



HAL
open science

Imprégnation magmatique de la lithosphère océanique: Etude microstructurale et géochimique des séries gabbroïques forées à la dorsale Médio-Atlantique

Marion Drouin

► **To cite this version:**

Marion Drouin. Imprégnation magmatique de la lithosphère océanique: Etude microstructurale et géochimique des séries gabbroïques forées à la dorsale Médio-Atlantique. Géochimie. Université Montpellier II - Sciences et Techniques du Languedoc, 2008. Français. NNT: . tel-00354807

HAL Id: tel-00354807

<https://theses.hal.science/tel-00354807>

Submitted on 21 Jan 2009

HAL is a multi-disciplinary open access archive for the deposit and dissemination of scientific research documents, whether they are published or not. The documents may come from teaching and research institutions in France or abroad, or from public or private research centers.

L'archive ouverte pluridisciplinaire **HAL**, est destinée au dépôt et à la diffusion de documents scientifiques de niveau recherche, publiés ou non, émanant des établissements d'enseignement et de recherche français ou étrangers, des laboratoires publics ou privés.

**UNIVERSITE MONTPELLIER II
SCIENCES ET TECHNIQUES DU LANGUEDOC**

T H E S E

pour obtenir le grade de

DOCTEUR DE L'UNIVERSITE MONTPELLIER II

*Discipline : Structure et Evolution de la Terre et des autres Planètes
École Doctorale : SIBAGHE (Systèmes Intégrés en Biologie, Agronomie, Géosciences,
Hydrosciences, Environnement)*

présentée et soutenue publiquement

par

Marion DROUIN

Le 26 Novembre 2008

**Imprégnation magmatique de la lithosphère océanique :
Étude microstructurale et géochimique de séries
gabbroïques forées à la dorsale Médio-Atlantique**

JURY

| | | |
|-------------------------|------------------------|------------------------|
| Mme Mathilde Cannat | DR, CNRS, IPGP | Rapporteur |
| M. Othmar Muntener | Professeur, Lausanne | Rapporteur |
| Mme Anne-Marie Boullier | DR, CNRS, UJF Grenoble | Examineur |
| M. Yves Lagabrielle | DR, CNRS, UM2 | Examineur |
| M. Benoît Ildefonse | DR, CNRS, UM2 | Directeur de Thèse |
| Mme Marguerite Godard | CR, CNRS, UM2 | Co-directrice de Thèse |

“Imagination is more important than knowledge”

Albert Einstein

Remerciements

Au terme de ces quatre années de thèse passées au laboratoire Géosciences Montpellier, le nombre de personnes que j'ai à remercier est conséquent ! Ces années ont été enrichissantes autant d'un point de vue intellectuel qu'humain mais aussi il faut le dire parfois très dures...Et oui la science ce n'est pas facile tous les jours, en tous cas j'aurai beaucoup appris !

Mes premiers remerciements vont à mon directeur de thèse Benoît Ildefonse sans qui je ne serais pas là en train d'écrire les dernières lignes de ce manuscrit ! Je le remercie avant tout pour m'avoir permis d'accéder à un de mes rêves qui était d'effectuer une campagne en mer. Enfin deux mois, c'est tout de même long mais bon, ce fut une expérience inoubliable... Je le remercie aussi pour sa grande disponibilité lors de la rédaction de ma thèse et les nombreux commentaires et réflexions dont il m'a fait part qui ont bien fait avancer le schmilblick !

Un grand merci à Margot, ma co-directrice de thèse, qui a toujours été là pour soutenir mon travail, pour passer derrière moi pour reprendre mes erreurs, hum ! Et me pousser et me motiver quand elle me sentait partir un peu loin de la science. Merci pour tout ce que tu m'as appris, pour nos discussions scientifiques et autres !

Je remercie mes rapporteurs Mathilde Cannat et Othmar Muntener d'avoir accepté de juger ce travail, ainsi que les autres membres du jury Anne-Marie Boullier et Yves Lagabrielle de participer à cette réflexion.

Je remercie toutes les personnes qui m'ont aidée dans l'acquisition de mes différentes données et participé à l'élaboration de ce travail : Christophe Névado et Doriane Delmas pour avoir réalisé mes centaines de lames minces très rapidement et surtout pour avoir toujours été disponible pour les dernières retouches avant le passage à l'EBS. Merci à Olivier Bruguier et Simone Pourtales pour leur aide dans l'utilisation de l'ICP-MS couplé à l'ablation laser et le traitement des données. D'ailleurs, ça doit être la seule machine qui n'a pas planté entre mes mains ! Merci aussi à Claude Merlet, pour la qualité des analyses à la microsonde, Pierre Azais pour son aide dans les manip de mesures électriques, Benoit, Alain Vauchez et surtout Andréa Tommasi que j'ai embêté cinquante mille fois pour l'EBS, je ne comprends vraiment pas pourquoi il y a tant de mauvaises ondes entre cette machine et moi ! Anne Delplanque pour les magnifiques dessins présents dans ce manuscrit et pour son aide précieuse lors de l'impression de mes posters toujours à la dernière minute avant de partir en conférence (encore de mauvaises ondes avec le matériel informatique...) et surtout sa bonne humeur permanente, Emmanuel Ball pour l'utilisation astucieuse d'illustrator et pour ces délicieuses confitures qui remontent le moral ! Jean-Marie Dautria pour ses coups de main en pétro.

Un grand merci à Françoise Boudier et Adolphe Nicolas de m'avoir fait découvrir l'ophiolite d'Oman (un autre de mes rêves !), ainsi que pour les innombrables discussions scientifiques ou non que l'on a pu avoir autour du feu dans les wadi d'Oman ou au labo. Françoise ton aide m'a été très précieuse !

Un immense merci à l'équipe enseignante qui m'a donné la chance d'enseigner la géologie au cours de ma thèse, travail qui me tient très à cœur, et plus particulièrement à Christine Lauer et Jean-Patrick Respaut qui m'ont inculqué l'art d'enseigner et surtout m'ont toujours soutenue dans les pires moments de la thèse....

Mes plus grands remerciements vont bien sûr à tous les thésards et autres personnes du laboratoire Géosciences Montpellier qui ont eu la dure tâche de me supporter au boulot pendant quatre ans et c'est pas peu dire: les anciens Andy, Marianne, Ingrid, Riccardo, Seb, Nicolas ; les éternelles : Véro, Vincent, Linda, Mickaël, Lydéric, Matthieu, Fabien, Florian, Bruno, Karen, Thomas, Titou, Pierre, Rémi, Lara, Marie, Magalie, Thomas et les autres pas ou plus thésards: Bernadette (ma deuxième maman), Marie-France, Nathalie, Céline, Marguerite, Eliane, Nicolas, Mickaël, Eric, Fred, Muriel (qui m'a supportée 2 mois sur le bateau !), Marie-Alix, Sylvie (merci pour les explications sur les processus de diffusion !), Florence, Ben. Une mention spéciale va à Andy et Vincent qui ont subi de l'intérieur toutes ces années, en tant que co-bureau, où les insultes fusaient contre l'ordinateur, mes sautes d'humeur mais aussi mes cris de joie (et oui parfois ça marche !), bref merci les gars, en même temps on s'est quand même bien marré ! Véro aussi, tu as toute ma gratitude car tu as toujours été là dans les bons et mauvais moments, nos grandes discussions philosophiques sur la vie vont me manquer ! Et aussi un grand merci à Akram parce que sans toi j'étais complètement paumée pour les mesures électriques ! Un remerciement spécial aussi à la dream team géophysique qui a bien voulu accepter une géochimiste au sein de leur groupe pour aller manger.

Merci enfin à tous mes amis pour leur soutien malgré la distance pour certains. Ne vous inquiétez plus, ça y est, je les ai finis mes études ! Merci à Josianne Lalanne pour ses petits plats et toutes ses bonnes intentions qui m'ont permis de décompresser et Jacques Lalanne car c'est l'une des rares personnes extérieures à comprendre ce que je fais en tant que cartographe marin ayant travaillé en 1972 sur la carte de la zone FAMOUS, rien que ça !!!

Un gros, gros merci à mes parents qui m'ont toujours soutenue et encouragée dans tous mes projets, et à ma famille toujours à fond derrière moi.

Aurélien, je te dédie ce travail, car c'est toi qui étais au cœur de toute cette tourmente, je ne te remercierai jamais assez...

Table des matières

| | |
|---|-----|
| <i>Introduction</i> | 1 |
| <i>Chapitre 1: Accrétion de la lithosphère océanique aux dorsales lentes, une revue</i> | 7 |
| <i>I. Structure de la lithosphère océanique et processus tectoniques</i> | 9 |
| 1. Morphologie axiale | 9 |
| 2. Structure lithologique, dénudation du manteau et failles de détachement | 13 |
| <i>II. Processus magmatiques dans la lithosphère océanique</i> | 31 |
| 1. Processus de cristallisation et d'accumulation | 33 |
| 2. Processus d'interaction magma/roche | 40 |
| 3. Comportement rhéologique et structural d'un cumulat partiellement cristallisé | 41 |
| 4. Implications des différents processus magmatiques sur la composition des MORBs | 46 |
| <i>Chapitre 2: Étude microstructurale et géochimique in-situ des troctolites riches en olivine du Puits IODP U1309D (dorsale Médio-Atlantique, 30°N)</i> | 51 |
| <i>I. Introduction</i> | 52 |
| 1. Le Massif Atlantis | 52 |
| 2. Les expéditions IODP 304 et 305 | 56 |
| 3. Caractéristiques pétrologiques et texturales des roches étudiées | 61 |
| <i>II. Preuve géochimique et pétrographique d'une imprégnation magmatique de la lithosphère océanique au Massif Atlantis, dorsale Médio-Atlantique (Puits IODP U1309D, 30°N)</i> | 71 |
| <i>Geochemical and petrographic evidence for magmatic impregnation in the oceanic lithosphere at Atlantis Massif, Mid-Atlantic Ridge (IODP Hole U1309D, 30°N), article accepté à Chemical Geology</i> | |
| <i>III. Caractérisation des variations chimiques observées au sein des minéraux des troctolites riches en olivine</i> | 128 |
| 1. Méthode d'analyse | 129 |
| 2. Résultats | 130 |
| 3. Discussion | 136 |

| | |
|--|------------|
| <i>IV. Microstructure d'une lithosphère océanique fortement imprégnée: étude des troctolites riches en olivine du Massif Atlantis (30°N, dorsale Médio-Atlantique, puits IODP U1309D)</i> | 143 |
|--|------------|

Microstructure of highly impregnated oceanic lithosphere: a study of the olivine-rich troctolites from the Atlantis Massif (Mid-Atlantic Ridge 30°N, IODP Hole U1309D), article en révision pour EPSL

| | |
|---|------------|
| <i>V. Revue des fabriques cristallographiques de l'olivine dans la zone de transition manteau/croûte de l'ophiolite d'Oman</i> | 179 |
|---|------------|

| | |
|------------------------------|------------|
| <i>VI. Conclusion</i> | 184 |
|------------------------------|------------|

| | |
|--|------------|
| <i>Chapitre 3: Étude géochimique in-situ des roches gabbroïques du Site ODP 1275 (Leg ODP 209, dorsale Médio-Atlantique 15°N)</i> | 188 |
|--|------------|

| | |
|-------------------------------|------------|
| <i>I. Introduction</i> | 189 |
|-------------------------------|------------|

| | |
|--|------------|
| <i>II. Description pétrologique des roches gabbroïques du site 1275</i> | 194 |
|--|------------|

| | |
|--------------------------------------|------------|
| <i>1. Les gabbros à oxyde</i> | 194 |
|--------------------------------------|------------|

| | |
|--|------------|
| <i>2. Les gabbros à olivine</i> | 195 |
|--|------------|

| | |
|----------------------------------|------------|
| <i>3. Les troctolites</i> | 197 |
|----------------------------------|------------|

| | |
|--|------------|
| <i>III. Analyses chimiques des minéraux des roches gabbroïques du site 1275</i> | 198 |
|--|------------|

| | |
|------------------------------|------------|
| <i>IV. Discussion</i> | 206 |
|------------------------------|------------|

| | |
|---------------------------|------------|
| <i>Conclusions</i> | 210 |
|---------------------------|------------|

| | |
|--------------------------|------------|
| <i>Références</i> | 216 |
|--------------------------|------------|

| | |
|-----------------------|------------|
| <i>Annexes</i> | 239 |
|-----------------------|------------|

Introduction

Les dorsales océaniques, longue chaîne volcanique sous-marine, parcourent l'ensemble des océans sur près de 55 000 km de long (Solomon, 1989). Limites divergentes entre deux plaques lithosphériques, elles sont le siège de l'accrétion et de l'expansion du plancher océanique. L'étude des dorsales océaniques nous renseigne sur les mouvements de convection et le mode de fusion du manteau terrestre, mais aussi sur les processus tectoniques et volcaniques permettant la genèse de la lithosphère océanique. La connaissance de ces structures est donc essentielle pour une compréhension globale de la dynamique de la Terre.

Les dorsales océaniques, du fait de leur inaccessibilité, ont été pendant longtemps les oubliées des Sciences de la Terre. Les campagnes océanographiques géologiques et géophysiques ainsi que, depuis 35 ans, les quelques campagnes de forage océanique ont permis de faire avancer l'état des connaissances sur ces montagnes sous-marines. Le forage, complémentaire des études géophysiques et géologiques en fond de mer, est le seul moyen pour échantillonner la lithosphère profonde et permettre ainsi de mieux cerner les processus de formation et d'évolution de la lithosphère océanique.

Les processus magmatiques et tectoniques au niveau des dorsales varient aussi bien spatialement, le long des segments d'accrétion, que temporellement, agissant sur la morphologie du plancher océanique et sur la structure lithologique de la lithosphère ainsi que sur sa composition chimique. Les dorsales lentes (< 50 mm/an de taux d'accrétion) représentent plus de la moitié des dorsales océaniques mondiales. Contrairement à la lithosphère litée des dorsales océaniques rapides (> 90 mm/an), la lithosphère océanique accrétée au niveau des dorsales lentes présente sur une partie de sa longueur une structure hétérogène, composée d'intrusions gabbroïques dans des péridotites plus ou moins serpentinisées (e.g., Lagabrielle & Cannat, 1990 ; Cannat, 1993, 1996; Canales et al., 2000).

La plupart des études réalisées sur les roches océaniques portent sur les deux termes extrêmes de la différenciation magmatique que sont les basaltes formant la croûte supérieure, et les péridotites abyssales, résidus de la fusion partielle à l'origine des liquides primaires. Depuis leur formation dans le manteau jusqu'à leur épanchement sur le plancher océanique, les liquides basaltiques sont le résultat de nombreux processus magmatiques successifs (extraction, migration, différenciation). Dès lors, ces études trouvent leurs limites dans le fait que ces différents processus sont compris uniquement entre les deux termes de la différenciation. De plus, dans les modèles géodynamiques (e.g., Hofmann, 1988), la composition de la croûte océanique est souvent assimilée à la composition des basaltes. Pourtant, ces roches représentent uniquement 10% de la croûte (Niu, 1997). A contrario, les roches gabbroïques, représentant l'étape intermédiaire entre les deux termes extrêmes de la

différenciation, sont peu étudiées du fait de leur rare échantillonnage. Pourtant, ces roches gabbroïques apparaissent comme des objets particulièrement appropriés pour contraindre les mécanismes de différenciation des MORB primitifs et les processus de réaction magma/roche, lors de la migration des liquides dans le manteau source puis dans la croûte.

Aux dorsales lentes, les roches gabbroïques et mantelliques sont mises à l'affleurement par l'intermédiaire de failles de détachement à faible pendage affectant tout ou une partie de la lithosphère. En perdurant dans le temps, certaines de ces failles créent des massifs qui se distinguent par leur forme caractéristique en dôme. Ces hauts topographiques nommés «core complexes» océaniques, ou encore mégamullions, sont des fenêtres tectoniques uniques sur la lithosphère profonde. L'étude des core complexes océaniques apparaît donc essentielle pour contraindre la lithologie et la structure de la lithosphère océanique aux dorsales lentes, et ainsi contraindre les processus tectoniques et magmatiques qui contrôlent la formation de cette lithosphère hétérogène.

Mon travail concerne l'étude de deux de ces core complexes océaniques forés le long de la dorsale lente Médio-Atlantique : le Massif Atlantis à 30°N (expéditions IODP 304-305) et le core complexe océanique situé à 15°45'N (Leg ODP 209). Le puits IODP U1309D (1415,5 mètres de profondeur) foré au cœur du Massif Atlantis, représente le second puits le plus profond foré sur une dorsale lente après le puits ODP 735B à la dorsale Sud-Ouest Indienne (Dick et al., 2000). Ces deux sites sont exceptionnels car, contrairement aux forages précédents (Leg ODP 153, Zone MARK à 23°N sur la dorsale Médio-Atlantique, puits ODP 735B sur la dorsale Sud-Ouest Indienne), ils ont permis, pour la première fois, d'échantillonner en abondance des roches riches en olivine dans une série de gabbros océaniques. Du fait de leur composition très primitive, les roches riches en olivine du puits IODP U1309D pourraient représenter le premier stade de différenciation d'un MORB. Alternativement, la texture poecilitique des roches riches en olivine n'est point sans rappeler celle des dunites et wehrlites de l'ophiolite d'Oman, initialement considérées comme des cumulats puis interprétées comme des péridotites mantelliques imprégnées par des liquides basaltiques (e.g., Nicolas and Prinzhofer, 1983; Boudier, 1991; Boudier and Nicolas, 1995). Les roches riches en olivine du puits IODP U1309D pourraient donc correspondre aussi à des roches mantelliques imprégnées dont la composition a été fortement modifiée par des réactions magma-roche (Kelemen et al., 2004). Dans les deux cas, la présence de ces « cumulats primitifs » ou « péridotites imprégnées » a une implication importante sur la compréhension des processus magmatiques et structuraux aux dorsales lentes puisqu'elles

impliquent des zones de transfert et d'accumulation magmatique importantes dans des régions supposées pauvres en magma.

Cette étude a donc pour objectif de déterminer la nature et l'origine de ces roches riches en olivine, la nature du magma à partir duquel elles ont cristallisé et de contraindre les interactions avec l'encaissant ainsi que les modifications microstructurales qui sont associées à ces processus magmatiques. De plus, le rôle du magmatisme dans le développement d'une lithosphère hétérogène est discuté, en s'appuyant sur l'analyse pétrologique et géochimique des roches gabbroïques composant les deux sites d'étude. Le travail présenté ici est pluridisciplinaire; sont étudiés les processus géochimiques ainsi que les microstructures des roches riches en olivine et des gabbros qui leur sont associés.

Le travail présenté dans ce mémoire porte essentiellement sur une série d'échantillons prélevés dans le puits IODP U1309D car la plupart des roches riches en olivine dans le bas du puits sont d'une fraîcheur exceptionnelle, unique dans l'histoire du forage de la croûte océanique (altération < 5%) permettant une analyse pétrologique, microstructurale et géochimique très détaillée. Au sommet du puits, par contre, les roches riches en olivine, nommée troctolites riches en olivine, présentent 30 à 90 % d'altération. Les roches gabbroïques (gabbros, gabbros à olivine, troctolites) voisines de ces roches riches en olivine ont aussi été intégrées à cette étude afin de définir le lien entre ces deux types de lithologies.

J'ai par ailleurs analysé une série d'échantillons de troctolites, gabbros à olivine et gabbros à oxyde provenant des puits ODP 1275B et 1275D forés au sein d'un core complexe océanique à 15°45'N sur la dorsale Médio-Atlantique. Les roches du Site ODP 1275 étant beaucoup plus altérées que celles du puits IODP U1309D, notamment les troctolites (80-90% d'altération), l'étude microstructurale de ces roches n'a pu être réalisée, de même seuls les gabbros à oxyde ont été analysés en éléments en trace.

Plusieurs méthodes analytiques ont été utilisées dans ce projet. Ces différentes méthodes sont décrites brièvement ci-dessous, ainsi que leur intérêt dans le cadre de mon travail (pour une description plus détaillée des techniques analytiques, se reporter à l'annexe A) :

⇒ *Mesure des éléments majeurs par Microsonde électronique (EPMA)* des différentes phases minérales (clinopyroxène, plagioclase, olivine, spinelle) constituant les troctolites riches en olivine et les roches gabbroïques qui leur sont associées dans le puits IODP U1309D, ainsi que les roches gabbroïques du Site ODP 1275. Ces analyses permettent de caractériser les minéraux, d'estimer les conditions

- ⇒ *Mesure in-situ des éléments en trace par ICP-MS et HR ICP-MS couplé à l'ablation laser* des minéraux (clinopyroxène, plagioclase, olivine) constituant les troctolites riches en olivine et les roches gabbroïques qui leur sont associées dans le puits IODP U1309D, ainsi que les gabbros à oxyde du Site ODP 1275. À partir de ces données en éléments en trace, nous pouvons déterminer et quantifier les processus pétrogénétiques à l'origine de ces différents types de roches. Les données en éléments en trace sont reportées dans le chapitre 2.
- ⇒ *Mesure quantitative de la déformation* grâce à une étude des *fabriques cristallographiques (méthode EBSD)* des minéraux constituant les troctolites riches en olivines et les roches gabbroïques qui leur sont associées dans le puits IODP U1309D. Ces données permettent de contraindre quantitativement le ou les mécanismes de déformation mis en jeu lors des différents stades structuraux de l'histoire de ces roches. Les données microstructurales sont reportées en annexe C.
- ⇒ *Mesures électriques* des troctolites riches en olivine et des roches gabbroïques du puits IODP U1309D afin de déterminer leur propriété électrique. Ces mesures ont pour but de caractériser la géométrie du réseau poreux de ces roches afin d'estimer leur contribution dans le système hydrothermal au niveau du Massif Atlantique. Du fait de la marginalité de cette étude dans le cadre de mon projet de thèse, les données électriques sont reportées en annexe D sous la forme d'une publication soumise à IODP.

La mise en œuvre de ces différentes techniques analytiques m'a permis d'obtenir de nombreux résultats qui sont discutés dans ce mémoire. Celui-ci s'articule en trois chapitres :

Le premier chapitre présente un état des lieux des connaissances sur l'accrétion de la lithosphère océanique aux dorsales lentes. Dans une première partie, je m'intéresse à la structure de la lithosphère ; les forages, les plongées en submersibles, les dragages et les mesures géophysiques ont permis de construire un modèle de lithosphère hétérogène différent du modèle classique de lithosphère litée. J'aborde aussi dans cette partie les processus tectoniques mis en jeu lors de l'accrétion des dorsales lentes. Dans une seconde partie, j'évoque les différents processus magmatiques s'enchaînant dans la lithosphère océanique au cours de la remontée des magmas vers la surface. Les conséquences de leur action dans la

lithosphère sur la composition des MORBs mais aussi sur la structure et la rhéologie des roches sont aussi exposées.

Le deuxième chapitre est consacré à l'étude des intervalles riches en olivine du Massif Atlantis. Ce chapitre débute par une description morphologique et géologique du Massif Atlantis et par un résumé des résultats obtenus lors des campagnes de forage IODP 304-305. L'étude pétro-texturale et géochimique des minéraux constituant les troctolites riches en olivines et les gabbros qui leur sont associées dans le puits IODP U1309D est présentée dans la seconde partie de ce chapitre. Cette étude nous permet de mettre en évidence de fortes interactions magma/roche à la base de la lithosphère dans la région du Massif Atlantis. Ce thème est discuté autour d'un article accepté à *Chemical Geology*. La troisième partie est consacrée à une étude préliminaire des variations chimiques observées au sein des minéraux des troctolites riches en olivine. Je m'intéresse, enfin dans la quatrième partie, à l'origine des troctolites riches en olivine du puits IODP U1309D, en mettant en relation les données pétrologiques et microstructurales acquises sur ces roches. Les résultats obtenus sont présentés et discutés dans un article en révision pour *EPSL*. Je clos ce chapitre en développant les différentes hypothèses avancées sur la nature des troctolites riches en olivines.

Le troisième chapitre concerne l'étude pétrologique et géochimique in-situ des roches gabbroïques composant le Site ODP 1275. Contrairement à l'étude précédente, je me focalise plus particulièrement sur les termes les plus évolués de cette série gabbroïque que sont les gabbros à oxyde. L'étude de ces roches révèle qu'aux dorsales lentes une certaine quantité de liquide basaltique cristallise sous forme de plutons interconnectés dans une lithosphère épaisse sans contrepartie volcanique.

Finalement, une synthèse des principales conclusions de ce mémoire est proposée. Les futures lignes de recherche sont aussi envisagées dans cette partie.

Chapitre 1

Accrétion de la lithosphère océanique aux dorsales lentes, une revue

L'étude des ophiolites contribue largement aux connaissances que l'on possède sur la nature et la structure de la lithosphère océanique (e.g., Nicolas, 1989). Elle vient compléter ce que nous révèlent la géologie et la géophysique marine, ainsi que les campagnes de forages réalisées dans le cadre des programmes DSDP, ODP puis IODP. Par exemple, la découverte récente d'une chambre magmatique au centre d'un segment de la dorsale lente Médio-Atlantique à 37°18'N (Singh et al., 2006) montre qu'une partie de ce segment, au budget magmatique plus élevé que les extrémités du même segment, a vraisemblablement un fonctionnement similaire à celui des dorsales rapides. De nombreuses questions subsistent néanmoins, concernant par exemple les modes de genèse des gabbros de la croûte océanique inférieure, tant aux dorsales rapides qu'aux dorsales lentes. Or ces roches qui sont le produit de la différenciation des liquides basaltiques peuvent nous apporter des informations importantes sur les processus magmatiques en contexte d'accrétion océanique comme la distribution des magmas, les réactions magma/roche agissant dans le manteau puis dans la croûte au cours de la remontée des magmas vers la surface, la composition chimique des magmas à l'origine des gabbros mais aussi des laves émises en surface. De même, les interactions entre magmatisme et tectonique, qui contrôlent en grande partie les mécanismes d'accrétion aux dorsales lentes, sont encore peu contraintes. Les travaux présentés dans ce manuscrit ont pour objectif, en premier lieu, de déterminer l'origine des troctolites riches en olivine du Massif Atlantis et leur relation avec les gabbros adjacents. Il s'agit donc d'établir quels processus magmatiques œuvrant au sein de la lithosphère profonde ont pu donner naissance à ce type de roche rarement échantillonné auparavant. L'objectif second de ce travail est de contraindre le rôle du magmatisme dans le développement d'une lithosphère hétérogène. Ce chapitre présente donc, en titre d'introduction à mon travail, un état des lieux des connaissances sur les processus tectoniques et magmatiques agissant au cours de l'accrétion de la lithosphère océanique aux dorsales lentes.

I. Structure de la lithosphère océanique et processus tectoniques

1. Morphologie axiale

Les dorsales océaniques présentent des morphologies et des structures très variables à l'échelle du globe. On distingue classiquement quatre grands types de dorsales selon leur taux d'expansion : ultra-lente ($\sim < 10\text{mm/an}$, par exemple la dorsale Sud-Ouest Indienne), lente (~ 10 à 50 mm/an , par exemple la dorsale Médio-Atlantique), intermédiaire ($\sim 50\text{mm}$ à 90 mm/an , par exemple la dorsale Juan de Fuca) et rapide (~ 90 à 180mm/an , par exemple la dorsale Est-Pacifique). Le taux d'accrétion des dorsales océaniques contrôle au premier ordre leur morphologie axiale. Ainsi, les dorsales rapides se distinguent par un bombement topographique axial; les dorsales intermédiaires présentent une morphologie plus variable avec un plateau axial peu élevé ou une vallée axiale; les dorsales lentes et ultra-lentes présentent un profond rift axial large d'une trentaine de kilomètres et d'une profondeur d'environ un kilomètre (Figure 1.1). Bien sûr, ces caractéristiques générales peuvent varier en fonction du budget magmatique local, et sont par exemple affectées par le voisinage d'un point chaud.

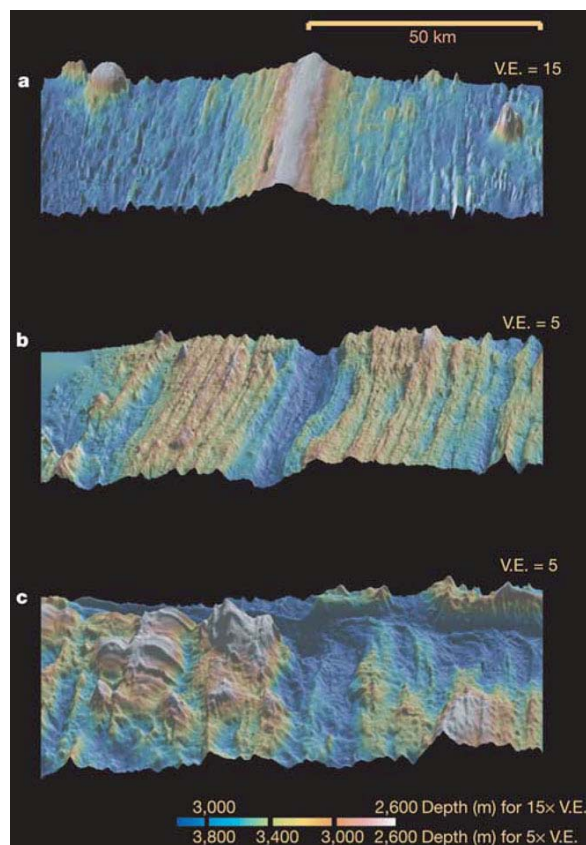


Figure 1.1 : Image bathymétrique présentant la morphologie axiale de dorsales à différents taux d'accrétion (Buck et al., 2005) : (a) rapide (dorsale Est-Pacifique 9°37'N), (b) intermédiaire (dorsale Sud-Est Indienne 115°E), (c) lente (dorsale Médio-Atlantique 23°25'N). L'abréviation V.E. correspond à l'exagération verticale.

Les dorsales, rapides ou lentes, se distinguent aussi par des variations morphologiques longitudinales traduisant une segmentation axiale de longueur d'onde variable décalant leur axe (e.g., Schouten et al., 1985 ; Macdonald et al., 1988). L'axe de la dorsale peut donc être décrit comme une suite de segments d'accrétion variant entre ~ dix et mille kilomètres de longueur et séparés par des discontinuités axiales. Dans le cas des dorsales lentes (Figure 1.2), ces discontinuités peuvent être de plusieurs sortes. On distingue principalement:

- Les discontinuités transformantes (segmentation de premier ordre). Ce sont des structures permanentes et stables dans le temps, parallèles à la direction d'expansion, qui découpent l'axe de la dorsale en segments de 200 à 1000 km de long.
- Les discontinuités non-transformantes (segmentation de second ordre). Ces structures, instables dans le temps avec une durée de vie de 3 à 9 Ma, délimitent des segments d'accrétion plus courts, qui varient entre 10 et 100 km de long (e.g., Sempéré et al., 1990, 1993 ; Fox et al., 1991 ; Grindley et al., 1992 ; Gente et al., 1995, Gràcia et al., 2000).

Enfin, des segmentations de troisième et quatrième ordres ont aussi été définies au niveau des dorsales lentes, comme des dorsales rapides, et correspondent à des variations morphologiques de plus faible ampleur (Gente et al., 1995).

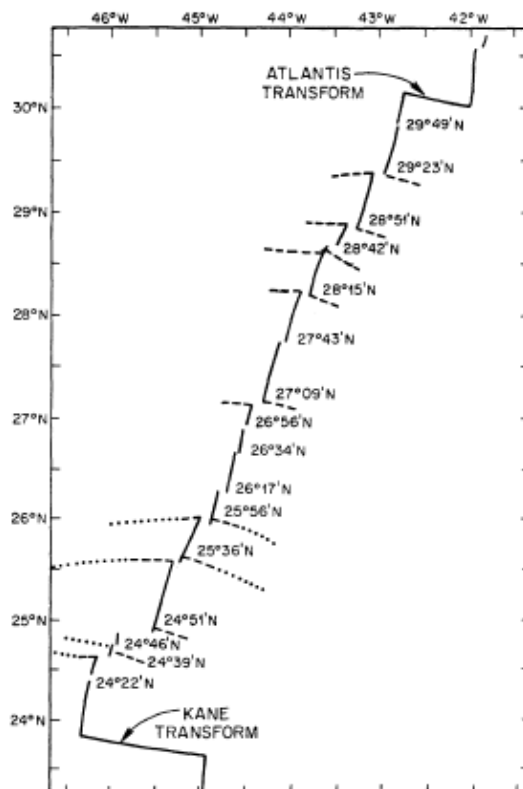


Figure 1.2 : Schéma de la segmentation de la zone axiale de la dorsale Médio-Atlantique entre la faille transformante Kane et la faille transformante Atlantis (segmentation de premier ordre). Les lignes épaisses indiquent les segments d'accrétion séparés par des discontinuités non-transformantes (segmentation de second ordre, indiquées par des tirets) (Sempéré et al., 1993).

Les observations effectuées le long de la dorsale Médio-Atlantique montrent que les caractéristiques morphologiques, géophysiques et pétrologiques varient communément du centre vers les extrémités des segments. Par exemple, les observations gravimétriques réalisées le long de plusieurs segments de la dorsale Médio-Atlantique (e.g., Kuo & Forsyth, 1988; Lin et al., 1990; Tolstoy et al., 1993; Detrick et al., 1995) montrent une augmentation systématique de l'anomalie de Bouguer réduite au manteau (MBA) du centre vers les extrémités des segments. Ces anomalies résiduelles de gravité ont été modélisées en supposant une croûte continue de densité et d'épaisseur constante. Ces variations le long des segments de la MBA sont donc interprétées comme une variation de l'épaisseur crustale (Tolstoy et al., 1993). Les anomalies gravimétriques négatives au centre des segments, nommées « Bull's eyes », reflètent une augmentation de l'épaisseur de la croûte de plus de 4

kilomètres depuis les extrémités vers le centre (Lin et al., 1990; Madge et al., 1997). La sismique réfraction montre aussi un épaississement crustal au centre des segments (Tolstoy et al., 1993; Canales et al., 2000; Hooft et al., 2000). Aux extrémités de segments, la croûte apparaît donc amincie (inférieure à 3 km), par opposition à une croûte épaisse, en moyenne de 6 km, au centre. De même, des laves enrichies ou moins appauvries sont présentes préférentiellement au centre des segments, ceci coïncidant avec la variation le long de l'axe de la MBA (Reynolds & Langmuir, 1997 ; Dosso et al., 1999 ; Niu et al., 2001). La focalisation de la remontée mantellique sous le centre des segments peut expliquer cette variation des caractères géophysiques, géochimiques et morphologiques entre centre et extrémités de segments (Lin et al., 1990, 1992). Ces différentes variations impliquent une variation importante de la structure thermique, lithologique et rhéologique de la lithosphère le long de l'axe.

L'architecture des dorsales lentes apparaît donc très variable. Elle varie avec le taux d'expansion, la géométrie de la dorsale, sa plus ou moins grande proximité avec un point chaud, la température potentielle du manteau (i.e., température adiabatique), la composition du manteau fertile et la production de magma. D'après Niu et al. (2001), la taille et la fertilité des hétérogénéités du manteau peuvent contrôler la création et l'évolution des segments des rides lentes. Ainsi, entre 35°N et 33°N sur la dorsale Médio-Atlantique, la température potentielle du manteau (estimée d'après la composition chimique des basaltes ou des magmas parents, e.g., Meyzen et al., 2003; Herzberg et al., 2007) et le taux d'expansion sont les mêmes, mais la fusion mantellique et la production crustale varient drastiquement. Le segment OH1, le plus au nord de cette zone, possède une croûte épaisse et des laves enrichies en éléments en trace incompatibles, alors que le segment OH3, au sud, possède une croûte fine et des laves appauvries en éléments en trace incompatibles. Une masse crustale importante révèle une plus grande quantité de liquide produite et extraite du manteau. Dès lors, la différence de compositions des basaltes entre ces deux segments serait contrôlée, d'après Niu et al. (2001), par la fusion de sources mantelliques hétérogènes de compositions distinctes. Les laves du segment OH1 reflètent une source hétérogène et enrichie en éléments en trace incompatibles, en alcalins et en eau, alors que les laves du segment OH3 reflètent une source hétérogène et appauvrie en éléments en trace incompatibles, en alcalins et en eau.

2. Structure lithologique, dénudation du manteau et failles de détachement

La structure lithologique de la croûte océanique a tout d'abord été appréhendée à partir de données sismiques, les profils de vitesses sismiques permettant d'accéder indirectement à la composition de la croûte océanique. Le premier modèle de structure de la croûte océanique, réalisé par Raitt (1963, dans Juteau & Maury, 1997) et basé sur le gradient des vitesses sismiques, correspond à un modèle en couches litées. Ce gradient, variant avec la profondeur, définit trois couches caractérisées par des vitesses sismiques qui leur sont propres. Ces couches sismiques ont plus tard été interprétées, en comparaison avec les ophiolites, comme formant trois unités lithologiques (Anonyme, 1972). La couche 1 ($V_p \sim < 3 \text{ km.s}^{-1}$) a ainsi été assimilée à une couche sédimentaire, la couche 2 ($V_p \sim 3\text{-}5 \text{ à } 6\text{-}7 \text{ km.s}^{-1}$) à des basaltes, et la couche 3 ($V_p \sim 6,7 \text{ à } 7,7 \text{ km.s}^{-1}$) à des gabbros. Ce modèle fut, plus en détail, décliné en modèle à sous-couches (sous-couches 2A, 2B, 2C, Houtz et Ewing, 1976; sous-couches 3A, 3B, Maynard, 1970 ; Sutton et al., 1971). La sous-couche 2A (vitesse des ondes P : $V_P \sim 3\text{-}4 \text{ km.s}^{-1}$) correspond à la couche la plus superficielle de la croûte océanique supérieure mise en place à l'axe de la dorsale. Elle est composée de basaltes avec une porosité importante et une densité anormalement faible, ce qui reflète une fracturation importante associée à l'altération hydrothermale. La sous-couche 2B est définie par des vitesses sismiques plus élevées ($V_P \sim 4,8\text{-}5,5 \text{ km.s}^{-1}$), et est interprétée comme étant des basaltes massifs ou métamorphisés. La sous-couche 2C ($V_P \sim 5,8\text{-}6,2 \text{ km.s}^{-1}$) décrit le complexe filonien. Enfin, les sous-couches 3A et 3B définissent la croûte océanique inférieure gabbroïque, avec tout d'abord les gabbros isotropes (3A ; $V_P \sim 6,8 \text{ km.s}^{-1}$) puis les gabbros lités, plus mafiques (3B ; $V_P \sim 7\text{-}7,7 \text{ km.s}^{-1}$).

En 1972, à partir principalement de l'étude des grandes ophiolites mondiales (Oman, Troodos) mais aussi de l'interprétation lithologique des profils sismiques de la lithosphère océanique, la « Penrose » Conférence impose le modèle d'une lithosphère océanique litée (Anonyme, 1972) dont la structure lithologique depuis le bas vers le haut (Figure 1.3) se décline comme suit:

- **Le complexe ultrabasique (manteau)** composé d'harzburgite, lherzolite et dunite en proportions variables.
- **Le complexe gabbroïque**, avec des roches à texture cumulative de type ultramafique à mafique ;
- **Le complexe filonien** formé par les filons mafiques verticaux.

- **Le complexe volcanique** composé de lave basaltique en coussin plus communément appelé « pillow lava ».

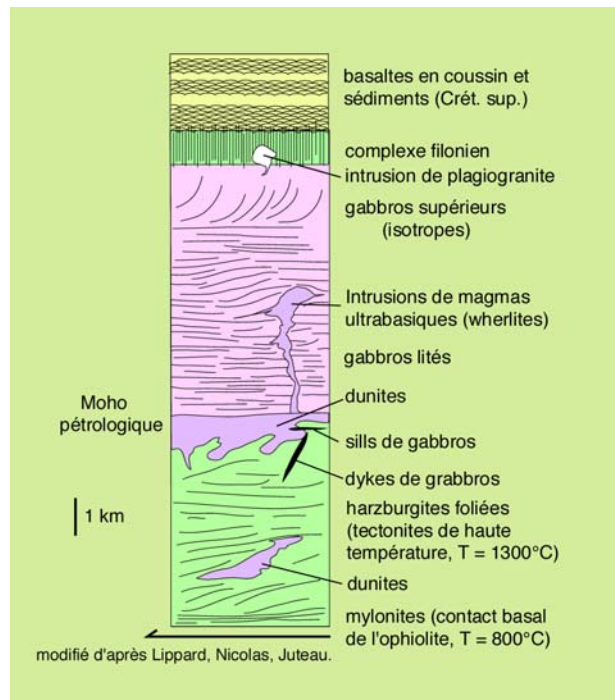


Figure 1.3 : Le modèle à 3 couches de la croûte océanique inspiré des observations effectuées dans l'ophiolite d'Oman (Boudier & Nicolas, 1985).

Pendant une vingtaine d'années, le modèle « ophiolitique » avec une croûte océanique inférieure composée de roches mafiques restera la référence. Toutefois, Hess (1962) et Dietz (1963) proposaient bien avant la Penrose Conférence, à partir de données sismiques, un modèle conceptuel dans lequel la croûte océanique inférieure était entièrement composée de roches mantelliques hydratées. Ces auteurs proposaient que le Moho, limite sismique entre la couche 3 et les vitesses supérieures correspondant au manteau, représentait la transition entre les péridotites serpentinisées et les péridotites du manteau sous-jacent.

Dès les années 60, les quelques données sismiques et de dragages existantes sur les dorsales lentes montrent la présence de roches ultramafiques à l'affleurement ou composant en partie la croûte océanique inférieure. Le modèle de croûte océanique litée semble alors mal s'appliquer aux dorsales lentes dans leur intégralité. Le long de l'axe de la dorsale Médio-Atlantique, des sables contenant une forte proportion de serpentine ont été dragués et carottés (Fox & Heezen, 1965; Figure 1.4). Des serpentinites ont été échantillonnées entre 29 et 31°N sur la dorsale Médio-Atlantique au niveau des zones de fracture Vema et Romanche (Van Andel & Bowin, 1968). La présence de ces serpentinites ainsi que la proportion importante de

basaltes échantillonnés, conduisent alors ces auteurs à considérer localement la croûte de la dorsale Médio-Atlantique comme une « pile » de basaltes reposant sur des serpentinites.

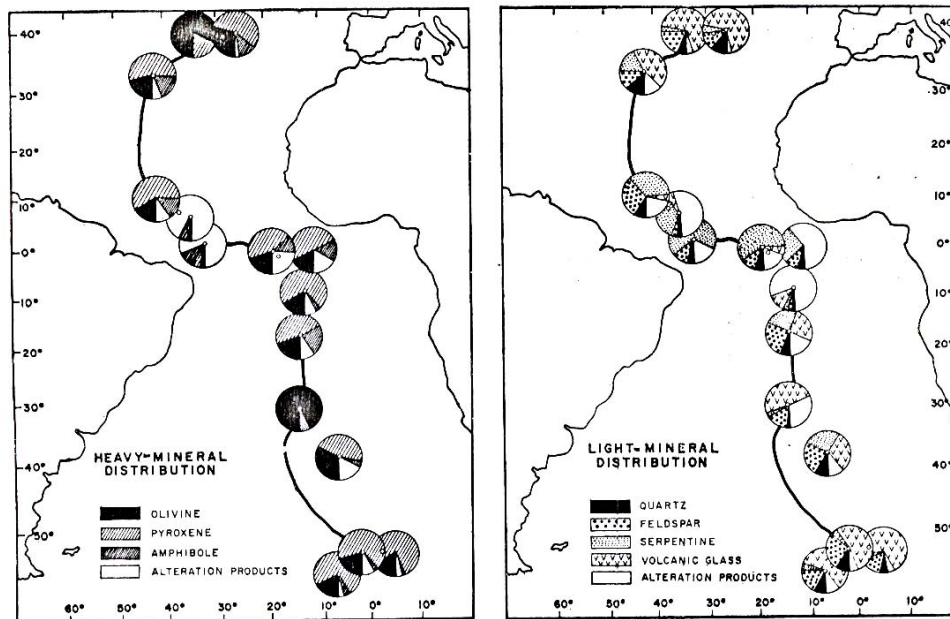


Figure 1.4 : Composition minérale des sables dragués et carottés le long de l'axe de la dorsale Médio-Atlantique (Fox et Heezen, 1965).

En 1971, Bonatti et al. montrent, grâce à des dragages effectués le long de la partie équatoriale de la dorsale Médio-Atlantique, l'abondance à l'affleurement de péridotites associées à des gabbros et des basaltes. Ces auteurs émettent alors l'hypothèse que les roches ultramafiques sont omniprésentes dans la croûte inférieure, sous l'Atlantique, aussi bien au niveau des zones de fracture que le long des segments axiaux. Ils proposent ainsi un modèle de lithosphère océanique applicable aussi bien à la dorsale Médio-Atlantique qu'à la dorsale Indienne, avec une zone du manteau supérieur composé de péridotites résiduelles de type « alpines » recoupées par du matériel basaltique qui remonte sous l'axe de la ride (Figure 1.5). Ce modèle fut l'un des premiers, avec celui de Van Andel et Bowin (1968), à prendre en compte l'abondance des roches mantelliques à faible profondeur, sous l'axe de la dorsale.

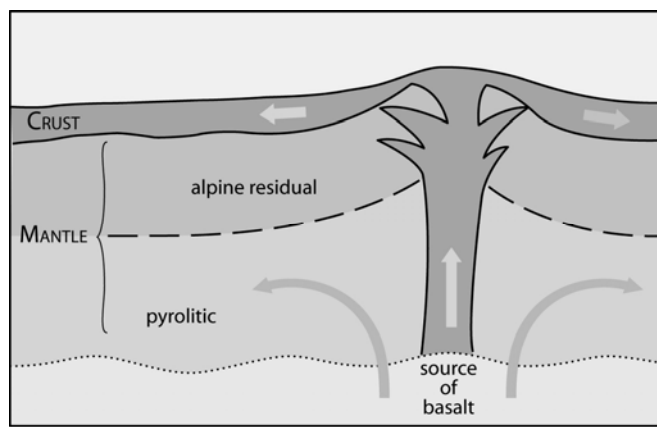


Figure 1.5 : Modèle de lithosphère océanique d'une dorsale lente, basé sur des dragages effectués dans la région équatoriale de la dorsale Médio-Atlantique. Ce modèle montre l'abondance de roches ultramafiques dans cette région. (Redessiné d'après Bonatti et al., 1971 par Lagabrielle, soumis)

Les roches mantelliques apparaissent donc comme un composant essentiel de la croûte océanique aux dorsales lentes. Toutefois, ces péridotites ont été majoritairement échantillonnées au niveau des principales zones de fractures, suggérant alors que seules ces structures sont capables de mettre à l'affleurement le manteau supérieur.

Dans les années 1980-90, les forages, les plongées en submersibles et les dragages effectués le long de la dorsale Médio-Atlantique en extrémité de segment mais en dehors des zones de fractures, montrent aussi la présence de roches mantelliques à l'affleurement directement sur le plancher océanique (e.g., Karson et al., 1987 ; Lagabrielle & Cannat, 1990 ; Juteau et al., 1990 ; Cannat, 1993, 1996 ; Cannat et al., 1995a). La croûte océanique basaltique apparaît alors très fine et localement discontinue le long de la dorsale Médio-Atlantique.

La lithosphère océanique accrétée aux dorsales lentes présente une structure hétérogène qui varie le long de l'axe (e.g., Dick et al., 1984 ; Karson et al., 1987 ; Dick, 1989 ; Lagabrielle & Cannat, 1990 ; Juteau et al., 1990 ; Cannat, 1993, 1996 ; Cannat et al., 1995a ; Lagabrielle et al., 1998 ; Canales et al., 2000 ; Carlson, 2001). L'activité volcanique est focalisée au centre des segments. Aux extrémités de ces mêmes segments, la lithosphère océanique est composée de corps gabbroïques intrusifs dans les roches ultramafiques, ces dernières étant, localement, directement recouvertes par des basaltes (Figures 1.6 et 1.7). La couche continue de gabbros, ainsi que le complexe filonien, sont souvent absents impliquant alors, pour les dorsales lentes, un modèle de croûte océanique localement très éloigné du modèle de croûte océanique litée de la « Penrose » conférence.

Grâce à des données de tomographie sismique, Madge et al. (2000) ont montré qu'au niveau de la vallée axiale de la dorsale Médio-Atlantique, il n'existait pas de chambre magmatique permanente et quasi-continue le long de l'axe comme aux dorsales rapides. Les profils de vitesses enregistrés évoquent plutôt une focalisation du flux magmatique dans la croûte inférieure puis une propagation sous forme de filons, verticalement et latéralement dans la croûte supérieure le long de l'axe pour aller alimenter des poches magmatiques individuelles et/ou les éruptions en surface. Néanmoins, les roches gabbroïques échantillonnées le long des dorsales lentes montrent une différenciation importante qui requiert la présence de chambres magmatiques, même si elles ne sont qu'éphémères et de petites tailles (Sinton & Detrick, 1992). Récemment, un réservoir magmatique, similaire à ceux présents sous la dorsale Est Pacifique, a été imagé sous la dorsale Médio-Atlantique au niveau du segment Lucky Strike (Singh et al., 2006). Cependant, cette chambre magmatique d'une longueur de 7 kilomètres n'est pas continue le long du segment contrairement aux chambres magmatiques des dorsales rapides et est focalisée au centre du segment.

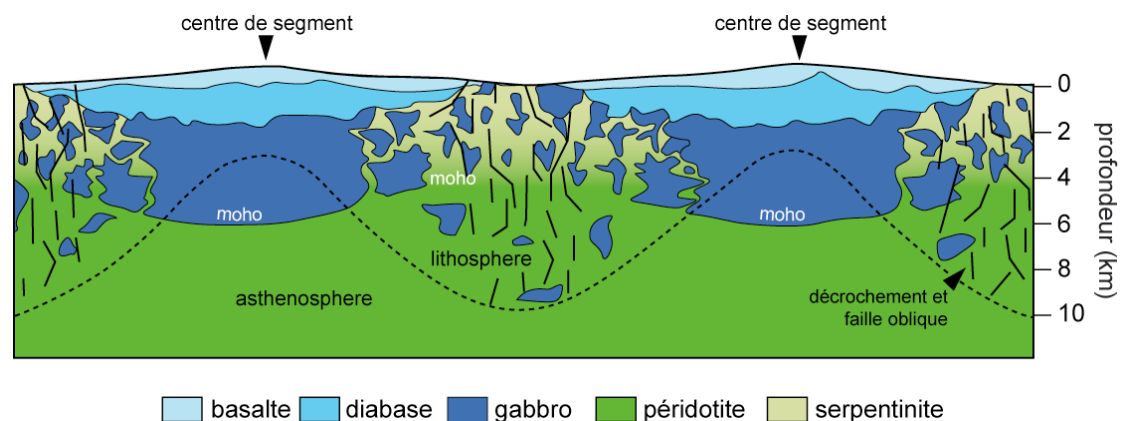


Figure 1.6 : Coupe géologique conceptuelle le long de l'axe d'une dorsale lente (Ildefonse et al., 2007a ; d'après Cannat et al., 1995a) basée sur la variation d'épaisseur de la croûte observée aux dorsales lentes à partir des données géophysiques (sismique et gravimétrie). La croûte magmatique est continue et supposée litée sous le centre des segments où l'approvisionnement magmatique est important ; et devient progressivement fine et composite aux extrémités des segments (région supposée moins riche en magma). Les roches ultramafiques sont à l'affleurement aux extrémités de segment, domaines avec des MBA positives. La ligne noire en pointillée marque la limite asthénosphère/lithosphère (isotherme 1100°C).

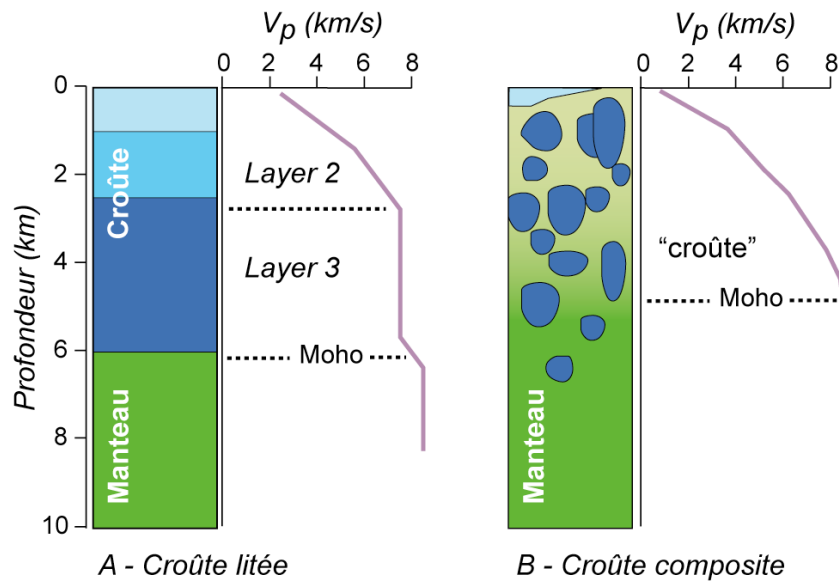


Figure 1.7 : Schéma présentant les deux types de croûte océanique associés à leurs profils types de vitesses sismiques (d'après Mével, 2003). (a) Croûte litée, de type « Penrose », constituée uniquement de roches magmatiques, (b) croûte composite comprenant des roches mantelliques plus ou moins serpentinisées. Bleu clair : basalte, bleu : complexe filonien, bleu foncé : gabbro, vert : péridotite.

L'accrétion de la croûte océanique aux dorsales lentes met en jeu deux processus principaux: l'accrétion magmatique et la dénudation tectonique des roches mantelliques et ignées profondes. L'absence de chambre magmatique continue traduit le fait que le magmatisme n'est globalement pas suffisant pour générer une croûte magmatique continue. Il a donc été proposé que l'accrétion procède par cycles volcano-tectoniques (magmatique/amagmatique) d'une durée de l'ordre de 2 Ma (e.g., Lagabrielle et al., 1998 ;Tucholke et al., 1998) qui modèlent ainsi de façon complexe le plancher océanique. Lors des phases d'accrétion "magmatique", une croûte continue se construit de manière similaire à celle des dorsales rapides, via une chambre magmatique comme celle imagée à Lucky strike (Singh et al., 2006). Lorsque l'accrétion "tectonique" domine, des failles de détachement dénudent la lithosphère profonde (e.g., Cannat et al., 1992; Cannat, 1993; Smith & Cann, 1993; Thatcher & Hill, 1995; Karson, 1999; Escartín et al., 2003; Buck et al., 2005; Ildefonse et al., 2007c; Tucholke et al., 2008). L'accrétion tectonique est généralement supposée intervenir principalement dans les régions au niveau des rides lentes où la lithosphère est plus froide et plus épaisse, c'est à dire majoritairement aux extrémités de segments, à proximité des failles transformantes (e.g., Dick et al., 1981; Cannat, 1993; Cannat et al., 1997; Tucholke & Lin, 1994; Cann et al., 1997; Lagabrielle et al., 1998; Tucholke et al., 1998; Ranero & Reston, 1999; Reston et al., 2002; Escartín et al., 2003; Fujiwara et al., 2003). Néanmoins, ceci résulte probablement d'un biais d'observation, les extrémités de

segment étant les zones majoritairement explorées lors des campagnes océanographiques. En réalité, lorsqu'on examine en détail une portion complète de dorsale lente ou ultra-lente, les failles de détachement apparaissent partout le long des segments et non pas exclusivement aux extrémités (Cannat et al., 2006 ; Smith et al., 2006, 2008 ; Escartín et al., 2008).

Dénudation du manteau : évolution des concepts

Entre 1920 et 1965, le concept de « mobilité du manteau », développé par Holmes (1929) puis par Wilson (1963) propose que l'accrétion océanique soit principalement accommodée par une tectonique extensive. Quelques années plus tard, pour expliquer la présence conjointe de péridotites serpentinisées, gabbros et basaltes à l'affleurement, Van Andel et Bowin (1968) ont fait appel au fonctionnement, à l'axe de la dorsale, d'une série de failles normales dont le pendage devient plus faible en surface (Figure 1.8). Ces auteurs énoncent pour la première fois le concept de faille de détachement océanique responsable de la dénudation des roches profondes de la lithosphère.

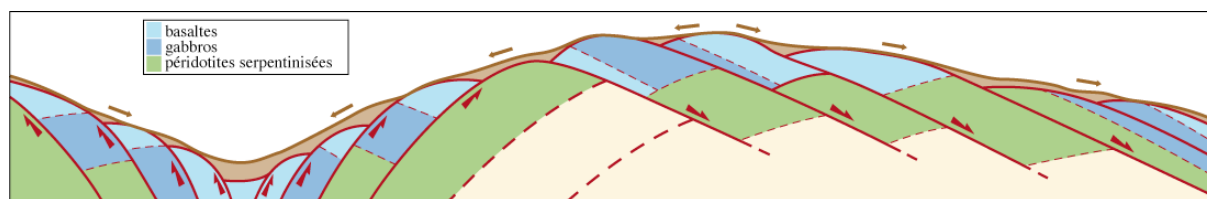


Figure 1.8 : Schéma montrant la mise à l'affleurement de péridotites plus ou moins serpentinisées par l'intermédiaire de grandes failles normales (Cortesogno et al., 1978 (redessiné) d'après Van Andel et Bowin, 1968).

Par la suite, les modèles de dénudation tectonique du manteau aux dorsales lentes se sont largement inspirés des modèles d'exhumation du manteau supérieur sous les marges passives comme la marge occidentale de la Galice. Dans la littérature, deux grands modèles d'exhumation du manteau au pied des marges passives s'opposent :

- **Le modèle dissymétrique** : La dénudation du manteau est le résultat d'un grand détachement crustale, voire lithosphérique, impliquant l'étirement non homogène de la lithosphère. D'après Wernicke (1981, 1985), l'amincissement de la croûte continentale et de la lithosphère peut s'expliquer par le jeu d'une faille normale faiblement inclinée (15°) affectant l'intégralité de la lithosphère (Figure 1.9). Boillot et al. (1986) reprennent le modèle de Wernicke pour expliquer la mise en place de péridotites au pied de la marge occidentale de la Galice: un grand détachement à l'échelle

lithosphérique, enraciné dans le manteau, permet la mise à l'affleurement du manteau supérieur à la fin du rifting de la marge. La formation des marges passives dans un tel modèle s'effectue en plusieurs stades. Dans un premier temps, la lithosphère est étirée, puis cisailée ; la déformation se localise alors sur un seul accident. Enfin, la progression de l'amincissement crustal conduit à la mise à l'affleurement du manteau.

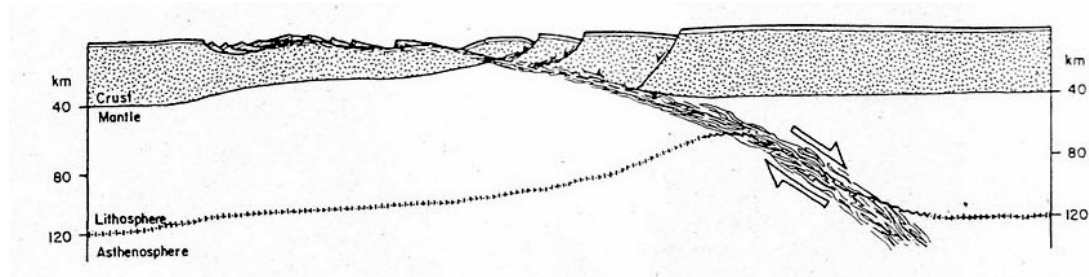


Figure 1.9: Modèle de cisaillement normal de la lithosphère (Boillot et al., 1986 d'après Wernicke, 1985).

- **Le modèle symétrique :** L'exhumation du manteau est le résultat d'un cisaillement simple conjugué de la lithosphère (e.g., Brun et Beslier, 1996; Figure 1.10). Ces auteurs montrent que mécaniquement une grande faille de détachement traversant toute la lithosphère n'est pas nécessaire pour exhumer le manteau. Le boudinage de la croûte fragile et du manteau fragile provoque l'apparition de zones de cisaillement conjuguées qui ont valeur de décollements (cisaillement à l'intérieur d'une couche incompetent). L'amincissement de la lithosphère induit une remontée asthénosphérique et l'exhumation du manteau par rupture du manteau fragile.

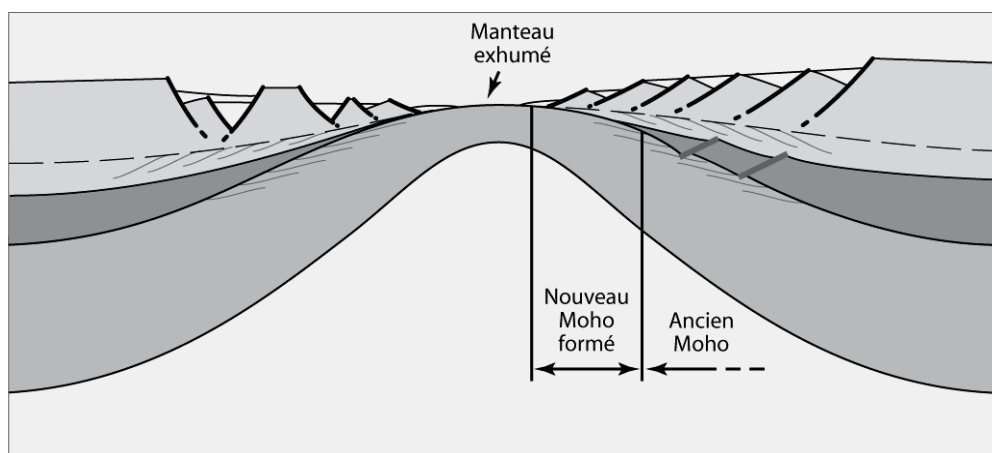


Figure 1.10 : Schéma, inspiré de modèles analogiques, illustrant la mise à l'affleurement du manteau à la limite continent-océan à la fin de la formation d'une marge passive (Redessiné d'après Brun et Beslier, 1996).

Dans les ophiolites des Alpes Occidentales, la présence de roches ultramafiques et gabbroïques à l’affleurement directement sous les basaltes a été expliquée à partir du modèle de cisaillement normal de la lithosphère de Wernicke (Lemoine, 1987; Figure 1.11).

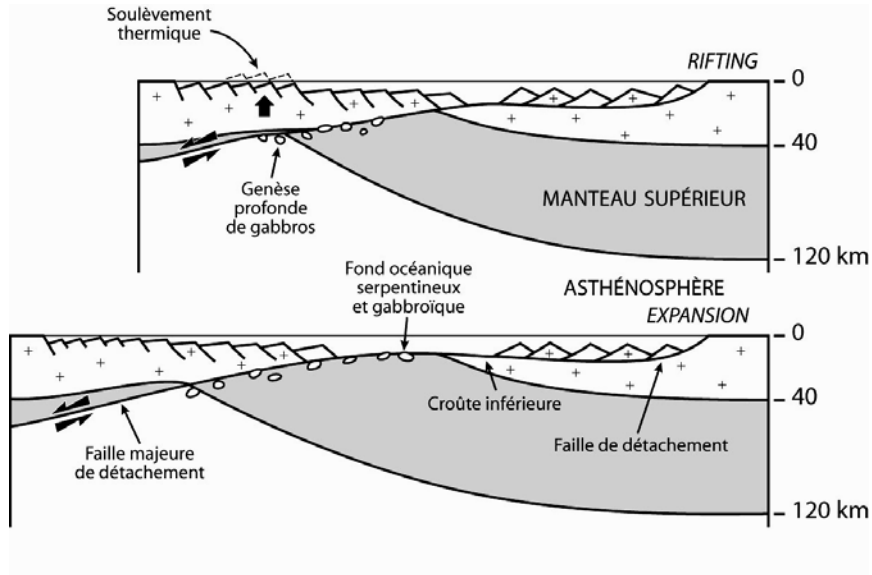


Figure 1.11 : Modèle de formation du fond océanique ultramafique de l’océan Piedmont-Ligurien par dénudation du manteau le long d’une faille de détachement majeure (Redessiné d’après Lemoine et al., 1987 par Lagabrielle, soumis).

De même, pour expliquer le mode d’extension asymétrique de la lithosphère océanique au niveau de la zone MARK (dorsale Médio-Atlantique, 23°N), Karson (1990) développe un modèle d’accrétion océanique aux dorsales lentes relativement similaire au modèle de Lemoine (1987) bien que n’étant pas à la même échelle spatiale (Figure 1.12).

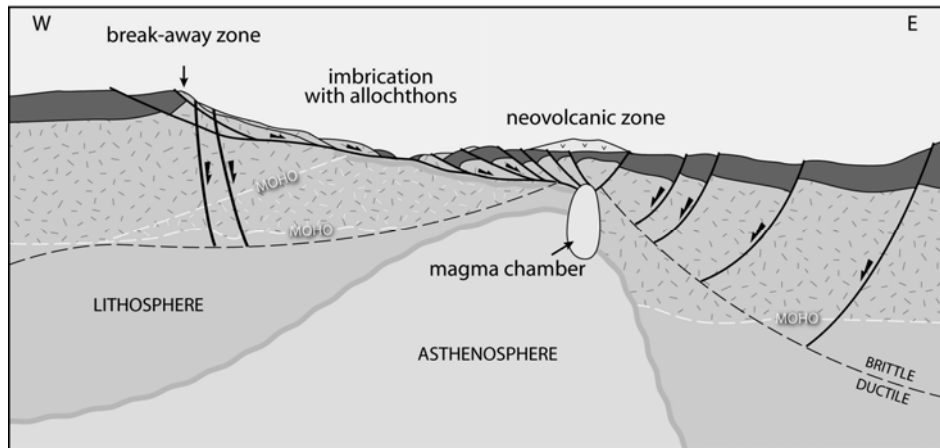


Figure 1.12 : Schéma illustrant une extension asymétrique au niveau de la Zone MARK (23°N) à la dorsale Médio-Atlantique (Redessiné d'après Karson, 1990 par Lagabrielle, soumis). La faille de détachement traverse la lithosphère et s'enracine dans l'asthénosphère. Gris foncé : laves basaltiques en coussin et complexe filonien, tirets noirs sur fond gris : roches gabbroïques, tirets noirs et blancs sur fond gris : serpentinites, gris clair : manteau; Les traits en tirets blancs indiquent la position du Moho sismique à différents stades de l'extension.

Le passage des grandes failles de détachement permettant l'ouverture de l'océan aux failles de détachement actives à l'axe de la dorsale traduit un changement d'échelles spatiales et temporelles. Les failles de détachement à l'axe fonctionnent pendant une durée plus limitée, typiquement 1 à 3 millions d'années (Tucholke et al., 1998), et génèrent une asymétrie du plancher océanique sur une distance parallèle à l'expansion océanique comprise entre 10 et 100 km, généralement de l'ordre de 10 à 20 km. Ces failles si elles perdurent dans le temps (i.e. > 1Ma, Smith et al., 2006, 2008), créent un haut topographique en forme de dôme. Ces dômes sont appelés "mégamullions" ou core complexes océaniques (CCO) dans la littérature en référence aux « core complexes » métamorphiques continentaux (e.g., Davis, 1983 ; Davis & Lister, 1988; John & Foster, 1993). Ils se caractérisent par leur forme en dôme et, en général, par une surface cannelée (« corrugated ») parallèlement à la direction d'accrétion de la lithosphère océanique (e.g., Karson, 1990, 1999 ; Dick et al., 1991, 2000 ; Tucholke & Lin, 1994 ; Cann et al., 1997 ; Tucholke et al., 1997, 1998 ; Blackman et al., 1998 ; 2002 ; Ohara et al., 2001, 2007; MacLeod et al., 2002; Escartín et al., 2003; Cannat et al., 2006; Smith et al., 2006, 2008; Tucholke et al., 2008). Les CCO se distinguent du modèle de faille de détachement à faible pendage de Wernicke (1985) par un plongement plus raide en profondeur (>45°) qui s'atténue progressivement en surface (<30°) pour devenir subhorizontal, en relation avec une rotation du mur de la faille (Buck, 1988 ; Buck, 1991 ; Tucholke et al, 1997 ; Lavier et al., 1999 ; Escartín et al., 2003 ; Smith et al., 2008 ; Figure

1.13). Ce fort pendage en profondeur des failles de détachement océaniques a été visualisé par tomographie sismique au niveau du site hydrothermal TAG à 26°N sur la dorsale Médio-Atlantique (DeMartin et al., 2007, Canales et al., 2007 ; Figure 1.14).

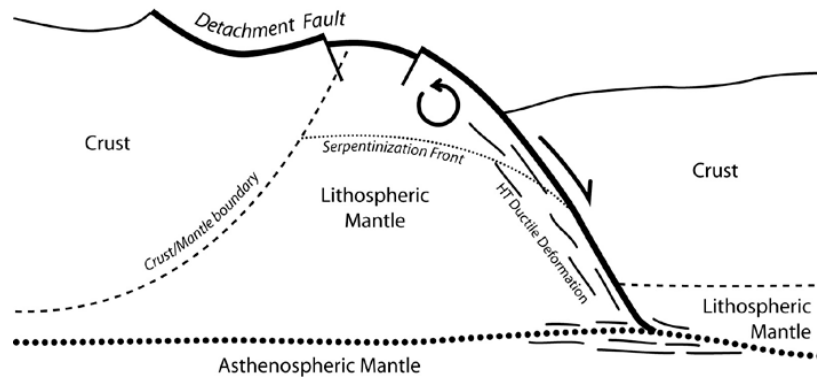


Figure 1.13 : Modèle d'évolution d'un core complexe océanique par rotation (roll-over) du mur de la faille (IODP Expeditions 304 and 305 Scientists, 2005 ; d'après Tucholke et al, 1997, et Escartín et al., 2003).

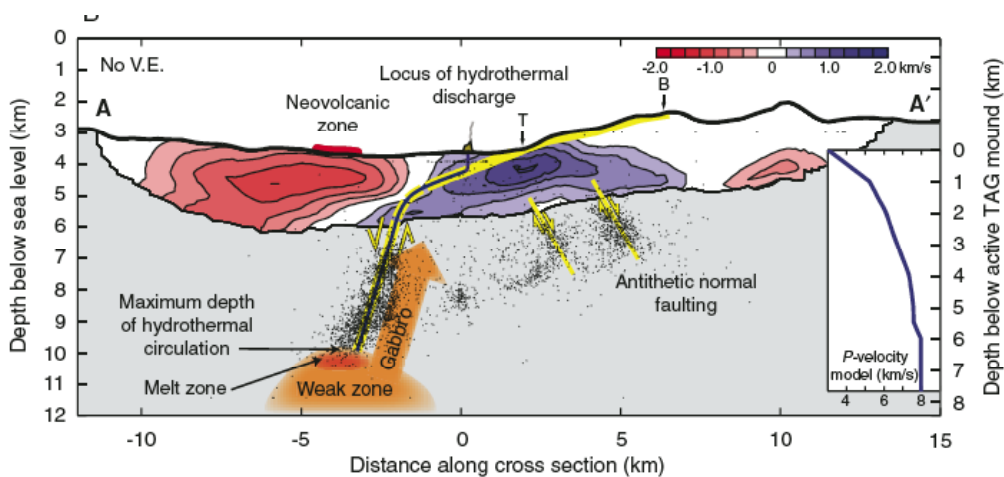


Figure 1.14 : Section à travers la vallée axiale du segment TAG à 26°N sur la dorsale Médio-Atlantique montrant le modèle tomographique calculé à partir des vitesses des ondes P. La faille de détachement, marquée en jaune, montre une surface en dôme, et pénètre à des profondeurs supérieures à 7 km sous le plancher océanique avec un pendage d'environ 70°. Le modèle tomographique des vitesses sismiques effectué à travers l'axe de la dorsale montre que le mur de la faille a subi une rotation importante mettant à l'affleurement les roches de la croûte inférieure le long d'une interface avec un pendage d'environ 20° (DeMartin et al., 2007). Les points noirs indiquent la localisation des hypocentres des micro-tremblements de terre liés à l'activité du détachement océanique. L'échelle de couleur allant du rouge au bleu correspond aux anomalies de vitesses sismiques par rapport à un modèle théorique de croûte océanique.

La plupart des CCO ont été observés au niveau des extrémités de segments, cependant nombre d'exemples dans l'Atlantique équatorial (~15°N) ainsi qu'à la dorsale Sud-Ouest indienne, ultra-lente, montrent que ces structures peuvent aussi se situer loin des extrémités et donc se rencontrer n'importe où le long de la dorsale (Escartín & Cannat, 1999; Cannat et al., 2006 ; Smith et al., 2006, 2008). De même, dans le bassin de Parece Vela (Pacifique Nord-Ouest), qui correspond à une dorsale intermédiaire éteinte, le mégamullion Godzilla, le plus grand CCO connu (~ 125 km de long sur ~ 55 km de large), occupe toute la longueur d'un segment (Ohara et al., 2001).

Plusieurs modèles de détachement océanique ont été proposés à partir des observations géologiques de différents CCO le long de la dorsale Médio-Atlantique (notamment le Massif Atlantis à 30°N et le massif à 15°45'N) et le long de la dorsale Sud-Ouest Indienne (Atlantis Bank à 32,72°S). On peut les regrouper en trois catégories (Escartín et al., 2003):

Modèle d'extension amagmatique

Ce modèle se base sur l'hypothèse selon laquelle une réduction de l'apport magmatique est un facteur critique pour l'initiation et la longévité de fonctionnement des failles de détachement (e.g., Karson, 1990 ; Tucholke et Lin, 1994 ; Tucholke et al., 1997, 1998). Les failles de détachements se développent pendant les périodes d'accrétion amagmatique. L'activité de ces failles s'arrête quand l'accrétion magmatique de la croûte océanique reprend. Ce modèle de faille qui s'enracine à la limite asthénosphère/lithosphère, développé par Tucholke et al. (1997, 1998, 2001), est très proche de certains modèles de core complexes continentaux (Figure 1.15). Il a été développé à partir des caractéristiques morphologiques et géologiques de différents CCO le long de la dorsale Médio-Atlantique (par exemple le Dôme de Dante à 26°40'N), notamment de la présence à l'affleurement de serpentinites. Ce modèle prévoit, du fait de l'enracinement profond de la faille, la présence d'une épaisse zone de déformation ductile associée à la faille, initiée à haute température, et la mise à l'affleurement du manteau lithosphérique.

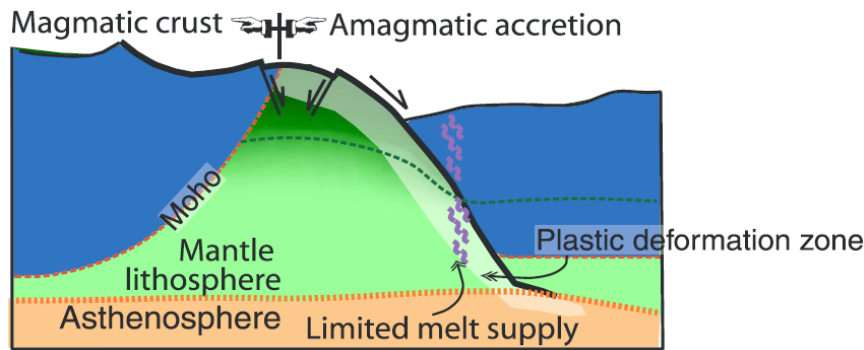


Figure 1.15 : Schéma illustrant le modèle d'extension amagmatique. La faille de détachement s'enracine à la base de la lithosphère. L'extension amagmatique a pour résultat la formation d'un détachement qui expose la croûte profonde et le manteau lithosphérique. (Escartín et al., 2003, d'après Tucholke et al., 1998)

Modèle d'extension tectonique en présence de magma

Dans ce modèle, la faille de détachement s'enracine dans une zone relativement riche en magma proche de la transition gabbro-dyke dans la croûte inférieure (Figure 1.16). Ce modèle, développé par Dick et al. (1991, 2000), est basé sur les observations géologiques du CCO Atlantis Bank (Dorsale Sud Ouest Indienne à 32,72°S). La présence en grande quantité de gabbros, la moindre abondance des serpentinites le long du plan de faille, et la présence d'une zone de cisaillement épaisse (>150m) en haut du puits, dont les microstructures témoignent d'une déformation démarrée à très haute température, en présence de liquide magmatique, montre que la faille de détachement a dans cet exemple largement interagi avec le système magmatique. Ce modèle propose que les grands détachements océaniques puissent s'enraciner au niveau d'un corps gabbroïque en cours de cristallisation. Une des faiblesses de ce modèle est l'absence d'hypothèse concernant le(s) facteur(s) permettant le déclenchement et la longévité de la faille de détachement.

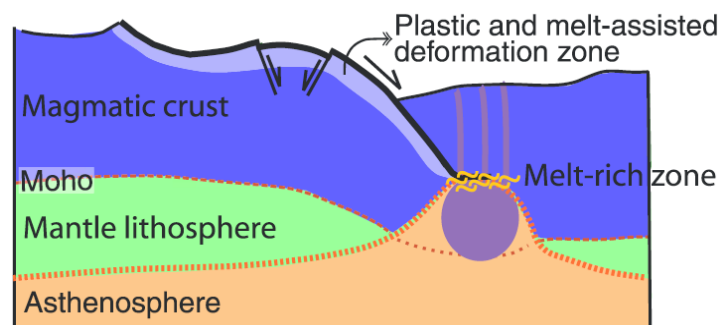


Figure 1.16 : Schéma illustrant le modèle d'extension tectonique en présence de magma. La faille de détachement s'enracine au niveau, ou proche d'une zone riche en magma à l'axe de la dorsale. Une croûte magmatique continue est créée pendant la phase tectonique de détachement et expose principalement des roches gabbroïques déformées à l'état magmatique, puis plastiquement à l'état solide. (Escartín et al., 2003, d'après Dick et al., 1991, 2000)

Modèle de faille de détachement enracinée à faible profondeur

Ce modèle (MacLeod et al., 2002; Escartín et al., 2003), est basé sur les observations géologiques du CCO à 15°45'N à l'ouest de la dorsale Médio-Atlantique (Figure 1.17). Les roches échantillonnées le long de la faille exposée sont déformées dans des conditions de température faible à modérée (essentiellement faciès schiste vert), impliquant une activité de la faille de détachement dans la lithosphère superficielle et froide. De plus, les péridotites sont altérées en talc et trémolite exclusivement le long de la faille de détachement, impliquant un drainage des fluides hydrothermaux le long de celle-ci. La circulation hydrothermale est globalement contrôlée par la structure, et les fluides circulent majoritairement le long des failles de détachement dans les cores complexes (McCaig et al., 2007). L'encaissant quant à lui présente une altération pénétrative. La minéralogie et la chimie des phases présentes le long du plan de faille sont complexes. L'enrichissement en silice et en calcium du protolithe, et donc la formation de talc et de trémolite, montre que les fluides hydrothermaux ont probablement interagi avec les péridotites et les gabbros à plus grande profondeur avant de remonter le long du plan de faille. Les roches se trouvant sous la faille de détachement sont peu ou pas déformées, ce qui montre que la déformation était localisée le long de la faille de détachement *sensu-stricto*. Ce modèle prend en compte le fait que la croûte est ici composite, et qu'il existe dans ce type de croûte la présence d'un front d'altération à relativement faible profondeur (<7km) qui représente une transition entre une lithosphère inférieure non altérée (rhéologiquement forte) et une lithosphère supérieure altérée (rhéologiquement faible). Dans la lithosphère fragile, ce front d'altération forme une limite rhéologique au niveau de laquelle les failles de détachement sont susceptibles de s'enraciner. La présence en abondance de

diabases déformés et non-déformés le long de la surface de la faille de détachement indique que celle-ci était active au cours du magmatisme (MacLeod et al., 2002 ; Escartín et al., 2003).

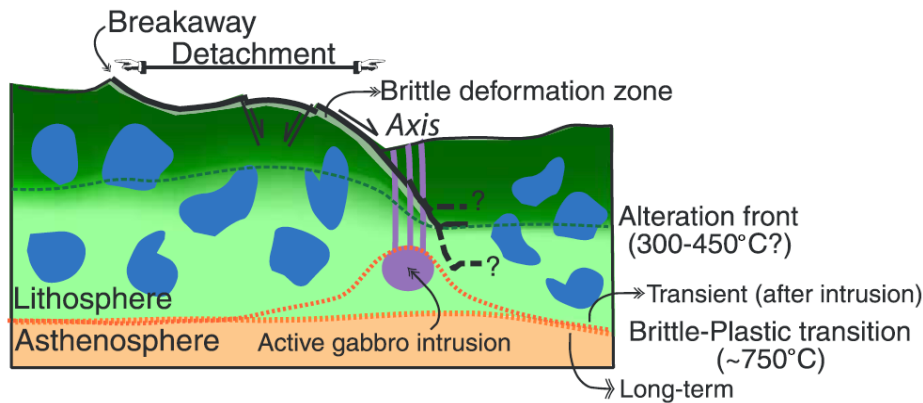


Figure 1.17 : Schéma illustrant le modèle de détachement s'enracinant à faible profondeur. Le front d'altération correspond à une limite rhéologique entre la lithosphère altérée (rhéologiquement faible) et non altérée (rhéologiquement forte) et permet l'enracinement du détachement (Escartín et al., 2003).

Dans la région entre les zones de fracture 15°20'N et Marathon à la dorsale Médio-Atlantique, quarante-cinq CCO, dispersés le long de deux segments d'accrétion (segments 13°N et 15°N), ont été identifiés (Smith et al., 2006, 2008). Cette multitude de core complexes conduit Smith et al. (2008) à proposer deux modèles distincts de formation, avec des implications différentes sur le mode d'accrétion de la lithosphère océanique. Dans un premier modèle, une faille de détachement majeure est continue le long de tout l'axe du segment (Figure 1.18). Dans ce cas, l'accrétion lithosphérique sur l'intégralité du segment est dominée par la remontée de gabbros et de péridotites mantelliques. Dans un deuxième modèle, une série de failles de détachements discontinues le long de l'axe forment les CCO qui sont séparés par des dépressions (Figure 1.18). L'accrétion lithosphérique par le biais des failles de détachement est alors, à l'échelle du segment, moins importante comparée à l'accrétion magmatique. La formation de nombreux CCO dans cette région est probablement liée à une production limitée de magma, ou tout au moins par une forte variation de celle-ci le long de l'axe. En effet, tout le long des segments 13°N et 15°N de fortes anomalies gravimétriques de Bouguer positives sont observées indiquant une croûte plus fine d'environ un kilomètre par rapport au segment volcanique 14°N formé de collines abyssales de chaque côté de la vallée axiale.

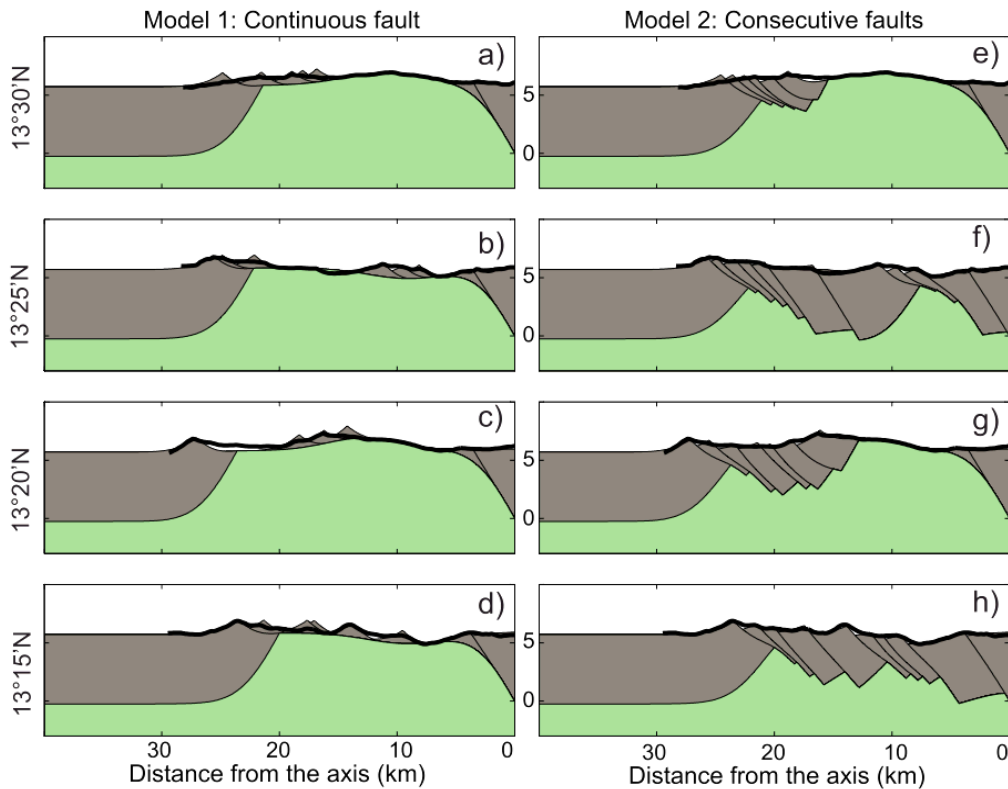


Figure 1.18 : Coupes sériées réparties du Nord au Sud le long de l'axe du segment 13°N sur la dorsale Médio-Atlantique présentant deux modèles possibles de formation des failles de détachement (Smith et al., 2008). Modèle 1 (a à d) : une seule faille de détachement est continue le long de l'axe sur tout le segment. Les nouvelles failles normales qui se forment à l'axe s'enracinent dans le détachement principal. Dans ce cas-là, l'accrétion de la lithosphère océanique est dominée par la mise à l'affleurement des roches mafiques et ultramafiques. Modèle 2 (e à h) : Succession de failles de détachement qui sont discontinues le long de l'axe. La lithosphère océanique est principalement accrétée par l'intermédiaire des processus magmatiques. Gris : croûte précédant la formation des failles; Vert : matériel profond remonté par glissement le long de la faille. La ligne noire épaisse représente la topographie du planché océanique.

Nous avons vu que le fonctionnement des détachements océaniques peut être associé à une activité magmatique. Le modèle, opposant phases tectonique et magmatique, semble donc inapproprié, tout au moins trop simpliste. Le développement d'une faille de détachement n'est donc pas nécessairement associé à une interruption de l'activité magmatique. Les modèles numériques, développés par Buck (1988), Buck et al. (2005) et Tucholke et al. (2008), montrent que les failles de détachement se forment seulement lorsque 30 à 50 % de l'expansion totale est accommodée par l'accrétion dite magmatique. Un budget magmatique trop faible, au même titre qu'un budget élevé, ne favorise pas la formation des failles de détachement. Ce résultat est confirmé par un examen systématique de la profondeur axiale de

la dorsale lorsque des CCO sont présents (Tucholke et al., 2008). Au premier ordre, la profondeur de l'axe peut être corrélée au volume de l'apport magmatique. Si la profondeur axiale est faible, inférieure à 3700m (i.e., l'apport magmatique est important), les CCO ne se développent pas. De même, lorsque la profondeur axiale est importante (i.e., l'apport magmatique est très faible) les CCO ne sont pas ou très peu présents. Les CCO ne témoignent donc pas du budget magmatique le plus réduit aux dorsales, mais représentent plutôt un stade intermédiaire entre l'accrétion volcanique et l'accrétion la plus pauvre en magma. Cette dernière est reliée par Cannat et al. (2006), sur la dorsale sud-ouest indienne, à un type de plancher océanique différent, moins rugueux, avec de larges rides parallèles à l'axe de la dorsale (« smooth seafloor »), systématiquement associé à la présence de serpentinites à l'axe, et correspondant donc à un cas extrême de dénudation du manteau. Ce type de plancher océanique est le siège d'anomalies gravimétriques de Bouguer positives, impliquant une très faible épaisseur de croûte (<3km). Ces domaines sont interprétés comme l'expression d'une succession de plans de failles normales à pendage variable (Figure 1.19).

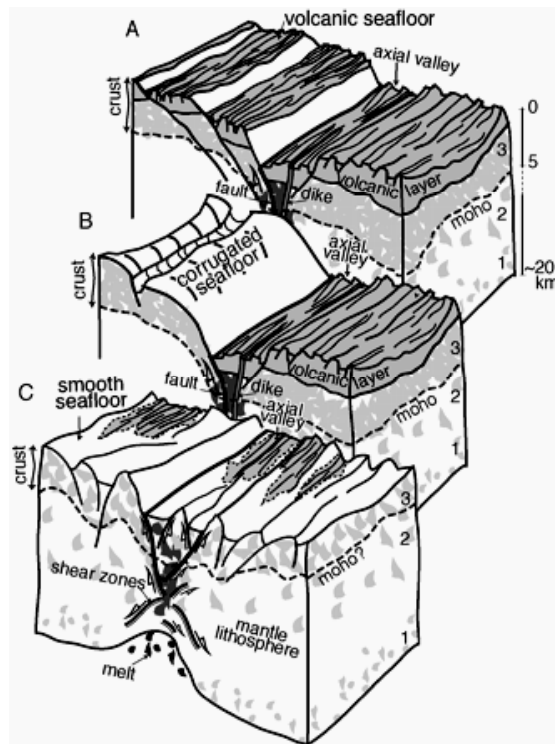


Figure 1.19 : Schéma présentant trois modes d'accrétion de la lithosphère dans les régions au budget magmatique réduit (Cannat et al., 2006). Les Modes A (volcanique) et B (cannelé; i.e. core complexes océaniques) définissent les régions des dorsales ultra-lentes où le budget magmatique est le plus important et s'appliquent aussi à la dorsale Médio-Atlantique. Le mode C (« smooth seafloor »), avec très peu ou pas de volcanisme à l'axe, semble spécifique des dorsales ultra-lentes, et correspond au budget magmatique le plus réduit. Noir: magma concentré dans l'asthénosphère, gris foncé : magma concentré dans la lithosphère, gris clair : roches magmatiques cristallisées.

Les forages effectués dans quatre CCO (*Atlantis Bank* : ODP Leg 118, Robinson et al., 1989 ; ODP Leg 176, Dick et al., 1999 ; ODP Leg 179, Pettigrew et al., 1999 ; *Zone MARK* : ODP Leg 153, Cannat et al., 1995b ; *le CCO à 15°45'N*: ODP Leg 209, Kelemen et al., 2004 ; *Massif Atlantis* : expédition IODP 304-305, Blackman et al., 2006) montrent la présence systématique de roches gabbroïques en leur cœur, suggérant un lien étroit entre le magmatisme et la formation des CCO (Ildefonse et al., 2007c). Dans le modèle proposé par Ildefonse et al. (2007c), une activité magmatique plus importante se manifeste épisodiquement aux extrémités de segments et permet la mise en place de plutons plus volumineux dans la croûte composite. La mise à l'affleurement de ces plutons est accommodée par une déformation très localisée, essentiellement dans les serpentinites à leur périphérie. Les CCO et les failles de détachement auxquelles ils sont associés sont donc, dans ce modèle, avant tout l'expression tectonique et morphologique de la présence épisodique de corps gabbroïques plus volumineux dans une lithosphère composite telle que définie par Cannat (1993, 1996).

Dans le schéma général présenté dans cette partie, les CCO apparaissent comme la manifestation la plus spectaculaire d'un mode d'accrétion plus général, via les failles de détachement. Ce mode d'accrétion apparaît fondamental au niveau des dorsales lentes : plus de 15% du nouveau plancher océanique accrété dans la région 13°-15°N être dominé par le développement de CCO (Smith et al., 2006). Escartín et al. (2008) montrent, grâce notamment à la sismicité enregistrée le long de la dorsale, qu'entre 12°N et 35°N sur la dorsale Médio-Atlantique, environ 50% du plancher océanique est accrété via des failles de détachement. Le mode d'accrétion de la lithosphère océanique est donc aussi un paramètre important contrôlant la morphologie axiale aux dorsales lentes (Figure 1.20). L'accrétion dite volcanique, dominée par les processus magmatiques éruptifs avec la formation de collines abyssales des deux côtés de l'axe, construit un plancher océanique symétrique de chaque côté de la vallée axiale (Figure 1.20b). À l'opposé, l'accrétion dite tectonique, liée à l'activité de failles de détachement le long d'un seul flanc de la vallée axiale, produit une morphologie axiale asymétrique (Figure 1.20a). De plus, ces auteurs montrent que le long des dorsales lentes, la chimie des basaltes est corrélée à la morphologie du plancher océanique donc au style d'accrétion de la lithosphère océanique (Escartín et al., 2008).

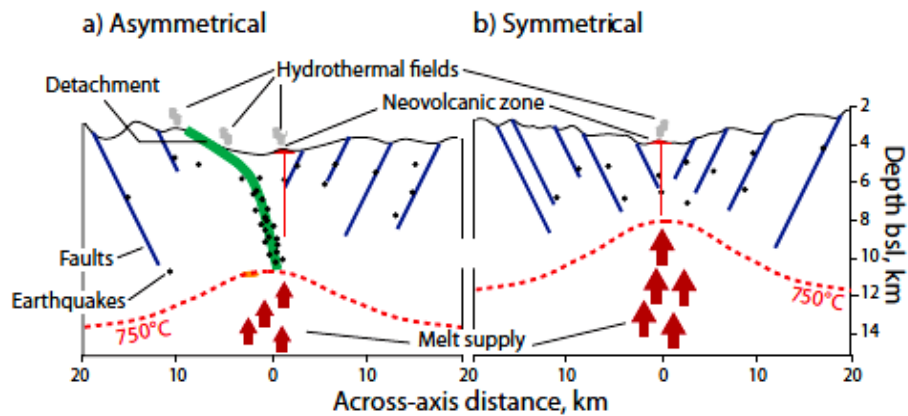


Figure 1.20 : Schéma présentant la morphologie axiale d'une dorsale lente en fonction du mode d'accrétion crustale (Escartín et al., 2008). (a) Section de dorsale asymétrique : un seul grand détachement sur un flanc de la dorsale accommode à peu près la moitié de l'extension de la lithosphère océanique créant alors une dissymétrie du plancher océanique de part et d'autre de l'axe (b) section de dorsale symétrique : de nombreuses failles sont présentes de chaque côté de l'axe et forment des collines abyssales.

II. Processus magmatiques dans la lithosphère océanique

Les magmas générés par la fusion partielle adiabatique du manteau sub-océanique ont été nommés magmas primaires (e.g., Elthon, 1979 ; Stolper, 1980). Ces magmas sont en équilibre avec les olivines du manteau source ($Fo \geq 0.89$; Dick & Bullen, 1984) et ont des compositions primitives (i.e., riche en magnésium $Mg\# = Mg/(Mg + Fe) \times 100 \geq 71$). La majorité des basaltes des dorsales océaniques (MORB pour Mid-Ocean Ridge Basalt) ont des compositions en éléments majeurs trop évoluées ($Mg\# < 70$) pour représenter des magmas primaires (Figure 1.21 ; e.g., Bender et al., 1978; Fujii and Bougault, 1983; Falloon and Green, 1987). Les magmas primaires ont donc subi une différenciation après leur extraction du manteau source qui a modifié leur composition chimique (e.g., Grove et al., 1992 ; O'Hara & Herzberg, 2002 ; Herzberg et al., 2007). Comment s'effectue la différenciation des liquides primaires et où?

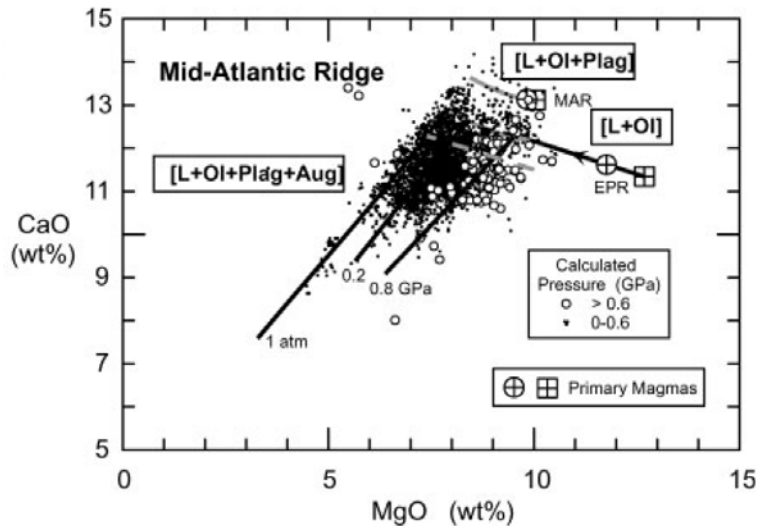


Figure 1.21 : Variation de la composition en CaO en fonction du MgO des verres basaltiques de la dorsale Médio-Atlantique et des verres basaltiques expérimentaux (Herzberg, 2004). Les ronds et carrés avec des croix indiquent la composition des liquides primaires pour les MORBs de la dorsale Est-Pacifique (EPR) et de la dorsale Médio-Atlantique (MAR). Cette figure montre que les basaltes des dorsales océaniques n'ont pas la même composition en éléments majeurs que les magmas primaires issus de la fusion partielle du manteau.

Les roches gabbroïques observées le long des dorsales présentent les caractères pétrologiques et géochimiques de cumulats. D'un point de vue pétrographique, le terme « cumulat » a été établi par Wager *et al.* (1960) et affiné par de nombreux auteurs (e.g., Wager, 1963; Jackson, 1967; Wager et Brown, 1968; Irvine, 1982) pour décrire les textures des roches ignées des grands complexes lités basiques ou ophiolitiques (Skaergaard, Stillwater, Rum, Bushveld ou Sudbury). Dans ce contexte, les cristaux qui précipitent en premier et qui s'accumulent sur le plancher de la chambre magmatique sont appelés minéraux cumulus. Le liquide piégé entre ces minéraux cumulus est nommé intercumulus. Les cumulats sont donc le produit d'une association dynamique d'une phase solide et d'une phase liquide (Wager et al., 1960). Les minéraux cumulus sont automorphes à subautomorphes et forment dans les cumulats un réseau de cristaux en contact les uns avec les autres. Les cristaux intercumulus, formés plus tardivement, cimentent les minéraux cumulus. Souvent xénomorphes, ils sont le produit de la cristallisation du matériel piégé entre les interstices du réseau formé par les minéraux cumulus. L'étude des cumulats apporte donc des renseignements sur la séparation des cristaux et du liquide (processus cumulus) mais aussi sur l'évolution, lors du refroidissement, de la pile cristalline et du liquide interstitiel formés lors du processus cumulus (processus post-cumulus).

La composition, le mode ainsi que la structure de ces roches gabbroïques océaniques sont des indicateurs de l'évolution chimique des magmas.

1. Processus de cristallisation et d'accumulation

La corrélation positive de la teneur en Mg des clinopyroxènes, traduite par l'indice Mg# ($Mg\# = \frac{Mg}{Mg+Fe} \times 100$), avec la teneur en anorthite des plagioclases dans les différentes roches gabbroïques océaniques définit généralement une évolution continue depuis des troctolites (roches gabbroïques composées d'olivine et de plagioclase) vers des gabbros à oxyde (roches gabbroïques composées de plagioclase, clinopyroxène, et oxydes). Si l'olivine, minéral riche en magnésium, précipite en premier, ceci aura pour conséquence d'abaisser le Mg# du liquide puisque le magnésium, élément compatible, se concentre dans le solide au cours de la différenciation magmatique. Les minéraux cristallisant en dernier verront donc leur composition s'enrichir en fer. Les gabbros à oxyde de part leur composition modale auront donc une composition chimique plus évoluée que les troctolites, plus riches en olivines.

Les gabbros océaniques des dorsales lentes sont en général caractérisés par des plagioclases avec une grande variabilité de composition (An_{95-30}) ; des clinopyroxènes avec des compositions très magnésiennes ($Mg\# > 88$), indiquant qu'ils ont cristallisé à partir d'un magma primitif (i.e., riche en magnésium), et des fortes teneurs en Na_2O ($> 0,35\%$) et en TiO_2 (Elthon et al., 1992; Figure 1.22). De même, les orthopyroxènes présentent aussi des Mg# très élevés (> 81). Or, ces teneurs ne sont pas en adéquation avec les compositions, aussi bien des clinopyroxènes ($Mg\# < 86$; $Na_2O < 0,35\%$), que des orthopyroxènes ($Mg\# < 81$) provenant de la cristallisation expérimentale d'un MORB à 1 atm (Elthon et al., 1992 ; Grove et al., 1992) (Figure 1.23). Par contre, les olivines n'ont pas de compositions « anormales » (FO_{70-90} et $NiO = 0-0,4\%$) et montrent une co-variation du nickel et de la Forstérite ($FO = \frac{Mg \times 100}{Mg+Mn+Fe}$) comparable à celle des phénocristaux des basaltes (Figure 1.24).

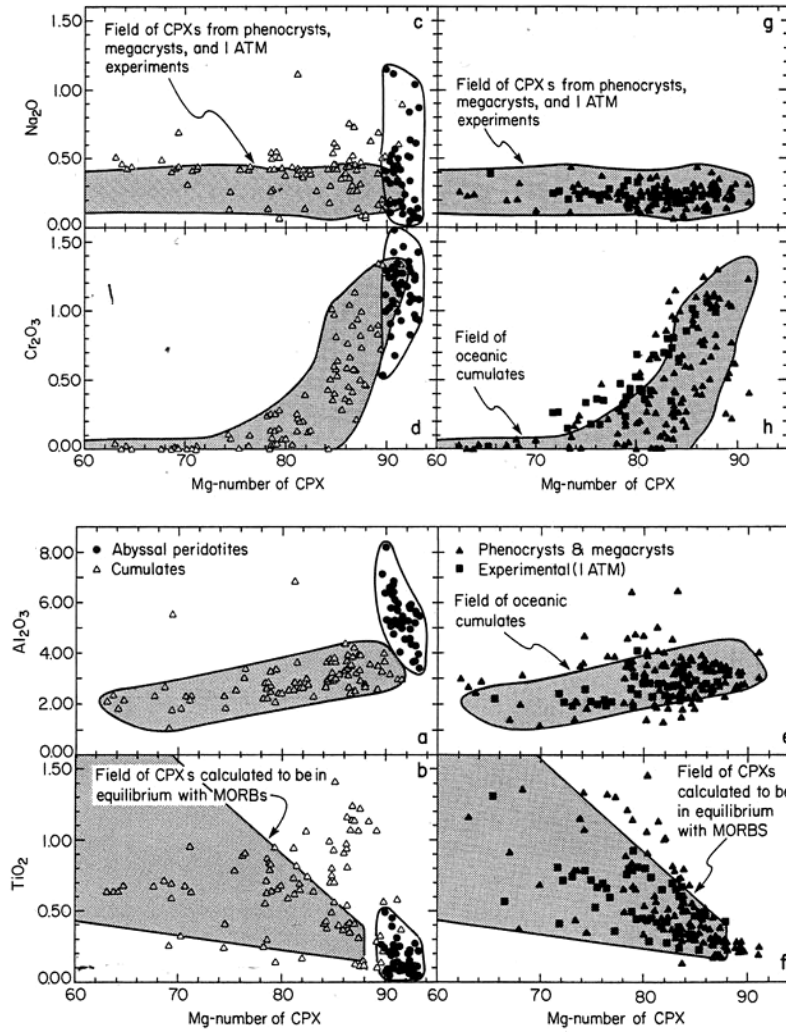


Figure 1.22 : Abondances en Al_2O_3 , TiO_2 , Na_2O et Cr_2O_3 dans les clinopyroxènes (CPX) des cumulats océaniques et des péridotites abyssales en fonction du Mg# des clinopyroxènes (a-d) comparées à l'abondance de ces mêmes oxydes dans les clinopyroxènes provenant des études expérimentales à 1 atm et les phénocristaux et mégacristaux des MORBs (e-h) (Elthon et al., 1992).

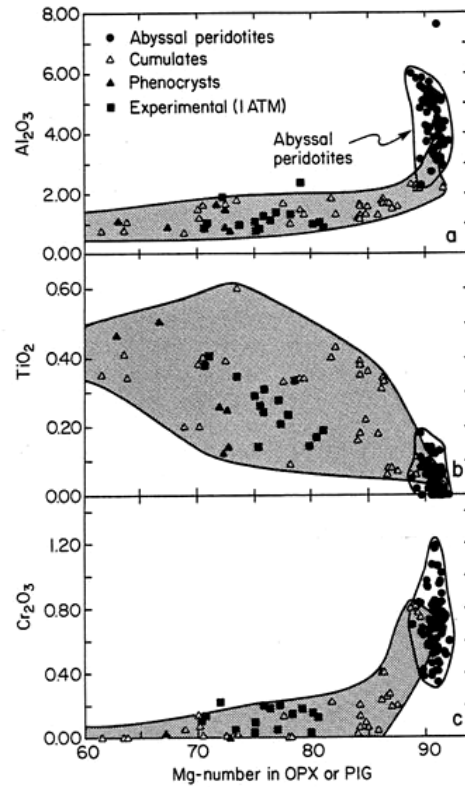


Figure 1.23 : Abondances en Al_2O_3 , TiO_2 et Cr_2O_3 dans les orthopyroxènes (OPX) et pigeonites (PIG) des cumulats océaniques (champ gris) et des péridotites abyssales en fonction du Mg# des pyroxènes comparées à l'abondance de ces mêmes oxydes dans les orthopyroxènes provenant des études expérimentales à 1 atm et les phénocristaux des MORBs (Elthon et al., 1992).

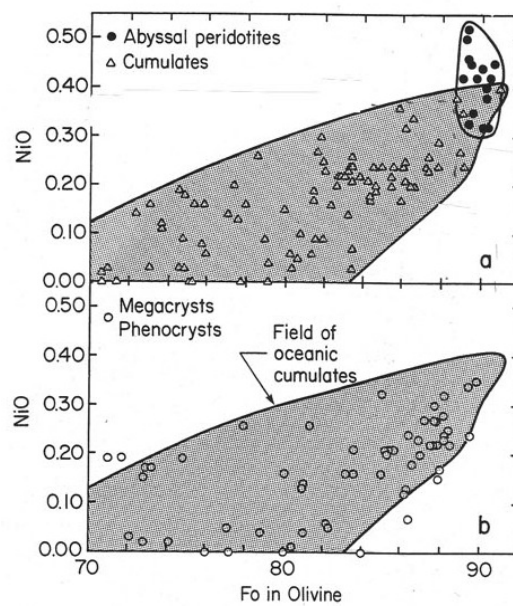
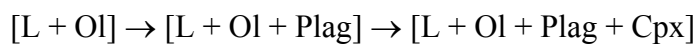


Figure 1.24: Composition en NiO en fonction de la teneur en Forstérite des olivines des cumulats océaniques et des péridotites abyssales (a) et des mégacristaux et phénocristaux des MORBs (b) (Elthon et al., 1992).

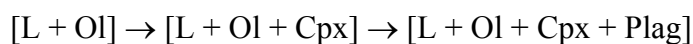
La composition chimique des minéraux qui constituent les gabbros océaniques est contrôlée par la température et la pression à laquelle s'effectue la cristallisation, ainsi que par la composition du liquide qui cristallise et par le type de processus de cristallisation.

Les études expérimentales sur les équilibres cristaux/liquide ont montré que l'ordre d'apparition des phases minérales au liquidus dépend de la pression, de la température et de la teneur en eau. Ainsi, à basse pression (< 2kbar), l'olivine arrive en premier au liquidus, suivit du plagioclase puis du clinopyroxène (Figure 1.25). Avec l'augmentation de la pression, l'intervalle entre la température du liquidus et la température de saturation des clinopyroxènes décroît (Figure 1.25). La figure 1.25, montre aussi qu'avec une augmentation de la teneur en eau des magmas, l'olivine et le clinopyroxène cristallisent aux dépens du plagioclase.

La suite de cristallisation d'un liquide de type MORB dans la croûte océanique (< 5 km de profondeur ; 2Kbar) est donc la suivante (Green & Ringwood, 1967; Grove & Bryan, 1983; Tormey et al., 1987; Juster et al., 1989; Grove et al., 1992 ; Herzberg, 2004):



La suite de cristallisation d'un liquide de type MORB dans le manteau supérieur (5-10Kbar) est la suivante (e.g., Bender et al., 1978 ; Grove et al., 1992 ; Herzberg, 2004) :



Les clinopyroxènes des gabbros océaniques formés dans la croûte océanique inférieure devraient donc avoir un Mg# relativement bas puisqu'ils cristallisent en dernier dans la suite de cristallisation à basse pression d'un MORB (e.g., Grove et al., 1992).

Plusieurs hypothèses ont été émises pour expliquer les teneurs très magnésiennes des pyroxènes des cumulats océaniques. L'une d'elles, de loin la plus citée dans la littérature, est la cristallisation des cumulats océaniques à pression modérée à forte (3-10 kbar) (e.g., Bender et al., 1978 ; Bence et al., 1979 ; Elthon et al., 1982, 1992 ; Elthon, 1987). Le clinopyroxène en cristallisant plus tôt dans la séquence de cristallisation, précipite à partir d'un liquide moins différencié, et acquiert un Mg# plus élevé.

Au niveau des dorsales lentes, la cristallisation des magmas dans le manteau est envisageable comme semble l'indiquer la convergence d'arguments pétrologiques, géophysiques ou paléomagnétiques très différents (e.g., Sleep et Barth, 1997; Meurer & Gee, 2002 ; Lizarralde et al., 2004 ; Cannat et al., 2004 ; Kelemen et al., 2004 ; Villiger et al., 2007). Comparés aux dorsales rapides, les apports magmatiques et la quantité de chaleur transportée sont globalement plus faibles. La croûte et le manteau sont plus froids et la

cristallisation peut se produire à des niveaux plus profonds (Michael & Cornell, 1998). La cristallisation peut démarrer dès l'extraction du liquide (Niu, 1997).

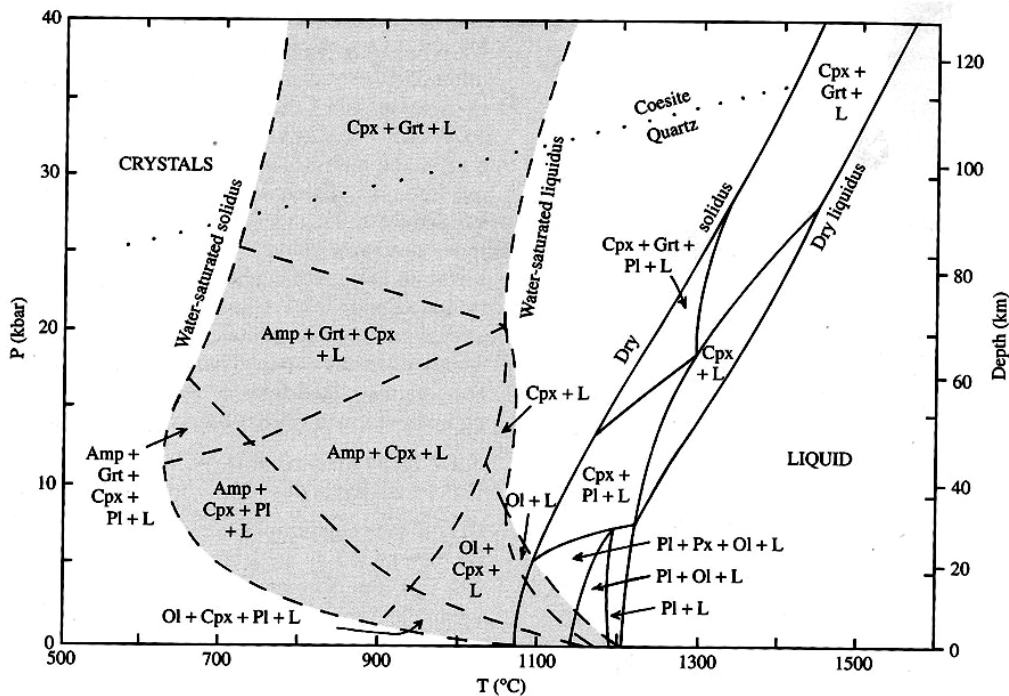


Figure 1.25 : Diagramme présentant les champs d'équilibres liquide/cristal dans un basalte tholéitique anhydre (ligne pleine) et en présence d'eau (ligne pointillé, champ gris) (Best, 2003).

Différents modèles géochimiques de différenciation en système clos d'un liquide magmatique ont été développés pour expliquer la variation de composition chimique des différents minéraux des roches gabbroïques et donc de ces dernières:

Lors de la cristallisation fractionnée, les minéraux sont immédiatement isolés et retirés du liquide dès qu'ils sont formés (Bowen, 1928 ; Bowen, 1941). Dans ce contexte aucune réaction entre les minéraux et le liquide résiduel n'est possible. La cristallisation fractionnée engendre donc des liquides et des solides de compositions chimiques différentes à chaque étape.

Lors de la cristallisation à l'équilibre (Shaw, 1970) les minéraux réagissent continuellement et sont rééquilibrés complètement avec le liquide. Ce mode d'évolution est théoriquement possible mais très peu réaliste, compte tenu des vitesses de diffusion intracristalline, voir même de diffusion dans le liquide. D'ailleurs, au cours de la cristallisation fractionnée la composition du liquide résiduel évoluera vers une gamme de composition beaucoup plus large que lors de la cristallisation à l'équilibre (Figure 1.26).

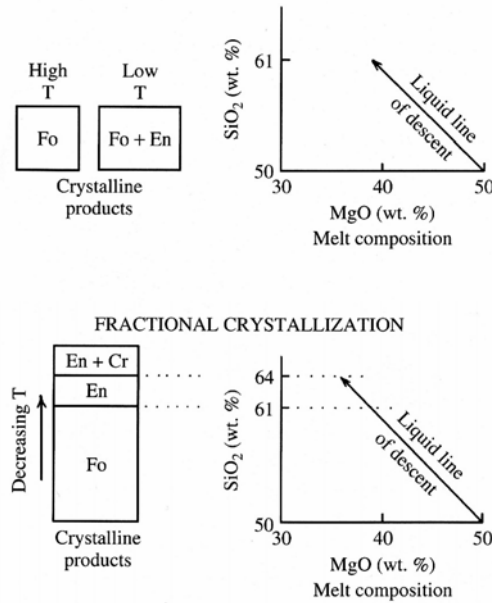


Figure 1.26 : Schéma présentant l'évolution de la composition des liquides et l'apparition des différents cristaux au cours de la cristallisation à l'équilibre (en haut) et de la cristallisation fractionnée (en bas) d'un liquide basaltique (composition initiale 50% de silice) dans le système binaire $Mg_2SiO_4-SiO_2$ à 1 atm (Best, 2003).

La cristallisation fractionnée se traduit aussi par une augmentation des éléments en trace incompatibles depuis les roches gabbroïques les plus primitives vers les plus évoluées. En effet, au cours de la cristallisation, les éléments incompatibles auront tendance à rester le plus longtemps possible dans le liquide puisque leur structure atomique (rayon ionique de grande taille par exemple) n'est pas compatible avec celle d'un minéral silicaté. Cependant, les éléments qui sont incorporés par préférence dans un minéral en particulier sont compatibles vis-à-vis de celui-ci. Par exemple, l'Eu et le Sr s'introduiront dans le plagioclase, le Ni est quant à lui compatible avec l'olivine. Ces éléments sont incompatibles si le plagioclase ou bien l'olivine sont absents. Par contre, ils deviennent compatibles quand le plagioclase ou l'olivine forme une portion significative de l'assemblage solide.

Pour rendre compte de la présence de phases évoluées dans des roches gabbroïques primitives, Langmuir (1989) puis O'Hara & Fry (1996) et Meurer & Boudreau (1998) ont proposé un processus combiné de cristallisation et d'interaction avec le liquide interstitiel dans la chambre magmatique: le modèle de cristallisation in-situ qui s'effectue en système clos (Figure 1.27). Dans ce modèle, la composition en éléments majeurs des cumulats est proche de celle du magma à partir duquel ils cristallisent et reste constante durant la différenciation, tandis que leur teneur en éléments en trace incompatibles est contrôlée par la

quantité variable de liquide interstitiel qui évolue dans la chambre magmatique (Langmuir, 1989).

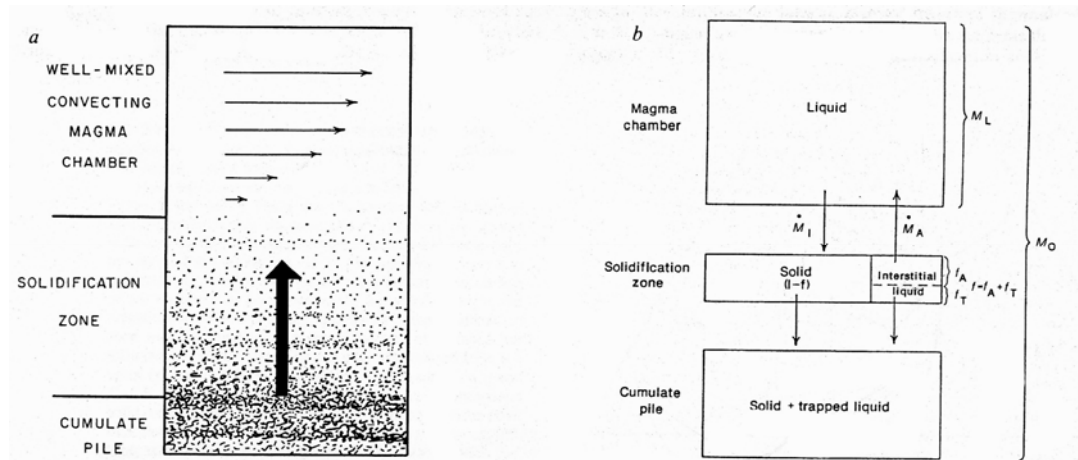


Figure 1.27 : (a) Schéma présentant la cristallisation in-situ (Langmuir, 1989). La flèche verticale montre le mouvement du liquide depuis la zone solidifiée vers l'intérieur de la chambre magmatique. Les flèches verticales désignent le courant convectif dans la chambre. La cristallisation a lieu dans la zone de solidification qui bouge progressivement dans la chambre magmatique au cours de la cristallisation. Une partie des liquides interstitiels migre dans la chambre magmatique après la cristallisation et se mélange avec les liquides présents dans la chambre. La composition, de ces derniers, change donc progressivement avec l'arrivée des nouveaux liquides interstitiels. (b) Modèle illustrant les différents paramètres pris en compte lors de la cristallisation à l'équilibre.

Le processus de cristallisation post-cumulus d'un liquide interstitiel évolué entre les minéraux cumulus est un autre modèle de différenciation magmatique développé pour expliquer la présence de larges clinopyroxènes poecilitiques intercumulus, zonés en éléments en trace, associés à des phases interstitielles évoluées comme les zircons, les amphiboles, les oxydes ou les apatites au sein même de cumulats primitifs (Meyer et al., 1989 ; Elthon et al., 1992 ; Bédard, 1994 ; Natland & Dick, 1996, 2001 ; Ross & Elthon, 1997 ; Tribuzio et al., 1999 ; Cortesogno et al., 2000 ; Gillis & Meyer, 2001 ; Coogan et al., 2000a-b ; Rampone et al., 1997 ; Borghini et al., 2007 ; Borghini & Rampone, 2007).

Cependant, dans la plupart des gabbros océaniques les plagioclases ne sont ni en équilibre textural ni en équilibre chimique avec les clinopyroxènes (Bloomer et al., 1989 ; 1991 ; Meyer et al., 1989 ; Elthon et al., 1992 ; Michael & Cornell, 1998 ; Dick et al, 2002 ; Kvassnes, 2004). Un simple modèle de différenciation en système clos ne peut décrire ces déséquilibres. D'autres processus, en système ouvert, sont donc requis pour rendre compte de ces observations.

2. Processus d'interaction magma/roche

Dans certaines roches gabbroïques océaniques riches en olivines, les olivines cumulatives montrent des textures résorbées et des contacts lobés avec les minéraux « secondaires » qui sont les plagioclases et les clinopyroxènes. Ces derniers montrent des variations de leur teneur en éléments en trace depuis le cœur vers la bordure, alors que le Mg# reste constant. Cette modification de la texture des cumulats, ainsi que le découplage entre les éléments de différentes compatibilités dans les plagioclases et les clinopyroxènes ont été interprétés comme des réactions magma/roche tardives par Mathez (1995).

Les troctolites du mégamullion Kane (23°N, dorsale Médio-Atlantique) montrent des textures poecilitiques avec des poeciloblastes de clinopyroxène qui englobent les cristaux d'olivines et de plagioclase corrodés (Lissenberg & Dick, 2008). Ces relations texturales indiquent que les clinopyroxènes ont bien cristallisé après l'olivine et le plagioclase comme prédit pour la cristallisation d'un MORB à basse pression. Les clinopyroxènes présentent des variations de leurs teneurs en Cr et Ti depuis le cœur vers la bordure plus enrichie. La concentration élevée en Ti et Cr de ces clinopyroxènes implique qu'ils ont cristallisé à partir d'un liquide évolué qui a donc subi un fractionnement important. Cependant, ces clinopyroxènes ont des Mg # élevés (> 88) allant à l'encontre d'une cristallisation poussée. De plus, les clinopyroxènes poecilitiques englobent des plagioclases résorbés avec des concentrations en anorthite faible (< 70), indiquant un déséquilibre entre ces deux phases. Pour rendre compte de l'ensemble des caractéristiques, texturales et chimiques, des clinopyroxènes à fort Mg# des troctolites, Lissenberg & Dick (2008) ont proposé un processus de réaction magma/roche entre des cumulats primitifs pré-existants et un liquide migrant de type MORB, dans la croûte océanique inférieure au cours de la cristallisation.

Bédard & Hébert (1996) et Bédard et al. (2000) ont montré que la croûte océanique froide peut être métasomatisée par les magmas basaltiques ascendants ayant une température plus élevée que le solidus des roches de la croûte. Le processus mécanique et chimique par lequel les magmas réagissent avec et assimilent les roches encaissantes a été nommé « syntexis » par ces auteurs. Lors de l'ascension des magmas dans la croûte inférieure, ces derniers dissolvent les roches gabbroïques préexistantes et créent un magma hybride (Kvassnes, 2004 ; Kvassnes & Grove, 2008). Ce processus d'assimilation correspondant à l'incorporation de roches solides dans un magma de composition différente est similaire au processus couplé de cristallisation et d'assimilation (De Paolo, 1981).

La présence systématique de roches mantelliques imprégnées, dans les ophiolites, à la transition entre le manteau et la croûte indique que les processus d'interaction entre les liquides basaltiques et le manteau superficiel sont aussi importants (e.g., Nicolas & Prinzhofer, 1983; Benn et al., 1988; Boudier, 1991; Boudier & Nicolas, 1995; Rampone et al., 1997, 2008; Koga et al., 2001; Dijkstra et al., 2003; Borghini et al., 2007; Piccardo et al., 2007). De même, aux dorsales rapides de nombreuses péridotites imprégnées ont été échantillonnées (e.g., Cannat et al., 1990; Constantin et al., 1995; Allan & Dick, 1996; Arai & Matsukage, 1996; Dick & Natland, 1996; Niu & Hekinian, 1997) ainsi qu'aux dorsales lentes (e.g., Dick, 1989; Cannat et al., 1992; Girardeau & Franchetau, 1993; Hekinian et al., 1993; Cannat et al., 1997; Seyler & Bonatti, 1997; Tartarotti et al., 2002; Kelemen et al., 2004; Paulick et al., 2006; Takazawa et al., 2007).

3. Comportement rhéologique et structural d'un cumulat partiellement cristallisé

L'augmentation de la fraction de liquide dans un milieu partiellement cristallisé a nécessairement des implications sur la rhéologie et la structure des roches composant la croûte océanique inférieure.

La présence d'un liquide magmatique au sein d'une matrice solide joue un rôle important sur les propriétés mécaniques de cette matrice (Figure 1.28). De plus, ce changement de rhéologie, lié à la fraction de liquide dans le système, peut agir sur les microstructures développées (e.g. Nicolas, 1992). La viscosité d'un mélange liquide/solide décroît brutalement lorsque la fraction liquide augmente et atteint un seuil critique ("Critical Melt Fraction" ou "Rheological Critical Melt Percentage" : e.g., Arzi, 1978 ; Van der Molen & Paterson, 1979 ; Nicolas et al., 1993; Rutter & Neumann, 1995 ; Lejeune & Richet, 1995 ; Vigneresse et al., 1996 ; Renner et al., 2000 ; Rabinowicz et al., 2001 ; Rosenberg & Handy, 2005 ; Scott & Kohlstedt, 2006). Cette fraction critique de liquide est généralement estimée autour de 0,3 : $0,2 \pm 0,1$ (Arzi, 1978) ou 0,3 à 0,35 (Van der Molen & Paterson, 1979) (Figure 1.29). Elle correspond au moment où la phase liquide devient connectée et le squelette solide se rompt. Au-dessus de ce seuil, la phase liquide domine le comportement du système liquide/solide (e.g., une roche partiellement fondue). Ce seuil représente la transition depuis une déformation plastique à l'état solide vers une déformation en suspension (magmatique dans le cas d'une roche partiellement fondue) (Figure 1.28). Inversement, lorsque la fraction

liquide est inférieure à la fraction critique, la rhéologie du système liquide/solide est dominée par les propriétés mécaniques de la phase solide.

Vignerresse et al. (1996) proposent que la rhéologie d'une roche qui fond diffère de celle d'une roche qui cristallise; la distribution du liquide n'est pas identique dans les deux cas. Quatre seuils sont alors décrits selon que la roche fond ou cristallise. Toutefois, Handy et al. (2001) et Rosenberg (2001) ont montré que la distribution du liquide est différente entre la cristallisation et la fusion seulement si ces deux processus sont très rapides.

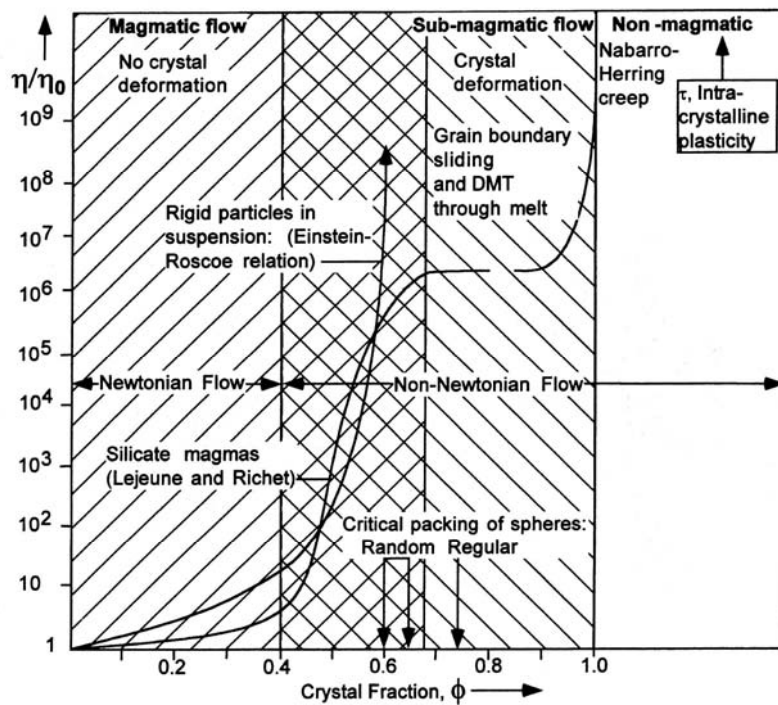


Figure 1.28: Diagramme montrant comment la rhéologie et les mécanismes de déformation varient en fonction de la fraction de cristaux dans un liquide. La viscosité (η) est normalisée à la viscosité du liquide (η_0) (Blenkinsop, 2000). DMT = Diffusive Mass Transfer soit déformation par diffusion.

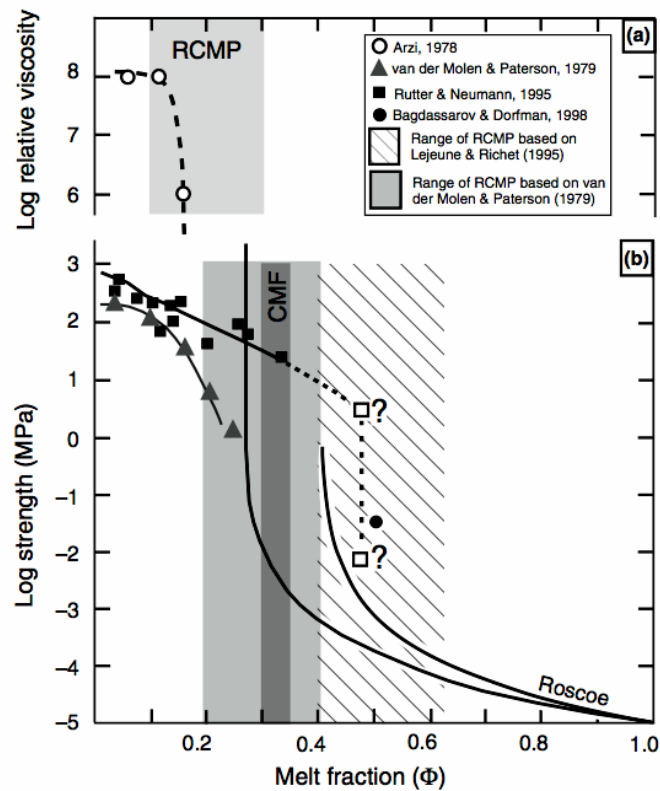


Figure 1.29 : Résistance/viscosité effective d'un mélange liquide/solide en fonction de la fraction de liquide (Rosenberg & Handy, 2005). (a) Cette partie du diagramme présente les résultats de l'étude de Arzi (1978) sur la viscosité relative (viscosité de l'échantillon/viscosité du liquide) de granites en fonction de la fraction de liquide. En gris clair : intervalle de fraction de liquide correspondant au pourcentage critique de liquide (Rheological Critical Melt Percentage) proposé par Arzi (1978). (b) Résultats des études de résistance d'un agrégat en fonction de la fraction de liquide de Rutter & Neumann (1995) pour des granites et de Van der Molen & Paterson (1979) pour des aplites. Les fractions critiques de liquide correspondant au RCMP sont indiquées en gris clair pour les données de Van der Molen & Paterson (1979) et en hachuré pour celles de Lejeune & Richet (1995) ; le champ gris foncé correspond au point où la réduction de la résistance avec l'augmentation de la fraction de liquide est au maximum, pour Van der Molen & Paterson (1979).

En résumé, le changement de rhéologie des roches à fort rapport liquide/solide est lié à une augmentation de l'interconnexion du liquide. La résistance d'une roche partiellement fondue entre le liquidus et le solidus est caractérisée par deux seuils (e.g. Rosenberg et Handy, 2005) : le premier coïncide avec la connexion du liquide, à une fraction de liquide d'environ 0,07 en moyenne pour un granite (Melt Connectivity Transition); le deuxième correspond à la rupture du réseau solide formé par les cristaux, à une fraction de liquide d'environ 0,4 (Solid-to-Liquid Transition). Ce deuxième seuil est similaire à la fraction critique de liquide décrite auparavant dans la littérature. Au-dessus de ce seuil, les cristaux sont en suspension dans le

liquide (Figures 1.30 et 1.31). Il en résulte l'alignement subparallèle des cristaux avec le plan de fluage (orientation préférentielle de forme), résultant de la rotation rigide des cristaux mais aussi des interactions mécaniques entre ces mêmes cristaux (Ildefonse et al., 1992; Tikoff & Teyssier, 1994; Ildefonse et al., 1997). Dans le cas de l'olivine, peu de fabrications dans les gabbros sont publiées: il semble que les axes [001] tendent à s'aligner avec la linéation magmatique (Benn et Allard, 1989).

La résistance des roches du manteau partiellement fondues décroît d'un facteur de 2 à 5 avec l'addition de 1 à 3% de liquide magmatique (Cooper & Kohlstedt, 1986 ; Zimmerman & Kohlstedt, 2004). Le RCMP dépend des angles de mouillages des phases cristallines en présence. Or l'angle de mouillage de l'olivine est très faible, donc la connexion du liquide s'effectue à une fraction de liquide très faible par exemple dans une dunite ($\phi < 0,05$) par rapport à un granite.

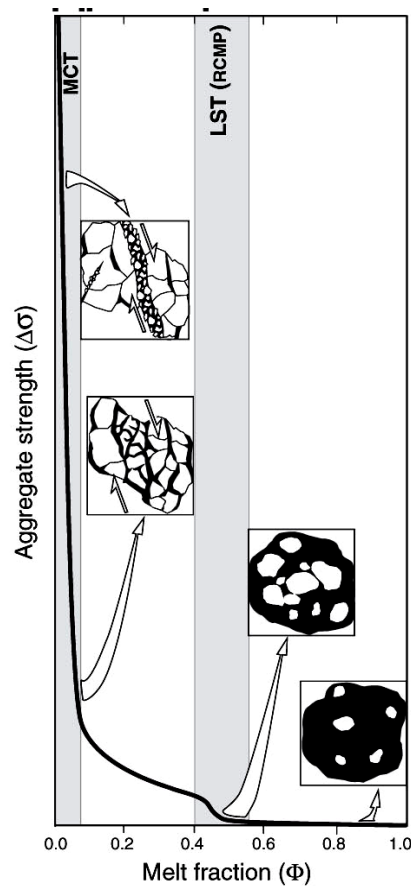


Figure 1.30 : Résistance d'un agrégat en fonction du pourcentage de liquide pour un granite partiellement fondu entre le liquidus et le solidus. MCT (Melt Connectivity Transition): connexion du liquide ; LST (Liquid-to-Solid Transition): transition solide-liquide. Les différents schémas illustrent la texture de la roche pour différentes fractions liquides : autour de $\Phi = 0,03$ la déformation se localise le long d'une bande de liquide ; à $\Phi = 0,07$ la déformation est plus distribuée à l'échelle de l'échantillon ; à $0,4 < \Phi < 0,6$ le réseau solide se brise, mais l'interaction entre les cristaux est encore possible ; à $\Phi = 0,6$ les cristaux sont suspendus dans le liquide et n'interagissent pas entre eux (Rosenberg & Handy, 2005).

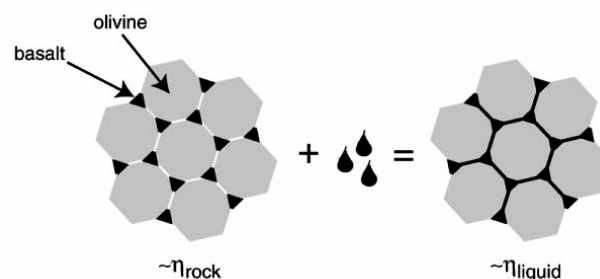


Figure 1.31 : Schéma présentant le changement de texture d'une roche partiellement fondue lorsque la fraction de liquide augmente (Scott & Kohlstedt, 2006). Au départ, le liquide est présent au joint de grains puis au-dessus du seuil critique, le réseau solide formé par les cristaux se rompt, les cristaux sont isolés dans le liquide, le comportement rhéologique de la roche est contrôlé par la phase liquide.

4. Implications des différents processus magmatiques sur la composition des MORBs

Il est généralement admis que les MORBs conservent les signatures géochimiques acquises en profondeur comme les modalités de fusion et la composition de la source (e.g., Klein & Langmuir, 1987). Ainsi, un faible taux de fusion engendre des magmas avec des concentrations plus élevées en Na₂O, K₂O et TiO₂ (Langmuir et al., 2002). Une fusion à haute pression augmente la concentration en FeO des magmas. De même, l'augmentation de la concentration en MgO et Al₂O₃ et la diminution de la concentration en SiO₂ et CaO des MORBs indiquent que ces magmas ont cristallisé à haute pression, c'est-à-dire à grande profondeur dans le manteau supérieur (e.g., Herzberg, 2004). L'augmentation du rapport isotopique ⁸⁷Sr/⁸⁶Sr dans les MORBs reflète un manteau enrichi en éléments en trace.

Ces différents indices chimiques requièrent que les magmas formés dans le manteau soient extraits rapidement et qu'ils n'aient pas subi d'interaction avec les roches composant le manteau ou la croûte. Sinon, l'indication du degré d'évolution ou du degré de fusion partielle par ces différents éléments peut être faussée.

O'hara (1998) montre que la présence, dans des phénocristaux des MORBs, d'inclusions magmatiques avec des compositions très faibles en éléments en trace incompatibles, peut être liée à de l'assimilation de gabbros fortement appauvris en éléments en trace incompatibles par les MORBs.

L'étude des roches gabbroïques océaniques montre que des processus autres que la cristallisation à haute pression ou un faible degré de fusion partielle d'un manteau hétérogène peuvent expliquer les différentes signatures chimiques des MORBs, mentionnées ci-dessus.

La figure 1.32 compare les évolutions chimiques au cours de la cristallisation fractionnée de différents liquides provenant de l'assimilation de roches gabbroïques par un liquide basaltique avec un liquide provenant de la cristallisation normale d'un MORB (Klein & Langmuir, 1987). L'assimilation de gabbros par des liquides basaltiques saturés en olivine augmente la teneur des magmas en Na₂O et CaO et la diminue en FeO (Figure 1.32 ; Kvassnes & Grove, 2008). Par contre, l'assimilation de troctolites par ces mêmes liquides basaltiques primitifs augmente la teneur de ces magmas en FeO et Na₂O et diminue leur teneur en CaO (Figure 1.32 ; Kvassnes & Grove, 2008).

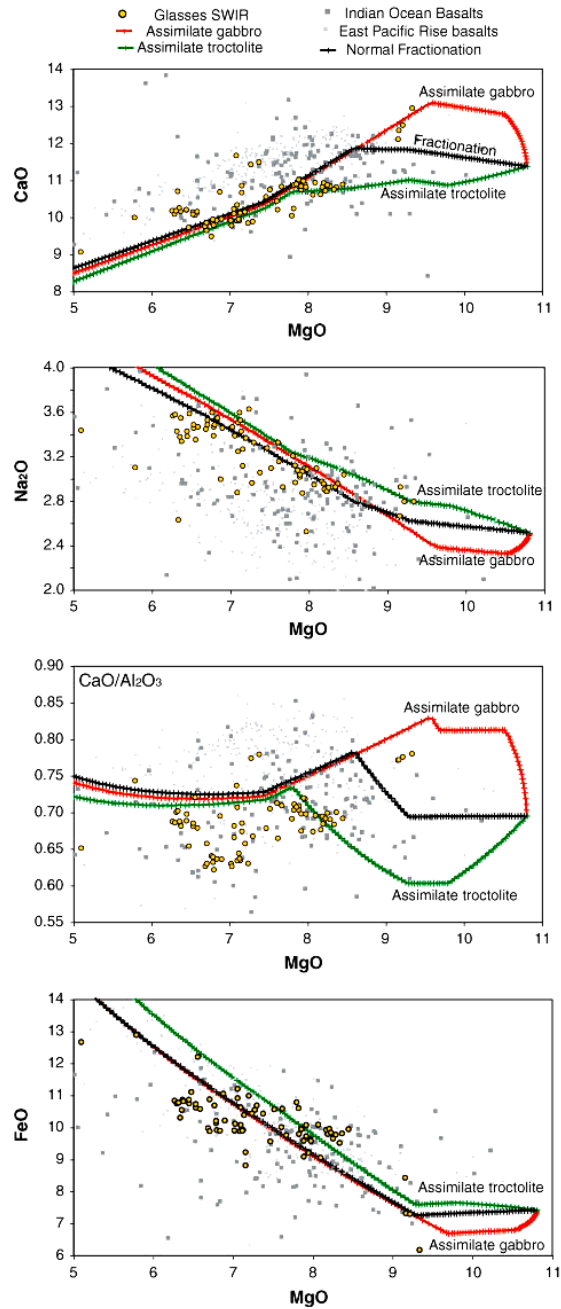


Figure 1.32 : Diagramme présentant les compositions en éléments majeurs de verres basaltiques provenant de la dorsale Est-Pacifique, de la dorsale Sud-Ouest Indienne et de la zone de fracture Atlantis II (dorsale Médio-Atlantique) et la composition de trois liquides évoluant par cristallisation fractionnée. Ligne noire : liquide évoluant par cristallisation fractionnée normale d'après Klein & Langmuir, 1987 ; ligne verte : liquide ayant assimilé des troctolites et ; ligne rouge : liquide ayant assimilé des gabbros), (Kvassnes & Grove, 2008).

Lissenberg & Dick (2008) montrent que l'assimilation de cumulats primitifs préexistants par un liquide de type MORB forme des magmas hybrides plus riches en Al_2O_3 et MgO et plus pauvres en CaO et SiO_2 (Figure 1.33). Or, certains auteurs utilisent ces changements de composition pour rétablir la pression de cristallisation des MORBs (Grove et al., 1992 ; Villiger et al., 2007). Dès lors, la pression calculée à partir de liquide basaltique ayant subi des réactions magma/roche dans la croûte inférieure peut être surestimée.

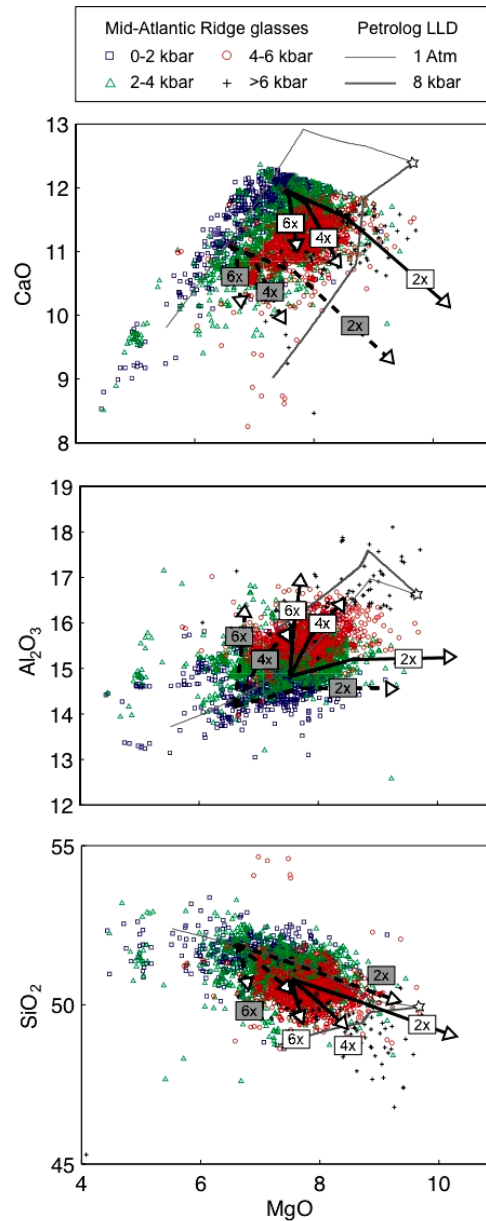


Figure 1.33 : Évolution des magmas en éléments majeurs durant une réaction magma/roche (ligne noire annotée des rapports de dissolution pl-ol) comparée à l'évolution des MORBs lors de la cristallisation à haute pression (ligne grise épaisse) et basse pression (ligne grise fine). La composition des verres basaltiques de la dorsale Médio-Atlantique est aussi reportée avec différentes couleurs en fonction de leur pression, calculée (Lissenberg & Dick, 2008).

Nonnotte et al. (2005) montrent à partir de l'étude des gabbronorites de la dorsale Médio-Atlantique que le mélange entre des MORB et des liquides issus de la fusion hydratée de la lithosphère peut contribuer à augmenter la valeur du rapport isotopique $^{87}\text{Sr}/^{86}\text{Sr}$.

De plus, Cannat et al. (1990) montrent que les compositions en certains éléments en trace d'un liquide magmatique, tels que le Ti, peuvent être modifiées par les interactions magma/roche existant lors de la circulation des liquides dans le manteau puis dans la croûte.

Les MORBs échantillonnés le long de différents segments d'accrétion sur la dorsale Médio-Atlantique montrent des variations de leurs teneurs en Fe_8 et Na_8 (Figure 1.34 ; Klein & Langmuir, 1989 ; Langmuir et al., 1992). Ces variations de composition d'un segment à l'autre peuvent être expliquées par l'assimilation de diverses roches gabbroïques de la croûte océanique inférieure (troctolite, gabbronorite..) par les magmas ascendants (Figure 1.34 ; Bédard et al., 2000). Cette assimilation engendre des liquides basaltiques avec des teneurs en Fe_8 et Na_8 différentes par rapport aux magmas issus de la cristallisation en milieu fermé.

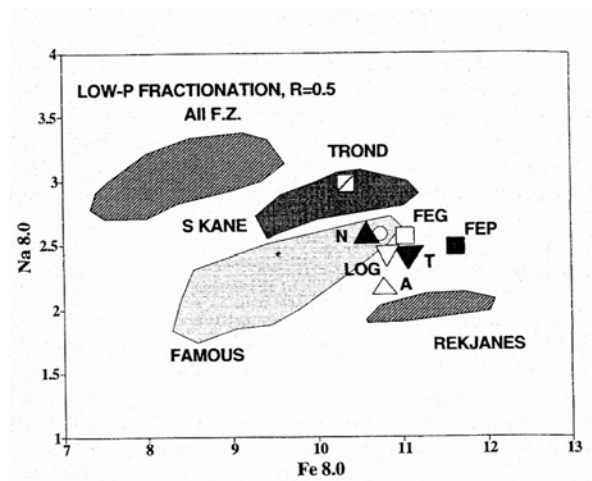


Figure 1.34 : Diagramme de la teneur en Na_8 (teneur en Na corrigé du fractionnement) en fonction de la teneur en Fe_8 de différents MORB cristallisés à basse pression. Légende : résidu de la cristallisation en système fermé à 8% de MgO (rond blanc), cristallisation couplée à de l'assimilation à 8% de MgO de gabbronorite (N), trondhjemite (TROND), ferrogabbro (FEG), ferropyroxénite (FEP), troctolite (T), leuco-gabbro à olivine (LOG), anorthosite (A).

Lissenberg & Dick (2008) montrent que les réactions magma/roche sont favorisées au niveau des dorsales lentes où la lithosphère épaisse et froide conduit au refroidissement rapide des magmas la percolant. Cet environnement augmente le taux de nucléation et de croissance des minéraux lors des premiers stades de la cristallisation, entraînant la formation rapide d'un réseau de cristaux d'olivine perméable dans lequel les liquides magmatiques migrent et réagissent efficacement. Cependant, l'ampleur avec laquelle la croûte océanique inférieure interagit avec les magmas basaltiques percolant est largement inconnue. Le taux d'assimilation est dépendant de la température de la lithosphère, du temps de résidence des magmas dans la croûte, de la composition et de la texture (tailles des minéraux) de l'assimilant.

C'est dans ce contexte que sont présentés les deux chapitres suivants, qui détaillent la microstructure et la géochimie in-situ de deux séries gabbroïques forées au sommet de deux core complexes océaniques sur la dorsale Médio-Atlantique (30°N et 15°45N).

Chapitre 2

Étude microstructurale et géochimique in-situ des troctolites riches en olivine du Puits IODP U1309D (dorsale Médio- Atlantique, 30°N)

I. Introduction

1. Le Massif Atlantis

Le Massif Atlantis, formé il y a 1,5 à 2 Ma, se situe sur le flanc ouest de la vallée médiane de la dorsale Médio-Atlantique à 30°N, à l'intersection avec la transformante Atlantis (Figure 2.1a). Ce massif s'étend sur environ une vingtaine de kilomètres le long de l'axe de la dorsale et dix à quinze kilomètres perpendiculairement à celle-ci (Figure 2.1b). Le site a été étudié pour la première fois en détail en 1996 lors d'une campagne du *R/V Charles Darwin* au cours de laquelle des échantillons ont été dragués et des données sonar ont été collectées (Cann et al., 1997 ; Blackman et al., 1998, 2002; Schroeder & John, 2004). Une autre campagne, *MARVEL 2000 (Novembre-Décembre 2000)*, a été effectuée sur ce massif afin de compléter les données préexistantes. Un total de 137 échantillons a alors été récolté durant 15 plongées du submersible *Alvin* (Blackman et al., 2002).

La partie centrale de ce massif (Figure 2.2), cannelée (cannelure d'une longueur d'onde d'environ 1000m, d'une amplitude d'une dizaine de mètres et d'une longueur de quelques kilomètres) présente des caractéristiques morphologiques et géophysiques typiques d'un core complexe océanique exhumé par une faille de détachement à faible pendage (Cann et al., 1997 ; Blackman et al., 1998, 2002 ; Schroeder & John, 2004). Le mur de la faille (compartiment sous le plan de faille), exhumé par la faille de détachement, est composé de roches de la croûte inférieure et du manteau supérieur. Le « bloc volcanique » composé de basalte à l'est du massif est interprété comme le toit de la faille de détachement (compartiment au-dessus du plan de faille ; Figure 2.2).

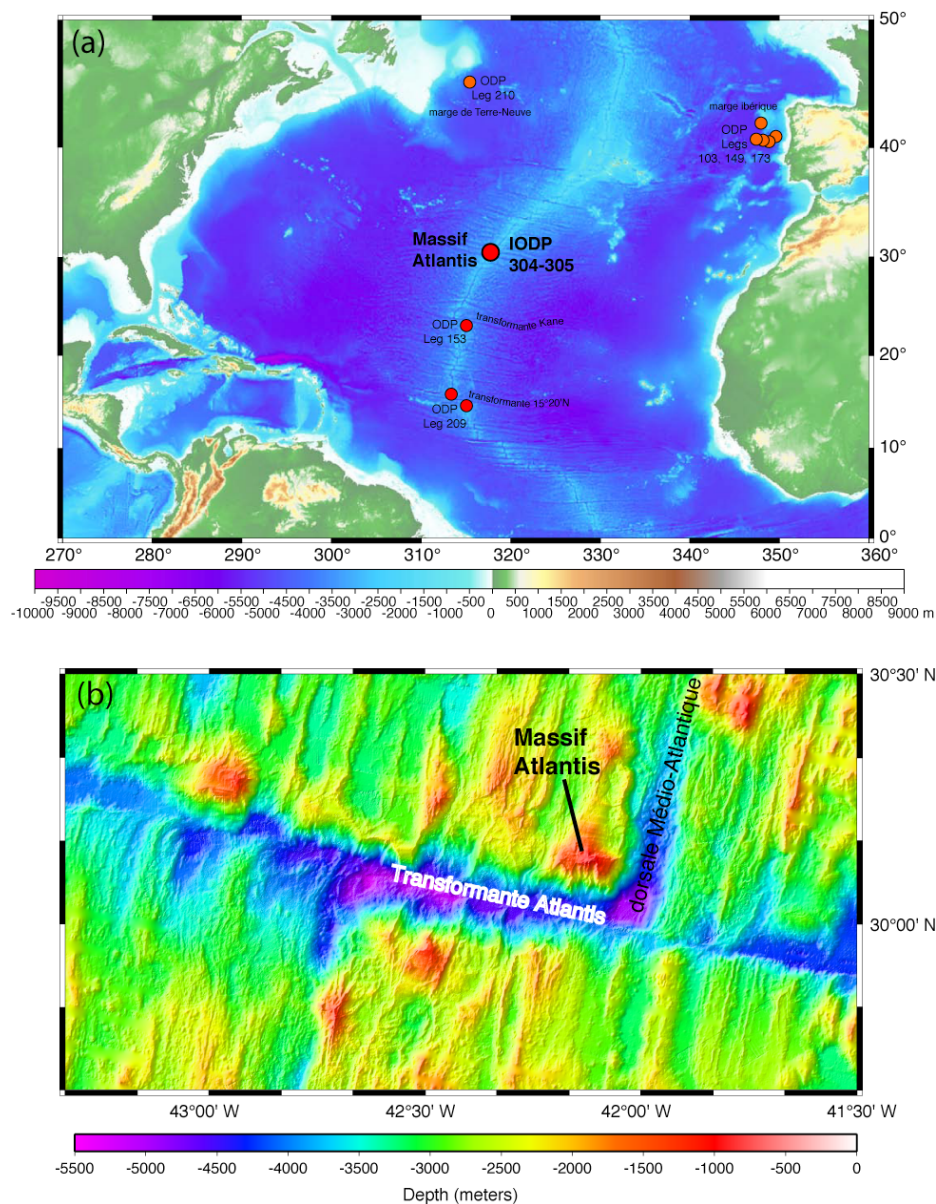


Figure 2.1 : (a) Carte bathymétrique de la dorsale Médio-Atlantique et localisation du massif Atlantis. Les points rouges indiquent la localisation des différentes campagnes de forages ODP effectuées dans l'Atlantique ; (b) Carte bathymétrique de la zone d'étude montrant le Massif Atlantis à l'intersection de la Faille Transformante Atlantis avec l'axe de la dorsale Médio-Atlantique (Blackman et al., 1998).

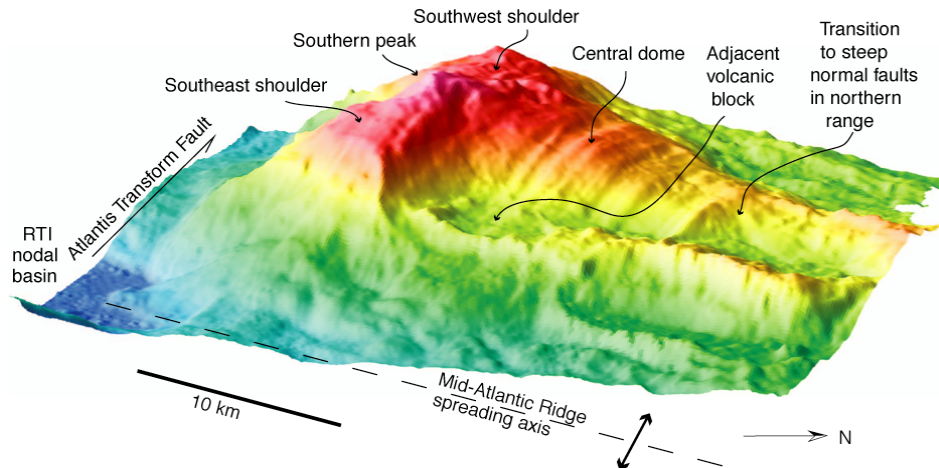


Figure 2.2: Morphologie du Massif Atlantis (Blackman et al., 2002).

Les résultats des deux campagnes océanographiques de 1996 et 2000 montrent que le Massif Atlantis est le siège d'anomalies gravimétriques de Bouguer positives indiquant la présence de roches, en son cœur, ayant des densités élevées (Blackman et al., 1998, 2002 ; Nooner et al., 2003). De même, les vitesses sismiques apparaissent élevées (8Km/s) à faible profondeur sous le plancher océanique (< 1Km), suggérant que l'intérieur du massif est composé de péridotites très peu altérées (Detrick et al., 1998 ; Canales et al., 2004). Les échantillons dragués lors de la campagne de 1996, au niveau du dôme central et du mur sud, comprennent des péridotites serpentinisées et des gabbros en proportion variable (Figure 2.3). Les roches échantillonnées avec le sous-marin *Alvin* sont en majorité des fragments de péridotites serpentinisées et des metabasaltes au niveau du dôme central (Figure 2.3 ; Cann et al., 2001 ; Blackman et al., 2002). Des serpentinites sont principalement échantillonnées sur le mur sud. Ces roches sont fréquemment recoupées par des veines gabbroïques fortement altérées, composées principalement de talc, trémolite, et chlorite (Früh-Green et al., 2001 ; Schroeder et al., 2002). Des schistes à talc dérivés des péridotites sont aussi présents sur le mur sud et délimitent la zone de détachement (Boschi et al., 2006).

Ces différentes données géophysiques et pétrologiques ont conduit à l'interprétation selon laquelle le massif a été formé probablement pendant un stade magmatique très limité, et a été le siège d'une tectonique extensive importante allant jusqu'à l'exhumation des roches mantelliques.

Les résultats des expéditions de forage IODP 304 et 305, en 2005 (voir ci-dessous), ont battu cette hypothèse en brèche, puisque les roches récupérées jusqu'à 1415 mètres de profondeur sont pour l'essentiel des gabbros.

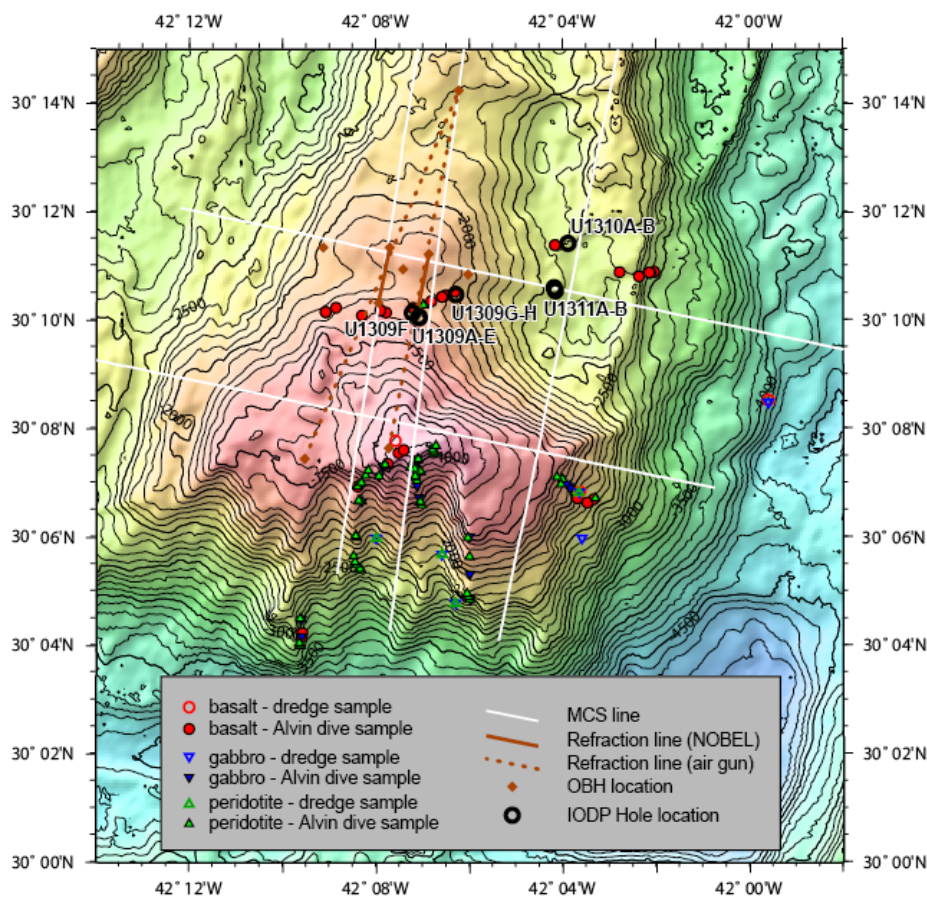


Figure 2.3: Carte du Massif Atlantis présentant les différentes données pétrologiques, les lignes sismiques ainsi que la localisation des différents puits forés lors de l'expédition IODP 304/305 (Blackman et al., 2006).

Une nouvelle analyse des données gravimétriques (Blackman et al., 2008) montre que les anomalies gravimétriques de Bouguer positives centrées sur le Massif Atlantis peuvent être interprétées différemment et sont compatibles avec la présence de roches essentiellement mafiques juste sous le plancher océanique (densité des gabbros = $2800-2900 \text{ kg/m}^3$). L'absence sur le dôme, d'une croûte supérieure basaltique ayant une densité plus faible ($\sim 2600 \text{ kg/m}^3$), ainsi que la présence des basaltes au toit de la faille immédiatement à l'est du dôme fournissent assez de contraste pour expliquer ces fortes anomalies gravimétriques. L'hypothèse d'un cœur gabbroïque pour le Massif Atlantis est aussi supportée par les modèles tomographiques plus récents de Canales et al. (2008) qui montrent de large corps gabbroïques (dizaine à centaine de km^2) inégalement distribués au sein des péridotites serpentinisées sous le dôme central du Massif Atlantis. Par contre, la lithosphère composant le sud du massif apparaît majoritairement ultramafique.

2. Les expéditions IODP 304 et 305

Les Expéditions IODP 304 et 305 (Nov. 2004 – Mars 2005; Blackman et al., 2006) ont permis de forer la lithosphère océanique présente au cœur du Massif Atlantis. Ces expéditions ont été réalisées dans le but d'identifier les différents processus qui contrôlent la formation des core complexes océaniques. Plusieurs sites ont été forés dans deux secteurs différents (Figure 2.3) : un dans le mur de la faille sous la faille de détachement au niveau du dôme central (Site U1309), et l'autre au toit de la faille (Site U1310 et U1311). En raison des difficultés à forer sur les deux derniers sites, le forage de ceux-ci a finalement été abandonné.

Site U1309

Deux puits profonds (U1309B à 30°10,11'N ; 42°07,11'W et U1309D à 30°10,12'N ; 42°07,11'W) ont permis d'échantillonner la section crustale, et cinq puits de faible profondeur (U1309A et U1309E-U1309H) ont échantillonné la couverture sédimentaire et les premiers mètres de la surface du dôme central afin de vérifier l'hypothèse selon laquelle la surface du dôme coïncide avec la faille de détachement.

Le puits le plus profond (1415,5 m), U1309D, a été foré au cœur du Massif Atlantis, avec une récupération moyenne de 75%. La majorité des roches récupérées (plus de 96%) sont de types gabbroïques, recoupées localement par des intrusions de diabases et de basaltes (Figure 2.4 et 2.6). Des péridotites sont aussi présentes, en très faible quantité (quelques dizaines de cm), dans les 180 premiers mètres du puits (Figure 2.6).

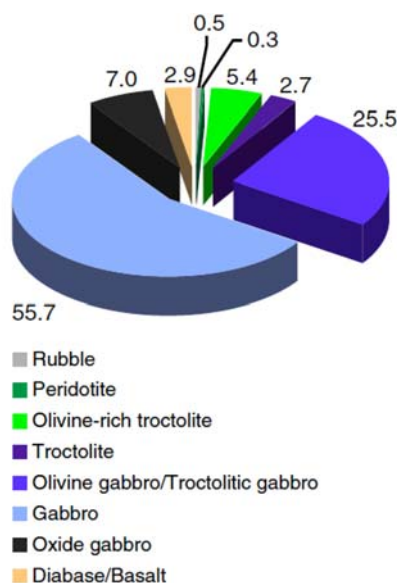


Figure 2.4 : Proportion de chaque lithologie échantillonnée dans le puits IODP U1309D (Blackman et al., 2006)

Ces péridotites ont des compositions relativement fertiles similaires aux péridotites imprégnées échantillonnées au niveau de la zone de fracture 15-20 (Sites ODP 1270 et 1271 ; Kelemen et al., 2004 ; Paulick et al., 2006), avec des faibles Mg# (89-90) et des teneurs en Ni supérieures à 2300 ppm. D'autre part, les péridotites du Site U1309 se distinguent par des teneurs relativement élevées en éléments en trace se situant entre la composition en éléments en trace des gabbros et du manteau résiduel ($La_N/Yb_N = 0,4-0,8$ et $Yb = 0,2-0,66 \times$ chondrites). La présence de plagioclase interstitiel dans ces péridotites suggère qu'un liquide magmatique ait pénétré ces roches. La composition chimique des péridotites, ainsi que leur texture suggèrent donc que ces roches ont interagi avec des magmas basaltiques.

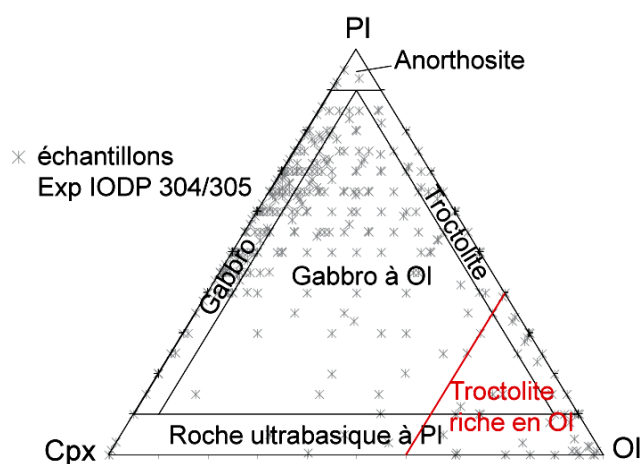


Figure 2.5 : Diagramme de classification des roches plutoniques selon leur composition modale (Strekeisen) dans lequel sont reportées les roches gabbroïques des expéditions IODP 304/305.

Les troctolites riches en olivine représentent 5,4% des roches récupérées dans le puits U1309D. Le terme « troctolite riche en olivine » regroupe différentes lithologies (dunite, wehrlite, troctolite) ayant en commun une texture poecilitique, plus de 60% d'olivines et une proportion variable de plagioclase, clinopyroxène et spinelles (Figure 2.5). La proportion des plagioclases et des clinopyroxènes variant à l'échelle du centimètre, il apparaît difficile d'appliquer la nomenclature standard des roches ultrabasiques ou plutoniques d'où l'adoption d'une appellation commune décrivant aussi bien la texture que la minéralogie de ces roches. Les troctolites riches en olivine sont interlitées au sein des séries gabbroïques, en contact soit franc soit diffus avec les gabbros. Elles ont été récupérées dans 22 intervalles de ~ 40 cm à 12m d'épaisseur le long du puits U1309D (Tableau 2.1). Entre 1092 et 1236 mbsf (meters below seafloor / mètres sous le plancher océanique) les troctolites riches en olivines sont la lithologie dominante. Les troctolites riches en olivines représentent le terme le plus primitif

de la série gabbroïque échantillonnée au Site U1309 et pourraient donc représenter le premier stade de cristallisation de la série gabbroïque. Ces roches ont des concentrations faibles en SiO₂ (< 45%), TiO₂ (< 0,1%) et en éléments en trace (Yb 0.06-0.8 ppm) mais présentent des Mg# élevés (82-89). Les troctolites riches en olivines chevauchent en composition les péridotites échantillonnées au Massif Atlantis et les péridotites imprégnées forées le long de la dorsale Médio-Atlantique (e.g., Site ODP 1271 à 15°20'N).

| Intervalle | Haut (mbsf) | Bas (mbsf) | Épaisseur (m) | Longueur de la carotte (m) | Récupération (m) | Numéro de la carotte |
|------------|-------------|------------|---------------|----------------------------|------------------|---------------------------|
| 1 | 132.42 | 133.76 | 1.34 | 1.34 | 1.00 | 23R1-142cm à 23R2-126cm |
| 2 | 311.69 | 320.02 | 8.33 | 5.66 | 0.68 | 60R2-36cm à 62R1-42cm |
| 3 | 324.51 | 336.05 | 11.54 | 7.84 | 0.68 | 63R1-11cm à 65R2-55cm |
| 4 | 339.58 | 342.18 | 2.60 | 2.60 | 1.00 | 66R1-78cm à 66R3-38cm |
| 5 | 496.60 | 497.88 | 1.28 | 1.28 | 1.00 | 100R1-0 à 128cm |
| 6 | 553.22 | 554.13 | 0.91 | 0.91 | 1.00 | 111R3-108cm à 111R4-56cm |
| 7 | 669.44 | 671.35 | 1.91 | 1.89 | 0.99 | 136R1-4cm à 136R2-58cm |
| 8 | 689.51 | 690.97 | 1.46 | 1.46 | 1.00 | 140R2-0 à 146cm |
| 9 | 1093.7 5 | 1097.75 | 4.00 | 3.47 | 0.87 | 227R2-32cm à 228R1-95cm |
| 10 | 1098.0 1 | 1100.19 | 2.18 | 2.18 | 1.00 | 228R2-0cm à 228R3-68cm |
| 11 | 1115.3 7 | 1116.19 | 0.82 | 0.82 | 1.00 | 232R1-27 à 109cm |
| 12 | 1121.9 1 | 1130.62 | 8.71 | 7.73 | 0.89 | 233R2-51cm à 235R1-112cm |
| 13 | 1130.8 8 | 1137.00 | 6.12 | 4.63 | 0.76 | 235R2-12cm à 236R2-135cm |
| 14 | 1139.7 1 | 1145.13 | 5.42 | 2.49 | 0.46 | 237R1-61cm à 238R1-123cm |
| 15 | 1154.6 5 | 1159.62 | 4.97 | 3.00 | 0.60 | 240R1-115cm à 241R1-132cm |
| 16 | 1159.9 5 | 1160.90 | 0.95 | 0.95 | 1.00 | 241R2-18 à 113cm |
| 17 | 1161.2 7 | 1163.80 | 2.53 | 0.77 | 0.30 | 241R3-0cm à 242R1-70cm |
| 18 | 1164.7 5 | 1168.29 | 3.54 | 1.03 | 0.29 | 242R2-38cm à 243R1-39cm |
| 19 | 1187.1 2 | 1187.59 | 0.47 | 0.47 | 1.00 | 247R1-2 à 49cm |
| 20 | 1188.2 7 | 1196.50 | 8.23 | 7.17 | 0.87 | 247R1-117cm à 248R4-58cm |
| 21 | 1230.3 4 | 1230.77 | 0.43 | 0.43 | 1.00 | 256R1-4 à 47cm |
| 22 | 1231.4 2 | 1235.84 | 4.42 | 3.11 | 0.70 | 256R1-112cm à 257R1-74cm |

Tableau 2.1 : Intervalles de troctolites riches en olivine le long du puits U1309D

Les gabbros et les gabbronorites sont le type de roches récupérées le plus abondant (56%). La composition modale ainsi que la taille des grains peut varier fortement à l'échelle du cm dans ce groupe de roches, ainsi que la proportion d'olivine, d'oxydes ferro-titanés et/ou d'orthopyroxène. En dessous de 600 mbsf, on observe une proportion importante d'orthopyroxènes dans les gabbros (orthopyroxène >5%). Intercalés au sein des gabbros, se trouvent des gabbros à olivine (28%) avec une proportion d'olivine variant de 5 à 50%. Le mode de ces roches étant fortement variable à l'échelle décimétrique, les gabbros à olivine évoluent localement vers des gabbros troctolitiques et des troctolites. Les gabbros, les gabbronorites et les gabbros à olivine du puits IODP U1309D avec des Mg# élevés (60-86) ont des compositions qui sont parmi les plus primitives des roches forées le long de la dorsale Médio-Atlantique (zone MARK, 23°N ; Agar et al., 1997 et 15°20'N ; Kelemen et al., 2004) et à la dorsale Sud-Ouest Indienne (Puits ODP 735B ; Dick et al., 1999).

Les gabbros à oxyde, définis par une proportion modale en oxydes ferro-titanés supérieure à 2%, représentent 7,7% des roches forées. Les oxydes se rencontrent majoritairement sous forme d'amas d'une dizaine de millimètres à un centimètre dans des gabbros à gros grains non-déformés (~ 80% des gabbros à oxyde). Ils sont aussi concentrés dans des filonets recoupant d'autres lithologies de façon diffuse ou nette, ou encore, moins fréquemment, associés à des zones de déformation ductiles. Une concentration importante d'intrusions de gabbros à oxyde est observée entre 1170 et 1270 mbsf. Les gabbros à oxyde, avec les dykes leucocratiques, représentent les termes les plus évolués de la suite gabbroïque avec des faibles Mg# (<50) et des teneurs élevées en éléments en trace (Yb = 1,2-26 ppm). La composition chimique de ces roches suggère qu'elles ont précipité à partir de liquides magmatiques différenciés.

Les contacts entre différentes lithologies, lorsqu'ils sont visibles, suggèrent que les gabbros sont généralement intrusifs dans les lithologies riches en olivines (gabbros à olivine et troctolites) et ces roches sont elles-mêmes recoupées par des veines felsiques et par les gabbros à oxyde qui représentent les roches gabbroïques les plus évoluées du puits U1309D.

L'ensemble de la carotte est modérément altéré dans des conditions de métamorphisme allant du faciès granulite au faciès zéolite. L'altération décroît vers le bas du puits et les troctolites riches en olivine sont, entre 1090 et 1236 mbsf, localement presque exemptes de toutes traces d'altération. La déformation magmatique, associée à la mise en place de la séquence gabbroïque du Puits U1309D, est toujours faible et affecte seulement 22% de la carotte. La déformation en conditions du faciès amphibolite est quasiment absente.

Plus généralement, le puits IODP U1309D se distingue par une déformation ductile rare, contrairement au puits ODP 735B foré sur la dorsale Sud-Ouest Indienne (Dick et al., 1999).

Cinq intervalles avec des inclinaisons magnétiques différentes ont été identifiés à partir des données magnétiques de rémanence (Figure 2.6 ; Blackman et al., 2006). Les limites entre ces groupes coïncident généralement avec des zones de failles ou de cisaillement (Figure 2.6). Ces différences d'inclinaisons par rapport à l'inclinaison attendue indiquent une histoire tectonique complexe pour la série gabbroïque échantillonnée. Au vue de ces résultats, la simple rotation d'un seul bloc du mur de la faille apparaît donc improbable.

L'analyse des âges de cristallisation des zircons provenant de différents échantillons le long du puits indiquent que la section de croûte échantillonnée s'est construite pendant ~ 200 mille ans (Grimes et al., 2008) par l'emplacement à différentes profondeurs sous la vallée axiale de multiples intrusions gabbroïques d'une dizaine de mètres (Blackman et al., 2006 ; Grimes et al., 2008 ; Godard et al., sous-presse).

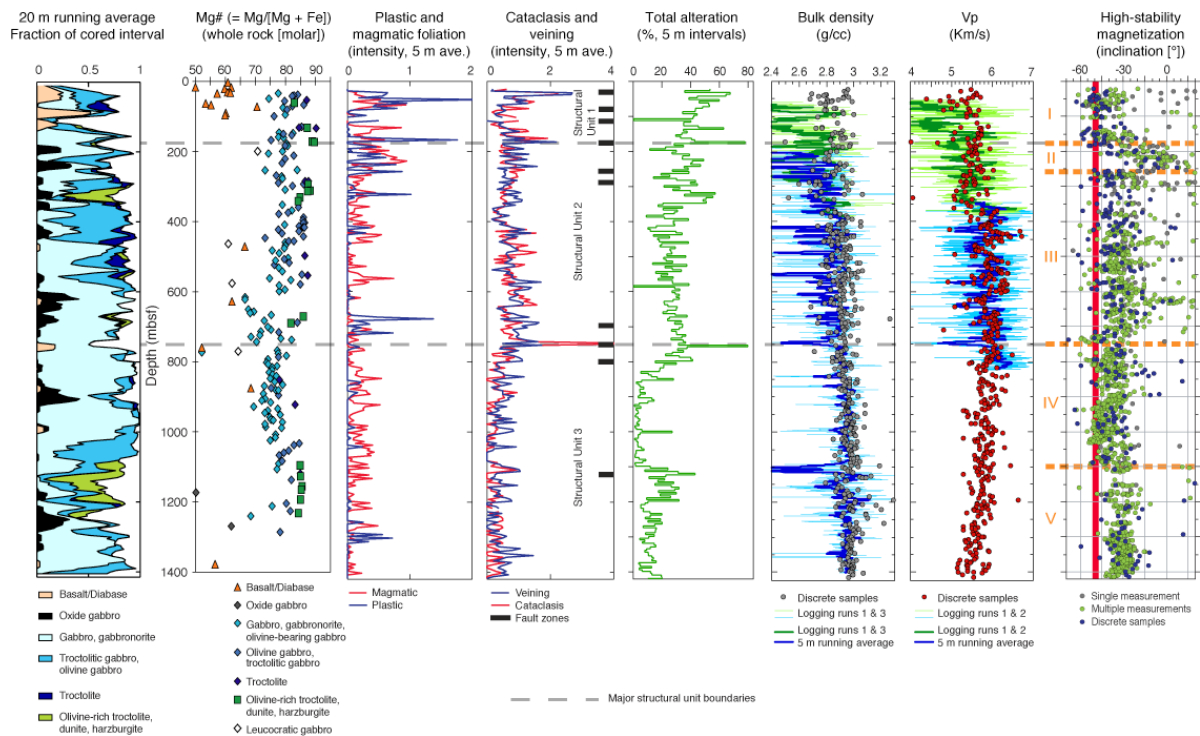


Figure 2.6: Variations le long du Puits IODP U1309D, du Mg# des roches totales, de la déformation magmatique et plastique, des veines d'altération, de l'altération, de la densité, et de l'inclinaison paléomagnétique des différents échantillons prélevés (Ildefonse et al., 2006).

Les puits U1309B et U1309D ne sont éloignés que de 20 mètres et pourtant le prolongement des unités magmatiques, métamorphiques et structurales entre les deux puits est

difficile à réaliser à petite échelle (< 10m ; Blackman et al., 2006). L'hétérogénéité latérale est donc très importante au cœur du Massif Atlantis.

Les roches récupérées dans les puits de faible profondeur U1309A et U1309E-U1309H sont principalement des sédiments et des fragments de basalte. Toutefois, dans le puits U1309H des fragments de diabase et de schiste à talc et trémolite ont été récupérés, ces derniers étant caractéristiques de la faille de détachement exposée sur le Massif Atlantis (Boschi et al., 2006). La présence de ces roches confirme l'hypothèse selon laquelle la surface cannelée du dôme central correspond à la surface de la faille de détachement.

3. Caractéristiques pétrologiques et texturales des roches étudiées

Sur la base d'observations texturales et de l'abondance modale, j'ai divisé mes échantillons en trois groupes : les troctolites riches en olivine, les troctolites, et les gabbros. Les principales caractéristiques pétrologiques et texturales de ces échantillons sont détaillées dans cette partie et résumées dans le tableau 2.2. Les conséquences, en termes de processus pétrogénétiques, découlant des observations pétrologiques de ces différentes roches, seront plus amplement débattues dans les parties 2 et 3 de ce chapitre. Les photographies des lames minces des échantillons sont disponibles en annexe de ce manuscrit.

Les troctolites riches olivines

Les troctolites riches en olivine sont composées de 64 à 85% d'olivines, 2 à 24 % de plagioclases et de 1 à 30 % de clinopyroxènes et 0,5% de spinelles. Ces roches se distinguent des autres roches gabbroïques échantillonnées dans le puits U1309D par des textures poecilites similaires aux textures d'hétéradcumulats (Figure 2.7): de larges cristaux poecilites de plagioclase et de clinopyroxène englobent des cristaux d'olivines plus ou moins arrondis. L'orthopyroxène a aussi été identifié dans un échantillon sous forme de large cristal poeciloblastique entourant les olivines. Les troctolites riches en olivines sont fortement serpentinisées dans la zone 1, au sommet du puits (30 à 90 % d'altération ; Tableau 2.2). Par contre les troctolites riches en olivine de la zone 4, dans le bas du puits, sont très peu serpentinisées (< 5% d'altération ; Tableau 2.2). Les minéraux composant les troctolites riches en olivine ne montrent pas ou très peu d'orientations préférentielles de forme ; aucune foliation ou linéation n'est visible dans nos échantillons.



Figure 2.7 : Photo au microscope optique en lumière polarisée d'une troctolite riche en olivine (247R3_16-18). Le clinopyroxène forme une large plage poecilitique englobant des cristaux d'olivines plus ou moins arrondis.

Les olivines se rencontrent sous plusieurs formes dans les troctolites riches en olivines (Figure 2.7):

- 1- Des cristaux subautomorphes de grande taille, avec des sous-joints selon (100) bien développés et des bordures plus ou moins corrodées. Dans certains échantillons (e.g., 233R3_21-24 ; 247R3_62-66) ces cristaux sont allongés et leur axe le plus long est parallèle à l'axe [001]. La décoration des lames minces par oxydation à 900°C (Kohlstedt et al., 1976) révèle la présence de dislocations et de parois de dislocations dans ces cristaux d'olivines subautomorphes. Ceci implique que les olivines ont été déformées plastiquement par fluage des dislocations.
- 2- Des chaînes de cristaux polygonaux avec des bordures curvilignes, des sous-joints selon (100) bien développés et montrant très peu de misorientation entre eux. Le clinopyroxène ou le plagioclase, selon le cas, semble s'être infiltré dans l'espace existant entre les bordures des cristaux adjacents.
- 3- Des cristaux arrondis de taille moyenne avec très peu ou pas de sous-structures et en continuité cristallographique avec les cristaux subautomorphes de grandes tailles. Ces cristaux d'olivines apparaissent dispersés au sein des larges plages de plagioclase et de clinopyroxène et semblent en partie assimilés.

Les cristaux d'olivine apparaissent beaucoup plus dispersés « au centre » des larges plages de plagioclases ou de clinopyroxène que sur « leur bordure » (Figure 2.7). Notons aussi la présence d'inclusions fluides de taille micrométrique dans la majorité des olivines sous forme

de traînées. Les inclusions fluides sont toutefois beaucoup plus rares dans les petits cristaux arrondis d'olivine.

Les plagioclases et les clinopyroxènes forment de grandes plages poecilitiques non-déformées (Figure 2.7). Ceci implique que ces minéraux ont cristallisé une fois que la déformation qui a affecté les olivines était terminée. Dans certaines troctolites riches en olivines, le clinopyroxène et le plagioclase sont interstitiels et forment une texture pénétrative similaire à la texture d'imprégnation observée dans les dunites de la zone de transition manteau/croûte des ophiolites (e.g., Boudier & Nicolas, 1995, Dijkstra et al., 2003) ou dans les péridotites abyssales (e.g., Takazawa et al., 2007). Dans la zone 3 d'échantillonnage, certaines troctolites riches en olivine (e.g., 136R1_35-39; 136R2_37-40) sont composées de larges clinopyroxènes (5 mm à 1.5 cm) entourant les cristaux d'olivine corrodés. Le plagioclase dans ces échantillons est généralement interstitiel. Les clinopyroxènes semblent donc avoir cristallisé avant ce dernier. L'ordre de cristallisation de ces échantillons est dans ce cas-là : Olivine-clinopyroxène-plagioclase (Tableau 2.2).

Les spinelles chromifères se présentent sous forme de petits cristaux polygonaux subautomorphes (0.5mm) inclus dans l'olivine, le clinopyroxène ou le plagioclase.

Séquence de cristallisation :

Dans les troctolites riches en olivine, les cristaux d'olivine corrodés semblent avoir été assimilés par les larges cristaux poeciloblastiques de plagioclases et de clinopyroxènes les entourant, indiquant donc un processus en déséquilibre. Le plagioclase et le clinopyroxène ont cristallisé à partir d'un liquide interstitiel dans l'espace existant entre les cristaux d'olivine avec lesquels il a certainement réagi. Les relations texturales entre les différentes phases minérales des troctolites riches en olivine montrent donc clairement que les plagioclases et les clinopyroxènes sont plus tardifs que les olivines. De plus, plagioclase et clinopyroxène semblent avoir cristallisé plus ou moins simultanément.

Relation avec les gabbros:

Les troctolites riches en olivine que j'ai échantillonnées sont souvent recoupées par des filonets gabbroïques. Les cristaux de plagioclases et de clinopyroxènes qui constituent ces filonets sont souvent résorbés et semblent « imprégner » les troctolites riches en olivine (Figure 2.8). Les troctolites riches en olivine sont aussi en contact soit franc (Figure 2.9) soit irrégulier (Figure 2.10) avec des gabbros. Dans le deuxième cas, les plagioclases et/ou les

clinopyroxènes semblent infiltrer les troctolites riches en olivine, et le changement de type de roche est surtout un changement modal et de taille des minéraux.



Figure 2.8 : Exemple de filonet gabbroïque pénétratif dans une troctolite riche en olivine. Carotte 233R3_31-51.



Figure 2.9 : Exemple de contact franc entre un gabbro (à gauche) et une troctolite riche en olivine (à droite). Carotte 235R2_0-28.



Figure 2.10 : Exemple de contact irrégulier entre une troctolite riche en olivine (à gauche) et un gabbro (à droite). Carotte 243R1_24-48.

Variation le long du puits :

La forme des olivines varie entre les différentes zones échantillonnées : dans les zones 1, 2 et 3 les olivines sont majoritairement subautomorphes alors que dans la zone 4 les olivines sont beaucoup plus rondes (Tableau 2.2). De même, les plagioclases sont

majoritairement interstitiels dans les zones 1, 2 et 3 et poecilites dans la zone 4 (Tableau 2.2). Les clinopyroxènes sont quant à eux majoritairement poecilites sauf dans la zone 1 (Tableau 2.2).

Les troctolites

Les troctolites sont composées de 45 à 64% d'olivines, 27 à 40 % de plagioclases et de 2 à 15 % de clinopyroxènes et 0,5 % de spinelles. Ces roches montrent des textures de mésocumulats avec l'olivine et le plagioclase en phase cumulus et le clinopyroxène en phase intercumulus (Figure 2.11). Aucune foliation n'est visible dans ces roches. Les troctolites ont principalement été échantillonnées dans la zone 1, où l'altération est assez importante. Toutefois, les troctolites sont un peu moins serpentinisées que les troctolites riches en olivine du fait de la présence en plus faible quantité d'olivines.

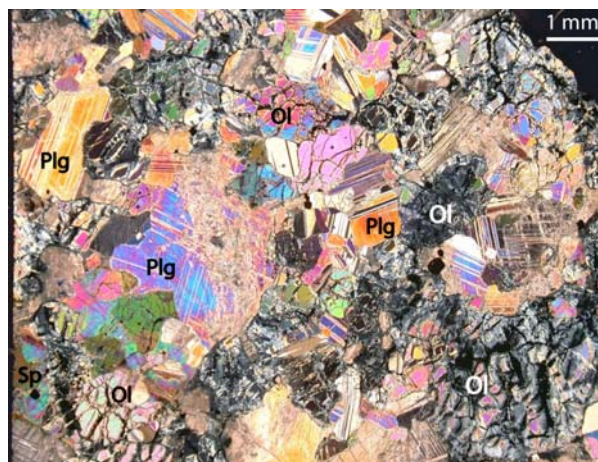


Figure 2.11 : Photo au microscope optique en lumière polarisée d'une troctolite (70R3_20-24). Les olivines, fortement serpentinisées, se présentent sous forme d'agrégats. Les plagioclases sont résorbés et entourent l'olivine.

Les olivines se présentent sous forme de cristaux subautomorphes de 1 à 2 mm partiellement à fortement serpentinisées (Figure 2.11). Certaines olivines sont très grosses et semblent avoir continué à grandir. La majorité des olivines des troctolites possèdent des sous-joints selon (100) bien définis. La technique de décoration a permis de mettre en évidence la présence de dislocations et de parois de dislocation dans la plupart des olivines (Figure 2.12). Ceci implique que les olivines ont été déformées plastiquement par fluage des dislocations.

Les plagioclases se présentent sous forme de lattes automorphes à subautomorphes de 2 à 4 mm trapues ou allongées (Figure 2.11). Les contours de ces cristaux sont généralement

résorbés. Les clinopyroxènes sont interstitiels et enveloppent l'olivine. Les spinelles se présentent sous forme de petits cristaux subautomorphes (0,5 mm) associés avec les olivines. Leur cristallisation est donc contemporaine de celle des olivines.

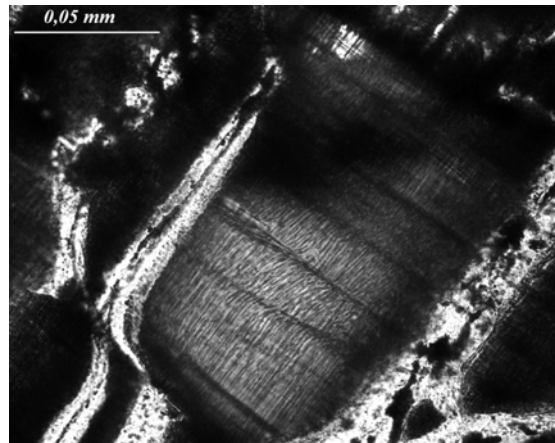


Figure 2.12 : Photo au microscope optique montrant la présence de dislocations et de parois de dislocation dans une olivine d'une troctolite (70R2_99-103).

Séquence de cristallisation :

Dans les troctolites, les olivines sont partiellement incluses dans les plagioclases. Le clinopyroxène est en position intercumulus, il occupe les interstices entre les olivines et les plagioclases. Ces relations texturales montrent une cristallisation sub-contemporaine des plagioclases et des olivines avec une précipitation légèrement plus précoce des olivines. Les clinopyroxènes sont tardifs. L'ordre de cristallisation est donc le suivant : Spinelle+Olivine – plagioclase - clinopyroxène.

Les gabbros

Le groupe des gabbros comprend deux lithotypes : les gabbros composés de 40 à 70% de plagioclases, de 25 à 60% de clinopyroxènes et moins de 5 % d'olivines et les gabbros à olivine qui se distinguent par la présence de plus de 5% d'olivines. Ces roches se distinguent des troctolites riches en olivine et des troctolites par l'absence de spinelles. Les gabbros et les gabbros à olivine possèdent une texture d'adcumulat typique des roches gabbroïques océaniques (Figure 2.13). Ces roches sont peu altérées, voir très fraîches dans la zone 4 (< 5% d'altération). Aucune foliation n'est visible dans nos échantillons.

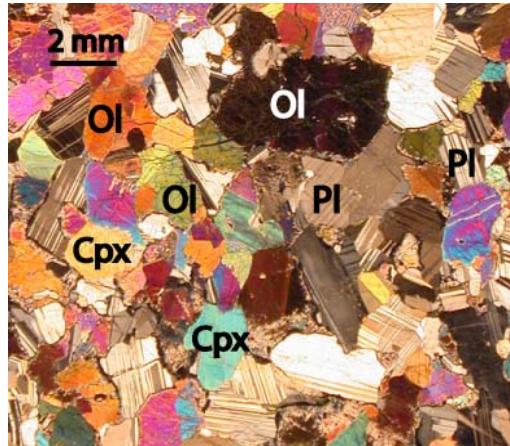


Figure 2.13 : Photo au microscope optique en lumière polarisée d'un gabbro à olivine avec une texture d'adcumulat (117R1_55-57).

Dans les gabbros, les clinopyroxènes se présentent sous forme de larges tablettes irrégulières de 2 mm à 1 cm avec de nombreuses lamelles d'exsolution d'orthopyroxène. Dans les gabbros à olivine, les clinopyroxènes sont xénomorphes et résorbés (Figure 2.13).

Les cristaux de plagioclases, phases majeures dans les gabbros et les gabbros à olivine, sont subautomorphes et généralement se présentent sous forme de lattes trapues à allongées de 1 mm à 1 cm (Figure 2.13).

Les olivines se présentent sous forme de cristaux lobés subautomorphes, généralement formant des agrégats avec les clinopyroxènes (Figure 2.13). La plupart des olivines des gabbros à olivine possèdent des sous-joints selon (100) bien définis. La présence de ces sous-joints indique une déformation plastique de ces olivines.

Séquence de cristallisation :

Les minéraux des gabbros et des gabbros à olivines semblent avoir grandi en même temps. Toutes les phases devaient être au liquidus en même temps. L'olivine en étant incluse dans les clinopyroxènes a sûrement cristallisé un petit peu avant. La cristallisation du clinopyroxène et du plagioclase est quant à elle contemporaine. L'ordre de cristallisation est donc le suivant : olivine – plagioclase – clinopyroxène. Cette séquence de cristallisation est typique des cumulats océaniques cristallisant à partir d'un MORB à faible pression (< 2kbar; Green & Ringwood, 1967; Grove & Bryan, 1983; Tormey et al., 1987; Juster et al., 1989; Grove et al., 1992).

En résumé, les troctolites et les gabbros montrent une séquence de cristallisation d'un MORB classique. Ceci indique que ces roches ont cristallisé à basse pression, c'est-à-dire dans la croûte océanique. Leur texture est similaire à celle des cumulats océaniques échantillonnés aux dorsales lentes. Les troctolites riches en olivine se distinguent par une texture poecilitique, en déséquilibre où le plagioclase et le clinopyroxène semblent cristalliser tardivement. Il est important de noter que le clinopyroxène est présent dans toutes les lithologies échantillonnées, même dans les troctolites riches en olivine, les plus primitives. Or l'ordre de cristallisation, généralement admis, d'un liquide de type MORB est : olivine, puis olivine-plagioclase et enfin olivine-plagioclase-clinopyroxène (Green and Ringwood, 1967; Grove and Bryan, 1983; Tormey et al., 1987; Juster et al., 1989; Grove et al., 1992). Cette observation semble confirmer la cristallisation tardive des clinopyroxènes dans les troctolites riches en olivine et implique une histoire complexe de cristallisation pour ces roches, certainement en plusieurs étapes. L'origine de ces roches ainsi que leur pétrogenèse et leur relation avec les roches gabbroïques auxquelles elles sont associées, sont discutées dans les deux parties suivantes.

II. Preuve géochimique et pétrographique d'une imprégnation magmatique de la lithosphère océanique au Massif Atlantis, dorsale Médio-Atlantique (Puits IODP U1309D, 30°N)

La composition globale du Puits U1309D montre que les roches gabbroïques sont appauvries en éléments en trace les plus incompatibles comme le Ba (40%), le Nb (40%) ou les Terres Rares (Ce =70%, Yb =95%) et enrichies en éléments compatibles et en éléments réfractaires comme Mg (120%), Ni (200%) ou Cr (200%) par rapport à la composition estimée des MORB parents ou des liquides primaires de la littérature (Godard et al., sous-*presse*). Ces différences de compositions pourraient s'expliquer par une surestimation de la proportion du terme le plus primitif ou une sous-estimation de la proportion des termes les plus évolués. Les calculs ont donc été refaits en enlevant les troctolites riches en olivine. La composition globale du Puits U1309D se rapproche dans ce cas-là de la composition des liquides primaires. Toutefois, la teneur globale en magnésium des roches gabbroïques du puits U1309D reste élevée. Cet excès de magnésium pourrait indiquer une interaction chimique importante, probablement durant la première phase de formation du corps gabbroïque du Site U1309, entre le magma parent et un composant riche en olivines. En effet, l'assimilation par les magmas ascendants d'olivines peut modifier la composition des liquides qui deviennent plus riches en magnésium et cristallisent donc des gabbros avec un Mg# élevé (Kvassnes & Grove, 2008 ; Lissenberg & Dick, 2008). Ce composant pourrait être un cumulat riche en olivine, formé avant l'emplacement du corps gabbroïque étudié, ou des péridotites mantelliques. Les troctolites riches en olivine pourrait représenter le résidu ultime de ce processus de réaction- assimilation entre le magma parent et la lithosphère intrudée.

Les variations chimiques observées en roche totale sont le résultat d'un effet de mode et de composition des minéraux. Il apparaît donc nécessaire de réaliser des analyses in situ des troctolites riches en olivine et des roches gabbroïques qui leur sont associées dans le puits U1309D, afin d'accéder à la composition des liquides en équilibre avec les différentes phases en présence et de contraindre l'histoire de ces roches. Nous avons donc mesuré les compositions en éléments majeurs et en trace des différents minéraux constituant les troctolites riches en olivine et les gabbros associés provenant de quatre intervalles riches en olivine le long du Puits U1309D. Les résultats de cette étude sont détaillés dans un article

accepté à Chemical Geology qui constitue la deuxième partie de ce chapitre. Ce travail montre que les troctolites riches en olivine ne représentent pas la première étape de différenciation d'un liquide basaltique mais qu'elles sont le résultat d'interactions magma/roche intenses :

1- La texture poecilitique des troctolites riches en olivines, avec l'olivine entourée par de larges cristaux de clinopyroxènes et de plagioclase, ainsi que la signature géochimique des olivines en déséquilibre avec des MORBs primaires montrent que les olivines se sont formées avant le processus magmatique qui a cristallisé les clinopyroxènes et les plagioclases. De plus la texture corrodée des olivines suggère que les magmas aient en parti assimilé cette phase.

2- Dans toutes les lithologies étudiées, les clinopyroxènes et les plagioclases ont des concentrations en éléments en trace similaires. Cette composition homogène en éléments en trace pourrait être expliquée par un apport constant de liquides indifférenciés dans les intervalles riches en olivine lors de la cristallisation des plagioclases et des clinopyroxènes.

3- Nous observons un enrichissement en élément en trace incompatible du cœur vers la bordure des clinopyroxènes et dans les clinopyroxènes interstitiels qui n'est pas en accord avec un processus simple de cristallisation fractionnée. Cette variation de composition résulterait d'une différenciation des liquides percolant dans les derniers stades de formation des troctolites riches en olivines.

Geochemical and petrographic evidence for magmatic impregnation in the oceanic lithosphere at Atlantis Massif, Mid-Atlantic Ridge (IODP Hole U1309D, 30°N)

Marion Drouin^{1*}, Marguerite Godard¹, Benoit Ildefonse¹, Olivier Bruguier¹, Carlos J. Garrido²

¹Géosciences Montpellier, CNRS & Université Montpellier 2, F-34095 Montpellier cedex5, France.

² Instituto Andaluz de Ciencias de la Tierra (IACT), CSIC & UGR, Facultad de Ciencias, Fuentenueva sn. 18002 Granada, Spain.

Article accepté à Chemical Geology

Abstract

IODP Hole U1309D (Atlantis Massif, Mid-Atlantic Ridge 30°N) is the second deepest hole drilled into slow spread gabbroic lithosphere. It comprises 5.4% of olivine-rich troctolites (~ >70% olivine), possibly the most primitive gabbroic rocks ever drilled at mid-ocean ridges. We present the result of an *in situ* trace element study carried out on a series of olivine-rich troctolites, and neighbouring troctolites and gabbros, from olivine-rich intervals in Hole U1309D. Olivine-rich troctolites display poikilitic textures; coarse-grained subhedral to medium-grained rounded olivine crystals are included into large undeformed clinopyroxene and plagioclase poikiloblasts. In contrast, gabbros and troctolites have irregularly seriate textures, with highly variable grain sizes, and locally poikilitic clinopyroxene oikocrysts in troctolites. Clinopyroxene is high Mg# augite (Mg# 87 in olivine-rich troctolites to 82 in gabbros), and plagioclase has anorthite contents ranging from 77 in olivine-rich troctolites to 68 in gabbros. Olivine has high forsterite contents (82-88 in olivine-rich troctolites, to 78-83 in gabbros) and is in Mg-Fe equilibrium with clinopyroxene. Clinopyroxene cores and plagioclase are depleted in trace elements (e.g., $Yb_{cpx} \sim 5-11 \times \text{Chondrite}$), they are in equilibrium with the same MORB-type melt in all studied rock-types. These compositions are not consistent with the progressively more trace element enriched (evolved) compositions expected from olivine rich primitive products to gabbros in a MORB cumulate sequence. They indicate that clinopyroxene and plagioclase crystallized concurrently, after melts having the same trace element composition, consistent with crystallization in an open system with a buffered magma composition. The slight trace element enrichments and lower Cr contents

* email: marion.drouin@gm.univ-montp2.fr, phone: +33-4671443941, fax: +33-467143603

observed in clinopyroxene rims and interstitial grains results from crystallization of late-stage differentiated melts, probably indicating the closure of the magmatic system. In contrast to clinopyroxene and plagioclase, olivine is not in equilibrium with MORB, but with a highly fractionated depleted melt, similar to that in equilibrium with refractory oceanic peridotites, thus possibly indicating a mantle origin. In addition, textural relationships suggest that olivine was in part assimilated by the basaltic melts after which clinopyroxene and plagioclase crystallized (impregnation). These observations suggest a complex crystallization history in an open system involving impregnation by MORB-type melt(s) of an olivine-rich rock or mush. The documented magmatic processes suggest that olivine-rich troctolites were formed in a zone with large magmatic transfer and accumulation, similar to the mantle-crust transition zone documented in ophiolites and at fast spreading ridges.

Keywords: troctolite; gabbro; LA-ICP-MS; trace elements; olivine; Atlantis Massif; Mid Atlantic Ridge; Integrated Ocean Drilling Program, cumulate, crust, mantle.

1 Introduction

Slow spreading ridges (full-spreading rate $< 50\text{mm/yr}$), such as the Mid Atlantic Ridge (MAR), represent about half of Earth's mid-ocean ridges. In contrast to the layered fast-spread crust (Penrose Conference participants, 1972; Ildefonse et al., 2007b), slow-spread crust is highly heterogeneous with, at least in some places, discrete gabbroic bodies intruded into serpentinized peridotites (e.g., Lagabrielle and Cannat, 1990; Cannat, 1993; Cannat, 1996; Canales et al., 2000; Carlson, 2001). Ocean Drilling has provided deep access to gabbroic rocks emplaced at depth in this type of heterogeneous lithosphere in various oceanic core complexes (Ildefonse et al., 2007a).

During IODP Expeditions 304 and 305 (Blackman et al., 2006; Ildefonse et al., 2006), a 1415.5 meter deep hole was drilled at 30°N near the Mid-Atlantic Ridge (Fig.1). IODP Hole U1309D is the second deepest hole in slow-spread lithosphere, after ODP Hole 735B on the Southwest Indian Ridge (Dick et al., 2000). Hole U1309D is almost exclusively made of gabbroic rocks (Blackman et al., 2006). Compared to ODP Hole 735B and other drilled gabbroic series, IODP Hole U1309D gabbroic rocks comprise a relatively large proportion of olivine-rich lithologies. The most olivine rich ones ($\sim >70\%$) were grouped as olivine-rich troctolites, and represent 5.4% of the rocks recovered at Hole U1309D (Blackman et al.,

2006). Such a large proportion of primitive crustal lithologies had never been drilled before in present-day mid-ocean ridge crust.

Geochemical studies show that MORB have compositions too evolved to represent primary mantle melts (e.g., Bender et al., 1978; Fujii and Bougault, 1983; Falloon and Green, 1987). Primitive MORB melts are saturated in olivine, and should first crystallized olivine-rich primitive cumulate. However, along slow-spreading ridges (e.g., MARK area at 23°N on the Mid-Atlantic Ridge, and ODP Hole 735B on the Southwest Indian Ridge), the occurrence of primitive cumulate had not been reported yet (e.g., Ross and Elthon, 1997; Bloomer et al., 1989; Dick et al., 2000; Coogan et al., 2001). Because of their very primitive composition, Hole U1309D olivine-rich troctolites are potential candidates for being these “missing” cumulates, and they may provide new insights on the early stages of MORB differentiation. On the other hand, some olivine-rich troctolites have textures suggesting melt impregnation and extensive melt-rock reaction processes (Blackman et al., 2006). The latter are shown to be important processes in both the lower crust (e.g., Bédard et al., 2000; Ridley et al., 2006; Kvassnes and Grove, 2008; Lissenberg and Dick, 2008) and the upper mantle (e.g., Boudier and Nicolas, 1995; Niu and Hekinian, 1997; Godard et al., 2000; Niu, 2004; Paulick et al., 2006; Takazawa et al., 2007).

We carried out an *in situ* geochemical study of troctolites and olivine-rich troctolites sampled in four intervals of Hole U1309D in which these lithologies are dominant, and of gabbros sampled next to these intervals. This study aimed at providing geochemical constraints on the origin of the olivine-rich lithologies in slow-spread lithosphere and its relationship with the formation of the oceanic crust in these environments.

2 Geological setting

Atlantis Massif, a ~2 Ma old Ocean Core Complex (OCC), is located at 30°N at the inside corner of the eastern intersection of the Mid-Atlantic Ridge (MAR) with the Atlantis Transform Fault (Fig.1a). This OCC extends approximately 20 km parallel to the ridge and 15 km across (Fig.1a); it is assumed to result from low-angle detachment faulting (Cann et al., 1997; Blackman et al., 1998; Blackman et al., 2002; Schroeder and John, 2004; Karson et al., 2006; Ildefonse et al., 2007a).

IODP Hole U1309D was drilled into the central part of the massif during IODP Expeditions 304 and 305 at 30°10.12'N, 42°07.11'W (Blackman et al., 2006). This borehole

penetrated 1415.5 meters below seafloor (mbsf). The recovered section comprises mainly of gabbroic rocks (>96%), although minor mantle peridotites (<< 1%) and diabases (2.9 %) were also sampled. Peridotite occurs at 172 mbsf as a 88cm interval of alternating dunites and harzburgites, with evidence of local melt impregnation in the vicinity of cross cutting gabbroic dykelets (Blackman et al., 2006; Tamura et al., 2007). ~10-20cm thick ultramafic intervals were drilled at 61, 155, and 224 mbsf; some may also represent serpentinized peridotite, but they were too altered for their origin to be reliably inferred. Most diabases were observed in the upper 130 meters of the borehole where they occur as 50 cm to 10 m thick intrusive intervals (Fig. 1b); they have MORB compositions (Blackman et al, 2006; Godard et al, in press).

The gabbroic rocks sampled during Expeditions 304-305 are characterized by a broad range of modal compositions: troctolite, olivine gabbro (including troctolitic gabbro), gabbro and oxide gabbro represent 2.7%, 28%, 56% and 7% respectively of the lithologies recovered at Hole U1309D (Blackman et al., 2006). The shipboard scientific party grouped an olivine rich subset of gabbroic samples as olivine-rich troctolite. Olivine-rich troctolite is characterized by more than ~65% olivine and it has a poikilitic texture (see rationale for using this terminology in Blackman et al., 2006). Its modal composition varies at the scale of a few centimeters to a few decimeters, locally grading to dunite, wehrlite, or troctolite. It represents 5.4 % of the lithologies recovered at Hole U1309D.

Olivine gabbro (>5% olivine) and gabbro are characterized by significant variations in grain size and modal composition on a decimeter-scale. Olivine gabbro locally grades to troctolitic gabbro and troctolite. Thin section observation reveals the occurrence of significant amounts of orthopyroxene (orthopyroxene>5%) in gabbros below 600 meters below sea floor (mbsf). Oxide gabbros (>2% modal Fe-Ti oxides) occur as disseminated patches, as dikelets crosscutting other lithologies, or less often associated with ductile deformation zones (Blackman et al., 2006). Gabbro and oxide gabbro are generally intrusive into troctolite and less evolved gabbro with either sharp or locally more diffusive contacts. Olivine-rich troctolite is observed along 22 discrete olivine-rich intervals in Hole U1309D with an average recovery of 75% (Fig. 1c). Olivine-rich troctolite occurs as <1 to ~50 m thick zones alternating with troctolite and gabbro intervals, with which they display either diffuse or sharp transitions. Olivine-rich troctolite is commonly intruded by thin (~1 to 20 cm) gabbroic intrusions. It is the dominant lithology between 1090 and 1236 mbsf (Fig. 1c).

The core is moderately altered at conditions ranging from granulite to zeolite facies. Overall, the alteration tends to decrease downhole and olivine-rich troctolite intervals between

1090 and 1230 mbsf are locally very fresh (< 1% serpentinisation). Magmatic deformation associated with the emplacement of Hole U1309D gabbroic intrusive suite is weak and affects only 22% of the recovered core. High-temperature (amphibolite to granulite facies) deformation is rare and high-strain ductile shear zones represent less than 3% of the recovered core.

3 Sampling

We selected 4 olivine-rich intervals in which we sampled the olivine-rich troctolites and the adjacent gabbroic rocks for petrographic and geochemical (major and trace element) analyses (Fig. 1b).

We collected 15 samples (10 olivine-rich troctolites, 3 troctolites, 1 olivine-gabbro and 1 gabbro) in a first interval from core 60R3 to 71R1 (~ 50m). This interval is composed of 22.5 m of fine-grained olivine-rich troctolites with abundant and large interstitial plagioclase occurrences. Small coarse-grained gabbro dikes cut through olivine-rich troctolites. Medium-grained troctolites are present at the bottom of the sampled interval, from core 69R3 to 71R1 (~ 6.8 m), and grade locally to olivine-gabbros, which are distinguished by their higher pyroxene content. Serpentinization is high in the upper part of the interval with not a lot of olivine preserved and decreases progressively down core with the appearance of troctolites.

In a second interval, from core 111R2 to 112R3 (~ 5.4 m), we collected 7 samples (5 olivine-rich troctolites, 1 troctolite and 1 gabbro). This interval is modally variable from fine-grained olivine-rich troctolites (~ 1 m) to medium-grained troctolites and coarse-grained olivine-gabbros. A continued pervasive serpentinization of olivine characterizes the interval, and some alteration veins of amphibole, talc and chlorite are also present.

We collected 5 samples (2 olivine-rich troctolites, 1 troctolite and 3 gabbros) in a third interval, from core 135R2 to 136R3 (~ 5.5 m). This zone is made of 1.91 m of medium-grained olivine-rich troctolites with large clinopyroxene oikocrysts including olivine chadacrysts, and interstitial plagioclases. Coarse-grained gabbros show sharp contacts with olivine-rich troctolites. Olivine-rich troctolites are moderate to highly altered compared to gabbro due to serpentinization of olivine.

In the fourth interval, from core 227R1 to 248R4 (~ 105 m), we collected 40 samples (28 olivine-rich troctolites, 2 troctolites, 4 olivine-gabbros and 6 gabbros). This zone is composed of several intervals (~ 48 m) of equigranular to seriate fine-grained olivine-rich troctolites cut by vertical gabbroic veins. Intervals of coarse-grained gabbro truncating

olivine-rich troctolites are also present along the section and plagioclase content increase toward contact to gabbro. Olivine-rich troctolites show also gradational contact with medium-grained troctolites and medium to coarse-grained olivine-gabbros. Alteration is very weak (<5% alteration) in this zone and consists mostly in olivine serpentinization.

4 Analytical methods

Modal compositions were determined by thin section observation and calculated on a subset of 42 samples using a mass-balance equation relating bulk rock and mineral compositions in the CFMAS system. Bulk rock major elements were analyzed by XRF, at Granada University (Spain) (Supplementary dataset). These two methods used for modal composition are in agreement. A subset of 34 samples (20 olivine-rich troctolites, 6 troctolites, 3 olivine gabbros and 5 gabbros) was selected for *in situ* trace element analyses.

Major element compositions of minerals were determined by Electron Probe Micro Analyser (EPMA) at Montpellier 2 University, using a CAMECA SX100 equipped with five wavelength-dispersive X-ray spectrometers (WDS). The analyses were done with 20 kV accelerating potential, 10 nA beam current and 30 s counting time for all elements. Concentrations were obtained from raw intensities using the “X-PHI” quantification procedure (Merlet and Bodinier, 1990). Natural minerals, synthetic oxides and pure metals were used as standards.

In situ trace element compositions were determined at Montpellier 2 University, using two different Inductively Coupled Plasma-Mass Spectrometers (ICP-MS) coupled with laser ablation (LA) system, a Geolas (Microlas) automated platform housing a 193 nm Compex 102 laser from LambdaPhysik. A first batch of clinopyroxenes and plagioclases was analyzed using a 1991 vintage VG Plasmaquad II turbo ICP-MS. Olivines and a subset of clinopyroxenes and plagioclases were analyzed on a ThermoFinnigan Element 2 High Resolution-ICP-MS (HR-ICP-MS) using a single collector double-focusing sector field Element XR (eXtended Range). Thin sections were polished to remove carbon coating after EPMA analyses, dried under into nitrogen and introduced into the ablation cell. Analyses were conducted using an in-house modified ablation cell of ca. 30 cm³, which resulted in a shorter washout time and an improved sensitivity compared to the initial larger ablation cell. Ablation experiments were conducted in a helium atmosphere, which enhances sensitivity and reduces inter-element fractionation (Gunther and Heinrich, 1999). The helium gas and particles from the sample were then mixed with argon before entering the plasma. Signals

were acquired in Time Resolved Acquisition, devoting 2 mn for the blank and 1 mn for measurement of the analyses. The laser was fired using an energy density of 15 Jcm^{-2} at a frequency of 5Hz and using a spot size of $122 \mu\text{m}$ for plagioclase, and $102 \mu\text{m}$ for clinopyroxene ($50 \mu\text{m}$, with HR-ICP-MS). This resulted in a sensitivity of ca. 4000 cps/ppm for in based on measurements on the NIST 612 certified reference material. For olivine analyses (HR-ICP-MS), the laser was used with a frequency of 10Hz and using a spot size of $122 \mu\text{m}$. Oxide level, measured using the ThO/Th ratio, was below 0.7%. ^{43}Ca and ^{29}Si were used as internal standards for clinopyroxene and plagioclase, and for olivine, respectively. Concentrations were calibrated against the NIST 612 rhyolitic glass using the values given in Pearce et al. (1997). Data were subsequently reduced using the GLITTER software (Van Achterberg et al., 2001) using the linear fit to ratio method. This typically resulted in a 5 to 10% precision (1sigma) for most analyses evaluated by repeated analyses of reference basalt BR (supplementary dataset - Table A8). Detection limits in plagioclase were between 0.2 and 5 ppm for REE, Hf, Y, Zr, Ti, V, Cr, and Ni and below 0.1 ppm for other elements by LA-ICP-MS, and below 0.05 ppm except Ti, Ni and Zn (1 to 2 ppm) by LA-HR-ICP-MS. In clinopyroxene, they were below 0.1 ppm for all elements except for Zr, Ti, V, Cr, and Ni (between 0.2 and 6 ppm) by LA-ICP-MS and below 0.02 ppm for all elements except for V, Cr, Co, Zn, Rb, Sr and Ba (between 0.03 to 0.3) and for Ti, Ni and Zn (between 2 and 4 ppm) by LA-HR-ICP-MS. Detection limits were below 0.08 ppm for all elements except Si, P, Ca, and Ni between 0.2 to 1.7 ppm for olivine analyses by LA-HR-ICP-MS.

Representative analyses are reported in Tables 1, 2 and 3. The complete dataset is available as on line supplementary dataset.

5 Petrographic description

5.1 Troctolite and olivine-rich troctolite

Troctolite contains olivine (45-64%, 1-4mm), plagioclase (27-40 %, 2-4mm), clinopyroxene (2-15 %, < 1mm) and spinel (0.5%, 0.5mm) (Fig.1c). It has a mesocumulate texture with olivine and plagioclase as cumulus phases and clinopyroxene as intercumulus phase (Fig.2A). Olivine (Ol) occurs as subhedral grains partly to highly serpentinized, partially included in plagioclase. This textural relationship shows a sub-contemporaneous crystallization of olivines and plagioclases with a precipitation slightly earlier for olivine. Plagioclase (Pl) has lath shaped, elongated or occur as blocky crystal, with resorbed grain

boundaries. Plagioclase crystals show polysynthetic twins develop during growth. Clinopyroxene (Cpx), when present, forms grains interstitial to olivine and plagioclase. Spinel (Sp) occurs as small subhedral grain associated with olivine. Crystallisation of spinel and olivine is also contemporaneous. The crystallization order in troctolite is inferred to be: Sp + Ol - Sp + Ol + Pl - Sp + Ol + Pl + Cpx.

Olivine-rich troctolite is made of olivine (64-85%, 1-5mm), plagioclase (2-24 %, 3mm to 1cm), clinopyroxene (1-30 %, 5mm to 1.5cm) and spinel (0.5%, 0.5mm). Olivine-rich troctolite has poikilitic textures with olivine chadacrysts embedded into large oikocrysts of clinopyroxene and plagioclase (Fig.2B, 2C). Based on morphology and grain size, several populations of olivine can be recognized (Fig.2B, 2C). The first population is composed of coarse-grained subhedral olivine crystals displaying smooth edges and common, well-defined and widely-spaced subgrain boundaries (Fig. 2B). The second population is formed by chains of polygonal olivine grains, with curvilinear boundaries, in optical continuity (Fig. 2C). Interstitial spaces between boundaries of adjacent olivines crystals are filled by clinopyroxene or plagioclase. This textural relationship suggests that the originally subhedral olivine was partly corroded. The third population comprises fine- to medium-grained, round olivine generally devoid of substructures, and occurring as dispersed chadacrysts in large clinopyroxene and plagioclase oikocrysts (Fig. 2B). Olivine appears more dispersed in the center of clinopyroxene and plagioclase oikocrysts than on their boundaries. Micron-size fluid inclusions are present in almost all olivine grains. They occur as trails in olivine crystals and can be locally very abundant, but they are rare in rounded grains. Clinopyroxene and plagioclase in olivine-rich troctolite do not show evidence of deformation. Plagioclase shows polysynthetic twins developed during growth. Clinopyroxene is locally interstitial (Fig.2D) and when the proportion of olivine is high, it forms, with plagioclase, a pervasive texture similar to that of impregnated dunites sampled at the mantle-crust transition zone in ophiolites (Boudier and Nicolas, 1995, Dijkstra et al., 2003), or in some abyssal peridotites (e.g., Takazawa et al., 2007). In some samples (136R1_35-39; 136R2_37-40), very large clinopyroxene oikocryst surrounds resorbed olivine, and plagioclase is generally interstitial in this case. In these samples, clinopyroxene crystallization seems to occur prior to plagioclase crystallization. Spinel occurs as small subhedral crystals (0.5mm) with polygonal shape, indifferently included in olivine, clinopyroxene or plagioclase. Textural relationships suggest that plagioclase and clinopyroxene crystallized more or less concurrently, after a melt that reacted with olivine.

In both troctolite and olivine-rich troctolite, plagioclase has the same anorthitic composition ($An_{69}-An_{82}$) and does not show any grain scale compositional variation (Fig.3a). Clinopyroxene is mainly augite ($En_{47-53}Fs_{6-10}Wo_{37-45}$) except in the topmost sampled interval, where clinopyroxenes from olivine-rich troctolites are distinguished by their diopside composition ($En_{47-49}Fs_{6-8}Wo_{44-47}$). We note also that clinopyroxene in troctolites 71R1_10-13 and 136R2_60-64 is characterized by an augite core with a diopside rim ($En_{46-48}Fs_{6-8}Wo_{45-46}$). Clinopyroxene have high Mg# values ($Mg\# = 100 \times \text{cationic Mg}/(\text{Mg}+\text{Fe}) = 85-90$) (Fig.3a). In both olivine-rich troctolites and troctolites, clinopyroxene is characterized by low TiO_2 (0.26-0.54 wt.%) and high Cr_2O_3 (0.48-1.45wt.%) contents except for the its that is enriched in Ti ($TiO_2 = 0.29-0.86$ wt.%) and depleted in Cr ($Cr_2O_3 = 0.48-1.33$ wt.%) (Fig.3b). Interstitial clinopyroxenes are characterized by high Ti ($TiO_2 = 0.33-0.72$ wt. %) and high Cr contents ($Cr_2O_3 = 0.97-1.45$ wt. %) similar to that of clinopyroxene rims (Fig.3b).

The different olivine populations in olivine-rich troctolite have similar major element compositions. Olivine in troctolites and olivine-rich troctolites displays a wide range of forsterite content ($Fo_{83}-Fo_{86}$ and $Fo_{82}-Fo_{88}$ respectively) and high Ni contents (1600-2100 ppm and 1440-2300 ppm respectively) (Fig.3c). These compositions are intermediate between that of oceanic gabbros and abyssal peridotites (Fig.3c). Some samples, mainly olivine-rich troctolites, are distinguished by high Ni values (2100-2300 ppm) for a given Fo content (Fo_{87}) compared to the most primitive gabbroic rocks sampled so far at slow-spreading ridges (Fig.3d) and show a linear correlation, atypical of oceanic cumulate trends (e.g., Ross and Elthon, 1997).

Spinel has high Cr and Fe contents ($Cr\# = 100 \times Cr/(Cr+Al) = 46-64$, and $FeO = 27\%$) and high Ti contents ($TiO_2 = 0.41-2.56$ wt. %). Overall, major element compositions of minerals in olivine-rich troctolites and troctolites are very primitive and plot at the most depleted end of the field of Mid-Ocean Ridge cumulate minerals (Fig.3).

Temperatures of plagioclase crystallization were calculated using an igneous thermometer based on plagioclase plus liquid equilibria (Putirka, 2005). This thermometer gives crystallization temperatures of $1230^\circ C$ (+/- $23^\circ C$) in troctolites and olivine-rich troctolites.

5.2 Gabbro and olivine gabbro

Gabbro is made of plagioclase (40-70%, 1mm to 1cm), clinopyroxene (25-60%, 2mm to 1cm) and less than 5 % olivine. No spinel is observed. Olivine-gabbro is distinguished

from gabbro by a modal content of olivine >5% (Fig. 1). Gabbros and olivine-gabbros have adcumulate textures, typical of oceanic gabbros, with plagioclase, clinopyroxene and olivine as cumulus phases (Fig. 2E). They are generally less altered than olivine-rich troctolites and troctolites, with the exception of some remarkably fresh olivine-rich troctolites sampled in the lowermost olivine-rich interval (Blackman et al., 2006; Ildefonse et al., 2006). No foliation is visible in these two types of rocks.

Plagioclase crystals, the main phase in gabbro and olivine-gabbro, are euhedral to subhedral and generally occur as elongated laths with polysynthetic twins and no optic zonation (Fig. 2F). In gabbro, clinopyroxene form irregular tablets with abundant thin exsolution lamellae of orthopyroxene. In olivine gabbro, clinopyroxene occurs as anhedral resorbed crystals. Olivine occurs as subhedral to lobed grains, generally forming aggregates with clinopyroxene. Textural relationships show that minerals in gabbros and olivine-gabbros seem to have grown at the same time. Olivine crystals are included into clinopyroxene, which suggests that olivine crystallized before clinopyroxene. The crystallization of clinopyroxene and plagioclase is concomitant. The crystallization order in gabbros and olivine-gabbros is: Ol - Ol + Pl + Cpx; it is consistent with the typical crystallization sequence of an oceanic cumulate from a MORB at low pressure (< 2kbar; Green and Ringwood, 1967; Grove and Bryan, 1983; Tormey et al., 1987; Juster et al., 1989; Grove et al., 1992).

The plagioclase anorthite content is An₅₆-An₇₄ in gabbros and An₆₉-An₇₇ in olivine gabbros (Fig.3a). Plagioclase does not exhibit core to rim variations. Clinopyroxene is augite (En₄₃₋₅₈Fs₉₋₁₇Wo₃₂₋₄₅); it is characterized by large variations in Mg# (73-86 in gabbros and 83-85 in olivine gabbros) (Fig.3a) and Cr contents (Cr₂O₃= 0.12-1.16 wt. %) at relatively constant Ti contents (TiO₂= 0.34-0.68 wt. %) (Fig.3c). Like in troctolite and olivine-rich troctolite, some clinopyroxenes show core-rim variations: TiO₂ increases (0.02 to 0.22 wt. %) and Cr₂O₃ decreases (0.03 to 0.62 wt.%) from cores to rims of crystals (Fig.3c). Olivine displays relatively low forsterite content (Fo₇₈-Fo₈₃) (Fig.3b). Gabbros and olivine gabbros have compositions comparable to that of oceanic gabbros from ODP Hole 735B or ODP Leg 153 (Fig.3; e.g., Natland et al., 1991; Ross and Elthon, 1997). Temperature of plagioclase crystallization, calculated using Putirka (2005)'s thermometer, is 1230°C (+/- 23°C) in olivine-gabbros and gabbros.

6 Minerals trace element compositions

6.1 Clinopyroxene

As illustrated in Figures 4 and 5, clinopyroxenes from olivine-rich troctolites, troctolites and gabbros have compositions similar to that of clinopyroxenes from gabbros sampled along the Mid-Atlantic Ridge. Clinopyroxene cores have on average low trace element contents, with Yb_N (N = normalized to chondrites) ranging from 5 to 11, and Light REE (LREE) depleted patterns ($La_N/Sm_N = 0.08-0.2$) with an almost flat Medium REE (MREE) to Heavy REE (HREE) segment ($Gd_N/Yb_N = 0.8-1$) (Fig.4a). Clinopyroxene cores have also slight negative Eu anomalies ($Eu/Eu^* = 0.8-0.9$) (Fig.4a). REE compositions of clinopyroxene from IODP hole U1309D are similar to that of clinopyroxenes from the most depleted gabbros sampled during ODP Leg 153 in the MARK area (Ross and Elthon, 1997; Coogan et al., 2000b) (Fig.4a). Clinopyroxene rims and interstitial clinopyroxenes are characterized by higher trace element contents ($Yb_N = 9-23$), and larger negative Eu anomalies ($Eu/Eu^* = 0.5-0.8$) (Fig.4b) although they display similar REE fractionation than clinopyroxene cores ($La_N/Yb_N = 0.05-0.15$) (Fig.4b). Some interstitial clinopyroxenes (troctolite 70R3_20-24 cm; troctolite 111R2_112-116 cm; olivine-rich troctolite 111R3_101-114 cm) are distinguished by higher HREE concentrations and they display the largest negative Eu anomaly. Two rims of clinopyroxene measured in olivine-rich troctolite 61R1_113-116 cm and in troctolite 71R1_10-13 cm display significantly distinct compositions: they have the highest trace element contents and relative enrichments in LREE ($La_N/Sm_N = 0.46$ and 0.2 respectively compared to $La_N/Sm_N < 0.2$ in clinopyroxene cores). These trace element enrichments are highly localized and appear atypical in the studied gabbroic series; they might reflect local (kinetic?) disequilibria during crystallization (e.g., Albarede and Bottinga, 1972).

Clinopyroxene, cores and rims, and interstitial clinopyroxenes display similar extended trace element patterns. They are characterized by a continuous depletion in incompatible trace elements, from REE to Ba ($< 10^{-1}$ x Primitive Mantle – PM-) then selective enrichments in Rb and Cs (up to 5x PM) (Fig.5a) as well as variable fractionation in U, Pb, Sr, Zr and Hf relative to neighboring elements. Clinopyroxene cores are systematically depleted in Zr and Hf relative to MREE ($Zr/Sm = 0.23-0.54$ x PM), they have high U positive anomalies (U/Th up to 74 xPM), moderate negative Pb anomalies to positive Pb anomalies ($Pb/Ce = 0.2-7.6$ x PM) and a moderate Sr negative anomaly ($Sr/Nd = 0.22-0.52$ x PM). Clinopyroxene rims and interstitial clinopyroxenes are characterized by higher trace element

contents and larger Sr negative anomalies ($Sr/Nd = 0.06-0.26 \times PM$) but lesser variations in U and Zr-Hf relative to neighboring elements ($U/Th = 1.08-14.4 \times PM$; $Zr/Sm = 0.26-1.02 \times PM$), the most enriched samples having no anomalies in Zr-Hf or U. Except for five olivine-rich troctolites, Pb is generally depleted relative to LREE ($Pb/Ce = 0.07-0.99 \times PM$), in clinopyroxene rims and interstitial clinopyroxenes, the strongest negative anomalies being observed in the most enriched samples. Finally, clinopyroxene have chondritic to sub-chondritic Zr/Hf ($18-37.4 - C1\text{-Chondrite} = 36.3$ (Sun and McDonough, 1989)) and Nb/Ta ($9.5-22; C1\text{-Chondrite} = 17.6$ (Sun and McDonough, 1989)) fractionations.

Similar trace element enrichments from core to rim as well as in interstitial clinopyroxene have been observed in gabbros from the MARK area (Ross and Elthon, 1997; Coogan et al., 2000b) but the extent of these variations is less in Hole U1309D samples than in the MARK gabbros (Fig.4b).

6.2 Plagioclase

All samples have low HREE contents ($Yb_N = 0.11-0.15$), LREE-enriched patterns with strong positive Eu anomalies ($Eu/Eu^* = 5-15$) a similar MREE/HREE fractionation ($Gd_N/Yb_N = 3.7-6.2$), but olivine-rich troctolites appear less LREE fractionated than neighboring troctolite and gabbro ($La = 0.7-1.1 - La_N/Sm_N = 1.1-1.9$ in olivine rich troctolites and $La = 0.6-2.7 - La_N/Sm_N = 0.7-2.8$ in troctolites and gabbros) (Fig.4c). Plagioclase do not display core to rim variations.

As illustrated on Figure 5c, plagioclases from olivine-rich troctolites, troctolites and gabbros at Hole U1309D have similar trace element patterns characterized by continuous enrichments in the most incompatible elements and positive anomalies in U and Sr relative to neighboring elements ($U/Th = 2.9-110.8 \times PM$; $Sr/Nd = 11-50.3 \times PM$). Pb displays moderate negative anomalies to strong positive anomalies ($Pb/Ce = 0.5-8.6 \times PM$). One of the most remarkable characteristics of the studied plagioclase is their strong depletion in Nb and Zr relative to neighboring elements, including Ta and Hf. This results in low sub-chondritic Nb/Ta and Zr/Hf ratios in these minerals ($Nb/Ta = 1.5-7.8$; $Zr/Hf = 1.6-30.1$).

Plagioclases from olivine-rich troctolites, troctolites and gabbros at Hole U1309D have trace element compositions similar to those of plagioclase cores of poikilitic olivine gabbros from Leg ODP 153 from the MARK area (Ross and Elthon, 1997; Coogan et al., 2000a). In detail, three gabbros are characterized by a slight increase in trace element contents, in particular in LREE, in plagioclase of samples. Cross-cutting relationships suggest

these three gabbros are late features: one is a gabbroic dikelet in an olivine-rich troctolite, the other two are associated to an oxide vein and a pegmatitic gabbro. They have compositions similar to that measured previously in plagioclase rims of poikilitic olivine gabbros from Leg ODP 153, which could point to late variations in the parental melts composition (Fig.4, Coogan et al., 2000a).

6.3 Olivine

The composition of olivine was measured in 3 olivine-rich troctolites (Fig. 4d and 5d). Olivine is depleted in trace elements in particular in LREE ($La_N \sim 0.001$; $Yb_N = 0.3-0.64$). It has strongly fractionated REE pattern showing a strong and continuous decrease from HREE to MREE ($Gd_N/Yb_N = 0.01-0.02$) then a relatively flat LREE segment ($La_N/Nd_N = 1-1.5$) (Fig.4d). Olivine displays spiked normalized trace element patterns (Fig.5d) characterized by selective enrichments in the most incompatible elements (except Ba) relative to LREE (e.g., $Th/Ce = 4.84-14.61 \times PM$) and in all High Field Strength Elements (HFSE: Nb, Ta, Zr, Hf and Y) relative to neighboring elements ($Zr/Sm = 4.07-5.03 \times PM$; $Y/Ho = 1.07-1.13 \times PM$; $Nb/Ce = 4.72-54.97 \times PM$). They display chondritic fractionations of Zr/Hf (35.1-43.3) and Nb/Ta (6.4-24.9).

Little data exist on the trace element composition of olivines in oceanic rock samples or in their ophiolite analogues. Most of the rare analyses were obtained on mantle peridotites from orogenic massifs and xenoliths (Sun and Kerrich, 1995; Bedini and Bodinier, 1999; Garrido et al, 2000). In comparison, the olivines in Hole U1309D olivine-rich troctolites are distinguished by their strongly fractionated REE patterns and their strong depletion in the most incompatible elements. In that respect, they resemble to olivine analyzed in peridotites from the Oman ophiolite (Gerbert-Gaillard, 2002), although they display slightly higher HREE and lower LREE contents, and they do not show the same large positive Pb anomaly (Fig.5d). Another characteristic of olivines from Hole U1309D is their large positive anomalies in HFSE, which distinguish these samples from all previously analyzed olivines.

7 Discussion

Hole U1309D gabbroic series are distinguished by the occurrence of olivine-rich lithologies, referred to as olivine-rich troctolites, in significant proportion compared to gabbroic series previously sampled at slow spreading ridges, such as at ODP Hole 735B on

the Southwest Indian Ridge (Dick et al., 1999, 2000). Olivine-rich troctolites occur as 1- to 10-m thick zones locally grading to or having sharp transition with either troctolites or gabbros. Olivine-rich troctolites and associated troctolites and gabbros form olivine-rich intervals; the largest one, which is ~100m thick, is observed at the bottom of the borehole. Olivine-rich troctolites and adjacent troctolites have high Mg# values in clinopyroxenes (85-90), high Fo and Ni content in olivines (82-88 and 1500-2200 ppm respectively) and high An content in plagioclase (69-82). These plagioclase and clinopyroxene compositions plot at the most primitive end of oceanic gabbroic series sampled so far at slow spreading ridges; we note also that plagioclase and clinopyroxene in studied olivine gabbros and gabbros overlap in composition with plagioclase and clinopyroxene sampled in the most primitive oceanic gabbros (Fig.3a; e.g., Ross and Elthon, 1997). Olivines in olivine-rich troctolites and troctolites have distinctly higher Fo and Ni contents compared to olivines analyzed previously in oceanic gabbroic series: their compositions are intermediate between that of oceanic gabbros and that of abyssal peridotites and fill the gap between these two-end members (Fig.3c). Variations of clinopyroxene Mg# are correlated to that of plagioclase An content from troctolites to gabbros (Fig.3a). This co-variation trend between the compositions of plagioclases and clinopyroxenes defines a continuous evolution from the most primitive troctolites to more evolved gabbros, possibly consistent with a sequence of fractional crystallization after a common MORB parental melt (Ross and Elthon, 1997), in which olivine-rich troctolites would represent the earliest stages of basaltic differentiation. The composition of olivines would require an Mg-Ni-rich, highly primitive parental melt.

One of the most striking feature of the olivine-rich intervals sampled at Hole U1309D is that clinopyroxene is present in all the studied rock types, even the most primitive olivine-rich troctolites. Yet, the order of fractional crystallization of MORB-type melts is generally inferred to be olivine, olivine-plagioclase then olivine-plagioclase-clinopyroxene (Green and Ringwood, 1967; Grove and Bryan, 1983; Tormey et al., 1987; Juster et al., 1989; Grove et al., 1992). In addition, clinopyroxene sampled with the olivine-rich intervals has Mg# values (85-90) higher than that expected for clinopyroxene crystallizing in a typical MORB fractional crystallization sequence (Mg# = 85 and 82 -at 5Kbar, 2Kbar respectively- using fractional crystallization models, Fig.3a, Mg# = 83 in Grove et al., 1992). On the other hand, high Mg# clinopyroxene is not uncommon in oceanic gabbro series (Meyer et al., 1989; Hébert et al., 1991; Elthon et al., 1992; Constantin et al., 1996; Ross and Elthon, 1997; Coogan et al., 2000a; Kvassnes, 2004; Lissenberg and Dick, 2008). Several hypotheses have

been proposed to explain the widespread occurrence of high Mg# clinopyroxene in the oceanic lower crust.

High clinopyroxene content together with their Mg# may indicate precipitation of clinopyroxene early in the MORB-crystallization sequence, that is at pressures higher (up to 10kbar) than that generally inferred for oceanic gabbros (~2kbar) (e.g., Bender et al. (1978), Bence et al. (1979), and Elthon et al. (1982, 1992)). This hypothesis seems to be consistent also with the occurrence of spinel in troctolites and olivine-rich troctolites of Hole U1309D, an oxide that crystallizes early in the crystallization sequence at high pressure (Sigurdson and Schilling, 1976; Fisk and Bence, 1980; Dick and Bullen, 1984). However, high pressure crystallization produces also high Al clinopyroxene (>6 wt.%; Stolper, 1980) whereas clinopyroxene in Hole U1309D olivine-rich troctolites and gabbros have low Al₂O₃ contents (3.5 wt.% in olivine-rich troctolites and 2.9 wt.% in gabbros) as expected for low pressure crystallization (e.g., Grove and Bryan, 1983). Therefore, this process cannot solely explain the high clinopyroxene content in the studied olivine-rich intervals or their high Mg # clinopyroxene.

Alternatively, these modes and the high Mg # clinopyroxene may indicate crystallization after melts of variable compositions, either incompletely aggregated melts (e.g., Coogan et al. (2000a)) or melts reacting with the wall rock. Several authors have suggested that high Mg# clinopyroxene result from chemical reequilibration between pre-existing gabbroic cumulates and percolating melt, by (i) late melt/rock reaction (Meyer et al., 1989): high Mg# clinopyroxene then corresponds to small amounts of trapped liquid which have been buffered in major elements by olivine matrix, or by (ii) crustal assimilation (Bédard et al., 2000; Kvassnes, 2004; Ridley et al., 2006; Kvassnes and Grove, 2008; Lissenberg and Dick, 2008) : interstitial melts in mush zone or ascending melts interact chemically with, and even dissolve, pre-existing cumulate minerals, thus changing melt composition. These assimilation/reaction processes are consistent with the characteristic texture of olivine-rich troctolites and troctolites of Hole U1309D, showing poikiloblasts or interstitial clinopyroxene enclosing resorbed olivine grains, which suggests that clinopyroxene crystallized within pores spaces from interstitial melts that had reacted with the olivine (Fig.2B).

Trace element geochemistry provides complementary information on the magmatic processes which led to the formation of the olivine-rich intervals sampled at Hole U1309D. Clinopyroxene and plagioclase have similar trace element concentrations in all the studied rock-types. We observe however trace element enrichments at clinopyroxene rims, and at the scale of the thin-section between large poikilitic and interstitial clinopyroxenes (Fig.4 and 5).

This variability at the grain and sample scale precludes a simple fractional crystallization process for the formation of the different lithologies sampled in the olivine-rich intervals, as crystallization would have resulted in an increase in trace element concentrations from primitive olivine-rich troctolites to the more evolved gabbros.

In the following, we discuss the formation of olivine-troctolites and its possible relationship with the earliest stages of the differentiation processes in a MORB cumulate series or to melt-rock interaction, as well as the importance of melt renewal and melt transport in the olivine rich intervals in Hole U1309D gabbroic sequence.

7.1 Olivine-rich troctolites: Geochemical evidence for melt impregnation

Textural relationships in olivine-rich troctolites indicate that clinopyroxene and plagioclase crystallized after a melt that was in chemical disequilibrium with, and partly corroded olivine (e.g., Donaldson, 1985). In addition, a companion study indicates that part of the olivine preserves a weak intra-crystalline evidence of deformation while clinopyroxene and plagioclase are undeformed (Drouin et al., 2007; in prep). These observations suggest that the formation and deformation of the olivine on one hand, and assimilation/crystallization processes, on the other hand, occurred as a multi-stage (at least two) process.

Assimilation of olivine induces changes in the crystallizing melt composition (Lissenberg and Dick, 2008). The addition of an olivine component may explain the particularly high contents in compatible and refractory elements, such as Mg or Ni, of the bulk gabbroic rocks composition at Hole U1309D (Godard et al, in press) compared to that of the bulk composition of Hole 735B (Hart et al., 1999; Dick et al., 2000) but also compared to primary mantle MORB melts (e.g., Kinzler & Grove, 1993). Olivine and high Mg# clinopyroxenes are in Fe-Mg equilibrium in olivine-rich troctolites and in neighbouring samples, in a way similar to what is described in the reacted troctolites sampled at the Kane Megamullion (Fig. 3c, Lissenberg and Dick, 2008). This indicates that elemental reequilibration occurs between melts and assimilated (and maybe also crystallizing) minerals in the olivine-rich intervals. The continuous melt/mineral chemical reequilibration produces geochemical trends analogue to those predicted by equilibrium crystallization models, for compatible elements such as Ni (Fig. 3d). This suggests that separation of melts and minerals (both wall rock and newly crystallized grains) is slow compared to the time-scale(s) over which Mg-Fe and Ni diffusive re-equilibration occurs.

In contrast, the olivines in olivine-rich troctolites are in disequilibrium with plagioclase and clinopyroxene for incompatible trace elements (Fig.6). The olivines are characterized by strongly fractionated trace element patterns, in equilibrium with a melt that is significantly more depleted in highly incompatible elements than MORB (Fig. 6), which precludes olivine formation after a MORB-type melt. Hence, although they are incorporated into the gabbroic sequence, olivines appear to preserve a primary trace element depleted signature similar, in part, to that of ophiolitic peridotites, which may point to a mantle origin. Their selective enrichments in the most incompatible elements may indicate a progressive reequilibration with the comparatively enriched MORB-type melts after which plagioclase and clinopyroxene were formed (chromatographic effect, e.g., Navon and Stolper, 1987; variable diffusion coefficients and reequilibration kinetics in the crystal for the different trace elements e.g., Kennedy et al, 1993; Van Orman et al, 2002). However, this suggests that melt/olivine reequilibration in our samples is much slower for trace element than for Mg-Fe. These results are in contradiction with the recent experimental results of Spandler et al (2007), who suggest that melt/olivine reequilibration is as fast for REE as for Mg-Fe. This discrepancy may relate to differences between natural and experimental conditions.

A distinctive signature of olivine of Hole U1309D olivine-rich troctolites is their strong HFSE enrichments, which seems to complement the strong depletion in these elements in plagioclase (Fig. 5); crystallization of the latter may have locally produced HFSE-rich melts with which olivine equilibrated. Alternatively, we cannot preclude the incorporation of trace-element rich, melt or solid micro-inclusion in olivine analyses (e.g., Schiano et al., 1995; Ionov, 1996; Rosenbaum et al., 1996; Garrido et al., 2000; Bodinier et al., 1996), as olivine crystallographic structure does not favor incorporation of trace elements. Olivine in the present study were analyzed using large spot sizes (~ 122 µm), therefore if micro-inclusions were present in the olivine grain, they were included in the analyses. Consequently, the differences in composition between Hole U1309D olivine and previously analyzed olivines could point to differences in the nature of the incorporated inclusions e.g. small spinel or oxides micro-inclusions similar to the larger spinel grains observed in olivines. Spinel and, more generally, oxides are extremely depleted in REE but they are HFSE enriched (e.g., Bedini and Bodinier, 1999; Garrido et al., 2000; Klemme et al, 2006) and therefore, they would not (or very little) contribute to the REE composition of Hole U1309D olivines but could affect their HFSE budget. In addition, refractory microphases (e.g., rutile) are often associated to spinel and have been shown to control its HFSE budget (Bodinier et al., 1996; Kalfoun et al., 2002). The distinctive HFSE signature of Hole U1309D olivines may

result from the incorporation of such refractory phases or of insignificant fractions of oxides, rather than a reequilibration with melts of different compositions.

Although further studies are needed to better understand the trace element distribution, and the kinetics of melt/rock reequilibration processes in olivines, our results indicate that the analyzed olivines do not have compositions consistent with crystallization after a MORB-type melt. We infer that (at least part of the) olivines were present before the onset of the cumulate crystallization sequence. Textural observations together with the partly equilibrated chemistry of olivines in Hole U1309D olivine-troctolites suggests that the latter were formed by continuous input and crystallization of melt into a solid or mushy reacting matrix, similar to melt impregnation of mantle peridotites observed at the mantle/crust transition zone in ophiolites (e.g., Boudier and Nicolas, 1995; Djistra et al., 2003) and at fast spreading ridges (e.g., Allan and Dick, 1996; Arai and Matsukage, 1996; Dick and Natland, 1996).

7.2 Melt accumulation processes in olivine-rich intervals in Hole U1309D

The lack of systematic petrographic and geochemical downhole variations in the gabbroic series sampled in IODP Hole U1309D is consistent with a formation of gabbroic rocks as a suite of magmatic intrusions (Blackman et al., 2006; Godard et al., in press). The more evolved rock types are generally intrusive into the more olivine-rich rock types (Blackman et al., 2006). Preservation of the compositional differences between the different gabbroic rock-types (Godard et al., in press; Miller et al., submitted) indicates little chemical reequilibration between the crystallizing gabbroic sequence and migrating melts. This suggests that focused flow (e.g., intermittent fracturing or high permeability channels) is the dominant mode of melt migration through the gabbro series (Korenaga et al., 1998). However, at the scale of olivine-rich intervals, we observed evidence for chemical reequilibration between minerals. In addition, there is no variation in trace element contents in plagioclase and clinopyroxene from olivine-rich troctolites to neighboring troctolites and gabbros. This suggests precipitation of plagioclase and clinopyroxene after a melt having the same trace element composition in all the rock-types forming the olivine-rich intervals at Hole U1309D. This suggests a complex magmatic sequence involving continuous renewal of melts of buffered trace element composition.

7.2.1 Plagioclase and clinopyroxene crystallization in an open system

Textural evidence suggests that plagioclase and clinopyroxene crystallization occurred more or less simultaneously in olivine-troctolites, while neighboring troctolites and gabbros record a classical MORB crystallization sequence. In both cases, plagioclase and clinopyroxene are in equilibrium with the same MORB-type melt, similar to basalt and diabase dykes that cross-cut the gabbroic series (Fig. 6). These basalts and diabases have the same trace element composition as the erupted basalts in the same region of the Mid-Atlantic ridge (Godard et al., in press). Furthermore, analyzed clinopyroxene cores are characterized by small (or the lack of) Eu negative anomalies, which indicates that they precipitated after melts that were little fractionated by plagioclase crystallization. This suggests that plagioclase and clinopyroxene could have precipitated from a chemically buffered reservoir similar to a large magmatic chamber, such as that suggested in “glacier” models (e.g., Quick and Denlinger, 1993; Phipps Morgan and Chen, 1993). This model however is not consistent with the complex architecture of the gabbroic sequence. Alternatively, the homogeneous trace element composition of crystallizing phases may indicate that a constant input of undifferentiated melts into the olivine-rich intervals occurred during their crystallization.

Olivine-rich troctolites were formed by melts impregnating and reacting with an olivine-rich matrix, of which remains rounded olivines scattered within large clinopyroxene and plagioclase oikocrysts. This texture as well as microstructural evidence (Drouin et al., in prep; Drouin et al., 2007) suggests that large volumes of melts infiltrated the original olivine matrix. Olivine-rich intervals could represent a reactive porous zone, where MORB-type melts migrated and crystallized via an open-system porous flow. This hypothesis implies that the temperature difference between melts and the olivine-rich matrix with which they interact is small as otherwise they would crystallize immediately. Two scenarios are envisaged to explain the relation between olivine-rich troctolites and gabbros at IODP Hole U1309D:

(1) Magma injections in cool lithosphere. Lissenberg and Dick. (2008) propose that the initially fast cooling of the intruding magma favors high rates of nucleation and crystal growth during the earliest stages of crystallization; this results in the formation of a permeable network (here formed mainly of olivine), in which melts can later migrate and react efficiently as the sill (or pluton) cools more slowly. However, this one-stage scenario is not consistent with our results that suggest that olivine-rich troctolites were formed as a two-stage process: first, formation of an olivine in equilibrium with a depleted melt and deformation, then MORB-melt infiltration and crystallization of plagioclase and clinopyroxene.

(2) Multiple magma injections in partially crystallized (molten) wall rock. MORB melts are injected in olivine-rich areas (probably mantle), which have already undergone deformation,

at near solidus temperature. Melt infiltrates the wall rock, and high temperature favors pervasive melt-rock interactions, melt impregnation, flow and slow cooling of the basaltic melts within the olivine matrix. Following multiple magmatic injections, slivers of olivine-rich areas are ultimately assimilated into the thus produced gabbroic series. This scenario is consistent with the high temperature of crystallization of plagioclase (~1230°C).

7.2.2 Late-stage crystallization and closure of the system: rims and interstitial clinopyroxenes

Significant enrichments in incompatible trace element content are observed at the rim of clinopyroxenes and in late interstitial grains, coupled to a narrow Mg# variation (Fig. 3, 4 & 5). Interstitial clinopyroxenes occur only in troctolites and olivine-rich troctolites and have the highest TiO₂ and Cr₂O₃ concentrations (Fig.3b) and the highest trace element concentrations (Fig 4 & 5). As illustrated in figure 3b, interstitial clinopyroxenes define a trend with steeply increasing TiO₂ as Cr₂O₃ slightly decreases. This contrasts with rims of large clinopyroxene oikocrysts or cumulus grains, which follow an evolutionary path with gently increasing TiO₂ as Cr₂O₃ decreases. These local variations in Cr and Ti are similar to the apparent differentiation trend from primitive olivine-rich troctolite (high Cr content, high Mg#) to more evolved gabbros (low Cr content, low Mg#), and labeled “cumulus trend” in the literature (Ross and Elthon, 1997; Borghini and Rampone, 2007). These variations recorded at clinopyroxene rims and in interstitial clinopyroxenes indicate crystallization after a trace element enriched, probably more evolved melt which is buffered in Mg-Fe by equilibration with olivine-rich matrix (Meyer et al., 1989). Similar variations of trace element contents within individual samples and grains of clinopyroxene has been described in oceanic gabbroic suites and ascribed either to equilibration with more differentiated migrating melts (Mathez, 1995; Natland and Dick, 1996; Tribuzio et al., 1999; Coogan et al., 2000a, 2000b; Gao et al., 2007), or to postcumulus crystallization of trapped interstitial melts (Meyer et al., 1989; Elthon et al., 1992; Bédard, 1994; Ross and Elthon, 1997; Rampone et al., 1997; Borghini et al., 2007).

Rims of clinopyroxenes and interstitial clinopyroxenes display strong negative Eu anomalies, in addition, there is a negative correlation between Eu/Eu* and the other REE concentration (Fig.7a). These chemical features are consistent with concomitant crystallization of plagioclase and clinopyroxene in a closed system (e.g., Bodinier et al., 2008) plagioclase crystallization results in Eu depletion and HREE enrichment in clinopyroxene (Mc Kay et al., 1986, Bodinier et al., 2008). Another geochemical characteristic of enriched

clinopyroxenes, compared to clinopyroxene cores, is their less fractionated compositions for Nb, Zr, Ba, Pb and Sr relative to neighboring elements. These variations seem to complement opposite trends in plagioclase (Fig 5). Interestingly, summing clinopyroxene rims and plagioclase compositions in roughly equal proportions reproduces the composition of clinopyroxene cores (Fig. 7b); this suggests that the same melt that produced plagioclase and clinopyroxene core, becomes locally more evolved due to plagioclase crystallization (hence plagioclase composition does not vary) then crystallizes clinopyroxene rims and interstitial clinopyroxenes. We infer that the incompatible trace element enrichments recorded by clinopyroxenes point to melt-mass reductions as interstitial melt / trapped melt crystallizes (Meyer et al., 1989) rather than the arrival of a more evolved melt coming from elsewhere in the crystallizing gabbroic sequence.

7.3 Possible origin of olivine-rich troctolites

We argue above that olivine-rich troctolites from IODP Hole U1309D are the product of intense melt-rock interactions with a basaltic melt. We argue also that the olivines in these rocks are not in equilibrium with a MORB-type melt (fig. 6). Texturally and compositionally, olivine-rich troctolites from Hole U1309D are similar to the ultramafic rocks sampled at ODP Site 1275 (ODP Leg 209, MAR 15°N, Kelemen, et al., 2004). The latter have been interpreted as residual peridotite that was "impregnated" by plagioclase and pyroxene crystallized from melt migrating along olivine grain boundaries (Kelemen et al., 2004). The interaction between a percolated MORB-type melt and peridotite results in large changes in mineral compositions. Indeed, most of impregnated mantle rocks in oceanic setting (e.g., Hébert et al., 1983; Dick, 1989; Cannat et al., 1990; Allan and Dick, 1996; Arai and Matsukage, 1996; Dick and Natland, 1996; Seyler and Bonatti, 1997; Kamenetsky and Crawford, 1998; Tartarotti et al., 2002) and ophiolite (e.g., Rampone et al., 1997, 2008; Koga et al., 2001; Dijkstra et al., 2003; Borghini et al., 2007; Marchesi et al., 2006) are characterized by Ti-rich clinopyroxene, Cr and Ti rich spinel and Fe enriched olivine. IODP Hole U1309D olivine-rich troctolites present the same chemical characteristic, suggesting a mantle origin for these rocks.

8 Conclusions

Olivine-rich troctolites, and neighboring troctolites and gabbros from IODP Hole U1309D provide textural and geochemical evidences of a multistage petrological history involving extensive melt-rock interactions.

A first stage is represented by corroded olivines in the olivine-rich troctolites. Olivines are characterized by geochemical signature in disequilibrium with MORB-type melts. In addition, they have chemistry and textures similar to impregnated peridotites described elsewhere in ophiolites and present-day oceanic settings. They could represent relicts of highly impregnated mantle.

A second stage involves the percolation of a MORB-type melt through the pre-existing olivine-rich matrix, and results in the crystallization of plagioclase and clinopyroxene oikocrysts.

In a third stage, the composition of clinopyroxene becomes more enriched in incompatible lithophile elements, as seen in the rims of large oikocrysts, and in smaller, interstitial grains. These grain-scale variations of the chemistry are observed in all samples from the four studied olivine-rich intervals in IODP Hole U1309D. We infer that these enrichments correspond to the progressive closure of the melt percolation system in a progressively more crystalline matrix,

Oceanic gabbros are generally considered as the complementary products of crystallization of MORB. Yet, clinopyroxene and plagioclase from the most primitive end-member of the gabbroic series sampled at IODP Hole U1309D precipitated after a MORB melt, having the same composition as the basaltic crust at 30°N. This suggests that the olivine-rich intervals feed in parallel the basaltic upper crust and the lower crustal gabbroic series.

Acknowledgements

We thank captains Pete Mowat and Alex Simpson, the operation superintendents Mike Storms, Stephen Midgley, and Ron Grout, the crew of the JOIDES Resolution, and the Integrated Ocean Drilling Program (IODP) United States Implementing Organization's technical staff for their outstanding work during IODP Expeditions 304 and 305. We are grateful to Christophe Nevado and Doriane Delmas for providing high-quality thin sections, to Claude Merlet for his assistance with the electron microprobe analyses and to Simone Pourtales for technical assistance on the ICP-MS. This study was supported by INSU program DyETI (Dynamique et Evolution de la Terre Interne). Carlos J. Garrido acknowledges funding from the Spanish MICINN (Grants CGL2006-04440/BTE, CGL2007-

61205 and PCI2006-A9-0580) and the “Junta de Andalucía” (research group RNM.131). We thank Jean Bédard for helpful review and comments and D.B. Dingwell for editorial handling.

References

- Aigner-Torres, M., Blundy, J., Ulmer, P., and Pettke, T., 2007. Laser Ablation ICPMS study of trace element partitioning between plagioclase and basaltic melts: an experimental approach. *Contribution to Mineralogy and Petrology*, 153:647-667.
- Albarede, F., and Bottinga, Y., 1972. Kinetic disequilibrium in trace element partitioning between phenocrysts and host lava. *Geochimica et Cosmochimica Acta*, 36(2): 141-156.
- Allan, J.F., and Dick, H.J.B., 1996. Cr-rich spinel as a tracer for melt migration and melt-wall rock interaction in the mantle: Hess Deep, Leg 147. In Mével, C., Gillis, K.M., Allan, J.F., and Meyer, P.S. (Eds.), *Proc. ODP, Sci. Results, 147: College Station, TX (Ocean Drilling Program)*, 157–172. doi:10.2973/odp.proc.sr.147.009.1996
- Anonymous, 1972. Penrose field conference on ophiolites. *Geotimes*, 17, pp. 24–25.
- Arai, S., and Matsukage, K., 1996. Petrology of gabbro-troctolite-peridotite complex from Hess Deep, equatorial Pacific: implications for mantle-melt interaction within the oceanic lithosphere. In Mével, C., Gillis, K.M., Allan, J.F., and Meyer, P.S. (Eds.), *Proc. ODP, Sci. Results, 147: College Station, TX (Ocean Drilling Program)*, 135–155. doi:10.2973/odp.proc.sr.147.008.1996
- Bédard, J.H., 1994. A procedure for calculating the equilibrium distribution of trace elements among the minerals of cumulate rocks, and the concentration of trace elements in coexisting liquids. *Chemical Geology*, 118: 143-153.
- Bédard, J.H., Hebert, R., Berclaz, A., and Varfalvy, V., 2000. Syntexis and the genesis of lower oceanic crust. *Geological Society of America*, 349: 105-119.
- Bedini, R.-M., and Bodinier, J.-L., 1999. Distribution of incompatible trace elements between the constituents of spinel peridotite xenoliths : ICP-MS data from the East African Rift. *Geochimica et Cosmochimica Acta*, 63(22): 3883-3900.
- Bence, A.E., D.M. Baylis, J.F. Bender, and T.L. Grove, 1979. Controls on the major and minor element chemistry of mid-ocean ridge basalts and glasses. In Talwani, M., Harrison, C.G., and Hayes, D.E. (Eds), *Deep Drilling Results in the Atlantic Ocean: Oceanic Crust, Maurice Ewing Symposium. AGU Washington D.C.* pp. 331-341.
- Bender, J.F., Hodges, F.N., and Bence, A.E., 1978. Petrogenesis of basalts from the project FAMOUS area : experimental study from 0 to 15 Kbars. *Earth and planetary Science Letters*, 41: 277-302.
- Blackman, D.K., Cann, J.R., Janssen, B., and Smith, D.K., 1998. Origin of extensional core complexes: evidence from the MAR at Atlantis Fracture Zone. *Journal of Geophysical Research*, 103: 21315-21334.
- Blackman, D.K., Karson, J.A., Kelley, D.S., Cann, J.R., Fruh-Green, G.L., Gee, J.S., Hurst, S.D., John, B.E., Morgan, J., Nooner, S.L., Ross, D.K., Schroeder, T.J., and Williams, E.A., 2002. Geology of the Atlantis Massif (MAR 30°N): implications for the evolution of an ultramafic oceanic core complex. *Marine Geophysical Researches*, 23(5-6): 443-469.
- Blackman, D.K., Ildefonse, B., John, B.E., Ohara, Y., Miller, D.J., MacLeod, C.J., and the Expedition 304/305 Scientists, 2006. *Proc. IODP, 304/305: College Station TX*

- (Integrated Ocean Drilling Program Management International, Inc.). doi:10.2204/iodp.proc.304305.2006
- Bloomer, S.H., Meyer, P.S., Dick, H.J.B., Ozawa, K., and Natland, J.H., 1991. Textural and mineralogic variations in gabbroic rocks from Hole 735B. In Von Herzen, R., Robinson, P.T., et al., Proc. ODP, Sci. Results, 118: College Station, TX (Ocean Drilling Program), 21–39. doi:10.2973/odp.proc.sr.118.136.1991
- Bloomer, S.H., Natland, J.H., and Fisher, R.L., 1989. Mineral relationships in gabbroic rocks from fracture zones of Indian Ocean Ridges: evidence for extensive fractionation, parental diversity and boundary-layer recrystallization. Geological Society of London Special Publications, 42: 107-124.
- Bodinier, J.-L., Merlet, C., Bedini, R.M., Simien, F., Remaïdi, M. and Garrido, C.J., 1996. Distribution of Nb, Ta and other highly incompatible trace elements in the lithospheric mantle : the spinel paradox. *Geochim. Cosmochim. Acta*, 60(3): 545-550.
- Bodinier, J. L., Garrido, C. J., Chanefo, I., Bruguier, O. and Gervilla, F., 2008. Origin of pyroxenite-peridotite veined mantle by refertilization reactions: Evidence from the Ronda peridotite (Southern Spain). *Journal of Petrology* 49, 999-1025. doi:10.1093/petrology/egn014.
- Bonatti, E., Ottonello, G., and Hamlyn, P.R., 1986. Peridotites from the Island of Zabargad (St John), Red Sea : Petrology and geochemistry. *Journal of Geophysical Research*, 91: 599-631
- Bonatti, E., Peyve, A., Kepezhinskas, P., Kurentsova, N., Seyler, M., Skolotnev, S., and Udintsev, G., 1992. Upper mantle heterogeneity below the Mid-Atlantic Ridge, 0-15°N. *Journal of Geophysical Research*, 97(B4): 4461-4476.
- Bonatti, E., Seyler, M., and Sushevskaya, N., 1993. A cold suboceanic mantle belt at the Earth's equator. *Science*, 261: 315-320.
- Borghini, G., Rampone, E., Crispini, L., De Ferrari, R., and Godard, M., 2007. Origin and emplacement of ultramafic-mafic intrusions in the Erro-Tobbio mantle peridotite (Ligurian Alps, Italy). *Lithos*, 94(1-4): 210-229.
- Borghini, G., and Rampone, E., 2007. Postcumulus processes in oceanic-type olivine-rich cumulates: the role of trapped melt crystallization versus melt/rock interaction. *Contribution to Mineralogy and Petrology*, 154(6): 619-633.
- Boudier, F., and Nicolas, A., 1995. Nature of the Moho transition zone in the Oman ophiolite. *Journal of Petrology*, 36(3): 777-796.
- Canales, J.P., Detrick, R.S., Lin, J., Collins, J.A., and Toomey, D.R., 2000. Crustal and upper mantle seismic structure beneath the rift mountains and across a nontransform offset at the Mid-Atlantic Ridge (35 degrees N). *J. Geophys. Res.*, 105: 2699-2719.
- Cann, J.R., Blackman D.K., Smith, D.K., McAllister, E., Janssen, B., Mello, S., Avgerinos, E., Pascoe, A.R., and Escartin J., 1997. Corrugated slip surfaces formed at ridge-transform intersections on the Mid-Atlantic Ridge. *Nature*, 385: 329-332.
- Cannat, M., 1993. Emplacement of mantle rocks in the seafloor at mid-ocean ridges. *Journal of Geophysical Research*, 98: 4163-4172.
- Cannat, M., 1996. How thick is the magmatic crust at slow spreading oceanic ridges? *Journal of Geophysical Research*, 101(B2): 2847-2857.
- Cannat, M., Bideau, D., and Hebert, R., 1990. Plastic deformation and magmatic impregnation in serpentinized ultramafic rocks from the Garrett transform fault (East Pacific Rise). *Earth and Planetary Science Letters*, 101: 216-232.
- Cannat, M., and Casey, J.F., 1995. An ultramafic lift at the Mid-Atlantic Ridge: successive stages of magmatism in serpentinized oceanic upper mantle: Mid-Atlantic Ridge 15°N. Mantle and lower crust exposed in oceanic ridges and in ophiolites.

- Carlson, R.L., 2001. The abundance of ultramafic rocks in Atlantic Ocean crust. *Geophys. J. Int.*, 144: 37-48.
- Constantin, M., Hekinian, R., Bideau, D., and Hebert, R., 1996. Construction of the oceanic lithosphere by magmatic intrusions: Petrological evidence from plutonic rocks formed along the fast-spreading East Pacific Rise. *Geology*, 24: 731-734.
- Coogan, L.A., Kempton, P.D., Saunders, A.D., and Norry, M.J., 2000a. Melt aggregation within the crust beneath the Mid-Atlantic Ridge: evidence from plagioclase and clinopyroxene major and trace element compositions. *Earth and Planetary Science Letters*, 176(2): 245-257.
- Coogan, L.A., Saunders, A.D., Kempton, P.D. and Norry, M.J., 2000b. Evidence from oceanic gabbros for porous melt migration within a crystal mush beneath the Mid-Atlantic Ridge. *Geochemistry, Geophysics, Geosystems - G3*, 1(9). doi: 10.1029/2000GC000072.
- Coogan, L.A., MacLeod, C.J., Dick, H.J.B., Edwards, S.J., Kvassnes, A., Natland, J.H., Robinson, P.T., Thompson, G., and O'Hara, M.J., 2001. Whole-rock geochemistry of gabbros from the Southwest Indian Ridge: constraints on geochemical fractionations between the upper and lower oceanic crust and magma chamber processes at (very) slow-spreading ridges. *Chemical Geology*, 178(1-4): 1-22.
- Dick, H.J.B., and Bullen, T., 1984. Chromian spinel as a petrogenetic indicator in abyssal and alpine-type peridotites and spatially associated lavas. *Contribution to Mineralogy and Petrology*, 86(1): 54-76.
- Dick, H.J.B., 1989. Abyssal peridotites, very slow spreading ridges and ocean ridge magmatism. In: A.D. Saunders and M.J. Norry (Editors), *Magmatism in the Ocean Basins*. Geological Society of London Special Publication, London, 42 : pp 71-105.
- Dick, H.J.B., and Natland, J.H., 1996. Late-stage melt evolution and transport in the shallow mantle beneath the East Pacific Rise. In Mével, C., Gillis, K.M., Allan, J.F., and Meyer, P.S. (Eds.), *Proc. ODP, Sci. Results*, 147: College Station, TX (Ocean Drilling Program), 103–134. doi:10.2973/odp.proc.sr.147.007.1996
- Dick, H.J.B., Natland, J.H., Miller, D.J., et al., 1999. *Proc. ODP, Init. Repts.*, 176: College Station, TX (Ocean Drilling Program). doi:10.2973/odp.proc.ir.176.1999
- Dick, H.J.B., Natland, J.H., Alt, J.C., Bach, W., Bideau, D., Gee, J.S., Haggas, S., Hertogen, J.G.H., Hirth, G., Holm, P.M., Ildefonse, B., Iturrino, G.J., John, B.E., Kelley, D.S., Kikawa, E., Kingdon, A., LeRoux, P.J., Maeda, J., Meyer, P.S., Miller, D.J., Naslund, H.R., Niu, Y., Robinson, P.T., Snow, J., Stephen, R.A., Trimby, P.W., Worm, H.-U., and Yoshinobu, A., 2000. A long in situ section of the lower ocean crust: results of ODP Leg 176 drilling at the Southwest Indian Ridge. *Earth Planet. Sci. Lett.*, 179:31-51. doi:10.1016/S0012-821X(00)00102-3
- Dijkstra, A.H., Barth, M.G., Drury, M.R., Mason, P.R.D., and Vissers R.M.L., 2003. Diffuse porous melt flow and melt-rock reaction in the mantle lithosphere at the slow-spreading ridge: a structural petrology and LA-ICP-MS study of the Othris Peridotite Massif (Greece). *Geochemistry, Geophysics, Geosystems*, 4: 1-24.
- Donaldson, C.H., 1985. A comment on crystal shapes resulting from dissolution in magmas. *Mineralogical Magazine*, 49: 129-132.
- Drouin, M., Godard, M., and Ildefonse, B., 2007. Origin of olivine-rich troctolites from IODP Hole U1309D in the Atlantis Massif (Mid-Atlantic Ridge): Petrostructural and geochemical study. *Eos Trans. AGU*, 88(52), Fall Meet. Suppl., Abstract T53B-1300.
- Drouin, M., Ildefonse, B., and Godard, M. Evidences of high degrees of melt impregnation in the mantle at slow spreading ridges: A petrological and microstructural study of the olivine-rich troctolites from Atlantis Massif (Mid-Atlantic Ridge 30°N, IODP Hole U1309D), *Earth Planet. Sci. Lett.*, in prep.

- Edwards, S.J., and Malpas, J., 1996. Melt-peridotite interactions in shallow mantle at the East Pacific Rise: evidence from ODP Site 895 (Hess Deep). *Mineralogical Magazine*, 60: 191-206.
- Elthon, D., Casey, J.F., and Komor, S., 1982. Mineral chemistry of ultramafic cumulates from the North Arm Mountain Massif of the Bay of Islands Ophiolite: implication for high pressure fractionation of oceanic basalts. *Journal of Geophysical Research*, 87.
- Elthon, D., Stewart, M., and Ross, D.K., 1992. Compositional trends of minerals in oceanic cumulates. *Journal of Geophysical Research*, 97(B11): 15,189-15,199.
- Falloon, T.J., and Green, D.H., 1987. Anhydrous partial melting of MORB pyroxene and other peridotite compositions at 10 kbar; implications for the origin of primitive MORB glasses. *Mineralogy and Petrology*, 37(3-4): 181-219.
- Fisk, M.R., and Bence, A.E., 1980. Experimental crystallization of chrome spinel in FAMOUS basalt 527-1-1. *Earth and Planetary Science Letters*, 48: 111-123.
- Fujii, N., and Bougault, H., 1983. Melting relations of a magnesian abyssal tholeiite and the origin of MORBs. *Earth and planetary Science Letters*, 62(2): 283-295.
- Fujii, T., 1990. Petrology of peridotites from Hole 670A, Leg 109. In Detrick, R., Honnorez, J., Bryan, W.B., Juteau, T., et al., Proc. ODP, Sci. Results, 106/109: College Station, TX (Ocean Drilling Program), 19–25. doi:10.2973/odp.proc.sr.106109.116.1990
- Gao, Y., Hoefs, J., Hellebrand, E., Von de Handt, A., and Snow, J.E., 2007. Trace element zoning in pyroxenes from ODP Hole 735B gabbros: diffuse exchange or synkinematic crystal fractionation? *Contribution to Mineralogy and Petrology*, 153: 429-442.
- Garrido, C.J., Bodinier, J.-L. and Alard, O., 2000. Distribution of LILE, REE and HFSE in anhydrous spinel peridotite and websterite minerals from the Ronda massif: insights into the nature of trace element reservoirs in the subcontinental lithospheric mantle. *Earth Planet. Sci. Lett.*, 181(3): 341-358.
- Gerbert-Gaillard, L., 2002. Caractérisation géochimique des peridotites de l'ophiolite d'Oman : Processus magmatiques aux limites lithosphère/asthénosphère. Doctorat Thesis, Montpellier 2, Montpellier, 266 pp. Available at <http://tel.archives-ouvertes.fr/tel-00002961/en/>
- Ghiorso, M.S., 1985. Chemical mass-transfer in magmatic processes. 1. Thermodynamic relations and numerical algorithms. *Contribution to Mineralogy and Petrology*, 90(2-3): 107-120.
- Ghiorso, M.S., and Sack R.O., 1995. Chemical mass transfer in magmatic processes IV. A revised and internally consistent thermodynamic model for the interpolation and extrapolation of liquid-solid equilibria in magmatic systems at elevated temperatures and pressures. *Contribution to Mineralogy and Petrology*, 119(2-3): 197-212.
- Godard, M., Jousset, D., and Bodinier, J.-L., 2000. Relationships between geochemistry and structure beneath a palaeo-spreading centre: A study of the mantle section in the Oman Ophiolite. *Earth and planetary Science Letters*, 180: 133-148.
- Godard, M., Awaji, S., Hansen, H.-E., Hellebrand, E., Brunelli, D., Johnson, K.T.M., Yamasaki, T., Maeda, J., Abratis, M., Christie, D., Kato, Y., Mariet, C. and Rosner, M., in press. Geochemistry of a long in-situ section of intrusive slow-spread lithosphere: Results from IODP Site U1309 (Atlantis Massif, 30°N Mid-Atlantic-Ridge). *Earth Planet. Sci. Lett.*
- Green, D.H., and Ringwood, A.E., 1967. The genesis of basaltic magmas. *Contribution to Mineralogy and Petrology*, 15: 103-190
- Grove, T.L., and Bryan, W.B., 1983. Fractionation of pyroxene-phyric MORB at low pressure-an experimental-study. *Contribution to Mineralogy and Petrology*, 84(4): 293-309.

- Grove, T.L., Kinzler, R.J., and Bryan, W.B., 1992. Fractionation of Mid-Ocean Ridge Basalt (MORB). In: J. Philipps Morgan, D.K. Blackman and J.M. Sinton (Eds.), *Mantle flow and melt generation at Mid-Ocean Ridges*. American Geophysical Union, pp. 281-311.
- Gunther, D., and Heinrich, C.A., 1999. Enhanced sensitivity in laser ablation-ICP mass spectrometry using helium-argon mixtures as aerosol carrier - Plenary lecture. *Journal of Analytical Atomic Spectrometry*, 14(9): 1363-1368.
- Hart, S.R., Blusztajn, J., Dick, H.J.B., Meyer, P.S., and Muehlenbachs, K., 1999. The fingerprint of seawater circulation in a 500-meter section of ocean crust gabbros. *Geochimica Et Cosmochimica Acta*, 63(23-24): 4059-4080.
- Hébert, R., Bideau, D., and Hékinian, R., 1983. Ultramafic and mafic rocks from the Garret transform fault near 13°30'S on the East Pacific Rise: igneous petrology. *Earth and Planetary Science Letters*, 65: 107-125.
- Hébert, R., Constantin, M., and Robinson, P.T., 1991. Primary mineralogy of Leg 118 gabbroic rocks and their place in the spectrum of oceanic mafic igneous rocks. In Von Herzen, R., Robinson, P.T., et al., *Proc. ODP, Sci. Results*, 118: College Station, TX (Ocean Drilling Program), 3–20. doi:10.2973/odp.proc.sr.118.119.1991
- Ildefonse, B., Blackman, D.K., John, B.E., Ohara, Y., Miller, D.J., MacLeod, C.J., and the IODP Expeditions 304-305 Scientists, 2006. IODP Expeditions 304 & 305 Characterize the Lithology, Structure, and Alteration of an Oceanic Core Complex. *Scientific Drilling*, 3, 4-11, doi:10.2204/iodp.sd.3.01.2006.
- Ildefonse, B., Blackman, D.K., John, B.E., Ohara, Y., Miller, D.J., MacLeod, C.J., and the IODP Expeditions 304-305 Scientists, 2007a. Oceanic Core Complexes and Crustal Accretion at Slow-Spreading Ridges. *Geology*, 35, 623-626; doi: 10.1130/G23531A.1.
- Ildefonse, B., Christie, D.M., and Mission Moho Workshop Steering Committee, 2007b. Mission Moho workshop : drilling through the oceanic crust to the Mantle. *Scientific Drilling*, 4:11-18. doi:10.2204/iodp.sd.4.02.2007.
- Ionov, D., 1996. Distribution and residence of lithophile trace elements in minerals of garnet and spinel peridotites: an ICP-MS study. *Journal of Conference Abstracts*, 1, 278.
- Juster, T.C., Grove, T.L. and Perfit, M.R., 1989. Experimental Constraints on the Generation of FeTi Basalts, Andesites, and Rhyodacites at the Galapagos Spreading Center, 85°W and 95°W. *Journal of Geophysical Research-Solid Earth and Planets*, 94(B7): 9251-9274.
- Juteau, T., Berger, E.T., and Cannat, M., 1990. Serpentinized, residual, mantle peridotites from the MAR Median valley, ODP Hole 670A (21°10N, 45°02W, Lag 109): primary mineralogy and geothermometry *Proceedings of Ocean Drilling Program, Scientific Results*, 106/109: 27-45.
- Kalfoun, F., Ionov, D., and Merlet, C., 2002. HFSE residence and Nb/Ta ratios in metasomatised, rutile-bearing mantle peridotites. *Earth and Planetary Science Letters*, 199(1-2): 49-65.
- Kamenetsky, V.S., and Crawford, A.J., 1998. Melt-peridotite reaction recorded in the chemistry of spinel and melt inclusions in basalt from 43 degrees N, Mid-Atlantic Ridge. *Earth and Planetary Science Letters*, 164(1-2): 345-352.
- Karson, J.A., Fruh-Green, G.L., Kelley, D.S., Williams, E.A., Yoerger, D.R., and Jakuba, M., 2006. Detachment shear zone of the Atlantis Massif core complex, Mid-Atlantic Ridge, 30°N. *Geochemistry, Geophysics, Geosystems* - G 3, 7. doi: 10.1029/2005GC001109.
- Kelemen, P.B., Kikawa, E., Miller, D.J., Abe, N., Bach, W., Carlson, R.L., Casey, J.F., Chambers, L.M., Cheadle, M., Cipriani, A., Dick, H.J.B., Faul, U., Garces, M., Garrido, C., Gee, J.S., Godard, M., Griffin, D.W., Harvey, J., Ildefonse, B., Iturrino,

- G.J., Josef, J., Meurer, W.P., Paulick, H., Rosner, M., Schroeder, T., Seyler, M. and Takazawa, E., 2004. Proc. ODP, Init. Repts., 209 [Online]. Available from World Wide Web: http://www-odp.tamu.edu/publications/209_IR/209ir.htm.
- Kennedy, A.K., Lofgren, G.E. and Wasserburg, G.J., 1993. An experimental study of trace element partitioning between olivine, orthopyroxene and melt in chondrules: equilibrium values and kinetic effects, *Earth and Planetary Science Letters*, 115 (1-4), 177-195.
- Kinzler, R.J. and Grove, T.L., 1993. Corrections and further discussion of the primary magmas of mid-ocean ridge basalts, 1 and 2. *Journal of Geophysical Research*, 98(B12): 22339-22347.
- Klemme, S., Günther, D., Hametner, K., Prowatke, S. and Zack, T., 2006. The partitioning of trace elements between ilmenite, ulvospinel, armalcolite and silicate melts with implications for the early differentiation of the moon. *Chem. Geol.*, 234: 251-263.
- Koga, K.T., Kelemen, P.B. and Shimizu, N., 2001. Petrogenesis of the crust-mantle transition zone and the origin of lower crustal wehrlite in the Oman ophiolite. *Geochemistry, Geophysics, Geosystems*.
- Korenaga, J., and Kelemen, P.B., 1998. Melt migration through the oceanic lower crust: a constraint from melt percolation modeling with finite solid diffusion. *Earth and Planetary Science Letters*, 156(1-2): 1-11.
- Komor, S., Grove, T.L., and Hébert, R., 1990. Abyssal peridotites from ODP Hole 670A (21°10N, 45°02W): residues of mantle melting exposed by non-constructive axial divergence. , *Proceedings of Ocean Drilling Program, Scientific Results*, pp. 85-101.
- Kvassness, A.J.S., 2004. Evolution of oceanic gabbros: in-situ and ancient examples. PhD Thesis, Woods Hole Oceanographic Institution. Available at <http://hdl.handle.net/1912/1860>.
- Kvassnes, A.J.S., and Grove, T.L., 2008. How partial melts of mafic lower crust affect ascending magmas at ocean ridges. *Contrib Mineral Petrol* (2008) 156:49–71.
- Lagabrielle, Y., and Cannat, M., 1990. Alpine jurassic ophiolites resemble the modern Central Atlantic basement. *Geology*, 18: 319-322.
- Lee, C.-T. A., Harbert, A., and Leeman, W.P., 2007. Extension of lattice strain theory to mineral/mineral rare-earth element partitioning: an approach for assessing disequilibrium and developing internally consistent partition coefficients between olivine, orthopyroxene, clinopyroxene and basaltic melt. *Geochimica et Cosmochimica Acta*, 71: 481-496.
- Lissenberg, C.J., and Dick, H.J.B., 2008. Melt-rock reaction in the lower oceanic crust and its implications for the genesis of mid-ocean ridge basalt. *Earth and Planetary Science Letters*, doi: 10.1016/j.epsl.2008.04.023
- Marchesi, C., Garrido, C., Godard, M., Proenza, J.A., Gervilla, F. and Blanco-Moreno, J., 2006. Petrogenesis of highly depleted peridotites and gabbroic rocks from the Mayari-Baracoa ophiolitic belt (Eastern Cuba). *Contributions to Mineralogy and Petrology*, 151: 717-736.
- Mathez, E.A., 1995. Magmatic metasomatism and formation of the Merensky reef, Bushveld Complex. *Contributions to Mineralogy and Petrology*, 119: 277-286.
- McKay, G.A., Wagstaff, J., and Yang, S.R., 1986. Clinopyroxene REE distribution coefficients for shergottites: The REE content of the Shergotty melt. *Geochimica et Cosmochimica Acta*, 50: 927-937.
- Merlet, C., and Bodinier, J.-L., 1990. Electron microprobe determination of minor and trace transition elements in silicate minerals: a method and its application to mineral zoning in the peridotite nodule PHN-1611. *Chemical Geology*, 83(Spc. Issue "Microanalytical methods in mineralogy and geochemistry"): 55-69.

- Meyer, P.S., Dick, H.J.B., and Thompson, G., 1989. Cumulate gabbros from the southwest Indian Ridge, 54°S-7°16'E: implications for magmatic processes at slow spreading ridge. *Contributions to Mineralogy and Petrology*, 103: 44-63.
- Miller, D.J., Abratis, M., Christie, D., Drouin, M., Godard, M., Ildefonse, B., Maeda, J., and Weinsteiger, A., submitted. Data Report: Microprobe analyses of primary mineral phases (plagioclase, pyroxene, olivine, and spinel) from Site U1309, Atlantis Massif, Integrated Ocean Drilling Program Expedition 304/305. In : Blackman, D.K., Ildefonse, B., John, B.E., Ohara, Y., Miller, D.J., MacLeod, C.J., and the Expedition 304/305 Scientists, 2006. *Proc. IODP, 304/305: College Station TX (Integrated Ocean Drilling Program Management International, Inc.)*.
- Natland, J.H., and Dick, H.J.B., 1996. Melt migration through high-level gabbroic cumulates of the East Pacific Rise at Hess Deep: the origin of magma lenses and the deep crustal structure of fast-spreading ridges. In Mével, C., Gillis, K.M., Allan, J.F., and Meyer, P.S. (Eds.), *Proc. ODP, Sci. Results, 147: College Station, TX (Ocean Drilling Program)*, 21–58. doi:10.2973/odp.proc.sr.147.002.1996
- Natland, J.H., Meyer, P.S., Dick, H.J.B., and Bloomer, S.H., 1991. Magmatic oxides and sulfides in gabbroic rocks from Hole 735B and the later development of the liquid line of descent. In Von Herzen, R., Robinson, P.T., et al., *Proc. ODP, Sci. Results, 118: College Station, TX (Ocean Drilling Program)*, 75–111. doi:10.2973/odp.proc.sr.118.163.1991
- Navon, O., and Stolper, E., 1987. Geochemical Consequences of Melt Percolation - the Upper Mantle as a Chromatographic Column. *Journal of Geology*, 95: 285-307.
- Niu, Y., 2004. Bulk-rock major and trace element compositions of abyssal peridotites: implications for mantle melting, melt extraction and post-melting processes beneath mid-ocean ridges. *Journal of Petrology*: 1-36.
- Niu, Y., and Hekinian, R., 1997. Basaltic liquids and harzburgitic residues in the Garrett Transform; a case study at fast-spreading ridges. *Earth and Planetary Science Letters*, 146(1-2): 243-258.
- Ozawa, K., Meyer, P.S., and Bloomer, S.H., 1991. Mineralogy and textures of iron-titanium oxide gabbros and associated olivine gabbros from Hole 735B. In Von Herzen, R., Robinson, P.T., et al., *Proc. ODP, Sci. Results, 118: College Station, TX (Ocean Drilling Program)*, 41–73. doi:10.2973/odp.proc.sr.118.125.1991
- Paulick, H., Bach, W., Godard, M., De Hoog, J.C.M., Suhr, G., and Harvey, J., 2006. Geochemistry of abyssal peridotites (Mid-Atlantic Ridge, 15°20'N, ODP Leg 209): implications for fluid/rock interaction in slow spreading environments. *Chemical Geology*, 234:179-210. doi:10.1016/j.chemgeo.2006.04.011
- Pearce, N.J.G., Perkins, W.T., Westgate, J.A., Gorton, M.P., Jackson, S.E., Neal, C.R., and Chenery S.P., 1997. A compilation of new and published major and trace element data for NIST SRM 610 and NIST SRM 612 glass reference materials. *Geostandards Newsletter- The journal of Geostandards and Geoanalysis* 21(1): 115-144.
- Phipps Morgan, J., and Chen, Y.J., 1993. The genesis of oceanic crust: magma injection, hydrothermal circulation, and crustal flow. *Journal of Geophysical Research*, 98: 6283-6297.
- Putirka, D., 2005. Igneous thermometers and barometers based on plagioclase + liquid equilibria: Tests of some existing models and new calibrations. *American Mineralogist*, 90: 336-346.
- Quick, J.E., and Denlinger, R.P., 1993. Ductile deformation and the origin of layered gabbro in ophiolites. *Journal of Geophysical Research*, 98:14015-14027.

- Rampone, E., Piccardo, G.B., Vannucci, R., and Bottazzi, P., 1997. Chemistry and origin of trapped melts in ophiolitic peridotites. *Geochimica and Cosmochimica Acta*, 61(21): 4557-4569.
- Rampone, E., Piccardo, G.B., and Hofmann, A.W., 2008. Multi-stage melt-rock interaction in the Mt. Maggiore (Corsica, France) ophiolitic peridotites: microstructural and geochemical evidence. *Contribution to Mineralogy and Petrology*, doi: 10.1007/s00410-008-0296-y.
- Ridley, W.I., Perfit, M.R., Smith, M.C., and Fornari, D.J., 2006. Magmatic processes in developing oceanic crust revealed in a cumulate xenolith collected at the East Pacific Rise, 9°50'N. *Geochemistry, Geophysics, Geosystems*, 7. doi:10.1029/2006GC001316.
- Roden, M.K., Hart, S.T., Frey, F.A., and Melson, W.G., 1984. Sr, Nd and Pb isotopic and REE geochemistry of St. Paul's Rocks: the metamorphic and metasomatic development of an alkali basalt mantle source. *Contribution to Mineralogy and Petrology*, 85: 376-390.
- Rosenbaum, J.M., Zindler, A., and Rubenstone, J.L., 1996. Mantle fluids: Evidence from fluid inclusions. *Geochimica et Cosmochimica Acta*, 60: 3229-3252.
- Ross, K., and Elthon, D., 1997. Cumulus and postcumulus crystallization in the oceanic crust: major- and trace-element geochemistry of Leg 153 gabbroic rocks. In Karson, J.A., Cannat, M., Miller, D.J., and Elthon, D. (Eds.), *Proc. ODP, Sci. Results*, 153: College Station, TX (Ocean Drilling Program), 333-350. doi:10.2973/odp.proc.sr.153.023.1997.
- Schiano, P., Clocchiatti, R., Shimizu, N., Maury, R.C., Jochum, K.P., and Hofmann, A.W., 1995. Hydrous, silica-rich melts in the sub-arc mantle and their relationship with erupted arc lavas. *Nature*, 377: 595-600.
- Schroeder, T.J., and John, B.E., 2004. Strain localisation on an oceanic detachment fault system, Atlantis Massif, 30°N, Mid-Atlantic Ridge., *Geochemistry, Geophysics, Geosystems*.
- Seyler, M., and Bonatti, E., 1997. Regional-scale melt-rock interaction in Iherzolitic mantle in the Romanche fracture zone (Atlantic Ocean). *Earth and Planetary Science Letters*, 146(1-2): 273-287.
- Seyler, M., Cannat, M., and Mével, C., 2003. Evidence for major element heterogeneity in the mantle source of abyssal peridotite from the Southwest Indian Ridge (52° to 68°E). *Geochemistry, Geophysics, Geosystems*, 10.
- Shibata, T., and Thompson, G., 1986. Peridotites from the Mid-Atlantic Ridge at 43°N and their petrogenetic relation to abyssal tholeiites. *Contribution to Mineralogy and Petrology*, 93: 144-159.
- Sigurdson, H., and Schilling, J.-G., 1976. Spinels in Mid-Atlantic Ridge basalts: Chemistry and occurrence. *Earth and Planetary Science Letters*, 29: 7-20.
- Spandler, C., O'Neill, H. St C. and Kamenetsky, V. S., 2007. Survival times of anomalous melt inclusions from element diffusion in olivine and chromite, *Nature*, 447, doi:10.1038/nature05759.
- Stolper, E.A., 1980. Phase diagram for Mid-Ocean Ridge basalts: preliminary results and implications for petrogenesis. *Contribution to Mineralogy and Petrology*, 74: 13-27.
- Sun, M., and Kerrich, R., 1995. Rare earth element and high field strength element characteristics of whole rocks and mineral separates of ultramafic nodules in Cenozoic volcanic vents of southeastern British Columbia, Canada. *Geochimica et Cosmochimica Acta*, 59(23): 4863-4879.
- Sun, S.S., and McDonough, W.F., 1989. Chemical and isotopic systematics of oceanic basalts: implications for mantle composition and processes. In: A.D. Saunders and

- M.J. Norry (Eds.), Magmatism in the ocean basins. Geological Society of London, pp. 313-345.
- Takazawa, E., Abe, N., Seyler, M., and Meurer, W.P., 2007. Hybridization of dunite and gabbroic materials in Hole 1271B from Mid-Atlantic Ridge 15°N: implications for melt flow and reaction in the upper mantle. In Kelemen, P.B., Kikawa, E., and Miller, D.J. (Eds.), Proc. ODP, Sci. Results, 209: College Station, TX (Ocean Drilling Program), 1–23. doi:10.2973/odp.proc.sr.209.005.2007
- Tartarotti, P., Susini, S., Nimis, P., and Ottolini, L., 2002. Melt migration in the upper mantle along the Romanche Fracture Zone (Equatorial Atlantic). *Lithos*, 63: 125-149.
- Tormey, D.R., Grove, T.L., and Bryan, W.B., 1987. Experimental petrology of normal MORB near the Kane fracture-zone, 22 degrees - 25-degrees N, Mid Atlantic Ridge. *Contribution to Mineralogy and Petrology*, 96(2): 121-139.
- Tribuzio, R., Tiepolo, M., Vannucci, R., and Bottazzi, P., 1999. Trace element distribution within olivine-bearing gabbros from the Northern Apennine ophiolites (Italy): evidence for post-cumulus crystallization in MOR-type gabbroic rocks. *Contribution to Mineralogy and Petrology*, 134(2-3): 123-133.
- Van Achterberg, E., Ryan, C.G., Jackson, S.E., and Griffin, W., 2001. Data reduction software for LA-ICP-MS. In: P. Sylvester (Ed.), *Laser ablation ICP-MS in the Earth Science*. Mineralogical Association of Canada, pp. 239-243.
- Van Orman, J.A., Grove, T.L., Shimizu, N., 2002. Diffusive fractionation of trace elements during production and transport of melt in Earth's upper mantle, *Earth and Planetary Science Letters* 198, 93-112.
- Workman, R.K., and Hart, S.R., 2005. Major and trace element composition of the depleted MORB mantle (DMM). *Earth and Planetary Science Letters*, 231(1-2): 53-72.

Figure Captions:

Fig. 1: (a) Bathymetric map of Atlantis Massif with location of Hole U1309D drilled during IODP expedition 304-305. (b) Lithology proportions in Hole U1309D, 20m vertical running average (Blackman et al., 2006) and localization of the four sampled olivine-rich intervals. (c) Streckeisen diagram of studied samples, and other samples from IODP Hole U1309D. Note that olivine-rich troctolites are characterized by their proportion of olivine (~ >70%), and by their texture (see text for further details).

Fig. 2: Representative rock textures in studied sampled from Hole U1309D (Ol : olivine, Pl : plagioclase, Cpx : clinopyroxene, Sp : Spinel). (A) Subhedral grains of olivine and subhedral laths of plagioclase in a troctolite. Spinel occurs as small subhedral grain between olivine and plagioclase crystals (sample 251R1_87-89). (B) Poikilitic texture in an olivine-rich troctolite characterized by subhedral olivine crystals with subgrain boundaries and small rounded olivine crystals embedded in large clinopyroxene and plagioclase poikiloblasts. Spinel occurs

as small subhedral crystals with polygonal shape, included in olivine, plagioclase or clinopyroxene crystals (sample 247R3_16-18). (C) Zoom on figure 2B: chains of polygonal olivine grains, with curvilinear boundaries, in optical continuity (sample 247R3_16-18). (D) Interstitial clinopyroxene in an olivine-rich troctolite showing lobate contact with rounded olivine (sample 241R2_94-97). (E) Euhedral plagioclase and cumulus clinopyroxene in a gabbro (sample 285R1_90-92). (F) Large and irregular cumulus grain of clinopyroxene and elongated laths of plagioclase in a gabbro (sample 291R3_39-41).

Fig. 3: (a) Plagioclase anorthite content (%) versus clinopyroxene Mg# ($Mg\# = 100 \times \text{cationic}$ in gabbros, troctolites and olivine-rich troctolites of Hole U1309D. (b) TiO_2 (wt. %) versus Cr_2O_3 (wt. %) in clinopyroxene in gabbros, troctolites and olivine-rich troctolites of Hole U1309D, with core-rim variations. (c) Clinopyroxene Mg# versus olivine Mg# in gabbros, troctolites and olivine-rich troctolites of Hole U1309D. The solid line illustrates equilibrium values between olivine and clinopyroxene (using olivine/liquid and clinopyroxene/liquid Fe-Mg partition coefficients of 0.3 and 0.23 respectively, Lissenberg and Dick, 2008). Dashed lines define equilibrium compositions with uncertainties of 0.02 for both partition coefficients (Lissenberg and Dick, 2008). (d) Ni content (ppm) in olivine versus olivine Mg# in gabbros, troctolites and olivine-rich troctolites of Hole U1309D. The following data are shown for comparison: average abyssal peridotites (Roden et al., 1984 ; Bonatti et al., 1986; Shibata and Thompson, 1986; Fujii, 1990; Juteau et al., 1990; Komor et al., 1990; Bonatti et al., 1992; Bonatti et al., 1993; Tartarotti et al., 2002; Seyler et al., 2003), impregnated peridotite from ODP Leg 147 (Hess Deep transition zone. Allan and Dick, 1996; Arai and Matsukage, 1996; Edwards and Malpas, 1996), impregnated dunite and gabbroic material from ODP hole 1271B (Takasawa et al., 2007), gabbros from MAR (Bloomer et al., 1991; Ozawa et al., 1991; Cannat and Casey, 1995; Ross and Elthon, 1997; Lissenberg and Dick, 2008), gabbros from ODP Hole 735B, at the SWIR (Hébert et al., 1991; Natland et al., 1991; Ozawa et al., 1991). Major element evolution during fractionation and equilibrium crystallization (noted CF and CE respectively) were calculated using a potential minimization program (PELE) based on the algorithms and database of Ghiorso (1985) and Ghiorso and Sack (1995), and are reported in a and d. PELE has been programmed by Alan E. Boudreau and can be downloaded at: <http://www.nicholas.duke.edu/people/faculty/boudreau/Downloads.html>. Initial melt composition is primary melt calculated after 10.3 % melting at 15Kbar (Kinzler and Grove, 1993). Symbols indicate appearance of each phase during process of crystallization, and associated labels in *italics* indicate the percentage of remaining liquid. Cpx: clinopyroxene, Ol:

olivine, Pl : plagioclase.

Fig. 4: Chondrites-normalized Rare Earth Element (REE) diagrams for (a) clinopyroxene cores; (b) clinopyroxene rims and interstitial clinopyroxenes ; (c) plagioclase from gabbros, troctolites and olivine-rich troctolites of Hole U1309D. REE abundances in clinopyroxene and plagioclase from gabbro of ODP Leg 153 (Coogan et al., 2000a, 2000b) are shown for comparison in a, b and c. (d) Chondrites-normalized Rare Earth Element diagrams for olivine in olivine-rich troctolites. The gray field is the field of REE abundances in mantle olivines from orogenic massifs and xenoliths (Sun and Kerrich, 1995; Bedini and Bodinier, 1999). REE patterns of olivine from cpx-harzburgite of the Oman Ophiolite (Gerbert-Gaillard, 2002) are also shown for comparison. Normalizing values after Sun and McDonough (1989).

Fig.5: Primitive mantle-normalized trace element abundances diagrams for: (a) clinopyroxene cores; (b) clinopyroxene rims and interstitial clinopyroxene ; (c) plagioclase from gabbros, troctolites and olivine-rich troctolites; (d) Primitive mantle-normalized trace element abundances diagrams for olivine in olivine-rich troctolites of Hole U1309D. Note that trace element abundances plot in plagioclase display reverse anomalies for the same elements as those in clinopyroxene rims and interstitial clinopyroxenes, which suggest concomitant crystallization of clinopyroxene and plagioclase. The gray field in (d) represents trace elements abundances in mantle olivines from orogenic massifs and xenoliths (Sun and Kerrich, 1995; Bedini and Bodinier, 1999). REE patterns of olivine from cpx-harzburgite of Oman Ophiolite (Gerbert-Gaillard, 2002) are also shown for comparison. Normalizing values after Sun and McDonough (1989).

Fig. 6: Chondrite-normalized Rare Earth Element abundances in calculated melts in equilibrium with clinopyroxenes, plagioclases and olivines from gabbros, troctolites and olivine-rich troctolites of Hole U1309D (using clinopyroxene/liquid and olivine/liquid partition coefficients from Lee et al., 2007, plagioclase/liquid partition coefficient from Aigner-Torres et al., 2007). The field of basalts from Hole U1309D is shown for comparison (Godard et al., submitted). The question mark on the diagram refers to uncertainty on partition coefficient values for incompatible elements. Normalizing values after Sun and McDonough (1989).

Fig. 7: (a) Eu/Eu^* versus Yb_N (normalized to Chondrites) in clinopyroxene cores and rims

and interstitial clinopyroxenes from gabbros, troctolites and olivine-rich troctolites of Hole U1309D. (b) Chondrites-normalized Rare Earth Element abundances for the average of plagioclase, clinopyroxene cores and rims and interstitial clinopyroxene from studied rocks of Hole U1309D. Composition of clinopyroxene cores is close to the composition of a mix of 40% plagioclase and 60% clinopyroxene rims and interstitial clinopyroxene. Normalizing values after Sun and McDonough (1989). Also shown on Figure 7a, is the chemical evolution of primary mantle melts during fractionation and equilibrium crystallization (calculated using PELE, details Fig.3). Primary mantle melt composition is calculated by 6% incremental melting of Depleted MORB Mantle (DMM) (Workman, 2005). Symbols indicate appearance of each phase during process of crystallization, and associated labels in italic indicate the percentage of remaining liquid.

Tables Captions

Table 1: Major and trace elements average compositions of clinopyroxene in 18 representative gabbros, troctolites and olivine-rich troctolites from IODP Hole U1309D.

Table 2: Major and trace elements average compositions of plagioclase in 9 representative gabbros, troctolites and olivine-rich troctolites from IODP Hole U1309D.

Table 3: Major and trace elements average compositions of olivine in troctolites and olivine-rich troctolites from IODP Hole U1309D.

Supplementary data:

Table A1: General characteristics of studied samples from IODP Hole U1309D.

Table A2: Major and trace elements average compositions of clinopyroxene from IODP Hole U1309D

Table A3: Major and trace element average compositions of plagioclases from IODP Hole U1309D

Table A4: Major element compositions of plagioclase from IODP Hole U1309D

Table A5: Major element compositions of olivine from IODP Hole U1309D

Table A6: Major element compositions of spinel from IODP Hole U1309D

Table A7: Whole rock major elements from IODP Hole U1309D

Table A8: Reference basalt BR analyses

Figure 1

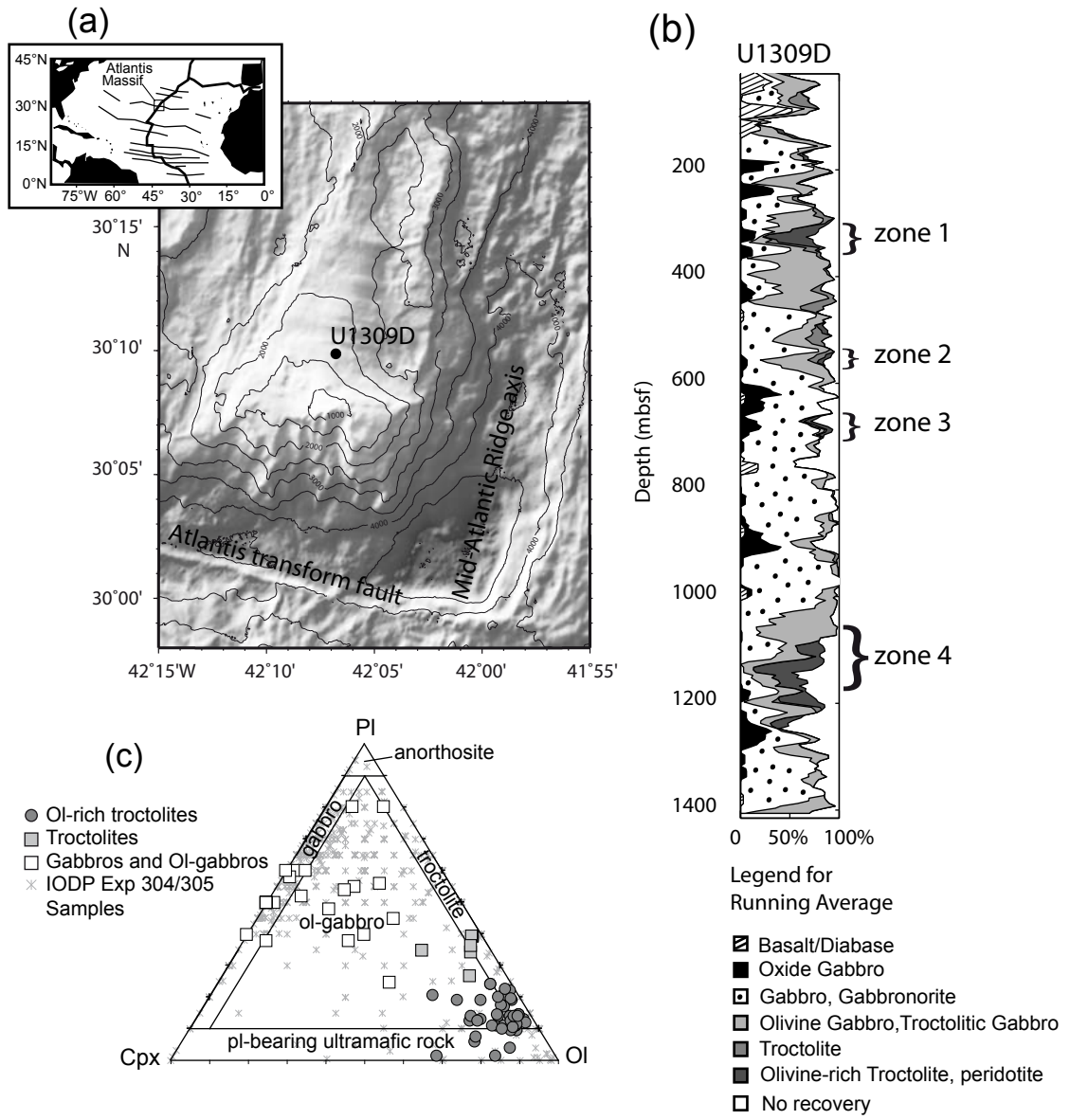


Figure 1

Figure 2

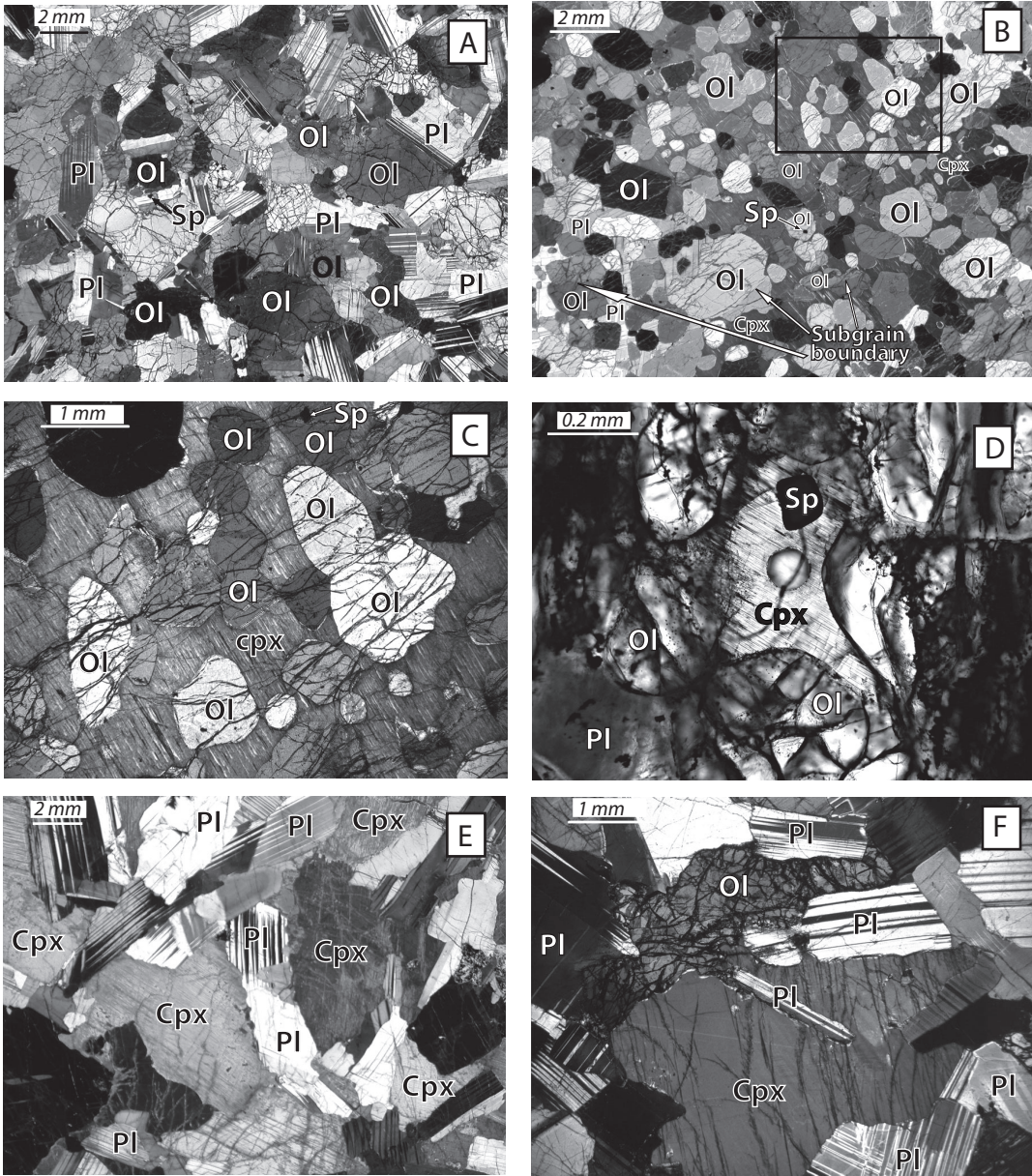


Figure 2

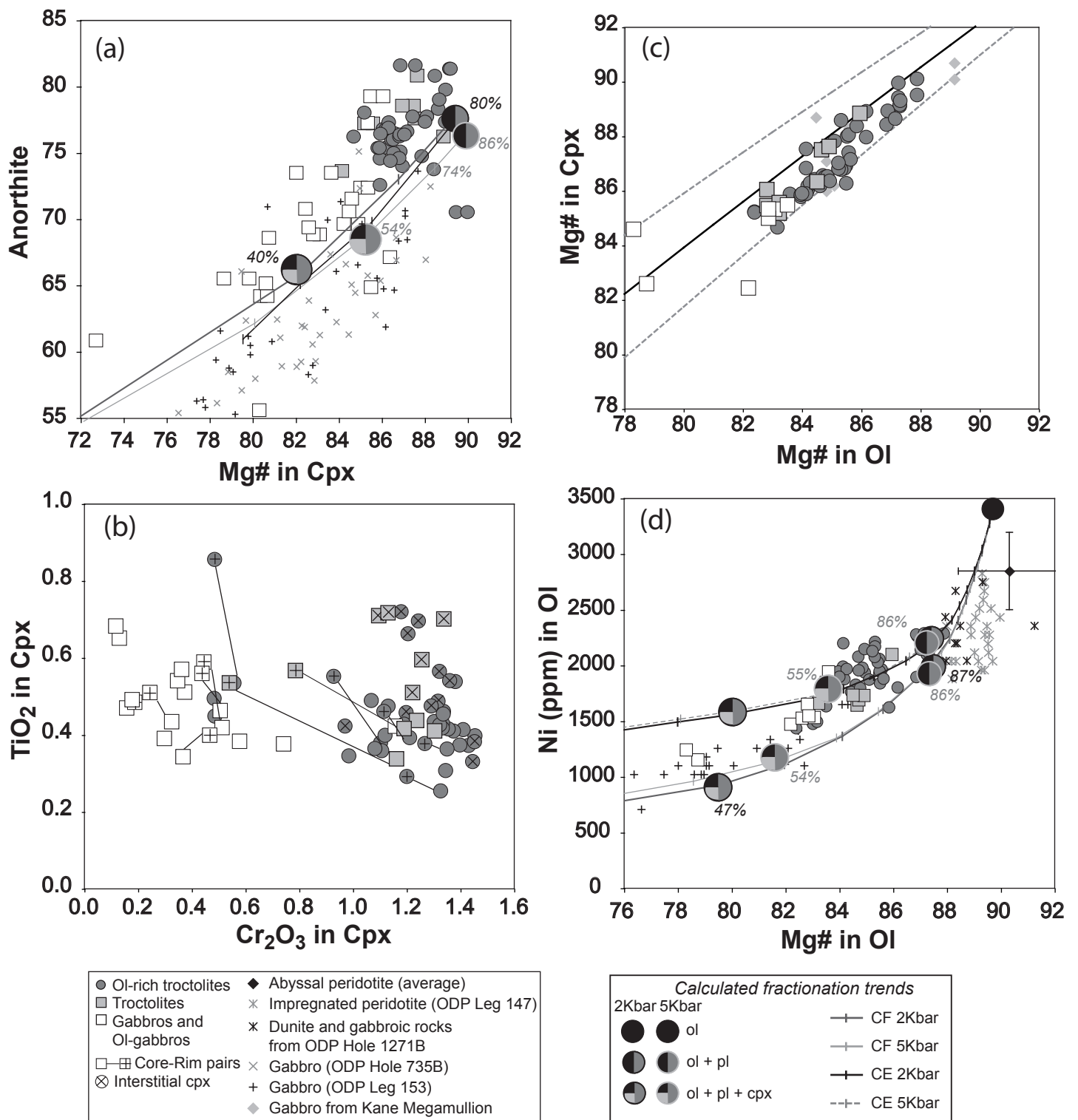


Figure 3

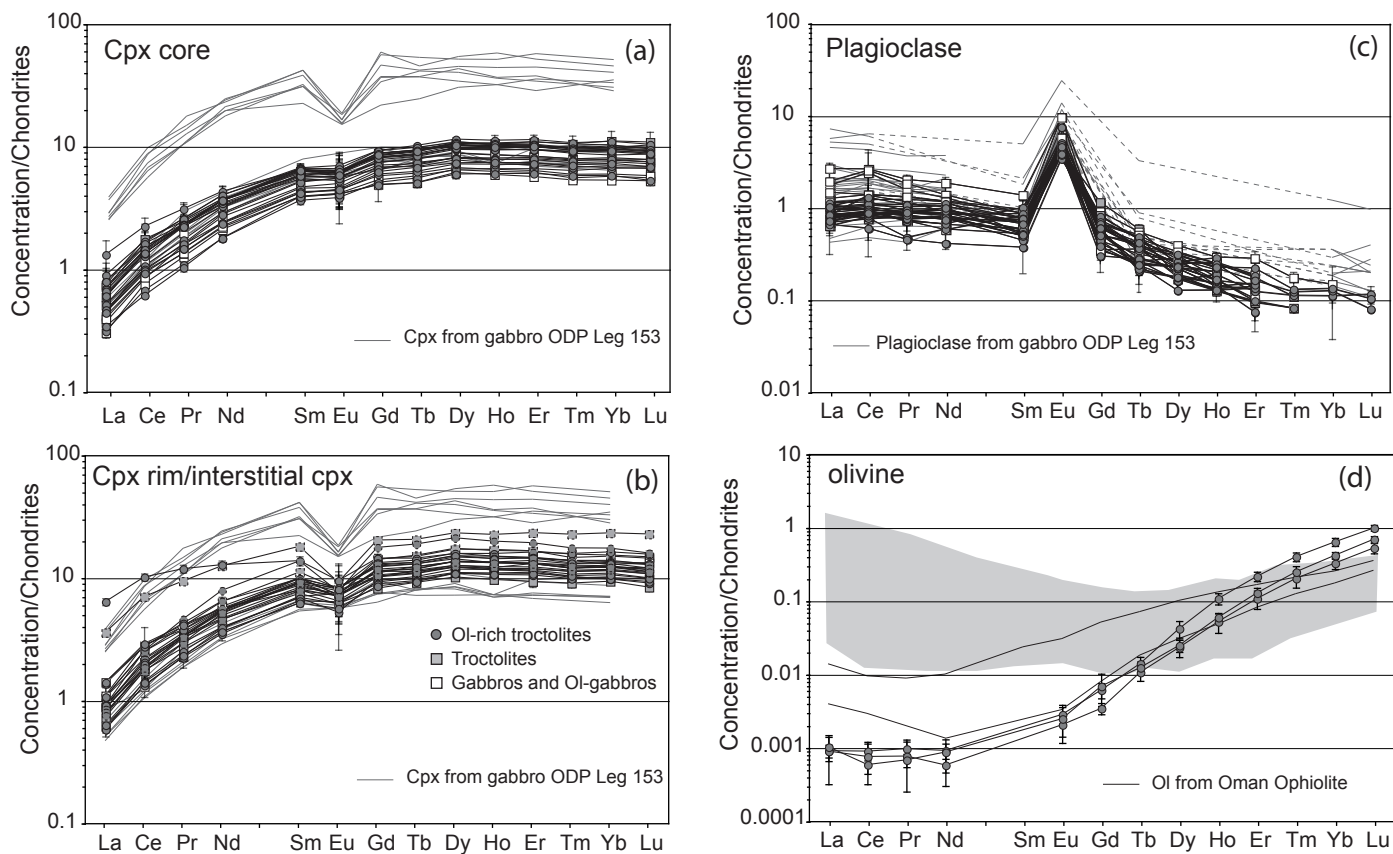


Figure 4

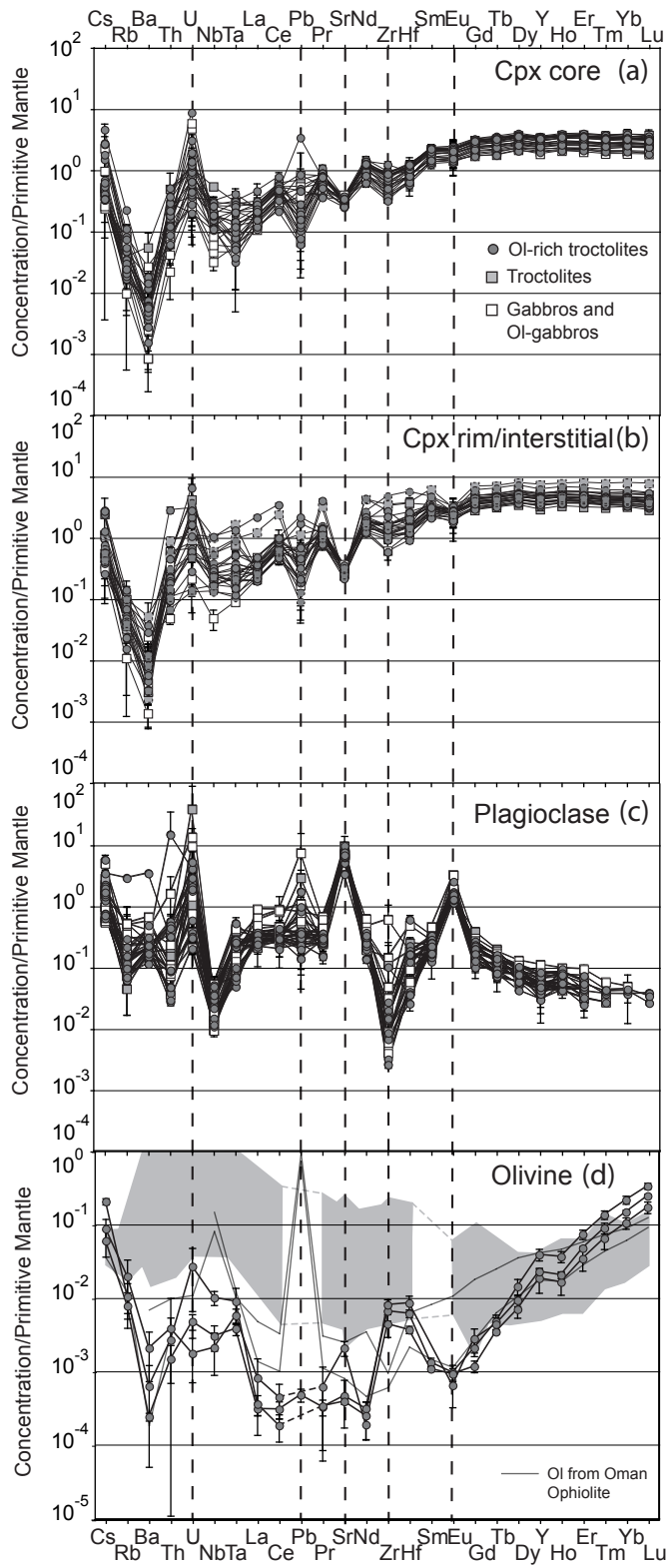


Figure.5

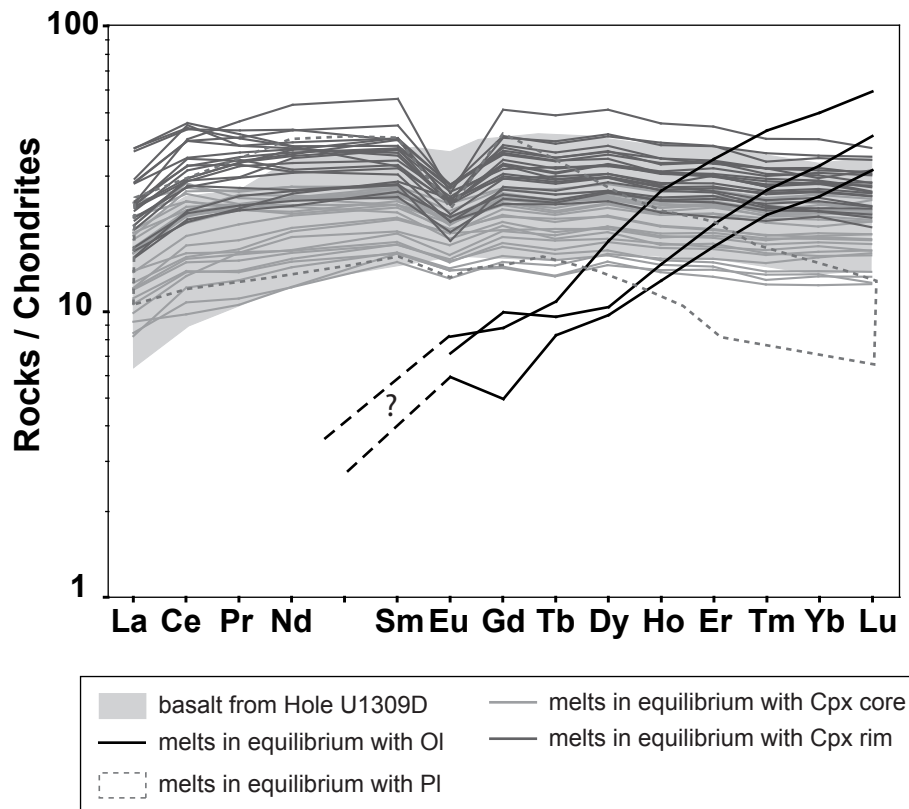


Figure.6

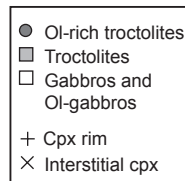
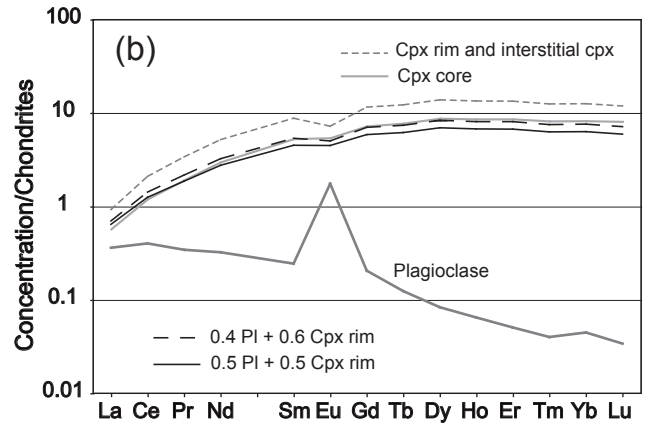
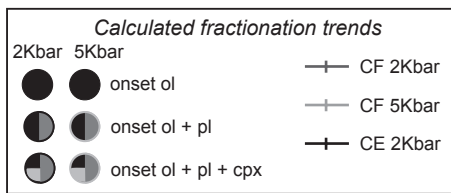
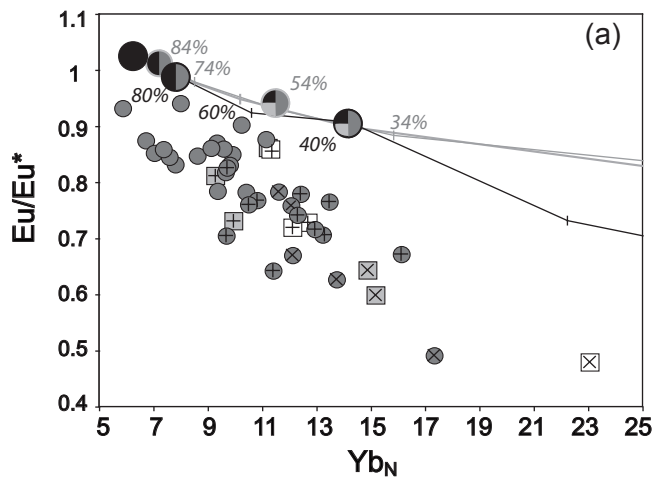


Figure.7

Table 1

Representative analyses of clinopyroxenes from IODP Hole U1309D^a

| Sample | 60R3_39-42 | 61R1_H3-116 | 62R1_4-7 | 70R3_20-24 | 71R1_10-13 | 111R2_112-116 | 111R3_101-114 | 136R1_35-39 | 136R2_37-40 | 227R2_106-109 | | | | | | | | |
|--|--------------------|-------------|--------------------|------------|--------------------|---------------|--------------------|-------------|--------------------|---------------|--------------------|-------|--------------------|-------|------------|-------|------------|-------|
| Rock type | ol-rich troctolite | | ol-rich troctolite | | ol-rich troctolite | | ol-rich troctolite | | ol-rich troctolite | | ol-rich troctolite | | ol-rich troctolite | | dikelet | | | |
| Depth(mbsf) | 313.22 | | 313.93 | | 319.64 | | 360.39 | | 362.9 | | 551.82 | | 553.13 | | 669.75 | | 1094.49 | |
| Zones | 1 | | 1 | | 1 | | 1 | | 1 | | 2 | | 2 | | 3 | | 4 | |
| Shape | poikilitic | | poikilitic | | poikilitic | | interstitial | | interstitial | | interstitial | | interstitial | | poikilitic | | poikilitic | |
| Location | c | | c | | c | | c | | c | | c | | c | | c | | c | |
| # | 5 | 2 | 3 | 5 | 5 | 10 | 8 | 3 | 2 | 9 | 5 | 1 | 6 | 1 | 6 | 9 | 6 | 2 |
| SiO ₂ | 51.52 | 0.27 | 51.27 | 0.08 | 51.94 | 0.39 | 51.92 | 0.34 | 52.03 | 0.41 | 51.75 | 0.39 | 51.35 | 0.09 | 51.88 | 0.00 | 52.01 | 0.30 |
| TiO ₂ | 0.37 | 0.06 | 0.46 | 0.07 | 0.51 | 0.03 | 0.38 | 0.18 | 0.42 | 0.42 | 0.20 | 0.09 | 0.18 | 0.10 | 0.35 | 0.10 | 0.38 | 0.10 |
| Al ₂ O ₃ | 3.87 | 0.08 | 3.76 | 0.09 | 3.73 | 0.08 | 3.80 | 0.22 | 3.68 | 0.37 | 3.56 | 0.25 | 3.62 | 0.46 | 3.58 | 0.29 | 3.49 | 0.09 |
| Cr ₂ O ₃ | 1.43 | 0.04 | 1.33 | 0.03 | 1.34 | 0.10 | 1.40 | 0.04 | 1.32 | 0.10 | 1.25 | 0.08 | 1.09 | 0.08 | 1.11 | 0.17 | 1.09 | 0.08 |
| F ₂ O | 3.54 | 0.21 | 3.49 | 0.04 | 3.87 | 0.48 | 3.54 | 0.21 | 3.49 | 0.04 | 3.54 | 0.29 | 4.18 | 0.41 | 3.52 | 0.04 | 3.66 | 0.28 |
| MnO | 0.14 | 0.01 | 0.14 | 0.01 | 0.14 | 0.01 | 0.15 | 0.01 | 0.15 | 0.01 | 0.17 | 0.02 | 0.17 | 0.01 | 0.16 | 0.01 | 0.14 | 0.02 |
| MgO | 16.27 | 0.42 | 16.14 | 0.12 | 16.62 | 1.42 | 16.56 | 0.80 | 15.92 | 0.13 | 16.61 | 0.94 | 17.17 | 1.76 | 16.11 | 0.72 | 16.37 | 0.36 |
| CaO | 21.82 | 0.60 | 22.21 | 0.15 | 20.70 | 1.90 | 20.94 | 1.32 | 22.05 | 0.51 | 21.07 | 1.19 | 20.00 | 2.75 | 21.45 | 1.04 | 22.00 | 0.39 |
| Na ₂ O | 0.39 | 0.01 | 0.40 | 0.03 | 0.39 | 0.08 | 0.42 | 0.02 | 0.43 | 0.02 | 0.34 | 0.03 | 0.37 | 0.07 | 0.40 | 0.05 | 0.41 | 0.02 |
| K ₂ O | 0.01 | 0.01 | 0.01 | 0.01 | 0.00 | 0.00 | 0.01 | 0.01 | 0.00 | 0.01 | 0.00 | 0.01 | 0.00 | 0.00 | 0.01 | 0.00 | 0.01 | 0.00 |
| NiO | 0.04 | 0.02 | 0.04 | 0.01 | 0.04 | 0.01 | 0.03 | 0.01 | 0.03 | 0.02 | 0.03 | 0.01 | 0.03 | 0.02 | 0.02 | 0.01 | 0.02 | 0.01 |
| Total | 99.38 | 0.32 | 99.27 | 0.09 | 99.09 | 0.14 | 99.83 | 0.35 | 100.06 | 0.21 | 99.55 | 0.27 | 99.77 | 0.59 | 99.24 | 0.36 | 99.35 | 0.24 |
| Mg# | 89.13 | 0.49 | 89.18 | 0.03 | 88.45 | 0.38 | 86.55 | 0.84 | 87.55 | 0.83 | 87.64 | 0.50 | 85.47 | 1.30 | 86.06 | 0.77 | 88.86 | 0.08 |
| Location | c | f | c | f | c | f | c | f | c | f | c | f | c | f | c | f | c | f |
| # | 6 | 1 | 7 | 7 | 7 | 7 | 2 | 3 | 2 | 2 | 2 | 2 | 3 | 4 | 3 | 4 | 6 | 2 |
| Ti | 2370 | 409 | 3119 | - | - | - | 4029 | 193 | - | - | 4948 | 4 | - | 393 | 8 | 386 | 308 | 19 |
| V | 319 | 20 | 358 | - | 301 | 27 | 310 | - | 343 | 15 | 322 | 18 | 420 | - | 393 | 8 | 297 | 9 |
| Cr | 8259 | 3740 | 5150 | - | 10421 | 716 | 10056 | - | 10061 | 255 | 9484 | 480 | 8887 | 715 | 9889 | 351 | 8670 | 10141 |
| Ni | 218 | 231 | 63 | - | 354 | 25 | 303 | - | 283 | 6 | 264 | 17 | 241 | 28 | 234 | 2 | 229 | 308 |
| Rb | 0.05 | 0.03 | 0.04 | - | 0.03 | 0.03 | 0.05 | - | 0.03 | 0.01 | 0.03 | 0.01 | 0.02 | 0.00 | 0.02 | 0.00 | 0.03 | 0.06 |
| Sr | 6.33 | 0.85 | 6.65 | - | 5.45 | 0.35 | 5.50 | - | 5.25 | 0.23 | 4.59 | 0.17 | 4.08 | 0.18 | 6.17 | 0.33 | 5.06 | 6.65 |
| Y | 13.76 | 2.06 | 13.57 | - | 11.67 | 1.22 | 23.76 | - | 9.87 | 1.02 | 17.38 | 3.38 | 24.42 | 1.07 | 15.33 | 2.43 | 33.69 | 23.38 |
| Zr | 6.32 | 1.94 | 13.51 | - | 5.07 | 1.09 | 30.73 | - | 4.11 | 0.20 | 15.14 | 4.09 | 37.09 | 8.20 | 8.81 | 2.17 | 39.02 | 17.78 |
| Nb | 0.11 | 0.02 | 0.23 | - | 0.13 | 0.05 | 0.74 | - | 0.10 | 0.02 | 0.12 | 0.01 | 0.72 | 0.08 | 0.39 | 0.04 | 0.43 | 0.19 |
| Ba | 0.08 | 0.01 | 0.09 | - | 0.02 | 0.02 | 0.02 | - | 0.01 | 0.00 | 0.01 | 0.00 | 0.01 | 0.00 | 0.01 | 0.00 | 0.01 | 0.02 |
| Cs | 0.03 | 0.02 | 0.03 | - | 0.02 | 0.03 | 0.26 | - | 0.13 | 0.02 | 0.08 | 0.05 | 0.02 | 0.01 | 0.38 | 0.27 | 0.19 | 0.37 |
| La | 0.108 | 0.023 | 0.203 | - | 0.107 | 0.023 | 1.500 | - | 0.075 | 0.003 | 0.137 | 0.006 | 0.206 | 0.049 | 0.188 | 0.029 | 0.844 | 0.520 |
| Ce | 0.659 | 0.142 | 1.104 | - | 0.591 | 0.109 | 6.150 | - | 0.416 | 0.037 | 0.866 | 0.061 | 1.128 | 0.024 | 1.088 | 0.358 | 4.260 | 1.522 |
| Pr | 0.167 | 0.034 | 0.276 | - | 0.141 | 0.021 | 1.116 | - | 0.104 | 0.009 | 0.237 | 0.027 | 0.309 | 0.007 | 0.234 | 0.025 | 0.884 | 0.379 |
| Nd | 1.356 | 0.296 | 2.370 | - | 1.133 | 0.159 | 5.910 | - | 0.841 | 0.122 | 1.813 | 0.252 | 2.535 | 0.262 | 1.696 | 0.264 | 5.790 | 2.960 |
| Sm | 0.805 | 0.153 | 1.380 | - | 0.708 | 0.091 | 2.090 | - | 0.563 | 0.089 | 1.040 | 0.153 | 1.520 | 0.057 | 0.965 | 0.158 | 2.740 | 1.685 |
| Eu | 0.333 | 0.052 | 0.449 | - | 0.271 | 0.036 | 0.545 | - | 0.224 | 0.030 | 0.302 | 0.036 | 0.415 | 0.018 | 0.370 | 0.042 | 0.529 | 0.470 |
| Gd | 1.618 | 0.315 | 2.230 | - | 1.359 | 0.139 | 2.940 | - | 1.059 | 0.183 | 1.931 | 0.326 | 2.865 | 0.318 | 1.748 | 0.173 | 4.140 | 2.908 |
| Tb | 0.314 | 0.058 | 0.458 | - | 0.266 | 0.025 | 0.535 | - | 0.209 | 0.039 | 0.380 | 0.051 | 0.565 | 0.021 | 0.342 | 0.054 | 0.764 | 0.554 |
| Dy | 2.425 | 0.421 | 3.380 | - | 2.089 | 0.240 | 3.980 | - | 1.675 | 0.201 | 2.964 | 0.445 | 4.380 | 0.014 | 2.715 | 0.332 | 5.840 | 4.305 |
| Ho | 0.536 | 0.096 | 0.751 | - | 0.462 | 0.047 | 0.887 | - | 0.378 | 0.037 | 0.653 | 0.124 | 0.934 | 0.023 | 0.612 | 0.098 | 1.267 | 0.954 |
| Er | 1.578 | 0.219 | 2.170 | - | 1.357 | 0.159 | 2.660 | - | 1.100 | 0.079 | 1.933 | 0.361 | 2.710 | 0.071 | 1.827 | 0.254 | 3.830 | 2.720 |
| Tm | 0.227 | 0.034 | 0.321 | - | 0.200 | 0.023 | 0.399 | - | 0.164 | 0.013 | 0.287 | 0.056 | 0.395 | 0.001 | 0.271 | 0.045 | 0.573 | 0.369 |
| Yb | 1.463 | 0.179 | 2.110 | - | 1.325 | 0.181 | 2.740 | - | 1.142 | 0.013 | 1.938 | 0.420 | 2.580 | 0.170 | 1.907 | 0.387 | 3.920 | 2.530 |
| Hf | 0.222 | 0.020 | 0.292 | - | 0.192 | 0.023 | 0.392 | - | 0.172 | 0.013 | 0.272 | 0.054 | 0.374 | 0.008 | 0.279 | 0.058 | 0.573 | 0.364 |
| Lu | 0.31 | 0.07 | 0.48 | - | 0.24 | 0.04 | 0.46 | - | 0.18 | 0.06 | 0.47 | 0.20 | 1.13 | 0.28 | 0.35 | 0.05 | 1.16 | 0.65 |
| Ta | 0.01 | 0.00 | 0.02 | - | 0.00 | 0.00 | 0.05 | - | 0.00 | 0.00 | 0.01 | 0.00 | 0.01 | 0.00 | 0.01 | 0.04 | 0.01 | 0.01 |
| Pb | 0.09 | 0.10 | 0.07 | - | 0.03 | 0.02 | 0.05 | - | 0.09 | 0.03 | 0.13 | 0.18 | 0.12 | 0.08 | 0.13 | 0.05 | 0.05 | 0.21 |
| Th | 0.01 | 0.00 | 0.02 | - | 0.01 | 0.01 | 0.24 | - | 0.01 | 0.00 | 0.01 | 0.00 | 0.08 | 0.01 | 0.04 | 0.00 | 0.05 | 0.02 |
| U | 0.04 | 0.04 | 0.01 | - | 0.02 | 0.01 | 0.06 | - | 0.01 | 0.01 | 0.01 | 0.01 | 0.02 | 0.01 | 0.02 | 0.01 | 0.02 | 0.01 |
| ^a Major element analyses were performed by electron microprobe (wt% and trace element analyses (ppm) by LA-ICP-MS. Abbreviation: n= number of analyses per mineral; σ = 1 standard deviation of multiple determinations; c= core; f= rim. | | | | | | | | | | | | | | | | | | |
| ^b Mg#=(Mg/(Mg+Fe))*100 | | | | | | | | | | | | | | | | | | |

Table 2

Representative analyses of plagioclase from IODP Hole U1309D*

| Sample | Rock type | Depth(mbsf) | Zones | 62R1-47 | 71R1-10-13 | 11R3-101-114 | 136R2-37-40 | 227R2-106-109 | 228R1-95-98 | 228R4-39-43 | 248R2-18-21 | 248R3-131-134 |
|--------------------------------|-----------|-------------|------------|--------------------|------------|--------------------|--------------------|---------------|--------------------|-------------|--------------------|--------------------|
| | | | | of-rich troctolite | ol-gabbro | of-rich troctolite | of-rich troctolite | di-ketel | of-rich troctolite | ol-gabbro | of-rich troctolite | of-rich troctolite |
| | | | | 319.64 | 362.9 | 553.13 | 671.13 | 1094.49 | 1097.75 | 1101.09 | 1193.32 | 1195.8 |
| | | | | 1 | 1 | 2 | 3 | 4 | 4 | 4 | 4 | 4 |
| | | | | σ | σ | σ | σ | σ | σ | σ | σ | σ |
| SiO ₂ | 47.51 | 0.16 | 47.62 | 0.53 | 47.90 | 0.59 | 48.65 | 0.51 | 51.44 | 0.11 | 48.68 | 0.53 |
| TiO ₂ | 0.02 | 0.01 | 0.04 | 0.02 | 0.05 | 0.02 | 0.03 | 0.01 | 0.08 | 0.02 | 0.05 | 0.02 |
| Al ₂ O ₃ | 33.79 | 0.04 | 33.25 | 0.45 | 32.84 | 0.35 | 33.25 | 0.43 | 30.68 | 0.13 | 32.26 | 0.39 |
| Cr ₂ O ₃ | 0.14 | 0.01 | 0.01 | 0.00 | 0.01 | 0.01 | 0.01 | 0.00 | 0.01 | 0.00 | 0.01 | 0.01 |
| FeO | 0.01 | 0.01 | 0.23 | 0.02 | 0.13 | 0.03 | 0.17 | 0.01 | 0.24 | 0.01 | 0.25 | 0.02 |
| MnO | 0.00 | 0.00 | 0.00 | 0.01 | 0.01 | 0.01 | 0.01 | 0.01 | 0.01 | 0.01 | 0.00 | 0.01 |
| MgO | 0.087 | 0.02 | 0.04 | 0.02 | 0.03 | 0.01 | 0.04 | 0.03 | 0.06 | 0.01 | 0.04 | 0.02 |
| CaO | 16.88 | 0.07 | 16.47 | 0.46 | 16.05 | 0.40 | 15.97 | 0.42 | 13.40 | 0.10 | 15.33 | 0.43 |
| Na ₂ O | 2.10 | 0.06 | 2.37 | 0.27 | 2.59 | 0.25 | 2.57 | 0.22 | 3.99 | 0.05 | 2.88 | 0.21 |
| K ₂ O | 0.01 | 0.01 | 0.02 | 0.01 | 0.01 | 0.00 | 0.02 | 0.01 | 0.02 | 0.00 | 0.01 | 0.03 |
| Total | 100.48 | 0.17 | 100.06 | 0.21 | 99.60 | 0.27 | 100.73 | 0.20 | 99.94 | 0.00 | 99.49 | 0.28 |
| An (Ca) | 81.61 | 0.52 | 79.27 | 2.32 | 77.37 | 2.10 | 77.37 | 1.98 | 64.91 | 0.46 | 74.61 | 1.95 |
| n | 3 | σ | 2 (core)** | σ | 2 (rim)** | σ | 3 | σ | 4* | σ | 4 | σ |
| Ti | 219 | - | 243 | 77 | 106 | 20 | 285 | 0.54 | 2.45 | 349 | 13 | 261 |
| V | 0.54 | 2.97 | 0.08 | 1.18 | 0.30 | 0.30 | 2.85 | 0.31 | 2.99 | 0.69 | 2.37 | 0.54 |
| Cr | <dl | 3.09 | 1.92 | 15.27 | 20.39 | <dl | <dl | <dl | 0.89 | 0.34 | <dl | <dl |
| Ni | 3.34 | 1.26 | 258.21 | 363.16 | 0.98 | 0.73 | 1.14 | 0.26 | 5.67 | 0.39 | 6.48 | 8.32 |
| Br | 0.04 | 0.02 | 0.24 | 0.10 | 0.36 | 0.34 | 0.34 | 0.05 | 0.01 | 0.24 | 0.02 | 0.04 |
| Sr | 110.62 | 7.99 | 128.34 | 6.99 | 177.89 | 50.84 | 132.63 | 8.29 | 139.63 | 3.10 | 182.49 | 5.34 |
| Y | 0.25 | 0.02 | 0.28 | 0.01 | 0.15 | 0.02 | 0.28 | 0.03 | 0.30 | 0.02 | 0.15 | 0.01 |
| Zr | 0.04 | 0.01 | 10.19 | 13.84 | 0.42 | 0.02 | 0.08 | 0.02 | 0.18 | 0.01 | 0.95 | 0.63 |
| Nb | 0.01 | 0.00 | 0.04 | 0.04 | 0.04 | 0.01 | 0.02 | 0.01 | 0.02 | 0.00 | 0.01 | 0.00 |
| Cs | 0.03 | 0.00 | 0.05 | 0.03 | 0.04 | 0.04 | 0.05 | 0.02 | 0.08 | 0.00 | 0.05 | 0.00 |
| Ba | 1.03 | 0.04 | 1.54 | 0.07 | 20.35 | 8.73 | 1.85 | 0.66 | 1.48 | 0.11 | 2.14 | 1.18 |
| La | 0.168 | 0.009 | 0.211 | 0.021 | 0.143 | 0.043 | 0.196 | 0.078 | 0.236 | 0.005 | 0.361 | 0.104 |
| Ce | 0.514 | 0.034 | 0.662 | 0.040 | 0.414 | 0.018 | 0.654 | 0.650 | 0.021 | 0.668 | 0.061 | 0.742 |
| Pr | 0.083 | 0.003 | 0.118 | 0.014 | 0.056 | 0.007 | 0.111 | 0.078 | 0.097 | 0.006 | 0.080 | 0.001 |
| Nd | 0.414 | 0.024 | 0.517 | 0.136 | 0.239 | 0.065 | 0.421 | 0.158 | 0.490 | 0.006 | 0.317 | 0.012 |
| Sm | 0.087 | 0.008 | 0.103 | 0.018 | 0.055 | 0.008 | 0.107 | 0.021 | 0.106 | 0.014 | 0.065 | 0.015 |
| Eu | 0.227 | 0.002 | 0.252 | 0.044 | 0.151 | 0.023 | 0.296 | 0.012 | 0.267 | 0.010 | 0.273 | 0.004 |
| Gd | 0.084 | 0.028 | 0.110 | 0.022 | 0.037 | 0.001 | 0.127 | 0.041 | 0.135 | 0.012 | 0.059 | 0.001 |
| Tb | 0.010 | 0.003 | 0.012 | 0.002 | 0.006 | 0.002 | 0.016 | 0.003 | 0.013 | 0.000 | 0.008 | 0.000 |
| Dy | 0.041 | 0.009 | 0.055 | 0.013 | 0.032 | 0.007 | 0.057 | 0.015 | 0.066 | 0.013 | 0.037 | 0.004 |
| Ho | 0.011 | 0.002 | 0.011 | 0.000 | 0.005 | 0.002 | 0.009 | 0.002 | 0.014 | 0.002 | 0.005 | 0.001 |
| Er | 0.020 | 0.006 | 0.023 | 0.000 | 0.010 | 0.003 | 0.030 | 0.001 | 0.030 | 0.001 | 0.011 | 0.000 |
| Tm | 0.003 | 0.000 | 0.003 | 0.001 | 0.001 | 0.000 | <dl | <dl | <dl | <dl | 0.002 | 0.000 |
| Yb | 0.019 | 0.003 | 0.015 | 0.002 | 0.007 | 0.007 | <dl | <dl | <dl | <dl | 0.006 | 0.001 |
| Lu | 0.003 | 0.001 | 0.001 | 0.001 | 0.000 | 0.000 | <dl | <dl | <dl | <dl | 0.001 | 0.001 |
| Hf | 0.01 | 0.00 | 0.00 | 0.00 | 0.03 | 0.01 | 0.04 | 0.01 | 0.06 | 0.00 | 0.02 | 0.02 |
| Ta | 0.00 | 0.00 | 0.01 | 0.01 | 0.01 | 0.00 | 0.01 | 0.00 | 0.01 | 0.00 | 0.01 | 0.00 |
| Pb | 0.04 | 0.02 | 0.60 | 0.02 | 0.40 | 0.26 | 0.07 | 0.03 | 0.05 | 0.01 | 0.31 | 0.33 |
| Th | 0.00 | 0.00 | 0.05 | 0.03 | 0.05 | 0.06 | 0.01 | 0.00 | 0.04 | 0.01 | 0.02 | 0.02 |
| U | 0.01 | 0.01 | 0.01 | 0.00 | 0.18 | 0.06 | 0.02 | 0.01 | 0.06 | 0.01 | 0.28 | 0.41 |

Major element analyses were performed by electron microprobe (wt%) and trace element analyses (ppm) by LA-ICP-MS or HR-ICP-MS (). Abbreviation: n= number of analyses per mineral; σ = 1 standard deviation of multiple determinations; <dl = below detection limit

Table 3

Composition of olivine from troctolite and olivine-rich troctolite at IODP Hole U1309D^a

| Sample | 232R1 112-116 | | 248R2 18-21 | | 248R3 131-134 | |
|--------------------------------|---------------|----------|--------------------|----------|--------------------|----------|
| Rock type | troctolite | | ol-rich troctolite | | ol-rich troctolite | |
| Depth(mbsf) | 1116.22 | | 1193.32 | | 1195.8 | |
| Zones | 4 | | 4 | | 4 | |
| <i>n</i> | 10 | σ | 9 | σ | 8 | σ |
| SiO ₂ | 39.54 | 0.12 | 40.12 | 0.14 | 40.67 | 0.13 |
| TiO ₂ | 0.02 | 0.01 | 0.02 | 0.01 | 0.02 | 0.01 |
| Al ₂ O ₃ | 0.01 | 0.01 | 0.01 | 0.01 | 0.01 | 0.01 |
| Cr ₂ O ₃ | 0.02 | 0.01 | 0.01 | 0.01 | 0.01 | 0.01 |
| FeO | 15.74 | 0.20 | 16.35 | 0.13 | 13.84 | 0.18 |
| MnO | 0.27 | 0.02 | 0.27 | 0.01 | 0.23 | 0.02 |
| MgO | 43.79 | 0.13 | 42.87 | 0.13 | 44.75 | 0.12 |
| CaO | 0.06 | 0.01 | 0.08 | 0.03 | 0.08 | 0.02 |
| Na ₂ O | 0.01 | 0.02 | 0.01 | 0.02 | 0.00 | 0.00 |
| K ₂ O | 0.01 | 0.01 | 0.01 | 0.01 | 0.00 | 0.00 |
| NiO | 0.21 | 0.02 | 0.18 | 0.01 | 0.27 | 0.01 |
| Total | 99.67 | 0.19 | 99.93 | 0.17 | 99.90 | 0.27 |
| Fo (M%) | 82.98 | 0.20 | 82.13 | 0.15 | 85.00 | 0.15 |
| Mg# | 83.22 | 0.21 | 82.37 | 0.15 | 85.21 | 0.15 |
| Ni (ppm) | 1665 | 182 | 1441 | 115 | 2134 | 112 |
| <i>n</i> | 3 | σ | 3 | σ | 3 | σ |
| P | 45 | 15 | 33 | 3 | 24 | 5 |
| Ca | 576 | 43 | 626 | 57 | 615 | 80 |
| Ti | 113 | 9 | 143 | 4 | 80 | 15 |
| V | 7.1 | 0.7 | 8.5 | 0.2 | 5.6 | 0.5 |
| Cr | 78 | 6 | 81 | 4 | 103 | 8 |
| Co | 176.1 | 1.3 | 179.3 | 1.4 | 168.0 | 3.2 |
| Ni | 1443 | 18 | 1601 | 30 | 2109 | 52 |
| Rb | 0.0065 | 0.0030 | 0.0051 | 0.0026 | 0.0127 | 0.0087 |
| Sr | 0.0075 | 0.0011 | 0.0100 | 0.0064 | 0.1341 | 0.1555 |
| Y | 0.1064 | 0.0085 | 0.1812 | 0.0324 | 0.0860 | 0.0321 |
| Zr | 0.0929 | 0.0174 | 0.0762 | 0.0207 | 0.0505 | 0.0172 |
| Nb | 0.0069 | 0.0009 | 0.0022 | 0.0008 | 0.0015 | 0.0009 |
| Cs | 0.0067 | 0.0007 | 0.0020 | 0.0008 | 0.0029 | 0.0010 |
| Ba | 0.0039 | 0.0032 | 0.0017 | 0.0002 | 0.0535 | 0.0664 |
| La | 0.0003 | 0.0001 | 0.0002 | 0.0000 | 0.0006 | 0.0005 |
| Ce | 0.0003 | 0.0001 | 0.0006 | 0.0001 | 0.0008 | 0.0004 |
| Pr | 0.0001 | 0.0001 | 0.0001 | 0.0000 | 0.0002 | 0.0001 |
| Nd | 0.0003 | 0.0002 | 0.0004 | 0.0001 | 0.0003 | 0.0001 |
| Sm | - | - | 0.0006 | 0.0001 | 0.0005 | 0.0000 |
| Eu | 0.0001 | 0.0000 | 0.0002 | 0.0000 | 0.0002 | 0.0000 |
| Gd | 0.0021 | 0.0007 | 0.0013 | 0.0003 | 0.0007 | 0.0001 |
| Tb | 0.0005 | 0.0001 | 0.0005 | 0.0001 | 0.0004 | 0.0000 |
| Dy | 0.0072 | 0.0014 | 0.0108 | 0.0027 | 0.0053 | 0.0013 |
| Ho | 0.0034 | 0.0003 | 0.0061 | 0.0011 | 0.0028 | 0.0009 |
| Er | 0.0234 | 0.0011 | 0.0360 | 0.0053 | 0.0168 | 0.0054 |
| Tm | 0.0068 | 0.0011 | 0.0102 | 0.0014 | 0.0049 | 0.0014 |
| Yb | 0.0746 | 0.0041 | 0.1089 | 0.0139 | 0.0529 | 0.0093 |
| Lu | 0.0186 | 0.0011 | 0.0252 | 0.0023 | 0.0130 | 0.0023 |
| Hf | 0.0026 | 0.0006 | 0.0019 | 0.0002 | 0.0012 | 0.0001 |
| Ta | 0.0003 | 0.0000 | 0.0002 | 0.0000 | 0.0002 | 0.0001 |
| Pb | - | - | 0.0153 | 0.0076 | - | - |
| Th | 0.0002 | 0.0002 | 0.0001 | 0.0001 | 0.0003 | 0.0005 |
| U | 0.0028 | 0.0046 | 0.0001 | 0.0000 | 0.0002 | 0.0002 |

^aMajor element analyses were performed by electron microprobe (wt%)

and trace element analyses (ppm) by HR-ICP MS.

Abbreviation: *n*= number of analyses per mineral; σ = 1 standard deviation of multiple determinations.

Mg# = (Mg/Mg+Fe)*100

Supplementary data table A1

General characteristics of studied samples from IODP Hole U1309D

| Leg | Site | H | Core | Type | Sample name | | | zone | Rock name | modal composition | | | | Alteration | Ol shape | Pl shape | Cpx shape | grain size | |
|-----|------|---|------|------|-------------|---------|---------|---------|-----------|--------------------------------|-------------|-------------|------------|------------|----------|----------|-----------|------------|------|
| | | | | | Section | Top(cm) | Bot(cm) | | | Depth(mbsf) | % Ol | % Pl | % Cpx | | | | | | % Sp |
| 304 | 1309 | D | 60 | R | 3 | 39 | 42 | 313.22 | 1 | Ol-rich troctolite | 70.5 | 13 | 16 | 0.5 | 2.5 | 0 | 1 | 1 | 2 |
| 304 | 1309 | D | 61 | R | 1 | 11 | 14 | 314.91 | 1 | Ol-rich troctolite | 75 | 6.5 | 18 | 0.5 | 2.5 | 0 | 1 | 1 | 2 |
| 304 | 1309 | D | 61 | R | 1 | 113 | 116 | 315.93 | 1 | Ol-rich troctolite | 77 | 19.5 | 3 | 0.5 | 2.5 | 0 | 2 | 1 | 2 |
| 304 | 1309 | D | 62 | R | 1 | 4 | 7 | 319.64 | 1 | Ol-rich troctolite | 70 | 19.5 | 10 | 0.5 | 2.5 | 0 | 1 | 1 | 2 |
| 304 | 1309 | D | 63 | R | 2 | 28 | 30 | 326.14 | 1 | Ol-rich troctolite +dykelet | 57 | 21 | 21 | 1 | 2.5 | 0 | 2 | 1 | 2 |
| 304 | 1309 | D | 63 | R | 3 | 36 | 39 | 327.72 | 1 | Ol-rich troctolite | 84 | 10 | 5.5 | 0.5 | 2.5 | 1 | 2 | 2 | 2 |
| 304 | 1309 | D | 64 | R | 1 | 13 | 16 | 329.33 | 1 | Ol-rich troctolite | 84 | 13.5 | 2 | 0.5 | 2.5 | 1 | 2 | 1 | 1 |
| 304 | 1309 | D | 64 | R | 1 | 53 | 56.5 | 329.73 | 1 | Ol-rich troctolite | 85 | 4.5 | 10 | 0.5 | 2.5 | 0 | 2 | 2 | 1 |
| 304 | 1309 | D | 65 | R | 2 | 16 | 19 | 335.66 | 1 | Ol-rich troctolite | 76 | 21.5 | 2 | 0.5 | 3 | 0 | 1 | | 1 |
| 304 | 1309 | D | 66 | R | 1 | 18 | 21 | 338.98 | 1 | gabbro | 2 | 50 | 48 | 0 | 2.5 | | 0 | 0 | 3 |
| 304 | 1309 | D | 66 | R | 1 | 18 | 21 | 338.98 | 1 | Ol-rich troctolite | 70 | 14.5 | 15 | 0.5 | 2.5 | 1 | 2 | 1 | 2 |
| 304 | 1309 | D | 67 | R | 2 | 47.5 | 51.5 | 345.495 | 1 | gabbro | 6 | 38 | 56 | 0 | 1 | | 0 | 0 | 3 |
| 304 | 1309 | D | 69 | R | 3 | 6 | 9 | 356.11 | 1 | troctolite | 63.5 | 27 | 9 | 0.5 | 2 | 0 | 2 | 1 | 2 |
| 304 | 1309 | D | 70 | R | 2 | 99 | 103 | 359.68 | 1 | troctolite | 58 | 39.5 | 2 | 0.5 | 1.5 | 0 | 0 | 2 | 2 |
| 304 | 1309 | D | 70 | R | 3 | 20 | 24 | 360.39 | 1 | troctolite | 58 | 39.5 | 2 | 0.5 | 1.5 | 0 | 0 | 2 | 2 |
| 304 | 1309 | D | 71 | R | 1 | 10 | 13 | 362.9 | 1 | ol-gabbro | 26 | 56 | 18 | 0 | 1 | 0 | 0 | 2 | 2 |
| 305 | 1309 | D | 111 | R | 2 | 112 | 116 | 551.82 | 2 | troctolite | 60 | 35 | 4.5 | 0.5 | 1.5 | 0 | 0 | 2 | 2 |
| 305 | 1309 | D | 111 | R | 3 | 101 | 114 | 553.13 | 2 | Ol-rich troctolite | 76 | 22.5 | 1 | 0.5 | 1 | 0 | 2 | 1 | 1 |
| 305 | 1309 | D | 111 | R | 4 | 14 | 17 | 553.71 | 2 | Ol-rich troctolite | 75 | 21 | 3.5 | 0.5 | 1.5 | 0 | 2 | 1 | 1 |
| 305 | 1309 | D | 111 | R | 4 | 50 | 54 | 554.07 | 2 | Ol-rich troctolite | 78 | 19.5 | 2 | 0.5 | 2.5 | 0 | 2 | 1 | 2 |
| 305 | 1309 | D | 112 | R | 1 | 69 | 73 | 554.89 | 2 | Ol-rich troctolite | 77.5 | 20 | 2 | 0.5 | 3 | 0 | 2 | 1 | 2 |
| 305 | 1309 | D | 112 | R | 2 | 16 | 20 | 555.86 | 2 | gabbro | 17 | 48 | 35 | 0 | 1 | 0 | 0 | 0 | 3 |
| 305 | 1309 | D | 112 | R | 3 | 22 | 25 | 557.24 | 2 | Ol-rich troctolite | 78 | 11.5 | 10 | 0.5 | 3 | 0 | 2 | 2 | 2 |
| 305 | 1309 | D | 135 | R | 2 | 82 | 85 | 666.8 | 3 | gabbro | 0 | 50 | 50 | 0 | 1.5 | | 0 | 0 | 3 |
| 305 | 1309 | D | 136 | R | 1 | 35 | 39 | 669.75 | 3 | Ol-rich troctolite | 64 | 19.5 | 16 | 0.5 | 2.5 | 1 | 2 | 1 | 2 |
| 305 | 1309 | D | 136 | R | 1 | 94 | 98 | 670.34 | 3 | gabbro | 0 | 50 | 50 | 0 | 1 | | 0 | 0 | 3 |
| 305 | 1309 | D | 136 | R | 1 | 94 | 98 | 670.34 | 3 | ol-gabbro | 30 | 40 | 30 | 0 | 2.5 | 0 | 2 | 0 | 2 |
| 305 | 1309 | D | 136 | R | 2 | 37 | 40 | 671.13 | 3 | Ol-rich troctolite | 73 | 13.5 | 13 | 0.5 | 2 | 1 | 1 | 1 | 2 |
| 305 | 1309 | D | 136 | R | 2 | 60 | 64 | 671.36 | 3 | Troctolite | 45 | 39.5 | 15 | 0.5 | 2 | 0 | 0 | 1 | 2 |
| 305 | 1309 | D | 136 | R | 3 | 21 | 26 | 672.33 | 3 | gabbro | 0 | 40 | 60 | 0 | 1 | | 0 | 0 | 3 |
| 305 | 1309 | D | 227 | R | 1 | 10 | 15 | 1092.1 | 4 | gabbro | 0 | 50 | 50 | 0 | 1.5 | | 0 | 0 | 2 |
| 305 | 1309 | D | 227 | R | 2 | 26 | 30 | 1093.69 | 4 | Ol-gabbro | 20 | 55 | 35 | 0 | 1.5 | 0 | 0 | 0 | 2 |
| 305 | 1309 | D | 227 | R | 2 | 71 | 74 | 1094.14 | 4 | Ol-rich troctolite | 80 | 11.5 | 8 | 0.5 | 2 | 1 | 2 | 1 | 1 |
| 305 | 1309 | D | 227 | R | 2 | 106 | 109 | 1094.49 | 4 | Ol-rich troctolite | 77 | 17.5 | 5 | 0.5 | 2 | 1 | 2 | 1 | 2 |
| 305 | 1309 | D | 227 | R | 2 | 106 | 109 | 1094.49 | 4 | dykelet | 0 | 50 | 50 | 0 | 1 | | 0 | 0 | 2 |
| 305 | 1309 | D | 227 | R | 3 | 121 | 124 | 1096.14 | 4 | Ol-rich troctolite | 72.5 | 13 | 14 | 0.5 | 2 | 2 | 1 | 1 | 1 |
| 305 | 1309 | D | 228 | R | 1 | 33 | 37 | 1097.13 | 4 | Ol-rich troctolite | 76 | 18 | 5 | 1 | 1.5 | 2 | 2 | 2 | 1 |
| 305 | 1309 | D | 228 | R | 1 | 66 | 70 | 1097.46 | 4 | gabbro | 2 | 60 | 35 | 0 | 1 | 0 | 0 | 0 | 3 |
| 305 | 1309 | D | 228 | R | 1 | 79 | 82 | 1097.59 | 4 | Ol-rich troctolite | 77 | 14.5 | 8 | 0.5 | 2 | 0 | 1.5 | 1 | 1 |
| 305 | 1309 | D | 228 | R | 1 | 95 | 98 | 1097.75 | 4 | gabbro | 2 | 58 | 40 | 0 | 1 | 0 | 0 | 0 | 3 |
| 305 | 1309 | D | 228 | R | 2 | 42 | 45 | 1098.43 | 4 | Ol-rich troctolite | 82.5 | 10 | 7 | 0.5 | 1.5 | 1 | 2 | 1 | 1 |
| 305 | 1309 | D | 228 | R | 3 | 22 | 25 | 1099.73 | 4 | Ol-rich troctolite | 80 | 14.5 | 5 | 0.5 | 1.5 | 0 | 2 | 1 | 2 |
| 305 | 1309 | D | 228 | R | 3 | 62 | 66 | 1100.13 | 4 | Ol-gabbro | 18 | 54 | 28 | 0 | 1.5 | 0 | 0 | 0 | 2 |
| 305 | 1309 | D | 228 | R | 3 | 62 | 66 | 1100.13 | 4 | Ol-rich troctolite | 85 | 12.5 | 2 | 0.5 | 3 | 0 | 2 | 1 | 2 |
| 305 | 1309 | D | 228 | R | 4 | 39 | 43 | 1101.09 | 4 | Ol-gabbro | 44 | 25 | 31 | 0 | 2 | 0 | 0 | 1 | 2 |
| 305 | 1309 | D | 231 | R | 3 | 0 | 3 | 1113.1 | 4 | Ol-gabbro | 35 | 45 | 20 | 0 | 2 | 0 | 0 | 0 | 3 |
| 305 | 1309 | D | 231 | R | 3 | 50 | 54 | 1113.6 | 4 | gabbro | 8 | 52 | 40 | 0 | 1 | 0 | 0 | 0 | 3 |
| 305 | 1309 | D | 232 | R | 1 | 9 | 13 | 1115.19 | 4 | Ol-rich troctolite | 70 | 24.5 | 5 | 0.5 | 2 | 1 | 1 | 1 | 2 |
| 305 | 1309 | D | 232 | R | 1 | 9 | 13 | 1115.19 | 4 | dykelet | 0 | 50 | 50 | 0 | 1 | | 0.5 | 0.5 | 2 |
| 305 | 1309 | D | 232 | R | 1 | 112 | 116 | 1116.22 | 4 | troctolite | 59 | 36.5 | 4 | 0.5 | 2 | 1 | 1 | 1 | 2 |
| 305 | 1309 | D | 233 | R | 1 | 31 | 34 | 1120.21 | 4 | Ol-rich troctolite | 74 | 20.5 | 5 | 0.5 | 2 | 0 | 1.5 | 2 | 2 |
| 305 | 1309 | D | 233 | R | 1 | 135 | 139 | 1121.25 | 4 | troctolite | 60 | 34.5 | 5 | 0.5 | 2.5 | 0 | 1 | 2 | 2 |
| 305 | 1309 | D | 233 | R | 2 | 109 | 112 | 1122.49 | 4 | Ol-rich troctolite | 74.5 | 23 | 2 | 0.5 | 1.5 | 1 | 1 | 2 | 2 |
| 305 | 1309 | D | 233 | R | 3 | 21 | 24 | 1123.06 | 4 | Ol-rich troctolite | 82 | 15 | 2.5 | 0.5 | 1.5 | 1.5 | 2 | 2 | 2 |
| 305 | 1309 | D | 234 | R | 1 | 22 | 26 | 1124.92 | 4 | Ol-rich troctolite | 82 | 15 | 2.5 | 0.5 | 1.5 | 1 | 1.5 | 2 | 2 |
| 305 | 1309 | D | 234 | R | 1 | 92 | 96 | 1125.62 | 4 | Ol-rich troctolite | 81 | 13 | 5.5 | 0.5 | 1.5 | 1.5 | 1.5 | 2 | 2 |
| 305 | 1309 | D | 234 | R | 2 | 127 | 130 | 1127.47 | 4 | Ol-rich troctolite | 82 | 15 | 2.5 | 0.5 | 2 | 1 | 2 | 2 | 2 |
| 305 | 1309 | D | 234 | R | 3 | 14 | 18 | 1127.74 | 4 | Ol-rich troctolite | 83 | 11.5 | 5 | 0.5 | 1.5 | 1 | 1 | 1 | 2 |
| 305 | 1309 | D | 235 | R | 1 | 29 | 34 | 1129.79 | 4 | gabbro | 5 | 60 | 35 | 0 | 2 | | 0 | 0 | 3 |
| 305 | 1309 | D | 235 | R | 1 | 29 | 34 | 1129.79 | 4 | Ol-rich troctolite | 83 | 11.5 | 5 | 0.5 | 2 | 0 | 2 | 2 | 2 |
| 305 | 1309 | D | 235 | R | 2 | 13 | 16 | 1130.89 | 4 | Ol-rich troctolite | 83 | 12 | 4.5 | 0.5 | 2 | 0 | 2 | | 2 |
| 305 | 1309 | D | 235 | R | 2 | 13 | 16 | 1130.89 | 4 | gabbro | 0 | 50 | 50 | 0 | 1 | | 0 | 0 | 3 |
| 305 | 1309 | D | 235 | R | 2 | 85 | 89 | 1131.61 | 4 | Ol-rich troctolite | 82.5 | 11 | 6 | 0.5 | 2 | 0 | 2 | 2 | 2 |
| 305 | 1309 | D | 236 | R | 1 | 122 | 126 | 1135.52 | 4 | Ol-rich troctolite | 70 | 24.5 | 5 | 0.5 | 2 | 0 | 1 | 1 | 2 |
| 305 | 1309 | D | 236 | R | 2 | 121 | 124 | 1136.86 | 4 | Ol-rich troctolite | 76.5 | 15 | 8 | 0.5 | 2 | 0 | 1 | 2 | 1 |
| 305 | 1309 | D | 237 | R | 2 | 40 | 43 | 1140.92 | 4 | Ol-rich troctolite | 81 | 14.5 | 4 | 0.5 | 2 | 1 | 1.5 | 1 | 2 |
| 305 | 1309 | D | 241 | R | 2 | 94 | 97 | 1160.71 | 4 | Ol-rich troctolite | 82 | 14.5 | 3 | 0.5 | 1 | 1 | 2 | 2 | 1 |
| 305 | 1309 | D | 242 | R | 1 | 123 | 126 | 1164.33 | 4 | gabbro | 7 | 80 | 13 | 0 | 1 | 0 | 0 | 0 | 2 |
| 305 | 1309 | D | 243 | R | 1 | 57 | 61 | 1168.47 | 4 | Ol-gabbro | 27 | 38 | 35 | 0 | 1.5 | 0 | 0 | 0 | 3 |
| 305 | 1309 | D | 247 | R | 3 | 62 | 66 | 1190.51 | 4 | Ol-rich troctolite | 67.5 | 2 | 30 | 0.5 | 1.5 | 2 | 2 | 1 | 2 |
| 305 | 1309 | D | 247 | R | 3 | 19 | 22 | 1190.08 | 4 | Ol-rich troctolite | 74.5 | 8 | 17 | 0.5 | 1 | 2 | 1 | 1 | 2 |
| 305 | 1309 | D | 248 | R | 2 | 18 | 21 | 1193.32 | 4 | Ol-rich troctolite | 77 | 11.5 | 11 | 0.5 | 1 | 2 | 1 | 1 | 2 |
| 305 | 1309 | D | 248 | R | 3 | 131 | 134 | 1195.8 | 4 | Ol-rich troctolite | 80 | 10.5 | 9 | 0.5 | 1.5 | 2 | 1 | 1 | 2 |
| 305 | 1309 | D | 248 | R | 4 | 19 | 23 | 1196.11 | 4 | gabbro | 15 | 80 | 5 | 0 | 1.5 | 0 | 0 | 0 | 3 |
| 305 | 1309 | D | 248 | R | 4 | 19 | 23 | 1196.11 | 4 | Ol-rich troctolite | 82.5 | 2 | 5 | 0.5 | 1.5 | 2 | 1 | 1 | 2 |
| 305 | 1309 | D | 248 | R | 4 | 65 | 69 | 1196.57 | 4 | gabbro | 0 | 60 | 40 | 0 | 1 | | 1 | 0 | 3 |

alteration: 0= no alteration; 1= low alteration; 2= highly altered; 3= completely altered

Ol (Olivine) shape: 0= anhedral; 1= more or less rounded; 2= rounded

Pl (Plagioclase) shape: 0= cumulus; 1= poikilitic; 2= interstitial

Cpx (Clinopyroxene) shape: 0= cumulus; 1= poikilitic; 2= interstitial

Supplementary data table A2

Major and trace element analyses of clinopyroxenes from IODP Hole U1309D^a

| Sample | 63R3 28-30 | 64R3 13-16 | 69R3 6-9 | 135R2 82-85 | 227R2 26-30 | 227R3 121-124 | 231R3 50-54 | 232R1 112-116 | 234R1 92-96 | 234R3 14-18 | 236R2 121-124 | 237R2 40-43 | 247R3 19-22 |
|--------------------------------|--------------------|--------------------|------------|-------------|-------------|--------------------|-------------|---------------|--------------------|--------------------|--------------------|--------------------|--------------------|
| Rock type | ol-rich troctolite | ol-rich troctolite | troctolite | gabbro | Oligabbro | ol-rich troctolite | gabbro | troctolite | ol-rich troctolite | ol-rich troctolite | ol-rich troctolite | ol-rich troctolite | ol-rich troctolite |
| Depth(m) | 326.14 | 329.33 | 356.11 | 666.8 | 1093.69 | 1096.14 | 1113.6 | 1127.74 | 1125.62 | 1127.74 | 1146.86 | 1140.92 | 1190.08 |
| Zone | 1 | 1 | 1 | 3 | 4 | 4 | 4 | 4 | 4 | 4 | 4 | 4 | 4 |
| Shape | poikilitic | poikilitic | poikilitic | Cumulus | cumulus | poikilitic | cumulus | poikilitic | interstitial | poikilitic | interstitial | poikilitic | poikilitic |
| Location | c | f | c | f | c | f | c | f | c | f | c | f | c |
| n | 4 | 7 | 10 | 9 | 55 | 7 | 15 | 13 | 13 | 19 | 23 | 23 | 23 |
| SiO ₂ | 51.54 | 0.25 | 51.73 | 0.29 | 51.60 | 52.17 | 0.32 | na | na | 51.86 | 0.39 | 51.86 | 0.39 |
| TiO ₂ | 0.42 | 0.05 | 0.44 | 0.09 | 0.49 | 0.44 | 0.08 | na | na | 0.57 | 0.02 | 0.57 | 0.02 |
| Al ₂ O ₃ | 3.89 | 0.21 | 3.75 | 3.39 | 3.59 | 3.34 | 0.33 | na | na | 3.65 | 0.19 | 3.65 | 0.19 |
| Cr ₂ O ₃ | 1.41 | 0.14 | 1.37 | 1.13 | 1.31 | 1.24 | 0.09 | na | na | 1.08 | 0.23 | 1.08 | 0.23 |
| FeO | 3.62 | 0.14 | 3.53 | 3.41 | 3.14 | 4.37 | 0.87 | na | na | 4.75 | 0.21 | 4.75 | 0.21 |
| MnO | 15.78 | 0.19 | 15.33 | 16.89 | 16.06 | 17.04 | 0.02 | na | na | 16.65 | 0.58 | 16.65 | 0.58 |
| MgO | 21.88 | 0.21 | 22.22 | 20.91 | 22.03 | 20.19 | 0.33 | na | na | 20.16 | 0.55 | 20.16 | 0.55 |
| CaO | 0.51 | 0.04 | 0.45 | 0.04 | 0.47 | 0.33 | 0.06 | na | na | 0.39 | 0.07 | 0.39 | 0.07 |
| Na ₂ O | 0.01 | 0.00 | 0.00 | 0.00 | 0.00 | 0.00 | 0.00 | na | na | 0.00 | 0.00 | 0.00 | 0.00 |
| K ₂ O | 0.05 | 0.01 | 0.04 | 0.01 | 0.03 | 0.03 | 0.01 | na | na | 0.04 | 0.01 | 0.04 | 0.01 |
| NiO | 0.05 | 0.01 | 0.04 | 0.01 | 0.03 | 0.03 | 0.01 | na | na | 0.04 | 0.01 | 0.04 | 0.01 |
| Total | 99.23 | 0.29 | 99.22 | 0.17 | 98.84 | 99.29 | 0.22 | na | na | 99.10 | 0.22 | 99.10 | 0.22 |
| Mg# | 88.60 | 0.48 | 89.53 | 0.65 | 90.12 | 87.52 | 1.24 | na | na | 86.20 | 0.25 | 86.20 | 0.25 |
| | 3022 | 170 | 298 | 496 | 10464 | 8816 | 337 | 2554 | 3786 | 6277 | 1692 | 8263 | 1330 |
| | 327 | 10 | 208 | 496 | 10464 | 8816 | 337 | 2554 | 3786 | 6277 | 1692 | 8263 | 1330 |
| | 400 | 10632 | 621 | 10049 | 496 | 10464 | 337 | 2554 | 3786 | 6277 | 1692 | 8263 | 1330 |
| | 466 | 422 | 52 | 314 | 23 | 338 | 297 | 12 | 174 | 102 | 174 | 280 | 10 |
| | 0.07 | 0.06 | 0.06 | 0.01 | 0.01 | 0.01 | 0.01 | 0.01 | 0.01 | 0.01 | 0.01 | 0.01 | 0.01 |
| | 0.09 | 0.08 | 0.09 | 0.03 | 0.09 | 0.08 | 0.04 | 0.02 | 0.05 | 0.04 | 0.02 | 0.05 | 0.02 |
| | 0.21 | 0.03 | 0.23 | 0.03 | 0.09 | 0.18 | 0.02 | 0.05 | 0.04 | 0.02 | 0.05 | 0.04 | 0.02 |
| | 0.09 | 0.01 | 0.08 | 0.01 | 0.02 | 0.01 | 0.00 | 0.01 | 0.01 | 0.00 | 0.03 | 0.04 | 0.05 |
| | 0.04 | 0.05 | 0.03 | 0.03 | 0.04 | 0.06 | 0.02 | 0.09 | 0.12 | 0.02 | 0.05 | 0.04 | 0.05 |
| | 0.214 | 0.032 | 0.252 | 0.037 | 0.149 | 0.172 | 0.023 | 0.099 | 0.122 | 0.029 | 0.094 | 0.024 | 0.190 |
| | 0.1048 | 0.215 | 1.521 | 0.285 | 0.849 | 1.060 | 0.103 | 0.536 | 0.711 | 0.011 | 0.532 | 0.079 | 0.998 |
| | 0.246 | 0.043 | 0.355 | 0.056 | 0.219 | 0.253 | 0.019 | 0.129 | 0.189 | 0.002 | 0.130 | 0.014 | 0.223 |
| | 1.890 | 0.380 | 2.564 | 0.378 | 1.679 | 1.830 | 0.097 | 1.033 | 1.497 | 0.042 | 1.057 | 0.058 | 1.632 |
| | 1.035 | 0.155 | 1.319 | 0.171 | 0.945 | 1.030 | 0.055 | 0.603 | 0.873 | 0.025 | 0.648 | 0.012 | 0.893 |
| | 0.410 | 0.046 | 0.408 | 0.037 | 0.324 | 0.354 | 0.014 | 0.239 | 0.334 | 0.001 | 0.259 | 0.006 | 0.349 |
| | 1.920 | 0.177 | 2.333 | 0.210 | 1.750 | 1.678 | 0.022 | 1.019 | 1.525 | 0.001 | 1.196 | 0.006 | 1.673 |
| | 0.386 | 0.039 | 0.439 | 0.037 | 0.345 | 0.340 | 0.014 | 0.192 | 0.304 | 0.004 | 0.229 | 0.011 | 0.319 |
| | 2.945 | 0.232 | 3.437 | 0.268 | 2.730 | 2.550 | 0.014 | 1.575 | 2.262 | 0.004 | 1.725 | 0.009 | 2.301 |
| | 0.643 | 0.045 | 0.756 | 0.057 | 0.601 | 0.543 | 0.022 | 0.338 | 0.488 | 0.001 | 0.372 | 0.019 | 0.538 |
| | 1.908 | 0.137 | 2.270 | 0.156 | 1.775 | 1.530 | 0.155 | 0.952 | 1.387 | 0.049 | 1.067 | 0.073 | 1.582 |
| | 0.277 | 0.021 | 0.338 | 0.029 | 0.263 | 0.229 | 0.008 | 0.138 | 0.206 | 0.001 | 0.153 | 0.009 | 0.234 |
| | 1.893 | 0.143 | 2.249 | 0.249 | 1.785 | 1.578 | 0.017 | 0.914 | 1.348 | 0.009 | 1.023 | 0.087 | 1.550 |
| | 0.268 | 0.011 | 0.321 | 0.037 | 0.250 | 0.212 | 0.017 | 0.135 | 0.193 | 0.004 | 0.149 | 0.017 | 0.223 |
| | 0.35 | 0.06 | 0.48 | 0.06 | 0.37 | 0.38 | 0.06 | 0.20 | 0.29 | 0.01 | 0.25 | 0.03 | 0.32 |
| | 0.01 | 0.00 | 0.02 | 0.01 | 0.00 | 0.01 | 0.00 | 0.01 | 0.00 | 0.00 | 0.00 | 0.01 | 0.01 |
| | 0.04 | 0.03 | 0.06 | 0.05 | 0.04 | 0.08 | 0.07 | 0.01 | 0.03 | 0.01 | 0.02 | 0.01 | 0.05 |
| | 0.03 | 0.01 | 0.03 | 0.01 | 0.01 | 0.02 | 0.01 | 0.01 | 0.00 | 0.00 | 0.01 | 0.01 | 0.02 |
| | 0.03 | 0.00 | 0.03 | 0.01 | 0.01 | 0.05 | 0.02 | 0.12 | 0.01 | 0.00 | 0.02 | 0.03 | 0.02 |

^aMajor element analyses were performed by electron microprobe (wtf%) and trace element analyses (ppm) by LA-ICP-MS. Abbreviation: P= not analysed; σ= standard deviation of multiple determinations.

Mg#=(Mg/Mg+Fe)*100

Supplementary data Table A3

Major and trace element analyses of plagioclases from IODP Hole U1309P*

| Sample | 63R2 28-30 | 69R3 6-9 | 70R2 99-103 | 70R3 20-24 | 111R2 11-2-116 | 135R2 82-85 | 136R3 21-26 | 221R2 26-30 | 231R3 50-54 | 232R1 112-116 | 241R1 22-26 | 241R3 14-18 | 251R2 85-89 | 256R2 121-124 | 241R2 94-97 | 242R1 123-126 | 243R1 57-61 | 247R2 19-22 | | | | | | | | | | | | | | | |
|--------------------------------|------------|----------|-------------|------------|----------------|-------------|-------------|-------------|-------------|---------------|-------------|-------------|-------------|---------------|-------------|---------------|-------------|-------------|--------|------|-------|------|-------|------|-------|------|-------|------|-------|------|--------|------|------|
| Rock Type | of-rich | of-rich | of-rich | of-rich | of-rich | gabbro | gabbro | of-gabbro | gabbro | of-rich | of-rich | of-rich | of-rich | of-rich | of-rich | of-gabbro | of-rich | | | | | | | | | | | | | | | | |
| Depth(mbsf) | 326.14 | 356.11 | 359.68 | 360.39 | 551.82 | 666.8 | 672.33 | 1093.69 | 1113.6 | 1116.22 | 1124.92 | 1127.74 | 1131.61 | 1136.86 | 1160.71 | 1164.33 | 1168.47 | 1190.51 | | | | | | | | | | | | | | | |
| Zones | 1 | 1 | 1 | 1 | 2 | 3 | 3 | 4 | 4 | 4 | 4 | 4 | 4 | 4 | 4 | 4 | 4 | 4 | | | | | | | | | | | | | | | |
| SiO ₂ | 48.43 | 48.32 | 0.32 | 47.80 | 0.43 | 47.70 | 0.51 | 48.35 | 0.39 | na | na | na | 50.74 | 0.59 | 47.89 | 0.51 | 48.36 | 0.83 | 49.21 | 0.54 | 48.67 | 0.89 | 48.93 | 0.70 | 47.88 | 0.32 | 49.10 | 1.04 | 49.49 | 0.55 | 49.63 | 0.37 | |
| TiO ₂ | 0.00 | 0.04 | 0.02 | 0.04 | 0.01 | 0.04 | 0.01 | 0.05 | 0.02 | na | na | na | 0.05 | 0.01 | 0.05 | 0.02 | 0.04 | 0.03 | 0.04 | 0.02 | 0.04 | 0.02 | 0.04 | 0.02 | 0.02 | 0.05 | 0.06 | 0.03 | 0.04 | 0.02 | 0.05 | 0.02 | |
| Al ₂ O ₃ | 33.59 | 32.99 | 0.21 | 33.33 | 0.31 | 33.56 | 0.29 | 32.81 | 0.26 | na | na | na | 31.57 | 0.38 | 32.50 | 0.38 | 32.55 | 0.63 | 32.59 | 0.30 | 32.70 | 0.68 | 32.32 | 0.30 | 32.80 | 0.27 | 32.11 | 0.68 | 31.60 | 0.47 | 32.31 | 0.30 | |
| Cr ₂ O ₃ | 0.00 | 0.00 | 0.00 | 0.00 | 0.01 | 0.01 | 0.01 | na | na | na | na | na | 0.00 | 0.01 | 0.01 | 0.01 | 0.01 | 0.01 | 0.01 | 0.01 | 0.01 | 0.01 | 0.01 | 0.01 | 0.01 | 0.00 | 0.01 | 0.00 | 0.01 | 0.00 | 0.00 | | |
| FeO | 0.11 | 0.18 | 0.04 | 0.02 | 0.02 | 0.02 | 0.02 | 0.17 | 0.04 | na | na | na | 0.29 | 0.03 | 0.02 | 0.25 | 0.02 | 0.23 | 0.02 | 0.24 | 0.02 | 0.24 | 0.02 | 0.23 | 0.03 | 0.24 | 0.02 | 0.24 | 0.03 | 0.26 | 0.02 | 0.26 | |
| MnO | 0.02 | 0.01 | 0.01 | 0.00 | 0.01 | 0.01 | 0.01 | na | na | na | na | na | 0.01 | 0.01 | 0.01 | 0.01 | 0.01 | 0.01 | 0.00 | 0.01 | 0.00 | 0.01 | 0.01 | 0.01 | 0.01 | 0.01 | 0.01 | 0.01 | 0.01 | 0.01 | 0.01 | 0.01 | |
| MgO | 0.05 | 0.05 | 0.02 | 0.06 | 0.02 | 0.06 | 0.02 | 0.04 | 0.01 | na | na | na | 0.04 | 0.02 | 0.04 | 0.01 | 0.04 | 0.01 | 0.04 | 0.01 | 0.05 | 0.03 | 0.05 | 0.01 | 0.05 | 0.02 | 0.05 | 0.06 | 0.05 | 0.02 | 0.05 | 0.02 | |
| CaO | 16.24 | 15.93 | 0.18 | 16.44 | 0.32 | 16.58 | 0.31 | 15.92 | 0.28 | na | na | na | 14.32 | 0.39 | 15.93 | 0.38 | 15.54 | 0.69 | 15.56 | 0.40 | 15.63 | 0.81 | 15.40 | 0.45 | 15.96 | 0.29 | 15.20 | 0.77 | 14.71 | 0.51 | 15.41 | 0.25 | |
| Na ₂ O | 2.47 | 2.53 | 0.13 | 2.27 | 0.18 | 2.17 | 0.17 | 2.23 | 0.17 | na | na | na | 3.60 | 0.22 | 2.29 | 0.22 | 2.22 | 2.66 | 2.39 | 2.84 | 0.23 | 2.63 | 0.38 | 2.83 | 0.26 | 2.57 | 0.14 | 3.01 | 0.45 | 3.21 | 0.28 | 2.92 | 0.13 |
| K ₂ O | 0.02 | 0.01 | 0.01 | 0.01 | 0.01 | 0.01 | 0.01 | na | na | na | na | na | 0.03 | 0.01 | 0.01 | 0.01 | 0.01 | 0.01 | 0.01 | 0.01 | 0.01 | 0.01 | 0.01 | 0.01 | 0.01 | 0.01 | 0.02 | 0.01 | 0.03 | 0.01 | 0.02 | 0.01 | |
| Total | 100.91 | 100.07 | 0.35 | 100.19 | 0.27 | 100.35 | 0.31 | 100.09 | 0.24 | na | na | na | 100.66 | 0.22 | 99.21 | 0.17 | 99.48 | 0.15 | 100.54 | 0.16 | 99.99 | 0.40 | 99.84 | 0.31 | 99.56 | 0.26 | 99.87 | 0.28 | 99.39 | 0.23 | 100.67 | 0.29 | |
| wt(%) | 78.33 | 77.61 | 1.09 | 80.80 | 1.60 | 80.83 | 1.48 | 76.26 | 1.42 | na | na | na | 68.62 | 1.89 | 77.24 | 1.95 | 76.27 | 3.47 | 75.13 | 1.95 | 76.64 | 3.52 | 75.01 | 2.22 | 77.44 | 1.26 | 73.53 | 3.87 | 71.58 | 2.30 | 74.42 | 1.16 | |

*Major element analyses were performed by electron microprobe (wt%) and trace element analyses (ppm) by LA-ICP-MS. Abbreviation: n= number of analyses per mineral, σ = 1 standard deviation of multiple determinations, <dl = below detection limit, n.a. = not analysed.

Supplementary data Table A4

Major element compositions of plagioclase from IODP Hole U1309D^a

| sample | 60R3_39-42 | | 61R1_113-116 | | 136R1_35-39 | | 227R3_121-124 | | 234R1_92-96 | | 237R2_40-43 | |
|-------------|------------|------------|--------------|------------|-------------|------------|---------------|------------|-------------|------------|-------------|------------|
| Rocke type | ol-rich | troctolite | ol-rich | troctolite | ol-rich | troctolite | ol-rich | troctolite | ol-rich | troctolite | ol-rich | troctolite |
| Depth(mbsf) | 313.22 | 315.93 | 669.75 | 1096.14 | 1125.62 | 1140.92 | | | | | | |
| Zones | 1 | 1 | 3 | 4 | 4 | 4 | 4 | 4 | 4 | 4 | 4 | 4 |
| n | 5 | 5 | 4 | 6 | 2 | 7 | | | | | | |
| wt% SiO2 | 47.20 | 47.09 | 49.31 | 48.65 | 48.75 | 48.58 | | | | | | |
| TiO2 | 0.04 | 0.03 | 0.04 | 0.04 | 0.04 | 0.05 | | | | | | |
| Al2O3 | 33.75 | 33.53 | 32.59 | 32.61 | 31.74 | 32.25 | | | | | | |
| Cr2O3 | 0.01 | 0.00 | 0.02 | 0.01 | 0.00 | 0.01 | | | | | | |
| FeO | 0.16 | 0.13 | 0.16 | 0.26 | 0.25 | 0.25 | | | | | | |
| MnO | 0.00 | 0.00 | 0.01 | 0.01 | 0.01 | 0.00 | | | | | | |
| MgO | 0.03 | 0.03 | 0.02 | 0.03 | 0.02 | 0.05 | | | | | | |
| CaO | 16.84 | 16.61 | 15.26 | 15.23 | 15.36 | 15.31 | | | | | | |
| Na2O | 2.13 | 2.15 | 2.99 | 2.73 | 2.97 | 2.87 | | | | | | |
| K2O | 0.01 | 0.04 | 0.02 | 0.01 | 0.02 | 0.01 | | | | | | |
| Total | 100.16 | 99.62 | 100.42 | 99.57 | 99.16 | 99.38 | | | | | | |
| An (Ca) | 81.37 | 80.83 | 73.79 | 75.43 | 74.02 | 74.64 | | | | | | |

σ

| | | | | | | |
|---------|------|------|------|------|------|------|
| SiO2 | 0.26 | 0.20 | 0.65 | 0.14 | 0.39 | 0.55 |
| TiO2 | 0.01 | 0.01 | 0.01 | 0.02 | 0.00 | 0.02 |
| Al2O3 | 0.28 | 0.04 | 0.36 | 0.05 | 0.12 | 0.39 |
| Cr2O3 | 0.01 | 0.01 | 0.01 | 0.01 | 0.00 | 0.01 |
| FeO | 0.02 | 0.03 | 0.01 | 0.07 | 0.02 | 0.02 |
| MnO | 0.00 | 0.01 | 0.01 | 0.01 | 0.01 | 0.01 |
| MgO | 0.00 | 0.01 | 0.00 | 0.01 | 0.02 | 0.02 |
| CaO | 0.32 | 0.12 | 0.44 | 0.27 | 0.66 | 0.43 |
| Na2O | 0.16 | 0.06 | 0.26 | 0.07 | 0.16 | 0.27 |
| K2O | 0.01 | 0.01 | 0.01 | 0.00 | 0.01 | 0.01 |
| Total | 0.30 | 0.19 | 0.23 | 0.26 | 0.07 | 0.13 |
| An (Ca) | 1.45 | 0.53 | 2.24 | 0.58 | 1.85 | 2.32 |

^aMajor element analyses were performed by electron microprobe (wt%). Abbreviation: n= number of analyses per mineral; σ = 1 standard deviation of multiple determinations.

Supplementary data table A5 (continued)

| sample | 227R3_121-124 | 228R4_39-43 | 232R1_112-116 | 234R1_22-26 | 234R1_92-96 | 234R3_14-18 | 235R2_85-89 | 236R2_121-124 | 237R2_40-43 | 241R2_94-97 | 243R1_57-61 | 247R3_19-22 | 248R2_18-21 | 248R3_131-134 |
|-------------|--------------------|-------------|---------------|--------------------|--------------------|--------------------|--------------------|--------------------|--------------------|--------------------|-------------|-------------|--------------------|--------------------|
| rock type | ol-rich troctolite | ol-gabbro | troctolite | ol-rich troctolite | ol-rich troctolite | ol-rich troctolite | ol-rich troctolite | ol-rich troctolite | ol-rich troctolite | ol-rich troctolite | ol-gabbro | troctolite | ol-rich troctolite | ol-rich troctolite |
| Depth(mbsf) | 1096.14 | 1101.09 | 1116.22 | 1124.92 | 1125.62 | 1127.74 | 1131.61 | 1136.86 | 1140.92 | 1160.71 | 1168.47 | 1190.08 | 1193.32 | 1195.8 |
| zones | 4 | 4 | 4 | 4 | 4 | 4 | 4 | 4 | 4 | 4 | 4 | 4 | 4 | 4 |
| n | 6 | 7 | 10 | 7 | 8 | 8 | 6 | 5 | 5 | 8 | 6 | 13 | 9 | 8 |
| wt% | | | | | | | | | | | | | | |
| SiO2 | 40.13 | 40.15 | 39.54 | 40.14 | 40.44 | 40.61 | 40.51 | 40.45 | 40.16 | 40.00 | 38.90 | 40.68 | 40.12 | 40.67 |
| TiO2 | 0.01 | 0.02 | 0.02 | 0.02 | 0.01 | 0.02 | 0.01 | 0.01 | 0.01 | 0.02 | 0.02 | 0.02 | 0.02 | 0.02 |
| Al2O3 | 0.01 | 0.01 | 0.01 | 0.01 | 0.01 | 0.01 | 0.02 | 0.01 | 0.01 | 0.01 | 0.00 | 0.02 | 0.01 | 0.01 |
| Cr2O3 | 0.02 | 0.01 | 0.02 | 0.02 | 0.02 | 0.02 | 0.02 | 0.02 | 0.02 | 0.02 | 0.01 | 0.01 | 0.01 | 0.01 |
| FeO | 14.35 | 15.74 | 15.74 | 13.82 | 13.76 | 13.86 | 13.44 | 14.23 | 13.77 | 14.35 | 19.81 | 14.08 | 16.35 | 13.84 |
| MnO | 0.23 | 0.25 | 0.27 | 0.22 | 0.23 | 0.23 | 0.23 | 0.24 | 0.22 | 0.23 | 0.29 | 0.23 | 0.27 | 0.23 |
| MgO | 44.19 | 43.29 | 43.79 | 45.02 | 45.41 | 45.51 | 44.91 | 44.68 | 44.82 | 44.59 | 40.11 | 44.48 | 42.87 | 44.75 |
| CaO | 0.09 | 0.07 | 0.06 | 0.09 | 0.08 | 0.08 | 0.08 | 0.08 | 0.09 | 0.08 | 0.07 | 0.09 | 0.08 | 0.08 |
| Na2O | 0.01 | 0.01 | 0.01 | 0.01 | 0.00 | 0.01 | 0.01 | 0.00 | 0.00 | 0.00 | 0.00 | 0.00 | 0.01 | 0.00 |
| K2O | 0.00 | 0.00 | 0.01 | 0.00 | 0.00 | 0.00 | 0.00 | 0.00 | 0.00 | 0.00 | 0.00 | 0.00 | 0.01 | 0.00 |
| NiO | 0.23 | 0.20 | 0.21 | 0.28 | 0.26 | 0.26 | 0.24 | 0.25 | 0.27 | 0.25 | 0.16 | 0.27 | 0.18 | 0.27 |
| Total | 99.26 | 99.75 | 99.67 | 99.64 | 100.22 | 100.62 | 99.46 | 99.98 | 99.36 | 99.55 | 99.39 | 99.89 | 99.93 | 99.90 |
| Fe (M%) | 84.38 | 82.83 | 82.98 | 85.11 | 85.26 | 85.20 | 85.41 | 84.62 | 85.09 | 84.50 | 78.05 | 84.70 | 82.13 | 85.00 |
| Mg# | 84.59 | 83.06 | 83.22 | 85.31 | 85.47 | 85.41 | 85.62 | 84.84 | 85.30 | 84.71 | 78.30 | 84.92 | 82.37 | 85.21 |
| Ni (ppm) | 1832.94 | 1536.53 | 1664.65 | 2174.62 | 2063.43 | 2033.58 | 1886.75 | 1983.70 | 2082.64 | 1961.12 | 1245.22 | 2151.91 | 1440.78 | 2134.23 |
| σ | | | | | | | | | | | | | | |
| SiO2 | 0.15 | 0.10 | 0.12 | 0.16 | 0.12 | 0.11 | 0.21 | 0.14 | 0.16 | 0.20 | 0.15 | 0.14 | 0.14 | 0.13 |
| TiO2 | 0.01 | 0.01 | 0.01 | 0.02 | 0.02 | 0.01 | 0.01 | 0.01 | 0.01 | 0.01 | 0.02 | 0.01 | 0.01 | 0.01 |
| Al2O3 | 0.01 | 0.01 | 0.01 | 0.01 | 0.01 | 0.01 | 0.01 | 0.00 | 0.00 | 0.01 | 0.00 | 0.01 | 0.01 | 0.01 |
| Cr2O3 | 0.02 | 0.01 | 0.01 | 0.02 | 0.01 | 0.01 | 0.02 | 0.01 | 0.01 | 0.01 | 0.01 | 0.01 | 0.01 | 0.01 |
| FeO | 0.15 | 0.13 | 0.13 | 0.20 | 0.12 | 0.11 | 0.21 | 0.32 | 0.04 | 0.15 | 0.07 | 0.09 | 0.13 | 0.18 |
| MnO | 0.02 | 0.01 | 0.02 | 0.02 | 0.01 | 0.01 | 0.02 | 0.02 | 0.01 | 0.02 | 0.01 | 0.02 | 0.01 | 0.02 |
| MgO | 0.15 | 0.13 | 0.13 | 0.15 | 0.13 | 0.21 | 0.15 | 0.06 | 0.14 | 0.21 | 0.13 | 0.21 | 0.13 | 0.12 |
| CaO | 0.03 | 0.01 | 0.01 | 0.01 | 0.01 | 0.01 | 0.02 | 0.01 | 0.02 | 0.01 | 0.02 | 0.02 | 0.03 | 0.02 |
| Na2O | 0.01 | 0.01 | 0.02 | 0.01 | 0.01 | 0.01 | 0.01 | 0.00 | 0.01 | 0.01 | 0.01 | 0.01 | 0.02 | 0.00 |
| K2O | 0.00 | 0.00 | 0.01 | 0.01 | 0.00 | 0.00 | 0.00 | 0.01 | 0.00 | 0.00 | 0.00 | 0.00 | 0.01 | 0.00 |
| NiO | 0.01 | 0.02 | 0.02 | 0.02 | 0.02 | 0.03 | 0.03 | 0.03 | 0.01 | 0.02 | 0.01 | 0.02 | 0.01 | 0.01 |
| Total | 0.14 | 0.15 | 0.19 | 0.30 | 0.30 | 0.18 | 0.31 | 0.19 | 0.14 | 0.24 | 0.11 | 0.32 | 0.17 | 0.27 |
| Fe (M%) | 0.16 | 0.15 | 0.20 | 0.33 | 0.30 | 0.12 | 0.19 | 0.30 | 0.06 | 0.17 | 0.07 | 0.07 | 0.15 | 0.15 |
| Mg# | 0.16 | 0.14 | 0.21 | 0.03 | 0.10 | 0.12 | 0.18 | 0.29 | 0.05 | 0.16 | 0.07 | 0.08 | 0.15 | 0.15 |
| Ni (ppm) | 90.29 | 171.88 | 182.47 | 143.64 | 150.55 | 273.91 | 239.79 | 61.25 | 116.25 | 172.78 | 77.71 | 187.89 | 115.39 | 112.13 |

^aMajor element analyses were performed by electron microprobe (wt%). Abbreviation: n= number of analyses per mineral; σ = 1 standard deviation of multiple determinations.
Mg#=(Mg/(Mg+Fe))*100

Supplementary data table A6

Major element compositions of spinel from IODP Hole U1309D^a

| Sample | 62R1_4-7 | 63R2_28-30 | 64R1_13-16 | 64R1_53-56.5 | 70R2_99-103 | 70R3_20-24 | 111R2_112-116 | 111R3_101-114 | 136R1_35-39 | 235R2_85-89 | 237R2_40-43 | 241R2_94-97 |
|-------------|--------------------|--------------------|--------------------|--------------|--------------|--------------|---------------|--------------------|--------------------|--------------------|--------------------|--------------------|
| rock type | Ol-rich troctolite | Ol-rich troctolite | Ol-rich troctolite | Dunite | Troctolite | Troctolite | Troctolite | Ol-rich troctolite | Ol-rich troctolite | Ol-rich troctolite | Ol-rich troctolite | Ol-rich troctolite |
| Depth(mbsf) | 319.64 | 326.14 | 329.33 | 329.73 | 359.680 | 360.390 | 551.820 | 553.130 | 669.75 | 1131.61 | 1140.92 | 1160.71 |
| zones | 1 | 1 | 1 | 1 | 1 | 1 | 2 | 2 | 3 | 4 | 4 | 4 |
| n | 2 | 1 | 3 | 4 | 1 | 2 | 1 | 4 | 1 | 1 | 2 | 2 |
| wt% | | | | | | | | | | | | |
| SiO2 | 0.18 | 0.25 | 0.13 | 0.13 | 0.09 | 0.12 | 0.11 | 0.11 | 0.10 | 0.20 | 0.25 | 0.18 |
| TiO2 | 0.69 | 0.87 | 1.01 | 0.88 | 2.23 | 2.34 | 2.28 | 1.59 | 0.41 | 1.41 | 1.85 | 1.90 |
| Al2O3 | 24.94 | 23.06 | 23.91 | 23.73 | 19.57 | 17.89 | 19.22 | 20.84 | 27.55 | 18.47 | 20.50 | 17.66 |
| Cr2O3 | 38.31 | 40.27 | 39.88 | 41.63 | 40.15 | 40.14 | 41.56 | 42.94 | 35.33 | 38.31 | 38.33 | 40.86 |
| FeO | 25.66 | 23.68 | 22.59 | 21.97 | 28.82 | 28.71 | 26.29 | 23.23 | 25.20 | 31.67 | 27.87 | 29.52 |
| MnO | 0.36 | 0.36 | 0.33 | 0.32 | 0.42 | 0.41 | 0.36 | 0.37 | 0.32 | 0.45 | 0.35 | 0.42 |
| MgO | 9.74 | 10.14 | 11.39 | 11.10 | 8.54 | 9.21 | 9.64 | 10.50 | 10.05 | 7.29 | 9.68 | 8.39 |
| CaO | 0.01 | 0.00 | 0.03 | 0.02 | 0.03 | 0.01 | 0.00 | 0.10 | 0.00 | 0.19 | 0.05 | 0.04 |
| Na2O | 0.01 | 0.00 | 0.00 | 0.01 | 0.00 | 0.00 | 0.01 | 0.02 | 0.00 | 0.00 | 0.00 | 0.01 |
| Total | 100.05 | 98.79 | 99.39 | 99.91 | 99.95 | 98.98 | 99.60 | 99.82 | 99.07 | 98.15 | 99.06 | 99.08 |
| Ct# | 50.83 | 53.95 | 52.81 | 54.07 | 57.92 | 60.08 | 59.20 | 58.09 | 46.25 | 58.18 | 55.78 | 61.17 |
| Mg# | 40.30 | 43.30 | 47.33 | 47.37 | 34.56 | 36.34 | 39.53 | 44.56 | 41.56 | 29.08 | 34.50 | 33.62 |
| σ | | | | | | | | | | | | |
| SiO2 | 0.02 | - | 0.01 | 0.02 | - | 0.00 | - | 0.02 | - | - | 0.01 | 0.01 |
| TiO2 | 0.29 | - | 0.10 | 0.08 | - | 0.12 | - | 0.39 | - | - | 0.59 | 0.37 |
| Al2O3 | 3.37 | - | 0.48 | 0.84 | - | 0.03 | - | 2.05 | - | - | 3.39 | 5.15 |
| Cr2O3 | 1.75 | - | 1.07 | 0.59 | - | 0.12 | - | 1.72 | - | - | 2.99 | 5.82 |
| FeO | 0.07 | - | 0.02 | 0.01 | - | 0.01 | - | 0.05 | - | - | 0.06 | 0.11 |
| MnO | 1.46 | - | 0.54 | 0.53 | - | 0.06 | - | 1.30 | - | - | 1.16 | 3.25 |
| MgO | 0.00 | - | 0.02 | 0.02 | - | 0.01 | - | 0.12 | - | - | 0.05 | 0.01 |
| CaO | 0.01 | - | 0.00 | 0.01 | - | 0.00 | - | 0.02 | - | - | 0.00 | 0.00 |
| Na2O | 2.66 | - | 0.43 | 0.85 | - | 0.05 | - | 1.14 | - | - | 0.74 | 1.68 |
| Total | 0.08 | - | 0.13 | 0.07 | - | 0.17 | - | 0.19 | - | - | 0.12 | 0.43 |
| Ct# | 5.12 | - | 0.48 | 1.36 | - | 0.01 | - | 3.02 | - | - | 4.57 | 7.96 |
| Mg# | 5.25 | - | 2.35 | 1.78 | - | 0.07 | - | 4.78 | - | - | 5.37 | 13.04 |

^aMajor element analyses were performed by electron microprobe (wt%). Abbreviation: n= number of analyses per mineral; σ = 1 standard deviation of multiple determinations

Mg# = (Mg/(Mg+Fe)) * 100

Ct# = (Cr/(Cr+Al)) * 100

Supplementary data Table A7

Whole Rock major elements from IODP Hole U1309D^a

| Sample | SiO ₂ | Al ₂ O ₃ | Fe ₂ O ₃ | MnO | MgO | CaO | Na ₂ O | K ₂ O | TiO ₂ | P ₂ O ₅ | Zr | LOI | Total |
|---------------|------------------|--------------------------------|--------------------------------|------|-------|-------|-------------------|------------------|------------------|-------------------------------|-------|-------|--------|
| | (%) | (%) | (%) | (%) | (%) | (%) | (%) | (%) | (%) | (%) | (ppm) | (%) | (%) |
| 60R3_39-42 | 39.04 | 5.07 | 9.00 | 0.16 | 32.50 | 5.42 | <d.l | <d.l | 0.10 | 0.01 | 7.80 | 8.42 | 99.72 |
| 61R1_11-14 | 39.09 | 3.15 | 9.74 | 0.14 | 33.91 | 4.11 | <d.l | <d.l | 0.09 | 0.01 | 7.50 | 9.52 | 99.76 |
| 61R1_113-116 | 36.81 | 7.01 | 9.42 | 0.16 | 32.50 | 3.76 | <d.l | <d.l | 0.07 | 0.01 | 5.60 | 9.88 | 99.62 |
| 62R1_4-7 | 38.48 | 6.65 | 9.77 | 0.15 | 30.28 | 5.28 | <d.l | <d.l | 0.08 | 0.01 | 5.80 | 9.02 | 99.72 |
| 63R2_28-30 | 39.13 | 7.81 | 9.18 | 0.24 | 26.31 | 7.90 | <d.l | 0.01 | 0.16 | 0.02 | 9.00 | 8.67 | 99.43 |
| 64R1_13-16 | 37.78 | 4.36 | 9.32 | 0.15 | 35.69 | 2.14 | <d.l | <d.l | 0.09 | 0.01 | 5.90 | 10.14 | 99.68 |
| 64R1_53-56 | 37.42 | 1.80 | 10.29 | 0.16 | 36.05 | 2.71 | <d.l | <d.l | 0.07 | 0.01 | 4.40 | 10.49 | 99.00 |
| 67R2_47-51 | 51.01 | 12.70 | 6.57 | 0.13 | 11.66 | 14.98 | 1.20 | 0.01 | 0.31 | 0.01 | 11.50 | 0.88 | 99.46 |
| 69R3_6-9 | 39.67 | 8.77 | 9.58 | 0.15 | 27.25 | 5.81 | <d.l | 0.08 | 0.08 | 0.02 | 10.20 | 7.79 | 99.20 |
| 70R2_99-103 | 40.27 | 12.85 | 8.75 | 0.12 | 24.82 | 6.41 | 0.39 | <d.l | 0.07 | 0.01 | 6.60 | 6.07 | 99.76 |
| 70R3_20-24 | 40.35 | 12.33 | 8.80 | 0.13 | 24.88 | 6.55 | 0.35 | <d.l | 0.08 | 0.01 | 5.80 | 5.82 | 99.30 |
| 71R1_10-13 | 45.67 | 19.05 | 5.76 | 0.09 | 14.06 | 12.37 | 0.87 | 0.02 | 0.15 | 0.02 | 19.20 | 1.46 | 99.52 |
| 111R3_109-113 | 39.01 | 7.23 | 9.70 | 0.15 | 33.44 | 3.41 | 0.05 | <d.l | 0.12 | 0.02 | 15.90 | 6.38 | 99.50 |
| 111R4_14-17 | 37.97 | 6.66 | 9.55 | 0.16 | 31.87 | 4.30 | <d.l | <d.l | 0.08 | 0.01 | 9.10 | 8.76 | 99.36 |
| 111R4_50-54 | 38.03 | 6.05 | 10.36 | 0.15 | 32.19 | 3.51 | <d.l | <d.l | 0.08 | 0.01 | 6.40 | 9.27 | 99.66 |
| 112R2_16-20 | 48.17 | 16.09 | 6.17 | 0.11 | 12.16 | 13.05 | 1.23 | 0.05 | 0.27 | 0.02 | 10.70 | 2.06 | 99.37 |
| 135R2_82-85 | 49.04 | 16.91 | 6.36 | 0.11 | 10.53 | 13.88 | 1.39 | 0.01 | 0.45 | 0.02 | 22.70 | 0.73 | 99.43 |
| 136R1_36-40 | 41.40 | 6.79 | 9.92 | 0.16 | 30.60 | 5.89 | 0.08 | 0.00 | 0.11 | 0.02 | 17.70 | 4.29 | 99.26 |
| 136R2_37-40 | 39.39 | 4.53 | 10.04 | 0.15 | 32.25 | 4.26 | <d.l | <d.l | 0.09 | 0.01 | 7.10 | 8.28 | 99.00 |
| 136R3_21-25 | 52.22 | 10.73 | 11.51 | 0.23 | 12.73 | 10.21 | 1.41 | 0.02 | 0.61 | 0.05 | 29.70 | 0.04 | 99.76 |
| 227R2_27-31 | 43.56 | 10.45 | 10.66 | 0.16 | 24.15 | 8.32 | 0.52 | 0.00 | 0.12 | 0.02 | 7.60 | 1.42 | 99.38 |
| 227R3_121-124 | 41.42 | 4.97 | 12.17 | 0.18 | 33.74 | 5.00 | <d.l | <d.l | 0.09 | 0.01 | 7.90 | 2.23 | 99.82 |
| 228R1_33-37 | 39.78 | 6.62 | 12.24 | 0.19 | 33.53 | 3.80 | 0.04 | <d.l | 0.06 | 0.01 | 6.70 | 3.44 | 99.71 |
| 228R1_95-98 | 44.83 | 4.71 | 9.94 | 0.16 | 27.65 | 9.83 | <d.l | <d.l | 0.23 | 0.01 | 11.10 | 2.01 | 99.38 |
| 228R2_42-45 | 38.94 | 3.67 | 12.44 | 0.18 | 35.14 | 3.15 | <d.l | <d.l | 0.07 | 0.01 | 7.80 | 6.05 | 99.65 |
| 228R4_39-43 | 44.82 | 9.46 | 9.27 | 0.15 | 24.03 | 9.75 | 0.40 | <d.l | 0.15 | 0.01 | 10.10 | 1.53 | 99.57 |
| 231R3_51-54 | 50.23 | 17.47 | 5.32 | 0.10 | 9.33 | 14.96 | 1.61 | <d.l | 0.25 | 0.01 | 11.00 | 0.38 | 99.66 |
| 232R1_112-116 | 41.74 | 11.78 | 10.17 | 0.15 | 25.71 | 6.45 | 0.58 | <d.l | 0.08 | 0.01 | 7.30 | 3.06 | 99.73 |
| 233R2_109-112 | 41.14 | 7.85 | 11.06 | 0.17 | 33.37 | 4.05 | 0.30 | <d.l | 0.04 | 0.01 | 5.30 | 1.67 | 99.66 |
| 234R1_22-26 | 40.54 | 5.23 | 12.15 | 0.18 | 36.54 | 2.97 | 0.12 | <d.l | 0.04 | 0.01 | 7.00 | 1.82 | 99.61 |
| 234R1_92-96 | 36.61 | 4.10 | 11.10 | 0.16 | 32.75 | 3.14 | <d.l | <d.l | 0.06 | 0.01 | 6.10 | 12.98 | 100.91 |
| 234R3_14-18 | 39.86 | 4.14 | 12.15 | 0.19 | 37.27 | 2.95 | <d.l | <d.l | 0.13 | 0.01 | 6.60 | 2.98 | 99.68 |
| 235R2_85-89 | 39.13 | 4.08 | 12.16 | 0.19 | 35.59 | 3.09 | <d.l | <d.l | 0.07 | 0.01 | 7.00 | 5.24 | 99.56 |
| 236R2_121-124 | 40.99 | 5.23 | 12.57 | 0.19 | 34.70 | 3.93 | 0.05 | <d.l | 0.07 | 0.01 | 7.00 | 1.89 | 99.63 |
| 237R2_40-43 | 38.59 | 5.04 | 11.58 | 0.18 | 34.51 | 3.37 | <d.l | <d.l | 0.06 | 0.01 | 6.50 | 5.66 | 99.00 |
| 241R2_94-97 | 40.56 | 6.85 | 11.35 | 0.17 | 34.38 | 3.45 | 0.18 | <d.l | 0.07 | 0.01 | 5.00 | 2.37 | 99.39 |
| 242R1_123-126 | 47.91 | 25.59 | 3.77 | 0.05 | 5.44 | 13.24 | 2.20 | 0.01 | 0.16 | 0.02 | 9.30 | 1.55 | 99.95 |
| 243R1_57-61 | 47.74 | 12.96 | 8.38 | 0.14 | 17.03 | 12.20 | 0.90 | <d.l | 0.26 | 0.02 | 13.40 | 0.01 | 99.63 |
| 247R3_19-22 | 42.66 | 3.59 | 12.07 | 0.19 | 35.77 | 5.07 | <d.l | <d.l | 0.10 | 0.01 | 8.00 | 0.06 | 99.52 |
| 247R3_62-66 | 42.56 | 1.75 | 12.21 | 0.19 | 34.26 | 6.58 | <d.l | <d.l | 0.16 | 0.01 | 8.00 | 1.57 | 99.30 |
| 248R2_18-21 | 41.88 | 4.20 | 13.81 | 0.21 | 34.71 | 4.09 | 0.11 | <d.l | 0.08 | 0.01 | 8.50 | 0.00 | 99.10 |
| 248R3_131-134 | 41.32 | 4.05 | 12.36 | 0.19 | 36.71 | 3.78 | <d.l | <d.l | 0.09 | 0.01 | 9.20 | 1.08 | 99.59 |

^aMajor element analyses were performed by XRF at the CIC (Universidad de Granada, Spain). Abbreviation: <d.l = below detection limit

Supplementary data Table A8

| Sample | 62R2_28-30 | 62R2_28-30 | 228R4_29-43 | 69R3_6-9 | 62R1_4-7 | 61R1_113-116 | 64R1_13-16 | 136R1_35-39 | 136R2_37-40 | 227R3_121-124 | 234R3_14-18 | 234R1_92-96 | 237R2_40-43 | 247R3_62-66 | 248R2_18-21 | 248R3_131-134 |
|---------|-------------|-------------|-------------|-------------|------------|--------------|-------------|-------------|-------------|---------------|-------------|-------------|-------------|------------------|-------------|---------------|
| Element | BR(basalt) | BR(basalt) | BR(basalt) | BR(basalt) | BR(basalt) | BR(basalt) | BR(basalt) | BR(basalt) | BR(basalt) | BR(basalt) | BR(basalt) | BR(basalt) | BR(basalt) | BR(basalt) | BR(basalt) | BR(basalt) |
| Cs | 0.66 | 0.58 | 0.62 | 0.72 | 0.59 | 0.62 | 0.59 | 0.67 | 0.56 | 0.89 | 0.66 | 0.68 | 0.71 | 0.71 | 0.48 | 0.61 |
| Rb | 41.21 | 40.80 | 42.97 | 42.23 | 40.21 | 40.34 | 37.67 | 40.85 | 35.21 | 39.38 | 39.68 | 41.72 | 42.79 | 42.38 | 41.34 | 40.90 |
| Ba | 1122.4 | 1043.07 | 1011.98 | 1011.98 | 945.51 | 962.85 | 952.75 | 1085.37 | 815.69 | 945.13 | 984.76 | 995.49 | 1017.17 | 1003.22 | 1009.57 | 994.81 |
| Th | 17.50 | 9.87 | 10.84 | 10.22 | 9.70 | 11.82 | 9.57 | 11.82 | 8.03 | 9.40 | 9.66 | 9.97 | 9.72 | 10.02 | 10.08 | 10.08 |
| U | 4.77 | 2.56 | 2.47 | 2.48 | 2.48 | 2.34 | 2.26 | 2.61 | 1.92 | 2.07 | 2.28 | 2.46 | 2.42 | 2.56 | 2.45 | 2.35 |
| Nb | 104.69 | 108.14 | 101.39 | 101.53 | 92.84 | 96.75 | 93.27 | 104.42 | 83.62 | 94.28 | 95.69 | 99.96 | 101.53 | 99.29 | 102.72 | 99.07 |
| Ta | 6.21 | 5.32 | 5.61 | 5.7 | 5.28 | 4.98 | 5.28 | 6.08 | 4.35 | 4.39 | 5.01 | 5.07 | 5.13 | 5.12 | 5.27 | 5.22 |
| La | 99.960 | 90.810 | 91.730 | 93.100 | 86.830 | 87.490 | 84.160 | 102.930 | 73.900 | 78.750 | 87.920 | 89.630 | 92.230 | 89.120 | 89.530 | 89.560 |
| Ce | 158.580 | 150.140 | 143.860 | 149.730 | 137.880 | 141.030 | 134.590 | 159.070 | 119.060 | 135.080 | 142.740 | 145.150 | 148.670 | 148.070 | 147.840 | 144.700 |
| Pr | 8.50 | 7.24 | 7.10 | 7.72 | 6.65 | 7.08 | 7.03 | 7.53 | 5.63 | 6.17 | 6.66 | 8.32 | 7.04 | 7.23 | 6.93 | 6.93 |
| Nd | 138.65 | 132.68 | 1290.06 | 1293.74 | 1216.71 | 1239.91 | 1208.87 | 1267.53 | 1036.28 | 1190.09 | 1233.19 | 1260.37 | 1271.17 | 1282.01 | 1283.91 | 1282.71 |
| Zr | 245.7 | 219.8 | 241.63 | 232.04 | 227.04 | 234.83 | 222.73 | 248.33 | 192.96 | 181.72 | 221.61 | 227.31 | 238.45 | 232.33 | 238.35 | 238.13 |
| Hf | 6.08 | 4.76 | 5.63 | 4.92 | 4.95 | 5.24 | 4.94 | 5.9 | 4.22 | 4.74 | 4.74 | 4.79 | 4.92 | 4.97 | 5.22 | 4.99 |
| Sm | 12.680 | 11.250 | 11.350 | 11.550 | 10.950 | 10.980 | 10.400 | 12.710 | 9.270 | 9.540 | 10.900 | 11.080 | 11.710 | 11.320 | 11.610 | 11.150 |
| Eu | 3.950 | 3.570 | 3.490 | 3.560 | 3.270 | 3.310 | 3.180 | 3.790 | 2.800 | 3.010 | 3.310 | 3.300 | 3.390 | 3.380 | 3.440 | 3.380 |
| Gd | 10.080 | 8.690 | 8.510 | 9.350 | 8.870 | 8.930 | 8.760 | 10.290 | 7.470 | 8.800 | 9.090 | 8.980 | 9.120 | 8.960 | 9.160 | 9.260 |
| Tb | 1.290 | 1.070 | 1.180 | 1.120 | 1.118 | 1.107 | 1.066 | 1.290 | 0.920 | 1.082 | 1.080 | 1.075 | 1.137 | 1.071 | 1.136 | 1.158 |
| Dy | 6.820 | 5.780 | 6.440 | 6.430 | 6.100 | 6.110 | 5.800 | 7.040 | 4.970 | 4.610 | 5.850 | 5.710 | 6.130 | 6.050 | 6.170 | 6.280 |
| Y | 27.36 | 23.65 | 26.21 | 25.07 | 25.74 | 26.6 | 24.85 | 27.4 | 21.3 | 19.62 | 24.79 | 25.32 | 26.9 | 25.84 | 26.36 | 26.57 |
| Ho | 1.130 | 0.960 | 1.030 | 1.060 | 1.030 | 1.018 | 0.963 | 1.160 | 0.846 | 0.739 | 0.960 | 0.992 | 0.999 | 1.001 | 1.032 | 1.032 |
| Er | 2.720 | 2.220 | 2.550 | 2.430 | 2.350 | 2.430 | 2.240 | 2.730 | 1.950 | 1.684 | 1.684 | 2.380 | 2.380 | 2.310 | 2.420 | 2.440 |
| Tm | 0.333 | 0.265 | 0.305 | 0.285 | 0.290 | 0.307 | 0.273 | 0.337 | 0.235 | 0.221 | 0.273 | 0.276 | 0.298 | 0.286 | 0.299 | 0.299 |
| Yb | 2.060 | 1.770 | 1.980 | 1.920 | 1.780 | 1.760 | 1.810 | 2.020 | 1.454 | 1.355 | 1.690 | 1.800 | 1.780 | 1.800 | 1.720 | 1.800 |
| Lu | 0.268 | 0.214 | 0.249 | 0.254 | 0.244 | 0.223 | 0.223 | 0.270 | 0.187 | 0.171 | 0.237 | 0.232 | 0.247 | 0.246 | 0.235 | 0.252 |
| Sample | 138R2_93-95 | 227R2_26-30 | 138R3_21-26 | 70R2_99-103 | 71R1_10-13 | 228R1_95-98 | 231R3_50-54 | 234R1_22-26 | 238R2_85-89 | 238R2_121-124 | 241R2_94-97 | average | std | reference values | | |
| Element | BR(basalt) | BR(basalt) | BR(basalt) | BR(basalt) | BR(basalt) | BR(basalt) | BR(basalt) | BR(basalt) | BR(basalt) | BR(basalt) | BR(basalt) | BR(basalt) | BR(basalt) | BR(basalt) | BR(basalt) | BR(basalt) |
| Cs | 0.61 | 0.72 | 0.67 | 0.71 | 0.66 | 0.71 | 0.67 | 0.65 | 0.67 | 0.71 | 0.70 | 0.66 | 0.07 | 0.8 | | |
| Rb | 40.90 | 42.31 | 43.11 | 44.36 | 42.27 | 41.82 | 42.32 | 41.13 | 40.56 | 44.19 | 43.98 | 41.36 | 1.84 | 47 | | |
| Ba | 994.81 | 1026.95 | 1064.84 | 1103.46 | 1039.66 | 1039.66 | 1015.75 | 1013.04 | 1049.49 | 1091.18 | 1096.52 | 1016.15 | 59.95 | 1050 | | |
| Th | 10.37 | 10.93 | 11.54 | 10.33 | 10.63 | 10.60 | 10.91 | 11.12 | 10.81 | 11.12 | 10.54 | 10.50 | 1.55 | 11 | | |
| U | 2.52 | 2.54 | 2.62 | 2.43 | 2.54 | 2.52 | 2.72 | 2.41 | 2.52 | 2.64 | 2.41 | 2.53 | 0.45 | 3 | | |
| Nb | 99.63 | 105.66 | 109.02 | 102.51 | 96.50 | 102.35 | 97.95 | 104.22 | 105.27 | 104.72 | 99.53 | 100.22 | 5.10 | 98 | | |
| Ta | 5.4 | 5.92 | 6.12 | 5.45 | 5.95 | 5.46 | 5.71 | 5.83 | 5.83 | 5.74 | 5.45 | 5.433 | 0.440 | 6 | | |
| La | 92.080 | 99.080 | 101.350 | 93.490 | 93.140 | 93.140 | 92.180 | 96.440 | 99.660 | 99.730 | 95.190 | 92.100 | 6.300 | 82 | | |
| Ce | 148.970 | 157.680 | 161.260 | 149.260 | 151.260 | 145.810 | 150.510 | 151.630 | 158.540 | 158.950 | 150.570 | 147.801 | 8.680 | 151 | | |
| Pr | 7.50 | 7.55 | 7.69 | 8.22 | 6.90 | 7.75 | 8.74 | 7.33 | 8.00 | 7.87 | 7.18 | 7.35 | 0.66 | 5.0 | | |
| Nd | 16.08 | 17.51 | 17.71 | 17.71 | 16.89 | 16.16 | 16.32 | 16.92 | 17.47 | 17.51 | 16.6 | 16.25 | 1.03 | 17.0 | | |
| Sr | 1271.81 | 1331.52 | 1423.64 | 1301.58 | 1194.09 | 1321.55 | 1298.76 | 1333.58 | 1364.86 | 1351.21 | 1317 | 1280.68 | 70.58 | 1320 | | |
| Zr | 64.16 | 69.7 | 70.66 | 65.42 | 65.98 | 64.16 | 64.3 | 66.06 | 67.39 | 68.75 | 66.58 | 63.80 | 4.20 | 65 | | |
| Nd | 229.55 | 254.86 | 266.32 | 234.47 | 234.47 | 249.81 | 237.5 | 255.23 | 249.02 | 255.91 | 235.14 | 235.49 | 16.96 | 260 | | |
| Hf | 5.33 | 5.67 | 6.32 | 5.3 | 5.04 | 5.56 | 5.74 | 5.6 | 5.6 | 5.89 | 5.7 | 5.271 | 0.857 | 5.6 | | |
| Sm | 11.400 | 12.580 | 12.860 | 11.610 | 12.090 | 11.390 | 11.630 | 11.940 | 12.430 | 12.320 | 12.010 | 11.511 | 0.824 | 12.2 | | |
| Ba | 3.400 | 3.740 | 3.780 | 3.580 | 3.590 | 3.400 | 3.580 | 3.600 | 3.620 | 3.690 | 3.460 | 3.458 | 0.230 | 3.7 | | |
| Gd | 9.810 | 10.110 | 10.350 | 9.550 | 9.880 | 9.480 | 9.590 | 9.770 | 9.810 | 10.090 | 9.720 | 9.209 | 0.760 | 9.5 | | |
| Tb | 1.146 | 1.267 | 1.363 | 1.192 | 1.087 | 1.164 | 1.140 | 1.201 | 1.213 | 1.290 | 1.185 | 1.145 | 0.103 | 1.3 | | |
| Dy | 6.430 | 6.880 | 7.030 | 6.350 | 6.220 | 6.520 | 6.490 | 6.620 | 6.640 | 7.010 | 6.160 | 6.276 | 0.564 | 6.4 | | |
| Y | 26.54 | 28.68 | 29.65 | 26.35 | 25.22 | 27.93 | 26.26 | 28.58 | 27.79 | 28.12 | 27.21 | 26.14 | 2.02 | 30 | | |
| Ho | 1.041 | 1.099 | 1.205 | 1.060 | 1.130 | 1.051 | 1.080 | 1.083 | 1.076 | 1.140 | 1.075 | 1.034 | 0.090 | 1.1 | | |
| Er | 2.530 | 2.570 | 2.680 | 2.490 | 2.540 | 2.450 | 2.650 | 2.660 | 2.730 | 2.730 | 2.520 | 2.445 | 0.229 | 2.5 | | |
| Tm | 0.306 | 0.331 | 0.360 | 0.297 | 0.328 | 0.338 | 0.313 | 0.332 | 0.310 | 0.347 | 0.306 | 0.300 | 0.029 | 0.3 | | |
| Yb | 1.870 | 2.090 | 1.940 | 1.790 | 2.310 | 1.930 | 2.020 | 2.020 | 2.050 | 2.060 | 1.840 | 1.866 | 0.186 | 1.8 | | |
| Lu | 0.255 | 0.268 | 0.283 | 0.228 | 0.282 | 0.244 | 0.268 | 0.282 | 0.278 | 0.298 | 0.241 | 0.247 | 0.027 | 0.3 | | |

III. Caractérisation des variations chimiques observées au sein des minéraux des troctolites riches en olivine

L'analyse de la texture des troctolites riches en olivine indique que les plagioclases et les clinopyroxènes ont cristallisé à partir d'un magma qui a imprégné une matrice d'olivines. L'olivine, emballée au sein des larges plages de clinopyroxène ou de plagioclase, présente une texture corrodée indiquant une dissolution de ce cristal. L'étude géochimique in-situ des troctolites riches en olivine indique un déséquilibre entre les olivines et les phases d'imprégnation (clinopyroxènes et les plagioclases).

Des profils géochimiques dans les clinopyroxènes, les plagioclases et les olivines de ces roches ont été réalisés afin de mieux comprendre les processus de résorption, de croissance et de rééquilibrage qui ont pu affecter ces différents minéraux. Cette étude des variations chimiques au sein des minéraux des troctolites riches en olivine est préliminaire, il ne sera donc noté dans cette partie que les premières interprétations que nous pouvons déduire des résultats obtenus. La poursuite de ces travaux est envisagée ultérieurement afin d'aborder les problèmes de diffusion au sein des minéraux et de rééquilibrage des roches au cours de la percolation d'un liquide. Les résultats de ces différentes analyses sont récapitulés en annexe B, tableaux B2.

L'imprégnation et la dissolution d'un minéral par un liquide impliquent des réactions chimiques à l'interface cristal/liquide gouvernées par la diffusion. La diffusion est un processus de migration de matière (atomes, ions, molécules) au sein d'un système en réponse à un gradient chimique. Dans une matrice cristalline, les réactions chimiques et les transferts de masse sont possibles seulement parce que ces solides contiennent des défauts ponctuels au sein de leur structure qui permettent la mobilité des espèces chimiques (lacune cationique par exemple pour la diffusion des Terres Rares). Pendant longtemps les processus de diffusion dans les minéraux ont été considérés comme des processus isotropes. Depuis une vingtaine d'années, les résultats expérimentaux ont montré que la diffusion des cations dans les minéraux silicatés dépend en partie de la direction cristallographique (voir revue de Brady, 1995). Par exemple, la diffusion dans l'olivine du Fe, Mg, Mn et Ni est beaucoup plus rapide parallèlement à l'axe [001] qu'à l'axe [100] ou [010] (e.g., Chakraborty, 1997 ; Petry et al., 2004 ; Costa & Dungan, 2005 ; Dohmen et al., 2007). Les profils en éléments majeurs et en trace ont donc été effectués le long des axes cristallographiques pour les olivines. Les

plagioclases et les clinopyroxènes se présentant sous forme de grands cristaux poeciloblastiques incluant de nombreuses olivines, les profils n'ont pas été réalisés selon leurs axes cristallographiques mais de façon transversale entre les grains d'olivines.

1. Méthode d'analyse

Profils dans l'olivine

Les orientations des axes cristallographiques de l'olivine ont été déterminées en utilisant un microscope électronique à balayage (MEB) couplé à un système d'imagerie EBSD (technique de diffraction d'électrons rétrodiffusés/Electron Back Scattered Diffraction) à l'université Montpellier 2. Dans chaque échantillon analysé, seules les olivines ayant leurs axes cristallographiques dans le plan de la lame mince ont été sélectionnées pour effectuer les profils. Ainsi, dans chaque cristal d'olivine choisi, un ou deux profils sont réalisés parallèlement à un ou deux axes cristallographiques (voir annexe B).

Les profils des teneurs en SiO₂, MgO, FeO, MnO, Cr₂O₃ et NiO dans l'olivine ont été réalisés à la microsonde électronique, à l'université Montpellier 2, dans quatre troctolites riches en olivine (234R1_22-26, 237R2_40-43, 248R2_18-21, 248R3_131-134). Les profils en éléments en trace ont été réalisés au HR-ICPMS couplé à un système d'ablation laser au laboratoire Géosciences Montpellier, dans deux troctolites riches en olivine (248R2_18-21 et 248R3_131-134). La présence de serpentine, d'inclusions fluides et de microfractures dans les grains d'olivines, ainsi que la taille importante du faisceau laser (120μ) ne m'a pas permis d'effectuer des profils rectilignes composés de nombreux points d'analyses.

Profils dans les phases d'imprégnation

Les profils dans les clinopyroxènes et les plagioclases ont été effectués du cœur vers la bordure de ces minéraux. Les profils en éléments en trace ont été réalisés dans cinq échantillons de troctolites riches en olivine (62R1_4-7 ; 136R2_37-40 ; 234R3_14-18 ; 248R2_18-21 ; 248R3_131-134).

2. Résultats

Profils dans les olivines

Pour illustrer les résultats obtenus, je prends pour exemple un cristal d'olivine peu serpentinisé et de grande taille provenant d'une troctolite riche en olivine qui a été pénétrée par un filonet gabbroïque (Figure 2.14a, échantillon 248R2_18-21 ; voir Figure 2.16). Ce filonet a envahi la troctolite riche en olivine et probablement assimilé en partie les olivines. Le cristal d'olivine analysé est polygonal, avec des bordures curvilignes indiquant une certaine corrosion par le magma ayant cristallisé le plagioclase adjacent.

Les profils en éléments majeurs réalisés dans les olivines ne montrent pas de variations chimiques le long de l'axe [001] (Figure 2.14b).

Les profils en éléments en trace n'étant pas rectilignes, les différents points d'analyses ont été projetés sur l'axe Y parallèle à l'axe [001]. La figure 2.14c montre une diminution des teneurs en P et Ca et une augmentation de la teneur en Ti, Cr et Yb depuis le cœur vers la bordure de l'olivine. La variation des teneurs en Ti (de 125 ppm au cœur à 154 ppm à la bordure) et Cr (70 ppm à 98 ppm) sont les plus marquées. Les Terres Rares varient peu du cœur vers la bordure du minéral contrairement au Ti et au Cr.

Les concentrations en Ti et en Ni de l'olivine ne sont pas en équilibre avec des liquides de type MORB (Ti~ 9700 ppm ; Ni~149 ppm ; Hofmann, 1988) mais avec des magmas plus pauvres en Ti (~ 4000 ppm) et plus riche en Ni (Ni~ 190 ppm).

Les liquides en équilibre avec les olivines, pour les Terres Rares, ont été calculés à partir des coefficients de partage utilisés dans la publication acceptée à Chemical Geology. La pertinence de ces coefficients de partage sera discutée dans la partie discussion. La concentration en Terres Rares Lourdes des points se situant à 0.5 mm de la bordure de l'olivine est proche de l'équilibre avec un liquide de type MORB (Yb= 3,77 ppm et pour un MORB Yb= 3,9 ppm d'après Hofmann, 1988). Par contre, les concentrations en Terres Rares Moyennes ne sont pas en équilibre avec un MORB mais avec un liquide très appauvri en ces éléments (Dy= 2,317 ppm et pour un MORB Dy= 6,304 ppm d'après Hofmann, 1988).

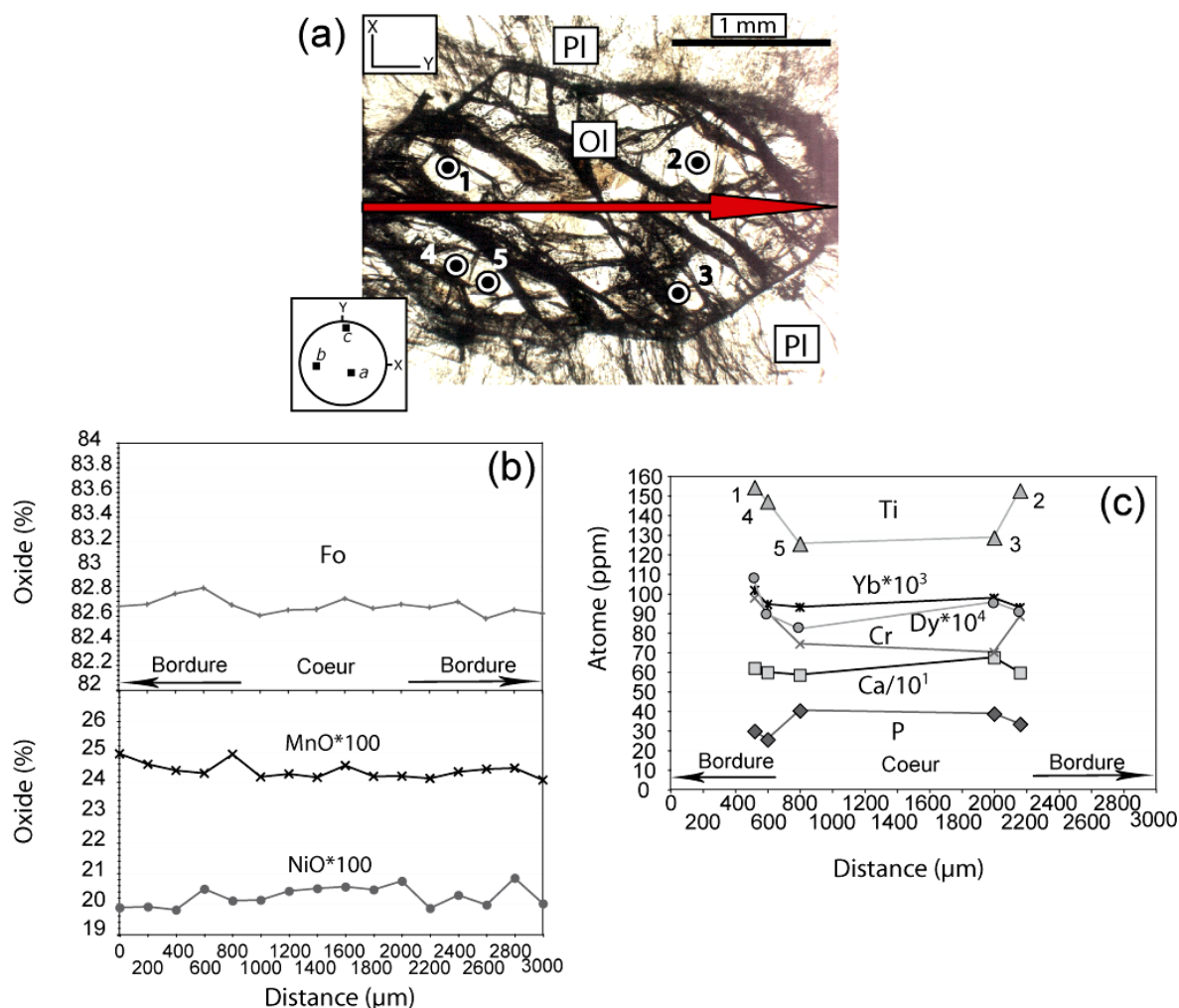


Figure 2.14 : Exemple d'un profil réalisé parallèlement à l'axe *c* d'un cristal d'olivine d'une troctolite riche en olivine (248R2_18-21). (a) Photo au microscope polarisant en lumière naturelle de l'olivine analysée. La flèche rouge indique la position du profil réalisé à la microsonde, dont les données sont exposées en (b). Les points d'analyses en éléments en trace sont aussi reportés. (b) Variation de la teneur en Forstérite (Fo), SiO₂, MnO et NiO le long du profil (en %). (c) Variation de la teneur en Ca, Ti, Cr, P, Yb et Dy (en ppm) le long du profil. Les numéros correspondent aux points d'analyse.

Profils dans les phases d'imprégnation

J'ai sélectionné à titre d'exemple deux clinopyroxènes : l'un caractéristique des troctolites riches en olivine du puits IODP U1309D avec une texture poecilitique entourant des olivines subautomorphes à rondes (234R3_14-18 ; Figure 2.15), l'autre appartenant à un filonet gabbroïque qui pénètre une troctolite riche en olivine et semble l'envahir et la démembrer (248R2_18-21 ; Figure 2.16).

J'observe systématiquement un enrichissement en éléments incompatibles et un appauvrissement en éléments compatibles depuis le cœur vers la bordure des clinopyroxènes

(Figures 2.15 et 2.16). Les clinopyroxènes étant de grands cristaux poecilitiques, la bordure est ici considérée comme étant la limite (moins de 1mm de distance) entre le clinopyroxène et un autre minéral (plagioclase ou olivine) qu'ils soient incorporés dans le clinopyroxène ou pas.

L'enrichissement en éléments incompatibles est observé à 1 mm du bord du clinopyroxène. Il s'accompagne de fortes anomalies négatives en Eu, Sr, et Ba. Comme nous avons pu le voir dans la partie 2 de ce chapitre, ces anomalies rendent compte de la cristallisation concomitante du plagioclase et du clinopyroxène.

Si nous regardons en détail la composition en éléments en trace de la bordure des clinopyroxènes, il ne semble pas avoir de variation dans la composition chimique selon que ce soit le plagioclase ou l'olivine au contact (Figure 2.16). Toutefois, cette observation mérite d'être documentée plus finement.

Pour les plagioclases, seuls deux de ces minéraux provenant de deux échantillons différents (62R1_4-7 et 248R2_18-21) montrent des variations cœur/bordure en éléments en trace qui sont opposées. Le premier échantillon provient de la zone d'échantillonnage numéro 1 dans le haut du puits, l'autre de la zone 4 à la base du puits. Les plagioclases dans la zone 1 sont souvent très altérés et montrent des textures plus interstitielles. Le plagioclase du deuxième échantillon appartient à un filonet gabbroïque qui pénètre une troctolite riche en olivine contrairement au plagioclase dans le premier échantillon ayant une texture caractéristique des troctolites riche en olivine du puits IODP U1309D.

Dans le premier échantillon (62R1_4-7), j'observe un appauvrissement en Terres Rares du cœur vers la bordure du plagioclase (Figure 2.17). Alors que dans l'autre échantillon (248R2_18-21), j'observe au contraire, un enrichissement en Terres Rares légères du cœur vers la bordure (Figure 2.18), comme décrit dans les plagioclases des gabbros océaniques (e.g., Coogan et al., 2000a). Ni la taille, ni la texture, ni la localisation des échantillons ne semblent expliquer ces différences de variations en éléments en trace.

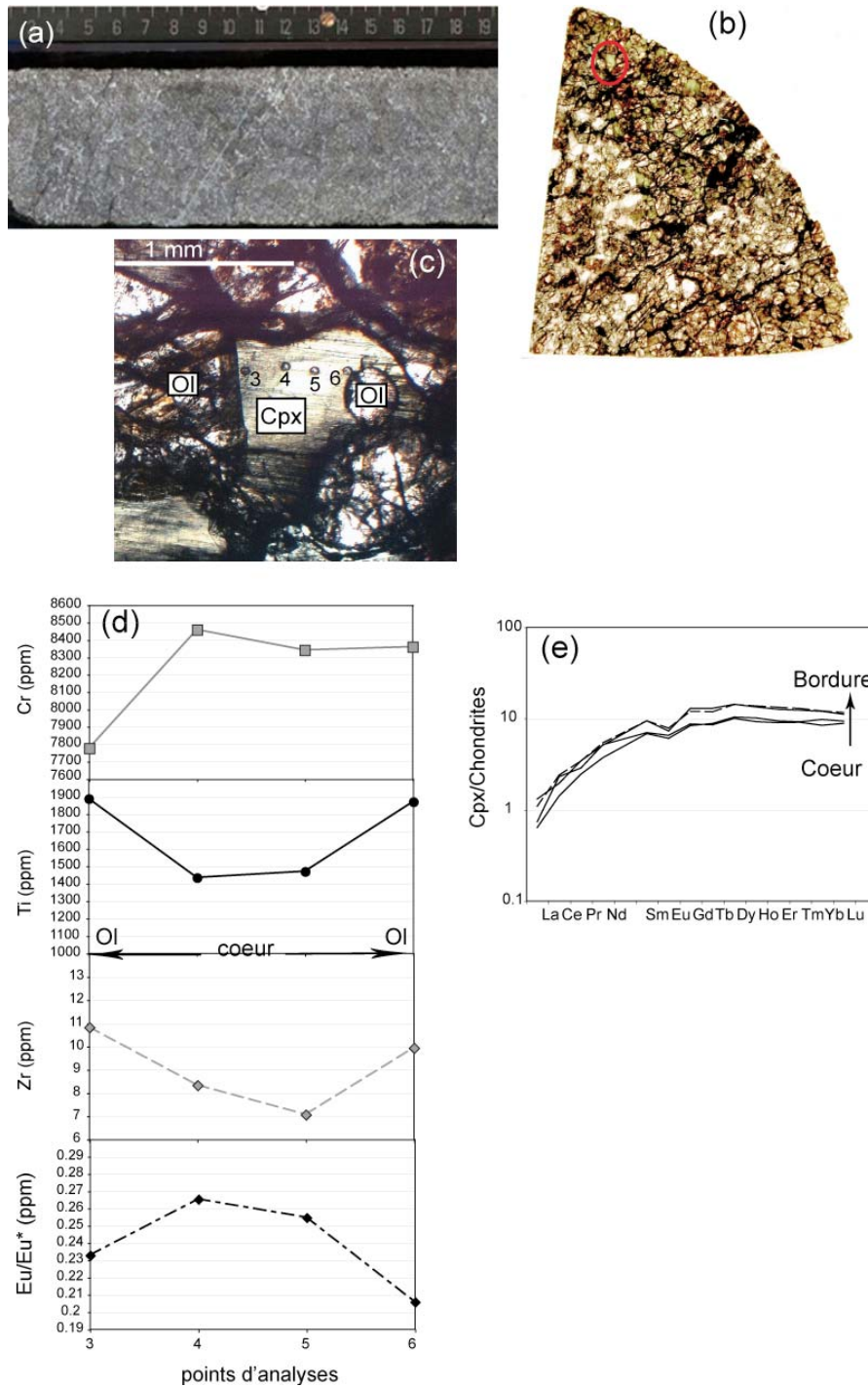


Figure 2.15 : (a) Photo d'un morceau de la carotte 234R3, montrant la texture pénétrative des plagioclases (en blanc) imprégnant la troctolite riche en olivine. (b) Photo de la lame mince de l'échantillon 234R3_14-18 montrant la texture poecilitique de cette troctolite riche en olivine. Le cercle rouge indique la zone où a été effectué le profil. (c) Photo au microscope polarisant en lumière naturelle montrant le profil effectué dans un clinopyroxène de l'échantillon 234R3_14-18 (les points d'analyses sont reportés pour indication). (d) variation de la concentration en Ti, Cr et Zr et du rapport Eu/Eu* le long du profil (en ppm). (e) diagramme de compositions en Terres Rares normalisées aux Chondrites (Sun et Mc Donough, 1989) des différents points d'analyses le long du profil.

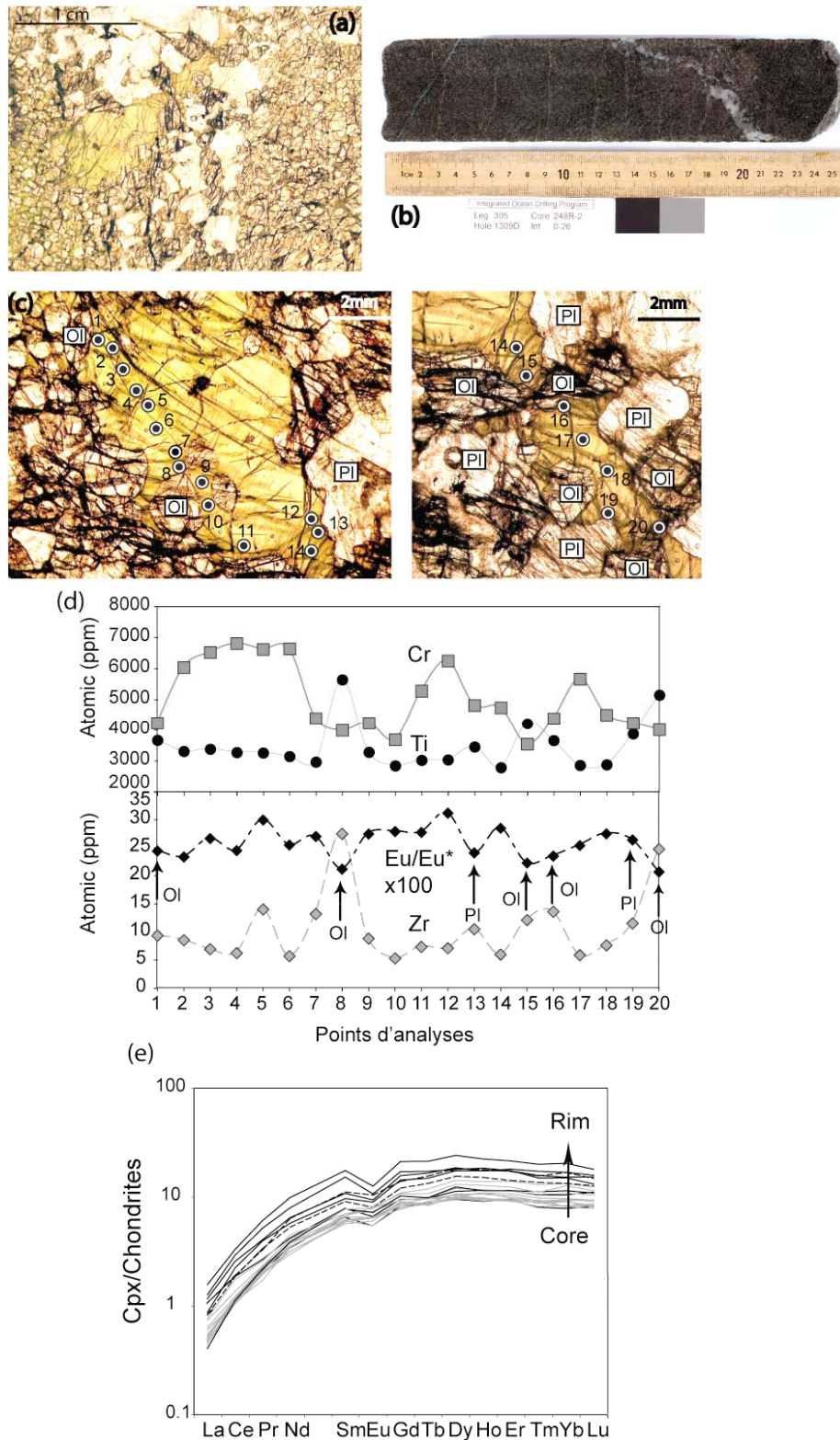


Figure 2.16 : (a) Photo d'un morceau de la carotte 248R2, montrant un filonet de gabbro recoupant la troctolite riche en olivine. (b) Photo de la lame mince de l'échantillon 248R2_18-21 montrant un seul grand cristal poecilitique de clinopyroxène (du filonet de gabbro) englobant des olivines arrondies, dans lequel a été réalisé le profil. (c) Photo au microscope polarisant en lumière naturelle montrant le profil effectué dans un clinopyroxène de l'échantillon 248R2_18-21 (les points d'analyses sont reportés pour indication). (d) variation de la concentration en Ti, Cr et Zr et du rapport Eu/Eu^*

le long du profil (en ppm). (e) diagramme de compositions en Terres Rares normalisées aux Chondrites (Sun et Mc Donough, 1989) des différents points d'analyses le long du profil (gris : cœur, pointillé : intermédiaire, noir : bordure).

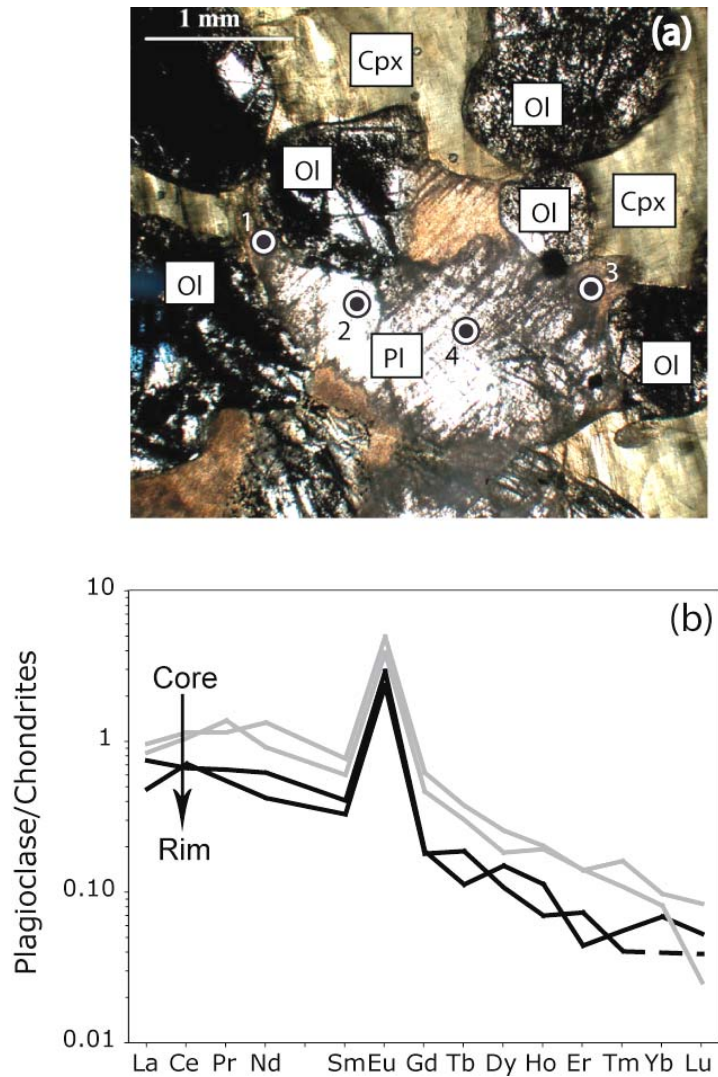


Figure 2.17: (a) Photo au microscope polarisant en lumière naturelle montrant le profil effectué dans un plagioclase de l'échantillon 62R1_4-7 (les points d'analyses sont reportés pour indication) ;(b) Diagramme de compositions en Terres Rares normalisées aux Chondrites (Sun et Mc Donough, 1989) des différents points d'analyses le long du profil effectué dans le plagioclase de l'échantillon 62R1_4-7.

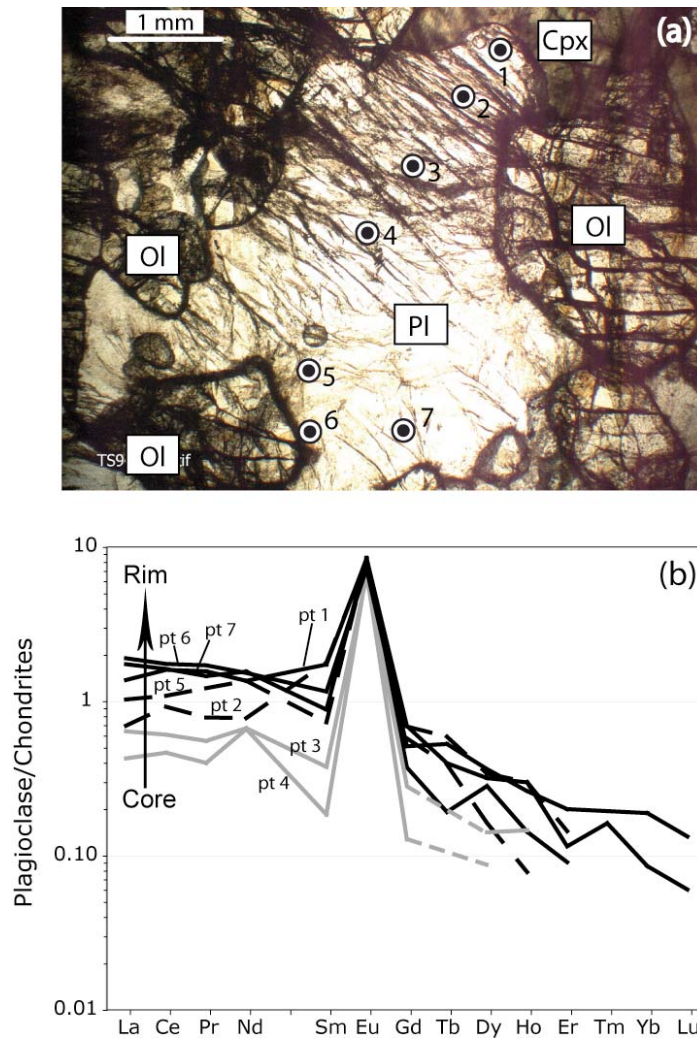


Figure 2.18 : (a) Photo au microscope polarisant en lumière naturelle montrant le profil effectué dans un plagioclase de l'échantillon 248R2_18-21 (les points d'analyses sont reportés pour indication) ;(b) Diagramme de compositions en Terres Rares normalisées aux Chondrites (Sun et Mc Donough, 1989) des différents points d'analyses le long du profil effectué dans le plagioclase de l'échantillon 248R2_18-21.

3. Discussion

Variations chimiques dans l'olivine

Les données en éléments en trace in-situ multi-élémentaires sur les olivines traitées dans ce travail sont les premières sur les olivines de gabbros océaniques. Ces olivines ne présentent pas de variations en éléments majeurs le long de l'axe cristallographique [001]. Ces olivines sont en équilibre en éléments majeurs avec les clinopyroxènes et les plagioclases. Par

contre, on observe des variations de compositions en éléments en trace au sein du cristal d'olivine.

La zonation chimique peut être soit liée à des changements de composition au cours de la cristallisation ou post-cristallisation comme des échanges diffusifs entre l'olivine et le liquide percolant. Dans les troctolites riches en olivines, les olivines, englobées par les cristaux poecilites de clinopyroxènes et de plagioclases, montrent une texture résorbée suggérant une dissolution de ces minéraux. La rééquilibration dépend de la vitesse de diffusion dans le minéral et de la vitesse de dissolution. Si la dissolution est plus rapide que l'échange diffusif dans le solide, le cristal dissous conservera sa composition antérieure qui n'a pas été affectée par la diffusion. Si la dissolution est moins rapide que la diffusion dans le solide, le cristal dissous aura une composition en équilibre avec le liquide et enregistre les variations de composition de ce dernier (Liang, 2000).

La composition en éléments en trace des olivines n'est pas en équilibre avec celle des clinopyroxènes et les plagioclases et donc avec un liquide de type MORB. Le déséquilibre entre les olivines et les phases d'imprégnations en éléments en trace est-il lié à la valeur des coefficients de partage olivine /liquide ? Ou bien est-ce un effet de la diffusion ?

Pertinence des coefficients de partage

Les coefficients de partage olivine/liquide silicaté pour les Terres Rares sont peu nombreux dans la littérature et montrent, en plus, une grande variabilité (Figure 2.19). Plusieurs paramètres contrôlent la variation des coefficients de partage entre l'olivine et un liquide : la température, la pression, la fugacité en oxygène, la composition de l'olivine (F_o) et la composition du liquide. De nombreuses études montrent que la composition du liquide a une influence considérable sur les coefficients de partage olivine/liquide (e. g., Watson, 1977; Hart & Davis, 1978; Mysen & Virgo, 1980; Libourel, 1999; Kushiro & Mysen, 2002; Toplis, 2005; Schmidt et al., 2006 ; Mysen, 2007). La valeur de ces derniers augmente avec la diminution des teneurs en MgO ou avec l'augmentation en SiO₂ du liquide (e.g., Bédard, 2005). La température est aussi un paramètre très important à prendre en compte puisque la valeur des coefficients de partage liquide/olivine augmente avec la diminution de la température (e.g., Bédard, 2005 ; Witt-Eickschen & O'Neill, 2005 ; Lee et al., 2007). De même, la composition du minéral joue un rôle important sur la distribution des éléments majeurs ou en trace entre l'olivine et un liquide silicaté (e.g. Blundy and Wood, 1991, 2003; Gaetani and Grove, 1995). Takahashi & Kushiro (1983) et Ulmer (1989) ont montré que les coefficients de partage olivine/liquide dans les systèmes péridotitique et basaltique dépendent

de la pression seulement au dessus de 4 GPa. La corrélation avec la fugacité en oxygène des coefficients de partage olivine/liquide est quant à elle assez faible (e.g., Bédard, 2005).

Différentes méthodes sont utilisées pour calculer les coefficients de partage olivine/liquide, dans différents laboratoires avec des outils d'analyse dont la précision peut varier. Chacun de ces éléments peut influencer sur la variation des coefficients de partage. Par exemple, l'avancée des techniques d'analyses in-situ (ICP-MS couplé à l'ablation laser) permet de mesurer les concentrations des minéraux en éléments en trace avec une précision de plus en plus élevée, qui peut expliquer en partie la différence entre les données actuelles et les plus anciennes.

La méthode dite « naturelle » analyse des paires de phénocristaux-verre basaltique. Les coefficients de partage mesurés par cette méthode montrent tous une sur-estimation de leur valeur en Terres Rares Légères (création d'un plateau) provoquée généralement par l'incorporation d'inclusion fluide microscopique, riche en Terres Rares Légères, lors de l'analyse de la composition de l'olivine (Figure 2.19 ; Kennedy et al., 1993 ; Beattie, 1994). En effet, la concentration en Terres Rares Légères de l'olivine est très sensible aux contaminations extérieures puisque très faibles (proche de la limite de détection). De plus, la température et la composition du liquide sont souvent difficiles à estimer pour les méthodes naturelles (e.g., altération des verres basaltiques). Lors des études expérimentales des effets cinétiques peuvent venir perturber les expériences (e.g., Bédard, 2005). De plus, dans la plupart de ces expériences la composition du liquide, la température et la pression varient simultanément. L'effet individuel de chacun de ces paramètres ne peut donc pas être isolé (Kushiro & Mysen, 2002).

Au vu des différents paramètres contrôlant les coefficients de partage, j'ai choisi de prendre pour mes calculs de liquide à l'équilibre avec les olivines, les coefficients de partage entre une olivine et un liquide basaltique, à 1300°C, de Lee et al. (2007). D'une part, ces auteurs combinent la mesure des coefficients de partage subsolidus minéral/minéral dans des xénolithes et la théorie physique pour développer des coefficients de partage olivine/liquide en accord avec ceux, mieux compris, du clinopyroxène. D'autre part, la concentration des olivines en éléments en trace est analysée par ICP-MS couplé à de l'ablation laser qui est une technique d'acquisition très précise. De plus, les calculs sont toujours corrigés de la température. Le calcul de la température de cristallisation du plagioclase dans les troctolites riches en olivine effectué dans la deuxième partie de ce chapitre, indique une température d'environ 1230°C d'où le choix de la température 1300°C. Enfin, les coefficients de partage des Terres Rares Légères sont déterminés à partir de l'extrapolation du modèle de contrainte

de réseau (e.g. Blundy & Wood, 2003) et non pas par une méthode naturelle ou expérimentale, éliminant ainsi la contamination par des inclusions fluides.

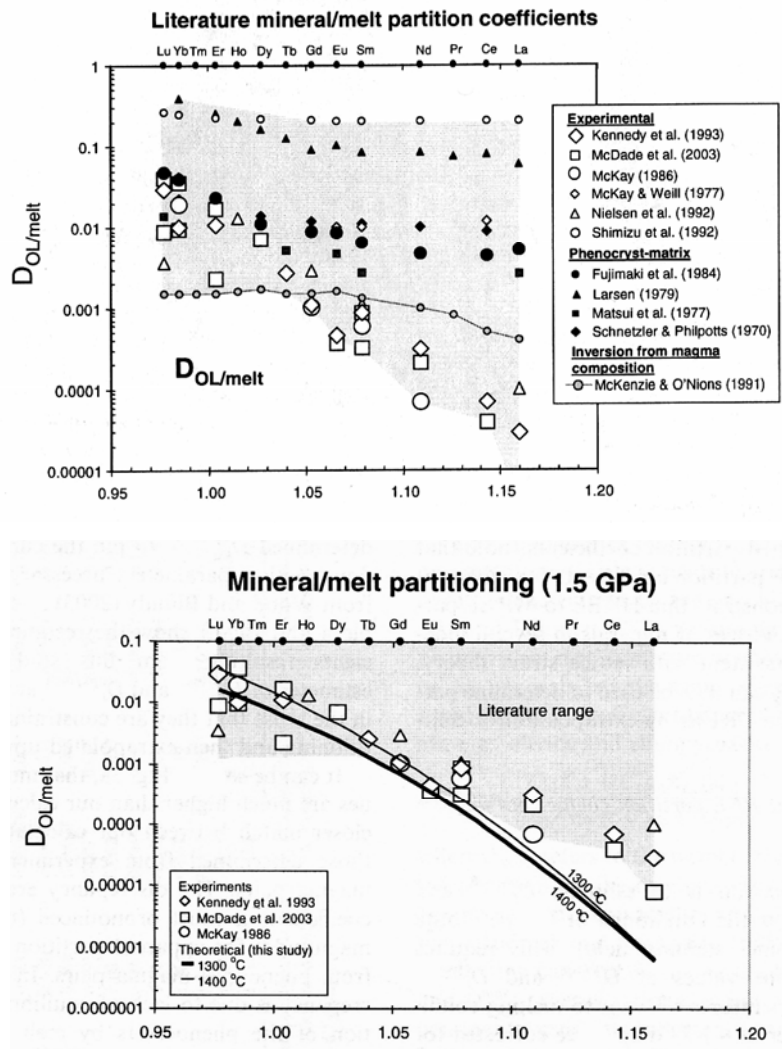


Figure 2.19: Compilation des coefficients de partage olivine/liquide silicaté de la littérature, tracés en fonction de la taille de rayon cationique (Lee et al., 2007). Les coefficients de partage sont classés selon le type de méthode utilisée pour les mesurer : expérimentale, sur des assemblages magma-phénocristaux, et à partir de la composition des magmas (méthode d'inversion). Le deuxième diagramme compare les coefficients de partages de Lee et al. (2007) que j'ai utilisés dans mon étude avec ceux de la littérature.

Diffusion dans l'olivine

Les études réalisées sur la diffusion ionique dans l'olivine (Houlier et al., 1988, 1990 ; Béjina & Jaoul, 1997 ; Dohmen et al., 2002) montrent qu'à 1400°C, la silice est l'espèce la plus lente à diffuser (10^{-20} m²/s) suivie par l'oxygène (10^{-18} m²/s) puis par les cations divalents

Mg-Fe (10^{-15} m²/s). La diffusion des Terres Rares dans l'olivine a toujours été considérée, plus ou moins implicitement, comme lente par rapport à la diffusion des cations divalents comme le Fer et le Magnésium (e.g., Qin et al., 1992 ; Cottrell et al., 2002). En effet, les Terres Rares possèdent de grands rayons ioniques, rendant difficile leur diffusion à travers le réseau cristallin d'un minéral silicaté.

La variation des valeurs des coefficients de diffusion observée dans la littérature peut être liée à différents paramètres comme la température, la pression, la fugacité en oxygène, la composition du minéral ou son orientation cristallographique qui contrôle la diffusion des espèces chimiques au sein d'un minéral (e.g., Chakraborty et al., 1994 ; Chakraborty, 1997 ; Meissner et al., 1998 ; Petry et al., 2004 ; Coogan et al., 2005, Dohmen et al., 2007). Par exemple, les coefficients de diffusion du Mg ou du Fe diminuent avec l'augmentation de la pression et la diminution de la fugacité en oxygène. La diffusion anisotrope dans l'olivine du Fe-Mg ne semble pas être liée à la température entre 800 et 1250°C (Dohmen et al., 2007).

Pourtant, Spandler et al. (2007) suggèrent que les Terres Rares diffusent aussi rapidement que le Fe-Mg dans l'olivine (Tableau 2.3). Nous pouvons estimer approximativement le temps de rééquilibration de l'olivine avec un liquide basaltique en assimilant l'olivine à une sphère vide de 1.5 mm de rayon, avec une composition du liquide constante à la bordure ; par la relation suivante développée par Vasseur et al. (1991 ; D'après Crank, 1979 ; page 37) :

$$t_{crit} = x^2 / \pi^2 D$$

où x correspond au rayon de la sphère (mètre), D est le coefficient de diffusion (m².s⁻¹) et t est le temps (seconde). Il faut une vingtaine d'années pour que ce cristal d'olivine s'équilibre complètement avec le liquide en Terres rares. Ces résultats ne correspondent pas à mes données.

Il existe une différence importante entre l'échelle de temps disponible en laboratoire pour étudier la diffusion et l'échelle de temps relevant des processus naturels de transport. Du reste, la détermination en laboratoire du coefficient de diffusion est souvent réalisée à des températures plus élevées (et à des échelles de temps plus courtes) que celles dans la nature.

Cherniak (2007) montre que la diffusion des Terres Rares dans l'olivine est trois fois plus lente que la diffusion déterminée par Spandler et al. (2007). La poursuite de travaux sur les phénomènes de diffusion est donc essentielle pour contraindre les temps de rééquilibrage des minéraux lors des réactions magma/roche.

| | Log $D_{Mg/Fe}$ (m^2/s) | Log D_{Ni} (m^2/s) | Log D_{Ca} (m^2/s) | Log D_{REE} (m^2/s) |
|---------------|---|----------------------------------|--|--|
| Olivine | -17 ⁽¹⁾ (1100°C) -16 ⁽²⁾ (1200°C) -15 ⁽²⁾ (1300°C) -16 à -18 ⁽⁹⁾ (980-1300°C) | -15 ⁽²⁾ (1200-1300°C) | -15 ⁽²⁾ (1300°C) -17 ⁽³⁾ (1300°C) | -15 ⁽⁴⁾ (1300°C) |
| Clinopyroxène | -22 à -20 ⁽⁸⁾ (950-1100°C) | — | -16 à -17 ⁽⁵⁾ (1100°C) -14 à -15 ⁽⁵⁾ (1300°C) | -20 à -18 ⁽⁶⁾ (1300°C) |
| Plagioclase | — | — | — | -19 à -20 ⁽⁷⁾ (1100°C) -18 à -17 ⁽⁷⁾ (1300°C) |

Tableau 2.3 : Coefficients de diffusion (D) en m^2/s (ordre de grandeur) du Fe/Mg, Ni, Ca et des Terres Rares (REE) pour l'olivine, le clinopyroxène et le plagioclase à des températures comprises entre 1100 et 1300°C. Les coefficients de diffusion pour l'olivine ont été choisis en fonction de l'axe cristallographique [001]. ⁽¹⁾ Dohmen et al. (2007); $Fo= 88$, parallèle à [001]. ⁽²⁾ Petry et al. (2004) ; $Fo= 90$, parallèle à [001]. ⁽³⁾Coogan et al. (2005) ; $Fo= 92$, parallèle à [001]. ⁽⁴⁾Spandler et al. (2007) ; $Mg\#= 90$, moyenne des différents axes cristallographiques. ⁽⁵⁾Dimanov & Jaoul (1998) ; diopside. ⁽⁶⁾Van Orman et al. (2001) ; diopside. ⁽⁷⁾Cherniack (2003); Labradorite (An_{67}). ⁽⁸⁾Azough & Freer (2000) ; diffusion du Fe, diopside (cristal naturel).⁽⁹⁾Chakraborty (1997) ; $Fo= 86$ à 95, parallèle à [001].

Variations chimiques dans les phases d'imprégnation

La teneur des éléments en trace dans les clinopyroxènes varie depuis le cœur vers la bordure de ces minéraux. Ces variations peuvent être dues à des changements de composition du liquide infiltré au cours de la cristallisation ou bien à la cristallisation d'un liquide exotique. La préservation de cette zonation est contrôlée par la diffusion des éléments chimiques au sein du cristal (Tableau 2.3 ; Van Orman et al., 2001).

Nous pouvons estimer approximativement le temps de rééquilibrage du clinopyroxène avec un liquide basaltique en assimilant la forme du minéral à une solide semi-fini et avec un liquide de composition constante à la bordure, par la relation suivante:

$$t_{crit} = x^2 / D$$

où x correspond à une bordure de 1 mm, D est le coefficient de diffusion ($m^2.s^{-1}$) et t est le temps (seconde). Il faut 3 millions d'années pour que la bordure du clinopyroxène s'équilibre en Terres Rares avec le liquide. Ce temps de rééquilibrage est bien plus long que l'âge du système magmatique (1,5-2 Ma), ce qui implique que cette zonation chimique a eu lieu au cours de la cristallisation du clinopyroxène.

La diffusion du Fe-Mg dans le clinopyroxène apparaît être bien plus lente que la diffusion des Terres Rares (Tableau 2.3). Ce résultat est assez surprenant puisque ces cations divalents ont des rayons ioniques plus petits que les Terres Rares impliquant une plus grande mobilité de ces espèces chimiques au sein d'un minéral silicaté. D'ailleurs, le Ca possède des coefficients de diffusions beaucoup plus rapides que les Terres Rares (Tableau 2.3).

Les relations texturales et la composition en éléments en trace de la bordure des clinopyroxènes montrent que ces minéraux ont cristallisé plus ou moins en même temps que les plagioclases dans un système fermé. La majorité des plagioclases ne montrent pas d'enrichissement en Terres Rares à leur bordure. Dès lors, cet enrichissement en éléments en trace à la bordure des clinopyroxènes correspondrait au résultat de la cristallisation du liquide percolant, plus différencié, dans le dernier stade de la cristallisation plutôt qu'à une source d'enrichissement exotique. L'absence de différence de composition de la bordure du clinopyroxène au contact d'une olivine ou d'un plagioclase pourrait indiquer un processus couplé de précipitation du plagioclase et de dissolution de l'olivine.

Pour conclure, ces données préliminaires montrent que :

- (1) Des variations de composition en éléments en trace dans l'olivine sont observées. Ces variations ne sont pas liées au choix des coefficients de partage.
- (2) Des variations de composition en éléments en trace sont observées du cœur vers la bordure des clinopyroxènes. Celles-ci sont le résultat de l'enrichissement en éléments en trace du liquide interstitiel dans le dernier stade de la cristallisation du à la fermeture progressive du système.
- (3) La variation de composition en éléments en trace du cœur vers la bordure des plagioclases n'est pas visible dans la majorité des plagioclases des troctolites riches en olivine.

IV. Microstructure d'une lithosphère océanique fortement imprégnée: étude des troctolites riches en olivine du Massif Atlantis (30°N, dorsale Médio-Atlantique, puits IODP U1309D)

L'étude géochimique *in-situ* des troctolites riches en olivine du puits IODP U1309D révèle que ces roches sont le résultat de l'imprégnation d'une matrice d'olivine par des liquides basaltiques de type MORB. La composition en éléments en trace des olivines indique une possible origine mantellique. La présence de sous-joints dans certaines de ces olivines suggère une déformation plastique de ces minéraux dans des conditions de haute température. L'étude des microstructures, et notamment des orientations préférentielles de réseau des olivines apparaît donc essentielle afin de discuter l'hypothèse d'une origine résiduelle pour ces roches. Les plagioclases et les clinopyroxènes dans les troctolites riches en olivine ont cristallisé, probablement en même temps, dans un système ouvert avec un apport constant, et sûrement important, de liquides de type MORB. Or, les processus pétrologiques impliquant la présence de liquide, comme la fusion partielle ou la percolation de magmas, modifient aussi bien la composition chimique que la microstructure des roches mantelliques (e.g., Lenoir et al., 2001; Vauchez & Garrido, 2001 ; Tommasi et al., 2004). Les questions de l'influence de l'imprégnation magmatique sur l'évolution des microstructures des troctolites riches en olivine, et de l'origine de ces roches sont traitées dans un article en révision pour EPSL qui constitue la quatrième partie de ce chapitre. Ce travail montre que les troctolites riches en olivine du puits IODP U1309D dérivent de péridotites mantelliques désagrégées par un flux important de liquide magmatique. L'interaction avec, et l'imprégnation par de larges volumes de magma ont fortement modifié la composition de la péridotite et sa microstructure :

- 1- La composition des minéraux des troctolites riches en olivine montre que ces roches sont le produit d'intenses interactions avec un liquide basaltique comme décrit pour les roches mantelliques imprégnées.
- 2- Les orientations préférentielles de réseau des olivines sont généralement cohérentes avec une déformation par fluage dislocation, avec l'activation du système de glissement de haute température (010) [100] comme classiquement observé dans les péridotites mantelliques.
- 3- Cependant, les fabriques cristallographiques des olivines sont faibles et montrent une plus forte concentration sur [001]. Ces fabriques de l'olivine, inhabituelles, sont

interprétées comme résultant d'une forte imprégnation magmatique d'une matrice d'olivine préalablement déformée à l'état solide et à haute température. Lorsque le rapport liquide/roche est suffisamment élevé, la matrice solide d'olivines se désagrège, et la fabrique plastique de haute température est perturbée. Cette dernière est progressivement détruite lorsque la déformation évolue, depuis un régime dominé par la phase solide vers un régime dominé par la phase liquide.

Microstructure of highly impregnated oceanic lithosphere: a study of the olivine-rich troctolites from the Atlantis Massif (Mid-Atlantic Ridge 30°N, IODP Hole U1309D)

Marion Drouin^{*}, Benoit Ildefonse, Marguerite Godard

Géosciences Montpellier, CNRS & Université Montpellier 2, F-34095 Montpellier cedex5, France.

Article en révision pour EPSL

Abstract

IODP Hole U1309D (IODP Expeditions 304 and 305) sampled the upper 1415 meters of the core of an oceanic core complex, at the slow-spreading Mid-Atlantic Ridge (30°N). The recovered core is mostly made of gabbroic rocks in which olivine-rich troctolites (ol > ~70%) represent 5.4% of the recovered rocks. These troctolites are the most primitive gabbroic rocks ever drilled at mid-ocean ridges. Olivine-rich troctolites from IODP Hole U1309D display poikilitic textures, with olivine ranging from coarse-grained subhedral crystals, with common well-developed subgrains, to medium-grained rounded crystals with fewer or no substructures, embedded in large, undeformed pyroxene and plagioclase poikiloblasts. Olivine crystallographic preferred orientations are weak, generally consistent with deformation by dislocation creep with activation of the high-temperature (010) [100] slip system, but often showing a relatively strong, uncommon [001] concentration. These unusual olivine fabrics are interpreted as resulting from abundant melt impregnation of a previously deformed olivine matrix. At high melt/rock ratio, the solid olivine framework is disrupted, and the high-temperature plastic fabric is disturbed when flow evolves from a solid-dominated regime to a liquid-dominated regime. Mineral compositions of olivine-rich troctolites show that they are the product of intense melt-rock interactions with a basaltic melt as described for impregnated mantle rocks. We conclude that olivine-rich troctolites derive from mantle peridotites disaggregated by large melt influx. Interaction with, and impregnation by large volumes of melt have strongly modified the mantle composition and its microstructure. Incorporation, at the base of the lithosphere, of small slivers of mantle/crust transition rocks to gabbroic sections may be a common mechanism of lower crustal accretion at ultra-slow and slow spreading ridges.

^{*} email: marion.drouin@gm.univ-montp2.fr, phone: +33-4671443941, fax: +33-467143603

Keywords: melt impregnation; mantle; olivine; crystallographic preferred orientations; EBSD, troctolite; gabbro; Atlantis Massif; Mid Atlantic Ridge; Integrated Ocean Drilling Program.

1 Introduction

Melt impregnation is observed at slow (e.g., Dick, 1989; Cannat et al., 1992; Girardeau and Franchetau, 1993; Hekinian et al., 1993; Cannat et al., 1997; Seyler and Bonatti, 1997; Tartarotti et al., 2002; Kelemen et al., 2004), and fast spreading ridges (e.g., Cannat et al., 1990; Constantin et al., 1995; Allan and Dick, 1996; Arai and Matsukage, 1996; Dick and Natland, 1996; Niu and Hekinian, 1997) as well as in ophiolites, which represent the relics of ancient oceanic lithosphere (e.g., Nicolas and Prinzhofer, 1983; Benn et al., 1988; Boudier, 1991; Boudier and Nicolas, 1995; Rampone et al., 1997, 2008; Koga et al., 2001; Dijkstra et al., 2003; Borghini et al., 2007; Piccardo et al., 2007). In these environments, melt impregnation corresponds to the crystallization of significant amount of plagioclase and/or clinopyroxene in peridotite and occurs in the shallowest part of the mantle, mostly at the mantle/crust transition. This process is associated with pervasive melt/rock interactions involving high melt volumes; it produces major changes not only in the composition but also in the physical properties and microstructures of mantle rocks, as observed at the asthenosphere/lithosphere transition above mantle plumes (Tommasi et al., 2004) and in peridotite massifs (e.g., Lenoir et al., 2001; Vauchez and Garrido, 2001).

Olivine-rich troctolites drilled during Expedition IODP 304-305 in the Atlantis Massif (Mid-Atlantic Ridge, 30°N) were sampled within a 1415 m thick gabbroic section. The geochemical characteristics of these rocks indicate that they have formed in a domain of large magmatic transfer and accumulation, similar to what is described in the mantle-crust transition zone in ophiolites and at fast spreading ridges (Drouin et al., accepted). In order to investigate the effect of melt/rock reaction and crystallization on mineral Crystallographic Preferred Orientations (CPO), and discuss the origin of olivine-rich troctolites, we performed coupled petrological and microstructural analyses of olivine-rich troctolites, and of neighboring troctolites and olivine gabbros collected from 4 olivine-rich intervals along IODP Hole U1309D.

2 The Atlantis Massif

The Atlantis Massif, a ~2 My old Oceanic Core Complex (OCC), is located at 30°N at the inside corner of the eastern intersection of the Mid-Atlantic Ridge with the Atlantis Transform Fault (Fig. 1a). This OCC extends approximately 20 km parallel to the ridge and 15 km across (Fig. 1a), and is shown to result from low-angle detachment faulting (e.g., Cann et al., 1997; Blackman et al., 2002; Karson et al., 2006; Ildefonse et al., 2007). The oceanic crust in this area is presumably highly heterogeneous with discrete gabbroic bodies intruded into serpentinized peridotites (e.g., Cannat, 1993, 1996; Ildefonse et al., 2007).

IODP Hole U1309D, the main hole drilled during IODP Expeditions 304-305, is located at the top of the central dome of Atlantis Massif (Fig. 1a) where the seafloor coincides with a corrugated detachment fault surface (Blackman et al., 2006). This hole penetrated 1415.5 meters below seafloor (mbsf) in basement, and is composed mainly of gabbroic rocks (Fig. 1b). Gabbro is the most abundant recovered rock (56%) with important variations in grain size and modal composition on a decimeter scale. Thin section observation reveals the occurrence of orthopyroxene (>5%) in many of these gabbros mostly below 600 mbsf. Olivine gabbro (Ol>5%) locally grades to troctolitic gabbro and troctolite, to represent the second most abundant recovered rock type (28%). Oxide gabbro (>2% modal Fe-Ti oxides) represents 7% of the recovered rocks and occurs as disseminated patches, as dikelets crosscutting other lithologies, or less commonly, associated with ductile deformation zones. Olivine-rich troctolite (>70% Ol; see rationale for using this terminology in Blackman et al., 2006) represents 5.4% of the recovered rocks, and are rarely sampled at mid-ocean ridges (Fig. 2). In contrast to olivine gabbro and troctolite, they display a distinctive, cumulate-like texture, with rounded olivine embedded in poikiloblastic clinopyroxene or/and plagioclase, and contain up to 2% chromium spinel. They are observed in 22 discrete intervals in Hole U1309D, ranging from ~40 cm to ~12 m in thickness, with an average recovery of 75%. These olivine-rich rocks are commonly intruded by thin (~1 to 20 cm) gabbroic intrusions, and are intercalated with olivine and troctolitic gabbro intervals in a given olivine-rich zone (Fig. 2), of which four have been sampled for this study (Table 1). Olivine-rich troctolite is the dominant lithology between 1090 and 1236 mbsf. The whole core in Hole U1309D is moderately altered at conditions ranging from granulite to zeolite facies. Overall, the alteration tends to decrease downhole and olivine-rich troctolite intervals between 1090 and 1236 mbsf are locally very fresh (down to < 1% serpentinisation). Magmatic deformation associated with the emplacement of Hole U1309D gabbroic intrusive suite is weak and affects

only 22% of the recovered core. High-temperature (amphibolite to granulite facies) deformation is rare and high-strain ductile shear zones represent less than 3% of the recovered core.

We primarily sampled olivine-rich troctolites and associated troctolites and olivine gabbros collected from 4 olivine-rich intervals in the core (zone 1 from ~301 to 363 mbsf, zone 2 from ~552 to 557 mbsf, zone 3 from ~667 to 672 mbsf, and zone 4 from 1092 to 1196 mbsf; Table 1, Figs. 1b, 2 and 3).

3 Composition of olivine-rich troctolites and neighboring gabbroic rocks

Major and trace element analyses of minerals from studied samples are presented and discussed in a companion paper (Drouin et al., accepted), and summarized below.

Olivine-rich troctolites are made of 64-85% olivine, 2-24 % plagioclase, 1-30 % clinopyroxene, 1% spinel. The occurrence of orthopyroxene oikocrysts has been noted in one sample (248R2_22-24; Fig. 3b). Spinel occurs as small subhedral crystals (0.5mm) with polygonal shape, included in olivine, clinopyroxene or plagioclase. Troctolites are made of 45-64% olivine, 27-40 % plagioclase, 2-15 % clinopyroxene, and 1% spinel, which occur as small subhedral grain (0.5 mm) associated with olivine in some samples. Olivine-gabbro is made of 40-70% plagioclase, 25-60% clinopyroxene and more than 5 % olivine. In contrast to olivine-rich troctolites and troctolites, spinel is absent in these rocks.

Clinopyroxene is high Mg# augite (Mg# 87 in olivine-rich troctolites to 82 in gabbros), and plagioclase has anorthite contents ranging from 77 in olivine-rich troctolites to 68 in gabbros. Olivine has high forsterite contents (82-88 in olivine-rich troctolites, to 78-83 in olivine-gabbros) and is in Mg-Fe equilibrium with clinopyroxene. Olivine in olivine-rich troctolite is also characterized by high Ni contents (1440-2300 ppm), intermediate between those of primitive oceanic gabbros and abyssal peridotites. Clinopyroxene and plagioclase have depleted trace element contents (e.g., Yb <11 and <0.15 x Chondrites, respectively) in equilibrium with MORB melts in both olivine-rich troctolites and neighboring troctolites and gabbros, which suggests that clinopyroxene and plagioclase crystallized simultaneously, after melts having similar trace element compositions, thus indicating an open system with a buffered magma composition (Drouin et al., accepted). In contrast, olivine has highly depleted

incompatible trace elements compositions, in disequilibrium with both plagioclase and clinopyroxene, which may point to a mantle origin.

Spinel is characterized by high Cr and Fe contents ($Cr\# = 100 \times \text{cationic Cr}/(\text{Cr} + \text{Al}) = 46-64$, and $FeO = 27\%$) in both olivine-rich troctolites and troctolites. A strong variation is also observed in Ti contents of spinel with TiO_2 ranging from 0.41 to 2.56 wt. % (Fig.4). Ti content is positively correlated with Cr# in spinel (Fig.4a). This co-variation trend defines a continuous evolution from olivine-rich troctolites to troctolites, similar to that is observed for spinels from ODP Hole 1271B, from reacted dunite to gabbroic rocks (Takazawa et al., 2007) and from Hess Deep ODP Site 895 (Allan and Dick, 1996; Arai and Matsukage, 1996; Dick and Natland, 1996). Furthermore, spinels show large increase in Ti content with little or no change in the forsterite content of coexisting olivine (Fig. 3b), as already described in impregnated dunites associated with abyssal peridotite or in ophiolite (Dick and Bullen, 1984; Allan and Dick, 1996; Arai and Matsukage, 1996; Dick and Natland, 1996; Takazawa et al., 2007). These high Cr, Fe and Ti contents in spinel from olivine-rich troctolite are consistent with extensive melt-rock interaction and interstitial crystallization of percolating melts, as these elements are excluded from plagioclase and olivine (e.g., Dick and Bullen, 1984; Allan et al., 1988; Allan and Dick, 1996; Kamenetsky and Crawford, 1998).

The mineral compositions of olivine-rich troctolites from IODP Hole U1309D suggest that they formed in a zone of large magmatic transfer and accumulation, and are the product of intense melt-rock interactions with a basaltic melt.

4 Microstructures of olivine-rich troctolites and neighboring gabbroic rocks

Olivine, pyroxene and plagioclase CPO of 20 olivine-rich troctolites, 3 troctolites, 1 troctolitic-gabbro and 3 olivine-gabbros were measured by indexation of electron back-scattered diffraction (EBSD) patterns using the SEM-EBSD facility at Geosciences Montpellier. EBSD patterns are generated by interaction of a vertical incident electron beam with a high-quality polished thin section tilted at 70° in a scanning electron microscope JEOL JSM 5600. The diffraction pattern is projected onto a phosphor screen and recorded by a digital CCD camera. This image is then processed and indexed for crystal orientation using the CHANNEL5 software from Oxford Instruments HKL. Crystallographic orientation maps were obtained for each sample, covering the thin section with a sampling step size ranging

from 30 to 80 μm (Fig. 5). Indexation rates in the raw maps range from 60 to 85% (Fig. 5a). Post-acquisition data treatment allowed to increase map quality by (i) automatically (using a filter that detects pixels having a minimum of 5 neighbors with the same orientation) and manually (when appropriate) filling the non-indexed pixels, (ii) identifying the grains, i.e., continuous domains characterized by an internal misorientation $<10^\circ$, and (iii) within each olivine crystal, searching and correcting for systematic indexation errors due to the olivine hexagonal pseudosymmetry, which results in similar diffraction patterns for orientations differing by a 60° rotation around [100]. Pole figures (Fig. 6) are presented using the average Euler angles for each grain (i.e., one measurement per grain) instead of the raw, gridded data to avoid the overrepresentation of larger grains when the grain size distribution is heterogeneous. A few samples, mostly in the upper part of the hole, are strongly serpentinized; olivine grains are then poorly indexed, and identification of single grains is consequently difficult resulting in strong biases in the pole figures. Therefore, these samples were excluded and we present the pole figures for a subset of 18 olivine-rich troctolites, 2 troctolites, and 2 olivine gabbros. Only nine of these samples (89R1_92-94, 90R3_8-10, 117R1_55-57, 227R3_124-126, 234R1_27-29, 247R3_16-18; 248R2_22-24; 248R3_36-38; 256R2_83-85) were oriented in the core reference frame (Fig. 6).

4.1 Olivine-rich troctolites

Olivine-rich troctolites display poikilitic textures with large clinopyroxene and plagioclase poikiloblasts, not deformed, enclosing coarse-grained subhedral crystal to medium-grained rounded olivine crystal (Fig. 3a). No shape-preferred orientation marking a visible foliation or lineation was measured in hand samples. In some olivine-rich troctolites (e.g., sample 60R3_39-42), clinopyroxene also occurs as interstitial grains and form, with plagioclases, pervasive textures (Fig. 3F) similar to impregnation textures in some Oman ophiolite dunites (e.g., Boudier and Nicolas, 1995), or abyssal peridotites (e.g., Takazawa et al., 2007). The fine- to medium-grained, rounded olivine crystals are generally devoid of substructures, and occur as chadacrysts in large clinopyroxene and plagioclase oikocrysts (Fig. 3a, e). Coarse-grained subhedral olivine crystals display smooth edges and common, well-defined and widely-spaced subgrain boundaries (Fig. 3a-c). In several samples, some subhedral olivine crystals are elongated, with the long axis commonly parallel to [001] axes, and with aspect ratios varying from 1:1.5 to 1:5. We also observe chains of olivine grains with curvilinear boundaries, and showing limited misorientation between each other (Fig. 3c). Decoration of thin sections by oxidation at 900°C in air (Kohlstedt et al., 1976) commonly

reveals free dislocations and dislocation walls in subhedral olivines (Fig. 3d), implying plastic deformation by dislocation creep.

Olivine CPOs in olivine-rich troctolites are very weak, with fabric strength (J index; Bunge, 1982; Ben Ismail and Mainprice, 1998) values ranging from 1.6 to 3.8 (Table 1). The CPO patterns, however, are remarkably consistent (Fig. 6), with [100] being generally the more scattered axis, a [010] concentration that possibly correspond to the pole to the foliation, and a relatively strong, uncommon [001] point or girdle cluster. The analysis of Misorientation Angle Distributions (MAD) of correlated (neighbour pairs) gridded data points gives indications on the active slip system(s) during deformation (Fig. 7). In most samples, the MAD of correlated data points shows a peak at low angles (2 to $\sim 15\text{-}20^\circ$), well above the theoretical random distribution, which is consistent with the likely occurrence of subgrains and/or adjacent grains derived from subgrains. The dominant associated rotation axis is close to [001] in most samples as indicated by the inverse pole figures of misorientation axes (Fig. 7; Table 1). They are consistent with the olivine crystal-plastic deformation and CPO being related to dislocation creep with activation of the (010) [100] slip system, the most commonly observed slip system in mantle peridotites (e.g., Tommasi et al., 2000). This is also consistent with observations made on EBSD maps (Fig. 5): we checked manually the latter for the subgrain rotation axes using misorientation profiles across subgrain boundaries when present (red lines in figure 5), which dominantly appear to be, or to be close to (100). [010] is a less common, but also observed rotation axis for low-angle misorientations, possibly indicating activation of the (001)[100] slip system (e.g., Tommasi et al., 2000).

4.2 Troctolites and olivine gabbros

Troctolites have igneous textures, with no foliation observed in our samples. Plagioclase forms large subhedral laths (2 to 4 mm) with aspect ratio ranging from 1:1.5 to 1:4. Clinopyroxene, when present, is interstitial. Olivine occurs as aggregates of subhedral, 1-2 mm large grains, with well-defined subgrain boundaries (Fig. 3g). In most olivines, decoration technique shows free dislocations and dislocation wall implying crystal-plastic deformation by dislocation creep.

Olivines in troctolites have weak CPO (Table 1), and show no consistent pattern, as illustrated by the two examples in Figure 6. The MAD analysis also shows a relatively high density of low misorientation angles, which are mainly characterized by rotation axes close to

[010] and [001]. Plagioclase and clinopyroxene do not show any significant CPO and are free of substructure related to crystal-plastic deformation.

Olivine gabbros exhibit igneous textures, with no foliation observed in our samples. Clinopyroxenes are large tablets of 2 mm to 1 cm and plagioclases, the major phase in these rocks, occur as elongated laths or tabular crystals of 1 mm to 1 cm with aspect ratios ranging from 1:1.5 to 1:5. Olivine occurs as aggregates of subhedral to lobed crystals, sometimes forming small chains with an average aspect ratio varying from 1:1.5 to 1:2. Well-defined olivine subgrain boundaries, indicative of crystal-plastic deformation, are also observed in olivine gabbros (Fig. 3h).

Olivine CPO in olivine gabbros are generally stronger than in olivine-rich troctolites and troctolites (Table 1), but with no clear, distinctive patterns (Fig. 6), which may be due to the relatively low number of grains (see examples in Figure 6). As in olivine-rich troctolites, analysis of misorientation angle distribution reveals well-developed (100) subgrain boundaries in olivines. CPO and misorientations in olivine from olivine-gabbros suggest deformation by dislocation creep with dominant activation of the high temperature (010) [100] slip systems (Tommasi et al., 2000). As in troctolites, plagioclase and clinopyroxene are not deformed.

5 Discussion

In olivine-rich troctolites, clinopyroxene and plagioclase poikiloblasts are not deformed. In contrast, the olivine grains enclosed within the poikiloblasts show evidences of high-temperature plastic deformation by dislocation creep. In addition, clinopyroxene and plagioclase crystallized after the same MORB melt that was in chemical disequilibrium with and partly corroded olivine (Drouin et al., accepted). This result excludes a common magmatic origin for clinopyroxene, plagioclase and olivine, and implies that plastic flow predates the crystallization of the melt. Clinopyroxene and plagioclase represent the cumulate phases of a MORB melt that impregnated a previously deformed olivine matrix. These observations suggest a complex crystallization history in an open system with percolation of MORB-type melt(s) in an olivine-rich rock or mush (Drouin et al., accepted). However, the origin of this olivine matrix remains ambiguous, and difficult to constrain. It could represent an earlier, very primitive cumulate or it could derive from mantle peridotite, as speculated in Drouin et al. (accepted) based on the in-situ geochemical arguments.

In the following sections, we discuss the potential effects of melt-rock interactions on the development of olivine CPOs, the different possible origins of olivine-rich troctolites, and the implications of the occurrence of the olivine-rich troctolites on accretion processes at slow-spreading ridges.

5.1 Olivine CPO in olivine-rich troctolite, typical of high melt-rock interaction?

The observed olivine microstructures, CPO and MAD in olivine-rich troctolites suggest that olivine deformation was accommodated by dislocation creep under high-temperature, with activation of the dominant (010) [100], which is classically observed in mantle peridotites as a result of asthenospheric flow (e.g., Avé-Lallemant & Carter, 1970; Nicolas et al., 1973; Poirier, 1975; Nicolas & Poirier, 1976; Tommasi et al., 2000). Olivine CPOs are weak in the olivine-rich troctolites, and most samples display a maximum concentration on [001]. The CPOs observed herein are uncommon in the mantle (Ben Ismail & Mainprice, 1998; Tommasi et al., 2000). This observation is not consistent with the high temperature (010) [100] slip system, which normally results in strong [100] clusters parallel to the lineation. Yet, similar olivine CPOs have been described in zones of melt accumulation and impregnation, such as the mantle transition zone of Oman Ophiolite (Nicolas & Prinzhofer, 1983; Boudier, 1991; Ceuleneer & Rabinowicz, 1992; Boudier & Nicolas, 1995; Jouselin et al., 1998; Dijkstra et al., 2002). Nicolas & Prinzhofer (1983), Boudier (1991), and Boudier & Nicolas (1995) proposed that the weaker olivine CPOs in wehrlite and impregnated dunite could result from the desegregation, by large volumes of magma, of a dunitic olivine matrix; olivine grains are dispersed in impregnating melt and lose their original fabric. We commonly observe in our samples chains of subhedral olivine grains showing limited misorientation between each other, with (100) subgrain boundaries and curvilinear grain boundaries (Fig. 3c). Interstitial spaces between boundaries of adjacent olivine crystals are filled by clinopyroxene or plagioclase (Fig. 3c). These observations suggest that, because diffusion is easier along dislocation walls, melt may have preferentially corroded olivine grains along (100) subgrain boundaries to form chains of new grains with smooth edges (Donaldson, 1985; Boudier, 1991). We interpret the dispersed, undeformed, smaller, rounded olivines that occur isolated in large clinopyroxene and plagioclase oikocryst (Fig. 3a,e) as the end product of such a corrosion/dissolution process. The absence of free

dislocations in the smallest rounded olivine crystals, observed in decorated thin sections, could also be enhanced by melt-assisted annealing.

Alternatively, the small, rounded grains could represent phenocrysts directly crystallized from the impregnating melt. We discard, however, this interpretation as i) these small olivine grains are commonly observed in crystallographic continuity with larger olivine grains (Fig. 3a), and ii) they are not in chemical equilibrium with the surrounding clinopyroxene and/or plagioclase (Drouin et al., accepted). We propose that the large impregnation by basaltic melt (Drouin et al., accepted) have significantly modified the original olivine CPO. In a first stage, the olivine-rich matrix was plastically deformed in the solid-state, producing fabrics that result from dislocation creep, which seem to be dominated by the most common (010) [100] slip system. Then, intergranular melt circulates within the olivine matrix and crystals begin to move relative to each other inducing a dispersion of the olivine CPO (e.g., Cannat et al., 1990). In some of our samples, olivine grains are elongated (maximum aspect ratios generally ranging from 1:4 to 1:6), and locally define weak to moderate shape-preferred orientations. Olivine crystals, when elongated, tend to have their long axis dominantly sub-parallel to [001] (Fig. 8). Crystal alignment in a flowing magma naturally results in the coincidence of the CPO and shape preferred. We interpret this observation as indicative of a transition from solid-state, plastic flow to local suspension flow with the increasing melt fraction, which must then locally exceed 20-30% (e.g., Van der Molen and Paterson, 1979; Vigneresse et al., 1996; Rosenberg and Handy, 2005).

The unusual clustering of [001] axes in the measured CPOs could result from the two combined processes outlined above: corrosion of preexisting olivine grains, preferentially along (100) subgrain boundaries, followed by misorientation of the newly formed grains by rotation preferentially around [001] (Poirier and Nicolas, 1975), and magmatic flow of olivine grains (with [001] being the longest axis when elongated) when the melt fraction is high enough to destroy the solid framework. Disruption of the solid olivine framework may happen locally, and/or episodically during the overall impregnation history recorded by the rock. This implies that, at least during part of this history, the volume of melt within the solid matrix is high enough to allow crystallization of relatively large amounts of clinopyroxene and/or plagioclase with constant and uniform chemistry, as detailed in Drouin et al. (accepted).

5.2 Olivine-rich troctolites: the ultimate residue of melt-mantle interactions?

High temperature plastic deformation of olivine can be observed in mantle rocks but also in primitive cumulate gabbros from the lower crust (e.g., Boudier et al., 1996; Dick et al., 1999; Yoshinobu and Hirth, 2002). Oceanic and ophiolitic gabbros commonly exhibit CPOs and subgrain microstructures in olivine crystals while there is no or little evidence for dislocation creep in coexisting plagioclase and pyroxene. At hypersolidus conditions, the olivine is the weakest phase, and responds passively to the deformation of a very thick, crystal-rich mush (Yoshinobu and Hirth, 2002). Olivine-rich troctolites sampled at IODP Hole U1309D, however, do not display the igneous texture typical of cumulate oceanic gabbros. Moreover, chemistry and microstructures show that olivine-rich troctolites were formed as a two stages process: the MORB melt after which clinopyroxene and plagioclase crystallized, impregnated a previously deformed olivine matrix. This early olivine matrix could have been a primitive MORB cumulate. Yet, the highly primitive major element compositions ($Fo= 82-88$ and $Ni= 1440-2300$ ppm) and the highly depleted incompatible trace element compositions of olivine in olivine-rich troctolites are not consistent with crystallization after a MORB-type melt (Drouin et al., accepted).

Olivine-rich troctolites display impregnation texture similar to the shallowest part of the mantle sampled at fast-spreading ridges (e.g., Cannat et al., 1990; Constantin et al., 1995; Allan and Dick, 1996; Arai and Matsukage, 1996; Dick and Natland, 1996; Niu and Hekinian, 1997). In addition, olivine CPOs are similar to those of wehrlites, troctolites and dunites in the mantle transition zone of Oman Ophiolite, which, from geochemical and/or microstructural arguments, are inferred to derive from mantle rocks (Nicolas & Prinzhofer, 1983; Boudier, 1991; Ceuleneer & Rabinowicz, 1992; Boudier & Nicolas, 1995; Jousset et al., 1998; Dijkstra et al., 2002). Hole U1309D olivine-rich troctolites could be considered as impregnated mantle rocks that have experienced strong structural and chemical changes due to extensive melt/rock interactions. We propose the following scenario for the formation of Hole U1309D olivine-rich troctolites (Fig. 9):

In a first stage, MORB melts are sporadically injected in the molten depleted mantle at near solidus temperature. High temperature favors pervasive melt-rock interactions, melt impregnation and orthopyroxene dissolution (e.g., Kelemen 1990; Kelemen et al., 1990; Niu, 2004; Tommasi et al., 2004). The solid matrix is progressively invaded by large melt fractions, locally dispersing the olivine network.

In a second stage, as temperature decreases, melt progressively crystallizes plagioclase and clinopyroxene within/around the assimilated olivine matrix (Drouin et al., accepted) to form the olivine-rich troctolite.

The gabbroic section that constitutes the Hole U1309D was built by multiple intrusive events at different depths in the axial lithosphere (Blackman et al., 2006; Grimes et al., 2008; Godard et al., in press). Narrow intervals of impregnated peridotites were sampled at the top of Hole U1309D (Blackman et al., 2006; Tamura et al., 2008) indicating that small slivers of mantle can be trapped within the gabbroic intrusions. Similarly, the olivine-rich troctolites may represent slivers of mantle; in contrast to the peridotite from the top of the borehole, olivine-rich troctolites have undergone extensive melt/rock interactions suggesting that melt infiltration occurred in hot lithosphere, probably at the asthenosphere/lithosphere transition.

The microstructures and the primitive composition of olivine in troctolites (Drouin et al., accepted) could reflect a continuous evolution from olivine-rich troctolites to troctolites, through increasing fraction of crystallized melt in the deformed olivine matrix, as proposed by Boudier and Nicolas (1995) in some lower crustal layered gabbros from the Oman ophiolite.

5.3 Implications on accretion processes at slow-spreading ridges

The formation of olivine-rich troctolite in the Hole U1309D gabbroic section, as described above, is associated to abundant melt accumulation and impregnation at the base of the lithosphere beneath the ridge axis in this area of the Mid-Atlantic ridge. The association of troctolite and olivine-gabbros with impregnated olivine-rich lithology in Hole U1309D is similar to what has been documented in fast-spreading mantle-crust transition zones in the Oman ophiolite (e.g., Boudier and Nicolas, 1995; Dijkstra et al., 2003) and at Hess Deep (Allan and Dick, 1996; Arai and Matsukage, 1996; Dick and Natland, 1996). However, in contrast to fast-spreading environments, the crust at 30°N is poor in volcanics, classically considered as "magma-poor", and accretion is dominated by detachment faulting (Cann et al., 1997; Blackman et al., 2002).

Our results, together with the abundance of igneous rocks in Hole U1309D (Blackman et al., 2006), suggest that magmatic activity, at the time of the formation of the gabbroic series that now constitutes the core of the Atlantis Massif, was relatively high. This is in apparent contradiction with the paucity of erupted basalts, the occurrence of outcropping mantle peridotites on the seafloor in this area, and with the traditional view that OCC formation is related to reduce magmatic activity (e.g., Tucholke and Lin, 1994). It suggests that most of the melt that produced the recovered crustal section remained trapped in the lithosphere, with

no or little erupted volcanic counterpart, resulting in a composite crust made of gabbroic plutons embedded in peridotites at depth or serpentinites closer to the seafloor and a reduced or locally absent basaltic upper crust, as already described at the mid-Atlantic and Southwest Indian Ridge (Cannat, 1993; Cannat et al., 1995; Lagabrielle et al., 1998; Cannat et al., 2008), and in Alpine ophiolites (Lagabrielle and Cannat, 1990). This interpretation is supported by the overall geochemical signature of Hole IODP U1309D (Godard et al., in press), and is consistent with the discrepancy between crustal thicknesses inferred from gravimetry and from melting models (Escartin and Cannat, 1999; Cannat et al., 2004). It is also consistent with thermal modeling (Sleep and Barth, 1997), and with the results of Lizarralde et al. (2004) who propose from seismic refraction and gravimetry data that, at spreading rates below 20mm/yr, significant amounts of melt might be retained in the mantle.

Extending our results to all volcanic-poor areas, where accretion is dominated by detachment faulting, and which could represent as much as 50% of slow-spreading ridges (Escartin et al., in press), we speculate that incorporation of impregnated mantle peridotites to gabbroic sections is a widespread, and fundamental way of building the lower crust at slow and ultra-slow spreading ridges. OCCs, which are a subset of detachment fault systems at slow and ultra-slow spreading ridges, represent a relatively magma-rich end-member of composite crust. Several recent studies, using independent arguments (gravimetry and bathymetry analysis, ocean drilling results) demonstrate that OCCs develop during or immediately after episodes of relatively high magma supply and do not represent the magma-starved end-member of accretion processes at mid-ocean ridges (Cannat et al., 2006; Ildefonse et al., 2007; Blackman et al., 2008; Tucholke et al., 2008). Ildefonse et al. (2007) have proposed that fully developed OCCs such as the Atlantis massif are the morphological expression of the occurrence of larger than usual, discrete gabbroic plutons in a composite crust, corresponding to episodically enhance magmatic activity.

6 Conclusion

Together with their in-situ mineral compositions (Drouin et al., accepted), the microstructures of olivine-rich troctolites from IODP Hole U1309D demonstrate that high degrees of melt impregnation contributed to their final texture, chemistry and microstructure. The observed olivine CPO and misorientations are consistent with deformation by dislocation creep, dominated by the high temperature (010) [100] slip system, as classically observed in mantle peridotites.

The measured CPOs differ from classical mantle fabrics in that they are much weaker, with slightly stronger [001] clusters. We interpret these fabrics as resulting from extensive melt impregnation of a previously deformed olivine-rich rock, with separation of olivine grains by preferred corrosion along (100) subgrain boundaries, possibly enhanced by magmatic flow when the melt-rock ratio is high enough to disrupt the solid olivine framework. Melt impregnation is also recorded by the rock texture, with the crystallization of poikilitic and interstitial pyroxene and plagioclase and corrosion of olivine that postdate olivine deformation.

Similar textures and CPO are classically observed in the mantle/transition zone of ophiolites and at present-day mid-ocean ridges. We propose that olivine in olivine-rich troctolites, and possibly in neighboring troctolites are derived from mantle peridotites. The composition of olivines and the Cr and Ti content in spinels indicate mantle/melt interaction at high melt/rock ratios. In this scheme, olivine-rich troctolites represent the ultimate product of a multistage melt-mantle reaction process.

The occurrence of a significant volume of olivine-rich troctolites in IODP Hole U1309D suggests then that magmatic activity at the ridge axis was high when the recovered crustal section was emplaced. This is consistent with the already stated hypotheses, inferred from several, independent constraints, that melt production in volcanic-poor areas of slow-spreading ridges is not necessarily low, and that the development of OCC is associated to relatively rich magmatic episodes in an overall composite crust. The olivine-rich troctolites were recovered as relatively thin (<12m), discrete intervals, which we interpret as relatively small slivers of impregnated mantle rocks, trapped in a stack of small gabbro intrusions. Extending this accretion mode to the entire portion of the mid-ocean ridge that is accreted through detachment faults (up to ~50%, Escartin et al., 2008), it may represent a fundamental way to build ultra-slow to slow-spread lithosphere.

Acknowledgements

This research used samples and data provided by the Integrated Ocean Drilling Program (IODP). We thank captains Pete Mowat and Alex Simpson, the operation superintendents Mike Storms, Stephen Midgley, and Ron Grout, the crew of the JOIDES Resolution, and the Integrated Ocean Drilling Program United States Implementing Organization's technical staff for their outstanding work during IODP Expeditions 304 and 305. We are grateful to Christophe Nevado and Doriane Delmas for

providing high-quality thin sections. We also thank F. Boudier, A. Tommasi, D. Mainprice, and G. Hirth for stimulating discussions. This study was supported by CNRS-INSU program DyETI (Dynamique et Evolution de la Terre Interne).

Reference

- Allan, J.F., Sack, R.O., Batiza, R., 1988. Cr-rich spinels as petrogenetic indicators: MORB-type lavas from the Lamont seamount chain, eastern Pacific. *American Mineralogist* 73, 741-753.
- Allan, J.F., and Dick, H.J.B., 1996. Cr-rich spinel as a tracer for melt migration and melt-wall rock interaction in the mantle: Hess Deep, Leg 147. In Mével, C., Gillis, K.M., Allan, J.F., and Meyer, P.S. (Eds.), *Proc. ODP, Sci. Results, 147: College Station, TX (Ocean Drilling Program)*, 157–172. doi:10.2973/odp.proc.sr.147.009.1996
- Arai, S., and Matsukage, K., 1996. Petrology of gabbro-troctolite-peridotite complex from Hess Deep, equatorial Pacific: implications for mantle-melt interaction within the oceanic lithosphere. In Mével, C., Gillis, K.M., Allan, J.F., and Meyer, P.S. (Eds.), *Proc. ODP, Sci. Results, 147: College Station, TX (Ocean Drilling Program)*, 135–155. doi:10.2973/odp.proc.sr.147.008.1996
- Avé-Lallemant, H.G., Carter, N.L., 1970. Syntectonic recrystallization of olivine and modes of flow in the upper mantle. *Geol. Soc. Am. Bull.* 81, 2003-2020.
- Ben Ismail, W., Mainprice, D., 1998. An olivine fabric database: An overview of upper mantle fabrics and seismic anisotropy. *Tectonophysics* 296, 145-158.
- Benn, K., Nicolas, A. and Reuber, I., 1988. Mantle-crust transition zone and origin of wehrlitic magmas : Evidence from the Oman ophiolite. *Tectonophysics*, 151: 75-85.
- Blackman, D.K., Karson, J.A., Kelley, D.S., Cann, J.R., Fruh-Green, G.L., Gee, J.S., Hurst, S.D., John, B.E., Morgan, J., Nooner, S.L., Ross, D.K., Schroeder, T.J., and Williams, E.A., 2002. Geology of the Atlantis Massif (MAR 30°N): implications for the evolution of an ultramafic oceanic core complex. *Marine Geophysical Researches* 23(5-6), 443-469.
- Blackman, D.K., Ildefonse, B., John, B.E., Ohara, Y., Miller, D.J., MacLeod, C.J., and the Expedition 304/305 Scientists, 2006. *Proc. IODP, 304/305: College Station TX (Integrated Ocean Drilling Program Management International, Inc.)*. doi:10.2204/iodp.proc.304305.2006

- Blackman, D. K., Karner, G.D., Searle, R.C., 2008. Three-Dimensional Structure of Oceanic Core Complexes : Effects on Gravity Signature and Ridge Flank Morphology, Mid-Atlantic Ridge 30°N. *Geochemistry, Geophysics, Geosystems*.
- Borghini, G., Rampone, E., Crispini, L., De Ferrari, R., and Godard, M., 2007. Origin and emplacement of ultramafic-mafic intrusions in the Erro-Tobbio mantle peridotite (Ligurian Alps, Italy). *Lithos* 94(1-4), 210-229.
- Boudier, F., 1991. Olivine xenocrysts in picritic magmas-An experimental and microstructural study. *Contrib. Mineral. Petrol.* 109(1), 114-123.
- Boudier, F., Nicolas, A., 1995. Nature of the Moho transition zone in the Oman Ophiolite. *J. Petrol.* 36, 777 – 796.
- Boudier, F., Nicolas, A. and Ildefonse, B., 1996. Magma chambers in the Oman ophiolite: fed from the top or from the bottom ? *Earth Planet. Sci. Lett.* 144, 239-250.
- Bunge, H.J., 1982. *Texture Analysis in Materials Science*. Butterworths, London, 599 pp.
- Cann, J.R., Blackman D.K., Smith, D.K., McAllister, E., Janssen, B., Mello, S., Avgerinos, E., Pascoe, A.R., and Escartin J., 1997. Corrugated slip surfaces formed at ridge-transform intersections on the Mid-Atlantic Ridge. *Nature* 385, 329-332.
- Cannat, M., Bideau, D., and Hebert, R., 1990. Plastic deformation and magmatic impregnation in serpentinized ultramafic rocks from the Garrett transform fault (East Pacific Rise). *Earth Planet. Sci. Lett.* 101, 216-232.
- Cannat, M., Bideau, D. and Bougault, H., 1992. Serpentinized peridotites and gabbros in the Mid-Atlantic Ridge axial valley at 15 37'N and 16 52'N. *Earth Planet. Sci. Lett.* 109, 87-106.
- Cannat, M., 1993. Emplacement of mantle-rocks in the seafloor at mid-ocean ridges. *Journal of Geophysical Research*, 98: 4163-4172.
- Cannat, M., Mevel, C., Maia, M., Deplus, C., Durand, C., Gente, P., Agrinier, P., Belarouchi, A., Dubuisson, G., Humler, E. and Reynolds, J., 1995. Thin crust, ultramafic exposures, and rugged faulting patterns at Mid-Atlantic Ridge (22 degrees 24 degrees N). *Geology*, 23(1): 49-52.
- Cannat, M., 1996. How thick is the magmatic crust at slow spreading oceanic ridges? *JGR* 101(B2), 2847-2857.
- Cannat, M., Cann, J., and MacLennan, J., 2004. Some hard rock constraints on the supply of heat to mid-ocean ridges. In C.R. German, J. Lin, L.M. Parson (Editors), *Mid-ocean ridges; hydrothermal interactions between the lithosphere and oceans*. Geophysical Monograph. American Geophysical Union, Washington, DC, United States, vol.148,

pp.111-149.

- Cannat, M., Chatin, F., Whitechurch, H., and Ceuleneer, G., 1997. Gabbroic rocks trapped in the upper mantle at the Mid-Atlantic Ridge. In Karson, J.A., Cannat, M., Miller, D.J., and Elthon, D. (Eds.), Proc. ODP, Sci. Results, 153: College Station, TX (Ocean Drilling Program), 243–264. doi:10.2973/odp.proc.sr.153.013.1997
- Cannat, M., Sauter, D., Mendel, V., Ruellan, E., Okino, K., Escartin, J., Combier, V., Baala, M., 2006. Modes of seafloor generation at a melt-poor ultraslow-spreading ridge. *Geology*, 34, 605-608, doi: 10.1130/G22486.1.
- Ceuleneer, G., Rabinowicz, M., 1992. Mantle flow and melt migration beneath oceanic ridges: Models derived from observation in ophiolites. In: . In J.P. Morgan, D.B. Blackman, J.M. Sinton (Editors), *Mantle Flow and Melt Generation at Mid-Ocean Ridges*. Geophysical Monograph. American Geophysical Union, Washington, DC, United States, vol.71, pp.123-154.
- Constantin, M., Hékinian, R., Ackermant, D. and Stoffers, P., 1995. Mafic and ultramafic intrusions into upper mantle peridotites from fast spreading centers of the Easter microplate (South East Pacific). In: R.L.M. Vissers and A. Nicolas (Editors), *Mantle and lower crust exposed in oceanic ridges and in ophiolites*. Petrology and Structural Geology. Kluwer Academic Press, Dordrecht, Boston, London, pp. 71-120.
- Dick, H.J.B., and Bullen, T., 1984. Chromian spinel as a petrogenetic indicator in abyssal and alpine-type peridotites and spatially associated lavas. *Contrib. Mineral. Petrol.* 86(1), 54-76.
- Dick, H.J.B., 1989. Abyssal peridotites, very slow spreading ridges and ocean ridge magmatism. In: A.D. Saunders and M.J. Norry (Editors), *Magmatism in the Ocean Basins*. Geological Society of London Special Publication, London, 42 : pp 71-105.
- Dick, H.J.B., and Natland, J.H., 1996. Late-stage melt evolution and transport in the shallow mantle beneath the East Pacific Rise. In Mével, C., Gillis, K.M., Allan, J.F., and Meyer, P.S. (Eds.), Proc. ODP, Sci. Results, 147: College Station, TX (Ocean Drilling Program), 103–134. doi:10.2973/odp.proc.sr.147.007.1996
- Dick, H.J.B., Natland, J.H., Miller, D.J., et al., 1999. Proc. ODP, Init. Repts., 176: College Station, TX (Ocean Drilling Program). doi:10.2973/odp.proc.ir.176.1999
- Dijkstra, A.H., Drury, M.R., Frijhoff, R.M., 2002. Microstructures and lattice fabrics in the Hilti mantle section (Oman Ophiolite): Evidence for shear localization and melt weakening in the crust-mantle transition zone? *JGR* 107(B11), 2270, doi: 10.1029/2001JB000458

- Dijkstra, A.H., Barth, M.G., Drury, M.R., Mason, P.R.D., and Vissers R.M.L., 2003. Diffuse porous melt flow and melt-rock reaction in the mantle lithosphere at the slow-spreading ridge: a structural petrology and LA-ICP-MS study of the Othris Peridotite Massif (Greece). *Geochemistry, Geophysics, Geosystems* 4, 1-24.
- Donaldson, C.H., 1985. A comment on crystal shapes resulting from dissolution in magmas. *Mineralogical Magazine* 49, 129-132. doi:10.1180/minmag.1985.049.350.19
- Drouin, M., Godard, M., Ildefonse, B. Geochemical and petrographic evidence for magmatic impregnation in the oceanic lithosphere at Atlantis Massif, Mid-Atlantic Ridge (IODP Hole U1309D, 30°N). Accepted to *Chemical Geology*.
- Edwards, S.J., and Malpas, J., 1996. Melt-peridotite interactions in shallow mantle at the East Pacific Rise: evidence from ODP site 895 (Hess Deep) *Mineralogical Magazine*, 60: 191-206.
- Escartin, J., Cannat, M., 1999. Ultramafic exposures and the gravity signature of the lithosphere near the fifteen-Twenty Fracture Zone (Mid-Atlantic Ridge, 14°-16.5°N). *Earth Planet. Sci. Lett.* 171, 411 – 424.
- Escartin, J., Smith, D.K., Cann, K., Schouten, H., C.L. Langmuir, and S. Escrig, in press. Central role of detachment faults in accretion of slow spreading oceanic lithosphere. *Nature*.
- Girardeau, J. and Franchetau, J., 1993. Plagioclase-wehrlites and peridotites on the East Pacific Rise (Hess Deep) and the Mid-Atlantic Ridge (DSDP Site 334) - evidence for magma percolation in the oceanic upper mantle. *Earth Planet. Sci. Lett.* 115, 137-149.
- Godard, M., Joussetin, D., Bodinier, J.-L., 2000. Relationships between geochemistry and structure beneath a palaeo-spreading centre: a study of the mantle section in the Oman Ophiolite. *Earth Planet. Sci. Lett.* 180, 133 – 148.
- Godard, M., Awaji, S., Hansen, H., Hellebrand, E., Brunelli, D., Johnson, K., Maeda, J., Yamasaki, T., Abratis, M., Christie, D., Kato, Y., Rosner, M., and Mariet, C., in press. Geochemistry of a long in-situ section of intrusive slow-spread crust: Results from IODP Site U1309 (Atlantis Massif, 30°N Mid-Atlantic-Ridge), *Earth. Planet. Sci. Lett.*
- Grimes, C.B., John, B.E., Cheadle, M.J., Wooden, J.L., 2008. Protracted construction of gabbroic crust at a slow-spreading ridge: Constraints from $^{206}\text{Pb}/^{238}\text{U}$ zircon ages from Atlantis Massif and IODP Hole U1309D (30°N, MAR). *Geochem. Geophys. Geosyst.*, doi:10.1029/2008GC002063
- Hébert, R., Bideau, D., and Hékinian, R., 1983. Ultramafic and mafic rocks from the Garret transform fault near 13°30'S on the East Pacific Rise: igneous petrology. *Earth Planet.*

- Sci. Lett. 65, 107-125.
- Hékinian, R., Bideau, D., Francheteau, J., Cheminée, J.L., Armijo, R., Lonsdale, P. and Blum, N., 1993. Petrology of the East Pacific Rise crust and upper mantle exposed in Hess deep (Eastern Equatorial Pacific). *JGR* 98(B5), 8069-8094.
- Ildefonse, B., Blackman, D.K., John, B.E., Ohara, Y., Miller, D.J., MacLeod, C.J., and the IODP Expeditions 304-305 Scientists, 2007. Oceanic Core Complexes and Crustal Accretion at Slow-Spreading Ridges. *Geology* 35, 623-626; doi: 10.1130/G23531A.1.
- Jousselin, D., Nicolas, A. and Boudier, F., 1998. Detailed mapping of a mantle diapir below a paleo-spreading center in the Oman ophiolite. *Journal of Geophysical Research-Solid Earth*, 103: 18153-18170.
- Kamenetsky, V.S., and Crawford, A.J., 1998. Melt-peridotite reaction recorded in the chemistry of spinel and melt inclusions in basalt from 43 degrees N, Mid-Atlantic Ridge. *Earth Planet. Sci. Lett.* 164(1-2), 345-352.
- Karson, J.A., Fruh-Green, G.L., Kelley, D.S., Williams, E.A., Yoerger, D.R., and Jakuba, M., 2006. Detachment shear zone of the Atlantis Massif core complex, Mid-Atlantic Ridge, 30°N. *Geochem. Geophys. Geosyst.*, 7. doi: 10.1029/2005GC001109.
- Kelemen, P.B., 1990. Reaction between ultramafic rock and fractionating basaltic magma. 1. Phase-relations, the origin of calc-alkaline magma series, and the formation of discordant dunite. *J. Pet.* 31(1), 51-98.
- Kelemen, P.B., Joyce, D.B., Webster, J.D., Holloway, J.R., 1990. Reaction between ultramafic rock and fractionating basaltic magma. 2. Experimental investigation of reaction between olivine tholeiite and harzburgite at 1150-degree-C-1050-degrees-C and 5Kb. *J. Pet.* 31(1), 99-134.
- Kelemen, P.B., Kikawa, E., Miller, D.J., et al., 2004. Proc. ODP, Init. Repts., 209: College Station, TX (Ocean Drilling Program). doi:10.2973/odp.proc.ir.209.2004
- Koga, K.T., Kelemen, P.B. and Shimizu, N., 2001. Petrogenesis of the crust-mantle transition zone and the origin of lower crustal wehrlite in the Oman ophiolite. *Geochem. Geophys. Geosyst.*, doi: 10.1029/2000GC000132.
- Kohlstedt, D.L., Goetze, C., Durham, W.B. and Vander Sande, J., 1976. New Technique for Decorating Dislocations in Olivine. *Science* 191(4231), 1045-1046.
- Lagabrielle, Y., Bideau, D., Cannat, M., Karson, J.A. and Mevel, C., 1998. Ultramafic-mafic plutonic rock suites exposed along the Mid-Atlantic Ridge (10 degrees N-30 degrees N); symmetrical-asymmetrical distribution and implications for seafloor spreading processes. In: W.R. Buck, P.T. Delaney, J.A. Karson and Y. Lagabrielle (Editors),

- Faulting and magmatism at mid-ocean ridges. Geophysical Monograph. American Geophysical Union, Washington, DC, United States, pp. 153-176.
- Lagabrielle, Y. and Cannat, M., 1990. Alpine Jurassic ophiolites resemble the modern central Atlantic basement. *Geology*, 18: 319-322.
- Lenoir, X., Garrido, C., Bodinier, J.-L., Dautria, J.-M., Gervilla, F., 2001. The recrystallization front of the Ronda peridotite: evidence for melting and thermal erosion of lithospheric mantle beneath the Alboran basin. *J. Petrol.* 42, 141–158.
- Lizarralde, D., Gaherty, J.B., Collins, J.A., Hirth, G. and Kim, S.D., 2004. Spreading-rate dependence of melt extraction at mid-ocean ridges from mantle seismic refraction data. *Nature* 432, 744-747.
- Nicolas, A., Boudier, F., and Boullier, A.M., 1973. Mechanism of flow in naturally and experimentally deformed peridotites, *Am. J. Sci.* 273, 853-876.
- Nicolas, A., Poirier, J.P., 1976. *Crystalline Plasticity and Solid State flow in Metamorphic Rocks*. John Willey, London, 444 pp.
- Nicolas, A., and Prinzhofer, A., 1983. Cumulative or residual origin for the transition zone in ophiolites: structural evidence. *J. petrol.* 24, 188-206.
- Niu, Y., and Hekinian, R., 1997. Basaltic liquids and harzburgitic residues in the Garrett Transform; a case study at fast-spreading ridges. *Earth Planet. Sci. Lett.* 146(1-2), 243-258.
- Niu, Y., 2004. Bulk-rock major and trace element compositions of abyssal peridotites: implications for mantle melting, melt extraction and post-melting processes beneath mid-ocean ridges. *J. Petrol* 45(12), 2423-2458.
- Poirier, J.P., 1975. Slip systems of olivine. *J. G. R.* 80(29), 4059-4061.
- Poirier, J.P. and Nicolas, A., 1975. Deformation-Induced Recrystallization Due to Progressive Misorientation of Subgrains, with Special Reference to Mantle Peridotites. *J. Geol.* 83, 707-720.
- Piccardo, G.B., Zanetti, A., Muntener, O., 2007. Melt/peridotite interaction in the Southern Lanzo peridotite: Field, textural and geochemical evidence. *Lithos* 94(1-4), 181-209.
- Rampone, E., Piccardo, G.B., Vannucci, R., and Bottazzi, P., 1997. Chemistry and origin of trapped melts in ophiolitic peridotites. *Geochimica and Cosmochimica Acta* 61(21), 4557-4569.
- Rampone, E., Piccardo, G.B., and Hofmann, A.W., 2008. Multi-stage melt-rock interaction in the Mt. Maggiore (Corsica, France) ophiolitic peridotites: microstructural and geochemical evidence. *Contrib. Mineral. Petrol.* doi: 10.1007/s00410-008-0296-y.

- Rosenberg, C.L., Handy, M.R., 2005. Experimental deformation of partially melted granite revisited: implications for the continental crust. *Journal of Metamorphic Geology* 23 (1), 19-28.
- Seyler, M. and Bonatti, E., 1997. Regional-scale melt-rock interaction in lherzolitic mantle in the Romanche Fracture Zone (Atlantic Ocean). *Earth and Planetary Science Letters*, 146(1-2): 273-287.
- Tamura, A., Arai, S., Ishimaru, S., Andal, E.S., 2008. Petrology and geochemistry of peridotites from IODP Site U1309 at Atlantis Massif, MAR30°N: micro- and macro-scale melt penetrations into peridotites. *Contrib. Mineral. Petrol.* 155 (4), 491-509.
- Takazawa, E., Abe, N., Seyler, M., and Meurer, W.P., 2007. Hybridization of dunite and gabbroic materials in Hole 1271B from Mid-Atlantic Ridge 15°N: implications for melt flow and reaction in the upper mantle. In Kelemen, P.B., Kikawa, E., and Miller, D.J. (Eds.), *Proc. ODP, Sci. Results, 209*: College Station, TX (Ocean Drilling Program), 1–23. doi:10.2973/odp.proc.sr.209.005.2007
- Tartarotti, P., Susini, S., Nimis, P., and Ottolini, L., 2002. Melt migration in the upper mantle along the Romanche Fracture Zone (Equatorial Atlantic). *Lithos* 63, 125-149.
- Tommasi, A., Mainprice, D., Canova, G., Chastel, Y., 2000. Viscoplastic self-consistent and equilibrium-based modeling of olivine lattice preferred orientations: Implications for the upper mantle seismic anisotropy. *J.G.R.* 105(B4), 7893-7908.
- Tommasi, A., Godard, M., Coromina, G., Dautria, J.-M. and Barszczus, H., 2004. Seismic anisotropy and compositionally induced velocity anomalies in the lithosphere above mantle plumes: a petrological and microstructural study of mantle xenoliths from French Polynesia. *Earth Planet. Sci. Lett.* 227, 539-556.
- Tucholke, B.E. and Lin, J., 1994. A geological model for the structure of ridge segments in slow spreading ocean crust. *Journal of Geophysical Research - Solid Earth*, 99(B6): 11937-11958.
- Tucholke, B.E., Behn, M.D., Buck, W.R., Lin, J., 2008. Role of melt supply in oceanic detachment faulting and formation of megamullions. *Geology* 36 (6), 455-458.
- Van der Molen, I., Paterson, M.S., 1979. Experimental deformation of partially melted granite. *Contrib. Mineral. Petrol.* 70, 299-318.
- Vauchez, A. and Garrido, C.J., 2001. Seismic properties of an asthenospherized lithospheric mantle: constraints from lattice preferred orientations in peridotite from the Ronda massif. *Earth Planet. Sci. Lett.* 192(2), 235-249.

Vigneresse, J.L., Barbey, P. and Cuney, M., 1996. Rheological transitions during partial melting and crystallization with application to felsic magma segregation and transfer. *J. Petrol.* 37, 1579-1600.

Yoshinobu, A.S. and Hirth, G., 2002. Microstructural and experimental constraints on the rheology of partially molten gabbro beneath oceanic spreading centers. *Journal of Structural Geology*, 24: 1101-1107.

Figures Captions

Figure 1: (a) Bathymetric map of the Atlantis Massif area, with the location of IODP Hole U1309D drilled during expedition IODP 304-305 (Blackman et al., 2008). (b) Lithologies recovered in Hole U1309D, 20m running average (Blackman et al., 2006) and depth localization of the sampled olivine-rich zones.

Figure 2: Examples of recovered cores of Olivine-rich troctolite (a to d), troctolitic gabbro (e), and olivine gabbro (f). a) Core 227R3, 63 to 83 cm. b) Core 232R1, 99 to 122 cm. Note the small-scale gradation in plagioclase content. c) Core 248R2, 0 to 25 cm, cross-cut by a cm-thick gabbroic vein. d) Core 256R2, 105 to 128 cm. Note the heterogeneous distribution of interstitial plagioclase, forming a pervasive, anastomosing network. e) Core 251R1, 70 to 91 cm. f) Core 268R2, 55 to 77 cm. Red areas indicate the localization of three samples (Table 1); thin rectangles : thin sections perpendicular to the core axis; square : parallel to the core axis.

Figure 3: Photomicrographs of representative microstructures in olivine-rich troctolites, troctolites and olivine-gabbros. (A) Rounded and subhedral olivine crystals (Ol) included in large clinopyroxene (Cpx) and plagioclase poikiloblasts forming poikilitic texture in olivine-rich troctolite (sample 247R3_16-18). (B) Coarse-grained subhedral olivine crystals with smooth edges and well-defined and widely-spaced subgrain boundaries, and poikiloblastic plagioclase (Pl) and orthopyroxene (Opx) (sample 248R2_22-24). (C) Olivines crystals in optical sub-continuity showing curvilinear boundaries and (100) subgrain boundaries in olivine-rich troctolite (sample 247R3_62-66). (D) Detail of dislocation sub-structures in deformed olivine of olivine-rich troctolite (decorated sample 248R2_18-21). (E) Chains of corroded olivines and rounded olivines embedded in a clinopyroxene oikocryst in olivine rich

troctolite. Spinel (Sp) occurs as small subhedral crystals with polygonal shape, included in olivine (sample 247R3_16-18). (F) Interstitial grains of clinopyroxene and plagioclase forming pervasive textures in olivine-rich troctolite (sample 64R1_58-60). Olivine crystals in this sample are highly serpentinized (G) Olivine crystals showing (100) subgrains boundaries and subhedral laths of plagioclase in a troctolite. Spinel occurs as small subhedral grain between olivine and plagioclase crystals (sample 251R1_87-89). (H) Well-defined subgrain boundaries in olivine from olivine-gabbro (sample 117R1_55-57). A, B, and E to H : cross-polarized light; C and D : plane-polarized light.

Figure 4: (a) Spinel TiO₂ content (wt.%) versus spinel Cr# (Cr# = 100 x cationic Cr/(Cr+Al)) in troctolites and olivine-rich troctolites of Hole U1309D. (b) Spinel TiO₂ content (wt. %) versus olivine Forsterite content (Fo) in troctolites and olivine-rich troctolites of Hole U1309D. The following data are shown for comparison: impregnated peridotites and gabbroic rocks from ODP Leg 147 (Hess Deep transition zone; Allan and Dick, 1996; Arai and Matsukage, 1996; Edwards and Malpas, 1996), impregnated dunite and gabbroic rocks from ODP hole 1271B (Takazawa et al., 2007).

Figure 5: EBSD maps of olivine-rich troctolites. a) sample 233R3_21-24. b) sample 247R3_16-18; the large and small rectangles indicate the localization of the microphotographs in Fig. 3a and 3e, respectively. c) sample 248R2_18-21 (from the core pictured in Figure 2c). d) sample 248R3_36-38. To the left : raw maps; each color corresponds to one mineralogical phase, red : olivine, blue : plagioclase, green : clinopyroxene, black : no results (i.e. no mineral, or non-indexed mineral. To the right : processed map for olivine (see text for further explanations on data processing); the color is a function of crystal orientation. Red lines : subgrain boundaries (misorientation <10°).

Figure 6: Olivine crystallographic preferred orientations (CPO) in olivine-rich troctolites, one troctolite, and one olivine gabbro. Equal-area, lower hemisphere stereographic projections; N is the number of measured grains; contours = x multiple of uniform distribution. The small black squares indicate the orientation of the maximum intensity in the pole figures. A small tick mark on the right side of some pole figures indicate the top of the core for oriented samples.

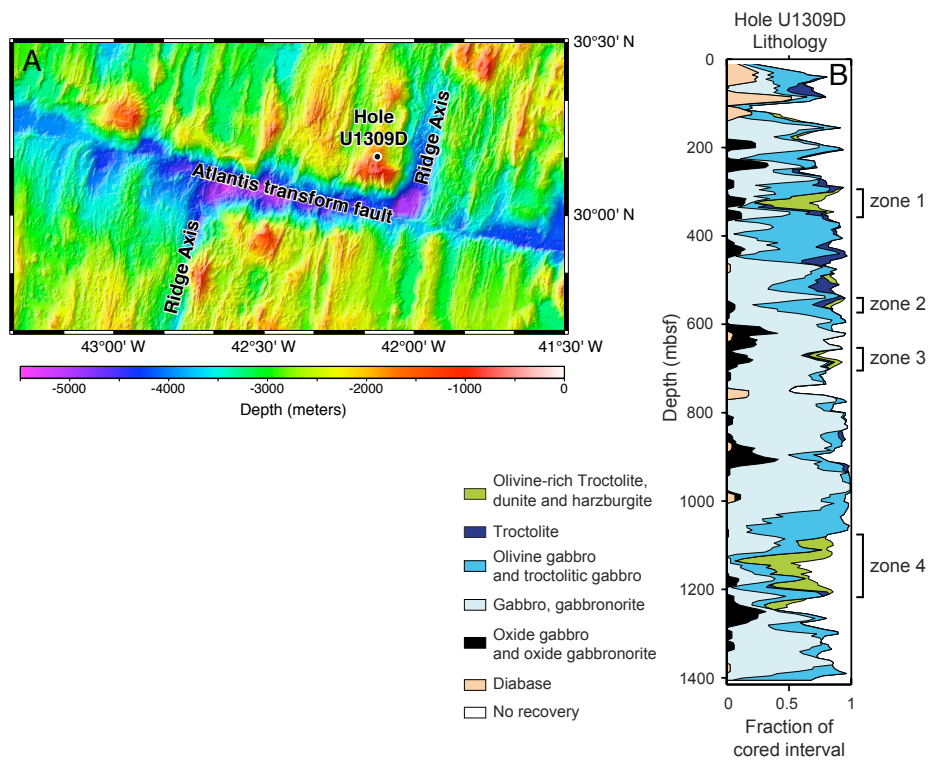
Figure 7: Misorientation angle distribution (MAD) and rotation axes for the low (2-15°) misorientation angles in the crystal reference frame. a) sample 248R2_22-24, b) sample 247R3_16-18, c) sample 227R3_121-124, d) sample 233R3_21-24. MOD histograms present data for correlated (angle between neighbor measurement points) and uncorrelated (angle between non-neighboring points randomly selected), compared to the theoretical random distribution. Contours in the inverse pole figures : x multiple of uniform distribution.

Figure 8: Crystallographic orientation map of olivine-rich troctolite: (a) sample 241R2_94-97, (b) 247R3_19-22, (c) sample 248R3_33-36. Color scale indicates the misorientation of olivine crystals with [001].

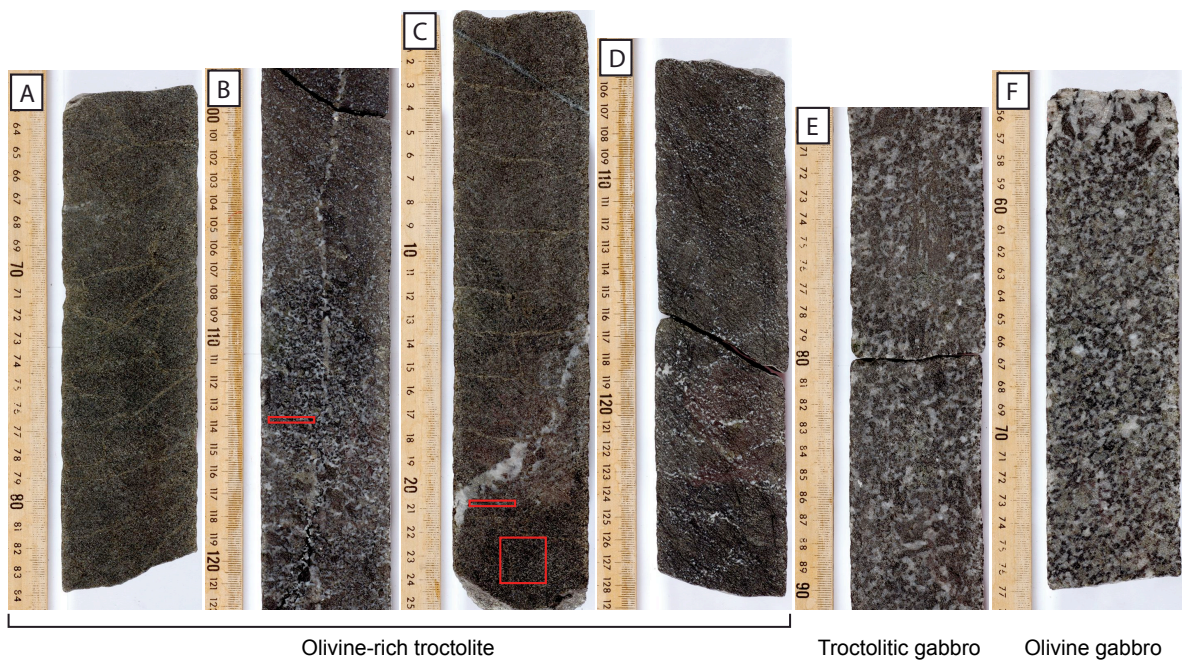
Figure 9: Sketch showing the proposed scenario for the formation of Hole U1309D olivine-rich troctolites. The transport of basaltic melts in depleted mantle at near solidus temperature and the impregnation of mantle involve orthopyroxene dissolution and formation of dunite with weakening of olivine fabrics (dunitisation process: $\text{Opx} + \text{melt} \Rightarrow \text{Cr-spinel} + \text{melt}$ 2); the increasing of melt fraction (melt fraction >30%) locally disrupt the olivine framework and modifies the original olivine fabric. The dunitisation process and the disruption of original fabric are probably concomitant. As temperature decreases, melt crystallizes plagioclase and clinopyroxene within the assimilated olivine matrix to form olivine-rich troctolite. The left schematic cross-section of the ridge axis is modified from Cannat (1996).

Tables captions

Table 1: General characteristics of studied samples from IODP Hole U1309D



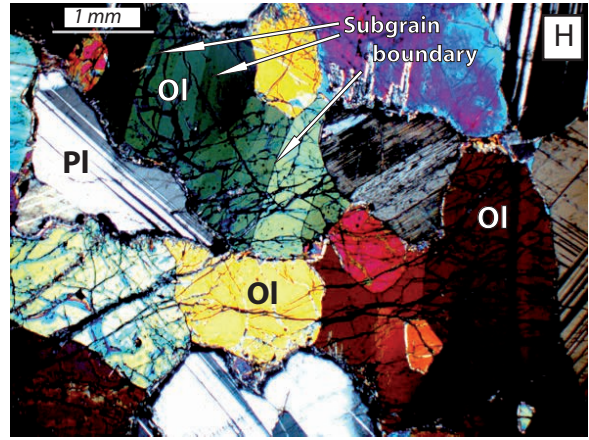
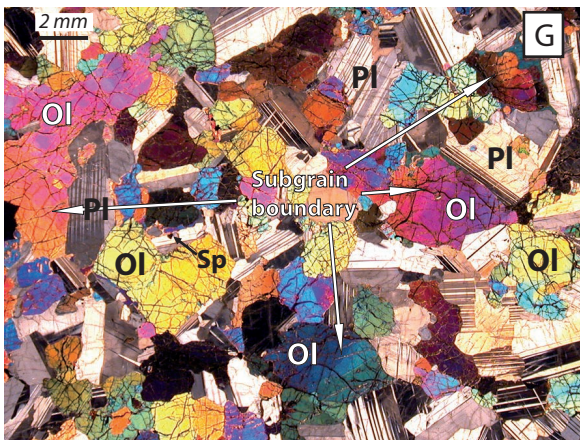
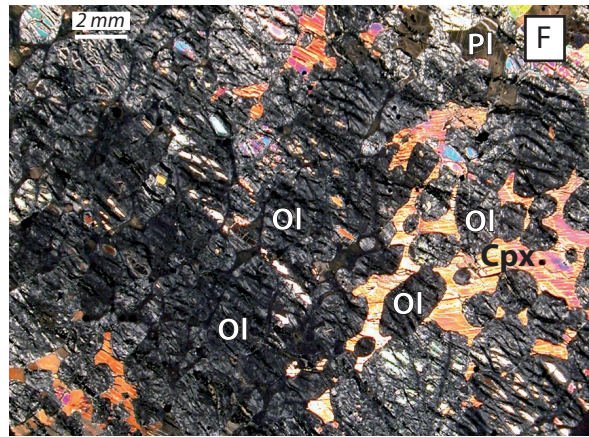
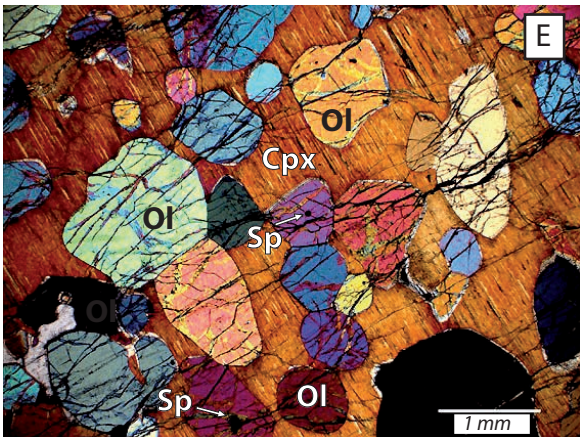
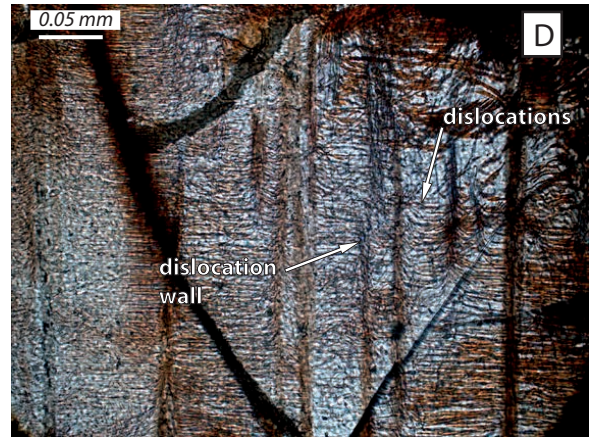
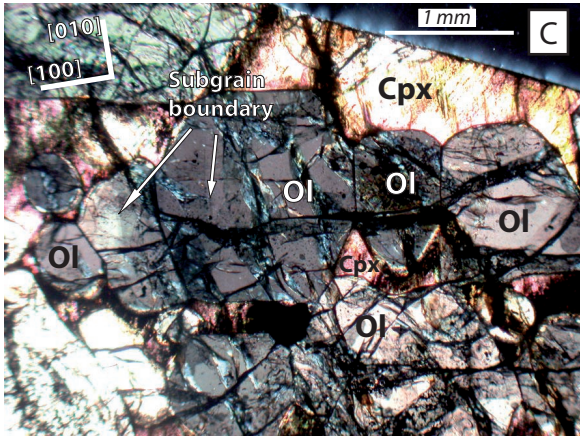
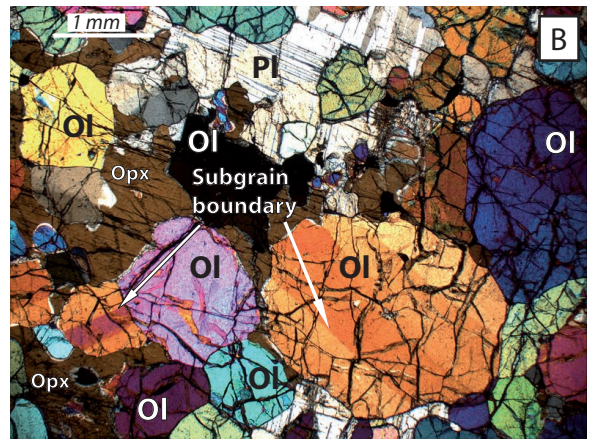
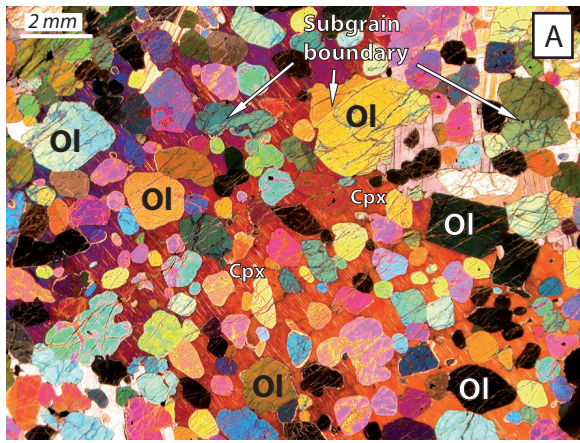
Drouin et al., Fig. 1



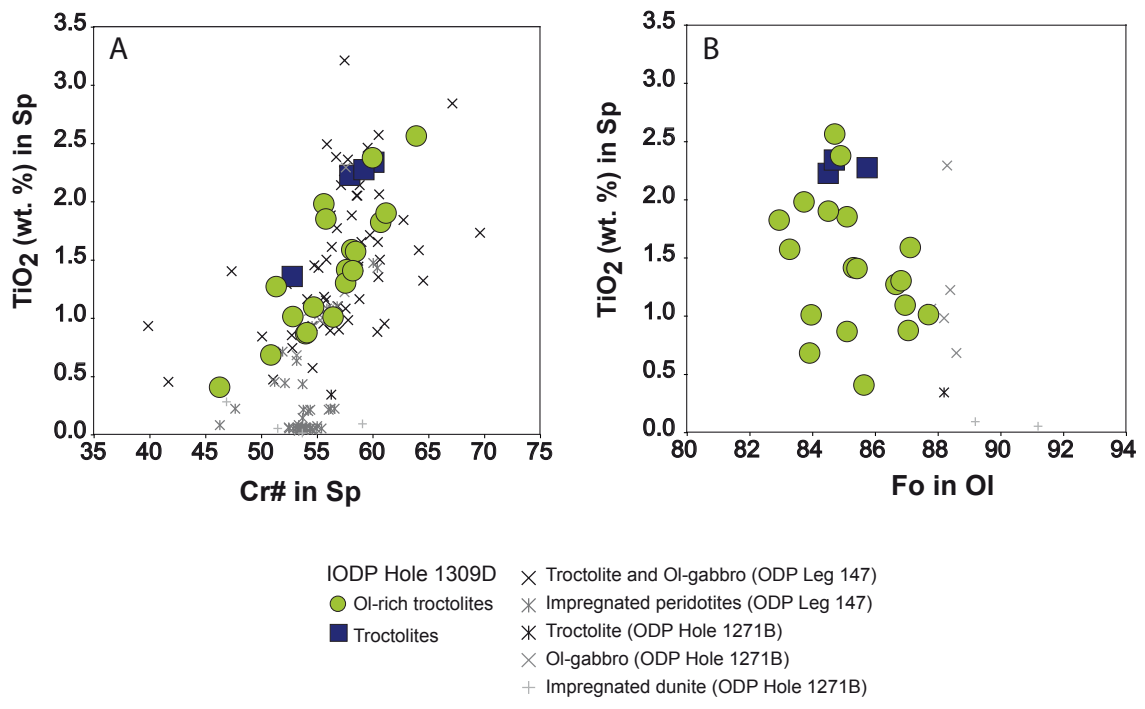
Olivine-rich troctolite

Troctolitic gabbro

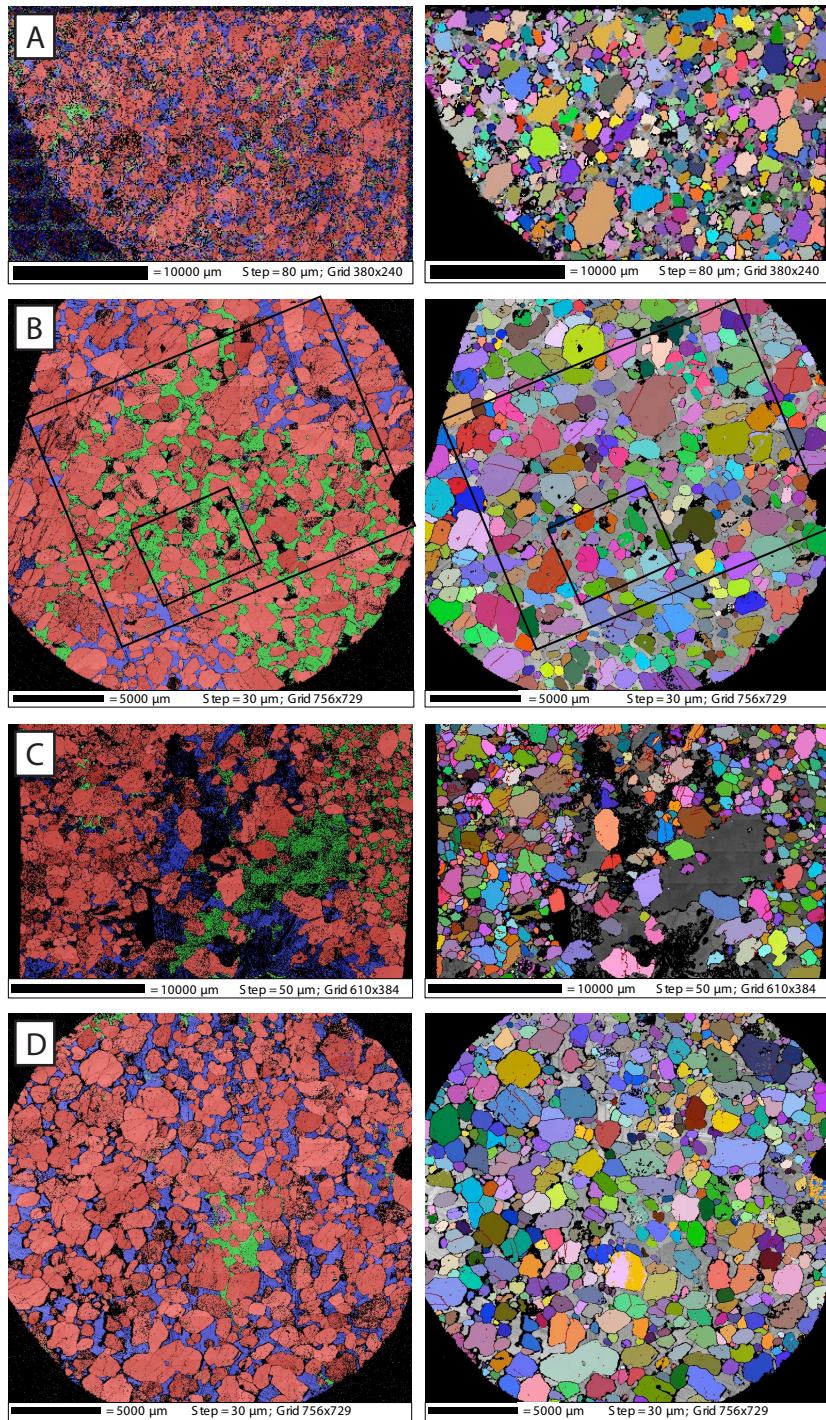
Olivine gabbro



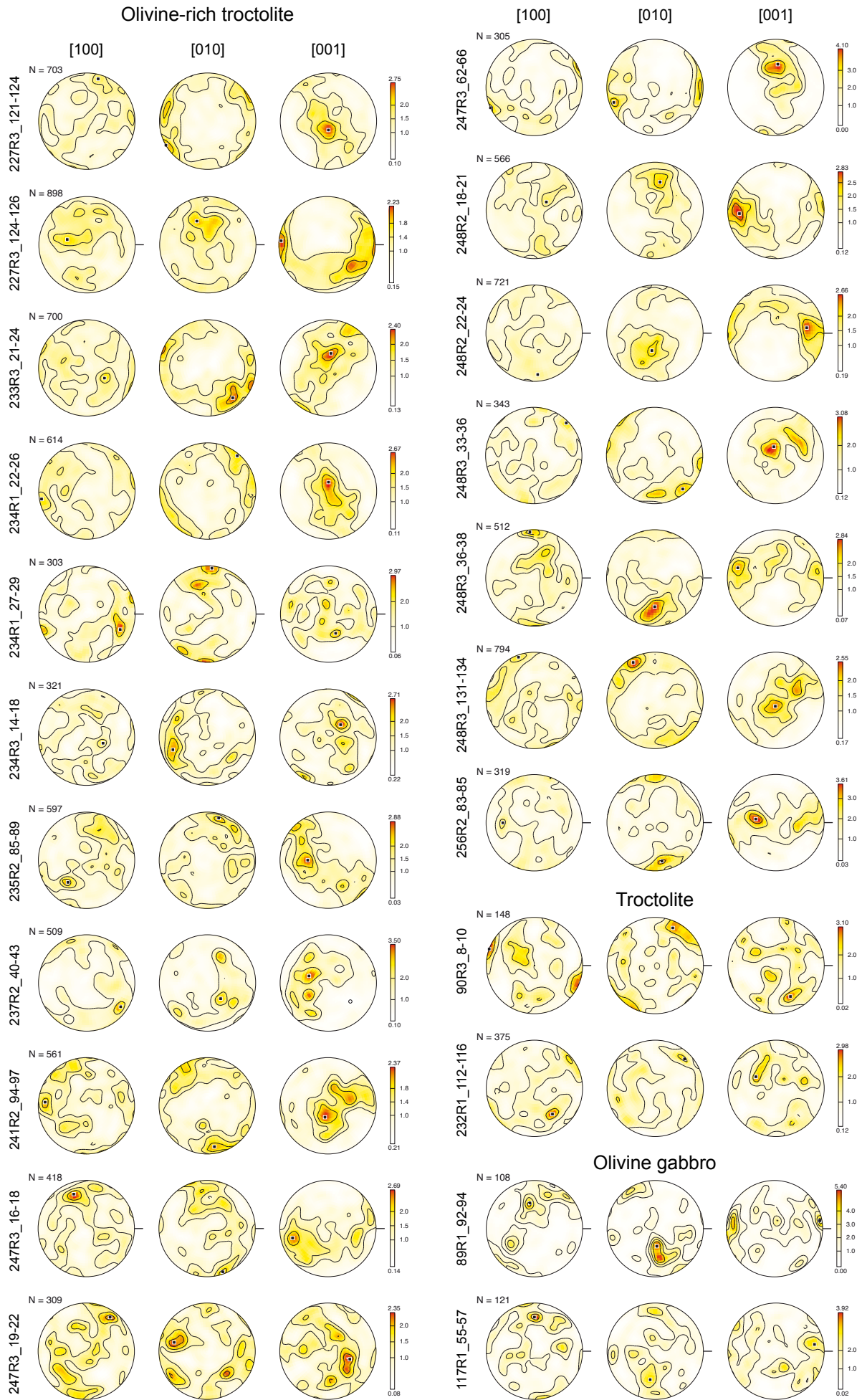
Drouin et al., Fig. 3



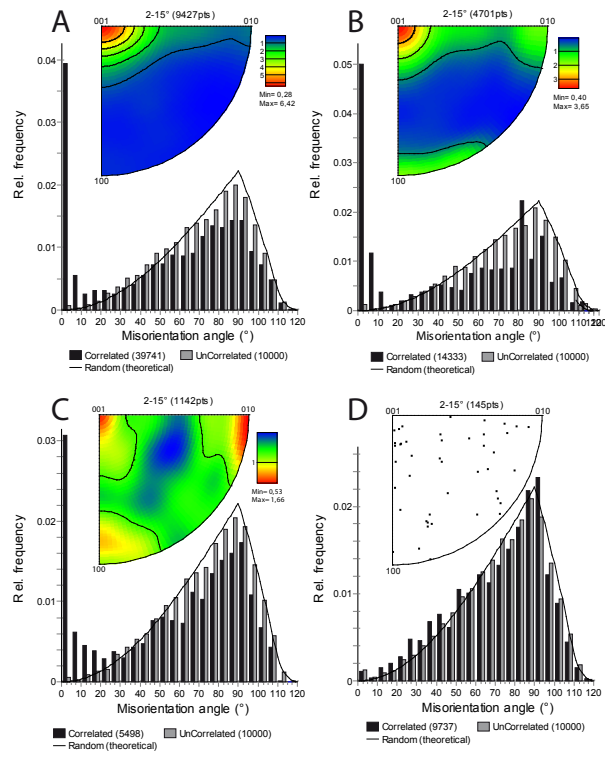
Drouin et al., Fig. 4



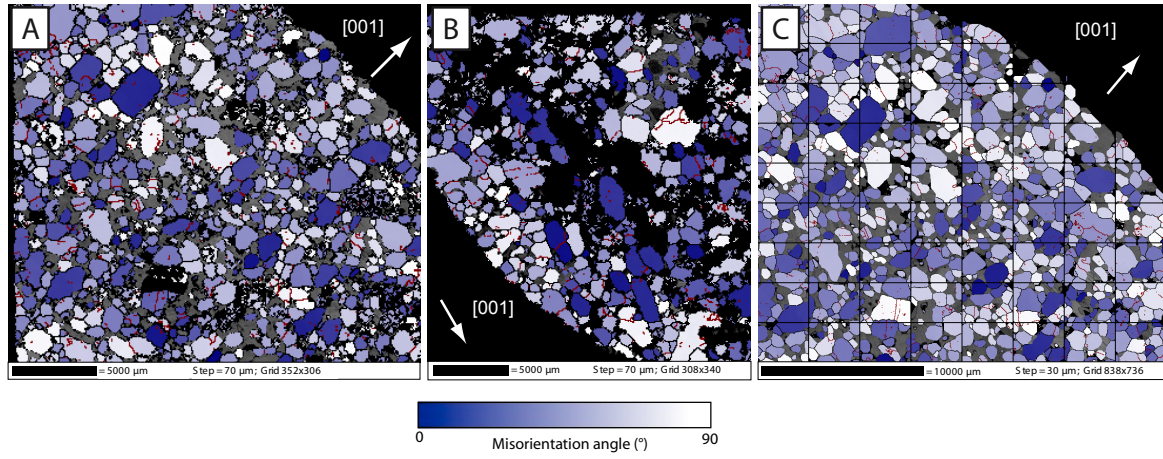
Drouin et al., Fig. 5



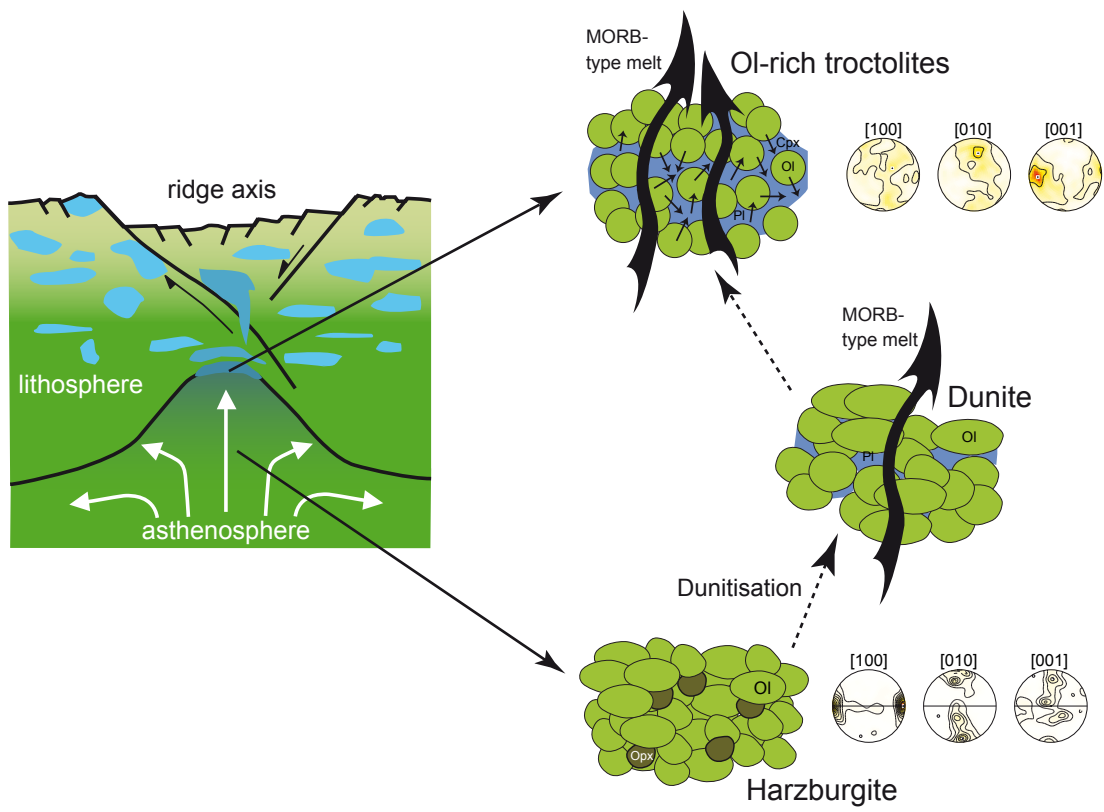
Drouin et al., Fig. 6



Drouin et al., Fig.7



Drouin et al., Fig. 8



Drouin et al., Fig. 9

Table 1

| Sample | Ol-rich zone | Depth (mbsf) | Rock type | J Index | | Misorientation (<15°) preferred rotation axis | Modal composition | | | | |
|---------------|--------------|--------------|--------------------|--------------------------------------|-------------------------------------|---|-------------------|------|-------|-------|------|
| | | | | Gridded data (1 meas. per grid node) | Detected grains (1 meas. per grain) | | % Ol | % Pl | % Cpx | % Opx | % Sp |
| 60R3_39-42 | 1 | 313.22 | Ol-rich troctolite | 10.87 | - | [010] | 70.5 | 13 | 16 | - | 0.5 |
| 70R2_99-103 | 1 | 359.68 | Troctolite | 6.83 | - | [010] & [001] | 58 | 39.5 | 2 | - | 0.5 |
| 89R1_92-94 | 1 | 444.72 | Ol-gabbro | 7.52 | 7.13 | [001] | 27 | 38 | 35 | - | 0 |
| 90R3_8-10 | 1 | 451.68 | Troctolite | 5.46 | 3.74 | [010] & [001] | 56 | 41.5 | 2 | - | 0.5 |
| 112R1_69-73 | 2 | 554.89 | Ol-rich troctolite | 6.46 | - | [001] | 77.5 | 20 | 2 | - | 0.5 |
| 117R1_55-57 | 2 | 578.75 | Ol-gabbro | 7.65 | 4.15 | [001] | 26 | 40 | 34 | - | 0 |
| 227R3_121-124 | 4 | 1096.14 | Ol-rich troctolite | 2.18 | 1.83 | undetermined | 72.5 | 13 | 14 | - | 0.5 |
| 227R3_124-126 | 4 | 1096.17 | Ol-rich troctolite | 1.67 | 1.61 | undetermined | 85 | 12 | 2.5 | - | 0.5 |
| 232R1_112-116 | 4 | 1116.22 | Troctolite | 3.57 | 2.35 | [001] ? | 59 | 36.5 | 4 | - | 0.5 |
| 233R3_21-24 | 4 | 1123.06 | Ol-rich troctolite | 1.63 | 1.75 | undetermined | 82 | 15 | 2.5 | - | 0.5 |
| 234R1_22-26 | 4 | 1124.92 | Ol-rich troctolite | 2.37 | 1.77 | [001] | 82 | 15 | 2.5 | - | 0.5 |
| 234R1_27-29 | 4 | 1124.97 | Ol-rich troctolite | 4.33 | 2.91 | [001] | 80 | 15 | 4.5 | - | 0.5 |
| 234R3_14-18 | 4 | 1127.74 | Ol-rich troctolite | 2.77 | 1.98 | [010] | 83 | 11.5 | 5 | - | 0.5 |
| 235R2_85-89 | 4 | 1131.61 | Ol-rich troctolite | 2.21 | 2.19 | undetermined | 82.5 | 11 | 6 | - | 0.5 |
| 237R2_40-43 | 4 | 1140.92 | Ol-rich troctolite | 2.69 | 3.02 | [001] | 81 | 14.5 | 4 | - | 0.5 |
| 241R2_94-97 | 4 | 1160.71 | Ol-rich troctolite | 2.11 | 1.88 | undetermined | 82 | 14.5 | 3 | - | 0.5 |
| 247R3_16-18 | 4 | 1190.05 | Ol-rich troctolite | 2.60 | 2.12 | [001] | 80 | 9 | 10.5 | - | 0.5 |
| 247R3_19-22 | 4 | 1190.08 | Ol-rich troctolite | 2.69 | 2.20 | [001] | 74.5 | 8 | 17 | - | 0.5 |
| 247R3_62-66 | 4 | 1190.51 | Ol-rich troctolite | 5.00 | 3.81 | [001] | 67.5 | 2 | 30 | - | 0.5 |
| 248R2_18-21 | 4 | 1193.32 | Ol-rich troctolite | 2.56 | 2.03 | [001] | 77 | 11.5 | 11 | - | 0.5 |
| 248R2_22-24 | 4 | 1193.36 | Ol-rich troctolite | 1.96 | 1.87 | [001] | 90 | 5 | 1.5 | 3 | 0.5 |
| 248R3_33-36 | 4 | 1194.82 | Ol-rich troctolite | 3.45 | 2.52 | [001] | 80 | 12 | 7.5 | - | 0.5 |
| 248R3_36-38 | 4 | 1194.85 | Ol-rich troctolite | 2.44 | 2.14 | [001] | 82 | 14.5 | 3 | - | 0.5 |
| 248R3_131-134 | 4 | 1195.80 | Ol-rich troctolite | 2.69 | 1.81 | [010] ? | 80 | 10.5 | 9 | - | 0.5 |
| 251R1_87-89 | 4 | 1207.17 | Troctolitic-gabbro | 8.94 | - | [001] | 40 | 55 | 5 | - | 0 |
| 256R2_83-85 | 4 | 1232.27 | Ol-rich troctolite | 3.04 | 3.03 | undetermined | 80 | 9 | 10.5 | - | 0.5 |
| 268R2_83-85 | - | 1290.06 | Ol-gabbro | 8.82 | 5.37 | undetermined | 10 | 55 | 35 | - | 0 |

V. Revue des fabriques cristallographiques de l'olivine dans la zone de transition manteau/croûte de l'ophiolite d'Oman

Nous avons vu dans le premier chapitre que l'augmentation de la fraction liquide au sein d'une matrice solide modifie les propriétés rhéologiques et la texture de cette dernière. L'étude microstructurale des troctolites riches en olivine du puits IODP U1309D montre que l'imprégnation magmatique modifie aussi les fabriques cristallographiques des olivines. L'argumentation est basée, entre autres, sur la similitude des textures et des fabriques cristallographiques des olivines entre les troctolites riches en olivine du puits IODP U1309D et les roches fortement imprégnées de la zone de transition manteau/croûte de l'ophiolite d'Oman (Nicolas & Prinzhofer, 1983; Boudier, 1991; Ceuleneer & Rabinowicz, 1992; Boudier & Nicolas, 1995; Joussetin et al., 1998; Dijkstra et al., 2002). Une revue de ces fabriques cristallographiques est présentée ici.

La zone de transition manteau /croûte à Maqсад dans l'ophiolite d'Oman est formée par 300 mètres de dunites interlitées avec des dunites imprégnées, des wehrlites, des lentilles de gabbros et des reliques de harzburgites, entre les harzburgites du manteau et les cumulats gabbroïques de la croûte (e.g., Boudier & Nicolas, 1995 ; Joussetin et al., 1998 ; Figure 2.20a et 2.21a). Certaines dunites imprégnées présentent une texture granulaire, avec des olivines polygonales ne présentant pas de sous-joints, entourées par des clinopyroxènes et des plagioclases interstitiels non-déformés (Figure 2.20b ; 90 OF 23, ID1). D'autres montrent des textures porphyroclastiques de haute température (Joussetin et al., 1998). Les wehrlites ont une texture poecilitique avec des olivines rondes entourées par des plagioclases et des clinopyroxènes interstitiels (Figure 2.20b ; 88 OF 5, W1). Les fabriques cristallographiques des olivines constituant les dunites imprégnées et les wehrlites sont faibles, désordonnées et montrent une distribution en guirlande sur l'axe [001] ; la linéation et la foliation sont difficiles à déterminer (Figure 2.20c et 2.21b). Les dunites imprégnées aux textures porphyroclastiques montrent une fabrique cristallographique de l'olivine modérée indiquant une déformation plastique avec l'activation du système de glissement de haute température (010) [100], communément décrit dans le manteau asthénosphérique (Figure 2.21b ; 95 OD 121). D'un point de vue général, les fabriques cristallographiques associées à la déformation plastique deviennent de plus en plus faibles et dispersées lorsque l'on passe des harzburgites mantelliques aux dunites de la zone de transition (Figure 2.22). Toutefois, les olivines

constituant ces dunites montrent souvent des sous-joints indiquant une déformation plastique de haute température (condition asthénosphérique) cohérente avec leur origine résiduelle. Les fabriques aléatoires des olivines constituant les dunites sont donc le résultat d'un fort rapport liquide/roche (supérieur à la fraction de liquide critique) qui a détruit la matrice solide mantellique et a dispersé les grains d'olivines dans le liquide basaltique imprégnant.

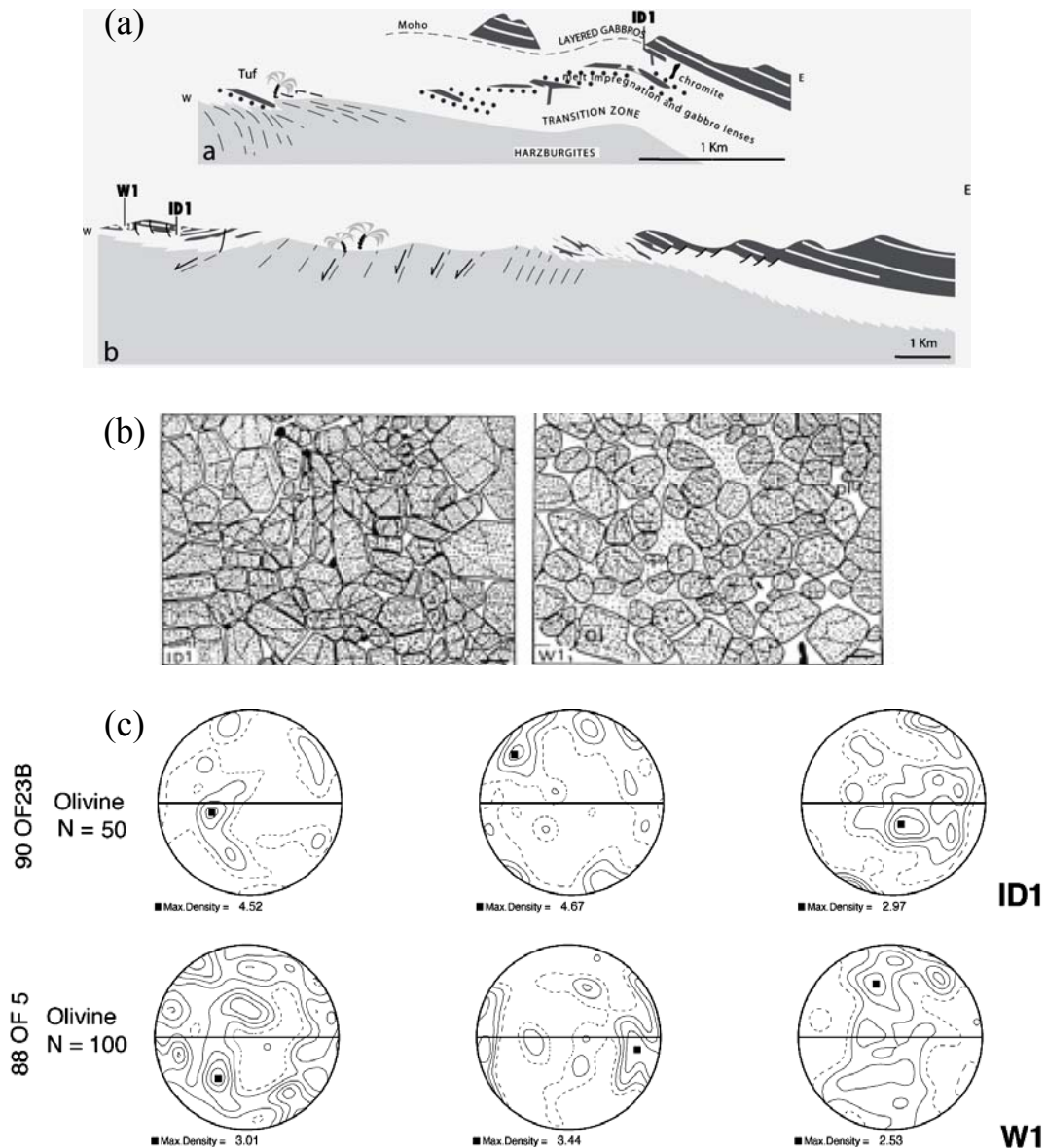


Figure 2.20: (a) Coupes dans la zone de transition manteau/croûte de Maqsad. La section mantellique est représentée en gris clair, les dunites en blanc, les gabbros en gris foncé, les points noirs marquent les amas irréguliers de plagioclase et de clinopyroxène. La localisation des échantillons de dunite imprégnée (ID1) et de wehrlite (W1) est aussi notée. (b) Textures des échantillons de dunite imprégnée (ID1) et de wehrlite (W1). (c) Fabriques cristallographiques de ces mêmes échantillons (Boudier & Nicolas, 1995).

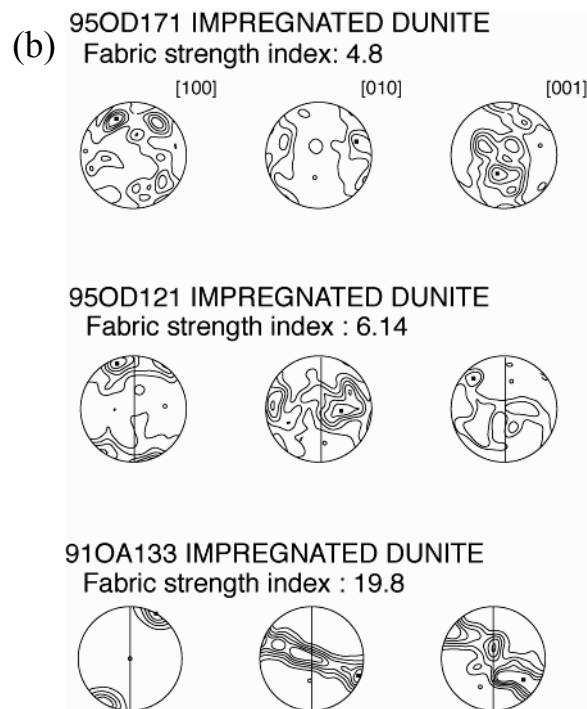
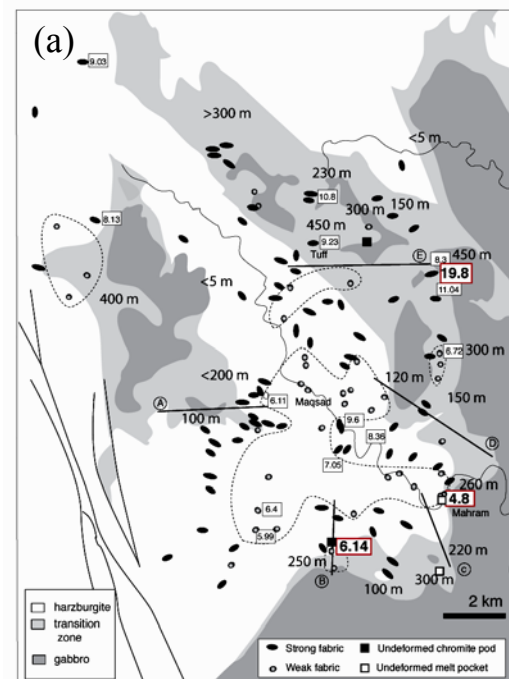


Figure 2.21 : (a) Carte de la zone de Maqsad (Ophiolite d'Oman) montrant la force des fabriques cristallographiques de 16 échantillons (marquées dans les rectangles). La zone de transition manteau/croûte est indiquée en gris claire, les gabbros en gris foncé et les harzburgites en blanc. (b) Exemples de fabriques cristallographiques des olivines de trois dunites imprégnées se situant à différents endroits dans la zone de transition manteau/croûte : cadre rouge sur la carte (Jousselin et al., 1998). L'échantillon 95 OD 171 provient d'une zone avec une forte imprégnation magmatique.

L'échantillon 95 OD 121 correspond à une dunite imprégnée présentant des textures porphyroclastiques de haute température.

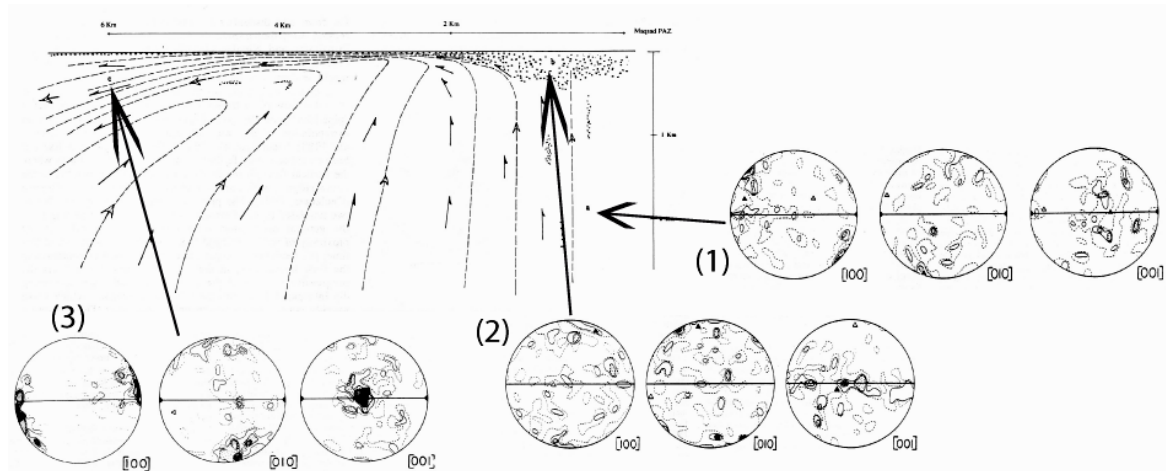


Figure 2.22 : Fabriques cristallographiques des olivines des péridotites de la zone de Maqsad dans l'ophiolite d'Oman (Ceuleneer & Rabinowicz, 1992). (1) Harzburgite dans la paléo zone de remontée asthénosphérique, (2) dunite de la zone de transition manteau/croûte, (3) Harzburgite dans la zone d'écoulement divergente.

La zone de transition manteau/croûte exposée dans la section mantellique de Hilti au nord de l'ophiolite d'Oman, est composée de wehrlites et de gabbros (Figure 2.23a ; Dijkstra et al., 2002). Les wehrlites sont formées de larges pœciloclastes de clinopyroxène et de plagioclase non-déformés qui sont le produit de la cristallisation fractionnée (Figure 2.23b). Les olivines, dans ces wehrlites, possèdent des fabriques cristallographiques faibles avec un maximum sur l'axe [001] et une distribution en guirlande sur cet axe (Figure 2.23c, échantillon A29). Ces fabriques cristallographiques contrastent avec celles des péridotites du manteau supérieur, montrant parfaitement une déformation plastique avec l'activation du système de glissement de haute température (010) [100], communément décrit dans le manteau asthénosphérique.

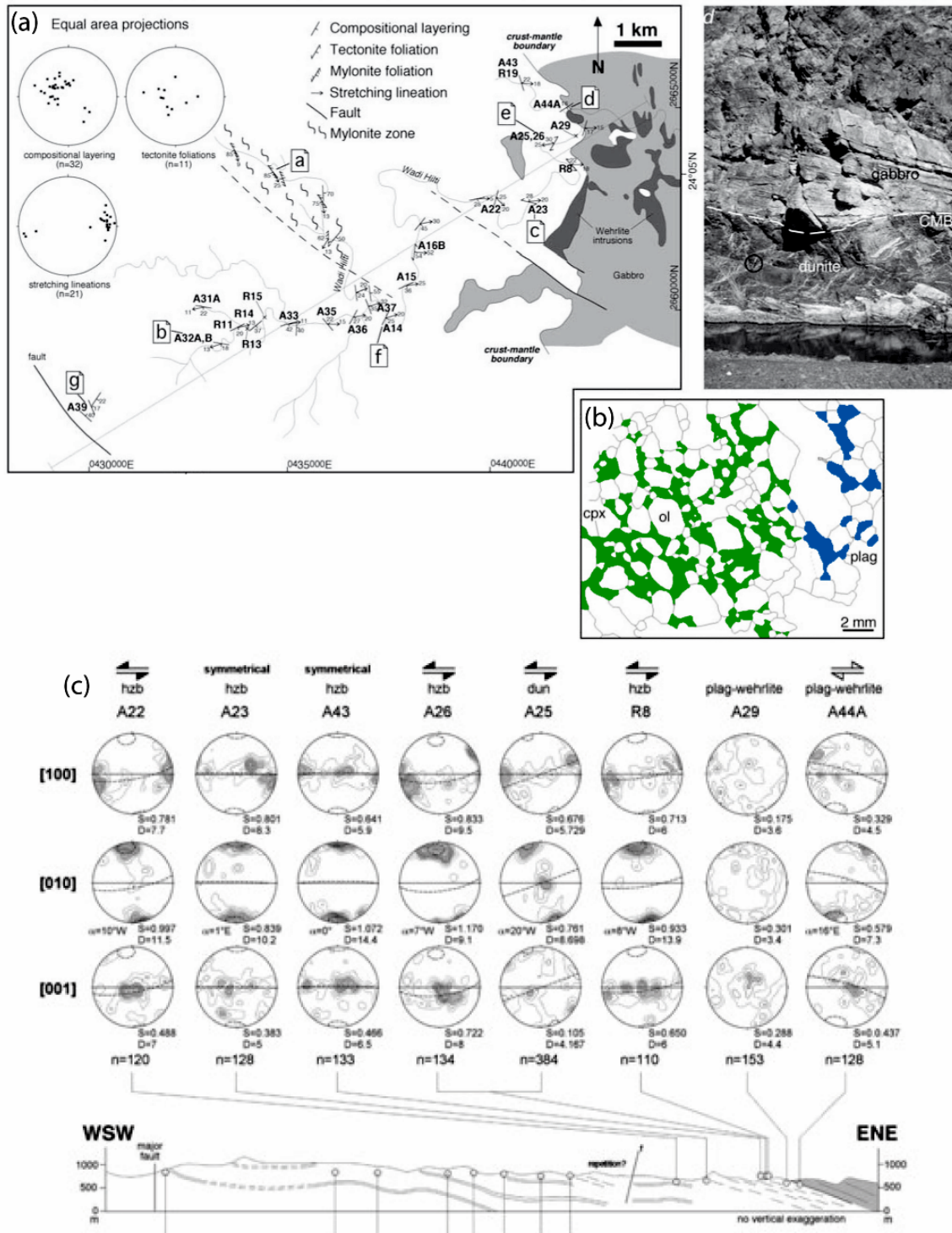


Figure 2.23 : (a) Carte de la section mantellique de Hilti dans l'ophiolite d'Oman montrant les données structurales et la localisation des échantillons (Dijkstra et al., 2002). Les wehrlites de la zone de transition manteau/croûte sont notées en gris foncé sur la carte. La photographie à droite de la carte montre la limite manteau/croûte (Crust-Mantle Boundary). (b) Texture de l'échantillon de wehrlite A29 : péciloblastes de clinopyroxène (vert) et de plagioclase (bleu). (c) Fabriques cristallographiques des olivines des péridotites du manteau supérieur et des wehrlites de la zone de transition manteau/croûte de la section mantellique de Hilti (figures extraites de Dijkstra et al., 2002).

Les textures des roches présentes dans ces zones de forte imprégnation magmatique sont similaires à celles des troctolites riches en olivine du puits IODP U1309D, avec des clinopyroxènes et plagioclases interstitiels à poeciloblastique et non-déformés. L'olivine se présente sous forme de cristaux communément polygonaux avec quelques sous-joints ou sous forme de cristaux arrondis (e.g., échantillon 88OF5, Figure 2.20b). Les fabriques cristallographiques des olivines présentes dans les wehrlites et les dunites imprégnées de la zone de transition manteau/croûte de l'ophiolite d'Oman sont plus faibles et plus dispersées que celles des péridotites asthénosphériques mesurées dans la même ophiolite. À la différence des fabriques étudiées dans le puits U1309D, celles-ci ne montrent pas systématiquement de maximum sur [001]. Cependant, elles présentent fréquemment une distribution en guirlande sur cet axe, comme les troctolites riches en olivine du puits IODP1309D. Une très grande similitude existe entre ces péridotites imprégnées et les troctolites riches en olivine du puits U1309D d'un point de vue aussi bien textural que microstructural, appuyant l'hypothèse proposée dans la quatrième partie de ce chapitre d'une origine résiduelle pour les troctolites riches en olivine.

VI. Conclusion

L'origine, résiduelle ou magmatique, des roches riches en olivine telles que les dunites, wehrlites et troctolites associées à des péridotites mantelliques dans les zones de transition manteau/croûte des ophiolites (e.g., Nicolas & Prinzhofer, 1983 ; Boudier ; 1991 ; boudier & Nicolas, 1995) ou des dorsales rapides (e.g. Cannat et al., 1990 ; Allan & Dick, 1996; Arai & Matsukage, 1996; Dick & Natland, 1996 ; Constantin, 1999) est depuis longtemps très controversée. Ce débat a concerné aussi les dunites en enclave dans les basaltes alcalins des îles océaniques (Berger & Vannier, 1984 ; Nicolas, 1985) ou bien les lherzolites à plagioclase de la dorsale Médio-Atlantique (Girardeau & Mercier, 1992 ; Girardeau & Francheteau, 1993). Ces différents auteurs ont tous proposé une origine mantellique pour ces roches riches en olivine considérée auparavant comme des cumulats. Cette affirmation, plus ou moins tranchée selon les auteurs, repose sur des arguments texturaux, structuraux et géochimiques comme :

- (1) La texture poecilitiques ou pénétrative de ces roches avec des clinopyroxène et/ou des plagioclases interstitiels ou poecilitiques qui ont cristallisé dans l'espace poreux entre les grains d'olivine.
- (2) La présence d'olivines corrodés, déformées plastiquement et entourées par des clinopyroxènes ou/et des plagioclases non-déformés.
- (3) Les fortes teneurs en Ni (0,29-0,38 % NiO) associées aux faibles Mg# (87-88) des olivines.

Il est vrai que la présence de minéraux résiduels au sein d'un magma est très difficile à prouver, en raison de la rééquilibration, souvent complète, des cristaux avec le liquide l'entourant. En effet, les éléments diffusant rapidement comme le fer et le magnésium se rééquilibrent rapidement avec le magma. Certaines roches ne conservent plus de reliques de la composition résiduelle de départ, et présentent donc toutes les caractéristiques chimiques d'un cumulat ultrabasique (i.e., faible concentration en Ni et Mg des olivines par rapport aux olivines mantelliques). De même, la texture ne permet pas vraiment de distinguer les cumulats des roches mantelliques fortement imprégnées par des magmas basaltiques puisque dans les deux cas ces processus forment des roches avec une texture poecilitique de type hétéradcumulat. Cependant d'autres outils comme l'analyse de la microstructure des minéraux, et notamment l'étude des fabriques cristallographiques de l'olivine ou l'analyse chimique in-situ des minéraux peuvent apporter des éléments de réponse à ce débat.

Les troctolites riches en olivine du puits IODP U1309D, de composition chimique très primitive, ont aussi été interprétées, dans un premier temps, comme des roches cumulatives. Cette interprétation est principalement due à leur présence au sein d'une série gabbroïque importante et à leur texture d'hétéradcumulat (Blackmann et al., 2006). Toutefois, dans ces troctolites riches en olivine, seules les olivines sont déformées plastiquement, ce qui exclut une origine magmatique commune entre ces minéraux et les plagioclases/clinopyroxènes. De plus, la texture de ces roches avec de larges plages de clinopyroxène et de plagioclase englobant des olivines corrodées et la géochimie in-situ indiquent que ces roches se sont formées au moins en deux étapes : (1) la cristallisation d'une matrice d'olivine, (2) l'imprégnation et la corrosion de cette matrice par un liquide basaltique de type MORB cristallisant des cristaux poecilitiques de clinopyroxènes et de plagioclases. La pétrogenèse de ces roches apparaît donc complexe : représentent-elles des cumulats primitifs à la base d'intrusions gabbroïques ou des fragments de manteau fortement imprégné dans une pile de petites intrusions gabbroïques ?

Les troctolites riches en olivine : des cumulats primitifs ?

Certains auteurs (Dick; 1989; Bloomer et al., 1989 ; Dick et al., 2000 ; Coogan et al., 2001) ont montré que les roches riches en olivines qui sont largement observées dans les zones de transition des ophiolites sont généralement absentes des échantillonnages effectués par forage sur les dorsales lentes. Pourtant, la présence de ces cumulats primitifs est requise pour produire la composition des MORBs que l'on observe en surface. Du fait de leur caractère très primitif, les troctolites riches en olivines du puits IODP U1309D pourraient représenter ces cumulats « manquants ». La matrice d'olivine composant les troctolites riches en olivine pourrait être un cumulat ultrabasique formé avant l'emplacement du corps gabbroïque composant le site U1309, puisque les contacts entre les différentes lithologies suggèrent que les gabbros sont généralement intrusifs dans les lithologies riches en olivines. Ce cumulat primitif aurait été, par la suite, imprégné par un liquide basaltique de type MORB à l'origine de la série gabbroïque du Site U1309. La déformation en base de croûte de ces cumulats primitifs pourrait expliquer la déformation plastique de haute température observée dans les olivines des troctolites riches en olivine (e.g., Boudier et al., 1996; Dick et al., 1999; Yoshinobu and Hirth, 2002).

Toutefois, les compositions très primitives en éléments majeurs (Fo= 82-88 et Ni= 1440-2300 ppm) et les teneurs très faibles en éléments en trace des olivines des troctolites riches en olivines ne sont pas en accord avec une cristallisation fractionnée à partir d'un liquide de type MORB (Drouin et al., accepté). Leur composition indiquerait qu'elles se soient formées à partir de magmas très magnésiens (> 12 % MgO). La production de tels magmas est associée à des taux de fusion partielle très élevés (~30%) d'un manteau très chaud (température potentielle > 1500°C) comme il a été démontré par Fitton & Godard (2004) pour les laves très magnésiennes du plateau d'Ontong Java dans le Pacifique Ouest. Les minéraux des gabbros échantillonnés au puits IODP U1309D sont en équilibre chimique avec des liquides de type MORB. De même, les basaltes du puits IODP U1309D ont des compositions typiques de N-MORB avec des teneurs en MgO d'environ 8% similaires aux basaltes échantillonnés à 30°N (Godard et al., 2000). Ces observations indiquent plutôt des taux de fusion partielle du manteau de l'ordre de 10% au niveau du Massif Atlantique en contradiction avec la formation de magma très magnésien. La production de ces magmas est généralement associée à des contextes géologiques de type points chaud (e.g., Herzberg & O'Hara, 1998) ou province basaltique continentale (e.g., Fitton & Godard, 2004). La présence de magma aussi magnésien est inconnue jusqu'à présent au niveau des rides océaniques.

Les troctolites riches en olivine : des roches mantelliques fortement imprégnées ?

La texture des troctolites riches en olivine du puits IODP U1309D est très similaire à celle des dunites et wehrlites de l'ophiolite d'Oman, interprétées comme des péridotites mantelliques imprégnées par des liquides basaltiques (e.g., Nicolas and Prinzhofer, 1983; Boudier, 1991; Boudier and Nicolas, 1995). Dans ces dunites imprégnées, une structure semblable aux cumulats ultrabasiques peut être créée par corrosion des olivines résiduelles qui produit des faces automorphes (e.g., Donaldson, 1985 ; Nicolas, 1985 ; Boudier, 1991). De plus, les fabriques cristallographiques des olivines des troctolites riches en olivines montrent une grande similitude avec celles des péridotites imprégnées de la zone de transition de l'ophiolite d'Oman.

L'interaction entre un liquide basaltique et une péridotite entraîne des variations importantes de compositions de leurs minéraux. Ainsi la plupart des roches mantelliques imprégnées dans les ophiolites (e.g., Rampone et al., 1997, 2008; Koga et al., 2001; Dijkstra et al., 2003; Borghini et al., 2007), ou bien sur les dorsales (e.g., Hébert et al., 1983; Dick, 1989; Cannat et al., 1990; Allan & Dick, 1996; Arai & Matsukage, 1996; Dick & Natland, 1996; Seyler & Bonatti, 1997; Kamenetsky & Crawford, 1998; Tartarotti et al., 2002) sont caractérisées par des olivines enrichies en Fe, des clinopyroxènes enrichies en Ti et des spinelles enrichies en Cr et en Ti. Les minéraux des troctolites riches en olivine partagent les mêmes caractéristiques chimiques que ces roches mantelliques imprégnées.

La texture, la microstructure et la composition chimique des phases minérales des troctolites riches en olivine indiquent plutôt une origine mantellique pour ces roches. Les olivines représentent des phases résiduelles plus ou moins modifiées chimiquement. Cependant, la formation de ces roches requiert l'interaction avec un grand volume de magma. Dans le puits IODP U1309D, la faible teneur en Fo des olivines et la présence de spinelles chromifères riches en Ti dans les péridotites indiquent que ces péridotites ont interagi avec de larges volumes de liquide basaltique (Tamura et al., 2007). Il est possible que certaines olivines dans les troctolites riches en olivine aient précipité directement à partir d'un magma basaltique. La mesure des concentrations en éléments en trace des olivines dans un plus grand nombre de troctolites riches en olivine ainsi que dans les troctolites et gabbros à olivine adjacents est donc requise.

Chapitre 3

Étude géochimique in-situ des roches gabbroïques du Site ODP 1275 (Leg ODP 209, dorsale Médio-Atlantique 15°N)

I. Introduction

Le leg ODP 209 s'est déroulé entre 14°43' et 15°44' N le long de la dorsale Médio-Atlantique en 2003. Le but de cette campagne était d'échantillonner des péridotites mantelliques le long de l'axe de la dorsale, à des distances variables par rapport à la zone de fracture 15°20'N, pour tester la variabilité de la composition et de la structure du manteau le long de l'axe (Kelemen et al., 2004). En effet, dans cette région, les péridotites mantelliques affleurent relativement bien le long de la dorsale. De plus, cet endroit se distingue par une forte anomalie négative de gravité (e.g., Escartin et Cannat, 1999; Fujiwara et al., 2003), une anomalie chimique de type « point chaud » centrée à 14°N (Dosso et al., 1991, 1993 ; Bonatti et al., 1992 ; Cannat et al., 1992), et des structures de core complexes océaniques qui sont interprétées comme de grandes failles de détachement exhument les roches de la lithosphère profonde (Escartin & Cannat, 1999 ; MacLeod et al., 2002 ; Escartin et al., 2003; Fujiwara et al., 2003; Smith et al., 2006). 19 puits ont été forés sur 8 sites différents le long de la dorsale (Figure 3.1; Kelemen et al., 2004). Je me suis particulièrement intéressée au Site 1275 qui se distingue des autres sites par la présence de roches gabbroïques en grande quantité (Figure 3.1), comme nous avons pu l'observer dans le puits IODP U1309D (Blackman et al., 2006; Ildefonse et al., 2007). De plus ce site de forage est le seul effectué dans un core complexe océanique dans cette zone de la dorsale médio-Atlantique.

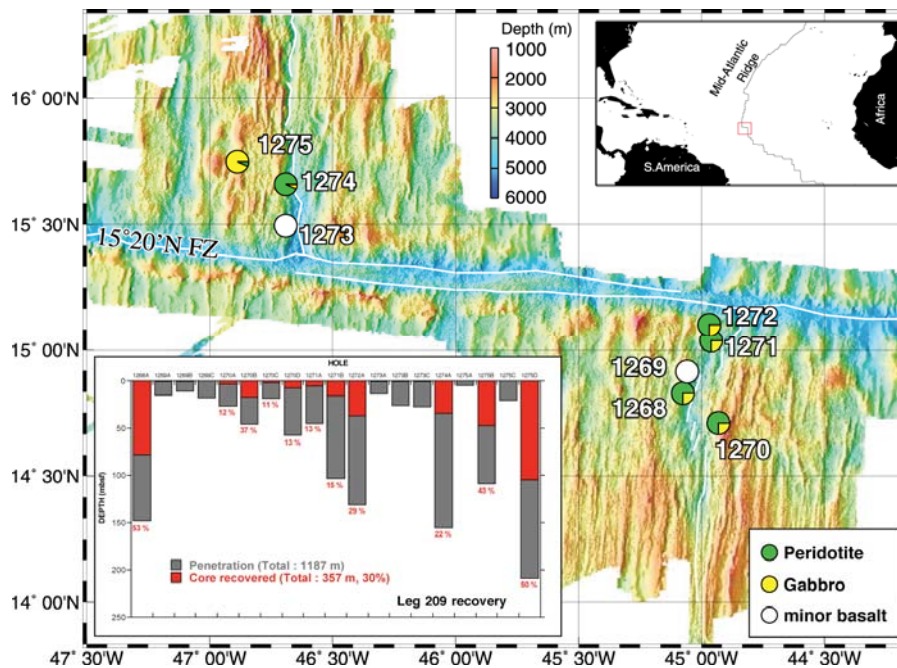


Figure 3.1: Localisation des différents sites forés lors du Leg ODP 109 et proportion de chaque lithologie échantillonnée pour les différents sites du Leg ODP 209 (d'après Kelemen et al., 2004). La bathymétrie est tirée de Fujiwara et al. (2003). Le cadre en bas à gauche indique la profondeur de chaque puits foré lors du Leg ODP 209 et la proportion de roches récupérées en mètres et en pourcentage dans ces différents puits.

Lors de la campagne JR63 (Avril-Mai 2001 ; MacLeod et al., 2002), la surface cannelée (cf. chapitre 1) de ce core complexe océanique a été échantillonnée par carottages (carottes orientées d'environ 1 m de longueur, prélevées grâce à l'outil de forage en fond de mer BRIDGE Drill) et de dragages (Figure 3.2). Des péridotites, des gabbros et des diabases plus ou moins altérés et déformés ont été récupérés (MacLeod et al., 2002 ; Escartin et al., 2003). Les roches fortement déformées (mylonites) sont très présentes au sommet de la surface cannelée et sur ses flancs (Figure 3.2). L'analyse de la distribution spatiale des différentes lithologies indique la présence d'un pluton gabbroïque de plus de 2 km, juste sous le détachement (MacLeod et al., 2002, Escartin et al., 2003).

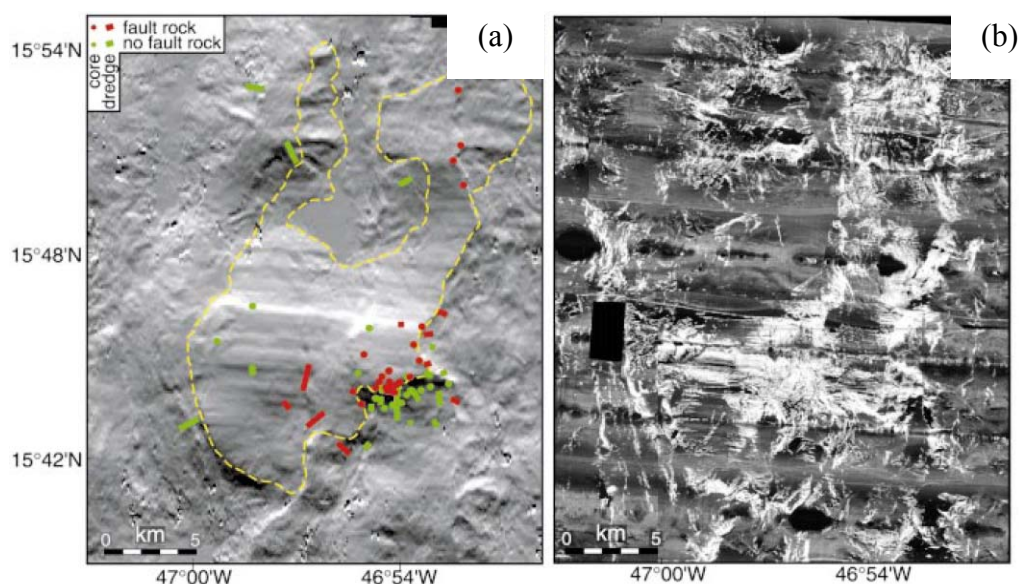


Figure 3.2: (a) Localisation des sites de carottage (cercles) et de dragages (barres) sur le « core complexe » océanique à 15°45'N effectués lors de la campagne océanographique JR63 (MacLeod et al., 2002). Les couleurs indiquent la présence (rouge) ou l'absence (vert) de roches fortement déformées. La surface cannelée est indiquée en trait discontinu jaune. (b) Image sonar présentant la surface cannelée du « core complexe » océanique. La longueur d'onde des cannelures est de l'ordre de quelques kilomètres à quelques centaines de mètres (MacLeod et al., 2002).

Lors du Leg ODP 209, 4 forages ont été réalisés sur le Site 1275, dont deux (1275B et 1275D) atteignent les profondeurs de 108,7 et 209 mbsf. Le puits 1275B est composé de 85.1% de gabbros et 5.5% de troctolites (terme englobant les lithologies suivantes : wehrlite, dunite, troctolite); les diabases et granophyres constituent quant à eux, respectivement 8.6% et 0.8% du volume total échantillonné. Le terme granophyre est utilisé ici pour désigner des roches qui sont composées principalement de feldspath et de quartz. Le puits 1275D est constitué de 64.4% de gabbros, 18.3% de troctolites et 4.7% de gabbros à olivine ; les diabase et les granophyres constituent respectivement 10.5% et 2.1% du volume total échantillonné. Les troctolites sont coupées par des filons et des veines (échelle centimétrique) gabbroïques ou felsiques.

Les troctolites sont composées d'olivine, d'orthopyroxène, de clinopyroxène, de plagioclase et de spinelle chromifère. Basées sur l'analogie avec les péridotites abyssales, ces troctolites ont été interprétées comme étant le produit de l'interaction d'un liquide basaltique interstitiel avec une péridotite (Shipboard Scientific Party, 2004a). Ce liquide magmatique en réagissant avec l'olivine le long des joints de grain a isolé ces dernières au sein d'une matrice gabbroïque. La cristallisation contemporaine du matériel gabbroïque entre les cristaux d'olivine et dans les gabbros séquents est démontrée par la croissance des pyroxènes

poecilitiques à travers le contact gabbro-troctolite. Les troctolites et les gabbros associés forment la roche hôte dans laquelle le liquide parent des gabbros à oxyde a été injecté. Les granophyres sont étroitement associés aux gabbros à oxyde et peuvent représenter le produit extrême de la cristallisation fractionnée.

Pour ce qui est des compositions des roches totales en éléments majeurs et en trace, trois groupes de roches sont distinguables au site 1275 : les troctolites d'une part, et deux groupes de roches gabbroïques d'autre part (groupe 1 : diabases et microgabbros, groupe 2 : gabbros à gros grains; Figure 3.3; Shipboard Scientific Party, 2004a). Les troctolites se distinguent par un Mg# élevé (87-89) comparé aux autres échantillons du Site 1275. Leur teneur en Ni et Cr est proche de celle des péridotites du Leg 209 (Figure 3.3). Le groupe 1 des roches gabbroïques possède des compositions chimiques semblables aux basaltes des dorsales océaniques alors que le groupe 2 présente des compositions plus évoluées avec des concentrations en MgO plus faible et des concentrations en Fe₂O₃ et TiO₂ plus élevées (Shipboard Scientific Party, 2004a).

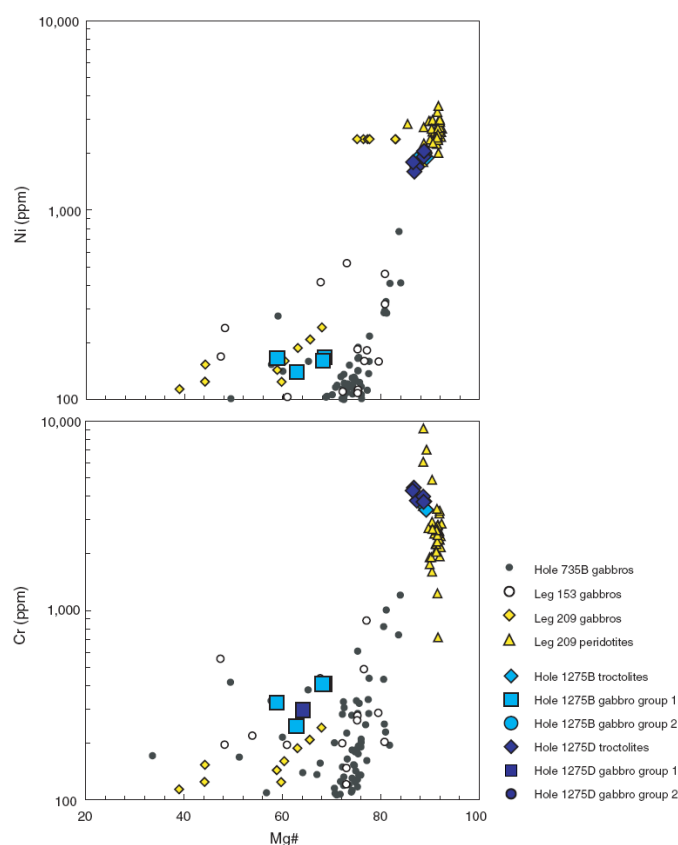


Figure 3.3: Teneur en Ni (ppm) et en Cr (ppm) en fonction du Mg# (données roche totale) dans les gabbros et les troctolites du Site ODP 1275 (Kelemen et al., 2004). Les données suivantes sont reportées en comparaison : Gabbros et péridotites du Leg 209 (Kelemen et al., 2004), gabbros du Leg ODP 153 (Agar al., 1997), gabbros du puits ODP 735B (Dick et al., 1999).

Mon étude pétro-géochimique du puits IODP U1309D à 30°N sur la dorsale Médio-Atlantique (chapitre 2 ; Drouin et al., accepté) a porté essentiellement sur le terme le plus primitif de la série gabbroïque, et m'amène, conjointement aux arguments pétrostructuraux (chapitre 2, Drouin et al., soumis), à proposer une origine mantellique pour ces troctolites riches en olivine. Le Site 1275 comprend aussi des roches riches en olivines, malheureusement celles-ci sont fortement altérées, rendant l'analyse chimique in-situ sensiblement plus difficile. Ces roches sont très similaires aux troctolites riches en olivine du puits U1309D, par leur texture (cristaux de clinopyroxènes et/ou d'orthopyroxènes et plagioclases interstitiels ou poecilitiques englobant des olivines résorbées) et leurs compositions chimiques très primitives. 55 échantillons (41 gabbros à oxyde, 6 troctolites, 5 gabbros à olivine, 2 gabbros et 1 veine felsique) ont été collectés le long des deux puits 1275B et 1275D (Figure 3.4) afin de déterminer la composition en éléments majeurs de leurs minéraux. Trois échantillons de gabbros à oxyde, représentant le terme le plus évolué de la série gabbroïque qui compose le Site 1275, ont aussi été sélectionnés pour l'analyse in-situ des éléments en trace. Ces roches évoluées amènent conjointement aux troctolites primitives, d'autres éléments sur le type de magmatisme associé au développement d'une lithosphère hétérogène. Je présente ci-dessous les premiers résultats de cette étude, réalisée en collaboration avec Carlos Garrido, et qui ont fait l'objet d'un résumé à l'EGU (Garrido et al., 2006).

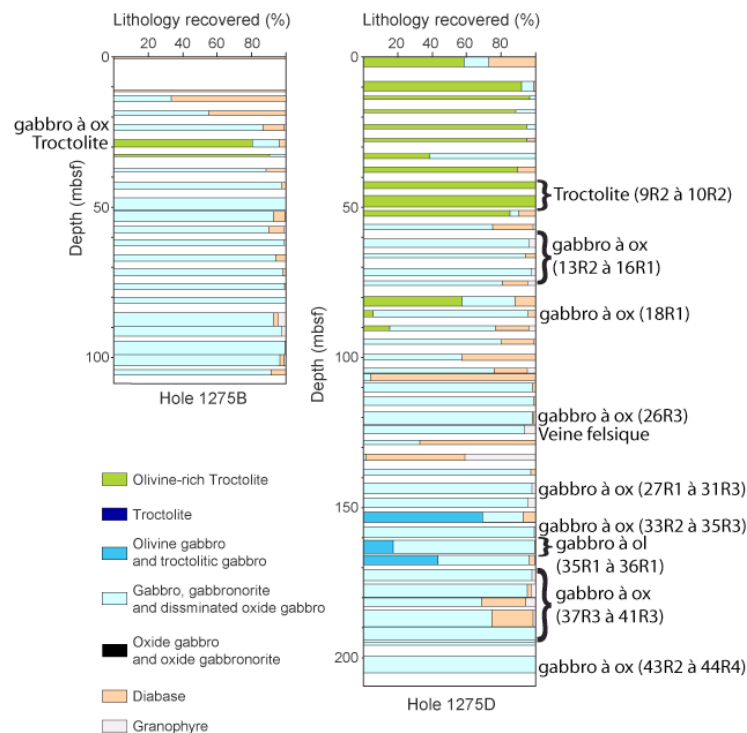


Figure 3.4: Proportion de chaque lithologie échantillonnée dans les puits ODP 1275B et 1275D (shipboard Scientific Party, 2004a) et localisation des échantillons analysés.

II. Description pétrologique des roches gabbroïques du site 1275

1. Les gabbros à oxyde

Les gabbros à oxyde sont composés de 5 à 15 % d'oxydes, 30 à 50% de plagioclases et 45 à 65% de clinopyroxènes. Ces roches présentent ou une texture grenue avec des minéraux majoritairement de grande taille (>4mm) ou une texture microgrenue (Figure 3.5a et b). Les plagioclases sont de deux types : certains sont xénomorphes, de grande taille, en latte ou trapus (Figure 3.5b) ; d'autres sont de petite taille, résorbés avec un contour dentelé (Figure 3.5a). De nombreuses microfractures, contenant des amphiboles vertes, recoupent ces minéraux. Les pyroxènes sont fortement altérés et souvent interstitiels. Les orthopyroxènes (hyperstène), majoritaires, sont de grande taille, à l'équilibre avec les clinopyroxènes, et présentent parfois des lamelles d'exsolution de clinopyroxène. Certains gabbros à oxyde ne contiennent cependant pas d'orthopyroxènes. Les oxydes sont interstitiels et/ou poecilitiques, parfois résorbés et souvent associés à de l'amphibole brune (Figure 3.5a). L'apatite est aussi présente en tant que minéral accessoire.

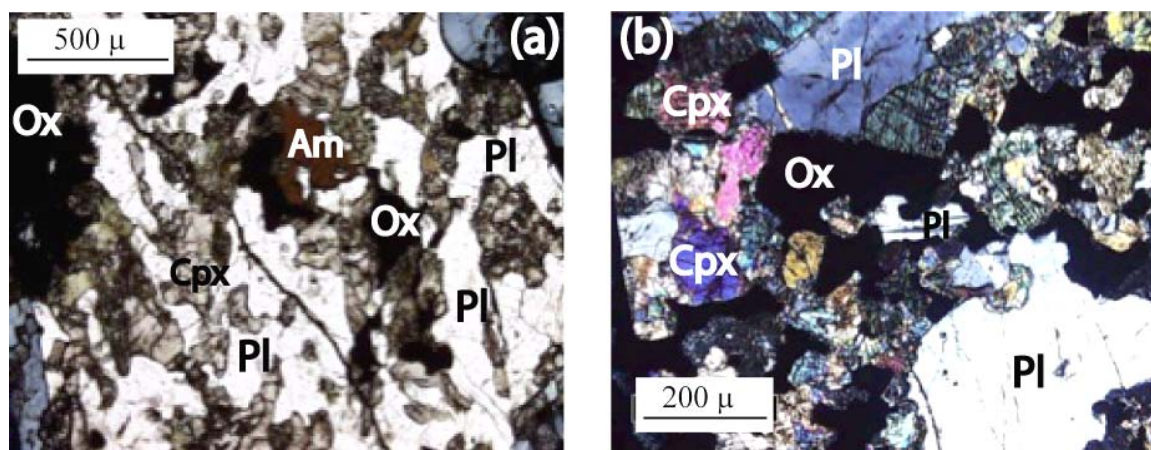


Figure 3.5 : Vues au microscope optique en lumière polarisée de la texture et de la minéralogie des gabbros à oxyde du Site 1275. (a) Cristaux de plagioclase et de clinopyroxène résorbés et cristaux d'oxyde résorbés associés à de l'amphibole brune dans un gabbro à oxyde à texture microgrenue (échantillon 1275D_27R1_133-145). (b) Cristaux de plagioclase, xénomorphes, en latte ; cristaux d'oxyde poecilitiques et cristaux de clinopyroxène résorbés dans un gabbro à oxyde à texture microgrenue (échantillon 1275D_26R3_112-120).

2. Les gabbros à olivine

Les gabbros à olivine sont composés de 5 à 20% d'olivines, 15 à 50% de clinopyroxènes, 5% d'orthopyroxènes et 20 à 60% de plagioclase. Ces roches ont des grains fins (texture microgrenue) à moyens (millimétrique). Les plagioclases, souvent très altérés, sont résorbés, et parfois interstitiels (Figure 3.6a). Les olivines sont plus ou moins arrondies et résorbées au contact du plagioclase, de l'orthopyroxène et du clinopyroxène (Figure 3.6b). Les clinopyroxènes sont interstitiels, mais peuvent parfois se présenter sous forme de cristaux pœcilitiques qui englobent les plagioclases (Figure 3.6a). Deux types d'orthopyroxènes sont présents dans les gabbros à olivine, n'ayant pas la même texture que ceux des troctolites riches en olivine du puits IODP U1309D. Le premier type regroupe des cristaux d'orthopyroxènes interstitiels à la bordure des olivines ou pœcilitiques entourant des cristaux de plagioclases et de clinopyroxènes résorbés ; le deuxième groupe est formé par des orthopyroxènes tardifs avec des lamelles d'exsolution de clinopyroxène le long de leurs plans de clivage et des inclusions globuleuses d'olivine (Figure 3.6d et schéma en Figure 3.7). Les orthopyroxènes du deuxième type semblent s'être développés au dépend des olivines. L'orthopyroxène est le résultat de la réaction olivine plus liquide (riche en eau; e.g., Kelemen et al., 1998 ; Smith et al., 1999 ; Arai et al., 2003). L'eau pourrait provenir du magma qui en fin de cristallisation va réagir avec l'olivine pour former des orthopyroxènes. Bien sûr, cette hypothèse est valable si le système reste fermé. Les oxydes sont interstitiels, et apparaissent donc comme tardifs et probablement liés aux orthopyroxènes. L'amphibole brune est aussi présente sous forme interstitielle, souvent associée aux oxydes (Figure 3.6c).

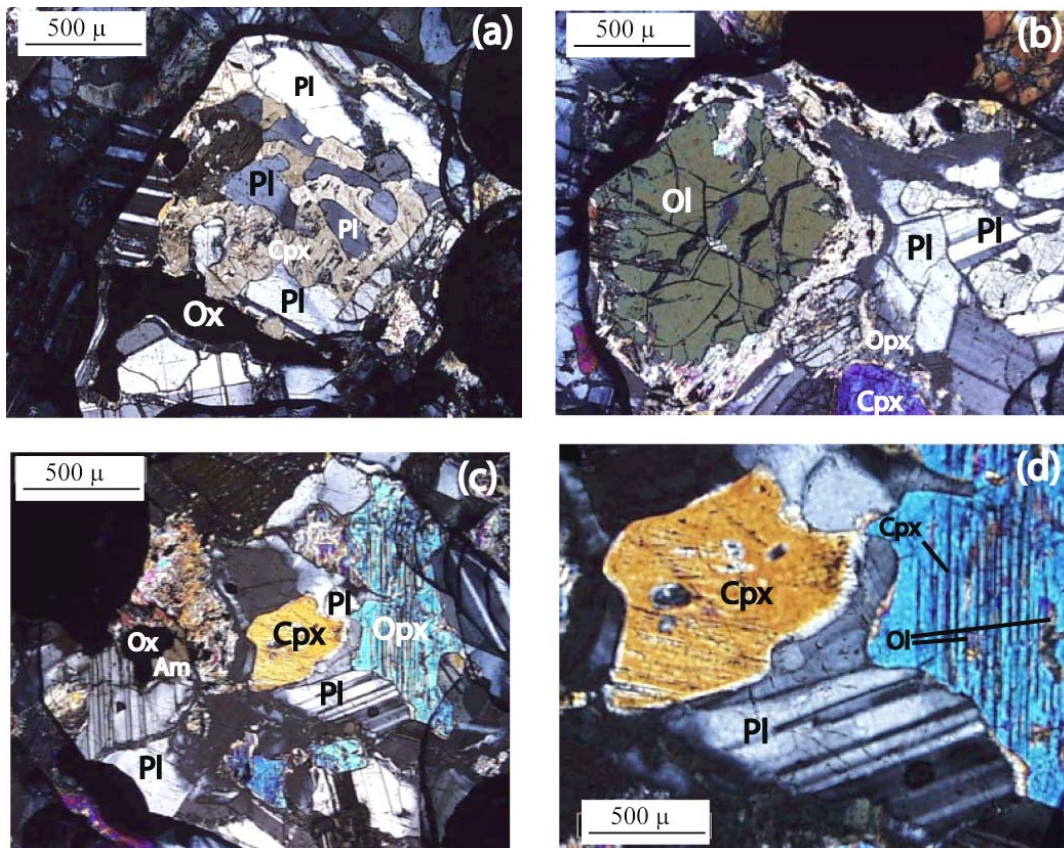


Figure 3.6 : Vues au microscope optique en lumière polarisée de la texture des gabbros à olivine du Site 1275 (échantillon 1275D_35R4_28-35). (a) Cristaux de plagioclase résorbés au sein d'un clinopyroxène. (b) Cristal d'olivine arrondi entouré par des plagioclases et des pyroxènes. (c) Amphibole brune associé à un oxyde, clinopyroxène, orthopyroxène et plagioclase montrant des textures résorbées. (d) Cristal d'orthopyroxène montrant des lamelles d'exsolution de clinopyroxène le long de ses plans de clivages et des inclusions d'olivines globuleuses (voir détail figure 5.7)

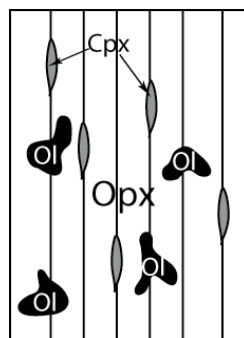


Figure 3.7 : Schéma représentant un orthopyroxène tardif, dans un gabbro à olivine, qui s'est développé au dépend de l'olivine comme le montrent les inclusions globuleuses d'olivines au sein du cristal d'orthopyroxène. Des exsolutions de clinopyroxènes sont aussi présentes le long des plans de clivages.

3. Les troctolites

Les troctolites sont composées 75 à 90% d'olivines, 5 à 10% de plagioclases et 5 à 10% de clinopyroxènes. Ces roches sont constituées de minéraux de taille moyenne (1 à 4 mm) et sont fortement altérées. L'olivine, fortement serpentinisée, se présente sous la forme d'agrégats de cristaux subautomorphes de 0,5 à 1 mm ou de cristaux arrondis et corrodés (Figure 3.8a). Les plagioclases de 0,5 à 4 mm sont très altérés et présentent une texture amiboïdale similaire aux textures d'imprégnation dans certaines péridotites abyssales (e.g., Takazawa et al., 2007 ; Figure 3.8b). Les pyroxènes, fortement altérés, sont interstitiels à pœcilitiques dans certains échantillons (6R2_106-110 ; 10R1_22-26 ; 10R2_43-46) et entourent les cristaux corrodés d'olivine. L'orthopyroxène est présent seulement dans l'échantillon 6R2_34-38 sous la forme de cristaux pœcilitiques xénomorphes de 5 mm entourant des cristaux d'olivine et d'oxyde (Figure 3.8c). Les oxydes (chromite) sont xénomorphes et souvent associés à des amphiboles brunes (Figure 3.8b). Les spinelles se présentent sous forme de petits cristaux subautomorphes (0,2 mm) associés à l'olivine.

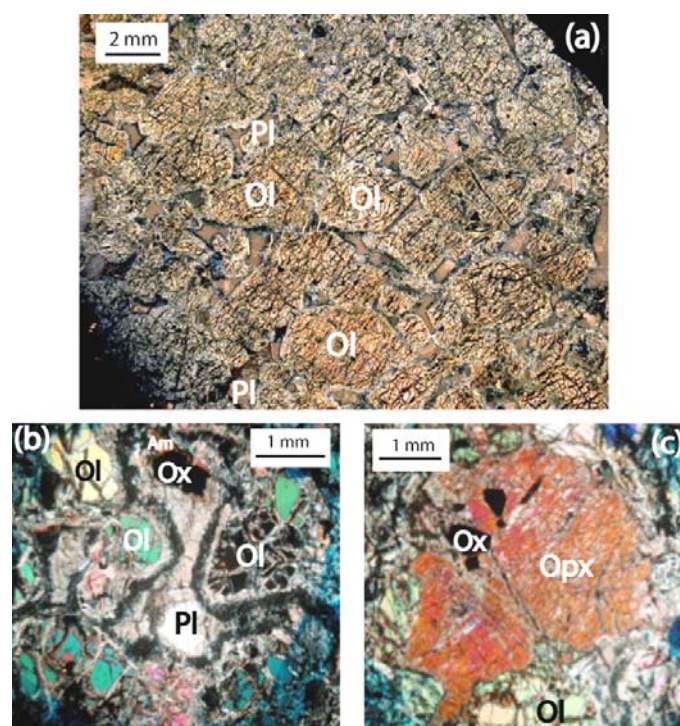


Figure 3.8 : Vues au microscope optique en lumière polarisée de la texture des troctolites du Site 1275. (a) Cristaux d'olivines, fortement serpentinisés et arrondis entourés par des plagioclases très altérés (échantillon 1275D_17R2_46-50). (b) Cristal de plagioclase très altéré présentant une texture amiboïdale et oxyde xénomorphe associé à de l'amphibole brune (échantillon 1275b_6R2_34-38). (c) Cristal pœcilitiques d'orthopyroxène entourant des cristaux d'olivine et d'oxyde (échantillon 1275b_6R2_34-38).

III. Analyses chimiques des minéraux des roches gabbroïques du site 1275

Éléments majeurs

Les données en éléments majeurs sont présentées dans les tableaux B3-a à B3-d en annexe B.

Dans les gabbros à oxyde, les plagioclases ont une composition plutôt albitique (An_{33-49}) (Figure 3.9a). Les clinopyroxènes sont majoritairement des augites ($En_{26-41}Fs_{18-32}Wo_{28-46}$) bien que quelques pigeonites soient présentes. Ils sont caractérisés par des Mg# moyens ($Mg\# = 100 \times \text{cationique } Mg/(Mg+Fe) = 46-68$) et des concentrations faibles en TiO_2 (0,10-0,90 %) et très faible en Cr_2O_3 (0,003-0,07 %). De même, les orthopyroxènes ont des Mg# moyens (41-65) et des concentrations moyennes en CaO (1,25-3,70 %), faibles en TiO_2 (0,11-0,49 %) et très faible en Cr_2O_3 (0-0,04 %).

Dans les gabbros à olivine, les plagioclases ont une composition un peu plus anorthitique (An_{47-62}) que dans les gabbros à oxyde (Figure 3.9a). Les clinopyroxènes sont des augites ($En_{47-52}Fs_{7-16}Wo_{36-45}$). Ils se distinguent par des Mg# élevés (75-88) et des concentrations variables en TiO_2 (0,29-1,24 %) et moyennes en Cr_2O_3 (0,21-0,87 %). Les orthopyroxènes ont des Mg# élevés (83-85) et des concentrations faibles en CaO (1,26-1,90 %) et en Cr_2O_3 (0,20-0,25 %). L'olivine dans les gabbros à olivine a une teneur en forsterite moyenne à élevée (Fo_{82-88}), et une concentration en Ni élevée (1832-2188 ppm), comparable aux olivines des troctolites et troctolites riches en olivine du puits U1309D (Figure 3.9b).

Dans les troctolites, les plagioclases ont une composition plus anorthitique (An_{48-80}) (Figure 3.9a). L'olivine a une teneur en forsterite élevée (Fo_{89}), et une concentration très élevée en Ni (2450-2584 ppm) comparable à celle des olivines des roches mantelliques imprégnées du Leg ODP 147 (Hess Deep, Océan Pacifique) et du Site ODP 1271 (Site au sud de la zone de fracture 15°20'N, foré pendant le Leg ODP 209; Figure 3.9b). Les clinopyroxènes sont des augites ($En_{34-51}Fs_{5-28}Wo_{37-47}$) et ont des Mg# très élevées (90-92) (Figure 3.9a). Ils ont des concentrations très variables en TiO_2 (0,35-1,02 %) et en Cr_2O_3 (0,01-1,35 %). Le seul orthopyroxène analysé dans les troctolites est très magnésien ($Mg\# = 90$) et possède des concentrations faibles en CaO (1,21 %) et en Cr_2O_3 (0,43 %).

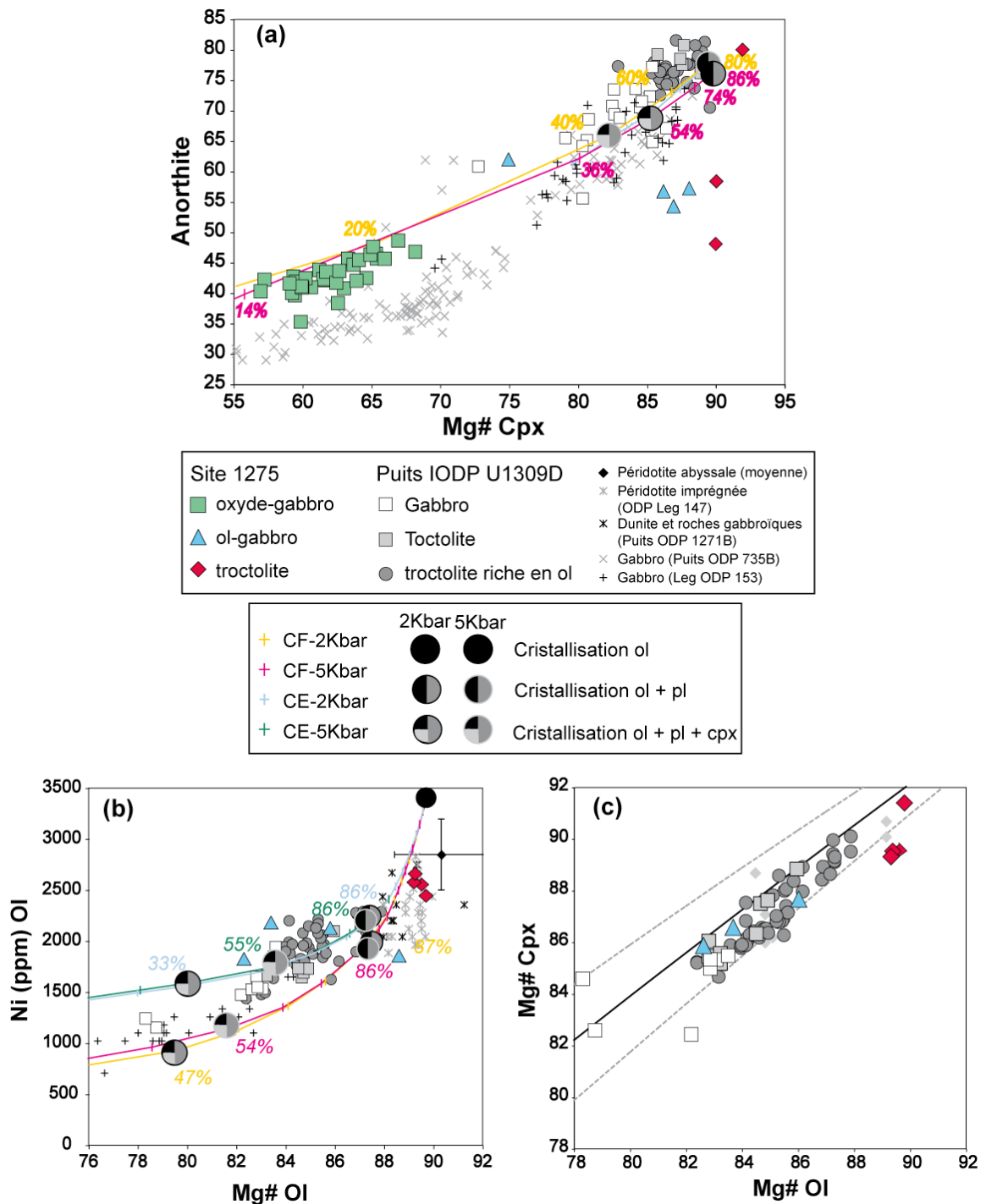


Figure 3.9 : (a) Teneur en anorthite (%) du plagioclase en fonction du Mg# ($Mg\# = 100 \times \text{cation } Mg/(Mg+Fe)$) du clinopyroxène dans les gabbros à oxyde, les gabbros à olivine et les troctolites du Site 1275. (b) Teneur en Ni de l'olivine en fonction du Mg# de l'olivine dans les gabbros à olivine et les troctolites du Site 1275. (c) Mg# dans les clinopyroxènes en fonction du Mg# dans les olivines dans les gabbros à olivine et les troctolites du Site 1275. La ligne noire correspond aux valeurs d'équilibre entre les olivines et les clinopyroxènes (avec $D^{Ol/Liq} = 0,3$ et $D^{Cpx/Liq} = 0,23$; Lissenberg & Dick, 2008). Les lignes grises en pointillés définissent les compositions à l'équilibre avec une incertitude de 0,02 pour chaque coefficient de partage (Lissenberg & Dick, 2008). Les données suivantes sont reportées pour comparaison: moyenne des péridotites abyssales (Roden et al., 1984;

Bonatti et al., 1986; Shibata & Thompson, 1986; Fujii, 1990; Juteau et al., 1990; Komor et al., 1990; Bonatti et al., 1992; Bonatti et al., 1993; Tartarotti et al., 2002; Seyler et al., 2003), péridotites imprégnées du Leg ODP 147, zone de transition à Hess Deep (Allan & Dick, 1996; Arai & Matsukage, 1996; Edwards & Malpas, 1996), dunite imprégnée et matériel gabbroïque du puits ODP 1271B (Takazawa et al., 2007b), gabbros de la dorsale Médio-Atlantique (Bloomer et al., 1991; Ozawa et al., 1991; Cannat & Casey, 1995; Ross & Elthon, 1997; Coogan et al., 2000b), gabbros du puits 735B, dorsale Sud-Ouest Indienne (Hebert et al., 1991; Natland et al., 1991; Ozawa et al., 1991), gabbros, troctolites et troctolites riches en olivine du puits U1309D (Drouin et al., accepté). L'évolution des éléments majeurs, durant la cristallisation fractionnée et à l'équilibre, a été calculée en utilisant le programme PELE (<http://www.nicholas.duke.edu/people/faculty/boudreau/DownLoads.html>). La composition initiale du liquide est celle d'un liquide primaire calculé après 10,3 % de fusion à 15Kbar (Kinzler & Grove, 1993). Les croix indiquent le pourcentage de liquide restant (indiqué en italique). cpx: clinopyroxène, ol: olivine.

Les minéraux des roches gabbroïques du site 1275 sont caractérisés par des compositions en éléments majeurs qui varient avec la lithologie. Les minéraux des gabbros à oxyde ont des compositions en éléments majeurs évoluées, comparables aux compositions préalablement analysées dans les gabbros océaniques (Figure 3.9a). Toutefois, à valeur égale en Mg# pour les clinopyroxènes, les plagioclases des gabbros à oxyde du Site 1275 ont des concentrations en anorthite plus élevées que les plagioclases des gabbros à oxyde de la dorsale Sud-Ouest Indienne. Les minéraux des gabbros à olivine ont des compositions en éléments majeurs un peu moins évoluées que celles des gabbros à oxyde, semblables à celles des gabbros du puits U1309D (Figure 3.9a). Les compositions en éléments majeurs des minéraux des troctolites du site 1275 sont quant à elles très primitives (Figure 3.9a). Cependant, la composition en anorthite des plagioclases de certains gabbros à olivine et des troctolites est très faible par rapport aux Mg# des clinopyroxènes associés. Ceci est vraisemblablement lié à la très forte altération (albitisation) des plagioclases.

Éléments en trace

Des analyses en éléments en traces de clinopyroxènes et de plagioclases ont été effectuées pour trois gabbros à oxyde du site 1275: 15R1_120-124 (gabbro à oxyde à grains fins) ; 16R1_30-34 et 19R1_50-54 (gabbros à oxyde à gros grains). Les résultats de ces analyses sont récapitulés dans les tableaux B3-f et B3-g en annexe B.

Clinopyroxènes

Afin de contraindre la pétrogenèse des gabbros à oxyde du Site 1275 nous avons comparé la composition en éléments en trace de leurs clinopyroxènes à celle des clinopyroxènes des gabbros et troctolites riches en olivine du puits U1309D et des gabbros de la zone MARK (dorsale Médio-Atlantique 23°N) (Figure 3.10 a et b). Les clinopyroxènes des gabbros à oxyde du Site 1275 ont des compositions en éléments en trace similaires à celles des bordures des clinopyroxènes des gabbros à olivine de la zone MARK. Toutefois, les clinopyroxènes des échantillons 16R1_30-34 et 19R1_50-54 ont des teneurs en Terres Rares Légères beaucoup plus élevées. Par ailleurs, les clinopyroxènes des gabbros à oxyde du Site 1275 sont 10 fois plus enrichis en éléments en trace que les clinopyroxènes des gabbros et troctolites riches en olivine du puits U1309D (Figure 3.10 a et b).

Les clinopyroxènes des gabbros à oxyde ont des teneurs élevées en éléments en trace, avec Yb_N (N = normalisé aux Chondrites) compris entre 32,91 et 62,69 et des spectres appauvris en Terres Rares Légères ($La_N/Sm_N = 0,15-0,49$) avec un segment plat des Terres Rares Moyennes aux Terres Rares Lourdes ($Gd_N/Yb_N = 0.8-1$) (Figure 3.10a). Cependant, les clinopyroxènes de l'échantillon 15R1_120-124 présentent un appauvrissement en terres rares légères plus important ($La_N = 4,25$) que ceux des échantillons 16R1_30-34 et 19R1_50-54 ($La_N =$ respectivement 24,94 et 15,37). L'enrichissement en Terres Rares Légères des clinopyroxènes des échantillons 16R1_30-34 et 19R1_50-54 pourrait être le résultat d'un déséquilibre cinétique pendant la cristallisation (Albarede & Bottinga, 1972). Les clinopyroxènes des échantillons 15R1_120-124 et 19R1_50-54 présentent une forte anomalie négative en Eu ($Eu/Eu^* = 0,4-0,5$), tandis que celle-ci est moins marquée pour les clinopyroxènes de l'échantillon 16R1_30-34 ($Eu/Eu^* = 0,7$) (Figure 3.10a).

Les clinopyroxènes des gabbros à oxyde 16R1_30-34 et 19R1_50-54 sont caractérisés par un appauvrissement continu des éléments en trace incompatibles depuis les Terres Rares jusqu'au Ba (<1 x Manteau Primitif –MP-) et enrichis en Rb et Cs ($> 2x$ MP) (Figure 3.10b). Dans ces mêmes échantillons, les clinopyroxènes sont appauvris en Zr et Hf par rapport aux Terres Rares Moyennes ($Zr/Sm = 0,27-0,28$ x MP), ont des fortes anomalies positives en U ($U/Th = 58$ x MP), et des fortes anomalies négatives en Pb ($Pb/Ce = 0,11-0,41$ x MP) et Sr ($Sr/Nd = 0,03-0,11$ x MP). Les clinopyroxènes de l'échantillon 16R1_30-34 sont caractérisés par un spectre d'éléments en trace plat avec un appauvrissement en éléments en trace les plus incompatibles ($< 2X$ MP) (Figure 3.10b). Ces clinopyroxènes se distinguent par des variations plus faibles en U et Zr-Hf par rapport aux éléments voisins ($U/Th = 7,8$ x MP; $Zr/Sm = 0,7$ x MP). De plus, ils présentent des anomalies négatives en Pb ($Pb/Ce = 0,48$ x

MP) et en Sr ($Sr/Nd = 0,16 \times MP$) moins marquées que pour les clinopyroxènes des gabbros à oxyde 16R1_30-34 et 19R1_50-54. De plus, les clinopyroxènes de l'échantillon 16R1_30-34 montrent de faibles anomalies positives en Ba ($Ba/Rb = 1,5 \times MP$). Finalement, les rapports Zr/Hf et Nb/Ta révèlent un fractionnement chondritique à sub-chondritique dans tous les clinopyroxènes ($Zr/Hf = 24-31$; Chondrite-C1 = 36,3 (Sun and McDonough, 1989) et $Nb/Ta = 7-24$; Chondrite-C1 = 17,6 (Sun and McDonough, 1989)) comme observé dans les clinopyroxènes du puits IODP U1309D.

Les anomalies négatives en Ba, Sr et Eu peuvent s'expliquer par le fractionnement du plagioclase, si les clinopyroxènes sont en équilibre avec ce dernier. Le fractionnement des oxydes ferro-titanés (minéraux incorporant le Nb) pourrait expliquer l'anomalie négative en Nb.

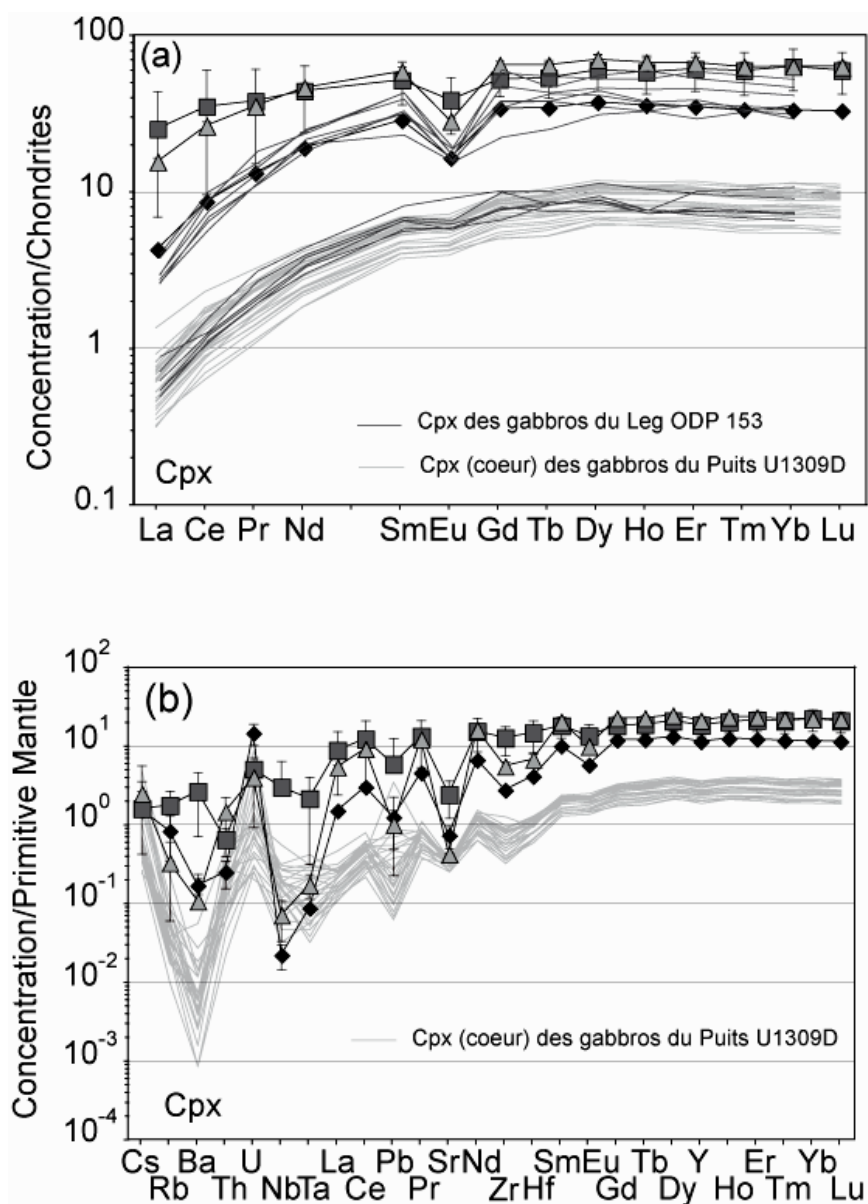


Figure 5.10 : Spectres de Terres Rares normalisés aux Chondrites (Sun et McDonough, 1989) (a) et spectres multi-élémentaires normalisés au manteau primitif (Sun et McDonough, 1989) (b) des clinopyroxènes des trois gabbros à oxyde analysés. Les données suivantes sont reportées pour comparaison : clinopyroxènes des gabbros, troctolites et troctolites riches en olivine du puits IODP U1309D (Drouin et al., accepté), clinopyroxène des gabbros du Leg ODP 153 (Ross et Elthon, 1997 ; Coogan et al., 2000b). Légende : carré= 16R1_ 30-34 (gabbro à oxyde à gros-grains) ; losange : 15R1_120-124 (gabbro à oxyde à grains fins) ; triangle= 19R1_ 50-54 (gabbro à oxyde à gros-grains).

Plagioclases

Les plagioclases des gabbros à oxyde du Site 1275 ont des fortes concentrations en Terres Rares Légères (Figure 3.11a) similaires à celles des bordures des plagioclases des gabbros à olivine et des plagioclases des gabbros à oxyde échantillonnés le long de la dorsale Médio-Atlantique (zone MARK). Par contre, leurs faibles teneurs en Terres Rares Lourdes sont similaires à celles des plagioclases des gabbros et troctolites riches en olivine du puits IODP U1309D.

Les plagioclases des gabbros à oxyde ont des faibles teneurs en Terres Rares Lourdes ($Yb_N = 0,13-0,14$) et des spectres enrichis en Terres Rares Légères avec de très fortes anomalies positives en Eu ($Eu_N/Eu^* = 37-41$). Ils montrent le même fractionnement en Terres Rares Moyennes/ Terres Rares Lourdes ($Gd_N/Yb_N = 3,6-5,9$; Figure 3.11a).

Ils ont des spectres d'éléments en trace similaires, caractérisés par un enrichissement continu en éléments en trace les plus incompatibles et des anomalies positives en U et Pb par rapport aux éléments voisins ($U/Th = 16,5-20,2 \times PM$; $Pb/Ce = 2,9-4,1 \times PM$) (Figure 3.11b). De plus, ces plagioclases montrent, comme les plagioclases du puits U1309D, de forts appauvrissements en Nb et Zr ainsi qu'en Ta et Hf par rapports aux éléments voisins. Ceci a pour conséquence des rapports Nb/Ta et Zr/Hf très fractionnés dans ces minéraux ($Nb/Ta = 1,8-5,4$ et $Zr/Hf = 20,7-24,3$). Les rapports en Nb/Ta des plagioclases du Site ODP 1275 sont similaires à ceux des plagioclases du puits IODP U1309D ($Nb/Ta = 1,5-7,8$), par contre les rapports en Zr/Hf sont légèrement plus faibles (IODP U1309D : $Zr/Hf = 1,6-30,1$).

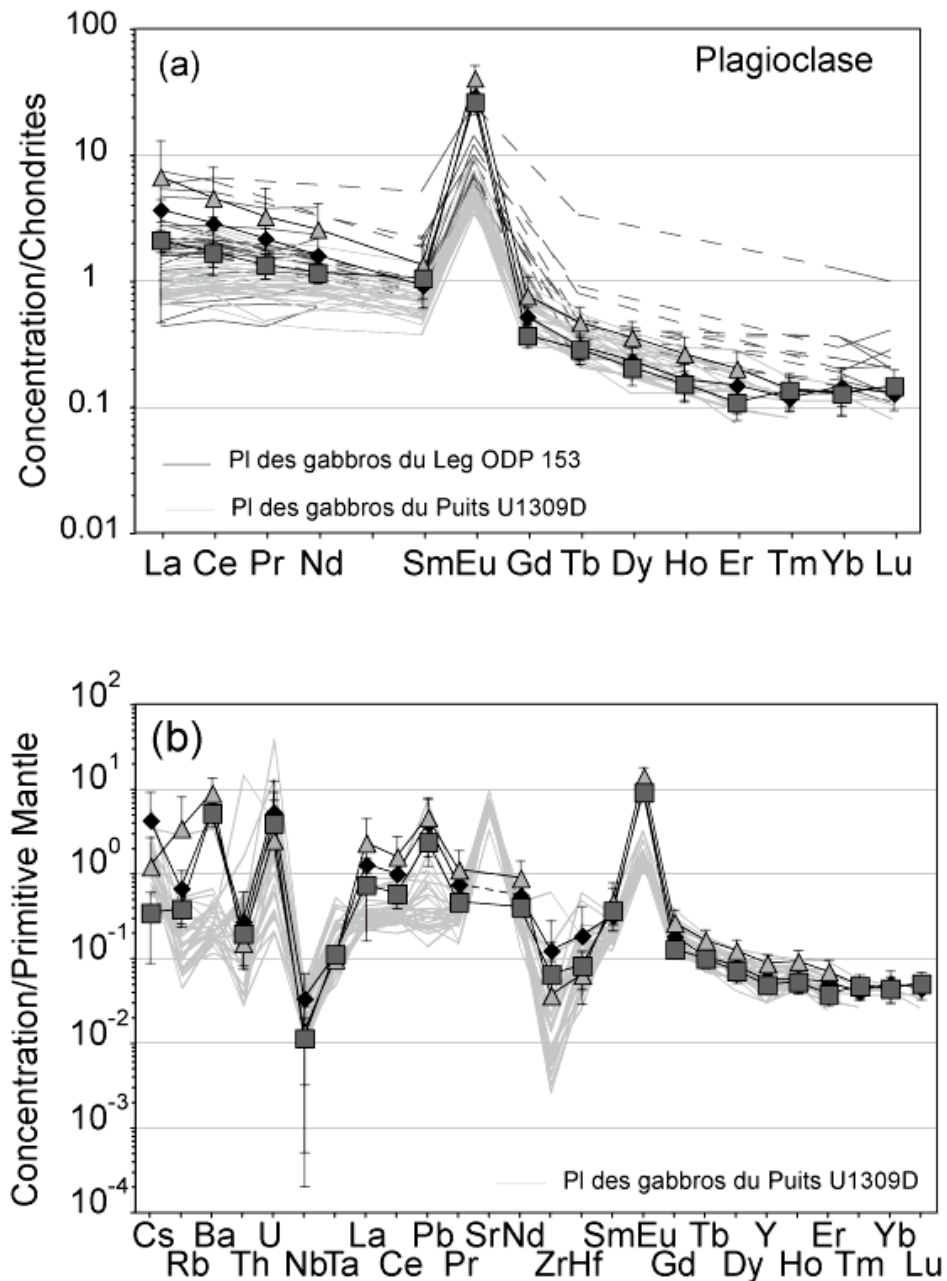


Figure 3.11: Spectres de Terres Rares normalisés aux Chondrites (Sun et McDonough, 1989) (a) et spectres multi-élémentaires normalisés au manteau primitif (Sun et McDonough, 1989) (b) des plagioclases des trois gabbros à oxyde analysés. Les données suivantes sont reportées pour comparaison : plagioclases des gabbros, troctolites et troctolites riches en olivine du puits IODP U1309D (Drouin et al., accepté), plagioclases des gabbros du Leg ODP 153 (Ross et Elthon, 1997 ; Coogan et al., 2000a), les pointillés indiquent l'absence de données. Légende : carré= 16R1_30-34 ; losange : 15R1_120-124 ; triangle= 19R1_50-54.

IV. Discussion

Les troctolites ont des compositions très primitives, avec des Mg# élevés dans les clinopyroxènes (90-92), des teneurs élevées en Forstérite dans les olivines (Fo₈₉) et des teneurs élevées en Anorthite dans les plagioclases (An₄₈₋₈₀). Ces résultats sont en accord avec les données géochimiques en roche totale pour les troctolites. Les olivines des troctolites du Site 1275 se distinguent par des teneurs élevées en Ni (2450-2584 ppm) pour une concentration en Forstérite donnée (Fo₈₉), similaires à celles des olivines des roches mantelliques imprégnées du Leg ODP 147 et du Site 1271 (Figure 3.9b). Les compositions très primitives des olivines des troctolites, ainsi que la texture de ces roches, similaire aux textures d'imprégnation dans certaines péridotites abyssales, confirment l'interprétation, proposée par Kelemen et al. (2004), pour les troctolites du Site 1275: elles seraient le produit de l'imprégnation par un/des liquide(s) basaltique(s) de péridotites résiduelles. De plus dans les troctolites, les olivines ne sont pas en équilibre en Mg/Fe avec les clinopyroxènes, à part dans un seul échantillon, contrairement aux olivines des troctolites riches en olivine du puits IODP U1309D (Figure 3.9c). Cette interprétation proposée pendant le Leg ODP 209 pour les troctolites du Site ODP 1275 (i.e., péridotites imprégnées; Shipboard Scientific Party, 2004b) contraste avec l'interprétation proposée lors des Expéditions IODP 304-305 pour les troctolites riches en olivine du puits IODP U1309D (i.e., cumulats primitifs). Pourtant, ces deux types de roches ont des caractéristiques texturales et pétrologiques très semblables. En effet, les deux roches sont formées de cristaux d'olivines arrondis et corrodés, entourés par des cristaux de plagioclases, de clinopyroxènes et d'orthopyroxènes interstitiels ou pœcilitiques. Les troctolites riches en olivine du puits IODP U1309D se distinguent des troctolites du Site ODP 1275, d'un point de vue composition minéralogique, par l'absence d'oxydes ferro-titanés. De plus, les olivines des troctolites riches en olivine du puits IODP U1309D présentent des concentrations en Ni (1440-2300) et en Forstérite (Fo₈₂-Fo₈₈) moins élevées que les olivines des troctolites du Site ODP 1275 (Figure 3.9b). Toutefois, ces concentrations sont très proches de celles des olivines des péridotites imprégnées et beaucoup plus primitives que celles des olivines des gabbros océaniques (Figure 3.9b). Les compositions en Ni et Fo des olivines des troctolites riches en olivine du puits U1309D peuvent s'expliquer par de forts taux d'interactions liquide/roche entre un magma basaltique et des péridotites. D'ailleurs, l'interprétation initiale de la pétrogenèse des troctolites riches en olivine a été révisée dans le chapitre 2 de ce mémoire. Au vu de cette révision, les troctolites

du Site ODP 1275 peuvent être le résultat d'une imprégnation magmatique moins intense que les troctolites riches en olivine du puits IODP U1309D.

Les olivines des gabbros à olivine du Site 1275 ont des teneurs en Ni et en Forstérite plus faibles que les olivines des troctolites du Site 1275 mais analogues à celles des olivines des troctolites riches en olivine du puits IODP U1309D (Figure 3.9b), interprétées comme des reliques de manteau fortement imprégné (Drouin et al., en révision). De plus, dans les gabbros à olivine, les olivines sont en équilibre avec les clinopyroxènes en Mg/Fe (Figure 3.9c). Les compositions de ces olivines peuvent être reproduites par des modèles géochimiques d'évolution par cristallisation à l'équilibre (Figure 3.9b). Ces résultats suggèrent une rééquilibration constante entre un liquide et les olivines pour les éléments compatibles (Drouin et al., accepté). L'association de gabbros à olivine avec des troctolites, interprétées comme du manteau imprégné, est similaire à ce qui a été observé dans le puits ODP 1271B, où les troctolites et les gabbros à olivine sont considérés comme le produit de l'interaction entre un liquide magmatique stagnant et les roches mantelliques encaissantes (Takazawa et al., 2007). Il est donc tentant de considérer les gabbros à olivine du Site 1275 comme le résultat de la cristallisation de magma basaltique dans une matrice péridotitique. Cependant, l'absence de données en éléments en trace pour les minéraux des gabbros à olivine, ainsi que l'absence de données microstructurales ne nous permet pas de conclure définitivement sur l'origine de ces roches.

Les gabbros à oxyde, avec des compositions plus évoluées, représentent le terme le plus différencié de la série gabbroïque du Site ODP 1275. Le Mg# des clinopyroxènes est positivement corrélé avec la teneur en anorthite des plagioclases dans les gabbros à oxyde. Cette co-variation de composition entre les plagioclases et les clinopyroxènes est comparable à celle des différentes suites de cumulats océaniques (Ross & Elthon, 1997) et compatible avec la cristallisation fractionnée d'un liquide de type MORB à faible profondeur (2Kbar) (Figure 3.9a). Les gabbros à oxyde représentent donc vraisemblablement le terme le plus évolué d'une suite de cristallisation d'un liquide primitif (Figure 3.9a). De même, les pyroxènes des gabbros à oxyde sont en équilibre avec des liquides évolués (100x Chondrites), suggérant que ces roches sont le produit d'une cristallisation fractionnée importante d'un MORB primitif. La composition des minéraux des gabbros à oxyde est en accord avec la composition en roche totale très évoluée des gabbros du groupe 2. Ces gabbros à oxyde très différenciés ne semblent donc pas être associés aux troctolites, roches mantelliques imprégnées, ni aux gabbros à olivine ayant des compositions plus primitives du type du groupe 1 en roche totale, et montrant une différenciation par cristallisation à l'équilibre.

Kelemen et al. (2004) suggèrent une seule et même histoire magmatique pour le Site ODP 1275. L'imprégnation magmatique du manteau serait contemporaine de la cristallisation des roches gabbroïques composant ce site. Mes résultats semblent suggérer que les gabbros à oxydes soient associés à des intrusions tardives de gabbros très évolués dans un encaissant formé de péridotites imprégnées associées à des gabbros primitifs.

De plus, mes données montrent que les gabbros à oxyde sont trop évolués pour représenter le produit complémentaire de la cristallisation des MORB, comme sont généralement considérés les gabbros océaniques. Ceci pourrait suggérer qu'il y a eu très peu d'extraction de magma de cette section gabbroïque. Ces gabbros à oxyde représentent des roches plutoniques qui ont cristallisé à différentes profondeurs dans la lithosphère océanique sans contreparties volcaniques, comme suggérés par Godard et al. (sous-pressé) pour les roches gabbroïques du Site IODP U1309.

Dans la région du Site 1275, la base de la lithosphère océanique semble être le siège d'une zone d'accumulation de magma importante où l'imprégnation et les réactions magma/roche sont fortes, comme cela a pu être observé dans les zones de transition manteau/croûte décrites dans les ophiolites (e.g., Boudier & Nicolas, 1995; Dijkstra et al., 2003) ou les dorsales rapides (e.g., Cannat et al., 1990; Allan & Dick, 1996; Arai & Matsukage, 1996; Dick & Natland, 1996). Ces résultats sont cohérents avec notre étude du Massif Atlantique (chapitre 2). D'ailleurs, la présence systématique de corps gabbroïques au cœur de différents core complexes océaniques forés le long de la dorsale Médio-Atlantique et la dorsale Sud-Ouest Indienne suggère que ce type de structure est associé à une activité magmatique non négligeable (Ildefonse et al., 2007). La présence en abondance de diabases recoupant la faille de détachement à 15°45'N indique que celle-ci était active au cours du magmatisme (MacLeod et al., 2002; Escartin et al., 2003).

Cette activité magmatique relativement forte se manifeste par la cristallisation de multiples plutons gabbroïques dans la lithosphère sans équivalent en surface, conduisant à la formation d'une croûte basaltique fine ou à son absence localement. Ceci est en accord avec les données gravimétriques qui montrent que les core complexes océaniques sont le siège d'anomalies gravimétriques de Bouguer positives (Tucholke et al., 2001; Searle et al., 2003; Fujiwara et al., 2003; Cannat et al., 2006; Blackman et al., 1998, 2008), résultant de la présence de gabbros (densité des gabbros = 2800-2900 kg/m³; Blackman et al., 2008) juste sous le plancher océanique (Blackman et al., 2008) et donc l'absence d'une croûte basaltique de densité plus faible (~2600 kg/m³). De plus, la présence de ces corps gabbroïques au sein des péridotites encaissantes, dans la lithosphère axiale, induit des hétérogénéités rhéologiques

qui favorisent la localisation de la déformation autour de ces plutons (Escartin & Cannat, 1999 ; Escartin et al., 2003; Ildefonse et al., 2007). L'activité magmatique apparaît donc comme un élément essentiel de la formation des core complexes océaniques.

Conclusions

Le fonctionnement d'une grande faille de détachement, à 30°N sur la dorsale Médio-Atlantique, a mis à l'affleurement la lithosphère profonde au niveau du Massif Atlantis, un core complexe océanique. Le forage du cœur de ce massif, au cours des expéditions IODP 304-305, en 2004-2005, a permis un échantillonnage unique de la croûte océanique inférieure. Le puits IODP U1309D, profond de 1415 mètres, se distingue par la présence de roches riches en olivine (ol \gg 70%) en quantité non négligeable (5,4% des roches récupérées), ayant les compositions les plus primitives des roches gabbroïques jamais forées aux dorsales. À 15°45'N, sur la dorsale Médio-Atlantique, les forages effectués au sommet d'un core complexe océanique (Site ODP 1275) lors du Leg ODP 209, ont aussi échantillonné majoritairement une série gabbroïque comprenant des roches riches en olivine. L'étude pétro-géochimique et microstructurale des roches riches en olivine du puits U1309D, ainsi que l'étude géochimique in-situ des roches gabbroïques du Site ODP 1275, m'ont permis d'apporter de nouveaux éléments quant à la compréhension des processus magmatiques et structuraux aux dorsales lentes.

Un des résultats principaux de ce travail est l'acquisition des premières données en éléments en trace in-situ multi-élémentaires sur des olivines mais aussi sur des clinopyroxènes et des plagioclases de gabbros océaniques.

Ceci m'a permis de montrer que dans les troctolites riches en olivine du puits IODP U1309D, les olivines ne sont pas en équilibre en éléments en trace avec les plagioclases et les clinopyroxènes. De plus, l'étude pétrologique et microstructurale des troctolites riches en olivine montre que les olivines ont subi une déformation par fluage-dislocation, avec l'activation du système de glissement de haute température (010) [100] comme on l'observe classiquement dans les péridotites mantelliques. Les plagioclases et les clinopyroxènes sont quant à eux non déformés. Ces résultats mettent en évidence une histoire complexe de cristallisation en plusieurs étapes pour ces roches très primitives. Les orientations cristallographiques préférentielles de l'olivine sont toutefois faibles et présentent un maximum d'intensité sur l'axe [001], peu commun pour les fabriques classiques du manteau. Ces fabriques sont interprétées comme étant le résultat d'une forte imprégnation magmatique d'une matrice d'olivine préalablement déformée. En effet, lorsque le rapport liquide/roche est suffisamment élevé ($> \sim 30\%$), l'agrégat solide d'olivine peut être disloqué, dispersant alors les grains d'olivines au sein du magma imprégnant et transformant la fabrique mantellique originelle. De plus, la corrosion des olivines se faisant préférentiellement le long des sous-joints (100), ce processus participe au renforcement de l'orientation préférentielle des axes

[001]. La quantité de magma qui imprègne les roches mantelliques apparaît donc comme un paramètre primordial, qui contrôle au premier ordre non seulement la chimie de la roche mais aussi sa microstructure.

Les troctolites riches en olivine du puits IODP U1309D ont donc cristallisé dans une zone de forte accumulation et imprégnation magmatique, similaire aux zones de transition croûte/manteau observées dans les ophiolites (e.g., Boudier & Nicolas, 1995) ou aux dorsales rapides (e.g., Cannat et al., 1990; Allan & Dick, 1996; Arai & Matsukage, 1996; Dick & Natland, 1996). La cristallisation du plagioclase et du clinopyroxène à partir d'un même liquide de type MORB, aussi bien dans les troctolites riches en olivine que dans les gabbros qui leurs sont associés, suggère que cette zone pourrait correspondre à une zone d'homogénéisation des liquides circulant dans le manteau.

L'étude pétro-géochimique et microstructurale des troctolites riches en olivines du puits IODP U1309D me permet de proposer le scénario suivant pour leur formation, et leur relation avec les gabbros voisins:

Des magmas de type MORB sont injectés sporadiquement dans le manteau partiellement fondu, proche de la température du solidus. La haute température du milieu favorise les interactions liquide/roche. L'invasion progressive par d'importants volumes de magma détruit localement le réseau rigide d'olivines. Le refroidissement plus ou moins lent du système conduit à la cristallisation des plagioclases et des clinopyroxènes au sein de la matrice d'olivine corrodée, disloquée et assimilée, pour former les troctolites riches en olivine. L'incorporation à la base de la lithosphère, sous l'axe de la dorsale, de petites unités de manteau imprégné pourrait constituer un mécanisme fondamental d'accrétion de la croûte océanique inférieure aux dorsales lentes.

Les roches gabbroïques forées au puits IODP U1309D à 30°N sur la dorsale Médio-Atlantique montrent une grande variété de lithologies, depuis les plus primitives jusqu'aux plus évoluées. Dans toutes les lithologies étudiées, les clinopyroxènes et les plagioclases ont des concentrations en éléments en trace similaires. Mes résultats supportent donc l'hypothèse selon laquelle l'imprégnation magmatique du manteau et la formation de la série gabbroïque sont deux événements contemporains au niveau du Massif Atlantis. Le Site ODP 1275 foré à 15°N sur la dorsale Médio-Atlantique comprend lui aussi une grande variété de lithologies gabbroïques. Cependant, la formation des roches les plus évoluées de cette série n'apparaît pas liée à l'évènement d'imprégnation. Ces roches correspondent à des injections tardives de magma qui ont entièrement cristallisé en profondeur sous forme de plutons intrusifs, sans équivalent en surface.

L'étude microstructurale et géochimique des deux séries gabbroïques présentées dans ce manuscrit indique une origine mantellique aussi bien pour les troctolites du Site ODP 1275 (cette étude et Kelemen et al., 2004) que pour les troctolites riches en olivine du puits IODP U1309D, correspondant aux termes les plus primitifs de ces séries. Qu'en est-il alors des cumulats primitifs ? En effet, la portion la plus primitive de la séquence cumulative n'a donc pas été échantillonnée au Site IODP U1309, ni au Site ODP 1275, comme au niveau de la zone de MARK sur la dorsale Médio-Atlantique ou dans le puits ODP 735B sur la dorsale Sud-Ouest Indienne ou elle est aussi absente. L'absence de cumulats primitifs dans les sections échantillonnées à ce jour pourrait n'être qu'un biais d'échantillonnage. Toutefois, contrairement à ces autres sites de forage, le bilan de masse pondéré des différents lithotypes du Site IODP U1309 calculé par Godard et al. (sous-presse) montre qu'il n'est pas nécessaire de faire appel à ces cumulats primitifs pour obtenir la composition des MORB primaires. Ceci indique que la série gabbroïque forée au Massif Atlantis ne correspond pas au complément chimique des MORB en surface. La composition primitive de l'ensemble des roches gabbroïques du site du Massif Atlantis se distingue donc de la zone de MARK et du puits ODP 735B, caractérisés par la présence de gabbros évolués plus abondants. Le Massif Atlantis est-il un cas exceptionnel ou bien les autres sites le sont-ils ? Un forage plus profond sur les sites préexistants ainsi que l'étude de plus de sections gabbroïques aux dorsales lentes permettront de répondre à la question de l'existence de ces cumulats primitifs.

L'abondance de roches gabbroïques et la présence de roches mantelliennes imprégnées dans le puits IODP U1309D et au Site ODP 1275 sont en accord avec l'hypothèse d'une activité magmatique relativement forte lors de la formation de la série gabbroïque qui constitue le cœur de ces deux core complexes océaniques. Ildefonse et al. (2007c) et Tucholke et al. (2008) montrent à partir d'observations géologiques et de modèles numériques que la formation des cores complexes océaniques est associée à des périodes de magmatisme élevé dans des régions des dorsales lentes au budget magmatique apparemment limité (absence, ou tout au moins présence discontinue, des extrusifs volcaniques basaltiques). Ce paradoxe apparent peut s'expliquer par la cristallisation de tout ou une partie du magma produit dans la lithosphère sans contrepartie volcanique en surface (Cannat, 1993; Cannat et al., 1995a; Cannat, 1996; Lagabriele et al., 1998; Lizarralde et al. ; 2004 ; Godard et al., sous-presse). Nos résultats montrent qu'au niveau des deux extrémités de segment considérées, et par extension dans toutes les zones "pauvres" en magma (i.e., pauvres en matériel volcanique) des dorsales lentes, une quantité importante de magma cristallise sous forme de plutons plus ou moins interconnectés dans la lithosphère. La croûte basaltique supérieure, lorsqu'elle est

présente, serait alors alimentée en parallèle de la série gabbroïque de la croûte inférieure, sans qu'il y ait nécessairement un lien pétrogénétique entre les deux. L'alimentation magmatique de la croûte supérieure peut par exemple s'effectuer, via des filons d'alimentation, depuis le centre du segment qui est une zone volcanique active, vers les extrémités.

Les différentes conclusions qui se dégagent de ce mémoire appellent d'autres questions, permettant de dégager quelques axes de recherches à mener afin de compléter ce travail :

L'échantillonnage du puits U1309D nous donne une vision unidimensionnelle du système core complexe océanique. Les dragages et plongées en submersible effectués sur le mur Sud du Massif Atlantis montrent que celui-ci est constitué principalement de serpentinites. La variation latérale de la croûte en termes de lithologie est donc connue. Cependant, nous connaissons très mal les relations tectoniques existant entre le cœur du massif et ses bordures. Il serait donc intéressant de forer à nouveau le Massif Atlantis pour mieux contraindre les relations entre la tectonique et le magmatisme lors de la formation des core complexes océaniques.

J'ai réalisé une étude préliminaire de la caractérisation des variations chimiques observées au sein des minéraux des troctolites riches en olivine (chapitre 2.III). La poursuite de ces travaux est essentielle pour contraindre les temps de rééquilibrage des minéraux lors des réactions magma/roche. Des profils plus détaillés en éléments en trace devront donc être réalisés dans les olivines, afin de pouvoir calculer de nouveaux coefficients de diffusion en fonction notamment des directions cristallographiques. Enfin, des profils de concentration en Al et P dans les olivines, deux éléments qui diffusent très lentement dans ce minéral contrairement aux cations divalents, doivent être réalisés pour contraindre plus avant l'origine des olivines et éventuellement confirmer l'origine mantellique des troctolites riches en olivines.

L'étude de l'interaction entre l'hydrothermalisme et le magmatisme apparaît aussi essentielle. En effet, Godard et al. (sous-pressé) ont montré que les gabbronorites présents dans le puits IODP U1309D ont les mêmes compositions appauvries en éléments en trace que les gabbros. Ceci peut signifier que les orthopyroxènes ont cristallisé très tôt dans la séquence de cristallisation d'un MORB donc à grande profondeur (~10Km ; e.g., Ghiorso, 1985), ou à partir d'un magma riche en eau (e.g., Koepke et al., 2007), ou encore ont été formés par refusion d'un manteau hydraté (Nonotte et al., 2005). Ces différentes hypothèses sont en contradiction avec : la faible teneur en Al_2O_3 des clinopyroxènes des gabbronorites (2,2 % ; Miller et al., soumis), indiquant qu'ils ont cristallisé à faible profondeur ; les compositions identiques des gabbros et des gabbronorites ; et l'absence de minéraux hydratés dans les

gabbronorites. La présence d'orthopyroxènes poecilitiques dans certaines troctolites riches en olivine est cohérente avec l'hypothèse avancée par Godard et al. (sous-presse) pour la formation des gabbronorites du puits IODP U1309D, par assimilation de lithosphère altérée (donc riche en eau) par les magmas basaltiques ascendants. La réaction entre un liquide basaltique et du manteau altéré a pu conduire à la cristallisation précoce des orthopyroxènes dans les troctolites riches en olivine.

Ainsi, le rôle de l'assimilation des roches encaissantes (mantelliques ou gabbroïques) par les magmas ascendants et des réactions liquide/roche associées apparaît fondamental dans les processus d'accrétion crustale aux dorsales lentes. Ces réactions semblent au cœur de nombreux processus pétrogénétiques dans la croûte comme le montre ce travail avec des roches "crustales" dérivées du manteau, mais aussi Lissenberg & Dick, (2008) et Kvasnes & Grove (2008) pour les cumulats primitifs.

Références

- Agar, S.M., Casey, J.F., Kempton, P.D., 1997. Textural, geochemical, and isotopic variations in gabbroic shear zones from the MARK area. In Karson, J.A., Cannat, M., Miller, D.J., and Elthon, D. (Eds.), Proc. ODP, Sci. Results, 153: College Station, TX (Ocean Drilling Program), 99–121. doi:10.2973/odp.proc.sr.153.007.1997
- Aigner-Torres, M., Blundy, J., Ulmer, P., Pettke, T., 2007. Laser Ablation ICPMS study of trace element partitioning between plagioclase and basaltic melts: an experimental approach. *Contrib. Mineral. Petrol.* 153, 647-667.
- Albarede, F., Bottinga, Y., 1972. Kinetic disequilibrium in trace element partitioning between phenocrysts and host lava. *Geochim. Cosmochim. Acta* 36(2), 141-156.
- Allan, J.F., Sack, R.O., Batiza, R., 1988. Cr-rich spinels as petrogenetic indicators: MORB-type lavas from the Lamont seamount chain, eastern Pacific. *Am. Mineral.* 73, 741-753.
- Allan, J.F., Dick, H.J.B., 1996. Cr-rich spinel as a tracer for melt migration and melt-wall rock interaction in the mantle: Hess Deep, Leg 147. In Mével, C., Gillis, K.M., Allan, J.F., and Meyer, P.S. (Eds.), Proc. ODP, Sci. Results, 147: College Station, TX (Ocean Drilling Program), 157–172. doi:10.2973/odp.proc.sr.147.009.1996
- Anonymous, 1972. Penrose field conference on ophiolites. *Geotimes*, 17, pp. 24–25.
- Arai, S., and Matsukage, K., 1996. Petrology of gabbro-troctolite-peridotite complex from Hess Deep, equatorial Pacific: implications for mantle-melt interaction within the oceanic lithosphere. In Mével, C., Gillis, K.M., Allan, J.F., and Meyer, P.S. (Eds.), Proc. ODP, Sci. Results, 147: College Station, TX (Ocean Drilling Program), 135–155. doi:10.2973/odp.proc.sr.147.008.1996
- Arai, S., Ishimaru, S., Okrugin, V.M., 2003. Metasomatized harzburgite xenoliths from Avacha volcano as fragments of mantle wedge of the Kamchatka arc : Implication for the metasomatic agent. *The Island Arc* 12, 233-246.
- Arzi, A., 1978. Critical phenomena in the rheology of partially melted rocks. *Tectonophysics* 44, 173-184.
- Aumento, F., Loubat, H., 1971. The Mid-Atlantic Ridge near 45°N, XVI, Serpentinized ultramafic intrusions. *Can. J. Earth Sci.* 8, 631-663.
- Avé-Lallemant, H.G., Carter, N.L., 1970. Syntectonic recrystallization of olivine and modes of flow in the upper mantle. *Geol. Soc. Am. Bull.* 81, 2003-2020.
- Azough, F., Freer, R., 2000. Iron Diffusion in Single-Crystal Diopside. *Phys. Chem. Minerals* 27, 732-740.
- Bédard, J.H., 1994. A procedure for calculating the equilibrium distribution of trace elements among the minerals of cumulate rocks, and the concentration of trace elements in coexisting liquids. *Chem. Geol.* 118, 143-153.
- Bédard, J.H., Hébert, R., 1996. The lower crust of the Bay of Islands ophiolite, Canada: Petrology, mineralogy, and the importance of syntexis in magmatic differentiation in ophiolites and at ocean ridges. *J. Geophys. Res.* 101, 25105-25124.
- Bédard, J.H., Hébert, R., Berclaz, A., Varfalvy, V., 2000. Syntexis and the genesis of lower oceanic crust. *Geol. Soc. Am.* 349, 105-119.
- Bédard, J.H., 2005. Partitioning coefficients between olivine and silicate melts. *Lithos* 83, 394-419.
- Béjina, F., Jaoul, O., 1997. Silicon diffusion in silicate minerals. *Earth. Planet. Sci. Lett.* 153, 229-238.
- Bedini, R.-M., Bodinier, J.-L., 1999. Distribution of incompatible trace elements between the constituents of spinel peridotite xenoliths : ICP-MS data from the East African Rift. *Geochim. Cosmochim. Acta* 63(22), 3883-3900.
- Bence, A.E., D.M. Baylis, J.F. Bender, Grove, T.L., 1979. Controls on the major and minor element chemistry of mid-ocean ridge basalts and glasses. In Talwani, M., Harrison,

- C.G., and Hayes, D.E. (Eds), Deep Drilling Results in the Atlantic Ocean: Oceanic Crust, Maurice Ewing Symposium. AGU Washington D.C. pp. 331-341.
- Bender, J.F., Hodges, F.N., Bence, A.E., 1978. Petrogenesis of basalts from the project FAMOUS area : experimental study from 0 to 15 Kbars. *Earth. Planet. Sci. Lett.* 41, 277-302.
- Ben Ismail, W., Mainprice, D., 1998. An olivine fabric database: An overview of upper mantle fabrics and seismic anisotropy. *Tectonophysics* 296, 145-158.
- Benn, K., Nicolas, A., Reuber, I., 1988. Mantle-crust transition zone and origin of wehrlitic magmas : Evidence from the Oman ophiolite. *Tectonophysics* 151, 75-85.
- Benn, K., Allard, B., 1989. Preferred mineral orientations related to magmatic flow in ophiolite layered gabbros. *J. Petrol.* 30(4), 925-946.
- Berger, E.T., Vannier, M., 1984. Les dunites en enclaves dans les basaltes alcalins des îles océaniques : approche pétrologique. *Bull. Mineral.* 107, 649-663.
- Best, M.G., 2003. *Igneous and metamorphic petrology*- 2nd ed. Blackwell Publishing, 729 pp.
- Blackman, D.K., Cann, J.R., Janssen, B., Smith, D.K., 1998. Origin of extensional core complexes: evidence from the MAR at Atlantis Fracture Zone. *J. Geophys. Res.* 103, 21315-21334.
- Blackman, D.K., Karson, J.A., Kelley, D.S., Cann, J.R., Fruh-Green, G.L., Gee, J.S., Hurst, S.D., John, B.E., Morgan, J., Noonan, S.L., Ross, D.K., Schroeder, T.J., Williams, E.A., 2002. Geology of the Atlantis Massif (MAR 30°N): implications for the evolution of an ultramafic oceanic core complex. *Mar. Geophys. Res.* 23(5-6), 443-469.
- Blackman, D.K., Ildefonse, B., John, B.E., Ohara, Y., Miller, D.J., MacLeod, C.J., and the Expedition 304/305 Scientists, 2006. Proc. IODP, 304/305: College Station TX (Integrated Ocean Drilling Program Management International, Inc.). doi:10.2204/iodp.proc.304305.2006
- Blackman, D. K., Karner, G.D., Searle, R.C., 2008. Three-Dimensional Structure of Oceanic Core Complexes : Effects on Gravity Signature and Ridge Flank Morphology, Mid-Atlantic Ridge 30°N. *Geochem. Geophys. Geosyst.*
- Blenkinsop, T. G., 2000. *Deformation Microstructures and Mechanisms in Minerals and Rocks*. Kluwer Academic, Dordrecht, pp 150.
- Bloomer, S.H., Natland, J.H., Fisher, R.L., 1989. Mineral relationships in gabbroic rocks from fracture zones of Indian Ocean Ridges: evidence for extensive fractionation, parental diversity and boundary-layer recrystallization. *Geol. Soc. London Special Publications* 42, 107-124.
- Bloomer, S.H., Meyer, P.S., Dick, H.J.B., Ozawa, K., Natland, J.H., 1991. Textural and mineralogic variations in gabbroic rocks from Hole 735B. In Von Herzen, R., Robinson, P.T., et al., Proc. ODP, Sci. Results, 118: College Station, TX (Ocean Drilling Program), 21–39. doi:10.2973/odp.proc.sr.118.136.1991
- Blundy, J.D., Wood, B.J., 1991. Crystal-chemical controls on the partitioning of Sr and Ba between plagioclase feldspar, silicate melts, and hydrothermal solutions. *Geochim. Cosmochim. Acta* 55, 193–209.
- Blundy, J., Wood, B.J., 2003. Partitioning of trace elements between crystals and melts. *Earth Planet. Sci. Lett.* 210, 383–397.
- Bodinier, J.-L., Menzies, M.A., Thirlwall, M.F., 1991. Continental to oceanic mantle transition - REE and Sr-Nd isotopic geochemistry of the Lanzo lherzolite massif. *J. Pet.*, sp. volume "Orogenic Lherzolites and Mantle Processes": 191-210.
- Bodinier, J.-L., Merlet, C., Bedini, R.M., Simien, F., Remaïdi, M. and Garrido, C.J., 1996. Distribution of Nb, Ta and other highly incompatible trace elements in the lithospheric mantle : the spinel paradox. *Geochim. Cosmochim. Acta*, 60(3): 545-550.

- Bodinier, J. L., Garrido, C. J., Chanefo, I., Bruguier, O. and Gervilla, F., 2008. Origin of pyroxenite-peridotite veined mantle by refertilization reactions: Evidence from the Ronda peridotite (Southern Spain). *Journal of Petrology* 49, 999-1025. doi:10.1093/petrology/egn014.
- Boillot, G., Recq, M., Winterer, E., and 21 others, 1986. Amincissement de la croûte continentale et dénudation tectonique du manteau supérieur sous les marges stables : à la recherche d'un modèle. L'exemple de la marge occidentale de la Galice (Espagne). *Bull. centres Rech. Explor.-Prod. Elf-Aquitaine*. 10, 1, 95-104.
- Bonatti, E., Honnorez, J., Ferrara, G., 1971. Peridotite-gabbro-basalt complex from the equatorial Mid-Atlantic Ridge, *Phil. Trans. R. Soc. London* 268, 385-402.
- Bonatti, E., Emiliani, C., Ferrara, G., Honnorez, J., Rydell, H., 1974. Ultramafic carbonate breccias from the equatorial MAR. *Mar. Geol.* 17, 83-102.
- Bonatti, E., Ottonello, G., Hamlyn, P.R., 1986. Peridotites from the Island of Zabargad (St John), Red Sea : Petrology and geochemistry. *J. Geophys. Res.* 91, 599-631
- Bonatti, E., Peyve, A., Kepezhinskas, P., Kurentsova, N., Seyler, M., Skolotnev, S., Udintsev, G., 1992. Upper mantle heterogeneity below the Mid-Atlantic Ridge, 0-15°N. *J. Geophys. Res.* 97(B4), 4461-4476.
- Bonatti, E., Seyler, M., Sushevskaya, N., 1993. A cold suboceanic mantle belt at the Earth's equator. *Science* 261, 315-320.
- Borghini, G., Rampone, E., Crispini, L., De Ferrari, R., Godard, M., 2007. Origin and emplacement of ultramafic-mafic intrusions in the Erro-Tobbio mantle peridotite (Ligurian Alps, Italy). *Lithos* 94(1-4), 210-229.
- Borghini, G., Rampone, E., 2007. Postcumulus processes in oceanic-type olivine-rich cumulates: the role of trapped melt crystallization versus melt/rock interaction. *Contrib. Mineral. Petrol.* 154(6), 619-633.
- Boschi, C., Früh-Green, G.L., Delacour, A.G., Karson, J.A., Kelley, D.S., 2006. Mass transfer and fluid flow during detachment faulting and development of an oceanic core complex, Atlantis Massif (MAR 30°N). *Geochem. Geophys. Geosyst.* - G 3, 7, 2005GC001074.
- Boudier, F., Nicolas, A., 1985. Harzburgite and lherzolite subtypes in ophiolitic and oceanic environments. *Earth Planet. Sci. Lett.* 76, 84-92.
- Boudier, F., 1991. Olivine xenocrysts in picritic magmas-An experimental and microstructural study. *Contrib. Mineral. Petrol.* 109(1), 114-123.
- Boudier, F., Nicolas, A., 1995. Nature of the Moho transition zone in the Oman ophiolite. *J. Petrol.* 36(3), 777-796.
- Boudier, F., Nicolas, A., Ildefonse, B., 1996. Magma chambers in the Oman ophiolite: fed from the top or from the bottom ? *Earth Planet. Sci. Lett.* 144, 239-250.
- Bowen, N.L., 1928. *The evolution of the Igneous Rocks*. Princeton University press, 332 pp.
- Bowen, N.L., 1941. Certain Singular Points on Crystallization Curves of Solid Solutions. *Proc. natn. Acad. Sci. USA* 27(6), 301-309.
- Brun J.P., Beslier M.O., 1996. Mantle exhumation at passive margin. *Earth Planet. Sci. Lett.* 142, 161-173.
- Bunge, H.J., 1982. *Texture Analysis in Materials Science*. Butterworths, London, 599 pp.
- Buck, W.R., 1988. Flexural rotation of normal faults. *Tectonics* 7, 959-973.
- Buck, W.R., 1991. Modes of continental lithospheric extension. *J. Geophys. Res.* 96(B12), 20161-20178.
- Buck, W.R., Lavier, L.L., Poliakov, A.N.B., 2005. Modes of faulting at mid-ocean ridges. *Nature* 434(7034), 719-723.

- Canales, J.P., Detrick, R.S., Lin, J., Collins, J.A., Toomey, D.R., 2000. Crustal and upper mantle seismic structure beneath the rift mountains and across a nontransform offset at the Mid-Atlantic Ridge (35 degrees N). *J. Geophys. Res.* 105: 2699-2719.
- Canales, J.P., Tucholke, B.E., Collins, J.A., 2004. Seismic reflection imaging of an oceanic detachment fault: Atlantis megamullion (Mid-Atlantic Ridge, 30 degrees 10 ' N). *Earth. Planet. Sci. Lett.* 222(2), 543-560.
- Canales, J.P., Sohn, R.A., Demartin, B.J., 2007. Crustal structure of the Trans-Atlantic Geotraverse (TAG) segment (Mid-Atlantic Ridge, 26 degrees 10-Minutes-N): Implications for the nature of hydrothermal circulation and detachment faulting at slow spreading ridges. *Geochem. Geophys. Geosyst.* -G3, 8. DOI: 10.1029/2007GC001629
- Canales, J.P., Tucholke, B.E., Xu, M., Collins, J.A., Dubois, D.L., 2008. Seismic evidence for large-scale compositional heterogeneity of oceanic core complexes. *Geochem. Geophys. Geosyst.* - G3, in-press.
- Cann, J.R., Blackman D.K., Smith, D.K., McAllister, E., Janssen, B., Mello, S., Avgerinos, E., Pascoe, A.R., Escartin J., 1997. Corrugated slip surfaces formed at ridge-transform intersections on the Mid-Atlantic Ridge. *Nature* 385, 329-332.
- Cann, J.R., Prichard, H.M., Malpas, J.G., Xenophontos, C., 2001. Oceanic inside corner detachments of the Limassol Forest area, Troodos ophiolite, Cyprus. *J. Geol. Soc.* 158, 757-767.
- Cannat, M., Bideau, D., Hebert, R., 1990. Plastic deformation and magmatic impregnation in serpentinized ultramafic rocks from the Garrett transform fault (East Pacific Rise). *Earth Planet. Sci. Lett.* 101, 216-232.
- Cannat, M., Bideau, D., Bougault, H., 1992. Serpentinized peridotites and gabbros in the Mid-Atlantic Ridge axial valley at 15 37'N and 16 52'N. *Earth Planet. Sci. Lett.* 109, 87-106.
- Cannat, M., 1993. Emplacement of mantle rocks in the seafloor at mid-ocean ridges. *J. Geophys. Res.* 98, 4163-4172.
- Cannat, M., Mevel, C., Maia, M., Deplus, C., Durand, C., Gente, P., Agrinier, P., Belarouchi, A., Dubuisson, G., Humler, E., Reynolds, J., 1995a. Thin crust, ultramafic exposures, and rugged faulting patterns at Mid-Atlantic Ridge (22 degrees 24 degrees N). *Geology* 23(1), 49-52.
- Cannat, M., Karson, J.A., Miller, D.J., et al., 1995b. Proc. ODP, Init. Repts, 153: College Station, TX (Ocean Drilling Program). doi:10.2973/odp.proc.ir.153.1995
- Cannat, M., Casey, J.F., 1995. An ultramafic lift at the Mid-Atlantic Ridge: successive stages of magmatism in serpentinized peridotites from the 15°N region, in: R.L.M. Vissers, A. Nicolas (Eds.), *Mantle and Lower Crust Exposed in Oceanic Ridges and in Ophiolites*, Kluwer, Dordrecht, 1995, pp. 5–34.
- Cannat, M., 1996. How thick is the magmatic crust at slow spreading oceanic ridges? *J. Geophys. Res.* 101(B2), 2847-2857.
- Cannat, M., Chatin, F., Whitechurch, H., Ceuleneer, G., 1997. Gabbroic rocks trapped in the upper mantle at the Mid-Atlantic Ridge. In Karson, J.A., Cannat, M., Miller, D.J., and Elthon, D. (Eds.), *Proc. ODP, Sci. Results, 153: College Station, TX (Ocean Drilling Program)*, 243–264. doi:10.2973/odp.proc.sr.153.013.1997
- Cannat, M., Cann, J., Maclennan, J., 2004. Some hard rock constraints on the supply of heat to mid-ocean ridges. In C.R. German, J. Lin, L.M. Parson (Editors), *Mid-ocean ridges; hydrothermal interactions between the lithosphere and oceans. Geophysical Monograph. Am. Geophys. Union, Washington, DC, United States, vol.148*, pp.111-149.

- Cannat, M., Sauter, D., Mendel, V., Ruellan, E., Okino, K., Escartin, J., Combier, V., Baala, M., 2006. Modes of seafloor generation at a melt-poor ultraslow-spreading ridge. *Geology* 34, 605-608, doi: 10.1130/G22486.1.
- Carlson, R.L., 2001. The abundance of ultramafic rocks in Atlantic Ocean crust. *Geophys. J. Int.* 144, 37-48.
- Casey, J.F., 1997. Comparaison of major- and trace element geochemistry of abyssal peridotites and mafic plutonic rocks with basalts from the Mark region of the Mid-Atlantic Ridge. In Karson, J.A., Cannat, M., Miller, D.J., and Elthon, D. (Eds.), *Proc. ODP, Sci. Results, 153: College Station, TX (Ocean Drilling Program)*, 181–241. doi:10.2973/odp.proc.sr.153.012.1997
- Chakraborty, S., Farvet, J.R., Yund, R.A., Rubie, D.C., 1994. Mg tracer diffusion in synthetic forsterite and San Carlos olivine as a function of P, T, and f_{O_2} , *Phys. Chem. Miner.* 21, 489-500.
- Chakraborty, S., 1997. Rates and Mechanisms of Fe-Mg interdiffusion in olivine at 980°C-1300°C. *J. Geophys. Res.* 102, 12317-12331.
- Cherniack, D. J., 2003. REE diffusion in feldspar. *Chem. Geol.* 193, 25-4.
- Cherniack, D.J., 2007. REE diffusion in olivine. AGU Fall Meeting 2007; MR13C-1397.
- Ceuleneer, G., Rabinowicz, M., 1992. Mantle flow and melt migration beneath oceanic ridges: Models derived from observation in ophiolites. In: . In J.P. Morgan, D.B. Blackman, J.M. Sinton (Editors), *Mantle Flow and Melt Generation at Mid-Ocean Ridges. Geophysical Monograph. Am. Geophys. Union, Washington, DC, United States*, vol.71, pp.123-154.
- Constantin, M., Hekinian, R., Bideau, D., Hebert, R., 1996. Construction of the oceanic lithosphere by magmatic intrusions: Petrological evidence from plutonic rocks formed along the fast-spreading East Pacific Rise. *Geology* 24, 731-734.
- Coogan, L.A., Kempton, P.D., Saunders, A.D., Norry, M.J., 2000a. Melt aggregation within the crust beneath the Mid-Atlantic Ridge: evidence from plagioclase and clinopyroxene major and trace element compositions. *Earth Planet. Sci. Lett.* 176(2), 245-257.
- Coogan, L.A., Saunders, A.D., Kempton, P.D., Norry, M.J., 2000b. Evidence from oceanic gabbros for porous melt migration within a crystal mush beneath the Mid-Atlantic Ridge. *Geochem. Geophys. Geosyst. - G3*, 1(9). doi: 10.1029/2000GC000072.
- Coogan, L.A., MacLeod, C.J, Dick, H.J.B., Edwards, S.J., Kvassnes, A., Natland, J.H., Robinson, P.T., Thompson, G., O'Hara, M.J., 2001. Whole-rock geochemistry of gabbros from the Southwest Indian Ridge: constraints on geochemical fractionations between the upper and lower oceanic crust and magma chamber processes at (very) slow-spreading ridges. *Chem. Geol.* 178(1-4), 1-22.
- Coogan, L. A., Hain, A., Stahl, S., Chakraborty, S., 2005. Experimental determination of the diffusion coefficient for calcium in olivine between 900°C and 1500°C. *Geochim. Cosmochim. Acta* 69(14), 3683-3694.
- Cooper, R.F., Kohlstedt, D.L., 1986. Rheology and structure of olivine basalt partial melts. *J. Geophys. Res.* 91, 93-15-9323.
- Cortesogno, L., Galbiati, B., Principi, G., Venturelli, G., 1978. La breccia ofiolitiche della Liguria orientale : nuovi dati e discussione sui modelli paleogeografici. *Ofioliti* 3, 99-160.
- Cortesogno, L., Gaggero, L., Zanetti, A., 2000. Rare earth and trace elements in igneous and high-temperature metamorphic minerals of oceanic gabbros (MARK area, Mid-Atlantic Ridge). *Contrib. Min. Petrol.* 139, 373-393.
- Costa, F., Dungan, M., 2005. Short time scales of magmatic assimilation from diffusion modeling of multiple elements in olivine. *Geology* 33(10), 837-840.

- Cottrell, E., Spiegelman, M., Langmuir, C.H., 2002. Consequences of diffusive reequilibration for the interpretation of melt inclusions. *Geochem. Geophys. Geosyst.* 3, 1026;
- Crank, J., 1979. *The Mathematics of diffusion*. Oxford University Press, Oxford.
- Davis, G.A., 1983. Shear-zone model for the origin of metamorphic core complexes. *Geology* 11, 342-347.
- Davis, G.A., Lister, G.A., 1988, Detachment faulting in continental extension; perspective from the southwestern U.S. Cordillera. In Clark, S. P., et al., eds., *Processes in continental lithospheric deformation: Geol. Soc. Am. Special Paper 218*, pp. 133–159.
- DeMartin, B.J., Canales, R.A.R., Canales, J.P., Humpris, S.E., 2007. Kinematics and geometry of active detachment faulting beneath the Trans-Atlantic Geotraverse (TAG) hydrothermal field on the Mid-Atlantic Ridge. *Geology* 35, 711-714.
- De Paolo, D.J., 1981. Trace element and isotopic effects of combined wallrock assimilation and fractional crystallization. *Earth Planet. Sci. Lett.* 53, 189-202.
- Detrick, R.S., Needham, H.D., Renard, V., 1995. Gravity anomalies and crustal thickness variations along the Mid-Atlantic Ridge between 33 degree N and 40 degree N. *J. Geophys. Res.* 100(B3), 3767-3787.
- Detrick, R.S., Toomey, D.R., Collins, J.A., 1998. Three-dimensional upper crustal heterogeneity and anisotropy around Hole 504B from seismic tomography. *J. Geophys. Res.* 103(B12), 30485-30504.
- Dick, H.J.B., Thompson, G., Bryan, W.B., 1981. Low-angle faulting and steady-state emplacement of plutonic rocks at ridge-transform intersections. *EOS, Trans. Am. Geophys. Union* 62 (1981), p. 406 (abstract).
- Dick, H.J.B., Bullen, T., 1984. Chromian spinel as a petrogenetic indicator in abyssal and alpine-type peridotites and spatially associated lavas. *Contrib. Mineral. Petrol.* 86(1), 54-76.
- Dick, H.J.B., 1989. Abyssal peridotites, very slow spreading ridges and ocean ridge magmatism. In: A.D. Saunders and M.J. Norry (Editors), *Magmatism in the Ocean Basins*. *Geol. Soc. London Special Publication*, London 42, pp 71-105.
- Dick, H.J.B., Schouten, H., Meyer, P.S., Gallo, D.G., Berg, H., Tyce, R., Patriat, P., Johnson, K., Snow, J., Fisher, A., Bathymetric map of the Atlantis II Fracture Zone, Southwest Indian Ridge, *Proc. ODP, Sci. Results* 118, 1991. Dick, H.J.B., Natland, J.H., 1996. Late-stage melt evolution and transport in the shallow mantle beneath the East Pacific Rise. In Mével, C., Gillis, K.M., Allan, J.F., and Meyer, P.S. (Eds.), *Proc. ODP, Sci. Results*, 147: College Station, TX (Ocean Drilling Program), 103–134. doi:10.2973/odp.proc.sr.147.007.1996
- Dick, H.J.B., Natland, J.H., Miller, D.J., et al., 1999. *Proc. ODP, Init. Repts.*, 176: College Station, TX (Ocean Drilling Program). doi:10.2973/odp.proc.ir.176.1999
- Dick, H.J.B., Natland, J.H., Alt, J.C., Bach, W., Bideau, D., Gee, J.S., Haggas, S., Hertogen, J.G.H., Hirth, G., Holm, P.M., Ildefonse, B., Iturrino, G.J., John, B.E., Kelley, D.S., Kikawa, E., Kingdon, A., LeRoux, P.J., Maeda, J., Meyer, P.S., Miller, D.J., Naslund, H.R., Niu, Y., Robinson, P.T., Snow, J., Stephen, R.A., Trimby, P.W., Worm, H.-U., Yoshinobu, A., 2000. A long in situ section of the lower ocean crust: results of ODP Leg 176 drilling at the Southwest Indian Ridge. *Earth Planet. Sci. Lett.*, 179:31-51. doi:10.1016/S0012-821X(00)00102-3
- Dick, H.J.B., Natland, J.H., Ildefonse, 2006. Past and Future Impact of Deep Drilling in the Ocean Crust and Mantle: An Evolving Order Out of New Complexity. *Oceanography* 19 (4), 72-80.

- Dick, H. J. B., Tivey, M.A., Tucholke, B.E., 2008. Plutonic foundation of a slow-spreading ridge segment: Oceanic core complex at Kane Megamullion, 23 degrees 30 ' N, 45 degrees 20 ' W. *Geochem. Geophys. Geosyst.* 9. DOI: 10.1029/2007GC001645.
- Dietz, R.S., 1963. Alpine serpentines as oceanic rind fragments. *Geol. Soc. Am. Bull.* 74(7), 947-952.
- Dijkstra, A.H., Drury, M.R., Fijhoff, R.M., 2002. Microstructures and lattice fabrics in the Hilti mantle section (Oman Ophiolite): Evidence for shear localization and melt weakening in the crust-mantle transition zone? *J. Geophys. Res.* 107(B11), 2270-2288.
- Dijkstra, A.H., Barth, M.G., Drury, M.R., Mason, P.R.D., Vissers R.M.L., 2003. Diffuse porous melt flow and melt-rock reaction in the mantle lithosphere at the slow-spreading ridge: a structural petrology and LA-ICP-MS study of the Othris Peridotite Massif (Greece). *Geochem. Geophys. Geosyst.* 4, 1-24.
- Dimanov, A., Jaoul, O., 1998. Calcium self-diffusion in diopside at high temperature: implications for transport properties. *Phys. Chem. Minerals* 26, 116-127.
- Dohmen, R., Becker, H.W., Meißner, E., Etzel, T., Chakraborty, S., 2002. Production of silicate thin films using pulsed laser deposit (PLD) and applications to studies in mineral kinetics. *Eur. J. Minerals* 14, 1155-1168.
- Dohmen, R., Becker, H.-W., Chakraborty, S., 2003. Point defect equilibration and diffusion in olivine at low temperatures ($T < 1000^{\circ}\text{C}$). *Eur. J. Mineral.* 15, p. 42.
- Dohmen, R., Becker, H.-W., Chakraborty, S., 2007. Fe–Mg diffusion in olivine I: experimental determination between 700 and 1200 C as a function of composition, crystal orientation and oxygen fugacity. *Phys Chem Minerals* 34, 389–407.
- Donaldson, C.H., 1985. A comment on crystal shapes resulting from dissolution in magmas. *Mineral. Mag.* 49, 129-132.
- Dosso, L., Barry, B.H., Bougault, H., Schilling, J.-G., Joron, J.-L., 1991. Sr-Nd-Pb geochemical morphology between 10° and 17°N on the Mid-Atlantic Ridge: A new MORB isotope signature. *Earth Planet. Sci. Lett.* 106(1-4), 29-43.
- Dosso, L., Bougault, H., Joron, J.-L., 1993. Geochemical morphology of the North Mid-Atlantic Ridge, 10°–24°N: Trace element-isotope complementarity. *Earth Planet. Sci. Lett.* 120(3-4), 443-462.
- Dosso, L., Bougault, H., Langmuir, C., Bollinger, C., Bonnier, O., Etoubleau, J., 1999. The age and distribution of mantle heterogeneity along the Mid-Atlantic Ridge (31-41 degrees N). *Earth. Planet. Sci. Lett.* 170,(3), 269-286.
- Drouin, M., Godard, M., Ildefonse, B., 2007. Origin of olivine-rich troctolites from IODP Hole U1309D in the Atlantis Massif (Mid-Atlantic Ridge): Petrostructural and geochemical study. *Eos Trans. AGU*, 88(52), Fall Meet. Suppl., Abstract T53B-1300.
- Drouin, M., Godard, M., Ildefonse, B. Geochemical and petrographic evidence for magmatic impregnation in the oceanic lithosphere at Atlantis Massif, Mid-Atlantic Ridge (IODP Hole U1309D, 30°N), *Chem. Geol.*, accepté.
- Drouin, M., Ildefonse, B., Godard, M. Melt impregnation of mantle peridotites at slow-spreading ridges: A petrological and microstructural study of the olivine-rich troctolites from the Atlantis Massif (Mid-Atlantic Ridge 30°N, IODP Hole U1309D). *Earth Planet. Sci. Lett.*, en révision.
- Edwards, S.J., Malpas, J., 1996. Melt-peridotite interactions in shallow mantle at the East Pacific Rise: evidence from ODP site 895 (Hess Deep) *Mineral. Mag.* 60, 191-206.
- Elthon, D., 1979. High magnesia liquids as the parental magma for ocean floor basalts. *Nature* 278, 514-518.

- Elthon, D., Casey, J.F., Komor, S., 1982. Mineral chemistry of ultramafic cumulates from the North Arm Mountain Massif of the Bay of Islands Ophiolite: implication for high pressure fractionation of oceanic basalts. *J. Geophys. Res.* 87, 8717-8734.
- Elthon, D., 1987. Petrology of gabbroic rocks from the Mid-Cayman rise spreading center. *J. Geophys. Res.* 92(B1), 658-682.
- Elthon, D., Stewart, M., Ross, D.K., 1992. Compositional trends of minerals in oceanic cumulates. *J. Geophys. Res.* 97(B11), 15189-15199.
- Escartin, J., Cannat, M., 1999. Ultramafic exposures and the gravity signature of the lithosphere near the fifteen-Twenty Fracture Zone (Mid-Atlantic Ridge, 14°-16.5°N). *Earth Planet. Sci. Lett.* 171, 411 – 424.
- Escartin, J., Mevel, C., MacLeod, C. J., McCaig, A. M., 2003. Constraints on deformation conditions and the origin of oceanic detachments: The Mid-Atlantic Ridge core complex at 15 degrees 45 ' N. *Geochem. Geophys. Geosyst.* 4. doi: 10.1029/2002GC000472.
- Escartín, J., Smith, D.K., Cann, J., Schouten, H., Langmuir, C.L., Escrig, S., 2008. Central role of detachment faults in accretion of slow spreading oceanic lithosphere. *Nature* 455, 790-794.
- Expedition Scientific Party, 2005. Oceanic core complex formation, Atlantis Massif—oceanic core complex formation, Atlantis Massif, Mid-Atlantic Ridge: drilling into the footwall and hanging wall of a tectonic exposure of deep, young oceanic lithosphere to study deformation, alteration, and melt generation. *IODP Prel. Rept.*, 305. doi:10.2204/iodp.pr.305.2005
- Falloon, T.J., Green, D.H., 1987. Anhydrous partial melting of MORB pyrolite and other peridotite compositions at 10 kbar; implications for the origin of primitive MORB glasses. *Mineral. Petrol.* 37(3-4), 181-219.
- Fisk, M.R., Bence, A.E., 1980. Experimental crystallization of chrome spinel in FAMOUS basalt 527-1-1. *Earth Planet. Sci. Lett.* 48, 111-123.
- Fitton, J.G., Godard, M., 2004. Origin and evolution of magmas on the Ontong Java Plateau. In Fitton, J.G., Mahoney, J.J., Wallace, P.J., Saunders, A.D. (eds). *Origin and evolution of the Ontong-Java Plateau*. *Geol. Soc. London, Special Publications* 229, 151-178.
- Fox, P.J., Heezen, B.C., 1965. Sands of the Mid-Atlantic Ridge. *Science* 149, 1367-1370.
- Fox, P.J., Grindley, N.R., Macdonald, K.C., 1991. The Mid-Atlantic ridge (31 degrees S- 34 degrees 30'S)- Temporal and spatial variation of accretionary processes. *Mar. Geophys. Res.* 13(1), 1-20.
- Früh-Green, G.L., Scambelluri, M., Vallis, F., 2001. O-H isotope ratios of high pressure ultramafic rocks: implications for fluid sources and mobility in the subducted hydrous mantle. *Contrib. Mineral. Petrol.* 141(2), 145-159.
- Fujii, N., Bougault, H., 1983. Melting relations of a magnesian abyssal tholeiite and the origin of MORBs. *Earth Planet. Sci. Lett.* 62(2), 283-295.
- Fujii, T., 1990. Petrology of peridotites from Hole 670A, Leg 109. In Detrick, R., Honnorez, J., Bryan, W.B., Juteau, T., et al., *Proc. ODP, Sci. Results*, 106/109: College Station, TX (Ocean Drilling Program), 19–25. doi:10.2973/odp.proc.sr.106109.116.1990
- Fujiwara, T., Lin J., Matsumoto, T., Kelemen, P.B., Tucholke, B.E., Casey, J.F., 2003. Crustal Evolution of the Mid-Atlantic Ridge near the Fifteen-Twenty Fracture Zone in the last 5 Ma. *Geochem. Geophys. Geosyst.* 4, doi: 10.1029/2002GC000364
- Gaetani, G.A., Grove, T.L., 1995. Partitioning of rare earth elements between clinopyroxene and silicate melt: crystal-chemical controls. *Geochim. Cosmochim. Acta* 59, 1951–1962.
- Garrido, C.J., Drouin, M., Godard, M., Paulick, H., 2006. Petrogenesis of a highly

- differentiated section of oceanic crust drilled at the Mid-Atlantic Ridge, 14-16°N (ODP Leg 209, Site 1275D). *Geophysical Research Abstracts*, Vol. 8, 10325, 2006. SRef-ID: 1607-7962/gra/EGU06-A-10325
- Gao, Y., Hoefs, J., Hellebrand, E., Von de Handt, A., Snow, J.E., 2007. Trace element zoning in pyroxenes from ODP Hole 735B gabbros: diffuse exchange or synkinematic crystal fractionation? *Contrib. Mineral. Petrol.* 153, 429-442.
- Garrido, C.J., Bodinier, J.-L. and Alard, O., 2000. Distribution of LILE, REE and HFSE in anhydrous spinel peridotite and websterite minerals from the Ronda massif: insights into the nature of trace element reservoirs in the subcontinental lithospheric mantle. *Earth Planet. Sci. Lett.*, 181(3): 341-358.
- Gente, P., Pockalny, R.A., Durand, C., Deplus, C., Maia, M., Ceuleneer, G., Mevel, C., Cannat, M., Laverne, C., 1995. Characteristics and evolution of the segmentation of the Mid-Atlantic Ridge between 20 degrees N and 24 degrees N during the last 10 million years. *Earth Planet. Sci. Lett.* 129(1-4): 55-71.
- Gerbert-Gaillard, L., 2002. Caractérisation géochimique des peridotites de l'ophiolite d'Oman : Processus magmatiques aux limites lithosphère/asthenosphère. Doctorat Thesis, Montpellier 2, Montpellier, 266 pp. Available at <http://tel.archives-ouvertes.fr/tel-00002961/en/>
- Ghiorso, M.S., 1985. Chemical mass-transfer in magmatic processes. 1. Thermodynamic relations and numerical algorithms. *Contrib. Mineral. Petrol.* 90(2-3), 107-120.
- Ghiorso, M.S., Sack R.O., 1995. Chemical mass transfer in magmatic processes IV. A revised and internally consistent thermodynamic model for the interpolation and extrapolation of liquid-solid equilibria in magmatic systems at elevated temperatures and pressures. *Contrib. Mineral. Petrol.* 119(2-3), 197-212.
- Gillis, K.M., Meyer, P.S., 2001. Metasomatism of oceanic gabbros by late stage melts and hydrothermal fluids: Evidence from the rare earth element composition of amphiboles. *Geochem. Geophys. Geosyst.* 2, 2000GC000087.
- Girardeau, J., Mercier, J.-C., 1992. Evidence for plagioclase-lherzolite intrusion in the Mid-Atlantic Ridge, DSDP Leg 37 from Parson, L.M., Murton, B.J., Browning, P. (eds), *Ophiolites and their modern oceanic analogues*. Geol. Soc. Sp. Publication 60, 241-250 pp.
- Girardeau, J., Franchetau, J., 1993. Plagioclase-wehrlites and peridotites on the East Pacific Rise (Hess Deep) and the Mid-Atlantic Ridge (DSDP Site 334) - evidence for magma percolation in the oceanic upper mantle. *Earth Planet. Sci. Lett.* 115, 137-149.
- Godard, M., Jousset, D., Bodinier, J.-L., 2000. Relationships between geochemistry and structure beneath a palaeo-spreading centre: A study of the mantle section in the Oman Ophiolite. *Earth Planet. Sci. Lett.* 180, 133-148.
- Godard, M., Awaji, S., Hansen, H., Hellebrand, E., Brunelli, D., Johnson, K., Maeda, J., Yamasaki, T., Abratis, M., Christie, D., Kato, Y., Rosner, M., Mariet, C., submitted June 2008. Geochemistry of a long in-situ section of intrusive slow-spread crust: Results from IODP Site U1309 (Atlantis Massif, 30°N Mid-Atlantic-Ridge), *Earth Planet. Sci. Lett.*, in press.
- Godard, M., Lagabrielle, Y., Alard, O., Harvey, J., 2008. Geochemistry of the highly depleted peridotites drilled at ODP Sites 1272 and 1274 (Fifteen-Twenty Fracture Zone, Mid-Atlantic Ridge): Implications for mantle dynamics beneath a slow spreading ridge. *Earth Planet. Sci. Lett.* 267(3-4), 410-425.
- Gràcia, E., Charlou, J.L., Radford-Knoery, J., Parson, L.M., 2000. Non-transform offsets along the Mid-Atlantic Ridge south of the Azores (38 degrees N-34 degrees N): ultramafic exposures and hosting of hydrothermal vents. *Earth Planet. Sci. Lett.* 177(1-2), 89-103.

- Green, D.H., Ringwood, A.E., 1967. The genesis of basaltic magmas. *Contrib. Mineral. Petrol.* 15, 103-190.
- Grimes, C.B., John, B.E., Cheadle, M.J., Wooden, J.L., 2008. Protracted construction of gabbroic crust at a slow-spreading ridge: Constraints from $^{206}\text{Pb}/^{238}\text{U}$ zircon ages from Atlantis Massif and IODP Hole U1309D (30°N, MAR). *Geochem. Geophys. Geosyst.*, doi:10.1029/2008GC002063
- Grindley, N.R., Fox, P.J., Vogt, P.R., 1992. Morphology and tectonics of the Mid-Atlantic Ridge (25°-27°30'S) from Sea Beam and magnetic data. *J. Geophys. Res.* 13, 15-80.
- Grove, T.L., Bryan, W.B., 1983. Fractionation of pyroxene-phyric MORB at low pressure-an experimental-study. *Contrib. Mineral. Petrol.* 84(4), 293-309.
- Grove, T.L., Kinzler, R.J., Bryan, W.B., 1992. Fractionation of Mid-Ocean Ridge Basalt (MORB). In: J. Philipps Morgan, D.K. Blackman and J.M. Sinton (Eds.), *Mantle flow and melt generation at Mid-Ocean Ridges*. Am. Geophys. Union, pp. 281-311.
- Gunther, D., Heinrich, C.A., 1999. Enhanced sensitivity in laser ablation-ICP mass spectrometry using helium-argon mixtures as aerosol carrier - Plenary lecture. *J. Anal. Atom. Spectrom.* 14(9), 1363-1368.
- Handy, M.R., Mulch, A., Roseneau, M., Rosenberg, C.L., 2001. A synthesis of the role of fault zones and melts as agents of weakening, hardening and differentiation of the continental crust. In: *the Nature and Tectonic Significance of Fault Zone Weakening*. Eds. Holdsworth, R.E., Strachan, R.A., Magloughlin, J.F and Knipe R.J., Geol. Soc. London, special publication 186, 305-332.
- Hart S. R., Davis K. (1978) Nickel partitioning between olivine and silicate melt. *Earth Planet. Sci. Lett.* 40, 203-219.
- Hart, S.R., Blusztajn, J., Dick, H.J.B., Meyer, P.S., Muehlenbachs, K., 1999. The fingerprint of seawater circulation in a 500-meter section of ocean crust gabbros. *Geochim. Cosmochim. Acta* 63(23-24), 4059-4080.
- Hébert, R., Bideau, D., Hékinian, R., 1983. Ultramafic and mafic rocks from the Garret transform fault near 13°30'S on the East Pacific Rise: igneous petrology. *Earth Planet. Sci. Lett.* 65, 107-125.
- Hébert, R., Constantin, M., Robinson, P.T., 1991. Primary mineralogy of Leg 118 gabbroic rocks and their place in the spectrum of oceanic mafic igneous rocks. In Von Herzen, R., Robinson, P.T., et al., *Proc. ODP, Sci. Results, 118: College Station, TX (Ocean Drilling Program)*, 3-20. doi:10.2973/odp.proc.sr.118.119.1991
- Hékinian, R., Bideau, D., Francheteau, J., Cheminée, J.L., Armijo, R., Lonsdale, P., Blum, N., 1993. Petrology of the East Pacific Rise crust and upper mantle exposed in Hess deep (Eastern Equatorial Pacific). *J. Geophys. Res.* 98(B5), 8069-8094.
- Herzberg, C., O'Hara, M. J., 1998. Phase equilibrium constraints on the origin of basalts, picrites, and komatiites. *Earth-Science Reviews* 44, 39-79.
- Herzberg, C., 2004. Partial crystallization of mid-ocean ridge basalts in the crust and mantle. *J. Petrol.* 45(12), 2389-2405.
- Herzberg, C., Asimow, P.D., Arndt, N., Niu, Y.L., Leshner, C.M., Fitton, J.G., Cheadle, M.J., et Saunders, A.D., 2007. Temperatures in ambient mantle and plumes: Constraints from basalts, picrites, and komatiites. *Geochem. Geophys. Geosyst.*, 8(2).
- Hess, H.H., 1962. History of ocean basins. in: *Petrologic Studies, Burlington Volume*, A.E.J.
- Hofmann, A.W., 1988. Chemical differentiation of the Earth: the relationship between mantle, continental crust, and oceanic crust. *Earth Planet. Sci. Lett.* 90, 297-314.
- Holmes, A. 1929. Radioactivity and Earth movements. *Trans. Geol. Soc. Glasg.* 18(3), 559-606.

- Hoofft, E. E. E., Detrick, R. S., Toomey, D. R., Collins, J. A., 2000. Crustal thickness and structure along three contrasting spreading segments of the Mid-Atlantic Ridge, 33.5 degrees-35 degrees N. *J. Geophys. Res.* 105(B4), 8205-8226.
- Houlier, B., Jaoul, O., Abel, F., Liebermann, R.C., 1988. Oxygen and silicon self-diffusion in natural olivine at T= 1300°C. *Phys. Earth. Planet. Inter.* 50, 240-250.
- Houlier, B., Cheraghmakani M., Jaoul, O., 1990. Silicon diffusion in San Carlos olivine. *Phys. Earth. Planet. Inter.* 62, 329-340.
- Lin, J., Houtz, R., Ewing, J., 1976. Upper crustal structure as a function of plate age. *J. Geophys. Res.* 81, 2490-2498.
- Ildefonse, B., Launeau, P., Bouchez, J.L., Fernandez, A., 1992. Effect of mechanical interactions on the development of shape preferred orientations: a two-dimensional experimental approach. *J. Struct. Geol.* 14(1), 73-83.
- Ildefonse, B., Arbaret, L., Diot, H., 1997. Rigid particles in simple shear flow: is their orientation periodic or steady-state? In: "Granite: from segregation of melt to emplacement fabrics" (J. L. Bouchez, D. Hutton & W. E. Stephens, eds.), Kluwer, Dordrecht, pp. 177-185.
- Ildefonse, B., Blackman, D.K., John, B.E., Ohara, Y., Miller, D.J., MacLeod, C.J., and the IODP Expeditions 304-305 Scientists, 2006. IODP Expeditions 304 & 305 Characterize the Lithology, Structure, and Alteration of an Oceanic Core Complex. *Scientific Drilling* 3, 4-11, doi:10.2204/iodp.sd.3.01.2006.
- Ildefonse, B., Christie, D.M., and Mission Moho Workshop Steering Committee, 2007a. Mission Moho workshop : drilling through the oceanic crust to the Mantle. *Scientific Drilling* 4, 11-18. doi:10.2204/iodp.sd.4.02.2007.
- Ildefonse, B., Rona, P.A., Blackman, D.K., 2007b. Deep Sampling of the Crust formed at Mid- Ocean Ridges: Scientific Ocean Drilling provides 'in-depth' perspective. *Oceanography* 20(1), 22-33.
- Ildefonse, B., Blackman, D.K., John, B.E., Ohara, Y., Miller, D.J., MacLeod, C.J., and the IODP Expeditions 304-305 Scientists, 2007c. Oceanic Core Complexes and Crustal Accretion at Slow-Spreading Ridges. *Geology* 35, 623-626; doi: 10.1130/G23531A.1.
- Ionov, D., 1996. Distribution and residence of lithophile trace elements in minerals of garnet and spinel peridotites: an ICP-MS study. *J. Conf. Abs.* 1, 278.
- IODP Expeditions 304-305 Scientists, 2005. IODP Expeditions 304 and 305: Oceanic Core Complex formation, Atlantis Massif. *Scientific Drilling* 1, 28-31.
- Irvin, T.N., 1982. Terminology for layered intrusions. *J. Petrol.* 23, 127-162.
- Jackson, E.D., 1967. Ultramafic cumulates in the Stillwater, Great Dyke, and Bushveld Intrusions. In Wyllie P.J. (ed), *Ultramafic and Related Rocks*, John Wiley and Sons, New-York, pp. 20-38.
- John, B.E., Foster, D.A., 1993, Structural and thermal constraints on the initiation angle of detachment faulting in the southern Basin and Range: The Chemehuevi Mountains case study: *Geol. Soc. Am. Bull.* 105, 1091-1108.
- Jousselin, D., Nicolas, A., Boudier, F., 1998. Detailed mapping of a mantle diapir below a paleo-spreading center in the Oman ophiolite. *J. Geophys. Res.* 103, 18153-18170.
- Jurewicz, A. J. G., Watson E. B., 1988. Cations in olivine, Part 2: Diffusion in olivine xenocrysts, with applications to petrology and mineral physics. *Contrib. Mineral. Petrol.* 99, 186-201.
- Juster, T.C., Grove, T.L., Perfit, M.R., 1989. Experimental Constraints on the Generation of FeTi Basalts, Andesites, and Rhyodacites at the Galapagos Spreading Center, 85°W and 95°W. *J. Geophys. Res.* 94(B7), 9251-9274.
- Juteau, T., Berger, E.T., Cannat, M., 1990. Serpentinized, residual, mantle peridotites from the MAR Median valley, ODP Hole 670A (21°10N, 45°02W, Lag 109): primary

- mineralogy and geothermometry Proceedings of Ocean Drilling Program, Scientific Results 106/109, 27-45.
- Juteau, T., Maury, R.C., 1997. *Géologie de la croûte océanique*. Masson, 367pp.
- Kalfoun, F., Ionov, D., Merlet, C., 2002. HFSE residence and Nb/Ta ratios in metasomatised, rutile-bearing mantle peridotites. *Earth Planet. Sci. Lett.* 199(1-2), 49-65.
- Kamenetsky, V.S., Crawford, A.J., 1998. Melt-peridotite reaction recorded in the chemistry of spinel and melt inclusions in basalt from 43 degrees N, Mid-Atlantic Ridge. *Earth Planet. Sci. Lett.* 164(1-2), 345-352.
- Karson, J.A., Thompson, G., Humphris, S.E., Edmond, J.M., Bryan, W.B., Brown, J.R., Winters, A.T., Pockalny, R.A., Casey, J.F., Campbell, A.C., Klinkhammer, G., Palmer, M.R., Kinzler R.J., Sulanowska, M.M., 1987. Along-axis variations in seafloor spreading in the MARK area. *Nature* 328, 681-685.
- Karson, J.A., 1990. Seafloor spreading on the Mid-Atlantic Ridge: implications for the structure of ophiolites and oceanic lithosphere produced in slow-spreading environments. In Malpas, J., Moores, E.M., Panayiotou, A., and Xenophontos, C. (Eds.), *Ophiolites: Oceanic Crustal Analogues: Proc. Symp. "Troodos 1987": Nicosia, Cyprus (Minist. Agric. Nat. Resour.)*, 547-555.
- Karson, J.A., 1999. Geological investigation of a lineated massif at the Kane transform fault: implications for oceanic core complexes. *Philos. Trans. R. Soc. Lond., A* 357, pp. 713-740.
- Karson, J.A., Fruh-Green, G.L., Kelley, D.S., Williams, E.A., Yoerger, D.R., Jakuba, M., 2006. Detachment shear zone of the Atlantis Massif core complex, Mid-Atlantic Ridge, 30°N. *Geochem. Geophys. Geosyst.*, 7. doi: 10.1029/2005GC001109.
- Kelemen, P.B., 1990. Reaction between ultramafic rock and fractionating basaltic magma.1. Phase-relations, the origin of calc-alkaline magma series, and the formation of discordant dunite. *J. Petrol.* 31(1), 51-98.
- Kelemen, P.B., Joyce, D.B., Webster, J.D., Holloway, J.R., 1990. Reaction between ultramafic rock and fractionating basaltic magma.2. Experimental investigation of reaction between olivine tholeiite and harzburgite at 1150-degree-C-1050-degrees-C and 5Kb. *J. Petrol.* 31(1), 99-134.
- Kelemen, P.B., Hart, S.R., Berstein, S., 1998. Silica enrichment in the continental upper mantle via melt/rock reaction. *Earth Planet. Sci. Lett.* 164(1-2), 387-406.
- Kelemen, P.B., Kikawa, E., Miller, D.J., Abe, N., Bach, W., Carlson, R.L., Casey, J.F., Chambers, L.M., Cheadle, M., Cipriani, A., Dick, H.J.B., Faul, U., Garces, M., Garrido, C., Gee, J.S., Godard, M., Griffin, D.W., Harvey, J., Ildefonse, B., Iturrino, G.J., Josef, J., Meurer, W.P., Paulick, H., Rosner, M., Schroeder, T., Seyler, M., Takazawa, E., 2004. Proc. ODP, Init. Repts., 209 [Online]. Available from World Wide Web: http://www-odp.tamu.edu/publications/209_IR/209ir.htm.
- Kennedy, A.K., Lofgren, G.E., Wasserburg, G.J., 1993. An experimental study of trace element partitioning between olivine, orthopyroxene and melt in chondrules: equilibrium values and kinetic effects. *Earth Planet. Sci. Lett.* 175, 177-195.
- Kinzler, R.J, Grove, T.L., 1993. Corrections and further discussion of the primary magmas of mid-ocean ridge basalts, 1 and 2. *J. Geophys. Res.* 98(B12), 22339-22347.
- Klein, E.M., Langmuir, C.H., 1987. Global correlations of ocean ridge basalt chemistry with axial depth and crustal thickness. *J. Geophys. Res.* 92(B8), 8089-8115.
- Klemme, S., Günther, D., Hametner, K., Prowatke, S. and Zack, T., 2006. The partitioning of trace elements between ilmenite, ulvospinel, armalcolite and silicate melts with implications for the early differentiation of the moon. *Chem. Geol.*, 234: 251-263.

- Koepke, J., Berndt, J., Feig, S.T., Holtz, F., 2007. The formation of SiO₂-rich melts within the deep oceanic crust by hydrous partial melting of gabbros. *Contrib. Mineral. Petrol.* 153, 67-84.
- Koga, K.T., Kelemen, P.B., Shimizu, N., 2001. Petrogenesis of the crust-mantle transition zone and the origin of lower crustal wehrlite in the Oman ophiolite. *Geochem. Geophys. Geosyst.* - G 3.
- Kohlstedt, D.L., Goetze, C., Durham, W.B., Vander Sande, J., 1976. New Technique for Decorating Dislocations in Olivine. *Science* 191(4231), 1045-1046.
- Komor, S., Grove, T.L., Hébert, R., 1990. Abyssal peridotites from ODP Hole 670A (21°10N, 45°02W): residues of mantle melting exposed by non-constructive axial divergence. , *Proceedings of Ocean Drilling Program, Scientific Results*, pp. 85-101.
- Korenaga, J., Kelemen, P.B., 1998. Melt migration through the oceanic lower crust: a constraint from melt percolation modeling with finite solid diffusion. *Earth Planet. Sci. Lett.* 156(1-2), 1-11.
- Kushiro, I., Mysen, B.O., 2002. A possible effect of melt structure on the Mg-Fe²⁺ partitioning between olivine and melt. *Geochim. Cosmochim. Acta.* 66(12), 2267-2272.
- Kuo, B.-Y., Forsyth, D.W., 1988. Gravity anomalies of the ridge-transform system in the South Atlantic between 31° and 34.5°S: Upwelling centres and variations in crustal thickness. *Mar. Geophys. Res.* 10, 205–232.
- Kvassness, A.J.S., 2004. Evolution of oceanic gabbros : in-situ and ancient examples. PhD Thesis, Woods Hole Oceanographic Institution. Available at <http://hdl.handle.net/1912/1860>.
- Kvassnes, A.J.S., Grove, T.L., 2008. How partial melts of mafic lower crust affect ascending magmas at ocean ridges. *Contrib. Mineral. Petrol.* 156, 49–71.
- Lagabrielle, Y., Cannat, M., 1990. Alpine jurassic ophiolites resemble the modern Central Atlantic basement. *Geology* 18, 319-322.
- Lagabrielle, Y., Bideau, D., Cannat, M., Karson, J.A., Mevel, C., 1998. Ultramafic-mafic plutonic rock suites exposed along the Mid-Atlantic Ridge (10 degrees N-30 degrees N); symmetrical-asymmetrical distribution and implications for seafloor spreading processes. In: W.R. Buck, P.T. Delaney, J.A. Karson and Y. Lagabrielle (Editors), *Faulting and magmatism at mid-ocean ridges. Geophysical Monograph. American Geophysical Union, Washington, DC, United States*, pp. 153-176.
- Lagabrielle, Y. Mantle exhumation and lithosphere spreading: An historical perspective from investigations in the Oceans and in the Alps-Appennines ophiolites. *Soumis à Boll. SGI*.
- Langmuir, C.H., 1989. Geochemical consequences of in situ crystallization. *Nature* 340, 199-205.
- Langmuir, C.H., Klein, E.M., Plank, T., 1992. Petrological constraints on melt formation and migration beneath mid-ocean ridges, in Phipps Morgan, J., Blackman, D., and Sinton, J.L., eds., *Mantle flow and melt generation at mid-ocean ridges: Washington, D.C., Am. Geophys. Union, Geophysical Series Monograph 71*, 183-230 pp.
- Lavier, L.L., Buck, W.R., Poliakov, A.N., 1999. Self-consistent rolling-hinge model for the evolution of large-offset low-angle normal faults. *Geology* 27(12), 1127-1130.
- Lee, C.-T. A., Harbert, A., Leeman, W.P., 2007. Extension of lattice strain theory to mineral/mineral rare-earth element partitioning: an approach for assessing disequilibrium and developing internally consistent partition coefficients between olivine, orthopyroxene, clinopyroxene and basaltic melt. *Geochim. Cosmochim. Acta* 71, 481-496.
- Lejeune, A., Richet, P., 1995. Rheology of crystal-bearing silicate melts: an experimental

- study at high viscosities. *J. Geophys. Res.* 100, 4215-4229.
- Lemoine M., Boillot G., Tricart P., 1987. Ultramafic and gabbroic ocean floor of the Ligurian Tethys (Alps, Corsica, Apennines): In search of a genetic model. *Geology* 15, 622-625.
- Lenoir, X., Garrido, C., Bodinier, J.-L., Dautria, J.-M., Gervilla, F., 2001. The recrystallization front of the Ronda peridotite: evidence for melting and thermal erosion of lithospheric mantle beneath the Alboran basin. *J. Petrol.* 42, 141–158.
- Liang, Y., 2000. Dissolution in molten silicates: effects of solid solution. *Geochim. Cosmochim. Acta* 64(9), 1617-1627.
- Libourel G., 1999. Systematics of calcium partitioning between olivine and silicate melt: implications for melt structure and calcium content of magmatic olivines. *Contrib. Mineral. Petrol.* 136, 63–80.
- Lin, J., Purdy, G.M., Schouten, H., Sempéré, J.C., Zervas, C., 1990. Evidence from gravity data for focused magmatic accretion along the Mid-Atlantic Ridge. *Nature*, 344: 627-632.
- Lin, J., Phipps Morgan, J., 1992. The Spreading Rate Dependence of 3-Dimensional Midocean Ridge Gravity Structure. *Geophys. Res. Lett.* 19(1), 13-16.
- Lissenberg, C.J., Dick, H.J.B., 2008. Melt-rock reaction in the lower oceanic crust and its implications for the genesis of mid-ocean ridge basalt. *Earth Planet. Sci. Lett.*, doi: 10.1016/j.epsl.2008.04.023
- Lizarralde, D., Gaherty, J.B., Collins, J.A., Hirth, G., Kim, S.D., 2004. Spreading-rate dependence of melt extraction at mid-ocean ridges from mantle seismic refraction data. *Nature* 432, 744-747.
- Macdonald, K.C., Fox, P.J., Perram, L.J., Eisen, M.F., Haymon, R.M., Miller, S.P., Carbotte, S.M., Cormier, M.H., Shor, A.N., 1988. A new view of the Mid-Atlantic Ridge from the behavior of ridge-axis discontinuities. *Nature* 335(6187), 217-225.
- MacLeod, C.J., Escartin, J., Banerji, D., Banks, G.J., Gleeson, M., Irving, D.H.B., Lilly, R.M., McCaig, A.M., Niu, Y.L., Allerton, S., Smith, D.K., 2002. Direct geological evidence for oceanic detachment faulting: The Mid-Atlantic Ridge, 15 degrees 45 ' N. *Geology* 30(10), 879-882.
- Madge, L.S., Sparks, D.W., Detrick, R.S., 1997. The relationship between buoyant mantle flow, melt migration, and gravity bull's eyes at the Mid-Atlantic Ridge between 33°N and 35°N. *Earth Planet. Sci. Lett.* 148, 59-68.
- Madge, L.S., Barclay, D.R., Toomey, R.S., Detrick, R.S., Collins, J.A., 2000. Crustal magma plumbing within a segment of the Mid-Atlantic Ridge, 35°N. *Earth Planet. Sci. Lett.* 175, 55-67.
- Marchesi, C., Garrido, C., Godard, M., Proenza, J.A., Gervilla, F. and Blanco-Moreno, J., 2006. Petrogenesis of highly depleted peridotites and gabbroic rocks from the Mayari-Baracoa ophiolitic belt (Eastern Cuba). *Contributions to Mineralogy and Petrology*, 151: 717-736.
- Mathez, E.A., 1995. Magmatic metasomatism and formation of the Merensky reef, Bushveld Complex. *Contrib. Mineral. Petrol.* 119 277-286.
- Maynard, G.L., 1970. Crustal layer of seismic velocity of 6.9-7.6 kilometers per second under deep oceans. *Science* 168, 120-121.
- McCaig, A., Cliff, R. A., Escartin, J. et al. , 2007. Oceanic deachment faults focus very large volumes of black smoker fluids. *Geology* 35, 935.
- McKay, G.A., Wagstaff, J., Yang, S.R., 1986. Clinopyroxene REE distribution coefficients for shergottites: The REE content of the Shergotty melt. *Geochim. Cosmochim. Acta* 50, 927-937.

- McKenzie, D., O'Nions, R.K., 1991. Partial Melt Distribution from Inversion of Rare Earth Element Concentrations. *J. Petrol.* 32(5), 1021-1091.
- Meissner, E., Sharp, T.G., Chakraborty S., 1998. Quantitative measurement of short compositional profiles using analytical transmission electron microscopy. *Am Miner* 83, 546–552.
- Merlet, C., Bodinier, J.-L., 1990. Electron microprobe determination of minor and trace transition elements in silicate minerals : a method and its application to mineral zoning in the peridotite nodule PHN-1611. *Chem. Geol.* 83(Spc. Issue "Microanalytical methods in mineralogy and geochemistry"), 55-69.
- Meurer, W.P., Boudreau, A.E., 1998. Compaction of igneous cumulates Part I: Geochemical consequences for cumulates and liquid fractionation trends. *J. Geol.* 106(3), 281-292.
- Meurer, W.P., Gee, J., 2002. Evidence for the protracted construction of slow-spread oceanic crust by small magmatic injections. *Earth Planet. Sci. Lett.* 201(1), 45-55.
- Mével, C., 2003. Serpentinization of abyssal peridotites at mid-ocean ridges. *Comptes Rendus Geoscience* 335(10-11), 825-852.
- Meyer, P.S., Dick, H.J.B., Thompson, G., 1989. Cumulate gabbros from the southwest Indian Ridge, 54°S-7°16'E: implications for magmatic processes at slow spreading ridge. *Contrib. Mineral. Petrol.* 103, 44-63.
- Meyzen, C.M., Toplis, M.J., Humler, E., Ludden, J.N., Mével, C., 2003. A discontinuity in mantle composition beneath the southwest Indian ridge. *Nature*, 421: 731-733.
- Michael, P.J., Cornell, W.C., 1998. Influence of spreading rate and magma supply on crystallization and assimilation beneath mid-ocean ridges: Evidence from chlorine and major element chemistry of mid-ocean ridge basalts. *J. Geophys. Res.* 103(B8), 18325-18356.
- Miller, D.J., Abratis, M., Christie, D., Drouin, M., Godard, M., Ildefonse, B., Maeda, J., Weinstieger, A., submitted. Data Report: Microprobe analyses of primary mineral phases (plagioclase, pyroxene, olivine, and spinel) from Site U1309, Atlantis Massif, Integrated Ocean Drilling Program Expedition 304/305. In : Blackman, D.K., Ildefonse, B., John, B.E., Ohara, Y., Miller, D.J., MacLeod, C.J., and the Expedition 304/305 Scientists, 2006. *Proc. IODP, 304/305: College Station TX (Integrated Ocean Drilling Program Management International, Inc.)*.
- Milman-Barris, M. S., Beckett, J. R., Baker, M. B., Hofmann, A. E., Morgan, Z., Crowley, M. R., Vielzeuf, D., Stolper, E., 2008. Zoning of phosphorus in igneous olivine. *Contrib. Mineral. Petrol.* 155(6), 739-765.
- Mysen B.O., Virgo D., 1980. Trace element partitioning and melt structure; an experimental study at 1 atm pressure. *Geochim. Cosmochim. Acta* 44, 1917–1930.
- Mysen, B.O., 2007. Olivine/melt transition metal partitioning, melt composition, and melt structure—Influence of Al³⁺ for Si⁴⁺ substitution in the tetrahedral network of silicate melts. *Geochim. Cosmochim. Acta* 71, 5500-5513.
- Natland, J.H., Meyer, P.S., Dick, H.J.B., Bloomer, S.H., 1991. Magmatic oxides and sulfides in gabbroic rocks from Hole 735B and the later development of the liquid line of descent. In Von Herzen, R., Robinson, P.T., et al., *Proc. ODP, Sci. Results, 118: College Station, TX (Ocean Drilling Program), 75–111.* doi:10.2973/odp.proc.sr.118.163.1991
- Natland, J.H., Dick, H.J.B., 1996. Melt migration through high-level gabbroic cumulates of the East Pacific Rise at Hess Deep: the origin of magma lenses and the deep crustal structure of fast-spreading ridges. In Mével, C., Gillis, K.M., Allan, J.F., and Meyer, P.S. (Eds.), *Proc. ODP, Sci. Results, 147: College Station, TX (Ocean Drilling Program), 21–58.* doi:10.2973/odp.proc.sr.147.002.1996

- Natland, J.H., Dick, H.J.B., 2001. Formation of the lower ocean crust and the crystallization of gabbroic cumulates at a very slowly spreading ridge. *J. volcanol. Geotherm. Res.* 110(3-4), 191-233.
- Navon, O., Stolper, E., 1987. Geochemical Consequences of Melt Percolation - the Upper Mantle as a Chromatographic Column. *J. Geol.* 95, 285-307.
- Nicolas, A., Boudier, F., Boullier, A.M., 1973. Mechanism of flow in naturally and experimentally deformed peridotites, *Am. J. Sci.* 273, 853-876.
- Nicolas, A., Poirier, J.P., 1976. Crystalline Plasticity and Solid State flow in Metamorphic Rocks. John Willey, London, 444 pp.
- Nicolas, A., Prinzhofer, A., 1983. Cumulative or residual origin for the transition zone in ophiolites: structural evidence. *J. petrol.* 24, 188-206.
- Nicolas, A., 1985. Residual origin of idiomorphic olivine crystals. *Bull. Mineral.* 108(5), 725-726.
- Nicolas, A., 1989. Structures of ophiolites and dynamics of oceanic lithosphere. Kluwer Acad. Publ. Dordrecht (Pays-Bas), 367pp.
- Nicolas, A., 1992. Kinematics in magmatic rocks with special reference to gabbros. *J. Petrol.* 33, 891-915.
- Nicolas, A., Freydier, C., Godard, M., Vauchez, A., 1993. Magma chambers at oceanic ridges: how large? *Geology* 21, 53-56.
- Niu, Y., Hekinian, R., 1997. Basaltic liquids and harzburgitic residues in the Garrett Transform; a case study at fast-spreading ridges. *Earth Planet.Sci. Lett.* 146(1-2), 243-258.
- Niu, Y., 1997. Mantle melting and melt extraction processes beneath ocean ridges: evidence from abyssal peridotites. *J. Petrol.* 38, 1047-1074.
- Niu, Y., Gilmore, T., Mackie, S., Greig, A., and Bach, W., 2002. Mineral chemistry, whole-rock compositions, and petrogenesis of Leg 176 gabbros: data and discussion. In Natland, J.H., Dick, H.J.B., Miller, D.J., and Von Herzen, R.P. (Eds.), *Proc. ODP, Sci. Results, 176: College Station, TX (Ocean Drilling Program), 1-60.* doi:10.2973/odp.proc.sr.176.011.2002
- Niu, Y., 2004. Bulk-rock major and trace element compositions of abyssal peridotites: implications for mantle melting, melt extraction and post-melting processes beneath mid-ocean ridges. *J. Petrol.* 45(12), 2423-2458.
- Nonotte, P., Ceuleneer, G., Benoit, M., 2005. Genesis of andesitic-boninitic magmas at mid-ocean ridges by melting of hydrated peridotites: Geochemical evidence from DSDP Site 334 gabbro-norites. *Earth. Planet. Sci. Lett.* 236, 632-653.
- Nooner, S. L., G. S. Sasagawa, D. K. Blackman, Zumberge, M. A., 2003. Structure of oceanic core complexes: Constraints from seafloor gravity measurements made at the Atlantis Massif, *Geophys. Res. Lett.* 30(8), 1446, doi:10.1029/2003GL017126.
- O'Hara, M.J., Fry, N., 1996. The highly compatible trace element paradox—Fractional crystallization revisited. *J. Petrol.* 37, 859-890.
- O'Hara, M.J., 1998. Volcanic Plumbing and the Space Problem-Thermal and Geochemical Consequences of Large-Scale Assimilation in Ocean Island Development. *J. Petrol.*, 1077-1089.
- Ohara, Y., Yoshida, T., Kato, Y., Kasuga, S., 2001. Giant megamullion in the Parece Vela Backarc Basin. *Mar. Geophys. Res.* 22(1), 47-61.
- Ohara, Y., Okino, K., Kasahara, J., 2007. Seismic study on oceanic core complexes in the Parece Vela back-arc basin. *Island Arc* 16(3), 348-360.
- Ozawa, K., Meyer, P.S., Bloomer, S.H., 1991. Mineralogy and textures of iron-titanium oxide gabbros and associated olivine gabbros from Hole 735B. In Von Herzen, R.,

- Robinson, P.T., et al., Proc. ODP, Sci. Results, 118: College Station, TX (Ocean Drilling Program), 41–73. doi:10.2973/odp.proc.sr.118.125.1991
- Paulick, H., Bach, W., Godard, M., De Hoog, J.C.M., Suhr, G., Harvey, J., 2006. Geochemistry of abyssal peridotites (Mid-Atlantic Ridge, 15°20'N, ODP Leg 209): implications for fluid/rock interaction in slow spreading environments. *Chem. Geol.* 234, 179-210. doi:10.1016/j.chemgeo.2006.04.011
- Pearce, N.J.G., Perkins, W.T., Westgate, J.A., Gorton, M.P., Jackson, S.E., Neal, C.R., Chenery S.P., 1997. A compilation of new and published major and trace element data for NIST SRM 610 and NIST SRM 612 glass reference materials. *Geostandards Newsletter- The journal of Geostandards and Geoanalysis* 21(1), 115-144.
- Petry; C., Chakraborty, S., Palme, H., 2004. Experimental determination of Ni diffusion coefficients in olivine and their dependence on temperature, composition, oxygen fugacity, and crystallographic orientation. *Geochim. Cosmochim. Acta* 68(20), 4179-4188.
- Pettigrew, T.L., Casey, J.F., Miller, D.J., et al., 1999. Proc. ODP, Init. Repts., 179: College Station, TX (Ocean Drilling Program). doi:10.2973/odp.proc.ir.179.1999
- Phipps Morgan, J., Chen, Y.J., 1993. The genesis of oceanic crust: magma injection, hydrothermal circulation, and crustal flow. *J. Geophys. Res.* 98, 6283-6297.
- Poirier, J.P., 1975. Slip systems of olivine. *J. Geophys. Res.* 80(29), 4059-4061.
- Poirier, J.P. and Nicolas, A., 1975. Deformation-Induced Recrystallization Due to Progressive Misorientation of Subgrains, with Special Reference to Mantle Peridotites. *J. Geol.* 83, 707-720.
- Piccardo, G.B., Zanetti, A., Muntener, O., 2007. Melt/peridotite interaction in the Southern Lanzo peridotite: Field, textural and geochemical evidence. *Lithos* 94(1-4), 181-209.
- Putirka, D., 2005. Igneous thermometers and barometers based on plagioclase + liquid equilibria: Tests of some existing models and new calibrations. *Am. Mineral.* 90, 336-346.
- Qin, Z., Lu, F., Anderson, A. T. Jr., 1992. Diffusive reequilibration of melt and fluid inclusions. *Am. Mineral.* 77, 565–576.
- Quick, J.E., 1981. The origin and significance of large, tabular dunite bodies in the Trinity peridotite, northern California. *Contrib. Mineral. Petrol.* 153(3), 303-319.
- Quick, J.E., Denlinger, R.P., 1993. Ductile deformation and the origin of layered gabbro in ophiolites. *J. Geophys. Res.* 98, 14015-14027.
- Rabinowicz, M., Genthon, P., Ceuleneer, G., Hillairet, M., 2001. Compaction in a mantle mush with high melt concentrations and the generation of magma chambers. *Earth Planet. Sci. Lett.* 188, 313-328.
- Raitt R.W, 1963. The crustal rocks. In: Hill M.N. (edit), "The sea", vol. 3, Wiley Interscience, New-York, pp. 85-102.
- Rampone, E., Piccardo, G.B., Vannucci, R., Bottazzi, P., 1997. Chemistry and origin of trapped melts in ophiolitic peridotites. *Geochim. Cosmochim. Acta* 61(21), 4557-4569.
- Rampone, E., Piccardo, G.B., Hofmann, A.W., 2008. Multi-stage melt-rock interaction in the Mt. Maggiore (Corsica, France) ophiolitic peridotites: microstructural and geochemical evidence. *Contrib. Mineral. Petrol.*, doi: 10.1007/s00410-008-0296-y.
- Ranero, C.R., Reston, T.J., 1999. Detachment faulting at ocean core complexes. *Geology* 27(11), 983-986.
- Renner, J., Evans, B., Hirth, G., 2000. On the rheologically critical melt fraction. *Earth Planet. Sci. Lett.* 181, 585-594.
- Reston, T.J., Weinrebe, W., Grevemeyer, I., Flueh, E.R., Mitchell, N.C., Kirstein, L., Kopp, C., Kopp, H., and participants of Meteor 47/2, 2002. A rifted inside corner massif on

- the Mid-Atlantic Ridge at 5°S. *Earth. Planet. Sci. Lett.* 200(3-4), 255-269.
- Reynolds, J.R., Langmuir, C.H., 1997. Petrological systematics of the Mid-Atlantic Ridge south of Kane: Implications for ocean crust formation. *J. Geophys. Res.* 102(B7), 14915-14946.
- Ridley, W.I., Perfit, M.R., Smith, M.C., Fornari, D.J., 2006. Magmatic processes in developing oceanic crust revealed in a cumulate xenolith collected at the East Pacific Rise, 9°50'N. *Geochem. Geophys. Geosyst.* - G3, 7. doi:10.1029/2006GC001316.
- Robinson, P.T., Von Herzen, R., et al., 1989. *Proc. ODP, Init. Repts.*, 118: College Station, TX (Ocean Drilling Program). doi:10.2973/odp.proc.ir.118.1989
- Roden, M.K., Hart, S.T., Frey, F.A., Melson, W.G., 1984. Sr, Nd and Pb isotopic and REE geochemistry of St. Paul's Rocks: the metamorphic and metasomatic development of an alkali basalt mantle source. *Contrib. Mineral. Petrol.* 85, 376-390
- Rosenbaum, J.M., Zindler, A., Rubenstone, J.L., 1996. Mantle fluids: Evidence from fluid inclusions. *Geochim. Cosmochim. Acta* 60, 3229-3252.
- Rosenberg, C.L., 2001. Deformation of partially-molten granite: a review and comparison of experimental and natural case studies. *Int. J. Earth Sci.* 90, 60-76.
- Rosenberg, C.L., Handy, M.R., 2005. Experimental deformation of partially melted granite revisited: implications for the continental crust. *J. Metam. Geol.* 23 (1), 19-28.
- Ross, K., Elthon, D., 1997. Cumulus and postcumulus crystallization in the oceanic crust: major- and trace-element geochemistry of Leg 153 gabbroic rocks. In Karson, J.A., Cannat, M., Miller, D.J., and Elthon, D. (Eds.), *Proc. ODP, Sci. Results*, 153: College Station, TX (Ocean Drilling Program), 333-350. doi:10.2973/odp.proc.sr.153.023.1997
- Rutter, E., Neumann, D.H.K., 1995. Experimental deformation of partially molten Westerly granite under fluid-absent conditions, with implications for the extraction of granitic magmas. *J. Geophys. Res.* 100, 15697-15715.
- Schiano, P., Clocchiatti, R., Shimizu, N., Maury, R.C., Jochum, K.P., Hofmann, A.W., 1995. Hydrous, silica-rich melts in the sub-arc mantle and their relationship with erupted arc lavas. *Nature* 377, 595-600.
- Schmidt M. W., Connolly J. A. D., Gunther D., Bogaerts M., 2006. Element partitioning: the role of melt structure and composition. *Science* 312, 1646-1650.
- Schouten, H., Klitgord, K.D., Whitehead, J.A., 1985. Segmentation of mid-ocean ridges. *Nature* 317, 225-229.
- Schroeder, T.J., John, B.E., Frost, B.R., 2002. Geologic implications of seawater circulation through peridotite exposed at slow-spreading mid-ocean ridges. *Geology* 30, 367-370.
- Schroeder, T.J., John, B.E., 2004. Strain localisation on an oceanic detachment fault system, Atlantis Massif, 30°N, Mid-Atlantic Ridge. *Geochem. Geophys. Geosyst.* - G 3.
- Scott, T., Kohlstedt, D.L., 2006. The effect of large melt fraction on the deformation behavior of peridotite. *Earth Planet. Sci. Lett.* 246, 177-187.
- Searle, R.C., Cannat, M., Fujioka, K., Mével, C., Fujimoto, H., Bralee, A., Parson, L., 2003. FUJI Dome: A large detachment fault near 64°E on the very slow-spreading southwest Indian Ridge. *Geochem. Geophys. Geosyst.* 4, doi: 10.1029/2003GC000519.
- Sempéré, J.C., Purdy, G.M., Schouten, H., 1990. Segmentation of the Mid-Atlantic Ridge between 24°N and 30°40'N. *Nature* 344, 427-431.
- Sempéré, J.C., Lin, J., Brown, H.S., Schouten, H., Purdy, G.M., 1993. Segmentation and morphotectonic variations along a slow spreading center: the Mid-Atlantic Ridge (24°00'N-30°40'N). *Marine Geophys. Res.* 15, 153-200.
- Seyler, M., Bonatti, E., 1997. Regional-scale melt-rock interaction in lherzolitic mantle in the Romanche fracture zone (Atlantic Ocean). *Earth Planet. Sci. Lett.* 146(1-2), 273-287.

- Seyler, M., Cannat, M., Mével, C., 2003. Evidence for major element heterogeneity in the mantle source of abyssal peridotite from the Southwest Indian Ridge (52° to 68°E). *Geochem. Geophys. Geosyst.* - G 3, 10.
- Shaw, D.M., 1970. Trace element fractionation during anatexis. *Geochim. Cosmochim. Acta* 34, 237-243.
- Shibata, T., Thompson, G., 1986. Peridotites from the Mid-Atlantic Ridge at 43°N and their petrogenetic relation to abyssal tholeiites. *Contrib. Mineral. Petrol.* 93, 144-159.
- Shipboard Scientific Party, 2004a. Site 1275. In Kelemen, P.B., Kikawa, E., Miller, D.J., et al., *Proc. ODP, Init. Repts.*, 209: College Station, TX (Ocean Drilling Program), 1–167. doi:10.2973/odp.proc.ir.209.110.2004
- Shipboard Scientific Party, 2004b. Leg 209 summary. In Kelemen, P.B., Kikawa, E., Miller, D.J., et al., *Proc. ODP, Init. Repts.*, 209: College Station, TX (Ocean Drilling Program), 1–139. doi:10.2973/odp.proc.ir.209.101.2004
- Sigurdson, H., Schilling, J.-G., 1976. Spinels in Mid-Atlantic Ridge basalts: Chemistry and occurrence. *Earth Planet. Sci. Lett.* 29, 7-20.
- Singh, S.C., Crawford, W.C., Carton, H., Seher, T., Combier, V., Cannat, M., Canales, J.P., Dusunur, D., Escartin, J., Miranda, J.M., 2006. Discovery of a magma chamber and faults beneath a Mid-Atlantic Ridge hydrothermal field. *Nature* 442, 1029-1032.
- Sinton, J.M., Detrick, R.S., 1992. Mid-ocean ridge magma chambers. *J. Geophys. Res.* 97(B1), 197-216.
- Sleep, N.H., Barth, G.A., 1997. The nature of oceanic lower crust and shallow mantle emplaced at low spreading rates. *Tectonophysics* 279(1-4), 181-191.
- Smith, D.K., Cann, J.R., 1993. Building the crust at the Mid-Atlantic Ridge. *Nature* 365, 707-715.
- Smith, D., Rite, J.C.A., Mertzman, S.A., 1999. Water-rock interactions, orthopyroxene growth, and Si-enrichment in the mantle: evidence in xenoliths from the Colorado Plateau, southwestern United States. *Earth Planet. Sci. Lett.* 165(1), 45-54.
- Smith, D.K., Cann, J.R., Escartín, J., 2006. Widespread active detachment faulting and core complex formation near 13°N on the Mid-Atlantic Ridge. *Nature* 442, doi: 10.1038/nature04950.
- Smith, D.K., Escartín, J., Schouten, H., Cann, J.R., 2008. Fault rotation and core complex formation: Significant processes in seafloor formation at slow-spreading mid-ocean ridges (Mid-Atlantic Ridge, 13-15°N). *Geochem. Geophys. Geosyst.* 9. Doi: 10.1029/2007GC001699.
- Solomon, S., 1989. In *Drilling the Oceanic Lower Crust and Mantle*, JOI/USSAC Workshop Report, Dick, H. J. B. ed., Woods Hole Oceanographic Institution, Woods Hole, MA, pp 73–74.
- Spandler, C., O'Neill, H. St C., Kamenetsky, V. S., 2007. Survival times of anomalous melt inclusions from element diffusion in olivine and chromite. *Nature* 447, 303-306.
- Spencer, J.E., Chase, C.G., 1989. Role of crustal flexure in initiation of low-angle normal faults and implications for structural evolution of the Basin and Range province. *J. Geophys. Res.* 94(B2), 1765-1775.
- Stolper, E.A., 1980. Phase diagram for Mid-Ocean Ridge basalts: preliminary results and implications for petrogenesis. *Contrib. Mineral. Petrol.* 74, 13-27.
- Sun, S.S., McDonough, W.F., 1989. Chemical and isotopic systematics of oceanic basalts: implications for mantle composition and processes. In: A.D. Saunders and M.J. Norry (Eds.), *Magmatism in the ocean basins*. *Geol. Soc. London*, pp. 313-345.
- Sun, M., Kerrich, R., 1995. Rare earth element and high field strength element characteristics of whole rocks and mineral separates of ultramafic nodules in Cenozoic volcanic vents

- of southeastern British Columbia, Canada. *Geochim. Cosmochim. Acta* 59(23), 4863-4879.
- Sutton, G.M., Maynard, G.L., Hussong, D.M., 1971. Widespread occurrence of a high-velocity basal layer in the Pacific crust found with repetitive sources and sonobuoys. *Geophysical Monograph Series*, J.G. Heacock edts, Am. Geophys. Union 14, 193-209.
- Takahashi, E., Kushiro, I., 1983. Melting of a dry peridotite at high pressures and basalt magma genesis. *Am. Mineral.* 68, 859–879.
- Takazawa, E., Abe, N., Seyler, M., Meurer, W.P., 2007. Hybridization of dunite and gabbroic materials in Hole 1271B from Mid-Atlantic Ridge 15°N: implications for melt flow and reaction in the upper mantle. In Kelemen, P.B., Kikawa, E., and Miller, D.J. (Eds.), *Proc. ODP, Sci. Results*, 209: College Station, TX (Ocean Drilling Program), 1–23. doi:10.2973/odp.proc.sr.209.005.2007
- Tamura, A., Arai, S., Ishimaru, S., Andal, E.S., 2008. Petrology and geochemistry of peridotites from IODP Site U1309 at Atlantis Massif, MAR30°N: micro- and macro-scale melt penetrations into peridotites. *Contrib. Mineral. Petrol.* 155 (4), 491-509.
- Tartarotti, P., Susini, S., Nimis, P., Ottolini, L., 2002. Melt migration in the upper mantle along the Romanche Fracture Zone (Equatorial Atlantic). *Lithos* 63, 125-149.
- Thatcher, W., Hill, D. P., 1995. A simple model for the fault-generated morphology of slow-spreading mid-oceanic ridges. *J. Geophys. Res.* 100(B1), 561–570.
- Tikoff, B., Teyssier, C., 1994. Strain and fabric analyses based on porphyroclast interaction. *Journal of Structural Geology* 16(4), 477-491.
- Tolstoy, M., Harding, A.J., Orcutt, J.A., 1993. Crustal thickness on the Mid-Atlantic Ridge: Bull's eye gravity anomalies and focused accretion. *Science* 262, 726-729.
- Tommasi, A., Mainprice, D., Canova, G., Chastel, Y., 2000. Viscoplastic self-consistent and equilibrium-based modeling of olivine lattice preferred orientations: Implications for the upper mantle seismic anisotropy. *J. Geophys. Res.* 105(B4), 7893-7908.
- Tommasi, A., Godard, M., Coromina, G., Dautria, J.-M., Barszczus, H., 2004. Seismic anisotropy and compositionally-induced velocity anomalies in the lithosphere above mantle plumes: A petrological and microstructural study of mantle xenoliths from French Polynesia. *Earth Planet. Sci. Lett.*, 227: 539– 556.
- Tommasi, A., Vauchez, A., Ionov, D.A., 2008. Deformation, static recrystallization, and reactive melt transport in shallow subcontinental mantle xenoliths (Tok Cenozoic volcanic field, SE Siberia). *Earth Planet. Sci. Lett.* 272, 65-77.
- Toplis M. J., 2005. The thermodynamics of iron and magnesium partitioning between olivine and liquid: criteria for assessing and predicting equilibrium in natural and experimental systems. *Contrib. Mineral. Petrol.* 149, 22–39.
- Tormey, D.R., Grove, T.L., Bryan, W.B., 1987. Experimental petrology of normal MORB near the Kane fracture-zone, 22 degrees - 25-degrees N, Mid Atlantic Ridge. *Contrib. Mineral. Petrol.* 96(2), 121-139.
- Tribuzio, R., Tiepolo, M., Vannucci, R., Bottazzi, P., 1999. Trace element distribution within olivine-bearing gabbros from the Northern Apennine ophiolites (Italy): evidence for post-cumulus crystallization in MOR-type gabbroic rocks. *Contrib. Mineral. Petrol.* 134(2-3), 123-133.
- Tucholke, B.E., Lin, J., 1994. A geological model for the structure of ridge segments in slow spreading ocean crust. *J. Geophys. Res.* 99(B6), 11937-11958.
- Tucholke, B.E., Lin, J., Tivey, M.A., Kleinrock, M.C., Reed, T.B., Goff, J.A., Jaroslow, G.E., 1997. Segmentation and crustal structure of the western Mid-Atlantic Ridge flank, 25°25′-27°10′N and 0-29 m.y., *J. Geophys. Res.* 102, 10203-10223.

- Tucholke, B.E., Lin, J., Kleinrock, M.C., 1998. Megamullions and mullion structure defining oceanic metamorphic core complexes on the Mid-Atlantic ridge. *J. Geophys. Res.* 103(B5), 9857-9866.
- Tucholke, B.E., Juioka, K., Ishihara, T., Hirth, G., Kinoshita, M., 2001. Submersible study of an oceanic megamullion in the central North Atlantic. *J. Geophys. Res.* 106, 16,145-116,161.
- Tucholke, B.E., Behn, M.D., Buck, W.R., Lin, J., 2008. Role of melt supply in oceanic detachment faulting and formation of megamullions. *Geology* 36 (6), 455-458.
- Ulmer, P., 1989. The dependence of the Fe²⁺-Mg cation-partitioning between olivine and basaltic liquid on pressure, temperature and composition. *Contrib. Mineral. Petrol.* 101, 261-273.
- Van Achterberg, E., Ryan, C.G., Jackson, S.E., Griffin, W., 2001. Data reduction software for LA-ICP-MS. In: P. Sylvester (Ed.), *Laser ablation ICP-MS in the Earth Science*. Mineralogical Association of Canada, pp. 239-243.
- Van Andel T. H., Bowin, C.O., 1968. Mid-Atlantic Ridge between 22° and 23° North Latitude and the Tectonics of Mid-Ocean Rise. *J. Geophys. Res.* 73(4), 1279-1298.
- Van der Molen, I., Paterson, M.S., 1979. Experimental deformation of partially melted granite. *Contrib. Mineral. Petrol.* 70, 299-318.
- Van Orman, J. A., Grove, T. L., Shimizu, N., 2001. Rare earth element diffusion in diopside : influence of temperature, pressure, and ionic radius, and an elastic model for diffusion in silicates. *Contrib. Mineral. Petrol.* 141, 687-703.
- Vasseur, G., Vernières, J., Bodinier, J.-L., 1991. Modelling of trace element transfer between mantle melt and heterogranular peridotite matrix. *J. Petrol.*, sp. volume "Orogenic lherzolites and mantle processes", 41-54.
- Vaucher, A., Garrido, C.J., 2001. Seismic properties of an asthenospherized lithospheric mantle: constraints from lattice preferred orientations in peridotite from the Ronda massif. *Earth Planet. Sci. Lett.* 192(2), 235-249.
- Vigneresse, J.L., Barbey, P., Cuney, M., 1996. Rheological transitions during partial melting and crystallization with application to felsic magma segregation and transfer. *J. Petrol.* 37, 1579-1600.
- Villiger, S., Ulmer, P., Müntener, O., Thompson, B., 2004. The Liquid Line of Descent of Anhydrous, Mantle-Derived, Tholeiitic Liquids by Fractional and Equilibrium Crystallization-an Experimental Study at 1.0 GPa. *J. Petrol.* 45(12), 2369-2388.
- Villiger, S., Müntener, O., Ulmer, P., 2007. Crystallization pressures of mid-ocean ridge basalts derived from major element variations of glasses from equilibrium and fractional crystallization experiments. *J. Geophys. Res.* 112, B01202, doi: 10.1029/2006JB004342
- Wager, L.R., Brown, G.M., Wadsworth, W.J., 1960. Types of igneous cumulates. *J. Petrol.* 1 (1), 73-85.
- Wager, L.R., 1963. The mechanism of adcumulus growth in the layered series of the Skaergaard Intrusion. *Mineral. Soc. Am. Special Paper* 1, 1-9.
- Wager, L.R., Brown, G.M., 1968. Layered igneous rocks. Olivier and Boyd, Edinburgh, 588pp.
- Watson E. B., 1977. Partitioning of manganese between forsterite and silicate liquid. *Geochim. Cosmochim. Acta* 41, 1363-1374.
- Wernicke, B., 1981. Low-angle normal faults in the Basin and Range Province-nappe tectonics in an extending orogen. *Nature* 291, 645-648.
- Wernicke, B., 1985. Uniform sense normal simple shear of the continental lithosphere. *Can. J. Earth Sci.* 22, 108-125

- Wilson, J. T., 1963. Evidence from islands on the spreading of ocean floors. *Nature* 197, 536-538.
- Witt-Eickschen, G., O'Neill, H. St. C., 2005. The effect of temperature on the equilibrium distribution of trace elements between clinopyroxene, orthopyroxene, olivine and spinel in upper mantle peridotite. *Chem. Geol.* 221, 65-101.
- Workman, R.K., Hart, S.R., 2005. Major and trace element composition of the depleted MORB mantle (DMM). *Earth Planet. Sci. Lett.* 231(1-2), 53-72.
- Yoshinobu, A.S., Hirth, G., 2002. Microstructural and experimental constraints on the rheology of partially molten gabbro beneath oceanic spreading centers. *J. Struct. Geol.* 24, 1101-1107.
- Zhang, Y., Walker, D., Leshner, C.E., 1989. Diffusive crystal dissolution. *Contrib. Mineral. Petrol.* 102, 492-513.
- Zimmerman, M.E., Kohlstedt, D.L., 2004. Rheological properties of partially molten lherzolite. *J. Petrol.* 45, doi : 10.1093/petrology/egg089.

Annexes

ANNEXE A

Techniques Analytiques

I. Échantillonnage

1. Puits U1309D (expédition IODP 304-305)

J'ai principalement échantillonné les troctolites riches en olivine et quelques gabbros associés dans les différentes zones « riches en olivine » le long du puits U1309D. Un total de 98 échantillons provenant de 4 zones riches en olivine constitue donc notre matériel d'étude (les photos des lames minces sont disponibles à la fin de cette annexe). Chaque échantillon est alors identifié par sa zone le long du puits. La zone 1 se situe entre 300.91 et 362.9 mbsf (mètres sous le plancher océanique/meters below sea floor); la zone 2 entre 551.82 et 557.24 mbsf; la zone 3 entre 666.8 et 672.33 mbsf et la zone 4 entre 1092.1 et 1196.57 mbsf (Figure A.1).

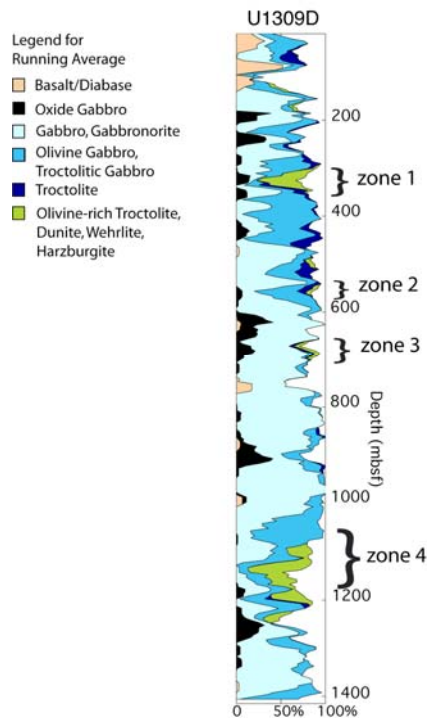


Figure A.1: Proportion de chaque lithologie échantillonnée le long du puits U1309D (moyenne sur 20m; Blackman et al., 2006) et localisation des différentes zones d'échantillonnage.

Dans un premier temps, une lame mince de 150 μm d'épaisseur a été réalisée à l'atelier de lithopréparation de l'université Montpellier 2 pour chaque échantillon. Ces lames minces « épaisses » ont été systématiquement produites dès le départ afin de prévoir des analyses en éléments en trace in situ par ICP-MS (Inductively Coupled Plasma-Mass Spectrometer) et HR-ICP-MS (High Resolution Inductively Coupled Plasma-Mass Spectrometer) couplé à l'ablation laser qui sont des méthodes d'analyse destructives demandant donc une certaine quantité de matériel.

Dans un deuxième temps, une étude pétrographique détaillée des lames minces, au microscope optique, a permis de réaliser un choix des échantillons à analyser. Différents critères ont été pris en compte dont le type de roche, l'altération, la forme et la taille des minéraux. Ainsi parmi la collection, 68 échantillons (44 troctolites riches en olivine, 5 troctolites, 7 gabbros à olivine et 12 gabbros) ont été désignés pour des analyses à la microsonde électronique. De ce groupe, un sous-ensemble de 34 échantillons (troctolites riches en olivine, 5 troctolites, 4 gabbros à olivine et 5 gabbros) a été choisi pour l'analyse des éléments en trace des clinopyroxènes, plagioclases et olivines par ICP-MS et HR-ICP-MS couplé à l'ablation laser. Ces 34 échantillons ont été sélectionnés par rapport à leur lithotype, leur profondeur (zone), leur bas degré d'altération, la taille et la forme de leurs minéraux.

De plus, afin de calculer le mode des roches analysées, 42 échantillons ont aussi été analysés en élément majeur par XRF (X-ray fluorescence) à l'université de Grenade en Espagne par Carlos Garrido.

2. Site 1275 (Leg ODP 209)

Lors de ma première année de thèse, j'ai effectué des analyses in-situ en éléments majeurs à la microsonde électronique et en trace par ICP-MS couplé à l'ablation laser des roches gabbroïques du site 1275 afin de pouvoir les comparer ultérieurement aux roches gabbroïques des expéditions IODP 304-305. Une partie de l'échantillonnage du site 1275 était présente (échantillonnage de Carlos Garrido), mais concernait surtout les gabbros à oxyde (35 échantillons de gabbros à oxyde, 2 gabbros, 5 gabbros à olivine et 1 veine felsique). J'ai effectué un nouvel échantillonnage afin de pouvoir analyser des troctolites, avec : 6 échantillons de troctolites et 6 échantillons de gabbros à oxyde. Tous ces échantillons, après une analyse pétrographique minutieuse des lames minces au microscope optique, ont fait l'objet d'analyses en éléments majeurs in-situ. Les échantillons du Site 1275 étant fortement altérés (surtout les troctolites) par rapport aux échantillons du Puits U1309D, je n'ai pu

effectuer des analyses in-situ en éléments en traces que dans trois gabbros à oxyde.

II. Analyse des échantillons à la microsonde électronique

La teneur en éléments majeurs des principales phases minérales des échantillons du puits U1309D a été analysée au Service Commun « Microsonde Sud » de l'université Montpellier 2, sur la microsonde électronique CAMECA SX100. Les analyses chimiques sont présentées en annexe B.

1. Préparations des lames minces

J'ai tout d'abord effectué un repérage préliminaire des zones à analyser, au microscope optique, avec photos à l'appui, afin de faciliter la reconnaissance des zones à analyser lors des séances d'analyse. Puis, les lames minces sont polies afin d'être les moins rugueuses possibles puis recouvertes de carbone et placées sous vide pour éviter toute contamination avant l'analyse.

2. Principe de la microsonde électronique

Le principe de la microsonde électronique a été défini par Castaing dans sa thèse en 1951. Cette technique est basée sur la spectrométrie des rayons X émis par un échantillon sous l'impact d'un faisceau incident d'électrons. Les électrons incidents vont ioniser les atomes du matériau analysé, le retour de l'atome à l'état initial s'accompagnant de l'émission d'un photon X d'énergie et de longueur d'onde caractéristique de l'atome émetteur. Pour ensuite pouvoir obtenir des résultats quantitatifs, on va comparer le matériau à analyser avec des témoins dont la composition a été déterminée par d'autres techniques analytiques. Le but est d'obtenir la composition chimique du matériau.

L'appareil utilisé par le laboratoire Géosciences Montpellier est une CAMECA SX100 équipé de cinq spectromètres à dispersion de longueur d'onde (WDS). Chacun des spectromètres est équipé de 1 ou plusieurs cristaux monochromateurs permettant à l'ensemble

de couvrir le spectre de longueurs d'onde caractéristiques des éléments depuis le Béryllium jusqu'à l'Uranium. L'intensité du rayonnement X est mesurée par cinq compteurs à remplissage gazeux (Figure A.2).

Les analyses ont été réalisées avec une accélération de 20 kV, une intensité de faisceau de 10 nA et un temps de comptage pour chaque élément de 30 s. Les concentrations sont obtenues à partir des intensités en utilisant la procédure de quantification "X-PHI" (Merlet, 1994). Les standards utilisés pour les calibrations sont des minéraux naturels, des oxydes synthétiques, et des métaux purs. La précision des analyses de la composition en éléments majeurs des minéraux est de +/-1%.

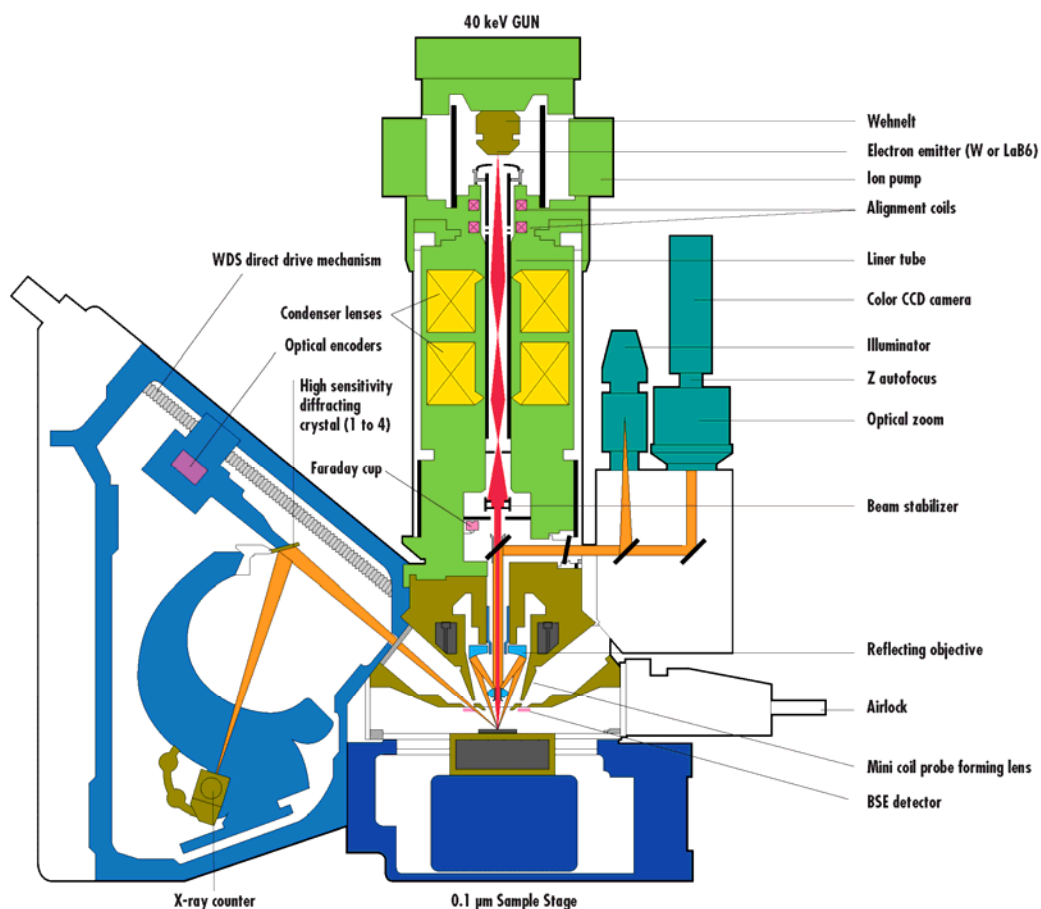


Figure A.2: Schéma de la microsonde électronique CAMECA SX100

III. Analyse des échantillons par ICP-MS couplé à l'ablation laser

La teneur en éléments en trace des clinopyroxènes, des plagioclases et des olivines a été analysée au laboratoire Géosciences Montpellier à l'université Montpellier 2, en utilisant deux ICP-MS différents couplés à un système d'ablation laser (Plateforme Geolas Q+ dotée d'un laser Excimer CompEx 102). Un premier groupe de clinopyroxènes et de plagioclases a été analysé en utilisant un spectromètre de masse à source plasma de type quadripôle VG Plasmaquad II Turbo. La teneur en éléments en trace des olivines et d'un deuxième groupe de clinopyroxènes et de plagioclases a été analysée par HR- ICP-MS en utilisant un spectromètre de masse à source plasma de type Element XR (eXtended Range). Les analyses chimiques sont présentées en Annexe B. Cette méthode d'analyse permet de déterminer de nombreux éléments du tableau périodique avec un fort degré de précision.

1. Préparations des lames minces

Après les analyses à la microsonde électronique, les lames minces sont repolies pour enlever l'enduit de carbone et coupées en carré de 3 cm afin de tenir dans la cellule d'ablation. Comme pour la préparation des analyses à la microsonde électronique, j'ai effectué un repérage des minéraux à analyser au microscope optique avant les mesures.

2. Principe de l'ICP-MS

L'ICP-MS est un spectromètre de masse dans lequel l'échantillon à analyser est introduit par l'intermédiaire d'une torche à plasma. Dans notre cas, l'échantillon est pulvérisé dans un courant d'argon grâce à un faisceau laser, puis ionisé dans une torche à plasma. Les éléments chimiques ionisés sont ensuite injectés dans le spectromètre de masse.

L'interface entre la torche et le spectromètre est constituée de deux cônes en métal percés d'un orifice et situés l'un derrière l'autre. La géométrie de ces cônes est telle que les ions sont accélérés à des vitesses supersoniques avant leur entrée dans le spectromètre. Cette partie est sensible, car l'on passe de la torche à pression atmosphérique à l'intérieur du

spectromètre qui est à une pression de 10^{-4} hPa à proximité de l'interface et de 10^{-7} hPa au niveau du détecteur. Le faisceau ionique est ensuite focalisé à l'intérieur du tube avant de pénétrer dans l'analyseur en masse.

a) Spectromètre de masse de type quadripôle

Le quadripôle est constitué de quatre barreaux traversés par un potentiel électrique. En fonction de ce potentiel et du rapport masse sur charge des ions un seul type d'ion aura une trajectoire rectiligne dans le quadripôle, les autres iront heurter les barreaux et seront pompés vers l'extérieur. Le détecteur se trouvant en fin de système correspond à un multiplicateur d'électrons. Ce type de fonctionnement en mode séquentiel permet un balayage très rapide de tout le spectre de masse et est donc très adapté à l'analyse multi-élémentaire.

b) Spectromètre de masse de type « Element XR »

Le spectromètre de masse Element XR est équipé d'un système à double focalisation : secteur magnétique et secteur électrostatique qui permet de réaliser un balayage magnétique ou électrique du faisceau d'ions. L'adjonction d'une cage de Faraday permet d'étendre la gamme dynamique de la machine à 109 cps. Il peut être utilisé à différentes résolutions de masse : basse (300), moyenne (4000) et haute (10 000), ce qui permet de séparer des ions ou molécules de masses très voisines.

3. Principe de l'analyse par ICP-MS couplé à un système d'ablation laser

L'ablation laser est une technique utilisée pour les analyses in situ des éléments en trace dans des échantillons solides.

La lame mince est placée dans une cellule d'ablation dans laquelle circule un flux continu d'hélium. Ceci permet d'augmenter la sensibilité et de réduire le fractionnement inter-éléments (Gunther et Heinrich, 1999). Les particules de l'échantillon pulvérisées par le laser sont entraînées par le courant d'hélium et mélangées à l'argon avant d'entrer dans le plasma.

L'analyse par ablation laser se fait en deux parties : dans un premier temps, on mesure le bruit de fond pendant 2 minutes ; le laser ne fonctionne pas et seul le courant d'hélium qui circule dans la chambre d'ablation est analysé. Dans un deuxième temps, le laser est activé

durant 1 minute et l'échantillon est vaporisé et analysé. L'analyse consiste à mesurer le nombre d'impacts par unité de temps sur le détecteur pour chaque isotope des éléments désirés. En fait, la durée d'analyse est divisée en cycles de 1,1 secondes durant lesquels le spectre de masse de l'ensemble des éléments à étudier est balayé par le quadripôle, d'où son nom « Time Resolved Acquisition » (TRA).

Chaque élément a été mesuré en utilisant un temps d'angles de saturation (dwell time) différent de 10.24 ms ou 20.48 ms pour plus de précision sur les Terres Rares (REE). Le laser est allumé en utilisant une densité d'énergie de 15 J cm^{-2} à une fréquence de 5Hz et en utilisant une taille de faisceau de 122 μm pour les plagioclases et de 102 μm pour les clinopyroxènes (50 μm avec le HR-ICP-MS). Pour l'analyse des olivines (HR-ICP-MS) le laser a été utilisé à une fréquence de 10Hz et une taille de faisceau de 120 μm .

4. Quantification-Standardisation

Pour parvenir à un résultat quantitatif il faut faire une standardisation interne et externe. La standardisation interne consiste à analyser un élément chimique dont on connaît déjà la concentration dans l'échantillon. Ces analyses sont réalisées en utilisant un isotope du calcium (^{43}Ca), élément abondant dans les clinopyroxènes et les plagioclases et un isotope de la silice (^{29}Si) pour les olivines. Le rapport entre l'intensité du signal obtenu pour un isotope donné et l'intensité du signal obtenu pour l'isotope choisi comme standard interne est alors comparé avec le même rapport mesuré dans un étalon externe. Cet étalon correspond à un verre rhyolitique synthétique dopé en éléments en trace, appelé NIST 612 (Pearce et al., 1997). Les données sont ensuite traitées par le logiciel GLITTER (Van Achterbergh et al., 1999).

L'analyse par ablation laser se déroule donc en plusieurs étapes :

- Analyse dans l'étalon externe (NIST 612)
- Plusieurs analyses dans les échantillons
- De nouveau analyse dans l'étalon externe
- Analyse dans le témoin de référence (BR)

5. Précision-limite de détection

Une bonne analyse est une analyse donnant à la fois un résultat juste et précis. La précision d'une analyse en ablation laser est souvent excellente, de l'ordre de 5 à 10% (1sigma RSD%). La justesse des analyses est évaluée en faisant des mesures répétées dans un verre basaltique de composition connue, BR (Govindaraju et Roelandts, 1988) (Tableau A.1).

La limite de détection peut être considérée comme la plus faible concentration pouvant être détecté au-dessus du bruit de fond. Les limites de détection sont variables selon le minéral analysé (Tableau A.2). Les plagioclases analysés au LA-ICP-MS ont des limites de détection entre 0.2 et 5 ppm pour les Terres Rares (REE), Hf, Y, Zr, Ti, V, Cr, et Ni et en dessous de 0.1 ppm pour les autres éléments. Les clinopyroxènes analysés avec le Laser-ICP-MS ont des limites de détection en dessous de 0.1 ppm pour tous les éléments exceptés Zr, Ti, V, Cr et Ni qui sont entre 0.2 et 6 ppm. Pour les analyses réalisées au LA-HR-ICP-MS, les plagioclases ont une limite de détection inférieure à 0.05 ppm excepté pour Ti, Ni et Zn (1 à 2 ppm); les clinopyroxènes ont une limite de détection inférieure à 0.02 ppm pour tous les éléments excepté pour Ti, Ni et Zn qui sont entre 2 et 4 ppm. Pour les éléments V, Cr, Co, Zn, Rb, Sr et Ba, les limites de détections sont entre 0.03 et 0.3 ppm. Les olivines ont une limite de détection inférieure à 0.08 ppm pour tous les éléments exceptés Si, P, Ca, et Ni qui sont entre 0.2 et 1.7 ppm.

IV. Analyse des échantillons à l'EBSD

L'analyse microstructurale des échantillons du puits U1309D a été réalisée à l'université Montpellier 2, en utilisant un microscope électronique à balayage (MEB) JEM-5600 SEM couplé à un système d'imagerie EBSD (Electron Back Scattered Diffraction). Les résultats sont présentés en Annexe C.

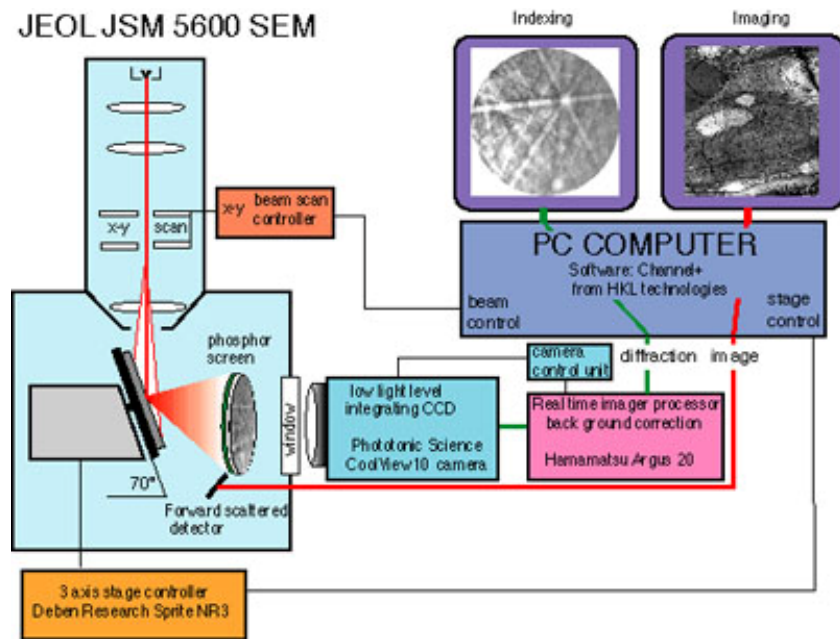
1. Préparations des lames minces

Avant chaque analyse à l'EBSD, les lames minces sont repolies afin d'avoir la surface la plus lisse possible pour une meilleure précision des analyses. J'ai choisi d'analyser à

l'EBSD principalement les troctolites riches en olivine (21 échantillons). En effet, leur texture poecilitique semble indiquer une histoire complexe, et cette technique d'analyse permet d'apporter une réponse sur l'origine de ces roches. Quelques roches gabbroïques (3 troctolites, 3 gabbros à olivine et 1 gabbro troctolitique) sont aussi analysées afin de comparer leur microstructure à celle des roches riches en olivine et de pouvoir ainsi retracer une histoire pétrostructurale.

2. Principe de l'EBSD

La technique de diffraction d'électrons rétrodiffusés (Electron Back Scattered Diffraction) permet de déterminer les orientations cristallographiques sur des matériaux mono- ou polycristallins. À chaque mesure, un diagramme de diffraction constitué de bandes de Kikuchi caractéristiques de l'orientation du grain analysé est produit dans la chambre du MEB (Figure A.3). Ce diagramme est projeté sur un écran de phosphore qui génère un signal de photon de ce dernier. L'image est acquise par un appareil photo numérique photonique CCD (Photonic Science CoolView CCD camera) et envoyée à un PC après le traitement des signaux (afin de réduire le bruit de fond et augmenter le signal lié au diagramme de diffraction). Le logiciel « CHANNEL5 » de « Oxford Instruments HKL Technology » est utilisé pour indexer les diagrammes de diffraction en termes d'orientation cristalline. Le processus complet prend environ 0.1 à 0.3 secondes. Une cartographie d'orientation des grains peut être obtenue en balayant avec le faisceau d'électrons la surface de l'échantillon.



Formation of a backscattered Kikuchi band

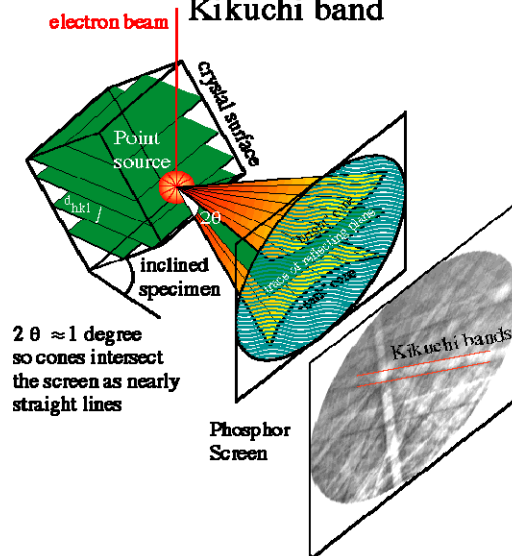


Figure A.3: Principe de fonctionnement d'une analyse EBSD

Tout d'abord la lame mince est orientée et fixée sur un support avec du ruban adhésif conducteur qui permet l'évacuation de la charge. Puis, la lame mince est placée à 70° dans la chambre d'observation du MEB, afin que soit réalisable la technique de diffraction des électrons. Ensuite, on effectue quelques réglages de calibration. Une pastille de silicium servant d'étalon est placée sur le support avec la lame mince. Le silicium permet d'ajuster les paramètres de détermination des minéraux et d'orientation des axes cristallins. Enfin, la cartographie de la lame mince est programmée en rentrant les différentes coordonnées spatiales de la lame et la taille du pas d'échantillonnage (entre 30 et 80 μm pour mes lames

minces) selon la taille des grains. Ces différents paramètres déterminent le temps d'analyse. Pour chaque échantillon, nous obtenons ainsi des cartes d'orientation cristallographique couvrant entièrement la lame mince (généralement 20*35mm). Le taux d'indexation dans les cartes brutes varie de 60 à 80%.

L'analyse à l'EBSD des échantillons se déroule donc ainsi (Figure A.3) :

- Acquisition d'une micrographie MEB
- Acquisition du cliché de Kikuchi pour le point d'analyse
- Détection des bandes de Kikuchi
- Détermination du minéral analysé à partir d'une base de donnée
- Détermination de l'orientation des axes cristallins pour ce point de mesure
- Changement de position de la sonde d'analyse, nouveau point de mesure et ainsi de suite.

3. Traitement des données

Le traitement des données EBSD s'effectue grâce à l'application « Tango » du logiciel « CHANNEL5 » qui permet d'augmenter le taux d'indexation :

- En comblant les pixels non-indexés qui ont plus de 8 voisins identiques avec la même orientation.
- En répétant cette opération en utilisant respectivement 7, 6, et 5 voisins identiques.
- En identifiant les grains, par exemple des domaines continus caractérisés par une misorientation interne $<10^\circ$.
- En corrigeant dans chaque cristal d'olivine les erreurs d'indexation systématiques dues aux pseudosymétries hexagonales de l'olivine, ayant pour conséquence des figures de diffraction similaires pour des orientations différant d'une rotation de 60° autour de l'axe [100].

À chaque étape, les cartes d'orientations sont vérifiées par l'utilisateur pour éviter l'extrapolation des données.

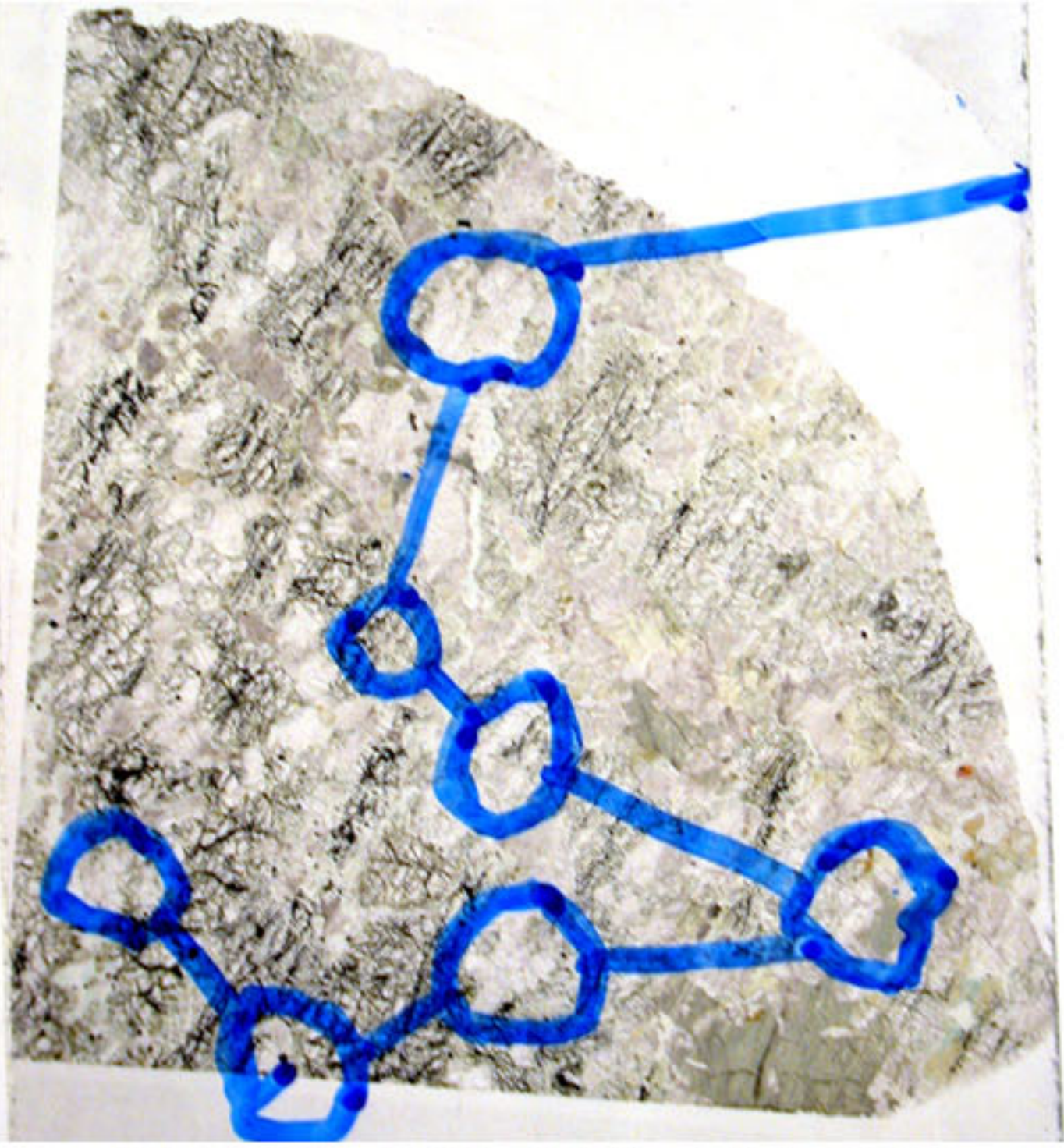
L'application « Mambo » du logiciel « CHANNEL5 » permet de visualiser les figures de pôles pour chaque minéral, ainsi que les axes de rotations des sous-joints (figures de pôles inverses). Les figures de pôles sont représentées en utilisant la moyenne des angles d'Euler pour chaque grain plutôt que des mesures individuelles pour éviter la surreprésentation des grains de grandes tailles dans les lames minces.

| Date de l'échantillon | numero de | Type | analyse | ppm Cs | ppm Rb | ppm Ba | ppm Th | ppm U | ppm Nb | ppm Ta | ppm La | ppm Ce | ppm Pb | ppm Pr | ppm Sr | ppm Nd | ppm Zn | ppm Hf | ppm Sm | ppm Eu | ppm Gd | ppm Tb | ppm Dy | ppm Y | ppm Ho | ppm Er | ppm Tm | ppm Yb | ppm Lu |
|-----------------------|---------------|-------------|-----------------------|--------|--------|----------|--------|-------|---------|--------|--------|---------|--------|--------|----------|--------|---------|--------|--------|--------|--------|--------|--------|--------|--------|--------|--------|--------|--------|
| 22/02/06 | 63R2_28-30 | BR(basalte) | JCBt1 | 0,66 | 41,21 | 1122,4 | 17,5 | 4,77 | 104,09 | 6,21 | 99,96 | 158,58 | 8,5 | 17,76 | 1386,5 | 70,04 | 245,7 | 6,08 | 12,68 | 3,95 | 10,08 | 1,29 | 6,82 | 27,36 | 1,13 | 2,72 | 0,333 | 2,06 | 0,268 |
| 22/02/06 | 63R2_28-30 | BR(basalte) | JCBt2 | 0,58 | 40,8 | 1043,07 | 10,84 | 2,56 | 108,14 | 5,52 | 90,81 | 150,14 | 7,24 | 16,24 | 1326,68 | 62,47 | 219,8 | 4,76 | 11,25 | 3,57 | 8,69 | 1,07 | 5,78 | 22,65 | 0,96 | 2,22 | 0,265 | 1,77 | 0,214 |
| 22/02/06 | 228R4_39-43 | BR(basalte) | JDBt1 | 0,622 | 42,97 | 1011,98 | 10,84 | 2,47 | 101,39 | 5,61 | 91,73 | 143,86 | 7,1 | 16,01 | 1290,06 | 64,49 | 241,63 | 5,63 | 11,35 | 3,49 | 9,51 | 1,18 | 6,44 | 26,21 | 1,03 | 2,55 | 0,305 | 1,98 | 0,249 |
| 22/02/06 | 69R3_6-9 | BR(basalte) | JEBt1 | 0,72 | 42,23 | 1064,619 | 10,22 | 2,48 | 101,53 | 5,7 | 93,1 | 149,73 | 7,22 | 16,5 | 1293,74 | 63,9 | 232,04 | 4,92 | 11,55 | 3,56 | 9,35 | 1,12 | 6,43 | 25,07 | 1,06 | 2,34 | 0,285 | 1,92 | 0,254 |
| 4/04/06 | 62R1_4-7 | BR(basalte) | LABt1 | 0,588 | 40,21 | 945,51 | 9,7 | 2,39 | 92,84 | 5,12 | 86,83 | 137,88 | 6,63 | 15,19 | 126,71 | 60,65 | 227,04 | 4,95 | 10,95 | 3,27 | 8,87 | 1,18 | 6,1 | 25,74 | 1,008 | 2,33 | 0,29 | 1,781 | 0,244 |
| 4/04/06 | 61R1_13-116 | BR(basalte) | LGBt1 | 0,624 | 40,34 | 962,85 | 10,01 | 2,26 | 96,75 | 5,28 | 87,49 | 141,03 | 7,08 | 15,39 | 1239,91 | 61,33 | 224,83 | 5,24 | 10,98 | 3,31 | 8,93 | 1,107 | 6,11 | 26,6 | 1,018 | 2,43 | 0,307 | 1,76 | 0,223 |
| 4/04/06 | 64R1_13-16 | BR(basalte) | LGBt1 | 0,591 | 37,67 | 932,75 | 9,57 | 2,26 | 93,27 | 4,98 | 84,16 | 134,59 | 7,03 | 14,86 | 1208,87 | 57,49 | 222,73 | 4,94 | 10,4 | 3,18 | 8,76 | 1,066 | 5,8 | 24,85 | 0,963 | 2,24 | 0,273 | 1,81 | 0,223 |
| 4/04/06 | 136R1_35-39 | BR(basalte) | LDBt1 | 0,672 | 40,85 | 1085,37 | 11,82 | 2,61 | 104,42 | 6,08 | 102,93 | 159,07 | 7,53 | 17,98 | 1267,53 | 69,49 | 248,33 | 5,9 | 12,71 | 3,79 | 10,29 | 1,29 | 7,04 | 27,4 | 1,16 | 2,73 | 0,337 | 2,02 | 0,27 |
| 4/04/06 | 136R2_37-40 | BR(basalte) | LEBt1 | 0,56 | 35,21 | 815,69 | 8,23 | 1,921 | 83,62 | 4,35 | 73,9 | 119,06 | 5,63 | 13,17 | 1036,28 | 52,14 | 192,96 | 4,22 | 9,27 | 2,8 | 7,47 | 0,92 | 4,97 | 21,3 | 0,846 | 1,95 | 0,235 | 1,454 | 0,187 |
| 4/04/06 | 227R3_121-124 | BR(basalte) | LFBt1 | 0,889 | 39,38 | 945,13 | 8,03 | 2,07 | 94,28 | 5,01 | 78,75 | 135,08 | 6,17 | 14,49 | 1190,09 | 54,61 | 181,72 | 3,76 | 9,54 | 3,01 | 6,8 | 0,852 | 4,61 | 19,62 | 0,739 | 1,684 | 0,221 | 1,355 | 0,171 |
| 4/04/06 | 234R3_14-18 | BR(basalte) | LGBt1 | 0,657 | 39,68 | 984,76 | 9,4 | 2,28 | 95,69 | 5,07 | 87,92 | 142,74 | 6,66 | 15,37 | 1233,19 | 59,91 | 221,61 | 4,74 | 10,9 | 3,31 | 9,09 | 1,08 | 5,85 | 24,79 | 0,96 | 2,28 | 0,288 | 1,69 | 0,237 |
| 6/04/06 | 234R1_92-96 | BR(basalte) | MHBt1 | 0,684 | 41,72 | 995,49 | 9,66 | 2,46 | 99,96 | 5,07 | 89,63 | 145,15 | 8,32 | 15,89 | 1260,37 | 62,17 | 227,31 | 4,79 | 11,08 | 3,3 | 8,98 | 1,075 | 5,71 | 25,32 | 0,992 | 2,38 | 0,276 | 1,8 | 0,232 |
| 6/04/06 | 237R2_40-43 | BR(basalte) | MIBt1 | 0,712 | 42,79 | 1017,17 | 9,97 | 2,419 | 101,53 | 5,13 | 92,23 | 148,67 | 7,04 | 16,31 | 1271,17 | 63,42 | 238,45 | 4,92 | 11,71 | 3,39 | 9,12 | 1,137 | 6,13 | 26,9 | 0,999 | 2,36 | 0,298 | 1,78 | 0,247 |
| 6/04/06 | 247R3_62-66 | BR(basalte) | MIBt1 | 0,707 | 42,38 | 1003,22 | 9,72 | 2,56 | 99,29 | 5,12 | 89,12 | 148,07 | 7,23 | 15,92 | 1282,01 | 62,51 | 232,35 | 4,97 | 11,32 | 3,38 | 8,96 | 1,071 | 6,05 | 25,84 | 1,001 | 2,31 | 0,286 | 1,75 | 0,246 |
| 6/04/06 | 248R3_131-134 | BR(basalte) | MKBt1 | 0,476 | 41,34 | 1009,57 | 10,02 | 2,45 | 102,72 | 5,27 | 89,53 | 147,84 | 6,93 | 16,06 | 1283,91 | 63,34 | 238,35 | 5,22 | 11,61 | 3,44 | 9,16 | 1,136 | 6,17 | 26,36 | 0,984 | 2,42 | 0,284 | 1,8 | 0,235 |
| 6/04/06 | 135R2_82-85 | BR(basalte) | MLBt1 | 0,612 | 40,9 | 994,81 | 10,08 | 2,35 | 99,07 | 5,22 | 89,56 | 144,7 | 6,93 | 15,87 | 1282,71 | 62,39 | 238,13 | 4,99 | 11,15 | 3,38 | 9,26 | 1,158 | 6,28 | 26,57 | 1,032 | 2,44 | 0,299 | 1,72 | 0,252 |
| 6/07/06 | 227R2_26-30 | BR(basalte) | MNBt1 | 0,72 | 42,31 | 1026,95 | 10,37 | 2,52 | 99,63 | 5,4 | 92,08 | 148,97 | 7,5 | 16,08 | 1271,81 | 64,16 | 239,55 | 5,33 | 11,49 | 3,4 | 9,81 | 1,146 | 6,43 | 26,54 | 1,041 | 2,53 | 0,306 | 1,87 | 0,255 |
| 6/07/06 | 135R3_21-26 | BR(basalte) | MOBt1 | 0,674 | 43,11 | 1064,84 | 11,54 | 2,62 | 109,02 | 6,12 | 101,35 | 161,26 | 7,69 | 17,71 | 1423,64 | 70,66 | 266,32 | 6,32 | 12,86 | 3,78 | 10,55 | 1,363 | 7,03 | 29,65 | 1,205 | 2,68 | 0,36 | 1,94 | 0,283 |
| 6/07/06 | 70R2_99-103 | BR(basalte) | MOBt1 | 0,712 | 44,36 | 1103,46 | 10,35 | 2,43 | 102,51 | 5,45 | 93,49 | 149,26 | 6,9 | 16,68 | 1301,58 | 65,42 | 237,43 | 5,3 | 11,61 | 3,58 | 9,55 | 1,192 | 6,36 | 26,35 | 1,06 | 2,49 | 0,297 | 1,79 | 0,228 |
| 10/07/06 | 71R1_10-13 | BR(basalte) | NABt1 | 0,663 | 42,27 | 1024,32 | 10,63 | 2,54 | 102,35 | 5,95 | 96,7 | 151,26 | 8,22 | 16,89 | 1194,09 | 69,98 | 234,47 | 5,04 | 12,09 | 3,59 | 9,98 | 1,087 | 7,21 | 25,22 | 1,13 | 2,54 | 0,299 | 2,31 | 0,282 |
| 10/07/06 | 228R1_95-98 | BR(basalte) | NDBt1 | 0,711 | 41,82 | 1039,66 | 10,6 | 2,52 | 102,35 | 5,46 | 93,14 | 145,81 | 7,75 | 16,16 | 1321,55 | 63,16 | 249,81 | 5,56 | 11,39 | 3,4 | 9,48 | 1,164 | 6,32 | 27,93 | 1,051 | 2,54 | 0,338 | 1,93 | 0,244 |
| 10/07/06 | 231R3_50-54 | BR(basalte) | NEBt1 | 0,67 | 42,32 | 1015,75 | 10,91 | 2,72 | 97,95 | 5,71 | 92,18 | 150,51 | 8,74 | 16,32 | 1298,76 | 64,3 | 237,5 | 5,74 | 11,63 | 3,38 | 9,59 | 1,14 | 6,49 | 26,26 | 1,08 | 2,65 | 0,313 | 2,02 | 0,268 |
| 10/07/06 | 234R1_22-26 | BR(basalte) | NFBt1 | 0,65 | 41,13 | 1013,04 | 11,12 | 2,55 | 104,22 | 5,59 | 96,44 | 151,63 | 7,33 | 16,92 | 1332,58 | 66,06 | 255,23 | 6,13 | 11,94 | 3,6 | 9,77 | 1,201 | 6,62 | 28,58 | 1,083 | 2,66 | 0,325 | 2,02 | 0,282 |
| 11/07/06 | 235R2_85-89 | BR(basalte) | NGBt1 | 0,668 | 40,56 | 1049,49 | 10,81 | 2,52 | 105,27 | 5,83 | 99,66 | 158,54 | 8 | 17,47 | 1364,86 | 67,39 | 249,02 | 5,6 | 12,43 | 3,62 | 9,81 | 1,213 | 6,64 | 28,17 | 1,076 | 2,73 | 0,31 | 2,05 | 0,278 |
| 11/07/06 | 236R2_121-124 | BR(basalte) | NHBt1 | 0,707 | 44,19 | 1091,18 | 11,12 | 2,64 | 104,72 | 5,74 | 99,73 | 158,95 | 7,87 | 17,51 | 1351,21 | 68,75 | 259,92 | 5,89 | 12,32 | 3,69 | 10,09 | 1,29 | 7,01 | 28,11 | 1,14 | 2,73 | 0,347 | 2,06 | 0,298 |
| 11/07/06 | 241R2_94-97 | BR(basalte) | NIBt1 | 0,699 | 43,98 | 1096,52 | 10,54 | 2,41 | 99,53 | 5,45 | 95,19 | 150,57 | 7,18 | 16,6 | 1317 | 66,58 | 235,14 | 5,7 | 12,01 | 3,46 | 9,27 | 1,185 | 6,16 | 27,21 | 1,073 | 2,52 | 0,306 | 1,84 | 0,241 |
| | | | MOYENNE | 0,661 | 41,837 | 1016,447 | 10,502 | 2,532 | 100,320 | 5,543 | 92,106 | 147,301 | 7,251 | 16,254 | 1280,639 | 63,297 | 235,839 | 5,291 | 11,511 | 3,458 | 9,309 | 1,185 | 6,216 | 26,185 | 1,034 | 2,445 | 0,300 | 1,866 | 0,247 |
| | | | SCART TYPE | 0,0701 | 13,84 | 59,947 | 1,553 | 0,453 | 5,496 | 0,244 | 6,300 | 10,680 | 0,655 | 1,043 | 70,583 | 4,201 | 16,957 | 0,557 | 0,824 | 0,230 | 0,760 | 0,103 | 0,564 | 2,022 | 0,090 | 0,299 | 0,099 | 0,186 | 0,077 |
| | | | valeurs de références | 0,8 | 47 | 1050 | 11 | 2,5 | 98 | 6,2 | 82 | 151 | 5 | 17 | 1320 | 65 | 260 | 5,6 | 12,2 | 3,7 | 9,5 | 1,25 | 6,4 | 30 | 1,1 | 2,5 | 0,3 | 1,8 | 0,25 |

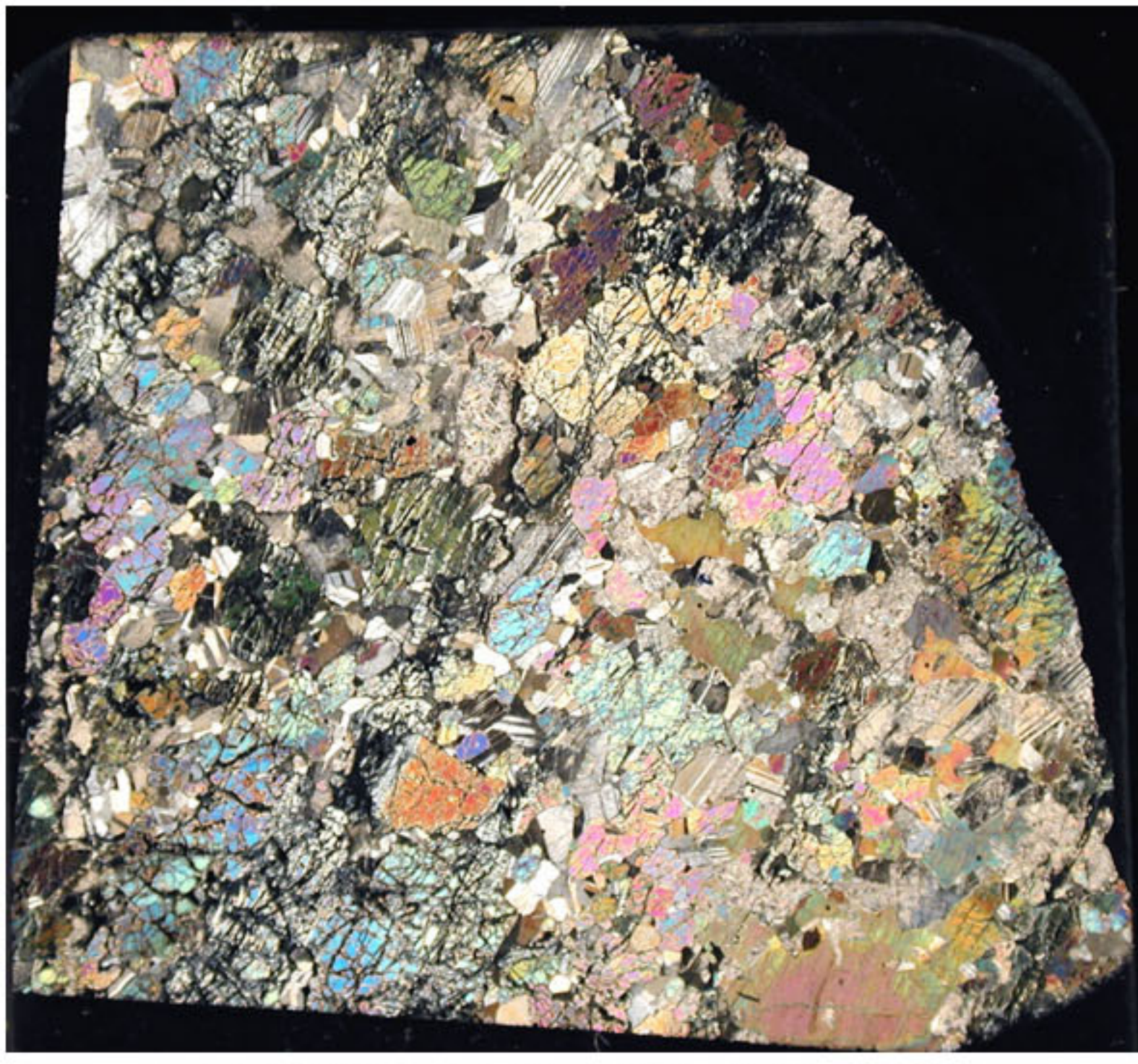
Tableau A2: Compositions des basaltes de référence

Tableau A2: Précision (ppm) sur les éléments mesurés avec le LA- ICP-MS et le LA-HR-ICP-MS*

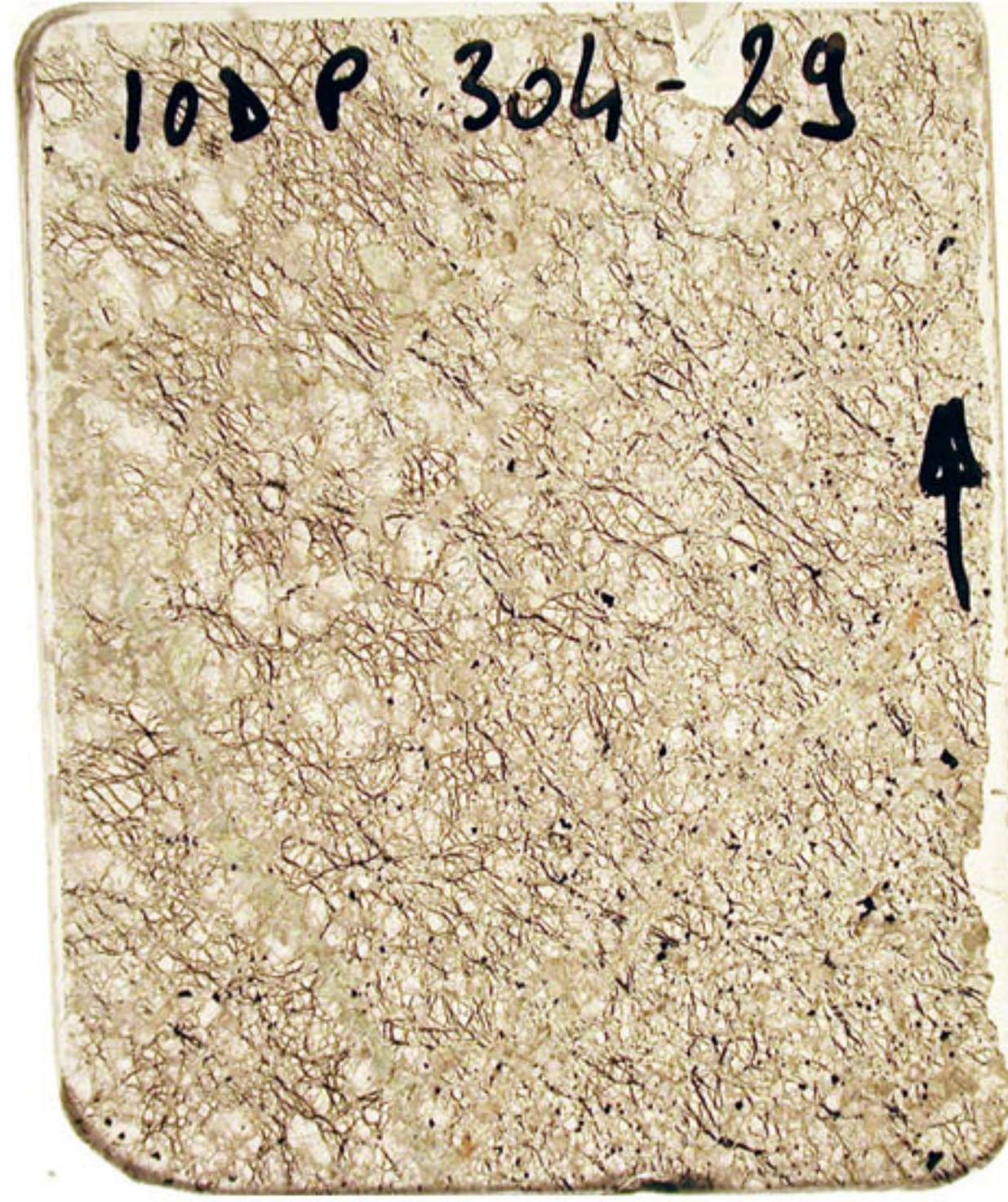
| | Plagioclase | Plagioclase* | Clinopyroxène | Clinopyroxène* | Olivine* |
|----|-------------|--------------|---------------|----------------|----------|
| Si | | | | | 1.75 |
| P | | | | | 0.29 |
| Ca | | | | | 1.18 |
| Ti | 2.24 | 1.20 | 3.43 | 2.23 | 0.08 |
| V | 3.460 | 0.018 | 0.200 | 0.030 | 0.002 |
| Cr | 5.28 | 0.22 | 6.83 | 0.37 | 0.03 |
| Co | | 0.055 | | 0.102 | 0.002 |
| Ni | 11.7 | 1.9 | 15.0 | 4.3 | 0.2 |
| Zn | | 0.26 | | 0.48 | 0.02 |
| Rb | 0.097 | 0.025 | 0.061 | 0.042 | 0.002 |
| Sr | 0.5550 | 0.0238 | 0.0990 | 0.0452 | 0.0009 |
| Y | 4.9600 | 0.0028 | 0.0710 | 0.0050 | 0.0002 |
| Zr | 0.9360 | 0.0034 | 0.2810 | 0.0071 | 0.0003 |
| Nb | 0.1740 | 0.0052 | 0.0321 | 0.0078 | 0.0003 |
| Cs | 0.1290 | 0.0104 | 0.1590 | 0.0178 | 0.0010 |
| Ba | 0.0432 | 0.0471 | 0.0412 | 0.0901 | 0.0015 |
| La | 0.25000 | 0.00099 | 0.03980 | 0.00250 | 0.00008 |
| Ce | 0.59000 | 0.00150 | 0.02180 | 0.00173 | 0.00013 |
| Pr | 1.05500 | 0.00086 | 0.02080 | 0.00082 | 0.00003 |
| Nd | 1.66300 | 0.00305 | 0.09510 | 0.00571 | 0.00030 |
| Sm | 3.12000 | 0.01530 | 0.12500 | 0.02470 | 0.00038 |
| Eu | 3.39000 | 0.00354 | 0.02750 | 0.00603 | 0.00005 |
| Gd | 4.48000 | 0.01130 | 0.16400 | 0.01930 | 0.00036 |
| Tb | 4.54000 | 0.00156 | 0.01570 | 0.00193 | 0.00007 |
| Dy | 5.26000 | 0.00185 | 0.05740 | 0.00298 | 0.00015 |
| Ho | 5.12000 | 0.00040 | 0.01430 | 0.00057 | 0.00003 |
| Er | 5.14000 | 0.00157 | 0.05010 | 0.00246 | 0.00014 |
| Tm | 4.90000 | 0.00221 | 0.01160 | 0.00294 | 0.00008 |
| Yb | 4.69000 | 0.00309 | 0.10700 | 0.00678 | 0.00019 |
| Lu | 4.41000 | 0.00151 | 0.01650 | 0.00206 | 0.00006 |
| Hf | 1.39000 | 0.00538 | 0.15300 | 0.01040 | 0.00015 |
| Ta | 0.12200 | 0.00243 | 0.01630 | 0.00438 | 0.00012 |
| Pb | 0.04880 | 0.00344 | 0.05580 | 0.00659 | 0.00041 |
| Th | 0.10800 | 0.00030 | 0.03770 | 0.00051 | 0.00002 |
| U | 0.01890 | 0.00225 | 0.04280 | 0.00036 | 0.00001 |



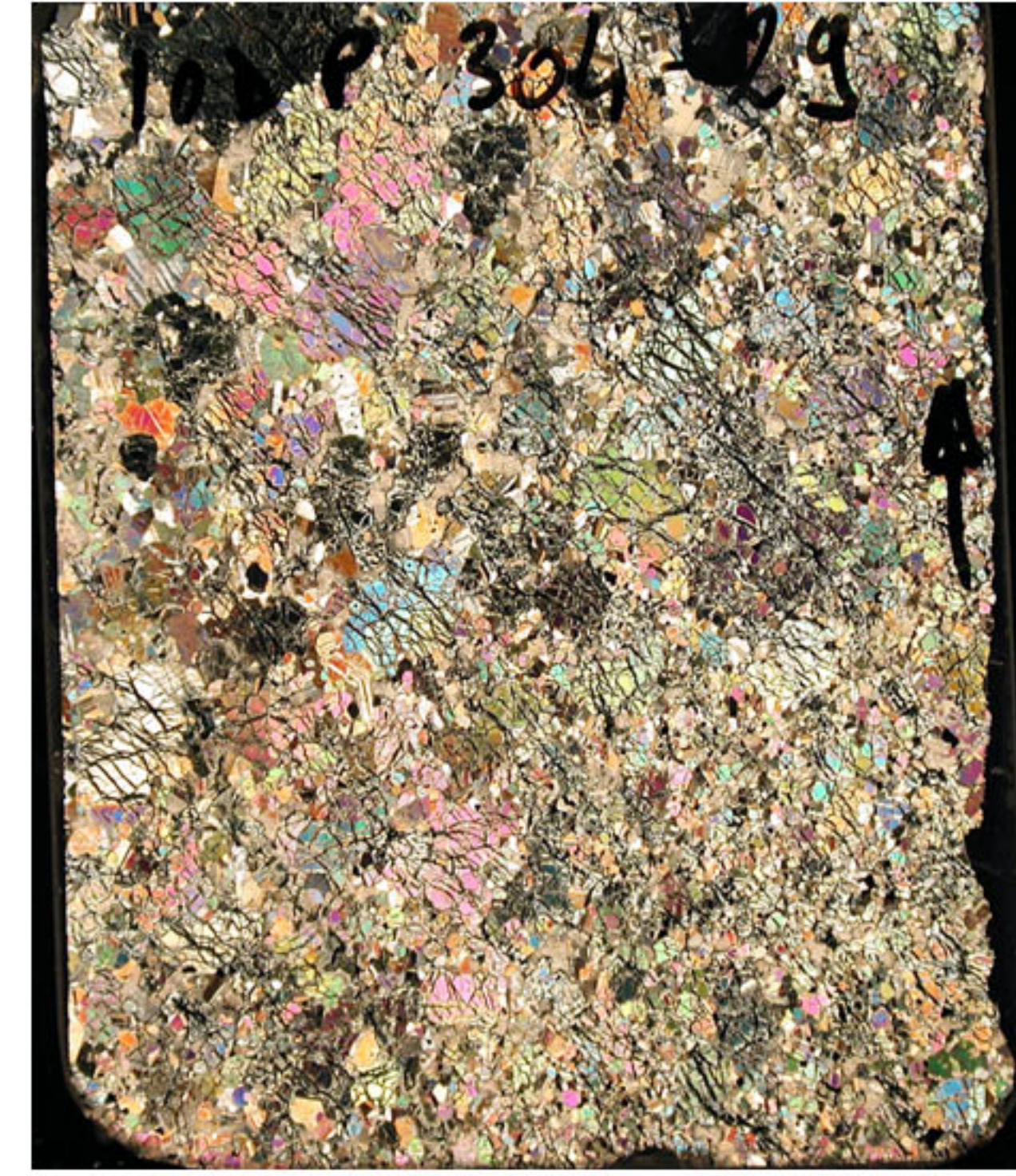
111R2_112-116_LN.JPG



111R2_112-116_LP.JPG



111R3_101-114_LN.JPG



111R3_101-114_LP.JPG



111R4_14-17_LN.JPG



111R4_14-17_LP.JPG



111R4_50-54_LN.JPG



112R1_69-73_LN.JPG



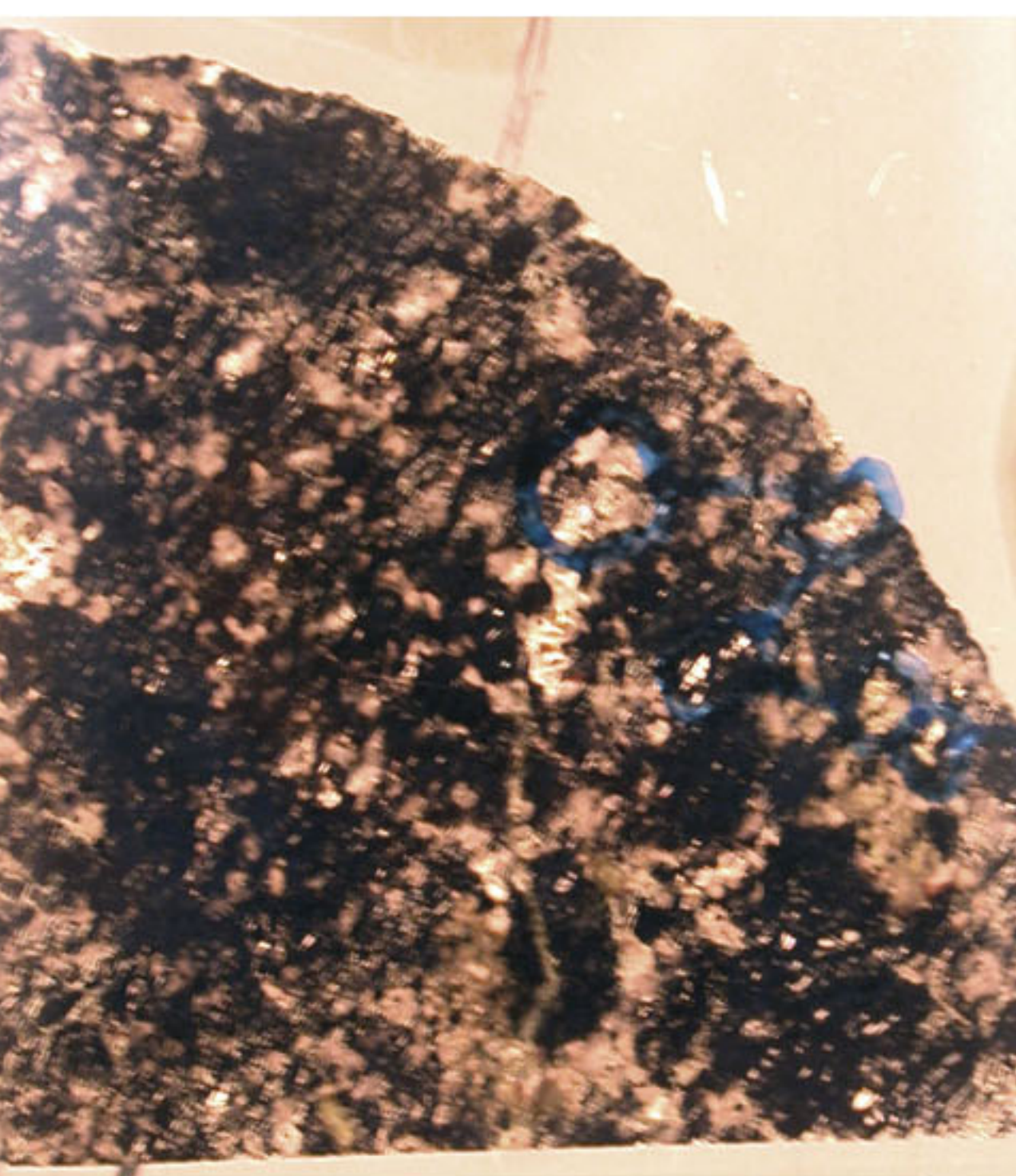
112R1_69-73_LP.JPG



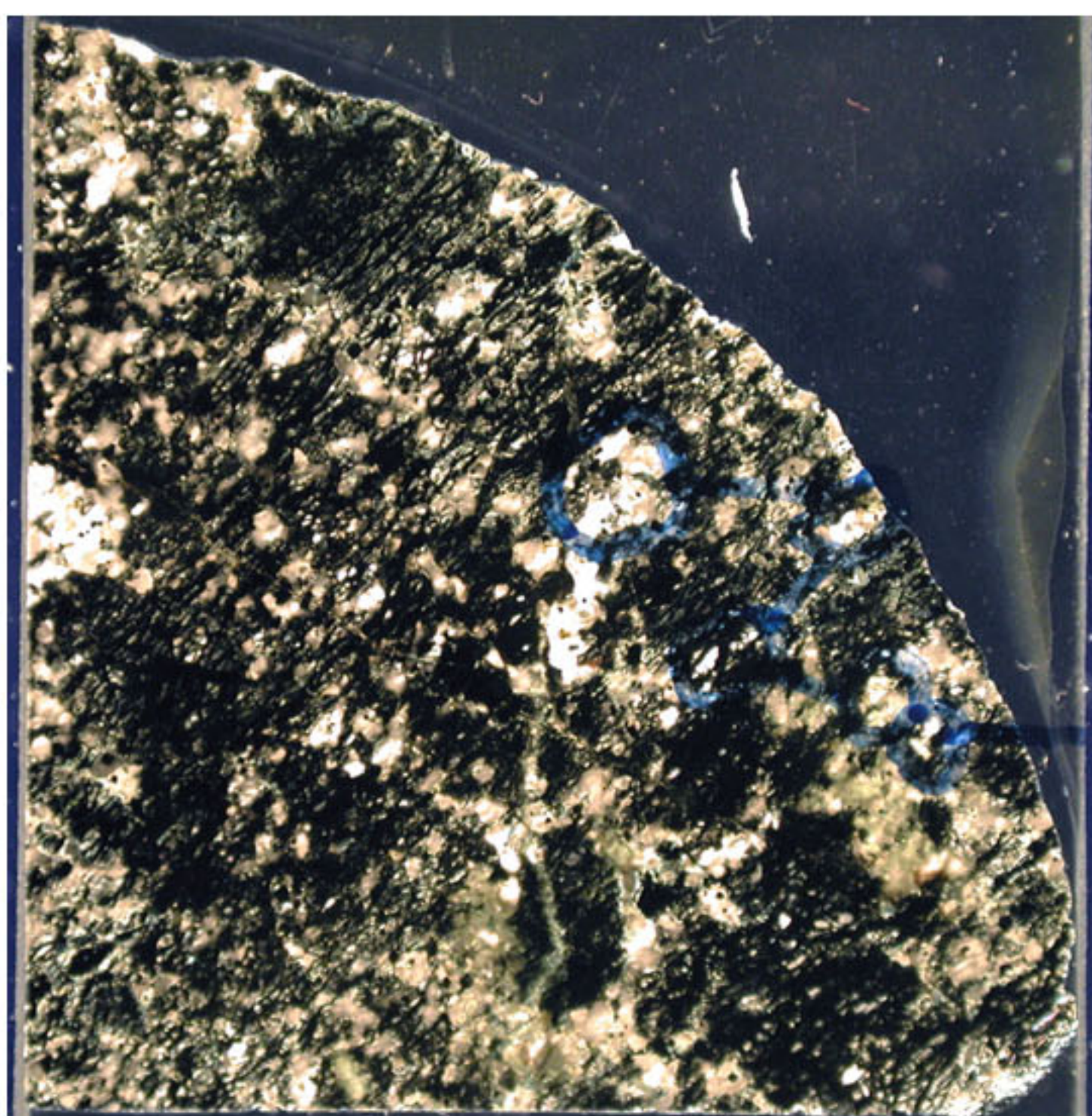
112R2_16-20_LN.JPG



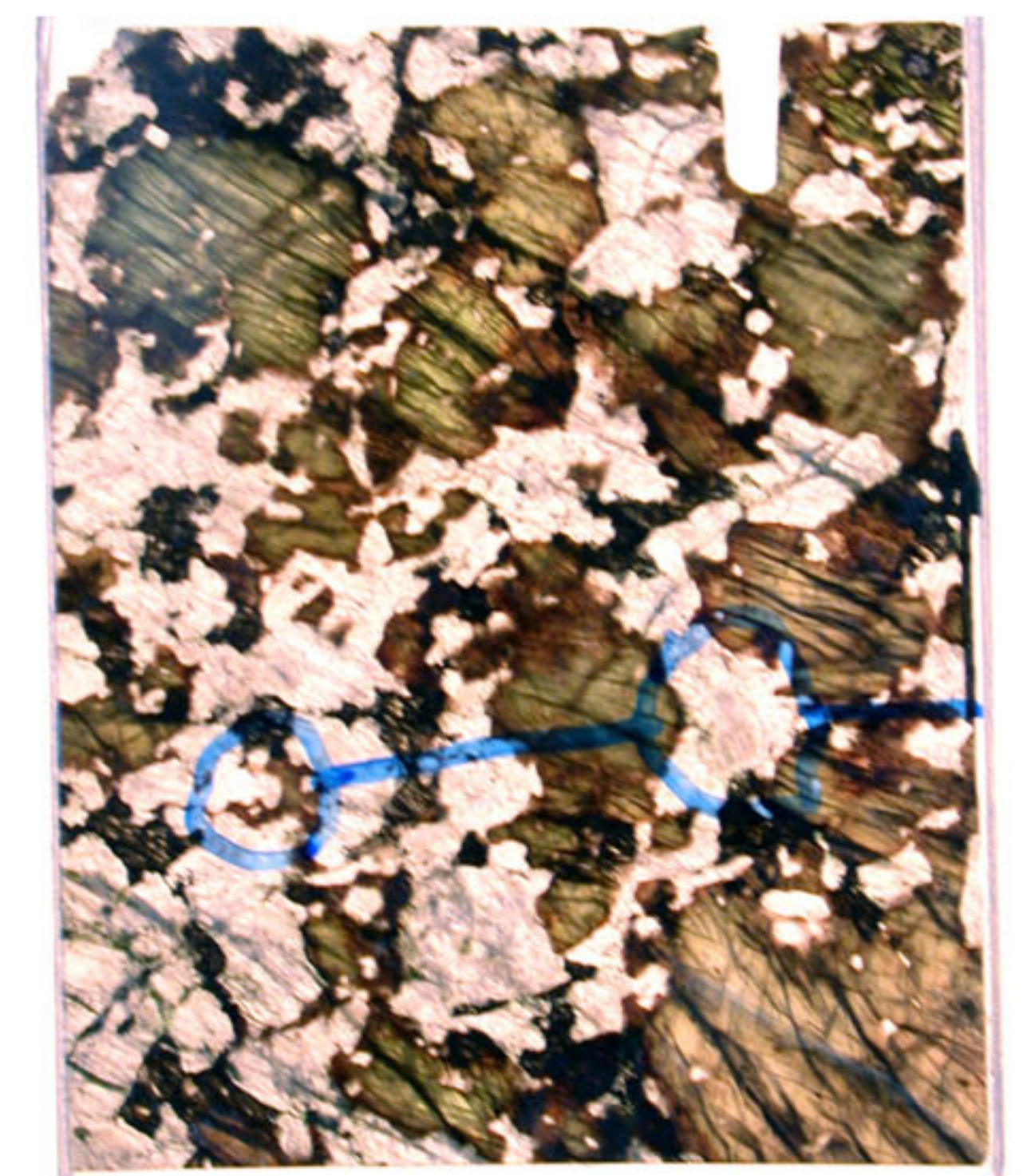
112R2_16-20_LP.JPG



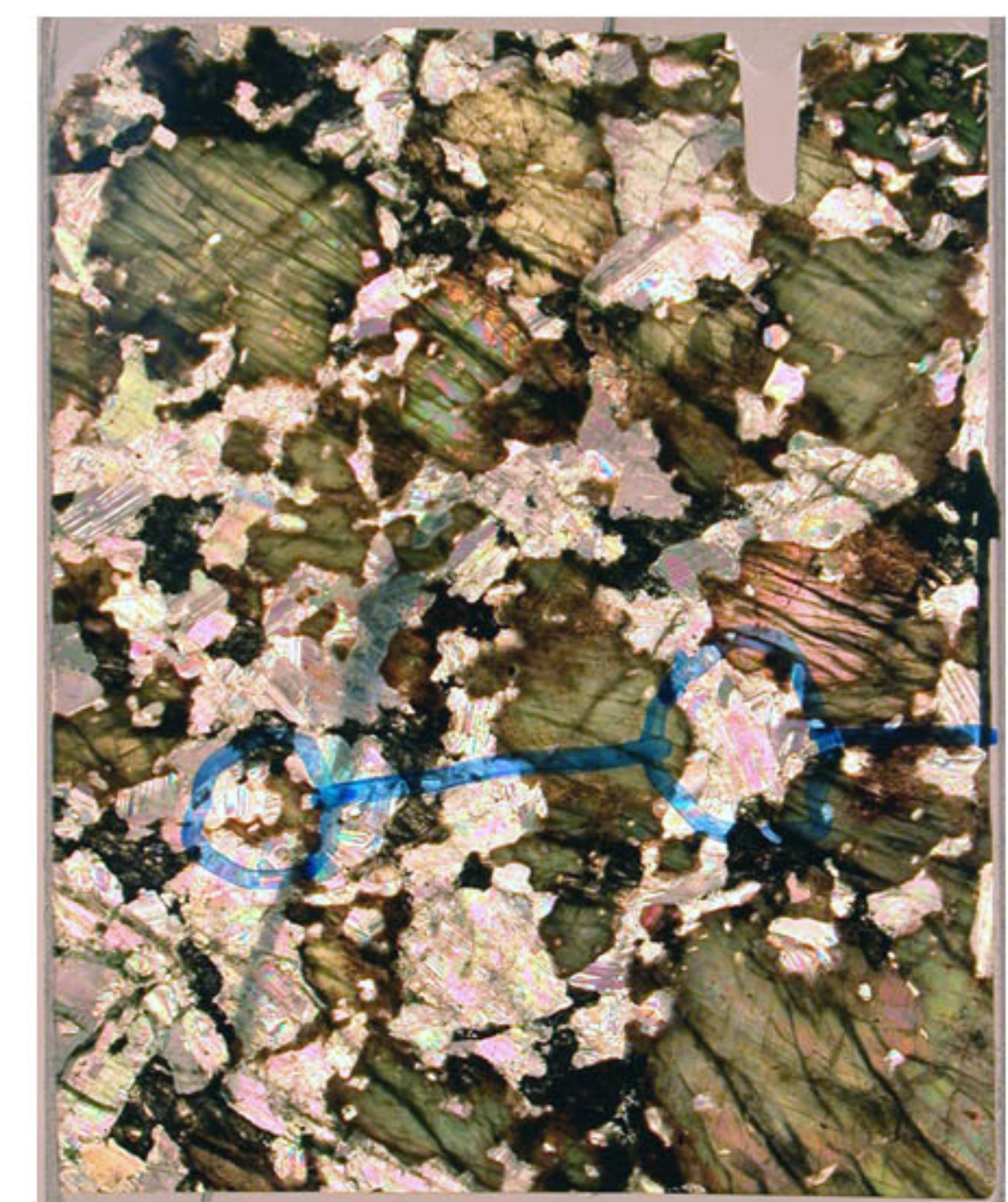
112R3_22-25_LN.JPG



112R3_22-25_LP.JPG



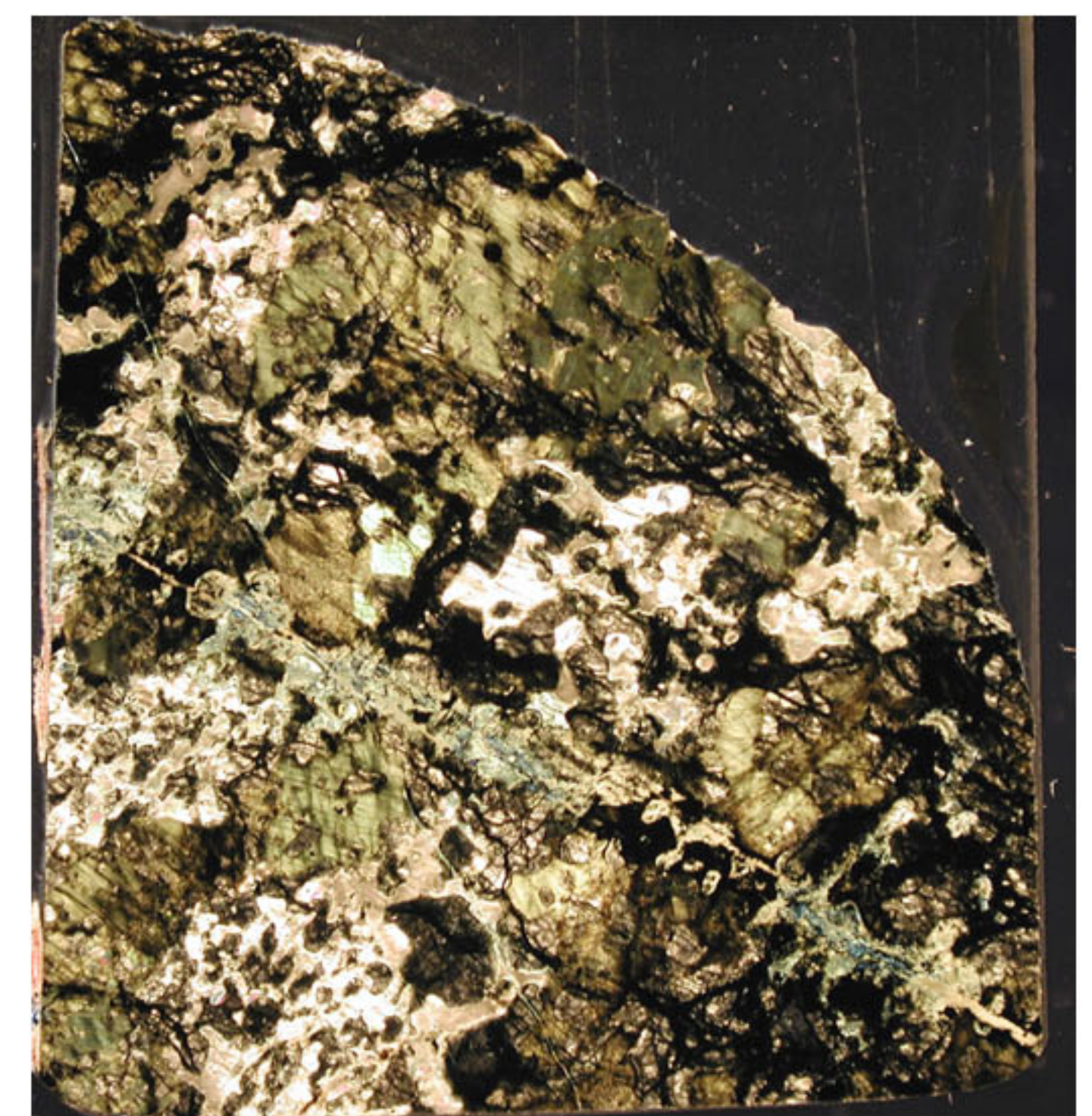
135R2_82-85_LN.JPG



135R2_82-85_LP.JPG



136R1_35-39_LN.JPG



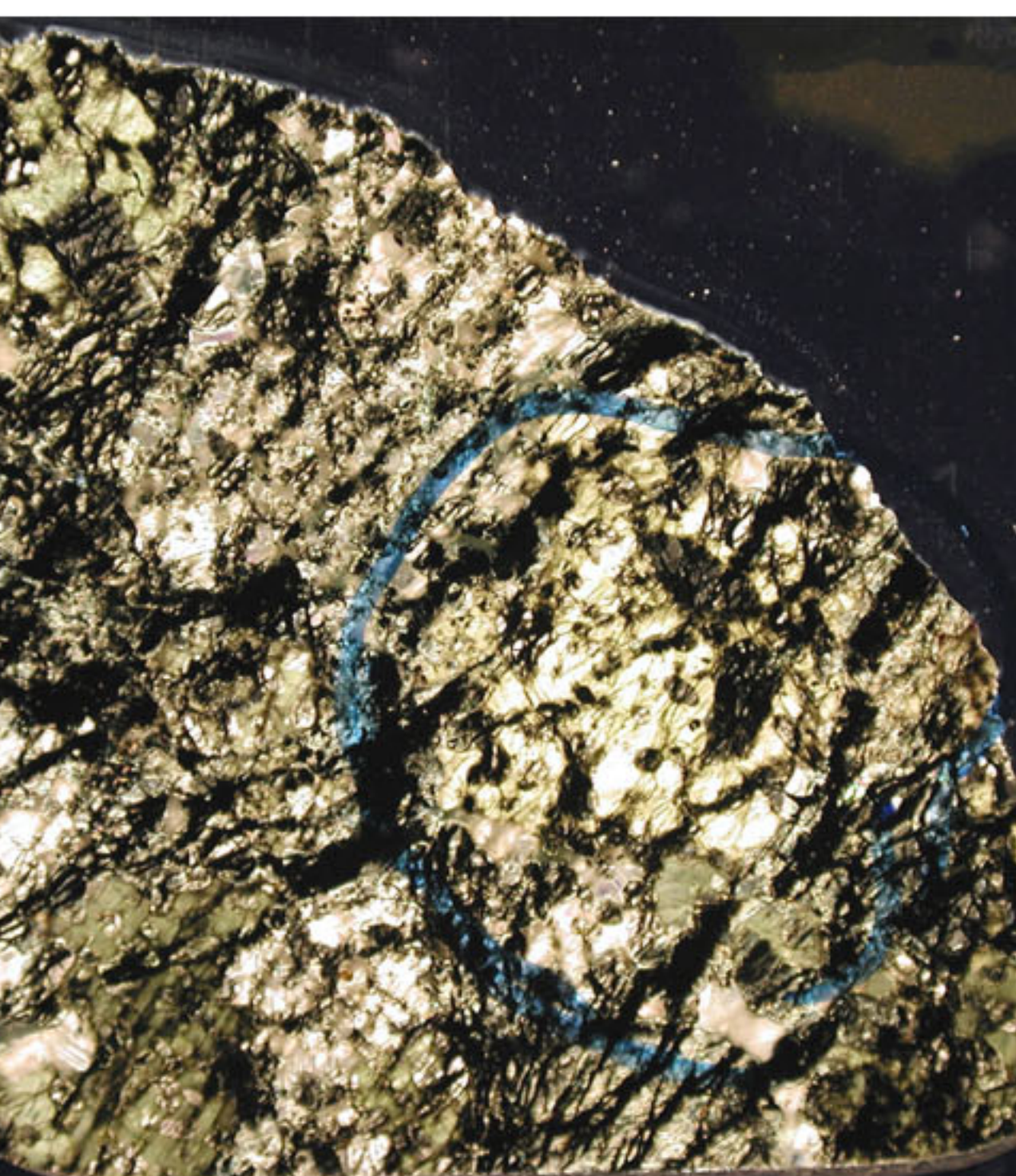
136R1_35-39_LP.JPG



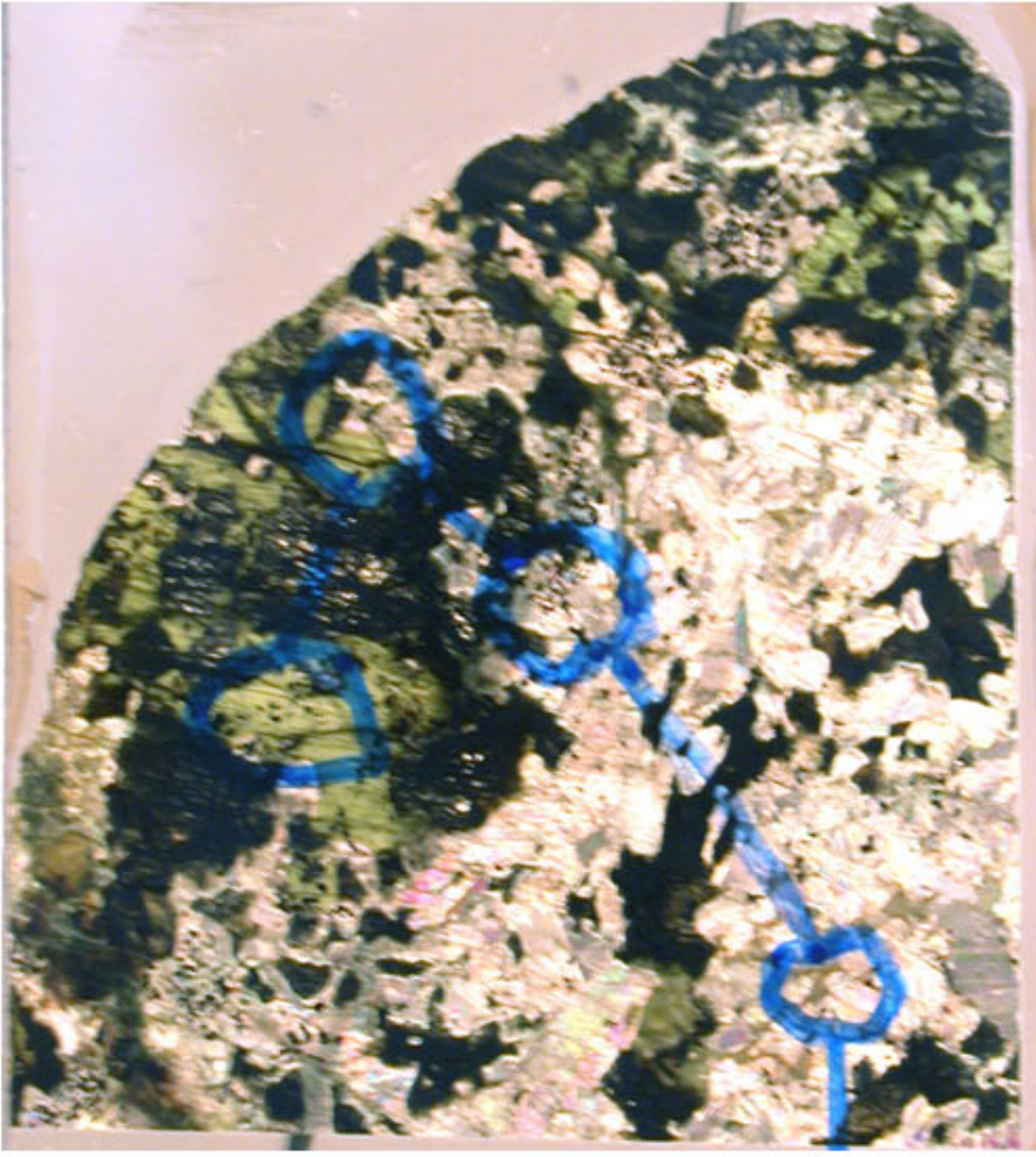
136R1_94-98_LN.JPG



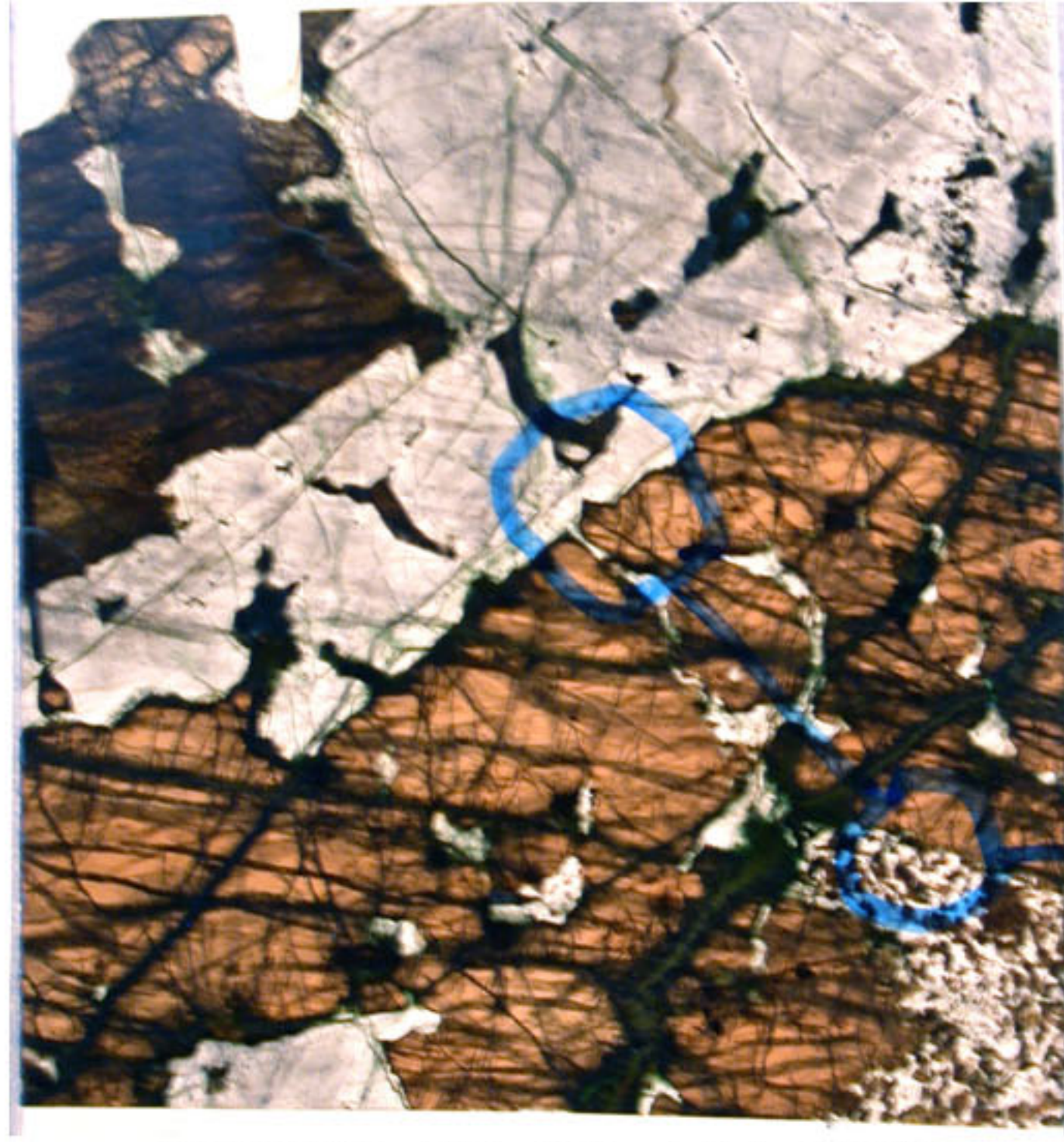
136R2_37-40_LN.JPG



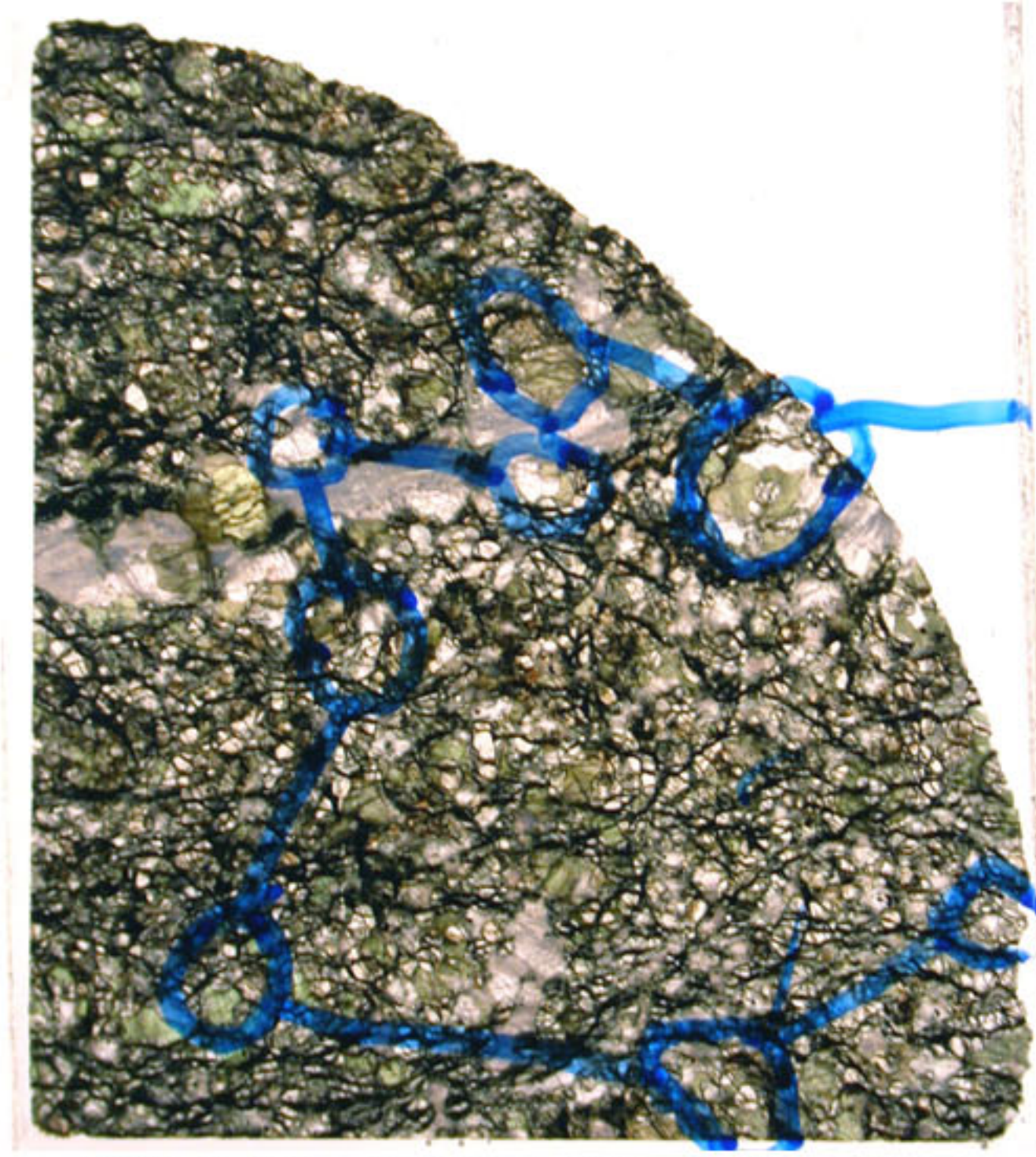
136R2_37-40_LP.JPG



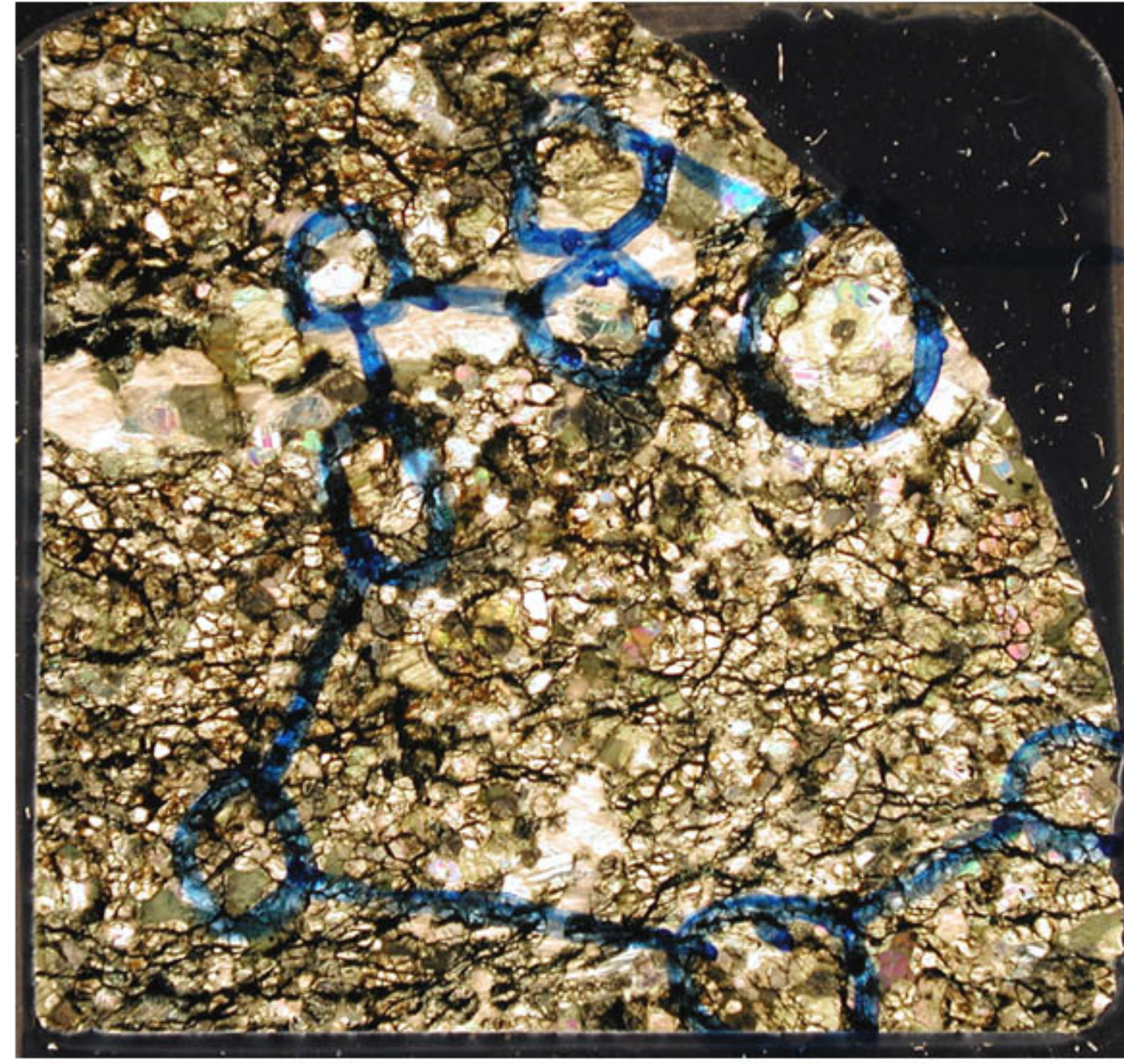
136R2_60-64_LN.JPG



136R3_21-26_LN.JPG



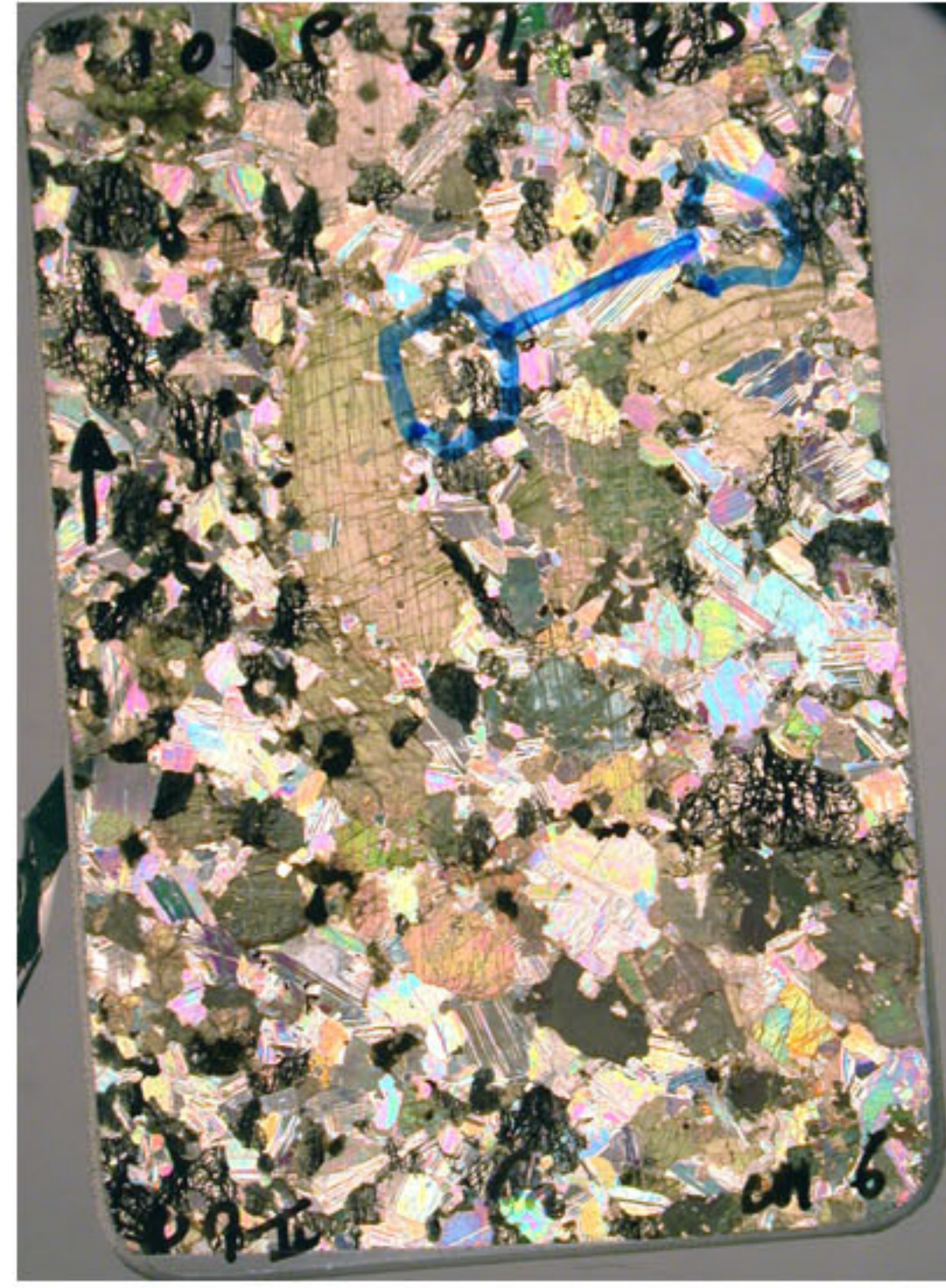
227R2_106-109_LN.JPG



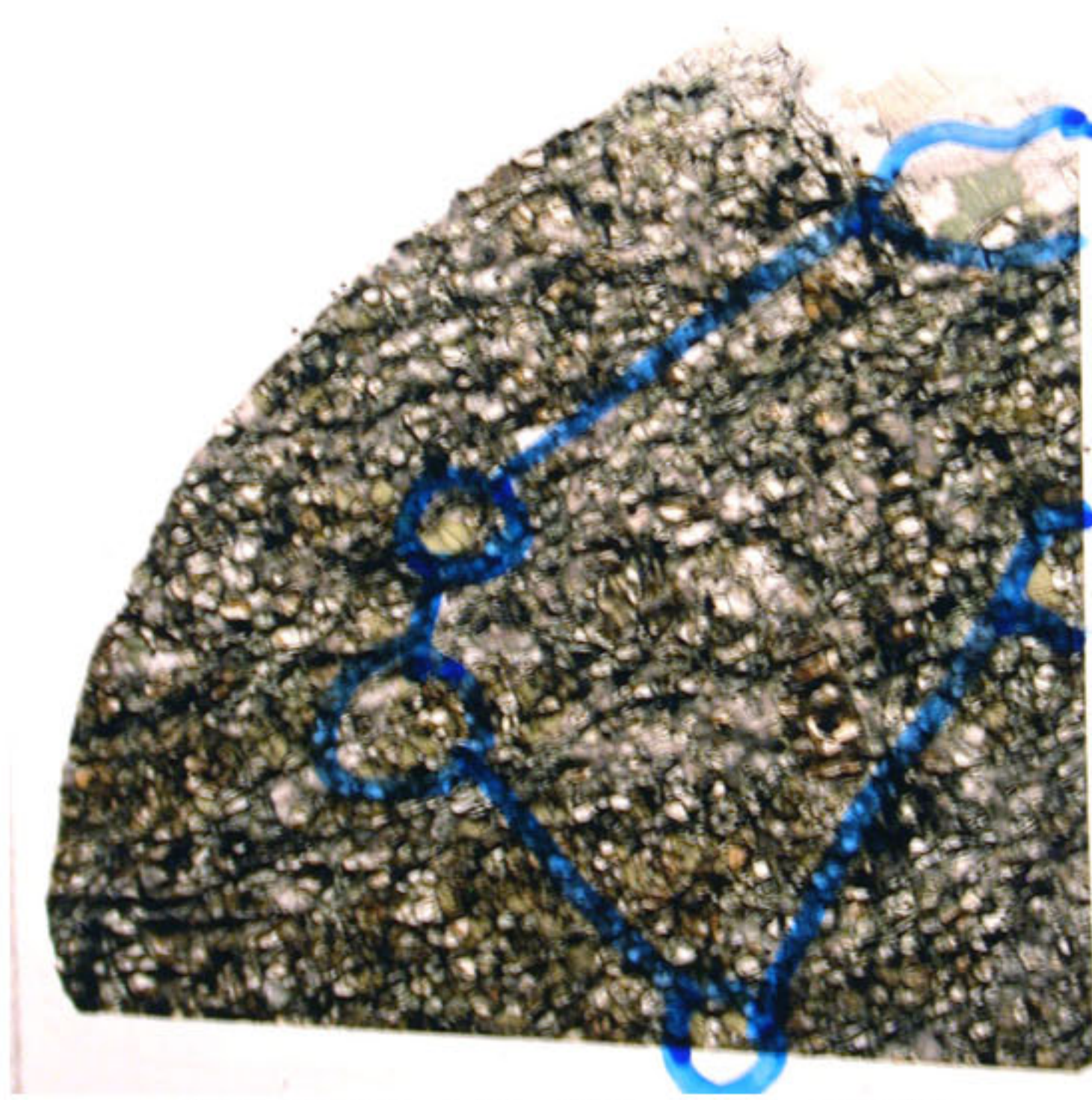
227R2_106-109_LP.JPG



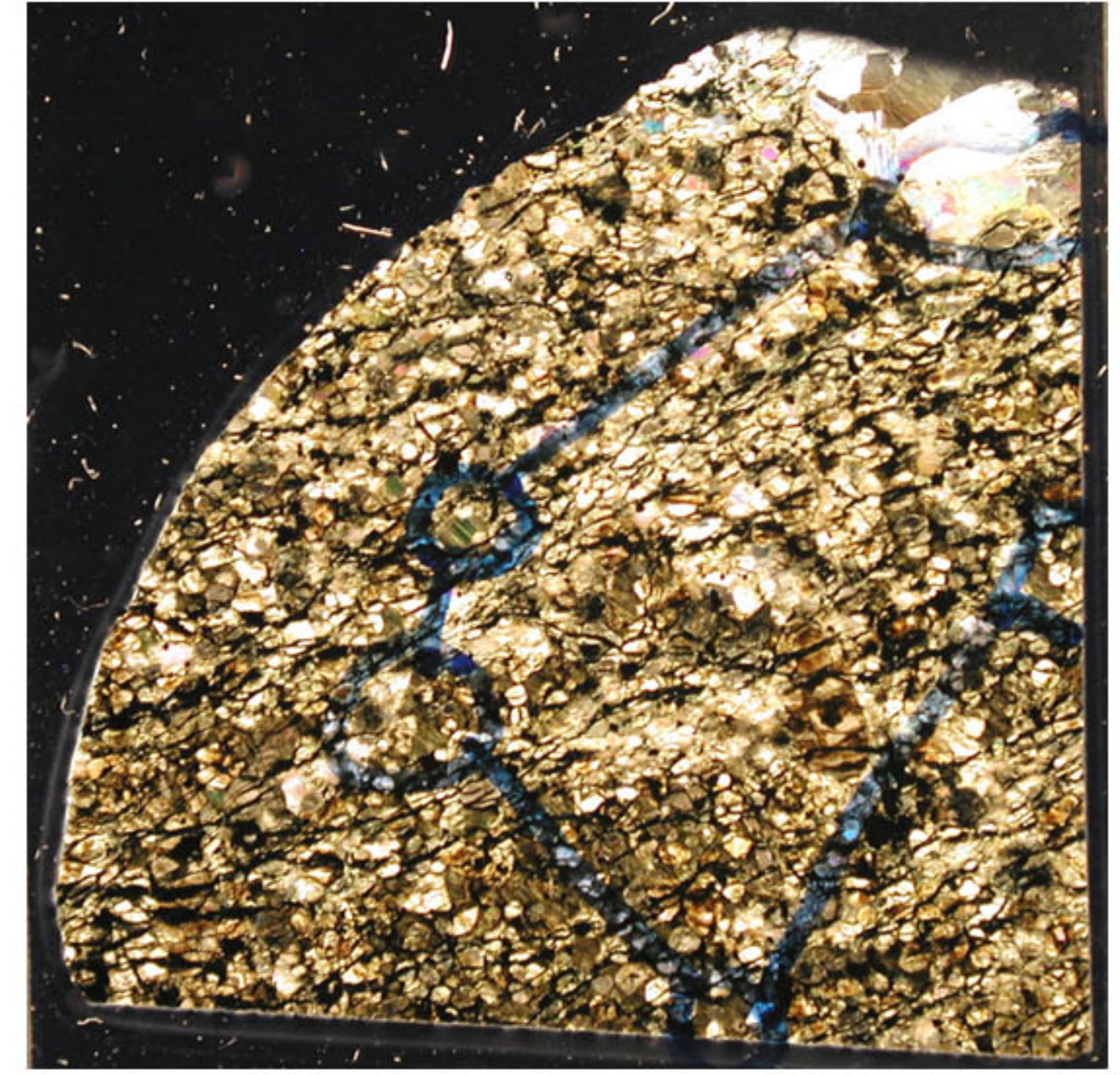
227R2_26-30_LN.JPG



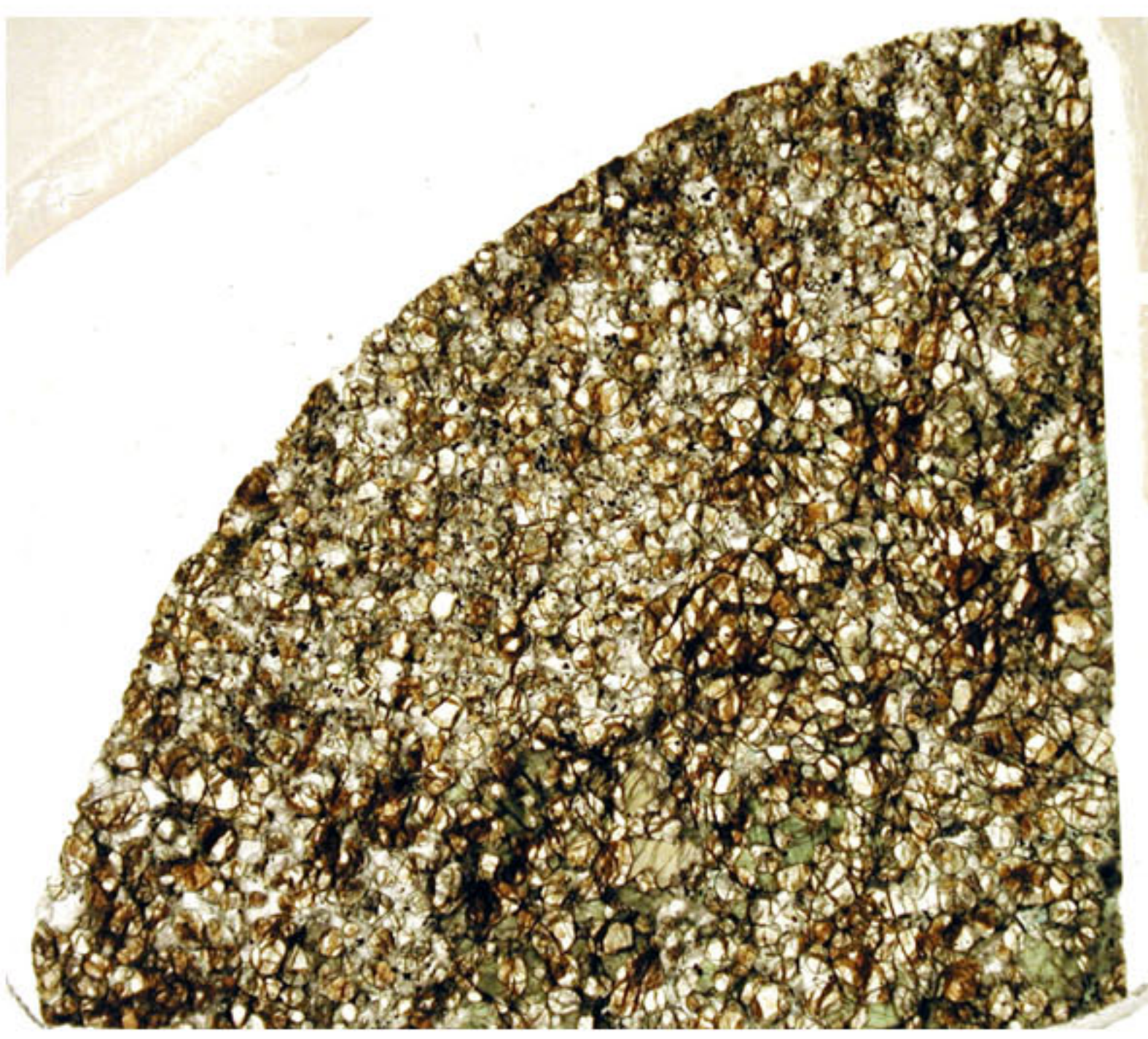
227R2_26-30_LP.JPG



227R2_71-74_LN.JPG



227R2_71-74_LP.JPG



227R3_121-124_LN.JPG



227R3_121-124_LP.JPG



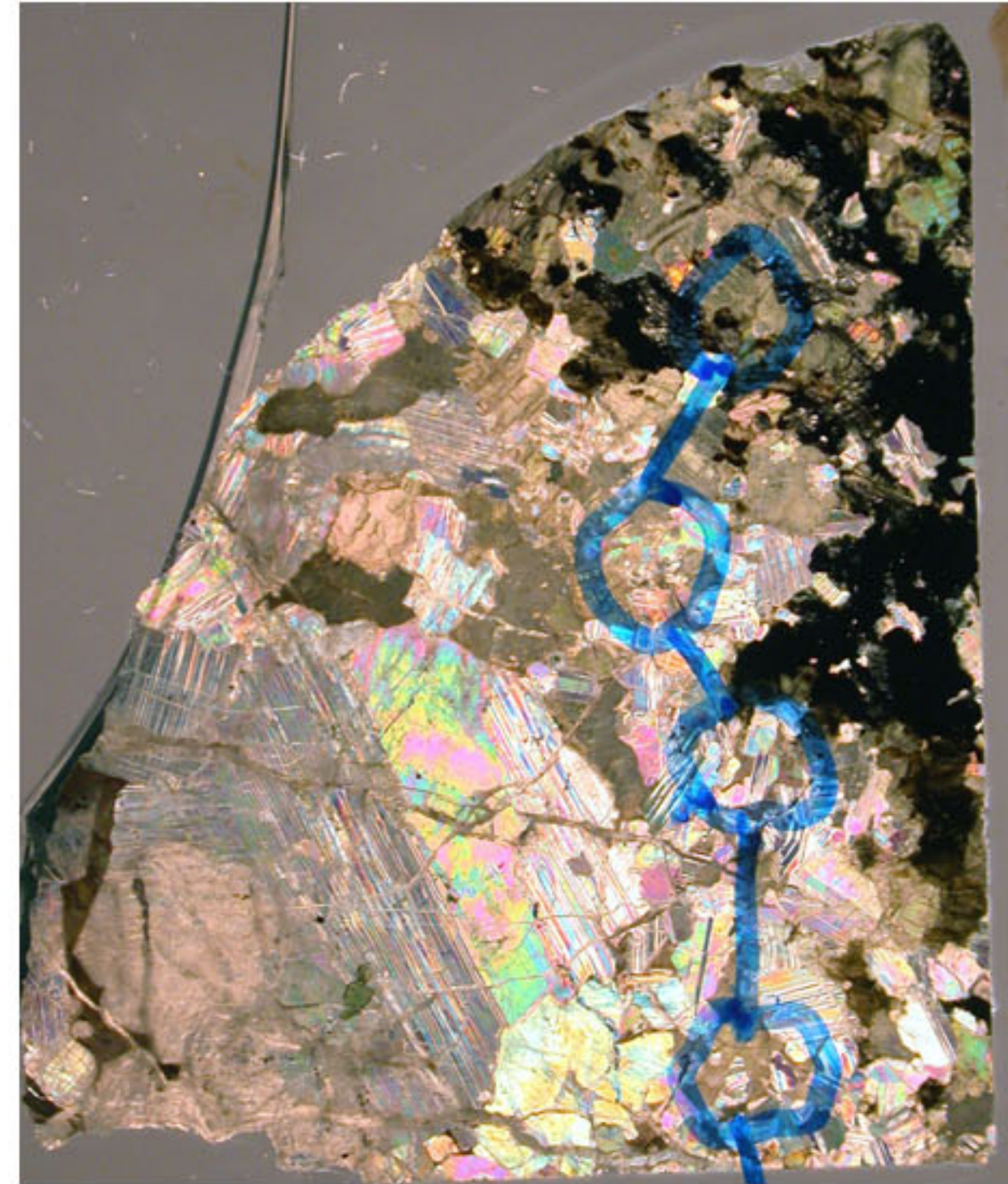
228R1_33-37_LN.JPG



228R1_33-37_LP.JPG



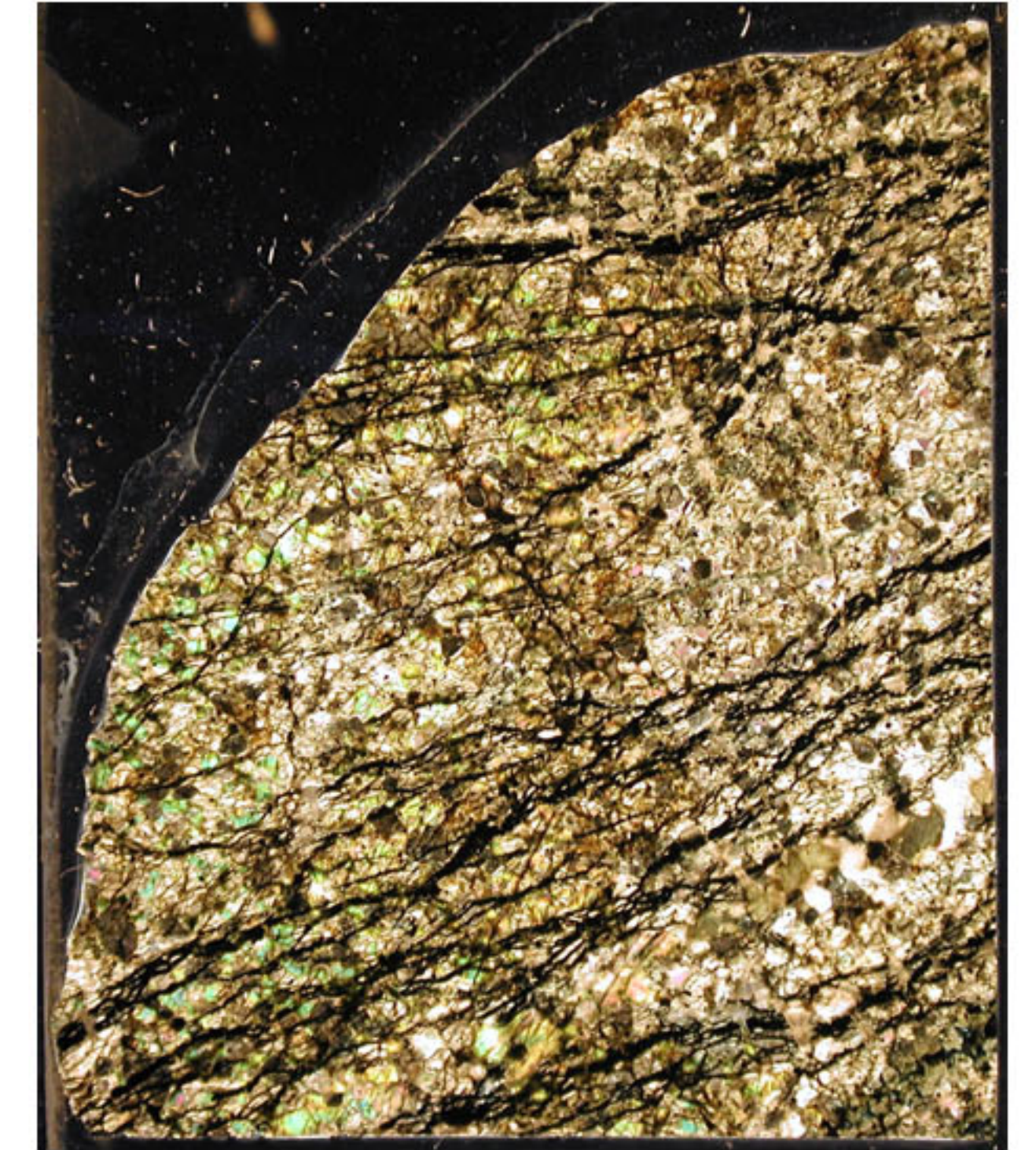
228R1_66-70_LN.JPG



228R1_66-70_LP.JPG



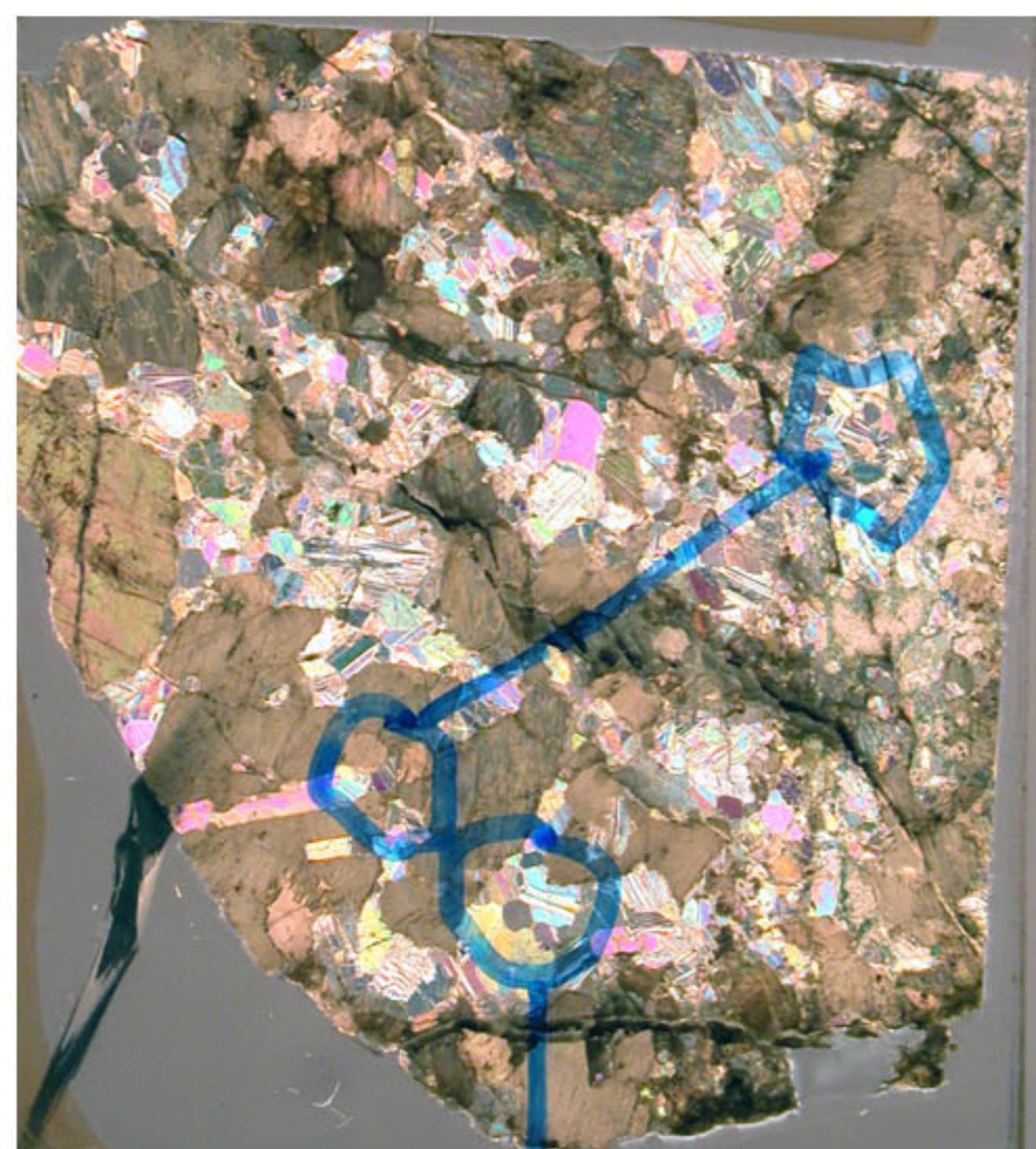
228R1_79-82_LN.JPG



228R1_79-82_LP.JPG



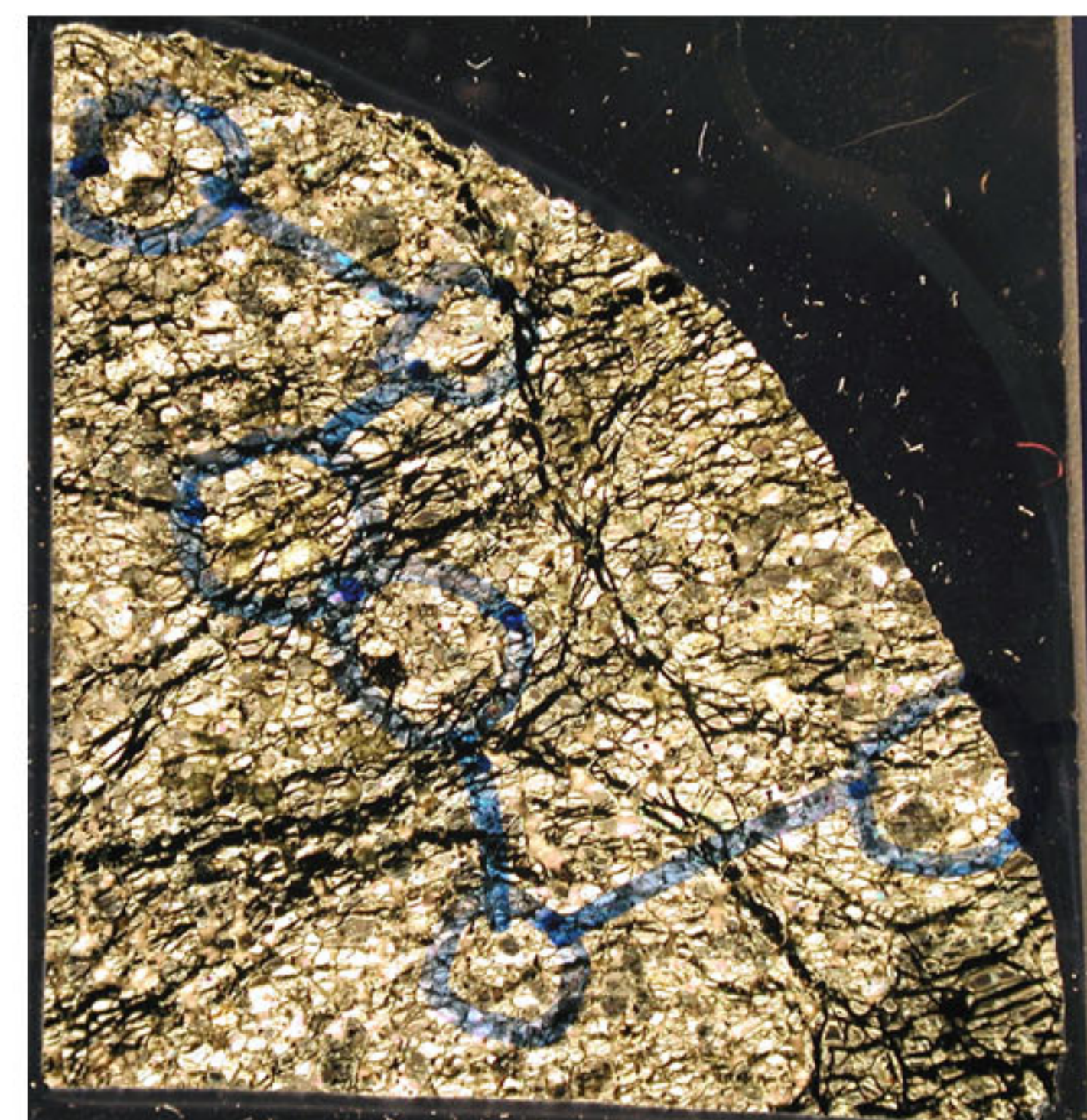
228R1_95-98_LN.JPG



228R1_95-98_LP.JPG



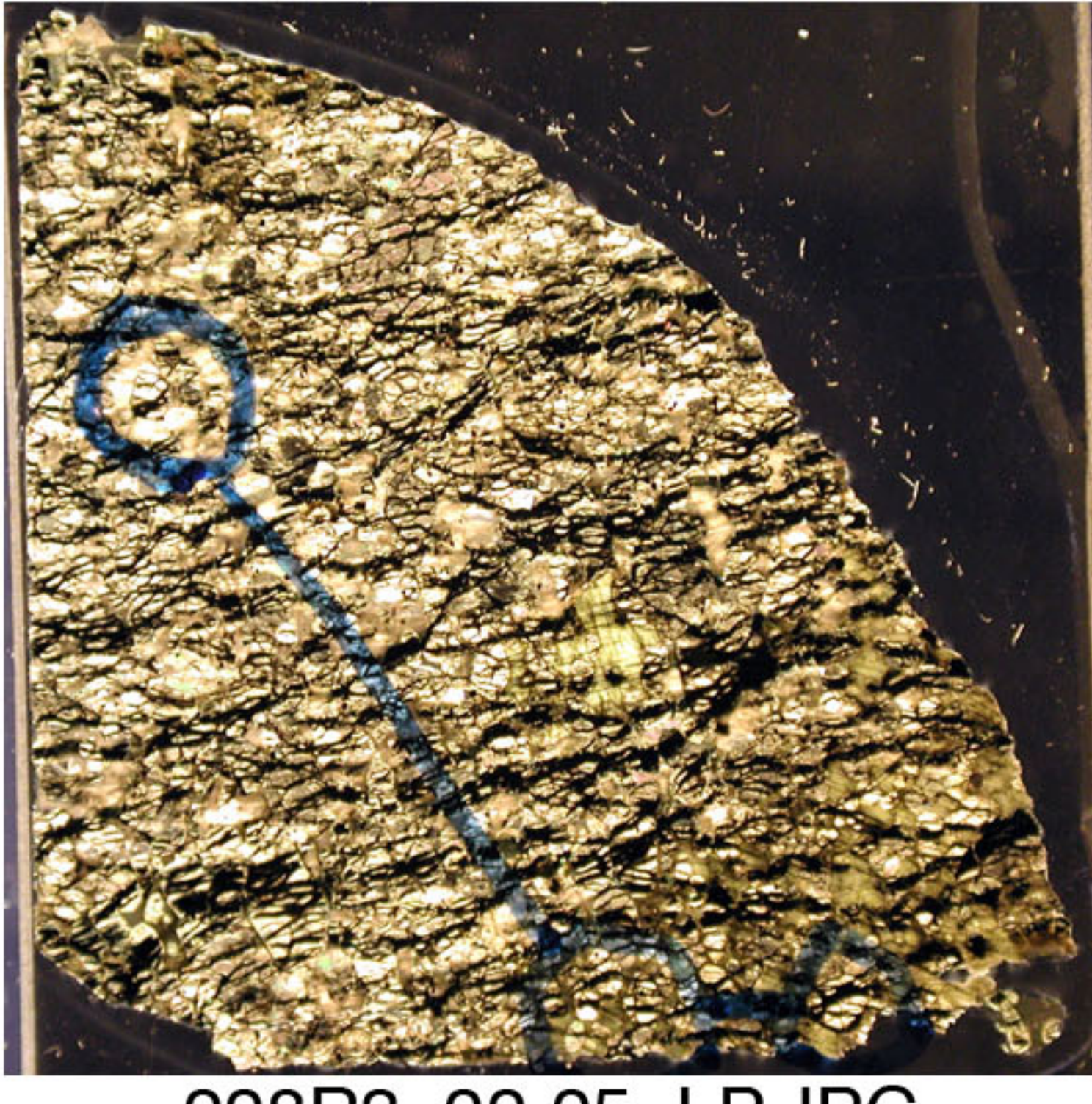
228R2_42-45_LN.JPG



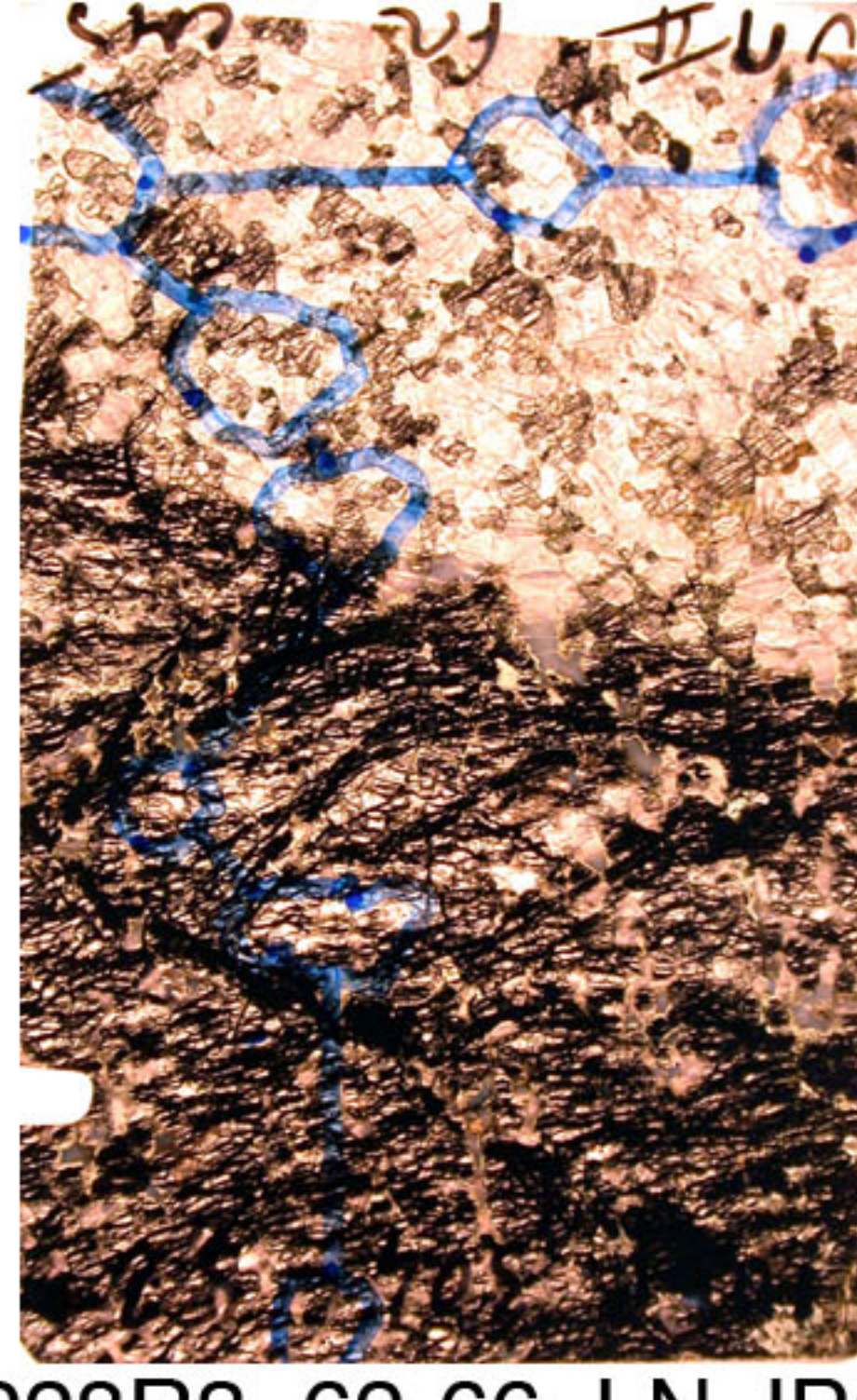
228R2_42-45_LP.JPG



228R3_22-25_LN.JPG



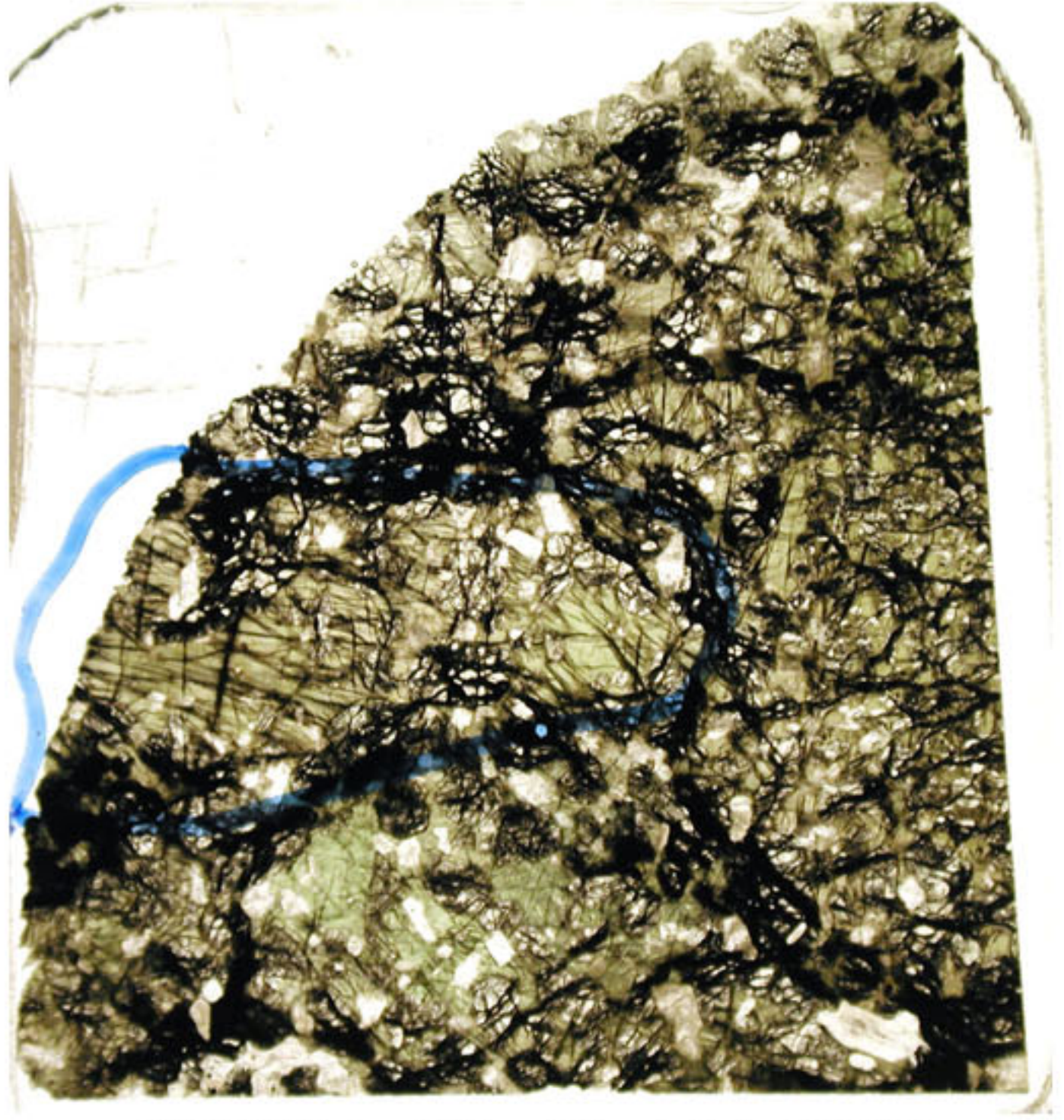
228R3_22-25_LP.JPG



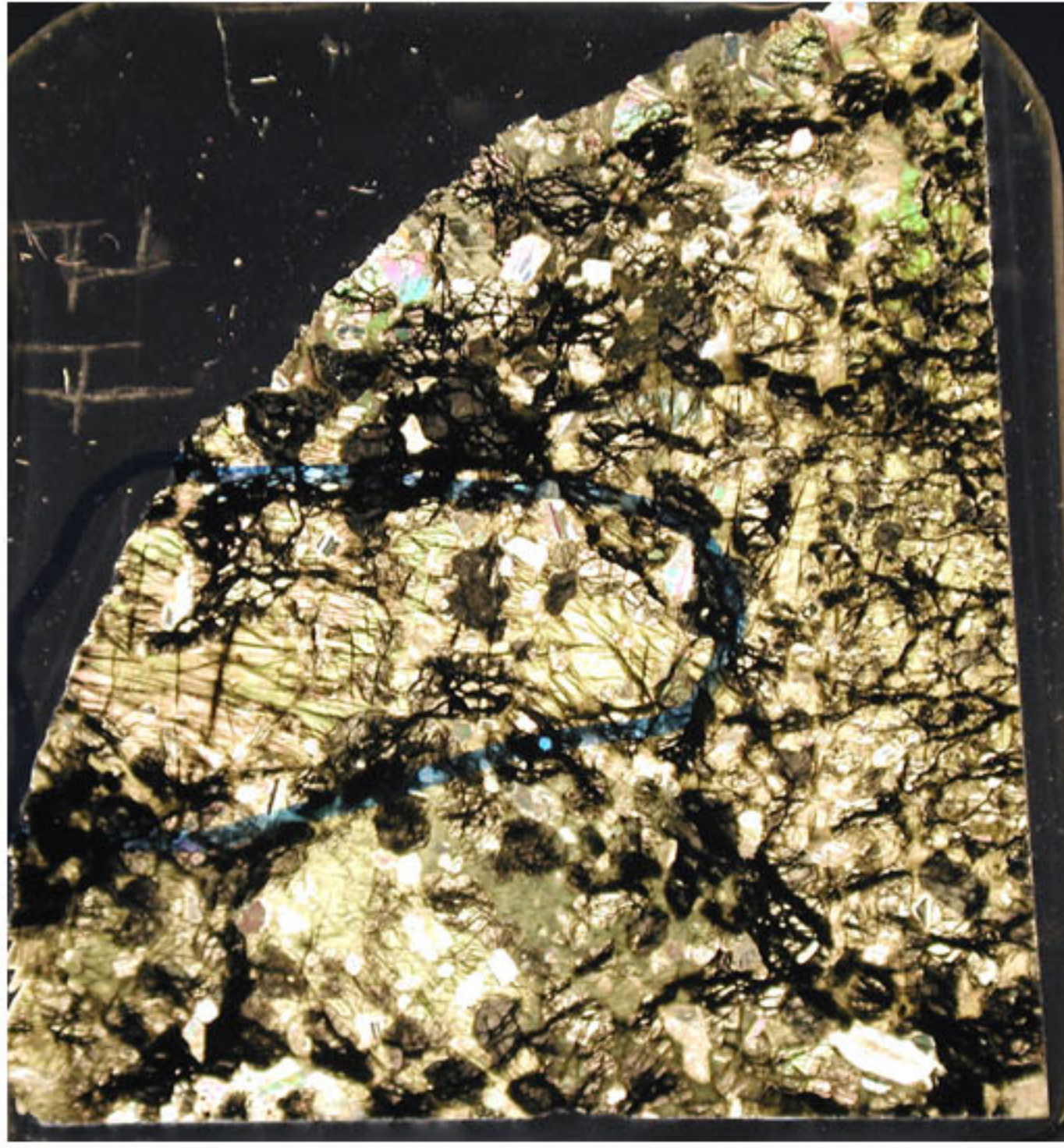
228R3_62-66_LN.JPG



228R3_62-66_LP.JPG



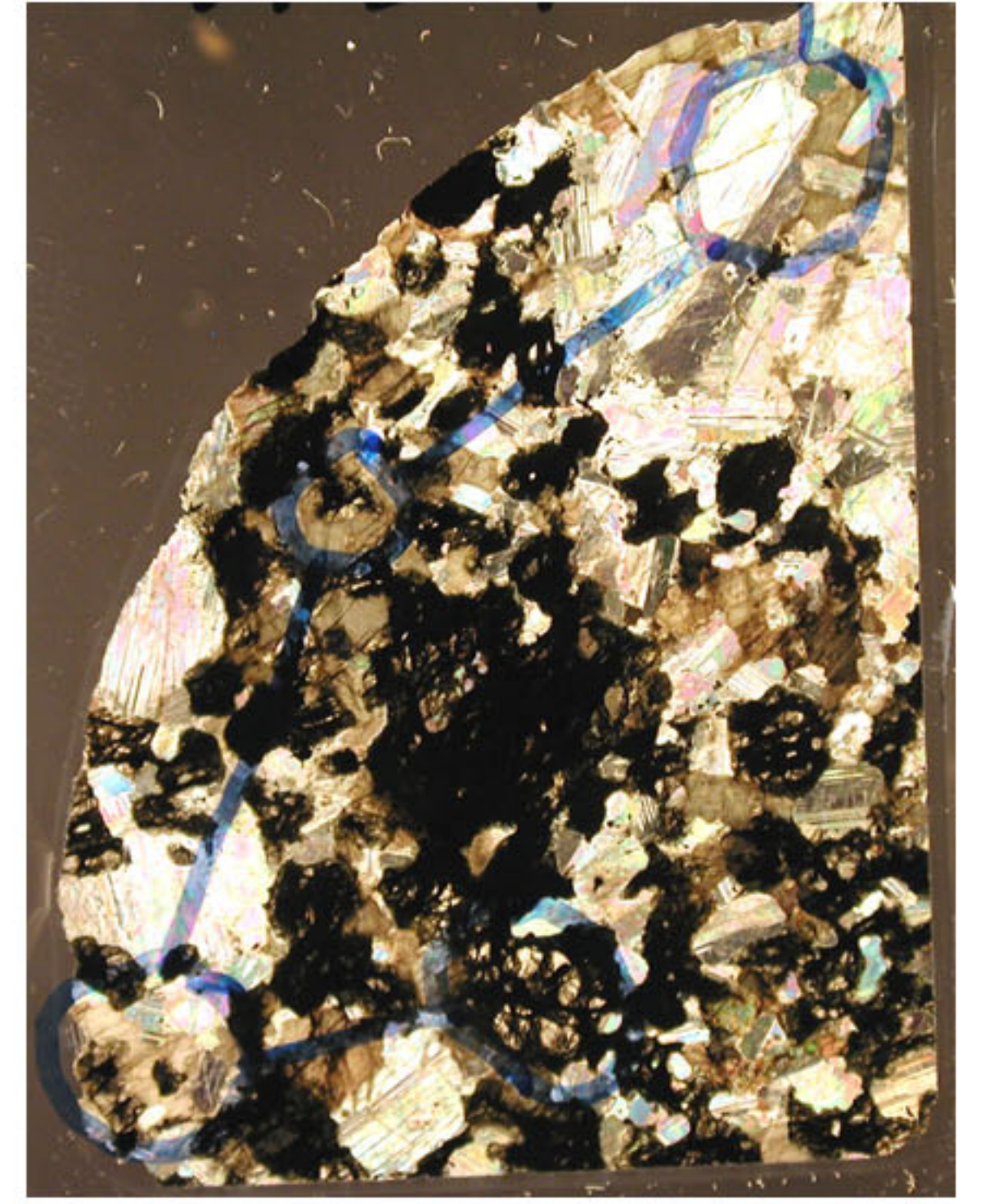
228R4_39-43_LN.JPG



228R4_39-43_LP.JPG



231R3_0-3_LN.JPG



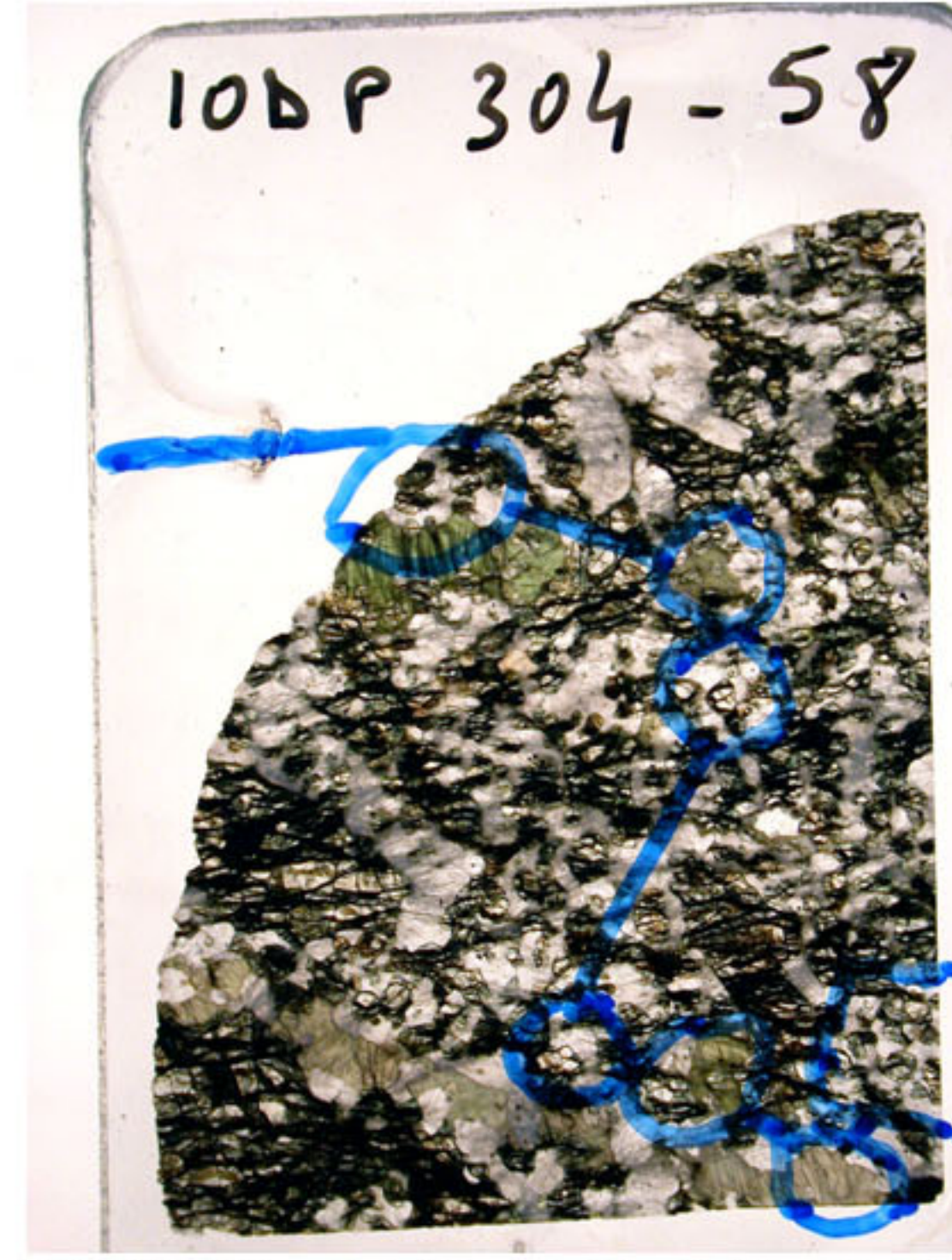
231R3_0-3_LP.JPG



231R3_50-54_LN.JPG



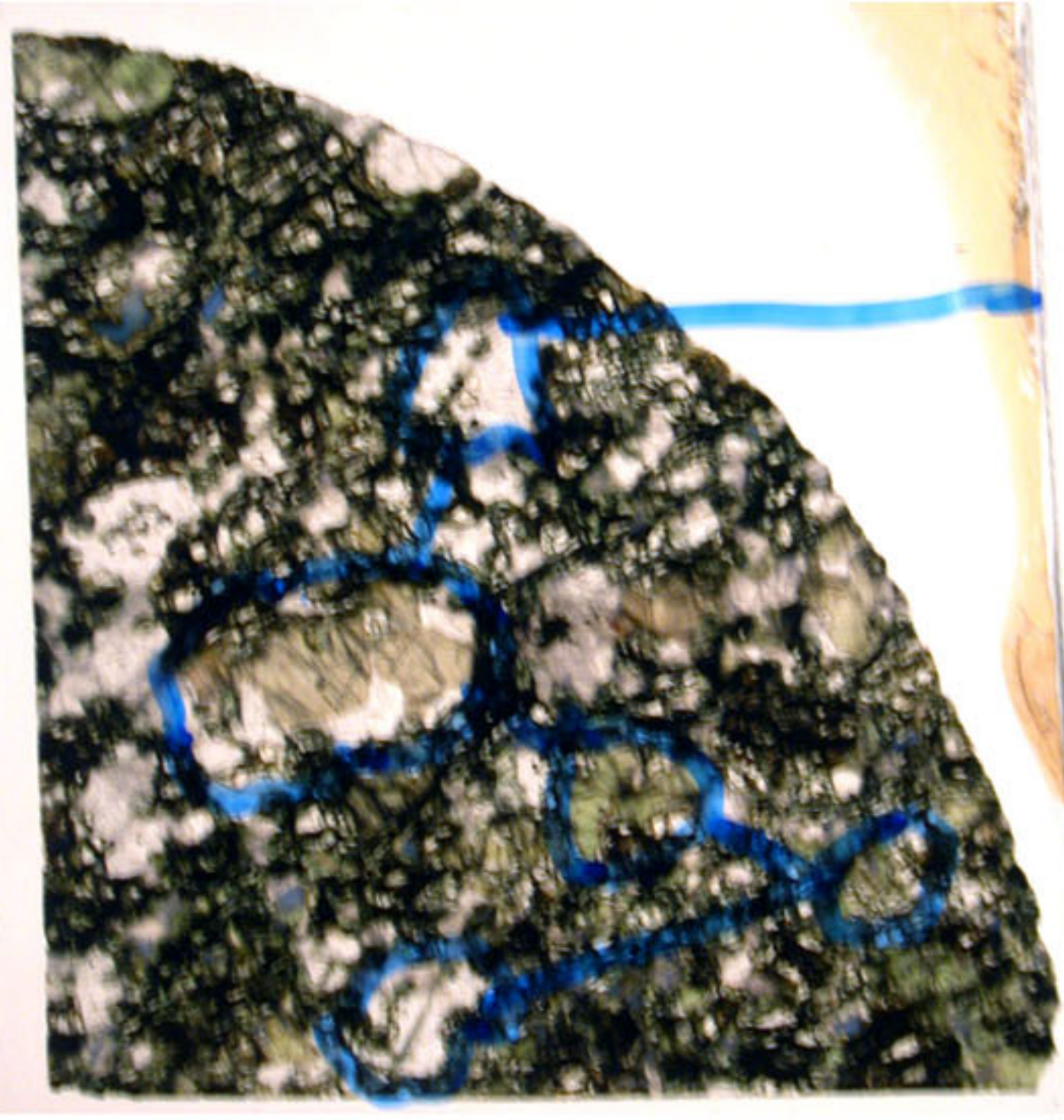
231R3_50-54_LP.JPG



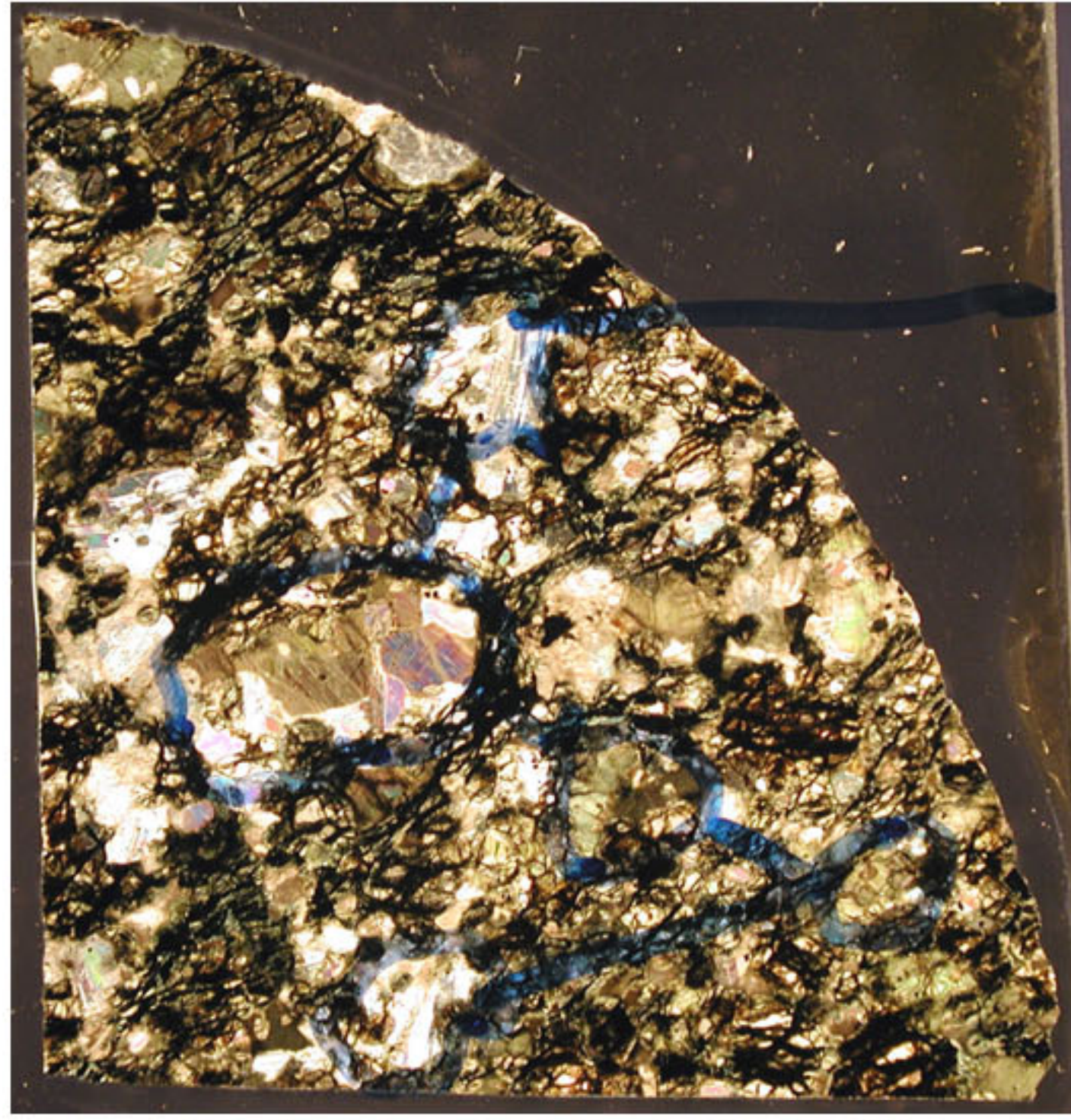
232R1_112-116_LN.JPG



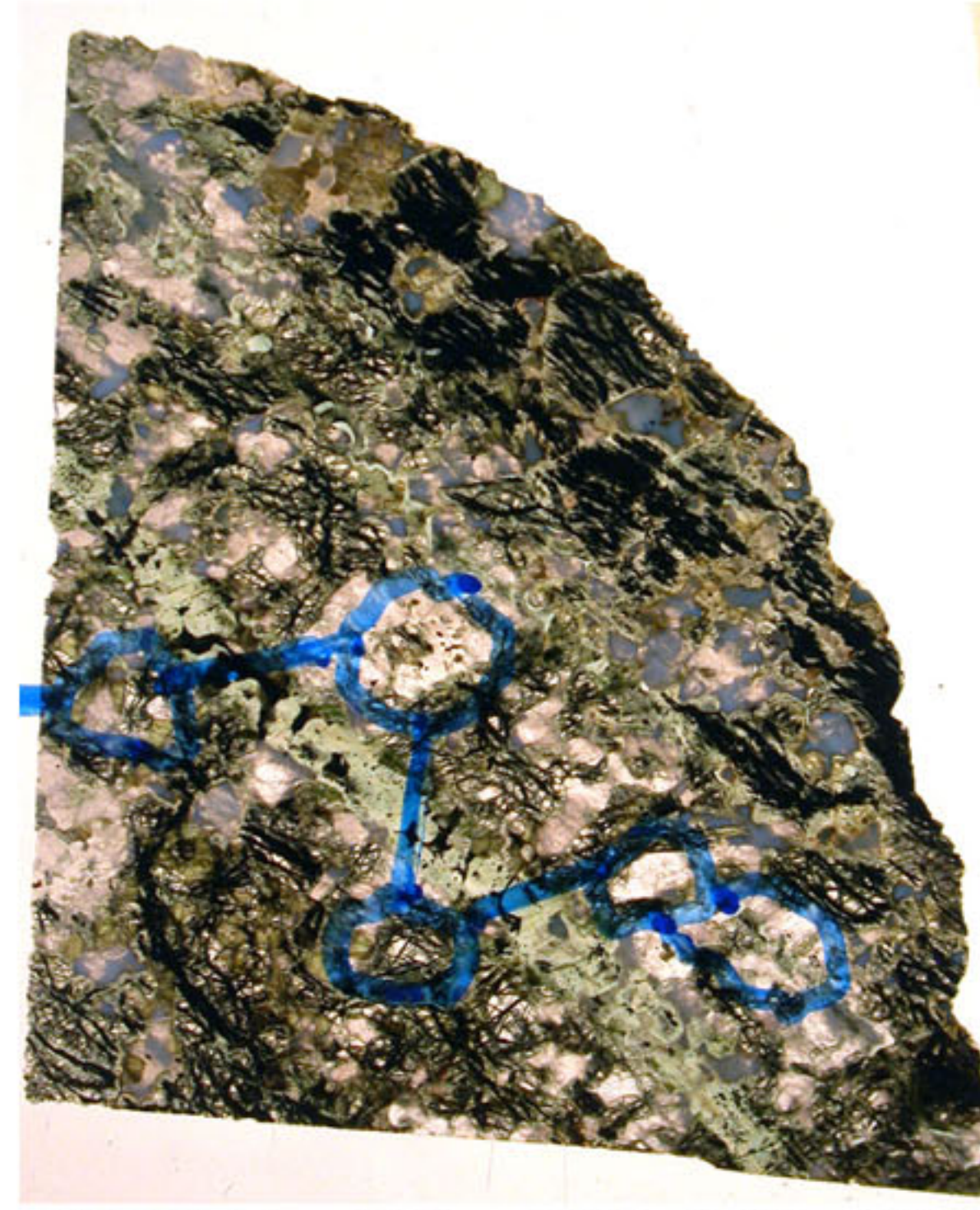
232R1_112-116_LP.JPG



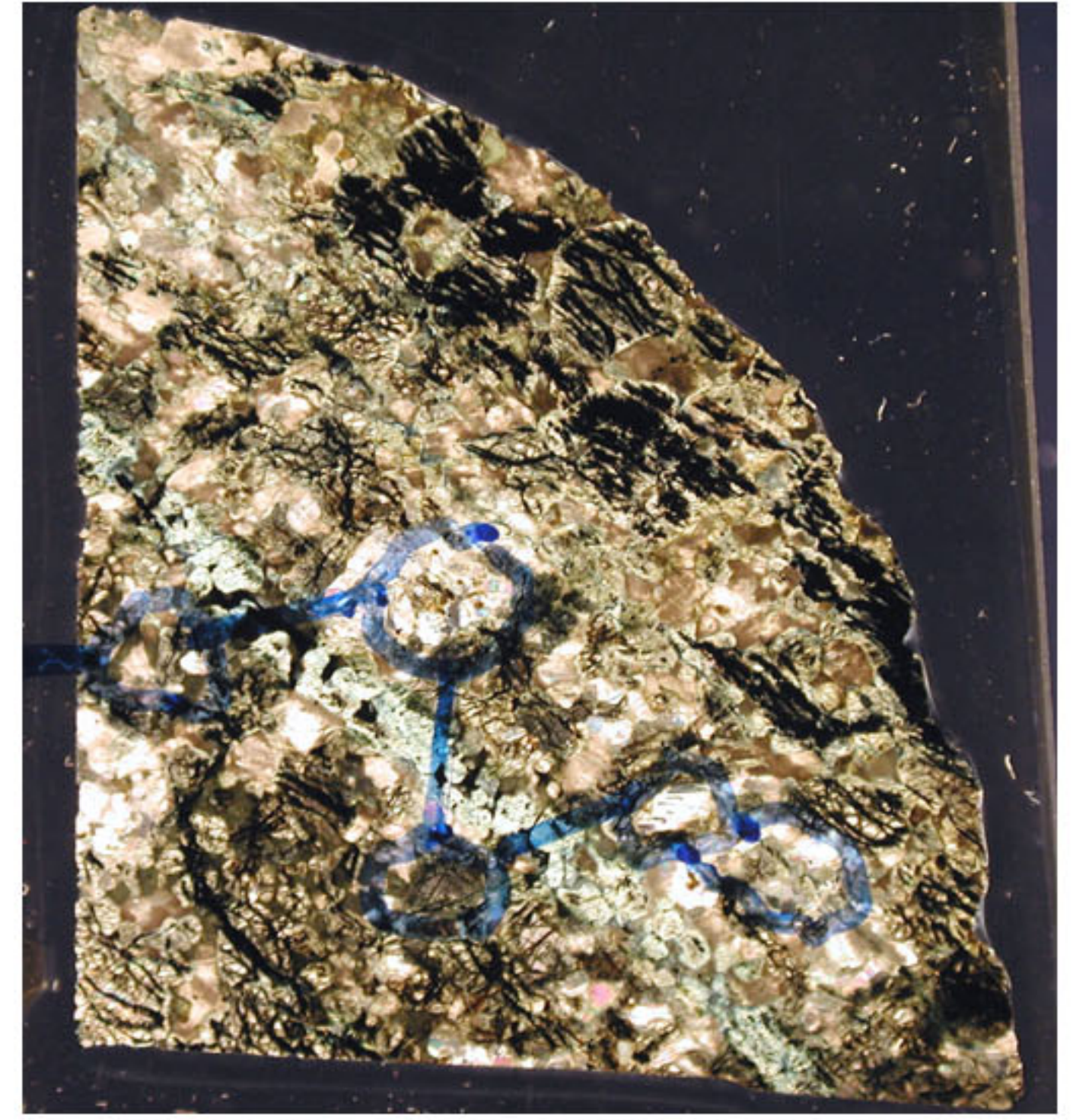
232R1_9-13_LN.JPG



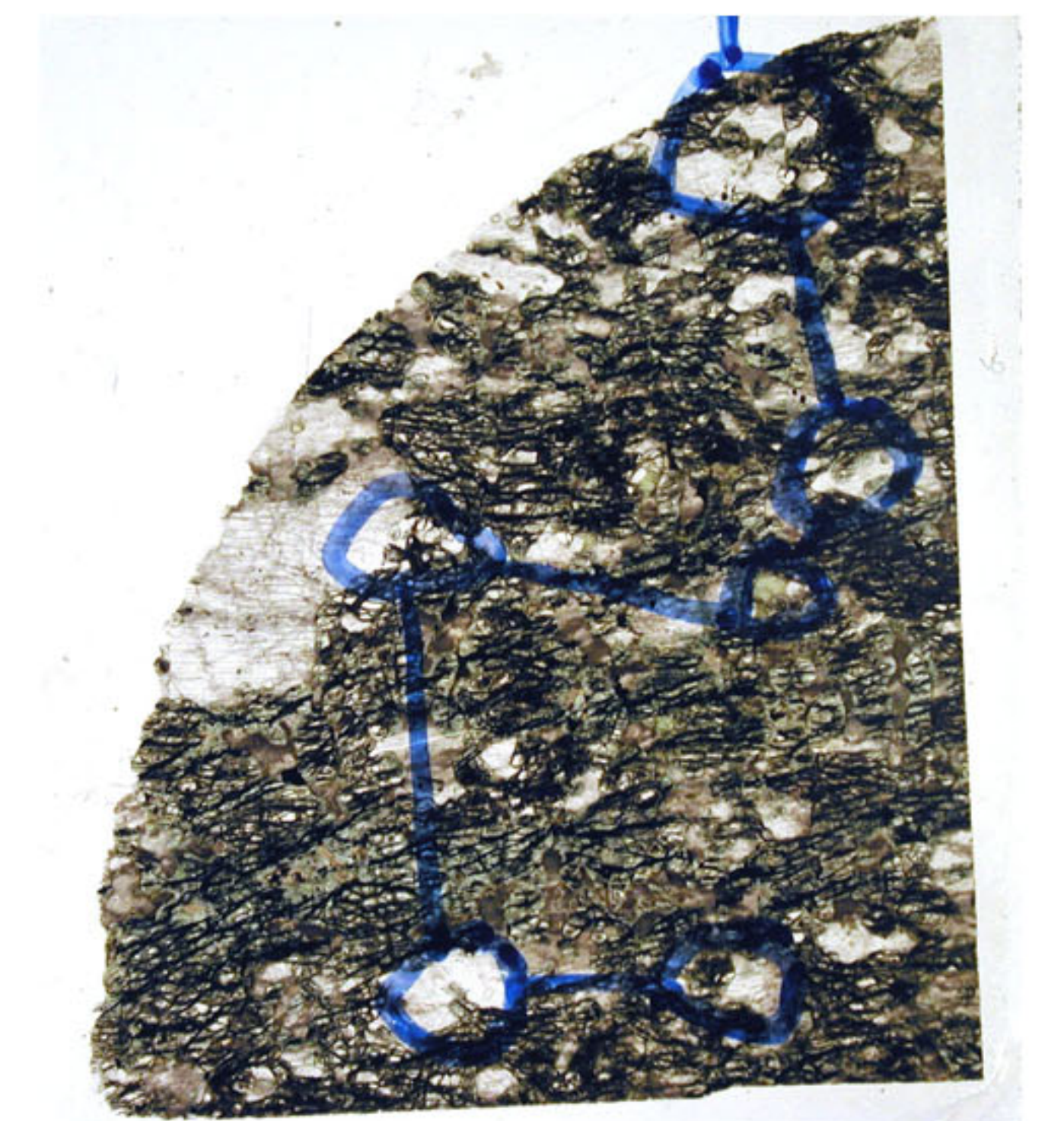
232R1_9-13_LP.JPG



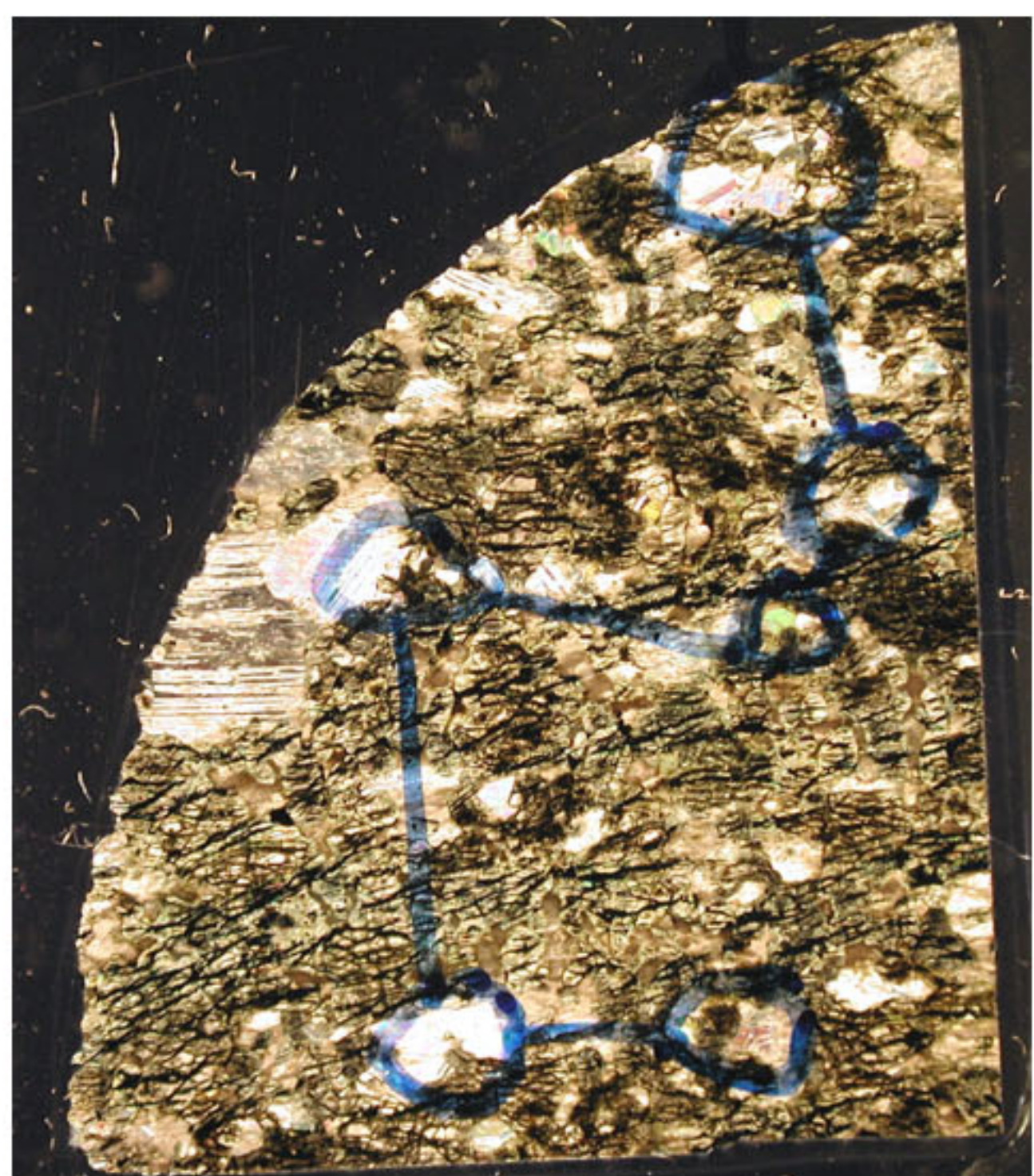
233R1_135-139_LN.JPG



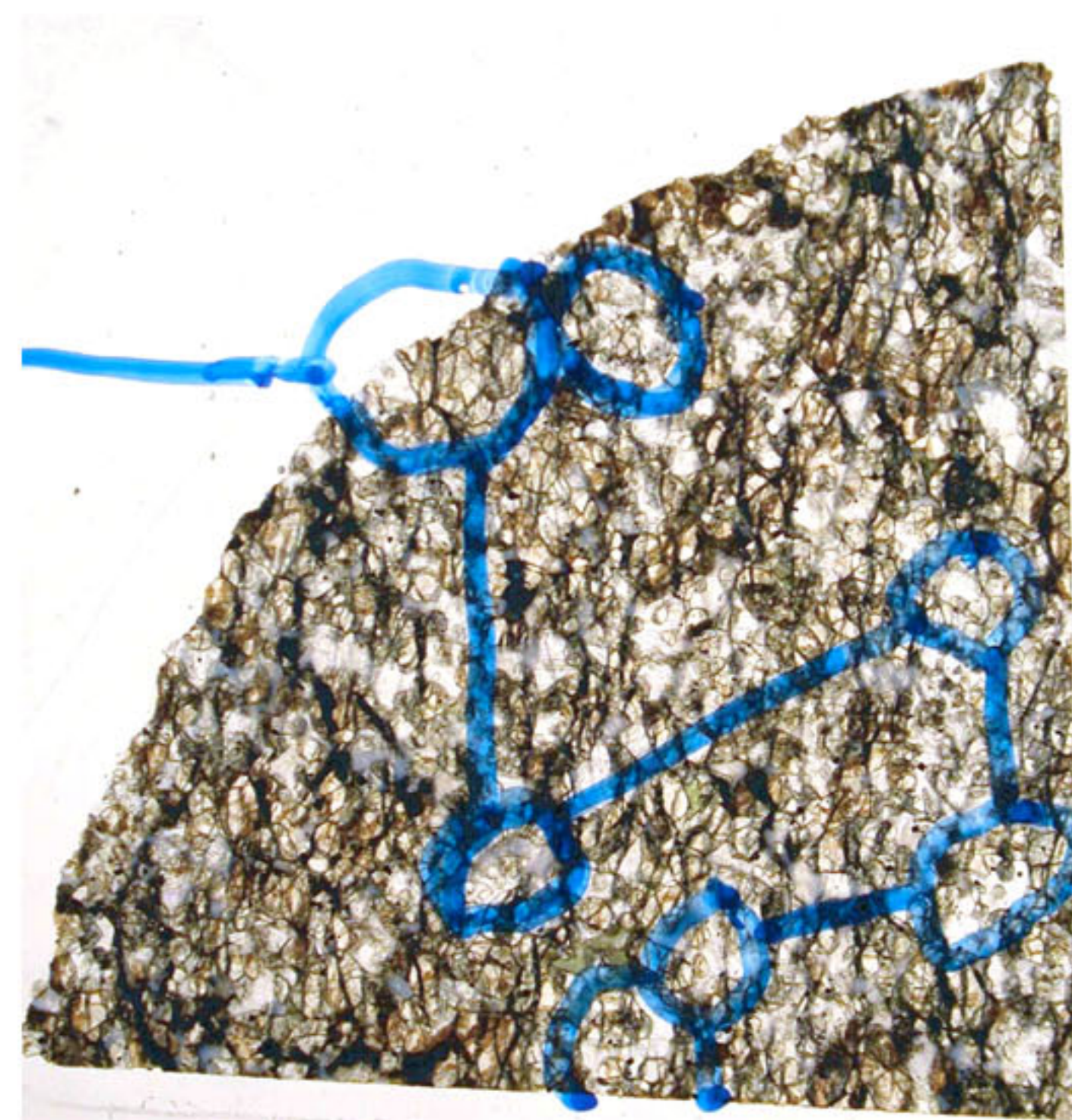
233R1_135-139_LP.JPG



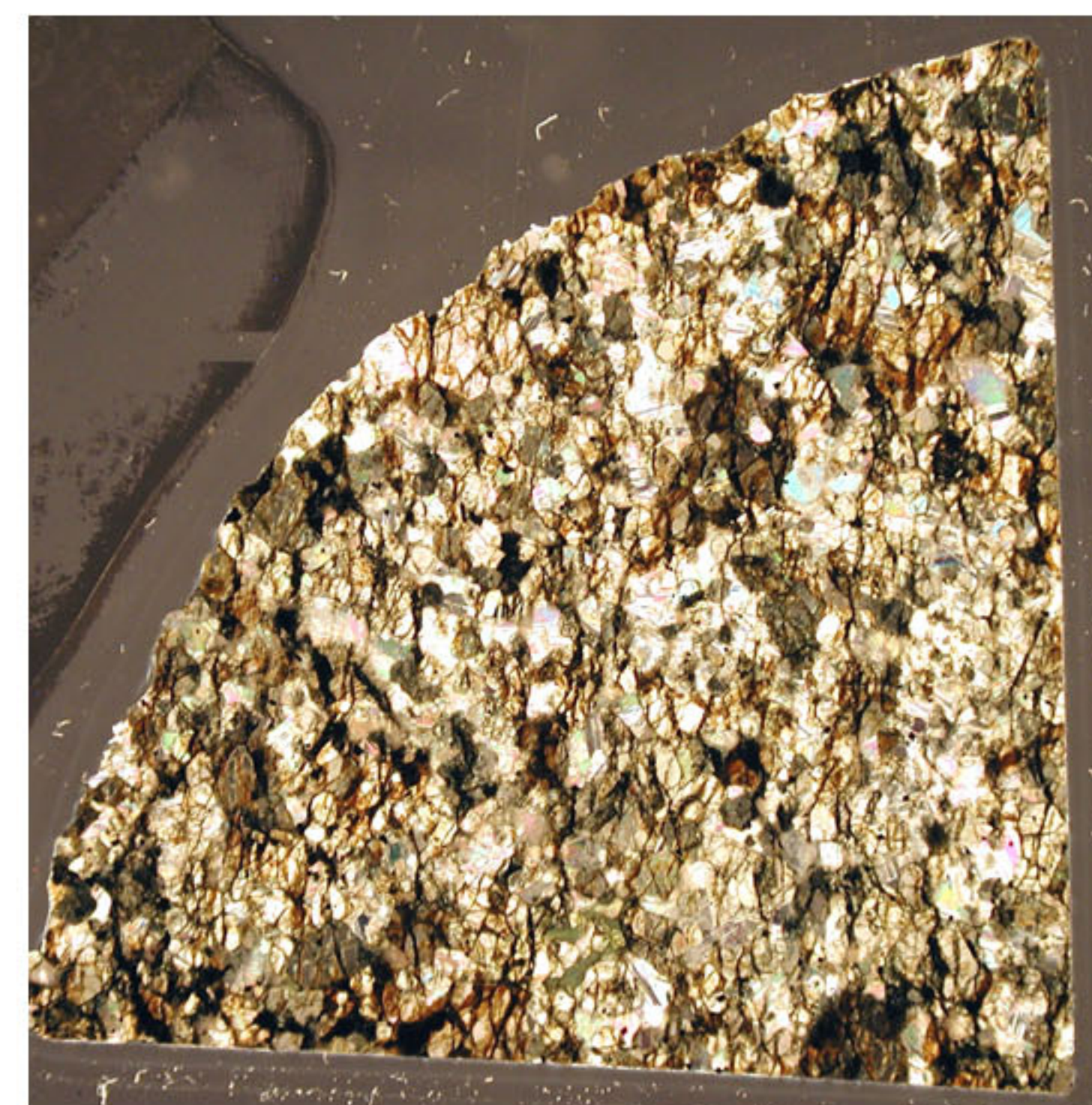
233R1_31-34_LN.JPG



233R1_31-34_LP.JPG



233R2_109-112_LN.jpg



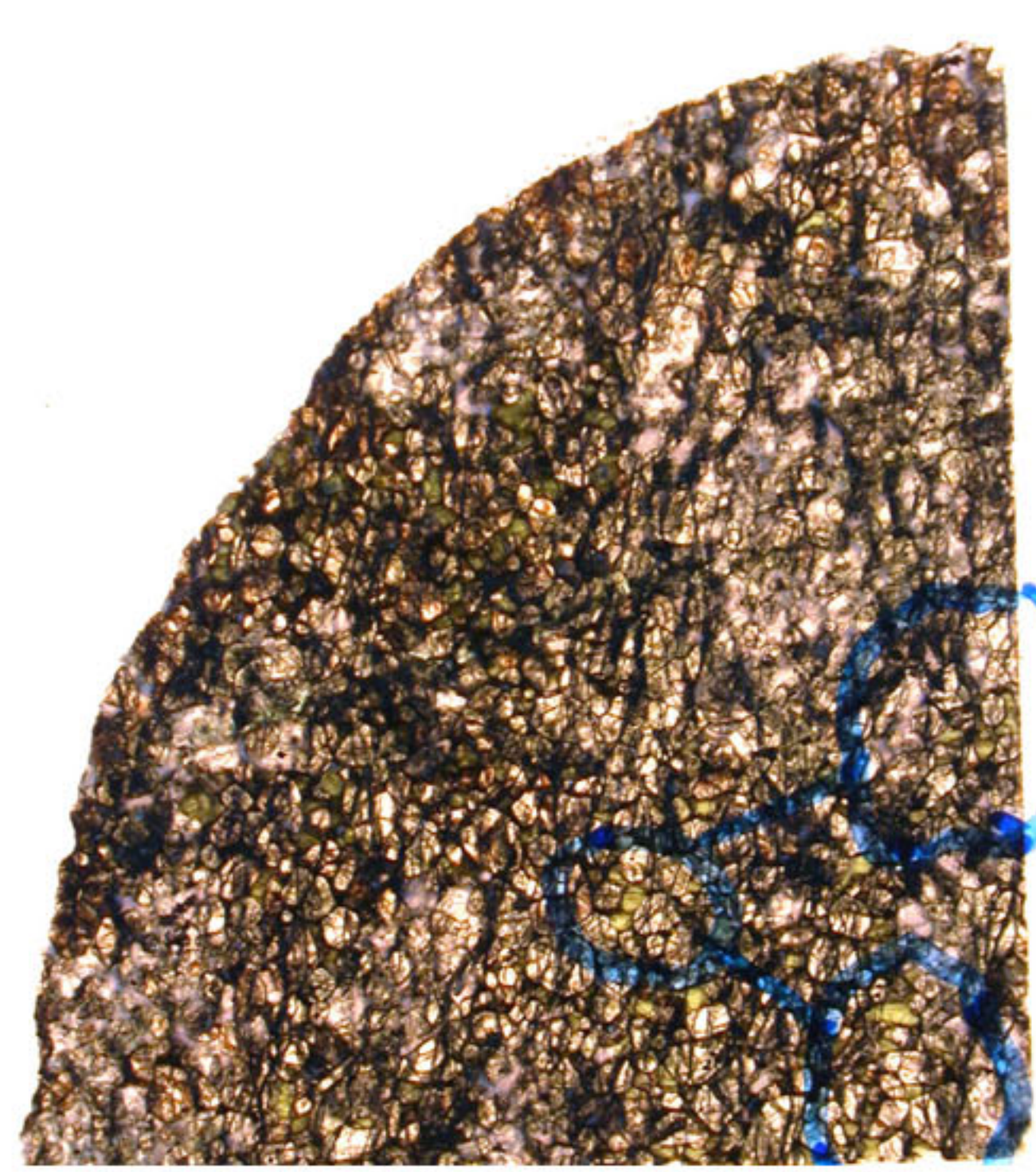
233R2_109-112_LP.JPG



234R1_22-26_LN.JPG



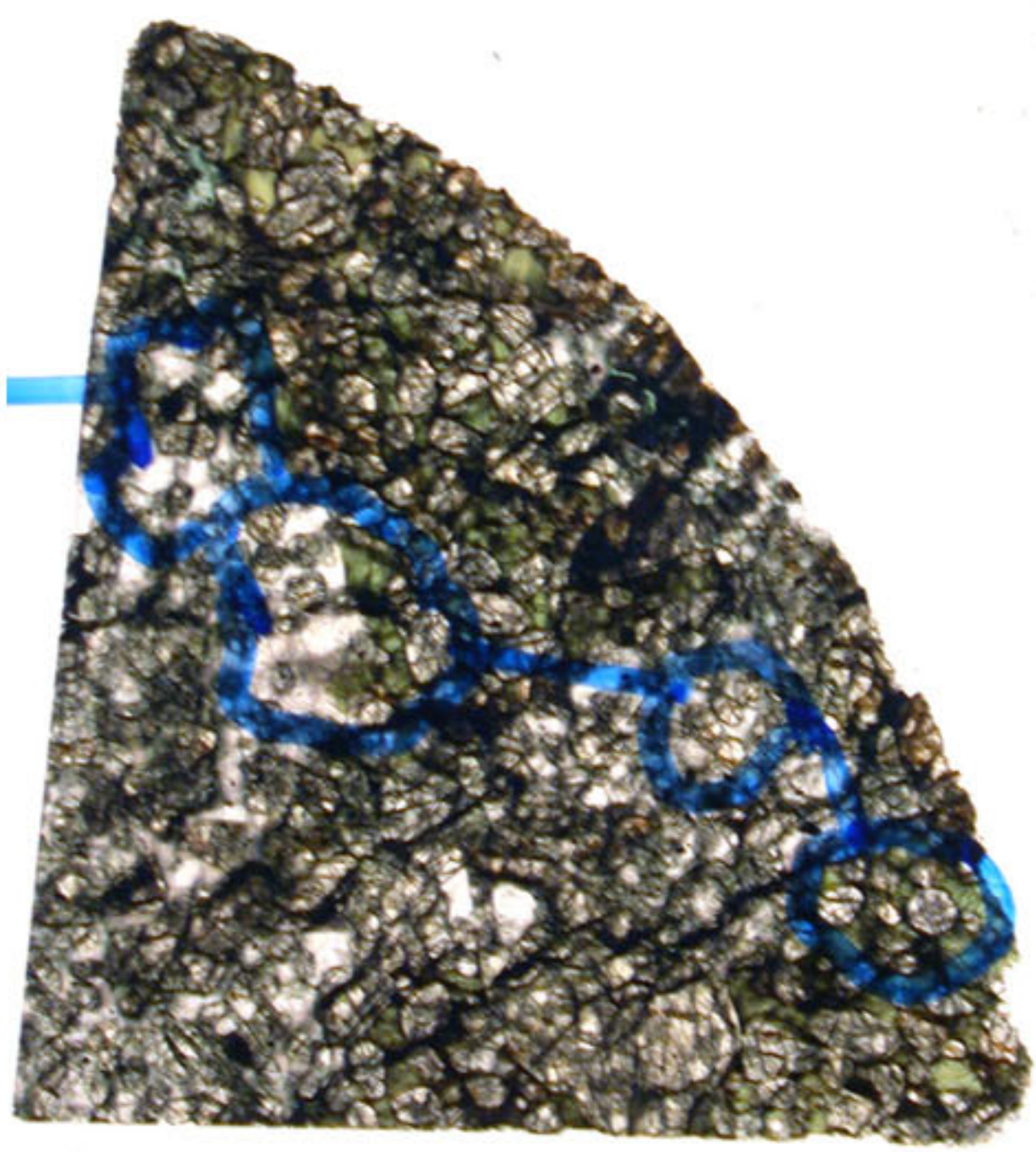
234R1_22-26_LP.JPG



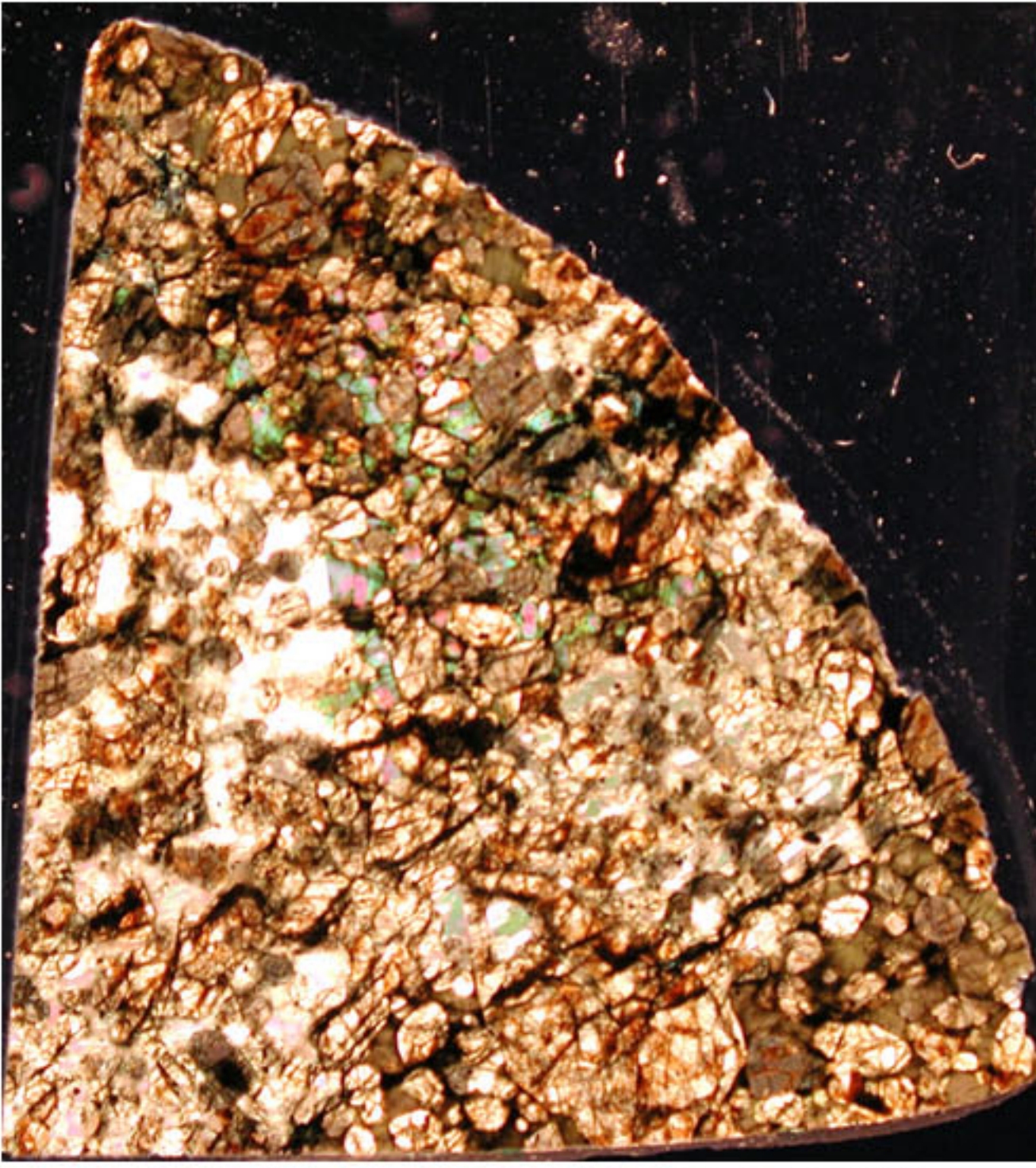
234R1_92-96_LN.JPG



234R1_92-96_LP.JPG



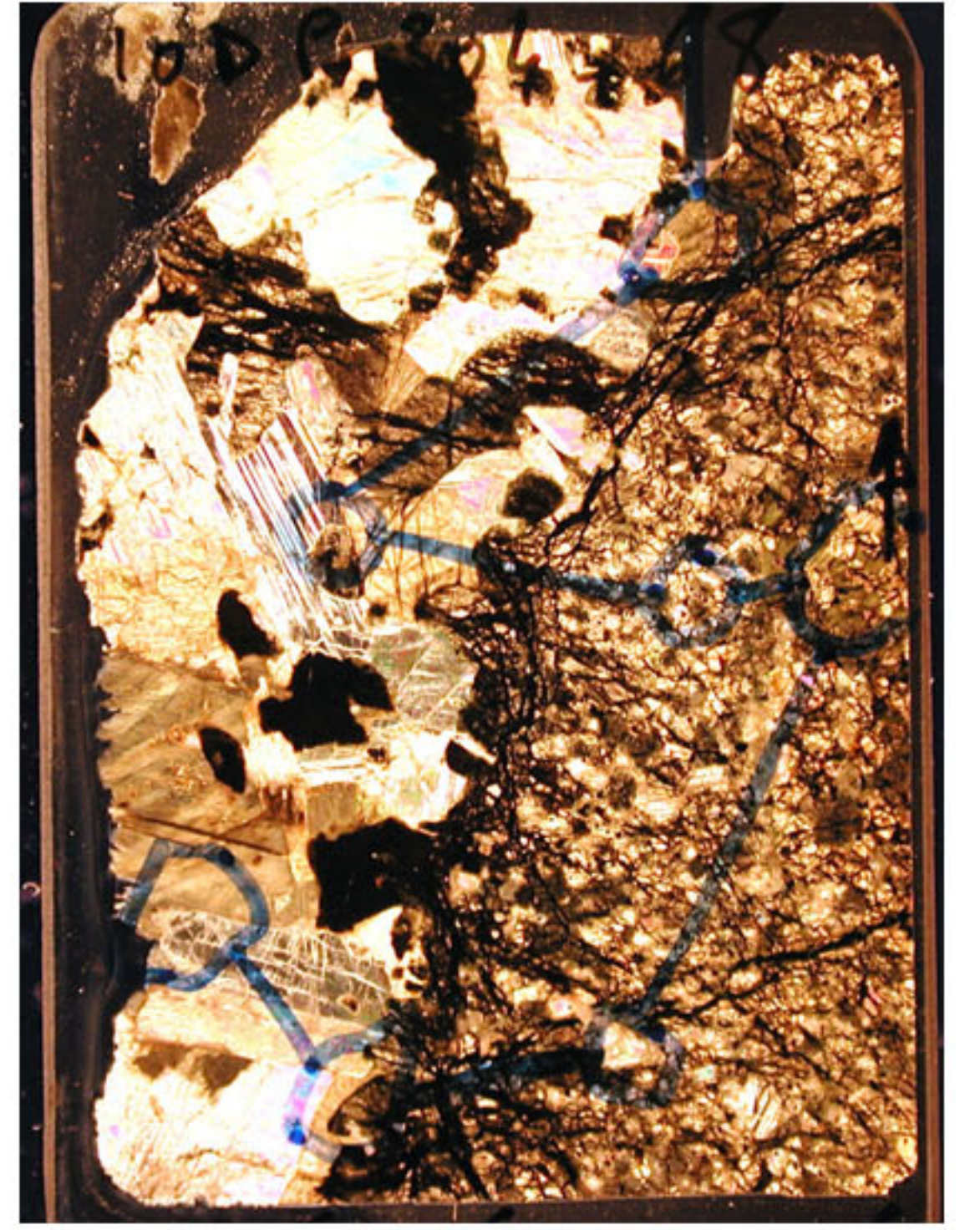
234R3_14-18_LN.JPG



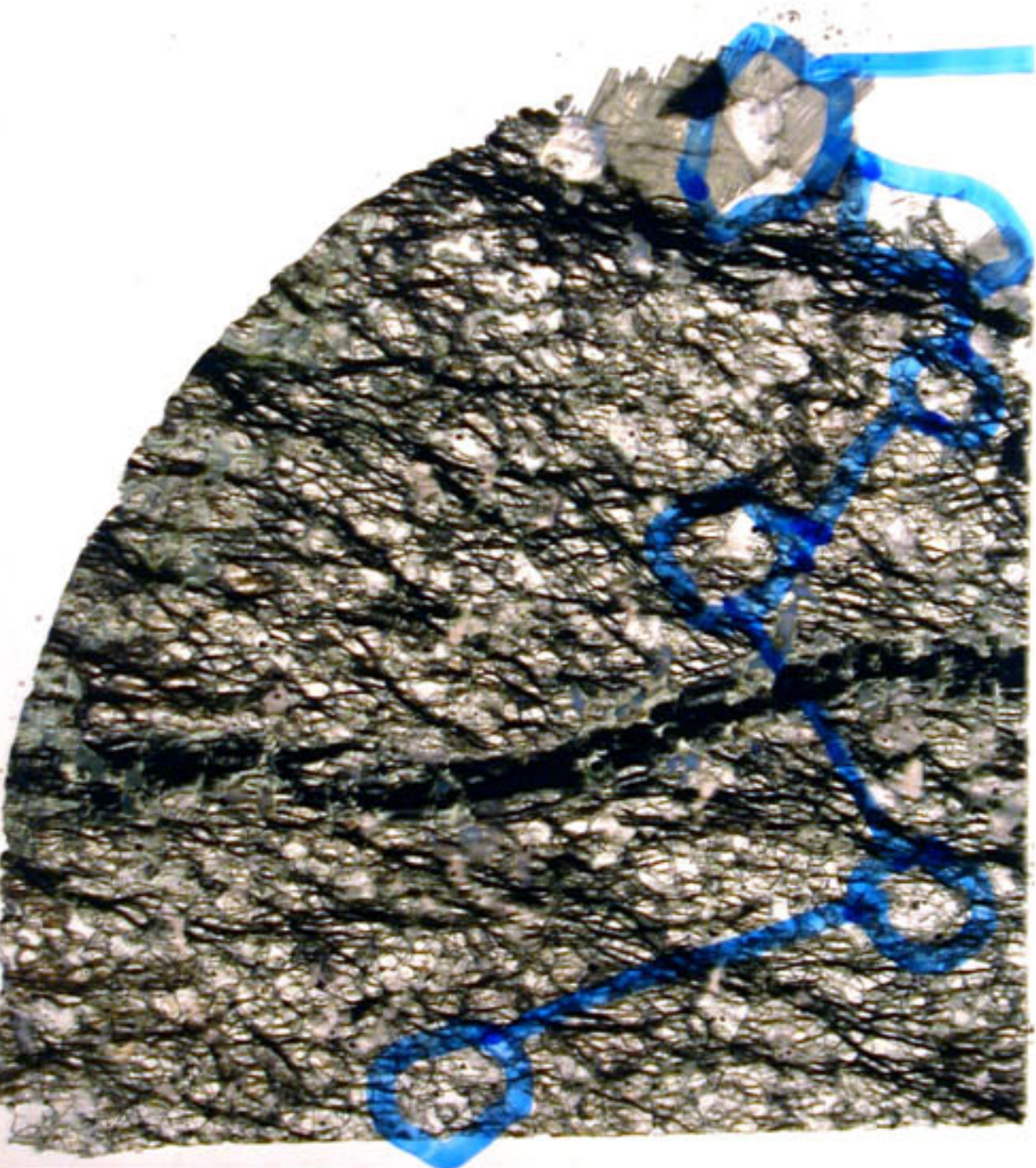
234R3_14-18_LP.JPG



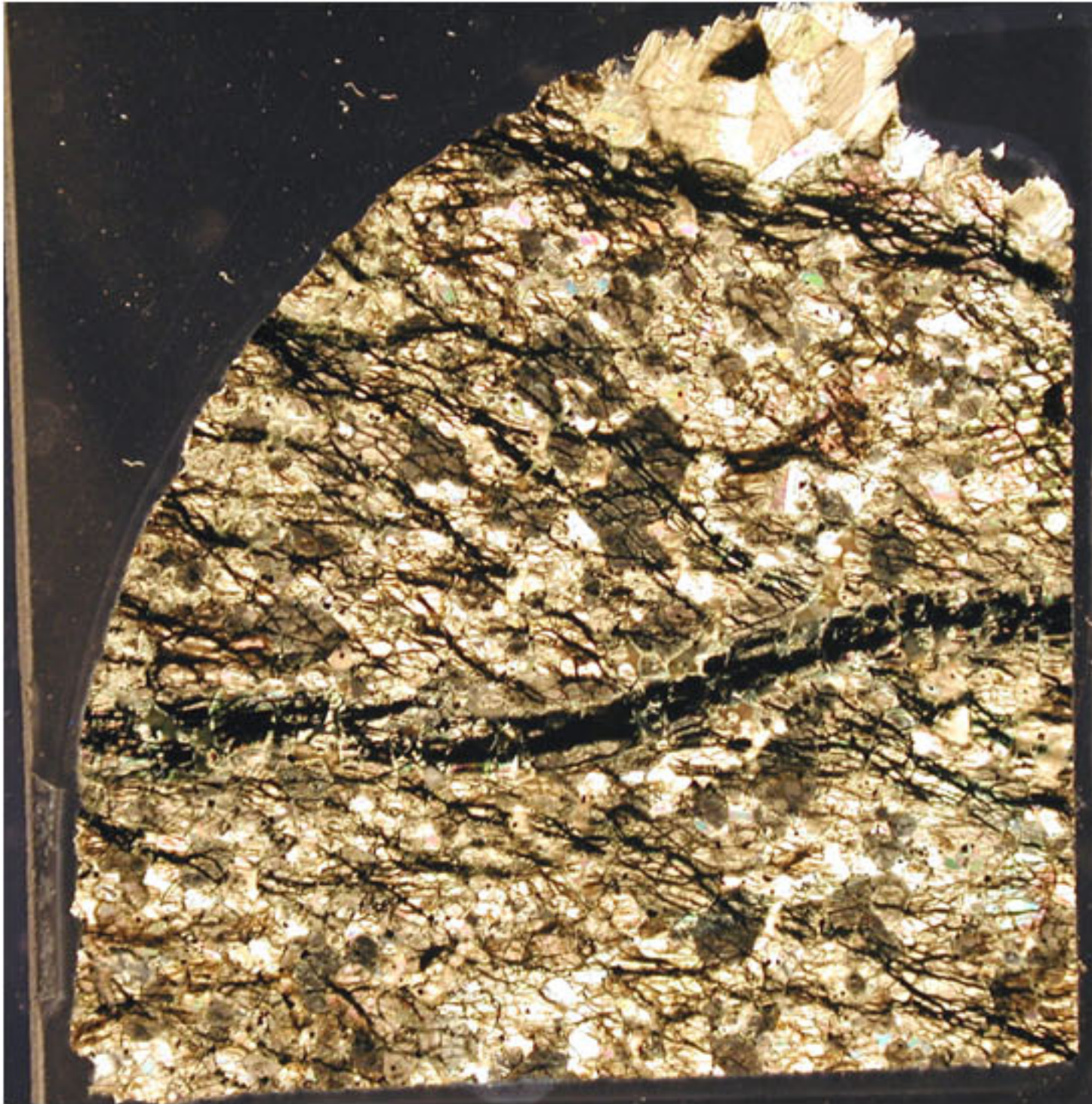
235R1_29-34_LN.JPG



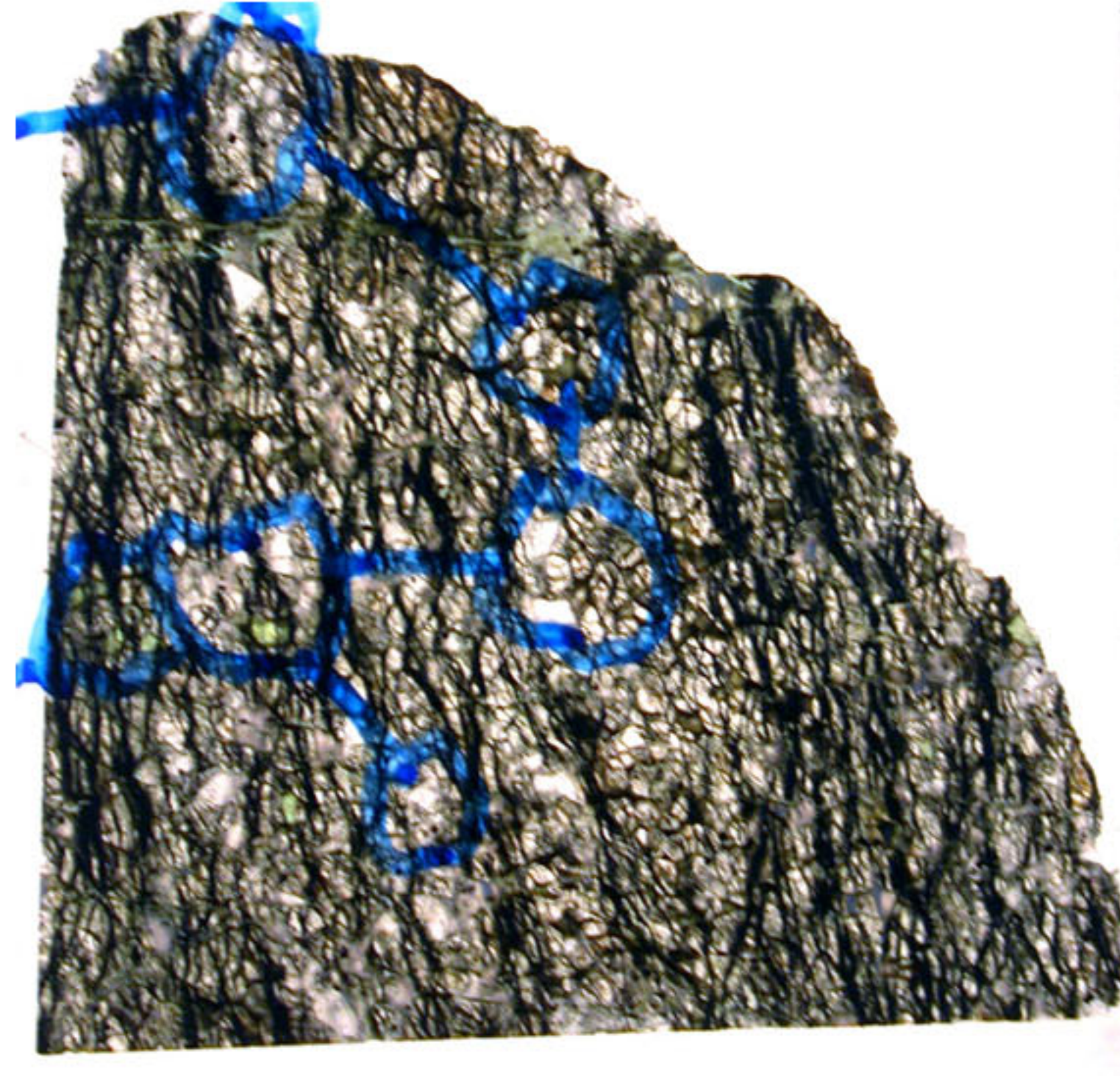
235R1_29-34_LP.JPG



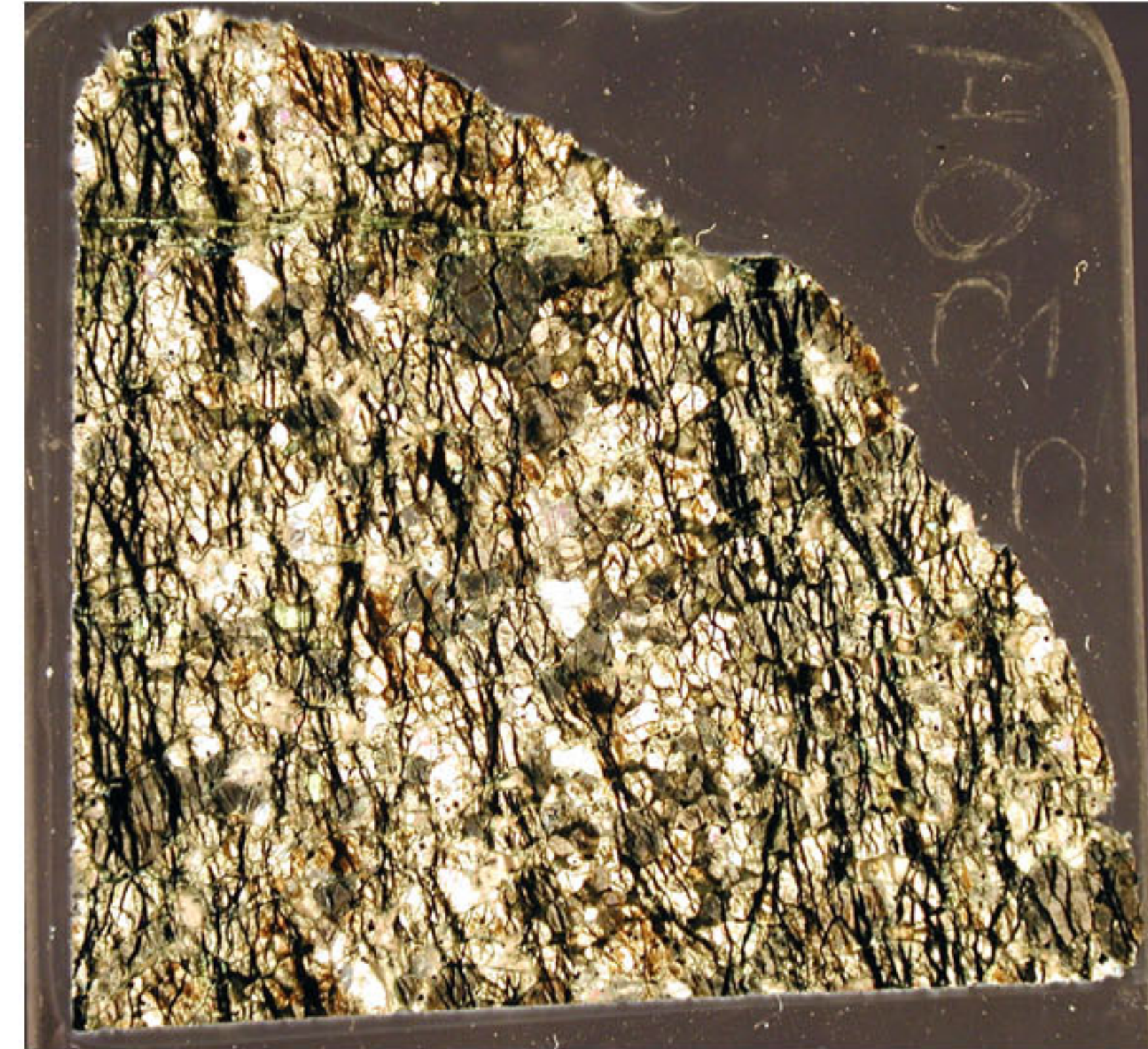
235R2_13-16_LN.JPG



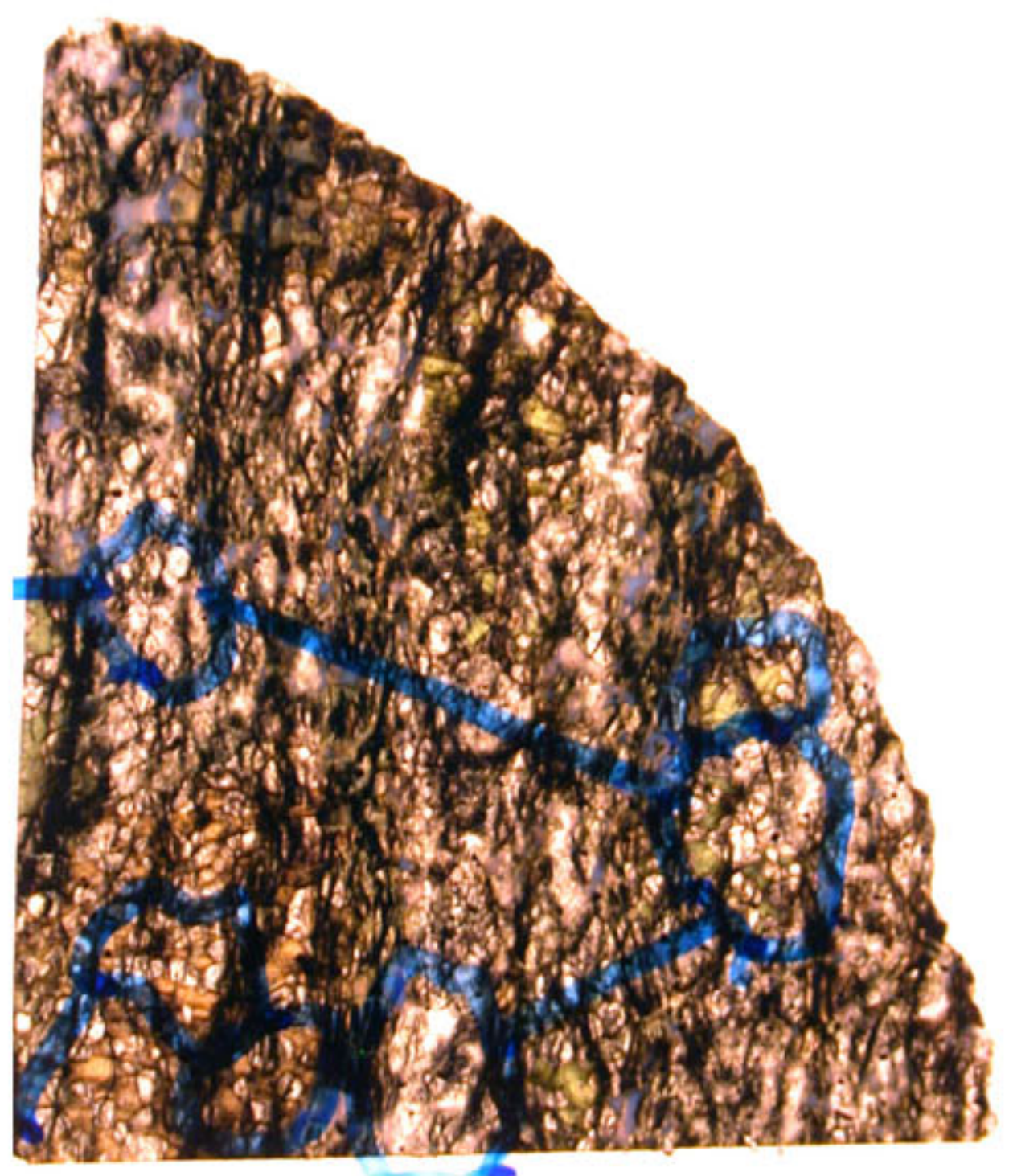
235R2_13-16_LP.JPG



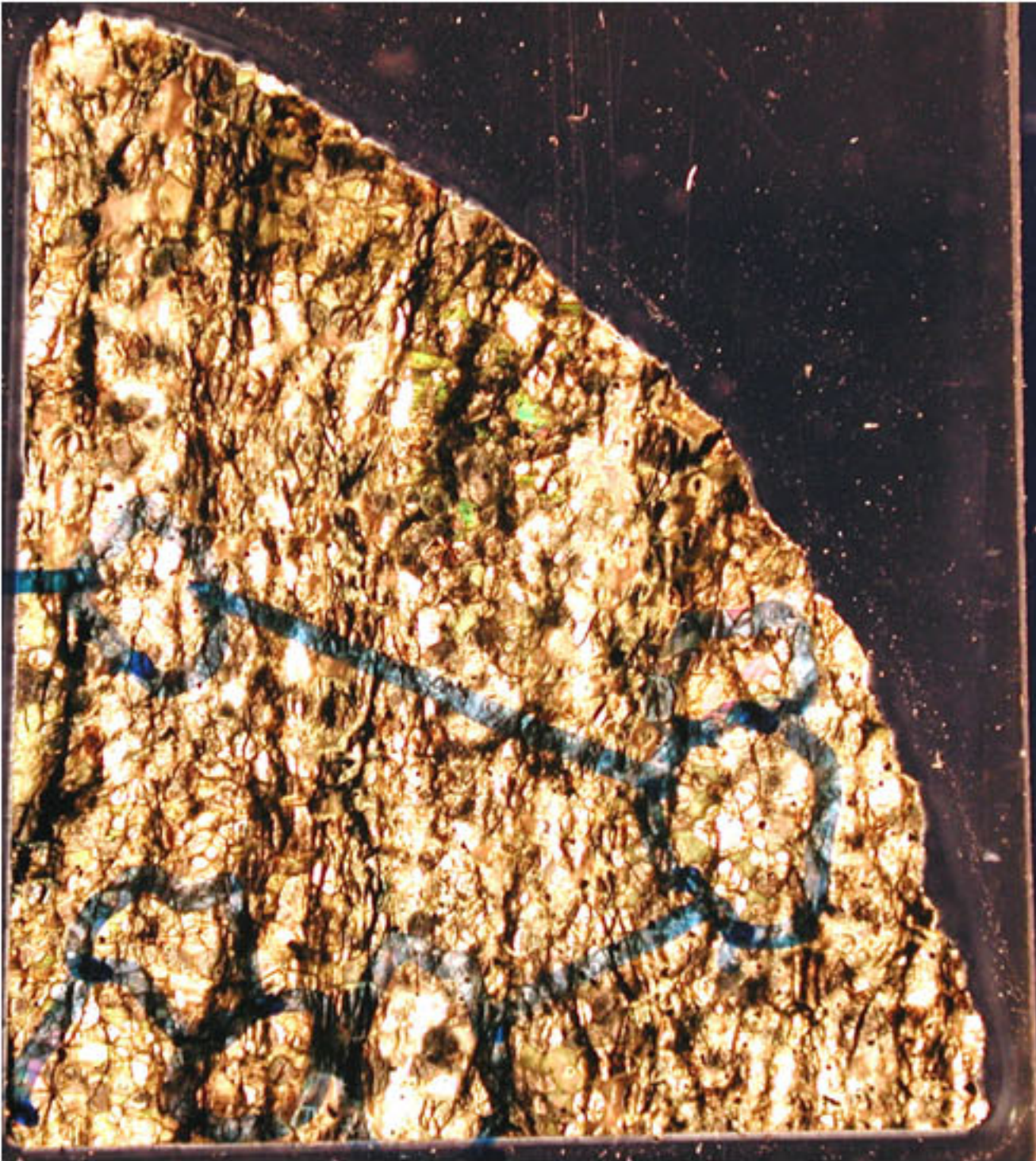
235R2_85-89_LN.JPG



235R2_85-89_LP.JPG



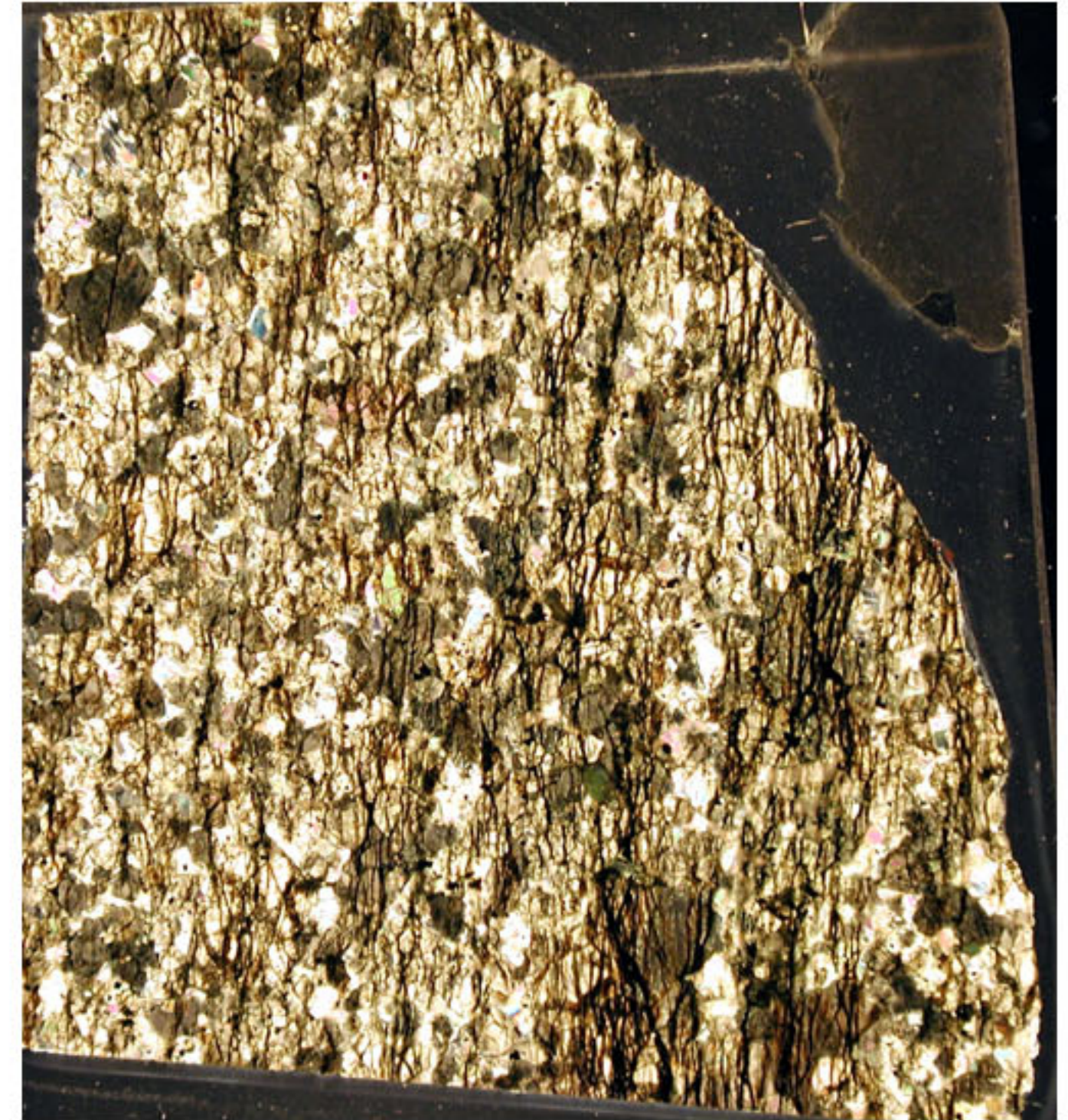
236R1_122-126_LN.JPG



236R1_122-126_LP.JPG



236R2_121-124_LN.JPG



236R2_121-124_LP.JPG



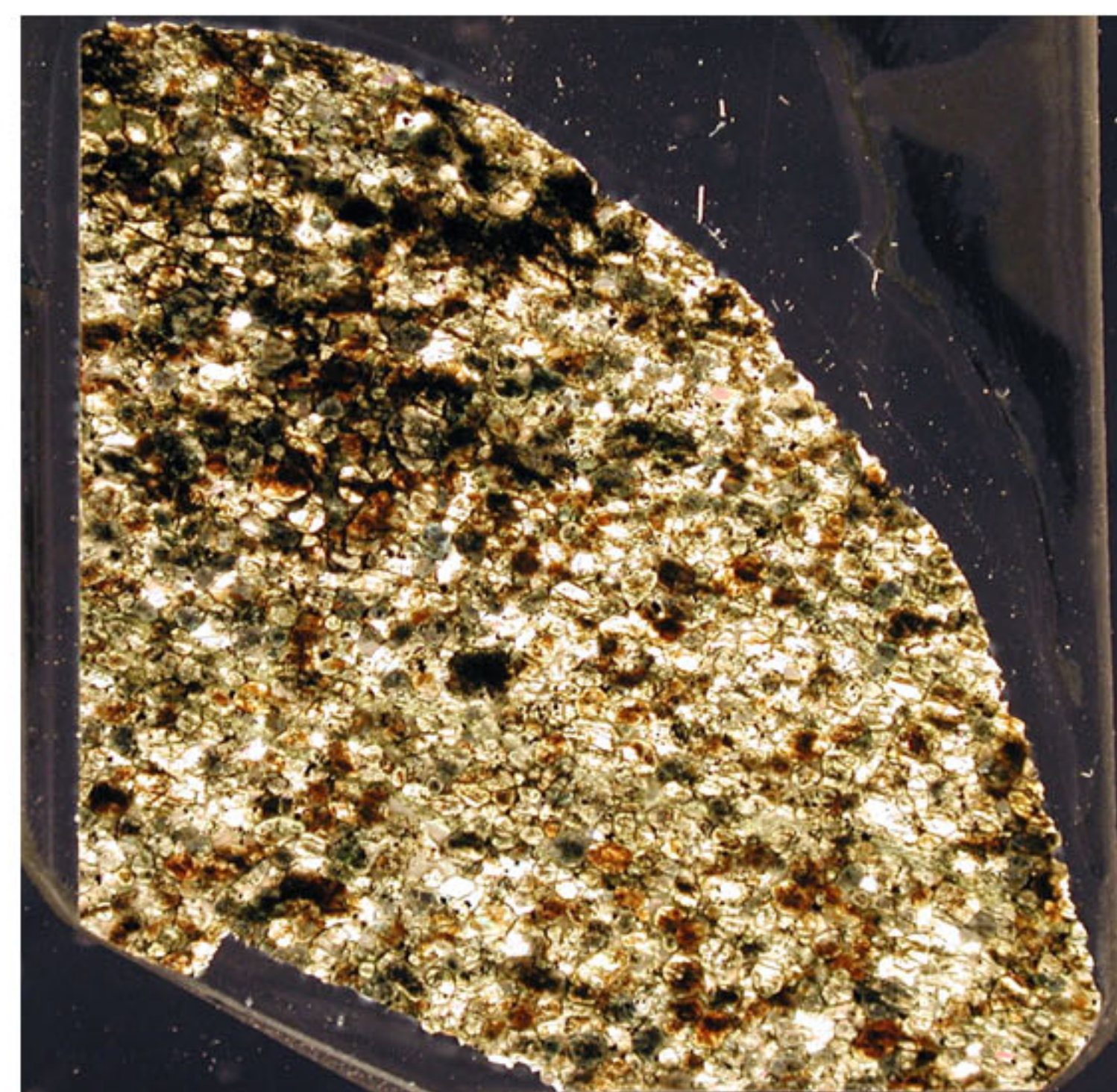
237R2_40-43_LN.JPG



237R2_40-43_LP.JPG



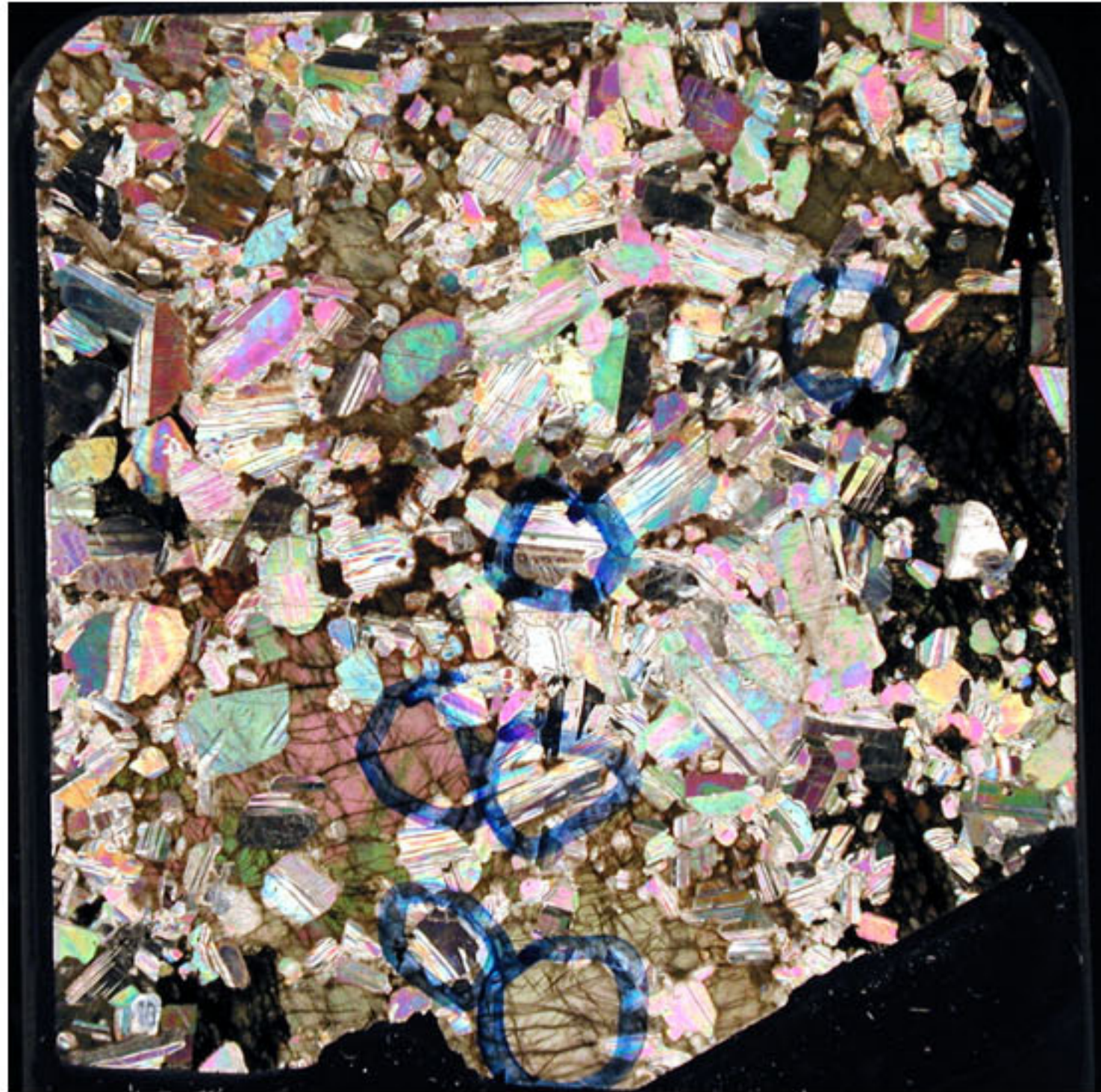
241R2_94-97_LN.JPG



241R2_94-97_LP.JPG



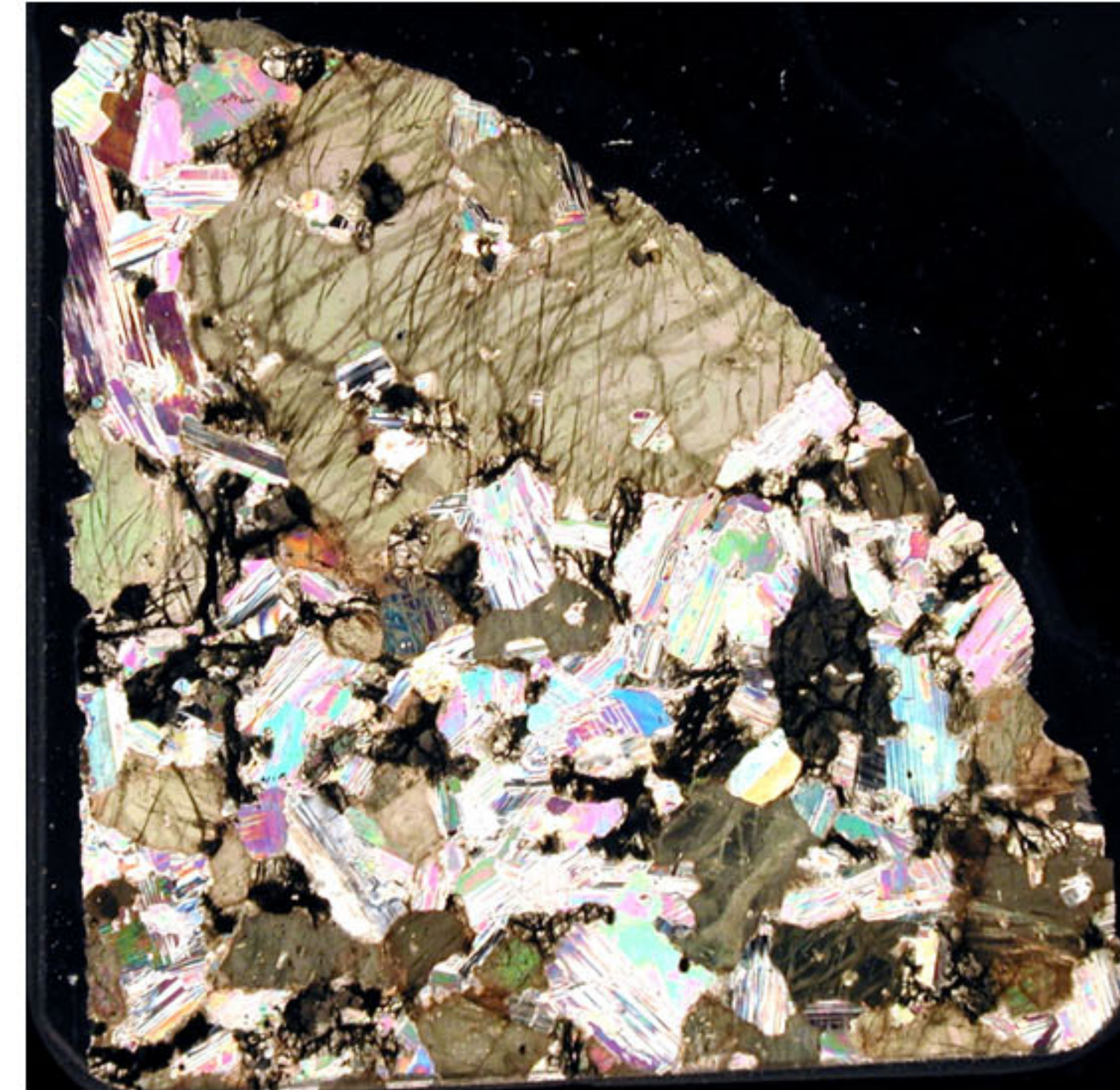
242R1_123-126_LN.JPG



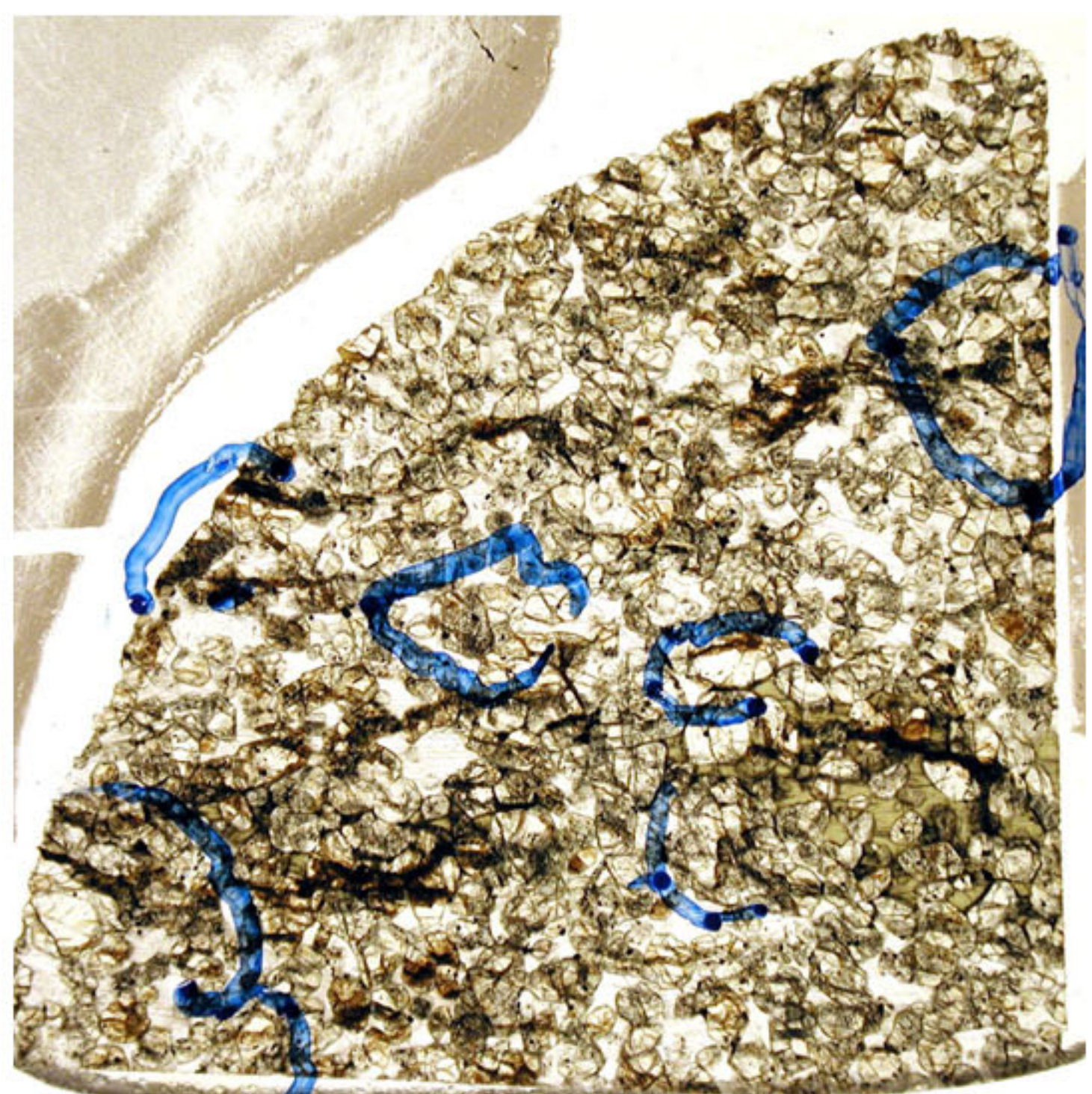
242R1_123-126_LP.JPG



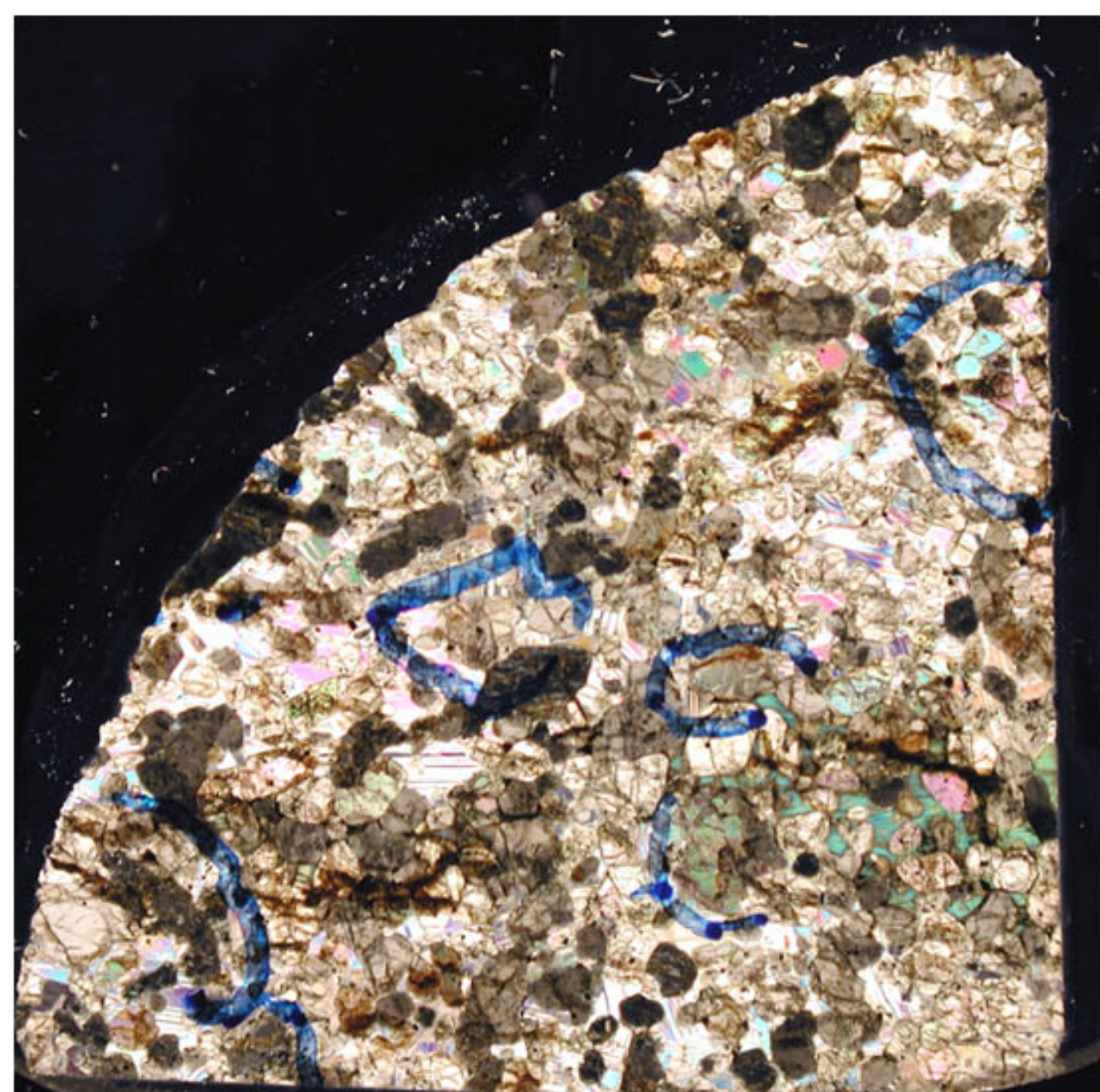
243R1_57-61_LN.JPG



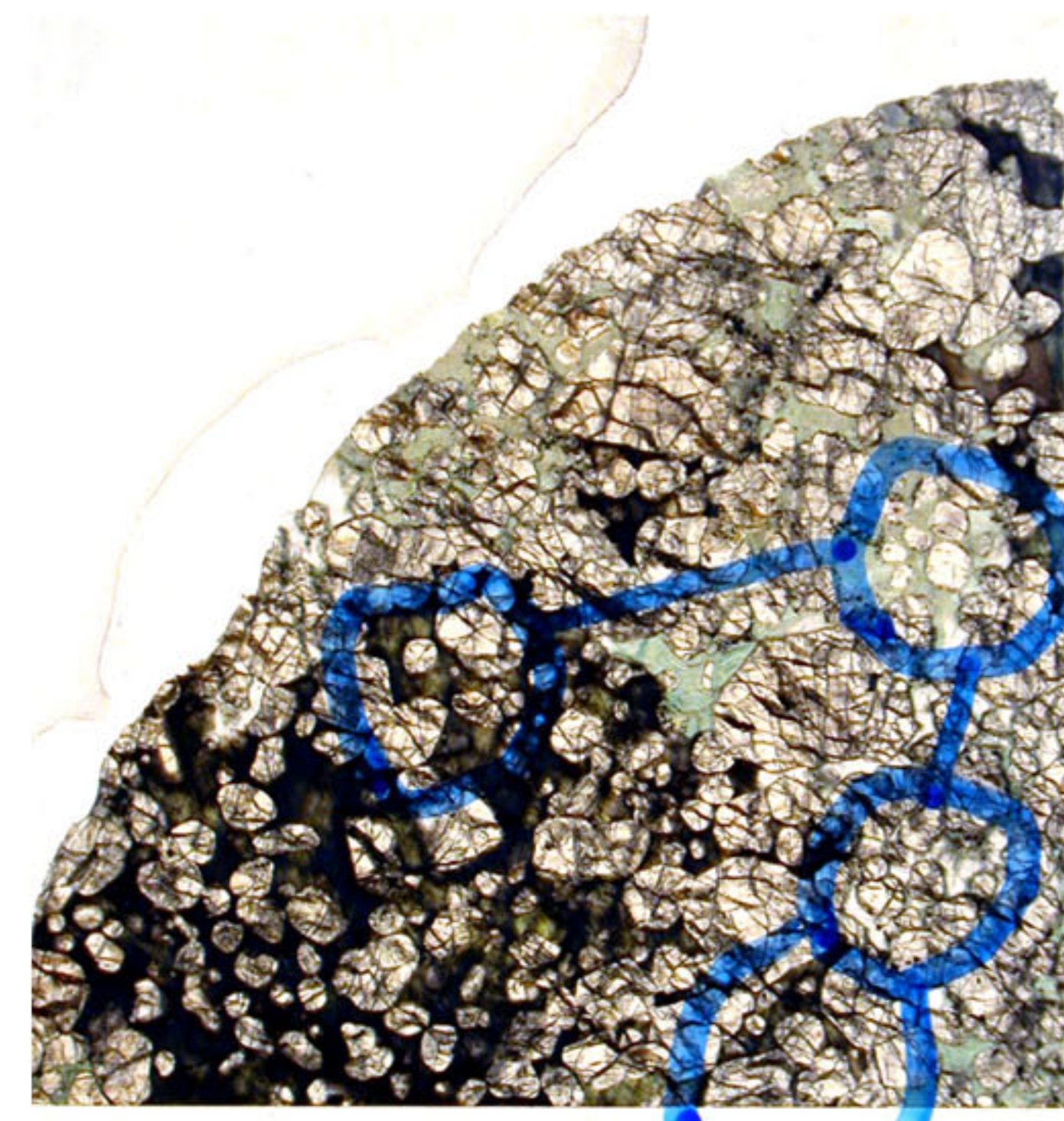
243R1_57-61_LP.JPG



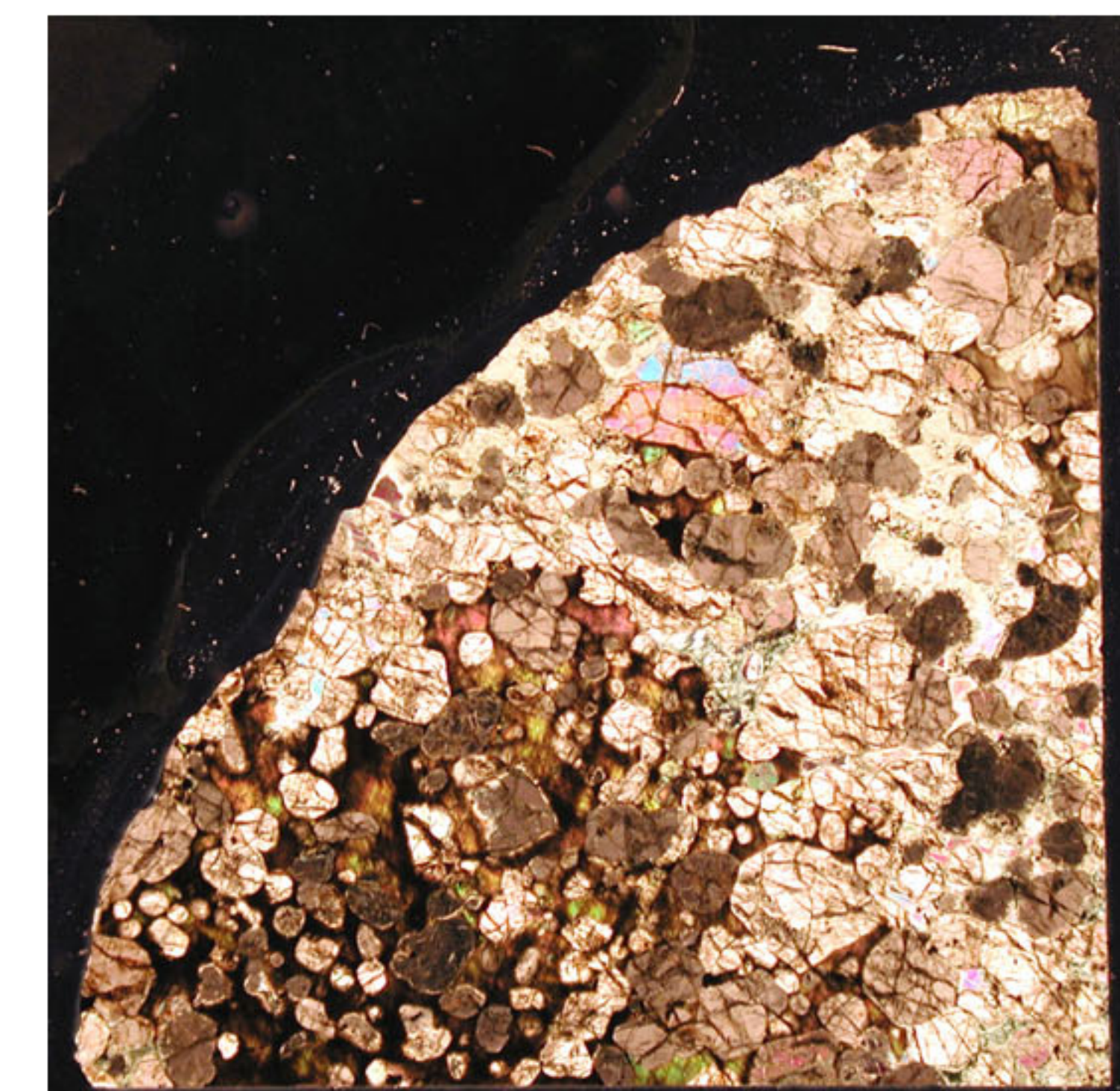
247R3_19-22_LN.JPG



247R3_19-22_LP.JPG



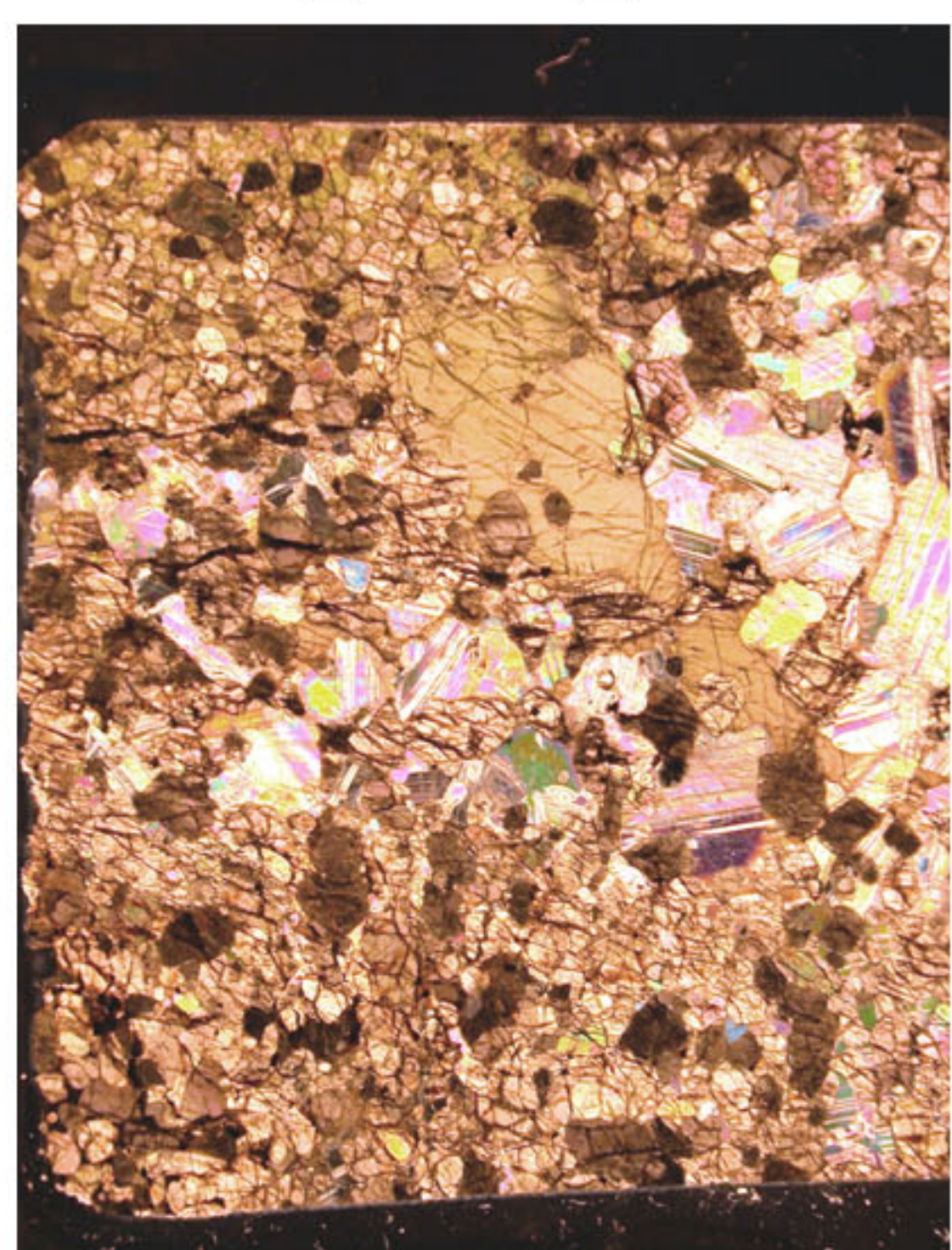
247R3_62-66_LN.JPG



247R3_62-66_LP.JPG



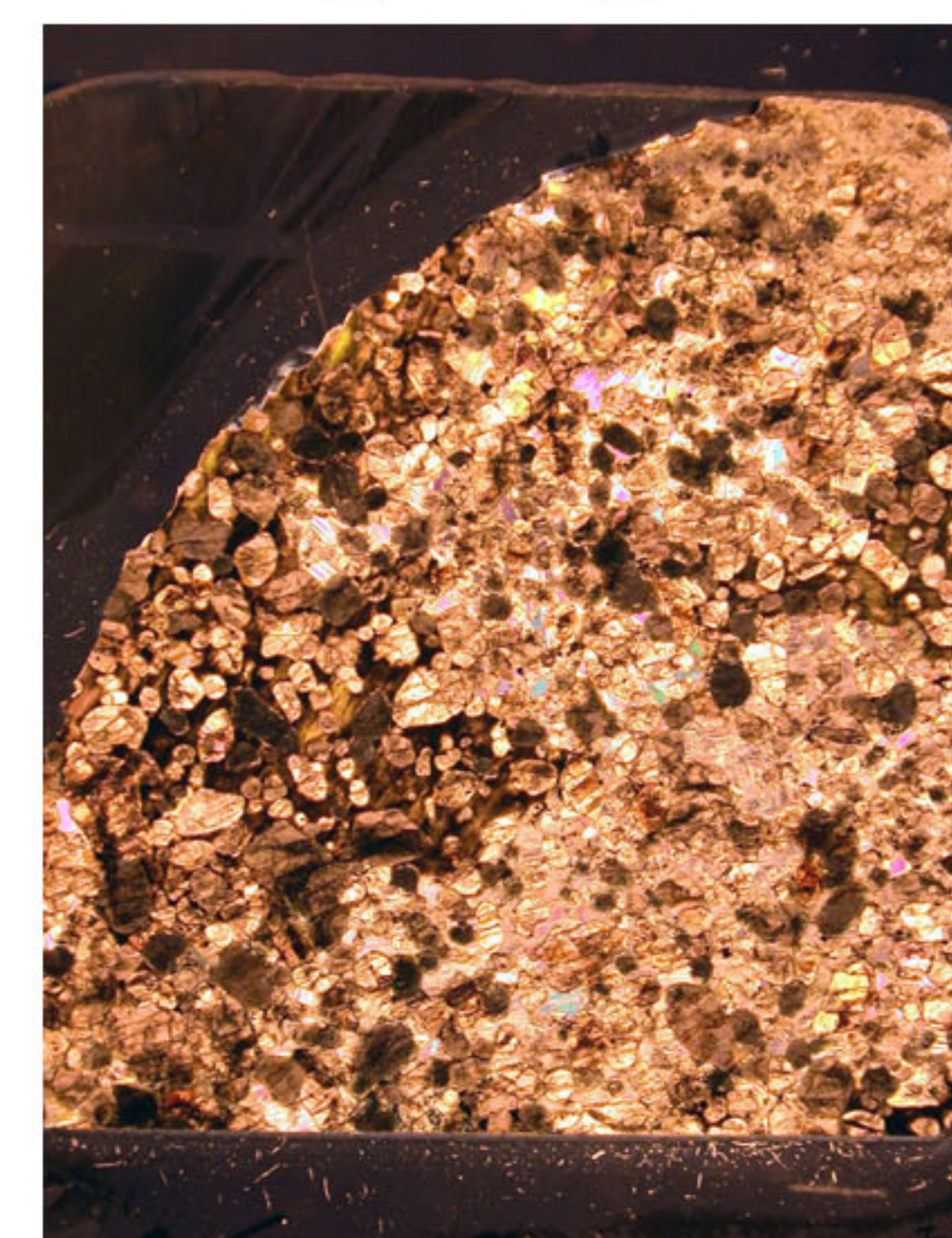
248R2_18-21_LN.JPG



248R2_18-21_LP.JPG



248R3_131-134_LN.JPG



248R3_131-134_LP.JPG



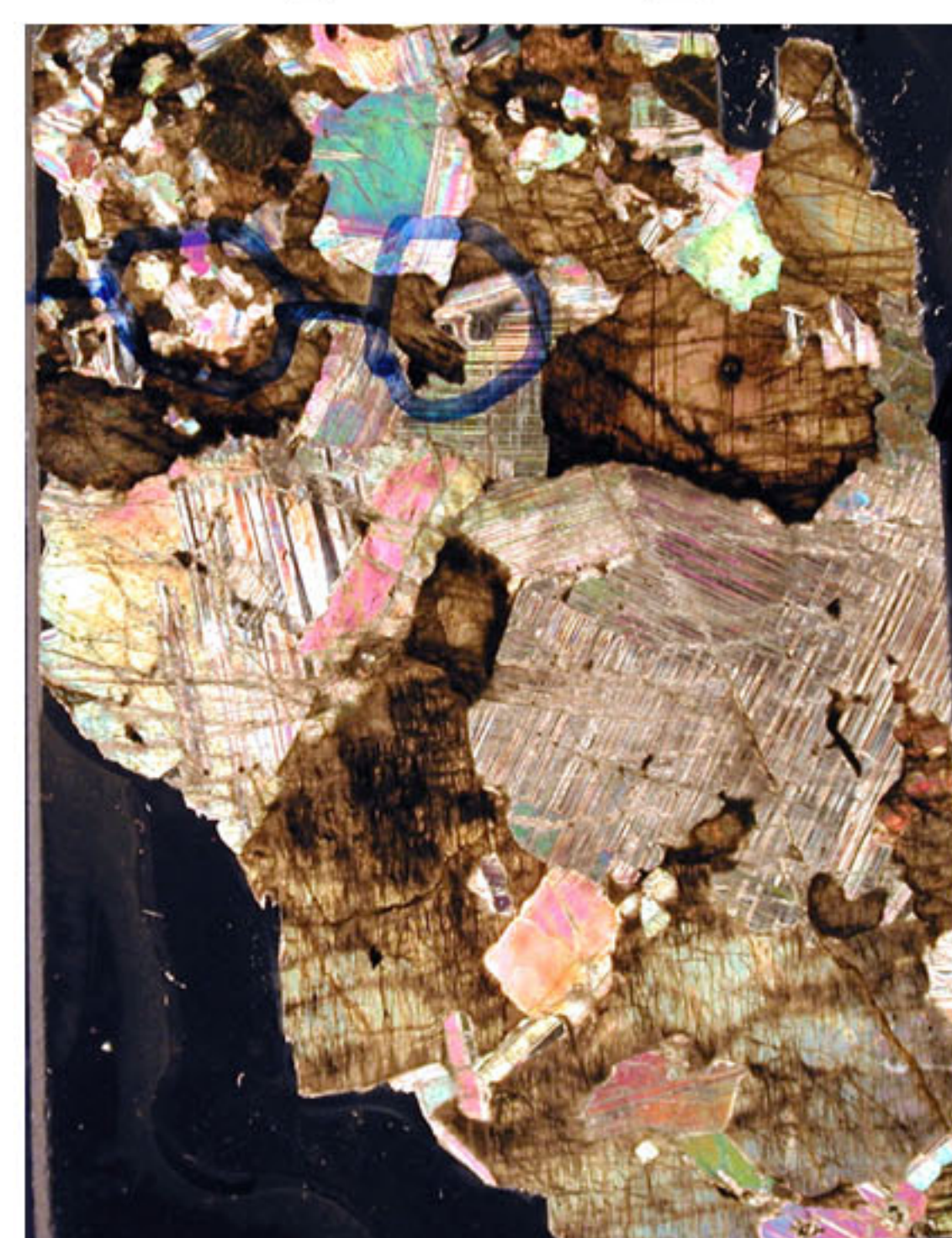
248R4_19-23_LN.JPG



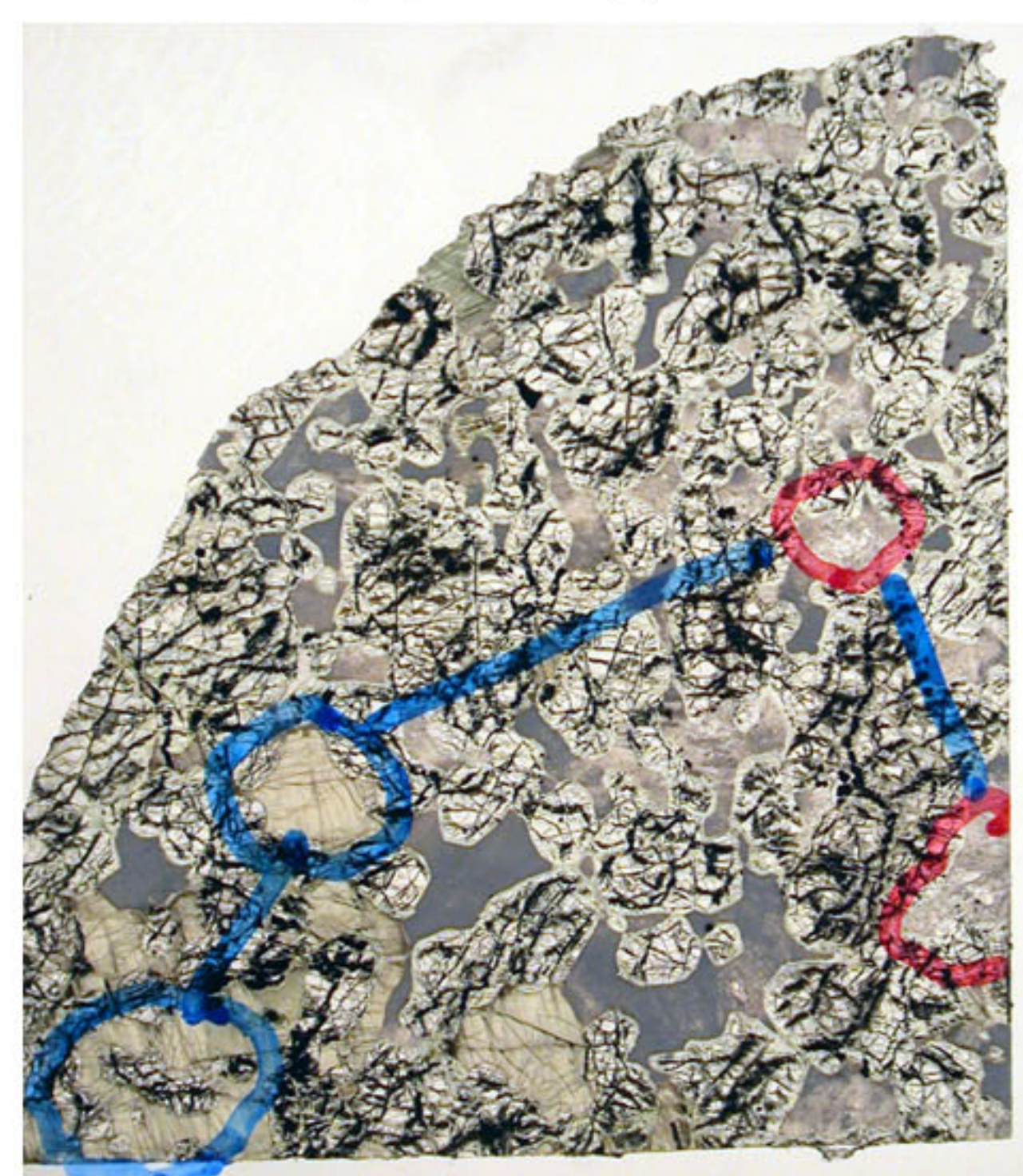
248R4_19-23_LP.JPG



248R4_65-69_LN.JPG



248R4_65-69_LP.JPG



60R3_39-42_LN.jpg



60R3_39-42_LP.JPG



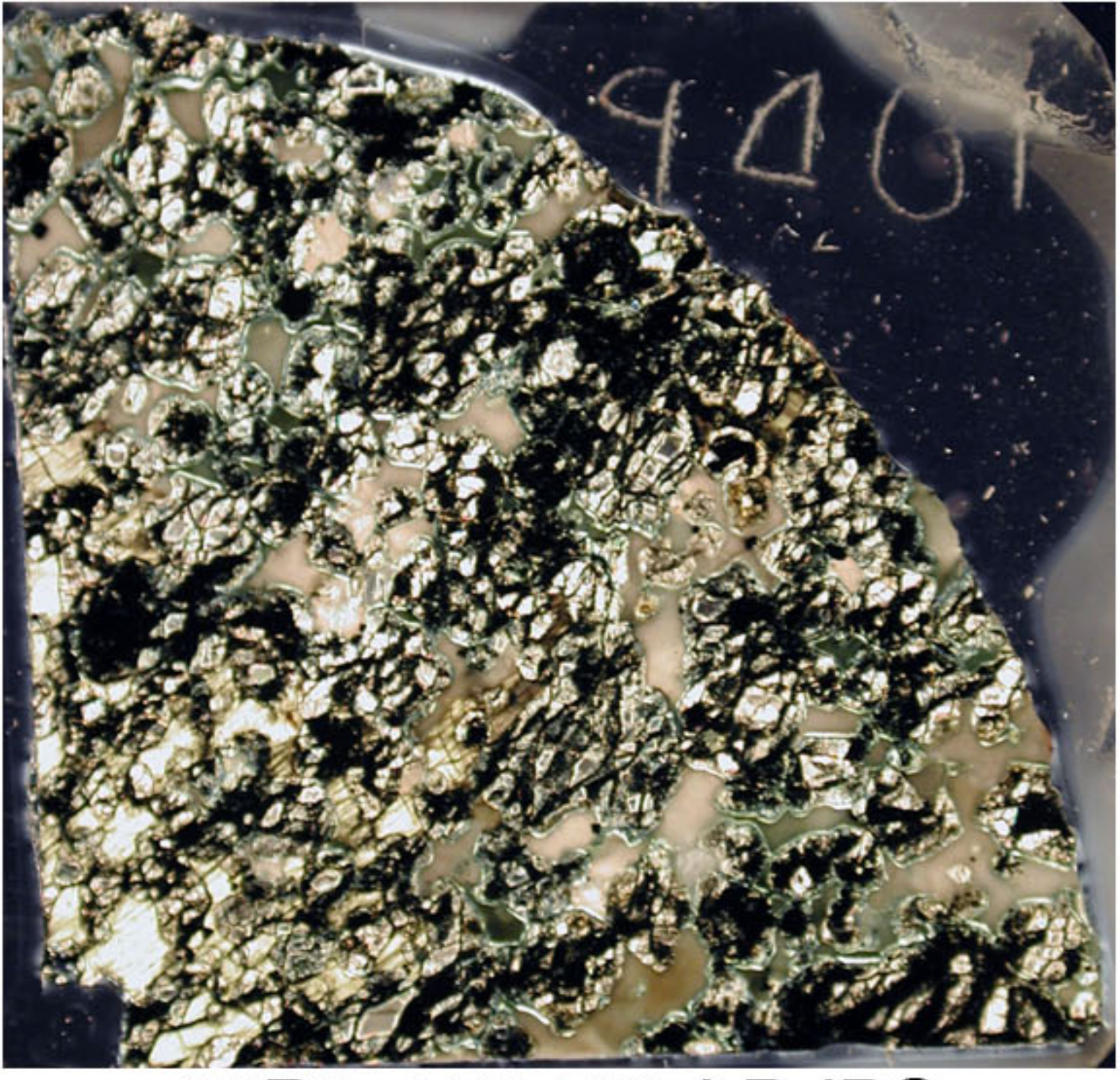
61R1_11-14_LN.jpg



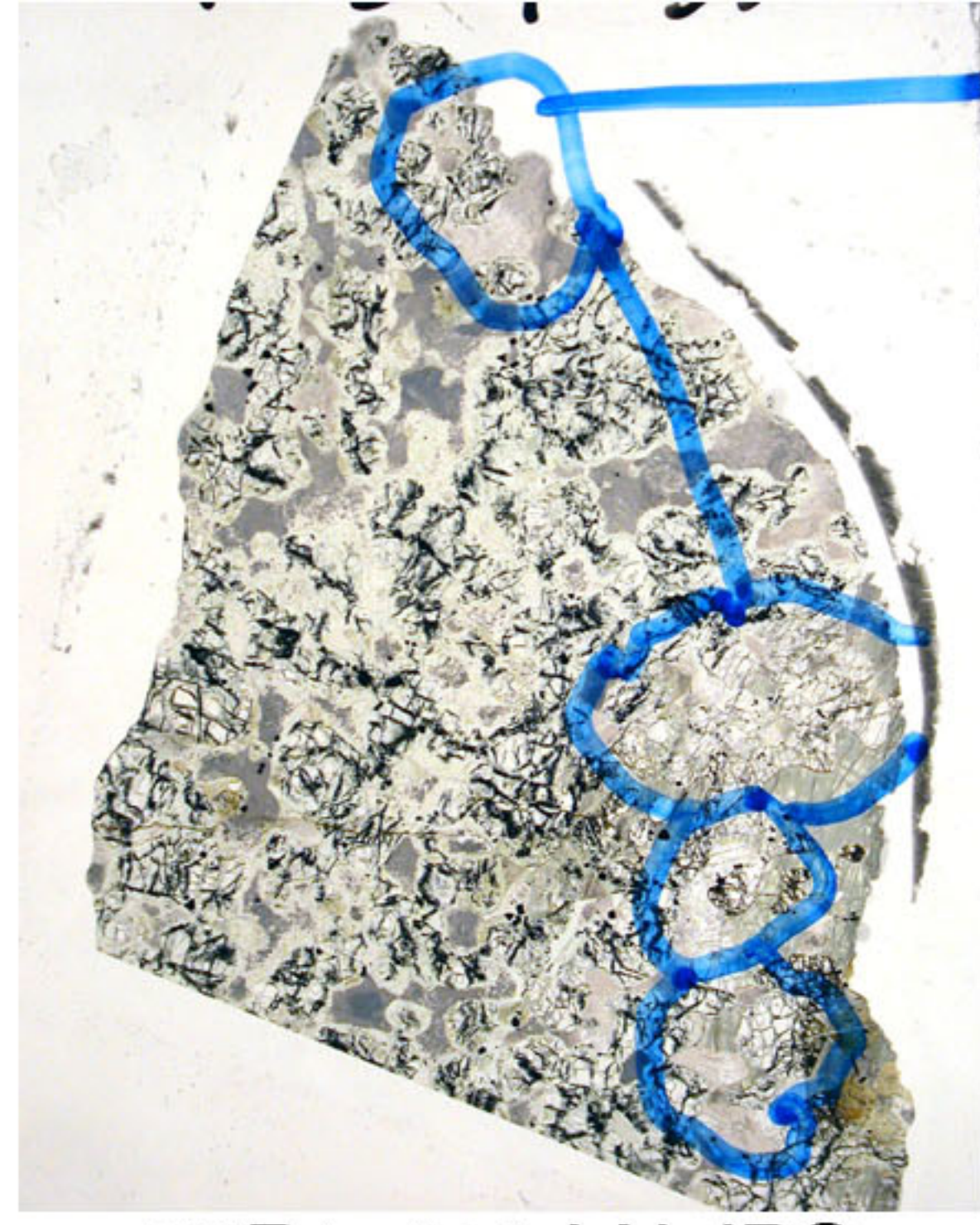
61R1_11-14_LP.JPG



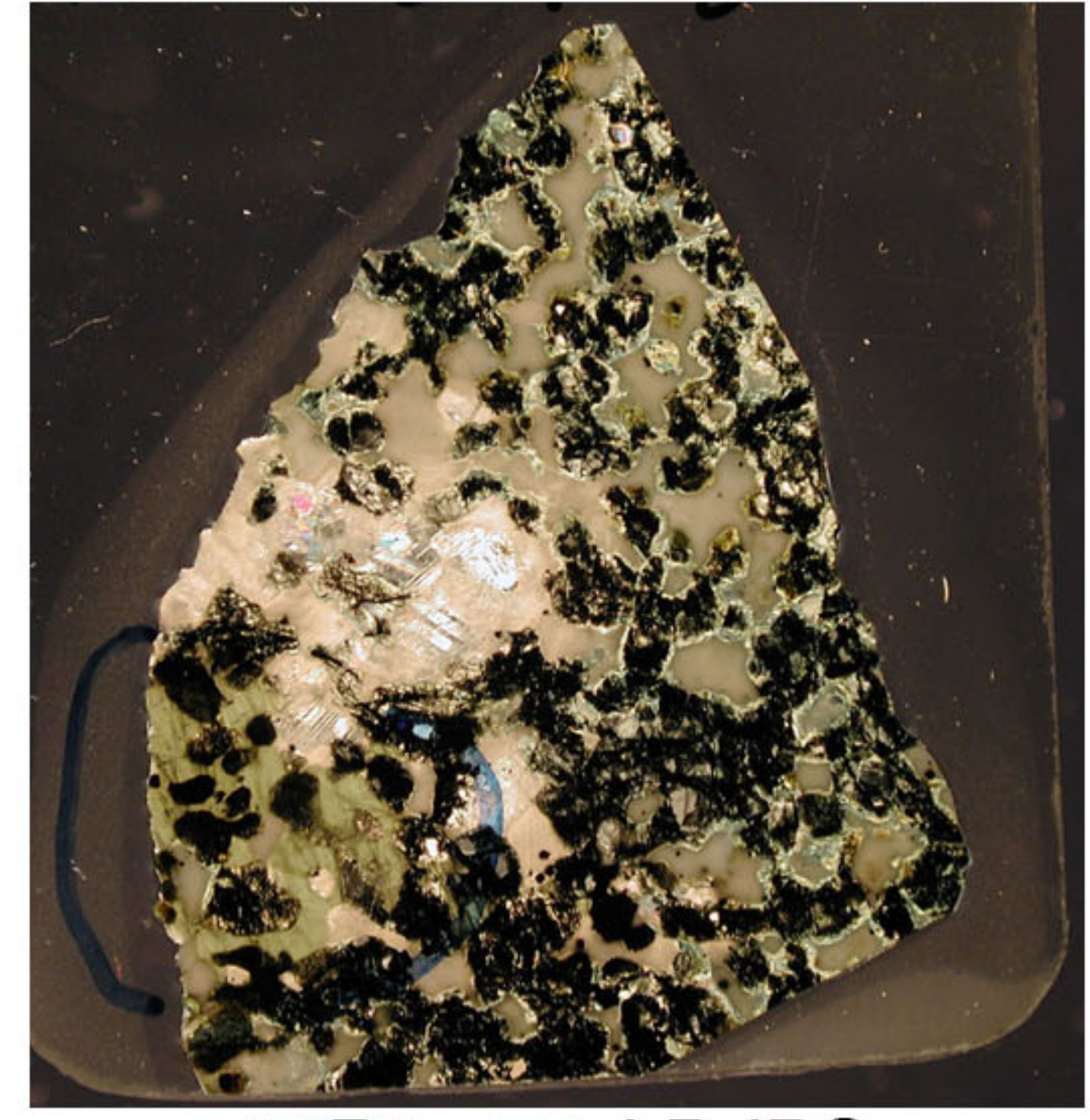
61R1_113-116_LN.JPG



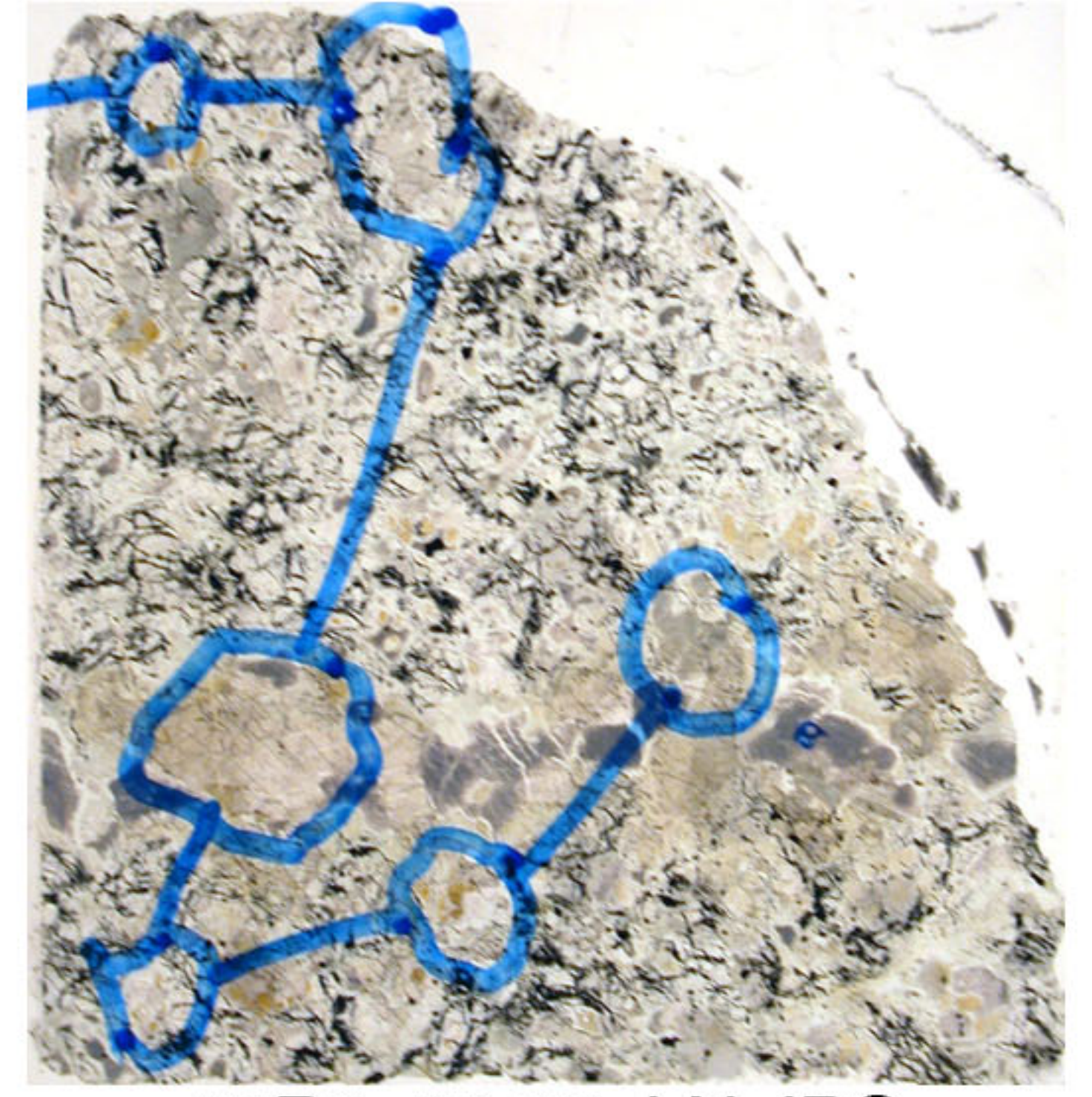
61R1_113-116_LP.JPG



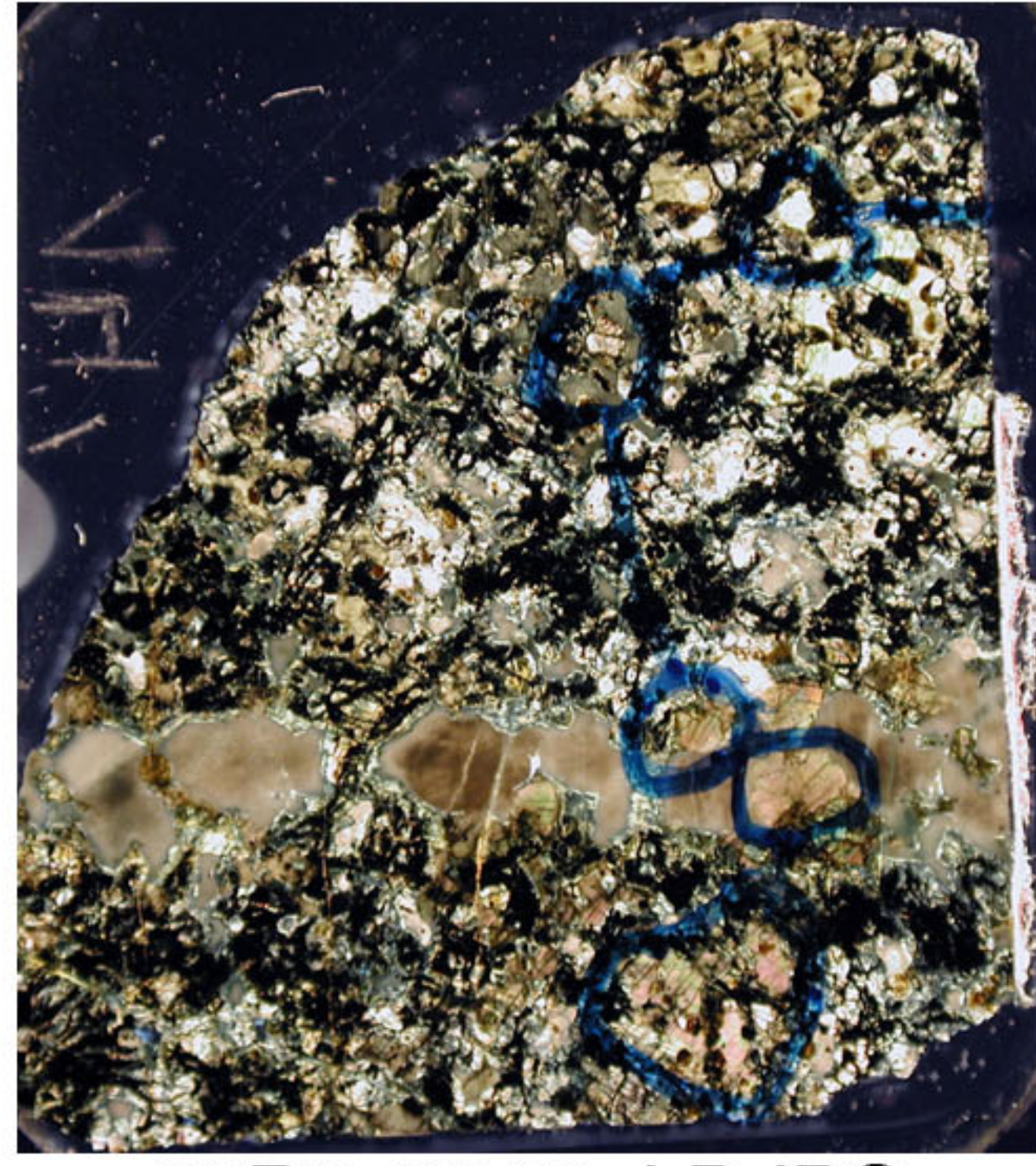
62R1_4-7_LN.JPG



62R1_4-7_LP.JPG



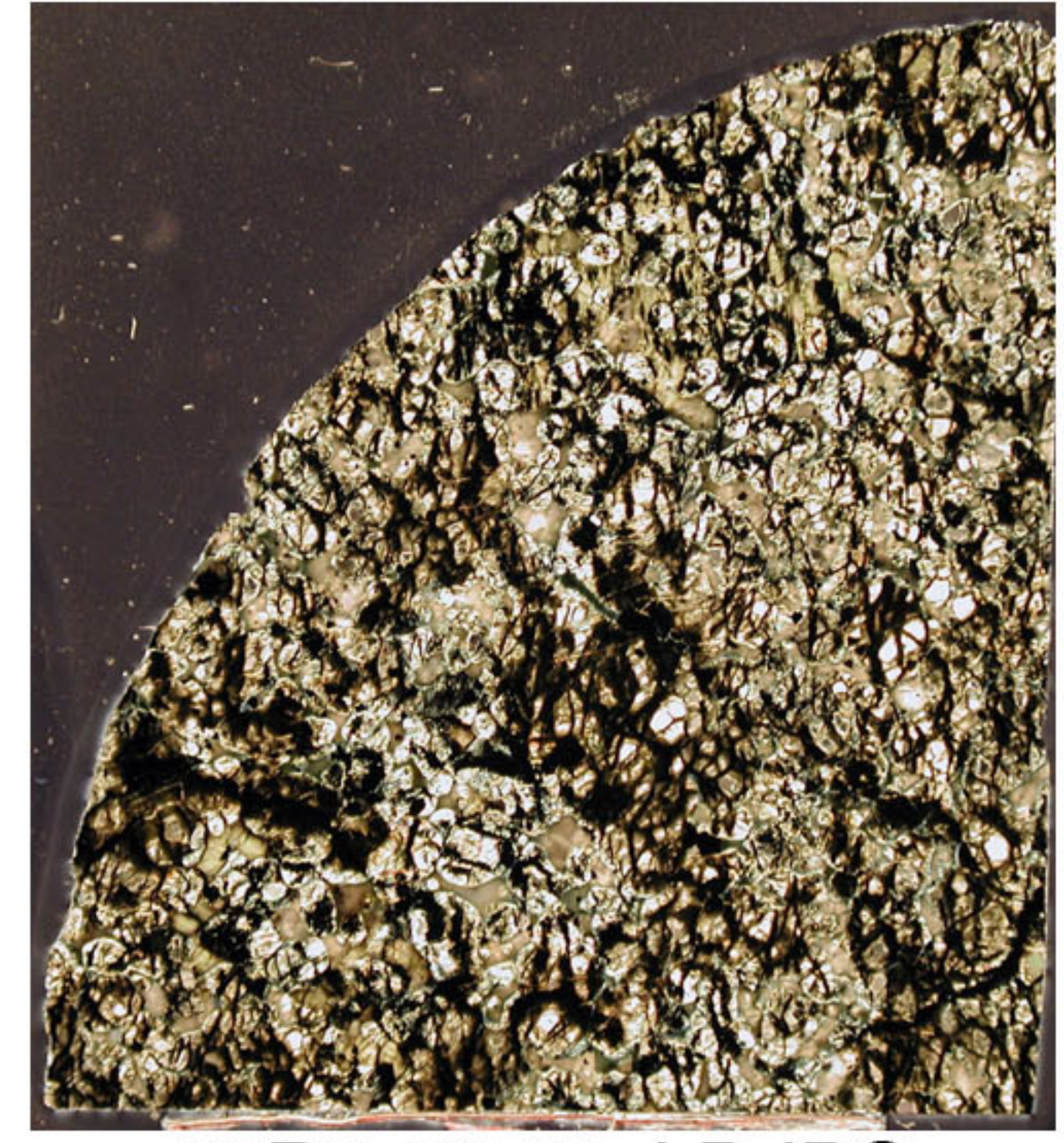
63R2_28-30_LN.JPG



63R2_28-30_LP.JPG



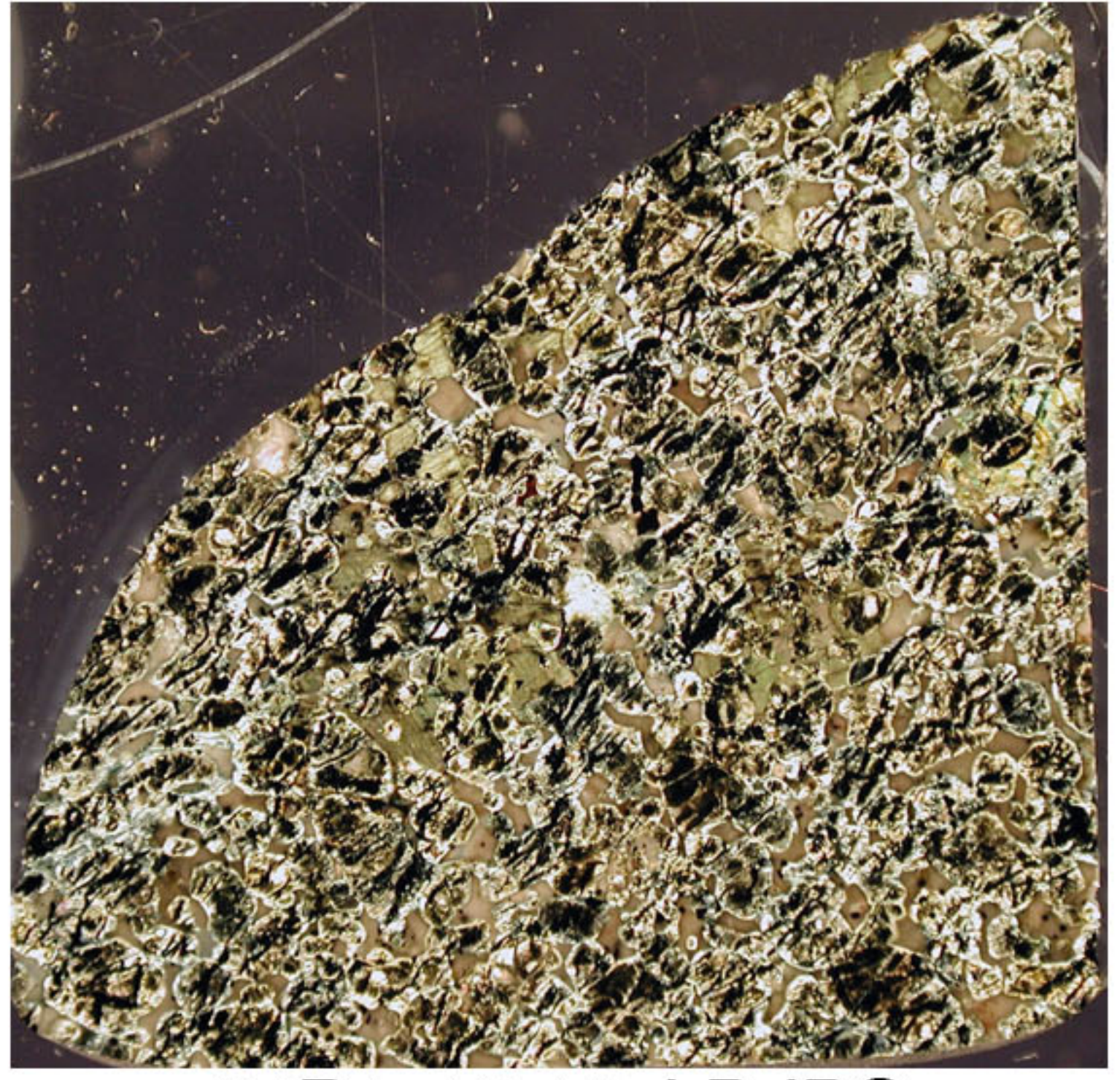
63R3_36-39_LN.JPG



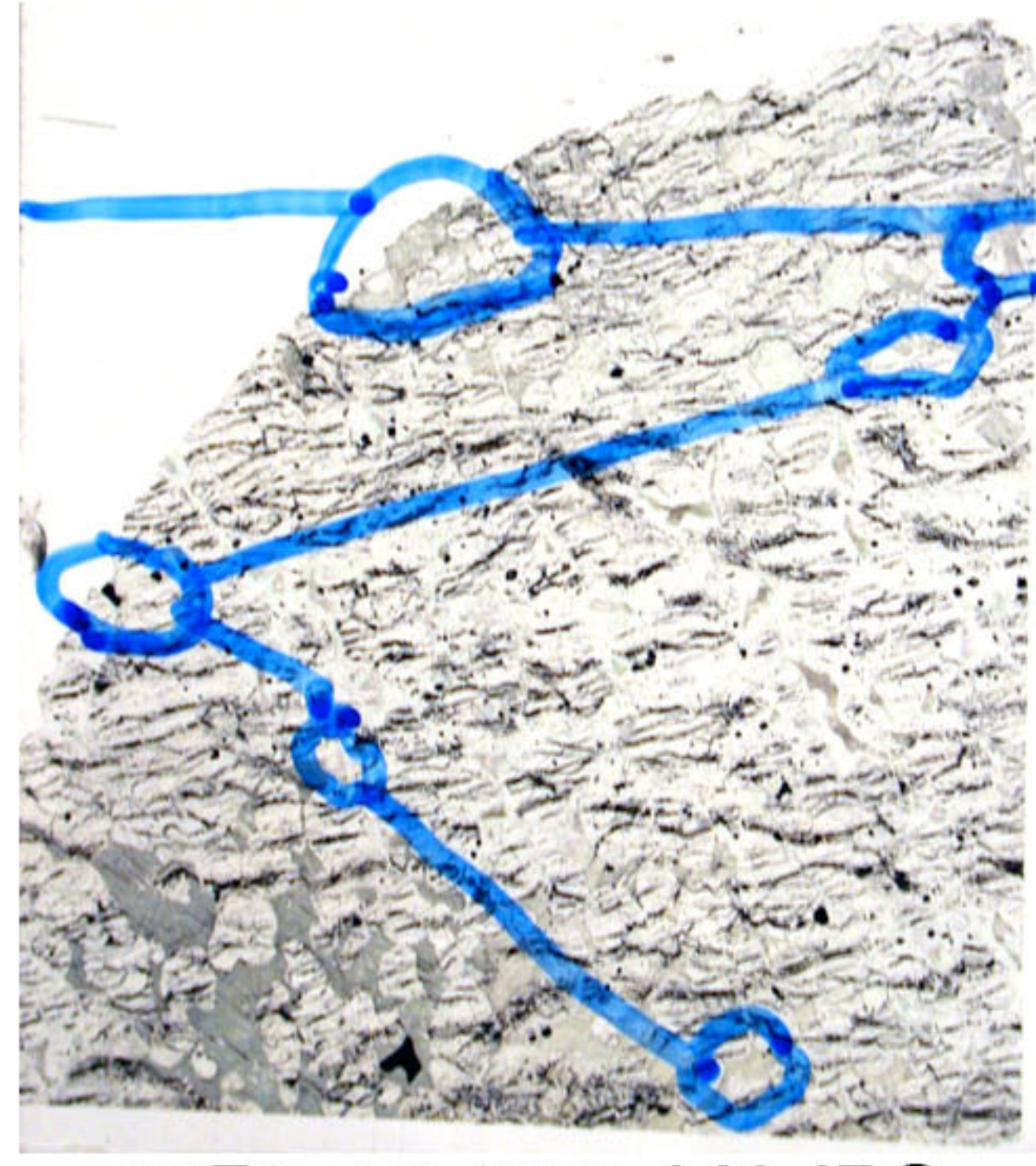
63R3_36-39_LP.JPG



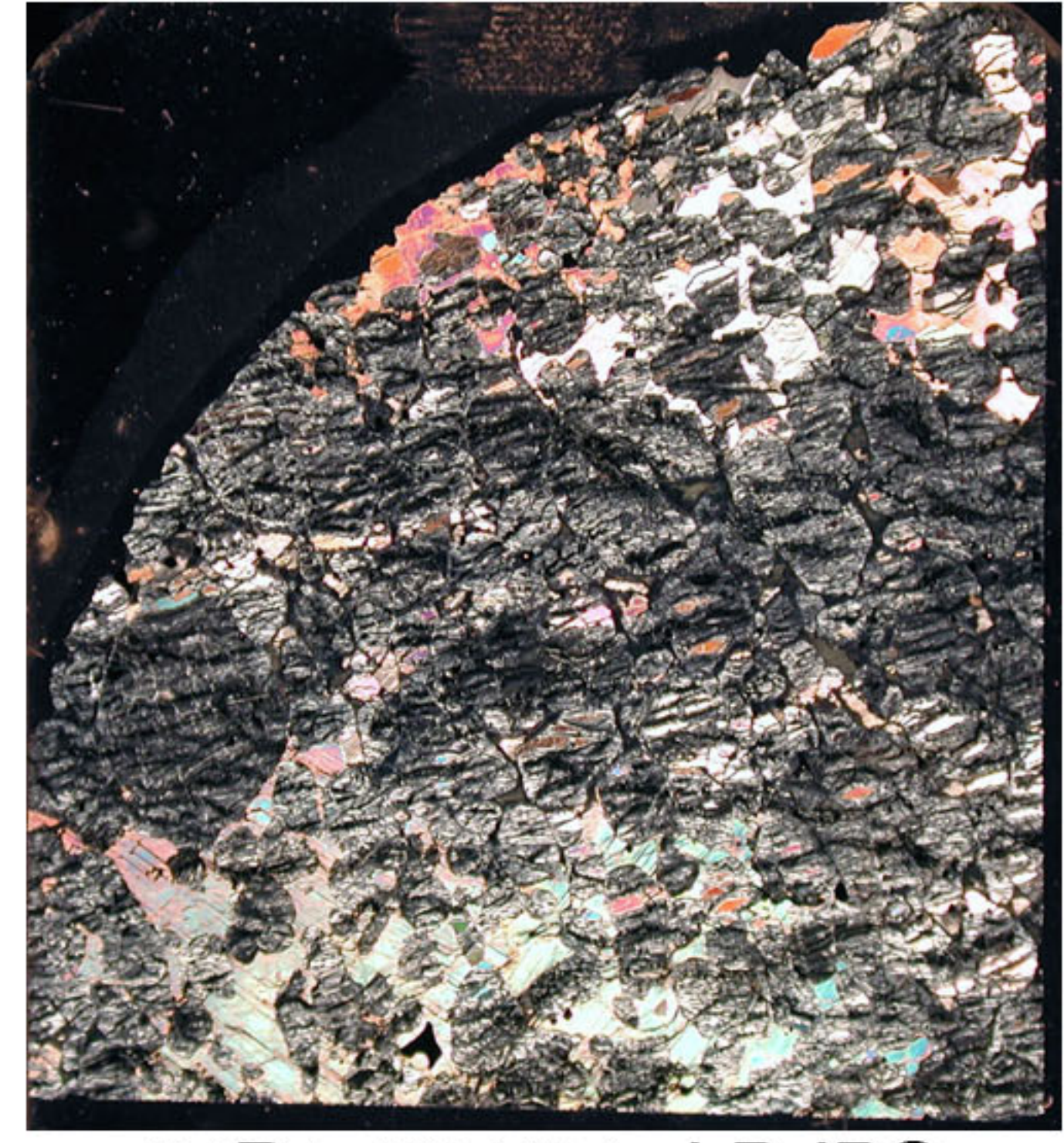
64R1_13-16_LN.jpeg



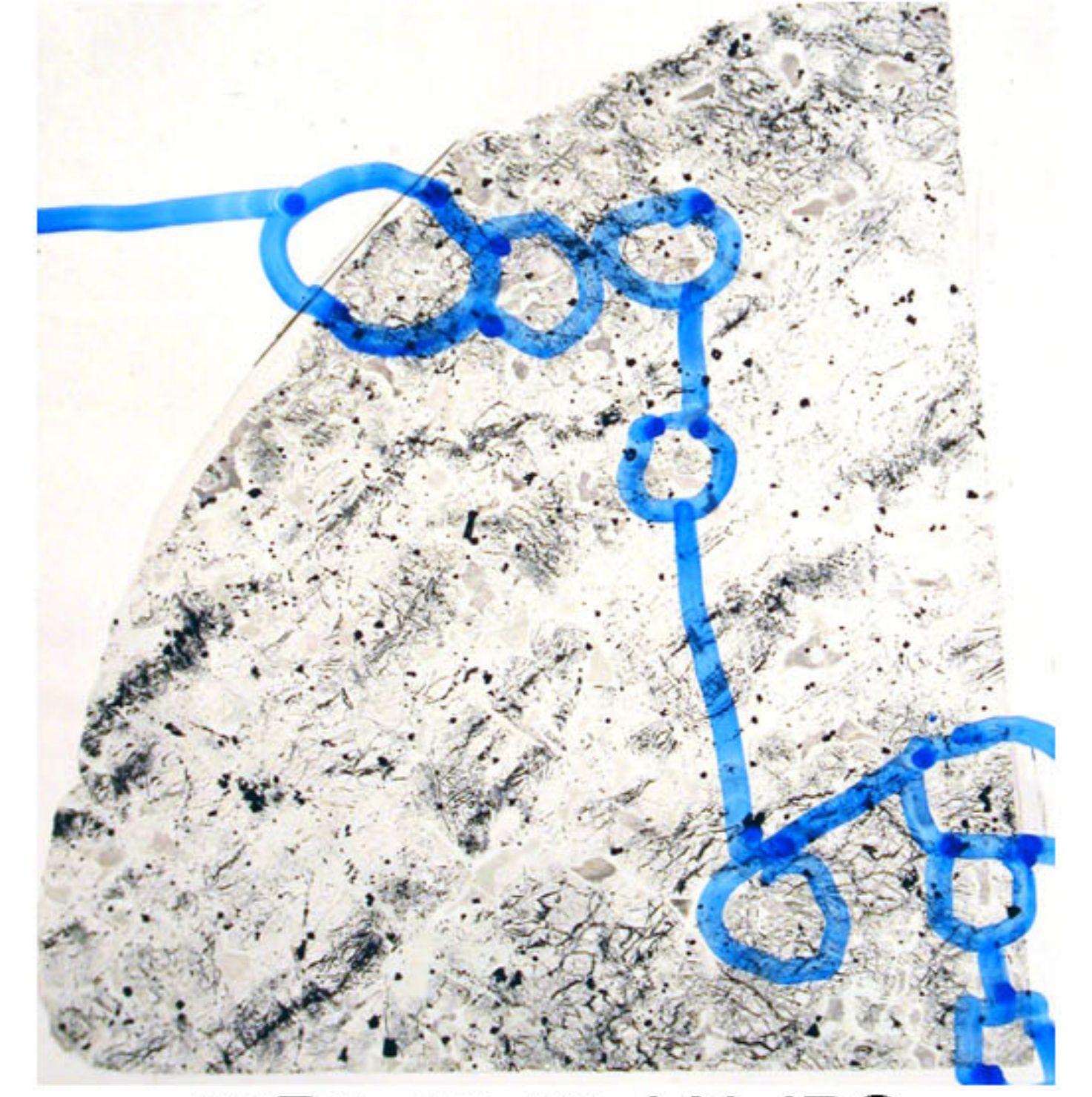
64R1_13-16_LP.JPG



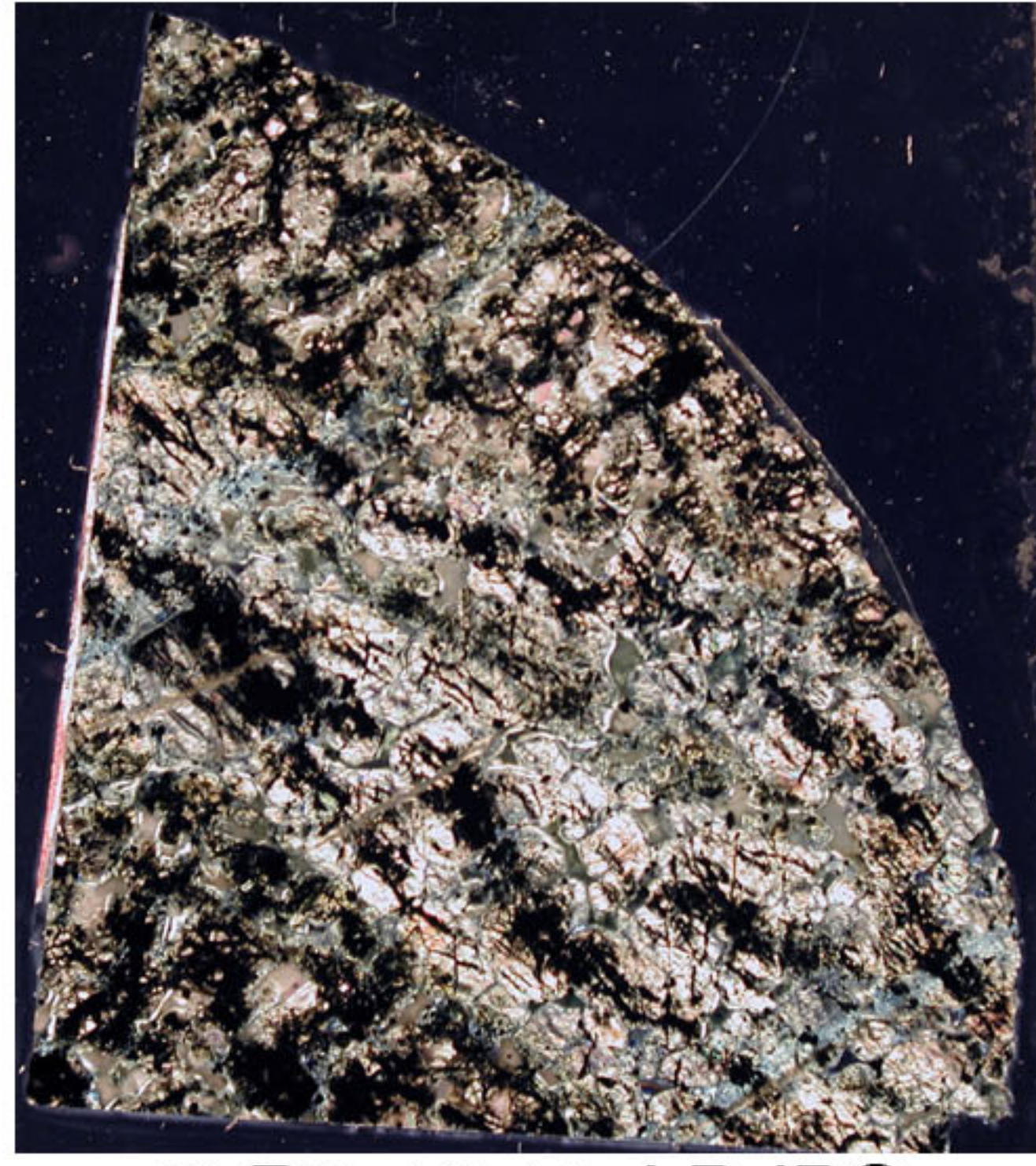
64R1_53-56.5_LN.JPG



64R1_53-56.5_LP.JPG



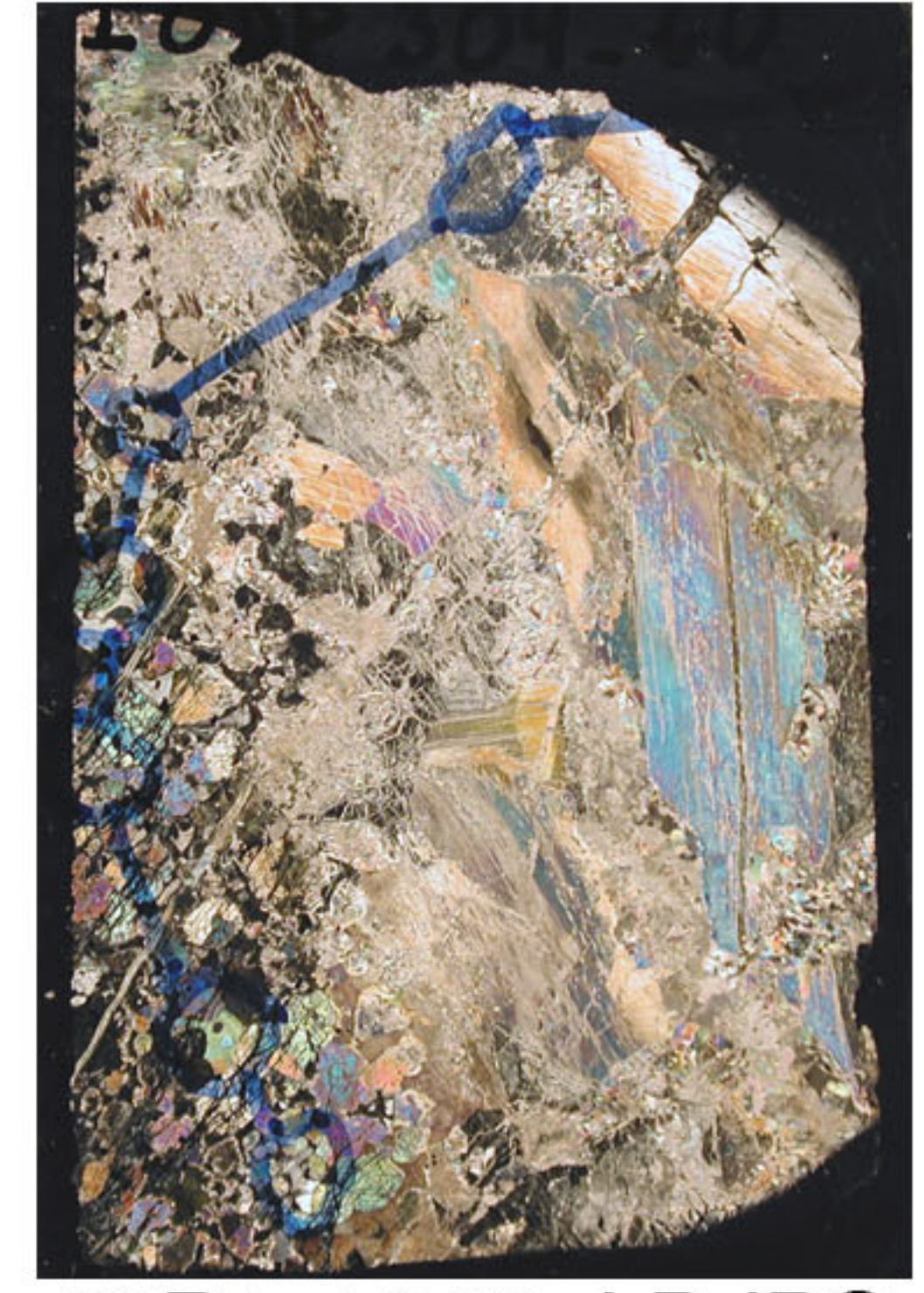
65R2_16-19_LN.JPG



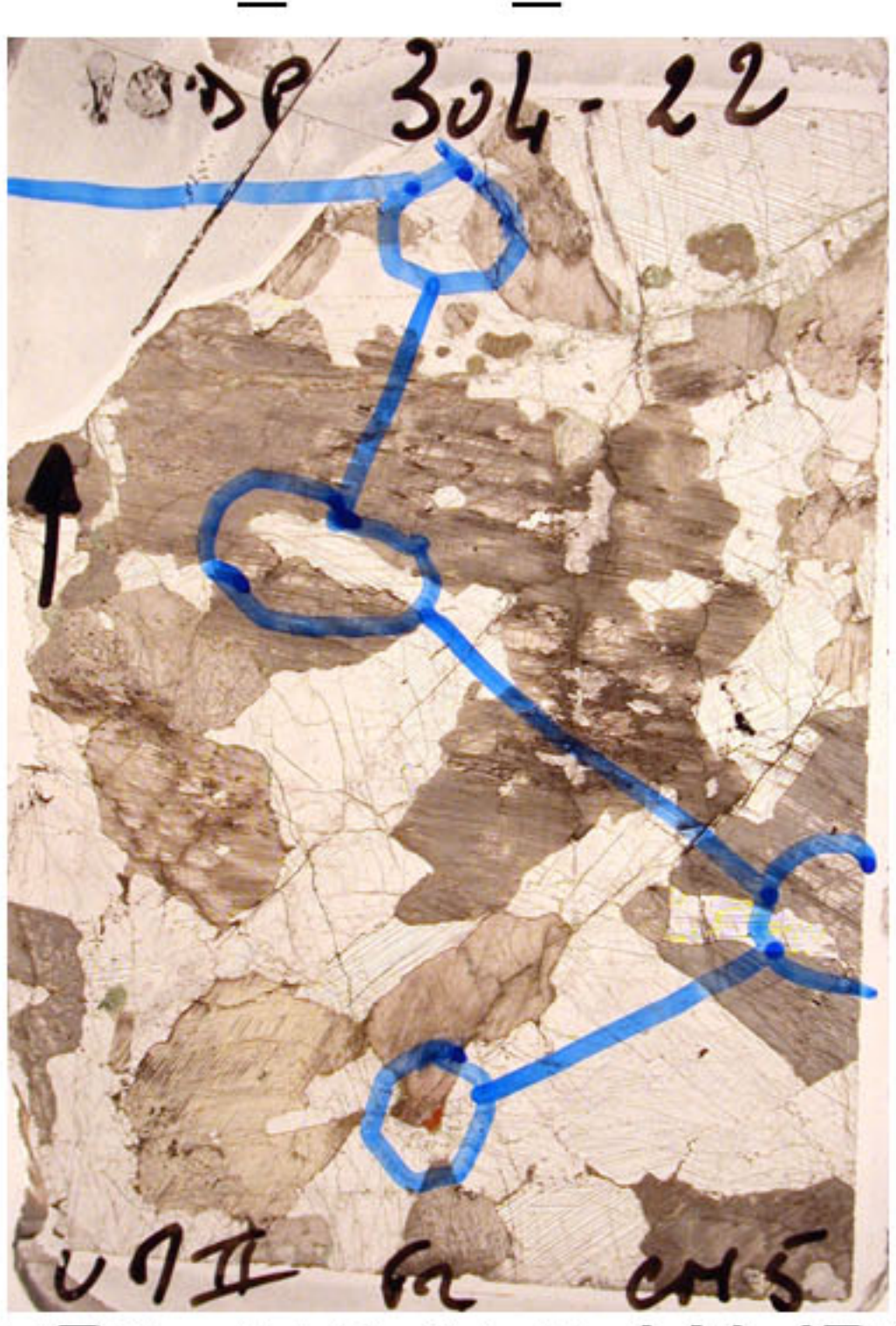
65R2_16-19_LP.JPG



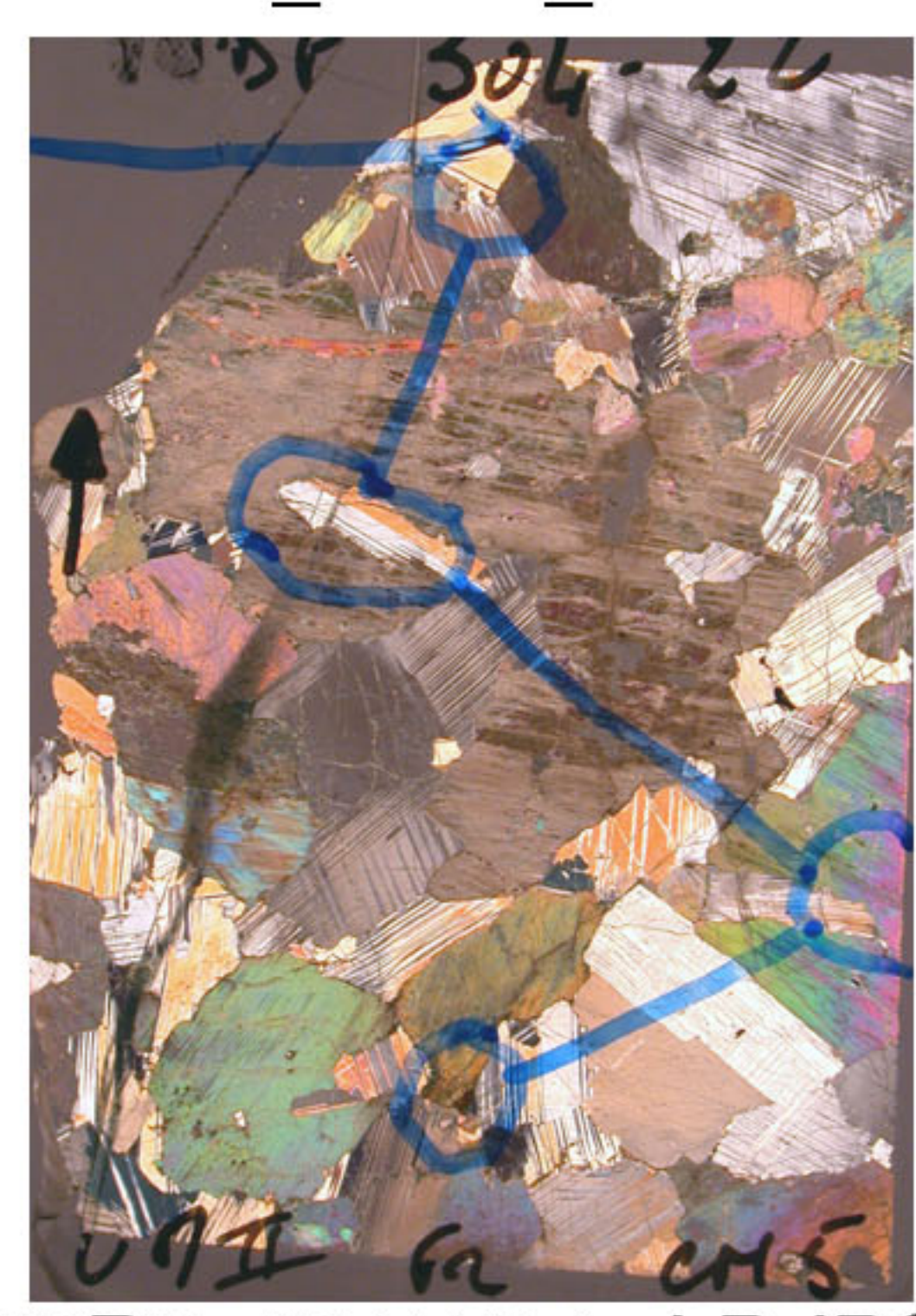
66R1_19-21_LN.JPG



66R1_19-21_LP.JPG



67R2_47.5-51.5_LN.JPG



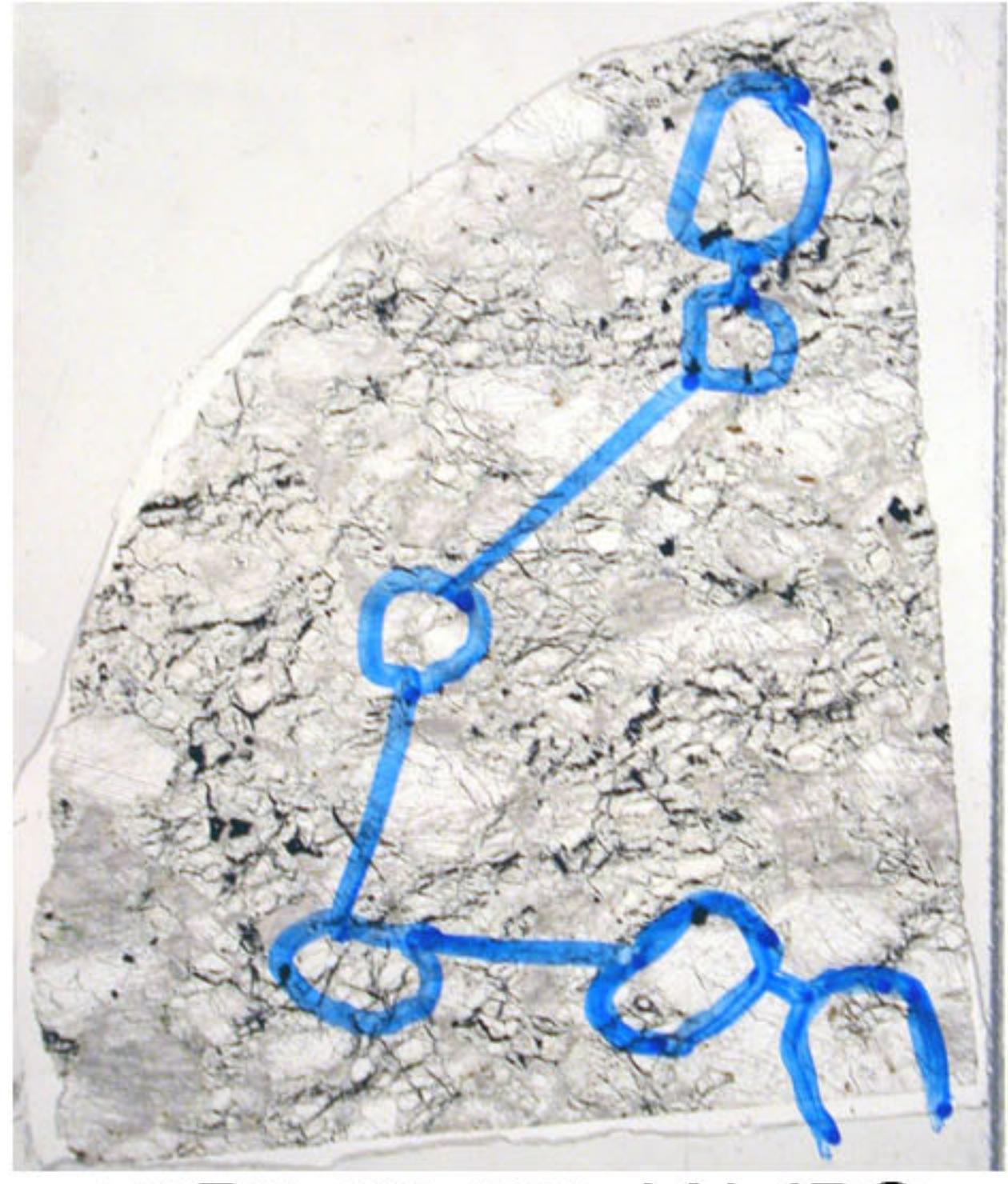
67R2_47.5-51.5_LP.JPG



69R3_6-9_LN.jpeg



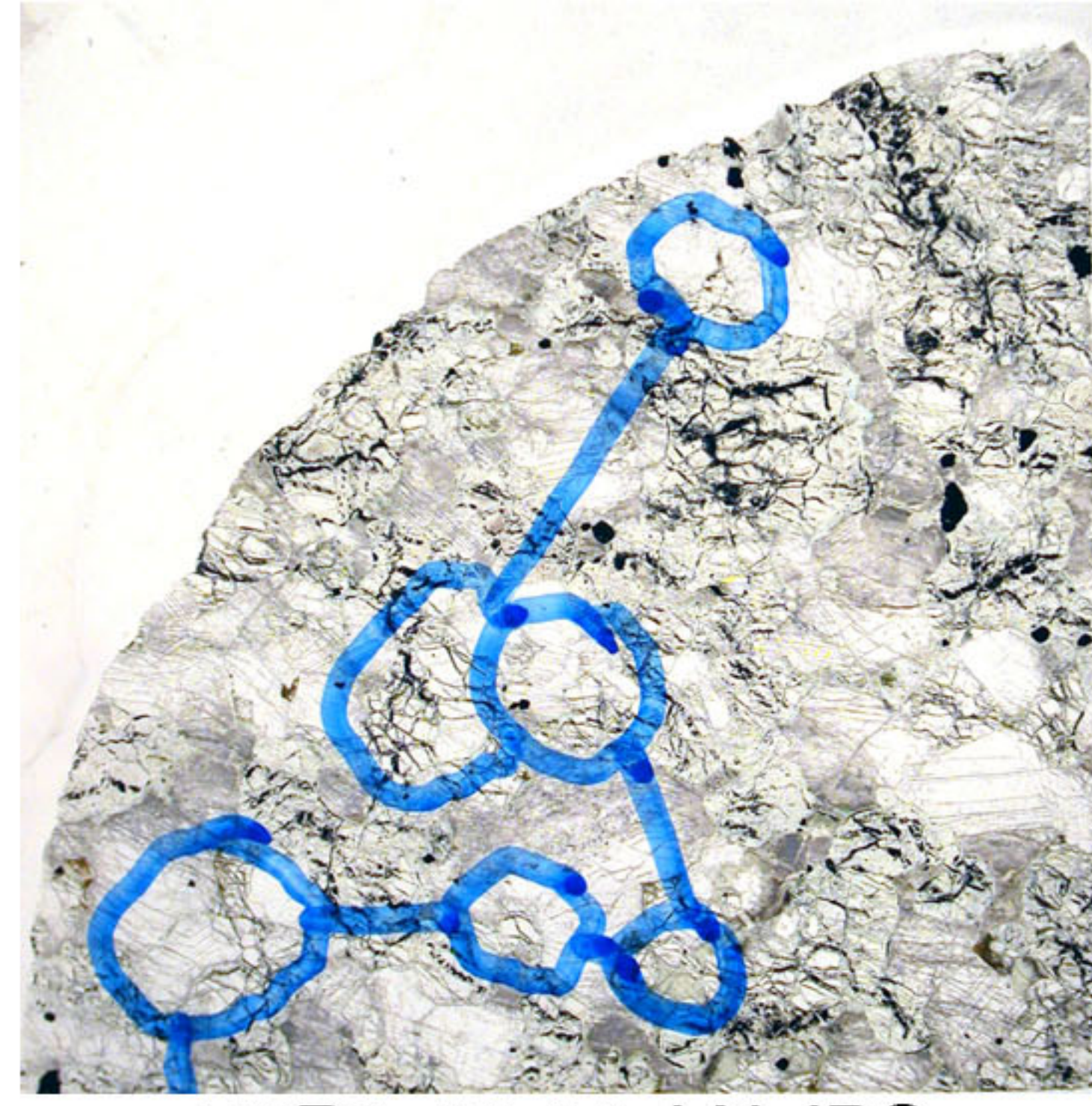
69R3_6-9_LP.JPG



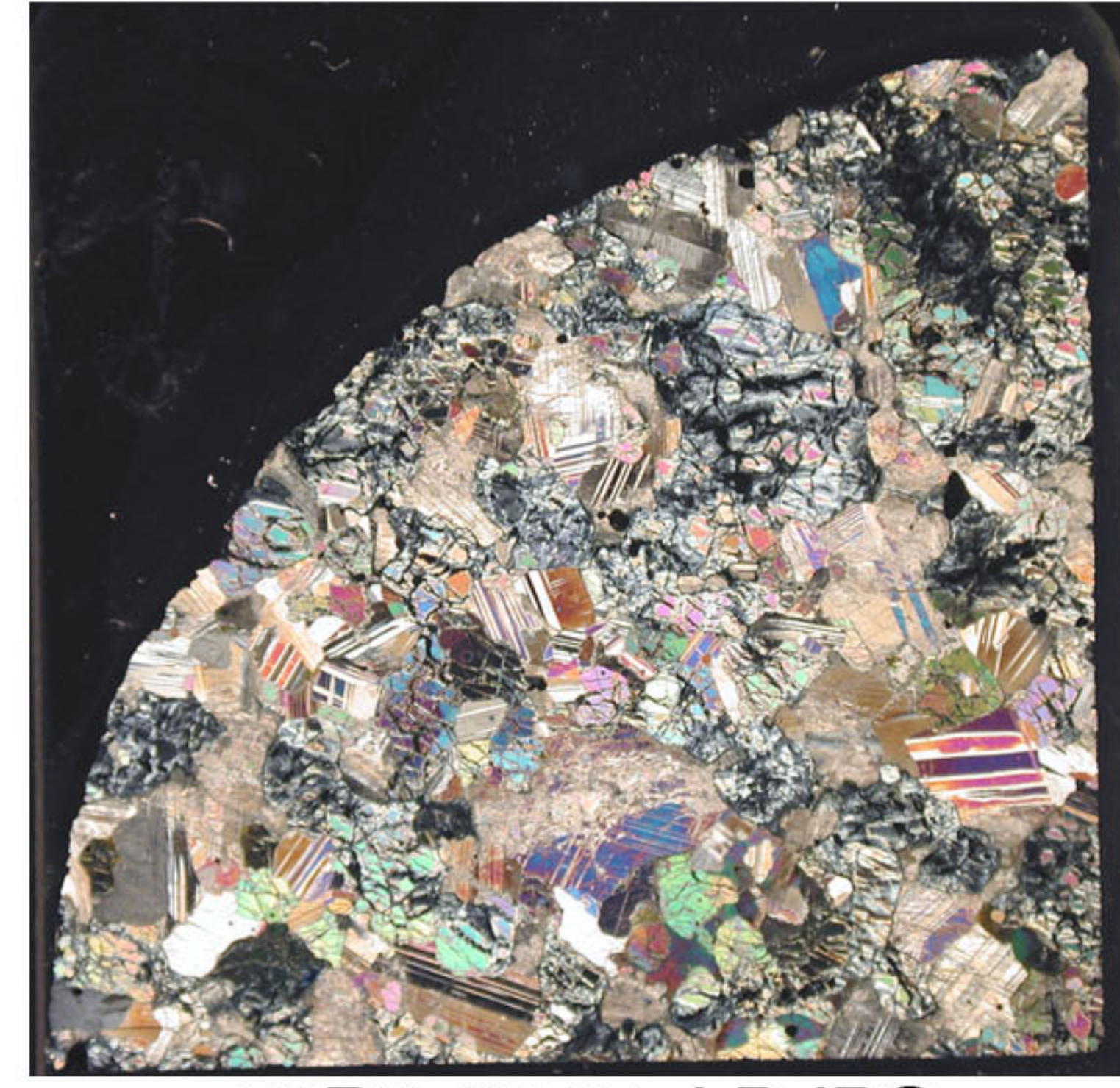
70R2_99-103_LN.JPG



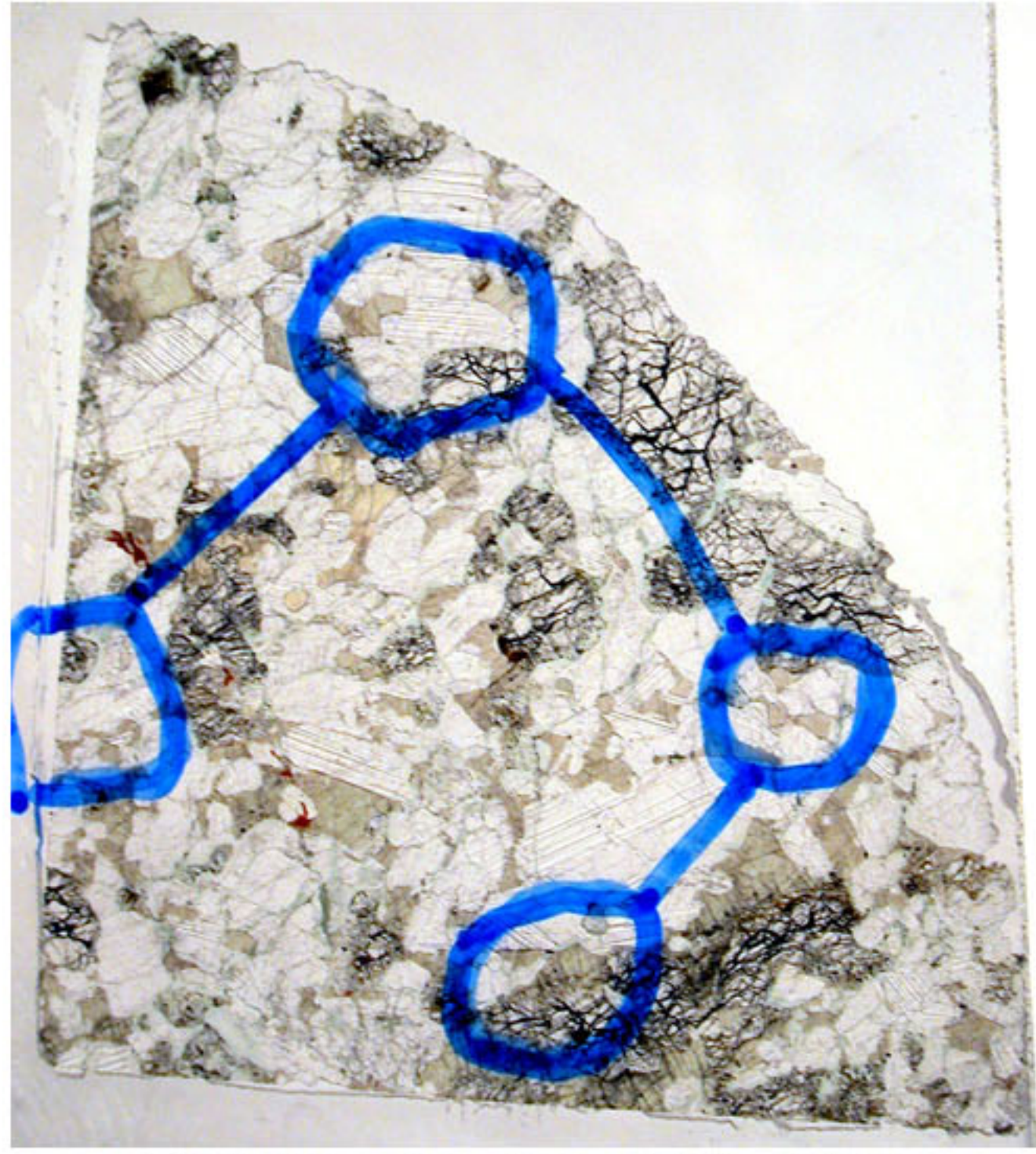
70R2_99-103_LP.JPG



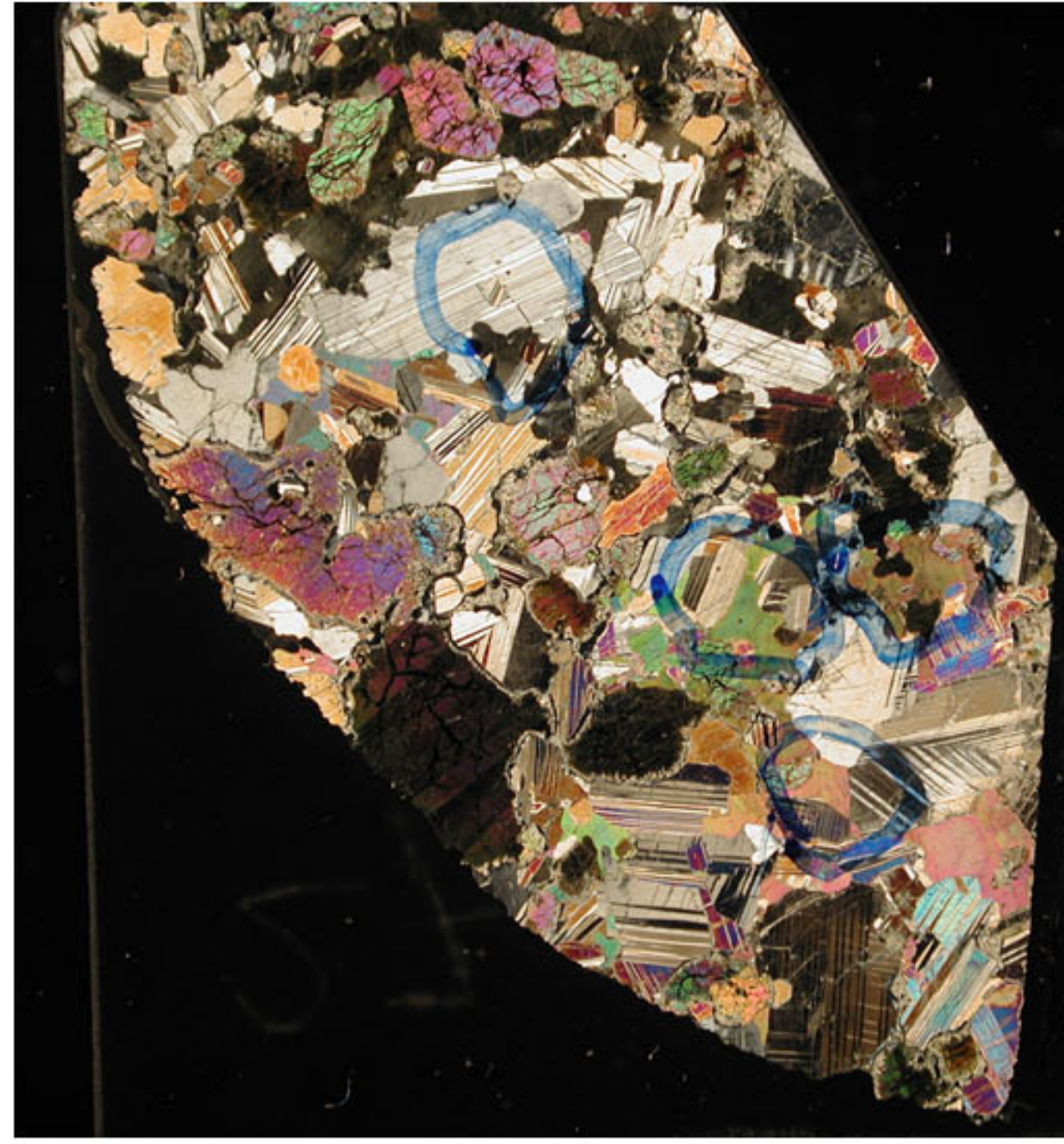
70R3_20-24_LN.JPG



70R3_20-24_LP.JPG



71R1_10-13_LN.JPG



71R1_10-13_LP.JPG

ANNEXE B

Données géochimiques

Annexe B1 : Analyse en éléments majeurs des minéraux des troctolites riches en olivine et des roches gabbroïques associées du puits IODP U1309D. Ces analyses sont reportées dans la publication suivante :

Data Report: Microprobe analyses of primary mineral phases (plagioclase, pyroxene, olivine, and spinel) from Site U1309, Atlantis Massif, Integrated Ocean Drilling Program Expedition 304/305. Miller et al. Soumis à IODP

B1-a : Composition moyenne en éléments majeurs des clinopyroxènes du puits IODP U1309D.

B1-b : Composition moyenne en éléments majeurs des plagioclases du puits IODP U1309D.

B1-c : Composition moyenne en éléments majeurs des olivines du puits IODP U1309D.

B1-d : Composition moyenne en éléments majeurs des spinelles du puits IODP U1309D.

Annexe B2 : Profils en éléments majeurs et en trace dans les minéraux des troctolites riches en olivine et des roches gabbroïques associées du puits IODP U1309D.

B2-a : Profils en éléments en trace dans les plagioclases du puits IODP U1309D.

B2-b : Profils en éléments en trace dans les clinopyroxènes du puits IODP U1309D.

B2-c : Profils en éléments en trace dans les olivines du puits IODP U1309D.

B2-d : Profils en éléments majeurs dans les olivines du puits IODP U1309D.

Annexe B3 : Analyse en éléments majeurs et en trace des minéraux des roches gabbroïques du Site ODP 1275.

B3-a : Composition moyenne en éléments majeurs des clinopyroxènes du Site ODP 1275.

B3-b : Composition moyenne en éléments majeurs des orthopyroxènes du Site ODP 1275.

B3-c : Composition moyenne en éléments majeurs des plagioclases du Site ODP 1275.

B3-d : Composition moyenne en éléments majeurs des olivines du Site ODP 1275.

B3-e : Composition moyenne en éléments majeurs des oxydes du Site ODP 1275.

B3-f : Composition moyenne en éléments en trace des clinopyroxènes du Site ODP 1275.

B3-g : Composition moyenne en éléments en trace des plagioclases du Site ODP 1275.

Data Report: Microprobe analyses of primary mineral phases (plagioclase, pyroxene, olivine, and spinel) from Site U1309, Atlantis Massif, Integrated Ocean Drilling Program Expedition 304/305¹

D. J. Miller,^{2,8} M. Abratis,³ D. Christie,⁴ M. Droin,⁵ B. Ildefonse,⁵ J. Maeda,⁶ and A. Weinsteiger⁷

¹ Submitted to Proc. IODP, Sci. Res, 304/305

² Integrated Ocean Drilling Program, Texas A&M University, 1000 Discovery Drive, College Station TX 77845-9547, USA. miller@iodp.tamu.edu

³ Institute of Geosciences, University of Jena, Burgweg 11, D-07749 Jena, GERMANY. michael.abratis@uni-jena.de

⁴ West Coast & Polar Regions Undersea Research Center, University of Alaska, Fairbanks, PO Box 757220, Fairbanks, AK 99775-7220, USA dchristie@guru.uaf.edu

⁵ Géoscience Montpellier, Université Montpellier 2, Place Eugène Bataillon, 34095 Montpellier cedex 5, FRANCE. marion.drouin@gm.univ-montp2.fr, Benoit.Ildefonse@um2.fr

⁶ Hokkaido University, Sapporo, Hokkaido 060-0810, JAPAN. jinmaeda@mail.sci.hokudai.ac.jp

⁷ College of Oceanic and Atmospheric Sciences, 104 Ocean Administration Building, Oregon State University, Corvallis OR 97331-5503, USA. weinstea@science.oregonstate.edu

⁸ Correspondence author

Abstract

This contribution is a compilation of electron microprobe analyses of primary minerals in mafic and ultramafic oceanic crustal rocks from the Atlantis Massif. The samples were recovered during Integrated Ocean Drilling Program (IODP) Expedition 304/305, which was designed to investigate the formation and evolution of oceanic core complexes. The analyses were performed at five different institutions and while common standard reference materials were not utilized at all institutions, internal standards and routine operational protocols were undertaken to assure analysis quality. More than 5000 analyses of plagioclase, pyroxene, olivine, and spinel are compiled here as a collaborative

effort to provide mineral analyses to the expedition shipboard science party and other interested researchers.

Background

IODP Expedition 304/305 was conceived to investigate the formation and evolution of oceanic core complexes exposing lithologies from the lower oceanic crust and upper mantle via long-lived detachment faulting. This expedition was the fourth location where drilling penetrated an inside corner high and/or a corrugated dome associated with a transform fault along a slow-spreading oceanic ridge. Atlantis Massif is located along the Mid Atlantic Ridge at 30°N (Fig. 1). Submersible surveys prior to this expedition suggested significant outcrops of serpentized peridotite were a characteristic feature of the Atlantis Massif. Particularly intriguing was gravity and seismic modeling which suggested high velocity, dense rock, potentially fresh mantle material, at a depth within the dome that could be attained via ocean drilling.

With a penetration of more than 1400m into oceanic basement and in excess of 80% recovery, Expedition 304/305 represents one of the hallmark achievements of scientific ocean drilling. To the delight of many and the dismay of some, the core was essentially entirely mafic, only rare thin screens of moderately to pervasive altered ultramafic rock were recovered. The primary lithologies represented in the Expedition 304/305 sample suite are, in decreasing abundance, gabbro, olivine gabbro, troctolite, oxide-bearing gabbro, oxide gabbro, gabbro-norite, and oxide- and olivine-bearing gabbro and gabbro-norite.

As a resource for researchers interested in compositional variability in ocean crust materials, several disciplinary groups from Expedition 304/305 expressed an interest in compiling data sets for publication in the Scientific Results volume of IODP. This volume presents an ideal venue for these data compilations, making vast amounts of data available to not only other members of the shipboard science party, but also to the earth sciences community.

Methods and data tables

Samples were processed at five institutions, Université Montpellier 2, France, University of Mainz, Germany, Hokkaido University, Sapporo, Japan, and Oregon State University and Texas A&M University, USA. Analytical conditions for each facility are listed in Table 1. Analytical results are presented in Table 2. All analytical data tables include estimated depth to the sample. This value is based on curated depth to the top of each core, thus the relative depth of samples in subsequent cores may be in error by as much as a few tens of cm. By IODP convention, when recovery is less than 100%, all the recovered material is curated from the top of the cored interval, thus introducing another shift in the reported recovery depth. Most analyses are reported individually, but in some cases are reported as the arithmetic average of several analyses (designated in data table by the number of individual analyses represented).

Acknowledgements

This research used samples provided by the Integrated Ocean Drilling Program (IODP).

References

Expedition 304/305 Scientists, 2006. Expedition 304/305 summary. In Blackman, D.K., Ildefonse, B., John, B.E., Ohara, Y., Miller, D.J., MacLeod, C.J., and the Expedition 304/305 Scientists, Proc. IODP, 304/305: College Station TX (Integrated Ocean Drilling Program Management International, Inc.). doi:10.2204/iodp.proc.304305.101.2006

Figure Caption

Figure F1. A Mid-Atlantic Ridge bathymetry (base image from www.ngdc.noaa.gov/mgg/image/2minrelief.html) B) Site U1309 on Atantis Massif. Base map from Expedition 304/305 Initial Report (Expedition 304/305 Scientists, 2006).

Table captions

Table 1. Analytical methods

Table 2. Mineral analyses

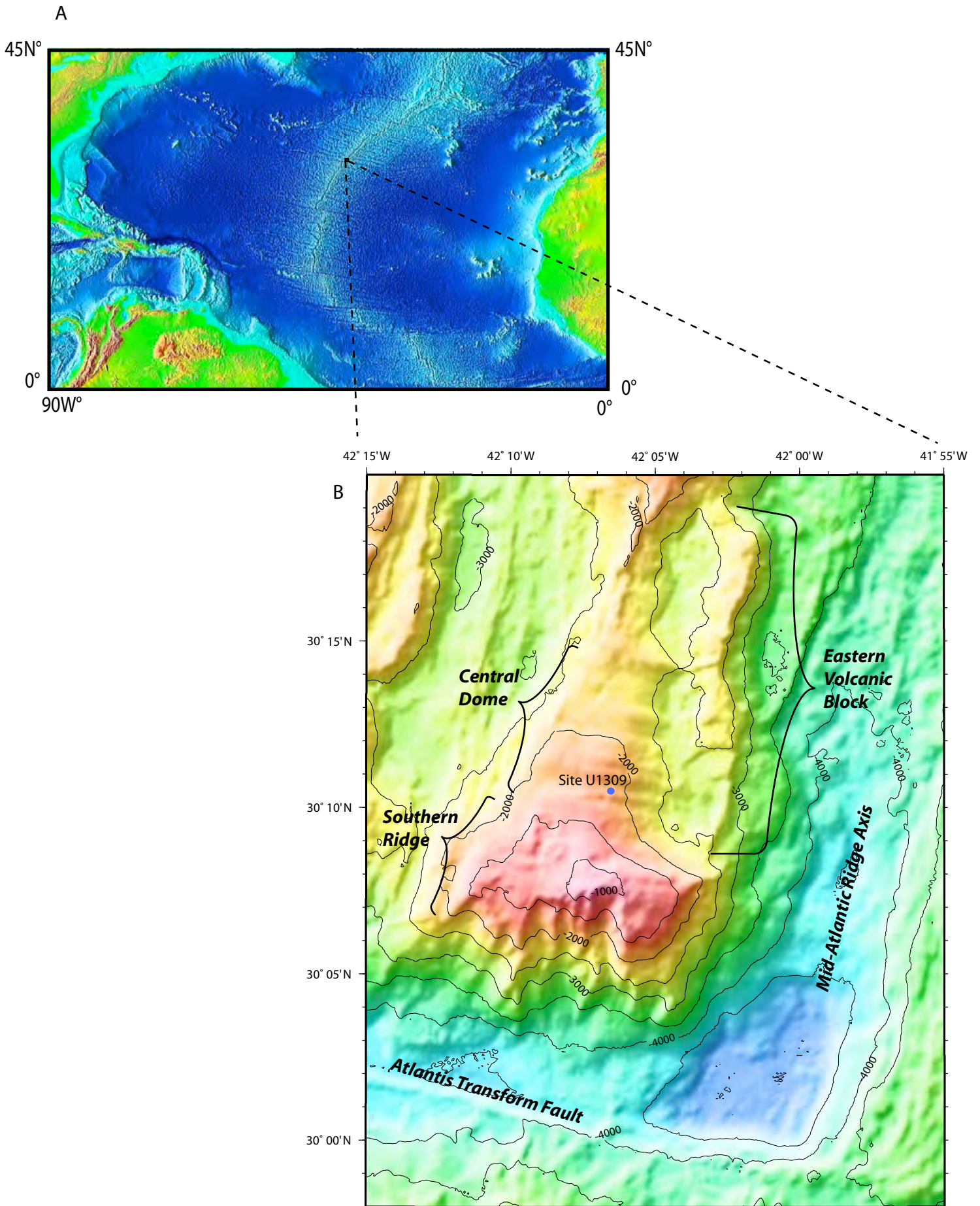


Figure 1.

Table 1

Laboratory: Institute of Geosciences, University of Mainz, Germany

EPMA Probe: JEOL JXA-8900RL

Acceleration voltage: 15 KV

Probe current: 12 nA

Beam diameter: 2 μm

Count time on peak:

Major elements (Si, Na, K, Ti, Fe, Al, Mg, Ca): 15 sec

Trace elements (Cr, Mn, Ni): 30 sec

Count time on background:

Major elements: 5 sec

Trace elements: 15 sec

SRM: wolla, cor, mg, fe, mn-ti, dio

Laboratory: Montpellier 2 University

EPMA Probe: Cameca SX100

Acceleration voltage: 20 KV

Probe current: 10 nA

Count time on peak: 30s for all elements

SRM: Al₂O₃, wolla, TiO₂, albite, forst, Cr₂O₃, rhodo, Fe₂O₃, orthose, Ni,

Laboratory: Oregon State University

EPMA Probe: Cameca SX100

Acceleration voltage: 15 KV

Probe current: 30 nA

Beam diameter: 1 mm

Count time on peak: 20-40 s

SRM: labradorite, kakanui augite, basalt, K-feldspar

Laboratory: Texas A&M University

EPMA Probe: Cameca SX50

Acceleration voltage: 15 KV

Probe current: 30 nA

Beam diameter: 10 μm

Count time on peak: 20-40 s

SRM: albite, fayalite, olivine, orthoclase, CaSiO₃, FeTiO₃, spessartine, spinel, chromite

Laboratory: Hokkaido University

EMPA probe: JEOL Superprobe 733 and JEOL 8800R Superprobe

Acceleration voltage: 15-keV

Probe current: 20 nA

Beam diameter: 10 μm

Count time on peak: 10-40s

SRM: synthetic oxides and natural minerals

SRM=standard reference materials

Tableau B1-a: Composition moyenne en éléments majeurs des clinopyroxènes du puits IODP U1309D non-analysés par LA-ICPMS et LA-HR-ICPMS*

| Echantillon | Profondeur (mbsf) | Zones | Type de roche | texture | Localisation | n | SiO2 | TiO2 | Al2O3 | Cr2O3 | FeO | MnO | MgO | CaO | Na2O | K2O | NiO | Total | Mg# |
|----------------|-------------------|-------|------------------------|--------------|--------------|----|-------|------|-------|-------|-------|------|-------|-------|------|------|------|--------|-------|
| 61R1_11-14 | 314.91 | 1 | troctolite riche en ol | poecilitique | | 11 | 51.89 | 0.40 | 3.82 | 1.45 | 3.58 | 0.13 | 16.18 | 21.82 | 0.40 | 0.00 | 0.04 | 99.71 | 88.96 |
| 63R3_36-39 | 327.72 | 1 | troctolite riche en ol | interstitiel | | 7 | 52.08 | 0.33 | 3.79 | 1.44 | 3.91 | 0.14 | 17.06 | 20.35 | 0.43 | 0.00 | 0.04 | 99.59 | 88.67 |
| 64R1_53-56.5 | 329.73 | 1 | troctolite riche en ol | interstitiel | c | 11 | 51.93 | 0.38 | 3.78 | 1.45 | 3.55 | 0.13 | 16.85 | 20.85 | 0.40 | 0.00 | 0.04 | 99.37 | 89.44 |
| | | | gabbro cumulus | | b | 3 | 52.16 | 0.42 | 3.34 | 1.35 | 3.24 | 0.12 | 16.30 | 21.81 | 0.43 | 0.00 | 0.03 | 99.20 | 89.98 |
| 66R1_18-21 | 338.98 | 1 | troctolite riche en ol | poecilitique | | 1 | 53.12 | 0.42 | 3.33 | 1.16 | 5.73 | 0.16 | 20.39 | 15.64 | 0.33 | 0.00 | 0.03 | 100.31 | 86.37 |
| | | | gabbro cumulus | | c | 3 | 52.02 | 0.43 | 3.65 | 1.33 | 4.07 | 0.14 | 16.73 | 20.64 | 0.41 | 0.00 | 0.04 | 99.45 | 88.01 |
| 67R2_47.5-51.5 | 345.495 | 1 | troctolite riche en ol | poecilitique | c | 7 | 52.73 | 0.47 | 2.58 | 0.16 | 7.50 | 0.22 | 17.04 | 18.84 | 0.27 | 0.00 | 0.02 | 99.82 | 80.36 |
| | | | gabbro cumulus | | b | 5 | 52.66 | 0.49 | 2.62 | 0.19 | 7.07 | 0.21 | 16.54 | 19.71 | 0.30 | 0.00 | 0.02 | 99.81 | 80.68 |
| 111R4_50-54 | 554.07 | 2 | troctolite riche en ol | poecilitique | c | 4 | 51.89 | 0.54 | 3.70 | 1.38 | 3.96 | 0.15 | 16.39 | 21.37 | 0.41 | 0.00 | 0.05 | 99.83 | 88.08 |
| | | | gabbro cumulus | | b | 2 | 52.26 | 0.42 | 3.73 | 1.41 | 4.33 | 0.14 | 16.86 | 20.51 | 0.39 | 0.00 | 0.03 | 100.08 | 87.43 |
| 112R2_16-20 | 555.86 | 2 | troctolite riche en ol | poecilitique | c | 3 | 52.08 | 0.42 | 3.14 | 0.51 | 6.11 | 0.17 | 16.84 | 19.71 | 0.33 | 0.00 | 0.02 | 99.33 | 83.11 |
| | | | gabbro cumulus | | b | 2 | 51.92 | 0.59 | 2.99 | 0.44 | 6.08 | 0.17 | 16.45 | 20.37 | 0.34 | 0.00 | 0.01 | 99.38 | 82.82 |
| 112R3_22-25 | 557.24 | 2 | troctolite riche en ol | interstitiel | | 4 | 52.54 | 0.66 | 3.18 | 1.20 | 4.26 | 0.16 | 17.21 | 20.33 | 0.43 | 0.00 | 0.04 | 100.01 | 87.84 |
| | | | gabbro cumulus | | | 1 | 52.78 | 0.65 | 2.84 | 0.13 | 6.72 | 0.19 | 15.39 | 21.33 | 0.38 | 0.01 | 0.01 | 100.41 | 80.32 |
| 136R1_94-98 | 670.34 | 3 | troctolite riche en ol | poecilitique | | 2 | 51.92 | 0.41 | 3.78 | 1.30 | 5.48 | 0.19 | 16.32 | 20.01 | 0.41 | 0.00 | 0.02 | 99.85 | 84.15 |
| 136R2_60-64 | 671.36 | 3 | troctolite riche en ol | poecilitique | c | 5 | 52.87 | 0.34 | 3.64 | 1.16 | 4.26 | 0.13 | 16.70 | 21.07 | 0.35 | 0.00 | 0.04 | 100.57 | 87.48 |
| | | | gabbro cumulus | | b | 1 | 53.05 | 0.54 | 2.94 | 0.54 | 4.31 | 0.15 | 16.10 | 22.33 | 0.35 | 0.00 | 0.06 | 100.35 | 86.95 |
| 227R1_10-15 | 1092.1 | 4 | troctolite riche en ol | poecilitique | c | 4 | 52.01 | 0.44 | 2.83 | 0.32 | 7.16 | 0.21 | 14.81 | 21.34 | 0.37 | 0.00 | 0.02 | 99.52 | 78.67 |
| | | | gabbro cumulus | | b | 2 | 52.11 | 0.51 | 2.75 | 0.24 | 6.82 | 0.23 | 15.15 | 21.75 | 0.34 | 0.00 | 0.04 | 99.94 | 79.84 |
| 227R2_71-74 | 1094.14 | 4 | troctolite riche en ol | poecilitique | c | 11 | 51.59 | 0.26 | 3.96 | 1.32 | 4.61 | 0.14 | 15.96 | 20.94 | 0.42 | 0.00 | 0.03 | 99.24 | 86.05 |
| | | | gabbro cumulus | | b | 3 | 51.50 | 0.29 | 3.73 | 1.20 | 4.84 | 0.16 | 16.95 | 20.32 | 0.37 | 0.00 | 0.04 | 99.39 | 86.19 |
| 228R1_33-37 | 1097.13 | 4 | troctolite riche en ol | poecilitique | c | 2 | 51.27 | 0.36 | 3.83 | 1.35 | 4.87 | 0.15 | 16.50 | 20.51 | 0.39 | 0.00 | 0.03 | 99.27 | 85.81 |
| 228R1_66-70 | 1097.46 | 4 | troctolite riche en ol | interstitiel | b | 2 | 51.40 | 0.38 | 3.64 | 1.27 | 5.09 | 0.16 | 17.35 | 19.65 | 0.34 | 0.01 | 0.04 | 99.31 | 85.88 |
| 228R1_79-82 | 1097.59 | 4 | troctolite riche en ol | interstitiel | | 5 | 51.98 | 0.51 | 2.70 | 0.37 | 6.27 | 0.20 | 16.54 | 20.18 | 0.31 | 0.00 | 0.02 | 99.08 | 82.45 |
| 228R2_42-45 | 1098.43 | 4 | troctolite riche en ol | poecilitique | | 10 | 52.03 | 0.40 | 3.54 | 1.12 | 4.75 | 0.16 | 16.94 | 19.93 | 0.36 | 0.00 | 0.03 | 99.26 | 86.45 |
| | | | gabbro cumulus | | | 4 | 51.71 | 0.42 | 3.73 | 1.33 | 4.46 | 0.13 | 16.14 | 21.07 | 0.44 | 0.00 | 0.05 | 99.48 | 86.59 |
| 228R3_22-25 | 1099.73 | 4 | troctolite riche en ol | poecilitique | | 6 | 51.70 | 0.44 | 3.69 | 1.30 | 4.61 | 0.14 | 16.29 | 20.74 | 0.40 | 0.00 | 0.04 | 99.35 | 86.32 |
| 231R3_0-3 | 1113.1 | 4 | gabbro à ol | cumulus | | 14 | 52.30 | 0.54 | 2.74 | 0.35 | 6.09 | 0.19 | 16.23 | 20.42 | 0.32 | 0.00 | 0.02 | 99.20 | 82.61 |
| | | | filonet | | c | 2 | 52.32 | 0.42 | 2.97 | 0.48 | 5.22 | 0.18 | 16.61 | 21.17 | 0.32 | 0.00 | 0.03 | 99.73 | 85.01 |
| 232R1_9-13 | 1115.19 | 4 | troctolite riche en ol | poecilitique | b | 2 | 52.36 | 0.48 | 2.87 | 0.48 | 5.17 | 0.17 | 16.91 | 20.84 | 0.34 | 0.00 | 0.03 | 99.66 | 85.35 |
| | | | gabbro cumulus | | | 6 | 52.34 | 0.45 | 2.92 | 0.48 | 5.19 | 0.17 | 16.76 | 21.01 | 0.33 | 0.00 | 0.03 | 99.70 | 85.18 |
| 233R1_31-34 | 1120.21 | 4 | troctolite riche en ol | poecilitique | | 1 | 51.79 | 0.42 | 3.39 | 0.97 | 4.58 | 0.14 | 16.49 | 20.31 | 0.42 | 0.00 | 0.05 | 98.56 | 86.52 |
| 233R1_135-139 | 1121.25 | 4 | troctolite riche en ol | interstitiel | | 4 | 51.51 | 0.51 | 3.64 | 1.22 | 4.67 | 0.16 | 16.58 | 20.56 | 0.41 | 0.01 | 0.05 | 99.31 | 86.35 |
| 233R2_109-112 | 1122.49 | 4 | troctolite riche en ol | interstitiel | | 1 | 52.17 | 0.48 | 3.52 | 1.29 | 4.94 | 0.15 | 17.45 | 19.01 | 0.37 | 0.01 | 0.02 | 99.40 | 86.30 |
| | | | gabbro cumulus | | c | 4 | 52.78 | 0.46 | 2.86 | 0.50 | 5.45 | 0.16 | 17.20 | 19.84 | 0.30 | 0.00 | 0.02 | 99.58 | 84.90 |
| 235R1_29-34 | 1129.79 | 4 | troctolite riche en ol | poecilitique | b | 2 | 52.47 | 0.56 | 2.83 | 0.44 | 5.41 | 0.18 | 16.17 | 21.04 | 0.32 | 0.00 | 0.03 | 99.44 | 84.24 |
| | | | gabbro cumulus | | | 3 | 52.68 | 0.50 | 2.85 | 0.48 | 5.44 | 0.16 | 16.85 | 20.24 | 0.31 | 0.00 | 0.02 | 99.53 | 84.68 |
| 235R2_13-16 | 1130.89 | 4 | troctolite riche en ol | interstitiel | | 4 | 52.94 | 0.39 | 2.79 | 0.30 | 5.61 | 0.16 | 17.09 | 19.90 | 0.28 | 0.00 | 0.03 | 99.50 | 84.48 |
| 247R3_62-66 | 1190.51 | 4 | troctolite riche en ol | poecilitique | | 5 | 51.84 | 0.43 | 3.52 | 1.19 | 4.97 | 0.14 | 16.95 | 19.67 | 0.39 | 0.00 | 0.04 | 99.16 | 85.91 |
| 248R4_19-23 | 1196.11 | 4 | troctolite riche en ol | poecilitique | | 6 | 52.16 | 0.49 | 3.33 | 1.07 | 4.78 | 0.17 | 16.35 | 20.35 | 0.39 | 0.00 | 0.02 | 99.12 | 85.93 |
| 248R4_65-69 | 1196.57 | 4 | troctolite riche en ol | poecilitique | | 6 | 51.43 | 0.68 | 2.47 | 0.12 | 10.11 | 0.28 | 15.03 | 18.83 | 0.35 | 0.00 | 0.02 | 99.31 | 72.73 |

*Les analyses en éléments majeurs ont été réalisées par microsonde électronique (% poids d'oxyde). Abbréviation: n= nombre d'analyses par mineral; c= cœur, b= bordure.
Mg# = (Mg/Mg+Fe)*100

Tableau B1-b: Composition moyenne en éléments majeurs des plagioclases du puits IODP U1309D*

| Echantillon | 63R3_36-39 | 64R1_53-56.5 | 65R2_16-19 | 66R1_18-21 | 67R2_47.5-51.5 | IIIR4_14-17 | IIIR4_50-54 | II2R1_69-73 | II2R3_22-25 | II2R2_16-20 | 136R1_94-98 | | | |
|---------------|------------------------|------------------------|------------------------|------------------------|----------------|------------------------|------------------------|------------------------|------------------------|-------------|-------------------|--------|--------|--------|
| Type de roche | troctolite riche en ol | troctolite riche en ol | troctolite riche en ol | troctolite riche en ol | gabbro | troctolite riche en ol | troctolite riche en ol | troctolite riche en ol | troctolite riche en ol | gabbro | troctolite gabbro | | | |
| Profondeur | 327.72 | 329.73 | 335.66 | 338.98 | 345.495 | 553.71 | 554.07 | 554.89 | 557.24 | 555.86 | 670.34 | 670.34 | | |
| Zones | 1 | 1 | 1 | 1 | 1 | 2 | 2 | 2 | 2 | 2 | 3 | 3 | | |
| n | 6 | 7 | 8 | 4 | 12 | 11 | 5 | 6 | 5 | 11 | 4 | 3 | | |
| % | | | | | | | | | | | | | | |
| SiO2 | 48.06 | 50.04 | 47.54 | 51.04 | 48.26 | 51.77 | 0.05 | 48.28 | 48.02 | 47.63 | 47.45 | 50.26 | 49.52 | 54.01 |
| TiO2 | 0.03 | 0.05 | 0.02 | 0.04 | 0.02 | 0.05 | 0.03 | 0.03 | 0.03 | 0.05 | 0.04 | 0.08 | 0.05 | 0.06 |
| Al2O3 | 33.32 | 31.96 | 33.51 | 31.05 | 32.95 | 30.73 | 33.02 | 33.02 | 33.05 | 32.87 | 31.51 | 31.40 | 32.43 | 29.29 |
| Cr2O3 | 0.01 | 0.00 | 0.01 | 0.00 | 0.01 | 0.01 | 0.01 | 0.01 | 0.01 | 0.01 | 0.01 | 0.01 | 0.01 | 0.00 |
| FeO | 0.15 | 0.10 | 0.11 | 0.32 | 0.16 | 0.22 | 0.14 | 0.14 | 0.15 | 0.16 | 0.16 | 0.23 | 0.22 | 0.37 |
| MnO | 0.01 | 0.01 | 0.01 | 0.01 | 0.01 | 0.01 | 0.00 | 0.00 | 0.01 | 0.01 | 0.17 | 0.01 | 0.01 | 0.00 |
| MgO | 0.02 | 0.03 | 0.01 | 0.06 | 0.01 | 0.03 | 0.03 | 0.03 | 0.04 | 0.05 | 1.51 | 0.05 | 0.03 | 0.03 |
| CaO | 16.28 | 14.63 | 16.38 | 13.87 | 15.91 | 13.34 | 15.87 | 16.07 | 16.07 | 15.91 | 13.95 | 14.15 | 15.30 | 11.67 |
| Na2O | 2.37 | 3.35 | 2.34 | 3.73 | 2.52 | 4.08 | 2.60 | 2.53 | 2.53 | 2.43 | 2.54 | 3.52 | 3.02 | 5.11 |
| K2O | 0.02 | 0.03 | 0.01 | 0.03 | 0.02 | 0.03 | 0.02 | 0.02 | 0.02 | 0.01 | 0.03 | 0.03 | 0.01 | 0.05 |
| Total | 100.27 | 100.20 | 99.93 | 100.15 | 99.87 | 100.28 | 100.02 | 99.92 | 99.92 | 99.13 | 100.48 | 99.73 | 100.60 | 100.61 |
| An (Ca) | 79.05 | 70.57 | 79.41 | 67.16 | 77.58 | 64.24 | 77.02 | 77.76 | 77.76 | 78.30 | 74.77 | 68.89 | 73.66 | 55.64 |
| σ | | | | | | | | | | | | | | |
| SiO2 | 0.22 | - | 0.37 | 0.14 | 0.09 | 0.74 | 0.14 | 0.52 | 0.62 | 0.62 | 3.95 | 0.41 | 0.52 | 0.09 |
| TiO2 | 0.01 | - | 0.01 | 0.01 | 0.01 | 0.01 | 0.01 | 0.02 | 0.01 | 0.01 | 0.01 | 0.02 | 0.01 | 0.03 |
| Al2O3 | 0.13 | - | 0.27 | 0.06 | 0.08 | 0.46 | 0.13 | 0.31 | 0.37 | 0.37 | 2.92 | 0.37 | 0.34 | 0.10 |
| Cr2O3 | 0.01 | - | 0.01 | 0.00 | 0.01 | 0.01 | 0.01 | 0.01 | 0.01 | 0.01 | 0.01 | 0.01 | 0.01 | 0.00 |
| FeO | 0.02 | - | 0.04 | 0.02 | 0.03 | 0.02 | 0.02 | 0.04 | 0.01 | 0.01 | 6.99 | 0.03 | 0.04 | 0.02 |
| MnO | 0.01 | - | 0.01 | 0.01 | 0.01 | 0.01 | 0.00 | 0.01 | 0.01 | 0.01 | 0.37 | 0.01 | 0.01 | 0.01 |
| MgO | 0.00 | - | 0.01 | 0.02 | 0.01 | 0.01 | 0.01 | 0.01 | 0.01 | 0.01 | 3.34 | 0.02 | 0.01 | 0.01 |
| CaO | 0.17 | - | 0.29 | 0.07 | 0.16 | 0.54 | 0.09 | 0.19 | 0.46 | 0.46 | 3.79 | 0.45 | 0.41 | 0.10 |
| Na2O | 0.09 | - | 0.16 | 0.05 | 0.07 | 0.33 | 0.07 | 0.15 | 0.33 | 0.33 | 0.56 | 0.26 | 0.23 | 0.10 |
| K2O | 0.02 | - | 0.01 | 0.01 | 0.02 | 0.02 | 0.01 | 0.01 | 0.01 | 0.01 | 0.02 | 0.00 | 0.00 | 0.01 |
| Total | 0.14 | - | 0.27 | 0.23 | 0.17 | 0.32 | 0.29 | 0.64 | 0.64 | 0.17 | 0.56 | 0.23 | 0.21 | 0.21 |
| An (Ca) | 0.75 | - | 1.40 | 0.32 | 0.59 | 2.79 | 0.50 | 1.17 | 2.77 | 2.77 | 1.62 | 2.27 | 1.93 | 0.58 |

* Les analyses en éléments majeurs ont été réalisées par microsonde électronique (% poids d'oxyde). Abbréviations: n= nombre d'analyses par minéral; σ = écart type.

Tableau B1-b (suite)

| Echantillon 136R2_60-64 | | 227R1_10-15 | | 227R2_71-74 | | 228R1_33-37 | | 228R1_66-70 | | 228R1_79-82 | | 228R2_42-45 | | 228R3_22-25 | | 228R3_62-66 | | 231R3_0-3 | | 232R1_9-13 | | |
|-------------------------|------------|-------------|------------------------|------------------|------------------------|------------------------|------------------------|------------------------|------------------------|------------------------|------------------------|------------------------|------------------------|-------------|-------------|-------------|---------|-----------|--|------------|--|--|
| Type de roche | troctolite | gabbro | troctolite riche en ol | troctolite en ol | troctolite riche en ol | troctolite riche en ol | troctolite riche en ol | troctolite riche en ol | troctolite riche en ol | troctolite riche en ol | troctolite riche en ol | troctolite riche en ol | troctolite riche en ol | gabbro | gabbro à ol | troctolite | filonet | | | | | |
| Profondeur | 671.36 | 1092.1 | 1094.14 | 1097.13 | 1097.46 | 1097.59 | 1098.43 | 1099.73 | 1100.13 | 1100.13 | 1100.13 | 1100.13 | 1100.13 | 1100.13 | 1113.1 | 1115.19 | 1115.19 | | | | | |
| Zones | 3 | 4 | 4 | 4 | 4 | 4 | 4 | 4 | 4 | 4 | 4 | 4 | 4 | 4 | 4 | 4 | 4 | | | | | |
| n | 4 | 13 | 6 | 6 | 7 | 5 | 10 | 3 | 6 | 15 | 20 | 11 | 3 | | | | | | | | | |
| % | | | | | | | | | | | | | | | | | | | | | | |
| SiO2 | 48.72 | 51.59 | 48.55 | 48.53 | 49.58 | 48.65 | 48.69 | 48.33 | 48.25 | 47.82 | 50.17 | 48.07 | 49.62 | | | | | | | | | |
| TiO2 | 0.04 | 0.05 | 0.01 | 0.03 | 0.04 | 0.04 | 0.04 | 0.02 | 0.08 | 0.06 | 0.07 | 0.05 | 0.06 | | | | | | | | | |
| Al2O3 | 33.33 | 30.86 | 32.75 | 32.52 | 31.36 | 32.71 | 32.44 | 32.69 | 32.62 | 32.70 | 31.00 | 32.84 | 31.91 | | | | | | | | | |
| Cr2O3 | 0.01 | 0.01 | 0.01 | 0.00 | 0.00 | 0.01 | 0.00 | 0.01 | 0.00 | 0.01 | 0.01 | 0.00 | 0.00 | | | | | | | | | |
| FeO | 0.18 | 0.42 | 0.26 | 0.24 | 0.32 | 0.25 | 0.27 | 0.29 | 0.33 | 0.33 | 0.30 | 0.25 | 0.24 | | | | | | | | | |
| MnO | 0.00 | 0.01 | 0.00 | 0.01 | 0.00 | 0.01 | 0.01 | 0.00 | 0.01 | 0.01 | 0.01 | 0.00 | 0.01 | | | | | | | | | |
| MgO | 0.02 | 0.06 | 0.04 | 0.04 | 0.06 | 0.04 | 0.04 | 0.05 | 0.05 | 0.06 | 0.05 | 0.03 | 0.05 | | | | | | | | | |
| CaO | 16.25 | 13.63 | 15.73 | 15.53 | 14.54 | 15.65 | 15.80 | 15.88 | 15.71 | 15.87 | 14.26 | 16.14 | 14.97 | | | | | | | | | |
| Na2O | 2.44 | 3.94 | 2.61 | 2.79 | 3.30 | 2.71 | 2.67 | 2.57 | 2.71 | 2.55 | 3.45 | 2.50 | 3.14 | | | | | | | | | |
| K2O | 0.02 | 0.03 | 0.02 | 0.02 | 0.03 | 0.03 | 0.01 | 0.01 | 0.02 | 0.02 | 0.03 | 0.01 | 0.02 | | | | | | | | | |
| Total | 101.02 | 100.60 | 100.00 | 99.72 | 99.23 | 100.11 | 99.97 | 99.86 | 99.78 | 99.44 | 99.34 | 99.90 | 100.04 | | | | | | | | | |
| An (Ca) | 78.57 | 65.55 | 76.82 | 75.40 | 70.80 | 76.02 | 76.51 | 77.34 | 76.11 | 77.34 | 69.42 | 78.06 | 72.39 | | | | | | | | | |
| g | | | | | | | | | | | | | | | | | | | | | | |
| SiO2 | 0.26 | 1.02 | 0.72 | 0.40 | 0.92 | 0.70 | 0.65 | 0.56 | 0.34 | 0.37 | 0.73 | 0.50 | 0.41 | | | | | | | | | |
| TiO2 | 0.02 | 0.01 | 0.01 | 0.02 | 0.03 | 0.02 | 0.01 | 0.02 | 0.02 | 0.02 | 0.01 | 0.01 | 0.01 | | | | | | | | | |
| Al2O3 | 0.21 | 0.70 | 0.39 | 0.18 | 0.65 | 0.43 | 0.26 | 0.17 | 0.18 | 0.23 | 0.38 | 0.33 | 0.19 | | | | | | | | | |
| Cr2O3 | 0.02 | 0.01 | 0.01 | 0.00 | 0.01 | 0.01 | 0.01 | 0.02 | 0.00 | 0.01 | 0.01 | 0.01 | 0.00 | | | | | | | | | |
| FeO | 0.02 | 0.03 | 0.02 | 0.03 | 0.04 | 0.02 | 0.03 | 0.05 | 0.04 | 0.04 | 0.06 | 0.04 | 0.02 | | | | | | | | | |
| MnO | 0.00 | 0.01 | 0.00 | 0.01 | 0.01 | 0.02 | 0.01 | 0.01 | 0.01 | 0.01 | 0.01 | 0.00 | 0.01 | | | | | | | | | |
| MgO | 0.01 | 0.06 | 0.01 | 0.02 | 0.01 | 0.02 | 0.01 | 0.00 | 0.01 | 0.01 | 0.02 | 0.01 | 0.01 | | | | | | | | | |
| CaO | 0.17 | 0.88 | 0.46 | 0.13 | 0.70 | 0.48 | 0.32 | 0.28 | 0.25 | 0.22 | 0.47 | 0.40 | 0.28 | | | | | | | | | |
| Na2O | 0.12 | 0.45 | 0.26 | 0.09 | 0.42 | 0.27 | 0.21 | 0.18 | 0.16 | 0.16 | 0.27 | 0.23 | 0.22 | | | | | | | | | |
| K2O | 0.00 | 0.01 | 0.01 | 0.01 | 0.01 | 0.02 | 0.00 | 0.01 | 0.01 | 0.03 | 0.01 | 0.01 | 0.00 | | | | | | | | | |
| Total | 0.06 | 0.18 | 0.36 | 0.32 | 0.13 | 0.41 | 0.37 | 0.32 | 0.15 | 0.22 | 0.50 | 0.38 | 0.21 | | | | | | | | | |
| An (Ca) | 1.00 | 4.08 | 2.31 | 0.64 | 3.60 | 2.37 | 1.76 | 1.54 | 1.40 | 1.34 | 2.32 | 1.95 | 1.73 | | | | | | | | | |

Tableau B1-b (suite)

| Echantillon | 233R1_31-34 | | 233R1_135-139 | | 233R2_109-112 | | 235R1_29-34 | | 235R2_13-16 | | 247R3_62-66 | | 248R4_19-23 | | 248R4_65-69 | |
|-------------|---------------|------------------------|---------------|------------|------------------------|------------------|-------------|------------|-------------|------------|-------------|------------------------|-------------|------------|-------------|--|
| | Type de roche | troctolite riche en ol | troctolite | troctolite | troctolite riche en ol | troctolite en ol | gabbro | troctolite | gabbro | troctolite | gabbro | troctolite riche en ol | gabbro | troctolite | gabbro | |
| Profondeur | 1120.21 | 1121.25 | 1122.49 | 1129.79 | 1129.79 | 1129.79 | 1130.89 | 1130.89 | 1130.89 | 1190.08 | 1196.11 | 1196.11 | 1196.11 | 1196.57 | | |
| Zones | 4 | 4 | 4 | 4 | 4 | 4 | 4 | 4 | 4 | 4 | 4 | 4 | 4 | 4 | 4 | |
| n | 11 | 14 | 13 | 5 | 8 | 10 | 3 | 8 | 8 | 8 | 4 | 4 | 7 | | | |
| wt% | | | | | | | | | | | | | | | | |
| SiO2 | 48.54 | 48.32 | 48.56 | 49.21 | 50.83 | 48.64 | 50.25 | 49.02 | 49.22 | 48.45 | 52.43 | | | | | |
| TiO2 | 0.06 | 0.06 | 0.05 | 0.04 | 0.04 | 0.03 | 0.05 | 0.07 | 0.08 | 0.04 | 0.07 | | | | | |
| Al2O3 | 32.16 | 32.83 | 32.55 | 32.53 | 31.26 | 32.53 | 31.48 | 31.98 | 32.06 | 32.70 | 29.85 | | | | | |
| Cr2O3 | 0.01 | 0.01 | 0.00 | 0.01 | 0.01 | 0.01 | 0.00 | 0.00 | 0.00 | 0.00 | 0.00 | | | | | |
| FeO | 0.26 | 0.29 | 0.25 | 0.28 | 0.34 | 0.31 | 0.32 | 0.26 | 0.29 | 0.34 | 0.45 | | | | | |
| MnO | 0.00 | 0.00 | 0.00 | 0.01 | 0.00 | 0.00 | 0.00 | 0.00 | 0.00 | 0.00 | 0.01 | | | | | |
| MgO | 0.05 | 0.05 | 0.05 | 0.06 | 0.08 | 0.07 | 0.06 | 0.06 | 0.07 | 0.05 | 0.05 | | | | | |
| CaO | 15.60 | 15.82 | 15.84 | 15.62 | 14.41 | 15.84 | 14.46 | 14.99 | 15.24 | 15.69 | 12.64 | | | | | |
| Na2O | 2.71 | 2.66 | 2.62 | 2.68 | 3.45 | 2.61 | 3.32 | 3.10 | 2.94 | 2.66 | 4.46 | | | | | |
| K2O | 0.02 | 0.02 | 0.01 | 0.01 | 0.02 | 0.01 | 0.02 | 0.03 | 0.02 | 0.01 | 0.04 | | | | | |
| Total | 99.41 | 100.06 | 99.95 | 100.46 | 100.44 | 100.07 | 99.97 | 99.53 | 99.93 | 99.96 | 100.00 | | | | | |
| An (Ca) | 76.03 | 76.59 | 76.92 | 76.24 | 69.67 | 76.95 | 70.61 | 72.62 | 74.03 | 76.46 | 60.90 | | | | | |
| Q | | | | | | | | | | | | | | | | |
| SiO2 | 0.61 | 0.65 | 0.80 | 0.41 | 0.34 | 0.70 | 0.34 | 0.70 | 1.05 | 0.33 | 0.29 | | | | | |
| TiO2 | 0.02 | 0.02 | 0.01 | 0.01 | 0.02 | 0.01 | 0.01 | 0.02 | 0.03 | 0.00 | 0.01 | | | | | |
| Al2O3 | 0.47 | 0.42 | 0.65 | 0.34 | 0.22 | 0.48 | 0.31 | 0.35 | 0.62 | 0.15 | 0.29 | | | | | |
| Cr2O3 | 0.01 | 0.01 | 0.01 | 0.01 | 0.01 | 0.01 | 0.00 | 0.00 | 0.00 | 0.01 | 0.01 | | | | | |
| FeO | 0.02 | 0.04 | 0.02 | 0.03 | 0.05 | 0.02 | 0.05 | 0.03 | 0.04 | 0.04 | 0.05 | | | | | |
| MnO | 0.00 | 0.01 | 0.00 | 0.01 | 0.01 | 0.01 | 0.00 | 0.01 | 0.00 | 0.01 | 0.01 | | | | | |
| MgO | 0.01 | 0.01 | 0.01 | 0.03 | 0.02 | 0.02 | 0.01 | 0.01 | 0.02 | 0.01 | 0.02 | | | | | |
| CaO | 0.49 | 0.45 | 0.64 | 0.28 | 0.15 | 0.48 | 0.12 | 0.42 | 0.86 | 0.16 | 0.29 | | | | | |
| Na2O | 0.28 | 0.29 | 0.38 | 0.23 | 0.12 | 0.30 | 0.06 | 0.25 | 0.41 | 0.15 | 0.17 | | | | | |
| K2O | 0.01 | 0.01 | 0.01 | 0.01 | 0.01 | 0.01 | 0.00 | 0.01 | 0.01 | 0.00 | 0.01 | | | | | |
| Total | 0.23 | 0.16 | 0.57 | 0.12 | 0.25 | 0.19 | 0.11 | 0.26 | 0.36 | 0.44 | 0.27 | | | | | |
| An (Ca) | 2.49 | 2.45 | 3.30 | 1.87 | 0.89 | 2.57 | 0.51 | 2.18 | 3.73 | 1.18 | 1.43 | | | | | |

Tableau B1-c: Composition moyenne en éléments majeurs des olivines du puits IODP U1309D*

| Echantillon | 61R1_11-14 | 63R3_36-39 | 64R1_53-56,5 | 65R2_16-19 | 66R1_18-21 | 111R4_14-17 | 111R4_50-54 | 112R1_69-73 | 112R3_22-25 | 227R2_71-74 | 228R1_33-37 | 228R1_66-70 | 228R1_79-82 | 228R2_42-45 |
|---------------|------------------------|------------------------|------------------|------------------------|------------------------|------------------------|------------------------|------------------------|------------------------|------------------------|------------------------|-------------|------------------------|------------------------|
| Type de roche | troctolite riche en ol | troctolite riche en ol | troctolite en ol | troctolite riche en ol | troctolite riche en ol | troctolite riche en ol | troctolite riche en ol | troctolite riche en ol | troctolite riche en ol | troctolite riche en ol | troctolite riche en ol | gabbro | troctolite riche en ol | troctolite riche en ol |
| Profondeur | 314,91 | 327,720 | 329,730 | 335,660 | 338,980 | 553,710 | 554,07 | 555 | 557,24 | 1094,14 | 1097,13 | 1097,46 | 1097,59 | 1098,43 |
| Zones | 1 | 1 | 1 | 1 | 1 | 2 | 2 | 2 | 2 | 4 | 4 | 4 | 4 | 4 |
| n | 10 | 10 | 7 | 7 | 7 | 9 | 9 | 6 | 3 | 6 | 5 | 2 | 6 | 15 |
| % | | | | | | | | | | | | | | |
| SiO2 | 40,73 | 40,86 | 40,88 | 40,44 | 40,61 | 40,74 | 40,54 | 39,93 | 40,73 | 40,20 | 40,01 | 39,72 | 40,48 | 40,46 |
| TiO2 | 0,01 | 0,01 | 0,02 | 0,01 | 0,01 | 0,01 | 0,00 | 0,01 | 0,01 | 0,01 | 0,02 | 0,01 | 0,01 | 0,01 |
| Al2O3 | 0,01 | 0,01 | 0,00 | 0,01 | 0,01 | 0,01 | 0,02 | 0,01 | 0,01 | 0,01 | 0,01 | 0,00 | 0,01 | 0,01 |
| Cr2O3 | 0,02 | 0,01 | 0,01 | 0,00 | 0,01 | 0,01 | 0,00 | 0,00 | 0,00 | 0,02 | 0,01 | 0,01 | 0,01 | 0,01 |
| FeO | 12,43 | 12,17 | 12,07 | 12,46 | 13,67 | 12,36 | 13,73 | 14,24 | 14,05 | 14,84 | 15,09 | 16,61 | 14,56 | 14,44 |
| MnO | 0,20 | 0,20 | 0,20 | 0,20 | 0,21 | 0,20 | 0,22 | 0,24 | 0,22 | 0,24 | 0,25 | 0,25 | 0,22 | 0,23 |
| MgO | 46,18 | 46,25 | 46,29 | 46,13 | 45,21 | 46,44 | 45,64 | 45,03 | 44,98 | 44,30 | 44,26 | 42,99 | 44,27 | 44,81 |
| CaO | 0,06 | 0,06 | 0,05 | 0,07 | 0,06 | 0,06 | 0,08 | 0,11 | 0,07 | 0,06 | 0,12 | 0,06 | 0,07 | 0,08 |
| Na2O | 0,00 | 0,01 | 0,01 | 0,01 | 0,01 | 0,01 | 0,01 | 0,00 | 0,01 | 0,01 | 0,01 | 0,00 | 0,02 | 0,01 |
| K2O | 0,00 | 0,00 | 0,00 | 0,01 | 0,01 | 0,00 | 0,01 | 0,00 | 0,00 | 0,00 | 0,00 | 0,01 | 0,00 | 0,00 |
| NiO | 0,29 | 0,29 | 0,27 | 0,24 | 0,23 | 0,27 | 0,25 | 0,25 | 0,24 | 0,24 | 0,25 | 0,19 | 0,23 | 0,27 |
| Total | 99,93 | 99,88 | 99,79 | 99,58 | 100,04 | 100,13 | 100,51 | 99,83 | 100,31 | 99,94 | 100,02 | 99,86 | 99,87 | 100,33 |
| Fo (M%) | 86,69 | 86,95 | 87,05 | 86,65 | 85,30 | 86,82 | 85,36 | 84,70 | 84,89 | 83,95 | 83,72 | 81,95 | 84,21 | 84,48 |
| Mg# | 86,88 | 87,13 | 87,24 | 86,84 | 85,50 | 87,00 | 85,56 | 84,92 | 85,09 | 84,17 | 83,94 | 82,18 | 84,41 | 84,68 |
| Ni (ppm) | 2266,14 | 2294,82 | 2101,78 | 1901,23 | 1843,79 | 2146,20 | 1968,58 | 1943,18 | 1878,76 | 1882,56 | 1949,73 | 1475,65 | 1768,53 | 2084,16 |
| σ | | | | | | | | | | | | | | |
| SiO2 | 0,14 | 0,20 | 0,08 | 0,22 | 0,14 | 0,17 | 0,19 | 0,10 | 0,03 | 0,14 | 0,21 | 0,06 | 0,12 | 0,22 |
| TiO2 | 0,01 | 0,01 | 0,01 | 0,01 | 0,01 | 0,01 | 0,01 | 0,01 | 0,01 | 0,01 | 0,01 | 0,01 | 0,01 | 0,01 |
| Al2O3 | 0,01 | 0,01 | 0,01 | 0,01 | 0,01 | 0,01 | 0,00 | 0,01 | 0,01 | 0,01 | 0,01 | 0,01 | 0,01 | 0,01 |
| Cr2O3 | 0,01 | 0,01 | 0,01 | 0,01 | 0,01 | 0,01 | 0,01 | 0,01 | 0,01 | 0,01 | 0,01 | 0,02 | 0,01 | 0,01 |
| FeO | 0,14 | 0,10 | 0,06 | 0,08 | 0,14 | 0,10 | 0,05 | 0,06 | 0,08 | 0,15 | 0,06 | 0,10 | 0,31 | 0,12 |
| MnO | 0,02 | 0,01 | 0,02 | 0,02 | 0,02 | 0,02 | 0,01 | 0,02 | 0,02 | 0,02 | 0,01 | 0,00 | 0,02 | 0,01 |
| MgO | 0,26 | 0,16 | 0,13 | 0,24 | 0,14 | 0,28 | 0,22 | 0,12 | 0,15 | 0,12 | 0,12 | 0,34 | 0,21 | 0,21 |
| CaO | 0,01 | 0,01 | 0,01 | 0,02 | 0,01 | 0,01 | 0,01 | 0,01 | 0,02 | 0,01 | 0,06 | 0,00 | 0,01 | 0,01 |
| Na2O | 0,00 | 0,01 | 0,01 | 0,01 | 0,01 | 0,01 | 0,01 | 0,01 | 0,01 | 0,01 | 0,01 | 0,00 | 0,02 | 0,01 |
| K2O | 0,00 | 0,00 | 0,01 | 0,01 | 0,01 | 0,00 | 0,01 | 0,00 | 0,00 | 0,01 | 0,01 | 0,01 | 0,00 | 0,00 |
| NiO | 0,02 | 0,02 | 0,02 | 0,02 | 0,02 | 0,02 | 0,02 | 0,02 | 0,04 | 0,02 | 0,04 | 0,04 | 0,02 | 0,02 |
| Total | 0,27 | 0,30 | 0,11 | 0,28 | 0,21 | 0,31 | 0,03 | 0,11 | 0,19 | 0,24 | 0,19 | 0,19 | 0,35 | 0,41 |
| Fo (M%) | 0,13 | 0,08 | 0,07 | 0,11 | 0,16 | 0,13 | 0,11 | 0,06 | 0,09 | 0,13 | 0,08 | 0,21 | 0,30 | 0,12 |
| Mg# | 0,12 | 0,08 | 0,06 | 0,10 | 0,16 | 0,13 | 0,10 | 0,06 | 0,10 | 0,12 | 0,07 | 0,21 | 0,31 | 0,12 |
| Ni (ppm) | 152,98 | 159,65 | 131,90 | 168,53 | 125,06 | 182,78 | 118,66 | 125,37 | 319,57 | 180,21 | 90,96 | 291,62 | 148,03 | 136,29 |

* Les analyses en éléments majeurs ont été réalisées par microsonde électronique (% poids d'oxyde). Abbréviation: n = nombre d'analyses par minéral; σ = écart type.

Tableau B1-c (suite)

| Echantillon | 228R3_22-25 | 228R3_62-66 | 231R3_0-3 | 232R1_9-13 | 233R1_31-34 | 233R1_135-139 | 233R2_109-112 | 235R1_29-34 | 235R2_13-16 | 247R3_62-66 | 248R4_19-23 | | |
|---------------|------------------------|------------------------|-------------|------------------------|------------------------|---------------|------------------------|------------------------|------------------------|------------------------|-------------|------------------------|---------|
| Type de roche | troctolite riche en ol | troctolite riche en ol | gabbro à ol | troctolite riche en ol | troctolite riche en ol | troctolite | troctolite riche en ol | troctolite riche en ol | troctolite riche en ol | troctolite riche en ol | gabbro | troctolite riche en ol | |
| Profondeur | 1099.73 | 1100.13 | 1100.13 | 1115.19 | 1115.19 | 1120.21 | 1121.25 | 1122.49 | 1129.79 | 1130.89 | 1190.51 | 1196.11 | 1196.11 |
| Zones | 4 | 4 | 4 | 4 | 4 | 4 | 4 | 4 | 4 | 4 | 4 | 4 | 4 |
| n | 10 | 5 | 6 | 8 | 5 | 9 | 4 | 14 | 4 | 5 | 11 | 3 | 7 |
| % | | | | | | | | | | | | | |
| SiO2 | 40.42 | 39.70 | 39.70 | 39.25 | 39.95 | 40.34 | 40.09 | 40.60 | 40.43 | 40.21 | 39.87 | 40.32 | 40.15 |
| TiO2 | 0.01 | 0.03 | 0.02 | 0.02 | 0.01 | 0.02 | 0.03 | 0.01 | 0.02 | 0.01 | 0.02 | 0.01 | 0.02 |
| Al2O3 | 0.01 | 0.02 | 0.01 | 0.01 | 0.01 | 0.01 | 0.01 | 0.01 | 0.01 | 0.01 | 0.01 | 0.01 | 0.02 |
| Cr2O3 | 0.01 | 0.02 | 0.02 | 0.01 | 0.01 | 0.01 | 0.02 | 0.01 | 0.01 | 0.01 | 0.01 | 0.01 | 0.01 |
| FeO | 14.68 | 16.04 | 16.18 | 19.45 | 15.90 | 14.29 | 14.53 | 13.63 | 15.69 | 15.44 | 14.83 | 15.12 | 14.85 |
| MnO | 0.23 | 0.26 | 0.24 | 0.30 | 0.25 | 0.23 | 0.25 | 0.22 | 0.25 | 0.25 | 0.24 | 0.23 | 0.24 |
| MgO | 44.08 | 43.47 | 43.09 | 40.41 | 43.55 | 44.59 | 44.45 | 45.02 | 43.44 | 43.80 | 44.09 | 43.21 | 43.69 |
| CaO | 0.10 | 0.08 | 0.07 | 0.09 | 0.05 | 0.06 | 0.07 | 0.08 | 0.07 | 0.09 | 0.08 | 0.08 | 0.06 |
| Na2O | 0.01 | 0.01 | 0.02 | 0.02 | 0.01 | 0.01 | 0.00 | 0.01 | 0.00 | 0.01 | 0.01 | 0.01 | 0.01 |
| K2O | 0.00 | 0.00 | 0.02 | 0.01 | 0.00 | 0.00 | 0.00 | 0.01 | 0.00 | 0.00 | 0.00 | 0.00 | 0.00 |
| NiO | 0.25 | 0.20 | 0.19 | 0.15 | 0.19 | 0.23 | 0.22 | 0.25 | 0.19 | 0.21 | 0.28 | 0.25 | 0.24 |
| Total | 99.82 | 99.82 | 99.58 | 99.70 | 99.92 | 100.06 | 99.67 | 99.86 | 100.11 | 100.04 | 99.43 | 99.25 | 99.30 |
| Feo (N%) | 84.04 | 82.61 | 82.38 | 78.47 | 82.77 | 84.54 | 84.27 | 85.27 | 82.93 | 83.26 | 83.91 | 83.37 | 83.76 |
| Mg# | 84.25 | 82.85 | 82.60 | 78.73 | 83.00 | 84.75 | 84.49 | 85.47 | 83.15 | 83.48 | 84.12 | 83.58 | 83.98 |
| Ni (ppm) | 1973.21 | 1554.60 | 1530.37 | 1156.23 | 1479.65 | 1551.45 | 1735.86 | 1952.03 | 1500.39 | 1638.33 | 2204.10 | 1945.54 | 1903.04 |
| g | | | | | | | | | | | | | |
| SiO2 | 0.14 | 0.15 | 0.25 | 0.13 | 0.12 | 0.19 | 0.11 | 0.12 | 0.12 | 0.21 | 0.16 | 0.18 | 0.21 |
| TiO2 | 0.01 | 0.02 | 0.01 | 0.01 | 0.01 | 0.02 | 0.02 | 0.01 | 0.01 | 0.01 | 0.01 | 0.01 | 0.02 |
| Al2O3 | 0.01 | 0.01 | 0.01 | 0.01 | 0.01 | 0.01 | 0.01 | 0.01 | 0.01 | 0.01 | 0.01 | 0.01 | 0.01 |
| Cr2O3 | 0.01 | 0.03 | 0.02 | 0.01 | 0.01 | 0.01 | 0.02 | 0.01 | 0.01 | 0.01 | 0.01 | 0.01 | 0.01 |
| FeO | 0.09 | 0.07 | 0.23 | 0.23 | 0.25 | 0.06 | 0.07 | 0.07 | 0.13 | 0.35 | 0.10 | 0.18 | 0.09 |
| MnO | 0.02 | 0.02 | 0.01 | 0.03 | 0.01 | 0.02 | 0.01 | 0.01 | 0.01 | 0.02 | 0.02 | 0.02 | 0.02 |
| MgO | 0.22 | 0.09 | 0.20 | 0.23 | 0.15 | 0.17 | 0.13 | 0.14 | 0.23 | 0.16 | 0.19 | 0.15 | 0.25 |
| CaO | 0.09 | 0.01 | 0.01 | 0.02 | 0.02 | 0.01 | 0.02 | 0.02 | 0.01 | 0.01 | 0.02 | 0.01 | 0.01 |
| Na2O | 0.01 | 0.01 | 0.03 | 0.01 | 0.01 | 0.01 | 0.00 | 0.01 | 0.00 | 0.01 | 0.01 | 0.01 | 0.01 |
| K2O | 0.00 | 0.00 | 0.04 | 0.01 | 0.00 | 0.00 | 0.00 | 0.01 | 0.00 | 0.00 | 0.01 | 0.00 | 0.00 |
| NiO | 0.01 | 0.01 | 0.02 | 0.02 | 0.02 | 0.02 | 0.02 | 0.02 | 0.01 | 0.02 | 0.02 | 0.01 | 0.01 |
| Total | 0.28 | 0.11 | 0.28 | 0.17 | 0.20 | 0.32 | 0.13 | 0.23 | 0.05 | 0.24 | 0.26 | 0.23 | 0.14 |
| Feo (N%) | 0.07 | 0.10 | 0.22 | 0.29 | 0.26 | 0.05 | 0.07 | 0.07 | 0.19 | 0.37 | 0.09 | 0.11 | 0.15 |
| Mg# | 0.06 | 0.09 | 0.22 | 0.29 | 0.25 | 0.05 | 0.07 | 0.07 | 0.18 | 0.35 | 0.10 | 0.12 | 0.15 |
| Ni (ppm) | 107.17 | 94.64 | 121.46 | 129.53 | 159.87 | 157.63 | 169.71 | 174.35 | 62.93 | 152.56 | 150.80 | 69.75 | 92.34 |

Tableau B1-d: Composition moyenne en éléments majeurs des spinelles du puits IODP U1309D*

| Echantillon | 63R3_36-39 | 64R1_53-56.5 | 65R2_16-19 | 66R1_18-21 | 111R4_14-17 | 112R1_69-73 | 112R3_22-25 | 136R2_60-64 | 227R2_71-74 | 228R1_33-37 | 235R1_29-34 | 235R2_13-16 |
|---------------|------------------------|------------------|------------------------|------------------------|------------------------|------------------------|------------------------|-------------|------------------------|------------------------|------------------------|------------------------|
| Type de roche | troctolite riche en ol | troctolite en ol | troctolite riche en ol | troctolite riche en ol | troctolite riche en ol | troctolite riche en ol | troctolite riche en ol | Troctolite | troctolite riche en ol | troctolite riche en ol | troctolite riche en ol | troctolite riche en ol |
| Profondeur | 327.72 | 329.73 | 335.66 | 338.98 | 553.710 | 555 | 557.24 | 671.36 | 1094.14 | 1097.13 | 1129.79 | 1130.89 |
| Zones | 1 | 1 | 1 | 1 | 2 | 2 | 2 | 3 | 4 | 4 | 4 | 4 |
| n | 3 | 4 | 7 | 6 | 4 | 2 | 1 | 6 | 1 | 2 | 1 | 3 |
| % | | | | | | | | | | | | |
| SiO2 | 0.20 | 0.13 | 0.15 | 0.18 | 0.12 | 0.14 | 0.14 | 0.12 | 0.15 | 0.17 | 0.17 | 0.15 |
| TiO2 | 1.10 | 0.88 | 1.27 | 1.42 | 1.30 | 2.56 | 2.38 | 1.36 | 1.01 | 1.98 | 1.83 | 1.58 |
| Al2O3 | 22.86 | 23.73 | 24.57 | 20.19 | 21.16 | 16.57 | 18.71 | 23.61 | 19.72 | 19.83 | 17.17 | 18.73 |
| Cr2O3 | 41.06 | 41.63 | 38.59 | 40.87 | 42.70 | 43.64 | 41.75 | 39.08 | 38.05 | 36.98 | 39.51 | 39.16 |
| FeO | 22.50 | 21.97 | 22.88 | 27.11 | 23.50 | 27.45 | 28.37 | 24.37 | 32.07 | 29.27 | 32.51 | 29.30 |
| MnO | 0.31 | 0.32 | 0.34 | 0.38 | 0.39 | 0.38 | 0.44 | 0.34 | 0.44 | 0.37 | 0.40 | 0.34 |
| MgO | 11.50 | 11.10 | 10.99 | 9.07 | 10.43 | 8.93 | 8.06 | 11.24 | 7.05 | 10.13 | 7.20 | 9.57 |
| CaO | 0.01 | 0.02 | 0.01 | 0.01 | 0.01 | 0.06 | 0.03 | 0.01 | 0.05 | 0.10 | 0.00 | 0.03 |
| Na2O | 0.01 | 0.01 | 0.01 | 0.00 | 0.01 | 0.00 | 0.01 | 0.00 | 0.00 | 0.02 | 0.00 | 0.02 |
| Total | 99.64 | 99.91 | 98.92 | 99.34 | 99.77 | 99.86 | 100.00 | 100.29 | 98.69 | 98.99 | 98.88 | 98.99 |
| Cr# | 54.66 | 54.07 | 51.31 | 57.62 | 57.53 | 63.87 | 59.95 | 52.77 | 56.41 | 55.59 | 60.68 | 58.43 |
| Mg# | 47.67 | 47.37 | 46.12 | 37.35 | 44.17 | 36.71 | 33.61 | 45.15 | 28.15 | 38.14 | 28.30 | 36.77 |
| σ | | | | | | | | | | | | |
| SiO2 | 0.00 | 0.02 | 0.03 | 0.01 | 0.02 | 0.02 | 0.02 | 0.02 | 0.15 | 0.01 | 0.17 | 0.03 |
| TiO2 | 0.18 | 0.08 | 0.47 | 0.16 | 0.17 | 0.25 | 0.25 | 0.64 | 0.13 | 0.13 | 0.13 | 0.24 |
| Al2O3 | 1.35 | 0.84 | 1.13 | 1.43 | 1.32 | 1.23 | 1.23 | 3.20 | 1.23 | 1.23 | 1.23 | 2.06 |
| Cr2O3 | 0.14 | 0.59 | 0.99 | 0.93 | 0.63 | 0.82 | 0.82 | 1.73 | 0.51 | 0.51 | 0.76 | 0.76 |
| FeO | 0.02 | 0.01 | 0.02 | 0.02 | 0.02 | 0.02 | 0.02 | 0.03 | 0.04 | 0.04 | 0.04 | 0.04 |
| MnO | 0.23 | 0.53 | 0.48 | 0.59 | 0.50 | 0.61 | 0.61 | 0.74 | 0.36 | 0.36 | 0.81 | 0.81 |
| MgO | 0.00 | 0.02 | 0.00 | 0.01 | 0.01 | 0.04 | 0.01 | 0.01 | 0.10 | 0.10 | 0.00 | 0.00 |
| CaO | 0.01 | 0.01 | 0.01 | 0.00 | 0.02 | 0.00 | 0.01 | 0.01 | 0.00 | 0.00 | 0.01 | 0.01 |
| Na2O | 1.05 | 0.85 | 1.44 | 0.71 | 0.92 | 0.97 | 0.97 | 1.47 | 1.28 | 1.28 | 1.75 | 1.75 |
| Total | 0.12 | 0.07 | 0.26 | 0.33 | 0.35 | 0.23 | 0.23 | 0.28 | 0.27 | 0.27 | 0.26 | 0.26 |
| Cr# | 2.07 | 1.36 | 1.89 | 2.18 | 2.02 | 2.22 | 2.22 | 4.17 | 2.39 | 2.39 | 3.66 | 3.66 |
| Mg# | 0.56 | 1.78 | 2.13 | 2.33 | 1.82 | 2.29 | 2.29 | 3.39 | 1.24 | 1.24 | 2.40 | 2.40 |

* Les analyses en éléments majeurs ont été réalisées par microsonde électronique (% poids d'oxyde). Abbréviation: n = nombre d'analyses par minéral; σ = écart type.

Tableau B-2a: Profils en éléments en trace dans les plagioclases du puits IODP U1309D*

| Echantillon | 62RI_4-7 | | | | 136R2_37-40 | | | | 248R2_18-21 | | | | | | | | | 248R3_131-134 | | | | | |
|-------------------|-----------------------------|--------|--------|--------|-----------------------------|--------|--------|--------|-----------------------------|--------|--------|--------|--------|--------|--------|--------|--------|-----------------------------|--------|--------|--------|--------|--------|
| Type de roche | Troctolite riche en olivine | | | | Troctolite riche en olivine | | | | Troctolite riche en olivine | | | | | | | | | Troctolite riche en olivine | | | | | |
| Profondeur (mbsf) | 319.64 | | | | 671.13 | | | | 1193.32 | | | | | | | | | 1196 | | | | | |
| Zones | 1 | | | | 3 | | | | 4 | | | | | | | | | 4 | | | | | |
| Point | 1 | 2 | 3 | 4 | 1 | 2 | 3 | 4 | A1 | A2 | A3 | A4 | A5 | A6 | A7 | B1 | B2 | B3 | 1 | 2 | 3 | 4 | 5 |
| Localisation | b | c | b | c | c | b | b | c | b | c | c | c | c | c | b | b | c | c | b | c | b | c | c |
| Ti | 120 | 188 | 92 | 297 | 333 | 264 | 253 | 265 | 385 | 312 | 301 | 217 | 264 | 420 | 517 | 646 | 711 | 640 | 276 | 295 | 295 | 243 | 309 |
| V | 1.39 | 3.03 | 0.97 | 2.91 | 2.41 | 2.43 | 2.42 | 2.07 | 4.75 | 4.64 | 4.54 | 3.80 | 4.63 | 4.38 | 4.21 | 4.08 | 4.68 | 4.72 | 2.41 | 3.98 | 4.37 | 3.41 | 2.65 |
| Cr | 29.69 | 1.73 | 0.85 | 4.44 | 2.71 | 0.82 | 0.59 | 1.26 | 0.88 | 2.36 | 1.15 | 0.39 | 0.74 | 5.38 | 3.08 | 0.47 | 0.35 | 0.63 | 0.36 | 8.72 | 2.51 | 0.62 | 0.22 |
| Co | 0.17 | 0.21 | 0.15 | 3.79 | 3.56 | 0.16 | 0.14 | 0.27 | 1.14 | 0.87 | 0.95 | 0.82 | 0.51 | 0.32 | 0.60 | 0.70 | 0.22 | 0.29 | 0.82 | 116.19 | 0.67 | 0.45 | 0.31 |
| Ni | 1.49 | 515.00 | 0.46 | 1.42 | 619.37 | 0.92 | 2.47 | 16.04 | 10.17 | 9.38 | 19.43 | 3.91 | 1.98 | 32.52 | 2.06 | 25.77 | 2.01 | 1.91 | 3.76 | 887.13 | 17.71 | 2.06 | 1.90 |
| Zn | 4.72 | 1.33 | 8.26 | 1.78 | 1.56 | 1.03 | 2.69 | 1.53 | 2.54 | 90.41 | 3.76 | 2.32 | 2.16 | 1.88 | 3.26 | 1.50 | 2.76 | 2.32 | 7.02 | 73.44 | 1.75 | 2.43 | 1.07 |
| Rb | 0.60 | 0.31 | 0.12 | 0.18 | 0.56 | 0.23 | 0.18 | 0.25 | 0.16 | 0.15 | 0.09 | 0.12 | 0.17 | 0.10 | 0.16 | 0.17 | 0.27 | 0.22 | 0.19 | 2.57 | 0.10 | 0.09 | 0.09 |
| Sr | 213.84 | 123.39 | 141.94 | 133.28 | 196.22 | 178.67 | 188.59 | 180.21 | 172.91 | 183.21 | 168.17 | 152.66 | 163.84 | 158.84 | 184.76 | 167.65 | 180.86 | 170.06 | 165.90 | 193.29 | 158.33 | 153.43 | 169.74 |
| Y | 0.16 | 0.27 | 0.14 | 0.29 | 0.15 | 0.21 | 0.17 | 0.14 | 0.60 | 0.38 | 0.30 | 0.28 | 0.43 | 0.53 | 0.36 | 0.42 | 0.47 | 0.45 | 0.23 | 0.39 | 0.28 | 0.27 | 0.24 |
| Zr | 0.40 | 19.98 | 0.44 | 0.40 | 1.56 | 6.29 | 0.31 | 0.99 | 0.14 | 1.33 | 0.16 | 0.02 | 2.19 | 1.94 | 0.23 | 0.04 | 1.44 | 0.09 | 0.93 | 0.40 | 0.74 | 0.17 | 0.02 |
| Nb | 0.04 | 0.01 | 0.03 | 0.06 | 0.00 | 0.01 | 0.02 | 0.01 | 0.02 | 0.06 | 0.02 | 0.01 | 0.01 | 0.00 | 0.01 | 0.00 | 0.01 | 0.01 | 0.02 | 0.02 | 0.02 | 0.01 | 0.01 |
| Cs | 0.01 | 0.03 | 0.07 | 0.07 | 0.08 | 0.05 | 0.05 | 0.03 | 0.03 | 0.24 | 0.03 | 0.01 | 0.01 | 0.05 | 0.01 | 0.03 | 0.01 | 0.01 | 0.02 | 0.05 | 0.02 | 0.01 | 2.87 |
| Ba | 26.52 | 1.49 | 14.18 | 1.58 | 3.21 | 2.34 | 1.98 | 2.11 | 5.61 | 3.89 | 4.46 | 3.42 | 3.53 | 3.56 | 5.60 | 4.42 | 5.34 | 4.61 | 1.98 | 16.88 | 1.25 | 1.24 | 1.54 |
| La | 0.174 | 0.196 | 0.113 | 0.225 | 0.304 | 0.591 | 0.481 | 0.298 | 0.323 | 0.163 | 0.150 | 0.100 | 0.241 | 0.446 | 0.408 | 0.618 | 0.535 | 0.469 | 0.230 | 0.293 | 0.220 | 0.240 | 0.274 |
| Ce | 0.401 | 0.634 | 0.426 | 0.690 | 0.625 | 0.866 | 0.738 | 0.642 | 0.969 | 0.559 | 0.369 | 0.282 | 0.659 | 1.061 | 0.981 | 1.484 | 1.424 | 1.264 | 0.590 | 0.720 | 0.603 | 0.619 | 0.658 |
| Pr | 0.061 | 0.128 | 0.051 | 0.108 | 0.080 | 0.079 | 0.082 | 0.094 | 0.147 | 0.074 | 0.052 | 0.038 | 0.114 | 0.161 | 0.137 | 0.212 | 0.192 | 0.176 | 0.094 | 0.111 | 0.086 | 0.106 | 0.092 |
| Nd | 0.285 | 0.420 | 0.194 | 0.613 | 0.331 | 0.360 | 0.309 | 0.312 | 0.627 | 0.360 | 0.310 | 0.306 | 0.628 | 0.706 | 0.721 | 0.993 | 0.966 | 0.779 | 0.408 | 0.562 | 0.408 | 0.496 | 0.455 |
| Sm | 0.061 | 0.090 | 0.049 | 0.115 | 0.059 | 0.097 | 0.082 | 0.053 | 0.263 | 0.270 | 0.057 | 0.028 | 0.111 | 0.175 | 0.134 | 0.174 | 0.185 | 0.176 | 0.094 | 0.115 | 0.114 | 0.134 | 0.094 |
| Eu | 0.167 | 0.221 | 0.134 | 0.283 | 0.277 | 0.277 | 0.270 | 0.270 | 0.482 | 0.478 | 0.370 | 0.397 | 0.479 | 0.416 | 0.489 | 0.444 | 0.472 | 0.474 | 0.290 | 0.297 | 0.263 | 0.264 | 0.266 |
| Gd | 0.038 | 0.094 | 0.036 | 0.126 | 0.060 | 0.073 | 0.058 | 0.048 | 0.076 | 0.117 | 0.058 | 0.026 | 0.140 | 0.104 | 0.141 | 0.143 | 0.188 | 0.176 | 0.104 | 0.104 | 0.068 | 0.077 | 0.097 |
| Tb | 0.004 | 0.011 | 0.007 | 0.014 | 0.008 | 0.008 | 0.007 | 0.007 | 0.007 | 0.014 | 0.023 | 0.013 | 0.022 | 0.020 | 0.015 | 0.021 | 0.021 | 0.020 | 0.008 | 0.015 | 0.007 | 0.010 | 0.005 |
| Dy | 0.037 | 0.046 | 0.027 | 0.064 | 0.029 | 0.043 | 0.040 | 0.034 | 0.071 | 0.041 | 0.036 | 0.022 | 0.086 | 0.092 | 0.080 | 0.079 | 0.089 | 0.104 | 0.051 | 0.077 | 0.045 | 0.059 | 0.049 |
| Ho | 0.006 | 0.011 | 0.004 | 0.011 | 0.005 | 0.005 | 0.006 | 0.004 | 0.008 | 0.004 | 0.008 | 0.010 | 0.017 | 0.015 | 0.017 | 0.016 | 0.016 | 0.021 | 0.008 | 0.016 | 0.009 | 0.013 | 0.009 |
| Er | 0.007 | 0.023 | 0.012 | 0.023 | 0.007 | 0.011 | 0.013 | 0.011 | 0.015 | 0.022 | 0.007 | 0.013 | 0.024 | 0.033 | 0.019 | 0.043 | 0.037 | 0.036 | 0.012 | 0.052 | 0.026 | 0.024 | 0.022 |
| Tm | 0.001 | 0.003 | 0.001 | 0.004 | 0.002 | 0.001 | 0.002 | 0.003 | 0.009 | 0.009 | 0.008 | 0.004 | 0.008 | 0.005 | 0.004 | 0.005 | 0.004 | 0.009 | 0.005 | 0.007 | 0.004 | 0.002 | 0.002 |
| Yb | 0.012 | 0.014 | 0.002 | 0.016 | 0.005 | 0.005 | 0.008 | 0.006 | 0.000 | 0.000 | 0.008 | 0.058 | 0.035 | 0.032 | 0.014 | 0.020 | 0.012 | 0.014 | 0.009 | 0.052 | 0.025 | 0.012 | 0.019 |
| Lu | 0.001 | 0.001 | 0.001 | 0.002 | 0.001 | 0.004 | 0.001 | 0.002 | 0.005 | 0.011 | 0.008 | 0.004 | 0.004 | 0.003 | 0.002 | 0.002 | 0.001 | 0.006 | 0.007 | 0.007 | 0.003 | 0.002 | 0.002 |
| Hf | 0.0379 | 0.003 | 0.029 | 0.0044 | 0.0213 | 0.1034 | 0.0033 | 0.0409 | 0.047 | 0.073 | 0.033 | 0.0125 | 0.108 | 0.0062 | 0.009 | 0.0061 | 0.0067 | 0.0052 | 0.0146 | 0.0128 | 0.0084 | 0.0063 | 0.066 |
| Ta | 0.00 | 0.01 | 0.01 | 0.02 | 0.00 | 0.01 | 0.00 | 0.01 | 0.01 | 0.01 | 0.02 | 0.05 | 0.01 | 0.01 | 0.00 | 0.00 | 0.00 | 0.02 | 0.00 | 0.01 | 0.00 | 0.02 | 0.00 |
| Pb | 0.59 | 0.62 | 0.21 | 0.59 | 0.21 | 0.68 | 2.44 | 0.05 | 0.14 | 0.05 | 0.05 | 0.07 | 0.07 | 0.06 | 0.07 | 0.06 | 0.06 | 0.04 | 0.20 | 0.21 | 0.03 | 0.04 | 0.04 |
| Th | 0.01 | 0.03 | 0.09 | 0.07 | 0.00 | 0.05 | 0.01 | 0.47 | 0.01 | 0.08 | 0.02 | 0.00 | 0.04 | 0.00 | 0.01 | 0.00 | 0.01 | 0.00 | 0.03 | 0.00 | 0.02 | 0.33 | 0.05 |
| U | 0.22 | 0.00 | 0.14 | 0.01 | 0.88 | 0.03 | 0.76 | 0.04 | 0.01 | 0.00 | 0.12 | 0.64 | 0.01 | 0.00 | 0.00 | 0.00 | 0.00 | 0.11 | 0.04 | 0.11 | 0.02 | 0.01 | 0.00 |

*Analyses en éléments en trace (ppm) par LA-ICP-MS. Abbréviation: c=cœur, b=bordure

Tableau B-2b. Profils en éléments en trace dans les clinopyroxènes du puits IODP U1309D*

| Echantillon | 62RI_47 | | | | | | | | | | 136R2_37-40 | | | | | | | | | |
|-------------------|-----------------------------|----------|----------|----------|----------|---------|---------|----------|---------|---------|-----------------------------|---------|---------|---------|---------|---------|---------|---------|---------|---------|
| | Troctolite riche en olivine | | | | | | | | | | Troctolite riche en olivine | | | | | | | | | |
| Type de roche | | | | | | | | | | | | | | | | | | | | |
| Profondeur (mbsf) | | | | | | | | | | | | | | | | | | | | |
| Zones | | | | | | | | | | | | | | | | | | | | |
| Point | 1 | | | | | | | | | | 3 | | | | | | | | | |
| Localisation | | | | | | | | | | | | | | | | | | | | |
| Point | 1 | 2 | 3 | 4 | 5 | 6 | 7 | 8 | 9 | 10 | 1 | 2 | 3 | 4 | 5 | 6 | 7 | 8 | 9 | 10 |
| Ti | 3263 | 1997 | 1970 | 2093 | 2255 | 2990 | 3053 | 1537 | 2610 | 2261 | 3117 | 2939 | 3859 | 2779 | 1857 | 3347 | 1926 | 2020 | 1231 | 2902 |
| V | 353.24 | 302.38 | 303.18 | 302.40 | 304.04 | 358.93 | 346.32 | 281.15 | 326.17 | 316.01 | 367.75 | 369.69 | 369.87 | 344.05 | 305.84 | 350.37 | 323.47 | 318.37 | 291.73 | 327.15 |
| Cr | 10130.10 | 10531.78 | 10634.40 | 10426.50 | 10161.13 | 9951.97 | 9389.08 | 10362.42 | 9426.71 | 9895.03 | 6441.54 | 7168.75 | 4796.39 | 5774.47 | 5085.79 | 5661.81 | 7477.78 | 5634.42 | 7721.97 | 5576.38 |
| Co | 26.79 | 29.99 | 32.44 | 33.00 | 32.05 | 28.37 | 27.08 | 30.97 | 25.94 | 29.89 | 31.61 | 32.10 | 29.60 | 29.02 | 30.21 | 25.74 | 31.89 | 30.10 | 37.80 | 23.67 |
| Ni | 110.87 | 120.43 | 135.09 | 211.91 | 134.73 | 143.90 | 114.17 | 120.90 | 111.91 | 126.58 | 181.73 | 230.59 | 77.49 | 88.13 | 101.44 | 380.27 | 1905.86 | 474.73 | 248.64 | 2661.89 |
| Zn | 22.02 | 27.20 | 20.07 | 22.98 | 24.46 | 19.61 | 20.23 | 24.96 | 20.85 | 22.71 | 19.75 | 19.00 | 19.12 | 16.74 | 16.02 | 13.12 | 18.31 | 19.31 | 17.96 | 13.59 |
| Rb | 0.07 | 0.19 | 0.17 | 0.76 | 1.10 | 0.80 | 0.05 | 0.37 | 0.10 | 0.02 | 0.04 | 0.45 | 0.57 | 0.03 | 0.06 | 0.03 | 0.03 | 0.39 | 0.49 | 0.02 |
| Sr | 4.20 | 4.99 | 6.99 | 5.30 | 5.53 | 4.81 | 5.06 | 5.53 | 4.70 | 5.40 | 7.53 | 8.03 | 7.32 | 7.29 | 7.79 | 6.92 | 8.04 | 8.44 | 7.79 | 7.75 |
| Y | 19.59 | 13.12 | 9.78 | 12.27 | 12.83 | 21.77 | 18.16 | 9.14 | 16.48 | 14.42 | 15.66 | 16.05 | 15.74 | 14.55 | 10.95 | 15.01 | 11.08 | 11.39 | 7.89 | 14.94 |
| Zr | 13.29 | 26.01 | 12.07 | 6.38 | 33.49 | 18.78 | 27.03 | 18.00 | 13.46 | 8.12 | 16.99 | 16.25 | 22.40 | 16.98 | 11.58 | 17.74 | 9.06 | 48.71 | 4.43 | 12.18 |
| Nb | 0.10 | 0.10 | 0.04 | 0.11 | 0.11 | 0.72 | 0.12 | 0.11 | 0.14 | 0.09 | 0.14 | 0.22 | 0.14 | 0.15 | 0.13 | 0.12 | 0.19 | 0.14 | 0.16 | 0.10 |
| Cs | 0.03 | 0.05 | 0.03 | 0.39 | 0.12 | 1.42 | 0.11 | 0.06 | 0.01 | 0.01 | 0.01 | 0.30 | 0.26 | 0.38 | 0.14 | 0.01 | 0.07 | 0.18 | 0.57 | 0.01 |
| Ba | 0.12 | 0.18 | 0.10 | 0.46 | 0.26 | 0.09 | 1.56 | 0.33 | 0.15 | 0.26 | 0.09 | 0.19 | 0.69 | 0.09 | 0.05 | 0.05 | 0.06 | 0.03 | 0.61 | 0.18 |
| La | 0.161 | 0.131 | 0.106 | 0.088 | 0.125 | 0.160 | 0.194 | 0.086 | 0.167 | 0.102 | 0.298 | 0.339 | 0.252 | 0.242 | 0.226 | 0.238 | 0.226 | 0.162 | 0.146 | 0.257 |
| Ce | 0.910 | 0.610 | 0.432 | 0.630 | 0.610 | 0.850 | 0.870 | 0.357 | 0.730 | 0.510 | 1.410 | 1.560 | 1.250 | 1.260 | 0.890 | 1.420 | 0.950 | 1.180 | 0.540 | 0.880 |
| Pr | 0.258 | 0.193 | 0.154 | 0.170 | 0.185 | 0.266 | 0.292 | 0.093 | 0.310 | 0.183 | 0.372 | 0.437 | 0.334 | 0.316 | 0.217 | 0.337 | 0.262 | 0.300 | 0.130 | 0.269 |
| Nd | 1.972 | 1.361 | 0.975 | 1.149 | 1.403 | 2.181 | 2.682 | 1.118 | 2.690 | 1.347 | 2.610 | 2.610 | 2.590 | 2.412 | 1.519 | 2.412 | 1.613 | 1.539 | 0.794 | 2.030 |
| Sm | 1.136 | 0.858 | 0.618 | 0.726 | 0.776 | 1.354 | 1.315 | 0.460 | 0.966 | 0.854 | 1.338 | 1.273 | 1.446 | 1.292 | 0.785 | 1.279 | 0.789 | 0.897 | 0.476 | 1.234 |
| Eu | 0.364 | 0.271 | 0.250 | 0.270 | 0.269 | 0.337 | 0.367 | 0.212 | 0.333 | 0.272 | 0.438 | 0.407 | 0.394 | 0.384 | 0.315 | 0.396 | 0.338 | 0.310 | 0.223 | 0.392 |
| Gd | 2.112 | 1.355 | 1.222 | 1.301 | 1.363 | 2.382 | 2.267 | 0.889 | 1.838 | 1.611 | 2.193 | 2.278 | 2.209 | 1.868 | 1.417 | 2.106 | 1.292 | 1.447 | 0.848 | 2.074 |
| Tb | 0.422 | 0.298 | 0.233 | 0.275 | 0.274 | 0.459 | 0.443 | 0.184 | 0.340 | 0.326 | 0.389 | 0.404 | 0.411 | 0.359 | 0.260 | 0.389 | 0.276 | 0.268 | 0.169 | 0.391 |
| Dy | 3.360 | 2.205 | 1.774 | 2.117 | 2.203 | 3.540 | 3.430 | 1.457 | 2.709 | 2.566 | 3.010 | 3.030 | 3.150 | 2.790 | 1.864 | 2.790 | 1.986 | 2.082 | 1.281 | 2.700 |
| Ho | 0.772 | 0.493 | 0.374 | 0.446 | 0.489 | 0.816 | 0.758 | 0.332 | 0.619 | 0.538 | 0.629 | 0.633 | 0.644 | 0.597 | 0.439 | 0.582 | 0.453 | 0.444 | 0.306 | 0.571 |
| Er | 2.236 | 1.462 | 1.124 | 1.311 | 1.421 | 2.376 | 2.264 | 1.009 | 1.858 | 1.644 | 1.666 | 1.803 | 1.781 | 1.625 | 1.285 | 1.616 | 1.230 | 1.277 | 0.897 | 1.686 |
| Tm | 0.354 | 0.222 | 0.158 | 0.207 | 0.210 | 0.364 | 0.329 | 0.159 | 0.280 | 0.236 | 0.250 | 0.269 | 0.244 | 0.232 | 0.163 | 0.232 | 0.183 | 0.172 | 0.137 | 0.211 |
| Yb | 2.179 | 1.522 | 1.113 | 1.457 | 1.427 | 2.408 | 2.082 | 1.037 | 1.843 | 1.577 | 1.673 | 1.665 | 1.664 | 1.580 | 1.218 | 1.599 | 1.243 | 1.231 | 0.943 | 1.369 |
| Lu | 0.315 | 0.214 | 0.149 | 0.199 | 0.172 | 0.354 | 0.301 | 0.159 | 0.257 | 0.237 | 0.226 | 0.231 | 0.228 | 0.210 | 0.174 | 0.208 | 0.178 | 0.175 | 0.150 | 0.222 |
| Hf | 0.45 | 0.22 | 0.18 | 0.27 | 0.26 | 0.63 | 0.59 | 0.14 | 0.46 | 0.30 | 0.75 | 0.55 | 0.93 | 0.65 | 0.30 | 1.10 | 0.46 | 0.16 | 0.57 | 0.01 |
| Ta | 0.05 | 0.01 | 0.00 | 0.02 | 0.00 | 0.02 | 0.04 | 0.00 | 0.01 | 0.00 | 0.04 | 0.03 | 0.04 | 0.02 | 0.04 | 0.02 | 0.02 | 0.00 | 0.01 | 0.01 |
| Pb | 0.37 | 0.32 | 0.07 | 0.13 | 0.22 | 0.07 | 0.38 | 0.01 | 0.01 | 0.04 | 0.03 | 0.04 | 6.28 | 0.38 | 0.27 | 1.11 | 0.08 | 5.16 | 0.30 | 2.47 |
| Th | 0.06 | 0.16 | 0.07 | 0.14 | 0.01 | 0.03 | 0.35 | 0.26 | 0.35 | 0.01 | 0.08 | 1.32 | 0.10 | 0.82 | 0.03 | 0.03 | 0.37 | 0.11 | 0.20 | 0.12 |
| U | 0.11 | 0.18 | 0.15 | 0.56 | 0.03 | 0.05 | 1.72 | 0.00 | 0.22 | 0.00 | 0.19 | 0.07 | 0.02 | 0.04 | 0.17 | 1.83 | 0.04 | 0.37 | 0.02 | 0.38 |

*Analyses en éléments en trace (ppm) par LA-CP-MC. Abbréviation: c=centre, b=bordure

Tableau B-2b (suite)

| Echantillon | 228R4 39-43 | | | | | | | | | | 238R3 14-18 | | | | | | | | | | 248R3 131-134 | | | | | | | | | |
|--------------------|------------------|--------|--------|--------|--------|--------|--------|--------|--------|--------|-----------------------------|--------|--------|--------|--------|--------|--------|--------|--------|--------|-----------------------------|------|--|--|--|--|--|--|--|--|
| | gabbro à olivine | | | | | | | | | | Troctolite riche en olivine | | | | | | | | | | Troctolite riche en olivine | | | | | | | | | |
| Type de roche | | | | | | | | | | | | | | | | | | | | | | | | | | | | | | |
| Profondeur (mbsf) | | | | | | | | | | | | | | | | | | | | | | | | | | | | | | |
| Zones | | | | | | | | | | | | | | | | | | | | | | | | | | | | | | |
| Point Localisation | | | | | | | | | | | | | | | | | | | | | | | | | | | | | | |
| Ti | 1 | 2 | 3 | 4 | 5 | 6 | 7 | 8 | 9 | 10 | 1 | 2 | 3 | 4 | 5 | 6 | 1 | 2 | 3 | 4 | 5 | | | | | | | | | |
| V | 3216 | 2338 | 2236 | 3170 | 2371 | 2354 | 2415 | 2575 | 2473 | 2785 | 1414 | 1522 | 1888 | 1435 | 1471 | 1870 | 3223 | 2234 | 3325 | 3325 | 2677 | 3398 | | | | | | | | |
| Cr | 35853 | 31708 | 30644 | 33210 | 31506 | 31013 | 30816 | 31840 | 30307 | 32171 | 33973 | 38952 | 40434 | 39193 | 39073 | 39377 | 35250 | 31392 | 35256 | 32224 | 35769 | | | | | | | | | |
| Co | 518034 | 559551 | 684126 | 427264 | 619997 | 719257 | 421314 | 349070 | 343829 | 360722 | 792350 | 802406 | 777677 | 845952 | 834155 | 836071 | 808179 | 726080 | 727827 | 751361 | 789588 | | | | | | | | | |
| Ni | 3851 | 3633 | 3443 | 3265 | 3470 | 3441 | 3484 | 3150 | 3302 | 3325 | 2983 | 3053 | 3649 | 3269 | 3338 | 3178 | 2956 | 3033 | 3181 | 2786 | 3038 | | | | | | | | | |
| Zn | 104364 | 25135 | 24429 | 25229 | 39508 | 23944 | 24452 | 22964 | 22676 | 89685 | 35499 | 26693 | 19879 | 51871 | 24315 | 22582 | 34100 | 34110 | 32569 | 172629 | 30182 | | | | | | | | | |
| Rb | 2310 | 2175 | 2060 | 1963 | 2279 | 2098 | 2077 | 1867 | 1967 | 2226 | 2296 | 2266 | 3079 | 2059 | 1908 | 2011 | 2091 | 1888 | 2239 | 1730 | 2074 | | | | | | | | | |
| Rb | 016 | 641 | 041 | 003 | 016 | 020 | 002 | 002 | 002 | 004 | 035 | 017 | 126 | 010 | 007 | 008 | 005 | 004 | 012 | 007 | 004 | | | | | | | | | |
| Sr | 589 | 743 | 705 | 1131 | 707 | 751 | 735 | 637 | 660 | 641 | 699 | 724 | 803 | 712 | 652 | 696 | 657 | 719 | 685 | 731 | 732 | | | | | | | | | |
| Y | 1332 | 1001 | 941 | 1310 | 982 | 1014 | 999 | 1274 | 1121 | 1345 | 1556 | 1601 | 1960 | 1421 | 1441 | 1871 | 1705 | 1042 | 1909 | 1556 | 2269 | | | | | | | | | |
| Zr | 1062 | 427 | 430 | 2002 | 592 | 543 | 742 | 3098 | 724 | 1013 | 1055 | 747 | 1083 | 834 | 708 | 995 | 1549 | 472 | 2511 | 1261 | 2964 | | | | | | | | | |
| Nb | 017 | 009 | 030 | 020 | 008 | 014 | 013 | 010 | 013 | 014 | 030 | 017 | 015 | 016 | 011 | 016 | 016 | 010 | 020 | 020 | 021 | | | | | | | | | |
| Cs | 001 | 001 | 001 | 015 | 012 | 010 | 014 | 001 | 016 | 001 | 002 | 017 | 005 | 013 | 019 | 026 | 002 | 002 | 004 | 004 | 030 | | | | | | | | | |
| Ba | 020 | 004 | 003 | 009 | 006 | 009 | 004 | 008 | 007 | 010 | 043 | 028 | 034 | 034 | 006 | 006 | 010 | 016 | 023 | 020 | 009 | | | | | | | | | |
| La | 0196 | 0078 | 0108 | 0230 | 0176 | 0141 | 0130 | 0178 | 0178 | 0204 | 0188 | 0201 | 0259 | 0175 | 0151 | 0310 | 0161 | 0109 | 0180 | 0185 | 0217 | | | | | | | | | |
| Ce | 1116 | 0438 | 0533 | 1043 | 0621 | 0624 | 0637 | 0961 | 0883 | 1016 | 0914 | 1148 | 1460 | 1404 | 0863 | 1190 | 0986 | 0559 | 1152 | 1101 | 1411 | | | | | | | | | |
| Pr | 0273 | 0118 | 0125 | 0285 | 0166 | 0155 | 0158 | 0235 | 0233 | 0236 | 0225 | 0298 | 0334 | 0272 | 0232 | 0325 | 0335 | 0148 | 0309 | 0326 | 0361 | | | | | | | | | |
| Nd | 1913 | 1002 | 1003 | 1825 | 1142 | 1237 | 1165 | 1635 | 1439 | 1696 | 1980 | 2002 | 2521 | 2407 | 1731 | 2371 | 1996 | 1052 | 2670 | 2022 | 3030 | | | | | | | | | |
| Sm | 0681 | 0539 | 0637 | 1019 | 0694 | 0701 | 0673 | 0790 | 0768 | 1025 | 1103 | 1122 | 1438 | 1068 | 1041 | 1439 | 0939 | 0619 | 1479 | 1096 | 1758 | | | | | | | | | |
| Eu | 0311 | 0266 | 0256 | 0379 | 0287 | 0268 | 0315 | 0337 | 0327 | 0346 | 0377 | 0422 | 0453 | 0378 | 0350 | 0421 | 0336 | 0282 | 0381 | 0380 | 0479 | | | | | | | | | |
| Gd | 1722 | 1258 | 1068 | 1651 | 1202 | 1203 | 1289 | 1594 | 1449 | 1521 | 1694 | 1938 | 2451 | 1781 | 1707 | 2649 | 1982 | 1076 | 2203 | 1898 | 2910 | | | | | | | | | |
| Tb | 0326 | 0239 | 0227 | 0331 | 0247 | 0273 | 0246 | 0296 | 0275 | 0310 | 0338 | 0400 | 0442 | 0318 | 0329 | 0483 | 0393 | 0238 | 0419 | 0369 | 0556 | | | | | | | | | |
| Dy | 2412 | 1829 | 1695 | 2325 | 1777 | 1893 | 1948 | 2343 | 2037 | 2467 | 2637 | 3020 | 3610 | 2530 | 2617 | 3620 | 2890 | 1732 | 3510 | 2742 | 4100 | | | | | | | | | |
| Ho | 0513 | 0384 | 0379 | 0539 | 0408 | 0412 | 0401 | 0511 | 0419 | 0517 | 0576 | 0647 | 0774 | 0520 | 0571 | 0753 | 0664 | 0374 | 0740 | 0584 | 0856 | | | | | | | | | |
| Er | 1741 | 1162 | 1078 | 1501 | 1136 | 1136 | 1166 | 1498 | 1284 | 1501 | 1656 | 1847 | 2185 | 1488 | 1547 | 2076 | 1873 | 1139 | 2271 | 1807 | 2485 | | | | | | | | | |
| Tm | 0225 | 0157 | 0165 | 0230 | 0171 | 0160 | 0162 | 0216 | 0200 | 0239 | 0256 | 0274 | 0327 | 0231 | 0234 | 0314 | 0266 | 0169 | 0312 | 0256 | 0365 | | | | | | | | | |
| Yb | 1467 | 1054 | 0972 | 1476 | 0994 | 1163 | 1100 | 1486 | 1188 | 1522 | 1793 | 1906 | 2006 | 1425 | 1651 | 2031 | 1697 | 1235 | 1857 | 1819 | 2330 | | | | | | | | | |
| Hf | 037 | 025 | 027 | 045 | 025 | 026 | 026 | 025 | 022 | 030 | 049 | 050 | 085 | 061 | 037 | 060 | 043 | 019 | 058 | 032 | 068 | | | | | | | | | |
| Ta | 001 | 000 | 004 | 001 | 000 | 000 | 000 | 000 | 001 | 004 | 002 | 002 | 001 | 009 | 000 | 001 | 002 | 002 | 002 | 002 | 003 | | | | | | | | | |
| Pb | 003 | 013 | 042 | 009 | 009 | 004 | 019 | 032 | 043 | 055 | 111 | 017 | 844 | 064 | 093 | 045 | 011 | 017 | 387 | 010 | 506 | | | | | | | | | |
| Th | 001 | 087 | 022 | 006 | 018 | 249 | 001 | 031 | 011 | 004 | 042 | 018 | 016 | 055 | 013 | 017 | 016 | 006 | 010 | 008 | 017 | | | | | | | | | |
| U | 074 | 004 | 009 | 001 | 000 | 001 | 000 | 001 | 048 | 001 | 026 | 044 | 018 | 088 | 012 | 024 | 025 | 032 | 004 | 001 | 001 | | | | | | | | | |

Tableau B-2b (suite)

| Échantillon | Trochilite riche en olivine | | | | | | | | | | | | | | | | | | | | | | | |
|--------------------|-----------------------------|--------|--------|--------|--------|--------|--------|--------|--------|--------|--------|--------|--------|--------|--------|--------|--------|--------|--------|--------|--------|--------|--------|--------|
| | 1193.32 | | | | | | | | | | | | | | | | | | | | | | | |
| Type de roche | | | | | | | | | | | | | | | | | | | | | | | | |
| Profondeur (mbsf) | | | | | | | | | | | | | | | | | | | | | | | | |
| Zones | | | | | | | | | | | | | | | | | | | | | | | | |
| Point Localisation | A1 | A2 | A3 | A4 | A5 | A6 | A7 | A8 | A9 | A10 | A11 | A12 | A13 | A14 | A15 | A16 | A17 | A18 | A19 | A20 | B1 | B2 | B3 | B4 |
| Ti | 3664 | 3308 | 3378 | 3270 | 3254 | 3143 | 2958 | 5636 | 3281 | 2838 | 3019 | 3035 | 3451 | 2779 | 4211 | 3659 | 2855 | 2877 | 3870 | 5144 | 7635 | 5637 | 4866 | 4366 |
| V | 36194 | 34891 | 36554 | 36211 | 36601 | 36531 | 36422 | 48374 | 39538 | 36301 | 38503 | 40159 | 42108 | 37747 | 47706 | 45048 | 39855 | 40874 | 47132 | 50708 | 41651 | 39249 | 39439 | 43990 |
| Cr | 422389 | 602630 | 651083 | 680453 | 661240 | 663359 | 438633 | 399117 | 422365 | 368883 | 527400 | 624404 | 481085 | 473736 | 353798 | 437630 | 565313 | 449810 | 422478 | 400693 | 865674 | 978466 | 964989 | 759817 |
| Co | 4138 | 3836 | 4069 | 4235 | 4281 | 4156 | 4212 | 4279 | 3930 | 4108 | 4035 | 4167 | 4060 | 4102 | 4363 | 4245 | 4200 | 4214 | 4269 | 3812 | 3251 | 3822 | 3856 | 3405 |
| Ni | 28928 | 28731 | 28419 | 30638 | 30771 | 30559 | 29115 | 37038 | 27511 | 29508 | 28245 | 28369 | 26754 | 27667 | 28531 | 27715 | 31090 | 27795 | 28101 | 26658 | 2753 | 3614 | 5261 | 7815 |
| Zn | 3124 | 2623 | 2883 | 2834 | 2738 | 2694 | 2714 | 2754 | 2458 | 2521 | 2512 | 2980 | 2487 | 2459 | 2907 | 2651 | 2532 | 2697 | 2497 | 2400 | 2548 | 2955 | 3056 | 2514 |
| Rb | 004 | 008 | 014 | 015 | 018 | 004 | 006 | 004 | 004 | 019 | 069 | 004 | 009 | 004 | 012 | 005 | 012 | 007 | 004 | 004 | 020 | 004 | 004 | 007 |
| Y | 659 | 737 | 698 | 734 | 692 | 686 | 657 | 691 | 688 | 655 | 693 | 710 | 681 | 695 | 667 | 679 | 640 | 674 | 648 | 658 | 799 | 736 | 688 | 671 |
| Zr | 1643 | 1356 | 1440 | 1364 | 1346 | 1328 | 1484 | 2560 | 1958 | 1453 | 1573 | 1650 | 2185 | 1475 | 2567 | 2368 | 1647 | 1738 | 2377 | 3141 | 1998 | 1830 | 1829 | 2158 |
| Y | 936 | 857 | 697 | 627 | 1405 | 574 | 1323 | 2752 | 883 | 532 | 738 | 712 | 1054 | 602 | 1215 | 1362 | 588 | 764 | 1153 | 2477 | 1016 | 744 | 677 | 2777 |
| Nb | 010 | 004 | 002 | 001 | 011 | 005 | 004 | 013 | 009 | 006 | 012 | 013 | 009 | 002 | 017 | 010 | 001 | 004 | 011 | 019 | 021 | 017 | 017 | 022 |
| Cs | 009 | 018 | 004 | 032 | 026 | 007 | 001 | 001 | 003 | 001 | 030 | 001 | 001 | 001 | 039 | 001 | 025 | 002 | 001 | 001 | 004 | 002 | 004 | 003 |
| Ba | 010 | 021 | 013 | 019 | 011 | 011 | 014 | 011 | 011 | 011 | 010 | 010 | 010 | 010 | 016 | 010 | 010 | 017 | 010 | 011 | 030 | 009 | 008 | 008 |
| La | 0248 | 0115 | 0109 | 0115 | 0107 | 0125 | 0149 | 0298 | 0182 | 0111 | 0120 | 0128 | 0195 | 0142 | 0274 | 0205 | 0096 | 0173 | 0251 | 0369 | 0286 | 0255 | 0178 | 0289 |
| Ce | 1118 | 0703 | 0668 | 0700 | 0633 | 0654 | 0741 | 1780 | 1071 | 0667 | 0727 | 0721 | 1136 | 0663 | 1560 | 1360 | 0683 | 0827 | 1160 | 2010 | 1071 | 0936 | 0916 | 1448 |
| Pr | 0250 | 0200 | 0223 | 0186 | 0184 | 0192 | 0215 | 0490 | 0244 | 0184 | 0197 | 0211 | 0319 | 0163 | 0384 | 0374 | 0207 | 0222 | 0309 | 0574 | 0336 | 0264 | 0284 | 0329 |
| Nd | 1936 | 1566 | 1644 | 1362 | 1479 | 1480 | 1630 | 3700 | 2083 | 1632 | 1742 | 1774 | 2460 | 1600 | 3010 | 2670 | 1800 | 1904 | 1944 | 2960 | 2207 | 1972 | 1897 | 2610 |
| Sm | 1185 | 0986 | 0944 | 0918 | 0898 | 0864 | 1001 | 2330 | 1069 | 0937 | 0942 | 1017 | 1386 | 1064 | 1645 | 1474 | 1182 | 1177 | 1693 | 2670 | 1398 | 1227 | 1201 | 1393 |
| Eu | 0380 | 0312 | 0371 | 0311 | 0371 | 0348 | 0373 | 0617 | 0453 | 0368 | 0378 | 0458 | 0465 | 0425 | 0543 | 0518 | 0416 | 0462 | 0600 | 0725 | 0566 | 0463 | 0456 | 0475 |
| Gd | 1923 | 1683 | 1839 | 1618 | 1577 | 1867 | 1762 | 3500 | 2230 | 1698 | 1780 | 1920 | 2470 | 1920 | 3220 | 2930 | 2090 | 2180 | 2850 | 4330 | 2335 | 2277 | 2175 | 2500 |
| Tb | 0358 | 0322 | 0323 | 0316 | 0340 | 0311 | 0332 | 0643 | 0441 | 0334 | 0361 | 0367 | 0496 | 0357 | 0619 | 0554 | 0367 | 0400 | 0581 | 0792 | 0475 | 0401 | 0435 | 0478 |
| Dy | 2820 | 2390 | 2426 | 2487 | 2454 | 2578 | 2710 | 4540 | 3590 | 2690 | 2640 | 3030 | 3930 | 2530 | 4700 | 4410 | 3120 | 3300 | 4620 | 6110 | 3610 | 3110 | 3300 | 3630 |
| Ho | 0444 | 0510 | 0539 | 0534 | 0520 | 0553 | 0597 | 1040 | 0780 | 0539 | 0615 | 0659 | 0854 | 0616 | 0978 | 0985 | 0643 | 0719 | 1009 | 1261 | 0800 | 0688 | 0688 | 814 |
| Er | 1858 | 1539 | 1502 | 1524 | 1522 | 1501 | 1687 | 2870 | 2300 | 1581 | 1768 | 1863 | 2340 | 1613 | 2970 | 2860 | 1890 | 2030 | 2830 | 3540 | 2360 | 2079 | 2024 | 2486 |
| Tm | 0263 | 0202 | 0239 | 0224 | 0208 | 0229 | 0233 | 0380 | 0339 | 0222 | 0248 | 0269 | 0345 | 0233 | 0438 | 0400 | 0284 | 0281 | 0397 | 0508 | 0376 | 0288 | 0318 | 0379 |
| Yb | 1756 | 1316 | 1378 | 1361 | 1409 | 1531 | 1607 | 2540 | 2250 | 1523 | 1637 | 1834 | 2260 | 1560 | 2860 | 2570 | 1930 | 2140 | 2840 | 3450 | 2484 | 2087 | 1944 | 2440 |
| Lu | 0278 | 0205 | 0197 | 0211 | 0220 | 0205 | 0231 | 0333 | 0312 | 0211 | 0237 | 0264 | 0331 | 0239 | 0401 | 0387 | 0275 | 0290 | 0374 | 0454 | 0364 | 0280 | 0266 | 0344 |
| Hf | 049 | 032 | 035 | 038 | 031 | 034 | 041 | 085 | 066 | 031 | 033 | 036 | 045 | 036 | 055 | 059 | 040 | 044 | 058 | 107 | 038 | 038 | 041 | 055 |
| Ta | 001 | 001 | 001 | 001 | 000 | 000 | 002 | 002 | 002 | 001 | 001 | 002 | 001 | 001 | 001 | 001 | 000 | 001 | 001 | 001 | 001 | 001 | 002 | 002 |
| Pb | 025 | 015 | 011 | 025 | 002 | 190 | 013 | 048 | 065 | 024 | 034 | 012 | 002 | 003 | 016 | 053 | 012 | 004 | 184 | 004 | 013 | 004 | 001 | 007 |
| Th | 004 | 022 | 001 | 007 | 007 | 007 | 000 | 028 | 002 | 003 | 001 | 011 | 001 | 000 | 005 | 021 | 002 | 001 | 007 | 003 | 013 | 002 | 002 | 002 |
| U | 046 | 000 | 007 | 007 | 071 | 005 | 054 | 109 | 003 | 004 | 003 | 000 | 002 | 000 | 002 | 006 | 008 | 000 | 014 | 003 | 002 | 000 | 001 | 001 |

Tableau B-2c: Profils en éléments en trace dans les olivines du puits IODP U1309D*

| Echantillon | | 232Rf 112-116 | | | | | | | | | | | | |
|-------------------|--------|---------------|--------|--------|--------|--------|--------|--------|--------|--------|--------|--------|--------|--------|
| Type de roche | | Troctolite | | | | | | | | | | | | |
| Profondeur (mbsf) | | 1116.22 | | | | | | | | | | | | |
| Zones Point | | 4 | | | | | | | | | | | | |
| Axe | o14_1 | o14_2 | o14_3 | o14_4 | O16_1 | O16_2 | O111_1 | O111_2 | O111_3 | O12_1 | O12_2 | O12_3 | O12_4 | O12_5 |
| Si | 184826 | 184826 | 184826 | 184826 | 184826 | 184826 | 184826 | 184826 | 184826 | 184826 | 184826 | 184826 | 184826 | 184826 |
| P | 40 | 77 | 61 | 18 | 45 | 152 | 36 | 64 | 20 | 41 | 57 | 60 | 68 | 51 |
| Ca | 421 | 592 | 579 | 526 | 417 | 435 | 595 | 528 | 550 | 484 | 577 | 658 | 596 | 662 |
| Ti | 122 | 132 | 125 | 122 | 110 | 88 | 108 | 106 | 131 | 91 | 104 | 113 | 106 | 114 |
| V | 7 | 8 | 7 | 7 | 7 | 5 | 8 | 7 | 8 | 5 | 7 | 7 | 6 | 7 |
| Cr | 85 | 93 | 75 | 78 | 79 | 52 | 84 | 79 | 94 | 65 | 94 | 73 | 64 | 70 |
| Co | 177.1 | 174.8 | 178.0 | 177.9 | 175.4 | 174.4 | 175.7 | 175.0 | 178.1 | 173.5 | 175.0 | 175.7 | 175.7 | 175.4 |
| Ni | 1442 | 1420 | 1455 | 1448 | 1472 | 1419 | 1424 | 1423 | 1449 | 1452 | 1462 | 1459 | 1459 | 1485 |
| Zn | 97 | 98 | 101 | 98 | 99 | 99 | 100 | 101 | 101 | 99 | 99 | 100 | 102 | 102 |
| Rb | 0.0298 | 0.0079 | 0.0116 | 0.0093 | 0.0094 | 0.0078 | 0.0079 | 0.0032 | 0.0042 | 0.0060 | 0.0036 | 0.0053 | 0.0090 | 0.0067 |
| Sr | 0.0093 | 0.0010 | 0.0036 | 0.0145 | 0.0122 | 0.0289 | 0.0080 | 0.0013 | 0.0091 | 0.0077 | 0.0027 | 0.0033 | 0.0281 | 0.0051 |
| Y | 0.0894 | 0.1332 | 0.1144 | 0.1180 | 0.0932 | 0.0784 | 0.1343 | 0.0919 | 0.1111 | 0.0750 | 0.1046 | 0.1091 | 0.0904 | 0.1160 |
| Zr | 0.7900 | 0.1143 | 0.1061 | 0.1092 | 0.0669 | 0.0727 | 0.5110 | 0.0628 | 0.0873 | 0.0709 | 0.5610 | 0.1256 | 0.0960 | 0.1162 |
| Nb | 0.0310 | 0.0054 | 0.0032 | 0.0151 | 0.0141 | 0.0063 | 0.0092 | 0.0055 | 0.0070 | 0.0044 | 0.0087 | 0.0078 | 0.0062 | 0.0067 |
| Cs | 0.0120 | 0.0020 | 0.0052 | 0.0068 | 0.0036 | 0.0018 | 0.0095 | 0.0042 | 0.0068 | 0.0030 | 0.0041 | 0.0493 | 0.0032 | 0.0243 |
| Ba | 0.0044 | 0.0194 | 0.0024 | 0.0159 | 0.0014 | 0.0055 | 0.0013 | 0.0367 | 0.0014 | 0.0034 | 0.0033 | 0.0012 | 0.0019 | 0.0159 |
| La | 0.0003 | 0.0004 | 0.0003 | 0.0003 | 0.0002 | 0.0004 | 0.0001 | 0.0003 | 0.0003 | 0.0004 | 0.0001 | 0.0001 | 0.0001 | 0.0008 |
| Ce | 0.0113 | 0.0002 | 0.0005 | 0.0004 | - | - | 0.0001 | 0.0023 | 0.0005 | 0.0003 | 0.0002 | 0.0001 | 0.0006 | 0.0001 |
| Pr | 0.0080 | 0.0001 | 0.0002 | 0.0002 | 0.0001 | 0.0001 | 0.0001 | 0.0001 | 0.0001 | 0.0002 | 0.0000 | 0.0001 | 0.0000 | 0.0000 |
| Nd | 0.0009 | 0.0001 | 0.0006 | 0.0005 | 0.0009 | 0.0003 | 0.0001 | 0.0002 | 0.0005 | 0.0006 | 0.0004 | 0.0004 | 0.0003 | 0.0001 |
| Sm | 0.0013 | 0.0003 | 0.0015 | 0.0021 | 0.0004 | 0.0004 | 0.0016 | 0.0006 | 0.0014 | 0.0034 | 0.0010 | 0.0007 | 0.0004 | 0.0011 |
| Eu | 0.0001 | 0.0004 | 0.0003 | 0.0001 | 0.0001 | 0.0001 | 0.0001 | 0.0001 | 0.0002 | 0.0003 | 0.0001 | 0.0007 | 0.0000 | 0.0001 |
| Gd | 0.0012 | 0.0018 | 0.0013 | 0.0032 | 0.0010 | 0.0007 | 0.0032 | 0.0006 | 0.0023 | 0.0020 | 0.0027 | 0.0006 | 0.0017 | 0.0038 |
| Tb | 0.0007 | 0.0008 | 0.0006 | 0.0005 | 0.0007 | 0.0002 | 0.0014 | 0.0003 | 0.0005 | 0.0003 | 0.0008 | 0.0006 | 0.0002 | 0.0009 |
| Dy | 0.0059 | 0.0093 | 0.0064 | 0.0093 | 0.0069 | 0.0034 | 0.0123 | 0.0044 | 0.0067 | 0.0041 | 0.0084 | 0.0084 | 0.0043 | 0.0083 |
| Ho | 0.0035 | 0.0042 | 0.0041 | 0.0035 | 0.0028 | 0.0027 | 0.0052 | 0.0031 | 0.0039 | 0.0024 | 0.0033 | 0.0054 | 0.0029 | 0.0036 |
| Er | 0.0178 | 0.0277 | 0.0261 | 0.0193 | 0.0162 | 0.0164 | 0.0259 | 0.0173 | 0.0234 | 0.0170 | 0.0233 | 0.0224 | 0.0215 | 0.0246 |
| Tm | 0.0048 | 0.0081 | 0.0079 | 0.0082 | 0.0054 | 0.0050 | 0.0061 | 0.0056 | 0.0067 | 0.0053 | 0.0061 | 0.0071 | 0.0061 | 0.0071 |
| Yb | 0.0957 | 0.0788 | 0.0802 | 0.0789 | 0.0658 | 0.0572 | 0.0731 | 0.0625 | 0.0720 | 0.0638 | 0.0670 | 0.0781 | 0.0719 | 0.0765 |
| Lu | 0.0164 | 0.0202 | 0.0203 | 0.0189 | 0.0162 | 0.0146 | 0.0174 | 0.0142 | 0.0182 | 0.0147 | 0.0170 | 0.0204 | 0.0174 | 0.0198 |
| Hf | 0.0089 | 0.0027 | 0.0038 | 0.0025 | 0.0015 | 0.0015 | 0.0022 | 0.0017 | 0.0032 | 0.0016 | 0.0035 | 0.0105 | 0.0024 | 0.0053 |
| Ta | 0.0003 | 0.0003 | 0.0004 | 0.0008 | 0.0005 | 0.0003 | 0.0003 | 0.0005 | 0.0004 | 0.0007 | 0.0002 | 0.0002 | 0.0007 | 0.0001 |
| Pb | 0.0075 | 0.0049 | 0.0051 | 0.0073 | 0.0104 | 0.0134 | 0.0090 | 0.0152 | 0.0079 | 0.0139 | 0.0121 | 0.0133 | 0.0091 | 0.1620 |
| Th | 0.0026 | 0.0001 | 0.0001 | 0.0002 | 0.0002 | 0.0202 | 0.0002 | 0.0001 | 0.0001 | 0.0000 | 0.0005 | 0.0017 | 0.0001 | 0.0148 |
| U | 0.0227 | 0.0662 | 0.0001 | 0.0017 | 0.0001 | 0.0003 | 0.0005 | 0.0000 | 0.0001 | 0.0005 | 0.0004 | 0.0001 | 0.0169 | 0.0002 |

* Analyses en éléments en trace (ppm) par LA-ICP-MS.

Tableau B-2c (suite)

| Echantillon | | Toxicologie riche en olivine | | | | | | | | | | | | | | | | | | | |
|---------------|--------|------------------------------|--------|--------|--------|--------|--------|--------|--------|--------|--------|--------|--------|--------|--------|--------|--------|--------|--|--|--|
| Type de roche | | 248R2 18-21 | | | | | | | | | | | | | | | | | | | |
| Profondeur | | 1193.32 | | | | | | | | | | | | | | | | | | | |
| Zones (mbsf) | | 4 | | | | | | | | | | | | | | | | | | | |
| Point | | Ol_e_1 | Ol_e_2 | Ol_e_3 | Ol_e_4 | Ol_e_5 | Ol_l_1 | Ol_l_2 | Ol_l_3 | Ol_l_4 | Ol_l_5 | Ol_a_1 | Ol_a_2 | O19_1 | O19_2 | O19_3 | O19_4 | | | | |
| Axe | | 001 | | | | | 001 | | | | | 001 | | | | | 001 | | | | |
| Si | 187537 | 187537 | 187537 | 187537 | 187537 | 187537 | 187537 | 187537 | 187537 | 187537 | 187537 | 187537 | 187537 | 187537 | 187537 | 187537 | 187537 | 187537 | | | |
| P | 38 | 40 | 31 | 42 | 29 | 30 | 33 | 39 | 26 | 40 | 22 | 34 | 27 | 30 | 36 | 30 | 30 | | | | |
| Ca | 587 | 685 | 666 | 638 | 778 | 620 | 596 | 674 | 599 | 585 | 532 | 393 | 641 | 522 | 552 | 619 | 619 | | | | |
| Ti | 111 | 169 | 128 | 125 | 130 | 154 | 153 | 129 | 147 | 126 | 112 | 141 | 137 | 154 | 140 | 150 | 150 | | | | |
| V | 7 | 9 | 9 | 8 | 8 | 9 | 8 | 8 | 9 | 8 | 7 | 8 | 8 | 8 | 9 | 10 | 10 | | | | |
| Cr | 66 | 92 | 94 | 88 | 57 | 98 | 88 | 70 | 91 | 74 | 74 | 75 | 69 | 60 | 85 | 91 | 91 | | | | |
| Co | 178.2 | 181.0 | 181.3 | 181.9 | 179.2 | 179.7 | 177.6 | 178.0 | 178.2 | 178.4 | 180.2 | 177.1 | 180.5 | 177.5 | 178.4 | 179.9 | 179.9 | | | | |
| Ni | 1667 | 1597 | 1599 | 1583 | 1563 | 1620 | 1594 | 1585 | 1566 | 1562 | 1548 | 1542 | 1628 | 1599 | 1643 | 1658 | 1658 | | | | |
| Zn | 110 | 111 | 113 | 112 | 113 | 115 | 112 | 112 | 114 | 118 | 111 | 109 | 111 | 109 | 110 | 113 | 113 | | | | |
| Rb | 0.0033 | 0.0054 | 0.0032 | 0.0136 | 0.0052 | 0.0037 | 0.0043 | 0.0094 | 0.0060 | 0.0084 | 0.0153 | 0.0085 | 0.0021 | 0.0026 | 0.0022 | 0.0021 | 0.0021 | | | | |
| Sr | 0.0175 | 0.0157 | 0.0164 | 0.0047 | 0.0299 | 0.0216 | 0.0025 | 0.0300 | 0.0047 | 0.0086 | 0.0197 | 0.0236 | 0.0228 | 0.0038 | 0.0025 | 0.0058 | 0.0058 | | | | |
| Y | 0.1298 | 0.2213 | 0.2033 | 0.1829 | 0.2470 | 0.1522 | 0.1480 | 0.1570 | 0.1460 | 0.1385 | 0.0786 | 0.0810 | 0.1878 | 0.1691 | 0.1567 | 0.1870 | 0.1870 | | | | |
| Zr | 0.0658 | 0.0801 | 0.0600 | 0.0597 | 0.0712 | 0.0956 | 0.0573 | 0.0691 | 0.0554 | 0.0622 | 0.0267 | 0.0408 | 0.0921 | 0.1073 | 0.0738 | 0.1430 | 0.1430 | | | | |
| Nb | 0.0014 | 0.0017 | 0.0015 | 0.0006 | 0.0018 | 0.0018 | 0.0019 | 0.0029 | 0.0020 | 0.0047 | 0.0039 | 0.0007 | 0.0023 | 0.0056 | 0.0013 | 0.0092 | 0.0092 | | | | |
| Cs | 0.0018 | 0.0033 | 0.0021 | 0.0038 | 0.0013 | 0.0026 | 0.0011 | 0.0067 | 0.0026 | 0.0024 | 0.0143 | 0.0037 | 0.0011 | 0.0010 | 0.0011 | 0.0011 | 0.0011 | | | | |
| Ba | 0.0033 | 0.0015 | 0.0017 | 0.0015 | 0.0029 | 0.0014 | 0.0015 | 0.0014 | 0.0027 | 0.0017 | 0.0038 | 0.0020 | 0.0018 | 0.0017 | 0.0016 | 0.0018 | 0.0018 | | | | |
| La | 0.0029 | 0.0001 | 0.0003 | 0.0004 | 0.0003 | 0.0002 | 0.0002 | 0.0005 | 0.0010 | 0.0005 | 0.0006 | 0.0037 | 0.0001 | 0.0003 | 0.0001 | 0.0006 | 0.0006 | | | | |
| Ce | 0.0099 | 0.0002 | 0.0009 | 0.0005 | 0.0005 | 0.0002 | 0.0002 | 0.0005 | 0.0010 | 0.0005 | 0.0006 | 0.0037 | 0.0006 | 0.0008 | 0.0002 | 0.0010 | 0.0010 | | | | |
| Pr | 0.0009 | 0.0002 | 0.0001 | 0.0001 | 0.0001 | 0.0002 | 0.0001 | 0.0001 | 0.0001 | 0.0000 | 0.0044 | 0.0003 | 0.0001 | 0.0001 | 0.0001 | 0.0001 | 0.0001 | | | | |
| Nd | 0.0013 | - | 0.0005 | 0.0008 | 0.0003 | 0.0008 | 0.0001 | 0.0004 | 0.0004 | 0.0004 | 0.0002 | 0.0025 | 0.0003 | 0.0248 | 0.0003 | 0.0005 | 0.0005 | | | | |
| Sm | 0.0010 | 0.0005 | 0.0007 | 0.0005 | 0.0005 | 0.0004 | 0.0008 | 0.0007 | 0.0006 | 0.0006 | 0.0005 | 0.0015 | 0.0050 | 0.0006 | 0.0008 | 0.0006 | 0.0006 | | | | |
| Eu | 0.0008 | 0.0001 | 0.0001 | 0.0001 | 0.0005 | 0.0001 | 0.0002 | 0.0001 | 0.0001 | 0.0001 | 0.0004 | 0.0010 | 0.0002 | 0.0002 | 0.0002 | 0.0003 | 0.0003 | | | | |
| Gd | 0.0012 | 0.0023 | 0.0015 | 0.0006 | 0.0020 | 0.0024 | 0.0009 | 0.0026 | 0.0007 | 0.0004 | 0.0005 | 0.0026 | 0.0018 | 0.0007 | 0.0006 | 0.0021 | 0.0021 | | | | |
| Tb | 0.0006 | 0.0005 | 0.0007 | 0.0005 | 0.0009 | 0.0005 | 0.0001 | 0.0006 | 0.0007 | 0.0004 | 0.0005 | 0.0006 | 0.0001 | 0.0003 | 0.0005 | 0.0009 | 0.0009 | | | | |
| Dy | 0.0068 | 0.0146 | 0.0136 | 0.0100 | 0.0175 | 0.0107 | 0.0091 | 0.0095 | 0.0089 | 0.0082 | 0.0052 | 0.0062 | 0.0102 | 0.0080 | 0.0093 | 0.0144 | 0.0144 | | | | |
| Ho | 0.0052 | 0.0075 | 0.0068 | 0.0061 | 0.0084 | 0.0056 | 0.0047 | 0.0052 | 0.0052 | 0.0049 | 0.0031 | 0.0025 | 0.0061 | 0.0058 | 0.0048 | 0.0063 | 0.0063 | | | | |
| Er | 0.0265 | 0.0441 | 0.0370 | 0.0380 | 0.0473 | 0.0319 | 0.0280 | 0.0314 | 0.0326 | 0.0273 | 0.0182 | 0.0192 | 0.0398 | 0.0330 | 0.0305 | 0.0379 | 0.0379 | | | | |
| Tm | 0.0074 | 0.0110 | 0.0110 | 0.0108 | 0.0130 | 0.0107 | 0.0084 | 0.0091 | 0.0093 | 0.0080 | 0.0056 | 0.0049 | 0.0105 | 0.0104 | 0.0097 | 0.0107 | 0.0107 | | | | |
| Yb | 0.0889 | 0.1191 | 0.1185 | 0.1097 | 0.1416 | 0.1017 | 0.0929 | 0.0977 | 0.0945 | 0.0931 | 0.0617 | 0.0638 | 0.1097 | 0.1163 | 0.1114 | 0.1088 | 0.1088 | | | | |
| Lu | 0.0206 | 0.0268 | 0.0256 | 0.0241 | 0.0290 | 0.0232 | 0.0219 | 0.0227 | 0.0226 | 0.0224 | 0.0153 | 0.0161 | 0.0266 | 0.0275 | 0.0234 | 0.0260 | 0.0260 | | | | |
| Hf | 0.0014 | 0.0028 | 0.0022 | 0.0016 | 0.0021 | 0.0019 | 0.0016 | 0.0020 | 0.0015 | 0.0017 | 0.0009 | 0.0009 | 0.0010 | 0.0025 | 0.0022 | 0.0105 | 0.0105 | | | | |
| Ta | 0.0013 | 0.0004 | 0.0001 | 0.0001 | 0.0002 | 0.0001 | 0.0002 | 0.0002 | 0.0001 | 0.0001 | 0.0003 | 0.0002 | 0.0002 | 0.0002 | 0.0001 | 0.0003 | 0.0003 | | | | |
| Pb | 0.0237 | 0.0187 | 0.0178 | 0.1955 | 0.0157 | 0.0144 | 0.0091 | 0.0102 | 0.0939 | 0.0059 | - | - | 0.0350 | 0.0741 | 0.0098 | 0.0173 | 0.0173 | | | | |
| Th | 0.0021 | 0.0002 | 0.0006 | 0.0000 | 0.0001 | 0.0000 | 0.0001 | 0.0001 | 0.0001 | 0.0002 | 0.0011 | 0.0001 | 0.0001 | 0.0017 | 0.0000 | 0.0001 | 0.0001 | | | | |
| U | 0.0091 | - | 0.0001 | 0.0001 | 0.0002 | 0.0003 | 0.0001 | 0.0001 | 0.0001 | 0.0001 | - | - | 0.0001 | 0.0002 | 0.0000 | 0.3370 | 0.3370 | | | | |

Tableau B-2c (suite)

| Echantillon | | 248R3 131-134 | | | | | | | | | |
|-------------------|--------|-----------------------------|--------|--------|--------|--------|--------|--------|--------|--------|--------|
| Type de roche | | Troctolite riche en olivine | | | | | | | | | |
| Profondeur (mbsf) | | 1195.8 | | | | | | | | | |
| Zones Point | | OL_a_1 | OL_a_2 | OL_6_1 | OL_6_2 | OL_6_3 | OL_6_4 | OL_5_1 | OL_5_2 | | |
| Axe | | 100 | 100 | 100 | 100 | 100 | 100 | 100 | 100 | | |
| Si | 190108 | 190108 | 190108 | 190108 | 190108 | 190108 | 190108 | 190108 | 190108 | 190108 | 190108 |
| P | 27 | 21 | 19 | 19 | 28 | 30 | 34 | 20 | 18 | 19 | |
| Ca | 639 | 537 | 694 | 758 | 766 | 828 | 668 | 681 | 566 | 536 | |
| Ti | 85 | 84 | 100 | 98 | 73 | 119 | 156 | 84 | 61 | 66 | |
| V | 5 | 5 | 5 | 5 | 5 | 7 | 7 | 5 | 5 | 6 | |
| Cr | 104 | 90 | 83 | 86 | 101 | 110 | 98 | 97 | 120 | 104 | |
| Co | 164.5 | 164.6 | 168.4 | 167.5 | 168.3 | 168.7 | 168.1 | 168.6 | 169.3 | 172.5 | |
| Ni | 2029 | 2083 | 2098 | 2081 | 2062 | 2164 | 2118 | 2103 | 2135 | 2183 | |
| Zn | 88 | 86 | 85 | 90 | 90 | 90 | 91 | 91 | 85 | 89 | |
| Rb | 0.0364 | 0.0087 | 0.0115 | 0.0045 | 0.0236 | 0.0026 | 0.0855 | 0.0021 | 0.0044 | 0.0078 | |
| Sr | 0.4990 | 0.1265 | 0.0073 | 0.0144 | 0.1502 | 0.0295 | 0.4330 | 0.0028 | 0.0089 | 0.0488 | |
| Y | 0.0822 | 0.0763 | 0.1110 | 0.1113 | 0.1105 | 0.1251 | 0.1272 | 0.1025 | 0.0556 | 0.0602 | |
| Zr | 0.0377 | 0.0388 | 0.2350 | 0.0454 | 0.0382 | 0.2438 | 0.0426 | 0.0485 | 0.1216 | 0.0188 | |
| Nb | 0.0009 | 0.0018 | 0.0010 | 0.0004 | 0.0035 | 0.0091 | 0.0032 | 0.0008 | 0.0004 | 0.0011 | |
| Cs | 0.0011 | 0.0026 | 0.0210 | 0.0011 | 0.0026 | 0.0132 | 0.0029 | 0.0035 | 0.0038 | 0.0038 | |
| Ba | 0.2451 | 0.0135 | 0.0013 | 0.0041 | 0.0651 | 0.0061 | 0.1758 | 0.0042 | 0.0013 | 0.0106 | |
| La | 0.0018 | 0.0004 | 0.0001 | 0.0001 | 0.0021 | 0.0002 | 0.0019 | 0.0002 | 0.0003 | 0.0001 | |
| Ce | 0.0008 | 0.0009 | 0.0004 | 0.0002 | 0.0020 | 0.0004 | 0.0022 | 0.0001 | 0.0005 | 0.0002 | |
| Pr | 0.0001 | 0.0002 | 0.0001 | 0.0000 | 0.0004 | 0.0001 | 0.0003 | 0.0005 | 0.0000 | 0.0001 | |
| Nd | 0.0002 | 0.0004 | 0.0002 | 0.0002 | 0.0002 | 0.0005 | 0.0004 | 0.0000 | 0.0002 | 0.0001 | |
| Sm | 0.0004 | 0.0005 | - | - | 0.0005 | 0.0006 | 0.0006 | 0.0008 | 0.0004 | 0.0006 | |
| Eu | 0.0002 | 0.0001 | 0.0001 | 0.0001 | 0.0003 | 0.0001 | 0.0006 | 0.0001 | 0.0002 | 0.0001 | |
| Gd | 0.0006 | 0.0008 | 0.0010 | 0.0005 | 0.0012 | 0.0006 | 0.0007 | 0.0005 | 0.0007 | 0.0010 | |
| Tb | 0.0004 | 0.0004 | 0.0005 | 0.0006 | 0.0006 | 0.0003 | 0.0004 | 0.0004 | 0.0003 | 0.0004 | |
| Dy | 0.0063 | 0.0043 | 0.0075 | 0.0069 | 0.0066 | 0.0082 | 0.0068 | 0.0063 | 0.0039 | 0.0041 | |
| Ho | 0.0023 | 0.0025 | 0.0037 | 0.0031 | 0.0039 | 0.0044 | 0.0039 | 0.0037 | 0.0020 | 0.0021 | |
| Er | 0.0154 | 0.0149 | 0.0209 | 0.0199 | 0.0215 | 0.0253 | 0.0278 | 0.0216 | 0.0108 | 0.0140 | |
| Tm | 0.0044 | 0.0046 | 0.0061 | 0.0061 | 0.0049 | 0.0068 | 0.0080 | 0.0062 | 0.0035 | 0.0039 | |
| Yb | 0.0552 | 0.0519 | 0.0632 | 0.0612 | 0.0578 | 0.0702 | 0.0799 | 0.0576 | 0.0389 | 0.0478 | |
| Lu | 0.0129 | 0.0137 | 0.0144 | 0.0141 | 0.0142 | 0.0170 | 0.0200 | 0.0142 | 0.0094 | 0.0117 | |
| Hf | 0.0012 | 0.0013 | 0.0032 | 0.0054 | 0.0012 | 0.0008 | 0.0012 | 0.0021 | 0.0009 | 0.0011 | |
| Ta | 0.0003 | 0.0002 | 0.0002 | 0.0015 | 0.0003 | 0.0002 | 0.0006 | 0.0001 | 0.0005 | 0.0002 | |
| Pb | - | - | - | - | 0.0200 | 0.0105 | 0.0468 | 0.0054 | - | 0.0127 | |
| Th | 0.0001 | 0.0000 | 0.0016 | 0.0007 | 0.0004 | 0.0023 | 0.0075 | 0.0001 | 0.0000 | 0.0000 | |
| U | 0.0013 | 0.0000 | - | - | 0.0001 | - | 0.0001 | 0.0000 | 0.0008 | 0.0000 | |

Tableau B-2d: Profils en éléments majeurs dans les olivines du puits IODP U1309D*

| Echantillon | Type de roche | Profondeur (mbsf) | Zones | Point | Axe | SiO2 | Cr2O3 | FeO | MnO | MgO | NiO | Total |
|---------------|-----------------------------|-------------------|-------|--------|------|-------|-------|--------|------|-------|------|--------|
| 248R3_131-134 | Troctolite riche en olivine | 1195.8 | 4 | OIA-1 | | 40.49 | 0.01 | 13.60 | 0.21 | 45.35 | 0.28 | 99.94 |
| | | | | OIA-2 | | 40.59 | 0.01 | 13.68 | 0.20 | 45.13 | 0.28 | 99.89 |
| | | | | OIA-3 | | 40.62 | 0.01 | 13.69 | 0.21 | 44.98 | 0.28 | 99.79 |
| | | | | OIA-4 | | 40.51 | 0.02 | 13.81 | 0.21 | 44.92 | 0.28 | 99.75 |
| | | | | OIA-5 | | 40.59 | 0.03 | 13.62 | 0.21 | 44.69 | 0.27 | 99.41 |
| | | | | OIA-6 | 100 | 40.65 | 0.02 | 13.75 | 0.21 | 45.04 | 0.27 | 99.94 |
| | | | | OIA-7 | | 40.64 | 0.01 | 13.69 | 0.21 | 44.94 | 0.28 | 99.77 |
| | | | | OIA-8 | | 40.80 | 0.00 | 13.68 | 0.21 | 44.80 | 0.29 | 99.79 |
| | | | | OIA-9 | | 40.68 | 0.02 | 13.62 | 0.20 | 44.75 | 0.28 | 99.54 |
| | | | | OIA-10 | | 40.32 | 0.01 | 13.90 | 0.22 | 45.13 | 0.27 | 99.85 |
| | | | | OIA-11 | | 40.40 | 0.01 | 13.71 | 0.21 | 45.13 | 0.28 | 99.74 |
| | | | | OIA-1 | | 40.60 | 0.01 | 13.36 | 0.21 | 44.80 | 0.26 | 99.23 |
| | | | | OIA-2 | | 40.61 | 0.01 | 13.81 | 0.21 | 45.00 | 0.28 | 99.91 |
| | | | | OIA-3 | | 40.67 | 0.00 | 13.73 | 0.21 | 44.95 | 0.27 | 99.83 |
| | | | | OIA-4 | 010 | 40.77 | 0.01 | 13.48 | 0.20 | 44.66 | 0.26 | 99.39 |
| | | | | OIA-5 | | 40.67 | 0.02 | 13.81 | 0.21 | 44.95 | 0.27 | 99.93 |
| | | | | OIA-6 | | 40.99 | 0.02 | 13.45 | 0.20 | 44.53 | 0.30 | 99.49 |
| | | | | OIS-1 | | 39.65 | 0.02 | 13.40 | 0.20 | 45.10 | 0.27 | 98.63 |
| | | | | OIS-2 | | 40.78 | 0.02 | 13.74 | 0.20 | 45.10 | 0.27 | 100.11 |
| | | | | OIS-3 | | 40.31 | 0.01 | 13.96 | 0.21 | 44.73 | 0.27 | 99.49 |
| | | | | OIS-4 | | 40.69 | 0.01 | 13.71 | 0.20 | 45.18 | 0.27 | 100.06 |
| | | | | OIS-5 | 100 | 40.63 | 0.02 | 13.65 | 0.21 | 44.89 | 0.27 | 99.67 |
| | | | | OIS-6 | | 40.96 | 0.02 | 13.75 | 0.21 | 44.89 | 0.27 | 100.10 |
| | | | | OIS-7 | | 40.58 | 0.00 | 13.79 | 0.21 | 45.11 | 0.27 | 99.96 |
| | | | | OIS-8 | | 41.00 | 0.01 | 13.87 | 0.21 | 45.06 | 0.27 | 100.42 |
| | | | | OIS-9 | | 39.44 | 0.03 | 13.20 | 0.27 | 45.58 | 0.26 | 98.77 |
| | | | | OIS-1 | | 40.81 | 0.01 | 13.72 | 0.21 | 45.13 | 0.29 | 100.16 |
| | | | | OIS-2 | | 40.85 | 0.01 | 13.64 | 0.20 | 45.17 | 0.28 | 100.16 |
| | | | | OIS-3 | 010 | 40.66 | 0.01 | 13.19 | 0.21 | 44.51 | 0.27 | 98.84 |
| | | | | OIS-4 | | 40.95 | 0.01 | 13.77 | 0.21 | 45.11 | 0.27 | 100.33 |
| | | | | OIS-5 | | 42.88 | 0.01 | 13.57 | 0.21 | 43.63 | 0.27 | 100.56 |
| | | | | OIS-1 | | 40.74 | 0.02 | 13.66 | 0.21 | 44.96 | 0.27 | 99.85 |
| | | | | OIS-2 | | 40.79 | 0.01 | 13.73 | 0.21 | 45.04 | 0.26 | 100.05 |
| | | | | OIS-3 | | 40.85 | 0.01 | 13.70 | 0.21 | 45.02 | 0.27 | 100.05 |
| | | | | OIS-4 | 100 | 41.11 | 0.01 | 13.74 | 0.21 | 44.81 | 0.27 | 100.15 |
| | | | | OIS-5 | | 40.76 | 0.01 | 13.76 | 0.21 | 45.01 | 0.27 | 100.02 |
| | | | | OIS-6 | | 40.83 | 0.01 | 13.75 | 0.21 | 44.95 | 0.27 | 100.02 |
| | | | | OIS-7 | | 40.95 | 0.00 | 13.67 | 0.21 | 44.99 | 0.28 | 100.10 |
| | | | | OIS-8 | | 40.76 | 0.01 | 13.71 | 0.21 | 44.97 | 0.27 | 99.93 |
| | | | | OIS-1 | | 40.74 | 0.01 | 13.47 | 0.20 | 45.19 | 0.27 | 99.89 |
| | | | | OIS-2 | | 40.78 | 0.01 | 13.71 | 0.21 | 45.06 | 0.27 | 100.04 |
| | | | | OIS-3 | | 40.74 | 0.01 | 13.70 | 0.21 | 45.14 | 0.27 | 100.06 |
| | | | | OIS-4 | | 40.73 | 0.01 | 13.70 | 0.21 | 45.21 | 0.27 | 100.13 |
| | | | | OIS-5 | 100 | 40.75 | 0.01 | 13.74 | 0.21 | 45.09 | 0.28 | 100.08 |
| | | | | OIS-6 | | 40.85 | 0.01 | 13.66 | 0.21 | 45.01 | 0.27 | 100.02 |
| | | | | OIS-7 | | 40.63 | 0.01 | 13.72 | 0.21 | 45.40 | 0.27 | 100.24 |
| | | | | OIS-8 | | 40.87 | 0.04 | 13.68 | 0.21 | 44.94 | 0.26 | 99.99 |
| | | | | OIS-9 | | 40.94 | 0.02 | 13.70 | 0.21 | 44.79 | 0.27 | 99.92 |
| OIS-10 | | 40.81 | 0.01 | 13.74 | 0.21 | 45.19 | 0.27 | 100.23 | | | | |
| OIS-1 | | 40.40 | 0.00 | 13.71 | 0.21 | 44.66 | 0.28 | 99.26 | | | | |
| OIS-2 | | 40.70 | 0.00 | 13.83 | 0.21 | 44.98 | 0.27 | 100.00 | | | | |
| OIS-3 | 010 | 40.80 | 0.01 | 13.81 | 0.21 | 45.01 | 0.27 | 100.10 | | | | |
| OIS-4 | | 40.85 | 0.01 | 13.72 | 0.21 | 44.92 | 0.27 | 99.99 | | | | |

| Echantillon | Type de roche | Profondeur (mbsf) | Zones | Point | Axe | SiO2 | Cr2O3 | FeO | MnO | MgO | NiO | Total |
|-------------|-----------------------------|-------------------|-------|--------|-----|-------|-------|-------|------|-------|------|-------|
| 248R2_18-21 | Troctolite riche en olivine | 1193.32 | 4 | OIA-1 | | 38.94 | 0.01 | 15.47 | 0.24 | 44.54 | 0.20 | 99.40 |
| | | | | OIA-2 | | 39.05 | 0.01 | 15.47 | 0.24 | 43.94 | 0.21 | 98.91 |
| | | | | OIA-3 | | 39.04 | 0.01 | 15.44 | 0.23 | 43.87 | 0.20 | 98.80 |
| | | | | OIA-4 | | 38.97 | 0.00 | 15.51 | 0.24 | 43.74 | 0.20 | 98.67 |
| | | | | OIA-5 | | 38.97 | 0.01 | 15.31 | 0.23 | 43.83 | 0.20 | 98.54 |
| | | | | OIA-6 | | 38.98 | 0.01 | 15.52 | 0.24 | 43.71 | 0.21 | 98.66 |
| | | | | OIA-7 | 001 | 38.88 | 0.01 | 15.50 | 0.24 | 43.73 | 0.20 | 98.56 |
| | | | | OIA-8 | | 38.87 | 0.01 | 15.51 | 0.24 | 43.73 | 0.20 | 98.55 |
| | | | | OIA-9 | | 39.32 | 0.01 | 15.48 | 0.24 | 43.66 | 0.20 | 98.91 |
| | | | | OIA-10 | | 39.15 | 0.01 | 15.45 | 0.23 | 43.85 | 0.20 | 98.91 |
| | | | | OIA-11 | | 39.12 | 0.01 | 15.49 | 0.24 | 43.76 | 0.20 | 98.82 |
| | | | | OIA-12 | | 39.00 | 0.01 | 15.50 | 0.24 | 43.72 | 0.20 | 98.66 |
| | | | | OIA-1 | | 39.01 | 0.01 | 15.91 | 0.24 | 43.58 | 0.20 | 98.95 |
| | | | | OIA-2 | | 39.02 | 0.01 | 15.92 | 0.24 | 43.44 | 0.20 | 98.84 |
| | | | | OIA-3 | 001 | 38.93 | 0.00 | 15.89 | 0.14 | 43.38 | 0.19 | 98.54 |
| | | | | OIA-4 | | 38.97 | 0.01 | 15.92 | 0.24 | 43.40 | 0.20 | 98.74 |
| | | | | OIA-5 | | 38.94 | 0.01 | 15.90 | 0.24 | 43.33 | 0.20 | 98.63 |
| | | | | OIA-1 | | 39.05 | 0.01 | 15.93 | 0.24 | 43.35 | 0.21 | 98.79 |
| | | | | OIA-2 | | 39.07 | 0.01 | 15.90 | 0.24 | 43.52 | 0.20 | 98.94 |
| | | | | OIA-3 | | 39.31 | 0.01 | 15.91 | 0.24 | 43.35 | 0.19 | 99.01 |
| | | | | OIA-4 | | 39.43 | 0.01 | 15.85 | 0.24 | 43.27 | 0.20 | 98.99 |
| | | | | OIA-5 | | 39.19 | 0.01 | 15.88 | 0.24 | 43.25 | 0.20 | 98.77 |
| | | | | OIA-6 | 100 | 39.18 | 0.01 | 15.82 | 0.24 | 43.49 | 0.20 | 98.95 |
| | | | | OIA-7 | | 39.35 | 0.01 | 15.88 | 0.24 | 43.30 | 0.19 | 98.98 |
| | | | | OIA-8 | | 39.14 | 0.01 | 15.56 | 0.30 | 42.74 | 0.19 | 98.94 |
| | | | | OIA-9 | | 39.16 | 0.01 | 15.88 | 0.24 | 43.46 | 0.21 | 98.95 |
| | | | | OIA-10 | | 39.20 | 0.01 | 15.80 | 0.24 | 43.39 | 0.20 | 98.84 |
| | | | | OII-1 | | 39.12 | 0.01 | 15.90 | 0.25 | 43.25 | 0.20 | 98.72 |
| | | | | OII-2 | | 39.16 | 0.01 | 15.93 | 0.25 | 43.39 | 0.20 | 98.94 |
| | | | | OII-3 | | 39.12 | 0.01 | 15.85 | 0.24 | 43.43 | 0.20 | 98.85 |
| | | | | OII-4 | | 38.98 | 0.01 | 15.83 | 0.24 | 43.51 | 0.20 | 98.79 |
| | | | | OII-5 | | 38.98 | 0.01 | 15.97 | 0.25 | 43.48 | 0.20 | 98.89 |
| | | | | OII-6 | | 39.08 | 0.00 | 15.91 | 0.24 | 43.05 | 0.20 | 98.49 |
| | | | | OII-7 | | 39.27 | 0.01 | 15.96 | 0.24 | 43.32 | 0.20 | 99.01 |
| | | | | OII-8 | 001 | 39.19 | 0.01 | 15.98 | 0.24 | 43.36 | 0.21 | 99.00 |
| | | | | OII-9 | | 39.30 | 0.01 | 15.91 | 0.25 | 43.48 | 0.21 | 99.16 |
| | | | | OII-10 | | 39.25 | 0.01 | 15.93 | 0.24 | 43.26 | 0.20 | 98.89 |
| | | | | OII-11 | | 39.28 | 0.01 | 15.90 | 0.24 | 43.29 | 0.21 | 98.93 |
| | | | | OII-12 | | 39.30 | 0.01 | 15.93 | 0.24 | 43.28 | 0.20 | 98.96 |
| | | | | OII-13 | | 39.20 | 0.01 | 15.88 | 0.24 | 43.31 | 0.20 | 98.85 |
| | | | | OII-14 | | 40.14 | 0.01 | 15.89 | 0.24 | 42.93 | 0.20 | 99.41 |
| | | | | OII-15 | | 39.34 | 0.00 | 15.97 | 0.24 | 43.35 | 0.21 | 99.12 |
| | | | | OII-16 | | 39.40 | 0.00 | 15.94 | 0.24 | 43.17 | 0.20 | 98.96 |
| | | | | OI9-1 | | 39.21 | 0.01 | 16.14 | 0.24 | 43.26 | 0.20 | 99.06 |
| | | | | OI9-2 | | 39.27 | 0.01 | 16.07 | 0.25 | 43.18 | 0.20 | 98.98 |
| | | | | OI9-3 | | 39.24 | 0.01 | 16.03 | 0.24 | 43.18 | 0.20 | 98.91 |
| | | | | OI9-4 | | 39.09 | 0.01 | 16.08 | 0.25 | 43.20 | 0.20 | 98.83 |
| | | | | OI9-5 | | 39.02 | 0.01 | 16.08 | 0.25 | 43.26 | 0.20 | 98.83 |
| | | | | OI9-6 | 001 | 38.94 | 0.00 | 16.06 | 0.25 | 43.23 | 0.19 | 98.68 |
| | | | | OI9-7 | | 39.12 | 0.01 | 16.05 | 0.25 | 43.19 | 0.20 | 98.82 |
| | | | | OI9-8 | | 39.00 | 0.01 | 16.12 | 0.24 | 43.24 | 0.20 | 98.81 |
| | | | | OI9-9 | | 39.41 | 0.01 | 16.06 | 0.24 | 42.97 | 0.19 | 98.89 |
| | | | | OI9-10 | | 39.41 | 0.01 | 15.95 | 0.24 | 43.25 | 0.21 | 99.07 |
| | | | | OI9-11 | | 39.26 | 0.01 | 16.01 | 0.25 | 43.15 | 0.21 | 98.87 |
| | | | | OID-1 | | 39.20 | 0.01 | 15.79 | 0.25 | 43.51 | 0.20 | 98.96 |
| | | | | OID-2 | | 39.29 | 0.01 | 15.61 | 0.24 | 43.66 | 0.20 | 99.01 |
| | | | | OID-3 | | 39.28 | 0.01 | 15.55 | 0.19 | 43.33 | 0.20 | 98.55 |
| | | | | OID-4 | 001 | 39.15 | 0.01 | 15.55 | 0.24 | 43.43 | 0.20 | 98.58 |
| | | | | OID-5 | | 39.31 | 0.01 | 15.63 | 0.24 | 43.62 | 0.21 | 99.03 |
| | | | | OID-6 | | 39.32 | 0.02 | 15.58 | 0.23 | 43.65 | 0.21 | 99.01 |
| | | | | OID-7 | | 39.29 | 0.01 | 15.58 | 0.24 | 43.66 | 0.20 | 98.98 |
| | | | | OIC-1 | | 40.01 | 0.01 | 15.22 | 0.23 | 43.50 | 0.20 | 99.18 |
| | | | | OIC-2 | | 39.48 | 0.01 | 15.54 | 0.24 | 43.74 | 0.20 | 99.21 |
| | | | | OIC-3 | | 39.06 | 0.01 | 15.02 | 0.22 | 45.13 | 0.19 | 99.62 |
| | | | | OIC-4 | 100 | 39.71 | 0.00 | 15.62 | 0.23 | 43.57 | 0.20 | 99.34 |
| | | | | OIC-5 | | 39.69 | 0.01 | 15.63 | 0.24 | 43.63 | 0.19 | 99.39 |
| | | | | OIC-6 | | 39.36 | 0.01 | 15.52 | 0.24 | 43.68 | 0.20 | 99.00 |
| | | | | OIC-7 | | 40.78 | 0.01 | 15.22 | 0.23 | 43.03 | 0.20 | 99.47 |

*Les analyses en éléments majeurs ont été réalisées par microsonde électronique (% poids d'oxyde)

Tableau B-2d suite

| Echantillon | Type de roche | Profondeur (mbsf) | Zones | Point | Axe | SiO2 | Cr2O3 | FeO | MnO | MgO | NiO | Total |
|-------------|-----------------------------|-------------------|-------|--------|-------|------|--------|------|-------|------|--------|-------|
| 237R2_40-43 | Troctolite riche en olivine | 1140.92 | 4 | O19-1 | 38.74 | 0.01 | 13.43 | 0.20 | 45.41 | 0.25 | 98.04 | |
| | | | | O19-2 | 38.93 | 0.01 | 13.51 | 0.21 | 45.36 | 0.25 | 98.27 | |
| | | | | O19-3 | 39.04 | 0.01 | 13.36 | 0.21 | 45.36 | 0.26 | 98.24 | |
| | | | | O19-4 | 39.06 | 0.01 | 13.36 | 0.20 | 45.37 | 0.25 | 98.26 | |
| | | | | O19-5 | 39.10 | 0.01 | 13.36 | 0.20 | 45.29 | 0.25 | 98.21 | |
| | | | | O19-6 | 39.05 | 0.01 | 13.39 | 0.21 | 45.22 | 0.25 | 98.13 | |
| | | | | O19-7 | 39.06 | 0.01 | 13.47 | 0.21 | 45.23 | 0.24 | 98.22 | |
| | | | | O19-8 | 39.13 | 0.01 | 13.44 | 0.21 | 45.02 | 0.25 | 98.07 | |
| | | | | O1A-1 | 40.07 | 0.02 | 13.38 | 0.21 | 45.68 | 0.25 | 99.60 | |
| | | | | O1A-2 | 40.15 | 0.02 | 13.39 | 0.21 | 45.58 | 0.25 | 99.60 | |
| | | | | O1A-3 | 40.12 | 0.02 | 13.33 | 0.21 | 45.37 | 0.25 | 99.30 | |
| | | | | O1A-4 | 40.20 | 0.01 | 13.37 | 0.21 | 45.43 | 0.25 | 99.47 | |
| | | | | O1A-5 | 40.21 | 0.02 | 13.38 | 0.21 | 45.44 | 0.26 | 99.51 | |
| | | | | O1A-6 | 40.20 | 0.02 | 13.40 | 0.21 | 45.32 | 0.25 | 99.39 | |
| | | | | O1A-7 | 40.22 | 0.01 | 13.40 | 0.21 | 45.29 | 0.25 | 99.38 | |
| | | | | O1A-8 | 40.23 | 0.02 | 13.38 | 0.21 | 45.30 | 0.25 | 99.39 | |
| | | | | O1A-9 | 40.24 | 0.01 | 13.39 | 0.21 | 45.33 | 0.25 | 99.43 | |
| | | | | O1A-10 | 40.25 | 0.01 | 13.36 | 0.21 | 45.33 | 0.25 | 99.41 | |
| | | | | O1A-11 | 40.28 | 0.01 | 13.41 | 0.21 | 45.35 | 0.25 | 99.51 | |
| | | | | O1A-12 | 40.30 | 0.01 | 13.40 | 0.21 | 45.35 | 0.25 | 99.52 | |
| | | | | O1A-13 | 40.37 | 0.01 | 13.36 | 0.21 | 45.37 | 0.25 | 99.56 | |
| | | | | O1A-14 | 40.30 | 0.02 | 13.37 | 0.21 | 45.53 | 0.25 | 99.66 | |
| | | | | O1A-15 | 40.34 | 0.01 | 13.32 | 0.21 | 45.29 | 0.25 | 99.42 | |
| | | | | O1A-16 | 40.37 | 0.02 | 13.29 | 0.21 | 45.22 | 0.25 | 99.35 | |
| | | | | O1A-17 | 40.34 | 0.01 | 13.32 | 0.21 | 45.32 | 0.25 | 99.46 | |
| | | | | O17-1 | 40.16 | 0.01 | 13.36 | 0.21 | 45.15 | 0.26 | 99.13 | |
| | | | | O17-2 | 40.28 | 0.01 | 13.38 | 0.21 | 45.42 | 0.25 | 99.56 | |
| | | | | O17-3 | 40.24 | 0.02 | 13.40 | 0.21 | 45.37 | 0.25 | 99.48 | |
| | | | | O17-4 | 40.33 | 0.02 | 13.38 | 0.21 | 45.32 | 0.26 | 99.52 | |
| | | | | O17-5 | 40.37 | 0.02 | 13.37 | 0.21 | 45.33 | 0.25 | 99.55 | |
| | | | | O17-6 | 40.38 | 0.01 | 13.36 | 0.21 | 45.34 | 0.25 | 99.55 | |
| | | | | O17-7 | 40.53 | 0.01 | 13.38 | 0.21 | 45.40 | 0.25 | 99.78 | |
| | | | | O17-8 | 40.28 | 0.01 | 13.32 | 0.21 | 45.39 | 0.25 | 99.47 | |
| | | | | O17-9 | 40.30 | 0.01 | 13.43 | 0.21 | 45.43 | 0.25 | 99.64 | |
| | | | | O17-10 | 40.33 | 0.01 | 13.38 | 0.21 | 45.54 | 0.26 | 99.73 | |
| | | | | O17-11 | 40.39 | 0.01 | 13.37 | 0.21 | 45.48 | 0.26 | 99.71 | |
| | | | | O17-12 | 40.48 | 0.01 | 13.34 | 0.21 | 45.48 | 0.26 | 99.77 | |
| | | | | O17-13 | 40.96 | 0.01 | 13.37 | 0.21 | 45.21 | 0.26 | 100.01 | |
| | | | | O17-14 | 40.42 | 0.00 | 13.46 | 0.22 | 45.40 | 0.25 | 99.75 | |
| | | | | O17-1 | 40.20 | 0.02 | 13.25 | 0.20 | 45.36 | 0.25 | 99.29 | |
| | | | | O17-2 | 40.44 | 0.02 | 13.35 | 0.20 | 45.32 | 0.26 | 99.58 | |
| | | | | O17-3 | 40.44 | 0.01 | 13.39 | 0.20 | 45.30 | 0.25 | 99.60 | |
| | | | | O17-4 | 40.43 | 0.02 | 13.40 | 0.21 | 45.17 | 0.26 | 99.48 | |
| | | | | O17-5 | 40.47 | 0.02 | 13.45 | 0.21 | 45.20 | 0.25 | 99.60 | |
| | | | | O17-6 | 40.44 | 0.02 | 13.42 | 0.21 | 45.22 | 0.25 | 99.55 | |
| | | | | O17-7 | 40.49 | 0.02 | 13.42 | 0.21 | 45.24 | 0.26 | 99.63 | |
| | | | | O17-8 | 40.61 | 0.02 | 13.43 | 0.21 | 45.36 | 0.26 | 99.88 | |
| O17-9 | 40.32 | 0.02 | 13.37 | 0.21 | 44.93 | 0.25 | 99.11 | | | | | |
| O17-10 | 40.39 | 0.02 | 13.35 | 0.21 | 45.24 | 0.25 | 99.46 | | | | | |
| O13-1 | 40.41 | 0.01 | 13.50 | 0.21 | 45.48 | 0.25 | 99.85 | | | | | |
| O13-2 | 40.43 | 0.01 | 13.41 | 0.21 | 45.41 | 0.24 | 99.71 | | | | | |
| O13-3 | 40.49 | 0.01 | 13.38 | 0.21 | 45.38 | 0.25 | 99.71 | | | | | |
| O13-4 | 40.46 | 0.01 | 13.41 | 0.20 | 45.31 | 0.25 | 99.64 | | | | | |
| O13-5 | 40.66 | 0.01 | 13.47 | 0.21 | 45.37 | 0.25 | 99.97 | | | | | |
| O13-6 | 40.70 | 0.01 | 13.48 | 0.21 | 45.25 | 0.24 | 99.90 | | | | | |
| O13-7 | 40.62 | 0.01 | 13.42 | 0.21 | 45.28 | 0.24 | 99.78 | | | | | |
| O13-8 | 40.70 | 0.01 | 13.46 | 0.21 | 45.23 | 0.24 | 99.86 | | | | | |
| O13-9 | 40.73 | 0.01 | 13.29 | 0.20 | 45.28 | 0.24 | 99.76 | | | | | |
| O13-10 | 40.72 | 0.01 | 13.35 | 0.21 | 45.25 | 0.25 | 99.78 | | | | | |
| O13-11 | 40.77 | 0.01 | 13.39 | 0.21 | 45.25 | 0.25 | 99.88 | | | | | |
| O13-12 | 40.88 | 0.01 | 13.36 | 0.21 | 45.16 | 0.24 | 99.87 | | | | | |
| O13-13 | 40.52 | 0.01 | 13.39 | 0.20 | 45.52 | 0.25 | 99.88 | | | | | |
| O13-14 | 40.60 | 0.01 | 13.34 | 0.21 | 45.36 | 0.25 | 99.76 | | | | | |
| O13-15 | 40.65 | 0.02 | 13.39 | 0.20 | 45.29 | 0.24 | 99.80 | | | | | |
| O13-16 | 40.67 | 0.01 | 13.41 | 0.21 | 45.29 | 0.24 | 99.84 | | | | | |
| O13-17 | 40.70 | 0.01 | 13.39 | 0.21 | 45.14 | 0.24 | 99.70 | | | | | |
| O13-18 | 40.66 | 0.02 | 13.38 | 0.21 | 45.32 | 0.25 | 99.83 | | | | | |
| O13-19 | 40.70 | 0.01 | 13.41 | 0.21 | 45.31 | 0.25 | 99.88 | | | | | |
| O13-20 | 40.66 | 0.01 | 13.39 | 0.21 | 45.28 | 0.24 | 99.80 | | | | | |
| O13-21 | 40.65 | 0.01 | 13.43 | 0.21 | 45.23 | 0.24 | 99.77 | | | | | |
| O13-22 | 40.58 | 0.02 | 13.46 | 0.21 | 45.37 | 0.25 | 99.88 | | | | | |
| O13-23 | 40.63 | 0.02 | 13.47 | 0.21 | 45.30 | 0.24 | 99.86 | | | | | |
| O13-24 | 40.60 | 0.02 | 13.57 | 0.21 | 45.22 | 0.24 | 99.85 | | | | | |
| O13-25 | 40.68 | 0.02 | 13.47 | 0.21 | 45.16 | 0.24 | 99.79 | | | | | |
| O13-26 | 40.65 | 0.02 | 13.49 | 0.21 | 45.04 | 0.25 | 99.65 | | | | | |
| O13-27 | 40.54 | 0.01 | 13.62 | 0.22 | 45.18 | 0.25 | 99.82 | | | | | |
| O13-28 | 40.58 | 0.02 | 13.56 | 0.21 | 44.97 | 0.26 | 99.59 | | | | | |
| O13-1 | 40.70 | 0.01 | 13.35 | 0.21 | 45.48 | 0.26 | 100.01 | | | | | |
| O13-2 | 40.49 | 0.01 | 13.38 | 0.21 | 45.44 | 0.25 | 99.79 | | | | | |
| O13-3 | 40.53 | 0.01 | 13.44 | 0.21 | 45.43 | 0.25 | 99.87 | | | | | |
| O13-4 | 40.46 | 0.01 | 13.38 | 0.21 | 45.39 | 0.26 | 99.70 | | | | | |
| O13-5 | 40.61 | 0.01 | 13.44 | 0.21 | 45.55 | 0.26 | 100.07 | | | | | |
| O13-6 | 40.58 | 0.01 | 13.34 | 0.21 | 45.40 | 0.25 | 99.79 | | | | | |
| O13-7 | 40.54 | 0.01 | 13.43 | 0.21 | 45.37 | 0.25 | 99.83 | | | | | |
| O13-8 | 40.46 | 0.01 | 13.43 | 0.21 | 45.30 | 0.25 | 99.67 | | | | | |
| O13-9 | 40.46 | 0.01 | 13.46 | 0.21 | 45.36 | 0.25 | 99.76 | | | | | |
| O13-10 | 40.44 | 0.01 | 13.43 | 0.21 | 45.31 | 0.25 | 99.66 | | | | | |
| O13-11 | 40.54 | 0.02 | 13.44 | 0.21 | 45.26 | 0.25 | 99.71 | | | | | |
| O13-12 | 40.36 | 0.01 | 13.29 | 0.20 | 45.60 | 0.25 | 99.71 | | | | | |
| O13-13 | 40.62 | 0.01 | 13.34 | 0.21 | 45.20 | 0.25 | 99.64 | | | | | |
| O13-14 | 40.50 | 0.01 | 13.34 | 0.21 | 45.20 | 0.25 | 99.52 | | | | | |
| O13-15 | 40.48 | 0.02 | 13.46 | 0.21 | 45.22 | 0.25 | 99.64 | | | | | |
| O13-16 | 40.51 | 0.02 | 13.39 | 0.21 | 45.24 | 0.25 | 99.62 | | | | | |
| O13-17 | 40.46 | 0.01 | 13.41 | 0.21 | 45.30 | 0.25 | 99.63 | | | | | |
| O13-18 | 40.45 | 0.01 | 13.47 | 0.21 | 45.23 | 0.25 | 99.62 | | | | | |
| O13-19 | 40.39 | 0.02 | 13.45 | 0.21 | 45.26 | 0.25 | 99.58 | | | | | |
| O13-20 | 40.38 | 0.01 | 13.43 | 0.21 | 45.31 | 0.24 | 99.59 | | | | | |
| O13-21 | 40.33 | 0.02 | 13.43 | 0.21 | 45.26 | 0.25 | 99.50 | | | | | |
| O13-22 | 40.07 | 0.02 | 13.41 | 0.21 | 45.29 | 0.24 | 99.32 | | | | | |
| O14-1 | 40.39 | 0.01 | 15.33 | 0.23 | 43.49 | 0.19 | 99.64 | | | | | |
| O14-2 | 40.42 | 0.01 | 15.32 | 0.23 | 43.67 | 0.19 | 99.85 | | | | | |
| O14-3 | 40.42 | 0.01 | 15.40 | 0.23 | 43.72 | 0.19 | 99.97 | | | | | |
| O14-4 | 40.40 | 0.00 | 15.25 | 0.23 | 43.91 | 0.19 | 99.98 | | | | | |
| O14-5 | 40.33 | 0.01 | 15.37 | 0.24 | 44.00 | 0.19 | 100.14 | | | | | |
| O14-6 | 40.44 | 0.01 | 15.36 | 0.23 | 43.49 | 0.19 | 99.72 | | | | | |
| O14-7 | 40.42 | 0.03 | 15.40 | 0.23 | 43.51 | 0.19 | 99.79 | | | | | |
| O14-8 | 40.41 | 0.05 | 15.45 | 0.24 | 43.57 | 0.19 | 99.91 | | | | | |
| O14-9 | 40.43 | 0.01 | 15.42 | 0.23 | 43.60 | 0.19 | 99.89 | | | | | |
| O14-10 | 40.49 | 0.01 | 15.38 | 0.23 | 43.61 | 0.19 | 99.91 | | | | | |
| O14-11 | 40.50 | 0.01 | 15.33 | 0.23 | 43.60 | 0.19 | 99.86 | | | | | |
| O14-12 | 40.52 | 0.01 | 15.32 | 0.23 | 43.66 | 0.19 | 99.92 | | | | | |
| O14-13 | 40.56 | 0.01 | 15.40 | 0.23 | 43.69 | 0.19 | 100.08 | | | | | |
| O14-14 | 40.54 | 0.03 | 15.44 | 0.23 | 43.63 | 0.19 | 100.05 | | | | | |
| O14-15 | 40.52 | 0.01 | 15.44 | 0.23 | 43.55 | 0.19 | 99.94 | | | | | |
| O14-16 | 40.52 | 0.01 | 15.39 | 0.23 | 43.66 | 0.19 | 100.00 | | | | | |
| O14-17 | 40.49 | 0.01 | 15.41 | 0.23 | 43.78 | 0.19 | 100.10 | | | | | |
| O10-1 | 40.42 | 0.01 | 15.31 | 0.23 | 43.56 | 0.19 | 99.72 | | | | | |
| O10-2 | 40.34 | 0.01 | 15.37 | 0.23 | 43.81 | 0.19 | 99.94 | | | | | |
| O10-3 | 40.82 | 0.00 | 15.30 | 0.22 | 43.56 | 0.20 | 100.11 | | | | | |
| O10-4 | 40.76 | 0.01 | 15.46 | 0.23 | 43.56 | 0.19 | 100.21 | | | | | |
| O10-5 | 40.80 | 0.01 | 15.42 | 0.23 | 43.42 | 0.19 | 100.06 | | | | | |
| O10-6 | 40.64 | 0.01 | 15.41 | 0.23 | 43.87 | 0.18 | 100.35 | | | | | |
| O10-7 | 40.25 | 0.01 | 15.51 | 0.23 | 43.88 | 0.20 | 100.08 | | | | | |

Tableau B-3a: Composition moyenne en éléments majeurs des clinopyroxènes du Site ODP 1275*

| Echantillon | 6R2_106-110 | 10R2_43-46 | 13R2_35-43 | 15R1_78-90 | 15R2_49-57 | 18R1_122-132 | 19R1_50-54 | 19R2_31-43 | 20R1_100-109 | 21R1_27-37 | 22R1_97-104 | 23R2_55-61 |
|---------------|-------------|------------|------------|------------|------------|--------------|------------|------------|--------------|------------|-------------|--------------|
| Puits | 1275B | 1275D | 1275D | 1275D | 1275D | 1275D | 1275D | 1275D | 1275D | 1275D | 1275D | 1275D |
| Type de roche | troctolite | troctolite | gab à ox | gab à ox | gab à ox | gab à ox | gab à ox | gab à ox | gab à ox | gab à ox | gab à ox | micro-gabbro |
| n | 3 | 1 | 1 | 5 | 5 | 8 | 9 | 8 | 8 | 12 | 5 | 4 |
| SiO2 | 52.04 | 51.44 | 51.93 | 50.08 | 50.75 | 50.90 | 50.32 | 50.77 | 51.28 | 50.51 | 51.03 | 52.39 |
| TiO2 | 0.42 | 1.02 | 0.10 | 0.62 | 0.42 | 0.48 | 0.51 | 0.88 | 0.52 | 0.65 | 0.54 | 0.51 |
| Al2O3 | 2.84 | 3.14 | 0.32 | 1.77 | 1.11 | 1.32 | 1.25 | 2.31 | 1.31 | 1.56 | 1.34 | 2.21 |
| Cr2O3 | 1.26 | 1.35 | 0.01 | 0.02 | 0.01 | 0.01 | 0.01 | 0.07 | 0.00 | 0.01 | 0.01 | 0.06 |
| FeO | 2.67 | 2.96 | 12.64 | 14.77 | 14.02 | 13.78 | 16.18 | 10.94 | 15.46 | 14.26 | 15.61 | 8.32 |
| MnO | 0.11 | 0.12 | 0.42 | 0.40 | 0.42 | 0.40 | 0.49 | 0.31 | 0.42 | 0.40 | 0.44 | 0.26 |
| MgO | 17.07 | 16.49 | 11.84 | 12.13 | 11.43 | 12.41 | 12.09 | 13.15 | 12.25 | 12.10 | 12.69 | 17.48 |
| CaO | 21.84 | 22.15 | 22.38 | 19.36 | 20.58 | 19.72 | 18.03 | 20.69 | 18.50 | 19.49 | 17.29 | 18.24 |
| Na2O | 0.48 | 0.57 | 0.14 | 0.40 | 0.30 | 0.33 | 0.31 | 0.39 | 0.35 | 0.35 | 0.29 | 0.29 |
| K2O | 0.00 | 0.00 | 0.00 | 0.02 | 0.00 | 0.00 | 0.00 | 0.01 | 0.00 | 0.01 | 0.01 | 0.00 |
| NiO | 0.05 | 0.06 | 0.03 | 0.02 | 0.01 | 0.01 | 0.00 | 0.01 | 0.01 | 0.01 | 0.00 | 0.02 |
| Total | 98.78 | 99.29 | 99.80 | 99.58 | 99.04 | 99.36 | 99.21 | 99.50 | 100.11 | 99.35 | 99.25 | 99.77 |
| Mg# | 91.92 | 90.84 | 62.55 | 59.43 | 59.23 | 61.64 | 57.33 | 68.17 | 59.04 | 60.21 | 59.49 | 78.93 |
| σ | | | | | | | | | | | | |
| SiO2 | 0.63 | - | - | 0.97 | 0.48 | 0.51 | 0.30 | 0.27 | 0.35 | 0.46 | 1.12 | 0.61 |
| TiO2 | 0.13 | - | - | 0.11 | 0.22 | 0.13 | 0.10 | 0.07 | 0.11 | 0.11 | 0.08 | 0.09 |
| Al2O3 | 0.16 | - | - | 0.47 | 0.56 | 0.18 | 0.14 | 0.31 | 0.29 | 0.20 | 0.28 | 0.48 |
| Cr2O3 | 0.16 | - | - | 0.02 | 0.02 | 0.01 | 0.01 | 0.07 | 0.01 | 0.01 | 0.01 | 0.10 |
| FeO | 0.06 | - | - | 1.11 | 0.53 | 0.66 | 2.58 | 0.51 | 4.46 | 0.60 | 3.81 | 0.50 |
| MnO | 0.01 | - | - | 0.04 | 0.02 | 0.02 | 0.06 | 0.02 | 0.09 | 0.02 | 0.07 | 0.04 |
| MgO | 0.21 | - | - | 0.54 | 0.41 | 0.21 | 0.58 | 0.42 | 1.41 | 0.18 | 1.64 | 0.31 |
| CaO | 0.67 | - | - | 0.79 | 0.90 | 0.70 | 2.77 | 0.29 | 5.06 | 0.78 | 5.64 | 0.41 |
| Na2O | 0.02 | - | - | 0.07 | 0.12 | 0.05 | 0.04 | 0.04 | 0.12 | 0.04 | 0.10 | 0.02 |
| K2O | 0.00 | - | - | 0.05 | 0.00 | 0.00 | 0.00 | 0.01 | 0.00 | 0.01 | 0.01 | 0.00 |
| NiO | 0.02 | - | - | 0.01 | 0.01 | 0.02 | 0.00 | 0.01 | 0.01 | 0.01 | 0.00 | 0.01 |
| Total | 0.03 | - | - | 0.79 | 0.31 | 0.38 | 0.69 | 0.15 | 0.64 | 0.47 | 0.61 | 0.40 |
| Mg# | 0.27 | - | - | 2.37 | 1.38 | 1.10 | 2.77 | 1.58 | 3.12 | 0.81 | 2.32 | 0.75 |

*Les analyses en éléments majeurs ont été réalisées par microsonde électronique (% poids d'oxyde). Abbréviation: n= nombre d'analyses par minéral; σ = écart type. Mg# = (Mg/Mg+Fe)*100

Tableau B-3a (suite)

| Echantillon | 24R2_121-128 | 24R3_11-20 | 26R1_60-70 | 26R3_112-121 | 27R1_10-17 | 27R1_70-80 | 17R1_133-141 | 27R2_31-37 | 29R2_52-58 | 30R2_54-63 | 31R3_0-5 | 31R3_71-76 |
|---------------|--------------|------------|------------|--------------|------------|------------|--------------|------------|------------|------------|----------|------------|
| Puits | 1275D | 1275D | 1275D | 1275D | 1275D | 1275D | 1275D | 1275D | 1275D | 1275D | 1275D | 1275D |
| Type de roche | gab à ox | gab à ox | gab à ox | gab à ox | gab à ox | gab à ox | gab à ox | gab à ox | gab à ox | gab à ox | gab à ox | gab à ox |
| n | 7 | 10 | 6 | 8 | 1 | 12 | 5 | 16 | 3 | 10 | 10 | 9 |
| SiO2 | 51.04 | 50.50 | 51.24 | 50.94 | 50.74 | 50.79 | 51.33 | 50.64 | 50.57 | 51.02 | 50.72 | 50.85 |
| TiO2 | 0.53 | 0.55 | 0.59 | 0.54 | 0.52 | 0.55 | 0.48 | 0.53 | 0.24 | 0.85 | 0.75 | 0.66 |
| Al2O3 | 1.48 | 1.46 | 1.39 | 1.52 | 1.47 | 1.52 | 1.31 | 1.80 | 0.69 | 1.87 | 1.88 | 1.67 |
| Cr2O3 | 0.01 | 0.01 | 0.01 | 0.02 | 0.00 | 0.01 | 0.01 | 0.01 | 0.01 | 0.01 | 0.02 | 0.01 |
| FeO | 14.74 | 13.99 | 14.05 | 13.30 | 12.23 | 13.68 | 12.24 | 14.50 | 18.22 | 13.81 | 12.26 | 12.98 |
| MnO | 0.41 | 0.39 | 0.40 | 0.41 | 0.39 | 0.41 | 0.40 | 0.41 | 0.55 | 0.38 | 0.35 | 0.37 |
| MgO | 12.25 | 12.08 | 11.81 | 12.70 | 13.12 | 12.71 | 12.81 | 12.09 | 8.72 | 13.44 | 12.98 | 12.81 |
| CaO | 18.99 | 19.73 | 19.89 | 19.46 | 19.51 | 19.09 | 20.47 | 19.15 | 20.41 | 17.60 | 19.83 | 19.53 |
| Na2O | 0.31 | 0.36 | 0.36 | 0.30 | 0.43 | 0.32 | 0.27 | 0.32 | 0.33 | 0.30 | 0.35 | 0.34 |
| K2O | 0.01 | 0.01 | 0.00 | 0.00 | 0.01 | 0.01 | 0.00 | 0.00 | 0.01 | 0.04 | 0.01 | 0.01 |
| NiO | 0.00 | 0.00 | 0.00 | 0.00 | 0.01 | 0.01 | 0.01 | 0.01 | 0.01 | 0.01 | 0.01 | 0.02 |
| Total | 99.77 | 99.08 | 99.75 | 99.20 | 98.43 | 99.10 | 99.34 | 99.09 | 99.75 | 99.34 | 99.16 | 99.24 |
| Mg# | 59.91 | 60.61 | 59.96 | 63.00 | 65.66 | 62.44 | 65.10 | 59.85 | 46.01 | 63.86 | 65.39 | 63.91 |
| d | | | | | | | | | | | | |
| SiO2 | 0.42 | 0.36 | 0.31 | 0.59 | - | 0.50 | 0.39 | 0.76 | 0.48 | 0.61 | 0.37 | 0.67 |
| TiO2 | 0.04 | 0.11 | 0.06 | 0.15 | - | 0.11 | 0.22 | 0.17 | 0.25 | 0.24 | 0.17 | 0.27 |
| Al2O3 | 0.18 | 0.31 | 0.09 | 0.15 | - | 0.14 | 0.55 | 1.08 | 0.60 | 0.42 | 0.32 | 0.57 |
| Cr2O3 | 0.01 | 0.01 | 0.01 | 0.01 | - | 0.01 | 0.01 | 0.01 | 0.01 | 0.01 | 0.01 | 0.01 |
| FeO | 2.59 | 0.43 | 0.43 | 0.42 | - | 1.51 | 0.31 | 3.02 | 0.86 | 3.89 | 0.74 | 2.03 |
| MnO | 0.07 | 0.03 | 0.03 | 0.01 | - | 0.04 | 0.03 | 0.05 | 0.07 | 0.08 | 0.03 | 0.04 |
| MgO | 0.53 | 0.17 | 0.13 | 0.14 | - | 0.47 | 0.13 | 1.31 | 0.59 | 1.87 | 0.30 | 0.48 |
| CaO | 2.81 | 0.44 | 0.55 | 0.92 | - | 1.91 | 0.59 | 3.66 | 1.00 | 5.19 | 1.14 | 2.16 |
| Na2O | 0.05 | 0.03 | 0.03 | 0.04 | - | 0.07 | 0.06 | 0.30 | 0.07 | 0.08 | 0.03 | 0.08 |
| K2O | 0.02 | 0.01 | 0.00 | 0.00 | - | 0.01 | 0.00 | 0.14 | 0.02 | 0.13 | 0.01 | 0.01 |
| NiO | 0.00 | 0.01 | 0.01 | 0.01 | - | 0.01 | 0.01 | 0.01 | 0.01 | 0.01 | 0.01 | 0.01 |
| Total | 0.74 | 0.62 | 0.47 | 0.39 | - | 0.26 | 0.77 | 0.49 | 0.44 | 0.61 | 0.61 | 0.81 |
| Mg# | 3.18 | 0.56 | 0.77 | 0.67 | - | 1.64 | 0.57 | 5.82 | 2.74 | 3.24 | 1.39 | 3.31 |

Tableau B-3a (suite)

| Echantillon | 31R3_140-147 | 33R2_23-30 | 33R2_80-90 | 34R4_36-44 | 35R1_90-100 | 35R2_71-80 | 35R3_86-97 | 35R3_115-119 | 35R4_28-35 | 35R4_47-57 | 36R1_74-79 | 37R1_69-75 |
|---------------|--------------|------------|------------|------------|-------------|------------|------------|--------------|------------|------------|------------|------------|
| Puits | 1275D | 1275D | 1275D | 1275D | 1275D | 1275D | 1275D | 1275D | 1275D | 1275D | 1275D | 1275D |
| Type de roche | gab à ox | gab à ox | gab à ol | gab à ox | gab à ox | gab à ox | gab à ox | gab à ox | gab à ol | gab à ox | gab à ol | gab à ox |
| n | 3 | 5 | 6 | 12 | 3 | 16 | 11 | 23 | 1 | 1 | 1 | 5 |
| SiO2 | 51.82 | 50.29 | 51.14 | 50.63 | 50.54 | 50.43 | 50.28 | 50.41 | 51.37 | 53.64 | 50.18 | 51.04 |
| TiO2 | 0.65 | 0.71 | 1.24 | 0.72 | 0.65 | 0.79 | 0.66 | 0.90 | 1.23 | 0.29 | 0.79 | 0.66 |
| Al2O3 | 1.49 | 1.72 | 2.77 | 1.77 | 1.75 | 1.97 | 1.71 | 1.80 | 2.59 | 2.28 | 5.07 | 1.60 |
| Cr2O3 | 0.00 | 0.02 | 0.87 | 0.04 | 0.03 | 0.02 | 0.02 | 0.04 | 0.51 | 0.21 | 0.24 | 0.01 |
| FeO | 15.80 | 13.49 | 3.96 | 12.36 | 12.02 | 11.62 | 14.00 | 12.95 | 4.70 | 4.84 | 9.14 | 12.36 |
| MnO | 0.42 | 0.38 | 0.14 | 0.35 | 0.36 | 0.36 | 0.41 | 0.38 | 0.18 | 0.22 | 0.21 | 0.37 |
| MgO | 14.19 | 12.66 | 16.35 | 13.32 | 12.70 | 13.20 | 12.36 | 13.50 | 16.42 | 18.04 | 15.22 | 12.66 |
| CaO | 15.22 | 19.17 | 21.59 | 19.17 | 20.40 | 19.91 | 19.09 | 19.21 | 21.82 | 19.14 | 16.61 | 19.90 |
| Na2O | 0.28 | 0.33 | 0.54 | 0.35 | 0.35 | 0.38 | 0.38 | 0.31 | 0.41 | 0.64 | 0.89 | 0.39 |
| K2O | 0.08 | 0.01 | 0.00 | 0.00 | 0.00 | 0.00 | 0.00 | 0.00 | 0.00 | 0.06 | 0.17 | 0.00 |
| NiO | 0.00 | 0.00 | 0.04 | 0.01 | 0.01 | 0.01 | 0.01 | 0.01 | 0.03 | 0.04 | 0.02 | 0.02 |
| Total | 99.96 | 98.79 | 98.64 | 98.71 | 98.81 | 98.69 | 98.93 | 99.51 | 99.25 | 99.40 | 98.55 | 99.00 |
| Mg# | 62.67 | 62.66 | 88.05 | 65.95 | 65.31 | 66.94 | 61.21 | 65.10 | 86.19 | 86.93 | 74.93 | 64.62 |
| d | | | | | | | | | | | | |
| SiO2 | 0.58 | 0.46 | 0.51 | 0.59 | 0.77 | 0.30 | 0.53 | 0.69 | 0.61 | | | 0.27 |
| TiO2 | 0.26 | 0.07 | 0.29 | 0.24 | 0.21 | 0.11 | 0.18 | 0.45 | 0.34 | | | 0.11 |
| Al2O3 | 0.69 | 0.14 | 0.28 | 0.57 | 0.50 | 0.35 | 0.42 | 0.39 | 0.49 | | | 0.17 |
| Cr2O3 | 0.01 | 0.01 | 0.03 | 0.02 | 0.00 | 0.02 | 0.02 | 0.03 | 0.18 | | | 0.01 |
| FeO | 7.02 | 1.43 | 0.37 | 2.14 | 0.37 | 0.60 | 1.23 | 2.09 | 0.40 | | | 0.62 |
| MnO | 0.15 | 0.04 | 0.02 | 0.03 | 0.01 | 0.02 | 0.04 | 0.09 | 0.02 | | | 0.04 |
| MgO | 2.01 | 0.48 | 0.48 | 0.72 | 0.26 | 0.34 | 0.28 | 1.14 | 0.45 | | | 0.34 |
| CaO | 7.92 | 1.68 | 0.97 | 2.78 | 0.19 | 0.57 | 1.29 | 2.46 | 0.85 | | | 0.37 |
| Na2O | 0.16 | 0.03 | 0.06 | 0.08 | 0.01 | 0.04 | 0.05 | 0.04 | 0.05 | | | 0.03 |
| K2O | 0.13 | 0.01 | 0.01 | 0.01 | 0.00 | 0.00 | 0.01 | 0.00 | 0.00 | | | 0.00 |
| NiO | 0.02 | 0.01 | 0.01 | 0.01 | 0.01 | 0.00 | 0.01 | 0.01 | 0.02 | | | 0.01 |
| Total | 0.77 | 0.60 | 0.22 | 0.33 | 0.26 | 0.06 | 0.37 | 0.52 | 0.59 | | | 0.45 |
| Mg# | 6.48 | 1.54 | 0.86 | 2.57 | 1.03 | 1.25 | 1.79 | 4.22 | 0.85 | | | 1.65 |

Tableau B-3a (suite)

| Echantillon | 38R2_44-53 | 38R3_90-100 | 39R1_7-16 | 39R1_48-59 | 40R1_119-121 | 40R3_58-63 | 41R1_100-104 | 41R3_91-101 | 43R2_4-13 | 44R4_22-31 |
|---------------|------------|-------------|-----------|------------|--------------|------------|--------------|-------------|-----------|------------|
| Puits | 1275D | 1275D | 1275D | 1275D | 1275D | 1275D | 1275D | 1275D | 1275D | 1275D |
| Type de roche | gab à ox | gab à ox | gab à ox | gab à ox | gab à ox | gab à ox | gab à ox | gab à ox | gab à ox | gab à ox |
| n | 10 | 8 | 5 | 1 | 13 | 9 | 3 | 3 | 6 | 5 |
| SiO2 | 50.74 | 50.72 | 50.98 | 49.94 | 50.95 | 50.20 | 50.36 | 50.58 | 50.48 | 50.37 |
| TiO2 | 0.77 | 0.70 | 0.64 | 0.53 | 0.65 | 0.70 | 0.67 | 0.73 | 0.74 | 0.50 |
| Al2O3 | 1.99 | 1.54 | 1.58 | 1.21 | 1.65 | 1.77 | 1.66 | 1.57 | 1.76 | 0.95 |
| Cr2O3 | 0.01 | 0.01 | 0.01 | 0.00 | 0.01 | 0.01 | 0.01 | 0.03 | 0.01 | 0.00 |
| FeO | 12.29 | 13.30 | 12.72 | 18.57 | 13.12 | 13.59 | 16.00 | 13.82 | 14.85 | 18.58 |
| MnO | 0.37 | 0.38 | 0.37 | 0.54 | 0.37 | 0.41 | 0.47 | 0.37 | 0.43 | 0.60 |
| MgO | 12.74 | 13.07 | 12.75 | 13.93 | 12.88 | 13.04 | 12.87 | 12.39 | 13.09 | 10.80 |
| CaO | 20.23 | 18.90 | 20.06 | 13.50 | 19.54 | 18.80 | 17.10 | 19.30 | 17.27 | 17.52 |
| Na2O | 0.38 | 0.35 | 0.36 | 0.32 | 0.31 | 0.30 | 0.36 | 0.33 | 0.34 | 0.29 |
| K2O | 0.01 | 0.00 | 0.00 | 0.04 | 0.00 | 0.00 | 0.00 | 0.00 | 0.00 | 0.01 |
| NiO | 0.01 | 0.01 | 0.01 | 0.00 | 0.01 | 0.01 | 0.01 | 0.00 | 0.01 | 0.00 |
| Total | 99.53 | 98.97 | 99.50 | 98.59 | 99.49 | 98.81 | 99.50 | 99.11 | 98.99 | 99.61 |
| Mg# | 64.90 | 63.69 | 64.08 | 57.21 | 63.70 | 63.29 | 59.32 | 61.50 | 61.71 | 51.06 |
| d | | | | | | | | | | |
| SiO2 | 0.28 | 0.29 | 0.53 | | 0.18 | 0.40 | 0.27 | 0.26 | 0.59 | 0.46 |
| TiO2 | 0.10 | 0.06 | 0.21 | | 0.14 | 0.08 | 0.26 | 0.07 | 0.16 | 0.06 |
| Al2O3 | 0.19 | 0.19 | 0.25 | | 0.23 | 0.15 | 0.74 | 0.33 | 0.35 | 0.34 |
| Cr2O3 | 0.01 | 0.01 | 0.02 | | 0.02 | 0.01 | 0.01 | 0.01 | 0.01 | 0.00 |
| FeO | 0.52 | 0.89 | 0.33 | | 1.23 | 2.34 | 3.85 | 0.35 | 4.39 | 2.84 |
| MnO | 0.02 | 0.03 | 0.03 | | 0.04 | 0.04 | 0.11 | 0.05 | 0.12 | 0.10 |
| MgO | 0.23 | 0.41 | 0.50 | | 0.32 | 0.92 | 0.70 | 0.55 | 0.90 | 0.70 |
| CaO | 0.51 | 1.08 | 0.31 | | 1.16 | 2.73 | 3.10 | 1.05 | 4.64 | 3.09 |
| Na2O | 0.03 | 0.05 | 0.04 | | 0.04 | 0.05 | 0.17 | 0.02 | 0.08 | 0.10 |
| K2O | 0.00 | 0.00 | 0.00 | | 0.00 | 0.00 | 0.00 | 0.00 | 0.00 | 0.00 |
| NiO | 0.01 | 0.01 | 0.01 | | 0.01 | 0.01 | 0.01 | 0.01 | 0.01 | 0.00 |
| Total | 0.62 | 0.36 | 0.42 | | 0.36 | 0.71 | 0.42 | 0.24 | 0.62 | 0.89 |
| Mg# | 0.94 | 1.02 | 1.46 | | 1.53 | 2.03 | 5.55 | 0.44 | 6.12 | 2.41 |

Tableau B-3b: Composition moyenne en éléments majeurs des orthopyroxènes du Site ODP 1275*

| Echantillon | 6R2_34-38 | 15R2_49-57 | 18R1_122-132 | 19R1_50-54 | 19R2_31-43 | 20R1_100-109 | 21R1_27-37 | 22R1_97-104 | 26R1_60-70 | 27R1_133-145 | 30R2_54-63 |
|---------------|------------|------------|--------------|------------|------------|--------------|------------|-------------|------------|--------------|------------|
| Puits | 1275B | 1275D | 1275D | 1275D | 1275D | 1275D | 1275D | 1275D | 1275D | 1275D | 1275D |
| Type de roche | troctolite | gab à ox | gab à ox | gab à ox | gab à ox | gab à ox | gab à ox | gab à ox | gab à ox | gab à ox | gab à ox |
| n | 8 | 3 | 1 | 1 | 3 | 4 | 1 | 2 | 5 | 1 | 1 |
| SiO2 | 53.93 | 50.37 | 51.02 | 52.55 | 52.46 | 51.56 | 50.81 | 50.69 | 51.08 | 51.40 | 51.83 |
| TiO2 | 0.45 | 0.27 | 0.29 | 0.16 | 0.49 | 0.33 | 0.29 | 0.27 | 0.33 | 0.28 | 0.36 |
| Al2O3 | 1.37 | 0.50 | 0.61 | 1.12 | 1.02 | 0.59 | 0.62 | 0.67 | 0.61 | 0.63 | 0.74 |
| Cr2O3 | 0.44 | 0.00 | 0.00 | 0.00 | 0.01 | 0.00 | 0.01 | 0.00 | 0.00 | 0.00 | 0.04 |
| FeO | 7.16 | 29.55 | 27.98 | 25.73 | 21.33 | 28.17 | 28.56 | 28.69 | 28.59 | 26.91 | 26.27 |
| MnO | 0.18 | 0.76 | 0.65 | 0.72 | 0.48 | 0.66 | 0.68 | 0.66 | 0.67 | 0.69 | 0.62 |
| MgO | 35.05 | 16.39 | 17.63 | 16.56 | 22.02 | 17.19 | 17.10 | 17.12 | 16.81 | 18.51 | 18.57 |
| CaO | 1.20 | 1.59 | 1.59 | 1.82 | 1.64 | 1.83 | 1.49 | 1.60 | 1.85 | 1.25 | 1.56 |
| Na2O | 0.03 | 0.02 | 0.04 | 0.20 | 0.04 | 0.05 | 0.05 | 0.04 | 0.05 | 0.01 | 0.02 |
| K2O | 0.00 | 0.00 | 0.01 | 0.02 | 0.00 | 0.01 | 0.00 | 0.01 | 0.00 | 0.00 | 0.17 |
| NiO | 0.11 | 0.02 | 0.01 | 0.00 | 0.02 | 0.00 | 0.00 | 0.01 | 0.01 | 0.02 | 0.01 |
| Total | 99.92 | 99.46 | 99.84 | 98.87 | 99.51 | 100.40 | 99.61 | 99.77 | 100.00 | 99.70 | 100.19 |
| Mg# | 89.76 | 49.71 | 52.90 | 53.42 | 64.79 | 52.10 | 51.63 | 51.55 | 51.18 | 55.08 | 55.75 |
| σ | | | | | | | | | | | |
| SiO2 | 5.38 | 0.09 | - | - | 0.06 | 0.22 | - | 0.03 | 0.20 | - | - |
| TiO2 | 0.18 | 0.02 | - | - | 0.08 | 0.02 | - | 0.07 | 0.05 | - | - |
| Al2O3 | 0.56 | 0.04 | - | - | 0.12 | 0.04 | - | 0.05 | 0.06 | - | - |
| Cr2O3 | 0.18 | 0.00 | - | - | 0.01 | 0.00 | - | 0.01 | 0.00 | - | - |
| FeO | 1.34 | 0.22 | - | - | 0.46 | 0.15 | - | 0.71 | 0.99 | - | - |
| MnO | 0.02 | 0.02 | - | - | 0.01 | 0.06 | - | 0.01 | 0.02 | - | - |
| MgO | 5.43 | 0.34 | - | - | 0.18 | 0.05 | - | 0.21 | 0.39 | - | - |
| CaO | 0.59 | 0.13 | - | - | 0.13 | 0.08 | - | 0.29 | 0.59 | - | - |
| Na2O | 0.03 | 0.02 | - | - | 0.02 | 0.01 | - | 0.01 | 0.03 | - | - |
| K2O | 0.00 | 0.00 | - | - | 0.01 | 0.01 | - | 0.01 | 0.00 | - | - |
| NiO | 0.09 | 0.01 | - | - | 0.02 | 0.01 | - | 0.00 | 0.01 | - | - |
| Total | 0.32 | 0.25 | - | - | 0.18 | 0.32 | - | 0.21 | 0.33 | - | - |
| Mg# | 0.25 | 0.65 | - | - | 0.61 | 0.13 | - | 0.92 | 1.41 | - | - |

*Les analyses en éléments majeurs ont été réalisées par microsonde électronique (% poids d'oxyde). Abbréviation: n= nombre d'analyses par minéral; σ = écart type.
Mg# = (Mg/(Mg+Fe))*100

Tableau B-3b (suite)

| Echantillon | 31R3_0-5 | 31R3_71-76 | 31R3_140-147 | 33R2_23-30 | 34R4_36-44 | 35R1_90-100 | 35R2_71-80 | 35R3_115-119 | 35R4_28-35 | 35R4_47-57 | 37R1_69-75 |
|---------------|----------|------------|--------------|------------|------------|-------------|------------|--------------|------------|------------|------------|
| Puits | 1275D | 1275D | 1275D | 1275D | 1275D | 1275D | 1275D | 1275D | 1275D | 1275D | 1275D |
| Type de roche | gab à ox | gab à ox | gab à ox | gab à ox | gab à ox | gab à ox | gab à ox | gab à ox | gab à ol | gab à ox | gab à ox |
| n | 5 | 5 | 6 | 1 | 3 | 4 | 2 | 9 | 4 | 2 | 9 |
| SiO2 | 52.18 | 51.72 | 52.85 | 50.20 | 51.55 | 51.33 | 51.23 | 51.50 | 55.03 | 55.01 | 51.54 |
| TiO2 | 0.46 | 0.43 | 0.43 | 0.32 | 0.44 | 0.42 | 0.35 | 0.44 | 0.66 | 0.60 | 0.41 |
| Al2O3 | 1.06 | 0.81 | 0.92 | 0.47 | 0.77 | 0.78 | 0.69 | 0.88 | 1.25 | 1.33 | 0.78 |
| Cr2O3 | 0.02 | 0.01 | 0.01 | 0.02 | 0.00 | 0.01 | 0.02 | 0.03 | 0.20 | 0.25 | 0.00 |
| FeO | 21.89 | 24.77 | 22.04 | 27.45 | 24.30 | 24.71 | 25.54 | 23.61 | 10.74 | 9.91 | 24.75 |
| MnO | 0.52 | 0.57 | 0.50 | 0.67 | 0.59 | 0.58 | 0.63 | 0.55 | 0.29 | 0.24 | 0.59 |
| MgO | 21.54 | 19.67 | 21.12 | 16.99 | 19.86 | 19.70 | 19.27 | 20.51 | 30.21 | 30.67 | 19.40 |
| CaO | 1.97 | 1.51 | 1.63 | 2.63 | 1.73 | 2.03 | 1.48 | 1.71 | 1.89 | 1.26 | 1.79 |
| Na2O | 0.04 | 0.03 | 0.03 | 0.01 | 0.03 | 0.04 | 0.03 | 0.02 | 0.04 | 0.01 | 0.04 |
| K2O | 0.01 | 0.00 | -0.05 | 0.01 | 0.00 | 0.00 | 0.00 | 0.00 | 0.00 | 0.01 | 0.00 |
| NiO | 0.00 | 0.01 | 0.01 | 0.00 | 0.01 | 0.01 | 0.02 | 0.01 | 0.04 | 0.07 | 0.01 |
| Total | 99.68 | 99.54 | 99.54 | 98.76 | 99.27 | 99.62 | 99.24 | 99.27 | 100.34 | 99.36 | 99.31 |
| Mg# | 63.67 | 58.60 | 63.04 | 52.46 | 59.30 | 58.69 | 57.35 | 60.75 | 83.38 | 84.65 | 58.28 |
| d | | | | | | | | | | | |
| SiO2 | 0.53 | 0.54 | 0.59 | - | 0.11 | 0.17 | 0.00 | 0.24 | 0.43 | 0.15 | 0.27 |
| TiO2 | 0.03 | 0.05 | 0.07 | - | 0.03 | 0.01 | 0.03 | 0.07 | 0.07 | 0.06 | 0.03 |
| Al2O3 | 0.24 | 0.08 | 0.11 | - | 0.09 | 0.03 | 0.06 | 0.16 | 0.06 | 0.01 | 0.12 |
| Cr2O3 | 0.02 | 0.01 | 0.01 | - | 0.00 | 0.01 | 0.02 | 0.02 | 0.03 | 0.02 | 0.01 |
| FeO | 2.79 | 0.78 | 1.80 | - | 0.47 | 0.77 | 0.04 | 0.98 | 0.17 | 0.09 | 1.21 |
| MnO | 0.07 | 0.01 | 0.05 | - | 0.03 | 0.01 | 0.01 | 0.06 | 0.01 | 0.03 | 0.06 |
| MgO | 1.77 | 0.53 | 1.38 | - | 0.23 | 0.46 | 0.05 | 0.66 | 0.36 | 0.11 | 0.78 |
| CaO | 0.79 | 0.42 | 0.26 | - | 0.17 | 0.12 | 0.24 | 0.22 | 0.50 | 0.05 | 0.34 |
| Na2O | 0.01 | 0.01 | 0.02 | - | 0.01 | 0.02 | 0.00 | 0.01 | 0.02 | 0.01 | 0.02 |
| K2O | 0.00 | 0.00 | 0.13 | - | 0.00 | 0.00 | 0.00 | 0.00 | 0.00 | 0.00 | 0.00 |
| NiO | 0.01 | 0.01 | 0.02 | - | 0.01 | 0.01 | 0.02 | 0.01 | 0.01 | 0.00 | 0.01 |
| Total | 0.38 | 0.80 | 0.31 | - | 0.11 | 0.17 | 0.38 | 0.48 | 1.09 | 0.21 | 0.20 |
| Mg# | 4.86 | 1.37 | 3.42 | - | 0.74 | 1.32 | 0.11 | 1.72 | 0.25 | 0.17 | 2.10 |

Tableau B-3b (suite)

| Echantillon | 37R3_104-112 | 38R2_44-53 | 38R3_90-100 | 39R1_7-16 | 39R1_48-59 | 40R1_119-124 | 40R3_58-63 | 41R1_100-108 | 41R3_91-101 | 43R2_4-13 |
|---------------|--------------|------------|-------------|-----------|------------|--------------|------------|--------------|-------------|-----------|
| Puits | 1275D | 1275D | 1275D | 1275D | 1275D | 1275D | 1275D | 1275D | 1275D | 1275D |
| Type de roche | gab à ox | gab à ox | gab à ox | gab à ox | gab à ox | gab à ox | gab à ox | gab à ox | gab à ox | gab à ox |
| n | 1 | 1 | 1 | 4 | 2 | 4 | 1 | 2 | 4 | 3 |
| SiO2 | 51.57 | 51.97 | 51.01 | 52.03 | 50.60 | 51.74 | 50.97 | 51.23 | 51.06 | 50.86 |
| TiO2 | 0.11 | 0.49 | 0.26 | 0.44 | 0.32 | 0.26 | 0.25 | 0.27 | 0.38 | 0.27 |
| Al2O3 | 0.92 | 0.90 | 0.73 | 0.82 | 0.59 | 0.69 | 0.58 | 0.81 | 0.72 | 0.59 |
| Cr2O3 | 0.02 | 0.02 | 0.00 | 0.00 | 0.01 | 0.01 | 0.03 | 0.01 | 0.00 | 0.01 |
| FeO | 31.01 | 22.77 | 24.69 | 24.18 | 27.28 | 25.70 | 26.74 | 26.04 | 27.16 | 27.92 |
| MnO | 0.62 | 0.52 | 0.65 | 0.57 | 0.66 | 0.64 | 0.66 | 0.64 | 0.60 | 0.73 |
| MgO | 12.18 | 21.07 | 18.54 | 20.17 | 17.16 | 19.10 | 17.76 | 18.95 | 17.89 | 17.31 |
| CaO | 1.47 | 2.94 | 3.70 | 1.95 | 2.28 | 1.64 | 2.34 | 1.75 | 1.96 | 1.82 |
| Na2O | 0.22 | 0.03 | 0.11 | 0.03 | 0.03 | 0.02 | 0.03 | 0.04 | 0.05 | 0.03 |
| K2O | 0.00 | 0.01 | 0.00 | 0.00 | 0.00 | 0.00 | 0.00 | 0.00 | 0.00 | 0.01 |
| NiO | 0.03 | 0.03 | 0.01 | 0.01 | 0.01 | 0.01 | 0.00 | 0.01 | 0.01 | 0.01 |
| Total | 98.14 | 100.75 | 99.70 | 100.20 | 98.94 | 99.81 | 99.36 | 99.77 | 99.83 | 99.55 |
| Mg# | 41.18 | 62.25 | 57.24 | 59.77 | 52.84 | 56.98 | 54.20 | 56.48 | 53.98 | 52.50 |
| d | | | | | | | | | | |
| SiO2 | - | - | - | 0.44 | 0.39 | 0.03 | - | 0.06 | 0.44 | 0.11 |
| TiO2 | - | - | - | 0.03 | 0.07 | 0.03 | - | 0.02 | 0.03 | 0.05 |
| Al2O3 | - | - | - | 0.21 | 0.06 | 0.03 | - | 0.11 | 0.09 | 0.06 |
| Cr2O3 | - | - | - | 0.01 | 0.01 | 0.01 | - | 0.01 | 0.00 | 0.01 |
| FeO | - | - | - | 1.99 | 1.03 | 0.58 | - | 0.22 | 1.42 | 0.71 |
| MnO | - | - | - | 0.06 | 0.10 | 0.03 | - | 0.04 | 0.03 | 0.04 |
| MgO | - | - | - | 1.34 | 0.80 | 0.29 | - | 0.20 | 1.00 | 0.10 |
| CaO | - | - | - | 0.31 | 0.76 | 0.79 | - | 0.64 | 0.15 | 0.92 |
| Na2O | - | - | - | 0.02 | 0.00 | 0.01 | - | 0.00 | 0.02 | 0.01 |
| K2O | - | - | - | 0.00 | 0.00 | 0.01 | - | 0.00 | 0.00 | 0.00 |
| NiO | - | - | - | 0.01 | 0.01 | 0.01 | - | 0.02 | 0.01 | 0.01 |
| Total | - | - | - | 0.22 | 0.57 | 0.15 | - | 0.26 | 0.13 | 0.40 |
| Mg# | - | - | - | 3.54 | 2.10 | 0.25 | - | 0.05 | 2.69 | 0.65 |

Tableau B-3c: Composition moyenne en éléments majeurs des plagioclases du Site ODP 1275*

| Echantillon | SR1_114-118 | SR2_48-52 | 6R2_106-110 | 9R2_22-26 | 9R2_34-36 | 10R1_22-26 | 10R2_43-46 | 13R2_35-43 | 13R2_96-100 | 15R1_78-90 | 15R1_120-124 |
|--------------------------------|-------------|-----------|-------------|-----------|-----------|------------|------------|------------|-------------|------------|--------------|
| Puits | 1275B | 1275B | 1275B | 1275D | 1275D | 1275D | 1275D | 1275D | 1275D | 1275D | 1275D |
| Type de roche | gab à ox | gab à ox | troctoïte | troctoïte | troctoïte | troctoïte | troctoïte | gab à ox | gab à ox | gab à ox | gab à ox |
| n | 11 | 10 | 2 | 5 | 7 | 6 | 3 | 6 | 18 | 12 | 26 |
| SiO ₂ | 57.82 | 57.59 | 48.71 | 52.57 | 50.94 | 52.53 | 54.86 | 57.53 | 57.32 | 57.28 | 57.70 |
| TiO ₂ | 0.06 | 0.06 | 0.03 | 0.11 | 0.09 | 0.11 | 0.10 | 0.08 | 0.07 | 0.07 | 0.07 |
| Al ₂ O ₃ | 25.67 | 25.88 | 31.84 | 30.23 | 31.17 | 29.82 | 28.06 | 26.00 | 26.21 | 26.25 | 26.47 |
| Cr ₂ O ₃ | 0.00 | 0.00 | 0.01 | 0.01 | 0.01 | 0.01 | 0.00 | 0.01 | 0.00 | 0.01 | 0.00 |
| FeO | 0.24 | 0.22 | 0.10 | 0.18 | 0.12 | 0.20 | 0.13 | 0.27 | 0.24 | 0.26 | 0.25 |
| MnO | 0.00 | 0.01 | 0.00 | 0.03 | 0.01 | 0.03 | 0.02 | 0.00 | 0.01 | 0.01 | 0.00 |
| MgO | 0.01 | 0.02 | 0.06 | 0.03 | 0.02 | 0.08 | 0.01 | 0.02 | 0.02 | 0.02 | 0.01 |
| CaO | 7.61 | 7.87 | 14.91 | 12.59 | 13.67 | 12.22 | 10.19 | 8.12 | 8.22 | 8.37 | 8.43 |
| Na ₂ O | 7.35 | 7.23 | 3.15 | 4.68 | 3.98 | 4.69 | 5.96 | 7.10 | 6.97 | 6.92 | 6.95 |
| K ₂ O | 0.22 | 0.17 | 0.06 | 0.14 | 0.06 | 0.16 | 0.16 | 0.16 | 0.24 | 0.17 | 0.13 |
| Total | 99.01 | 99.05 | 98.88 | 100.58 | 100.07 | 99.84 | 99.49 | 99.30 | 99.30 | 99.34 | 100.02 |
| An (Ca) | 35.94 | 37.23 | 72.09 | 59.34 | 65.28 | 58.48 | 48.17 | 38.38 | 38.94 | 39.67 | 39.83 |
| σ | | | | | | | | | | | |
| SiO ₂ | 0.46 | 0.24 | 0.39 | 1.03 | 0.27 | 0.30 | 4.02 | 0.35 | 0.36 | 0.52 | 0.29 |
| TiO ₂ | 0.02 | 0.03 | 0.00 | 0.03 | 0.02 | 0.02 | 0.05 | 0.02 | 0.02 | 0.03 | 0.02 |
| Al ₂ O ₃ | 0.33 | 0.17 | 0.52 | 0.66 | 0.26 | 0.29 | 2.55 | 0.14 | 0.25 | 0.29 | 0.18 |
| Cr ₂ O ₃ | 0.00 | 0.01 | 0.02 | 0.01 | 0.00 | 0.01 | 0.00 | 0.01 | 0.01 | 0.01 | 0.01 |
| FeO | 0.03 | 0.02 | 0.00 | 0.11 | 0.04 | 0.08 | 0.08 | 0.04 | 0.03 | 0.03 | 0.05 |
| MnO | 0.01 | 0.01 | 0.00 | 0.03 | 0.01 | 0.02 | 0.02 | 0.01 | 0.01 | 0.01 | 0.01 |
| MgO | 0.01 | 0.01 | 0.02 | 0.01 | 0.02 | 0.08 | 0.01 | 0.01 | 0.01 | 0.01 | 0.01 |
| CaO | 0.46 | 0.16 | 0.39 | 0.74 | 0.28 | 0.10 | 3.15 | 0.13 | 0.28 | 0.33 | 0.17 |
| Na ₂ O | 0.24 | 0.10 | 0.20 | 0.42 | 0.18 | 0.09 | 1.65 | 0.15 | 0.17 | 0.16 | 0.10 |
| K ₂ O | 0.06 | 0.01 | 0.00 | 0.05 | 0.02 | 0.02 | 0.14 | 0.01 | 0.04 | 0.01 | 0.02 |
| Total | 0.20 | 0.22 | 0.32 | 0.35 | 0.44 | 0.53 | 0.08 | 0.30 | 0.21 | 0.27 | 0.21 |
| An (Ca) | 2.22 | 0.72 | 1.80 | 3.73 | 1.45 | 0.51 | 14.88 | 0.80 | 1.37 | 1.47 | 0.80 |

*Les analyses en éléments majeurs ont été réalisées par microsonde électronique (% poids d'oxyde). Abbréviations: n= nombre d'analyses par minéral; σ = écart type.

Tableau B-3c (suite)

| Echantillon | 15R2_49-57 | 16R1_30-34 | 18R1_122-132 | 19R1_50-54 | 19R2_31-43 | 20R1_100-109 | 21R1_27-37 | 22R1_97-104 | 23R2_55-61 | 24R2_121-128 | 24R3_11-20 |
|---------------|------------|------------|--------------|------------|------------|--------------|------------|-------------|--------------|--------------|------------|
| Puits | 1275D | 1275D | 1275D | 1275D | 1275D | 1275D | 1275D | 1275D | 1275D | 1275D | 1275D |
| Type de roche | gab à ox | gab à ox | gab à ox | gab à ox | gab à ox | gab à ox | gab à ox | gab à ox | micro-gabbro | gab à ox | gab à ox |
| n | 11 | 35 | 9 | 31 | 13 | 12 | 13 | 11 | 15 | 12 | 13 |
| SiO2 | 56.81 | 58.48 | 56.73 | 56.94 | 55.91 | 57.70 | 56.83 | 56.67 | 51.24 | 57.65 | 56.98 |
| TiO2 | 0.08 | 0.07 | 0.09 | 0.07 | 0.09 | 0.09 | 0.08 | 0.10 | 0.05 | 0.08 | 0.08 |
| Al2O3 | 26.23 | 25.98 | 26.73 | 26.44 | 27.60 | 26.56 | 26.76 | 26.71 | 30.35 | 26.51 | 26.54 |
| Cr2O3 | 0.00 | 0.01 | 0.01 | 0.01 | 0.01 | 0.01 | 0.01 | 0.01 | 0.00 | 0.00 | 0.00 |
| FeO | 0.25 | 0.24 | 0.24 | 0.31 | 0.22 | 0.29 | 0.26 | 0.34 | 0.45 | 0.28 | 0.27 |
| MnO | 0.01 | 0.01 | 0.01 | 0.01 | 0.01 | 0.00 | 0.01 | 0.00 | 0.01 | 0.00 | 0.01 |
| MgO | 0.01 | 0.01 | 0.02 | 0.03 | 0.02 | 0.01 | 0.02 | 0.02 | 0.18 | 0.02 | 0.02 |
| CaO | 8.47 | 7.84 | 8.91 | 8.53 | 9.95 | 8.83 | 8.91 | 8.78 | 13.87 | 8.71 | 8.59 |
| Na2O | 6.86 | 7.30 | 6.66 | 6.85 | 6.16 | 6.73 | 6.54 | 6.59 | 3.92 | 6.78 | 6.71 |
| K2O | 0.21 | 0.24 | 0.17 | 0.20 | 0.12 | 0.16 | 0.18 | 0.19 | 0.03 | 0.16 | 0.20 |
| Total | 98.94 | 100.18 | 99.56 | 99.38 | 100.07 | 100.38 | 99.60 | 99.40 | 100.11 | 100.21 | 99.40 |
| An (Ca) | 40.06 | 36.76 | 42.12 | 40.32 | 46.86 | 41.65 | 42.49 | 41.94 | 60.17 | 41.16 | 40.98 |
| σ | | | | | | | | | | | |
| SiO2 | 0.63 | 2.27 | 0.60 | 0.87 | 1.20 | 0.33 | 0.24 | 0.22 | 2.72 | 0.19 | 0.30 |
| TiO2 | 0.02 | 0.03 | 0.01 | 0.04 | 0.02 | 0.01 | 0.03 | 0.04 | 0.03 | 0.02 | 0.03 |
| Al2O3 | 0.23 | 1.48 | 0.21 | 0.45 | 0.67 | 0.18 | 0.13 | 0.09 | 1.99 | 0.18 | 0.13 |
| Cr2O3 | 0.01 | 0.01 | 0.01 | 0.01 | 0.01 | 0.01 | 0.01 | 0.01 | 0.01 | 0.01 | 0.00 |
| FeO | 0.03 | 0.03 | 0.02 | 0.27 | 0.03 | 0.07 | 0.02 | 0.23 | 0.14 | 0.03 | 0.02 |
| MnO | 0.01 | 0.01 | 0.01 | 0.01 | 0.01 | 0.00 | 0.01 | 0.01 | 0.01 | 0.01 | 0.01 |
| MgO | 0.01 | 0.01 | 0.01 | 0.06 | 0.02 | 0.01 | 0.01 | 0.01 | 0.04 | 0.01 | 0.01 |
| CaO | 0.32 | 1.78 | 0.15 | 0.53 | 0.81 | 0.16 | 0.13 | 0.10 | 2.25 | 0.15 | 0.11 |
| Na2O | 0.21 | 0.90 | 0.16 | 0.32 | 0.47 | 0.11 | 0.10 | 0.08 | 1.30 | 0.09 | 0.14 |
| K2O | 0.02 | 0.14 | 0.01 | 0.03 | 0.02 | 0.01 | 0.01 | 0.03 | 0.02 | 0.02 | 0.02 |
| Total | 0.44 | 0.28 | 0.89 | 0.74 | 0.30 | 0.15 | 0.25 | 0.34 | 0.32 | 0.13 | 0.27 |
| An (Ca) | 1.62 | 8.35 | 0.88 | 2.62 | 3.92 | 0.79 | 0.70 | 0.53 | 5.33 | 0.65 | 0.80 |

Tableau B-3c (suite)

| Echantillon | 26R1_60-70 | 26R3_112-120 | 27R1_10-17 | 27R1_70-80 | 27R1_133-145 | 27R2_31-37 | 29R2_52-58 | 30R2_54-63 | 31R3_0-5 | 31R3_71-76 | 31R3_140-147 |
|---------------|------------|--------------|-------------|------------|--------------|------------|------------|------------|----------|------------|--------------|
| Puits | 1275D | 1275D | 1275D | 1275D | 1275D | 1275D | 1275D | 1275D | 1275D | 1275D | 1275D |
| Type de roche | gab à ox | gab à ox | Felsic veim | gab à ox | gab à ox | gab à ox | gab à ox | gab à ox | gab à ox | gab à ox | gab à ox |
| n | 13 | 12 | 20 | 10 | 9 | 21 | 13 | 11 | 16 | 17 | 12 |
| SiO2 | 57.46 | 56.84 | 60.11 | 56.75 | 55.56 | 58.41 | 58.26 | 56.49 | 55.82 | 56.80 | 56.61 |
| TiO2 | 0.08 | 0.11 | 0.04 | 0.07 | 0.06 | 0.06 | 0.06 | 0.08 | 0.08 | 0.07 | 0.08 |
| Al2O3 | 26.56 | 26.66 | 24.13 | 26.83 | 27.84 | 25.59 | 25.76 | 27.47 | 27.39 | 26.73 | 27.31 |
| Cr2O3 | 0.01 | 0.00 | 0.00 | 0.01 | 0.01 | 0.01 | 0.01 | 0.01 | 0.01 | 0.00 | 0.01 |
| FeO | 0.39 | 0.63 | 0.25 | 0.27 | 0.31 | 0.39 | 0.24 | 0.25 | 0.28 | 0.28 | 0.30 |
| MnO | 0.01 | 0.01 | 0.00 | 0.01 | 0.01 | 0.01 | 0.01 | 0.01 | 0.01 | 0.00 | 0.01 |
| MgO | 0.01 | 0.03 | 0.01 | 0.02 | 0.01 | 0.04 | 0.01 | 0.02 | 0.02 | 0.01 | 0.04 |
| CaO | 8.62 | 8.62 | 5.61 | 8.74 | 9.79 | 7.34 | 7.56 | 9.60 | 9.57 | 8.91 | 9.46 |
| Na2O | 6.78 | 6.80 | 8.46 | 6.66 | 6.10 | 7.33 | 7.13 | 6.19 | 6.20 | 6.68 | 6.21 |
| K2O | 0.15 | 0.15 | 0.31 | 0.13 | 0.10 | 0.18 | 0.26 | 0.47 | 0.11 | 0.16 | 0.37 |
| Total | 100.07 | 99.85 | 98.92 | 99.48 | 99.79 | 99.35 | 99.28 | 100.58 | 99.48 | 99.66 | 100.34 |
| An (Ca) | 40.93 | 40.85 | 26.57 | 41.72 | 46.76 | 35.31 | 36.39 | 45.05 | 45.73 | 42.07 | 44.81 |
| σ | | | | | | | | | | | |
| SiO2 | 0.91 | 1.13 | 3.61 | 0.46 | 1.09 | 3.43 | 0.53 | 0.72 | 0.70 | 1.58 | 1.01 |
| TiO2 | 0.04 | 0.15 | 0.03 | 0.02 | 0.02 | 0.03 | 0.02 | 0.01 | 0.02 | 0.03 | 0.02 |
| Al2O3 | 0.45 | 0.23 | 2.41 | 0.32 | 0.70 | 1.89 | 0.42 | 0.37 | 0.59 | 0.82 | 0.64 |
| Cr2O3 | 0.01 | 0.01 | 0.01 | 0.01 | 0.01 | 0.01 | 0.01 | 0.01 | 0.01 | 0.01 | 0.01 |
| FeO | 0.51 | 1.28 | 0.09 | 0.09 | 0.21 | 0.42 | 0.05 | 0.04 | 0.05 | 0.05 | 0.19 |
| MnO | 0.01 | 0.01 | 0.01 | 0.01 | 0.01 | 0.01 | 0.01 | 0.00 | 0.01 | 0.00 | 0.01 |
| MgO | 0.01 | 0.04 | 0.01 | 0.01 | 0.01 | 0.13 | 0.01 | 0.01 | 0.01 | 0.01 | 0.07 |
| CaO | 0.56 | 0.19 | 2.80 | 0.34 | 0.78 | 2.32 | 0.39 | 0.41 | 0.45 | 1.24 | 0.75 |
| Na2O | 0.34 | 0.10 | 1.69 | 0.17 | 0.43 | 1.31 | 0.18 | 0.24 | 0.25 | 0.60 | 0.40 |
| K2O | 0.03 | 0.05 | 0.30 | 0.02 | 0.02 | 0.10 | 0.04 | 0.94 | 0.02 | 0.07 | 0.68 |
| Total | 0.36 | 0.27 | 0.62 | 0.39 | 0.40 | 1.07 | 0.25 | 0.80 | 1.01 | 0.54 | 0.68 |
| An (Ca) | 2.73 | 0.87 | 13.54 | 1.51 | 3.74 | 11.26 | 1.78 | 2.78 | 2.11 | 5.61 | 3.78 |

Tableau B-3c (suite)

| Echantillon | 33R2_23-30 | 33R2_80-90 | 34R4_36-44 | 35R1_90-101 | 35R2_71-80 | 35R3_86-97 | 35R3_115-119 | 35R4_28-35 | 35R4_47-57 | 36R1_74-79 | 37R1_69-75 |
|---------------|------------|------------|------------|-------------|------------|------------|--------------|------------|------------|------------|------------|
| Puits | 1275D | 1275D | 1275D | 1275D | 1275D | 1275D | 1275D | 1275D | 1275D | 1275D | 1275D |
| Type de roche | gab à ox | gab à ol | gab à ox | gab à ox | gab à ox | gab à ox | gab à ox | gab à ol | gab à ox | gab à ol | gab à ox |
| n | 7 | 10 | 15 | 6 | 5 | 17 | 15 | 29 | 9 | 14 | 8 |
| SiO2 | 56.29 | 52.62 | 55.71 | 55.48 | 54.92 | 56.09 | 55.03 | 52.71 | 53.29 | 51.83 | 56.62 |
| TiO2 | 0.08 | 0.09 | 0.08 | 0.09 | 0.09 | 0.08 | 0.07 | 0.11 | 0.10 | 0.05 | 0.09 |
| Al2O3 | 26.85 | 29.59 | 27.23 | 27.43 | 27.58 | 27.08 | 27.66 | 29.39 | 29.09 | 30.17 | 27.14 |
| Cr2O3 | 0.00 | 0.01 | 0.00 | 0.00 | 0.00 | 0.01 | 0.01 | 0.00 | 0.01 | 0.01 | 0.00 |
| FeO | 0.32 | 0.13 | 0.29 | 0.32 | 0.29 | 0.27 | 0.26 | 0.13 | 0.16 | 0.31 | 0.31 |
| MnO | 0.01 | 0.00 | 0.01 | 0.01 | 0.02 | 0.00 | 0.01 | 0.00 | 0.01 | 0.01 | 0.01 |
| MgO | 0.02 | 0.02 | 0.02 | 0.02 | 0.02 | 0.02 | 0.02 | 0.02 | 0.10 | 0.15 | 0.01 |
| CaO | 9.11 | 11.99 | 9.52 | 9.78 | 10.14 | 9.22 | 10.02 | 12.09 | 11.35 | 12.75 | 8.97 |
| Na2O | 6.42 | 4.82 | 6.17 | 6.12 | 5.85 | 6.44 | 6.05 | 4.97 | 5.15 | 4.29 | 6.60 |
| K2O | 0.12 | 0.18 | 0.12 | 0.14 | 0.09 | 0.14 | 0.05 | 0.16 | 0.17 | 0.08 | 0.15 |
| Total | 99.21 | 99.43 | 99.16 | 99.39 | 98.99 | 99.34 | 99.18 | 99.60 | 99.43 | 99.64 | 99.89 |
| An (Ca) | 43.67 | 57.33 | 45.71 | 46.54 | 48.68 | 43.85 | 47.67 | 56.81 | 54.38 | 50.47 | 42.54 |
| σ | | | | | | | | | | | |
| SiO2 | 0.76 | 0.86 | 0.67 | 0.89 | 0.28 | 0.59 | 1.31 | 1.21 | 1.16 | 4.69 | 1.00 |
| TiO2 | 0.02 | 0.02 | 0.02 | 0.01 | 0.02 | 0.02 | 0.02 | 0.02 | 0.02 | 0.03 | 0.04 |
| Al2O3 | 0.53 | 0.51 | 0.40 | 0.52 | 0.17 | 0.36 | 0.88 | 0.82 | 0.96 | 2.73 | 0.64 |
| Cr2O3 | 0.01 | 0.01 | 0.00 | 0.00 | 0.01 | 0.01 | 0.01 | 0.01 | 0.01 | 0.01 | 0.01 |
| FeO | 0.04 | 0.03 | 0.04 | 0.05 | 0.04 | 0.04 | 0.06 | 0.03 | 0.03 | 0.14 | 0.13 |
| MnO | 0.01 | 0.01 | 0.01 | 0.01 | 0.02 | 0.01 | 0.01 | 0.01 | 0.01 | 0.01 | 0.01 |
| MgO | 0.01 | 0.01 | 0.01 | 0.01 | 0.01 | 0.03 | 0.01 | 0.02 | 0.24 | 0.22 | 0.01 |
| CaO | 0.60 | 0.70 | 0.49 | 0.62 | 0.10 | 0.42 | 1.04 | 1.06 | 1.01 | 3.46 | 0.81 |
| Na2O | 0.37 | 0.45 | 0.25 | 0.39 | 0.08 | 0.25 | 0.58 | 0.55 | 0.52 | 2.03 | 0.46 |
| K2O | 0.02 | 0.02 | 0.04 | 0.04 | 0.01 | 0.03 | 0.04 | 0.06 | 0.04 | 0.06 | 0.03 |
| Total | 0.21 | 0.23 | 0.64 | 0.37 | 0.26 | 0.42 | 0.42 | 0.81 | 0.59 | 0.81 | 0.29 |
| An (Ca) | 3.05 | 3.69 | 2.26 | 3.22 | 0.50 | 2.07 | 4.97 | 4.75 | 4.69 | 9.11 | 3.95 |

Tableau B-3c (suite)

| Echantillon | 37R3_104-112 | 38R2_44-53 | 38R3_90-100 | 39R1_7-16 | 39R1_48-59 | 40R1_119-124 | 40R3_58-63 | 41R1_100-108 | 41R3_91-101 | 43R2_4-13 | 44R4_22-31 |
|---------------|--------------|------------|-------------|-----------|------------|--------------|------------|--------------|-------------|-----------|------------|
| Puits | 1275D | 1275D | 1275D | 1275D | 1275D | 1275D | 1275D | 1275D | 1275D | 1275D | 1275D |
| Type de roche | gab à ox | gab à ox | gab à ox | gab à ox | gab à ox | gab à ox | gab à ox | gab à ox | gab à ox | gab à ox | gab à ox |
| n | 8 | 14 | 9 | 12 | 11 | 12 | 9 | 8 | 8 | 18 | 12 |
| SiO2 | 55.74 | 55.97 | 55.89 | 55.94 | 56.47 | 56.29 | 55.56 | 56.40 | 56.47 | 56.17 | 59.24 |
| TiO2 | 0.08 | 0.08 | 0.08 | 0.08 | 0.08 | 0.08 | 0.07 | 0.07 | 0.08 | 0.08 | 0.05 |
| Al2O3 | 27.33 | 27.91 | 27.13 | 27.32 | 26.91 | 27.34 | 27.07 | 26.88 | 26.82 | 26.94 | 25.22 |
| Cr2O3 | 0.01 | 0.00 | 0.01 | 0.00 | 0.00 | 0.01 | 0.00 | 0.00 | 0.01 | 0.01 | 0.01 |
| FeO | 0.33 | 0.29 | 0.28 | 0.27 | 0.25 | 0.30 | 0.31 | 0.26 | 0.36 | 0.30 | 0.29 |
| MnO | 0.01 | 0.01 | 0.01 | 0.01 | 0.00 | 0.00 | 0.00 | 0.00 | 0.01 | 0.01 | 0.00 |
| MgO | 0.02 | 0.01 | 0.02 | 0.02 | 0.01 | 0.02 | 0.02 | 0.02 | 0.04 | 0.02 | 0.01 |
| CaO | 9.56 | 9.80 | 9.44 | 9.56 | 9.00 | 9.40 | 9.50 | 9.00 | 8.86 | 9.11 | 6.94 |
| Na2O | 6.21 | 6.19 | 6.32 | 6.26 | 6.65 | 6.36 | 6.17 | 6.58 | 6.56 | 6.44 | 7.68 |
| K2O | 0.16 | 0.12 | 0.11 | 0.12 | 0.20 | 0.10 | 0.10 | 0.12 | 0.17 | 0.13 | 0.26 |
| Total | 99.48 | 100.39 | 99.28 | 99.58 | 99.56 | 99.90 | 98.81 | 99.34 | 99.37 | 99.20 | 99.70 |
| An (Ca) | 45.58 | 46.34 | 44.95 | 45.48 | 42.25 | 44.70 | 45.70 | 42.80 | 42.36 | 43.57 | 32.83 |
| σ | | | | | | | | | | | |
| SiO2 | 1.12 | 0.52 | 0.58 | 0.70 | 0.95 | 0.55 | 0.61 | 0.88 | 1.03 | 0.64 | 1.57 |
| TiO2 | 0.02 | 0.02 | 0.02 | 0.01 | 0.02 | 0.02 | 0.02 | 0.04 | 0.02 | 0.02 | 0.03 |
| Al2O3 | 0.61 | 0.35 | 0.37 | 0.41 | 0.59 | 0.27 | 0.41 | 0.36 | 0.56 | 0.39 | 1.01 |
| Cr2O3 | 0.01 | 0.01 | 0.01 | 0.01 | 0.01 | 0.01 | 0.01 | 0.01 | 0.01 | 0.01 | 0.01 |
| FeO | 0.10 | 0.07 | 0.06 | 0.04 | 0.05 | 0.09 | 0.04 | 0.02 | 0.37 | 0.06 | 0.11 |
| MnO | 0.01 | 0.01 | 0.01 | 0.01 | 0.00 | 0.01 | 0.01 | 0.01 | 0.01 | 0.01 | 0.01 |
| MgO | 0.02 | 0.01 | 0.01 | 0.03 | 0.01 | 0.01 | 0.01 | 0.01 | 0.08 | 0.01 | 0.01 |
| CaO | 0.74 | 0.34 | 0.43 | 0.57 | 1.02 | 0.39 | 0.42 | 0.53 | 0.74 | 0.44 | 1.20 |
| Na2O | 0.47 | 0.21 | 0.27 | 0.33 | 0.36 | 0.23 | 0.24 | 0.38 | 0.44 | 0.26 | 0.62 |
| K2O | 0.06 | 0.03 | 0.01 | 0.02 | 0.05 | 0.01 | 0.01 | 0.01 | 0.03 | 0.03 | 0.10 |
| Total | 0.44 | 0.45 | 0.18 | 0.54 | 0.59 | 0.41 | 0.59 | 0.40 | 0.38 | 0.35 | 0.36 |
| An (Ca) | 3.87 | 1.67 | 2.12 | 2.78 | 3.97 | 1.92 | 2.04 | 2.86 | 3.67 | 2.17 | 5.69 |

Tableau B-3d: Composition moyenne en éléments majeurs des olivines du Site ODP 1275*

| Echantillon | 6R2_34-38 | 6R2_106-110 | 10R1_22-26 | 10R2_43-46 | 33R2_80-90 | 34R4_47-57 | 35R4_28-35 | 36R1_74-79 |
|--------------------------------|------------|-------------|------------|------------|-------------|-------------|-------------|-------------|
| Puits | 1275B | 1275B | 1275D | 1275D | 1275D | 1275D | 1275D | 1275D |
| Type de roche | troctolite | troctolite | troctolite | troctolite | gabbro à ol | gabbro à ol | gabbro à ol | gabbro à ol |
| n | 15 | 8 | 2 | 4 | 7 | 8 | 5 | 7 |
| SiO ₂ | 40.65 | 40.54 | 40.93 | 40.34 | 39.95 | 39.70 | 39.49 | 40.70 |
| TiO ₂ | 0.01 | 0.01 | 0.01 | 0.01 | 0.01 | 0.02 | 0.02 | 0.02 |
| Al ₂ O ₃ | 0.01 | 0.01 | 0.00 | 0.01 | 0.01 | 0.02 | 0.01 | 0.03 |
| Cr ₂ O ₃ | 0.01 | 0.01 | 0.01 | 0.00 | 0.01 | 0.01 | 0.01 | 0.05 |
| FeO | 10.49 | 9.93 | 10.17 | 10.43 | 13.59 | 15.80 | 16.77 | 11.05 |
| MnO | 0.17 | 0.17 | 0.16 | 0.19 | 0.22 | 0.26 | 0.28 | 0.17 |
| MgO | 48.59 | 48.50 | 48.70 | 48.60 | 45.61 | 44.04 | 43.27 | 47.72 |
| CaO | 0.08 | 0.08 | 0.09 | 0.08 | 0.06 | 0.06 | 0.07 | 0.17 |
| Na ₂ O | 0.01 | 0.00 | 0.00 | 0.00 | 0.01 | 0.01 | 0.01 | 0.00 |
| K ₂ O | 0.00 | 0.00 | 0.00 | 0.00 | 0.00 | 0.00 | 0.00 | 0.00 |
| NiO | 0.33 | 0.31 | 0.33 | 0.34 | 0.27 | 0.24 | 0.23 | 0.28 |
| Total | 100.34 | 99.58 | 100.39 | 100.00 | 99.75 | 100.17 | 100.16 | 100.58 |
| Fo (M%) | 89.04 | 89.54 | 89.36 | 89.08 | 85.47 | 83.00 | 81.89 | 88.33 |
| Mg# | 89.04 | 89.54 | 89.36 | 89.08 | 85.79 | 83.38 | 82.29 | 88.59 |
| Ni (ppm) | 2583.92 | 2449.92 | 2560.88 | 2666.93 | 2133.32 | 1861.74 | 1831.89 | 2188.31 |
| σ | | | | | | | | |
| SiO ₂ | 0.13 | 0.15 | 0.24 | 0.26 | 0.23 | 0.29 | 0.10 | 0.44 |
| TiO ₂ | 0.01 | 0.01 | 0.00 | 0.01 | 0.01 | 0.02 | 0.01 | 0.01 |
| Al ₂ O ₃ | 0.01 | 0.01 | 0.00 | 0.01 | 0.01 | 0.01 | 0.00 | 0.02 |
| Cr ₂ O ₃ | 0.01 | 0.01 | 0.01 | 0.00 | 0.01 | 0.01 | 0.01 | 0.02 |
| FeO | 0.07 | 0.06 | 0.15 | 0.20 | 0.11 | 0.14 | 0.06 | 1.93 |
| MnO | 0.02 | 0.02 | 0.01 | 0.01 | 0.01 | 0.01 | 0.01 | 0.02 |
| MgO | 0.13 | 0.14 | 0.14 | 0.15 | 0.14 | 0.26 | 0.25 | 1.57 |
| CaO | 0.02 | 0.02 | 0.00 | 0.01 | 0.01 | 0.01 | 0.01 | 0.09 |
| Na ₂ O | 0.01 | 0.01 | 0.00 | 0.00 | 0.01 | 0.01 | 0.01 | 0.01 |
| K ₂ O | 0.00 | 0.00 | 0.00 | 0.00 | 0.00 | 0.00 | 0.00 | 0.00 |
| NiO | 0.02 | 0.02 | 0.02 | 0.03 | 0.02 | 0.02 | 0.01 | 0.07 |
| Total | 0.19 | 0.26 | 0.27 | 0.26 | 0.11 | 0.62 | 0.35 | 0.95 |
| Fo (M%) | 0.08 | 0.04 | 0.18 | 0.21 | 0.11 | 0.10 | 0.11 | 2.13 |
| Mg# | 0.08 | 0.04 | 0.18 | 0.21 | 0.11 | 0.10 | 0.10 | 2.10 |
| Ni (ppm) | 157.26 | 154.53 | 133.31 | 228.62 | 172.28 | 170.97 | 53.10 | 574.59 |

*Les analyses en éléments majeurs ont été réalisées par microsonde électronique (% poids d'oxyde).

Abbréviations: n= nombre d'analyses par mineral; σ = écart type.

Mg# = (Mg/Mg+Fe)*100

Tableau B-3e: Composition moyenne en éléments majeurs des oxydes du Site ODP1275*

| Echantillon | SR1_114-118 | SR2_48-52 | 6R2_106-110 | 9R2_22-26 | 9R2_34-36 | 10R1_22-26 | 10R2_43-46 | 13R2_35-43 | 15R1_78-90 | 15R1_120-124 | 15R2_49-57 | 16R1_30-34 |
|----------------------|-------------|-----------|-------------|------------|------------|------------|------------|------------|------------|--------------|------------|------------|
| Puits | 1275B | 1275B | 1275B | 1275D | 1275D | 1275D | 1275D | 1275D | 1275D | 1275D | 1275D | 1275D |
| Type de roche | gab à ox | gab à ox | troctolite | troctolite | troctolite | troctolite | troctolite | gab à ox | gab à ox | gab à ox | gab à ox | gab à ox |
| n | 2 | 1 | 1 | 2 | 5 | 3 | 2 | 1 | 5 | 5 | 2 | 5 |
| SiO2 | 0.09 | 0.10 | 0.10 | 0.12 | 0.06 | 0.05 | 0.07 | 0.09 | 0.13 | 0.10 | 0.09 | 0.06 |
| TiO2 | 50.02 | 49.34 | 0.89 | 50.79 | 2.51 | 2.06 | 2.24 | 49.77 | 51.79 | 50.29 | 50.51 | 49.74 |
| Al2O3 | 0.02 | 0.15 | 24.04 | 0.03 | 21.15 | 19.83 | 19.80 | 0.01 | 0.04 | 0.02 | 0.02 | 0.03 |
| Cr2O3 | 0.01 | 0.03 | 40.75 | 0.02 | 42.69 | 44.17 | 42.45 | 0.00 | 0.01 | 0.02 | 0.00 | 0.02 |
| FeO | 47.19 | 47.37 | 19.96 | 47.05 | 21.79 | 22.76 | 23.14 | 48.77 | 45.79 | 47.72 | 47.91 | 48.59 |
| MnO | 0.84 | 0.79 | 0.25 | 1.06 | 0.36 | 0.37 | 0.36 | 0.97 | 1.16 | 1.05 | 0.95 | 0.95 |
| MgO | 0.21 | 0.28 | 13.28 | 0.22 | 11.70 | 10.87 | 11.09 | 0.19 | 0.25 | 0.14 | 0.38 | 0.15 |
| CaO | 0.01 | 0.01 | 0.02 | 0.00 | 0.00 | 0.01 | 0.01 | 0.01 | 0.01 | 0.00 | 0.00 | 0.01 |
| Na2O | 0.00 | 0.00 | 0.01 | 0.00 | 0.00 | 0.00 | 0.01 | 0.00 | 0.02 | 0.02 | 0.00 | 0.04 |
| Total | 98.39 | 98.07 | 99.47 | 99.29 | 100.45 | 100.30 | 99.36 | 99.80 | 99.21 | 99.36 | 99.88 | 99.60 |
| σ | | | | | | | | | | | | |
| SiO2 | 0.00 | - | - | 0.05 | 0.02 | 0.02 | 0.01 | - | 0.07 | 0.02 | 0.00 | 0.01 |
| TiO2 | 0.03 | - | - | 0.93 | 0.44 | 0.21 | 0.15 | - | 0.34 | 0.32 | 0.15 | 0.56 |
| Al2O3 | 0.00 | - | - | 0.01 | 0.44 | 0.45 | 0.01 | - | 0.02 | 0.00 | 0.01 | 0.01 |
| Cr2O3 | 0.01 | - | - | 0.01 | 0.57 | 0.19 | 0.19 | - | 0.01 | 0.01 | 0.01 | 0.02 |
| FeO | 0.12 | - | - | 0.24 | 0.25 | 0.48 | 0.70 | - | 0.64 | 0.17 | 0.20 | 0.24 |
| MnO | 0.04 | - | - | 0.05 | 0.02 | 0.02 | 0.03 | - | 0.09 | 0.07 | 0.01 | 0.10 |
| MgO | 0.00 | - | - | 0.00 | 0.48 | 0.47 | 0.68 | - | 0.09 | 0.02 | 0.13 | 0.06 |
| CaO | 0.00 | - | - | 0.01 | 0.00 | 0.01 | 0.01 | - | 0.01 | 0.00 | 0.00 | 0.01 |
| Na2O | 0.00 | - | - | 0.00 | 0.00 | 0.01 | 0.02 | - | 0.02 | 0.02 | 0.01 | 0.03 |
| Total | 0.20 | - | - | 0.80 | 0.22 | 0.19 | 0.08 | - | 0.27 | 0.51 | 0.22 | 0.46 |

* Les analyses en éléments majeurs ont été réalisées par microsonde électronique (% poids d'oxyde). Abbréviation: n= nombre d'analyses par minéral; σ = écart type.

Tableau B-3e (suite)

| Echantillon | 18R1_122-132 | 19R1_50-54 | 26R3_112-120 | 27R1_10-17 | 27R1_70-80 | 27R1_133-145 | 27R2_31-37 | 31R3_0-5 | 31R3_71-76 | 33R2_23-30 | 34R4_36-44 | 35R3_86-97 | 35R3_115-119 |
|---------------|--------------|------------|--------------|-------------|------------|--------------|------------|----------|------------|------------|------------|------------|--------------|
| Puits | 1275D | 1275D | 1275D | 1275D | 1275D | 1275D | 1275D | 1275D | 1275D | 1275D | 1275D | 1275D | 1275D |
| Type de roche | gab à ox | gab à ox | gab à ox | Felsic vein | gab à ox | gab à ox | gab à ox | gab à ox | gab à ox | gab à ox | gab à ox | gab à ox | gab à ox |
| # | 3 | 6 | 3 | 1 | 4 | 3 | 5 | 1 | 2 | 1 | 1 | 3 | 3 |
| SiO2 | 0.04 | 0.06 | 0.11 | 0.07 | 0.08 | 0.07 | 0.09 | 0.09 | 0.08 | 0.09 | 0.08 | 0.13 | 0.07 |
| TiO2 | 3.10 | 50.40 | 51.69 | 50.93 | 52.04 | 51.99 | 51.69 | 50.06 | 50.02 | 50.46 | 51.32 | 50.45 | 51.15 |
| Al2O3 | 18.61 | 0.05 | 0.07 | 0.03 | 0.02 | 0.04 | 0.01 | 0.03 | 0.06 | 0.08 | 0.03 | 0.02 | 0.03 |
| Cr2O3 | 44.85 | 0.02 | 0.02 | 0.00 | 0.03 | 0.01 | 0.03 | 0.00 | 0.06 | 0.01 | 0.04 | 0.03 | 0.07 |
| FeO | 21.56 | 47.76 | 46.32 | 45.91 | 46.05 | 45.75 | 46.66 | 48.03 | 47.82 | 46.22 | 47.39 | 48.03 | 46.89 |
| MnO | 0.38 | 1.09 | 1.20 | 1.09 | 1.12 | 1.12 | 1.24 | 1.32 | 1.19 | 0.85 | 1.09 | 1.05 | 1.52 |
| MgO | 12.08 | 0.19 | 0.19 | 0.17 | 0.35 | 0.42 | 0.16 | 0.16 | 0.17 | 0.83 | 0.33 | 0.51 | 0.29 |
| CaO | 0.01 | 0.01 | 0.04 | 0.00 | 0.01 | 0.04 | 0.02 | 0.00 | 0.46 | 0.00 | 0.01 | 0.00 | 0.00 |
| Na2O | 0.01 | 0.02 | 0.01 | 0.01 | 0.01 | 0.00 | 0.01 | 0.04 | 0.00 | 0.00 | 0.01 | 0.01 | 0.01 |
| Total | 100.81 | 99.62 | 99.65 | 98.22 | 99.70 | 99.44 | 99.90 | 99.73 | 99.87 | 98.55 | 100.29 | 100.23 | 100.02 |
| o | | | | | | | | | | | | | |
| SiO2 | 0.01 | 0.01 | 0.02 | - | 0.01 | 0.01 | 0.02 | - | 0.02 | - | - | 0.00 | 0.02 |
| TiO2 | 0.20 | 0.45 | 0.68 | - | 0.34 | 0.46 | 0.33 | - | 0.87 | - | - | 0.58 | 0.68 |
| Al2O3 | 0.60 | 0.08 | 0.07 | - | 0.01 | 0.04 | 0.00 | - | 0.06 | - | - | 0.01 | 0.01 |
| Cr2O3 | 0.73 | 0.02 | 0.02 | - | 0.01 | 0.01 | 0.01 | - | 0.00 | - | - | 0.03 | 0.01 |
| FeO | 0.19 | 0.39 | 0.41 | - | 0.17 | 0.36 | 0.43 | - | 0.86 | - | - | 0.60 | 0.41 |
| MnO | 0.02 | 0.10 | 0.15 | - | 0.08 | 0.10 | 0.35 | - | 0.00 | - | - | 0.28 | 0.05 |
| MgO | 0.19 | 0.05 | 0.05 | - | 0.11 | 0.16 | 0.12 | - | 0.01 | - | - | 0.41 | 0.03 |
| CaO | 0.01 | 0.00 | 0.05 | - | 0.00 | 0.06 | 0.03 | - | 0.66 | - | - | 0.00 | 0.00 |
| Na2O | 0.01 | 0.03 | 0.01 | - | 0.01 | 0.00 | 0.02 | - | 0.01 | - | - | 0.01 | 0.01 |
| Total | 0.24 | 0.41 | 0.16 | - | 0.17 | 0.41 | 0.64 | - | 0.71 | - | - | 0.16 | 0.42 |

Tableau B-3e (suite)

| Echantillon | 35R4_28-35 | 36R1_74-79 | 37R1_69-75 | 7R3_104-11 | 38R2_44-53 | 38R3_90-100 | 39R1_7-16 | 40R1_119-124 | 40R3_58-63 | 41R1_100-108 | 41R3_91-101 | 44R4_22-31 |
|---------------|------------|------------|------------|------------|------------|-------------|-----------|--------------|------------|--------------|-------------|------------|
| Puits | 1275D | 1275D | 1275D | 1275D | 1275D | 1275D | 1275D | 1275D | 1275D | 1275D | 1275D | 1275D |
| Type de roche | gab à ol | gab à ol | gab à ox | gab à ox | gab à ox | gab à ox | gab à ox | gab à ox | gab à ox | gab à ox | gab à ox | gab à ox |
| n | 4 | 5 | 1 | 1 | 1 | 3 | 1 | 8 | 4 | 3 | 3 | 4 |
| SiO2 | 0.11 | 0.15 | 0.09 | 0.09 | 0.06 | 0.15 | 0.11 | 0.10 | 0.11 | 0.11 | 0.10 | 0.12 |
| TiO2 | 28.60 | 41.12 | 50.56 | 50.13 | 50.80 | 44.90 | 50.13 | 51.06 | 49.10 | 52.00 | 50.08 | 51.34 |
| Al2O3 | 8.29 | 7.79 | 0.03 | 0.02 | 0.05 | 1.13 | 0.03 | 0.01 | 0.03 | 0.03 | 0.10 | 0.03 |
| Cr2O3 | 19.54 | 5.57 | 0.03 | 0.02 | 0.02 | 0.02 | 0.03 | 0.02 | 0.01 | 0.02 | 0.04 | 0.01 |
| FeO | 37.77 | 41.11 | 46.54 | 48.79 | 48.37 | 51.73 | 48.64 | 47.78 | 48.11 | 45.96 | 48.17 | 46.68 |
| MnO | 1.83 | 1.48 | 1.77 | 1.10 | 0.93 | 1.30 | 1.33 | 1.33 | 1.27 | 0.91 | 0.81 | 1.28 |
| MgO | 3.88 | 2.71 | 0.19 | 0.19 | 0.23 | 0.24 | 0.16 | 0.15 | 0.18 | 0.29 | 0.34 | 0.13 |
| CaO | 0.22 | 0.13 | 0.01 | 0.01 | 0.00 | 0.02 | 0.01 | 0.02 | 0.01 | 0.03 | 0.01 | 0.00 |
| Na2O | 0.00 | 0.00 | 0.01 | 0.00 | 0.02 | 0.01 | 0.01 | 0.01 | 0.00 | 0.01 | 0.00 | 0.00 |
| Total | 100.23 | 100.07 | 99.23 | 100.34 | 100.49 | 99.50 | 100.43 | 100.48 | 98.82 | 99.36 | 99.66 | 99.59 |
| o | | | | | | | | | | | | |
| SiO2 | 0.01 | 0.02 | - | - | - | 0.04 | - | 0.01 | 0.01 | 0.01 | 0.02 | 0.04 |
| TiO2 | 28.55 | 22.86 | - | - | - | 10.08 | - | 0.38 | 0.45 | 1.26 | 0.40 | 0.55 |
| Al2O3 | 9.58 | 17.39 | - | - | - | 1.85 | - | 0.01 | 0.02 | 0.02 | 0.10 | 0.04 |
| Cr2O3 | 22.31 | 12.32 | - | - | - | 0.04 | - | 0.02 | 0.01 | 0.02 | 0.00 | 0.02 |
| FeO | 6.64 | 11.30 | - | - | - | 7.30 | - | 0.30 | 0.59 | 1.38 | 0.32 | 0.91 |
| MnO | 1.59 | 0.67 | - | - | - | 0.12 | - | 0.13 | 0.05 | 0.02 | 0.03 | 0.16 |
| MgO | 3.88 | 5.72 | - | - | - | 0.02 | - | 0.05 | 0.09 | 0.13 | 0.09 | 0.05 |
| CaO | 0.43 | 0.11 | - | - | - | 0.02 | - | 0.03 | 0.00 | 0.02 | 0.01 | 0.00 |
| Na2O | 0.01 | 0.00 | - | - | - | 0.01 | - | 0.01 | 0.00 | 0.02 | 0.01 | 0.00 |
| Total | 1.37 | 0.63 | - | - | - | 0.36 | - | 0.23 | 0.18 | 0.25 | 0.58 | 0.25 |

**Tableau B-3f: Analyses en éléments en trace des clinopyroxenes
du Leg ODP 209 Puits 1275D***

| Echantillon | 15R1_120-124 | | 16R1_30-34 | | 19R1_50-54 | |
|----------------------|---------------------|----------|-------------------|----------|-------------------|----------|
| Type de roche | gabbro à oxyde | | gabbro à oxyde | | gabbro à oxyde | |
| n | 5 | σ | 4 | σ | 6 | σ |
| Ti | 3511 | 211 | 19217 | 9695 | - | - |
| Rb | 0.51 | 0.30 | 1.09 | 0.55 | 0.21 | 0.17 |
| Sr | 15.22 | 4.95 | 50.02 | 24.91 | 8.71 | 0.27 |
| Y | 50.75 | 1.84 | 82.32 | 23.21 | 94.25 | 5.63 |
| Zr | 30.33 | 1.98 | 138.43 | 55.36 | 60.64 | 8.23 |
| Nb | 0.02 | 0.01 | 2.09 | 2.34 | 0.05 | 0.03 |
| Cs | 0.05 | 0.03 | 0.05 | 0.06 | 0.08 | 0.10 |
| Ba | 1.15 | 0.26 | 18.15 | 13.25 | 0.74 | 0.87 |
| La | 1.008 | 0.029 | 5.910 | 4.290 | 3.643 | 0.227 |
| Ce | 5.248 | 0.093 | 21.173 | 15.353 | 15.988 | 1.017 |
| Pr | 1.238 | 0.030 | 3.576 | 2.143 | 3.313 | 0.250 |
| Nd | 8.814 | 0.199 | 20.378 | 9.231 | 21.380 | 1.486 |
| Sm | 4.354 | 0.109 | 7.840 | 2.400 | 8.908 | 0.597 |
| Eu | 0.945 | 0.039 | 2.218 | 0.868 | 1.626 | 0.074 |
| Gd | 6.934 | 0.201 | 10.673 | 2.398 | 13.130 | 0.846 |
| Tb | 1.275 | 0.022 | 1.986 | 0.509 | 2.398 | 0.167 |
| Dy | 9.426 | 0.190 | 15.045 | 3.978 | 17.625 | 1.340 |
| Ho | 2.003 | 0.036 | 3.260 | 0.897 | 3.758 | 0.273 |
| Er | 5.742 | 0.216 | 9.985 | 2.785 | 10.953 | 0.904 |
| Tm | 0.845 | 0.038 | 1.503 | 0.459 | 1.587 | 0.121 |
| Yb | 5.594 | 0.287 | 10.628 | 3.167 | 10.657 | 0.948 |
| Lu | 0.826 | 0.033 | 1.504 | 0.441 | 1.586 | 0.124 |
| Hf | 1.24 | 0.11 | 4.43 | 1.93 | 2.04 | 0.33 |
| Ta | 0.00 | 0.00 | 0.09 | 0.07 | 0.01 | 0.00 |
| Pb | 0.22 | 0.18 | 1.06 | 1.19 | 0.18 | 0.09 |
| Th | 0.02 | 0.01 | 0.05 | 0.02 | 0.12 | 0.06 |
| U | 0.30 | 0.09 | 0.10 | 0.02 | 0.08 | 0.06 |

*Analyses en éléments en trace (ppm) par LA-ICP-MS. Abbreviation:

n= nombre d'analyses par mineral; σ = écart type.

**Tableau B-3g: Analyses en éléments en trace des plagioclases
du Leg ODP 209 Puits 1275D***

| Echantillon | 15R1_120-124 | | 16R1_30-34 | | 19R1_50-54 | |
|----------------------|---------------------|----------------------------|-------------------|----------------------------|-------------------|----------------------------|
| Type de roche | gabbro à oxyde | | gabbro à oxyde | | gabbro à oxyde | |
| <i>n</i> | <i>12</i> | σ | <i>11</i> | σ | <i>12</i> | σ |
| Ti | 499 | 116 | 613 | 100 | 4711 | 1480 |
| Rb | 0.42 | 0.26 | 0.24 | 0.09 | 30.48 | 41.87 |
| Y | 0.25 | 0.04 | 0.22 | 0.04 | 4.85 | 1.29 |
| Zr | 1.36 | 1.72 | 0.72 | 0.98 | 6.45 | 11.50 |
| Nb | 0.02 | 0.02 | 0.01 | 0.01 | 0.12 | 0.11 |
| Cs | 0.14 | 0.15 | 0.01 | 0.01 | 0.33 | 0.39 |
| Ba | 37.69 | 1.24 | 35.81 | 11.01 | 721.57 | 368.03 |
| La | 0.868 | 0.176 | 0.497 | 0.099 | 21.287 | 19.537 |
| Ce | 1.743 | 0.215 | 1.019 | 0.237 | 33.713 | 25.336 |
| Pr | 0.205 | 0.041 | 0.126 | 0.028 | 3.656 | 2.498 |
| Nd | 0.739 | 0.059 | 0.541 | 0.098 | 15.130 | 9.225 |
| Sm | 0.140 | 0.047 | 0.160 | 0.182 | 2.628 | 1.212 |
| Eu | 1.685 | 0.067 | 1.518 | 0.307 | 32.623 | 8.770 |
| Gd | 0.107 | 0.020 | 0.075 | 0.015 | 1.860 | 0.751 |
| Tb | 0.011 | 0.003 | 0.011 | 0.003 | 0.223 | 0.075 |
| Dy | 0.059 | 0.015 | 0.052 | 0.014 | 1.102 | 0.369 |
| Ho | 0.009 | 0.003 | 0.009 | 0.002 | 0.187 | 0.065 |
| Er | 0.025 | 0.010 | 0.018 | 0.005 | 0.388 | 0.144 |
| Tm | 0.003 | 0.001 | 0.003 | 0.001 | 0.042 | 0.013 |
| Yb | 0.025 | 0.010 | 0.021 | 0.004 | 0.268 | 0.084 |
| Lu | 0.003 | 0.000 | 0.004 | 0.001 | 0.044 | 0.012 |
| Hf | 0.06 | 0.07 | 0.03 | 0.01 | 0.27 | 0.15 |
| Ta | 0.00 | 0.00 | 0.00 | 0.00 | 0.04 | 0.01 |
| Pb | 0.71 | 0.73 | 0.43 | 0.21 | 9.37 | 5.51 |
| Th | 0.02 | 0.03 | 0.02 | 0.01 | 0.16 | 0.08 |
| U | 0.11 | 0.15 | 0.08 | 0.11 | 0.82 | 1.34 |

*Analyses en éléments en trace (ppm) par LA-ICP-MS. Abbréviation:

n= nombre d'analyses par mineral; σ = écart type.

ANNEXE C

Données microstructurales

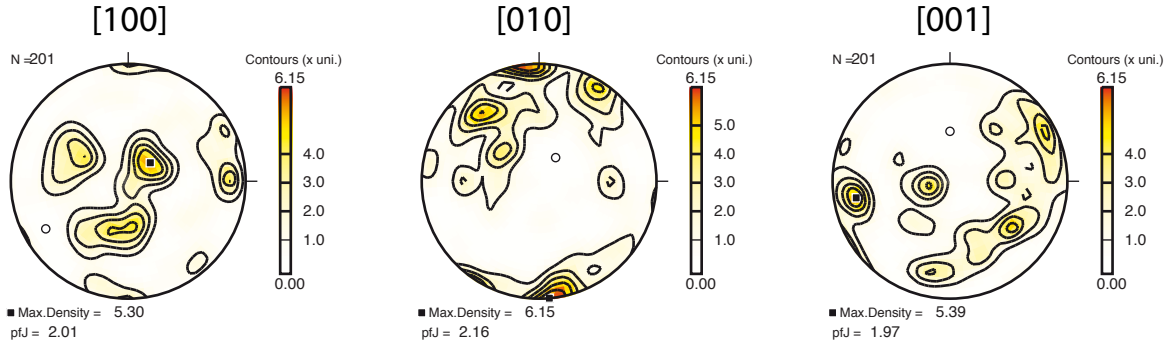
Dans cette annexe sont reportées, sous forme de planche graphique, pour chaque échantillon du puits U1309D analysé à l'EBSD: les figures de pôle des orientations préférentielles de réseau, la distribution des angles de misorientations sous forme d'histogramme, les figures de pôles inverses des axes de rotation pour les angles de faible misorientation (2-15°) pour les cristaux d'olivine ; les images de la texture de chaque échantillon avec les différentes orientations des angles d'Euler (associées à une couleur) pour chaque phase analysée à l'EBSD.

60R3_39-42

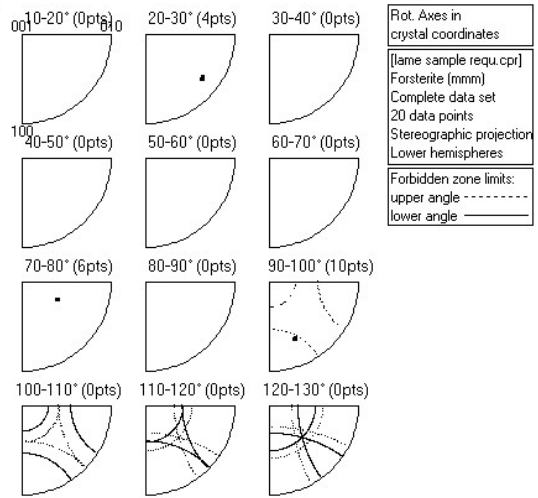
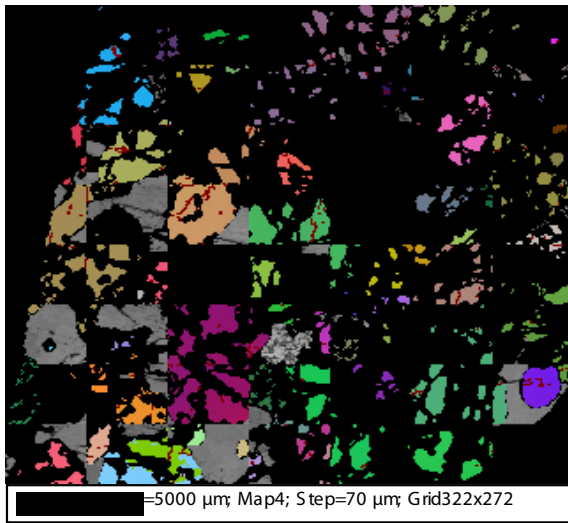
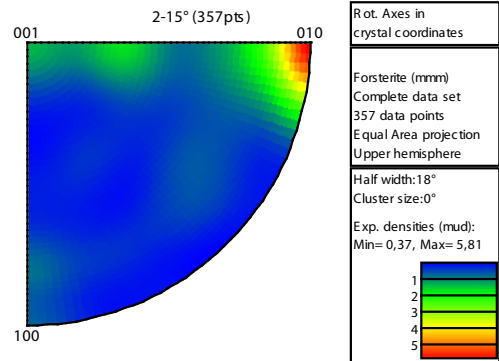
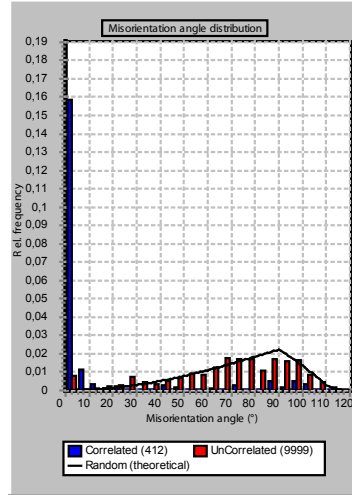
Troctolite riche en olivine

70% Ol 13% Pl 16% Cpx

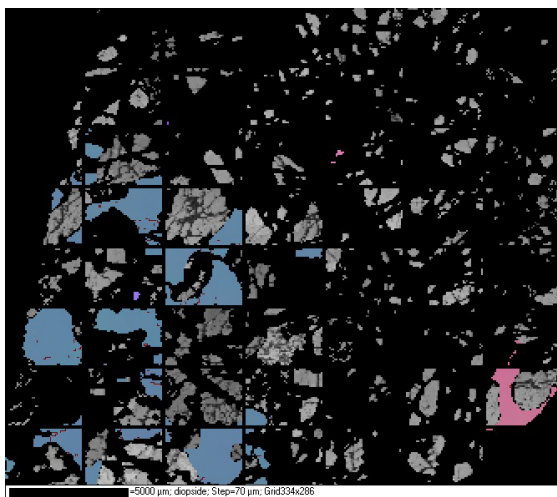
Olivine



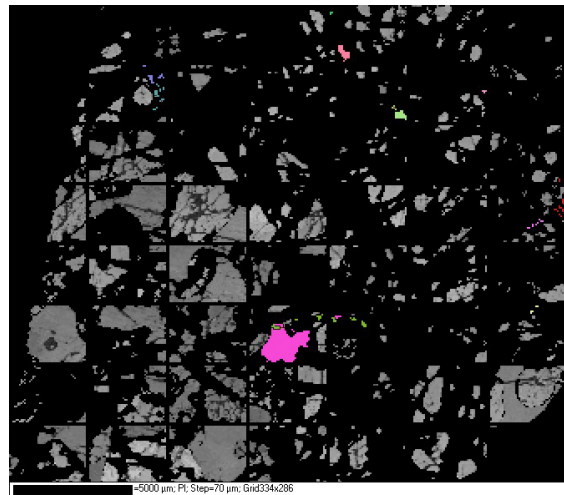
Olivine misorientation



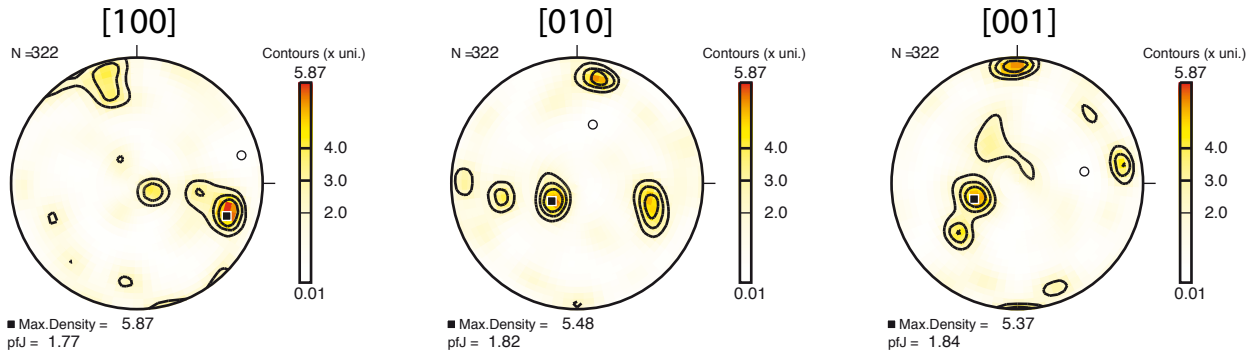
Clinopyroxene



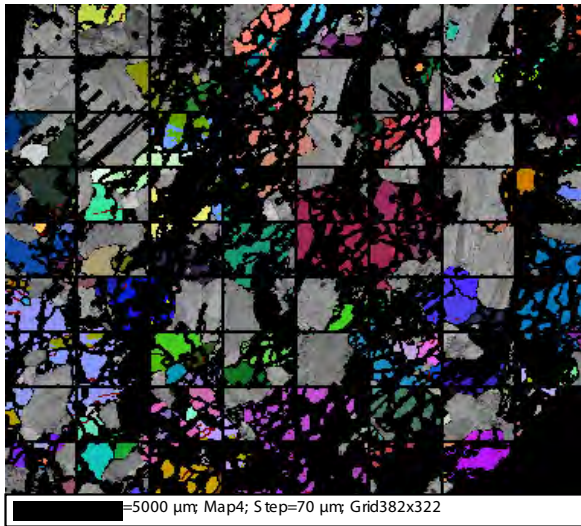
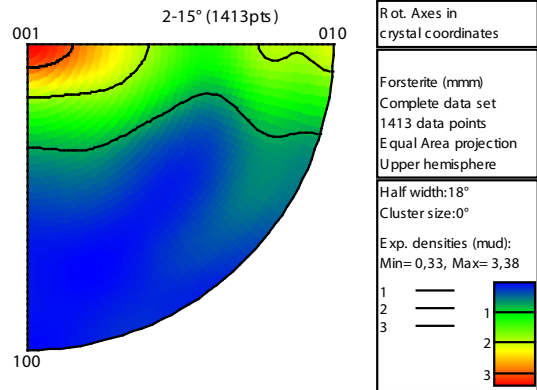
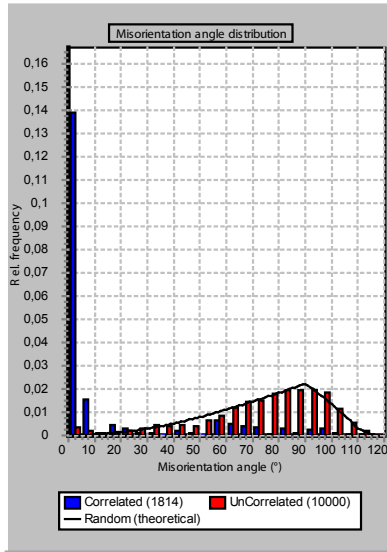
Plagioclase



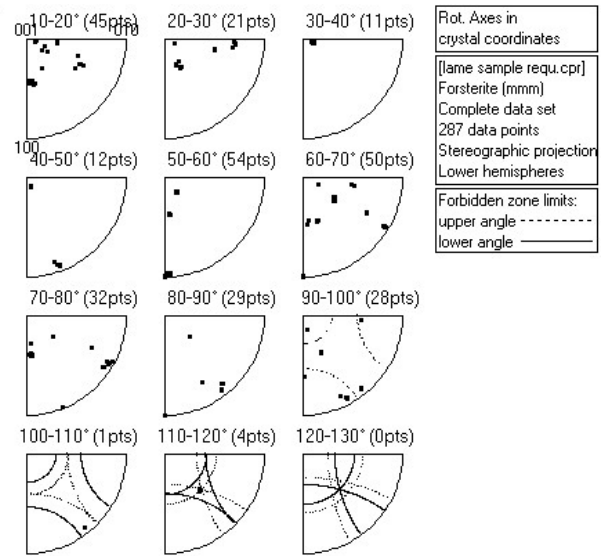
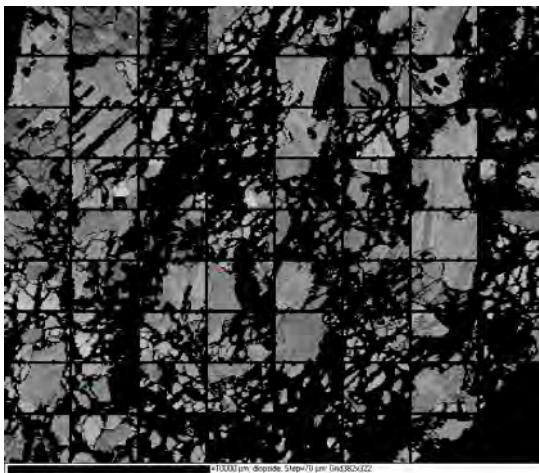
Troctolite 70R2_99-103 58% ol 40% Pl 2% Cpx



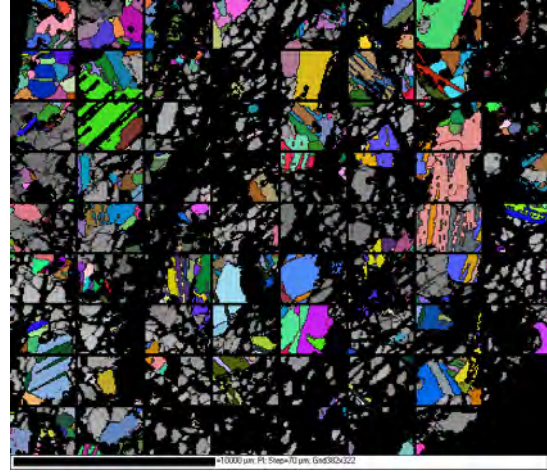
Olivine misorientation



Clinopyroxene



Plagioclase

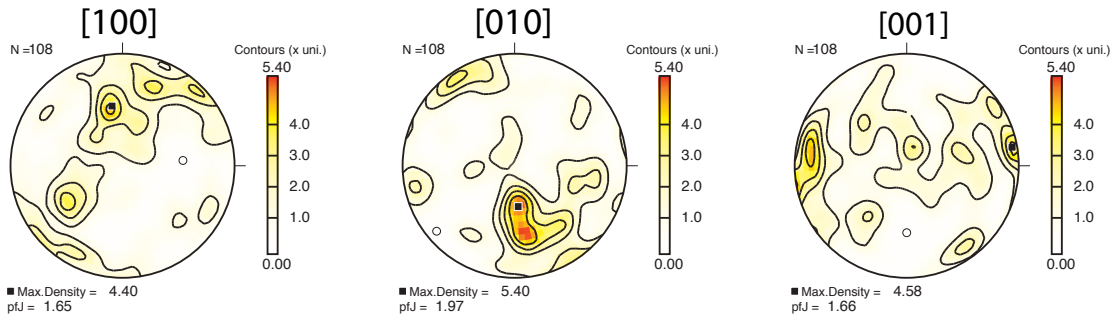


89R1_92-94

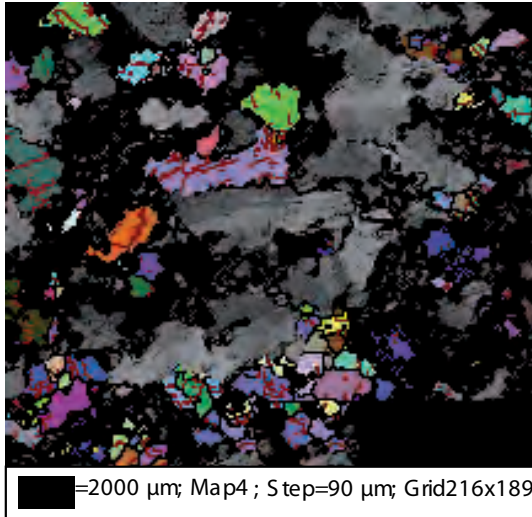
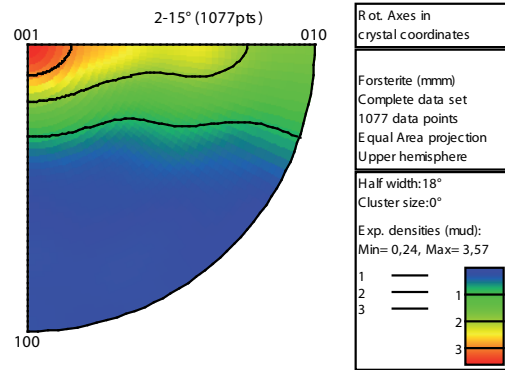
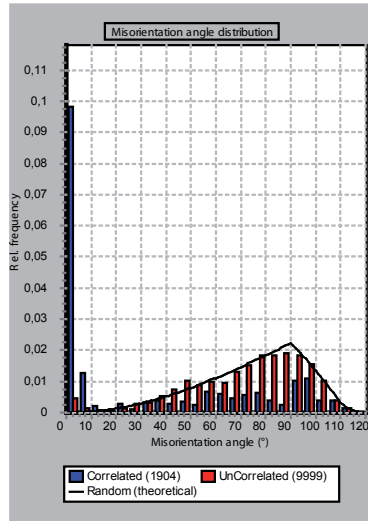
Olivine-gabbro

27% Ol 38% Pl 35% Cpx

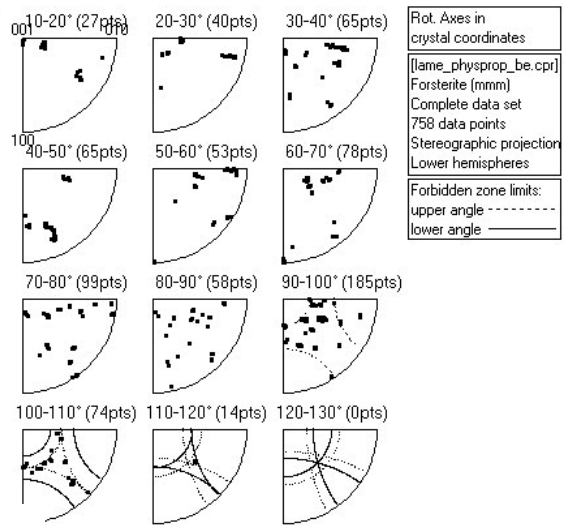
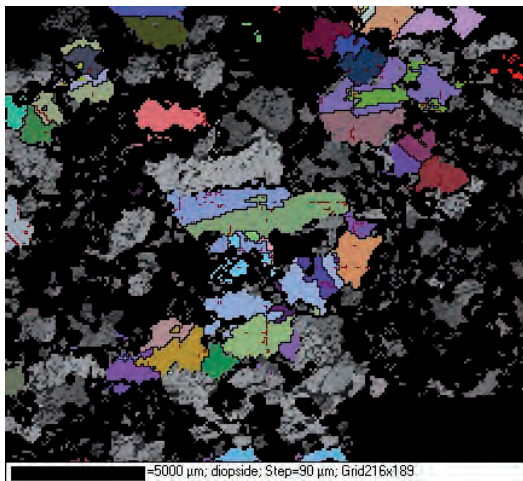
Olivine



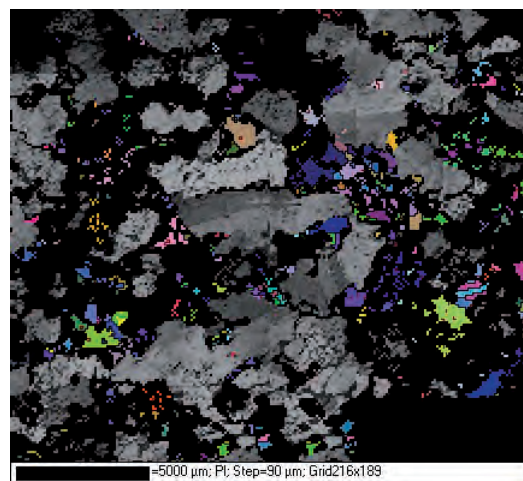
Olivine
misorientation



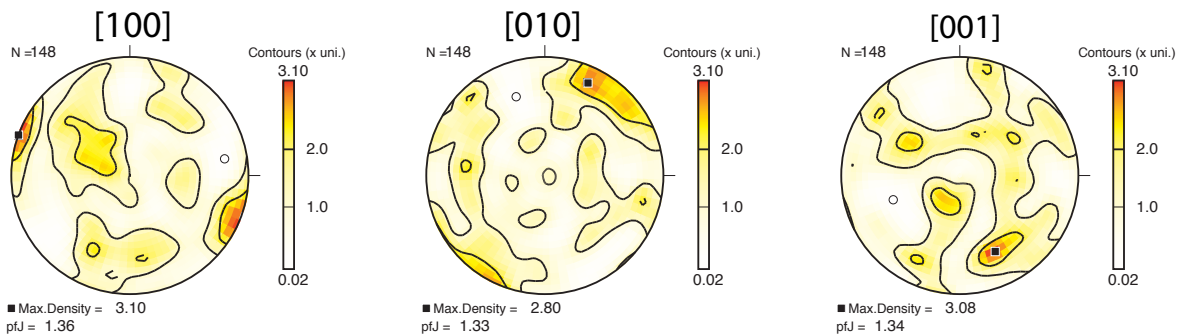
Clinopyroxene



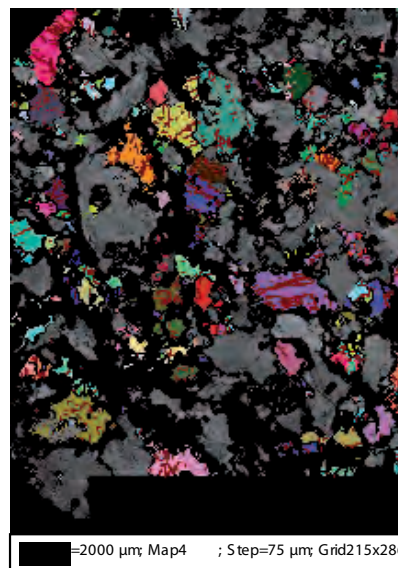
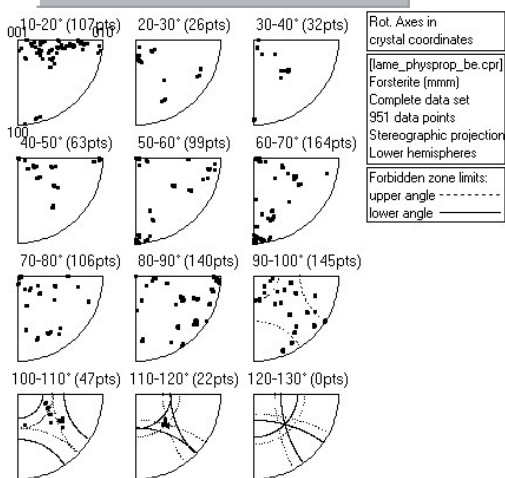
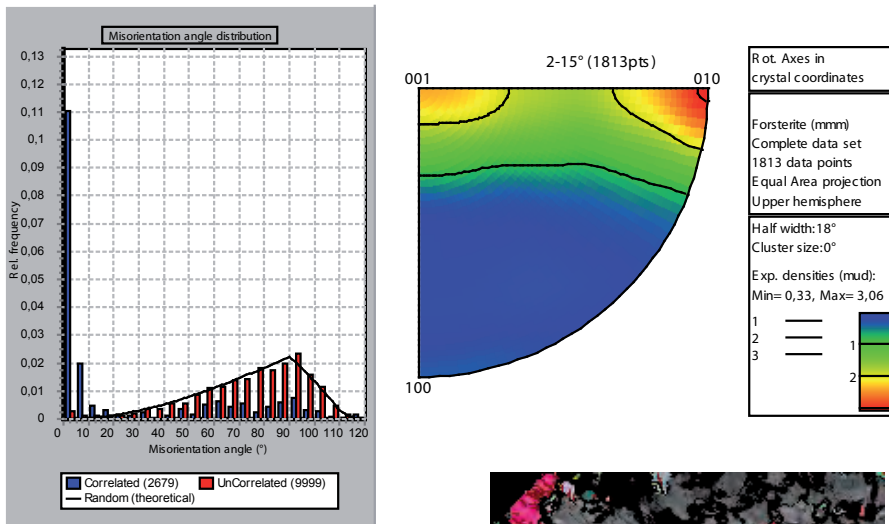
Plagioclase



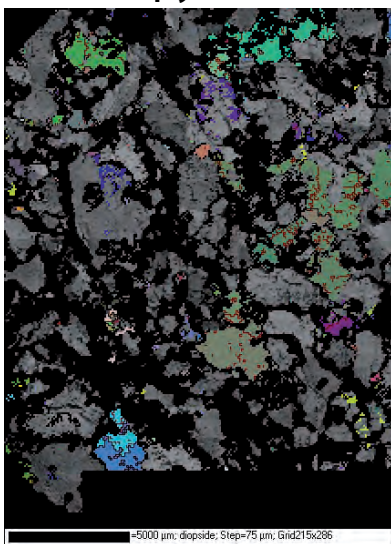
Troctolite 90R3_8-10 Olivine 56% Ol 42% Pl 2% Cpx



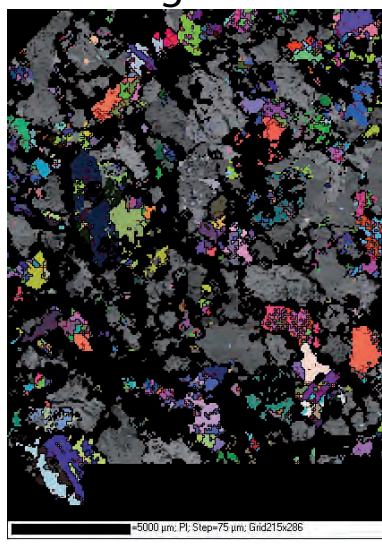
Olivine misorientation



Clinopyroxene



Plagioclase

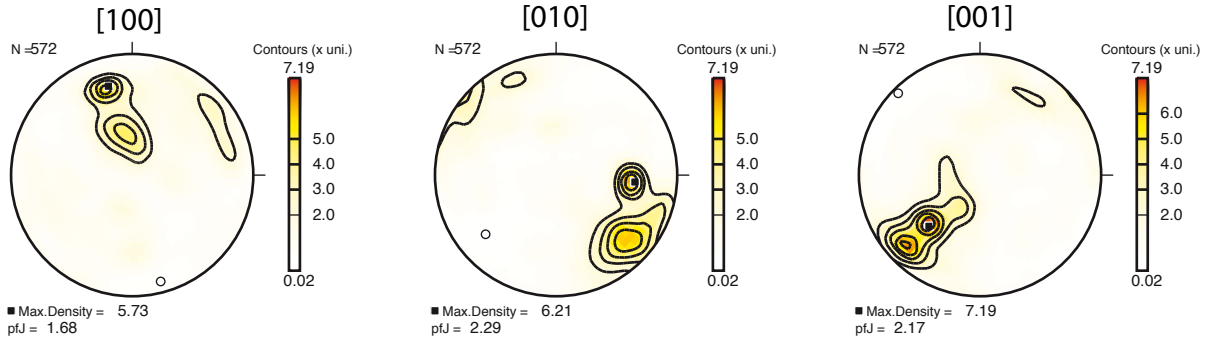


112R1_69-73

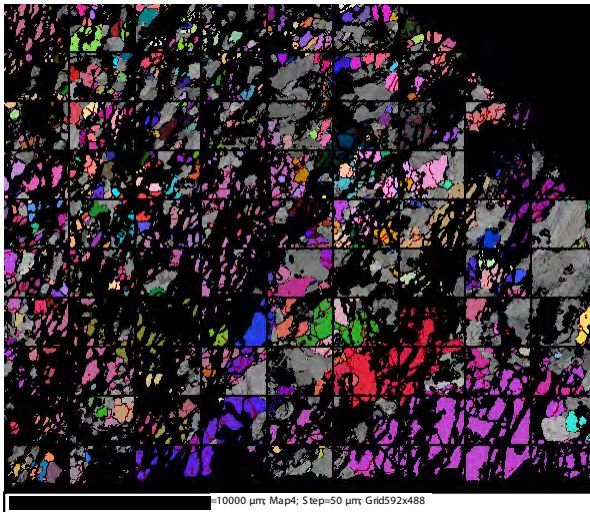
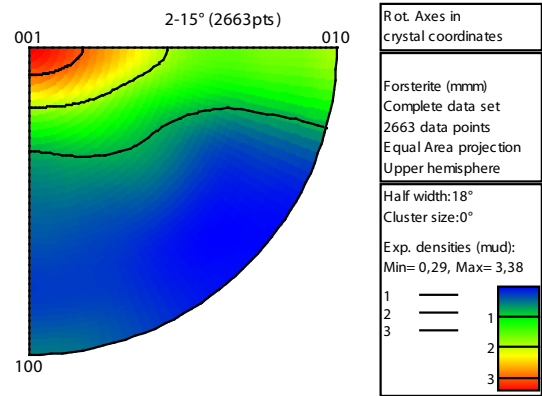
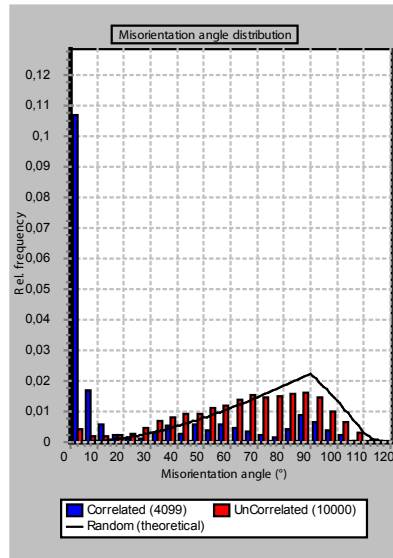
Troctolite riche en olivine

78% Ol 20% Pl 2% Cpx

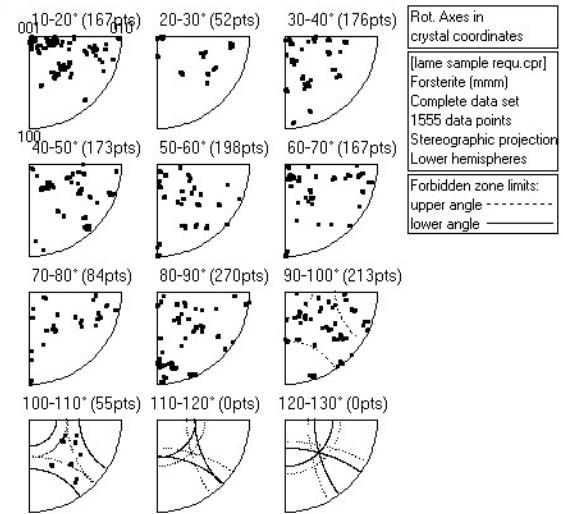
Olivine



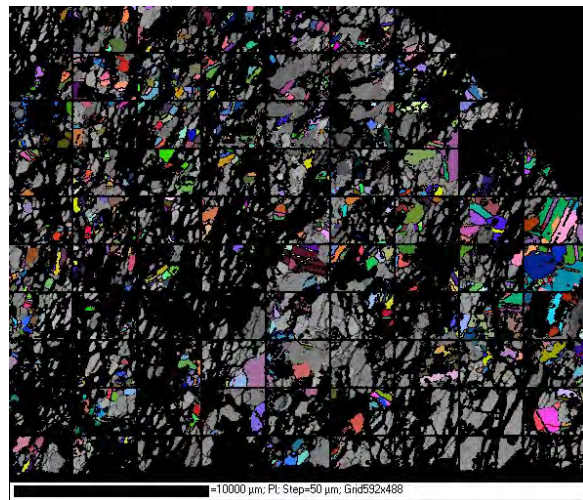
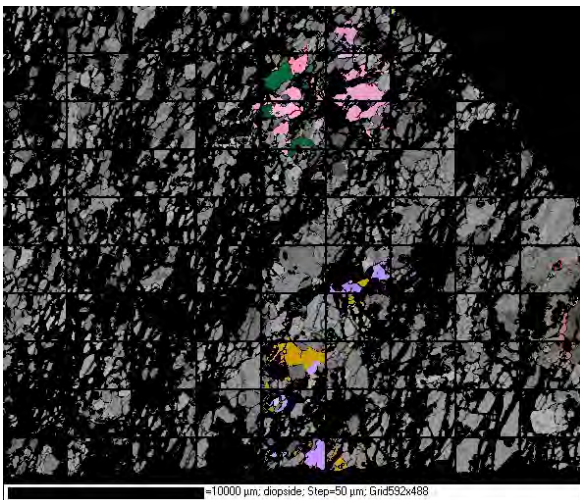
Olivine misorientation



Clinopyroxene



Plagioclase

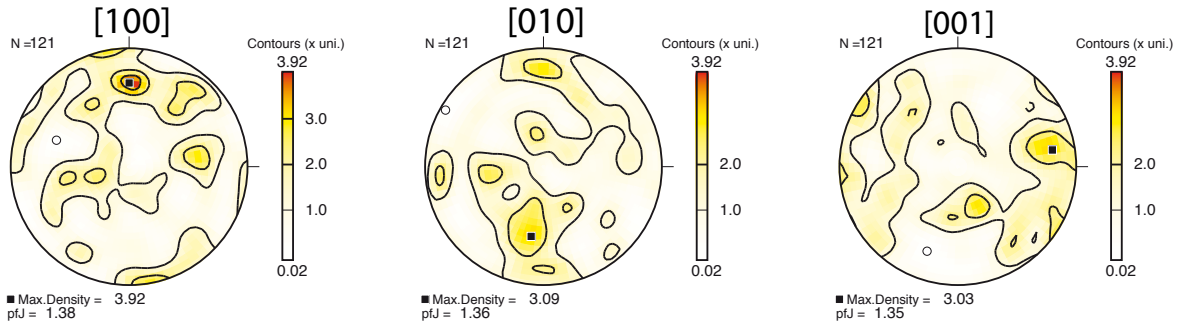


117R1_55-57

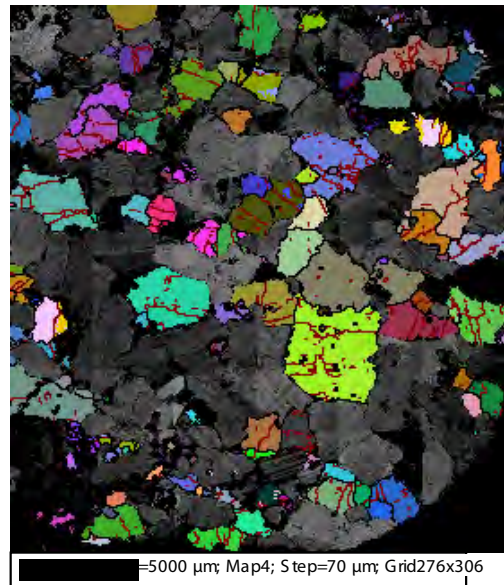
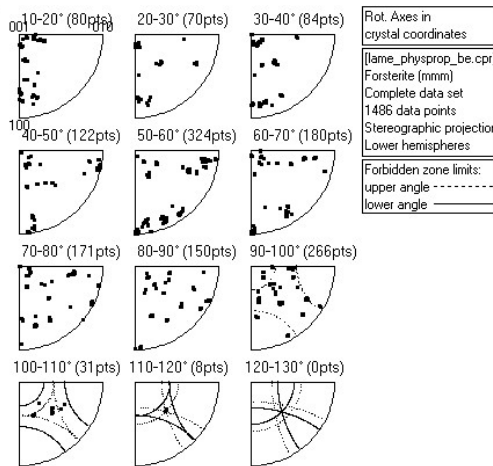
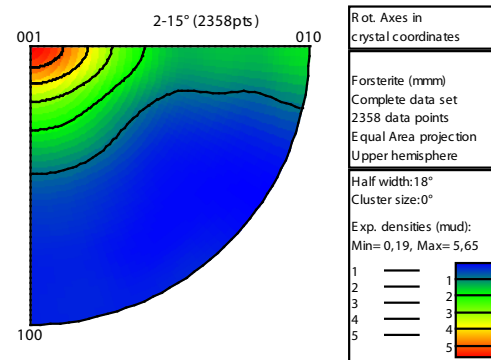
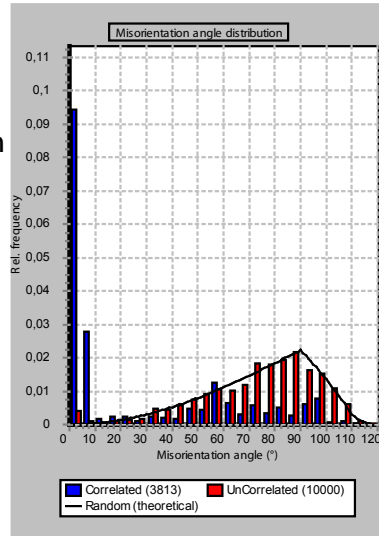
olivine-gabbro

26% Ol 40% Pl 34% Cpx

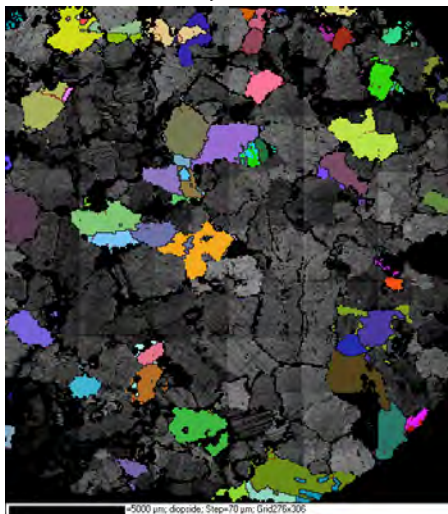
Olivine



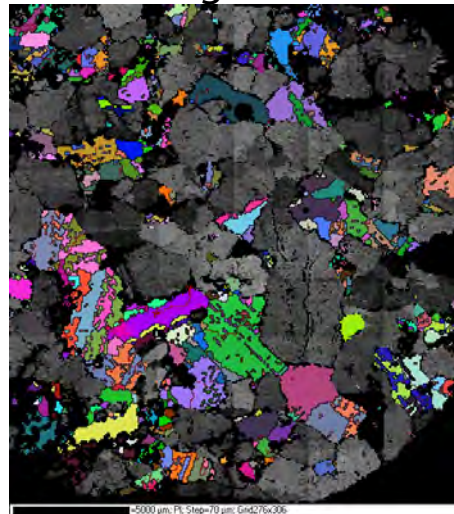
Olivine misorientation



Clinopyroxene



Plagioclase

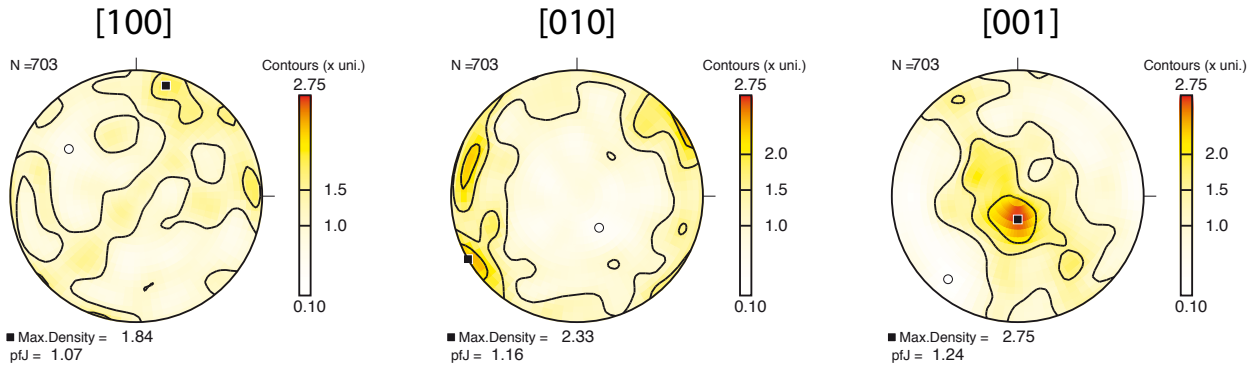


227R3_121-124

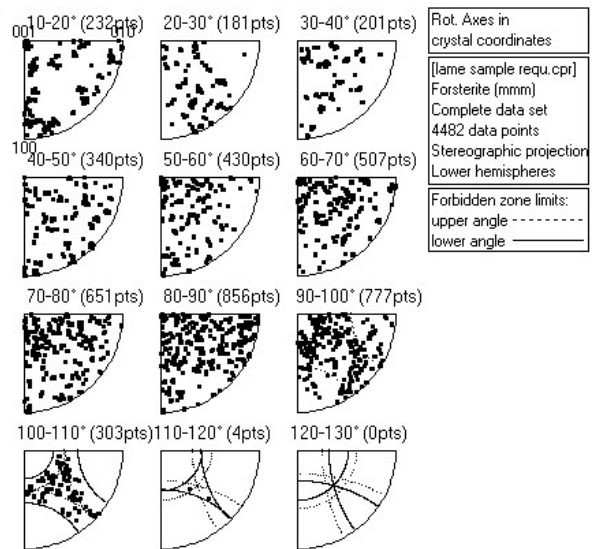
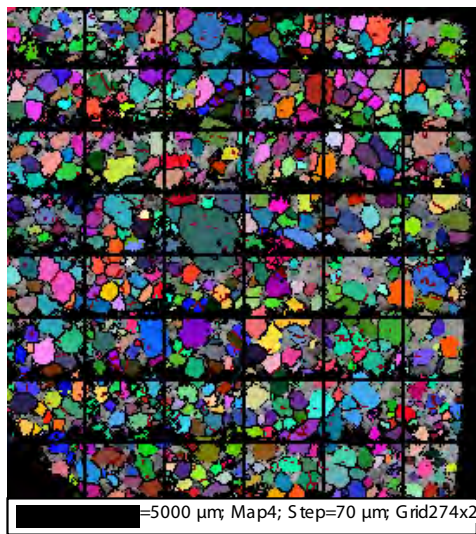
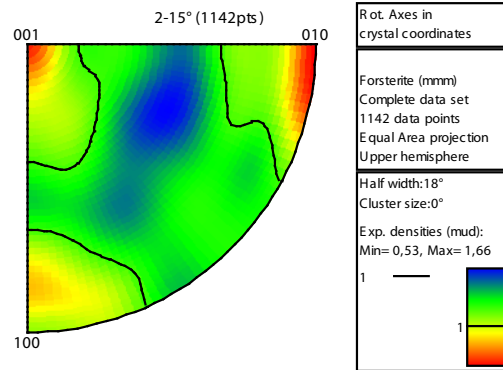
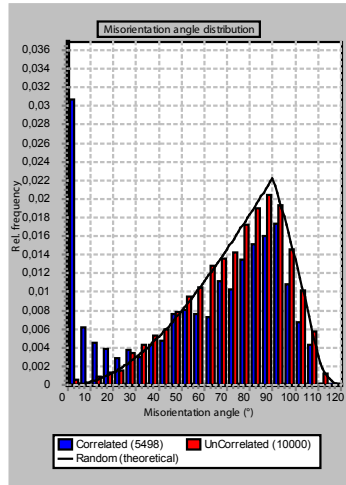
Troctolite riche en olivine

73% Ol 13% Pl 14% Cpx

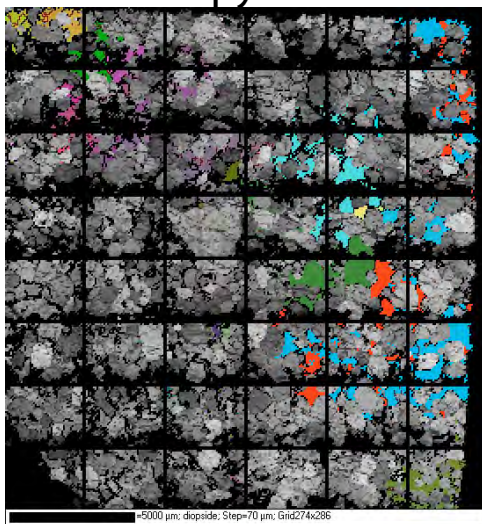
Olivine



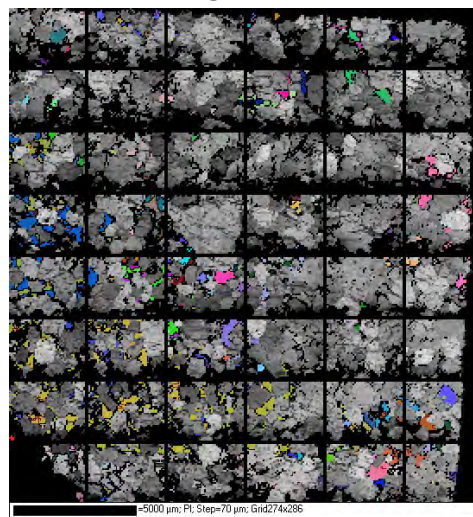
Olivine misorientation



Clinopyroxene

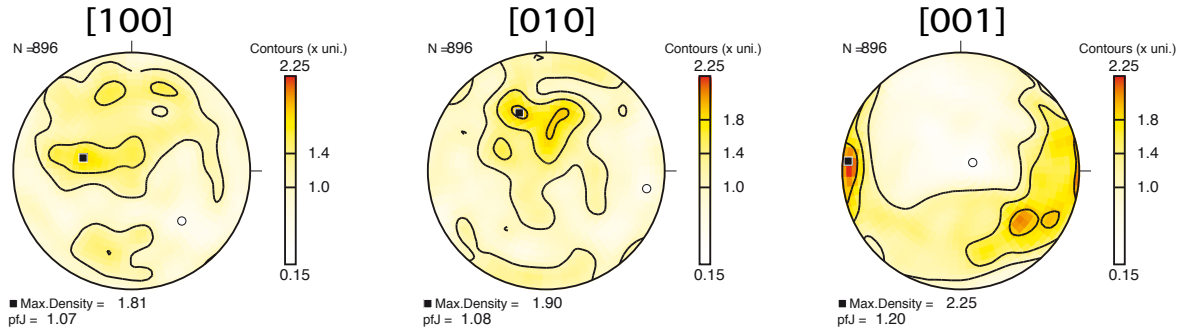


Plagioclase

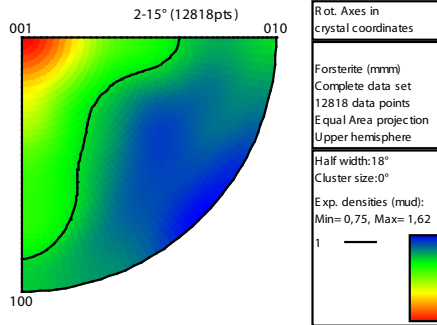
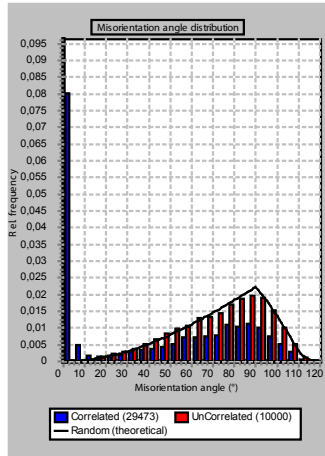


227R3_124-126

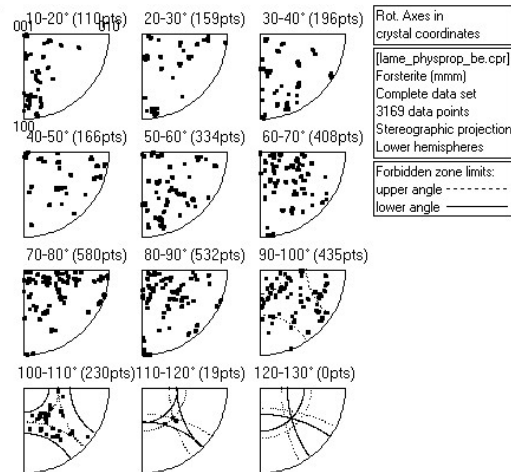
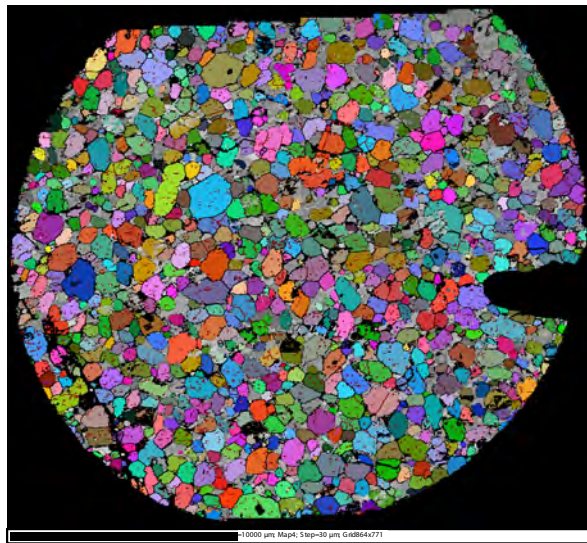
Troctolite riche en olivine Olivine 85% Ol 12% Pl 3% Cpx



Olivine misorientation

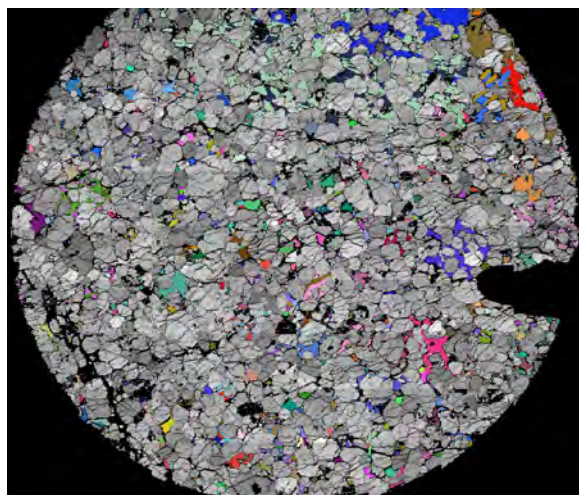
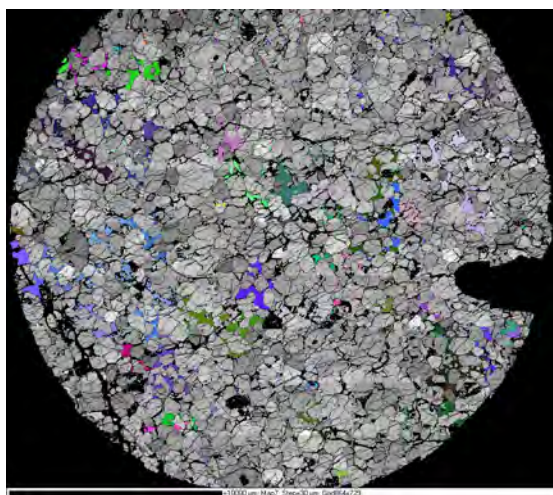


| |
|----------------------------------|
| Rot. Axes in crystal coordinates |
| Forsterite (mmm) |
| Complete data set |
| 12818 data points |
| Equal Area projection |
| Upper hemisphere |
| Half width: 18° |
| Cluster size: 0° |
| Exp. densities (mud): |
| Min = 0,75, Max = 1,62 |
| 1 |



Clinopyroxene

Plagioclase

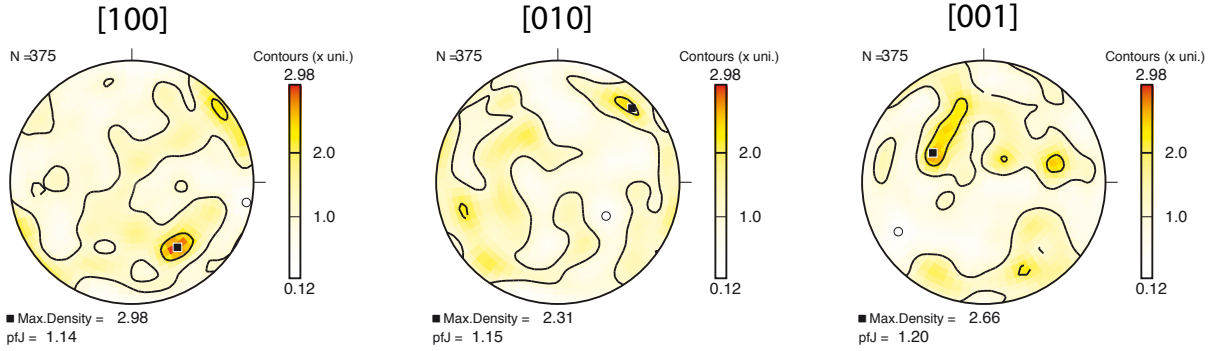


232R1_112-116

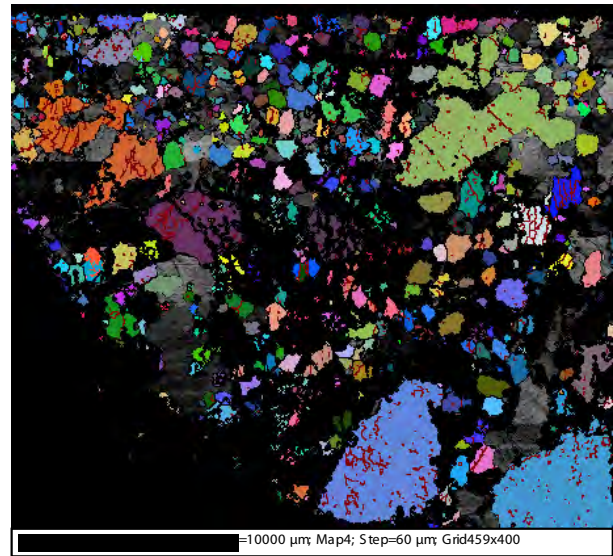
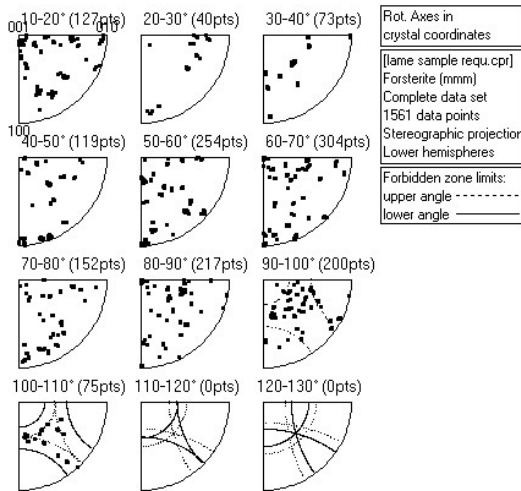
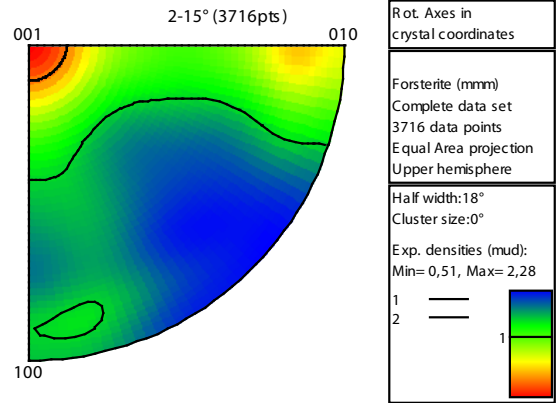
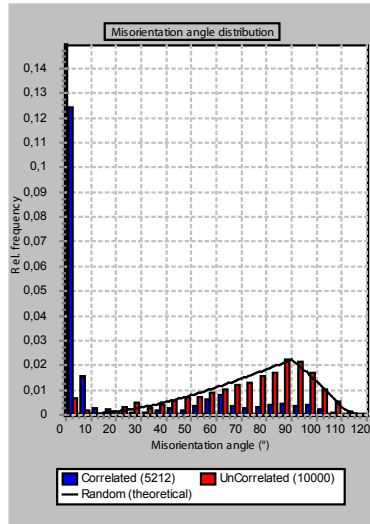
Troctolite

59% Ol 37% Pl 4% Cpx

Olivine

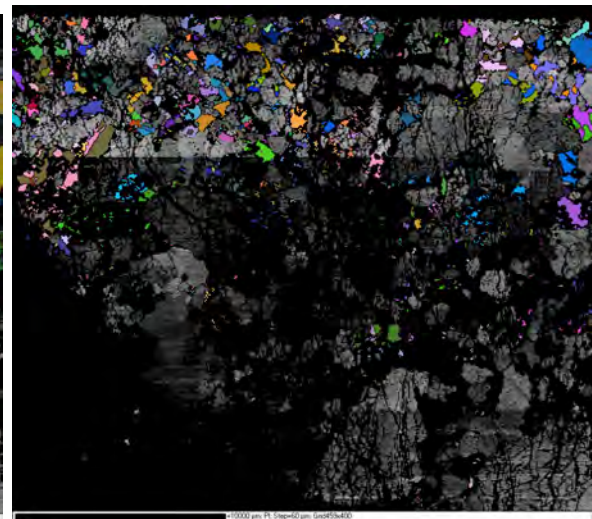
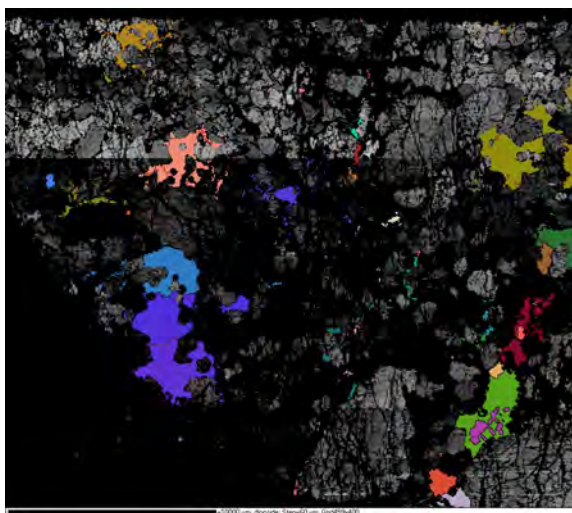


Olivine misorientation



Clinopyroxene

Plagioclase

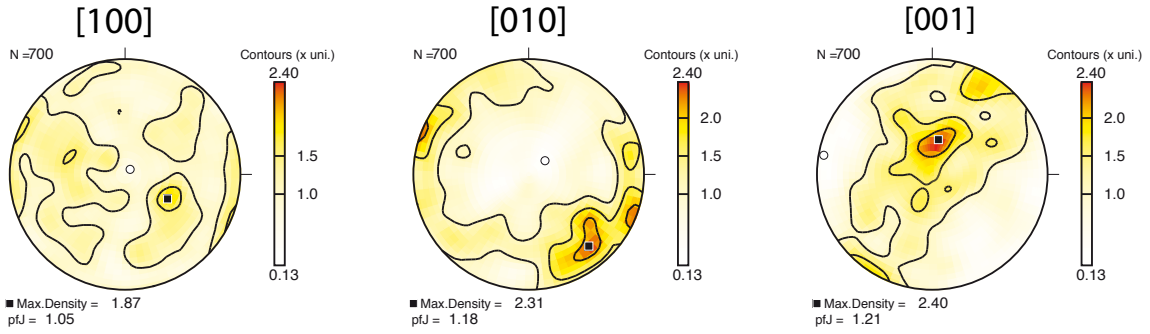


233R3_21-24

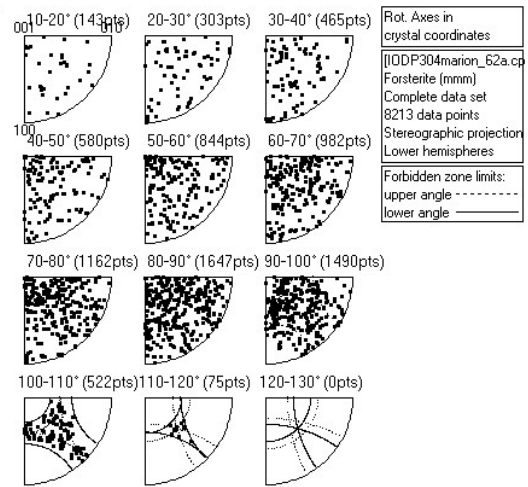
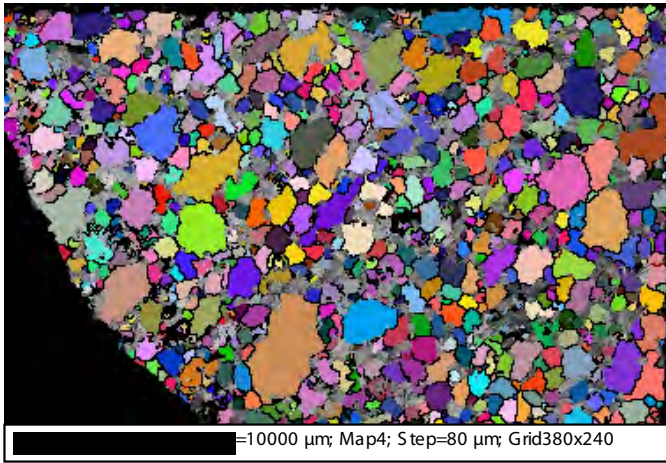
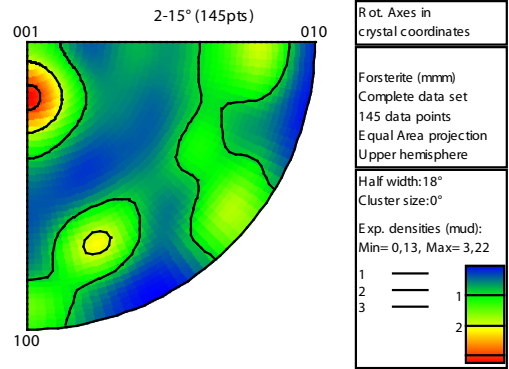
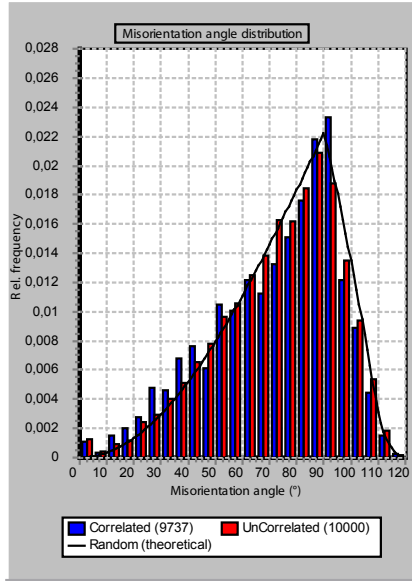
Troctolite riche en olivine

82% Ol 15% Pl 3% Cpx

Olivine

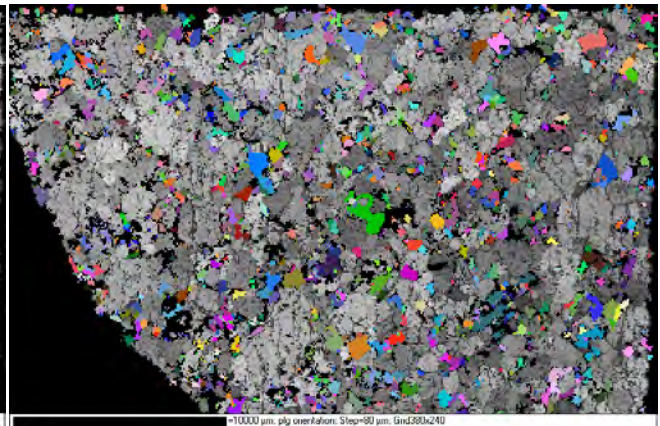
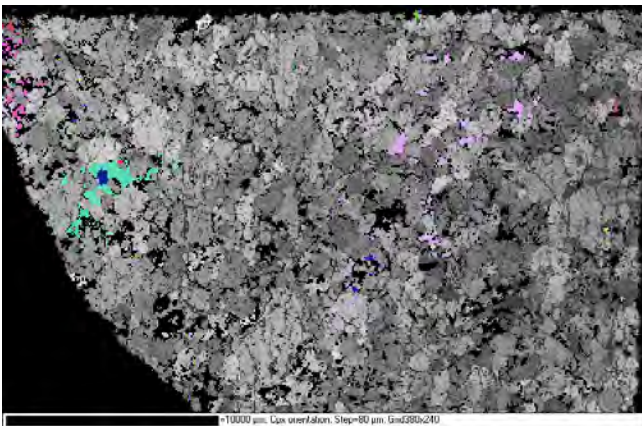


Olivine misorientation



Clinopyroxene

Plagioclase

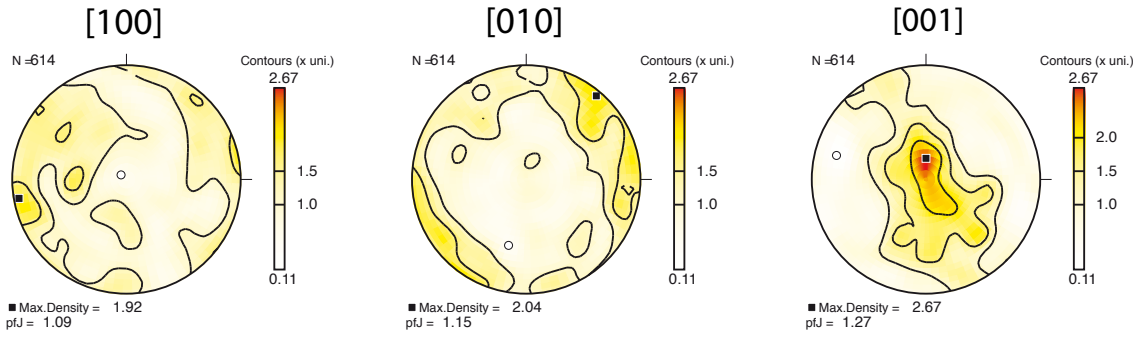


234R1_22-26

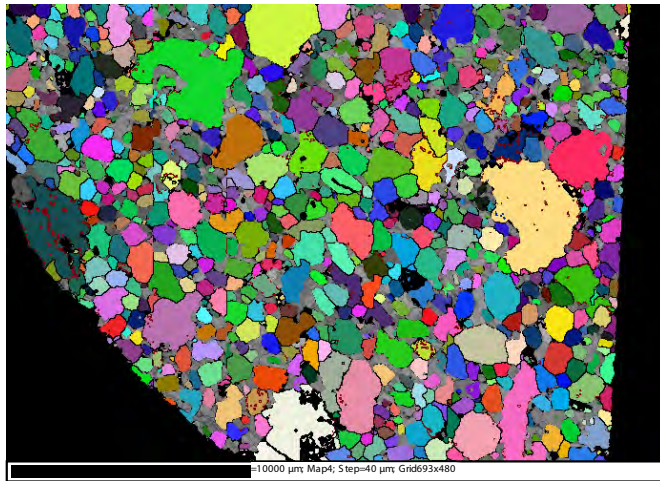
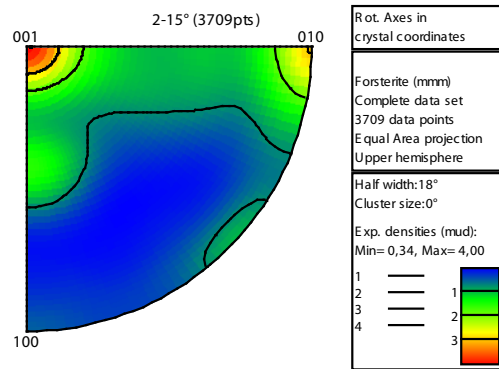
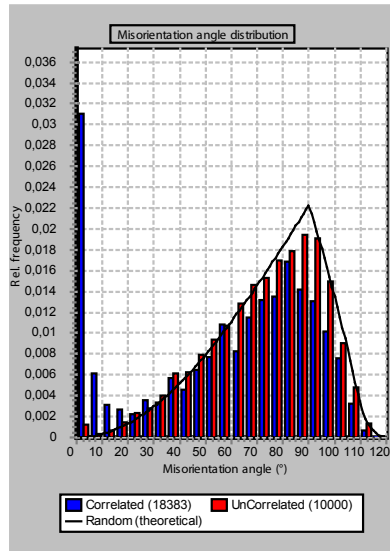
Troctolite riche en olivine

82% Ol 15% Pl 3% Cpx

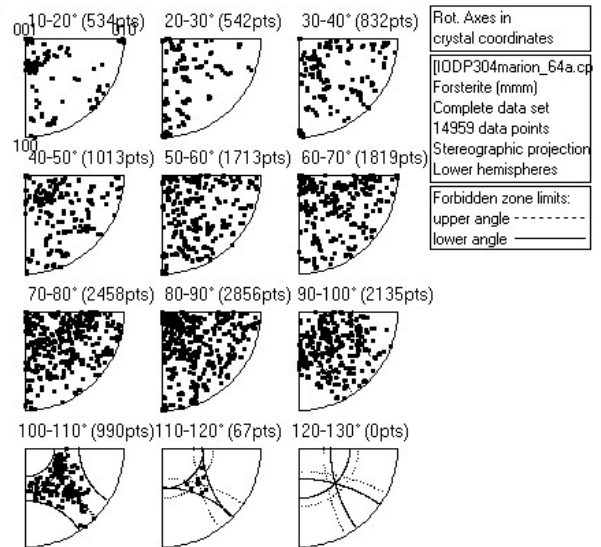
Olivine



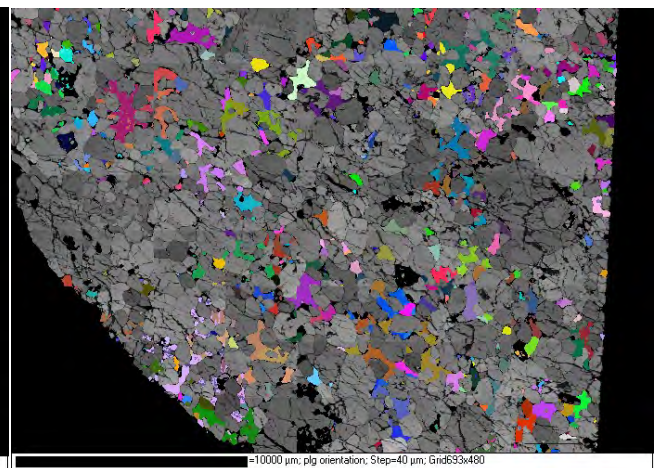
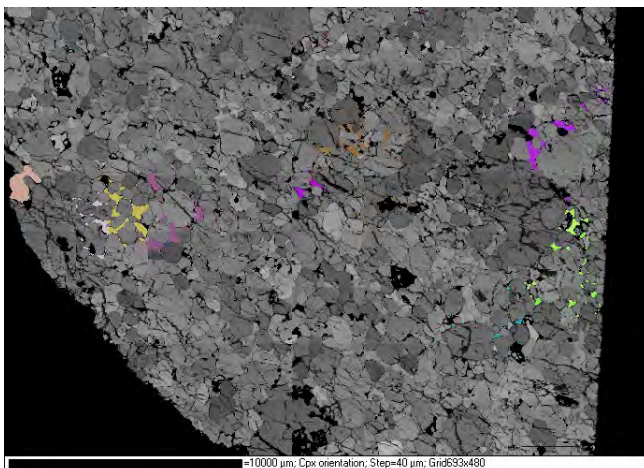
Olivine misorientation



Clinopyroxene



Plagioclase

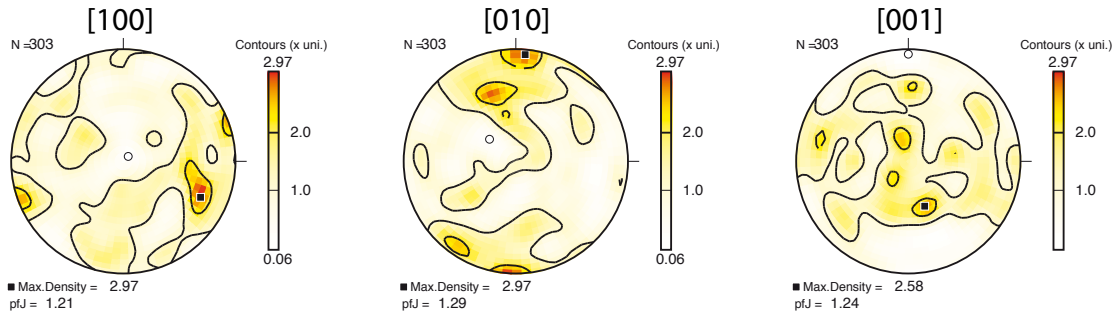


234R1_27-29

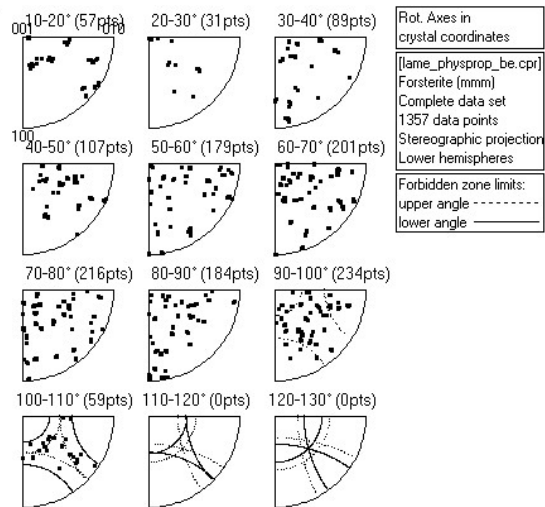
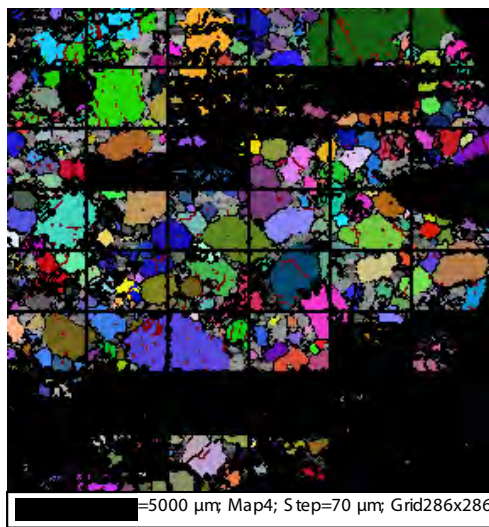
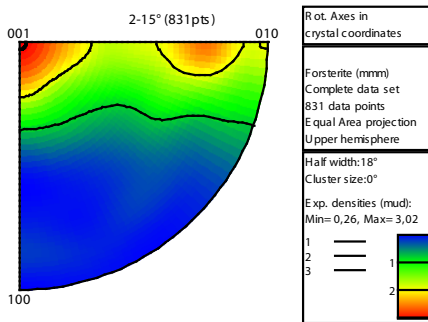
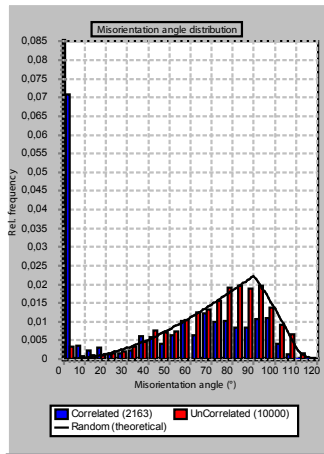
Troctolite riche en olivine

80% Ol 15% Pl 5% Cpx

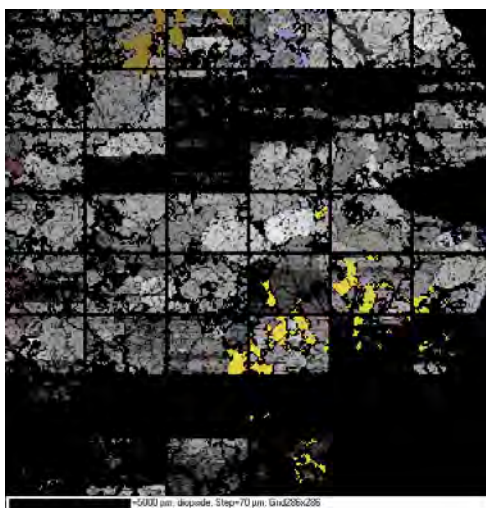
Olivine



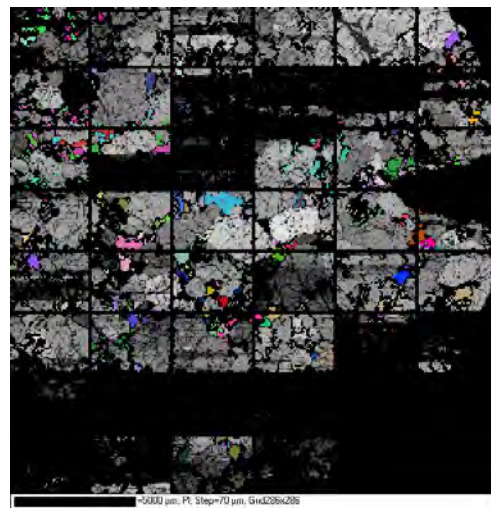
Olivine misorientation



Clinopyroxene



Plagioclase

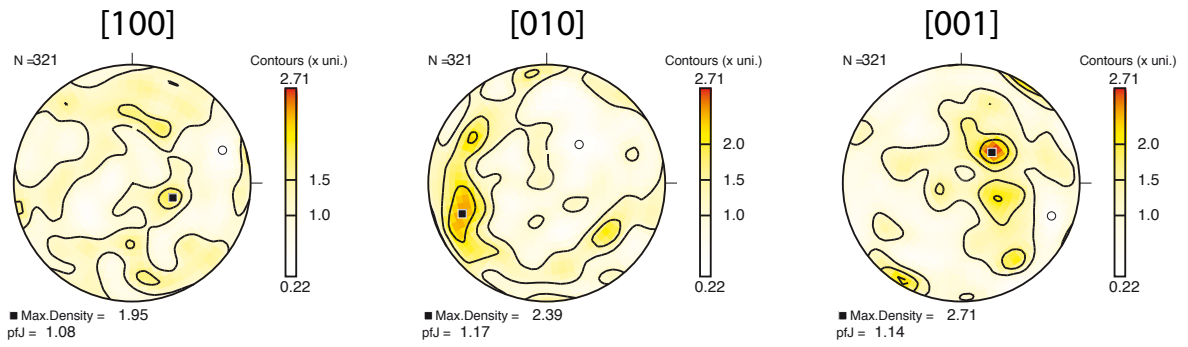


234R3_14-18

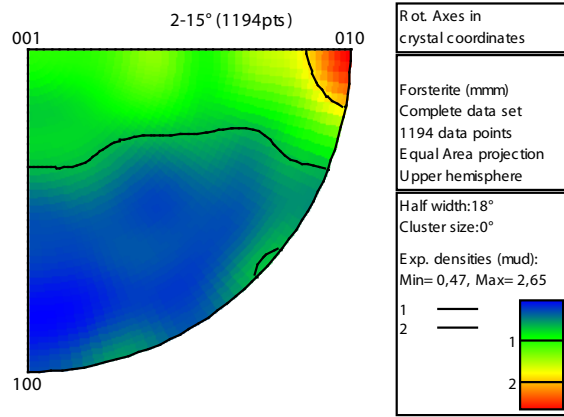
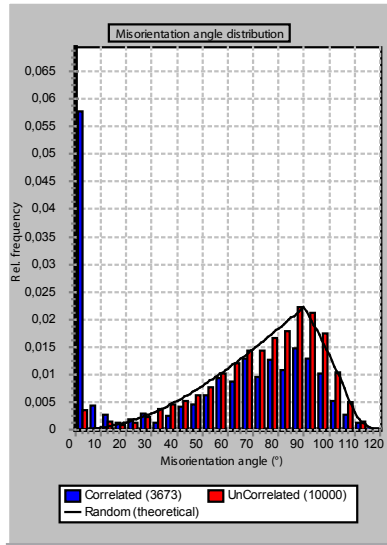
Troctolite riche en olivine

83% Ol 12% Pl 5% Cpx

Olivine



Olivine misorientation



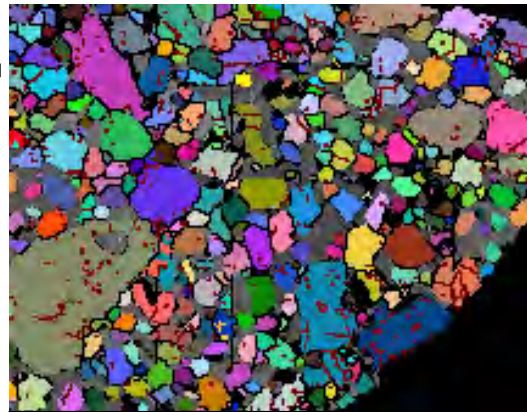
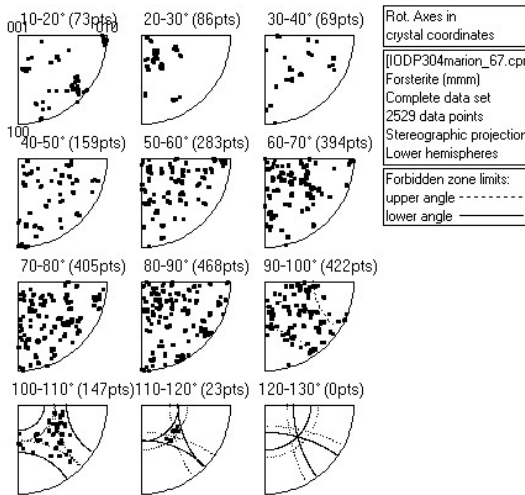
Rot. Axes in crystal coordinates

Forsterite (mmm)
Complete data set
1194 data points
Equal Area projection
Upper hemisphere

Half width: 18°
Cluster size: 0°

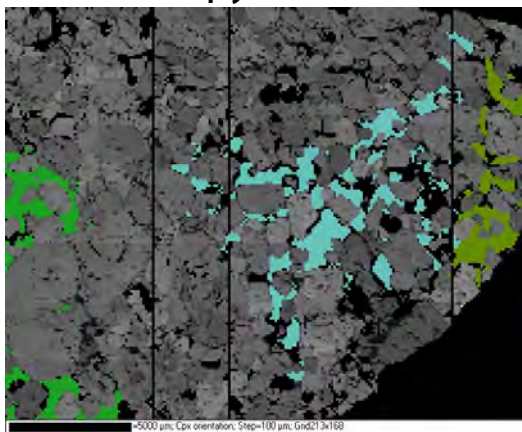
Exp. densities (mud):
Min= 0,47, Max= 2,65

1 ——— 1
2 ——— 2

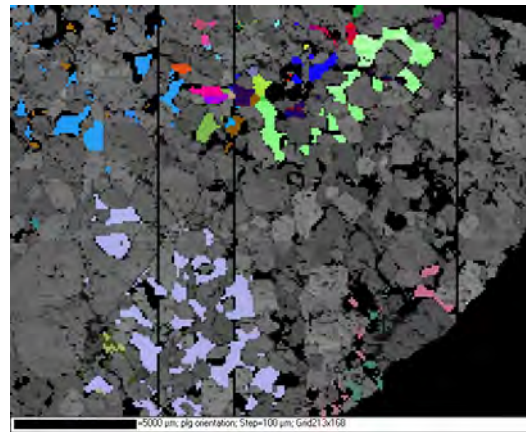


2000 μm; Map4; Step=100 μm; Grid213x168

Clinopyroxene



Plagioclase

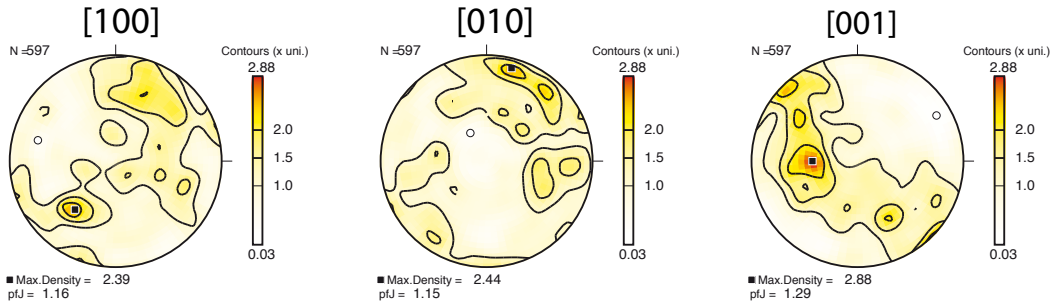


235R2_85-89

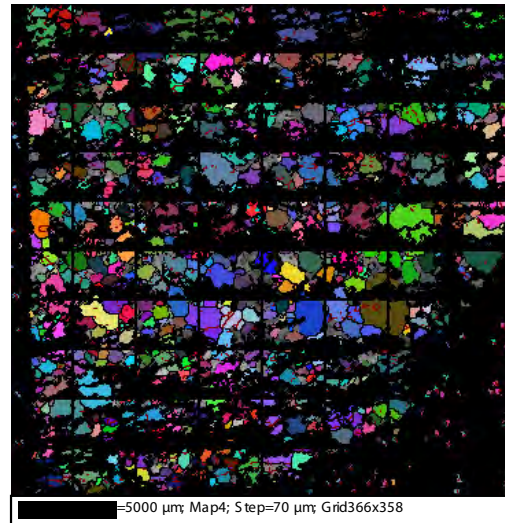
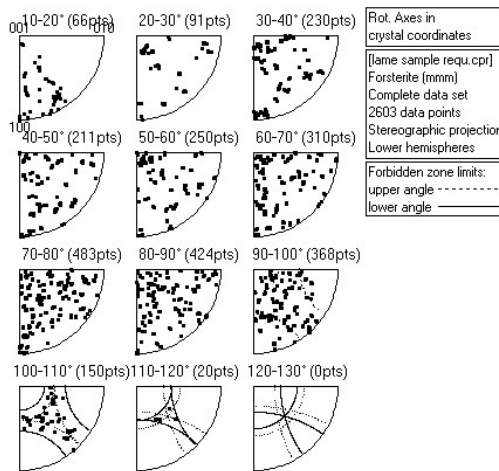
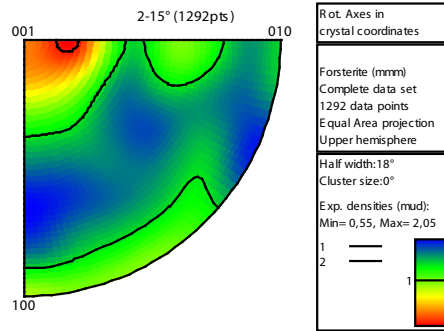
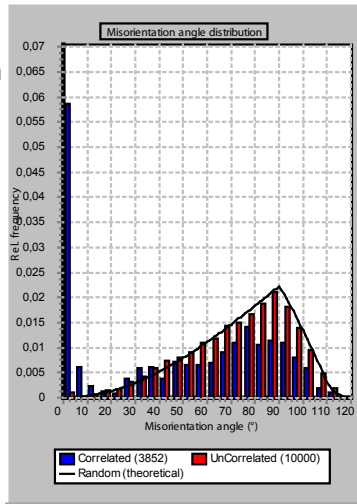
Troctolite riche en olivine

83% Ol 11% Pl 6% Cpx

Olivine

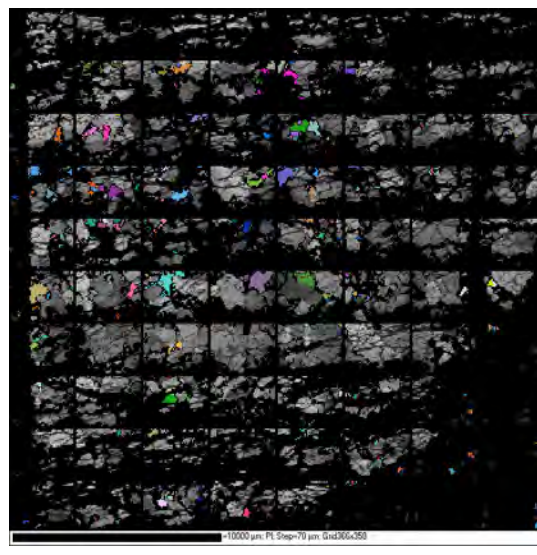
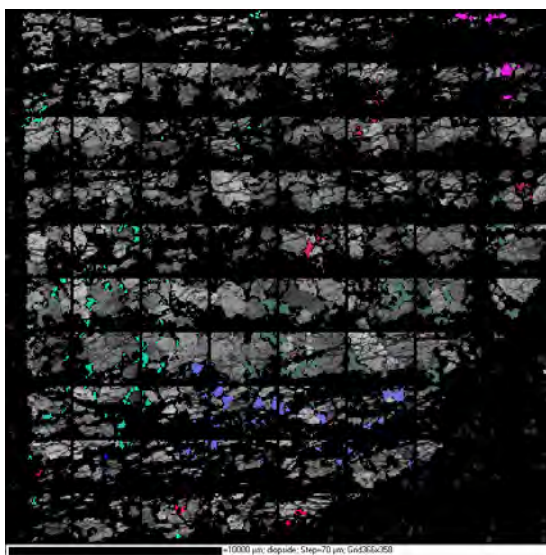


Olivine misorientation



Clinopyroxene

Plagioclase

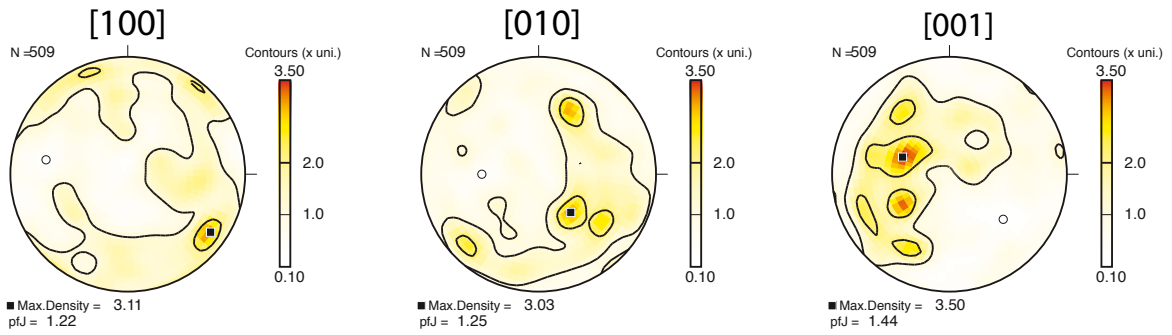


237R2_40-43

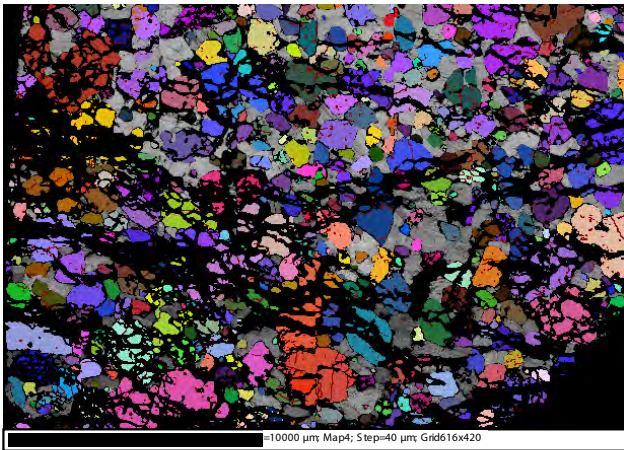
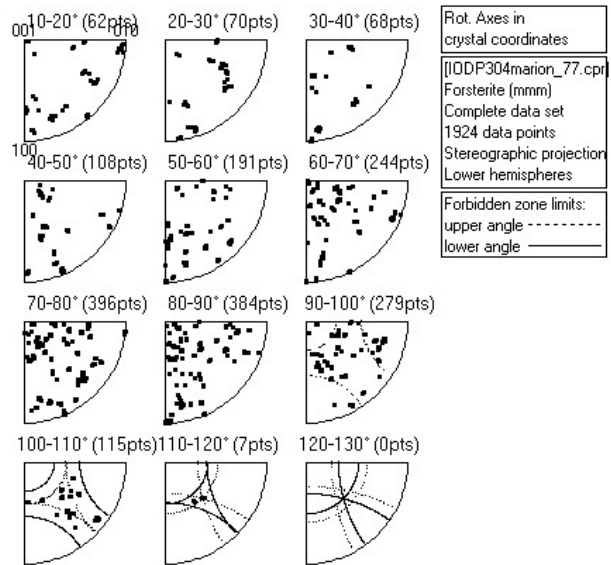
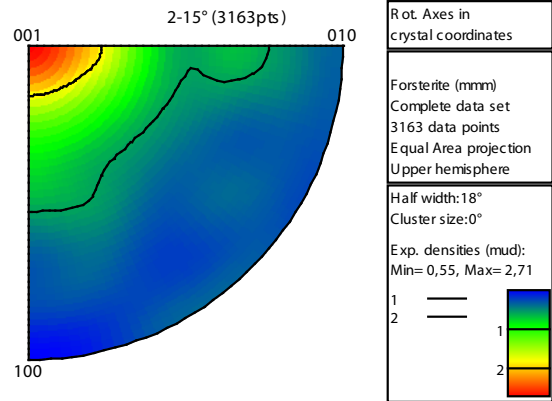
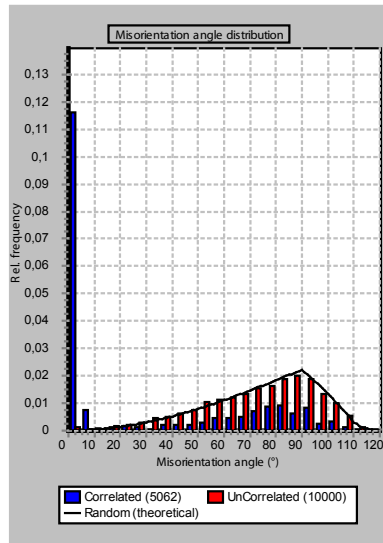
Troctolite riche en olivine

Olivine

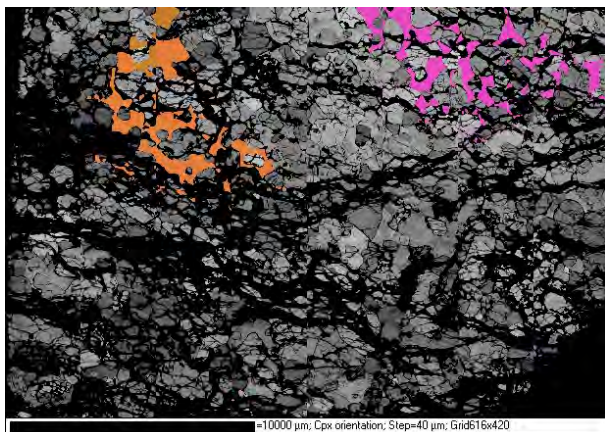
81% Ol 15% Pl 4% Cpx



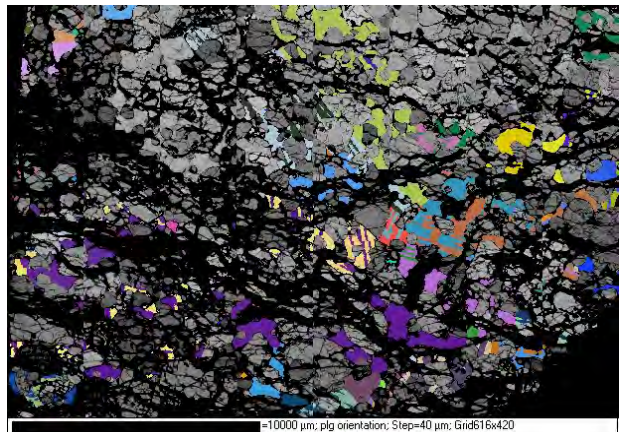
Olivine misorientation



Clinopyroxene



Plagioclase

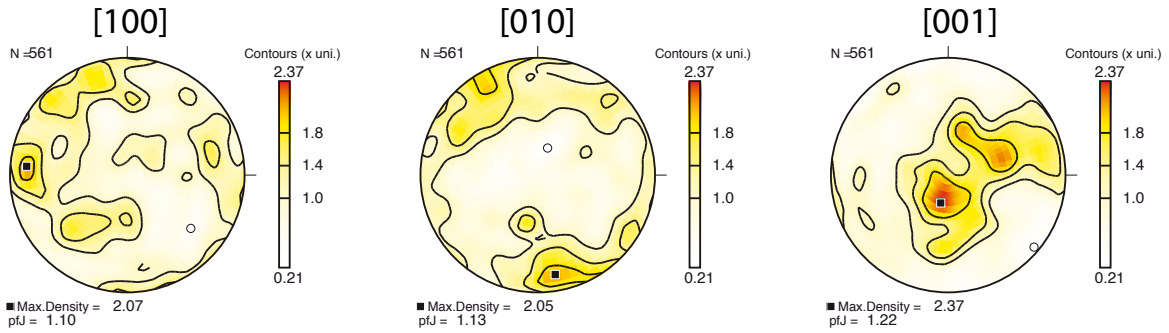


241R2_94-97

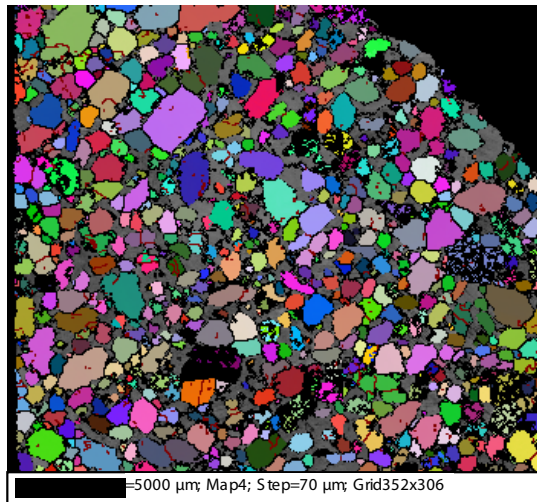
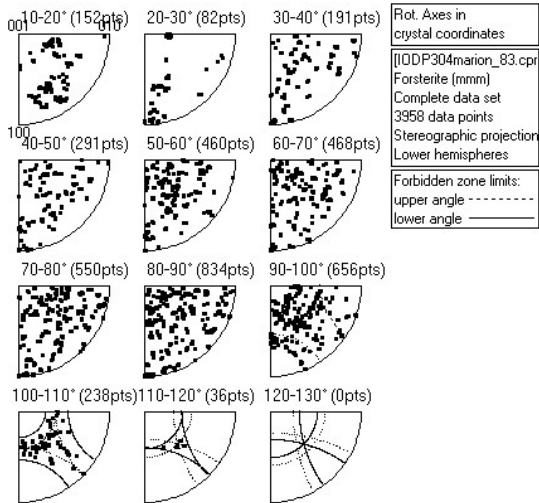
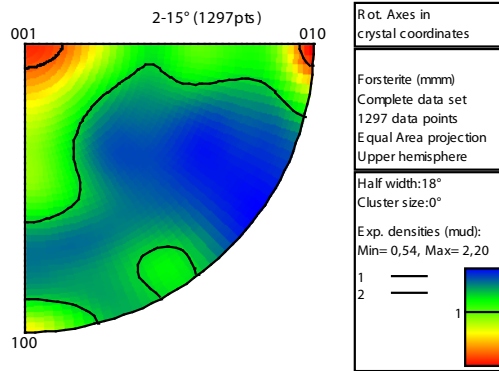
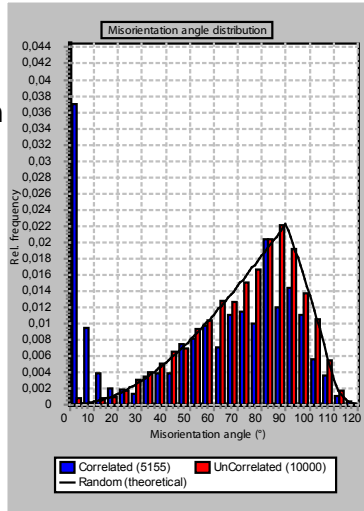
Troctolite riche en olivine

82% Ol 15% Pl 3% Cpx

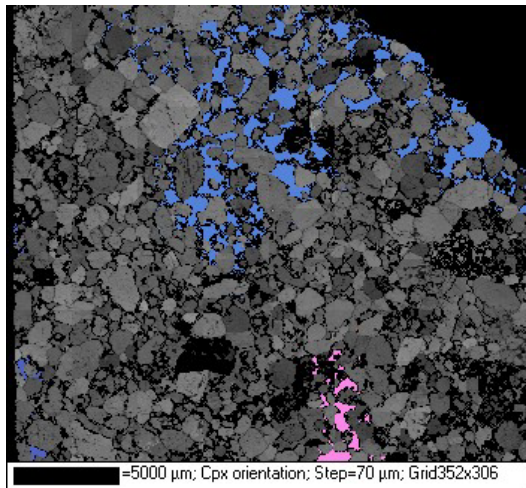
Olivine



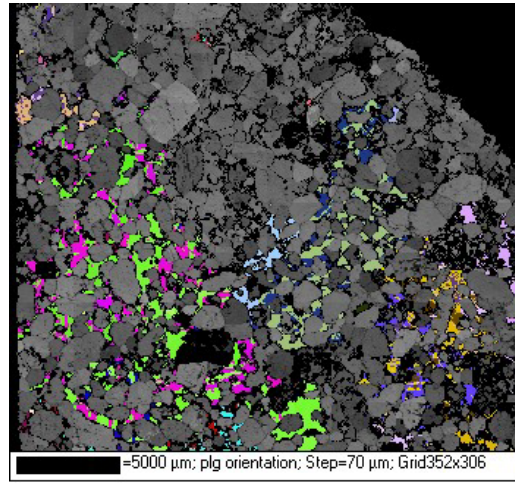
Olivine misorientation



Clinopyroxene



Plagioclase

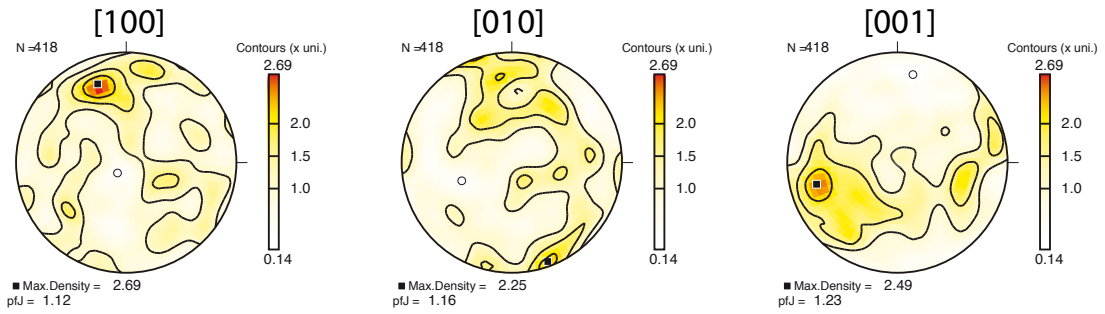


247R3_16-18

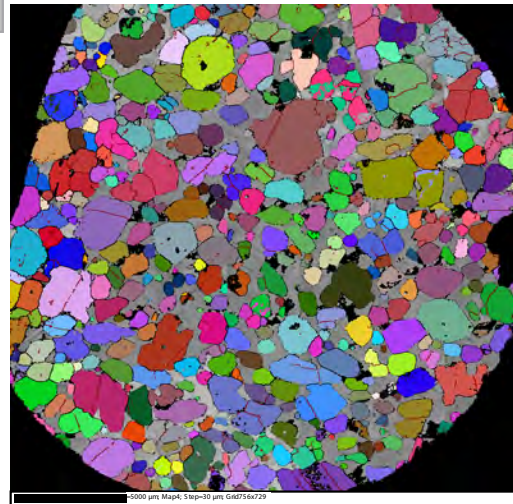
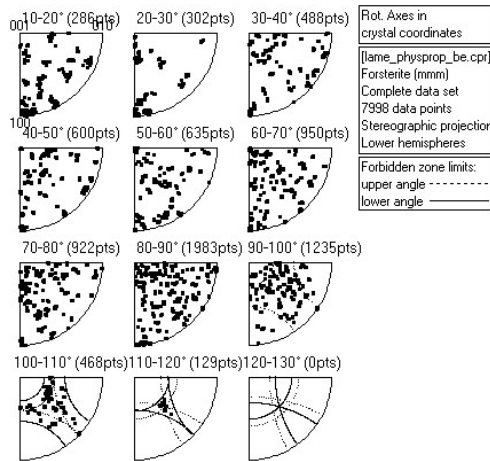
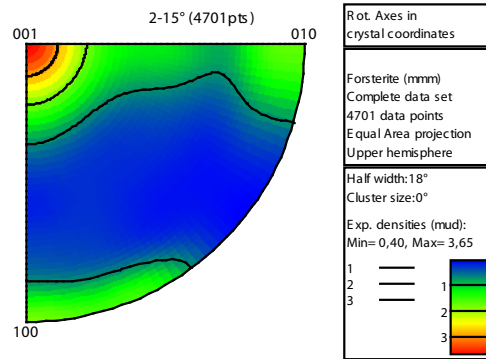
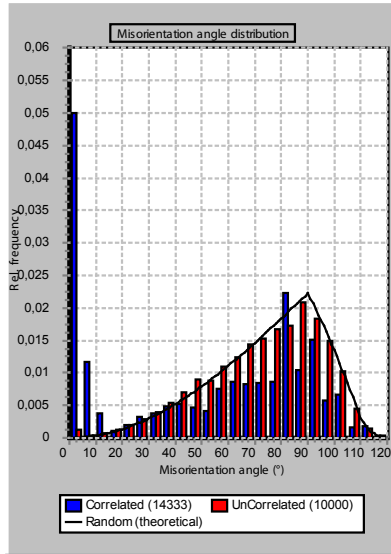
Troctolite riche en olivine

80% Ol 9% Pl 11% Cpx

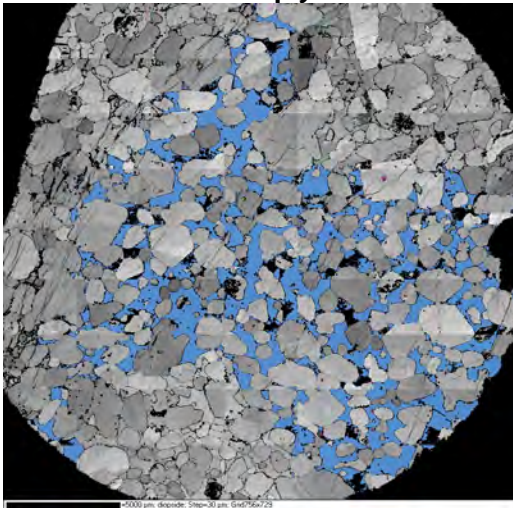
Olivine



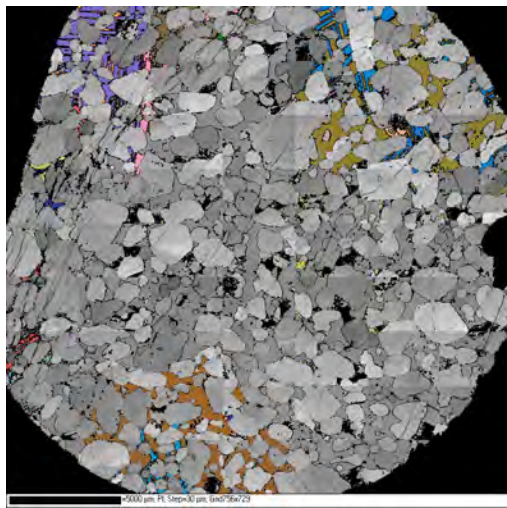
Olivine misorientation



Clinopyroxene



Plagioclase

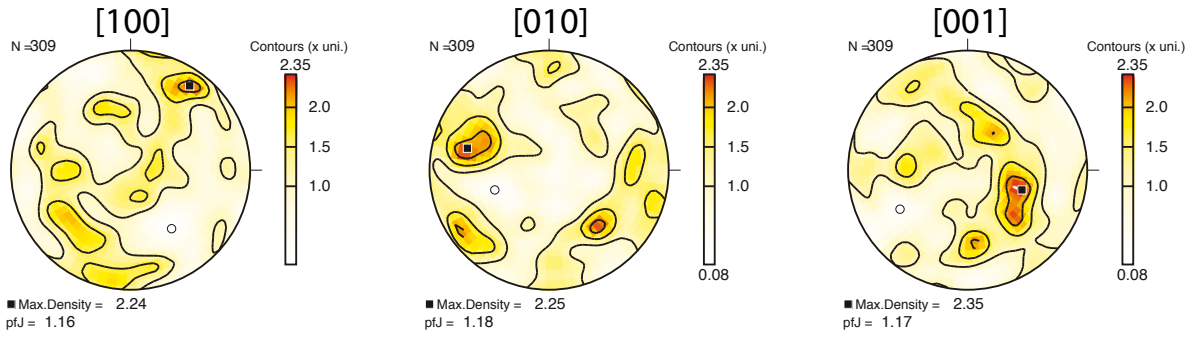


247R3_19-22

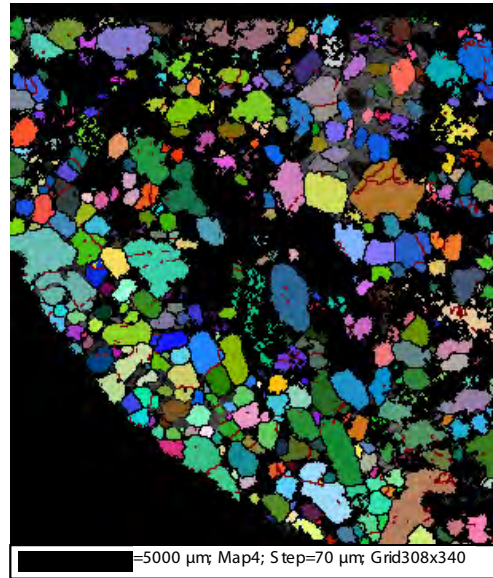
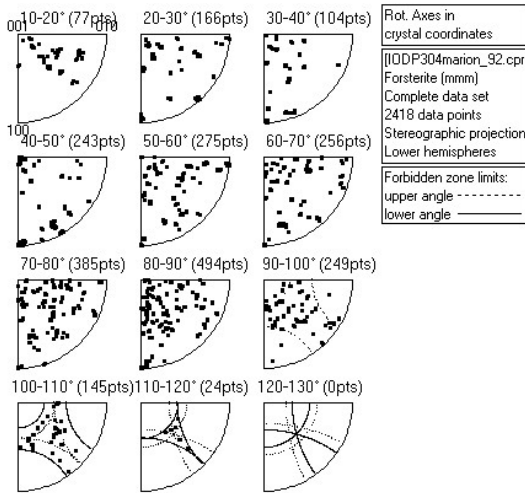
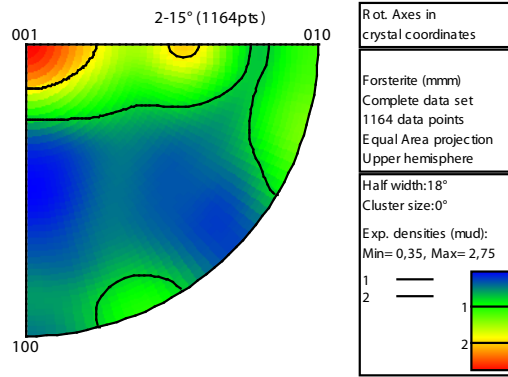
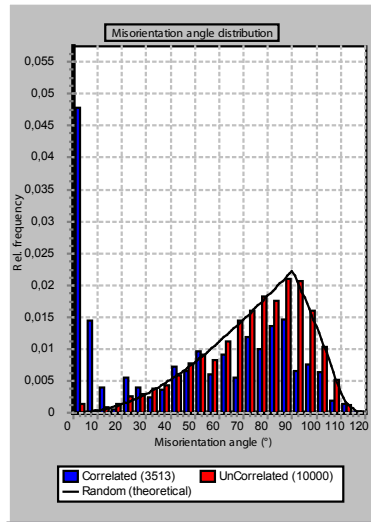
Troctolite riche en olivine

74% Ol 9% Pl 17% Cpx

Olivine

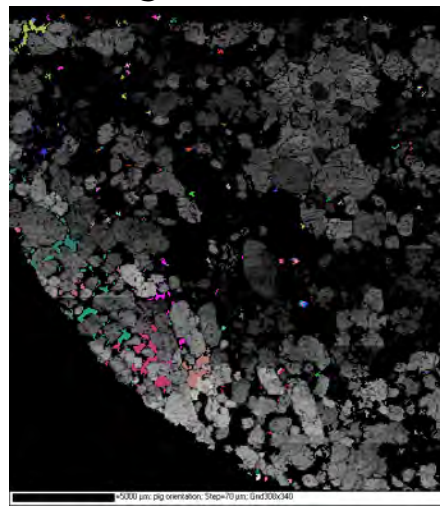


Olivine misorientation



Clinopyroxene

Plagioclase

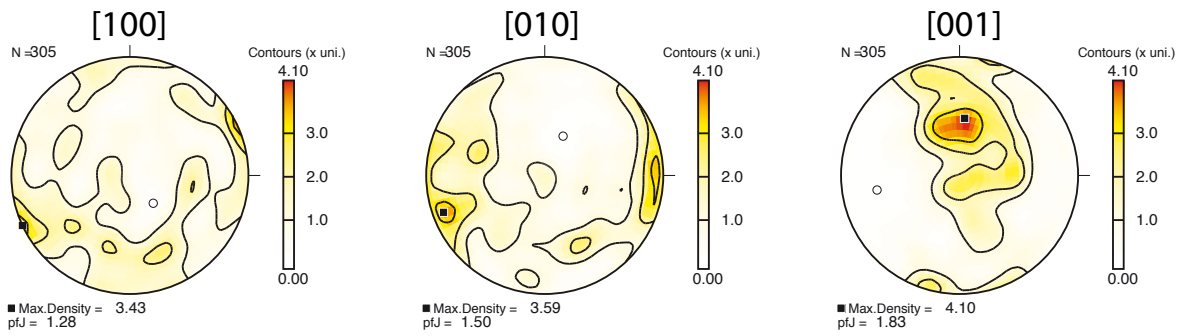


247R3_62-66

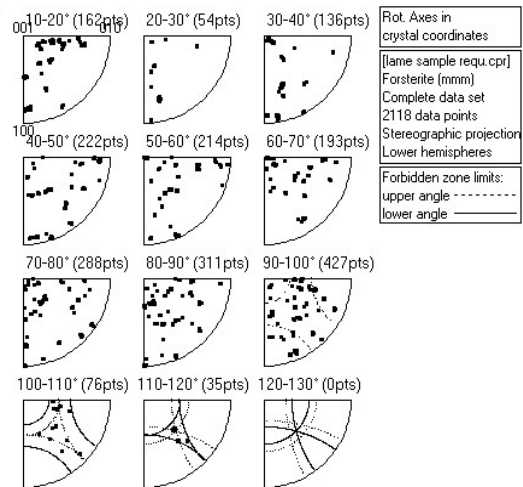
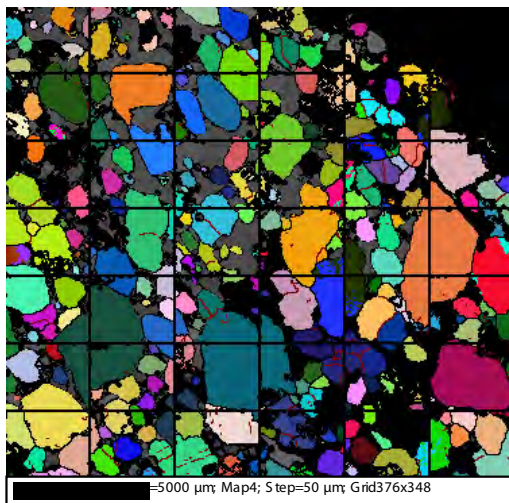
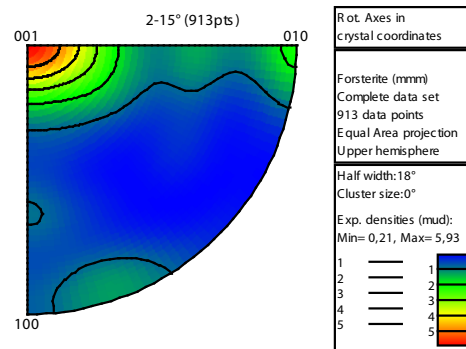
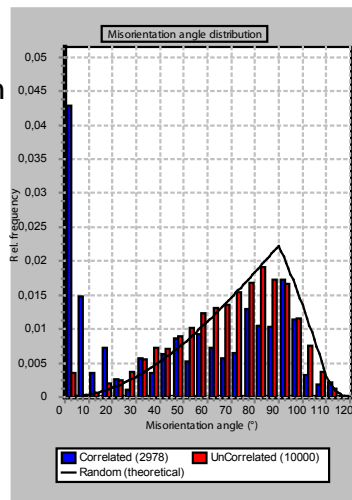
Troctolite riche en olivine

68% Ol 2% Pl 30% Cpx

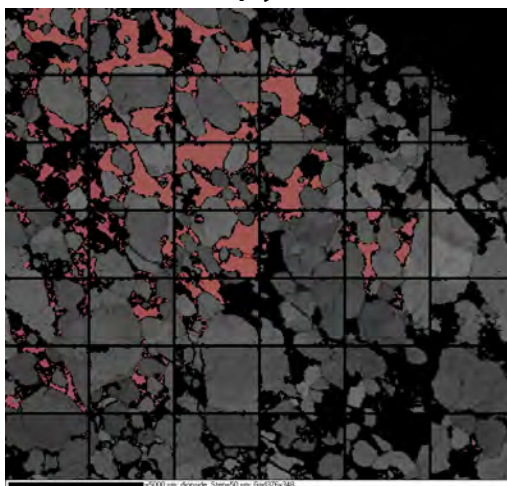
Olivine



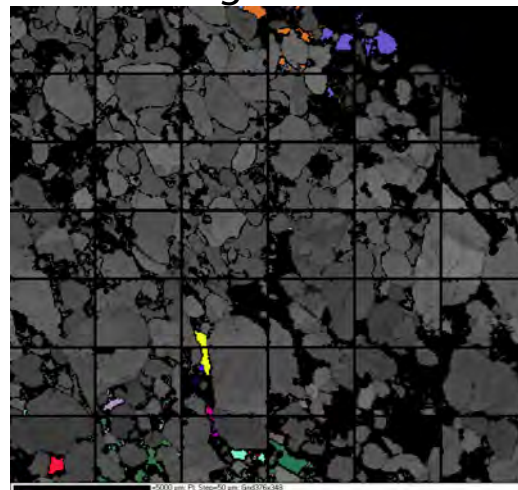
Olivine misorientation



Clinopyroxene



Plagioclase



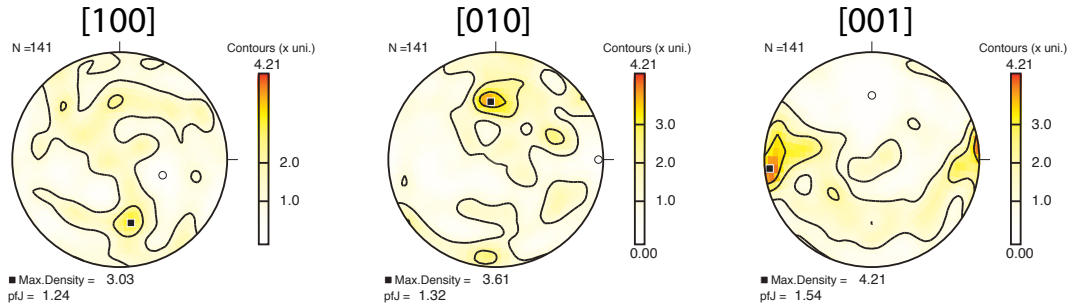
248R2_18-21

Troctolite riche en olivine
+ dykelet

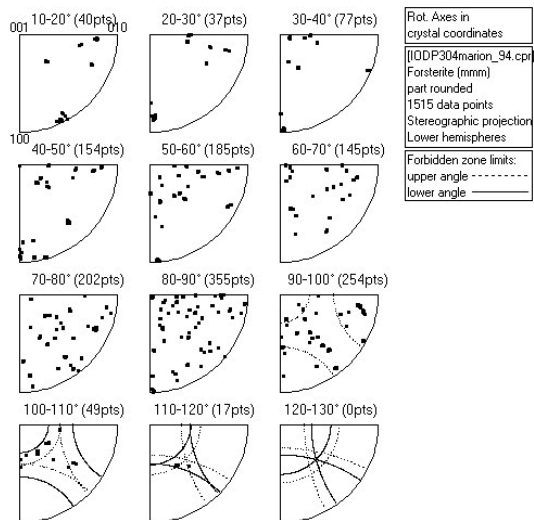
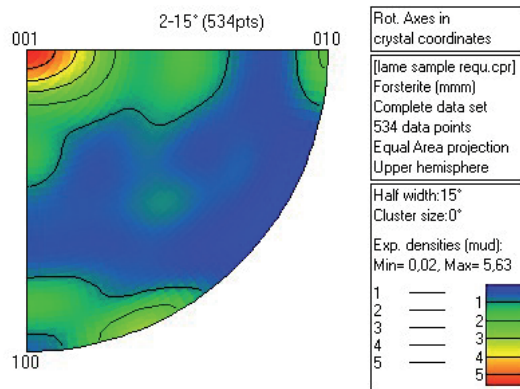
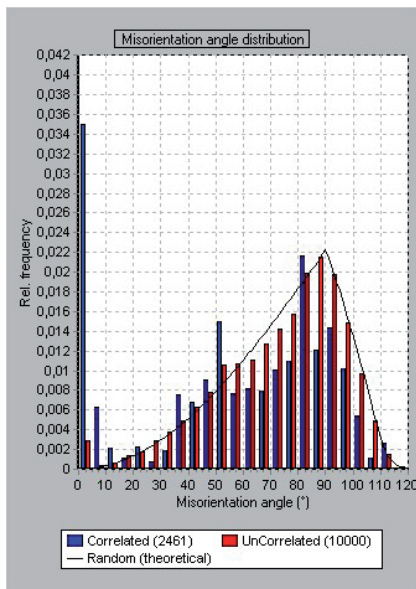
77% Ol 12% Pl 11% Cpx

Olivine

Rounded grain



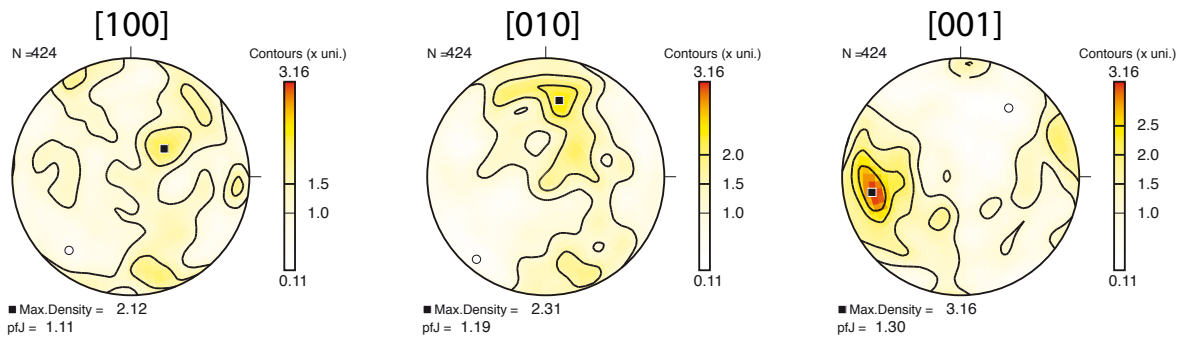
Olivine misorientation



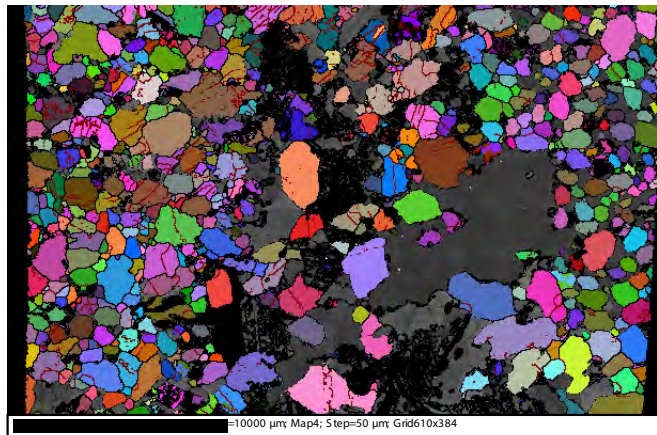
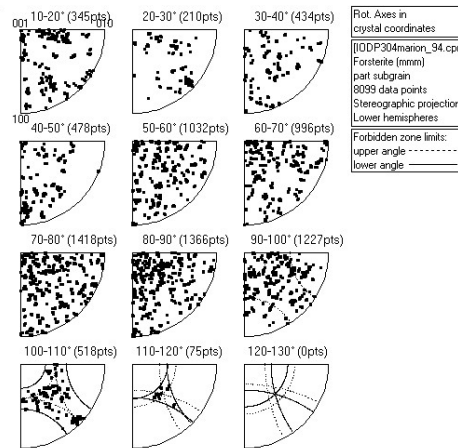
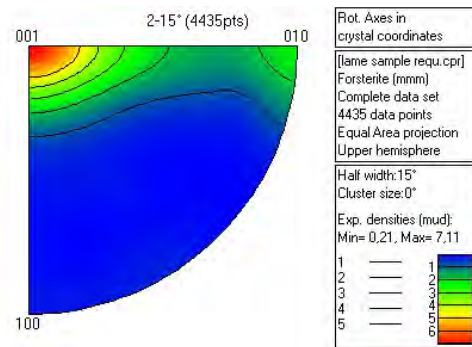
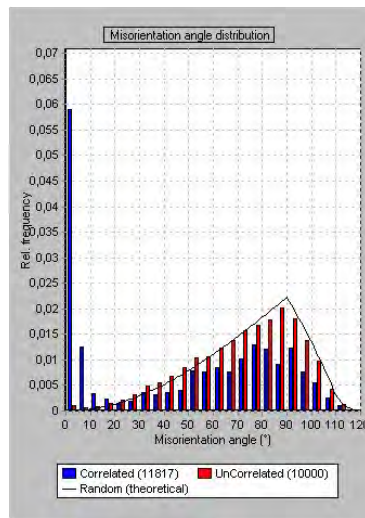
248R2_18-21

Troctolite riche en olivine
+ dykelet

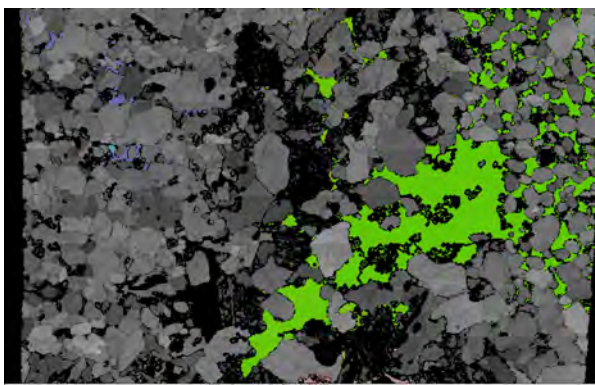
77% Ol 12% Pl 11% Cpx



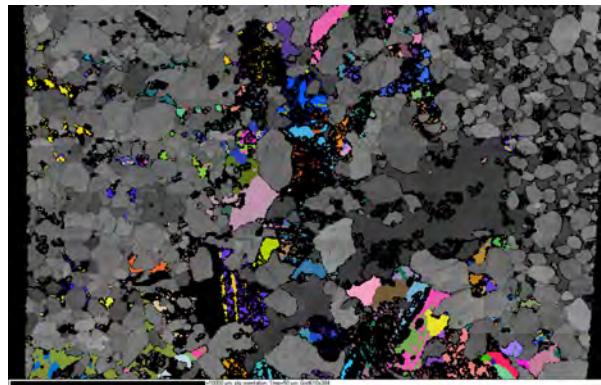
Olivine
misorientation



Clinopyroxene



Plagioclase

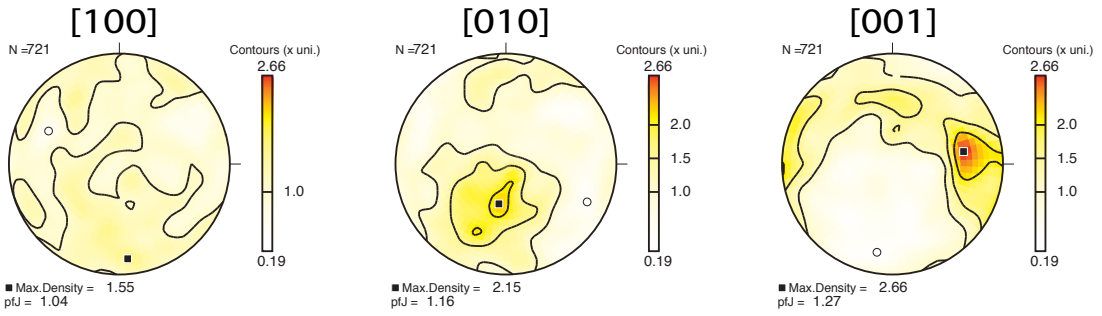


248R2_22-24

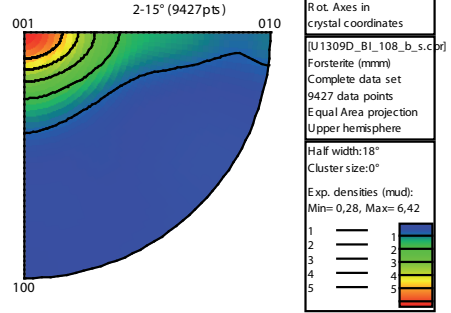
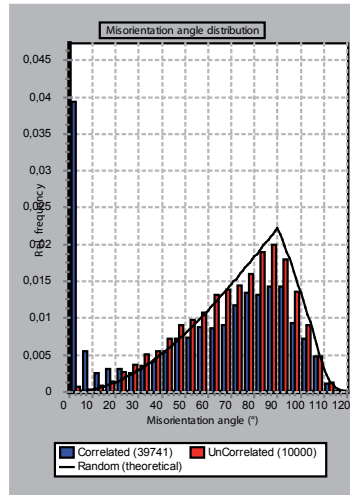
Troctolite riche en olivine

Olivine

90% Ol 5% Pl 2% Cpx 3%opx

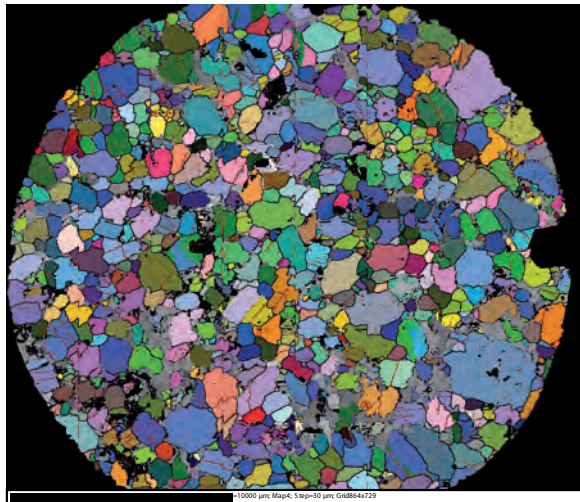
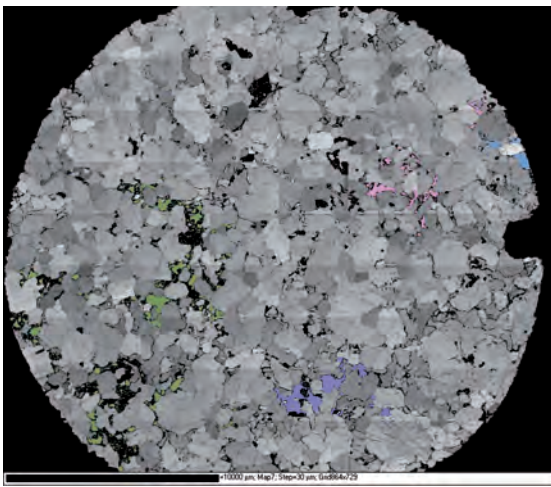


Olivine misorientation



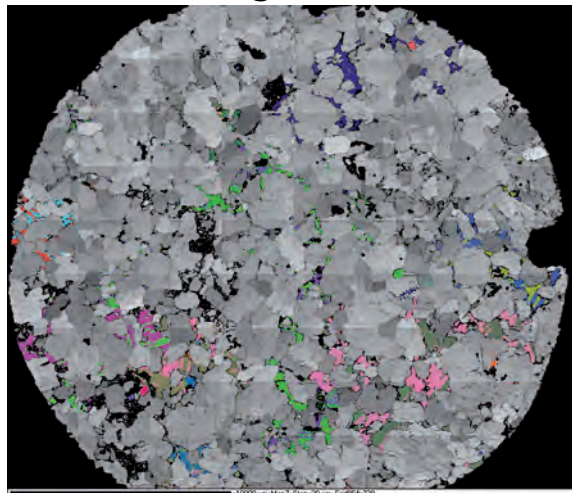
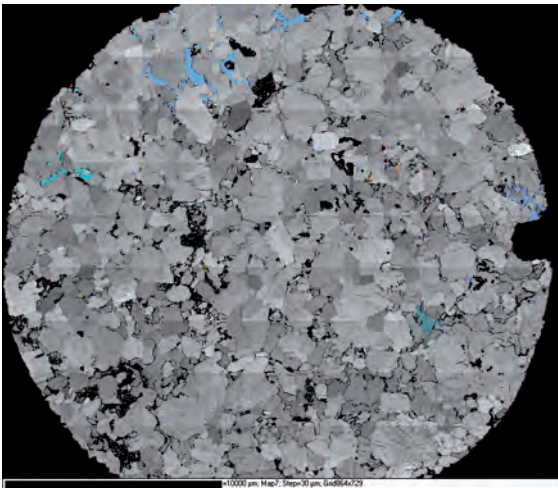
Orthopyroxène

Olivine



Clinopyroxène

Plagioclase

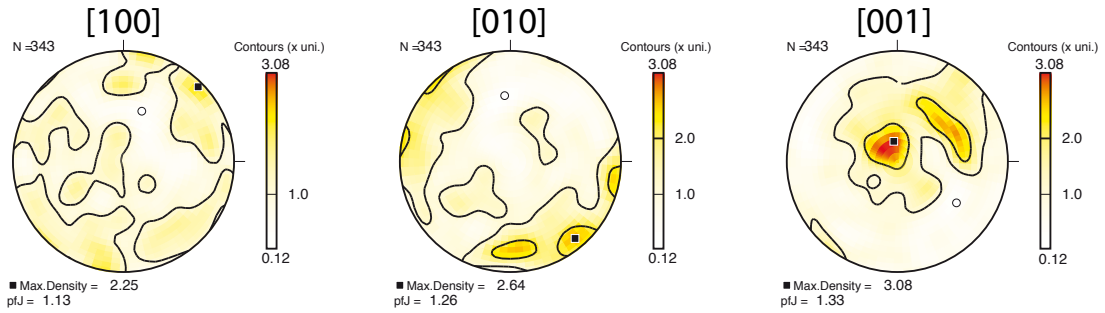


248R3_33-36

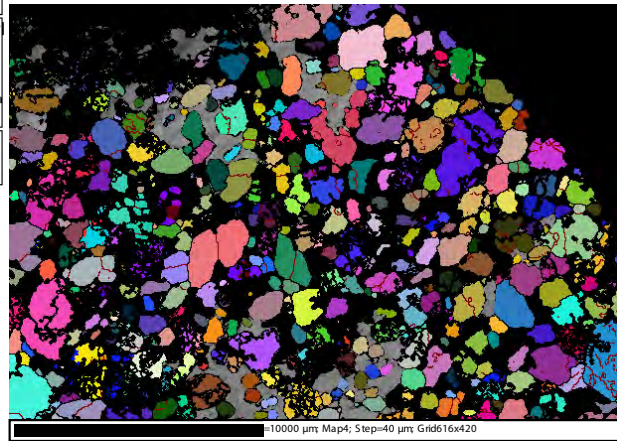
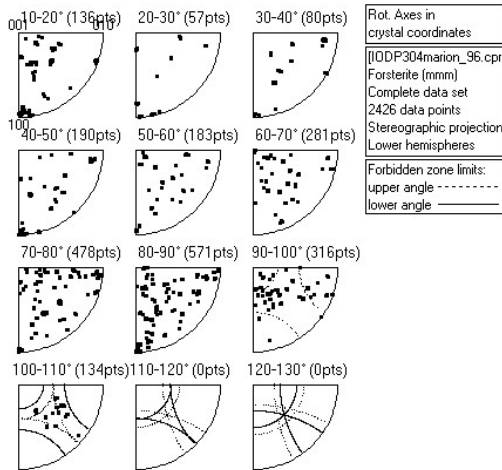
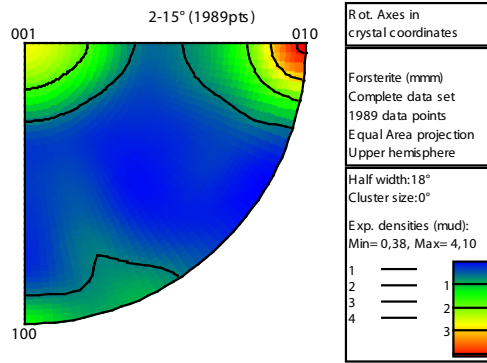
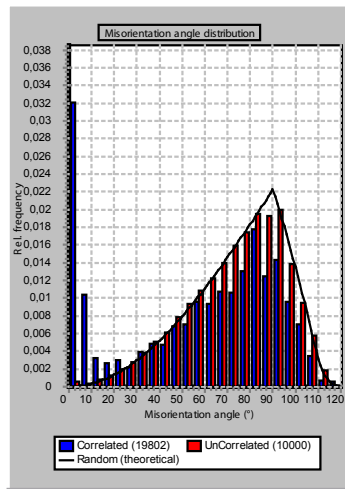
Troctolite riche en olivine

80% Ol 11% Pl 9% Cpx

Olivine

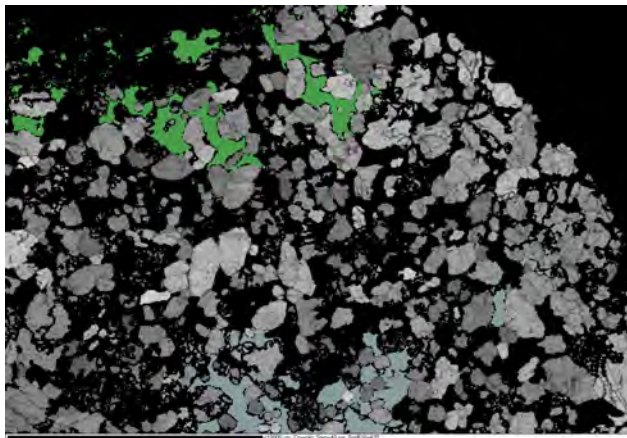


Olivine misorientation



Clinopyroxene

Plagioclase



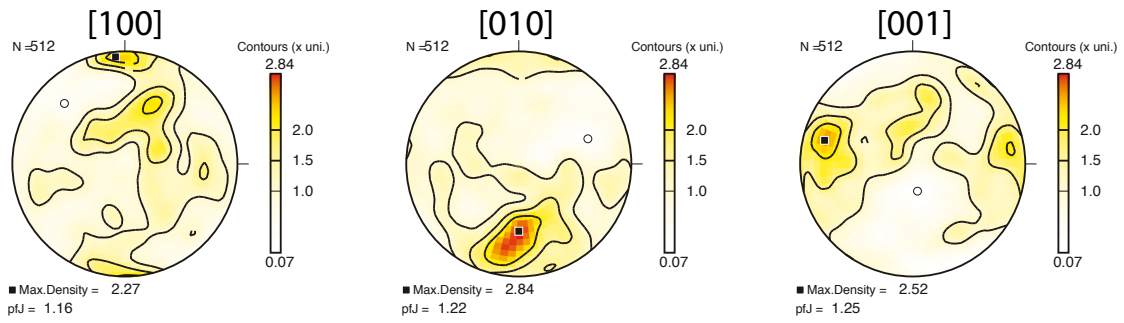
Non-annexé

248R3_36-38

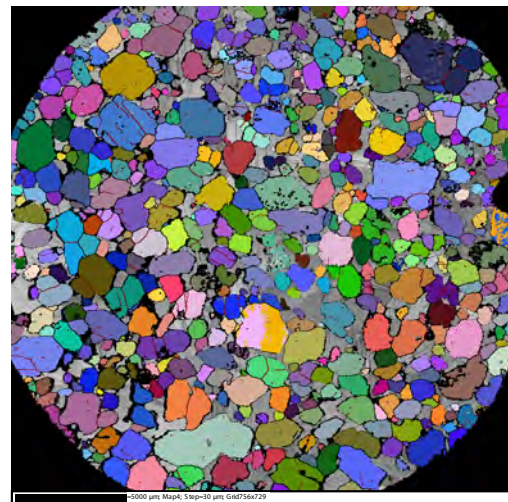
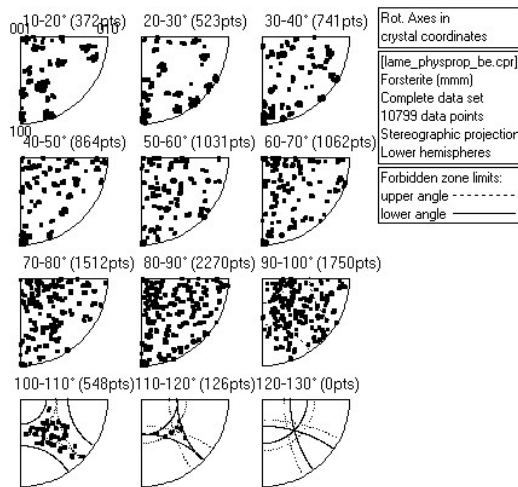
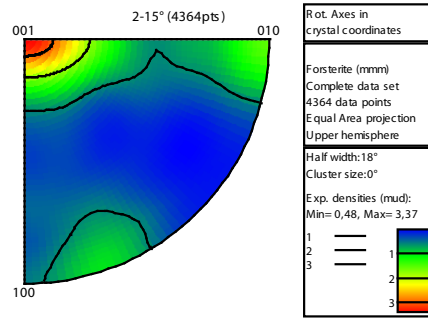
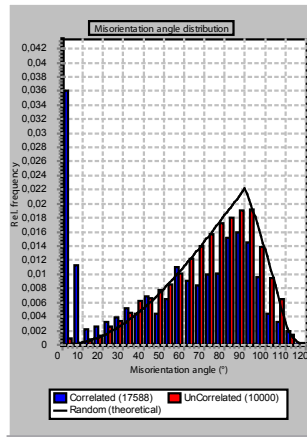
Troctolite riche en olivine

82% Ol 15% Pl 3% Cpx

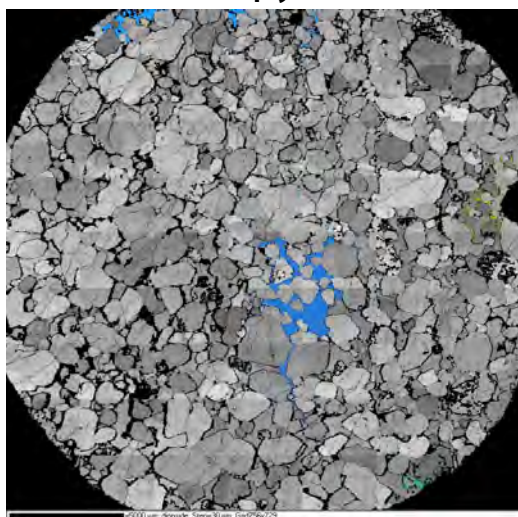
Olivine



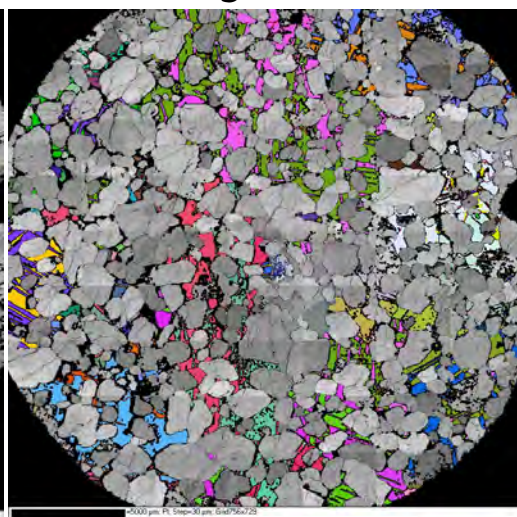
Olivine misorientation



Clinopyroxene



Plagioclase

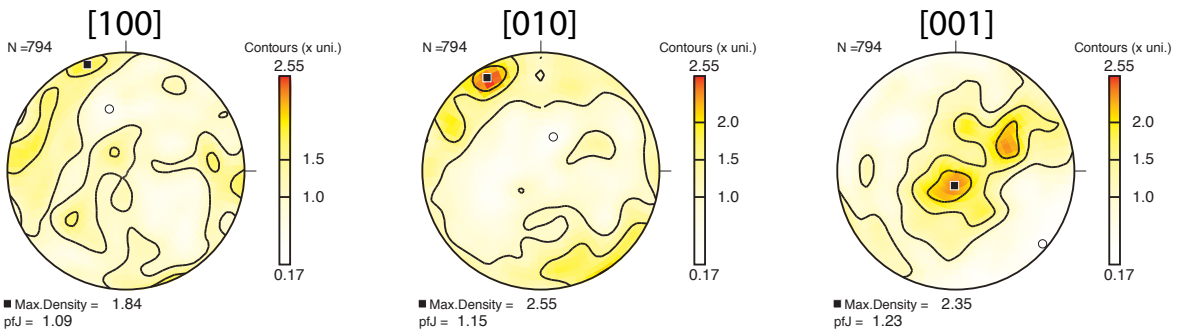


248R3_131-134

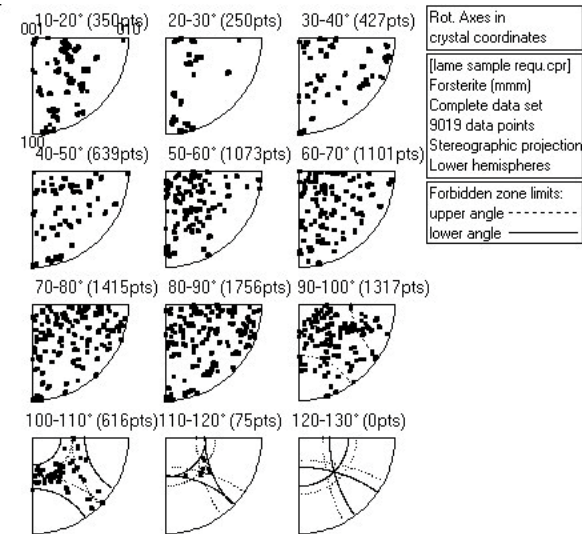
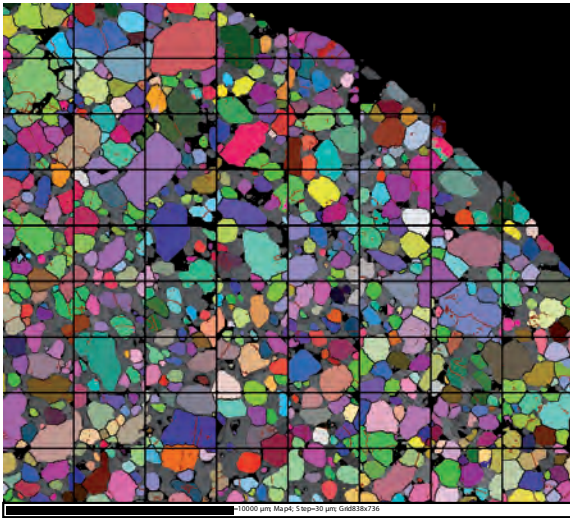
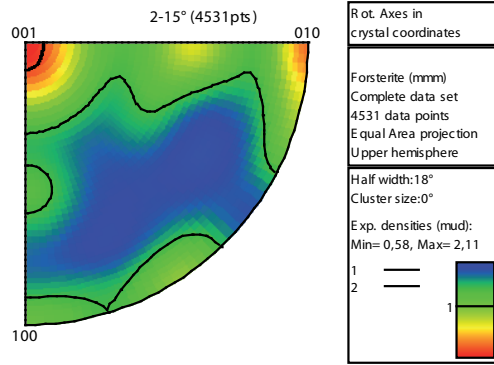
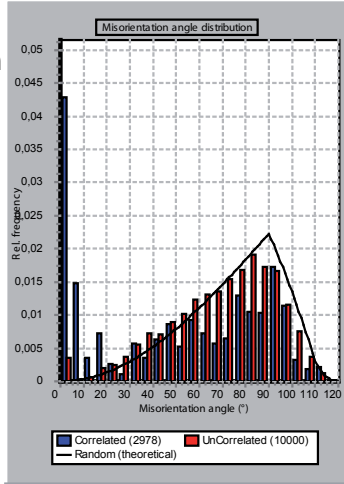
Troctolite riche en olivine

80% Ol 11% Pl 9% Cpx

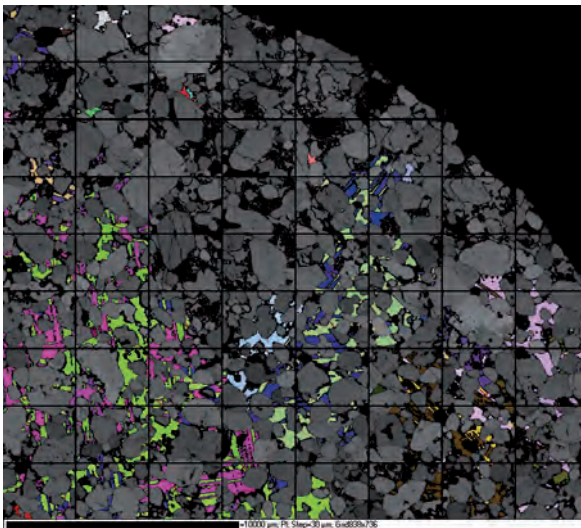
Olivine



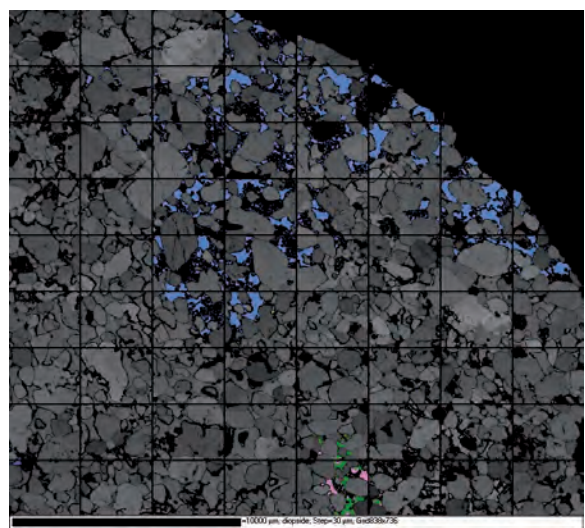
Olivine misorientation



Clinopyroxene



Plagioclase

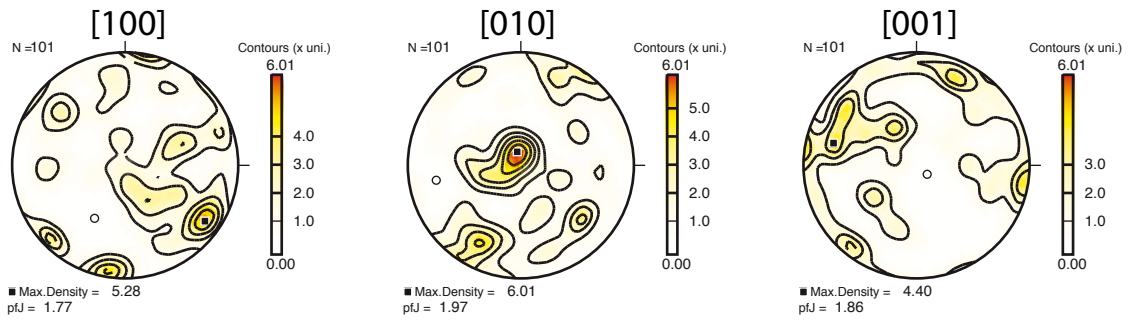


251R1_87-89

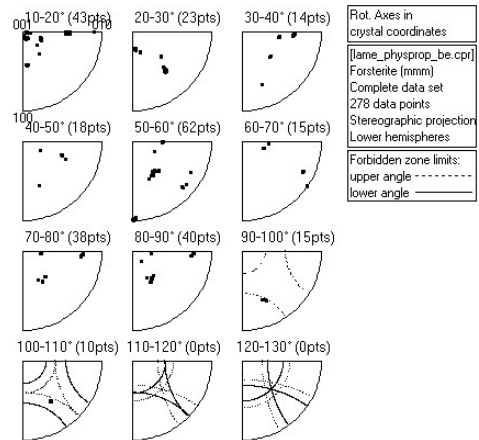
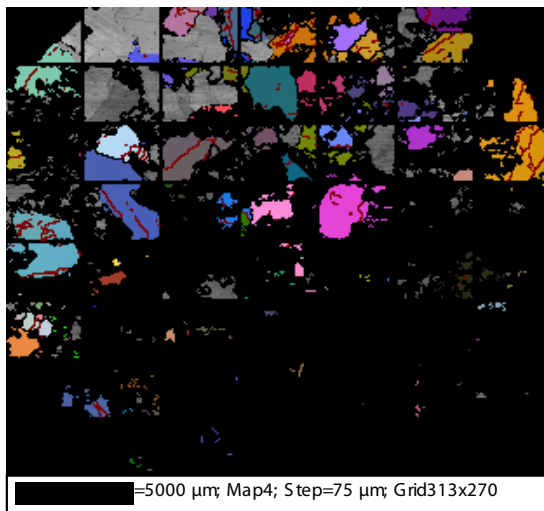
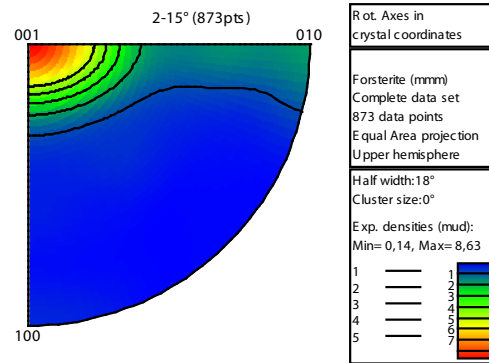
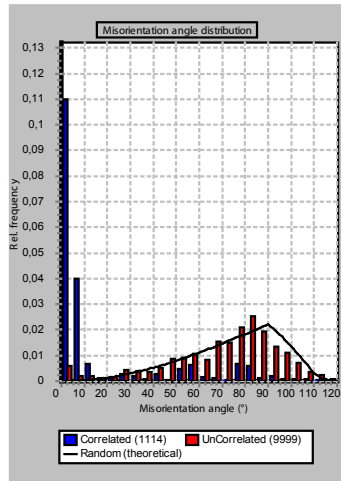
Gabbro troctolitique

40% Ol 55% Pl 5% Cpx

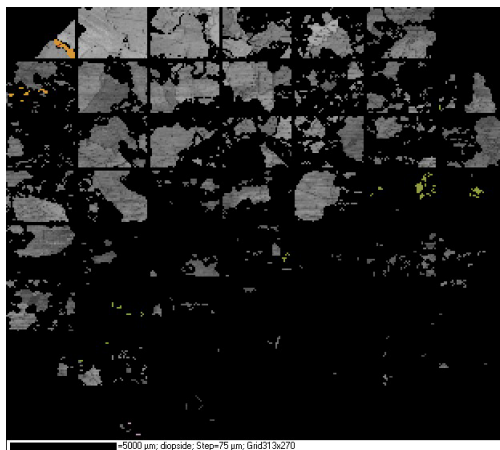
Olivine



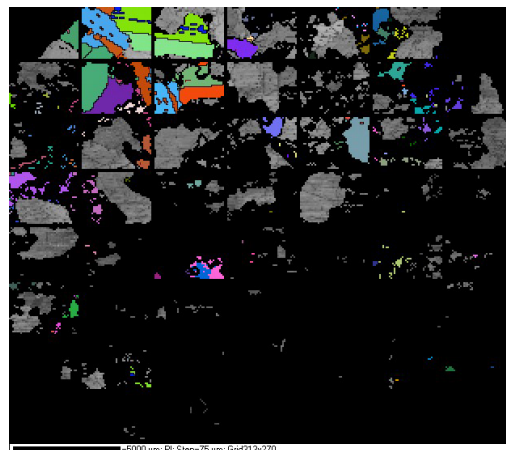
Olivine
misorientation



Clinopyroxene



Plagioclase

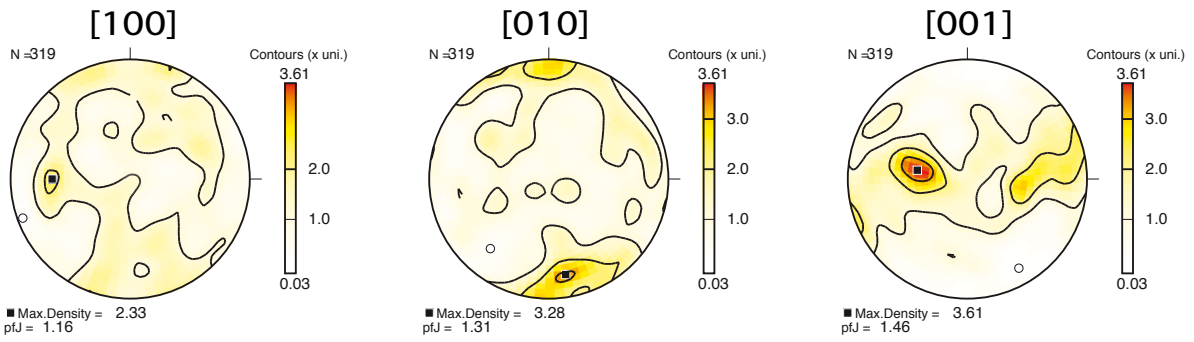


256R2_83-85

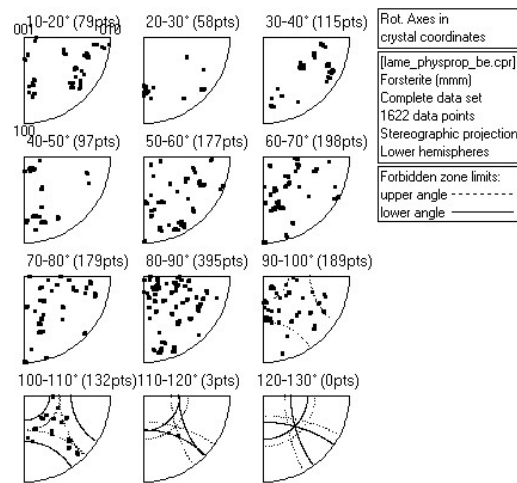
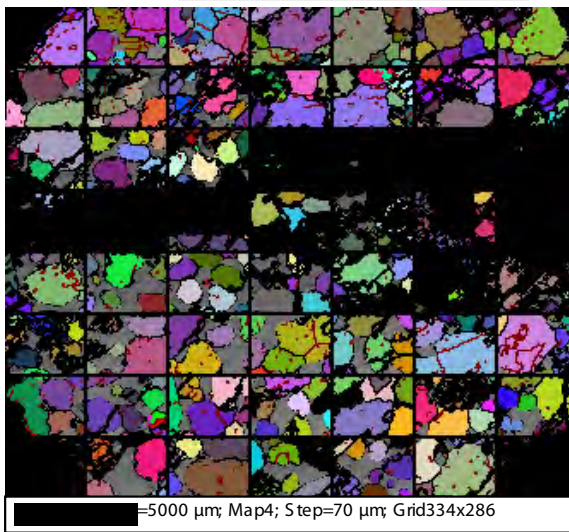
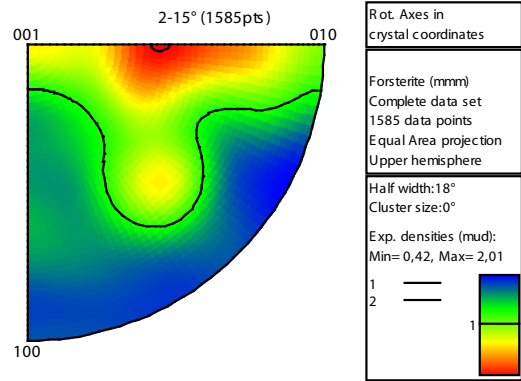
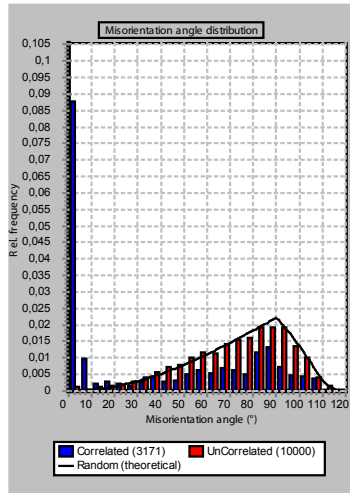
Troctolite riche en olivine

80% Ol 9% Pl 11% Cpx

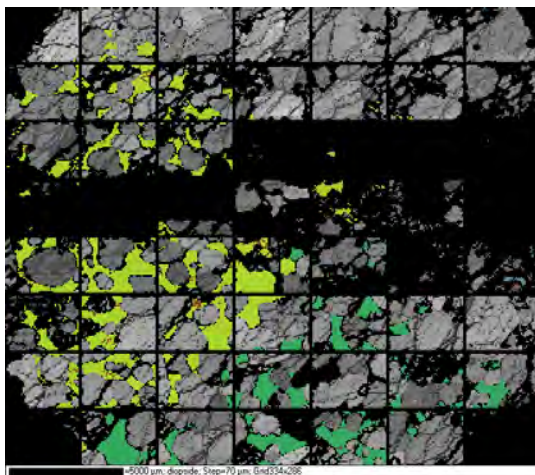
Olivine



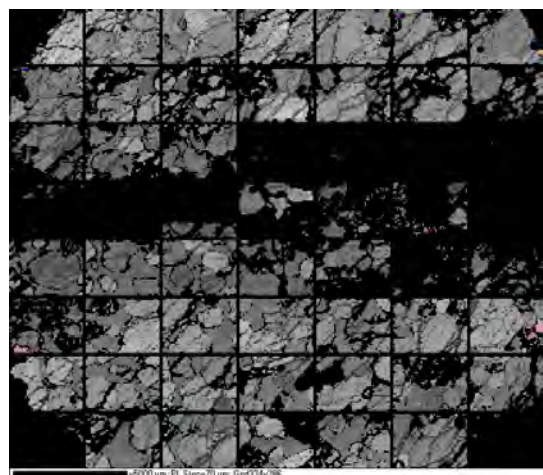
Olivine misorientation



Clinopyroxene



Plagioclase

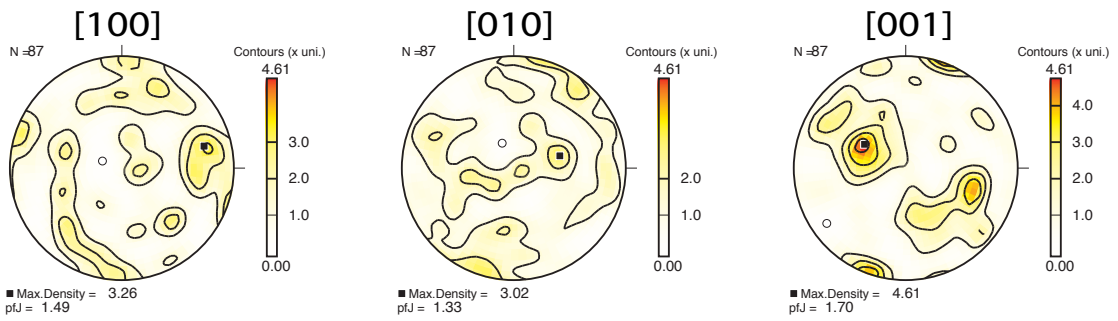


268R2_83-85

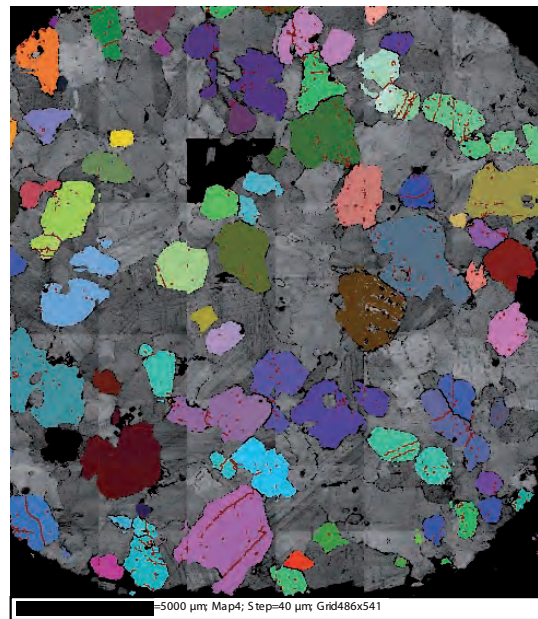
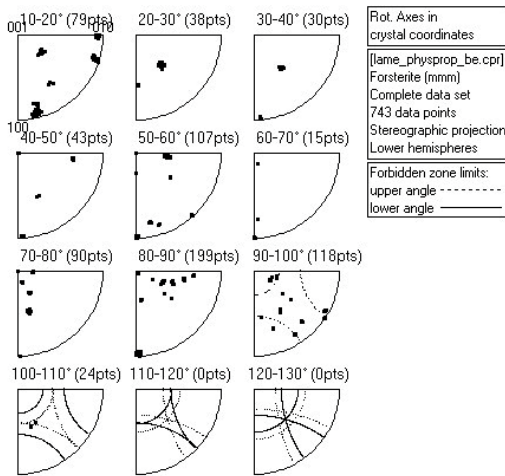
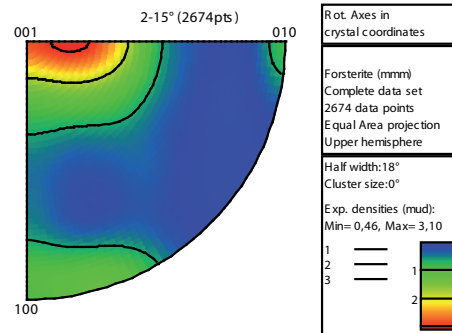
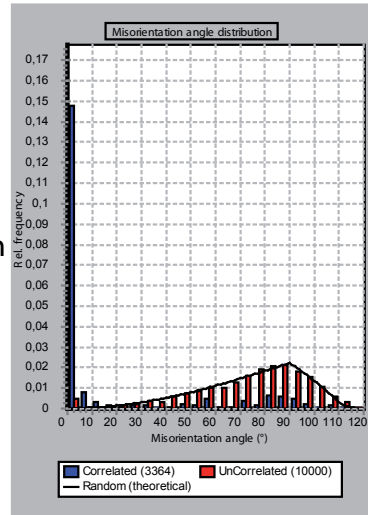
olivine-gabbro

10% Ol 55% Pl 35% Cpx

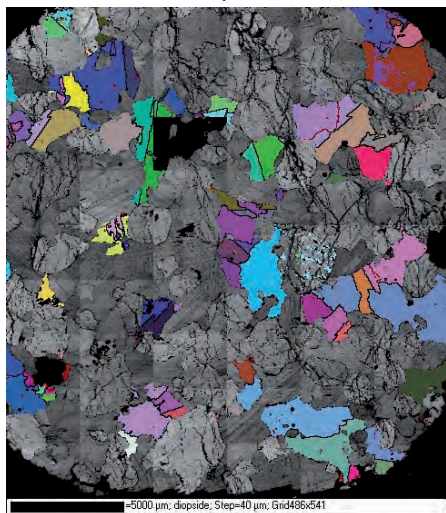
Olivine



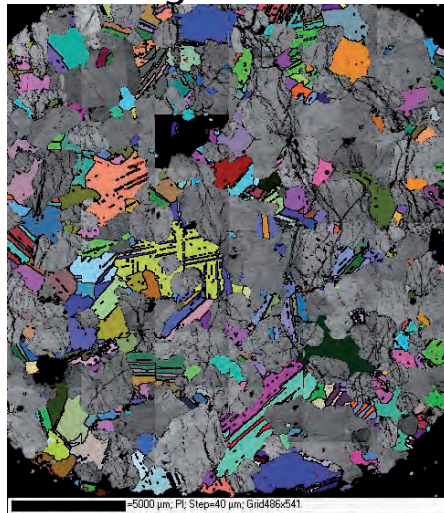
Olivine misorientation



Clinopyroxene



Plagioclase



ANNEXE D

Propriétés électriques des roches gabbroïques et troctolitiques du puits IODP U1309D

Dans cette annexe sont reportés les résultats des mesures de conductivité électriques, de densité et de porosité des roches gabbroïques du puits IODP U1309D sous forme d'une publication soumise à IODP. Ces mesures ont été réalisées en laboratoire sur 109 mini-carottes d'environ 2 cm de hauteur et 2,5 cm de diamètre. Pour déterminer la porosité et la densité des échantillons chaque mini-carotte est préalablement mesurée précisément (moyenne sur 4 mesures) à l'aide d'un pied à coulisse. Puis, les mesures de porosité et de densité sont effectuées par la méthode de « triple pesée ». Cette méthode consiste à mesurer la masse de l'échantillon : (1) à sec, (2) saturé avec une solution saline (30g/l), (3) immergé dans cette même solution saline. La densité et la porosité sont obtenues par la suite par des calculs simples à partir des différentes masses mesurées (voir détail dans la publication ci-jointe). Pour déterminer leur conductivité électrique, chaque mini-carotte est saturée successivement avec 6 solutions salines de salinités croissantes (0,06g/l à 60g/l). Les mesures de conductivité électrique des différents échantillons ont été réalisées avec deux électrodes mises en contact avec les faces des mini-carottes à une fréquence fixe de 1000Hz. Les valeurs de conductivité de la roche sont ensuite reportées dans un diagramme en fonction des différentes valeurs de conductivité du fluide saturant. De ce graphique sont extraits le facteur de formation et la conductivité de surface (voir détail dans la publication ci-jointe). Le facteur de formation renseigne sur la topologie du réseau poreux, tandis que la conductivité de surface permet d'évaluer l'état de surface des pores, soit le degré d'altération de la roche. À partir de ces paramètres, on peut déduire la tortuosité et le facteur de cimentation en appliquant la loi d'Archie (voir détail dans la publication ci-jointe). Ces deux variables décrivent la géométrie et la structure du réseau poreux.

La caractérisation des propriétés électriques des roches gabbroïques du puits IODP U1309D montre que :

- Les échantillons ont une porosité comprise entre 0,005 et 0,039

- Le facteur de formation décroît et la conductivité de surface, le facteur de cimentation et la tortuosité augmente avec la porosité comme généralement observé dans les gabbros (Ildefonse & Pezard , 2001 ; Einaudi et al., 2005).
- La tortuosité et le facteur de cimentation sont plus dispersés dans les échantillons riches en olivines et donc en serpentines.
- La porosité, la tortuosité et le facteur de cimentation augmentent avec le taux de fracturation des roches.

1 **Data report : Electrical properties of gabbroic and troctolitic rocks from IODP**
2 **Hole U1309D, Atlantis Massif**

3

4 Benoit Ildefonse, Marion Drouin, Marie Violay, and Philippe Pezard

5 Géosciences Montpellier, CNRS & Université Montpellier 2, F-34095 Montpellier cedex5,
6 France

7

8 Corresponding author :

9 Benoît Ildefonse
10 Géosciences Montpellier
11 Université Montpellier 2
12 CC 60
13 34095 Montpellier cedex 05
14 France
15 Phone : +33 (0)467143818
16 Fax : +33 (0)467143603
17 Email : benoit.ildefonse@univ-montp2.fr

18 IODP Exp 305, Sample request 20111

19

20

21

22 Keywords : IODP, Integrated Ocean Drilling Program, JOIDES Resolution, Expedition
23 304-305, Oceanic Core Complex, Site U1309, electrical properties, oceanic crust, gabbro,
24 troctolite

25

26

27

28

29

30 **Abstract** _ We report here on the results of laboratory measurements carried out to
31 explore the electrical properties of gabbroic and troctolitic samples from IODP Hole
32 U1309D, in the Atlantis massif, an oceanic core complex located at 30°N on the Mid-
33 Atlantic Ridge. Oceanic core complex are presumably localized in portions of

34 heterogeneous oceanic crust that are relatively rich in igneous rocks, and are the locus
35 of significant hydrothermal activity. Electrical properties are used in igneous rocks to
36 discuss their porosity structure as a function of mineralogy, alteration processes, and
37 deformation. Electrical properties of the gabbroic suites sampled during IODP
38 Expeditions 304 and 305 can contribute to the understanding of these processes in the
39 Atlantis Massif. We present the full suite of electrical data together with density and
40 porosity measurements on the same suite of samples.

41

42 **Introduction**

43 One of the main objectives of IODP Expeditions 304 and 305 was to drill a deep hole
44 inside the Atlantis Massif, an oceanic core complex located at 30°N in the inside corner
45 of the intersection of the Mid-Atlantic ridge with the Atlantis Fracture Zone (Blackman,
46 Ildefonse, John, Ohara, Miller, MacLeod et al., 2006). IODP Hole U1309D was drilled
47 down to 1415.5 meters below seafloor (mbsf); it is the second deepest hole in slow-
48 spread crust, after ODP Hole 735B on the Southwest Indian Ridge (Dick et al., 2000). We
49 report here on a series of laboratory measurements carried out at Géosciences
50 Montpellier, to quantify the electrical properties of the oceanic crustal rocks recovered
51 in Hole U1309D. Our knowledge of the in-situ structure of oceanic crust is partly based
52 on geophysical investigations, including downhole measurements (e.g., Goldberg, 1997).
53 The analysis of marine geophysical data requires a complete understanding of the
54 intrinsic physical properties of investigated crustal sections. Electrical measurements
55 are used to evaluate the porosity structure of low-porosity, igneous rocks (e.g., Pezard,
56 1990), and are presented herein together with density and porosity measurements. This

57 work follows the study of electrical properties of gabbroic rocks sampled in ODP hole
58 735B at the Southwest Indian ridge (Pezard et al., 1991; Ildefonse and Pezard, 2001)

59

60 **Geological setting**

61 Hole U1309D is almost exclusively made of gabbroic and troctolitic rocks, to the
62 exception of a few tens of centimeters of mantle peridotites in the upper 225 meters
63 (Blackman, Ildefonse, John, Ohara, Miller, MacLeod et al., 2006; Ildefonse et al., 2006). In
64 comparison with gabbroic sections previously recovered by drilling in oceanic crust
65 (Robinson, Von Herzen et al., 1989; Gillis, Mével, Allan et al., 1993; Cannat, Karson, Miller
66 et al., 1995; Dick, Natland, Miller et al., 1999; Pettigrew, Casey, Miller et al., 1999;
67 Kelemen, Kikawa, Miller et al., 2004), the core recovered in IODP Hole U1309D
68 comprises a larger proportion of olivine-rich lithologies. On the basis of their modal
69 abundance in olivine, plagioclase, clinopyroxene, and Fe-Ti oxide, gabbroic rocks were
70 grouped after shipboard descriptions (Blackman, Ildefonse, John, Ohara, Miller, MacLeod
71 et al., 2006) into olivine-rich troctolite (5,4% of recovered rocks), troctolite (2.7%),
72 olivine to troctolitic gabbro (28%), gabbro (56%) and oxide gabbro (7%). Olivine-rich
73 troctolites have more than ~70% olivine, as subhedral or rounded grains included in
74 interstitial to poikilitic plagioclase and clinopyroxene. Their modal compositions vary at
75 the scale of a few centimeters to a few decimeters, locally grading to dunite, wehrlite, or
76 olivine gabbro. Olivine gabbro (>5% olivine) and gabbro display seriated textures, and
77 are characterized by significant variations in grain size and modal composition on a
78 decimeter-scale. Olivine gabbro locally grades to troctolitic gabbro and troctolite.
79 Gabbro is generally intrusive into troctolite and olivine gabbro with either sharp or
80 locally more diffuse contacts. Thin section observation reveals the occurrence of

81 significant amounts of orthopyroxene in gabbros below 600 mbsf. Oxide gabbros (>2%
82 modal Fe-Ti oxides) occur as disseminated patches, as dikelets crosscutting other
83 lithologies, or less often associated with ductile deformation zones (Blackman, Ildefonse,
84 John, Ohara, Miller, MacLeod et al., 2006). Late-stage dikes of coarse-grained gabbro and
85 microgabbro commonly intrude troctolite units. The core is variably altered at
86 conditions ranging from granulite to zeolite facies. Overall, the alteration tends to
87 decrease downhole and olivine-rich troctolite intervals between 1090 and 1230 mbsf
88 are locally exceptionally fresh. Magmatic deformation associated with the emplacement
89 of Hole U1309D gabbroic intrusive suite is weak and affects only 22% of the recovered
90 core. High temperature (Amphibolite facies) deformation is rare, and high-strain ductile
91 shear zones represent less than 3% of the recovered core.

92 IODP Hole U1309D is the last of 16 holes drilled in 4 different oceanic core complexes
93 in the Atlantic and Indian oceans, and (ODP Legs 118, 153, 176, 179, 209; IODP
94 Expeditions 304 & 305), all of which recovered only gabbroic sections. This common
95 geological feature in boreholes, contrasting with the more variable seafloor geology in
96 the same areas, including serpentinites, was the basis for a revised model of oceanic core
97 complex development, in which the core is dominantly made of gabbro intrusion(s),
98 surrounded by faults preferentially localized in serpentinitized peridotites (Ildefonse et
99 al., 2007). The detachment fault that caps the Atlantis Massif and other oceanic core
100 complexes is the locus of abundant hydrothermal fluid circulation (McCaig et al., 2007).
101 Characterizing the electrical properties the gabbroic series recovered in IODP Hole
102 U1309D sheds light on their porosity structure, which is an important parameter,
103 together with alteration petrology, to take into account to discuss their contribution to
104 the hydrothermal system.

105

106 **Background and methods**

107 Electrical properties of porous media are sensitive to fluid content and to alteration;
108 they can thus be used to detect conductive features in a resistive matrix (e.g., Walsh and
109 Brace, 1984; Pezard and Luthi, 1988). The modes of electrical conduction are identified
110 in the laboratory from resistivity measurements at various salinities of the saturating
111 fluid, and provide information on the porosity structure and the degree of alteration.
112 The method has been initially proposed for sandstones and clays (Waxman and Smits,
113 1968; Revil and Glover, 1998), but has been successfully applied to various low-porosity
114 igneous rocks such as basalts (e.g., Pezard, 1990; Einaudi et al., 2000), gabbros (Pezard
115 et al., 1991; Ildefonse and Pezard, 2001), peridotites (Ildefonse et al., 1999), and granites
116 (Pape et al., 1985; Pezard et al., 1999; Belghoul, 2007).

117 In a porous media comprising a matrix considered as infinitely resistive and a
118 connected pore space saturated with a conductive electrolyte, two main mechanisms are
119 responsible for electrical conduction: (i) an electrolytic conduction mechanism in pore
120 volumes, and (ii) a surface conduction mechanism at the interface between the
121 electrolyte and minerals. Electrolytic conduction is related to the nature and salinity of
122 the saturating fluid; surface conduction is related to the presence along pore surfaces of
123 charges, which is related on the first order to alteration (e.g., Revil and Glover, 1998).
124 The measured electrical conductivity can be written (Waxman and Smits, 1968) :

$$125 \quad (1) \quad C_0 = \frac{C_w}{F} + C_s ,$$

126 with C_0 the total conductivity of the pore space, C_w the conductivity of water, the
127 saturating fluid, F the electrical formation factor, and C_s the surface conductivity. C_s is

128 related to clay-like silicates, hence to alteration through the cation exchange capacity
129 (Waxman and Smits, 1968). While this model works well at high salinity, it tends to
130 overestimate C_s at low salinity. We can use, alternatively, the non-empirical, statistical
131 approach proposed by Revil and Glover (1998), based on the micro-geometry of the
132 porous space. The conductivity of the sample is then given by a complex model that has
133 two simpler forms at high and low salinities (see equations in Revil and Glover, 1998;
134 Ildefonse and Pezard, 2001).

135 To characterize their electrolytic and surface conduction components, each sample
136 (minicores) was analyzed with measurements of electrical resistivity performed at 1
137 kHz, and variable saturating fluid salinity (six series of measurements, from 0.06 g/l to
138 60 g/l; datafile; Fig. 1, Tables 1 and 2). The measurements were done with 2 electrodes;
139 the polarizing effect at the electrode/sample interface was reduced by using paper filter
140 to separate the electrodes from the sample (see Pezard, 1990, for a detailed description
141 of the experimental protocole).

142 The contribution of surface conduction to the total, measured electrical conductivity
143 can be estimated by using β (Ildefonse and Pezard, 2001) :

144 (2)
$$\beta = \frac{F \times C_s}{(F \times C_s) + C_w},$$

145 with $C_w = 5000 \text{ mS}\cdot\text{m}^{-1}$ (for sea water at 24°C).

146 The intrinsic electrical formation factor F and the surface conductivity are extracted,
147 from the high- and low-salinity parts of the curves, respectively, using both the Waxman
148 and Smits (1968) and Revil and Glover (1998) models.

149 F depends only on the microstructural characteristics of the rock, and is classically
150 considered to characterize the 3D topology of the pore space (e.g., Guéguen and
151 Palciauskas, 1992). An empirical relationship between the electrical formation factor F
152 and porosity ϕ was proposed by Archie (1942) with :

$$153 \quad (3) \quad F = \phi^{-m} ,$$

154 in which the exponent m is called cementation index in oil industry. m typically varies
155 from ~1.5 to 2.5 in crystalline rocks (e.g., Guéguen and Palciauskas, 1992).

156 The relation between F and ϕ can also be expressed in terms of degree of connectivity
157 of the inner pore space, characterized by the electrical tortuosity τ (Walsh and Brace,
158 1984; Pezard, 1990; Pezard et al., 1991; Guéguen and Palciauskas, 1992) :

$$159 \quad (4) \quad F = \frac{\tau}{\phi} .$$

160 While the "cementation index" m describes the non-uniformity of the section of the
161 conductive channels, the electrical tortuosity τ relates to the complexity of the path
162 followed by the electrical current (e.g., Guéguen and Palciauskas, 1992) or, in a more
163 general sense, the efficiency of electrical flow processes (Clennell, 1997). In igneous,
164 low-porosity rocks, the average electrical tortuosity is generally of the order of 10 (e.g.,
165 Pezard et al., 1991; Ildefonse and Pezard, 2001).

166 Density and porosity were measured using the classical triple weighing method, with
167 an OHAUS precision scale (10^{-4} g accuracy). Samples were first weighed after being
168 dried in an oven at $\sim 50^{\circ}\text{C}$, then re-saturated for "wet" weight measurements in air and
169 immersed.

170 The bulk density ρ_b and grain density ρ_g are given by :

171 (5)
$$\rho_b = \frac{M_{\text{sat}}}{(M_{\text{sat}} - M_{\text{imm}})} \times \rho_{\text{water}}, \text{ and}$$

172 (6)
$$\rho_g = \frac{M_{\text{dry}}}{(M_{\text{dry}} - M_{\text{imm}})} \times \rho_{\text{water}},$$

173 with M_{dry} , the mass of the dry sample, M_{sat} the mass of the saturated sample, M_{imm} the
174 mass of the immersed, saturated sample, and ρ_{water} : 1.02 g/cc for a 30g/l salinity, at 0.1
175 MPa and 20-25°C.

176 The closed, unconnected porosity is supposed to be negligible; the connected porosity
177 (in %) is :

178 (7)
$$\phi = 100 \times \frac{(M_{\text{sat}} - M_{\text{dry}})}{(M_{\text{sat}} - M_{\text{imm}})}.$$

179

180

181 **Results**

182 Measurements have been carried out on a series of 109 samples (Table1, 2 and 3,
183 Plate 1) taken from the entire core in IODP Hole U1309D, which group as 7 oxide
184 gabbros (oxide content > 2%), 72 gabbros and olivine gabbros, 14 troctolitic gabbros
185 and troctolites, 16 olivine-rich troctolites (Olivine > ~70%) (see Blackman, Ildefonse,
186 John, Ohara, Miller, MacLeod et al., 2006, for further descriptions of the lithologies
187 recovered in IODP Hole U1309D).

188 The data quality is variable and has been visually assessed on a case-by-case basis
189 (using an empirical scale for the fit quality from 1_good_ to 3_bad_, Fig. 1, Table 3). In 25
190 cases, the lowest salinity point tends to be low enough that it causes a deflection of the

191 Revil and Glover (1998) model fit curve toward lower C_s values (Fig. 1c). This behavior
192 was observed by Revil et al (2002) in volcanoclastic material, and ascribed to the
193 occurrence of zeolite in the samples. It is also seen together with unusually high surface
194 conductivities, which is also the case in our sample set; the 25 samples that show a
195 deflection in the fit curve have high surface conductivities, > 2.5 mS/m (mean = 19.7
196 mS/m) while the others have much lower surface conductivities, < 2.6 mS/m (mean =
197 0.57 mS/m). Zeolite was described in Hole U1309D rocks (Blackman, Ildefonse, John,
198 Ohara, Miller, MacLeod et al., 2006), hence a similar behavior may be seen here.
199 However, zeolite occurrence was only shown in the lower half of the hole, below ~ 700
200 mbsf (Blackman, Ildefonse, John, Ohara, Miller, MacLeod et al., 2006), while this
201 electrical behavior is observed in 14 samples evenly distributed above 700 mbsf.
202 Assessing the potential role of zeolite in the measured samples requires characterizing
203 their alteration mineralogy, which is beyond the objective of this data report. An
204 alternative, or complementary contributor could be serpentinite and/or associated
205 minerals (brucite, talc, magnetite, ...), as many of these samples have a primary olivine-
206 rich composition. We could not, though, identify a simple relationship between this
207 peculiar electrical behavior and a simple compositional or textural parameter such as
208 the amount of serpentinite (several heavily serpentinitized samples do not show this
209 behavior), or the degree of fracturation. One additional complexity to the problem of
210 understanding this behavior is that in several cases, the low salinity deflection of the
211 Revil and Glover (1998) model fit curve is not observed, while the lowest salinity
212 measurements clearly lies below the fit curve (e.g., Fig. 1b). Some poor quality
213 measurements in the higher salinity range, for example, may preclude the model to
214 properly fit the whole data set. When removing these samples from the data set, the

215 remaining samples that show the standard curve fit as shown in figure 1a all correspond
216 to sample with low degree (<10%) of serpentinization.

217 In 21 samples, one (or two in a few cases) point in the series of conductivity
218 measurements was so out of range (2 or more orders of magnitude) compared to the
219 other points that we decided to remove them (Fig. 1c). In the majority of these 21 cases,
220 the "bad" point was the lowest salinity one, as illustrated in figure 1c, and we cannot
221 exclude that these correspond to end-member versions of the zeolite-like behavior
222 described above. Except for one oxide gabbro, these contain significant amount of more
223 or less altered olivine (olivine gabbro to olivine-rich troctolite).

224 The standard errors on F and C_s obtained from the analysis detailed above are given
225 in table 2, and shown in downhole distributions of F and C_s for both the Waxman and
226 Smits (1968), and Revil and Glover (1998) models (Fig. 2). In most cases, the largest
227 errors are smaller than the small-scale trends observed in these distributions, which
228 then must correspond to real changes in some first-order controlling parameter(s) such
229 as porosity or alteration. Downhole distributions of electrical properties are also shown
230 in figure 3, together with porosity, density, and compared to the downhole distribution
231 of lithology, variation of hand sample alteration, and borehole electrical resistivity.

232 As classically done for electrical properties, they are shown in figure 4 as a function of
233 sample porosity ϕ . The already know correlations in gabbros (i.e., \sim linear decrease of F
234 and increase of C_s , τ and m with ϕ , Ildefonse and Pezard, 2001; Einaudi et al., 2005), also
235 seen in granites (Belghoul, 2007), are still present, but somehow disturbed by samples
236 that tend to have higher C_s and lower F at more or less constant ϕ (\sim 1%). As a result, τ
237 and m tend to be more scattered, especially when abundant olivine/serpentine is
238 present. Figure 5 shows the variations of ϕ , τ and m as a function of the degree of

239 fracturation (intensity of cataclastic fabric, as characterized onboard on hand samples)
240 and the degree of serpentinization. Note that stronger serpentinization does not change
241 (or even decreases slightly) porosity, and tends to correspond to a simpler geometry of
242 the porous network (slightly lower τ and m). Not surprisingly, ϕ , τ and m tend to
243 increase in more fractured rocks.

244

245 **Acknowledgements** - This research used samples and/or data provided by the
246 Integrated Ocean Drilling Program (IODP). Funding for this research was provided by
247 the CNRS-INSU program DyETI (Dynamique et Evolution de la Terre Interne). We are
248 grateful to Christophe Nevado and Doriane Delmas for providing high-quality thin
249 sections.

250

251

252 **References**

253 Archie, G.E., 1942. The electrical resistivity log as an aid in determining some reservoir
254 characteristics. J. Pet. Techn., 5: 1-8.

255 Belghoul, A., 2007. Caractérisation petrophysique et hydrodynamique du socle cristallin.
256 Unpublished "thèse de doctorat", Université Montpellier 2.

257 Blackman, D.K., Ildefonse, B., John, B.E., Ohara, Y., Miller, D.J., MacLeod, C.J., and the
258 Expedition 304/305 Scientists, 2006. Proc. IODP, 304/305: College Station TX
259 (Integrated Ocean Drilling Program Management International, Inc.).

260 doi:10.2204/iodp.proc.304305.2006

261 Cannat, M., Karson, J.A., Miller, D.J., et al., 1995. Proc. ODP, Init. Repts, 153: College
262 Station, TX (Ocean Drilling Program). doi:10.2973/odp.proc.ir.153.1995

263 Clennell, M.B., 1997. Tortuosity: a guide through the maze. In: M.A. Lovell and P.K.
264 Harvey (Editors), Developments in petrophysics. Geol. Soc. Spec. Pub., London, pp.
265 299-344. doi:10.1144/GSL.SP.1997.122.01.18

266 Dick, H.J.B., Natland, J.H., Miller, D.J., et al., 1999. Proc. ODP, Init. Repts., 176: College
267 Station, TX (Ocean Drilling Program). doi:10.2973/odp.proc.ir.176.1999

268 Einaudi, F., Pezard, P.A., Cochemé, J.J., Coulon, C., Laverne, C., and Godard, M., 2000.
269 Petrography, geochemistry, and physical properties of a continuous extrusive
270 section from the Hilti massif, Semail ophiolite. Mar. Geoph. Res., 21, 387-407.
271 doi:10.1023/A:1026752415989

272 Einaudi, F., Pezard, P., Ildefonse, B., and Glover, P., 2005. Electrical properties of gabbros
273 from Hole 1105A, SW Indian Ridge. In "Petrophysics of Crystalline Rocks" (P.K.
274 Harvey, T.S. Brewer, P.A. Pezard, and V.A. Petrov, eds), Geological Society Spec. Pub.,
275 240, 179-193. doi:10.1144/GSL.SP.2005.240.01.14

276 Expedition 304/305 Scientists, 2006. Methods. In Blackman, D.K., Ildefonse, B., John,
277 B.E., Ohara, Y., Miller, D.J., MacLeod, C.J., and the Expedition 304/305 Scientists, Proc.
278 IODP, 304/305: College Station TX (Integrated Ocean Drilling Program Management
279 International, Inc.). doi:10.2204/iodp.proc.304305.102.2006

280 Gillis, K., Mével, C., Allan, J., et al., 1993. Proc. ODP, Init. Repts., 147: College Station, TX
281 (Ocean Drilling Program). doi:10.2973/odp.proc.ir.147.1993

282 Goldberg, D., 1997. The role of downhole measurements in marine geology and
283 geophysics. *Rev. Geophys.* 35, 315–342. doi:10.1029/97RG00221

284 Guéguen, Y. and Palciauskas, V., 1992. *Introduction à la physique des roches*. Hermann,
285 Paris, 299 pp.

286 Ildefonse, B., Blackman, D.K., John, B.E., Ohara, Y., Miller, D.J., MacLeod, C.J., and the IODP
287 Expeditions 304-305 Scientists, 2006. IODP Expeditions 304 & 305 Characterize the
288 Lithology, Structure, and Alteration of an Oceanic Core Complex. *Scientific Drilling*,
289 3, 4-11, doi:10.2204/iodp.sd.3.01.2006.

290 Ildefonse, B., Blackman, D.K., John, B.E., Ohara, Y., Miller, D.J., MacLeod, C.J., and
291 Integrated Ocean Drilling Expeditions 304/305 Science Party, 2006. Oceanic core
292 complexes and crustal accretion at slow-spreading ridges. *Geology*, 35(7):623–626.
293 doi:10.1130/G23531A.1

294 Ildefonse, B., and Pezard, P., 2001. Electrical properties of slow-spreading ridge gabbros
295 from ODP Site 735, Southwest Indian Ridge. *Tectonophysics*, 330:69-92.
296 doi:10.1016/S0040-1951(00)00220-1

297 Ildefonse, B., Valsardieu, B., Pezard, P., Mainprice, D. and Garrido, C.J., 1999. Petrophysics
298 and anisotropy of gabbros and peridotites from the Oman ophiolite. In: B. Leiss, K.
299 Ullemeyer and K. Weber (Editors), *Textures and physical properties of rocks*.
300 *Göttinger Arbeiten zur Geologie und paläontologie*. Geologische Institute,
301 Universität Göttingen, pp. 73-74.

302 Kelemen, P.B., Kikawa, E., Miller, D.J., et al., 2004. *Proc. ODP, Init. Repts.*, 209: College
303 Station, TX (Ocean Drilling Program). doi:10.2973/odp.proc.ir.209.2004

304 McCaig, A.M., Cliff, R.A., Escartin, J., Fallick, A.E. and MacLeod, C.J., 2007. Oceanic
305 detachment faults focus very large volumes of black smoker fluids. *Geology*, 35: 935-
306 938. doi: 10.1130/G23657A.1

307 Pettigrew, T.L., Casey, J.F., Miller, D.J., et al., 1999. Proc. ODP, Init. Repts., 179: College
308 Station, TX (Ocean Drilling Program). doi:10.2973/odp.proc.ir.179.1999

309 Pape, H., Riepe, L. and Schopper, J.R., 1985. Petrophysical detection of microfissures in
310 granite. *Trans. SPWLA, 26th Ann. Log. Symp.*, Paper P.

311 Pezard, P.A., 1990. Electrical properties of Mid-Ocean Ridge basalt and implications for
312 the structure of the upper oceanic crust in Hole 504B. *J. Geophys. Res.* 95, 9237-
313 9264. doi:10.1029/JB095iB06p09237

314 Pezard, P.A. et al., 1999. Physical properties of granite, with application to nuclear waste
315 storage in subsurface. In: B. Leiss, K. Ullemeyer and K. Weber (Editors), *Textures*
316 *and physical properties of rocks. Göttinger Arbeiten zur Geologie und paläontologie.*
317 *Geologische Institute, Universität Göttingen*, pp. 149-151.

318 Pezard, P.A., Howard, J.J., and Goldberg, D., 1991. Electrical conduction in oceanic
319 gabbros, Hole 735B, Southwest Indian Ridge. In Von Herzen, R., Robinson, P.T., et al.,
320 *Proc. ODP, Sci. Results*, 118: College Station, TX (Ocean Drilling Program), 323-331.
321 doi:10.2973/odp.proc.sr.118.161.1991

322 Pezard, P.A., Luthi, S.M., 1988. Borehole electrical images in the basement of the Cajon
323 Pass Scientific Drillhole, California; fracture identification and tectonic implications.
324 *Geophys. Res. Lett.* 15, 1017-1020. doi:10.1029/GL015i009p01017

325 Revil, A. and Glover, P.W.J., 1998. Nature of surface electrical conductivity in natural
326 sands, sandstones, and clays. *Geoph. Res. Lett.*, 25: 691-694.
327 doi:10.1029/98GL00296

328 Revil, A., D. Hermitte, E. Spangenberg, and J. J. Cochemé (2002), Electrical properties of
329 zeolitized volcanoclastic materials, *J. Geophys. Res.*, 107(B8), 2168,
330 doi:10.1029/2001JB000599.

331 Robinson, P.T, Von Herzen, R., et al., 1989. *Proc. ODP, Init. Repts.*, 118: College Station, TX
332 (Ocean Drilling Program). doi:10.2973/odp.proc.ir.118.1989

333 Walsh, J.B., Brace, W.F., 1984. The effect of pressure on porosity and the transport
334 properties of rocks. *J. Geophys. Res.* 89, 9425–9431. doi:10.1029/JB089iB11p09425

335 Waxman, M.H. and Smits, L.J.M., 1968. Electrical conductivities in oil-bearing shaly
336 sands. *Soc. Pet. Eng. J.*, 8: 107-122. doi:10.2118/1863-A

337

338

339 **Figure, Table, and Plate Captions**

340 Figure 1 - Examples of plots of the core conductivities as a function of the saturating
341 fluid conductivities. Best-fit curves are calculated using the Waxman and Smits (1968),
342 and Revil and Glover (1998) models (orange curve, WG, and purple curve, RG,
343 respectively). a) Example of good fit. b) Example of bad fit (higher errors on F and C_s
344 estimates, see Fig. 2). c) Example of good fit, with the deflection of the RG fit curve at low
345 salinities, pointing to lower Surface conductivities. d) Example of curve where a good fit
346 is obtained by removing a point (in the case the lowest salinity one) that is several

347 orders of magnitudes out of range compared to the adjacent one. See text for further
348 explanations.

349

350 Figure 2 – Downhole distributions of the electrical formation factor F and surface
351 Conductivity C_s calculated using both the Waxman and Smits (1968), and the Revil and
352 Glover (1998) models. The error bars show the standard error obtained for F and C_s
353 from the fit curves (see examples in Fig. 1).

354

355 Figure 3 – Compared downhole distributions of a) lithology, b) hand sample alteration,
356 c) borehole electrical resistivity, d) porosity, e) grain density, and f to i) electrical
357 properties (F , C_s , τ and m).

358

359 Figure 4 – Variations of the electrical properties (a : Formation factor F , b : Surface
360 conductivity C_s , c: tortuosity τ , d : cementation index m) with sample porosity. Electrical
361 properties are calculated from the Revil and Glover (1998) model.

362

363 Figure 5 – Variations of porosity f (a and b), electrical tortuosity (c and d), and electrical
364 cementation index m (e and f) with the cataclastic fabric intensity, and the degree of
365 serpentinization, respectively. The cataclastic fabric intensity scale is the one used
366 during shipboard core descriptions (Expedition 304/305 Scientists, 2006), with 0 =
367 undeformed, 1 = minor fracturing, 2 = moderate fracturing, 3 = dense, anastomosing
368 fracturing and incipient brecciation (<20% matrix), 4 = well-developed fault brecciation

369 (20-70% matrix), and clast rotation, 5 = cataclasite (>70% matrix). Both the cataclastic
370 fabric intensity and the degree of serpentinization are the one of the intervals from
371 where the measured sample come from, as estimated onboard from macroscopic
372 observation of hand samples. Electrical tortuosity and cementation index are calculated
373 from the Revil and Glover (1998) model.

374

375 Table 1 – List of measured samples, and their resistivity (in $\Omega.m$) at 6 different salinities
376 of the saturating fluid. The sample batch number refers to the Table 2 data.

377

378 Table 2 – Resistivity of the saturating fluid at the 6 different salinities in the 5 separate
379 sample batches (the deviations from the nominal resistivity at the given fluid salinity are
380 due to progressive re-equilibration between the samples and the fluid before the
381 measurements are done).

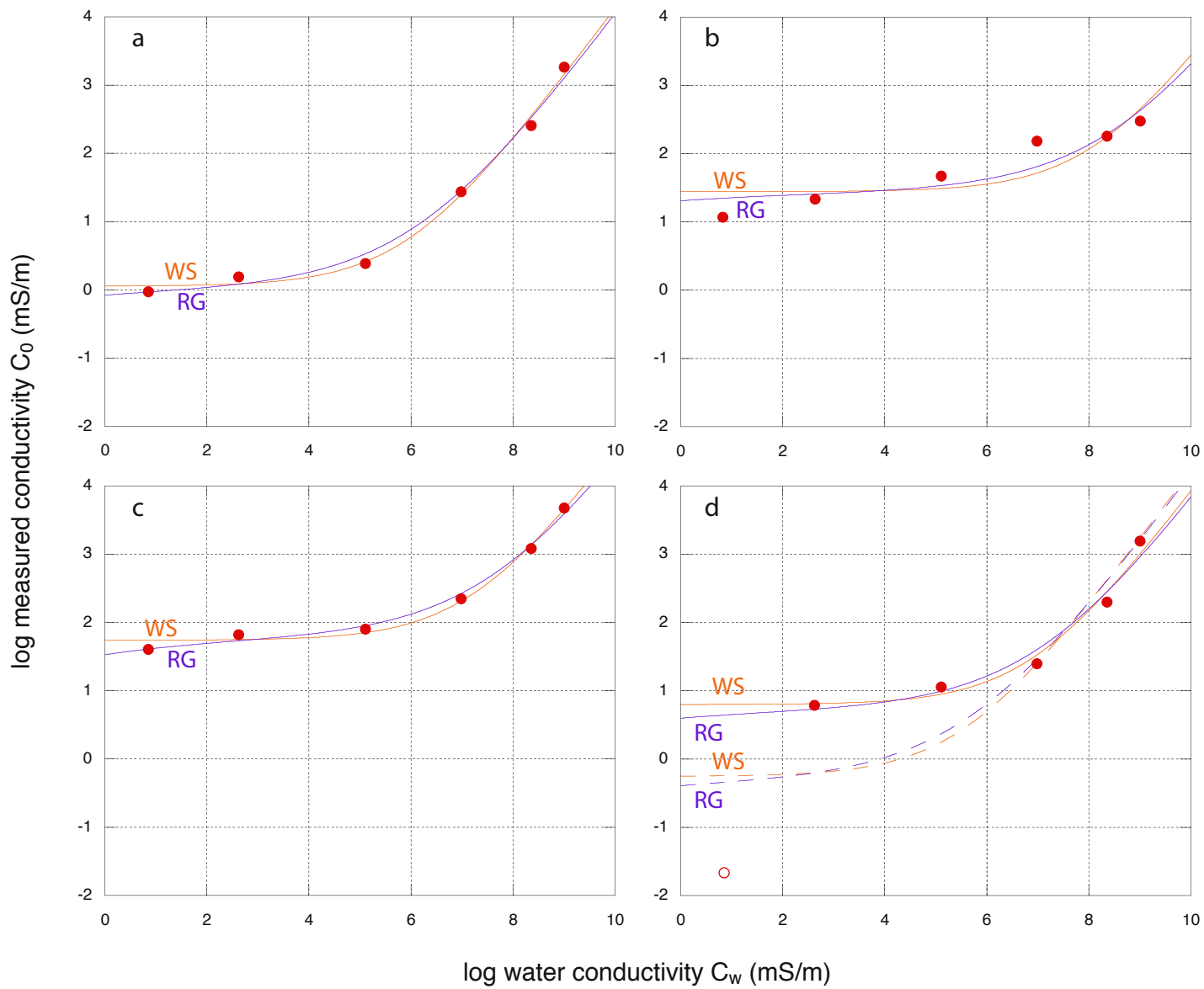
382

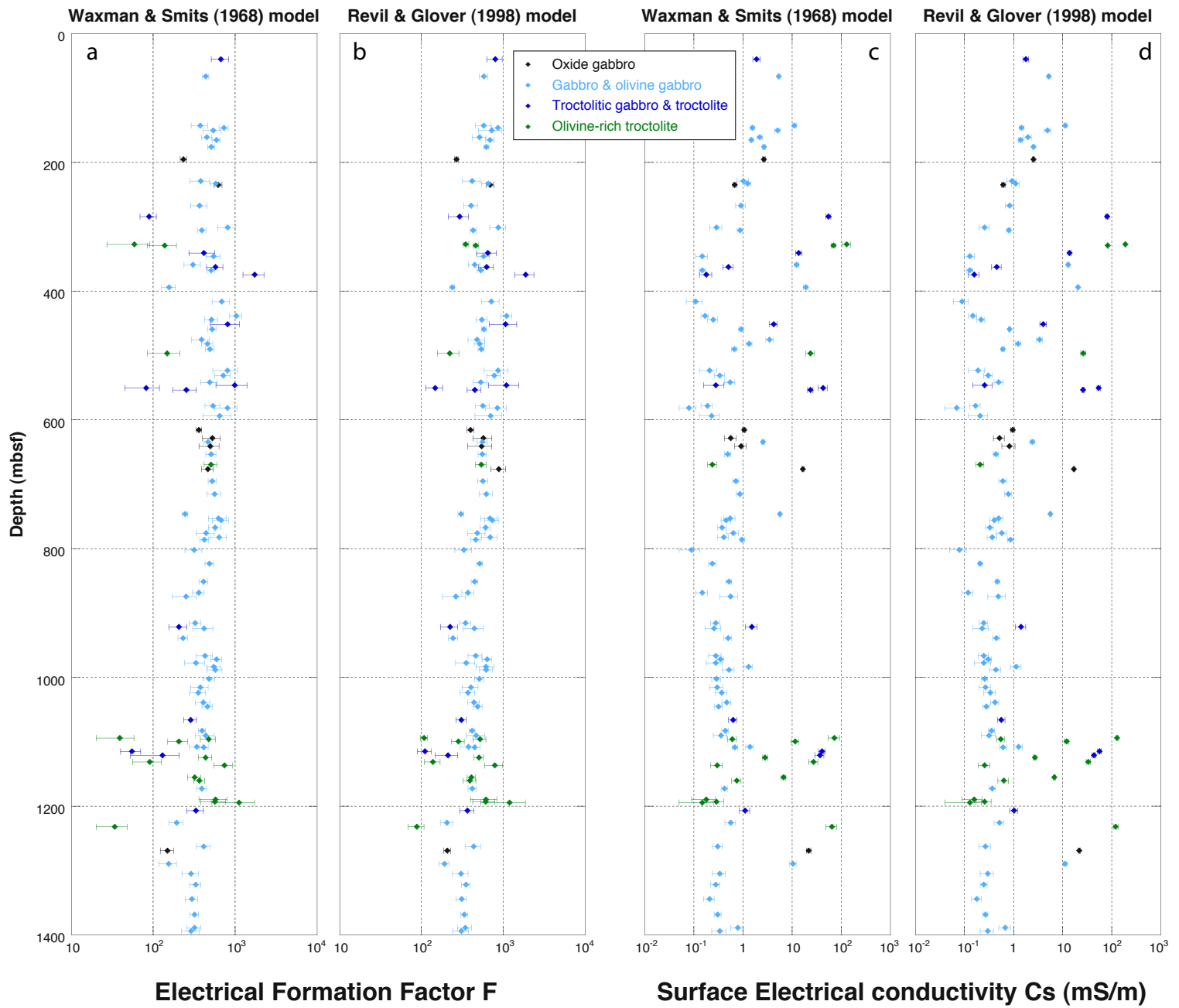
383 Table 3 – Porosity, Bulk and grain density, electrical properties, core bulk alteration,
384 degree of serpentinization, and cataclastic fabric intensity of the measured samples.

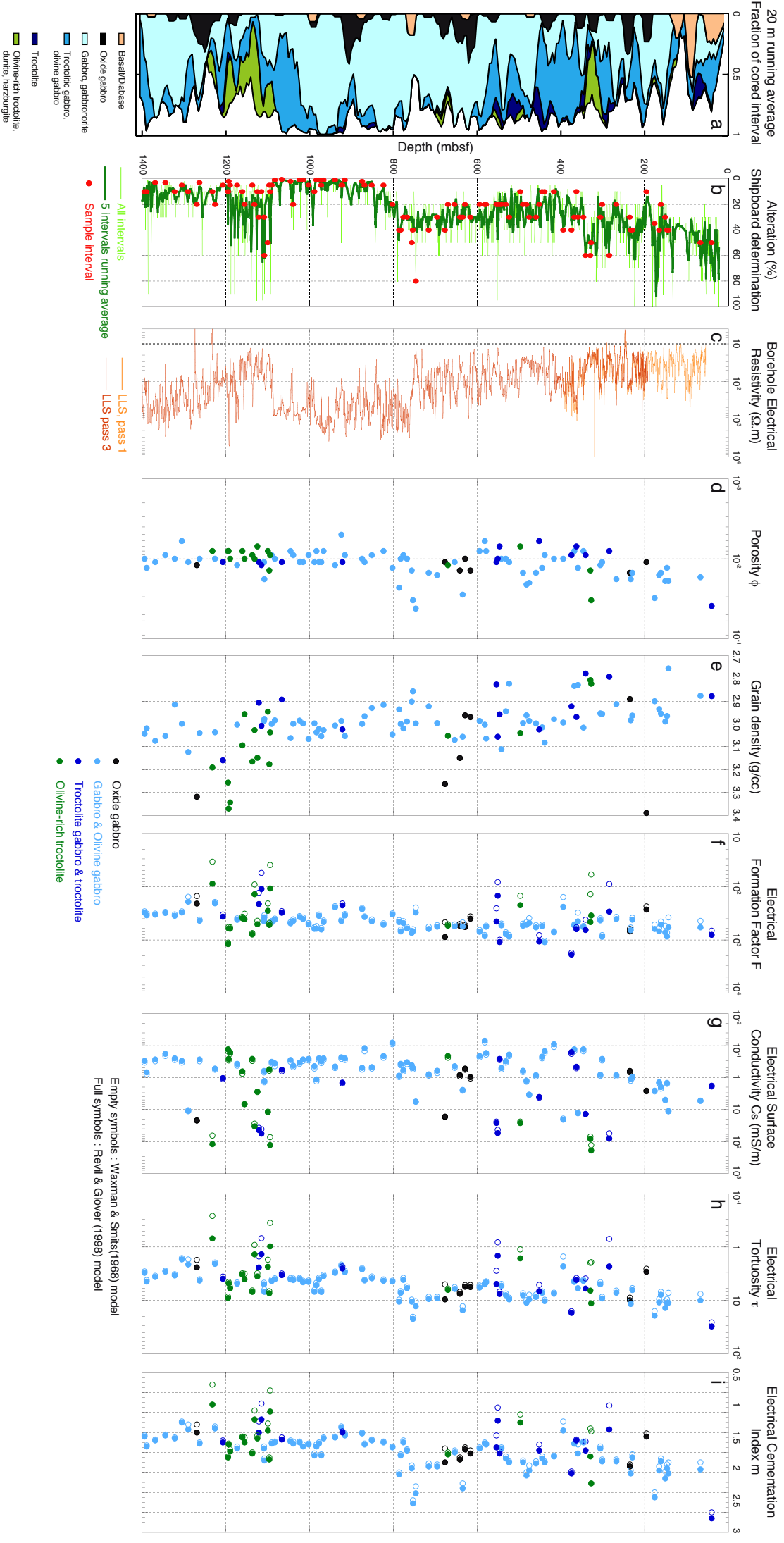
385

386 Plate 1 – Microphotographs of sample thin sections in plane- and cross-polarized light.

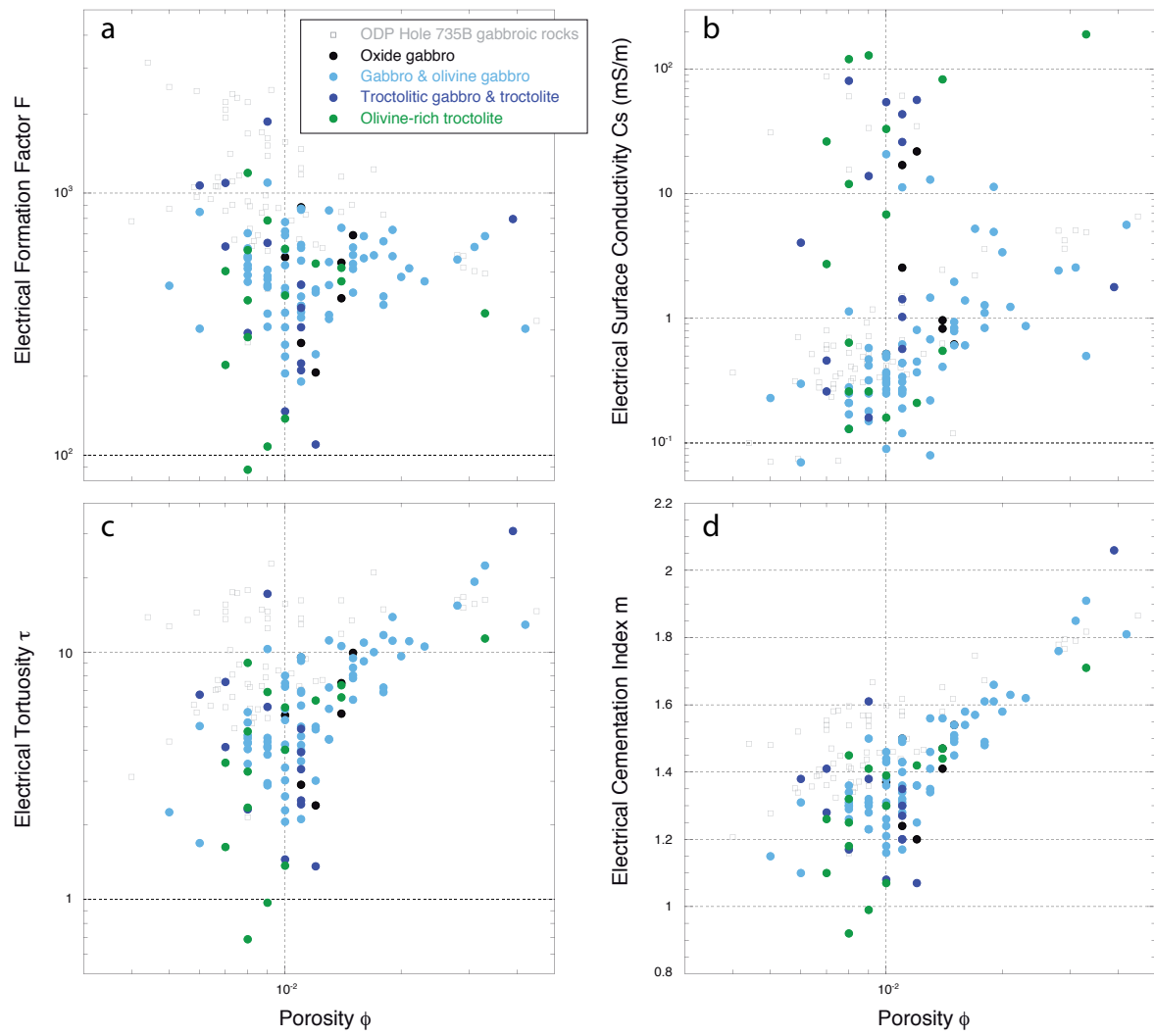
387 Thin section were done after chips taken from the minicore ends; each section is about
388 2,54 cm in diameter (1 inch).

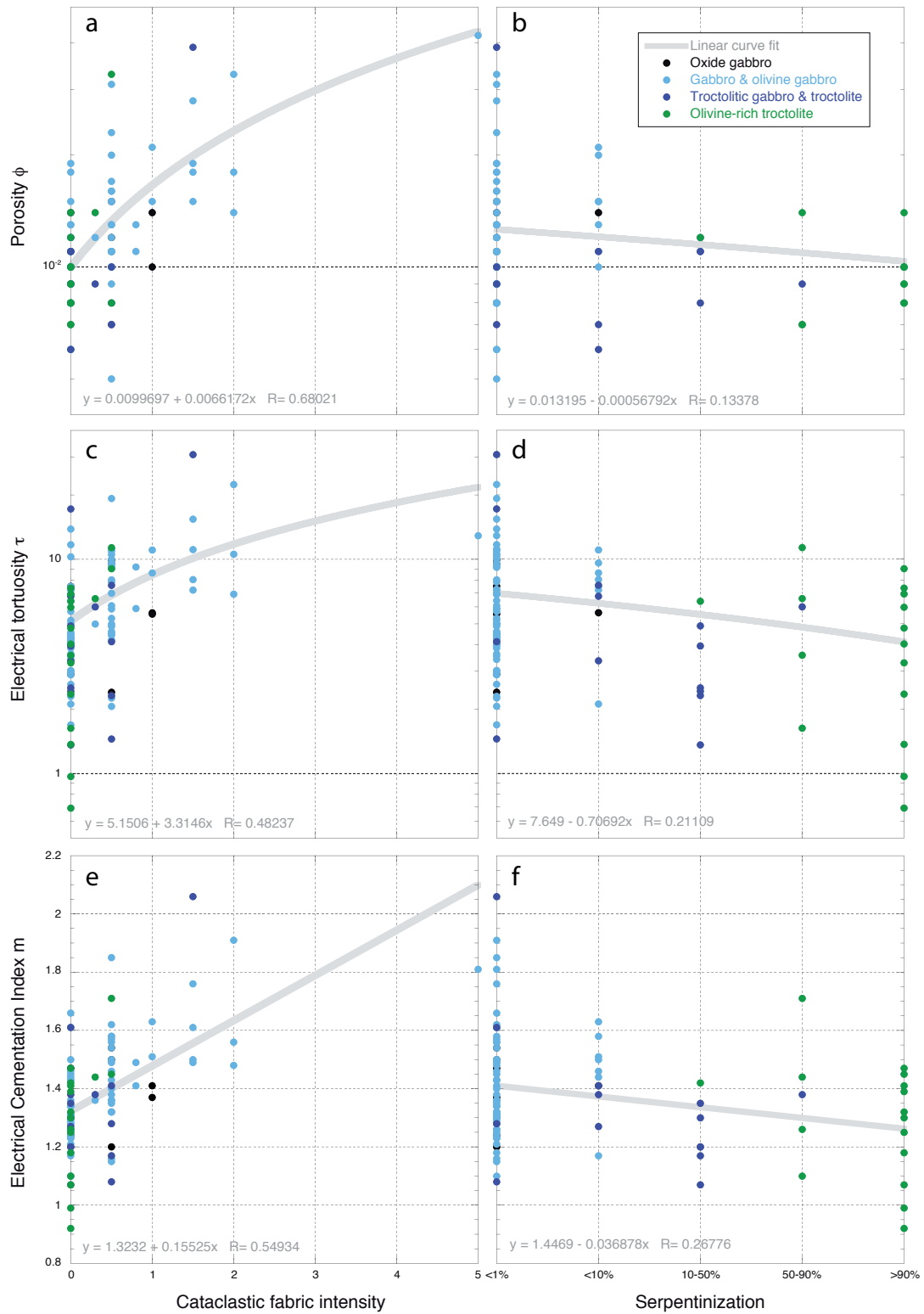






Ildefonse et al. Fig 3



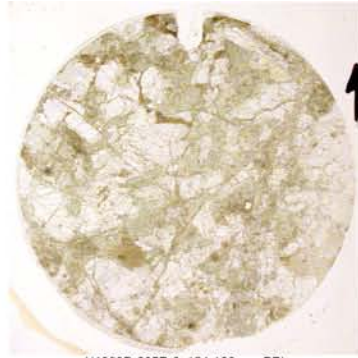


| Sample batch | Resistivity @ ~0.006 g/l (Ohm.m) | Resistivity @ ~0.06 g/l (Ohm.m) | Resistivity @ ~0.6 g/l (Ohm.m) | Resistivity @ ~6 g/l (Ohm.m) | Resistivity @ ~30 g/l (Ohm.m) | Resistivity @ ~60 g/l (Ohm.m) |
|--------------|--|---------------------------------------|--------------------------------------|------------------------------------|-------------------------------------|-------------------------------------|
| 1 | 427.4 | 72.46 | 6.068 | 0.9272 | 0.2347 | 0.1233 |
| 2 | 440.5 | 73.53 | 6.057 | 0.9275 | 0.2353 | 0.1230 |
| 3 | 432.9 | 72.99 | 6.079 | 0.9273 | 0.2358 | 0.1227 |
| 4 | 436.7 | 71.94 | 6.079 | 0.9272 | 0.2347 | 0.1227 |
| 5 | 438.6 | 73.53 | 6.075 | 0.9301 | 0.2353 | 0.1230 |

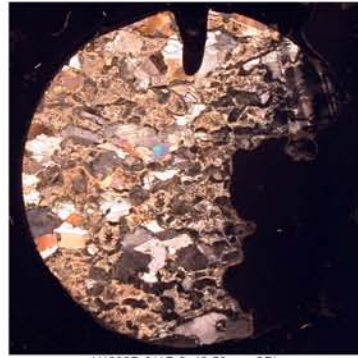
| Sample ID | Depth (m) | Lithology | Porosity P_v | Waxman & Smits (1968) model | | | | | | Revil & Glover (1998) model | | | | | | catenatic fabric | | | | | | | | | | |
|-------------------------------|-----------|---------------------------|---------------------------|----------------------------------|------------------------------|-----------------------------------|------------------------------|--------------------|---------|-----------------------------|-------------------------|---------------------|-----------|--------------------|------|------------------|------------|-------------|---------------------|------|----------------------|------|------------------|------------------|------------------|-----|
| | | | | Bulk density ρ_b | | Grain density ρ_g | | Surface conduction | | Electrical Tomuosity | | Cementation index m | | Surface conduction | | | Tortuosity | | Cementation index n | | core bulk alteration | | | | | |
| | | | | ρ_b | (ρ_b/ρ_w) | ρ_g | (ρ_g/ρ_w) | F. st. | Cs. st. | F. fit | fraction R | F. Error | Cs. Error | fit quality | R | | R | fit quality | R | R | | | | | | |
| 304-U1300D-3R-3, 124-126 cm | 40.11 | Tractolite Gabbro | 0.039 | 2.81 | 2.88 | 671 | 160 | 1.90 | 0.32 | 0.95 | 0.2 | 26.0 | 2.00 | 797 | 167 | 1.79 | 0.24 | 0.97 | 0.22 | 30.9 | 2.06 | 30 | <math><10</math> | 1.5 | | |
| 304-U1300D-11R-2, 48-50 cm | 66.77 | Gabbro | 0.017 | 2.84 | 2.88 | 438 | 37 | 5.37 | 0.26 | 0.99 | 0.2 | 6.7 | 1.50 | 579 | 68 | 5.25 | 0.30 | 0.99 | 0.18 | 10.0 | 1.57 | 50 | <math><10</math> | 0.5 | | |
| 304-U1300D-25R-1, 33-35 cm | 143.03 | Gabbro | 0.019 | 2.72 | 2.76 | 375 | 85 | 11.22 | 1.09 | 0.94 | 0.2 | 0.46 | 7.2 | 575 | 122 | 11.39 | 0.83 | 0.97 | 0.57 | 11.1 | 1.61 | 40 | <math><10</math> | 1.5 | | |
| 304-U1300D-25R-3, 84-86 cm | 166.49 | Olivine Bearing Gabbro | 0.015 | 2.94 | 2.98 | 592 | 59 | 1.50 | 0.12 | 0.99 | 0.15 | 9.4 | 1.54 | 859 | 140 | 1.47 | 0.29 | 0.94 | 0.32 | 10.2 | 1.56 | 30 | <math><10</math> | 1.5 | | |
| 304-U1300D-26R-3, 83-85 cm | 150.94 | Olivine Bearing Gabbro | 0.019 | 2.95 | 2.99 | 540 | 133 | 5.10 | 0.66 | 0.94 | 0.2 | 0.36 | 10.3 | 724 | 230 | 4.96 | 0.71 | 0.94 | 0.2 | 13.9 | 1.66 | 30 | <math><10</math> | 0 | | |
| 304-U1300D-28R-4, 45-47 cm | 161.38 | Gabbro | 0.015 | 2.93 | 2.95 | 453 | 63 | 2.23 | 0.29 | 0.99 | 0.17 | 6.9 | 1.46 | 514 | 97 | 1.97 | 0.33 | 0.98 | 0.17 | 7.8 | 1.49 | 20 | <math><10</math> | 0.5 | | |
| 304-U1300D-29R-3, 64-66 cm | 165.45 | Gabbro | 0.016 | 2.90 | 2.94 | 592 | 59 | 1.50 | 0.12 | 0.99 | 0.15 | 9.4 | 1.54 | 859 | 140 | 1.47 | 0.29 | 0.94 | 0.16 | 10.9 | 1.58 | 40 | <math><10</math> | 0.5 | | |
| 304-U1300D-32R-1, 9-11 cm | 176.39 | Olivine Bearing Gabbro | 0.031 | 2.84 | 2.90 | 514 | 52 | 2.70 | 0.19 | 0.99 | 0.2 | 0.22 | 15.9 | 623 | 38 | 2.57 | 0.10 | 1.00 | 0.24 | 19.3 | 1.85 | 35 | <math><10</math> | 0.5 | | |
| 304-U1300D-36R-1, 10-12 cm | 195.7 | Oxide Gabbro | 0.011 | 3.36 | 3.39 | 235 | 21 | 2.67 | 0.21 | 0.99 | 0.2 | 0.11 | 2.6 | 268 | 15 | 2.56 | 0.12 | 1.00 | 0.12 | 2.9 | 1.24 | 10 | <math><10</math> | 0 | | |
| 304-U1300D-43R-1, 57-79 cm | 229.37 | Olivine Gabbro | 0.015 | 2.93 | 2.96 | 382 | 103 | 10.2 | 0.27 | 0.96 | 0.3 | 0.07 | 5.9 | 417 | 99 | 0.94 | 0.21 | 0.97 | 0.07 | 6.4 | 1.45 | 40 | <math><10</math> | 0 | | |
| 304-U1300D-44R-1, 18-20 cm | 216.58 | Olivine Gabbro | 0.012 | 2.95 | 2.98 | 583 | 82 | 1.26 | 0.18 | 0.99 | 0.1 | 10.4 | 1.58 | 835 | 117 | 1.15 | 0.20 | 0.99 | 0.13 | 11.7 | 1.61 | 40 | <math><10</math> | 0.5 | | |
| 304-U1300D-44R-2, 83-85 cm | 235.53 | Disseminated Oxide Gabbro | 0.015 | 2.86 | 2.89 | 621 | 68 | 0.68 | 0.06 | 1.00 | 1.0 | 0.08 | 8.9 | 691 | 69 | 0.62 | 0.05 | 1.00 | 0.18 | 9.9 | 1.54 | 30 | <math><10</math> | 0.5 | | |
| 304-U1300D-51R-1, 74-76 cm | 267.54 | Gabbro | 0.018 | 2.88 | 2.91 | 369 | 82 | 0.91 | 0.20 | 0.97 | 0.2 | 0.06 | 6.6 | 404 | 77 | 0.84 | 0.16 | 0.98 | 0.06 | 7.2 | 1.49 | 20 | <math><10</math> | 1.5 | | |
| 304-U1300D-54R-3, 45-47 cm | 284.34 | Tractolite | 0.008 | 2.78 | 2.79 | 89 | 20 | 55.22 | 6.24 | 0.96 | xx3 | 0.50 | 0.07 | 293 | 81 | 80.92 | 6.40 | 0.98 | xx3 | 0.83 | 2.3 | 117 | 60 | 10-50% | 0.5 | |
| 304-U1300D-55R-1, 110-112 cm | 301.54 | Olivine Gabbro | 0.010 | 2.94 | 2.96 | 810 | 196 | 0.29 | 0.08 | 0.97 | 0.2 | 0.05 | 8.8 | 873 | 191 | 0.26 | 0.06 | 0.98 | 0.04 | 9.2 | 1.49 | 20 | <math><10</math> | 0.8 | | |
| 304-U1300D-59R-1, 58-60 cm | 305.78 | Olivine Gabbro | 0.012 | 2.93 | 2.95 | 393 | 48 | 0.88 | 0.11 | 0.99 | 0.2 | 0.06 | 4.6 | 429 | 35 | 0.81 | 0.07 | 1.00 | 0.1 | 0.6 | 5.0 | 1.36 | 30 | <math><10</math> | 0.3 | |
| 304-U1300D-63R-3, 41-43 cm | 327.77 | Olivine-rich Tractolite | 0.033 | 2.77 | 2.82 | 59 | 32 | 130.26 | 23.33 | 0.77 | xx3 | 0.60 | 1.9 | 348 | 29 | 190.94 | 3.82 | 1.00 | 0.1 | 0.93 | 11.4 | 1.71 | 50 | 50-90% | 0.5 | |
| 304-U1300D-64R-1, 58-60 cm | 329.78 | Olivine-rich Tractolite | 0.014 | 2.78 | 2.81 | 138 | 53 | 70.20 | 7.09 | 0.82 | 0.3 | 0.66 | 2.0 | 461 | 31 | 83.12 | 0.94 | 1.00 | 1.0 | 0.88 | 6.6 | 1.44 | 60 | 50-90% | 0.3 | |
| 304-U1300D-66R-2, 93-95 cm | 341.23 | Tractolite | 0.009 | 2.76 | 2.78 | 405 | 144 | 13.75 | 1.74 | 0.86 | 0.3 | 0.53 | 3.9 | 646 | 174 | 13.91 | 1.10 | 0.95 | 0.3 | 0.64 | 6.0 | 1.38 | 60 | 50-90% | 0.3 | |
| 304-U1300D-67R-3, 17-19 cm | 346.43 | Gabbro (fine-grained) | 0.008 | 3.00 | 3.02 | 548 | 105 | 0.15 | 0.04 | 0.99 | 0.2 | 0.02 | 4.1 | 574 | 95 | 0.13 | 0.03 | 0.99 | 0.2 | 0.02 | 4.3 | 1.30 | 30 | <math><10</math> | 0 | |
| 304-U1300D-70R-2, 76-78 cm | 359.45 | Olivine Gabbro | 0.013 | 2.81 | 2.83 | 306 | 69 | 12.39 | 1.34 | 0.96 | 0.2 | 0.43 | 4.0 | 426 | 73 | 13.04 | 0.82 | 0.99 | 0.2 | 0.54 | 5.9 | 1.41 | 30 | <math><10</math> | 0.8 | |
| 304-U1300D-71R-1, 14-16 cm | 362.94 | Tractolite/Gabbro | 0.007 | 2.96 | 2.97 | 576 | 129 | 0.51 | 0.12 | 0.98 | 0.2 | 0.06 | 3.8 | 127 | 66 | 130 | 0.46 | 0.10 | 0.98 | 0.2 | 0.05 | 4.1 | 1.28 | 10 | <math><10</math> | 0.5 |
| 304-U1300D-71R-5, 13-15 cm | 368.26 | Olivine Gabbro | 0.008 | 2.94 | 2.96 | 510 | 52 | 0.15 | 0.02 | 0.99 | 0.2 | 0.02 | 6.3 | 531 | 51 | 0.13 | 0.03 | 0.99 | 0.2 | 0.01 | 4.5 | 1.31 | 40 | <math><10</math> | 0.5 | |
| 304-U1300D-73R-2, 86-88 cm | 374.71 | Tractolite/Gabbro | 0.009 | 2.91 | 2.92 | 1742 | 497 | 0.18 | 0.05 | 0.96 | 0.2 | 0.06 | 16.0 | 159 | 1875 | 489 | 0.16 | 0.04 | 0.97 | 0.2 | 0.06 | 17.2 | 1.61 | 40 | <math><10</math> | 0 |
| 304-U1300D-77R-3, 21-23 cm | 394.34 | Olivine Gabbro | 0.010 | 2.98 | 2.99 | 156 | 30 | 19.03 | 1.90 | 0.96 | 0.2 | 0.37 | 1.5 | 238 | 17 | 20.84 | 0.61 | 1.00 | 1.0 | 0.50 | 2.3 | 1.18 | 40 | <math><10</math> | 0 | |
| 305-U1300D-33R-2, 29-31 cm | 416.44 | Olivine Gabbro | 0.011 | 2.96 | 2.98 | 486 | 164 | 0.11 | 0.04 | 0.98 | 0.2 | 0.01 | 7.2 | 146 | 686 | 0.64 | 0.05 | 1.00 | 1.0 | 0.61 | 7.5 | 1.44 | 50 | <math><10</math> | 0 | |
| 305-U1300D-35R-1, 12-14 cm | 439.02 | Olivine Gabbro | 0.009 | 3.06 | 3.08 | 1035 | 178 | 0.17 | 0.03 | 0.99 | 0.2 | 0.03 | 9.7 | 1097 | 163 | 0.15 | 0.03 | 0.99 | 1.0 | 0.03 | 10.3 | 1.50 | 10 | <math><10</math> | 0 | |
| 305-U1300D-39R-1, 92-94 cm | 447.72 | Olivine Gabbro | 0.013 | 2.99 | 3.02 | 515 | 94 | 0.25 | 0.06 | 0.99 | 0.2 | 0.03 | 6.8 | 546 | 83 | 0.22 | 0.04 | 0.99 | 1.0 | 0.02 | 7.2 | 1.46 | 10 | <math><10</math> | 0 | |
| 305-U1300D-90R-3, 8-10 cm | 451.68 | Tractolite | 0.006 | 3.01 | 3.02 | 814 | 315 | 4.24 | 0.78 | 0.85 | 0.3 | 0.41 | 5.1 | 132 | 1070 | 393 | 4.06 | 0.62 | 0.91 | 0.3 | 0.46 | 6.7 | 1.38 | 20 | <math><10</math> | 0 |
| 305-U1300D-121R-1, 123-125 cm | 459.43 | Olivine Bearing Gabbro | 0.015 | 2.97 | 3.00 | 525 | 99 | 0.92 | 0.10 | 0.99 | 0.2 | 0.09 | 7.8 | 581 | 44 | 0.84 | 0.05 | 1.00 | 1.0 | 0.09 | 8.6 | 1.51 | 30 | <math><10</math> | 1 | |
| 305-U1300D-95R-3, 35-37 cm | 475.73 | Olivine Bearing Gabbro | 0.020 | 2.95 | 2.99 | 390 | 97 | 3.51 | 0.61 | 0.95 | 0.2 | 0.22 | 7.8 | 153 | 479 | 109 | 3.40 | 0.49 | 0.97 | 0.2 | 0.25 | 9.6 | 1.58 | 30 | <math><10</math> | 0.5 |
| 305-U1300D-97R-1, 6-8 cm | 482.26 | Olivine Bearing Gabbro | 0.021 | 2.92 | 2.96 | 461 | 75 | 1.34 | 0.19 | 0.98 | 0.2 | 0.11 | 9.9 | 160 | 517 | 75 | 1.24 | 0.15 | 0.99 | 0.2 | 0.11 | 11.1 | 1.63 | 20 | <math><10</math> | 1 |
| 305-U1300D-98R-3, 96-98 cm | 490.66 | Olivine Bearing Gabbro | 0.015 | 2.97 | 3.00 | 493 | 61 | 0.67 | 0.08 | 0.99 | 0.2 | 0.06 | 7.4 | 148 | 537 | 46 | 0.61 | 0.05 | 1.00 | 1.0 | 0.06 | 8.0 | 1.50 | 20 | <math><10</math> | 1.5 |
| 305-U1300D-100R-1, 2-4 cm | 494.62 | Olivine-rich Tractolite | 0.007 | 3.03 | 3.04 | 148 | 63 | 23.72 | 4.76 | 0.82 | 0.4 | 1.1 | 1.02 | 221 | 65 | 26.40 | 3.02 | 0.95 | 0.5 | 1.6 | 11.0 | 1.10 | 40 | 50-90% | 0 | |
| 305-U1300D-105R-3, 46-48 cm | 523.65 | Olivine Gabbro | 0.011 | 2.80 | 2.82 | 806 | 270 | 0.21 | 0.08 | 0.95 | 0.2 | 0.03 | 8.9 | 149 | 864 | 280 | 0.19 | 0.07 | 0.96 | 0.2 | 0.03 | 9.5 | 1.50 | 30 | <math><10</math> | 0.5 |
| 305-U1300D-107R-2, 52-54 cm | 531.72 | Olivine Bearing Gabbro | 0.010 | 2.92 | 2.94 | 721 | 154 | 0.34 | 0.08 | 0.98 | 0.2 | 0.05 | 7.5 | 144 | 776 | 147 | 0.31 | 0.06 | 0.99 | 0.2 | 0.05 | 8.0 | 1.46 | 20 | <math><10</math> | 0.5 |
| 305-U1300D-109R-2, 69-71 cm | 541.84 | Olivine Bearing Gabbro | 0.010 | 3.09 | 3.11 | 491 | 112 | 0.55 | 0.13 | 0.88 | 0.3 | 0.05 | 4.9 | 135 | 531 | 103 | 0.50 | 0.10 | 0.98 | 0.2 | 0.05 | 5.3 | 1.36 | 20 | <math><10</math> | 0.5 |
| 305-U1300D-110R-2, 74-76 cm | 546.76 | Olivine Gabbro | 0.007 | 2.94 | 2.96 | 689 | 404 | 0.28 | 0.12 | 0.99 | 0.2 | 0.05 | 6.8 | 139 | 1094 | 406 | 0.26 | 0.11 | 0.99 | 0.2 | 0.05 | 7.6 | 1.41 | 20 | <math><10</math> | 0.5 |
| 305-U1300D-111R-2, 17-19 cm | 548.87 | Tractolite/Gabbro | 0.010 | 3.04 | 3.06 | 82 | 37 | 42.80 | 9.11 | 0.81 | 0.3 | 0.41 | 0.8 | 0.95 | 147 | 34 | 54.58 | 4.75 | 0.97 | 0.2 | 0.62 | 1.5 | 1.08 | 20 | <math><10</math> | 0.5 |
| 305-U1300D-111R-4, 19-21 cm | 553.76 | Tractolite | 0.011 | 2.81 | 2.83 | 255 | 81 | 23.74 | 2.88 | 0.91 | xx3 | 0.55 | 2.8 | 123 | 448 | 88 | 26.10 | 1.43 | 0.98 | 0.2 | 0.70 | 4.9 | 1.35 | 20 | 10-50% | 0 |
| 305-U1300D-117R-1, 55-57 cm | 578.75 | Olivine Gabbro | 0.008 | 3.05 | 3.06 | 537 | 109 | 0.19 | 0.05 | 0.99 | 0.2 | 0.02 | 4.4 | 131 | 564 | 106 | 0.17 | 0.04 | 0.99 | 0.2 | 0.02 | 4.6 | 1.32 | 20 | <math><10</math> | 0.5 |
| 305-U1300D-117R-4, 22-24 cm | 582.63 | Gabbro (fine-grained) | 0.012 | 3.03 | 3.05 | 507 | 89 | 0.24 | 0.11 | 0.99 | | | | | | | | | | | | | | | | |



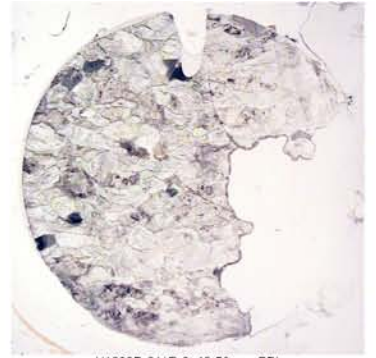
U1309D-005R-3, 124-126 cm, CPL



U1309D-005R-3, 124-126 cm, PPL



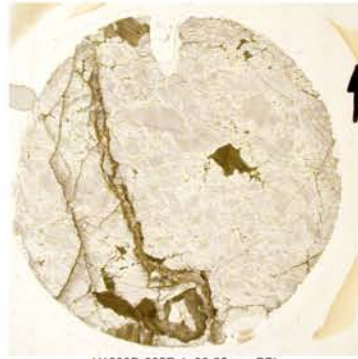
U1309D-011R-2, 48-50 cm, CPL



U1309D-011R-2, 48-50 cm, PPL



U1309D-025R-1, 33-35 cm, CPL



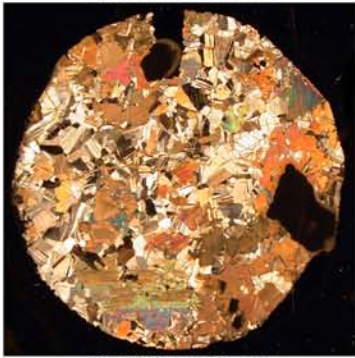
U1309D-025R-1, 33-35 cm, PPL



U1309D-025R-3, 94-96 cm, CPL



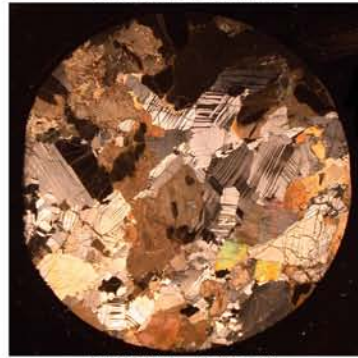
U1309D-025R-3, 94-96 cm, PPL



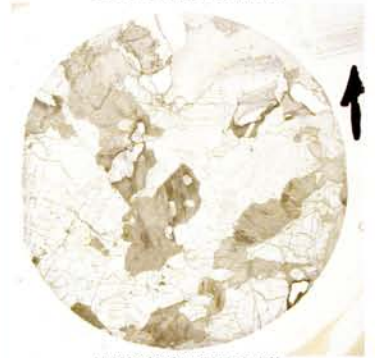
U1309D-026R-3, 83-85 cm, CPL



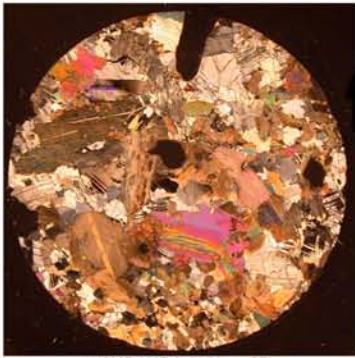
U1309D-026R-3, 83-85 cm, PPL



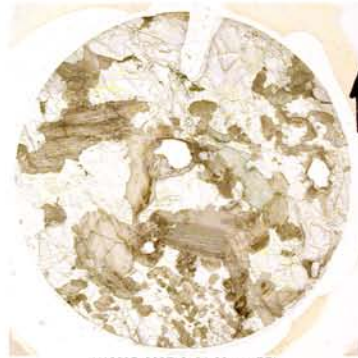
U1309D-028R-4, 45-47 cm, CPL



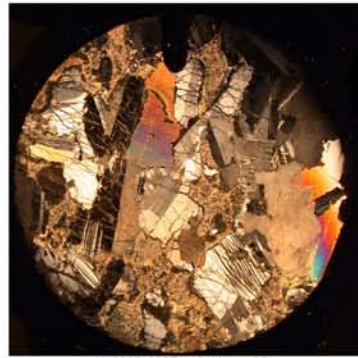
U1309D-028R-4, 45-47 cm, PPL



U1309D-029R-3, 64-66 cm, CPL



U1309D-029R-3, 64-66 cm, PPL



U1309D-032R-1, 9-11 cm, CPL



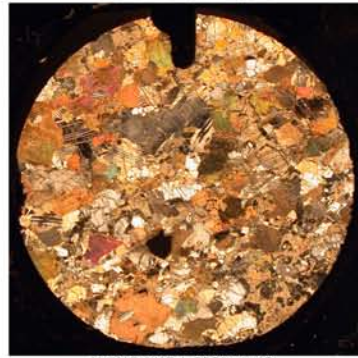
U1309D-032R-1, 9-11 cm, PPL



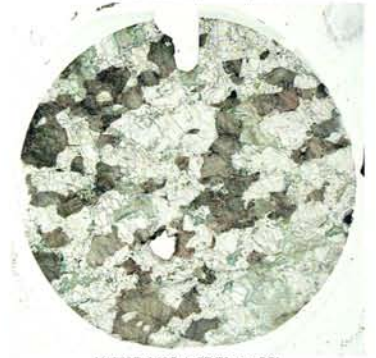
U1309D-036R-1, 10-12 cm, CPL



U1309D-036R-1, 10-12 cm, PPL



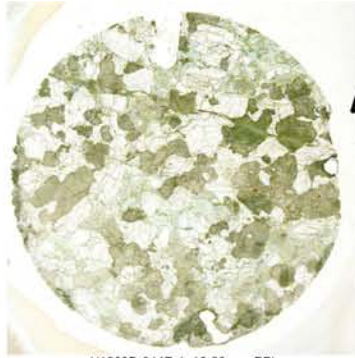
U1309D-043R-1, 57-79 cm, CPL



U1309D-043R-1, 57-79 cm, PPL



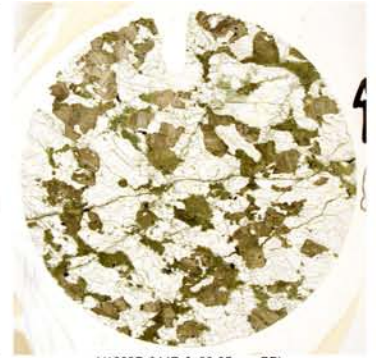
U1309D-044R-1, 18-20 cm, CPL



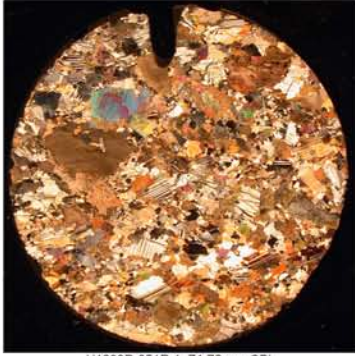
U1309D-044R-1, 18-20 cm, PPL



U1309D-044R-2, 83-85 cm, CPL



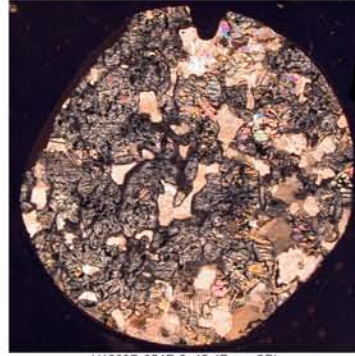
U1309D-044R-2, 83-85 cm, PPL



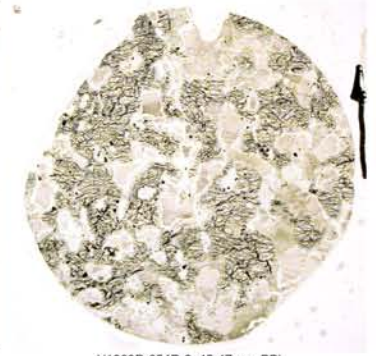
U1309D-051R-1, 74-76 cm, CPL



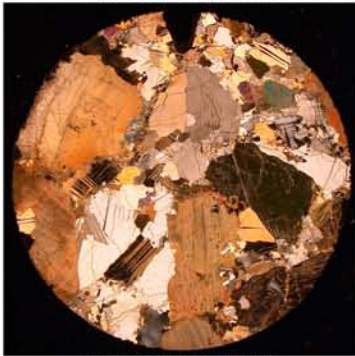
U1309D-051R-1, 74-76 cm, PPL



U1309D-054R-3, 45-47 cm, CPL



U1309D-054R-3, 45-47 cm, PPL



U1309D-058R-1, 110-112 cm, CPL



U1309D-058R-1, 110-112 cm, PPL



U1309D-059R-1, 58-60 cm, CPL



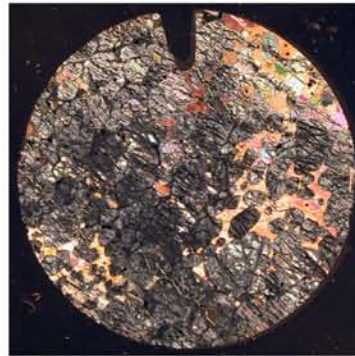
U1309D-059R-1, 58-60 cm, PPL



U1309D-063R-3, 41-43 cm, CPL



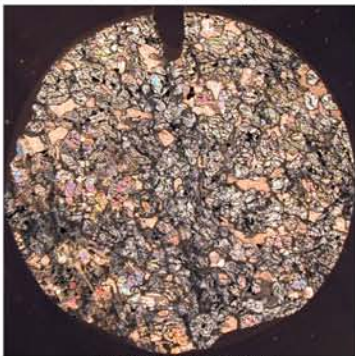
U1309D-063R-3, 41-43 cm, PPL



U1309D-064R-1, 58-60 cm, CPL



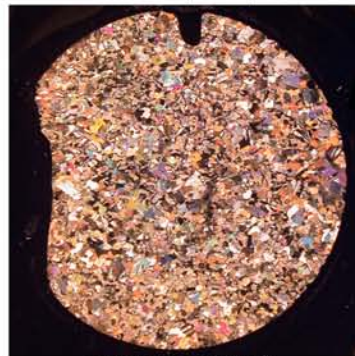
U1309D-064R-1, 58-60 cm, PPL



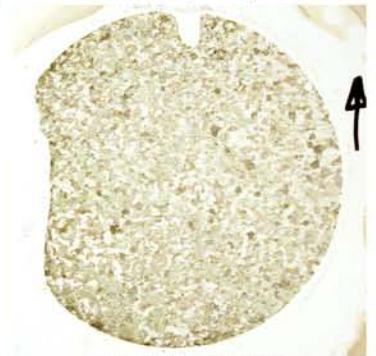
U1309D-066R-2, 93-95 cm, CPL



U1309D-066R-2, 93-95 cm, PPL



U1309D-067R-3, 17-19 cm, CPL



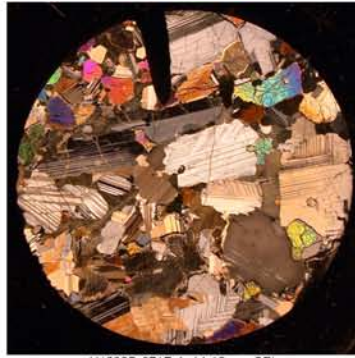
U1309D-067R-3, 17-19 cm, PPL



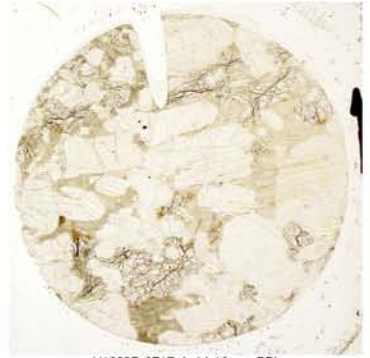
U1309D-070R-2, 76-78 cm, CPL



U1309D-070R-2, 76-78 cm, PPL



U1309D-071R-1, 14-16 cm, CPL



U1309D-071R-1, 14-16 cm, PPL



U1309D-071R-5, 13-15 cm, CPL



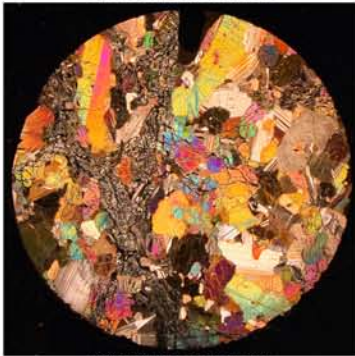
U1309D-071R-5, 13-15 cm, PPL



U1309D-073R-2, 86-88 cm, CPL



U1309D-073R-2, 86-88 cm, PPL



U1309D-077R-3, 21-23 cm, CPL



U1309D-077R-3, 21-23 cm, PPL



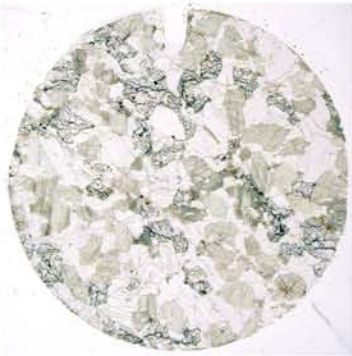
U1309D-083R-2, 29-31 cm, CPL



U1309D-083R-2, 29-31 cm, PPL



U1309D-088R-1, 2-4 cm, CPL



U1309D-088R-1, 2-4 cm, PPL



U1309D-089R-1, 92-94 cm, CPL



U1309D-089R-1, 92-94 cm, PPL



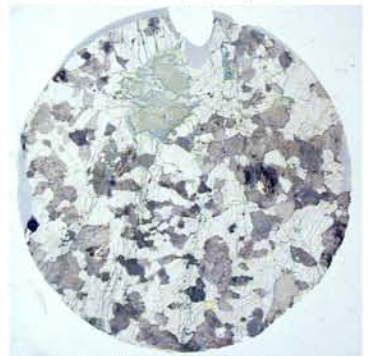
U1309D-090R-3, 8-10 cm, CPL



U1309D-090R-3, 8-10 cm, PPL



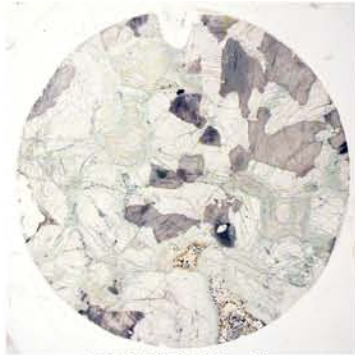
U1309D-092R-1, 123-125 cm, CPL



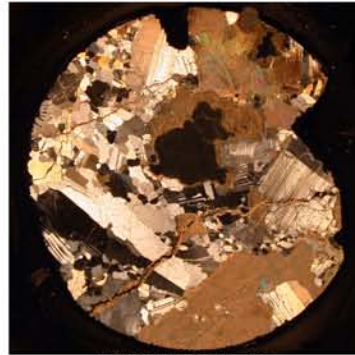
U1309D-092R-1, 123-125 cm, PPL



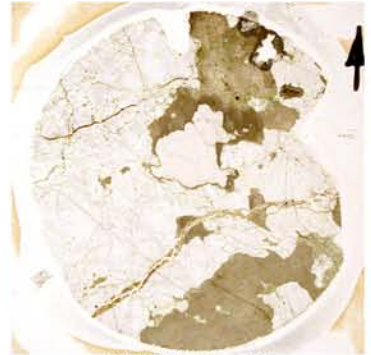
U1309D-095R-3, 35-37 cm, CPL



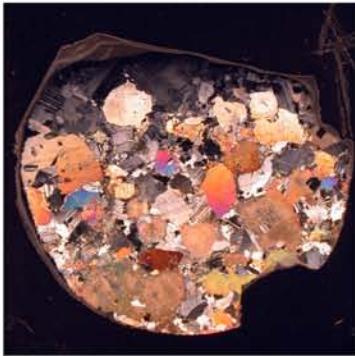
U1309D-095R-3, 35-37 cm, PPL



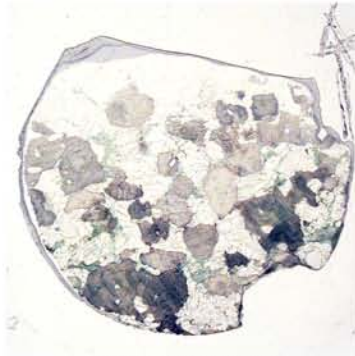
U1309D-097R-1, 6-8 cm, CPL



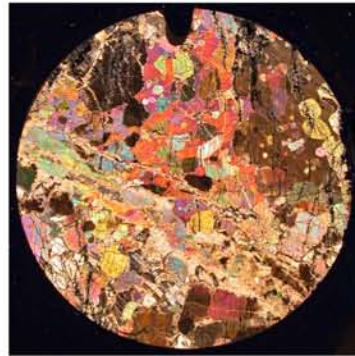
U1309D-097R-1, 6-8 cm, PPL



U1309D-098R-3, 96-98 cm, CPL



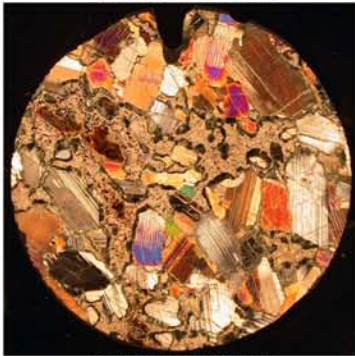
U1309D-098R-3, 96-98 cm, PPL



U1309D-100R-1, 32-34 cm, CPL



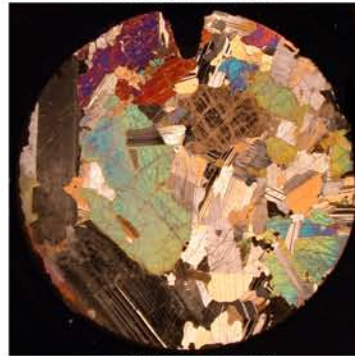
U1309D-100R-1, 32-34 cm, PPL



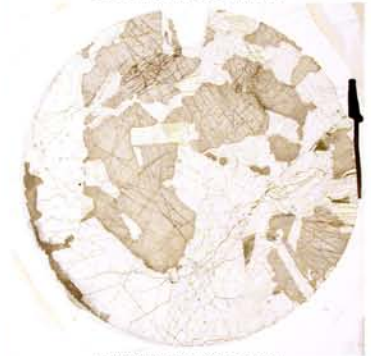
U1309D-105R-3, 46-48 cm, CPL



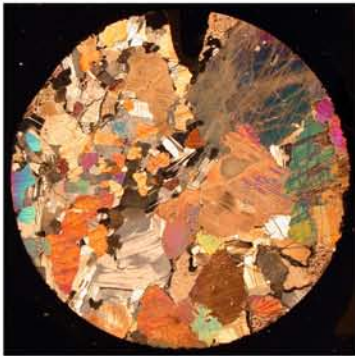
U1309D-105R-3, 46-48 cm, PPL



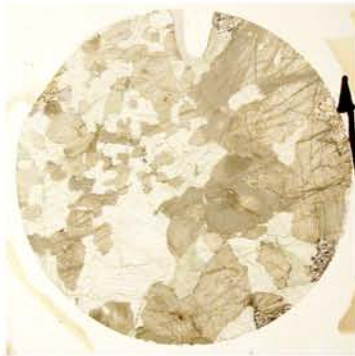
U1309D-107R-2, 52-54 cm, CPL



U1309D-107R-2, 52-54 cm, PPL



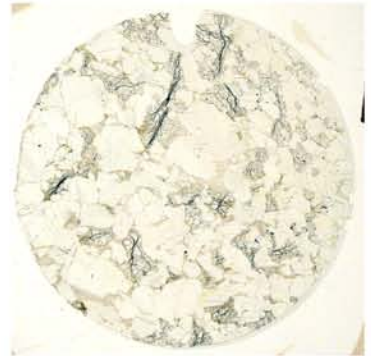
U1309D-109R-2, 69-71 cm, DPL



U1309D-109R-2, 69-71 cm, PPL



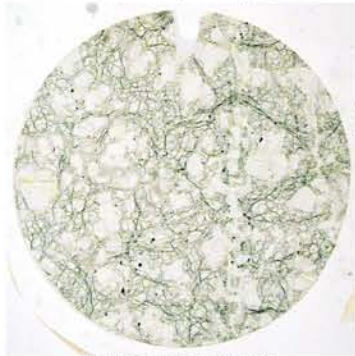
U1309D-110R-2, 74-76 cm, CPL



U1309D-110R-2, 74-76 cm, PPL



U1309D-111R-2, 17-19 cm, CPL



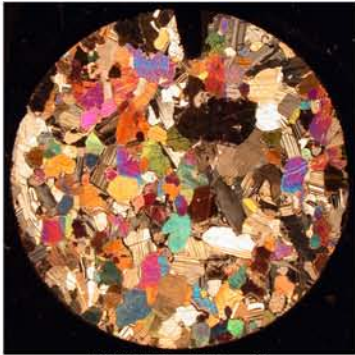
U1309D-111R-2, 17-19 cm, PPL



U1309D-111R-4, 19-21 cm, CPL



U1309D-111R-4, 19-21 cm, PPL



U1309D-117R-1, 55-57 cm, CPL



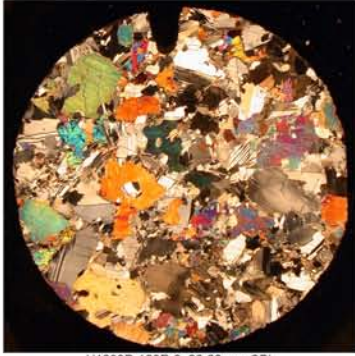
U1309D-117R-1, 55-57 cm, PPL



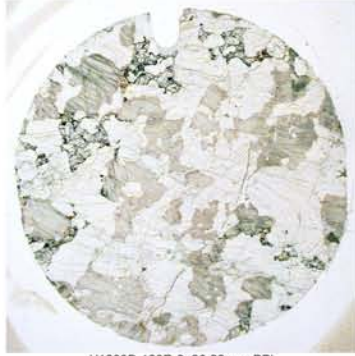
U1309D-117R-4, 27-29 cm, CPL



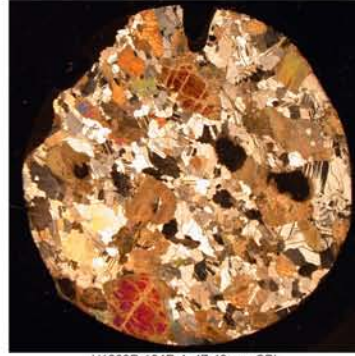
U1309D-117R-4, 27-29 cm, PPL



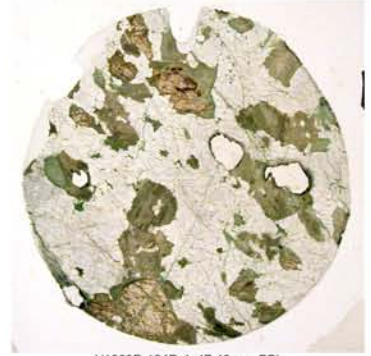
U1309D-120R-2, 26-28 cm, CPL



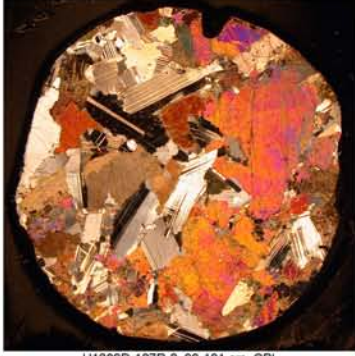
U1309D-120R-2, 26-28 cm, PPL



U1309D-124R-4, 47-49 cm, CPL



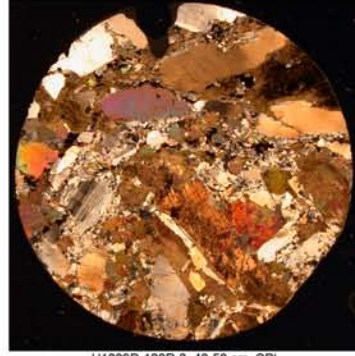
U1309D-124R-4, 47-49 cm, PPL



U1309D-127R-2, 99-101 cm, CPL



U1309D-127R-2, 99-101 cm, PPL



U1309D-128R-3, 48-50 cm, CPL



U1309D-128R-3, 48-50 cm, PPL



U1309D-130R-1, 44-46 cm, CPL



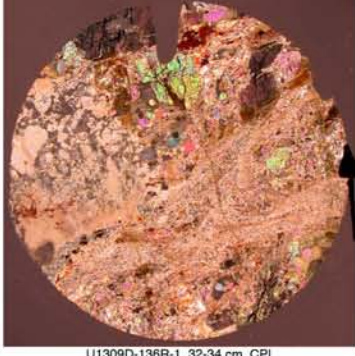
U1309D-130R-1, 44-46 cm, PPL



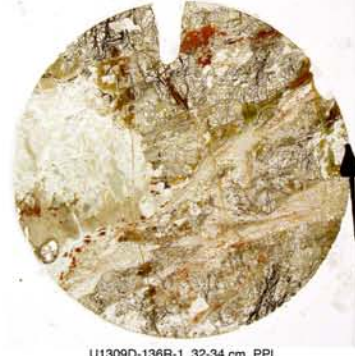
U1309D-132R-3, 106-108 cm, CPL



U1309D-132R-3, 106-108 cm, PPL



U1309D-136R-1, 32-34 cm, CPL



U1309D-136R-1, 32-34 cm, PPL



U1309D-137R-2, 126-128 cm, CPL



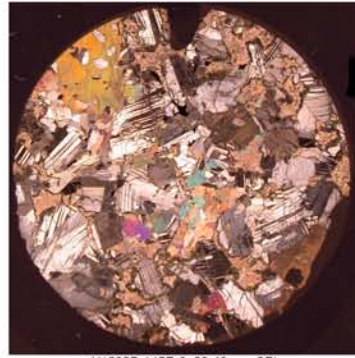
U1309D-137R-2, 126-128 cm, PPL



U1309D-141R-2, 63-65 cm, CPL



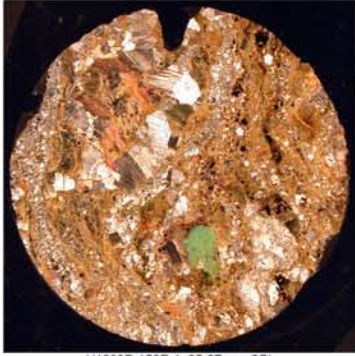
U1309D-141R-2, 63-65 cm, PPL



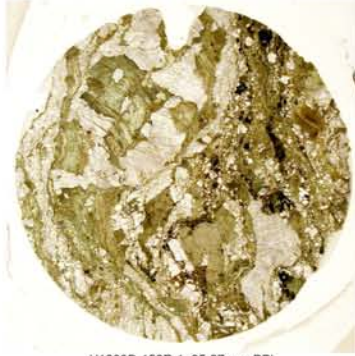
U1309D-145R-3, 38-40 cm, CPL



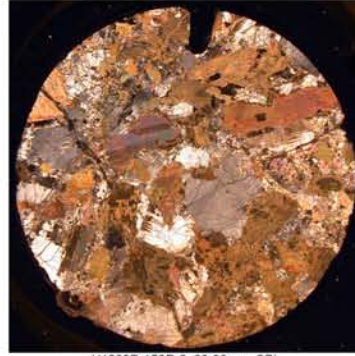
U1309D-145R-3, 38-40 cm, PPL



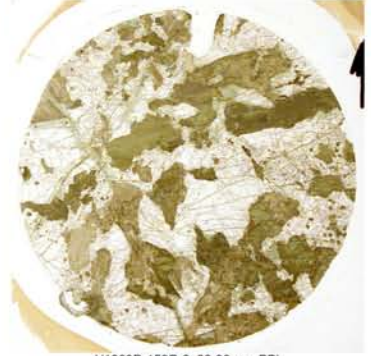
U1309D-152R-1, 35-37 cm, CPL



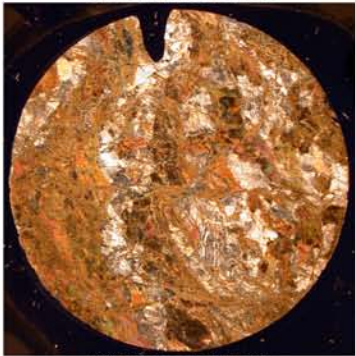
U1309D-152R-1, 35-37 cm, PPL



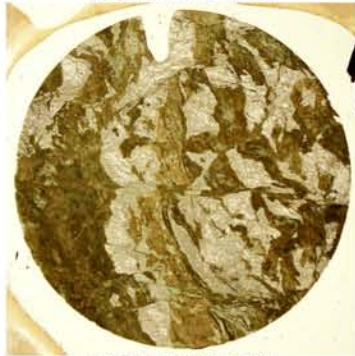
U1309D-153R-2, 88-90 cm, CPL



U1309D-153R-2, 88-90 cm, PPL



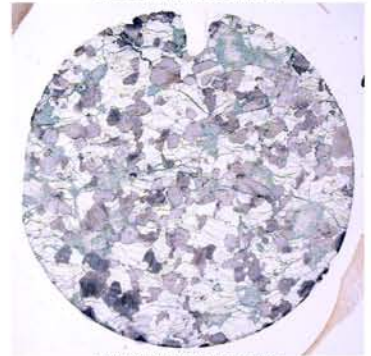
U1309D-154R-1, 30-32 cm, CPL



U1309D-154R-1, 30-32 cm, PPL



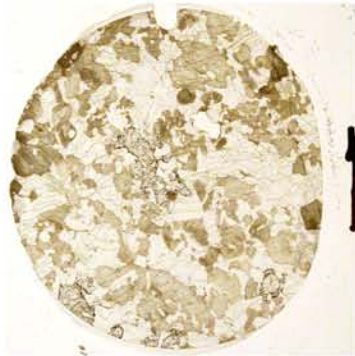
U1309D-157R-2, 75-77 cm, CPL



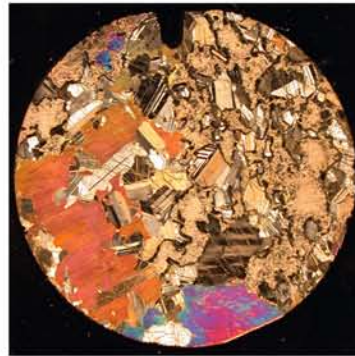
U1309D-157R-2, 75-77 cm, PPL



U1309D-159R-1, 104-106 cm, CPL



U1309D-159R-1, 104-106 cm, PPL



U1309D-160R-2, 117-119 cm, CPL



U1309D-160R-2, 117-119 cm, PPL



U1309D-161R-2, 44-46 cm, CPL



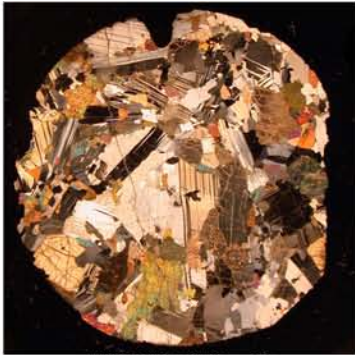
U1309D-161R-2, 44-46 cm, PPL



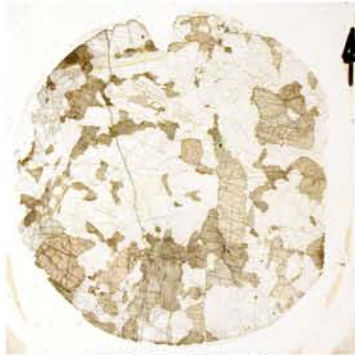
U1309D-164R-3, 110-112 cm, CPL



U1309D-164R-3, 110-112 cm, PPL



U1309D-169R-1, 64-66 cm, CPL



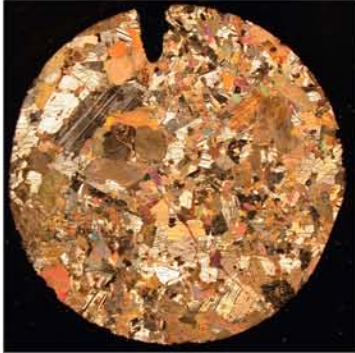
U1309D-169R-1, 64-66 cm, PPL



U1309D-170R-4, 77-79 cm, CPL



U1309D-170R-4, 77-79 cm, PPL



U1309D-174R-4, 53-55 cm, DPL



U1309D-174R-4, 53-55 cm, PPL



U1309D-178R-3, 8-10 cm, CPL



U1309D-178R-3, 8-10 cm, PPL



U1309D-188R-2, 37-39 cm, CPL



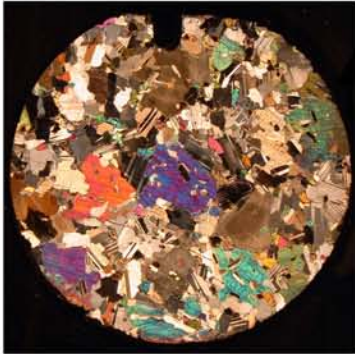
U1309D-188R-2, 37-39 cm, PPL



U1309D-189R-3, 40-42 cm, CPL



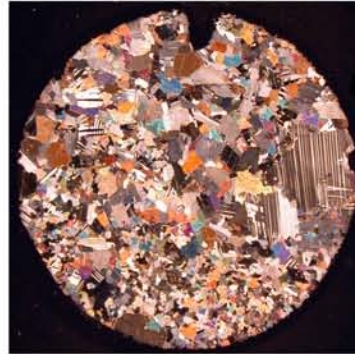
U1309D-189R-3, 40-42 cm, PPL



U1309D-190R-1, 31-33 cm, CPL



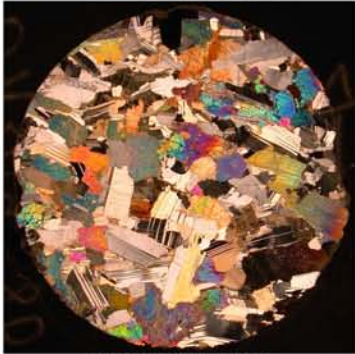
U1309D-190R-1, 31-33 cm, PPL



U1309D-194R-2, 27-29 cm, CPL



U1309D-194R-2, 27-29 cm, PPL



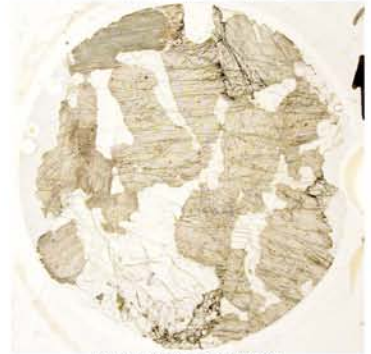
U1309D-200R-2, 31-33 cm, CPL



U1309D-200R-2, 31-33 cm, PPL



U1309D-202R-1, 40-42 cm, CPL



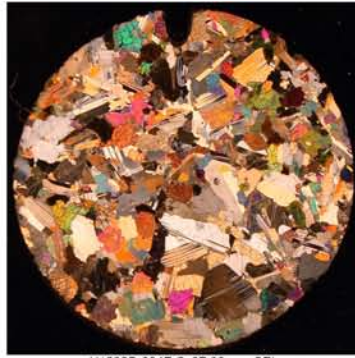
U1309D-202R-1, 40-42 cm, PPL



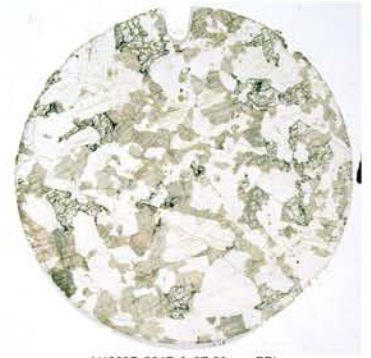
U1309D-203R-1, 99-101 cm, CPL



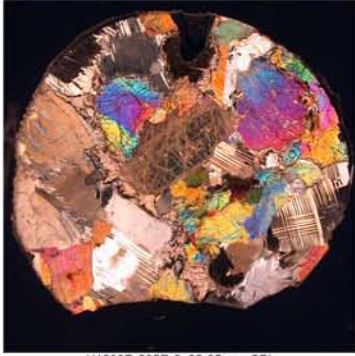
U1309D-203R-1, 99-101 cm, PPL



U1309D-204R-2, 97-99 cm, CPL



U1309D-204R-2, 97-99 cm, PPL



U1309D-205R-2, 83-85 cm, CPL



U1309D-205R-2, 83-85 cm, PPL



U1309D-208R-2, 74-76 cm, CPL



U1309D-208R-2, 74-76 cm, PPL



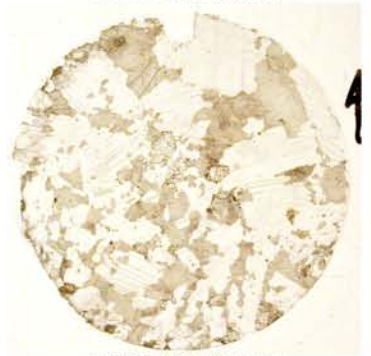
U1309D-211R-1, 64-66 cm, CPL



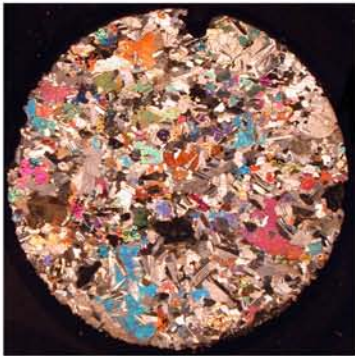
U1309D-211R-1, 64-66 cm, PPL



U1309D-212R-4, 65-67 cm, CPL



U1309D-212R-4, 65-67 cm, PPL



U1309D-216R-1, 17-19 cm, CPL



U1309D-216R-1, 17-19 cm, PPL



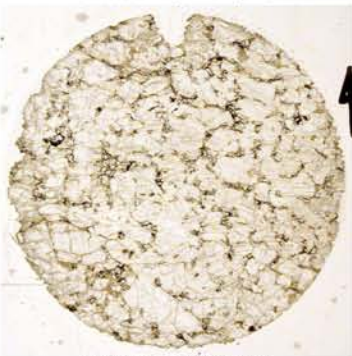
U1309D-217R-2, 23-25 cm, CPL



U1309D-217R-2, 23-25 cm, PPL



U1309D-221R-3, 64-66 cm, CPL



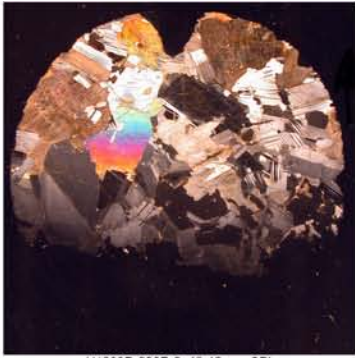
U1309D-221R-3, 64-66 cm, PPL



U1309D-225R-1, 72-74 cm, CPL



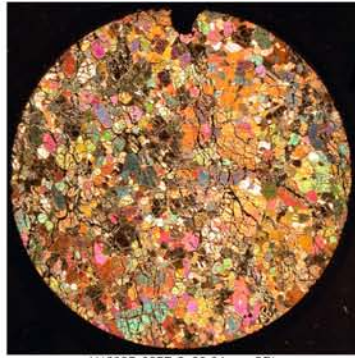
U1309D-225R-1, 72-74 cm, PPL



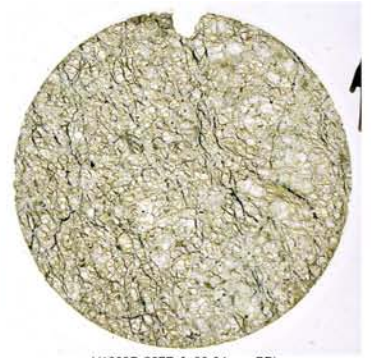
U1309D-226R-3, 40-42 cm, CPL



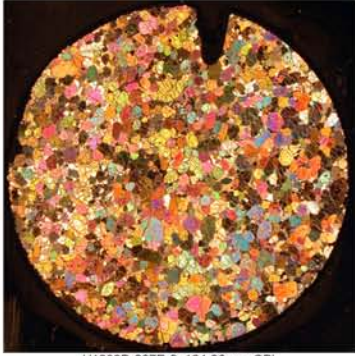
U1309D-226R-3, 40-42 cm, PPL



U1309D-227R-2, 82-84 cm, CPL



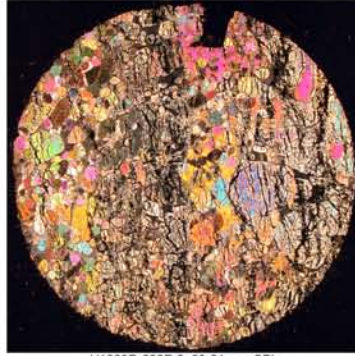
U1309D-227R-2, 82-84 cm, PPL



U1309D-227R-3, 124-26 cm, CPL



U1309D-227R-3, 124-26 cm, PPL



U1309D-228R, 29-31 cm, CPL



U1309D-228R, 29-31 cm, PPL



U1309D-230R, 2, 125-127 cm, CPL



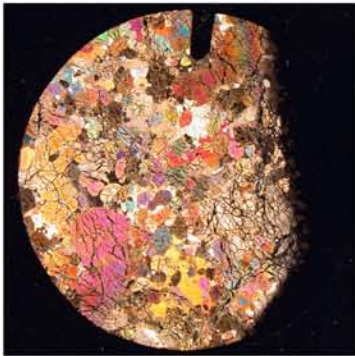
U1309D-230R, 2, 125-127 cm, PPL



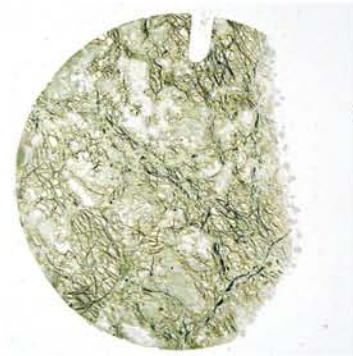
U1309D-230R-3, 28-30 cm, CPL



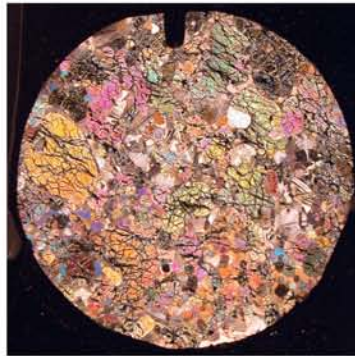
U1309D-230R-3, 28-30 cm, PPL



U1309D-232R-1, 15-17 cm, CPL



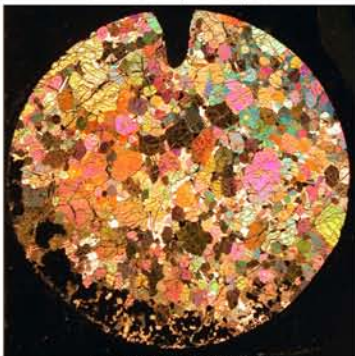
U1309D-232R-1, 15-17 cm, PPL



U1309D-233R-1, 141-143 cm, CPL



U1309D-233R-1, 141-143 cm, PPL



U1309D-234R-1, 27-29 cm, CPL



U1309D-234R-1, 27-29 cm, PPL



U1309D-235R-2, 91-93 cm, CPL



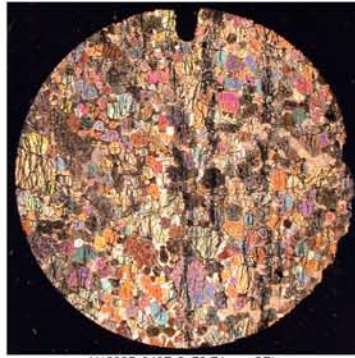
U1309D-235R-2, 91-93 cm, PPL



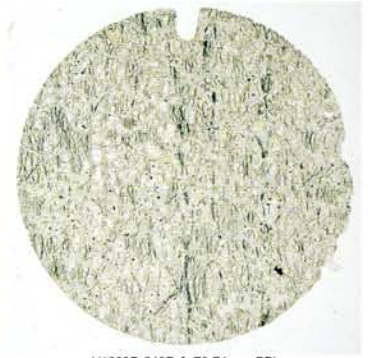
U1309D-236R-2, 125-127 cm, CPL



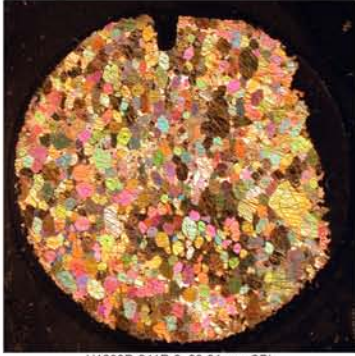
U1309D-236R-2, 125-127 cm, PPL



U1309D-240R-2, 72-74 cm, CPL



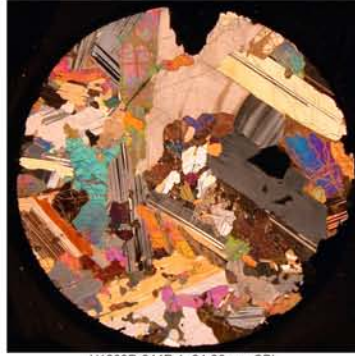
U1309D-240R-2, 72-74 cm, PPL



U1309D-241R-2, 89-91 cm, CPL



U1309D-241R-2, 89-91 cm, PPL



U1309D-244R-1, 34-36 cm, CPL



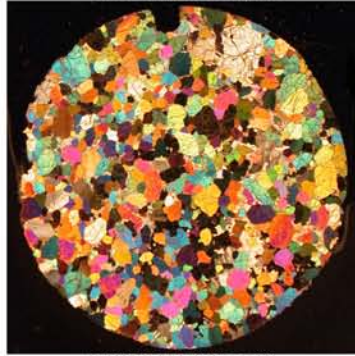
U1309D-244R-1, 34-36 cm, PPL



U1309D-247R-3, 16-18 cm, CPL



U1309D-247R-3, 16-18 cm, PPL



U1309D-248R-2, 22-24 cm, CPL



U1309D-248R-2, 22-24 cm, PPL



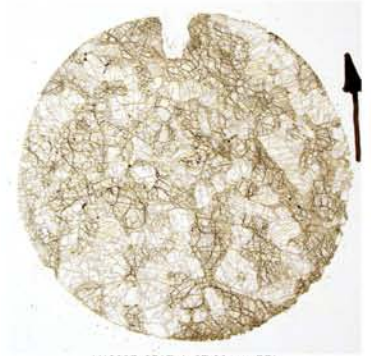
U1309D-248R-3, 36-38 cm, CPL



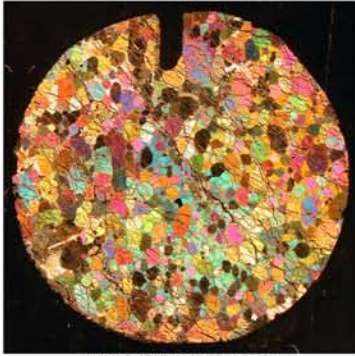
U1309D-248R-3, 36-38 cm, PPL



U1309D-251R-1, 87-89 cm, CPL



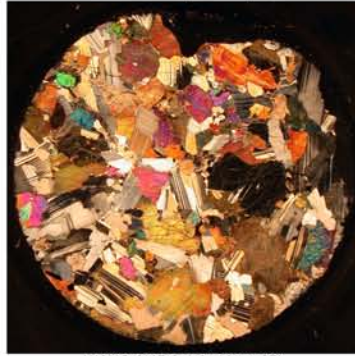
U1309D-251R-1, 87-89 cm, PPL



U1309D-256R-2, 83-85 cm, CPL



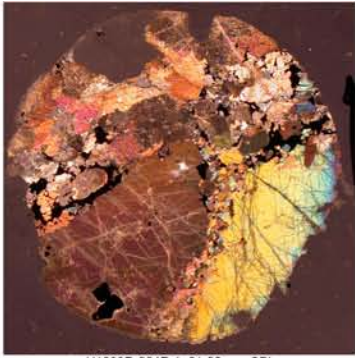
U1309D-256R-2, 83-85 cm, PPL



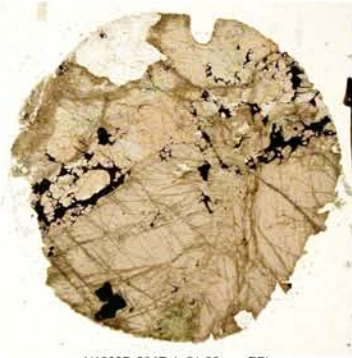
U1309D-262R-3, 112-114 cm, CPL



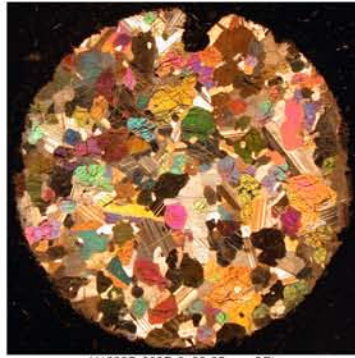
U1309D-262R-3, 112-114 cm, PPL



U1309D-264R-1, 81-83 cm, CPL



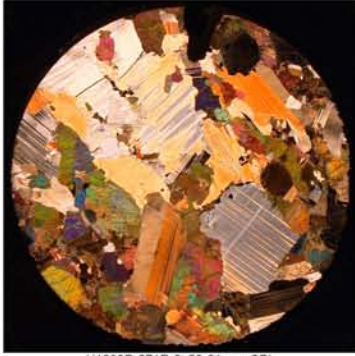
U1309D-264R-1, 81-83 cm, PPL



U1309D-268R-2, 83-85 cm, CPL



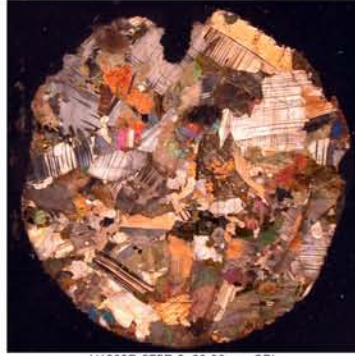
U1309D-268R-2, 83-85 cm, PPL



U1309D-271R-3, 59-61 cm, CPL



U1309D-271R-3, 59-61 cm, PPL



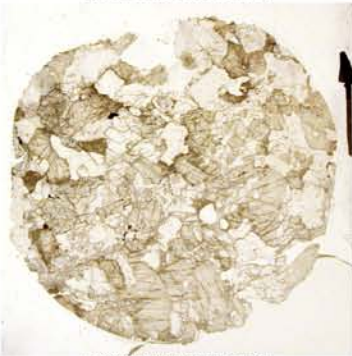
U1309D-275R-3, 88-90 cm, CPL



U1309D-275R-3, 88-90 cm, PPL



U1309D-280R-1, 88-90 cm, CPL



U1309D-280R-1, 88-90 cm, PPL



U1309D-285R-1, 90-92 cm, CPL



U1309D-285R-1, 90-92 cm, PPL



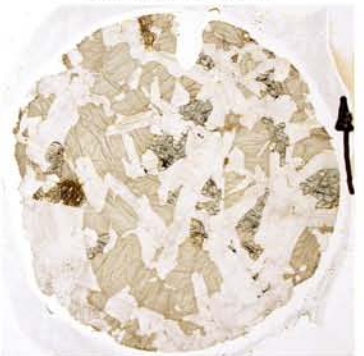
U1309D-290R-2, 89-91 cm, CPL



U1309D-290R-2, 89-91 cm, PPL



U1309D-291R-3, 39-41 cm, CPL



U1309D-291R-3, 39-41 cm, PPL

ANNEXE E

Articles publiés

« Oceanic cores complexes and crustal accretion at slow-spreading ridges. » (2007) Ildefonse, B., Blackman, D.K., John, B.E., Ohara, Y., Miller, D.J., MacLeod, C.J., **Integrated Ocean Drilling Program Expeditions 304/305 Science Party**, *Geology* 35(7), 623-626.

« IODP Expeditions 304 & 305 Characterize the Lithology, Structure, and Alteration of an Oceanic Core Complex. » (2006) Ildefonse, B., Blackman, D.K., John, B.E., Ohara, Y., Miller, D.J., MacLeod, C.J., **Integrated Ocean Drilling Program Expeditions 304/305 Science Party**, *Scientific Drilling* 3.

« Pervasive melt percolation reactions in ultra-depleted refractory harzburgites at the Mid-Atlantic Ridge, 15°20'N: ODP Hole 1274A. » (2007) Seyler, M., Lorand, J.-P., Dick, H.J.B., **Drouin, M.**, *Contrib. Mineral. Petrol.* 153(3), 303-319.

« Bulk-rock geochemistry and plagioclase zoning in lavas exposed along the northern flank of the Western Blanco Depression (Northeast Pacific): Insight into open-system magma chamber processes. » (2007) Cordier, C., Caroff, M., Juteau, T., Fleutelot, C., Hemond, C., **Drouin, M.**, Cotten, J., Bollinger, C., *Lithos* 99(3-4), 289-311.

Oceanic core complexes and crustal accretion at slow-spreading ridges

B. Ildefonse* Géosciences Montpellier, CNRS, Université Montpellier 2, CC 60, 34095 Montpellier cedex 05, France

D.K. Blackman Scripps Institution of Oceanography, La Jolla, California 92093, USA

B.E. John Department of Geology and Geophysics, University of Wyoming, 1000 East University Avenue, Department 3006, Laramie, Wyoming 82071, USA

Y. Ohara Ocean Research Laboratory, Hydrographic and Oceanographic Department of Japan, 5-3-1 Tsukiji, Chuo-ku, Tokyo 104-0045, Japan

D.J. Miller Integrated Ocean Drilling Program, Texas A&M University, 1000 Discovery Drive, College Station, Texas 77845-9547, USA

C.J. MacLeod School of Earth, Ocean and Planetary Sciences, Cardiff University, Main Building, Park Place, Cardiff CF10 3YE, UK Integrated Ocean Drilling Program Expeditions 304/305 Science Party^{†1}

ABSTRACT

Oceanic core complexes expose gabbroic rocks on the seafloor via detachment faulting, often associated with serpentinized peridotite. The thickness of these serpentinite units is unknown. Assuming that the steep slopes that typically surround these core complexes provide a cross section through the structure, it has been inferred that serpentinites compose much of the section to depths of at least several hundred meters. However, deep drilling at oceanic core complexes has recovered gabbroic sequences with virtually no serpentinized peridotite. We propose a revised model for oceanic core complex development based on consideration of the rheological differences between gabbro and serpentinized peridotite: emplacement of a large intrusive gabbro body into a predominantly peridotite host is followed by localization of strain around the margins of the pluton, eventually resulting in an uplifted gabbroic core surrounded by deformed serpentinite. Oceanic core complexes may therefore reflect processes associated with relatively enhanced periods of mafic intrusion within overall magma-poor regions of slow- and ultra-slow-spreading ridges.

Keywords: Integrated Ocean Drilling Program, Ocean Drilling Program, oceanic lithosphere, mid-ocean ridges, Mid-Atlantic Ridge, oceanic core complex, gabbro, serpentinite.

INTRODUCTION

Oceanic core complexes (OCCs) have been recognized along both slow- and ultra-slow-spreading ridges (e.g., Tucholke et al., 1998; Cannat et al., 2006; Smith et al., 2006), and are characterized by domal bathymetric highs interpreted as portions of the lower crust and/or upper mantle denuded via low-angle normal or detachment faulting (e.g., Tucholke and Lin, 1994; Cann et al., 1997). The spreading-parallel extents of the cores of OCCs are typically tens of kilometers. OCCs are interpreted to form episodically at or near the spreading axis, beneath detachment faults that typically slip for periods of ~1–3 m.y. before becoming inactive (e.g.,

Tucholke et al., 1998). At slow spreading rates (i.e., <~5 cm/yr), the style of axial magmatism (both volcanism and plutonism) varies along strike and over time, and plays a key role in controlling seafloor morphology as well as the compositional architecture of the lithosphere. This has led to the concept that the oceanic crust at some slower spreading ridges is a heterogeneous “plum pudding” of discrete gabbro bodies hosted by peridotite, locally capped by a thin layer of extrusive basalt (Cannat, 1996).

Many models of OCC formation (e.g., Karson, 1990; Tucholke and Lin, 1994; Escartin et al., 2003; Buck et al., 2005) emphasize the role of reduced magma supply in the development and long-term localization of strain along detachment faults. OCCs are therefore often inferred to represent periods of reduced magmatism at a given section of the spreading segment.

Our revised model is motivated by recent deep (>100 m below seafloor, mbsf) drilling results from three OCCs: (1) Atlantis Bank, Southwest Indian Ridge, Ocean Drilling Program (ODP) Holes 735B (Robinson et al., 1989; Dick et al., 2000) and 1105A (Pettigrew et al., 1999); (2) the 15°45'N OCC on the Mid-Atlantic Ridge, ODP Site 1275 (Kelemen et al., 2004); and (3) Atlantis Massif, Mid-Atlantic Ridge, 30°N, Integrated Ocean Drilling Program (IODP) Site U1309 (Blackman et al., 2006). In this paper we emphasize new results from Site U1309, mak-

ing comparisons to Hole 735B and Hole 1275D in conjunction with geophysical and geological mapping data. Although the mechanisms and structures required in our model are not new, we show that by considering the rheological properties of a heterogeneous “plum pudding” crust, a revised view emerges as to how episodes of OCC formation fit within the overall history of a given section of the mid-ocean ridge system.

ATLANTIS MASSIF, 30°N, Mid-Atlantic Ridge

Atlantis Massif formed within the past 1.5–2 m.y. (Blackman et al., 1998, 2002), and bounds the median valley on the western flank of the Mid-Atlantic Ridge (Fig. 1). The core of the massif, exposed on its upper surface by a corrugated detachment fault, comprises upper mantle rocks and gabbroic intrusions. The basaltic block to the east is interpreted as the hanging wall to the detachment fault system.

Exposures along the south face of the massif are interpreted as providing cross-sectional views into the core complex; collected samples comprise ~30% gabbro (+basalt and/or diabase dikes) and ~70% serpentinized harzburgites (Blackman et al., 2002; Karson et al., 2006).

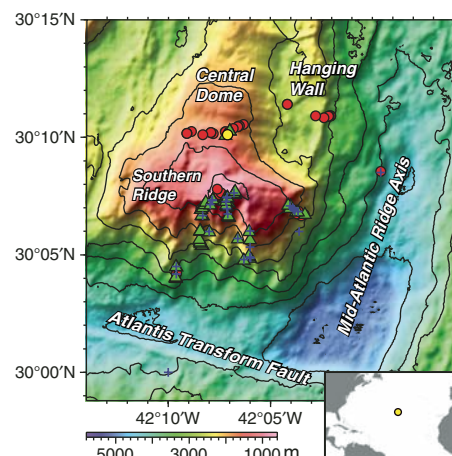


Figure 1. Bathymetric map of Atlantis Massif showing location of Site U1309 (yellow) and seafloor samples. Red—basalt, blue—gabbro, green—serpentinized peridotite.

*E-mail: benoit.ildefonse@univ-montp2.fr.

^{†1}N. Abe, M. Abratis, E.S. Andal, M. Andréani, S. Awaji, J.S. Beard, D. Brunelli, A.B. Charney, D.M. Christie, A.G. Delacour, H. Delius, M. Drouin, F. Einaudi, J. Escartin, B.R. Frost, P.B. Fryer, J.S. Gee, M. Godard, C.B. Grimes, A. Halfpenny, H-E. Hansen, A.C. Harris, N.W. Hayman, E. Hellebrand, T. Hirose, J.G. Hirth, S. Ishimaru, K.T.M. Johnson, G.D. Karner, M. Linek, J. Maeda, O.U. Mason, A.M. McCaig, K. Michibayashi, A. Morris, T. Nakagawa, T. Nozaka, M. Rosner, R.C. Searle, G. Suhr, A. Tamura, M. Tominaga, A. von der Handt, T. Yamasaki, X. Zhao.

^{†2}GSA Data Repository item 2007165, affiliations of all 51 co-authors, is available online at www.geosociety.org/pubs/ft2007.htm, or on request from editing@geosociety.org or Documents Secretary, GSA, P.O. Box 9140, Boulder, CO 80301, USA.

Gravity modeling (Blackman et al., 2002) suggests that rocks within the central and southern dome have a density 200–400 kg/m³ greater than the surrounding rock. Rock samples from the top of the central dome are mostly angular talus and rubble of serpentinized peridotite, metabasalt, and limestone. Highly altered gabbroic veins, now dominantly talc, tremolite, and chlorite, commonly cut these rocks (Schroeder and John, 2004; Boschi et al., 2006).

IODP EXPEDITIONS 304 AND 305 RESULTS

IODP Expeditions 304 and 305 penetrated 1415.5 m of the footwall of the central dome of Atlantis Massif at Site U1309 (average core recovery 75%). Hole U1309D is dominantly gabbroic, and is thus far unique in its highly primitive nature (Fig. 2; Blackman et al., 2006). Holes U1309B and U1309D have interfingered intrusive units that vary in thickness from centimeters to ~100–200 m. Contact relations suggest that gabbro is generally intrusive into more olivine-rich rocks, and is in turn intruded by oxide gabbro and leucocratic dikes. Three thin (<1 m) intervals of ultramafic rocks interpreted as residual mantle peridotite are intercalated with gabbro in the upper 225 m of Site U1309. Diabase intrudes all rock types throughout the section, but forms a greater proportion of the core in the upper 150 mbsf. These tholeiitic basalts overlap glass compositions typical of the Mid-Atlantic Ridge. The relative intensity of alteration and vein development of intrusive contacts suggest that some of the diabase dikes were emplaced late in the history of the footwall.

Overall, the recovered section is moderately altered at conditions ranging from magmatic to zeolite facies, and little deformed (Fig. 2C). While there is a spectrum of metamorphic facies, an overall decrease in total alteration and a change in style of alteration occur with depth. Whereas the upper 380 m of the core shows an alteration profile characteristic of pervasive static infiltration of seawater with decreasing temperature, at greater depths alteration is generally restricted to halos adjacent to veins, fractures, and igneous contacts. Extensive amphibolite facies metamorphism and deformation are lacking and high-strain ductile shear zones are rare. High-strain crystal-plastic deformation is typically restricted to a few, mostly granulite grade, shear zones ranging in width from millimeters to a few meters. In many places, weak crystal-plastic deformation seems to overprint magmatic foliation. The amount of strain recorded by brittle fracture and cataclasis is limited overall, except for fault zones concentrated in the upper 150 m of Hole U1309D and a few discrete intervals downhole. Fragments of schistose talc-bearing fault rock recovered at the seafloor are likely derived from the detachment fault.

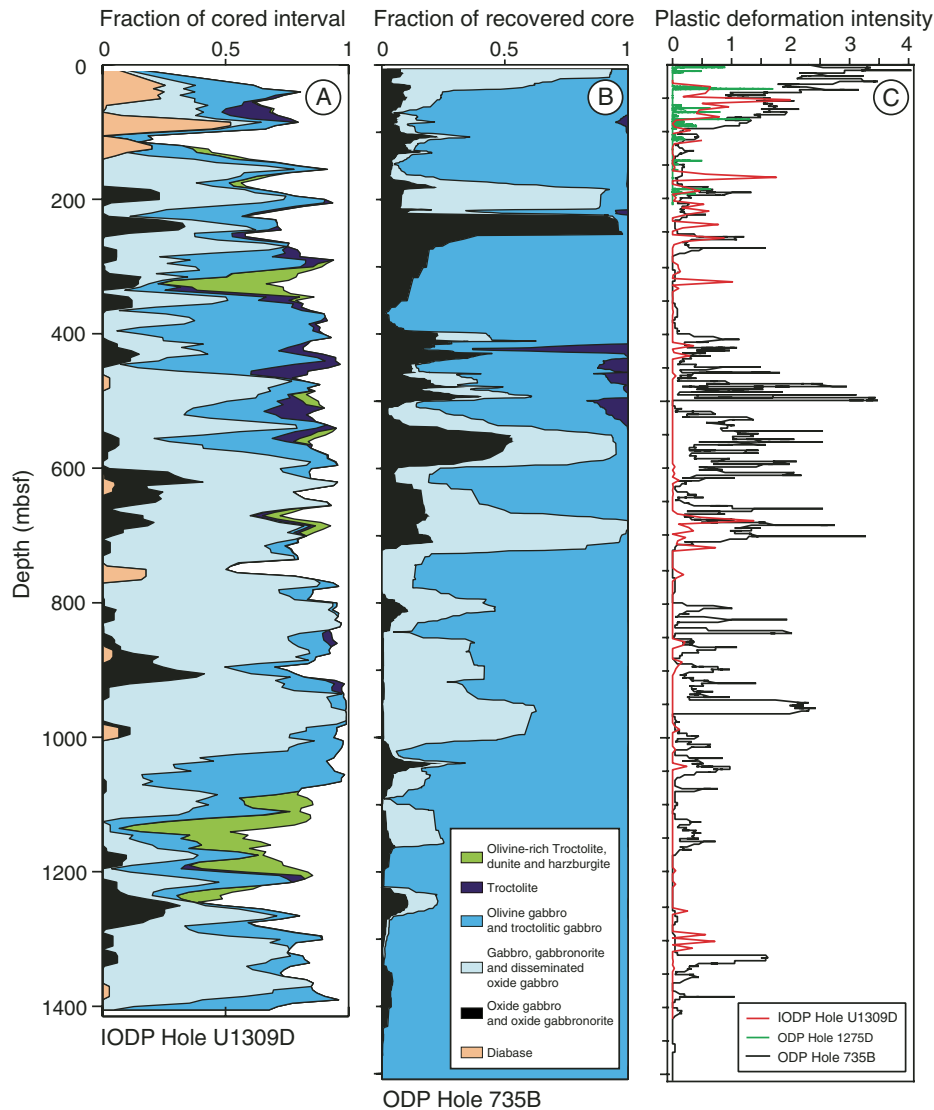


Figure 2. Summary of lithology and deformation in boreholes penetrating oceanic core complex. A: Core U1309D lithology (20 m running average). B: Core 735B lithology (20 m running average) (after Dick et al., 2000). C: Crystal-plastic deformation intensities for all cores. Deformation intensity scale: 0 = undeformed, 1 = weakly foliated, 2 = strongly foliated, 3 = porphyroclastic, 4 = mylonitic. ODP—Ocean Drilling Program; IODP—Integrated Ocean Drilling Program; mbsf—meters below seafloor.

COMPARISON WITH PREVIOUSLY DRILLED OCC

The deepest hole drilled to date in slow-spreading ocean crust is the 1508-m-deep ODP Hole 735B, at Atlantis Bank, adjacent to the Atlantis II transform and ~90 km south of the active Southwest Indian Ridge. Hole 735B recovered a gabbroic series (Fig. 2B), dominated by olivine gabbro, gabbro, and oxide gabbro (Dick et al., 2000). The 158-m-deep ODP Hole 1105A, ~1.3 km NE of Hole 735B, recovered the same rock types. Short seabed rock drill cores from the flat top of Atlantis Bank show it to be dominated by amphibolite facies gabbro mylonite with subhorizontal fabrics, suggesting that it is an OCC denuded by a detachment fault

(MacLeod et al., 1999). Talc-tremolite schists, inferred to be derived from serpentinized peridotite, are described at Atlantis Bank, due west of Hole 735B (Dick et al., 2001).

In the Atlantic, an OCC has also been investigated at 15°45'N, ~25 km west of the Mid-Atlantic Ridge axis. ODP Holes 1275B and 1275D were drilled into the OCC to depths of 108.7 and 209 mbsf, respectively (Kelemen et al., 2004). Prior to drilling, this corrugated domal bathymetric high was sampled by submersible (Fujiwara et al., 2003), dredging, and an oriented seabed rock-coring device (MacLeod et al., 2002; Escartin et al., 2003). These studies suggest that a discrete (≥30 km² in map) body of gabbro and accompanying diabase dikes intruded

peridotite. The roof of the gabbro body is tens to a couple of hundred meters below a detachment fault zone composed of talc-chlorite-tremolite schists (MacLeod et al., 2002; Escartin et al., 2003). ODP Cores 1275B and 1275D recovered troctolitic rocks above gabbroic rocks (Kelemen et al., 2004). The olivine-rich troctolites in the upper few tens of meters of the section are similar in composition and texture to those in the lower part of Hole U1309D, but were tentatively interpreted as impregnated mantle peridotite (Kelemen et al., 2004). They are interpreted on the basis of regional data to be part of the country rock to the gabbro intrusion (MacLeod et al., 2002; Escartin et al., 2003).

The similarity between Atlantis Massif and 15°45'N OCC in particular is striking. In both cases serpentinized peridotites are exposed on the seafloor but nearly absent in deep boreholes. Both have fault rocks (mostly talc-chlorite-tremolite or serpentinite schists) at the seafloor and late intrusion of basaltic dikes. In both cases the gabbro bodies have undergone little high-temperature deformation. Atlantis Bank is similar in many respects, although evidence for low-temperature deformation of serpentinized peridotite is rare. The major difference between the three OCCs is the thickness and intensity of deformation recorded by the gabbroic sections (Fig. 2C). Core from Hole 735B is spectacularly more deformed than the gabbros of Sites U1309 and 1275, with extensive, high-temperature crystal-plastic plastic deformation, including numerous mylonitic shear zones as thick as 20 m (Dick et al., 2000). The upper ~100 m in Core 735B is a mylonite zone, with a downward-decreasing deformation intensity.

REVISED MODEL

Our revised model builds on the concept (e.g., Cannat, 1996) that at least part of the oceanic lithosphere formed at slow-spreading centers comprises peridotite with gabbroic intrusions in varying proportions (the “plum pudding” concept). Because significant weakening of peridotite occurs in response to even small degrees of serpentinization (Escartin et al., 1997, 2001), the peridotite host will rapidly become weaker than the solidified gabbro intrusions as cracking and fluid penetration initiate. This may occur by two complementary mechanisms: local alteration associated with magmatic fluids escaping around the edges of a mafic intrusion within peridotite, and faulting of the lithosphere to allow seawater to penetrate from above. Geological relationships at 15°45'N clearly show how extensive strain can localize on low-temperature structures once seawater has penetrated, and weak hydrous minerals formed (MacLeod et al., 2002).

We posit that “plum pudding” lithosphere at the ridge axis is likely to be rheologically heterogeneous on a plate scale because of the con-

trast between the stronger gabbro and weaker hydrated mantle peridotite. Ongoing extensional deformation during regional plate separation is therefore likely to be concentrated in the altered peridotites, at the margins of the larger gabbro bodies. With progressive strain weakening, displacement localizes onto fewer, larger-offset shear zones, and a single detachment fault eventually forms. Such a feedback mechanism combined with the lateral rheological heterogeneities would likely promote an asymmetric rather than symmetric style of faulting, and lead to development of the sheath-like serpentinite and/or talc-lubricated detachment around the low-strain core of the gabbro body (Fig. 3).

In light of the “plum pudding” model for the architecture of magma-poor slow-spreading ocean lithosphere (Cannat, 1996), and consequent potential for strain localization around the gabbro bodies, it follows that most or many OCCs should have a gabbroic core. It is clear that magma supply to slow-spreading ridges can be episodic; some episodes may generate intrusion of larger magma bodies (Figs. 3B, 3C). Such episodes could be related to enhanced melt delivery from the underlying mantle, and/or (when OCCs are located at segment ends) enhanced melting at the segment center and along-axis magma transport. If the intrusion occurs at the base of the lithosphere, it would be surrounded by fresh peridotite and would thus

be buoyant; alternatively it could be emplaced at shallower levels directly, possibly intruded up shear zones (Allerton and MacLeod, 1998). As magmatic activity wanes, continuous spreading results in stretching of the lithosphere, accommodated by conjugate normal faults (Fig. 3D), enabling uplift of gabbro and mantle blocks from the base of the lithosphere (e.g., Lagabrielle et al., 1998). The lack of extensive ductile deformation within the section recovered at U1309D and at the 15°45'N OCC suggests that crystallization of the intrusion was nearly complete before large strains were achieved. In contrast, at Atlantis Bank it is clear that deformation must have accompanied or closely followed intrusion (Dick et al., 2000). In this so-far unique example, the role of surrounding serpentinized peridotites may be less critical.

Relative slip between the intrusive body when it is at depth and the overlying sequence probably reflects a combination of buoyancy (gabbro less dense than relatively fresh peridotite) and spreading forces (uplift and transfer via alternating axial faults). The gabbro body rises to the depth where it is captured by a fault that becomes the long-lived detachment fault to unroof the core (Fig. 3E). The shallow dip and longevity of the exposed detachment fault reflect the scale of the large competent gabbro body (Fig. 3F). During stages E to F (Fig. 3), diabase dikes may cut through the crystal-

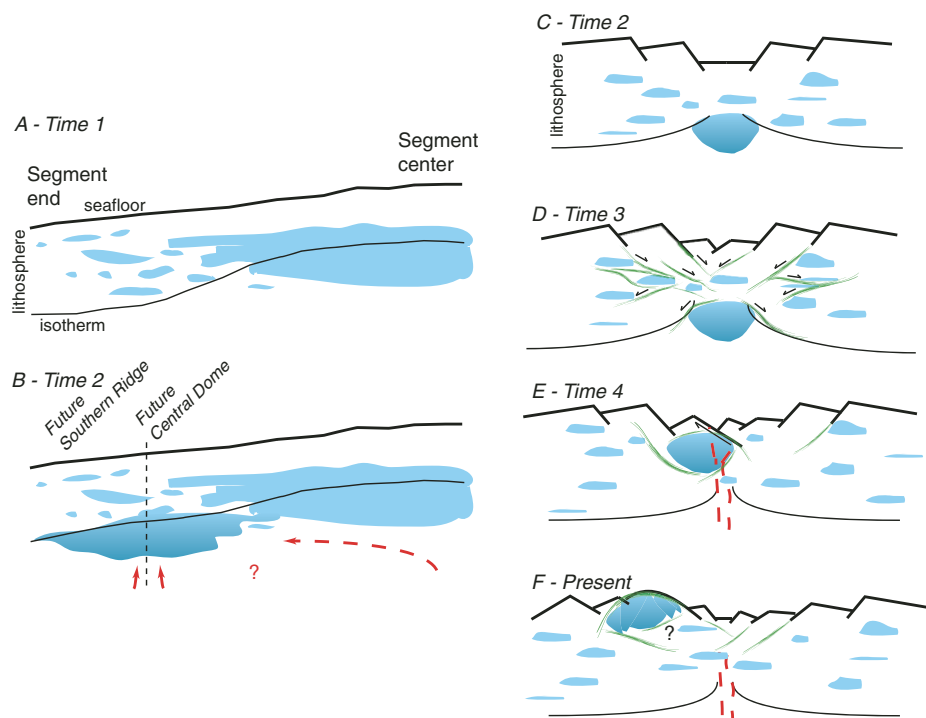


Figure 3. Sketch of revised model for oceanic core complex formation. A, B: Along-axis sections. Vertical dashed line shows location of cross sections. C–F: Spreading-parallel cross sections. For simplicity, only gabbro intrusions are pictured. White part of lithosphere is presumed to be dominantly peridotite at segment end; basalt cover, if present, is concentrated via detachment faulting toward flank opposite to core complexes.

lized gabbro body and faulted serpentinites, as observed at Site U1309, and in short cores from the 15°45'N OCC (MacLeod et al., 2002).

The model implies that serpentinized fault zones envelop the gabbro bodies, explaining the paradox of dominantly gabbroic cores in the vicinity of seafloor serpentinites on top or flanks of OCCs. Further work is required to determine the location of the peridotite-gabbro boundary at Atlantis Massif. Does the active serpentinization signature of venting at the Lost City hydrothermal field just below the peak of Atlantis Massif (Kelley et al., 2001) indicate multi-kilometer thickness of peridotite there? Or, do recent three-dimensional gravity models (Blackman and Collins, 2006) with gabbroic densities throughout the core (both central dome and southern ridge) of the massif better represent the structure? Peridotite is dominant over gabbro on the most intensively studied upper few hundred meters of the southern wall (Boschi et al., 2006; Karson et al., 2006), but the extent to which this is true for the entire southern ridge is unknown. Deep drilling on the southern ridge could provide answers and direct testing of southward extent of the gabbroic pluton sampled down to 1415 mbsf at IODP Site U1309.

ACKNOWLEDGMENTS

We thank captains Pete Mowat and Alex Simpson, the operation superintendents Mike Storms, Stephen Midgley, and Ron Grout, the crew of the JOIDES *Resolution*, and the Integrated Ocean Drilling Program (IODP) United States Implementing Organization's technical staff for their outstanding work during IODP Expeditions 304 and 305. The manuscript benefited from reviews by Roger Buck, Henry Dick, and an anonymous reviewer.

REFERENCES CITED

- Allerton, S., and MacLeod, C.J., 1998, Fault-controlled magma transport in the mantle lithosphere at slow-spreading ridges, in Mills, R.A., and Harrison, K., eds., *Modern ocean floor processes and the geological record: Geological Society [London] Special Publication 148*, p. 29–42.
- Blackman, D., and Collins, J., 2006, Structure and development of MAR30°N oceanic core complex [abs.]: *Ofioliti*, v. 31, p. 227.
- Blackman, D.K., Cann, J.R., Janssen, B., and Smith, D.K., 1998, Origin of extensional core complexes: Evidence from the Mid-Atlantic Ridge at Atlantis Fracture Zone: *Journal of Geophysical Research*, v. 103, p. 21,315–21,333, doi: 10.1029/98JB01756.
- Blackman, D.K., Karson, J.A., Kelley, D.S., Cann, J.R., Fruh-Green, G.L., Gee, J.S., Hurst, S.D., John, B.E., Morgan, J., Nooner, S.L., Ross, D.K., Schroeder, T.J., and Williams, E.A., 2002, Geology of the Atlantis Massif (Mid-Atlantic Ridge, 30 degrees N): Implications for the evolution of an ultramafic oceanic core complex: *Marine Geophysical Research*, v. 23, p. 443–469, doi: 10.1023/B:MARI.0000018232.14085.75.
- Blackman, D.K., Ildefonse, B., John, B.E., Ohara, Y., Miller, D.J., MacLeod, C.J., and Expedition 304/305 Scientists, 2006, Proceedings of the Integrated Ocean Drilling Program, Volume 304/305: College Station, Texas, Integrated Ocean Drilling Program Management International, Inc., doi: 10.2204/iodp.proc.304305.2006.
- Boschi, C., Früh-Green, G.L., Delacour, A., Karson, J.A., and Kelley, D.S., 2006, Mass transfer and fluid flow during detachment faulting and development of an oceanic core complex, Atlantis Massif (MAR 30°N): *Geochemistry, Geophysics, Geosystems*, v. 7, doi: 10.1029/2005GC001074.
- Buck, W.R., Lavier, L.L., and Poliakov, A.N.B., 2005, Modes of faulting at mid-ocean ridges: *Nature*, v. 434, p. 719–723, doi: 10.1038/nature03358.
- Cann, J.R., Blackman, D.K., Smith, D.K., McAllister, E., Janssen, B., Mello, S., Aygerinos, E., Pascoe, A.R., and Escartin, J., 1997, Corrugated slip surfaces formed at ridge-transform intersections on the Mid-Atlantic Ridge: *Nature*, v. 385, p. 329–332, doi: 10.1038/385329a0.
- Cannat, M., 1996, How thick is the magmatic crust at slow spreading oceanic ridges?: *Journal of Geophysical Research*, v. 101, p. 2847–2857, doi: 10.1029/95JB03116.
- Cannat, M., Sauter, D., Mendel, V., Ruellan, E., Okino, K., Escartin, J., Combier, V., and Baala, M., 2006, Modes of seafloor generation at a melt-poor ultraslow-spreading ridge: *Geology*, v. 34, p. 605–608.
- Dick, H.J.B., and 27 others, 2000, A long in-situ section of the lower ocean crust: Results of ODP Leg 176 drilling at the Southwest Indian Ridge: *Earth and Planetary Science Letters*, v. 179, p. 31–51, doi: 10.1016/S0012-821X(00)00102-3.
- Dick, H.J.B., Arai, S., Hirth, G., John, B.J., and KR00–06 Scientific Party, 2001, A sub-horizontal cross-section through the crust mantle boundary at the SW Indian Ridge: *Geophysical Research Abstracts*, v. 3.
- Escartin, J., Hirth, G., and Evans, B., 1997, Effects of serpentinization on the lithospheric strength and the style of normal faulting at slow-spreading ridges: *Earth and Planetary Science Letters*, v. 151, p. 181–189, doi: 10.1016/S0012-821X(97)81847-X.
- Escartin, J., Hirth, G., and Evans, B., 2001, Strength of slightly serpentinized peridotites: Implications for the tectonics of oceanic lithosphere: *Geology*, v. 29, p. 1023–1026, doi: 10.1130/0091-7613(2001)029<1023:SOSSPI>2.0.CO;2.
- Escartin, J., Mével, C., MacLeod, C.J., and McCaig, A.M., 2003, Constraints on deformation conditions and the origin of oceanic detachments: The Mid-Atlantic Ridge core complex at 15: *Geochemistry, Geophysics, Geosystems*, v. 4, doi: 10.1029/2002GC000472.
- Fujiwara, T., Lin, J., Matsumoto, T., Kelemen, P.B., Tucholke, B.E., and Casey, J.F., 2003, Crustal evolution of the Mid-Atlantic Ridge near the Fifteen-Twenty Fracture Zone in the last 5 Ma: *Geochemistry, Geophysics, Geosystems*, v. 4, doi: 10.1029/2002GC000364.
- Karson, J.A., 1990, Seafloor spreading on the Mid-Atlantic Ridge: Implications for the structure of ophiolites and oceanic lithosphere produced in slow-spreading environments, in Malpas, J., et al., eds., *Ophiolites and oceanic crustal analogues: Proceedings of the Symposium "Troodos 1987"*: Nicosia, Cyprus, Geological Survey Department, p. 125–130.
- Karson, J.A., Früh-Green, G.L., Kelley, D.S., Williams, E.A., Yoerger, D.R., and Jakuba, M., 2006, Detachment shear zone of the Atlantis Massif core complex, Mid-Atlantic Ridge, 30°N: *Geochemistry, Geophysics, Geosystems*, v. 7, doi: 10.1029/2005GC001109.
- Kelemen, P.B., Kikawa, E., Miller, D.J., and Shipboard Science Party, 2004, Proceedings of the Ocean Drilling Program, Initial reports, Volume 29: College Station, Texas, Ocean Drilling Program, doi: 10.2973/odp.proc.ir.209.2004.
- Kelley, D.S., Karson, J.A., Blackman, D.K., Fruh-Green, G.L., Butterfield, D.A., Lilley, M.D., Olson, E.J., Schrenk, M.O., Roe, K.K., Lebon, G.T., and Rivizzigno, P., 2001, An off-axis hydrothermal vent field near the Mid-Atlantic Ridge at 30 degrees N: *Nature*, v. 412, p. 145–149, doi: 10.1038/35084000.
- Lagabrielle, Y., Bideau, D., Cannat, M., Karson, J.A., and Mevel, C., 1998, Ultramafic-mafic plutonic rock suites exposed along the Mid-Atlantic Ridge (10°N–30°N). Symmetrical-asymmetrical distribution and implications for seafloor spreading processes, in Buck, W.R., et al., eds., *Faulting and magmatism at mid-ocean ridges: American Geophysical Union Geophysical Monograph 106*, p. 153–176.
- MacLeod, C.J., Dick, H.J.B., Allerton, S., Robinson, P.T., and the JR31 Scientific Party, 1999, Structure of Atlantis Bank, SW Indian Ridge: An eroded megamullion surface?: *Geophysical Research Abstracts*, v. 1, p. 186.
- MacLeod, C.J., Escartin, J., Banerji, D., Banks, G.J., Gleeson, M., Irving, D.H.B., Lilly, R.M., McCaig, A.M., Niu, Y., Allerton, S., and Smith, D.K., 2002, Direct geological evidence for oceanic detachment faulting: The Mid-Atlantic Ridge, 15°45'N: *Geology*, v. 30, p. 879–882, doi: 10.1130/0091-7613(2002)030<0879:DGEFOD>2.0.CO;2.
- Pettigrew, T.L., Casey, J.F., Miller, D.J., and Shipboard Science Party, 1999, Proceedings of the Ocean Drilling Program, Initial reports, Volume 179: College Station, Texas, Ocean Drilling Program, doi: 10.2973/odp.proc.ir.179.1999.
- Robinson, P.T., Von Herzen, R., and Shipboard Science Party, 1989, Proceedings of the Ocean Drilling Program, Initial reports, Volume 118: College Station, Texas, Ocean Drilling Program, doi: 10.2973/odp.proc.ir.118.1989.
- Schroeder, T., and John, B.E., 2004, Strain localization on an oceanic detachment fault system, Atlantis Massif, 30 degrees N, Mid-Atlantic Ridge: *Geochemistry, Geophysics, Geosystems*, v. 5, p. Q11007, doi: 10.1029/2004GC000728.
- Smith, D.K., Cann, J.R., and Escartin, J., 2006, Widespread active detachment faulting and core complex formation near 13 degrees N on the Mid-Atlantic Ridge: *Nature*, v. 442, p. 440–443, doi: 10.1038/nature04950.
- Tucholke, B.E., and Lin, J., 1994, A geological model for the structure of ridge segments in slow spreading ocean crust: *Journal of Geophysical Research*, v. 99, p. 11,937–11,958, doi: 10.1029/94JB00338.
- Tucholke, B.E., Lin, J., and Kleinrock, M.C., 1998, Megamullions and mullion structure defining oceanic metamorphic core complexes on the mid-Atlantic ridge: *Journal of Geophysical Research*, v. 103, p. 9857–9866, doi: 10.1029/98JB00167.

Manuscript received 14 November 2006

Revised manuscript received 27 February 2007

Manuscript accepted 3 March 2007

Printed in USA

IODP Expeditions 304 & 305 Characterize the Lithology, Structure, and Alteration of an Oceanic Core Complex

by Benoit Ildefonse, Donna Blackman, Barbara E. John, Yasuhiko Ohara, D. Jay Miller, Christopher J. MacLeod, and the IODP Expeditions 304-305 Scientists

doi:10.2204/iodp.sd.3.01.2006

Introduction and Goals

More than forty years after the Mohole Project (Bascom, 1961), the goal of drilling a complete section through *in situ* oceanic crust remains unachieved. Deep Sea Drilling Project – Ocean Drilling Program (DSDP-ODP) Hole 504B within the eastern Pacific (Alt et al., 1993) is the deepest hole ever drilled into ocean crust (2111 mbsf), but it failed to reach lower crustal plutonic rocks below the pillow basalts and sheeted dikes. IODP Expeditions 309 and 312 eventually recovered the long-sought transition from sheeted dikes into underlying gabbros by drilling into very fast-spreading Pacific crust (Wilson et al., 2006). The lithology and structure of oceanic crust produced at slow-spreading ridges are heterogeneous (e.g., Cannat et al., 1997) and offer unique drilling access to lower crust and upper mantle rocks. After

ODP Hole 735B penetrated 1500 m of gabbro at the Southwest Indian Ridge (Dick et al., 2000), IODP Expeditions 304 and 305 recently recovered just over 1400 m of little-deformed, gabbroic lower crust from a tectonic window along the slow-spreading Mid-Atlantic Ridge.

IODP Expeditions 304 and 305 at the Atlantis Massif, Mid-Atlantic Ridge 30°N, were designed to investigate the processes that control oceanic core complex (OCC) formation and exposure of lower crust and upper mantle rocks in young (<2 Ma) oceanic lithosphere accreted at slow-spreading ridges. The corrugated, central portion of this domal massif (Fig. 1) displays morphologic and geophysical characteristics inferred to be representative of an OCC exposed via long-lived, low-angle, normal or detachment faulting (Cann et al., 1997; Blackman et al., 1998, 2004). Geophysical inter-

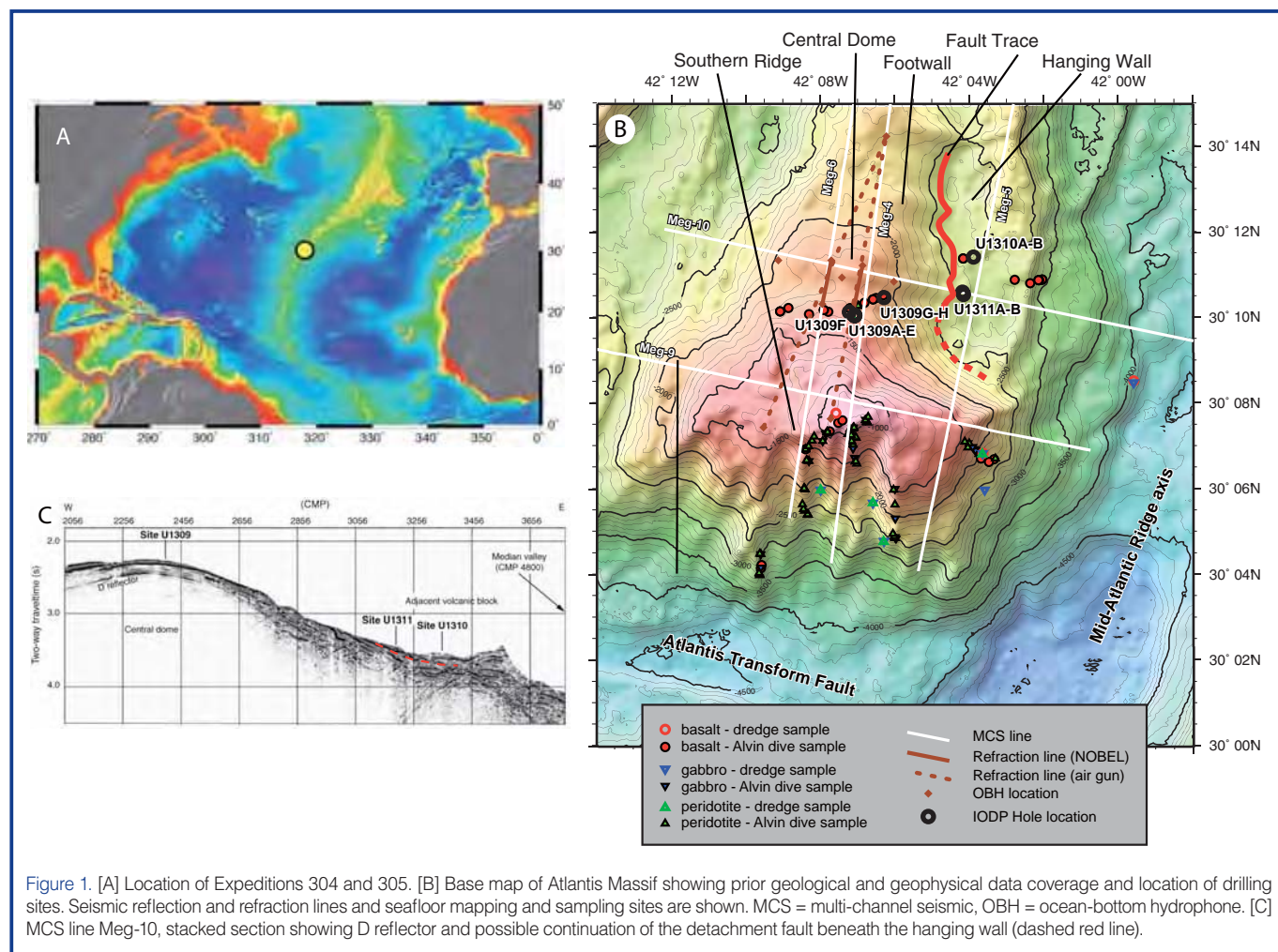


Figure 1. [A] Location of Expeditions 304 and 305. [B] Base map of Atlantis Massif showing prior geological and geophysical data coverage and location of drilling sites. Seismic reflection and refraction lines and seafloor mapping and sampling sites are shown. MCS = multi-channel seismic, OBH = ocean-bottom hydrophone. [C] MCS line Meg-10, stacked section showing D reflector and possible continuation of the detachment fault beneath the hanging wall (dashed red line).

pretations suggested that unaltered mantle rock occurred <1 km below the seafloor (Collins et al., 2003; Blackman et al., 2004; Canales et al., 2004), implying that drilling through an alteration front in ultramafic rocks could be achieved and that fresh mantle peridotite could be recovered at moderate depths. Additional objectives of drilling at the footwall concerned the dominant mechanism(s) of footwall uplift and the interactions between tectonics and magmatism in OCCs. Drilling within the hanging wall and through the detachment fault system was aimed at sampling and further constraining the latter and at assessing petrogenetic relationships between volcanic rocks in the hanging wall and potential source rocks recovered in the footwall.

We attempted drilling at three sites (Fig. 1 [C]), one in the footwall through the inferred detachment fault and two in the hanging wall, but we did not succeed in drilling the fractured basalt in the hanging wall. In contrast, Hole U1309D, in the footwall of the detachment fault, penetrated 1415.5 m below the seafloor, and recovery averaged 75% (IODP Expeditions 304-305 Scientists, 2005). Shallow holes on the footwall provided limited samples whose composition and structure support the hypothesis that the corrugated dome coincides with an exposed detachment fault.

Geological and Geophysical Background

The Atlantis Massif formed within the past 1.5–2 My. and was exhumed along a detachment fault exposed over an 8–10-km-wide, 15-km-long area that forms the elongate, doubly plunging domal seafloor morphology (Fig. 1). Adjacent basaltic rocks to the east are interpreted as part of a hanging-wall block above the detachment fault. Multi-channel seismic data (Canales et al., 2004) suggest that the fault system may dip gently under the seafloor at the base of the dome and continue at a shallow angle (<15°) beneath the eastern block toward the present-day ridge axis (Fig. 1C). The Southern Ridge is shallower than the central dome, shoaling to 700 m below sea level, and its corrugated surface extends eastward to the median valley wall.

Prior to IODP drilling, the core of the Atlantis Massif was inferred to comprise dominantly mantle peridotite. The peridotite-hosted, possibly serpentinization-driven Lost City hydrothermal vent field (Früh-Green et al., 2003; Kelley et al., 2005) is located just below the summit of the Southern Ridge, approximately 5 km south of Site U1309. Analysis of seismic refraction data across the central dome of the Atlantis Massif (Collins et al., 2003) indicated, at least locally, P-wave velocities of ~8 km·s⁻¹ within several hundred meters below the seafloor, possibly indicative of pristine mantle rocks. Interpretation of multi-channel seismic reflection data suggested a major difference in structure between the outside (conjugate) corner lithosphere versus that hosting the Atlantis Massif (Canales et al., 2004). A strong reflector is visible at 0.2–0.5 s below much of the domal surface and coincides roughly with the depth below which mantle

velocities were inferred from the seismic refraction data. One interpretation of this “D reflector” suggested that it marks an alteration front within the peridotite-dominated massif. The multi-channel seismic (MCS) processing employed by Canales et al. (2004) resulted in the D reflector being quite continuous across the dome. A subsequent study by Singh et al. (2004) using different processing parameters to emphasize deep reflectivity produced a less continuous, but still pervasive interval of reflectivity whose top generally coincided with Canales’ D reflector. Modeling of sea-surface gravity and sparse seafloor data (Blackman et al., 1998, 2004; Nooner et al., 2003) suggests that rocks beneath the central and southern dome have densities 200–400 kg·m⁻³ greater than rock to either side.

Rock samples collected from the central dome by the manned submersible *Alvin* are dominated by angular talus and rubble of serpentinized peridotite, metabasalt, and limestone (Blackman et al., 2004). A few samples from the central dome show cataclastic deformation or are highly serpentinized or metasomatically altered peridotite. The protolith of most of the serpentinite sampled on the south wall (Fig. 1) is inferred to be harzburgite. Talc-rich fault rocks preserve textural and geochemical characteristics of their ultramafic protoliths (Boschi et al., 2006). Microstructural analysis of samples from the south wall (Schroeder and John, 2004) indicates ductile deformation initially at granulite facies, overprinted by semi-brittle and brittle deformation down to subgreenschist facies. The observations and sample distribution suggest that strong semi-brittle and brittle deformation is concentrated at shallow structural levels (~100 m beneath the domal surface) along the Southern Ridge (Schroeder and John, 2004; Karson et al., 2006). Rocks sampled from the hanging wall by manned submersible are wholly basalt (Blackman et al., 2004).

Drilling at the Atlantis Massif Reveals Dominantly Gabbroic Core

Igneous rocks recovered from Site U1309 span a broad range in composition, from the most primitive crustal rocks ever cored in slow-spreading oceanic lithosphere (Mg# up to ~90) to highly evolved rock types (Fig. 2). To a first order, the gabbroic section can be divided into two major igneous units (Johnson et al., 2005). The upper unit extends to ~600 mbsf and broadly shows an increase downhole in olivine-rich rock types, although the detailed lithostratigraphy is more complicated. There is a sharp decrease in whole-rock Mg# of the gabbros at ~600 mbsf (Fig. 2). Oxide-rich gabbros are concentrated in a zone between these upper and lower units. The lower unit also shows a general increase downhole in olivine-rich rock types, with oxide-rich intervals near the base of the hole. At least two thin, mantle-peridotite intervals are recognized in the upper 180 m of the section, implying that the gabbroic section recovered in Hole U1309D was in part intruded into mantle peridotite.

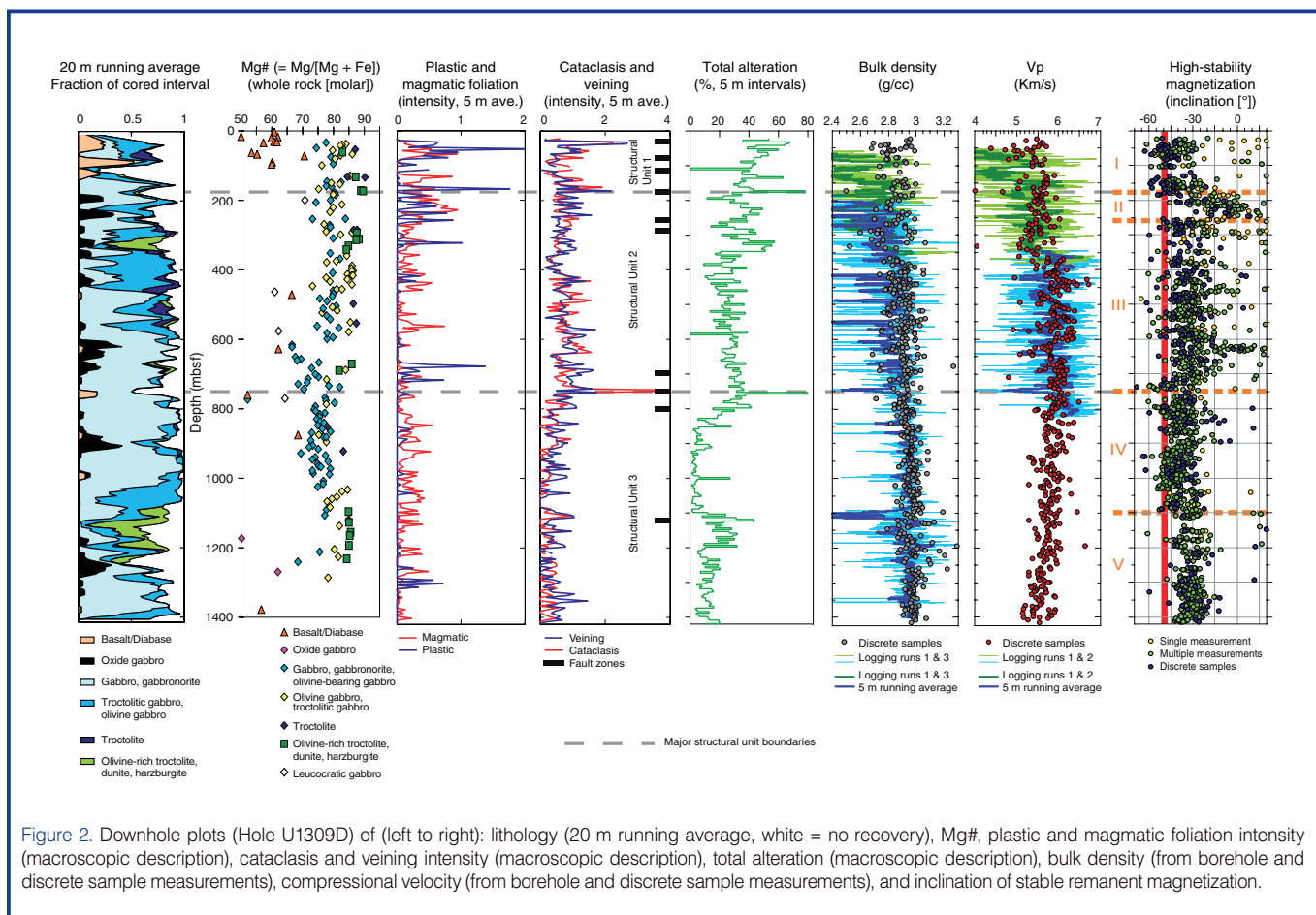


Figure 2. Downhole plots (Hole U1309D) of (left to right): lithology (20 m running average, white = no recovery), Mg#, plastic and magmatic foliation intensity (macroscopic description), cataclasis and veining intensity (macroscopic description), total alteration (macroscopic description), bulk density (from borehole and discrete sample measurements), compressional velocity (from borehole and discrete sample measurements), and inclination of stable remanent magnetization.

Holes U1309B and U1309D have interfingered lithologic units that vary in thickness from centimeters up to ~100–200 m where intrusive contacts are preserved. Contact relations where visible between gabbro and other rock types, except diabase at Site U1309, suggest that gabbro is generally intrusive into more olivine-rich rock types, such as olivine gabbro and troctolite, and in turn intruded by felsic (“leucocratic”) dikes and oxide gabbro. These relationships are more common between 400 and 650 mbsf than in the lower part of the hole, where gabbro contacts are commonly more diffuse. The ~140-m-thick interval of olivine-rich troctolite and minor associated lithologic units from 1094 to 1236 mbsf in Hole U1309D forms an integral lithologic package that has been intruded by numerous crosscutting gabbroic dikes of variable thickness at temperatures below the troctolite solidus. Broader-scale contacts with adjacent olivine gabbro appear to be dominantly intrusive and formed under hyper-solidus conditions. Late diabase intrusions are found in several places throughout Holes U1309B and U1309D.

The most abundant rock type recovered is gabbroic in composition and spans a wide range of modal composition, including minor (rarely exceeding a few percent) amounts of olivine, Fe-Ti oxides, and orthopyroxene. Gabbros and gabbronorites exhibit significant variation in grain size (<1 mm to >10 cm), occasionally within a single section of core. Olivine gabbro, the second-most abundant rock type, has highly variable modal compositions on a submeter scale

and grades locally into troctolitic gabbro; it is commonly spatially associated with troctolites. A series of olivine-rich rocks (~5% in hole U1309D; dunites, wehrlites, troctolites), grouped as olivine-rich troctolites, are interlayered with gabbroic rocks. In contrast to troctolite, olivine-rich troctolite displays subhedral to rounded medium-grained olivine and interstitial to poikilitic plagioclase and clinopyroxene in variable proportions. These rocks may represent primitive cumulates.

Fe-Ti oxide gabbro, resulting from pervasive, late-magmatic-stage infiltration of evolved melt, composes 7% of the rocks recovered from Hole U1309D. The most common occurrence of oxide concentrations (~80% of the oxide gabbros) is seen as randomly dispersed patches in undeformed, generally coarse-grained gabbro. They are also found as discrete dikelets or layers cutting other rock types with either sharp or diffuse boundaries, and associated with intervals of ductile deformation.

Structure and Alteration

The core from Hole U1309D can be divided structurally into three major units (Fig. 2):

- Structural Unit 1 (0–170 mbsf) is marked by a high but decreasing degree of cataclasis downhole; abundant, late, relatively undeformed diabase; a high degree of green-

schist-grade alteration; and a near-present-day orientation of the paleomagnetic inclination. The boundary to structural Unit 2 at ~170 mbsf is marked by a subhorizontal to moderately dipping crystal-plastic shear zone within gabbroic rocks, a high intensity of veining, strong cataclasis, and a ~2-m-thick interval of altered ultramafic rocks.

- Structural Unit 2 (~170 to ~785 mbsf) is marked by a relatively high intensity of veining, including the presence of sulfide minerals. Paleomagnetic inclinations are ~10°–30° shallower than present-day values. The base of structural Unit 2 is defined by a series of greenschist-grade cataclastic fault zones between 695 and 785 mbsf.
- Structural Unit 3 extends beyond 785 mbsf and is characterized by an overall low intensity of cataclastic deformation, veining, and plastic deformation.

Overall, the section is moderately altered at conditions ranging from granulite to zeolite facies and dominated by static, greenschist facies assemblages. Pseudomorphs of igneous textures remain largely unmodified. Magmatic deformation fabrics, as defined by the preferred orientation of plagioclase, were recorded in 22% of the recovered rocks. These fabrics are weak to very weak, except in local intervals, and tend to be developed more clearly in gabbroic rocks with finer initial grain size; foliation is also well developed in the rare layered intervals. In many places, weak crystal-plastic deformation seems to overprint magmatic foliations (Fig. 3). High-strain, crystal-plastic shear zones are rare (Figs. 2 and 3) and are typically restricted to clearly defined, mostly granulite-grade shear zones ranging in width from millimeters to a few meters. This contrasts markedly with the much larger number of high-strain shear zones recorded in the gabbroic complex at ODP Site 735B (Fig. 3A) on the Southwest Indian Ridge (Dick et al., 1999, 2000). Vein intensity in Hole 1309D decreases significantly below 785 mbsf (Fig. 2) and tends to correlate with cataclastic deformation in general and with fault zones on a local scale. On the scale of the entire core, there is no systematic, lithology-dependent distribution of vein type downhole. The amount of strain recorded by brittle fracture and cataclasis is limited overall, except for a few fault zones concentrated in the upper 50 m of Hole U1309D and in discrete intervals downhole, some of which correspond to the boundaries of the defined major structural units, in particular at ~750 mbsf (Fig. 2). Cataclasis is associated locally with oxide gabbro intervals and dikelets, leucocratic veins, and contact zones between diabase intrusions and their gabbroic host rocks.

The lack of significant structures indicative of high displacement by either ductile or brittle processes severely limits the possible thickness of fault zones that could compose a detachment system over the central dome. Poor recovery of the upper 20 m of the footwall allows the possibility that this narrow zone accommodated very high strain along a dominantly brittle fault, as documented at the 15°45'N OCC (MacLeod et al., 2002; Escartín et al., 2003). If so, the fault

zone thickness differs from the 50–100 m estimates at the Southern Ridge (Williams et al., 2003; Schroeder and John, 2004; Karson et al., 2006). This difference results either from a decreasing thickness of the fault from the south to the center of the dome or from an overestimated thickness at the Southern Ridge because of limitations in accurately determining the structural depth of subsurface samples. Extensive amphibolite facies deformation is lacking, and high-strain ductile shear zones are rare. The absence of a thick zone of high-temperature ductile deformation in the footwall and the apparent tectonic history (less rotation in the upper 180 m and variable rotations between several distinct, few-hundred-meter sections downhole, Fig. 2) suggested by paleomagnetic inclination measurements indicate complexity in structural evolution that differs from a simple model of a deep-rooted detachment fault, predicted to be associated with high-temperature deformation, and with constant or monotonically varying footwall rotation with depth.

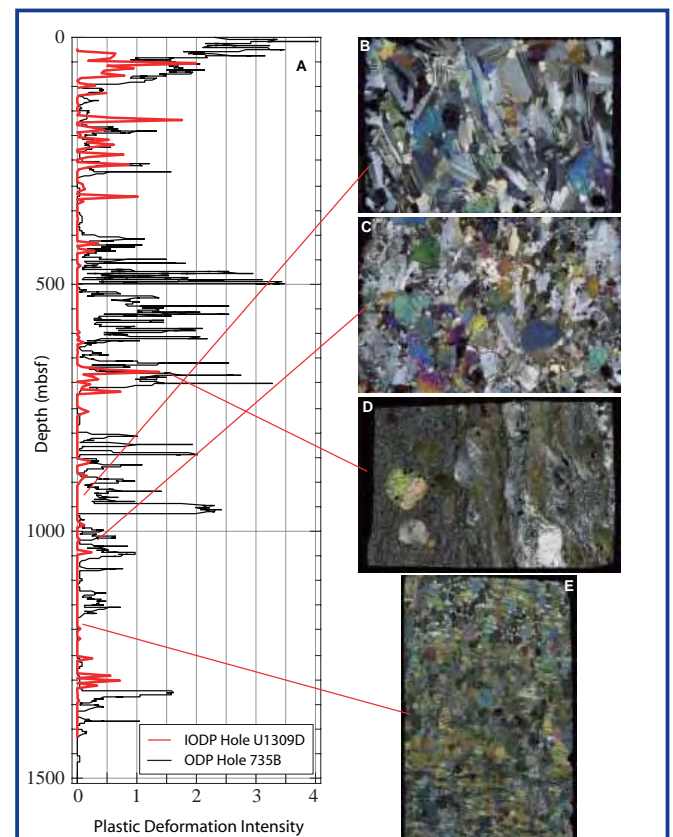


Figure 3. Intensity of crystal-plastic deformation and microstructural characters of magmatic and plastic foliations (cross-polarized light, field of view ~2 cm). [A] Compared deformation intensities (5 m running average) in ODP Hole 735B and IODP Hole U1309D (Crystal-plastic deformation scale: 0 = undeformed, 1 = weakly foliated, 2 = strongly foliated, 4 porphyroclastic). [B] Magmatic foliation. [C] High-temperature, low-stress, crystal-plastic foliation. Note the dynamic recrystallization of plagioclase and olivine. Crystal-plastic strain probably overprints a pre-existing magmatic foliation. [D] Mylonitic foliation (low temperature, high stress) with relict plagioclase and clinopyroxene porphyroclasts. [E] Olivine-rich troctolite with alignment, possibly magmatic, of weakly elongated olivines. Note that poikilitic plagioclase and clinopyroxene grains are not elongated parallel to foliation.

Altered mineral assemblages in rocks from Site U1309 record cooling of mafic plutonic rocks from submagmatic conditions (>1000°C) to zeolite facies temperatures (<200°C) during the unroofing and uplift of the Atlantis Massif. Individual samples generally display a range of superimposed metamorphic conditions, but no single sample records the entire cooling history of the site. Overall, alteration intensity is moderate, tends to decrease downhole, and is commonly related to vein intensity (Fig. 2). Local exceptions to this general downhole decrease in alteration intensity often correlate with an increase in modal abundance of olivine. Coarser-grained gabbro intervals are generally more altered than medium- to coarse-grained units. Intervals of olivine-rich troctolite show alteration restricted to heterogeneous serpentine networks, with strong alteration gradients from the contact with intensely veined intercalated gabbros to fresher cores. The latter contain local intervals of very fresh (as low as 1% serpentinization) olivine-rich (as much as >90%) rocks.

The metamorphic and alteration history recorded at Site U1309 is summarized as follows:

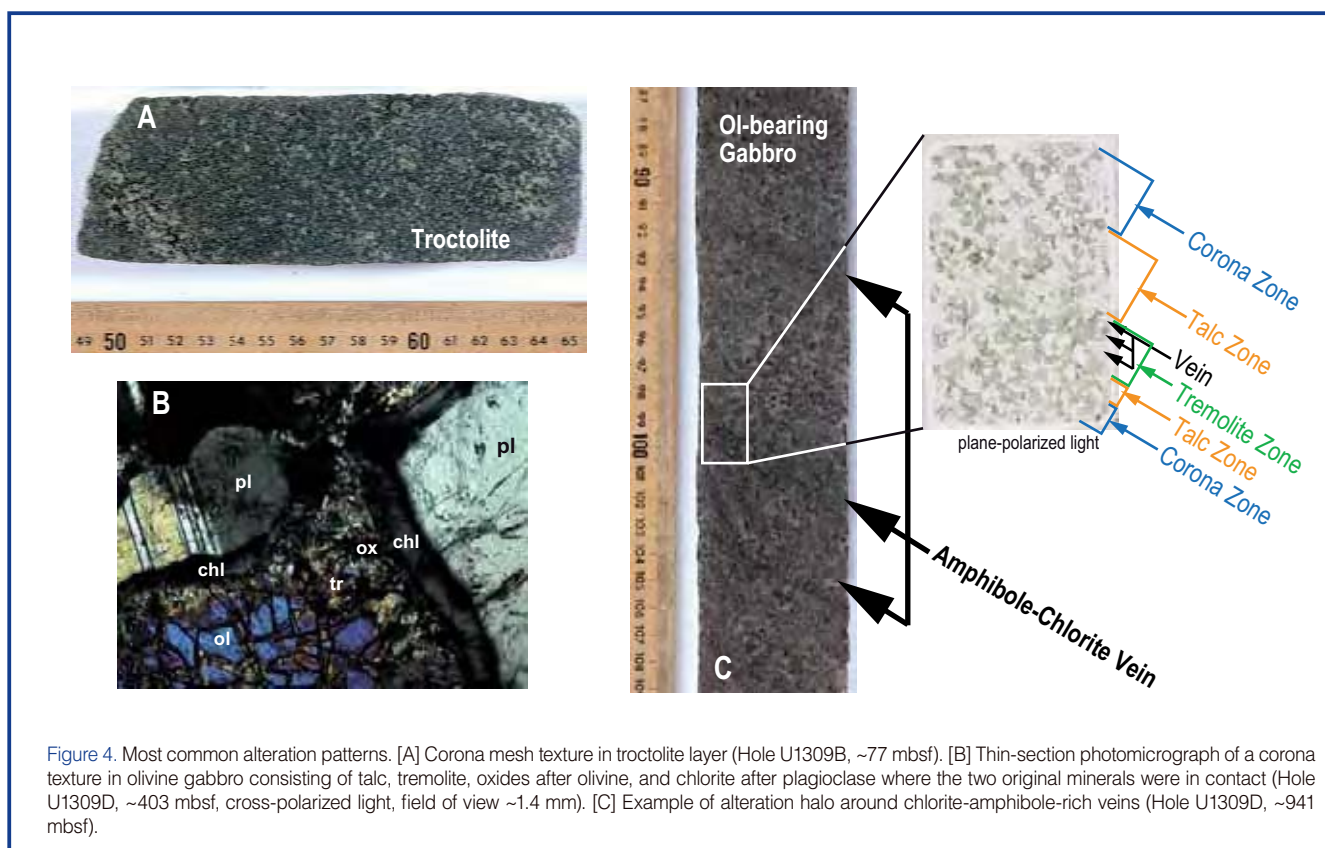
1. High-temperature, near-solidus, mylonitic deformation and recrystallization at granulite- to upper-amphibolite-facies conditions.
2. A widespread, largely static upper-greenschist-facies to lower-amphibolite-facies event (Figs. 2 and 4). The upper ~380 m of the core shows a beautiful alteration profile with evidence for pervasive static infiltration of seawater with decreasing temperature. In addition, these same rocks show

localized alteration superimposed in some cases on pervasive alteration, presumably reflecting localized fluid flow and metasomatism. Below this depth, alteration is generally restricted to halos around veins, fractures, and igneous contacts.

3. Static, lower greenschist to subgreenschist metamorphism. Serpentinization above ~300 mbsf is restricted to rocks where olivine was in excess over plagioclase and was therefore still present after the corona-forming reaction between olivine and plagioclase (stage 2) went to completion. At deeper levels, serpentine, prehnite, and hydrogrossular are often localized on closely spaced, variably oriented fractures.

Correlations Between Alteration and Geophysical Signature

Downhole logging and physical property measurements on core samples do not correlate strongly with rock type (Fig. 2). Instead, alteration may play a stronger role in determining the geophysical signature of the upper 1.5 km of the central dome. Average sample density varies only slightly, from 2.800 g·cm⁻³ in the upper 380 mbsf to 2.900 g·cm⁻³ in the lower ~1 km (Fig. 2). Meter-scale intervals show more variability in both sample and logging measurements, with oxide gabbro sometimes reaching >3.200 g·cm⁻³ and highly altered olivine-rich zones dropping to <2.700 g·cm⁻³. Average compressional velocity is 5.6 km·s⁻¹ in the upper ~400 m and 5.8 km·s⁻¹ for the interval ~500–800 mbsf. The mid-expedition checkshot experiment extended to 840 mbsf, the base of the hole at that stage. Instrument failure and poor weather



precluded acquisition of seismic data in the final logging run. Seismic velocity values obtained by sample and sonic log measurements range from ~ 5.1 to $6.8 \text{ km}\cdot\text{s}^{-1}$. Values less than $5.5 \text{ km}\cdot\text{s}^{-1}$ are common in the upper 180 mbsf and in the olivine-rich interval $\sim 280\text{--}380$ mbsf, below which values near $6 \text{ km}\cdot\text{s}^{-1}$ are most common. Only thin intervals have a velocity greater than $6.5 \text{ km}\cdot\text{s}^{-1}$ corresponding to olivine gabbro or olivine-rich troctolite units with little alteration.

Shipboard processing of the checkshot data revealed only first-arrival information. Although the signal-to-noise ratio was generally good for the stacked data, considerable noise was present due to impacts of the pipe in the upper part of the hole. After the expedition, individual traces were analyzed, and particularly noisy records were removed prior to re-stacking and bandpass filtering (5–120 Hz). The processed data (Fig. 5) show a secondary arrival that trails the first peak by a time that decreases from 41 ms to essentially zero between stations at 275 and 435 mbsf. Using the delays at the 275 and 345 mbsf stations and a velocity of $5.5 \text{ km}\cdot\text{s}^{-1}$, a reflector at ~ 390 mbsf could produce the secondary arrival that also corresponds to a strong reflector on the MCS line closest to Hole U1309D. It is likely that this represents the D reflector in this part of the dome.

The temperature-acceleration-pressure (TAP) tool recorded a temperature of 120°C at the bottom of the hole (Fig. 6). Temperature increased with depth as expected but was somewhat lower than predicted from a simple cooling-

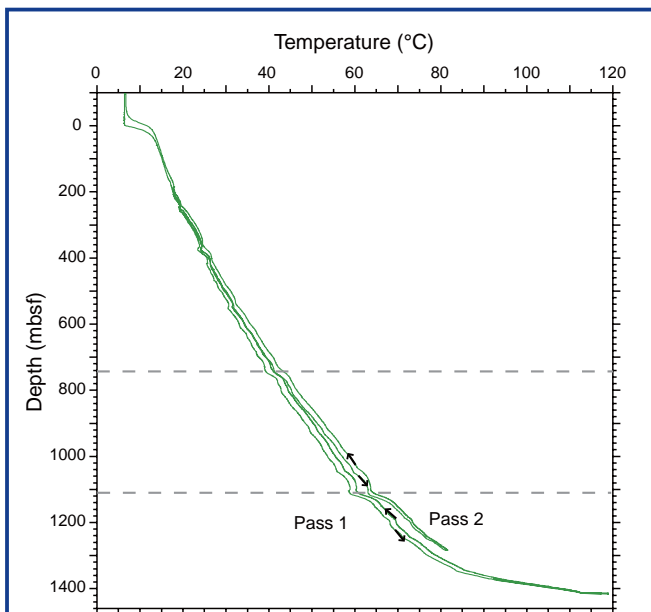


Figure 6. Temperature recorded by TAP tool. Increase in borehole temperature with time is recorded during downhole and uphole logging runs and during repeated logging passes. Dashed lines indicate recognized fault zones (see Fig. 2) which coincide with local dips in temperature.

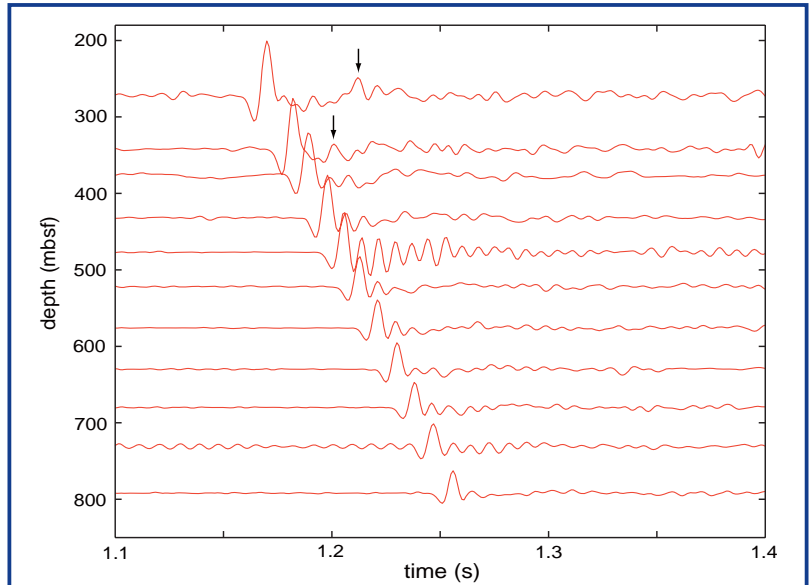


Figure 5. Filtered waveforms for checkshot experiment in upper part of Hole U1309D. Main arrival has strong signal-to-noise ratio. Removal of especially noisy traces brings out character of later arrivals. At upper stations, a secondary arrival (arrows) probably corresponds to D reflector of Canales et al., (2004).

plate model of a spreading ridge flank with an age of ~ 2 Ma. The measured temperatures are a minimum estimate, however, because of hole cooling during coring. These initial results suggest that thermally driven flow is likely to occur in the hole. Several drops of a few degrees were recorded in narrow intervals (two of which coincide with documented fault zones at ~ 750 and 1110 mbsf) on repeated TAP runs (Fig. 6), perhaps indicating localized fluid flow.

Concluding Remarks

Igneous rocks recovered at Site U1309 provide an exceptional record of magmatic accretion, tectonic exposure, and hydrothermal alteration in a slow-spreading ridge environment. The exposures of peridotite along the southern wall of the Atlantis Massif, the geophysical results suggesting that at least portions of the dome contain fresh olivine-rich rock (possibly olivine-rich troctolites), and the down-hole variability at Site U1309 all likely indicate significant lateral lithological heterogeneity over distances as short as hundreds of meters across the footwall.

The Atlantis Massif is the fourth location where drilling an OCC (i.e., a corrugated massif, or an inside corner high capped by fault rocks) at a slow-spreading ridge has been attempted by ODP or IODP. A total of fourteen holes (>10 m deep) were cored at seven different sites in three different OCCs during ODP Legs 118, 153, 176, 179, and 209 (Robinson, et al., 1989; Cannat, et al., 1995; Dick, et al., 1999; Pettigrew et al., 1999; Kelemen, et al., 2004). Those efforts recovered only gabbroic sections, ranging from Fe-Ti oxide gabbros to troctolites, locally intruded by diabase. The latest results of IODP Expeditions 304 and 305 point to the need for a new paradigm of crustal accretion in regions that are classically inferred to be representative of magma-starved portions of

the ridge. One possible working model relates the development of OCCs to the occurrence of periodically larger gabbroic bodies beneath slow-spreading ridge segment ends (Ildefonse et al., 2006). Uplift and exhumation of these gabbroic bodies would be enabled by deformation that localized predominantly within the serpentinized peridotite that initially surrounded them. The northward extension, inside the core of the Atlantis Massif, of the serpentinites outcropping at the southern wall is presently unknown. These serpentinites could represent a relatively thin sheet of mantle rocks surrounding a dominantly gabbroic core. Alternatively, a significant, but unknown part of the Atlantis Massif footwall may be composed primarily of serpentinite and peridotite. Further IODP operations in this region should combine deeper drilling in Hole U1309D and drilling the southeast shoulder of the Atlantis Massif.

Acknowledgements

We thank Captains Pete Mowat and Alex Simpson, the operation superintendents Mike Storms, Stephen Midgley, and Ron Grout, the crew of the *JOIDES Resolution*, and the IODP United States Implementing Organization's technical staff for their commitment and hard work during Expeditions 304 and 305.

IODP Expeditions 304 and 305 Scientists

D. Blackman (Co-Chief Scientist), B. Ildefonse (Co-Chief Scientist), B.E. John (Co-Chief Scientist), Y. Ohara (Co-Chief Scientist), D.J. Miller (Expedition Project Manager/Staff Scientist), C.J. MacLeod (Shore-based Contributor), N. Abe, M. Abratis, E.S. Andal, M. Andréani, S. Awaji, J.S. Beard, D. Brunelli, A.B. Charney, D.M. Christie, A.G. Delacour, H. Delius, M. Drouin, F. Einaudi, J. Escartin, B.R. Frost, P.B. Fryer, J.S. Gee, M. Godard, C.B. Grimes, A. Halfpenny, H-E. Hansen, A.C. Harris, A.T. Hasebe, N.W. Hayman, E. Hellebrand, T. Hirose, J.G. Hirth, S. Ishimaru, K.T.M. Johnson, G.D. Karner, M. Linek, J. Maeda, O.U. Mason, A.M. McCaig, K. Michibayashi, A. Morris, T. Nakagawa, T. Nozaka, M. Rosner, R.C. Searle, G. Suhr, M. Tominaga, A. von der Handt, T. Yamasaki, and X. Zhao.

References

- Alt, J.C., Kinoshita, H., Stokking, L.B., et al., 1993. Proc. ODP, Init. Repts., 148: College Station, Texas, U.S.A. (Ocean Drilling Program).
- Bascom, W.N., 1961. A Hole in the Bottom of the Sea: The Story of the Mohole Project. Garden City, New York (Doubleday and Company, Inc.).
- Blackman, D.K., Cann, J.R., Janssen, B., and Smith, D.K., 1998. Origin of extensional core complexes: evidence from the MAR at Atlantis fracture zone. *J. Geophys. Res.*, 103:21315–21334. doi:10.1029/98JB01756
- Blackman, D.K., Karson, J.A., Kelley, D.S., Cann, J.R., Früh-Green, G.L., Gee, J.S., Hurst, S.D., John, B.E. Morgan, J., Nooner, S.L., Ross, D.K., Schroeder, T.J., and Williams, E.A., 2004. Geology of the Atlantis Massif (MAR 30°N): implications for the evolution of an ultramafic oceanic core complex. *Mar. Geophys. Res.*, 23:443–469. doi:10.1023/B:MARI.0000018232.14085.75
- Boschi, C., Früh-Green, G.L., Delacour, A., Karson, J.A., and Kelley, D.S., 2006. Mass transfer and fluid flow during detachment faulting and development of an oceanic core complex, Atlantis Massif (MAR 30°N), *Geochem. Geophys. Geosyst.*, 7:Q01004, doi:10.1029/2005GC001074.
- Canales, J.P., Tucholke, B.E., and Collins, J.A., 2004. Seismic reflection imaging of an oceanic detachment fault: Atlantis megamullion (Mid-Atlantic Ridge, 30°10'N). *Earth Planet. Sci. Lett.*, 222:543–560; doi:10.1016/j.epsl.2004.02.023.
- Cann, J.R., Blackman, D.K., Smith, D.K., McAllister, E., Janssen, B., Mello, S., Avgerinos, E., Pascoe, A.R., and Escartin, J., 1997. Corrugated slip surfaces formed at ridge-transform intersections on the Mid-Atlantic Ridge. *Nature*, (London, U. K.), 385:329–332; doi:10.1038/385329a0.
- Cannat, M., Karson, J.A., Miller, D.J., et al., 1995. Proc. ODP, Init. Repts., 153: College Station, TX (Ocean Drilling Program).
- Cannat, M., Lagabriele, Y., Bougault, H., Casey, J., de Coutures, N., Dmitriev, L., and Fouquet, Y., 1997. Ultramafic and gabbroic exposures at the Mid-Atlantic Ridge: geological mapping in the 15 degrees N region. *Tectonophysics*, 279:193–213; doi:10.1016/S0040-1951(97)00113-3.
- Collins, J., Canales, J., and Tucholke, B., 2003. Seismic velocity structure of mid-Atlantic ridge core complexes: Geophysical Research Abstracts, Vol. 5, 10390.
- Dick, H.J.B., Natland, J.H., Miller, D.J., et al., 1999. Proc. ODP, Init. Repts., 176. Available at http://www-odp.tamu.edu/publications/176_IR/176TOC.HTM.
- Dick, H.J.B., Natland, J.H., Alt, J.C., Bach, W., Bideau, D., Gee, J.S., Haggas, S., Hertogen, J.G.H., Hirth, G., Holm, P.M., Ildefonse, B., Iturrino, G.J., John, B.E., Kelley, D.S., Kikawa, E., Kingdon, A., LeRoux, P.J., Maeda, J., Meyer, P.S., Miller, D.J., Naslund, H.R., Niu, Y.-L., Robinson, P.T., Snow, J., Stephen, R.A., Trimby, P.W., Worm, H.-U., and Yoshinobu, A., 2000. A long in situ section of the lower ocean crust: results of ODP Leg 176 drilling at the Southwest Indian Ridge. *Earth Planet. Sci. Lett.*, 179:31–51; doi:10.1016/S0012-821X(00)00102-3.
- Escartin, J., Mével, C., MacLeod, C.J., and McCaig, A., 2003. Constraints on deformation conditions and the origin of oceanic detachments, the Mid-Atlantic Ridge core complex at 15°45'N. *Geochem. Geophys. Geosyst.*, 4(8):1067; doi:10.1029/2002GC000472.
- Früh-Green, G.L., Kelley, D.S., Bernasconi, S.M., Karson, J.A., Ludwig, K.A., Butterfield, D.A., Boschi, C., and Proskurowski, G., 2003. 30,000 years of hydrothermal activity at the Lost City vent field. *Science*, 301:495–498; doi:10.1126/science.1085582.
- IODP Expeditions 304-305 Scientists, 2005. IODP Expeditions 304 and 305: Oceanic Core Complex formation, Atlantis Massif. *Scientific Drilling*, 1:28-31.
- Ildefonse, B., Blackman, D., John, B.E., Ohara, Y., Miller, D.J., MacLeod, C.J., and IODP Expeditions 304-305 Scientific Party, 2006. A revised model of oceanic core complex structure? Indications from IODP Expeditions 304-305, Mid-Atlantic Ridge, 30°N, and previous ocean drilling results.

Geophysical Research Abstracts, 8:05723; SRef-ID: 1607-7962/gra/EGU06-A-05723.

- Johnson, K.T., Hellebrand, E., Abe, N., Andal, E., Brunelli, D., Charney, A., Christie, D., Hansen, H., Ishimaru, S., Maeda, J., Ohara, Y., Suhr, G., Tamura, A., Van der Handt, A., Yamasaki, T., and IODP Expedition 304-305 Scientific Party, 2005. Igneous petrology of Hole U1309D, IODP Expeditions 304/305 at the Atlantis Massif, MAR 30°N, Eos Trans. AGU, 86(52), Fall Meet. Suppl., Abstract T41D-1336.
- Karson, J.A., Früh-Green, G.L., Kelley, D.S., Williams, E.A., Yoerger, D.R., and Jakuba, M., 2006. Detachment shear zone of the Atlantis Massif core complex, Mid-Atlantic Ridge, 30°N, *Geochem. Geophys. Geosyst.*, 7:Q06016; doi:10.1029/2005GC001109.
- Kelemen, P.B., Kikawa, E., Miller, D.J., et al., 2004. Proc. ODP, Init. Repts., 209 Available at http://www-odp.tamu.edu/publications/209_IR/209ir.htm.
- Kelley, D.S., Karson, J.A., Früh-Green, G.L., Yoerger, D.R., Shank, T.M., Butterfield, D.A., Hayes, J.M., Schrenk, M.O., Olson, E.J., Proskurowski, G., Jakuba, M., Bradley, A., Larson, B., Ludwig, K., Glickson, D., Buckman, K., Bradley, A.S., Brazelton, W.J., Roe, K., Elend, M.J., Delacour, A., Bernasconi, S.M., Lilley, M.D., Baross, J.A., Summons, R. E., and Sylva, S.P., 2005. A serpentinite-hosted ecosystem: the Lost City hydrothermal field. *Science*, 307:1428–1434; doi:10.1126/science.1102556.
- MacLeod, C.J., Escartin, J., Banerji, D., Banks, G.J., Gleeson, M., Irving, D.H.B., Lilly, R.M., McCaig, A.M., Niu, Y., Allerton, S., and Smith, D.K., 2002. Direct geological evidence for oceanic detachment faulting: the Mid-Atlantic Ridge, 15°45'N. *Geology*, 30:10:879–882; doi:10.1130/0091-7613(2002)030<0879:DGEFOD> 2.0.CO;2.
- Nooner, S.L., Sasagawa, G.S., Blackman, D.K., and Zumberge, M.A., 2003. Constraints on crustal structure at the Mid-Atlantic Ridge from seafloor gravity measurements made at the Atlantis Massif. *Geophys. Res. Lett.*, 30:1446; doi:10.1029/2003GL017126.
- Pettigrew, T.L., Casey, J.F., Miller, D.J., et al., 1999. Proc. ODP, Init. Repts., 179. Available from World Wide Web: http://www-odp.tamu.edu/publications/179_IR/179TOC.HTM.
- Robinson, P.T., Von Herzen, R., et al., 1989. Proc. ODP, Init. Repts., 118: College Station, TX (Ocean Drilling Program).
- Schroeder, T., and John, B.E., 2004. Strain localization on an oceanic detachment fault system, Atlantis Massif, 30°N, Mid-Atlantic Ridge. *Geochem. Geophys. Geosyst.*, 5(11):Q11007 doi:10.1029/2004GC000728.
- Singh, S.C., Collins, J.A., Canales, J.P., Tucholke, B.E., and Detrick, R.S., 2004. New insights into serpentinitization at Atlantis Massif. *Eos Trans. AGU* 85(47), Fall Meet. Suppl., Abstract V23B-0628.
- Williams, E.A., Karson, J.A., Kelley, D.S., and Früh-Green, G.L., 2003. Cross-section of the Atlantis Massif - Geologic Framework for the Lost City Hydrothermal Vent Field. *Eos Trans. AGU*, 84(46), Fall Meet. Suppl., Abstract B12A-0774.
- Wilson, D.S., Teagle, D.A.H., Alt, J.C., Banerjee, N.R., Umino, S., Miyashita, S., Acton, G.D., Anma, R., Barr, S.R., Belghoul, A., Carlut, J., Christie, D.M., Coggon, R.M., Cooper, K.M., Cordier, C., Crispini, L., Durand, S.R., Einaudi, F., Galli, L., Gao, Y.J., Geldmacher, J., Gilbert, L.A., Hayman, N.W., Herrero-Bervera, E., Hirano, N., Holter, S., Ingle, S., Jiang, S.J., Kalberkamp, U., Kerneklian, M., Koepke, J., Laverne, C., Vasquez, H.L.L., MacLennan, J., Morgan, S., Neo, N., Nichols, H.J., Park, S.H., Reichow, M.K., Sakuyama, T., Sano, T., Sandwell, R., Scheibner, B., Smith-Duque, C.E., Swift, S.A., Tartarotti, P., Tikku, A.A., Tominaga, M., Veloso, E.A., Yamasaki, T., Yamazaki, S., and Ziegler, C., 2006. Drilling to gabbro in intact ocean crust. *Science*, 312:1016–1020; doi:10.1126/science.1126090.

Authors

Benoit Ildefonse, CNRS, Laboratoire de Tectonophysique, Université Montpellier 2, 34095 Montpellier cedex 5, France, e-mail : benoit.ildefonse@univ-montp2.fr

Donna Blackman, Scripps Institution of Oceanography, University of California, San Diego, 9500 Gilman Drive, La Jolla, Calif. 92093-0225, U.S.A.

Barbara E. John, Department of Geology and Geophysics, University of Wyoming, 1000 East University Avenue, Department 3006, Laramie, Wyo. 82071, U.S.A.

Yasuhiko Ohara, Ocean Research Laboratory, Hydrographic and Oceanographic Department of Japan, 5-3-1 Tsukiji, Chuo-ku, Tokyo 104-0045, Japan

D. Jay Miller, Integrated Ocean Drilling Program, Texas A&M University, 1000 Discovery Drive, College Station, Texas 77845-9547, U.S.A.

Christopher J. MacLeod, School of Earth, Ocean and Planetary Sciences, Cardiff University, Main Building, Park Place, Cardiff CF10 3YE, U.K.

and the IODP Expeditions 304–305 Scientists

Related Web Links

- <http://iodp.tamu.edu/scienceops/expeditions/exp304.html>
<http://iodp.tamu.edu/scienceops/expeditions/exp305.html>
http://www-odp.tamu.edu/publications/176_IR/176TOC.HTM.
http://www-odp.tamu.edu/publications/209_IR/209ir.htm

Pervasive melt percolation reactions in ultra-depleted refractory harzburgites at the Mid-Atlantic Ridge, 15° 20'N: ODP Hole 1274A

Monique Seyler · J. -P. Lorand · H. J. B. Dick ·
M. Drouin

Received: 14 June 2006 / Accepted: 14 September 2006 / Published online: 9 November 2006
© Springer-Verlag 2006

Abstract ODP Leg 209 Site 1274 mantle peridotites are highly refractory in terms of lack of residual clinopyroxene, olivine Mg# (up to 0.92) and spinel Cr# (~0.5), suggesting high degree of partial melting (>20%). Detailed studies of their microstructures show that they have extensively reacted with a pervading intergranular melt prior to cooling in the lithosphere, leading to crystallization of olivine, clinopyroxene and spinel at the expense of orthopyroxene. The least reacted harzburgites are too rich in orthopyroxene to be simple residues of low-pressure (spinel field) partial melting. Cu-rich sulfides that precipitated with the

clinopyroxenes indicate that the intergranular melt was generated by no more than 12% melting of a MORB mantle or by more extensive melting of a clinopyroxene-rich lithology. Rare olivine-rich lherzolitic domains, characterized by relics of coarse clinopyroxenes intergrown with magmatic sulfides, support the second interpretation. Further, coarse and intergranular clinopyroxenes are highly depleted in REE, Zr and Ti. A two-stage partial melting/melt–rock reaction history is proposed, in which initial mantle underwent depletion and refertilization after an earlier high pressure (garnet field) melting event before upwelling and remelting beneath the present-day ridge. The ultra-depleted compositions were acquired through melt re-equilibration with residual harzburgites.

Communicated by T.L. Grove.

Electronic supplementary material Supplementary material is available in the online version of this article at <http://dx.doi.org/10.1007/s00410-006-0148-6> and is accessible for authorized users.

M. Seyler · J. -P. Lorand
Museum National d'Histoire Naturelle,
CNRS UMR7160 Minéralogie—Pétrologie,
61 rue Buffon, 75005 Paris, France

H. J. B. Dick
Woods Hole Oceanographic Institution,
Woods Hole, MA 02543, USA

M. Drouin
Laboratoire de Tectonophysique,
CNRS UMR 5568, Université de Montpellier 2,
Place Eugène Bataillon,
Montpellier Cedex 05 34095, France

M. Seyler (✉)
Université Lille1, UFR Sciences de la Terre,
Bât. SN5, Villeneuve d'Ascq cedex 59655, France
e-mail: Monique.Seyler@univ-lille1.fr

Introduction

Abysal peridotites are widely considered as complementary residues of mid-oceanic ridge basalts (MORBs) after variable degree of adiabatic melting resulting from decompression of the mantle beneath spreading ridges. In this view, their structure, texture and composition must provide valuable information on melting and melt extraction processes and source composition. Current models assume that melts segregate from their sources after melting for a very low percent melting and are rapidly extracted from the surrounding mantle to be transferred into high-porosity channels, where they are transported to the surface with no chemical interaction with the shallow mantle (Kelemen et al. 1997). Strongly depleted light to heavy rare earth element ratios (LREE/HREE) in residual clinopyroxene (Cpx) are

indeed indisputable evidence for near-fractional melt extraction beneath spreading ridges (Johnson et al. 1990; Johnson and Dick 1992). On the other hand, it is argued that the last melt fractions produced by low-P partial melting of depleted peridotites may travel by diffuse porous flow, leading to extensive melt–rock reaction and peridotite refertilization in the shallow mantle (Kelemen et al. 1997; Asimow 1999; Dijkstra et al. 2003). Recently, it was recognized that a small proportion of Cpx in abyssal peridotites is not residual, but crystallized from melt as the partially molten mantle enters into the conductive thermal layer (Seyler et al. 2001; Hellebrand et al. 2002; Brunelli et al. 2006). This observation supports the idea of refertilization of the fractional melting residues by basaltic melt, which was first suggested by Elthon (1992). Reactive porous flow and refertilization are two important processes that are potentially able to deeply modify textures, mineral modes and chemical compositions of residual peridotites. Melt–rock interaction and refertilization were principally studied in plagioclase-bearing peridotites, in which feldspar-bearing veins and strong chemical gradients make these reactions immediately recognizable. In contrast, coarse-grained, plagioclase-free spinel peridotites show no obvious evidence of these reactions, because they theoretically cool at a greater depth. At a temperature close to the peridotite solidus and condition of low-strain deformation, residual and igneous minerals tend to textural and chemical equilibria. Serpentinization will then tend to blur or destroy any fragile evidence of reaction. As a consequence, description of reactional textures in abyssal peridotites is very few and little is known about the nature of reactions really involved in these processes. Hence, the extent of the reactions and the magnitude of the compositional changes they induce are poorly evaluated.

Ocean Drilling Program Leg 209 Site 1274 mantle peridotites appear to be most suitable to study these two aspects. They experienced a relatively low degree of serpentinization, and textures show greater extent of diffuse melt–rock reaction than commonly observed in most abyssal peridotites. In this paper we describe in detail a variety of these high-T microstructures, which are believed to result from pervasive melt–rock reaction in partially molten peridotites. Petrographic observation coupled with in situ mineral chemistry allows us to investigate the nature and conditions of melt–rock reactions and to constrain some aspects of the melting history of the peridotites. Fe–Ni–Cu sulfides of magmatic origin have been studied in addition to major minerals. These base metal sulfides are important petrogenetic indicators of partial melting degree and

melt–rock interactions, because they concentrate chalcophile trace elements (S, Cu) that partition very similarly to CaO and Al₂O₃ (Lorand 1988, 1991; Luguet et al. 2003).

Geological setting

The region of the Mid-Atlantic Ridge (MAR) extending across the 15°20'N Fracture Zone (FZ) has been the focus of numerous geophysical, dredging and submersible surveys, and was recently drilled at eight sites during Leg 209 of the Ocean Drilling Program (Escartin and Cannat 1999; Fujiwara et al. 2003; Kelemen et al. 2004, and reviews therein). In this region, basaltic crust is thin and discontinuous, and mantle peridotites with gabbroic intrusions crop out nearly continuously on both sides of the rift valley from 14°40'N to 15°40'N. The overall quantity of gabbroic rocks is estimated to be 20–40%, a proportion that would correspond to 5 km of “normal” oceanic crust (Kelemen 2003). Two gravity lows, centered at ~14°N and ~16°N, are interpreted as centers of magmatic segments where thick igneous crust accreted. While the peridotites appear to have undergone an unusually high degree of melting (Bonatti et al. 1992; Cannat et al. 1992, 1997), the basalt compositions evolve from enriched-type MORBs in the 14°N region to normal-type MORBs in the 16°N region (Dosso et al. 1991, 1993).

ODP Leg 209, Site 1274, located 31 km north (15°65'N–46°68'W) of the NW intersection of the MAR with the 15°20'N FZ (Fig. 1), has drilled into 156 m of mantle peridotite, with 35% recovery. Cores recovered are mainly residual peridotite, with a few m-scale gabbroic intrusions, and a large proportion of dunites (77% harzburgite; 20% dunite; 3% gabbros). Site 1274 peridotites contain the smallest proportion of gabbros with respect to other Leg 209 sites (Fig. 1). Thick fault gouge forms about 7% of the recovered cores, in the lower part of the hole, between ~95 and ~145 mbsf. Site 1274 peridotites are less serpentinized and weathered (up to 35% of the original mantle preserved) than Sites 1268 and 1272 peridotites (>99% serpentinization). In the three sites, the peridotite protolith is dominated by harzburgites varying in composition from orthopyroxene (Opx)-rich (28–30 vol% Opx) to Opx-poor (10 vol%) to dunites. Cpx content represents 1–2 vol% of the peridotites (visual estimation), with rare, local concentrations, up to 4 vol%. In a few places, a rough Opx layering can be observed, but in general, rocks have coarse granular textures lacking high-T foliation and lineation.

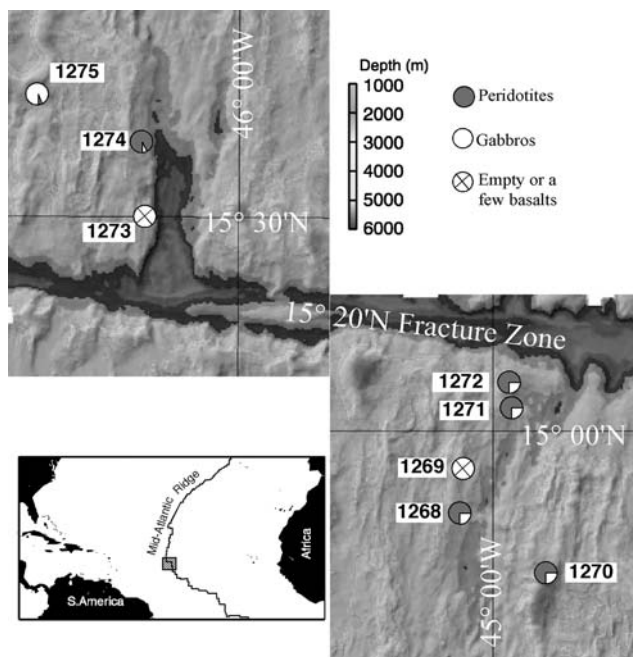


Fig. 1 Location and lithologies of ODP Leg 209 drill sites, shown on bathymetric map from Fujiwara et al. (2003)

Sample selection and analytical methods

The studied sample set comprises 36 harzburgites, 1 Cpx-rich harzburgite and 1 dunite. Harzburgites were sampled away from dunite bands and gabbros (Table 1; Fig. 2a). Each sample consists of a 35 × 25 mm billet, 0.5 to 0.75 cm thick, in which 1 to 3 standardized thin sections have been cut. Primary modal proportions of 12 samples were reconstructed, using relict primary phases and their pseudomorphs, by point counting (steps of 1/3 mm; ~6,000 points per sample). Detailed textural observation and modes of fine-grained mineral intergrowths were completed by analyzing backscattered electron images. In addition, the 25 SEY samples were investigated in reflected light microscopy to identify base metal sulfides (BMS); their modal abundances (two polished thin sections per sample) were determined using a procedure reported in detail by Lorand and Grégoire (2006). Mineral compositions were analyzed with a CAMECA SX-100 electron microprobe at the University of Paris VI and at Woods Hole Oceanographic Institute. The accelerating voltage was 15 kV and beam current was 40 nA (15 nA for Na). A 2 μm beam size was used for all minerals, except a subset of pyroxenes, for which average compositions including exsolution lamellae were obtained with a defocused beam (10–15 μm). Selected Cpx were analyzed for REEs, Zr, Ti and Sr by secondary ion mass spectrometry, using an upgraded

Table 1 Sample numbers and their position in Hole 1274A cores

| Hole 1274A sample no. | Core | Section | Interval (cm) | Piece |
|-----------------------|------|---------|---------------|-------|
| SEY01 | 1R | 1 | 4–5 | 1 |
| SEY02 | 1R | 1 | 27–31 | 4 |
| SEY03 | 1R | 1 | 65–66 | 8 |
| SEY04 | 1R | 1 | 88–90 | 10 |
| SEY05 | 2R | 1 | 33–36 | 6 |
| SEY06 | 3R | 1 | 44–45 | 6 |
| SEY07 | 3R | 1 | 85–86 | 9 |
| SEY08 | 4R | 1 | 15–18 | 1B |
| SEY09 | 4R | 1 | 44–46 | 2B |
| SEY10 | 4R | 2 | 1–3 | 1 |
| SEY11 | 5R | 1 | 3–5 | 1 |
| SEY12 | 5R | 1 | 45–49 | 7 |
| HJBD01 | 6R | 1 | 38–48 | 6 |
| HJBD02 | 6R | 3 | 40–50 | 1B |
| SEY13 | 7R | 1 | 48–50 | 4 |
| HJBD03 | 7R | 2 | 20–30 | 2A |
| SEY14 | 8R | 1 | 40–43 | 7 |
| HJBD04 | 8R | 1 | 46–52 | 8 |
| SEY15 | 8R | 2 | 9–11 | 1 |
| HJBD05 | 9R | 1 | 14–16 | 3 |
| SEY16 | 11R | 1 | 11–13 | 2 |
| HJBD06 | 11R | 1 | 117–121 | 17 |
| SEY17 | 12R | 1 | 2–4 | 1 |
| SEY18 | 12R | 1 | 65–67 | 10 |
| SEY19 | 12R | 1 | 72–75 | 10 |
| SEY20 | 12R | 2 | 10–14 | 3 |
| HJBD07 | 13R | 1 | 81–85 | 9 |
| HJBD08 | 14R | 1 | 102–106 | 12 |
| SEY21 | 18R | 1 | 13–16 | 3 |
| SEY22 | 18R | 1 | 112–113 | 19 |
| HJBD09 | 19R | 1 | 17–22 | 4 |
| HJBD10 | 20R | 1 | 18–24 | 4 |
| HJBD11 | 23R | 1 | 53–57 | 11 |
| HJBD12 | 24R | 1 | 90–95 | 5 |
| HJBD13 | 26R | 1 | 52–56 | 9 |
| SEY23 | 27R | 1 | 87–90 | 7 |
| SEY24 | 27R | 1 | 112–116 | 8 |
| SEY25 | 27R | 2 | 18–21 | 2 |

Cameca IMS-4f ion microprobe at the University of Montpellier and following procedures described in Bottazzi et al. (1994).

Analytical results

Modal compositions

Olivine (Ol) and Opx contents in the studied harzburgites vary from 70.3 to 84.1 vol% and 13.4 to 27.2 vol%, respectively (Table 2). Cpx content is in the 0.7–2.6 vol% range in the harzburgites, and is 4.7 vol% in the Cpx-rich harzburgite; this sample, very close to lherzolite in Streckeisen's classification (1976), is referenced as lherzolite herein. Spinel (Sp) is ubiquitous and may be abundant in some samples (0.5–1.3 vol%).

Fig. 2 ODP Leg 209 Hole 1274A. **a** Stratigraphic summary of lithologies with a graphical depiction of the recovery for each interval (TD = total depth; after Kelemen et al. 2004). **b** Distribution of magmatic sulfides in 25 samples. **c** Ranges of Na₂O contents in clinopyroxenes from 36 samples

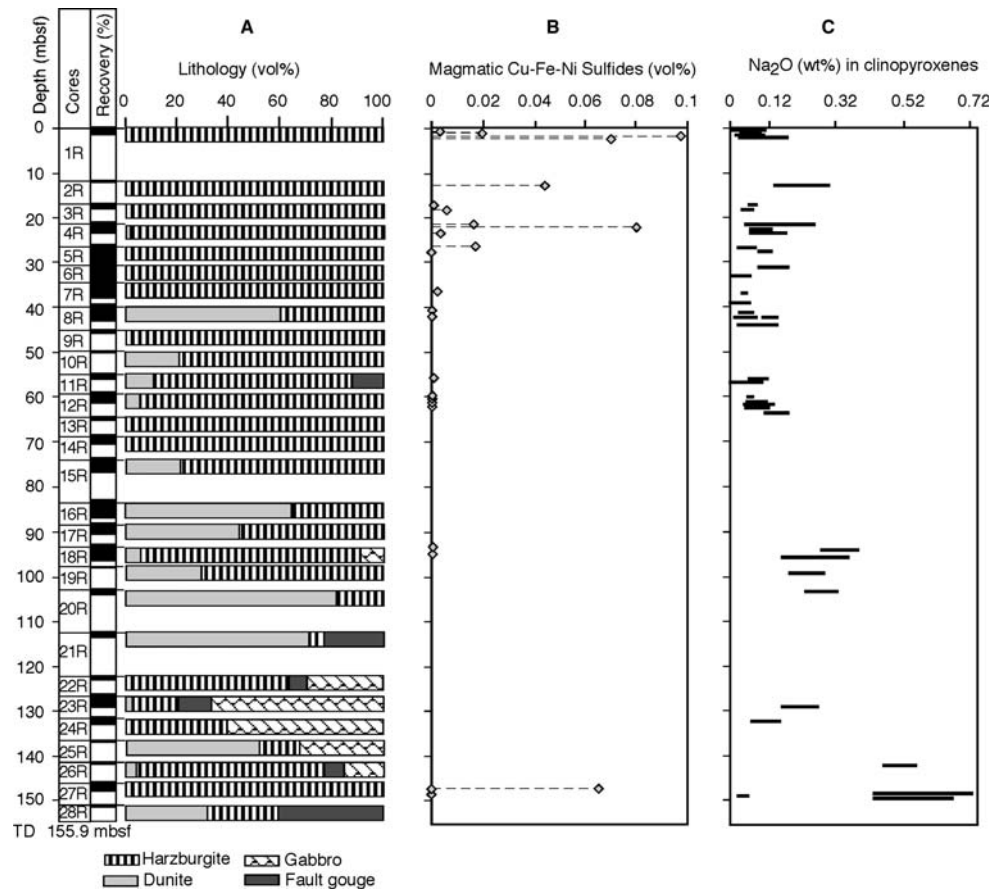


Table 2 Reconstructed primary modal compositions (vol%) of representative ODP Leg 209 Hole peridotites

| | Li | Ol | Opx | Tot. Cpx | Tot. Sp | Cpx* | S1 |
|-------|----|------|------|----------|---------|------|------|
| SEY02 | H | 81.1 | 17.6 | 0.71 | 0.57 | 0.36 | 0.58 |
| SEY03 | H | 72.3 | 24.2 | 2.30 | 1.24 | 1.56 | 1.22 |
| SEY04 | L | 77.2 | 17.1 | 4.72 | 0.51 | 3.48 | 2.07 |
| SEY07 | H | 74.2 | 23.7 | 1.57 | 0.57 | 0.87 | 1.17 |
| SEY11 | H | 77.1 | 19.9 | 2.20 | 0.80 | 1.09 | 1.84 |
| SEY14 | H | 70.3 | 27.2 | 2.06 | 0.49 | 1.32 | 1.23 |
| SEY15 | D | 96.2 | 0.1 | 2.2 | 1.5 | 1.2 | 1.5 |
| SEY16 | H | 72.8 | 25.1 | 1.68 | 0.45 | 1.02 | 1.10 |
| SEY21 | H | 74.1 | 22.0 | 2.58 | 1.27 | 1.56 | 1.70 |
| SEY22 | H | 80.5 | 16.8 | 1.82 | 0.80 | 1.21 | 1.01 |
| SEY23 | H | 84.1 | 13.4 | 1.74 | 0.77 | 1.18 | 0.94 |
| SEY25 | H | 77.3 | 19.9 | 1.99 | 0.75 | 0.86 | 1.88 |

Sample composition is represented by a single, standard-sized, thin section (~6,000 points)

Li Lithology, *H* harzburgite, *L* lherzolite, *D* dunite. Mineral abbreviations: *Ol* olivine; *Opx* orthopyroxene; *Tot. Cpx* total clinopyroxene; *Tot. Sp* total spinel; *Cpx** interstitial clinopyroxene grains not intergrown with spinel, and selvages on orthopyroxenes; *S1* Type 1 clinopyroxene-spinel symplectites

The average composition of the 11 harzburgites/lherzolite is 76.5% Ol, 20.6% Opx, 2.1% Cpx and 0.7% Sp, in the average of the visually estimated composition of Hole 1274A harzburgites (Kelemen et al. 2004). No correlation was found between Cpx and Opx or Ol contents, and the lherzolite is especially poor in Opx.

Base metal sulfides have been detected in 75% of the studied thin sections (Fig. 2b). Owing to the average degree of serpentinization, all the BMS assemblages except a few inclusions in the Opx described subsequently, systematically display partial replacement of primary sulfides (pentlandite Fe₄Ni₅S₈ to

Fe₅Ni₄S₈ (unpublished EMP data), chalcopyrite Cu-FeS₂, bornite Cu₅FeS₄) by native copper, Ni₃Fe alloys and/or magnetite, and occasionally by heazlewoodite Ni₃S₂ and secondary Cu-rich sulfides (digenite Cu₉S₅ and valleriite CuFe₂S₃, Mg(OH)₂). This alteration sequence is common to abyssal peridotites (Luguet et al. 2003). Serpentinization-related opaque minerals preserved the original shape of magmatic sulfide grains, i.e. polyhedral (not euhedral) blebs with generally concave inward grain boundaries. Only such grains were used for modal abundance estimates.

Site 1274 peridotites may be as BMS-rich as fertile mantle lherzolites (up to 0.1 vol%), despite their average harzburgitic modal compositions. However, BMS are heterogeneously distributed, being concentrated in the uppermost 25 m of Hole 1274A and in the deeper Ol-rich harzburgite SEY23; two zones that yielded only harzburgites (Fig. 2a, b). The highest BMS concentrations correspond to high (>0.1) Cpx/Opx modal ratios (SEY03; SEY04; SEY23) and the lowest to Opx-rich samples (>20% Opx). However, BMS are strongly heterogeneously distributed at the hand-sample scale which generated strong random sectioning effects. For example, one thin section in SEY09 contains almost no BMS whereas the other is the second richest one (0.08 vol% BMS). The near-zero BMS content of samples from 40 to 145 mbsf is worthy of note, because it seems to correspond with the occurrence of numerous dunites (although there are sampling gaps in our studied sample set).

Microstructures and grain morphology

Centimeter-sized, rounded olivine domains are mosaics of 3–4 mm-sized grains. Gently curved to polygonal grain boundaries, with an occasional subgrain boundary, suggests recrystallization of very coarse primary crystals. Opx porphyroclasts are highly variable in grain shape and size. Coarse to very coarse (>1–2 cm), equant Opx are occasionally broken with formation of wedge-shaped fractures (Fig. 3a) which affect only the Opx grains and not adjacent Ol and display no specific orientation. Opx grain boundaries commonly display cusped embayments filled with secondary Ol, varying in size from a few micrometer to a few millimeter. In many instances, Ol sides in contact with reacted Opx have developed faceted crystal boundaries, which suggests growth from, or re-equilibration with, a melt film that was present at the Ol–Opx interface; in some cases, this melt film is interpreted to have left behind a stringer of Cpx. With increasing degree of dissolution, some Opx grains become ovoid and define a flow structure. More typically, strong dissolution results in

the formation of anhedral, thin, elongate grains, interstitial to Ol. Replacive Ol commonly penetrates Opx along cleavage planes (Fig. 3b). Extensive replacement of Opx by Ol results in the parceling of the original, very coarse grains into what appears in thin section as clusters of variously shaped (angular to rounded) Opx clasts within a matrix of newly crystallized Ol. Ends of Opx porphyroclasts are preferentially corroded or intergrown with Sp several millimeters long and a few 100 μm wide (Fig. 3c). These aggregates are interpreted as recrystallized Opx parcels cemented by Sp and minor Cpx. This secondary material is arranged along the crystallographic directions of the host mineral and likely results from the infiltration of melt which reacted with the Opx, then precipitated Sp ± Cpx. This material steps out the Opx in between adjacent Ol grains (Fig. 3c); at these sites, Ol is resorbed into tiny grains poikilitically enclosed in Sp. A few samples show high strain deformation, with mosaics of very fine grained (20–50 μm) Ol replacing Opx along kink bands and grain boundaries. However, Opx dynamic recrystallization was not observed in any samples.

Clinopyroxene occurs in two major textural types. The first type characterizes the lherzolite sample, where coarse (up to 5 mm) Cpx grains, with large exsolution lamellae of Opx and occasional twinning, form diffuse, one crystal thick, discontinuous veins (Fig. 4a); some partially replace Opx (Fig. 4b). Crystal boundaries show large embayments filled with Ol (Fig. 4a), similar to those in Opx porphyroclasts. However, in contrast with Opx, these Cpx have poikiloblastic rims, associated with tiny grains of Sp, that enclose adjacent Ol or Opx (Fig. 4a) and can be followed over several millimeters (Fig. 4c). Both cores and rims display intergrowths with magmatic sulfides (Fig. 4c, d). The second Cpx texture type, ubiquitous in the lherzolite and all harzburgites, consists of smaller grains, up to 2 mm in size, with thin exsolution lamellae of Opx and rare twinning. They typically form selvages on Opx, with Opx–Cpx contacts characterized by strong Opx resorption: Opx display convex-out grain boundaries and tends to be poikilitically enclosed by Cpx (Fig. 4e). Cpx selvages show thin extensions between adjacent Ol grains, locally widen into small to medium-sized, intergranular Cpx. Late-stage Cpx also fills low-angle triple junctions, V-shaped fractures in Opx, and small cracks in the Ol matrix.

Spinel is found with recrystallized Opx (described in Opx section) or associated with late-stage Cpx. Sp shapes range from anhedral to blocky, subhedral porphyroblasts up to 2 mm sized, that are often overgrown by a corona of Cpx in spatial continuity with the Cpx

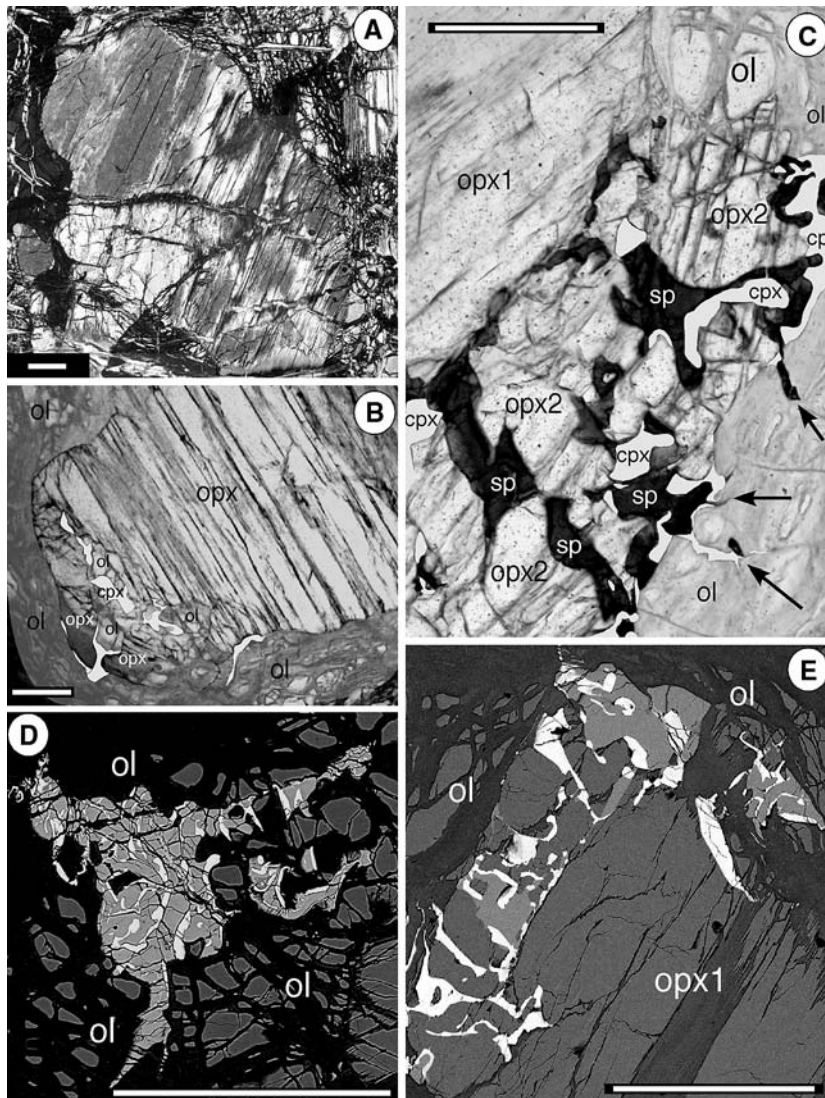


Fig. 3 Photomicrographs of Site 1274 harzburgite textures, indicative of reactions with a porous melt. **a** Wedge-shaped fracture in a coarse orthopyroxene porphyroblast. The *broken part* had slightly rotated and fracture is filled with secondary clinopyroxene. In *bottom*, large embayment filled with a single olivine grain. Crossed polarizers. **b** Detail of oval, resorbed orthopyroxene. *Left end of the crystal* was corroded by melt that penetrated following a cleavage plane. Secondary olivine (ol) and clinopyroxene (cpx; colored in white for clarity) now fill the space. Transmitted light. **c** *Right end* of same orthopyroxene porphyroblast (opx1) as in **b** formerly percolated by melt that followed the cleavages before precipitating spinel (sp; dark

brown) and clinopyroxene (cpx; colored in white) intergrowth. This new material seals texturally re-equilibrated subgrains of the orthopyroxene (opx2), and continues as intergranular extensions between adjacent olivine (arrows). Transmitted light. **d** Backscattered electron image of clinopyroxene (light gray) and spinel (white) S1 symplectite, filling serpentinized olivine (ol; dark) triple junction. **e** Backscattered electron image of clinopyroxene (light gray), orthopyroxene (gray) and spinel (white) S2 symplectite developed at the interface of orthopyroxene porphyroblast (opx1) and olivine (ol). Scale bar for all micrographs represents 500 μ m

selvages. Pyroxenes and Sp commonly form two types of fine-grained symplectites representing 0.5–2% of harzburgite modes. One symplectite type (S1) consists of Cpx grains intergrown with skeletal Sp in ~40:60 volume proportions, respectively, with no Opx (Fig. 3d). It occupies the same textural sites as the discrete Cpx, with both occurrences grading into each other. In particular, it fills Ol or Ol–Opx triple

junctions, and surrounds the ovoid Opx. Thin stringers of S1 may also be observed at the edges of coarse Cpx in the lherzolite. A second symplectite type (S2) contains Opx in addition to Cpx and Sp rods. It forms bulbous, myrmekite-like assemblage, ~200 μ m across, at Opx–Ol interfaces, with convex side of Opx toward Ol (Fig. 3e) and Sp branching perpendicular to the adjacent Ol. Although separated by Sp, Opx in S2

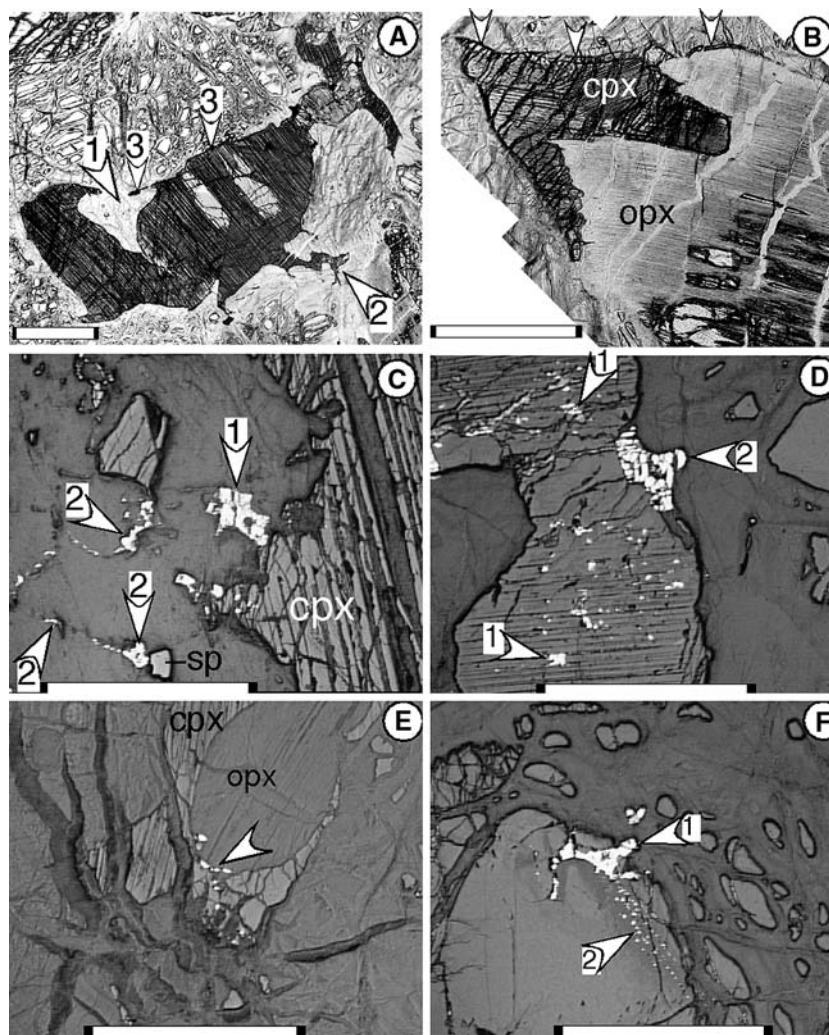


Fig. 4 a–d Photomicrographs of Site 1274 Iherzolite sample SEY04. **a** Part of vein-like, coarse-grained clinopyroxene in serpentinized olivine matrix. *Arrow 1* shows embayment filled with secondary olivine. *Arrow 2* shows intergranular extension of the grain boundary in adjacent (now serpentinized) olivine matrix. *Arrows 3* show a stringer of Al-Cr-poor clinopyroxene rimming the coarse clinopyroxene. Transmitted light. **b** Coarse clinopyroxene (cpx) developed at the border of altered orthopyroxene porphyroclast (opx), and replacing it deeply inside. Note that the two pyroxenes share common (001) planes. *Arrows at the top* show a rim of secondary Al-Cr-poor clinopyroxene (*left*) grading to clinopyroxene-spinel intergrowth (*right*). The latter surrounds almost completely the orthopyroxene. Transmitted light. **c** Rims of coarse clinopyroxene with large BMS

blebs attached (*arrow 1*). These rims extend in thin intergranular veins associated with spinel (sp) and sulfide (*arrows 2*), suggesting that the melt reached interconnection through the silicate matrix. Reflected light. **d** BMS grains enclosed in cleavage planes of a coarse clinopyroxene (*white and arrows 1*). Note the large BMS grain attached on the clinopyroxene (*arrow 2*). Reflected light. **e** Continuous poikiloblastic clinopyroxene rim sealing BMS micrograins (*white and arrow*) at the outer margin of a highly resorbed orthopyroxene. Reflected light. **f** A large BMS grain penetrating into a corroded orthopyroxene (*arrow 1*). Note the secondary sulfide inclusion networks inside the orthopyroxene (*arrow 2*). Scale bar for all micrographs represents 500 μm

symplectite is in optical continuity with the primary Opx grain.

The average size of BMS grains range between 100×50 and $200 \times 100 \mu\text{m}$, but larger grains (up to $500 \times 300 \mu\text{m}$ in maximum dimensions) occur in the Iherzolite. BMS are not randomly distributed at the thin section scale. Most BMS grains occur at Opx–Ol or Cpx–Opx grain boundaries. Except in SEY23, very

few BMSs are surrounded by Ol alone. BMS occur in sites of Opx consumption, either protruding into Opx margins in contact with secondary Ol (15%) or as disseminated blebs adjacent Cpx selvages (50%). Respectively 40% and 30% of about 300 counted grains of BMS share a grain boundary with an Opx or a Cpx crystal, whereas the latter two silicates account for only 20 and 2%, respectively, of harzburgite modes. In

some cases, BMS are sealed at the Opx outer margins by a continuous poikiloblastic Cpx rims. Sulfide melts penetrated corrosion paths, thus creating secondary sulfide inclusion networks within the Opx (Fig. 4f). Their BMS assemblages (pentlandite + chalcopyrite + bornite in unfractured, closed inclusions; abundant native Cu in fractured, open inclusions) provide evidence for Cu-rich sulfide parent melts. Another sulfide population (25%) is intimately associated with the interstitial Cpx separate from the Opx, either as swarms of droplets (1–10 μm) or as convoluted patches showing low dihedral angles and grading into vein-like extensions. The diffuse discontinuous veins of coarse Cpx in the lherzolite are BMS-rich, BMS occupying the same microstructural sites as the Cpx (Fig. 4c, d). Large BMS blebs are attached to Cpx crystals that also contain concentrated sprays of hundreds of BMS inclusions oriented parallel to cleavage planes (Fig. 4d). In this peculiar sample, sulfide melt reached interconnection through the silicate matrix, as suggested by the thin sulfide veins that surround relict Opx crystals (Fig. 4c). A minor proportion of BMS (2–4%) is attached to Sp, especially S1 Sp. By contrast, no sulfide has been found in S2 symplectites.

Major element mineral compositions

Ol Mg# [= molar $\text{Mg}/(\text{Mg} + \text{Fe})$] and NiO contents (eTable 1) from 0.903 to 0.917 and from 0.30 to 0.43 wt%, respectively, vary little, with identical within- and inter-sample standard deviations. Sample set average is Mg# 0.9107 ± 0.0015 and NiO 0.38 \pm 0.03 wt%. CaO contents are very low (<0.1 wt%) except in the dunite (0.22 wt%) and one harzburgite (0.24 wt% in SEY18).

Orthopyroxene (eTable 2) shows limited within- and inter-sample compositional ranges for Mg# and CaO (0.911 ± 0.024 and 1.91 ± 0.34 wt%, respectively). Al_2O_3 and Cr_2O_3 are positively correlated (Fig. 5a), with the highest concentrations in the cores of the largest porphyroclasts (≥ 5 mm). However, many coarse porphyroclasts have cores depleted in Al_2O_3 and Cr_2O_3 . There is no difference in concentration of Al_2O_3 and Cr_2O_3 between the smaller porphyroclasts and the grains forming intergrowths with Sp. In addition, Cr_2O_3 is low (~ 0.9 wt%) relative to Al_2O_3 concentrations (~ 3 wt%), and only a few Opx compositions plot on the extension of the abyssal Opx compositional trend, defined by the cores of similarly sized porphyroclasts (Fig. 5a; Seyler et al. 2003). This suggests that Hole 1274A Opx have been more extensively re-equilibrated to lower T than commonly observed in typical abyssal peridotites. Because Al_2O_3

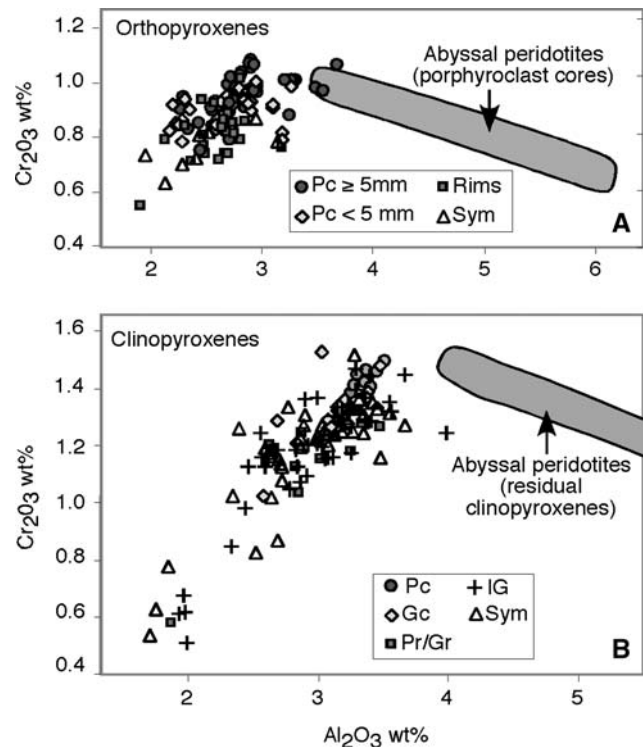


Fig. 5 Cr_2O_3 versus Al_2O_3 (wt%) in pyroxenes of Hole 1274A peridotites. *Point symbols* represent sample averages. **a** Pc = porphyroclast cores; Sym = in S2 symplectites and other intergrowths with spinel. Field of abyssal peridotite orthopyroxene porphyroclast cores ≥ 5 mm (Seyler et al. 2003). **b** Pc = coarse grain cores; Gc = medium grain cores; Pr/Gr = coarse and medium grain rims; IG = small interstitial grains and selvages on orthopyroxene; Sym = in S1 and S2 symplectites and in intergrowths with orthopyroxene and spinel. Field of abyssal peridotite residual clinopyroxene cores (Seyler et al. 2003)

and Cr_2O_3 decrease together, Cr# decreases only slightly and can thus still be used to compare the different samples.

Clinopyroxene compositions are given in eTable 3. Overall, Cpx are characterized by low Al_2O_3 and Cr_2O_3 contents compared with common abyssal Cpx and both oxides decrease simultaneously (Fig. 5b). The lherzolite coarse Cpx grains are slightly zoned, with the highest Al_2O_3 , Cr_2O_3 and the lowest CaO (in integrating exsolution lamellae) contents in cores. Coarse grain rims and small Cpx grains that crystallized at the edges of coarse crystals are poorer in Al_2O_3 and Cr_2O_3 and richer in CaO. Similar compositional ranges also characterize all Cpx textural types in harzburgites, although some larger Cpx cores tend to have higher Al_2O_3 and Cr_2O_3 . It is noteworthy that within a thin section, tiny Cpx in symplectites has similar compositional ranges to the cores and rims of medium-sized grains not in intimate contact with Sp. In contrast with Al_2O_3 and Cr_2O_3 , Mg-numbers

are systematically higher in the rims and tiny grains, indicating subsolidus Fe–Mg exchange reactions with the other silicate minerals and Sp upon cooling. Thus Al_2O_3 and Cr_2O_3 variations cannot be attributed to simple subsolidus re-equilibration and will be discussed further. TiO_2 contents are very low ≤ 0.05 wt% in most samples, increasing to 0.15 wt% in a few samples. Na_2O contents display a wide range of concentrations from near 0 up to 0.72 wt% (Fig. 2c). Most samples (75% of the sample set), including the lherzolite and the dunite, contain Cpx with very low $\text{Na}_2\text{O} \leq 0.13$ wt%; such concentrations are among the lowest Na_2O concentrations reported in abyssal peridotites. Na_2O and TiO_2 are positively correlated in these very low- Na_2O Cpx. The other samples have Cpx moderately or strongly enriched in Na_2O (0.15–0.3 wt% in six samples and >0.4 wt% in three samples, respectively) with no enrichments in TiO_2 . Such high concentrations of Na_2O are at odds with the overall ultra-depleted compositions of the peridotites. Cpx grains are unzoned for Na_2O and TiO_2 , and, at a thin section scale, their concentration ranges are similar within grains and from grain to grain. High Na_2O samples cannot be distinguished from low Na_2O samples by any textural features or other major element compositions. Eight of nine samples enriched in Na_2O come from the base of the hole, in the section with gabbroic intercalations and fault gouges (Fig. 2a,c). In particular, the three samples with the highest Na_2O contents (SEY23, SEY25 and HJBD13) were sampled in the bottom, close to fault gouge horizons. However, sample SEY24, extremely poor in Na_2O and TiO_2 , is intercalated in the Na_2O -rich section.

Spinel Cr# [= molar $\text{Cr}/(\text{Cr} + \text{Al})$] vary in a very narrow range from 0.43 to 0.51 (average 0.47 ± 0.011) in all the harzburgites and the lherzolite. Sample SEY02 is characterized by significantly lower Cr# (0.36); the dunite is only slightly higher with 0.52 (eTable 4). Within-sample variations do not exceed 5%, except in one sample (SEY05) where Cr# variation is up to 10%. TiO_2 contents vary from 0.01 to 0.15 wt% (average 0.07 wt%). Such values (<0.2 wt%) are commonly considered as a characteristic of plagioclase-free, spinel peridotites that did not react with MORB liquid at low-P (Dick 1989; Seyler and Bonatti 1997). In the entire sample set, except SEY02, Sp compositions thus define a unique, restricted, compositional field, with no correlation between Cr# and TiO_2 . Average Cr# and Mg# in Sp, Ol and Opx are well correlated from sample to sample. In Ol Mg# vs Sp Cr# diagram, Hole 1274A peridotites plot at the higher Cr# end-member (except SEY02) of the abyssal peridotite

array (Fig. 6). These compositions are similar to those of dredged samples from the entire 14° – 16°N region (Bonatti et al. 1992; Cannat et al. 1992, 1997) and also characterize abyssal peridotites from the 43°N area at the MAR (Shibata and Thompson 1986).

Trace elements in clinopyroxenes

Six samples have been selected for trace element study, including five harzburgites and the lherzolite SEY04. Cpx in harzburgite samples SEY03, SEY21, SEY22 and the lherzolite have low to very low Na_2O contents (≤ 0.3 wt%), whereas harzburgite samples SEY23 and SEY25 have Cpx enriched in Na_2O (0.45–0.55 wt%). Within-sample variability for REEs, Sr, Zr and Ti was investigated by analyzing Cpx of several textural occurrences (selvages on Opx, intergranular grains, core and rim, symplectites, and crack-filling); in addition, three samples were analyzed in two thin sections cut from the same slab, to study centimeter scale variability. Results are presented in eTable 5. Trace element concentrations show no significant intra- or inter-grain variations at a sample scale (except in sample SEY25), and as a consequence, show no texture-related variation. Thus, only average concentrations are hereafter considered for these samples. Near-homogeneous trace element contents in Cpx, suggestive of equilibrium at the thin section scale, is a typical feature of abyssal Cpx, for which with few exceptions, no significant texture-dependence is observed (Hellebrand et al. 2002). In contrast, the two grains analyzed in SEY25 show different compositions. The low-Na Cpx

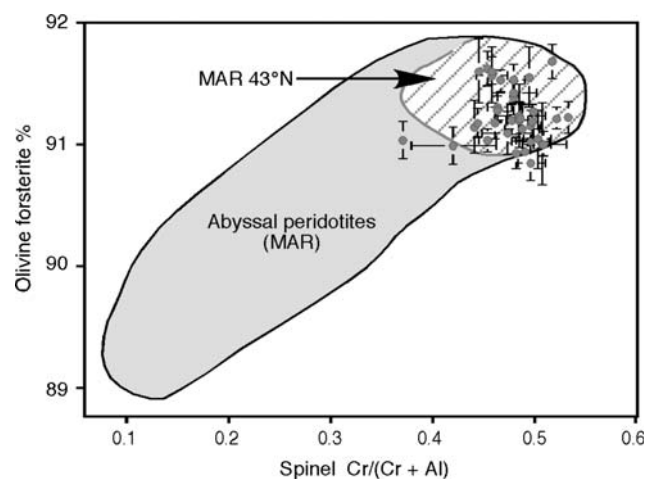


Fig. 6 Olivine forsterite contents versus spinel Cr# [= molar $\text{Cr}/(\text{Cr} + \text{Al})$] in Hole 1274A peridotites. Point symbols represent sample averages. Bars represent 1σ sample variations. Field of Mid-Atlantic Ridge (MAR) peridotites from Seyler et al. (2003). Field of peridotites from 43°N at the MAR after Shibata and Thompson (1986)

group has ultra-depleted trace element compositions, in accordance with the extreme depletion in major elements. HREE concentrations are twofold lower than in Cpx from the hotspot-influenced Bouvet FZ (Johnson et al. 1990). REE absolute and relative concentrations in Site 1274 low-Na Cpx are nearly identical to Cpx from Marie Celeste FZ harzburgites in the Central Indian Ridge. The latter are also the most depleted Cpx reported for abyssal peridotites (sample ANTP84-11 in Hellebrand et al. 2002; Fig. 7). Both sets of Cpx are characterized by very steep positive Nd to Lu slope, LREE upward inflection and downward inflection in Eu. This apparent negative Eu anomaly is not coupled with a negative Sr anomaly, which would have been the signature of coexisting plagioclase (this mineral has not been observed in Hole 1274A harzburgites). In contrast, Sr is strongly enriched relative to the adjacent REEs, a feature also commonly observed in the Cpx from very depleted harzburgites, which has been explained by increased difference between Sr and REE bulk partition coefficients, as continuous melting approaches the point of Cpx exhaustion (Parkinson et al. 1992). Because all these Cpx are selectively enriched in LREEs relative to MREEs, we interpret the $(\text{Sm}/\text{Eu})_N$ ratios >1 as an effect of Sm enrichment with respect to Eu. SEY23 REE patterns are characterized by higher concentrations in MREEs relative to HREEs and by less fractionated $(\text{Nd}/\text{Yb})_N$ ratios. La, Ce and Sr enrichments are similar to those observed in SEY21 and SEY22 Cpx, although Na_2O is twice more concentrated. SEY25 Cpx are globally enriched in the trace elements. Starting from similar Lu and Yb concentrations, the magnitude of the enrichments increases toward the more incompatible REEs up to Ce, and then slightly decreases for La. Their REE concentrations thus define patterns characterized by a

concave downward shape with $(\text{La}/\text{Ce})_N < 1$, which are unusual in abyssal peridotites but have been reported from two ultra-slow spreading ridge segments, the Gakkel peridotites in the Arctic ocean (Hellebrand and Snow 2003) and the Southwest Indian Ridge near the Rodrigues Triple Junction (Toplis et al. 2003). SEY25 Cpx patterns display other unusual features for mantle peridotites equilibrated in the spinel stability field, such as strong negative Eu, Sr and Zr anomalies.

Discussion

Constraints from textures and in situ major elements

Structures, textures and compositions of the high-T mineral assemblages confirm the highly refractory compositions of Site 1274 harzburgites. No evidence for truly residual Cpx has been found. Detailed microstructures clearly demonstrate that the variability of Opx mode results from two major melt–mineral reaction events leading to different extents of replacement of the Opx either by Ol (reaction 1) or by $\text{Cpx} \pm \text{Sp}$ (reaction 2), and resulting in the dm to m scale alternation of harzburgites with variable Ol/Opx and Cpx/Opx ratios observed in the drill core. In addition to modal and textural changes, melt–mineral diffusive exchange reactions occurred concurrently, which allow us to better constrain some aspects of the late magmatic history.

Interpretation of orthopyroxene resorption

A first interpretation of reaction 1 textures is to consider them as “asthenospheric” textures formed in the

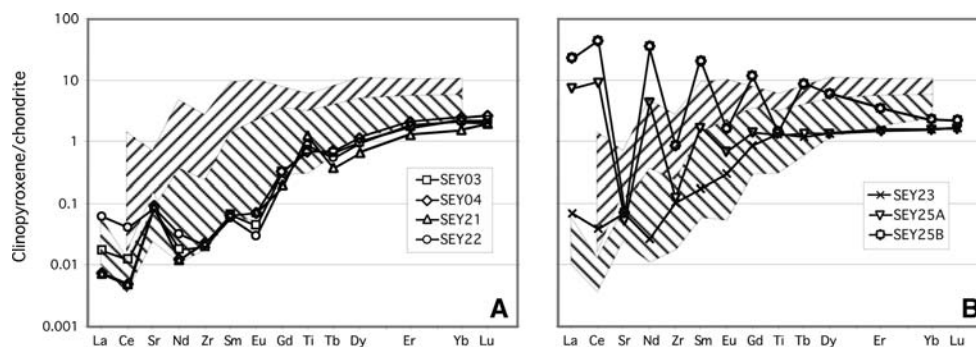


Fig. 7 Chondrite-normalized clinopyroxene rare earth element, Sr, Zr and Ti patterns of Hole 1274A peridotites. **a** Low-Na clinopyroxenes. **b** High-Na clinopyroxenes. Upper hatched field represents the range for abyssal peridotites after Johnson et al. (1990), Ross and Elthon (1997), Hellebrand et al. (2002) and

Brunelli et al. (2006). Lower hatched field is the range for Marie Celeste Fracture Zone peridotites in the Central Indian Ocean after Hellebrand et al. (2002). CI chondrite normalization values from Anders and Grevesse (1989)

upwelling melting mantle (Nicolas 1986; Ceuleneer et al. 1988). In this interpretation, secondary Ol is a reaction product of Opx + Cpx + Sp incongruent melting (Kinzler and Grove 1992). On the other hand, similar textures may develop where incremental or aggregated melts, generated at deeper levels, migrate upward through residual peridotites (Daines and Kohlstedt 1993). In this second interpretation, Ol precipitation and Opx dissolution result from reaction between adiabatically ascending melts that become saturated in Ol and undersaturated in Opx and surrounding mantle (Kelemen 1990). This reaction may occur in the convecting mantle, in regions of incipient melt focusing, where interaction between ascending partial melts and wall rock results in randomly distributed porous flow (Kelemen et al. 1995a,b; Aharonov et al. 1995), or at a higher level in the thermal boundary layer (TBL), where convection changes to, then is dominated by, conductive cooling. In Site 1274, the large (>1 mm) size of the replacive Ol grains suggests that the reaction mostly occurred at, or close to, the peridotite solidus; it continued at relatively low T and high stress as indicated by the few samples where Opx, affected by crystal plastic deformation, is also deeply corroded and replaced by tiny grains of Ol.

Reaction 2, characterized by Cpx \pm Sp replacing Opx, indicates that the melt was not only undersaturated in Opx (or silica) but also saturated in Cpx. Such reaction combined with reaction 1 may lead to wherlitic compositions through melt–peridotite interaction. Cpx replacing Opx textures are commonly observed in some mantle xenoliths (Zinnegrebe and Foley 1995; Klügel 2001) and lherzolite massifs (Fabriès et al. 1989) where mantle peridotites have been percolated by alkaline melts, but are not a characteristic feature of abyssal peridotites (Seyler et al. 2001). Similar textures are produced experimentally during Opx assimilation in basanitic liquid (Shaw 1999). In Shaw's (1999) experiments, crystallization of Ol and Cpx after dissolution of Opx occurs in two stages. Stage 1 produces Ol and a modified melt enriched in silica and saturated in Cpx, stage 2 crystallizes Cpx selvages on residual Opx by diffusion of Ca from the modified melt. In contrast, primitive, tholeiitic liquids, in equilibrium with mantle minerals at high pressure, become undersaturated in both Opx and Cpx and oversaturated in Ol as they begin to cool at a lower P, and Ol is the only silicate phase to crystallize within residual peridotites at the base of the TBL (Kelemen 1990; Kelemen et al. 1995a, b; Wagner and Grove 1998). Cpx precipitation will follow as Ol fractionation drives the liquids to saturation in Cpx at moderate P (0.7–1.2 GPa; Stolper 1980). At this stage, the liquid composition has signi-

ficantly evolved and the peridotite has cooled well below its solidus, leading to the formation of thin metasomatic dykelets. Lack of Fe–Ti enrichments and diffuse Cpx textures in Site 1274 peridotites do not support such a conclusion. In contrast, the petrographic study indicates that both reactions, and thus the Cpx crystallization, occurred at similar conditions of low strain and high temperature of the solid matrix, prior to the formation of the lithosphere.

Additional evidence for high-T conditions comes from the observation that in spite of the fact that Opx was, in general, extensively dissolved, this mineral did not reprecipitate along with Cpx. Fractionating liquids are driven to Opx saturation if they derive from high-P partial melts that extensively reacted with wall peridotites, beyond the point of the exhaustion of Cpx (Kelemen et al. 1995a, b), or if they are silica-rich, low-P melts produced by partial melting of a depleted peridotite, in equilibrium with a Cpx-free residue. Indeed, in many ophiolites, mantle harzburgites as refractory as Site 1274 harzburgites, which show similar textures of Opx dissolution–Ol crystallization, do contain secondary Opx (Barth et al. 2003; Dijkstra et al. 2003). In addition, these Opx have very low CaO contents (<0.8%; Barth et al. 2003), in contrast with Site 1274 Opx (ave. CaO ~1.96%, Wo ~3.8%). Application of Ca-in-Opx geothermometer of Brey and Kohler (1990) leads to an equilibrium temperature of ~1,250°C at 1 GPa, suggesting that Hole 1274 peridotites cooled rapidly at depth in the TBL before uplift. This result also reflects probable dry melting Site 1274 peridotites as opposed to assumed hydrous condition in many ophiolites.

Al–Cr exchange reactions and origin of late-stage Sp and Cpx

Although Al₂O₃ and Cr₂O₃ behave in the opposite way during partial melting (Jacques and Green 1980), in Site 1274, both oxides decrease from core to rim in Opx, to the point where a large proportion of coarse Opx cores acquire low Al₂O₃ and Cr₂O₃ contents. Enhanced Al₂O₃ and Cr₂O₃ depletions indicate that re-equilibration of the Opx to lower *P–T* condition occurred in high-T peridotites in presence of melt, which increased Al and Cr diffusion out of Opx into the interstitial melt. This process, which occurred concurrently with the Opx resorption, leads to the complex Opx + Sp \pm Ol intergrowths through a suite of reactions: (1) dissolution of high-T (Al-, Cr-rich) Opx along grain boundaries and cleavages and reprecipitation of Sp, in situ, or at sites of low stress where the melt was driven by shearing of the

matrix, according to the reaction $\text{Mg}(\text{Al,Cr})\text{AlSiO}_6 = \text{Mg}(\text{Al,Cr})_2\text{O}_4 + (\text{SiO}_2)_{\text{melt}}$, (2) dissolution of adjacent Ol by modified melt locally oversaturated in silica, leading to enclosure of Ol into Sp neoblasts. During these reactions, residual Opx and Ol texturally re-equilibrated with the newly formed minerals.

Clinopyroxene selvages on Opx may result from another melt-to-mineral diffusive reaction: $0.5 \text{Mg}_2\text{Si}_2\text{O}_6 + (\text{CaSiO}_3)_{\text{melt}} = \text{CaMgSi}_2\text{O}_6$. Minor amounts of Cpx in the Opx + Sp ± Ol intergrowths, as well as the formation of the S2 symplectites at the Opx–Ol interfaces, may also involve Cpx exsolution from Opx and/or a calcic melt component according to the reactions: $\text{Mg}_2\text{SiO}_4 + \text{Mg}(\text{Al,Cr})\text{AlSiO}_6 + (\text{CaSiO}_3)_{\text{melt}} = \text{Mg}(\text{Al,Cr})\text{O}_4 + \text{CaMgSi}_2\text{O}_6 + 0.5 \text{Mg}_2\text{Si}_2\text{O}_6$ or $\text{Mg}_2\text{SiO}_4 + (\text{CaAl}_2\text{SiO}_6)_{\text{melt}} = \text{CaMgSi}_2\text{O}_6 + \text{MgAl}_2\text{O}_4$. In contrast, the Cpx grains that fill low-angle Ol and Ol–Opx triple junctions and the S1 symplectites, for which no evidence for Opx- or Ol–melt reaction has been observed, probably precipitated from melt as Cpx or Cpx–Sp cotectic crystals, respectively. The ranges of Al_2O_3 and Cr_2O_3 concentrations in the Cpx likely reflect variable Al_2O_3 and Cr_2O_3 saturations of the interstitial melt under condition of rapidly decreasing temperature as the peridotite entered into the TBL, conditions that also permit the preservation of the delicate symplectites.

Lherzolic domains

Hole 1274A peridotites display lherzolic domains, as exemplified by sample SEY04 which is enriched in both Ol and Cpx. The coarse Cpx crystals are constituents of the protogranular texture, and their orientation defines a high-T lineation; they show resorption features similar to Opx; they contain coarse (up to 4 μm) Opx exsolution lamellae; they also display Cu-rich sulfide intergrowths. All these features are in contrast with textures and compositions of late-stage Cpx (+ Sp ± sulfides) that overgrew the coarse Cpx as poikiloblastic rims or discrete crystals. Similar Cpx + Sp ± sulfides are also abundant around reacted Opx. This second Cpx generation is characteristically small-sized, enriched in wollastonite (thin Opx exsolutions; high whole-grain CaO contents) and impoverished in Al_2O_3 and Cr_2O_3 relative to the coarse Cpx. The coarse Cpx crystals are thus interpreted to have crystallized from a sulfide-rich melt at higher *P–T* conditions than the late-stage Cpx grains. However, elemental compositions which are mainly controlled by melt composition (Na, Ti and incompatible trace elements) are similar between coarse and late-stage Cpx. Therefore, texture and composition relationships

between the two generations of Cpx might be interpreted as the result of a dissolution–reprecipitation process at decreasing *P–T* conditions, that partially preserved relicts of earlier Cpx. Because late-stage Cpx in the lherzolite shows mineral association, texture and compositions identical to the Cpx in the harzburgites, we suggest that Cpx saturation in the percolating melt might have been promoted by melting or selective dissolution of previous Cpx veins within residual mantle. During this process, the primary Cpx and the percolating melt evolved toward chemical equilibrium. Such melt will be especially reactive with Opx.

Constraints from trace element and mode modeling

A number of numerical models have been developed, which describe the behavior of trace elements during melt–rock interaction involving elemental exchanges both by diffusive and by mineral (e.g. with modal ± porosity changes) reactions (e.g. Godard et al. 1995; Vernières et al. 1997; Suhr et al. 1998). They show that extensive interaction between migrating melt, derived from adiabatic decompression, and depleted uppermost mantle approaches equilibrium between melt and peridotite and rapidly depletes the melt in incompatible elements. Because the least incompatible trace elements are controlled by mineral reactions and are buffered by the peridotite, the HREE patterns in melt and solid, after melt–rock interaction, reflect the composition of the residual solid (except at high melt/solid ratios in high-porosity channels). In contrast, concentrations of the most incompatible trace elements (LREEs) are mostly controlled by the porosity, being partially buffered by percolating melt. If melt–rock equilibration is not totally achieved, then REE patterns will show selective enrichments in LREEs quite similar to those observed in Site 1274 depleted Cpx.

As a first step in modeling the reactions, we assumed that melt–rock equilibration in Site 1274 peridotites was achieved through partial melting alone. Theoretical extents of melting of the solid residue was calculated using the concentrations of the Cpx moderately incompatible elements (Eu to Lu), that are the least sensitive to melt percolation. In this model, Cpx fractionated at the top of the melting zone from intergranular melt in equilibrium with a near-Cpx free residual harzburgite. Composition of this melt can be modeled as the composition of the last melt fraction generated at the shallowest pressure during continuous decompressional partial melting. The results of these calculations are then used as end-members to discuss the effects of additional reactions between percolating

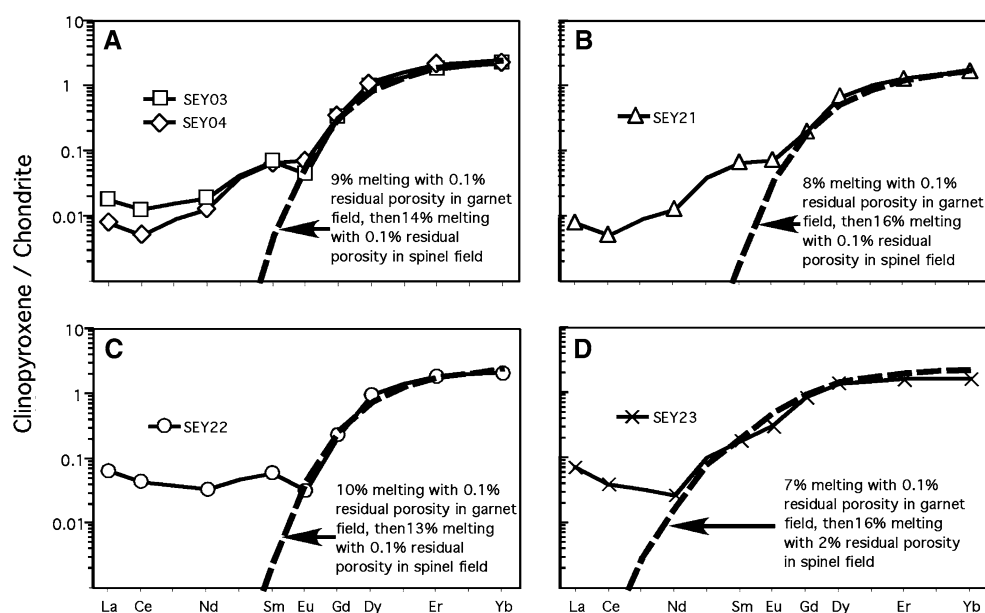
melt and residue. Our calculations, using nonmodal melting equations (Shaw 2000) and a conventional Sp-hertzolite source, cannot reproduce the M/HREE fractionations of the low-Na Cpx, whatever the melting process (batch, Raleigh, critical). To reproduce simultaneously the low Lu and Yb contents and the very low Eu/Lu ratios, melting must begin in the garnet stability field, in agreement with previous modeling of strongly depleted abyssal Cpx compositions (Johnson et al. 1990; Hellebrand et al. 2002; Brunelli et al. 2006). Polybaric, near-fractional melting models (Brunelli et al. 2006) reproduce the M-HREEs contents in our four most depleted samples after 9–10% melting in the garnet stability field, followed by 12–14% melting in the spinel stability field (Fig. 8a–c). Na-rich Cpx SEY23 cannot be reproduced in a satisfying way. Best fits are obtained after 7–9% fractional melting in the garnet stability field followed by 14–16% melting in the spinel stability field with higher residual porosity (~2–7%; Fig. 8d). This suggests that other processes, such as melt entrapment or melt mixing, contributed to the SEY23 REE pattern. SEY25 cannot be modeled by partial melting alone, except for Lu and Yb whose concentrations are nearly identical to those measured in the other samples.

Because melting reactions in the garnet stability field produced Opx (Kinzler 1997), calculated residual modes contain ~30 wt% Opx, a proportion which is very close to the Opx contents of the least reacted Site 1274 harzburgites (Opx ~28 vol%). Departure from this theoretical mode toward lower, variable, and heterogeneously distributed Opx/Ol proportions is one of the most convincing pieces of evidence for additional

mineral reactions accompanying advecting melt percolation. Pervasive or poorly focused partial melt migrating upward in the upwelling molten mantle, or in the shallow mantle at a temperature close to the peridotite solidus, enhances pyroxene dissolution and Ol crystallization, the magnitude of which increases with the quantity of melt passing through the peridotite (Aharonov et al. 1995; Kelemen et al. 1995a, b; Asimow and Stolper 1999). Thus, an alternative model would be to assume that the peridotite underwent a lower degree of adiabatic melting than the one calculated above, leaving a substantial amount of residual Cpx (for instance ~10% upon 12% melting in the spinel field) that would disappear by additional dissolution. In this case, residual intergranular melt would equilibrate with Cpx-free harzburgites characterized by low and highly fractionated REE contents. During this process, both Opx and Cpx are subject to dissolution with Opx more rapidly dissolving as pressure decreases (Kelemen et al. 1995b). However, Site 1274 Opx-rich harzburgites are also devoid of residual Cpx; it is thus likely that low-P melt–rock interaction involved a harzburgite mantle already depleted in Cpx and, thus, that partial melting did start in the garnet stability field.

Selective LREE enrichments in the depleted Cpx, and the occurrence of Na-rich, REE-enriched Cpx (samples SEY23 and 25), may reflect incomplete or local equilibrium between percolating melt and residue, the former being more enriched in REE than the latter, or may be explained by a later event that occurred during or just after the Cpx crystallization (Navon and Stolper 1987; Bodinier et al. 1990; Takazawa

Fig. 8 Results of polybaric continuous (critical) melting models in the garnet, then the spinel peridotite fields (*thick dashed lines*). Equations for continuous melting from Shaw (2000). Polybaric model and melting parameters (initial and melt modes, source composition, melt/peridotite partition coefficients) same as in Brunelli et al. (2006). Departure of Site 1274 samples from calculated patterns for Sm to La is attributed to late-stage chromatographic fractionation (not modeled here)



et al. 1992), in relation to the presence of former melt channels.

Additional constraints from BMS distribution

Base metal sulfides provide further evidence supporting variable degrees of reactions of a highly refractory mantle with a percolative melt. It is now well demonstrated that S behaves as a moderately incompatible element during mantle melting, because basaltic melts dissolve five to ten times more S than the estimated S content of the upper mantle (Lorand 1991; and references therein). At 1.5 GPa, conventional fractional melting predicts total consumption of BMS for $F \leq 12$ –16% if the depleted MORB mantle contains about 150 ppm S (Saal et al. 2002; Luguët et al. 2003). Because the solubility of S decreases with increasing pressure (Mavrogènes and O'Neill 1999), a partial melting event starting in the garnet lherzolite stability field would allow BMS to persist in residual solids at higher F ($\leq 20\%$). The near-zero S contents of certain Site 1274 Opx-rich harzburgites are therefore consistent with a high degree of partial melting that has progressed beyond complete resorption of the sulfides.

The remainder of Site 1274 harzburgites is much too rich in BMS to be interpreted as simple melting residues. Assuming that all of the S is residing in BMS, the highest BMS content (0.1 vol%) corresponds to ca 300 ± 30 ppm S (based on pentlandite and chalcopyrite S concentrations of 33 and 35 wt%, respectively; unpublished data). This bulk-rock S content is twice the “best estimate” for the convecting depleted mantle. In theory, the conventional fractional melting model predicts a regular decrease of S contents negatively correlated with melt depletion indexes such as Ol Mg# and Sp Cr#. There is no such correlation in Site 1274 harzburgites which, on the contrary, display huge variations of BMS modal abundances, sometimes at the hand-sample scale, in spite of nearly constant Ol Mg# and Sp Cr#. Such heterogeneous distribution can be understood if BMS are “cumulate minerals” of a heterogeneously distributed percolating melt in disequilibrium with harzburgites. The common occurrence of BMS in microstructural sites of melt–rock reactions (Opx–Ol and Cpx–Opx) provide strong support to this interpretation, as does the overabundance of Cu-rich sulfides in Opx-hosted inclusions and of native copper in intergranular BMS that have experienced strong reduction by serpentinization fluids. The assemblage Pn + Cp + Bo (which was protected from serpentinization) is characteristic of oceanic peridotites that have been refertilized in Cpx + Sp by basaltic melts (Lorand 1988; Luguët et al. 2003). Experimental

phase diagrams in the Cu–Fe–Ni–S system (Craig and Kullerud 1969) show this assemblage to be a crystallization product of a Cu-enriched Ni–Fe sulfide melt with metal/sulfur atomic ratio > 1 .

The fact that the highest BMS concentrations correspond to rocks with high (> 0.1) Cpx/Opx modal ratios (SEY03, SEY04, SEY23) outlines the main effect of Cpx fractionation. As suggested earlier, Cpx crystallization in Site 1274 harzburgites was promoted by rapid temperature decrease at relatively high pressure (~ 0.8 –1 GPa). Such P – T conditions enhance BMS precipitation by reducing the solubility of S in the percolating melt (Naldrett 1989). In the lherzolite SEY04, the volume of sulfide liquid was high enough for sulfide melt films to be locally interconnected through the interstitial pores of the silicate matrix (Fig. 4c). Experimental data (Gaetani and Grove 1999) suggests that interconnection can occur for 0.1 vol% intergranular sulfides, which is very close to the BMS modal abundance measured in this sample. It is likely that, after such a massive coprecipitation of BMS and Cpx, S was exhausted from the residual silicate melt and no BMS precipitated inside S2 symplectites.

The BMS embedded in Opx porphyroclasts is a common occurrence in ophiolitic and abyssal harzburgites and interpreted as incompletely extracted residual sulfides that have survived partial melting (Lorand 1988; Luguët et al. 2003). This interpretation does not pertain to Site 1274 harzburgites that experienced high degrees of melting beyond complete resorption of BMS. In these rocks, the BMS embedded in Opx contain a high proportion of Cu-rich minerals and are often rimmed by Sp or discrete Cpx crystals. These chemical and microstructural criteria suggest that BMS actually precipitated from trapped, Cu-rich, melts and then infiltrated the corroded Opx at temperatures below the peridotite solidus via the numerous corrosion embayments and fractures. Cu–Ni sulfide melts have depressed solidus temperatures compared to major silicates of anhydrous peridotites ($< 1,000^\circ\text{C}$ vs. $1,300^\circ\text{C}$ at 1 GPa) and high wetting capacity (Ballhaus et al. 2001), which can explain the secondary sulfide inclusion networks within the Opx.

A two-stage partial melting/melt–rock reaction model for Site 1274 peridotites?

The wealth of textural, mineralogical and geochemical data obtained from this study yields some contradictions and inconsistencies. A high degree of melting of peridotite, starting in the garnet stability field, is inconsistent with normal mantle temperature inferred from the chemistry of the basalts and gabbros sampled

north of the 15°20'N FZ, which have normal MORB compositions (Dosso et al. 1991, 1993; Kelemen 2003) and from the structure of the lithosphere, which is typical of a slow-spreading ridge (thin crust but thick lithospheric mantle, in which a large quantity of gabbroic rocks have frozen; Cannat 1996). The Cu–Ni-rich composition of the metasomatic BMS also argues against a refractory percolating melt.

We propose to solve these inconsistencies by assuming that the convective mantle at the Mid-Atlantic Ridge, 15°–16°N contained harzburgitic blobs that have already been affected by early high-P history of melt depletion and refertilization before upwelling and remelting beneath the present-day ridge. Such a two-stage petrogenetic model has been suggested for other abyssal peridotites from ultra-slow spreading ridges (Seyler et al. 2004) and is supported by Os model ages indicating a long-term Re depletion (Brandon et al. 2000; Alard et al. 2005). For this to apply for Hole 1274A peridotites requires the garnet signature and the high Opx contents of the least reacted harzburgites.

Pyroxene layering in the peridotites may be partially inherited from former pyroxenite veins. This pyroxenitic component preferentially melted to produce a melt undersaturated in Opx and saturated in Cpx. Experimental melting of Cpx-rich lithologies with MORB affinity demonstrate that melts have major element compositions in the range of normal MORB compositions (Pickering-Witter and Johnston 2000; Schwab and Johnston 2001). In addition, experimental melting of Cpx + Sp layer enclosed within a peridotite matrix, with bulk composition similar to MORB composition, releases a melt strongly undersaturated in Opx, which upon reaction with surrounding residual harzburgite, yields normal MORB liquid and residual Ol + Sp assemblage (Bulatov et al. 2002). Mantle pyroxenites are four to five times more enriched in S and Cu than fertile lherzolite (Lorand 1991). Therefore a high degree of melting of Cpx-rich veins may produce a melt saturated in Cu-rich sulfide phases. This melt is just as capable to precipitate Cu-rich BMS as is a low-degree melt of peridotite of similar major element composition in the percolated mantle column. In this interpretation, the coarse Cpx + Ol + sulfides assemblages in the lherzolite sample represent relics of early cumulate veins that partially melted and/or reacted with peridotitic melt. Lack of a geochemical anomaly in the regional basalts does not preclude our model, as very small amounts of Cpx-rich melt will be highly diluted after mixing with partial melts from the melting of surrounding depleted peridotites that had some remaining Cpx.

Concluding remarks

Leg 209 Hole 1274A harzburgites differ from common abyssal peridotites by extreme refractory compositions and by well-developed textures of Opx dissolution and Ol + Cpx + Sp + sulfides crystallization. They also show more extensive melt–mineral elemental exchange reactions, resulting in lower Al and Cr contents in residual Opx and in anomalously depleted, U-shaped REE patterns in Cpx. Although Site 1274 peridotites may resemble some ophiolitic and forearc mantle harzburgites, lack of secondary Opx and higher temperature of equilibration show that the extra-depletion was not caused by late-stage hydrous melting. Characteristics of Site 1274 samples indicate reaction with a melt in strong disequilibrium with the peridotite matrix at a temperature close to its solidus.

Acknowledgments This research used samples and data supplied by the Ocean Drilling Program (ODP). ODP is sponsored by the U.S. National Science Foundation (NSF) and participating countries under management of Joint Oceanographic Institutions (JOI), Inc. We thank D. Brunelli for discussion, and B. Boyer for his assistance with the SIMS analyses. Comments from two anonymous reviewers are gratefully acknowledged. Funding for this research was provided by Centre National de la Recherche Scientifique-Institut National des Sciences de l'Univers (Programme Dynamique et Evolution de la Terre Interne).

References

- Alard O, Luguet A, Pearson N J, Griffin W L, Lorand J-P, Gannoun A, Burton KW, O'Reilly SY (2005) In-situ Os analyses bridging the isotopic gap between abyssal peridotites and Mid-Oceanic Ridge Basalts. *Nature* 436:1005–1008
- Aharonov E, Whitehead JA, Kelemen PB, Spiegelman M (1995) Channeling instability of upwelling melt in the mantle. *J Geophys Res* 100:20433–20450
- Anders E, Grevesse N (1989) Abundances of the elements: meteoritic and solar. *Geochim Cosmochim Acta* 53:197–214
- Asimow PD (1999) A model that reconciles major- and trace-element data from abyssal peridotites. *Earth Planet Sci Lett* 169:303–319
- Asimow PD, Stolper EM (1999) Steady-state mantle–melt interactions in one dimension: I. Equilibrium transport and melt focusing. *J Petrol* 40:475–494
- Ballhaus C, Tredoux M, Spaeth A. (2001) Phase relations in the Fe–Ni–Cu–PGE–S system at magmatic temperature and application to massive sulfide ores of Sudbury Igneous Complex. *J Petrol* 42:1991–1926
- Barth MG, Mason PRD, Davies GR, Dijkstra AH, Drury MR (2003) Geochemistry of the Othris Ophiolite, Greece: evidence for refertilisation? *J Petrol* 44:1759–1785
- Bodinier JL, Vasseur G, Dupuy C, Fabrics J (1990) Mechanisms of mantle metasomatism: geochemical evidence from the Lherz orogenic peridotite. *J Petrol* 31:597–628
- Bonatti E, Peyve A, Kepezhinskas P, Kurentsova N, Seyler M, Skolotnev S, Udintsev G (1992) Upper mantle heterogeneity below the Mid-Atlantic Ridge, 0–15°N. *J Geophys Res* 97:4461–4476

- Bottazzi P, Ottolini L, Vannucci R, Zanetti A (1994) An accurate procedure for the quantification of rare elements in silicates. In: Proceedings of the 9th international conference on secondary ion mass spectrometry SIMS IX. Wiley, New York, pp 927–930
- Brandon AD, Snow JE, Walker RJ, Morgan JW, Mock TD (2000) $^{190}\text{Pt}/^{186}\text{Os}$ and $^{187}\text{Re}/^{187}\text{Os}$ systematics of abyssal peridotites. *Earth Planet Sci Lett* 177:319–335
- Brey GP, Kohler T (1990) Geothermobarometry in 4-phase lherzolites. 2. New thermobarometers and practical assessment of existing thermobarometers. *J Petrol* 31:1353–1378
- Brunelli D, Seyler M, Cipriani A, Ottolini L, Bonatti E (2006) Discontinuous melt extraction and weak refertilization of mantle Peridotites at the Vema Lithospheric Section (Mid-Atlantic Ridge). *J Petrol* 47:745–771
- Bulatov VK, Girmis AV, Brey GP (2002) Experimental melting of a modally heterogeneous mantle. *Mineral Petrol* 75:131–152
- Cannat M (1996) How thick is the magmatic crust at slow-spreading oceanic ridges?. *J Geophys Res* 101:2847–2857
- Cannat M, Bideau D, Bougault H (1992) Serpentinized peridotites and gabbros in the Mid-Atlantic Ridge axial valley at 15°37'N and 16°52'N. *Earth Planet Sci Lett* 109:87–106
- Cannat M, Lagabrielle Y, de Coutures N, Bougault H, Dmitriev L, Fouquet Y (1997) Ultramafic and gabbroic exposures at the Mid-Atlantic Ridge: geological mapping in the 15°N region. *Tectonophysics* 279:193–213
- Ceuleneer G, Nicolas A, Boudier F (1988) Mantle flow patterns at an oceanic spreading centre: the Oman peridotite record. *Tectonophysics* 151:1–26
- Craig JR, Kullerud G (1969) Phase relations in the Cu-Fe-Ni-S system and their applications to magmatic ore deposits. In: *Magmatic ore deposits*. Econ Geol Monogr 4, pp 343–358
- Daines MJ, Kohlstedt DL (1993) Melting and melt movement in the Earth. *Phys Sci Eng* 342:43–52
- Dick HJB (1989) Abyssal peridotites, very slow spreading ridges and ocean ridge magmatism. In: Saunders AE, Norris MJ (eds) *Magmatism in the ocean basins*. Geol Soc Spec Public 42, pp 71–105
- Dijkstra AH, Barth MG, Drury MR, Mason PRD, Vissers RLM (2003) Diffuse porous melt flow and melt–rock reaction in the mantle lithosphere at a slow-spreading ridge: A structural petrology and LA-ICP-MS study of the Othris Peridotite Massif (Greece). *Geochem Geophys Geosyst* DOI: 10.1029/2001GC000278
- Dosso L, Bougault H, Schilling JG, Joron JL (1991) Sr-Nd-Pb geochemical morphology between 10° and 17°N on the Mid-Atlantic Ridge: a new MORB isotope signature. *Earth Planet Sci Lett* 106:29–43
- Dosso L, Bougault H, Joron JL (1993) Geochemical morphology of the north Mid-Atlantic Ridge, 10°–24°N, trace element-isotope complementarity. *Earth Planet Sci Lett* 120:443–462
- Elthon D (1992) Chemical trends in abyssal peridotites: refertilization of depleted suboceanic mantle. *J Geophys Res* 97:9015–9025
- Escartin J, Cannat M (1999) Ultramafic exposures and the gravity signature of the lithosphere near the Fifteen–Twenty Fracture Zone (Mid-Atlantic Ridge, 14°–16.5°N). *Earth Planet Sci Lett* 171:411–424
- Fabriès J, Bodinier JL, Dupuy C, Lorand JP, Benkerrou C (1989) Evidence of modal metasomatism in the orogenic spinel lherzolite body from Caussou (Northern Pyrenees, France). *J Petrol* 30:199–228
- Fujiwara T, Lin J, Matsumoto T, Kelemen PB, Tucholke BE, Casey J (2003) Crustal evolution of the Mid-Atlantic Ridge near the Fifteen–Twenty Fracture Zone in the last 5 Ma. *Geochem Geophys Geosyst* DOI: 10.1029/2002GC000364
- Gaetani GA, Grove TL (1999) Wetting of mantle olivine by sulphide melt: implications for Re/Os ratios in the mantle peridotite and late-stage core formation. *Earth Planet Sci Lett* 169:147–163
- Godard M, Bodinier JL, Vasseur G (1995) Effects of mineralogical reactions on trace element redistributions in mantle rocks during percolation processes: a chromatographic approach. *Contrib Mineral Petrol* 133:449–461
- Hellebrand E, Snow JE (2003) Deep melting and sodic metasomatism underneath the highly oblique-spreading Lena Trough (Arctic Ocean). *Earth Planet Sci Lett* 216:283–299
- Hellebrand E., Snow JE, Hoppe P, Hofman AW (2002) Garnet-field melting and late-stage refertilization in ‘residual’ abyssal peridotites from the Central Indian Ridge. *J Petrol* 43:2305–2338
- Jacques AL, Green DH (1980) Anhydrous melting of peridotite at 0–15 kb pressure and the genesis of tholeiitic basalts. *Contrib Mineral Petrol* 73:287–310
- Johnson KTM, Dick HJB (1992) Open system melting and the temporal and spatial variation of peridotite and basalt compositions at the Atlantis II F.Z. *J Geophys Res* 97:9219–9241
- Johnson KTM, Dick HJB, Shimizu N (1990) Melting in the oceanic upper mantle: an ion microprobe study of diopsides in abyssal peridotites. *J Geophys Res* 95:2661–2678
- Kelemen PB (1990) Reaction between ultramafic rock and fractionating basaltic magma, I. Phase relations, the origin of calc-alkaline magma series, and the formation of discordant dunite. *J Petrol* 31:51–98
- Kelemen PB (2003) Igneous crystallization beginning at 20 km beneath the Mid-Atlantic Ridge, 14° to 16°N. *EOS Trans AGU* 84 (46) Fall Meet Suppl Abstr V22H-03 invited
- Kelemen PB, Shimizu N, Salters VJM (1995a) Extraction of mid-ocean-ridge basalt from the upwelling mantle by focused flow of melt in dunite channels. *Nature* 375:747–753
- Kelemen PB, Whitehead JA, Aharonov E, Jordahl KA (1995b) Experiments on flow focusing in soluble porous media, with applications to melt extraction from the mantle. *J Geophys Res* 100:475–496
- Kelemen PB, Hirth G, Shimizu N, Spiegelman M, Dick HJB (1997) A review of melt migration processes in the adiabatically upwelling mantle beneath oceanic spreading ridges. *Phil Trans R Soc Lond* 355:283–318
- Kelemen PB, Kikawa E, Miller DJ et al (2004) Proc ODP Init Repts 209 [CD-ROM]. Available from: Ocean Drilling Program, Texas A&M University, College Station TX 77845–9547, USA. Proc ODP Init Repts 209 [Online]. Available from World Wide Web: http://www.odp.tamu.edu/publications/209_IR/209ir.htm
- Kinzler RJ (1997) Melting of mantle peridotite at pressures approaching the spinel to garnet transition: application to mid-ocean ridge basalt petrogenesis. *J Geophys Res* 102:853–874
- Kinzler RJ, Grove TL (1992) Primary magmas of mid-ocean ridge basalts, 2. Applications *J Geophys Res* 97:6907–6926
- Klügel A (2001) Prolonged reactions between harzburgite xenoliths and silica-undersaturated melt: implications for dissolution and Fe–Mg interdiffusion rates of orthopyroxene. *Contrib Mineral Petrol* 141:1–14
- Lorand J-P (1988) The Cu-Fe-Ni sulfide assemblages of tectonic peridotites from the Maqсад district, Sumail ophiolite, Southern Oman: implications for the origin of the sulfide component in the oceanic upper-mantle. In: Boudier F,

- Nicolas A (eds) “The ophiolites of Oman”. *Tectonophysics* 151:57–74
- Lorand J-P (1991) Sulfide petrology and sulfur geochemistry of orogenic lherzolites : a comparative study between Pyrenean bodies (France) and the Lanzo massif (Italy). In: Menzies MA et al (eds) *Orogenic Lherzolites and mantle processes*. *J Petrol*, pp 77– 95
- Lorand J-P, Grégoire M (2006) Petrogenesis of base metal sulfides of some peridotites of the Kaapvaal craton (south Africa). *Contrib Mineral Petrol* 151:495–520
- Luguet A, Lorand J-P, Seyler M (2003) A coupled study of sulfide petrology and highly siderophile element geochemistry in abyssal peridotites from the Kane Fracture Zone (MARK area, Mid-Atlantic Ridge). *Geochim Cosmochim Acta* 67:1553–1570
- Mavrogènes JA, O’Neill HSC (1999) The relative effects of pressure, temperature and oxygen fugacity on the solubility of sulfide in mafic magmas. *Geochim Cosmochim Acta* 63:1173–1180
- Naldrett AJ (1989) Sulfide melt crystallization temperatures, solubilities in silicate melts, and Fe, Ni, and Cu partitioning between basaltic magmas and olivine. In: Whitney JA, and Naldrett AJ (eds) *Ore depositions associated with magmas*. *Rev Econ Geol* 4:5–20
- Navon O, Stolper E (1987) Geochemical consequences of melt percolation: the upper mantle as a chromatographic column. *J Geol* 95:285–307
- Nicolas A (1986) A melt extraction model based on structural studies in mantle peridotites. *J Petrol* 27:999–1022
- Parkinson IJ, Pearce JA, Thirlwall MF, Johnson KTM, Ingram G (1992) Trace element geochemistry of peridotites from the Izu-Bonin-Mariana forearc, Leg 125. In: Fryer P, Pearce JA, Stokking LB et al (eds) *Proc ODP Sci Results* 125. Ocean Drilling Program, College Station, Texas, pp 487–506
- Pickering-Witter J, Johnston AD (2000) The effects of variable bulk composition on the melting systematics of fertile peridotitic assemblages. *Contrib Mineral Petrol* 140:190–211
- Ross K, Elthon D (1997) Extreme incompatible trace-element depletion of diopside in residual mantle from south of the Kane Fracture Zone. In: Karson JA, Cannat M, Miller DJ, Elton D (eds) *Proc ODP Sci Results*, vol 153. College Station, Texas, pp 277–284
- Saal AE, Hauri EH, Langmuir CH, Perfit MR (2002) Vapour undersaturation in primitive mid-ocean-ridge basalt and the volatile content of Earth’s upper mantle. *Nature* 419:451–455
- Schwab BE, Johnston AD (2001) Melting systematics of modally variable, compositionally intermediate peridotites and the effects of mineral fertility. *J Petrol* 42:1789–1811
- Seyler M, Bonatti E (1997) Regional-scale melt–rock interaction in lherzolitic mantle in the Romanche Fracture Zone (Atlantic ocean). *Earth Planet Sci Lett* 146:273–287
- Seyler M, Toplis MJ, Lorand JP, Luguet A, Cannat M (2001) Clinopyroxene microtextures reveal incompletely extracted melts in abyssal peridotites. *Geology* 29:155–158
- Seyler M, Cannat M, Mével C (2003) Evidence for major-element heterogeneity in the mantle source of abyssal peridotites from the Southwest Indian Ridge (52° to 68°E). *Geochem Geophys Geosyst*. DOI: 10.1029/2002GC000305
- Seyler M, Lorand JP, Toplis M, Godard G (2004) Asthenospheric metasomatism beneath the mid-oceanic ridge: evidence from depleted abyssal peridotite. *Geology* 32:301–304
- Shaw CSJ (1999) Dissolution of orthopyroxene in basaltic magma between 0.4 and 2 GPa: further implications for the origins of Si-rich alkaline glass inclusions in mantle xenoliths. *Contrib Mineral Petrol* 135:114–132
- Shaw DM (2000) Continuous (dynamic) melting theory revisited. *Can Mineral* 38:1041–1063
- Shibata T, Thompson G (1986) Peridotites from the Mid-Atlantic Ridge at 43°N and their petrogenetic relation to abyssal tholeiites. *Contrib Mineral Petrol* 93:144–159
- Stolper E (1980) A phase diagram for mid-ocean ridge basalts: preliminary results and implications for petrogenesis. *Contrib Mineral Petrol* 74:13–27
- Streckeisen A (1976) To each plutonic rock its proper name. *Earth Sci Rev* 12:1–33
- Suhr G, Seck HA, Shimizu N, Günther D, Jenner G (1998) Infiltration of refractory melts into the lowermost oceanic crust: evidence from dunite- and gabbro-hosted clinopyroxenes in the Bay of Islands Ophiolite. *Contrib Mineral Petrol* 131:136–154
- Takazawa E, Frey FA, Shimizu N, Obata M, Bodinier JL (1992) Geochemical evidence for melt migration and reaction in the upper mantle. *Nature* 359:55–58
- Toplis MJ, Seyler M, Mével C (2003) Trace element concentrations of clinopyroxenes in peridotites from the eastern section of the ultra-slow spreading Southwest Indian ridge (40°E–69°E). *EGS Geophys Res Abstr* 5:07305
- Vernières J, Godard M, Bodinier JL (1997) A plate model for the simulation of trace elements during partial melting and magma transport in the Earth’s upper mantle. *J Geophys Res* 102:24771–24784
- Wagner TP, Grove TL (1998) Melt/harzburgite reaction in the petrogenesis of tholeiitic magma from Kilauea volcano, Hawaii. *Contrib Mineral Petrol* 131:1–12
- Zinnegrebe E, Foley SF (1995) Metasomatism in mantle xenoliths from Gees, West Eiffel, Germany: evidence for the genesis of calc-alkaline glasses and metasomatic Ca-enrichment. *Contrib Mineral Petrol* 122:75–96

Bulk-rock geochemistry and plagioclase zoning in lavas exposed along the northern flank of the Western Blanco Depression (Northeast Pacific): Insight into open-system magma chamber processes

Carole Cordier*, Martial Caroff, Thierry Juteau, Corinne Fleutelot, Christophe Hémond, Marion Drouin¹, Joseph Cotten, Claire Bollinger

Laboratoire des Domaines Océaniques (UMR6538), Université de Bretagne Occidentale et Centre Nationale de la Recherche Scientifique, Institut Universitaire Européen de la Mer (IUEM), Place Copernic, 29280 Plouzané, France

Received 17 May 2006; accepted 15 June 2007
Available online 23 June 2007

Abstract

The present study is based on a set of lavas and crosscutting dikes collected by dives along detailed vertical transects on the northern flank of the western part of the Blanco Transform Fault, Northeast Pacific. The studied area consists of a small basin, the Western Blanco Depression (WBD), extending from the southern end of the Juan de Fuca ridge to a pseudofault trace 60 km eastward. The Northern Scarp of the WBD comprises a volcanic unit overlying a sheeted-dike complex. Major and trace element data, coupled with Sr–Nd isotope ratios, reveal a two-component mantle source, composed by an isotopically depleted matrix variably veined by more enriched material. One chemical group (NS2), indistinguishable from the other Northern Scarp samples on the basis of trace element data, has an unusually depleted isotopic composition typical of a nearly pure mantle end-member. Some cogenetic samples of the Northern Scarp have been used to constrain the differentiation modalities. Anorthite and MgO content profiles in plagioclase xenocrysts and phenocrysts reveal (i) the existence of H₂O-bearing evolved melts in the mushy zones and (ii) the occurrence of mixing process between these melts and anhydrous mafic liquids. The hydration is supported by other petrographic features such as high magmatic fO_2 values, calculated from Fe–Ti oxide pairs, and the presence of pyroxene inclusions in plagioclase phenocrysts. Mixing, consistent with the existence of Ni-rich ferrobasalts, is interpreted to be the consequence of the reservoir refilling by mafic liquids (Mg# = 70). These petrological and geochemical evidences are combined with the evolution of Mg# with depth to suggest a periodic open-system magma chamber evolution beneath the southern end of the Juan de Fuca ridge.

© 2007 Elsevier B.V. All rights reserved.

Keywords: Transform fault; Plagioclase zoning; Crystallization; Hydration; Mushy zone; Magma mixing

1. Introduction

Transform zones belong to oceanic plate frontiers, sometimes separating two geochemically contrasted segments and revealing mantle segmentation (Sinton et al., 1991; Smith et al., 1998; Niu et al., 2001). Between transforms and beneath fast and intermediate spreading

* Corresponding author. Tel.: +33 29 8017289; fax: +33 29 8016620.
E-mail address: carole.cordier@sdt.univ-brest.fr (C. Cordier).

¹ Present address: Laboratoire de Tectonophysique, Université Montpellier II, 34095 Montpellier Cedex, France.

ridges, the axial magma reservoirs are thought to be composite with a thin melt lens overlying a large zone of crystal mush (Sinton and Detrick, 1992; Singh et al., 1998; Dunn and Toomey, 2000). Geological and geochemical studies have shown that these reservoirs are generally long-lived and periodically refilled (e.g. Caroff et al., 1997; Lagabrielle and Cormier, 1999). Close to or within the transform zones, fractionated basalts (ferrobasalts) are frequently sampled (Sinton et al., 1983; Juteau et al., 1995; Cotsonika et al., 2005; Stakes et al., 2006).

In this study, we focus on the Northern Scarp of the Western Blanco Transform Zone (southern end of the Juan de Fuca ridge). Contrary to some other transform zones, the outcropping crustal section has been only slightly tectonized. Thus, the Northern Scarp provides a remarkable petrographic window into the upper oceanic crust down to the sheeted-dike complex and an opportunity to study the temporal variations of the lava composition through the volcanic pile. New geochemical data (major and trace elements, Sr–Nd isotopic ratios)

from the extrusive unit outcropping along the Western Blanco Depression are used to compare the chemistry of lavas from both flanks. Once determined which samples are cogenetic, we focus on the differentiation of the northern flank lavas using a detailed study of the geochemistry and plagioclase zoning of remarkable samples collected along one dive.

2. Geological setting

2.1. The Blanco Transform Fault and the Western Blanco Depression

The Blanco Transform Fault (BTF) is a 360-km-long, left-stepping, dextrally-slipping fault that bounds the north of the Gorda ridge and the south of the Cleft segment of the Juan de Fuca ridge (Fig. 1, inset). The BTF comprises five segments roughly perpendicular to the Juan de Fuca ridge and separated by small basins. The Western Blanco Depression (WBD) extends parallel to the BTF from the southern end of the Juan de Fuca ridge

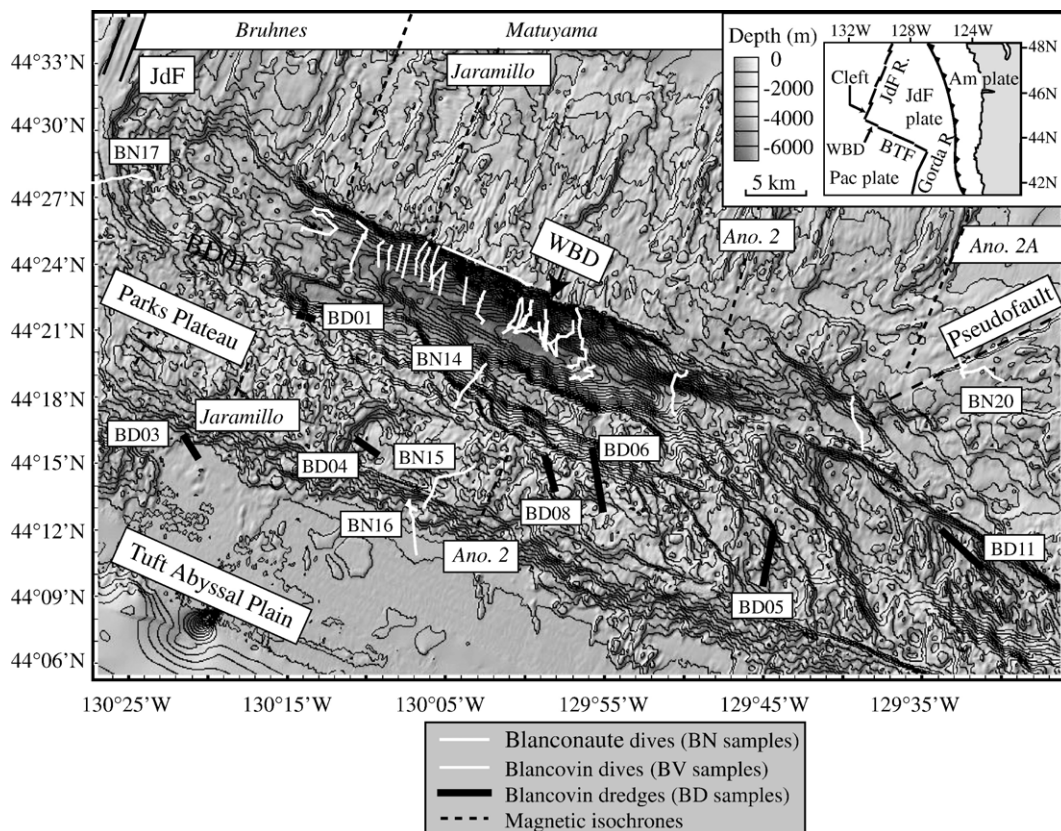


Fig. 1. Bathymetric map of the Western Blanco Depression (WBD) with superimposed magnetic isochrones (Embley and Wilson, 1992). Submersible dives and dredge paths from the Blanconaute and Blancovin cruises are reported. The dives and dredges not shown in Fig. 2 are given here. Inset: location map of the WBD in the NE Pacific. JdF plate: Juan de Fuca plate; Am plate: American plate; Pac plate: Pacific plate; JdF R.: Juan de Fuca ridge; Gorda R.: Gorda ridge.

to a pseudofault trace 60 km to the east (Fig. 1). It is a N112°E-trending 10 km-wide trough, which reaches a maximum depth of 4860 m. The pseudofault trace indicates earlier southward propagation of the Juan de Fuca ridge. The most recent propagating rift reached the BTF 1.4 My ago (Wilson et al., 1984; Embley and Wilson, 1992). For 1.4 My, spreading has been accommodated by accretion. Thus, the lithosphere presently exposed along the Northern Scarp originated to the north of the ridge-transform intersection, in the southern end of the Cleft segment at an intermediate full spreading rate of 56 mm/yr (Wilson, 1992).

2.2. Lithology of the crust exposed along the WBD

The Northern Scarp of the WBD truncates the ridge-parallel lineated magnetic anomalies formed at the Juan de Fuca ridge (from Brunhes to Anomaly 2A, Tivey, 1994). It is a linear cliff (dip 45–50°S) with continuous outcrops reaching up to hundreds of meters and separated by small steps covered with talus debris and sediments. Along this scarp, a 900–1000 m-thick volcanic unit is separated from a sheeted-dike complex by a slight drop in the cliff slope (Juteau et al., 1995; Karson et al., 2002). The volcanic unit consists mainly of basaltic pillow-lavas, with a few massive flows, intruded by sparse feeder dikes. The lava flows dip northwesterly (toward the spreading axis) gradually more with depth (Karson

et al., 2002). This dip evolution with depth has been attributed to a rapid subsidence beneath the spreading axis (1–3 km), which quickly diminishes off-axis (Karson et al., 2002; Pollock et al., 2005). Late top flows, channeled away from the axis, underwent a more moderated subsidence. The dikes of the sheeted complex roughly strike north–northeast and typically dip of 30–50° to the southeast (Karson et al., 2002). They show evidence of an intensive hydrothermal alteration, with development of numerous whitish veins at the dike joints (Manac'h et al., 1999). A few massive coarse-grained rocks have been observed at the bottom of the scarp (Fig. 2). In the neighboring dives BN24 and BV2963 (spaced by 100 m), the lithological succession is complicated by tectonic offsets due to normal faulting and the transition between sheeted dikes and extrusives is crossed twice (Fig. 2). Based on the repetition of this transition, the collapse of the lower block in both dives can be estimated at 550–700 m. Furthermore, due to their steepness, the slopes are gravitationally unstable and the dives BN07, BN08 and BN10 have sampled cliff sectors affected by a major landslide (0.85 km³). The slide block has slipped down over 600 m (Juteau et al., 1995).

To the south, the WBD is flanked by the Parks Plateau, lying at present on the Pacific plate. It is a 1650 m-high, 12 km-wide, and 70 km-long structure. The lithologic succession of the south wall of the WBD (northern flank of the Parks Plateau) differs from the

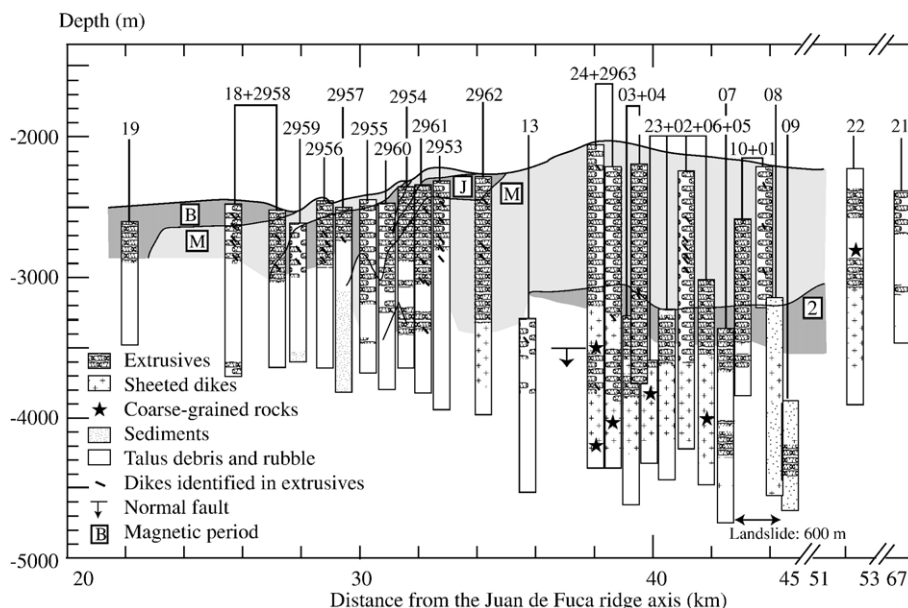


Fig. 2. Schematic representation of the lithologies observed along the Northern Scarp of the WBD superimposed on the magnetic cross section modified after Tivey (1996) and Tivey et al. (1998). Normal polarity crust is shaded in light gray (M: Matuyama) and is separated by isochrones from inverse polarity crust in dark gray (B: Brunhes, J: Jaramillo, 2: Anomaly 2). The dives are labeled at the top of the scarp (29XX names referring to the Alvin dives, the other names to the Nautila dives) and the dives that will be combined together in Section 7 are linked by horizontal lines.

Northern Scarp by the lack of sheeted-dike complex and the presence of hyaloclastites in the lower part of the scarp. The top of the Parks Plateau is capped by small, isolated volcanoes, out of which erupted the lava flows covering its southern flank.

Two models have been proposed for the geodynamical evolution of the WBD area (Dauteuil, 1995):

- (1) The southern flank (Parks Plateau) would correspond to a seamount. This model is supported by (i) the present position of the plateau, at the edge of a transform fault where off-axis magmatism is frequently observed; (ii) the abundance of small volcanic edifices in its central part and the lack of any sheeted-dike complex; and (iii) its elongated morphology suggesting a volcanic origin (Fig. 1).
- (2) Both flanks of the WBD would have evolved together on the Juan de Fuca plate until 0.4–0.2 My. Then, minor changes in relative motion between Juan de Fuca and Pacific plates would have caused a northward jump of the transform, from the southern flank of the Parks Plateau to the present-day location along the northern flank of the WBD (Embley and Wilson, 1992; Dauteuil, 1995; Juteau et al., 1995). This model is supported by (i) the shift of the seafloor magnetic anomalies between the two sides of the WBD (Fig. 1); (ii) the similar average depth of the Parks Plateau and the Juan de Fuca plate (Fig. 1); and (iii) the similar trend of the tectonic structures in both the Parks Plateau and the Juan de Fuca plate.

2.3. Temporal and spatial relationships along the Northern Scarp

Along the Northern Scarp, the temporal evolution of the lava chemistry can be investigated by studying lavas both horizontally and vertically. Horizontally, lavas become older with increasing distance to the Juan de Fuca ridge, consistently with the succession of measured seafloor magnetic boundaries (Fig. 1) and with the increasing damage of the flow morphology eastward. The vertical succession has a temporal significance only throughout the extrusives (Fig. 2). Lava tilting (Karson et al., 2002) and magnetization profiles versus depth (Tivey et al., 1998) suggest that the isochrones form curved trends that dip toward the Juan de Fuca ridge. Consequently, each overlying lava was emplaced further off-axis than the one below it. Even if the dive paths are not perpendicular to the isochrones, the vertical succession of lavas is thought to record increasing age lavas with depth (Pollock et al., 2005).

3. Petrology of the lavas and crosscutting dikes from the Northern Scarp

3.1. Sampling

The crust exposed along the Northern Scarp of the WBD was the object of several geological, geophysical, and geochemical studies (Delaney et al., 1987; Gaetani et al., 1995; Juteau et al., 1995; Tivey, 1996; Fleutelot, 1997; Naidoo, 1998; Tivey et al., 1998; Manac'h et al., 1999; Karson et al., 2002; Pollock et al., 2005). They were all based on samples and observations achieved through three cruises between 1987 and 1995. The present study uses samples collected from the extrusive unit (lavas and crosscutting dikes) during the Blanconaute (1991) and Blancovin (1995) programs. During the Blanconaute cruise, twenty Nautille dives sampled the Northern Scarp (acronym BN ahead of the sample numbers) from the Juan de Fuca ridge axis (BN17) to the pseudofault (BN20, Figs. 1 and 2). Three additional Blanconaute dives were performed on the Parks Plateau (Fig. 1). The Blancovin cruise (Figs. 1 and 2) completed the sampling of the Northern Scarp with eleven Alvin upslope dives (acronym BV), mainly located less than 35 km from the Juan de Fuca ridge axis. In addition, eight dredges (acronym BD) sampled the Parks Plateau and an eastern intratransform basin (BD11).

3.2. Textures and mineralogy

The secondary mineralogy of the extrusive unit samples has been detailed in Juteau et al. (1995) and Manac'h et al. (1999). In summary, the lavas are characterized by a low-temperature oxidative alteration (<100 °C), with local development of brown alteration halos in the pillow-lava margins (palagonite, celadonite, smectite, and Fe-oxyhydroxides).

In the lavas, the groundmass texture shows a progressive evolution over less than 5 cm from fresh or palagonitized glassy margins to microlitic cores. The transition zones display spherulitic/variolitic texture characterized by fan-like arrangement of thin plagioclase and fibrous clinopyroxene crystals, enclosing small granular clinopyroxenes or olivines. In more crystallized samples, the texture tends to become intergranular.

Sparse autoclastic breccias (hyaloclastites) have been collected. Clasts consist of rounded to angular hyaline/fine-grained basalt fragments (up to 2.5 cm) cemented by a matrix of crushed and altered glass bearing finely broken phenocrysts (mainly plagioclases).

Lavas are slightly vesicular (<8 vol.%). In the outer part of the flows, amygdules are filled from rims to cores

Table 1
Representative microprobe analyses^a of plagioclase from BV2958 dive samples

| Sample | BV2958-2 | | | | | | | | | | | | BV2958-3 | | | | | | BV2958-4 | | | | | |
|--------------------------------|----------------------|--------|--------|--------|--------|--------|--------|---------|--------|--------|--------|--------|----------|--------|--------|--------|--------|--------|----------|------|--|--|--|--|
| | Crystal ^b | X. A | X. A | X. A | X. A | X. B | X. B | X. B | X. B | X. B | X. C | X. C | P. D | P. D | P. E | P. E | P. F | P. F | P. F | P. F | | | | |
| L (µm) ^c | 2650 | 2650 | 2650 | 2650 | 1925 | 1925 | 1925 | 1925 | 1925 | 1925 | 835 | 835 | 700 | 700 | 1600 | 1600 | 1600 | 1600 | 1600 | 1600 | | | | |
| D (µm) ^c | 139 | 171 | 708 | 1083 | 133 | 227 | 842 | 842 | 842 | 1222 | 1592 | 2322 | 3 | 83 | 4 | 40 | 63 | 142 | 312 | 346 | | | | |
| Zone ^d | An-low | Ca-M | Core | Ca-M | Ca-M | An-low | Core | Inner P | Rim | Rim | Core | Rim | Core | Rim | Core | Ca-R | Core | Ca-R | Core | Ca-R | | | | |
| SiO ₂ | 49.86 | 47.77 | 48.83 | 47.33 | 47.60 | 49.74 | 48.88 | 48.09 | 48.59 | 46.29 | 56.76 | 54.56 | 57.77 | 54.06 | 54.19 | 55.13 | 53.27 | 54.58 | | | | | | |
| TiO ₂ | 0.03 | 0.04 | 0.02 | 0.02 | 0.01 | 0.01 | 0.03 | 0.05 | 0.01 | 0.00 | 0.09 | 0.16 | 0.00 | 0.00 | 0.08 | 0.09 | 0.14 | 0.11 | | | | | | |
| Al ₂ O ₃ | 31.79 | 33.57 | 32.43 | 33.98 | 33.20 | 31.97 | 32.66 | 32.69 | 32.84 | 34.19 | 26.48 | 27.91 | 25.91 | 28.51 | 29.01 | 28.33 | 29.47 | 28.17 | | | | | | |
| FeO ^e | 0.46 | 0.53 | 0.48 | 0.51 | 0.53 | 0.52 | 0.58 | 0.33 | 0.42 | 0.43 | 0.84 | 0.86 | 0.81 | 0.80 | 0.71 | 0.82 | 0.84 | 0.87 | | | | | | |
| MnO | 0.00 | 0.13 | 0.03 | 0.06 | 0.03 | 0.06 | 0.00 | 0.00 | 0.03 | 0.03 | 0.13 | 0.00 | 0.00 | 0.00 | 0.00 | 0.05 | 0.12 | 0.05 | | | | | | |
| MgO | 0.21 | 0.18 | 0.17 | 0.20 | 0.20 | 0.22 | 0.23 | 0.21 | 0.19 | 0.16 | 0.11 | 0.13 | 0.05 | 0.14 | 0.17 | 0.10 | 0.11 | 0.15 | | | | | | |
| CaO | 15.46 | 17.47 | 16.50 | 17.65 | 17.17 | 15.65 | 16.45 | 16.77 | 16.59 | 18.45 | 9.79 | 11.75 | 8.96 | 11.99 | 12.43 | 11.64 | 12.64 | 11.56 | | | | | | |
| Na ₂ O | 3.00 | 1.94 | 2.35 | 1.63 | 1.95 | 2.70 | 2.59 | 2.05 | 2.35 | 1.29 | 6.06 | 5.15 | 6.48 | 4.64 | 4.55 | 5.03 | 4.52 | 4.91 | | | | | | |
| K ₂ O | 0.00 | 0.00 | 0.05 | 0.03 | 0.01 | 0.04 | 0.04 | 0.00 | 0.01 | 0.00 | 0.09 | 0.06 | 0.06 | 0.04 | 0.01 | 0.13 | 0.03 | 0.06 | | | | | | |
| P ₂ O ₅ | 0.00 | 0.00 | 0.05 | 0.00 | 0.00 | 0.00 | 0.06 | 0.05 | 0.00 | 0.00 | 0.02 | 0.08 | 0.03 | 0.05 | 0.00 | 0.03 | 0.00 | 0.06 | | | | | | |
| Cr ₂ O ₃ | 0.00 | 0.00 | 0.00 | 0.00 | 0.00 | 0.01 | 0.05 | 0.00 | 0.00 | 0.00 | 0.00 | 0.02 | 0.03 | 0.00 | 0.01 | 0.14 | 0.00 | 0.00 | | | | | | |
| SO ₂ | 0.01 | 0.00 | 0.00 | 0.00 | 0.00 | 0.01 | 0.00 | 0.00 | 0.03 | 0.00 | 0.00 | 0.04 | 0.00 | 0.00 | 0.00 | 0.00 | 0.05 | 0.03 | | | | | | |
| Total | 100.82 | 101.62 | 100.90 | 101.40 | 100.76 | 100.92 | 101.55 | 100.24 | 101.06 | 100.85 | 100.37 | 100.73 | 100.08 | 100.24 | 101.17 | 101.50 | 101.20 | 100.55 | | | | | | |
| An (%) | 74 | 83 | 79 | 86 | 83 | 76 | 78 | 82 | 80 | 89 | 47 | 56 | 43 | 59 | 60 | 56 | 61 | 56 | | | | | | |

^a Compositions were determined using a Cameca SX 50 automated electron microprobe (Microsonde Ouest, Brst, France). Analytical conditions were 15 kV accelerating voltage, 15 nA beam current on a Faraday cup, 6 s counting time, and correction by the ZAF method. Concentrations lower than 0.1 wt.% are considered not representative. Chemical distribution maps (Fig. 9) were obtained in plagioclase xenocrysts (sample BV2958-2) by electron microprobe, with a 10 µm electron beam, a 13 µm analysis step, a 15 kV accelerating voltage, and a 60 nA current.

^b X. = xenocryst, P. = phenocryst. X. and P. are followed by the letter used to identify the crystals in the text and in Fig. 9. Analyzed points are shown in the profiles of Fig. 9.

^c L. = length of the crystal, D. = distance of the analyzed point from the right crystal edge.
^d An-low = An-poor zone, Ca-M = calcic mantle, Inner P. = inner part, Ca-R = calcic rim (for the definition of these zones, see text and Fig. 9).
^e Total Fe calculated as FeO.

with Fe-oxyhydroxydes, celadonite plus smectite, then calcite (Manac'h et al., 1999). Spherical segregation vesicles are common, sometimes surrounded by tangential plagioclase microlites. They are partially (crescent-shape) or totally filled with more or less recrystallized glass.

Most of the intrusive samples, together with some lava flow cores, have a moderately coarse-grained doleritic texture, generally intergranular, more rarely ophitic.

Consistently with descriptions presented by Juteau et al. (1995), Fleutelot (1997), and Naidoo (1998), lavas are aphyric to moderately phyrlic (phenocrysts <10 vol.%). Only BN22-14 exhibits olivine accumulation (10–15 vol.%). Plagioclase is the dominant phenocrystic phase (<1 mm long) that frequently forms glomerocrysts. They may enclose small inclusions of plagioclase and/or devitrified glass (<150 μm in diameter) in both rims and cores. The phenocryst margins commonly present a slight optical zoning. A few samples (e.g. BV2955-7 and BV2958-2) host plagioclasic coarse-grained xenoliths (~0.5 cm). Olivine phenocrysts, with Cr-spinel inclusions, are less frequent and partially to completely bowlingitized. Sparse clinopyroxene phenocrysts have been observed, independently of the differentiation degree of the lava. In most cases, small laths of plagioclase are present on the margin of clinopyroxene phenocrysts but in a few lavas (e.g. BV2958-3 and -4) plagioclase phenocrysts partially or totally include clinopyroxenes.

3.3. Mineralogical compositions

Plagioclase phenocrysts and xenocrysts range from andesine to anorthite ($37 \leq \text{An} \leq 98$, Table 1). Microlites have compositions ranging from An_{32} to An_{82} . Sparse

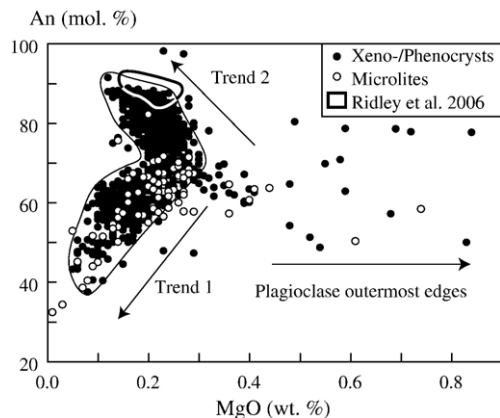


Fig. 3. MgO versus An content in the plagioclases of the Northern Scarp lavas, compared with the plagioclase compositions measured by Ridley et al. (2006) in a cumulate xenolith (EPR, 9°50'N). Selected analyses are given in Table 1.

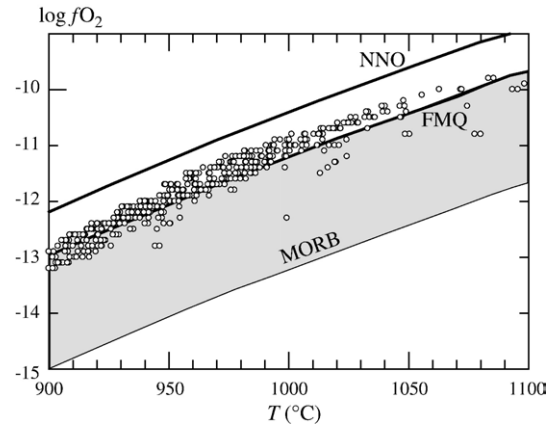


Fig. 4. Plot of $\log f_{\text{O}_2}$ versus temperature for coexisting groundmass titanomagnetite-hemoilmenite pairs analyzed in the lava BV2958-3. FMQ: quartz-fayalite-magnetite buffer; NNO: Ni-NiO buffer. MORB field is drawn after Christie et al. (1986) and Lee et al. (2005).

secondary albite has also been identified (pillow-lava BN17-04, hyaloclastite BN18-02). An contents of plagioclase microlites and phenocrysts have been reported versus MgO in the Fig. 3 diagram. Two main trends are identified. Trend 1, including both microlites and phenocrysts, shows a concomitant decrease of MgO and An contents. Trend 2, including mainly phenocrysts plus xenocrysts, is characterized by an increase of An when MgO decreases. The two trends intersect around $\text{MgO} = 0.25$ wt.% and An_{70} . These trends are disturbed by MgO-rich compositions ($\text{MgO} > 0.3$ wt.%), corresponding to the outermost edges of plagioclase phenocrysts.

The olivine phenocrysts range from Fo_{76} to Fo_{85} except the cumulus crystals in the pillow-lava BN22-14 that are more magnesian (Fo_{87-90}). The $\text{Fe-Mg}K_D$ values suggest that the olivines with $\text{Fo}_{<85}$ have crystallized in equilibrium with the host rock (following Roeder and Emslie, 1970). In BN22-14, the olivine crystals are fresh, euhedral, and do not show any sign of resorption or mechanical stress as expected for peridotite xenocrysts. Consequently, these forsteritic olivines might have crystallized in equilibrium with a not sampled, highly mafic melt ($\text{Mg\#} \sim 74$, considering a $\text{Fe-Mg}K_D$ value of 0.3).

Clinopyroxene is augitic, except rare pigeonite in the crosscutting dikes BN18-05, -06, and BV2958-2. Their Mg# values ($= 100 \text{Mg} / [\text{Mg} + \text{Fe}^{2+} + \text{Mn}]$) range from 64 to 89 in phenocrysts and from 54 to 86 in groundmass crystals.

Groundmass Fe-Ti oxides are mainly granular Ti-magnetite ($59 < \text{Usp} < 87$). Haemoilmenite microlites have also been identified ($89 < \text{Ilm} < 98$) in the sample BV2958-3. The occurrence of coexisting Fe-Ti oxides in this lava allows estimating the oxygen fugacity (f_{O_2}) and crystallization temperature (T). The calculations have

Table 2
Chemical data^a (wt.% oxide, ppm element) of representative samples from Northern Scarp and Parks Plateau

| Location | JdF ridge | | NS (west) | | | | | | |
|---|-----------|-----------|-----------|----------|---------|----------|-----------|-----------|-----------|
| | Sample | BN17-02 | BN17-11 | BN18-01 | BN18-03 | BN18-07 | BV2958-1 | BV2958-1s | BV2958-1s |
| Reference ^b | 1 and 3 | 1 and 2 | 3 | 1 | 3 | 1 | 1 | 1 | 1 |
| Type ^c | Basalt | Fe-basalt | Basalt | Basalt | Basalt | Basalt | Seg. Ves. | Seg. Ves. | Diabase |
| Latitude | 44.5 | 44.5 | 44.4 | 44.4 | 44.4 | 44.4 | 44.4 | 44.4 | 44.4 |
| Longitude | 130.4 | 130.5 | 130.2 | 130.2 | 130.2 | 130.2 | 130.2 | 130.2 | 130.2 |
| Depth (m) | −2852 | −2174 | −3681 | −2877 | −2501 | −2956 | −2956 | −2956 | −2949 |
| Dist. (km) ^d | 8.1 | 3 | 24.9 | 26 | 26.3 | 27.1 | 27.1 | 27.1 | 27.1 |
| SiO ₂ | 50.50 | 50.20 | 49.85 | 50.50 | 49.70 | 50.00 | 53.00 | 57.40 | 49.50 |
| TiO ₂ | 1.55 | 2.02 | 1.83 | 1.70 | 1.82 | 1.98 | 3.97 | 2.68 | 1.64 |
| Al ₂ O ₃ | 14.82 | 13.87 | 14.00 | 14.28 | 14.30 | 14.20 | 12.69 | 10.51 | 14.10 |
| Fe ₂ O ₃ t ^c | 12.13 | 13.67 | 12.93 | 11.55 | 12.70 | 12.80 | 16.26 | 17.04 | 12.20 |
| MnO | 0.21 | 0.23 | 0.22 | 0.21 | 0.21 | 0.20 | 0.32 | 0.20 | 0.20 |
| MgO | 7.63 | 6.91 | 7.12 | 7.12 | 7.06 | 6.20 | 1.96 | 0.44 | 7.00 |
| CaO | 12.15 | 11.70 | 11.50 | 11.70 | 11.68 | 11.15 | 7.68 | 4.76 | 11.30 |
| Na ₂ O | 2.38 | 2.46 | 2.48 | 2.56 | 2.56 | 2.53 | 4.03 | 3.92 | 2.60 |
| K ₂ O | 0.17 | 0.20 | 0.32 | 0.21 | 0.20 | 0.24 | 0.36 | 0.78 | 0.08 |
| P ₂ O ₅ | 0.17 | 0.21 | 0.21 | 0.16 | 0.17 | 0.19 | 0.64 | 1.15 | 0.15 |
| LOI | −0.62 | −0.67 | −0.11 | −0.13 | 0.10 | 0.28 | | | 0.83 |
| Total | 101.09 | 100.80 | 100.35 | 99.86 | 100.50 | 99.77 | 99.31 | 97.27 | 99.60 |
| Mg# ^f | 60.9 | 55.6 | 57.7 | 60.4 | 57.9 | 54.5 | 25.4 | 7.3 | 58.7 |
| Rb | 1.7 | 2.3 | 3.3 | 1.2 | 2.5 | 3.2 | n.d. | n.d. | 0.8 |
| Sr | 107 | 104 | 110 | 112 | 105 | 99 | n.d. | n.d. | 109 |
| Ba | 12 | 16 | 18 | 17 | 15 | 22 | n.d. | n.d. | 13 |
| Sc | 43 | 45 | 43 | 45 | 44 | 43 | n.d. | n.d. | 43 |
| V | 335 | 409 | 360 | 372 | 377 | 403 | n.d. | n.d. | 350 |
| Cr | 288 | 188 | 215 | 158 | 175 | 130 | n.d. | n.d. | 155 |
| Co | 45 | 45 | 46 | 47 | 46 | 40 | n.d. | n.d. | 40 |
| Ni | 91 | 63 | 75 | 74 | 71 | 56 | n.d. | n.d. | 59 |
| Y | 38 | 48 | 45 | 38 | 41 | 45 | n.d. | n.d. | 36 |
| Zr | 101 | 130 | 129 | 102 | 111 | 117 | n.d. | n.d. | 94 |
| Nb | 2.5 | 4.0 | 4.6 | 3.8 | 3.6 | 4.0 | n.d. | n.d. | 3.5 |
| La | 3.9 | 5.0 | 5.2 | 3.9 | 4.4 | 4.3 | n.d. | n.d. | 3.5 |
| Ce | 12.0 | 14.0 | 16.0 | 11.3 | 12.0 | 12.6 | n.d. | n.d. | 10.5 |
| Nd | 12.0 | 16.0 | 16.0 | 11.2 | 14.0 | 12.1 | n.d. | n.d. | 9.8 |
| Sm | n.d. | n.d. | n.d. | 3.5 | n.d. | 4.3 | n.d. | n.d. | 3.5 |
| Eu | 1.2 | 1.5 | 1.6 | 1.4 | 1.0 | 1.5 | n.d. | n.d. | 1.3 |
| Gd | n.d. | n.d. | n.d. | 5.3 | n.d. | 6.4 | n.d. | n.d. | 5.0 |
| Dy | 6.1 | 7.7 | 7.4 | 6.4 | 6.9 | 7.3 | n.d. | n.d. | 5.9 |
| Er | 4.5 | 5.4 | 5.2 | 3.8 | 4.6 | 4.5 | n.d. | n.d. | 3.4 |
| Yb | 3.8 | 4.7 | 4.5 | 3.8 | 4.2 | 4.5 | n.d. | n.d. | 3.5 |
| (La/Yb) _N ^g | 0.7 | 0.8 | 0.8 | 0.7 | 0.8 | 0.7 | | | 0.7 |
| (La/Nd) _N ^g | 0.6 | 0.6 | 0.6 | 0.7 | 0.6 | 0.7 | | | 0.7 |
| (Dy/Yb) _N ^g | 1.1 | 1.1 | 1.1 | 1.1 | 1.1 | 1.1 | | | 1.1 |
| ⁸⁷ Sr/ ⁸⁶ Sr | 0.702488 | 0.702486 | | 0.702461 | | 0.702440 | | | |
| ¹⁴³ Nd/ ¹⁴⁴ Nd | 0.513173 | 0.513166 | | 0.513177 | | 0.513197 | | | |

(continued on next page)

The full Table 2 is available in the online version of this article; See Appendix A.

^a Major and trace element analyses were performed by ICP-AES at Brest for whole rocks and by electron microprobe for glass of segregation vesicles (see text). For ICP-AES, the analytical method is described in Cotten et al. (1995). Relative standard deviations are <2% for major elements, Rb and Sr; and <5% for other trace elements. Sr and Nd isotope ratios were measured following the procedure described in Dosso et al. (1991) and using a Thermo-Electron Triton T1 mass spectrometer (UMR6538 “Domaines Océaniques”, IUEM, Brest) in dynamic mode for Sr and in static mode for Nd. Sr isotope compositions were corrected for mass fractionation to ⁸⁸Sr/⁸⁶Sr=8.375209 and normalized to a value of 0.710254 for standard NBS SRM987 (*n*=18 during the analyses period). Nd isotope compositions were corrected for mass fractionation to ¹⁴⁶Nd/¹⁴⁴Nd=0.721903 and normalized to a value of 0.511866 for standard La Jolla (*n*=14).

^b References: 1, this work; 2, Juteau et al. (1995); 3, Fleutelot (1997) and Naidoo (1998).

Table 2 (continued)

| Location | NS (west) | | | | | | NS (center) | | |
|--|------------|------------|----------|-----------|----------|----------|-------------|-----------|----------|
| Sample | BV2958-3 | BV2958-4 | BV2958-5 | BV2960-2 | BV2960-4 | BV2960-7 | BV2963-9 | BN04-09 | BN04-12 |
| Reference ^b | 1 | 1 | 1 | 1 | 1 | 1 | 1 | 1 and 3 | 1 |
| Type ^c | Ni-Fe-bas. | Ni-Fe-bas. | Basalt | Fe-basalt | Basalt | Basalt | Fe-basalt | Fe-basalt | Basalt |
| Latitude | 44.4 | 44.4 | 44.4 | 44.4 | 44.4 | 44.4 | 44.4 | 44.4 | 44.4 |
| Longitude | 130.2 | 130.2 | 130.2 | 130.1 | 130.1 | 130.1 | 130.0 | 130.0 | 130.0 |
| Depth (m) | -2765 | -2643 | -2549 | -3190 | -3036 | -2492 | -2271 | -2742 | -2291 |
| Dist. (km) ^d | 27.3 | 27.4 | 27.5 | 30.8 | 31 | 31.4 | 39.3 | 40.1 | 40.1 |
| SiO ₂ | 48.00 | 49.20 | 50.20 | 49.20 | 49.50 | 49.50 | 49.70 | 49.50 | 50.20 |
| TiO ₂ | 3.55 | 3.20 | 1.81 | 2.13 | 1.85 | 1.36 | 2.37 | 2.52 | 1.98 |
| Al ₂ O ₃ | 12.55 | 13.17 | 14.70 | 13.50 | 13.70 | 15.15 | 13.80 | 13.45 | 13.70 |
| Fe ₂ O _{3t} ^e | 16.80 | 15.00 | 11.75 | 13.70 | 13.10 | 10.80 | 13.50 | 14.65 | 13.05 |
| MnO | 0.24 | 0.23 | 0.20 | 0.21 | 0.20 | 0.19 | 0.22 | 0.23 | 0.21 |
| MgO | 4.98 | 4.69 | 6.50 | 6.20 | 6.85 | 8.05 | 5.60 | 5.58 | 6.30 |
| CaO | 9.35 | 9.94 | 12.00 | 10.90 | 11.00 | 12.00 | 11.00 | 10.13 | 11.40 |
| Na ₂ O | 2.89 | 2.78 | 2.57 | 2.60 | 2.55 | 2.30 | 2.79 | 2.82 | 2.63 |
| K ₂ O | 0.22 | 0.43 | 0.23 | 0.20 | 0.11 | 0.15 | 0.32 | 0.38 | 0.26 |
| P ₂ O ₅ | 0.35 | 0.35 | 0.17 | 0.21 | 0.19 | 0.14 | 0.23 | 0.30 | 0.19 |
| LOI | 0.27 | 0.38 | -0.01 | 0.93 | 0.46 | -0.15 | 0.18 | 0.34 | -0.18 |
| Total | 99.20 | 99.37 | 100.12 | 99.78 | 99.51 | 99.49 | 99.71 | 99.90 | 99.74 |
| Mg# ^f | 42.3 | 43.6 | 57.8 | 52.8 | 56.4 | 64.9 | 50.7 | 48.5 | 54.4 |
| Rb | 2.4 | 4.8 | 2.4 | 2.5 | 1.2 | 1.4 | 3.0 | 3.1 | 1.6 |
| Sr | 104 | 104 | 110 | 108 | 108 | 101 | 126 | 131 | 108 |
| Ba | 28 | 25 | 17 | 16 | 14 | 11 | 25 | 30 | 15 |
| Sc | 44 | 44 | 44 | 46 | 44 | 40 | 46 | 44 | 47 |
| V | 600 | 530 | 390 | 440 | 390 | 305 | 445 | 450 | 408 |
| Cr | 110 | 157 | 190 | 66 | 109 | 275 | 94 | 55 | 111 |
| Co | 48 | 49 | 45 | 49 | 43 | 45 | 44 | 47 | 46 |
| Ni | 100 | 116 | 80 | 65 | 52 | 102 | 58 | 40 | 57 |
| Y | 77 | 75 | 42 | 48 | 42 | 32 | 52 | 57 | 45 |
| Zr | 240 | 240 | 113 | 130 | 120 | 76 | 156 | 181 | 121 |
| Nb | 8.4 | 7.6 | 3.8 | 4.0 | 4.6 | 3.0 | 6.4 | 7.3 | 4.1 |
| La | 8.5 | 8.7 | 4.6 | 4.8 | 4.7 | 3.1 | 6.4 | 8.2 | 4.3 |
| Ce | 25.0 | 25.8 | 12.9 | 14.4 | 14.2 | 9.6 | 18.5 | 23.0 | 13.0 |
| Nd | 24.0 | 24.0 | 12.0 | 13.6 | 12.7 | 8.3 | 16.5 | 22.0 | 12.5 |
| Sm | 8.0 | 7.8 | 4.3 | 4.6 | 4.3 | 3.1 | 5.4 | n.d. | 4.3 |
| Eu | 2.5 | 2.4 | 1.4 | 1.7 | 1.5 | 1.1 | 1.8 | 2.0 | 1.6 |
| Gd | 10.8 | 10.6 | 5.6 | 6.8 | 5.6 | 4.3 | 7.2 | n.d. | 6.1 |
| Dy | 12.7 | 12.8 | 6.9 | 7.7 | 7.0 | 5.3 | 8.6 | 9.5 | 7.3 |
| Er | 7.8 | 7.7 | 4.2 | 4.8 | 4.3 | 3.1 | 5.2 | 6.1 | 4.6 |
| Yb | 7.7 | 7.6 | 4.1 | 4.7 | 4.1 | 3.1 | 5.0 | 5.5 | 4.4 |
| (La/Yb) _N ^g | 0.8 | 0.8 | 0.8 | 0.7 | 0.8 | 0.7 | 0.9 | 1.1 | 0.7 |
| (La/Nd) _N ^g | 0.7 | 0.7 | 0.8 | 0.7 | 0.7 | 0.7 | 0.8 | 0.7 | 0.7 |
| (Dy/Yb) _N ^g | 1.1 | 1.1 | 1.1 | 1.1 | 1.1 | 1.1 | 1.2 | 1.2 | 1.1 |
| ⁸⁷ Sr/ ⁸⁶ Sr | 0.702457 | | 0.702490 | 0.702462 | 0.702460 | 0.702479 | 0.702497 | 0.702481 | 0.702453 |
| ¹⁴³ Nd/ ¹⁴⁴ Nd | 0.513185 | | 0.513171 | 0.513184 | 0.513181 | 0.513188 | 0.513169 | 0.513158 | 0.513179 |

^c Seg. ves.: glass in segregation vesicles; Fe-basalt: ferrobasalt; Fe-diabase: ferrodibase; Ni-: Ni-rich subaphyric sample; Ol-: sample with olivine accumulation; Hcumulate: heteradcumulate.

^d Dist.: distance from the Juan de Fuca axis.

^e Total iron expressed as Fe₂O₃.

^f Mg# calculated with Fe₂O₃/Fe₂O_{3t} ratios from Middlemost (1989).

^g Chondrite-normalized incompatible trace element ratios (normalization values from Sun and McDonough, 1989).

Table 2 (continued)

| Location | NS (center) | | | | | | | | NS (east) | |
|---|-------------|----------|-----------|----------|----------|-----------|----------|----------|-----------|-----------|
| | BN23-09 | BN02-10 | BN02-12 | BN06-07 | BN06-14 | BN10-13 | BN10-17 | BN01-03 | BN22-14 | BN22-19 |
| Reference ^b | 1 | 1 and 3 | 1 and 2 | 1 and 3 | 1 and 3 | 1 and 3 | 1 | 1 and 3 | 2 | 1 and 3 |
| Type ^c | Basalt | Basalt | Fe-basalt | Basalt | Basalt | Fe-basalt | Basalt | Basalt | Ol-basalt | Fe-basalt |
| Latitude | 44.4 | 44.4 | 44.4 | 44.4 | 44.4 | 44.4 | 44.4 | 44.4 | 44.3 | 44.3 |
| Longitude | 130.0 | 130.0 | 130.0 | 130.0 | 130.0 | 130.0 | 129.9 | 129.9 | 129.8 | 129.8 |
| Depth (m) | −3638 | −3600 | −3409 | −3062 | −2300 | −3457 | −2993 | −2492 | −2613 | −2292 |
| Dist. (km) ^d | 40.4 | 40.9 | 40.9 | 41.5 | 41.4 | 43.2 | 43.8 | 44.3 | 52.3 | 53.3 |
| SiO ₂ | 49.30 | 48.90 | 48.85 | 49.80 | 50.20 | 47.60 | 49.20 | 50.70 | 45.00 | 49.80 |
| TiO ₂ | 1.18 | 1.06 | 3.61 | 1.66 | 1.65 | 2.34 | 1.68 | 2.38 | 1.36 | 2.42 |
| Al ₂ O ₃ | 15.00 | 15.58 | 11.62 | 14.30 | 14.54 | 13.54 | 14.10 | 14.60 | 13.70 | 13.25 |
| Fe ₂ O ₃ t ^e | 9.74 | 9.59 | 19.10 | 12.30 | 11.80 | 14.10 | 12.00 | 12.73 | 10.23 | 14.55 |
| MnO | 0.19 | 0.16 | 0.26 | 0.20 | 0.20 | 0.21 | 0.21 | 0.21 | 0.20 | 0.23 |
| MgO | 7.80 | 8.15 | 4.27 | 7.20 | 7.32 | 6.25 | 7.43 | 5.14 | 15.00 | 6.05 |
| CaO | 11.45 | 11.87 | 7.78 | 11.73 | 11.85 | 10.00 | 11.70 | 11.49 | 9.30 | 10.98 |
| Na ₂ O | 2.86 | 2.27 | 3.10 | 2.51 | 2.56 | 2.97 | 2.46 | 2.69 | 2.47 | 2.54 |
| K ₂ O | 0.10 | 0.13 | 0.34 | 0.15 | 0.21 | 0.10 | 0.12 | 0.38 | 0.05 | 0.35 |
| P ₂ O ₅ | 0.11 | 0.12 | 0.52 | 0.17 | 0.17 | 0.28 | 0.17 | 0.26 | 0.12 | 0.26 |
| LOI | 1.81 | 2.38 | 1.08 | −0.35 | −0.26 | 2.50 | 0.77 | 0.10 | 2.31 | −0.04 |
| Total | 99.54 | 100.21 | 100.53 | 99.67 | 100.24 | 99.89 | 99.90 | 100.68 | 99.75 | 100.39 |
| Mg# ^f | 66.5 | 67.8 | 35.6 | 59.2 | 60.6 | 52.3 | 60.5 | 50 | 78.4 | 50.7 |
| Rb | 0.3 | 2.5 | 4.7 | 1.7 | 2.0 | 1.1 | 0.5 | 4.4 | 0.6 | 4.7 |
| Sr | 116 | 117 | 115 | 101 | 104 | 108 | 119 | 117 | 250 | 108 |
| Ba | 21 | 12 | 38 | 12 | 13 | 11 | 12 | 23 | 3 | 21 |
| Sc | 43 | 39 | 40 | 44 | 44 | 45 | 45 | 46 | 31 | 44 |
| V | 282 | 157 | 410 | 356 | 345 | 418 | 365 | 445 | 185 | 460 |
| Cr | 304 | 272 | 8 | 206 | 200 | 122 | 280 | 105 | 460 | 120 |
| Co | 44 | 44 | 46 | 43 | 43 | 44 | 44 | 46 | 64 | 44 |
| Ni | 77 | 108 | 15 | 69 | 71 | 48 | 75 | 49 | 580 | 50 |
| Y | 27 | 24 | 100 | 38 | 38 | 62 | 37 | 53 | 27 | 54 |
| Zr | 69 | 64 | 332 | 99 | 100 | 190 | 112 | 155 | 115 | 165 |
| Nb | 2.9 | 2.5 | 12.0 | 3.2 | 2.8 | 5.6 | 4.3 | 5.3 | 1.2 | 4.5 |
| La | 2.7 | 3.2 | 13.3 | 3.7 | 4.0 | 6.9 | 4.4 | 6.0 | 3.8 | 6.0 |
| Ce | 6.4 | 9.5 | 42.0 | 12.5 | 12.0 | 21.0 | 13.0 | 18.5 | 13.0 | 17.5 |
| Nd | 7.7 | 10.0 | 40.0 | 12.0 | 11.5 | 22.0 | 11.4 | 18.0 | 10.5 | 19.0 |
| Sm | 2.5 | n.d. | n.d. | n.d. | n.d. | n.d. | 3.70 | n.d. | n.d. | n.d. |
| Eu | 1.1 | 0.95 | 3.3 | 1.4 | 1.3 | 2.1 | 1.4 | 2.0 | 1.2 | 1.4 |
| Gd | 3.5 | n.d. | n.d. | n.d. | n.d. | n.d. | 5.1 | n.d. | n.d. | n.d. |
| Dy | 4.5 | 3.9 | 16.2 | 6.1 | 6.3 | 9.9 | 6.2 | 8.7 | 4.2 | 9.2 |
| Er | 2.6 | 2.6 | 10.7 | 4.1 | 3.9 | 6.3 | 3.6 | 5.7 | 2.8 | 6.1 |
| Yb | 2.6 | 2.3 | 9.7 | 3.7 | 3.7 | 6.1 | 3.7 | 5.2 | 2.5 | 5.5 |
| (La/Yb) _N ^g | 0.8 | 1.0 | 1.0 | 0.7 | 0.8 | 0.8 | 0.9 | 0.8 | 1.1 | 0.8 |
| (La/Nd) _N ^g | 0.7 | 0.6 | 0.7 | 0.6 | 0.7 | 0.6 | 0.8 | 0.7 | 0.7 | 0.6 |
| (Dy/Yb) _N ^g | 1.2 | 1.1 | 1.1 | 1.1 | 1.2 | 1.1 | 1.1 | 1.1 | 1.1 | 1.1 |
| ⁸⁷ Sr/ ⁸⁶ Sr | 0.702304 | 0.702281 | 0.702445 | 0.702430 | 0.702469 | 0.702413 | 0.702510 | 0.702494 | | 0.702482 |
| ¹⁴³ Nd/ ¹⁴⁴ Nd | 0.513287 | 0.513288 | 0.513172 | 0.513175 | 0.513175 | 0.513188 | 0.513156 | 0.513167 | | 0.513181 |

(continued on next page)

been made from the compositions of mineral pairs, using the ILMAT program of [Lepage \(2003\)](#) and the thermobarometer equations of [Andersen and Lindsley \(1985\)](#). Calculated temperatures vary from 760 °C to 1398 °C. Only Fe–Ti oxides equilibrated at 900 < *T* < 1100 °C have been considered to constrain the magmatic *f*O₂ values. Results, shown in [Fig. 4](#), yield to *f*O₂ values plotting between the FMQ and NNO buffers.

4. Geochemistry of the WBD samples

4.1. Methods

31 samples of the lava unit from the Northern Scarp (lavas and crosscutting dikes), with loss on ignition (LOI) lower than 3 wt.%, were selected for chemical analyses ([Table 2](#)) to complete the available WBD data of [Juteau](#)

Table 2 (continued)

| Location | PP (west) | PP (center) | | PP (east) | | | | | Intratransform basin |
|--|-----------|-------------|-----------|-----------|------------|-----------|-----------|-----------|----------------------|
| Sample | BD01-02C | BD04-01A | BN14-07 | BD05-21A | BD08-01E | BD08-02 | BD08-04B | BD08-05 | BD11-01 |
| Reference ^b | 1 and 3 | 1 and 3 | 2 | 1 and 3 | 3 | 3 | 1 and 3 | 3 | 1 and 3 |
| Type ^c | Basalt | Basalt | OI-basalt | OI-basalt | Ni-Fe-bas. | Ni-basalt | Ni-basalt | Ni-basalt | Ni-basalt |
| Latitude | 44.4 | 44.3 | 44.3 | 44.2 | 44.3 | 44.3 | 44.3 | 44.3 | 44.2 |
| Longitude | 130.2 | 130.2 | 130.1 | 129.7 | 130.0 | 130.0 | 130.0 | 130.0 | 129.5 |
| Depth (m) | -2850 | -2530 | -3561 | -2650 | -2000 | -2000 | -2000 | -2000 | -3287.5 |
| Dist. (km) ^d | 3 | 32 | 35.4 | 54 | 42 | 42 | 42 | 42 | 72 |
| SiO ₂ | 49.20 | 49.60 | 47.90 | 47.75 | 48.85 | 48.40 | 49.00 | 49.00 | 50.00 |
| TiO ₂ | 1.43 | 1.63 | 1.54 | 1.14 | 2.65 | 2.22 | 2.41 | 2.40 | 1.85 |
| Al ₂ O ₃ | 17.10 | 15.80 | 15.20 | 15.74 | 14.20 | 15.30 | 14.75 | 14.60 | 14.50 |
| Fe ₂ O _{3t} ^c | 9.87 | 11.25 | 10.40 | 11.08 | 14.25 | 11.60 | 12.60 | 12.52 | 12.40 |
| MnO | 0.16 | 0.27 | 0.16 | 0.18 | 0.23 | 0.16 | 0.26 | 0.28 | 0.20 |
| MgO | 6.08 | 7.14 | 10.20 | 10.45 | 6.70 | 5.60 | 7.00 | 7.00 | 8.08 |
| CaO | 12.05 | 11.30 | 10.80 | 10.45 | 9.50 | 9.70 | 9.05 | 8.92 | 10.00 |
| Na ₂ O | 2.66 | 2.73 | 2.65 | 2.45 | 3.10 | 3.20 | 3.40 | 3.50 | 2.80 |
| K ₂ O | 0.15 | 0.22 | 0.26 | 0.27 | 0.37 | 1.41 | 0.88 | 0.88 | 0.21 |
| P ₂ O ₅ | 0.17 | 0.20 | 0.17 | 0.13 | 0.35 | 0.40 | 0.44 | 0.44 | 0.22 |
| LOI | 1.20 | -0.53 | 0.80 | 0.36 | -0.59 | 2.23 | 0.28 | -0.04 | -0.55 |
| Total | 100.07 | 99.61 | 100.08 | 100.00 | 99.61 | 100.28 | 100.07 | 99.50 | 99.71 |
| Mg# ^f | 60.4 | 61.1 | 70.8 | 70 | 53.8 | 54.4 | 57.9 | 58.1 | 61.7 |
| Rb | 2.0 | 2.8 | 2.7 | 4.5 | 4.8 | 25.0 | 12.5 | 12.5 | 3.1 |
| Sr | 158 | 155 | 165 | 140 | 165 | 357 | 270 | 270 | 140 |
| Ba | 20 | 30 | 18 | 12 | 44 | 148 | 127 | 156 | 30 |
| Sc | 39 | 40 | 36 | 37 | 37 | 32 | 34 | 34 | 36 |
| V | 272 | 295 | 270 | 205 | 345 | 270 | 300 | 300 | 285 |
| Cr | 187 | 218 | 450 | 375 | 190 | 237 | 225 | 225 | 295 |
| Co | 39 | 45 | 58 | 53 | 43 | 41 | 43 | 43 | 44 |
| Ni | 50 | 79 | 330 | 272 | 94 | 128 | 112 | 120 | 148 |
| Y | 29 | 32 | 32 | 24 | 53 | 40 | 47 | 46 | 36 |
| Zr | 96 | 112 | 108 | 74 | 208 | 205 | 220 | 225 | 125 |
| Nb | 4.5 | 5.7 | 4.3 | 3.3 | 11.7 | 21.4 | 21.5 | 21.4 | 6.8 |
| La | 4.6 | 5.5 | 4.7 | 3.4 | 10.5 | 16.6 | 16.3 | 16.4 | 6.1 |
| Ce | 13.0 | 15.0 | 13.0 | 9.0 | 28.0 | 36.0 | 37.0 | 36.0 | 16.0 |
| Nd | 10.5 | 12.5 | 11.5 | 8.0 | 22.0 | 23.0 | 23.5 | 24.0 | 13.0 |
| Sm | n.d. | n.d. | n.d. | n.d. | n.d. | n.d. | n.d. | n.d. | n.d. |
| Eu | 1.2 | 1.3 | 1.4 | 1.0 | 2.1 | 1.8 | 2.0 | 1.9 | 1.5 |
| Gd | n.d. | n.d. | n.d. | n.d. | n.d. | n.d. | n.d. | n.d. | n.d. |
| Dy | 5.0 | 5.6 | 5.0 | 4.3 | 9.0 | 6.8 | 8.0 | 8.0 | 6.1 |
| Er | 2.9 | 3.3 | 3.0 | 2.5 | 5.3 | 3.9 | 4.6 | 4.6 | 3.6 |
| Yb | 2.8 | 3.2 | 2.9 | 2.6 | 5.1 | 3.8 | 4.6 | 4.5 | 3.5 |
| (La/Yb) _N ^g | 1.2 | 1.2 | 1.2 | 1.0 | 1.5 | 3.1 | 2.6 | 2.6 | 1.3 |
| (La/Nd) _N ^g | 0.9 | 0.9 | 0.8 | 0.8 | 0.9 | 1.4 | 1.4 | 1.3 | 0.9 |
| (Dy/Yb) _N ^g | 1.2 | 1.2 | 1.2 | 1.1 | 1.2 | 1.2 | 1.2 | 1.2 | 1.2 |
| ⁸⁷ Sr/ ⁸⁶ Sr | 0.702356 | 0.702347 | | 0.702451 | | | 0.702700 | | 0.702367 |
| ¹⁴³ Nd/ ¹⁴⁴ Nd | 0.513227 | 0.513227 | | 0.513208 | | | 0.513182 | | 0.513245 |

et al. (1995), Fleutelot (1997), and Naidoo (1998). Major and trace elements were measured at Brest University on whole rock powders by inductively coupled plasma atomic emission spectrometer (ICP-AES). Some Blancovin analyses (DCP and ICP spectrometries) on different powders have already been presented in Pollock et al. (2005). Concentrations diverge from our analyses up to 130 relative percent (for Ni in BV2958-1, in which Pollock et al. (2005) reported excess olivine, contrary to us). Consequently, we

repeated the concentration determination on new powders, using both ICP-AES and ICP-MS, for the five samples of the dive BV2958 (Table 3). Differences between our triplicates are minor, except for the mobile elements K₂O, Rb, and Ba. To avoid introducing an analytical bias in our interpretations, we choose in this instance to use only chemical data obtained by ICP-AES. In samples BV2958-1 and BV2963-8, glass of segregation vesicles was analyzed for major elements by electron microprobe (Table 2).

Sr and Nd isotope ratio determination of twenty-six samples from the Northern Scarp and Parks Plateau were performed (Table 2). In order to remove seawater alteration effects, the whole-rock powders were leached with 2.5 N HCl for one hour and rinsed in ultrapure water three times. Sample BD08-04B, clearly shifted toward high $^{87}\text{Sr}/^{86}\text{Sr}$ values, was subjected to a more aggressive leaching in 6 N HCl during one hour. However, the 6 N HCl leached composition does not significantly differ from that leached with 2.5 N HCl.

4.2. Loss on ignition, major and compatible trace elements

In each dive, LOI values tend to increase with depth. No clear correlation between LOI and major elements concentrations has been observed for the whole dataset (e.g. K_2O versus LOI, Fig. 5a).

All the WBD lavas and crosscutting dikes are basalts, except the basaltic andesite BN13-08 (total alkali-silica diagram of Le Bas et al., 1986). Their compositions range from mafic terms to ferrobasalts ($\text{FeO}^t > 12$ wt.% and $\text{TiO}_2 > 2$ wt.%, Byerly, 1980). The Northern Scarp samples display the most differentiated compositions. The major element variations in segregation vesicle glasses of BV2958-1 and BV2963-8 (Northern Scarp) are studied together with the whole rock analyses on the Fig. 5 diagrams. Even if such compositions are the result of local post-emplacement *in situ* crystallization, they can be used as rough equivalents of the products of magma chamber differentiation. They range from basaltic to dacitic and tend toward the composition of a dacite collected on the Cleft segment (Stakes et al., 2006). In major elements versus MgO diagrams (Fig. 5b and d), compositions of samples and segregation vesicles display the typical crystallization trends of tholeiites: TiO_2 and $\text{Fe}_2\text{O}_3'$ increase when MgO decreases (from 9 to ~ 3 wt.%, Fig. 5b), then decrease in segregation vesicles; CaO and Al_2O_3 decrease (Fig. 5c), and Na_2O , K_2O and P_2O_5 increase continuously (Fig. 5d). While the Northern Scarp and Parks Plateau variation trends appear largely similar, the Parks Plateau data are more widely scattered and do not fall along a well-defined crystallization trend like the Northern Scarp samples. In addition, the Parks Plateau lavas are characterized by the highest Al_2O_3 values and sometimes by lower TiO_2 contents. Three samples show evidence for olivine accumulation ($\text{MgO} > 10$ wt.%). Finally, some non-cumulative samples from both the Northern Scarp and Parks Plateau (including three samples of the BD08 dredge) fall to the right of the main trend in the TiO_2 and P_2O_5 versus MgO diagrams (Fig. 5b and d).

Differentiation results in a decrease of the compatible trace element contents when La, taken here as the reference highly incompatible element, increases (Ni in Fig. 5e and Cr not shown). The olivine-cumulative samples are shifted toward high Ni concentrations (> 250 ppm). However, crystallization and accumulation cannot explain the extent of the observed variations. Even if poor in olivine phenocrysts, the samples shifting apart in the TiO_2 and P_2O_5 diagrams also fall clearly above the main trend in the Ni versus La diagram (Fig. 5e). This is also true for Cr (Table 2). Two of these Ni-rich samples have been triplicated and the shift in compatible elements is still observed, regardless of the powder and the analytical method (Table 3).

4.3. Incompatible trace elements and Sr–Nd isotopes

As it is difficult to clearly distinguish samples from the Northern Scarp and Parks Plateau with major elements and Ni, moderately to highly incompatible trace elements can be used to discriminate lavas from both sites. First, Sr is systematically lower in the Northern Scarp ($\text{Sr} < 130$ ppm, except BN22-14) than in the Parks Plateau lavas (Table 2). Low-temperature reactions with seawater cannot account for such a geographical distribution of Sr as alteration does not differ between both flanks. Moreover, in incompatible trace element versus La diagrams (Fig. 5f–h), the Northern Scarp and Parks Plateau basalts define two linear contrasted trends. The Northern Scarp samples, which display the lowest Nb/La ($\text{Nb/La} = 0.9 \pm 0.2$), La/Nd ($\text{La/Nd}_N = 0.7 \pm 0.1$), and La/Yb ratios ($\text{La/Yb}_N = 0.7 \pm 0.6$), somehow mimic the Cleft variations in the Yb–La diagram (Fig. 5h). These features characterize normal MORBs (N-MORBs). In this way, the normalized rare earth element (REE) patterns of the Northern Scarp lavas are grossly parallel, depleted in LREE and flat between MREE and HREE (Fig. 6a). Consistently with the effects of fractional crystallization, the less mafic samples are characterized by higher abundances in REE and also the development of a slight negative Eu anomaly (e.g. dive BV2958, Fig. 6a). Three out of four Ni-rich samples of the dredge BD08 from the Parks Plateau (except BD08-01) shift apart from the variation trends of the Plateau due to their very high La and Nb and low Nd and Yb contents (Fig. 5f–h). Such features resemble those of one Gorda sample (Davis et al., 1998, Fig. 5g–h). The REE patterns of the BD08 basalts also have the steepest slopes in chondrite normalized diagrams, characteristic of enriched MORBs ($\text{La/Yb}_N = 2.8 \pm 0.6$ and $\text{Dy/Yb}_N = 1.2 \pm 0.1$, Fig. 6b).

Sr–Nd isotope ratios of the WBD samples are shown in the $^{143}\text{Nd}/^{144}\text{Nd}$ versus $^{87}\text{Sr}/^{86}\text{Sr}$ diagram of Fig. 7,

Table 3

Comparison of composition of samples from dive BV2958 determined using different analytical methods

| Sample | 2958-1 | 2958-1 | 2958-1 | 2958-1 | 2958-2 | 2958-2 | 2958-2 | 2958-2 | 2958-2 | 2958-3 | 2958-3 | 2958-3 | 2958-3 | 2958-3 | 2958-5 | 2958-5 | 2958-5 | 2958-5 |
|---|--------|--------|--------|---------|--------|--------|--------|---------|--------|--------|--------|---------|--------|--------|--------|---------|--------|--------|
| Method ^a | AES | AES* | MS | Pollock | AES | AES* | MS | Pollock | AES | AES* | MS | Pollock | AES | AES* | MS | Pollock | | |
| SiO ₂ | 50.00 | 49.70 | | 49.51 | 49.50 | 49.80 | | 49.87 | 48.00 | 48.20 | | 50.03 | 50.20 | 50.20 | | 50.86 | | |
| TiO ₂ | 1.98 | 2.00 | | 2.43 | 1.64 | 1.66 | | 2.94 | 3.55 | 3.65 | | 2.16 | 1.81 | 1.81 | | 2.00 | | |
| Al ₂ O ₃ | 14.20 | 14.45 | | 13.20 | 14.10 | 14.30 | | 13.09 | 12.55 | 12.53 | | 13.58 | 14.70 | 14.80 | | 14.04 | | |
| Fe ₂ O ₃ ^b | 12.80 | 12.80 | | 14.58 | 12.20 | 12.16 | | 15.63 | 16.80 | 17.00 | | 13.31 | 11.75 | 11.55 | | 12.07 | | |
| MnO | 0.20 | 0.21 | | 0.21 | 0.20 | 0.19 | | 0.21 | 0.24 | 0.25 | | 0.22 | 0.20 | 0.20 | | 0.20 | | |
| MgO | 6.20 | 6.20 | | 6.67 | 7.00 | 7.11 | | 5.79 | 4.98 | 5.04 | | 6.47 | 6.50 | 6.60 | | 6.48 | | |
| CaO | 11.15 | 11.25 | | 10.53 | 11.30 | 11.60 | | 9.82 | 9.35 | 9.40 | | 11.33 | 12.00 | 11.75 | | 11.22 | | |
| Na ₂ O | 2.53 | 2.57 | | 2.61 | 2.60 | 2.57 | | 2.76 | 2.89 | 2.90 | | 2.83 | 2.57 | 2.55 | | 2.72 | | |
| K ₂ O | 0.24 | 0.20 | | 0.28 | 0.08 | 0.10 | | 0.17 | 0.22 | 0.23 | | 0.21 | 0.23 | 0.24 | | 0.26 | | |
| P ₂ O ₅ | 0.19 | 0.19 | | n.d. | 0.15 | 0.15 | | n.d. | 0.35 | 0.36 | | n.d. | 0.17 | 0.16 | | n.d. | | |
| LOI | 0.28 | 0.20 | | 0.50 | 0.83 | 0.42 | | 0.70 | 0.27 | 0.06 | | 0.20 | -0.01 | -0.07 | | 0.70 | | |
| Total | 99.77 | 99.77 | | 100.02 | 99.60 | 100.06 | | 100.29 | 99.20 | 99.62 | | 100.14 | 100.12 | 99.79 | | 99.87 | | |
| Rb | 3.2 | n.d. | 1.5 | 2.8 | 0.8 | n.d. | 0.6 | 0.7 | 2.4 | n.d. | 1.8 | 1.8 | 2.4 | n.d. | 2.1 | 2.6 | | |
| Sr | 99 | 102 | 104 | 112 | 109 | 110 | 111 | 106 | 104 | 105 | 105 | 108 | 110 | 110 | 111 | 113 | | |
| Ba | 22 | 50 | 49 | 20 | 13 | 15 | 14 | 11 | 28 | 30 | 29 | 25 | 17 | 19 | 18 | 16 | | |
| Sc | 43 | 45 | 46.6 | 44.0 | 43 | 45 | 46.9 | 46.3 | 44 | 46 | 48.2 | 44.5 | 44 | 45 | 46.6 | 45.6 | | |
| V | 403 | 415 | 402 | 405 | 350 | 364 | 356 | 343 | 600 | 630 | 639 | 506 | 390 | 385 | 385 | 383 | | |
| Cr | 130 | 132 | 125 | 144 | 155 | 165 | 156 | 183 | 110 | 111 | 105 | 146 | 190 | 185 | 179 | 193 | | |
| Co | 40 | 49 | 48 | 52 | 40 | 45 | 45 | 42 | 48 | 56 | 56 | 48 | 45 | 42 | 44 | 42 | | |
| Ni | 56 | 75 | 75 | 129 | 59 | 64 | 63 | 87 | 100 | 109 | 105 | 98 | 80 | 72 | 69 | 92 | | |
| Y | 45 | 46 | 49.6 | 46.0 | 36 | 38 | 39.7 | 34.0 | 77 | 79 | 86.3 | 75.0 | 42 | 42 | 44.8 | 42.0 | | |
| Zr | 117 | 125 | 131 | 122 | 94 | 100 | 105 | 97 | 240 | 245 | 264 | 220 | 113 | 115 | 119 | 121 | | |
| Nb | 4.0 | 4.5 | 4.1 | 3.9 | 3.5 | 3.9 | 4.0 | 3.1 | 8.4 | 8.5 | 8.6 | 7.0 | 3.8 | 4.1 | 4.5 | 4.1 | | |
| La | 4.3 | 4.7 | 4.4 | 4.0 | 3.5 | 4.1 | 3.8 | 3.1 | 8.5 | 9.2 | 8.9 | 7.5 | 4.6 | 4.5 | 4.4 | 4.2 | | |
| Ce | 12.6 | 13.5 | 13.5 | 12.6 | 10.5 | 11.4 | 11.3 | 9.8 | 25.0 | 26.5 | 26.6 | 23.0 | 12.9 | 13.5 | 13.0 | 13.0 | | |
| Nd | 12.1 | 13.0 | 12.9 | 12.1 | 9.8 | 11.0 | 10.7 | 9.3 | 24.0 | 25.0 | 24.7 | 22.0 | 12.0 | 12.0 | 12.1 | 12.2 | | |
| Sm | 4.3 | 4.5 | 4.55 | 4.29 | 3.5 | 3.7 | 3.75 | 3.22 | 8.0 | 8.2 | 8.37 | 7.47 | 4.3 | 4.1 | 4.21 | 4.16 | | |
| Eu | 1.5 | 1.6 | 1.56 | 1.38 | 1.3 | 1.3 | 1.36 | 1.13 | 2.5 | 2.5 | 2.58 | 2.21 | 1.4 | 1.4 | 1.49 | 1.41 | | |
| Gd | 6.4 | 6.6 | 6.23 | 6.21 | 5.0 | 5.1 | 5.07 | 4.84 | 10.8 | 11.0 | 11.01 | 10.59 | 5.6 | 5.6 | 5.61 | 6.00 | | |
| Dy | 7.4 | 7.6 | 7.74 | 7.07 | 5.9 | 6.2 | 6.32 | 5.63 | 12.7 | 13.0 | 13.51 | 12.17 | 6.9 | 6.7 | 7.09 | 6.97 | | |
| Er | 4.5 | 4.6 | 4.92 | 4.46 | 3.4 | 3.8 | 3.99 | 3.41 | 7.8 | 8.0 | 8.63 | 7.26 | 4.2 | 4.2 | 4.48 | 4.33 | | |
| Yb | 4.5 | 4.7 | 4.55 | 4.32 | 3.5 | 3.8 | 3.70 | 3.20 | 7.7 | 7.9 | 8.07 | 6.94 | 4.1 | 4.2 | 4.24 | 3.98 | | |

^a AES: ICP-AES analyses (Brest); AES*: ICP-AES re-analyses on a new powder (Brest); MS: ICP-MS re-analyses on the same powder than AES*; Pollock: analyses of Pollock et al. (2005) by DCP (elements marked in *italic*) and by ICP-MS (other elements). Our ICP-MS analyses were conducted using a procedure modified after Barrat et al. (1996), on a Thermo-Finnigan Element 2. The external standard used to calculate element concentration is the U.S. Geological Survey standard BHVO-2. BIR-1 and PMS were standards used to check the validity of the method.

^b Total iron expressed as Fe₂O₃.

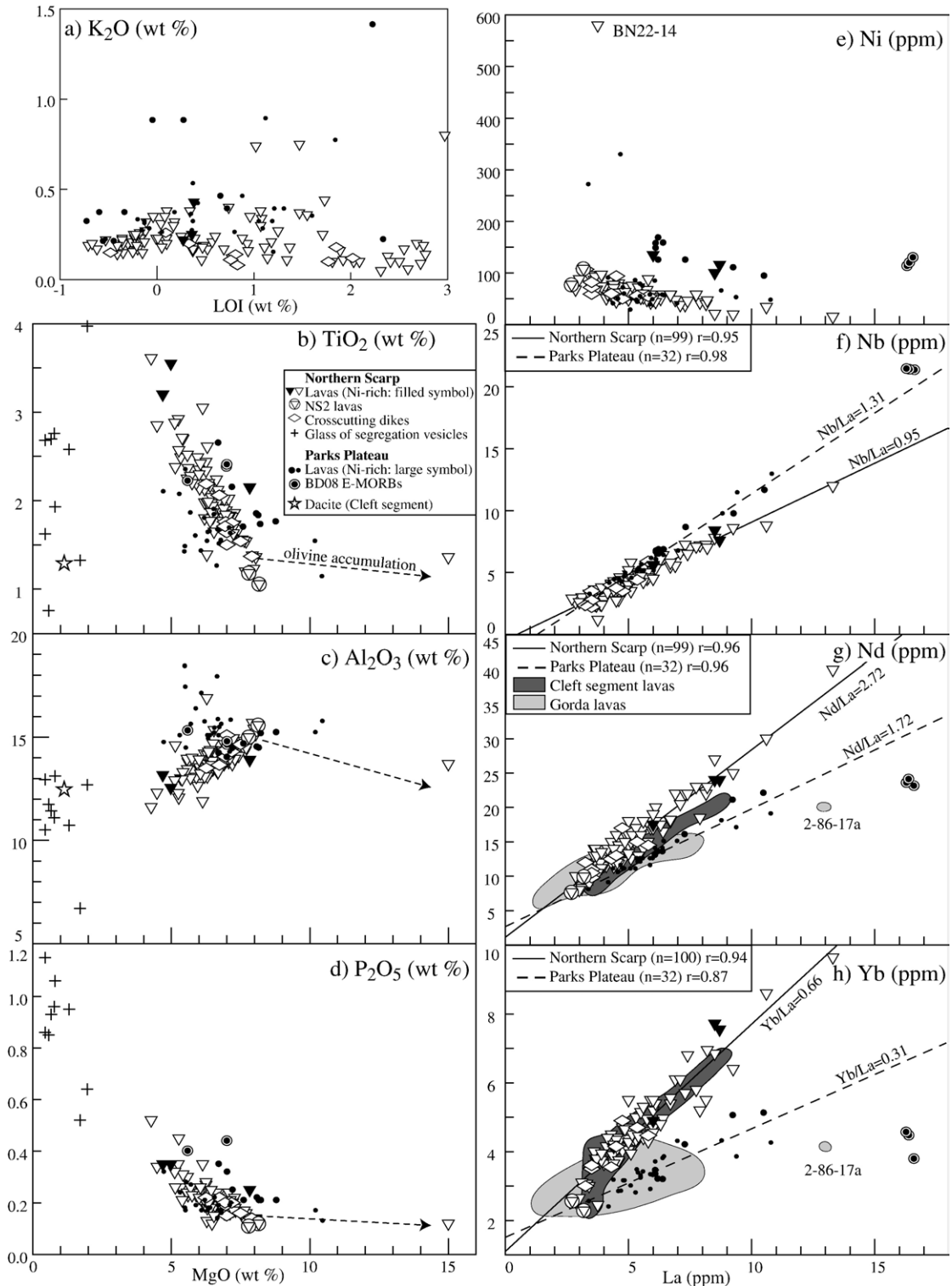


Fig. 5. a) K₂O versus LOI variations for relatively fresh Northern Scarp and Parks Plateau lavas and crosscutting dikes (LOI < 3 wt.%). b–h) Selected major oxide (wt.%) and trace element (ppm) variation diagrams versus MgO and La, respectively. The major element composition of the RC10 dacite collected on the Cleft segment is shown for comparison (Stakes et al., 2006). The dashed arrows illustrate the chemical effects induced by olivine accumulation. Linear regressions in incompatible trace element diagrams are shown for both the Northern Scarp and Parks Plateau (except BD08) samples. Cleft field: Smith et al. (1994); Rhodes et al. (1990). Gorda field and sample 2-86-17A: Davis and Clague (1987); Davis et al. (1998).

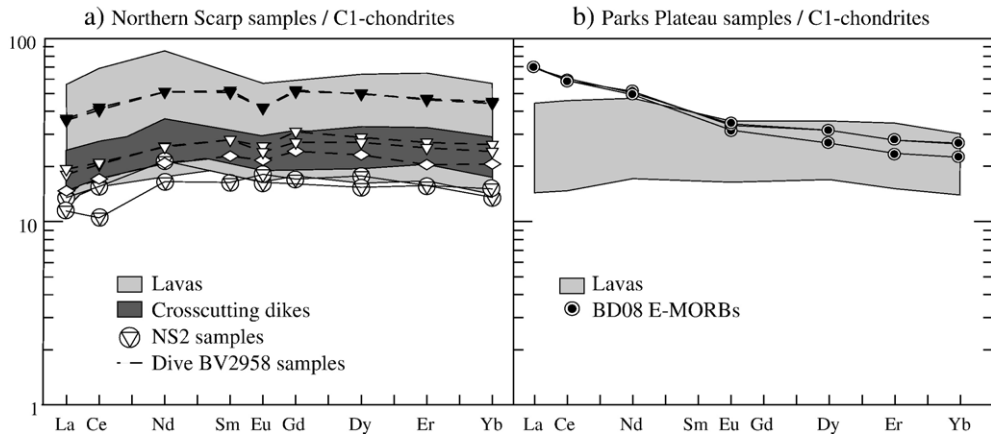


Fig. 6. Fields for C1-chondrite-normalized REE patterns for a) the Northern Scarp samples and b) the Parks Plateau samples (normalization values from Sun and McDonough, 1989). Patterns of representative samples of the dive BV2958 (Northern Scarp) are shown. The NS2 (defined from isotopic features) and BD08 samples are also plotted. Symbols as in Fig. 5.

together with fields for the lavas from the Juan de Fuca Ridge, including the Cleft segment, and the Gorda ridge. Data from the WBD define an array with a negative slope.

Most of the Northern Scarp lavas (18 N-MORBs, NS1) have homogeneous isotope compositions. NS1 samples have the lowest $^{143}\text{Nd}/^{144}\text{Nd}$ of the WBD dataset (≤ 0.513172), comparable to those measured in the Cleft Segment lavas. Two Northern Scarp basalts (BN02-10 and BN23-09, NS2), collected at the sheeted-dike complex/extrusive boundary, shift toward high $^{143}\text{Nd}/^{144}\text{Nd}$ values (> 0.513250), above the Juan de Fuca field. The four Parks Plateau basalts (PP) plot between NS1 and NS2 ($0.513208 \leq ^{143}\text{Nd}/^{144}\text{Nd} \leq 0.513245$), except the enriched MORB BD08-04B, which is characterized by an elevated $^{87}\text{Sr}/^{86}\text{Sr}$ ratio. This sample plots outside the Juan de Fuca field but inside the Gorda one. All BD08 samples should share this isotopic signature except for BD08-01E which appears to have different trace element ratios, similar to those of other Parks Plateau samples.

Isotope and trace element data can be used to distinguish the samples with respect to the geographic area (NS/PP) or their specific location in the lithological succession (NS1 within the extrusive unit and NS2 at the sheeted-dike/extrusive transition). The distribution of the Northern Scarp samples in the Sr–Nd diagram (Fig. 7) is consistent with a binary mixing between a Cleft-type mantle component and a depleted NS2-type mantle source. Such a highly depleted isotopic composition is not observed elsewhere in the Pacific, except in the western rift of the Easter Microplate, the Lamont seamounts, and the Garrett Transform Zone (Wendt et al., 1999; our unpublished data). It might be considered representative of

a nearly pure depleted end-member and interpreted as the residue of a previous low-extent mantle melting event (Wendt et al., 1999).

The geochemical characteristics of the Parks Plateau lavas do not help to decipher the plateau origin (seamount versus accretion at the Cleft segment tip). Most of the PP samples fall within the Juan de Fuca field but BD08-04B plots within the Gorda isotope field (Fig. 7) and presents trace element features similar to Gorda MORBs (Fig. 5g–h). However, discussing the geodynamic significance of the Parks Plateau is out of scope

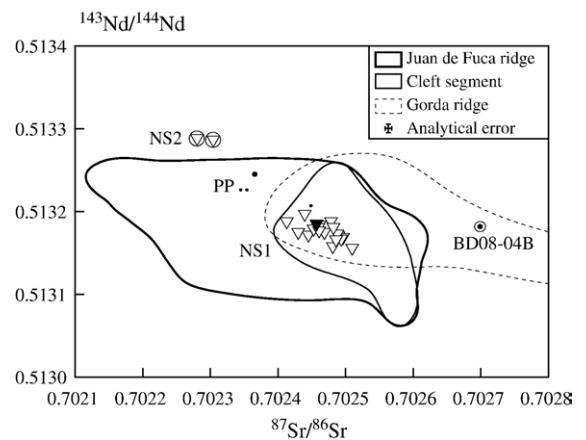


Fig. 7. $^{143}\text{Nd}/^{144}\text{Nd}$ versus $^{87}\text{Sr}/^{86}\text{Sr}$ diagram showing the isotope ratios of the Northern Scarp and Parks Plateau samples, compared with the lavas of the Juan de Fuca and Gorda ridges. Juan de Fuca and Cleft segment fields: Cohen et al. (1980); Hegner and Tatsumoto (1987); Ito et al. (1987); White et al. (1987); Rhodes et al. (1990); Cousens et al. (1995); Chadwick et al. (2005). Gorda field: White et al. (1987); Goldstein et al. (1991); Volpe and Goldstein (1993); Davis et al. (1998). Symbols as in Fig. 5.

of this study and additional data would be required before drawing any general conclusion.

5. Identification of the main magmatic processes operating in the Northern Scarp magma reservoir

Given the relative constancy of incompatible trace element and isotope ratios within the NS1 group (Figs. 5 and 7), the corresponding lavas can be regarded as issued from a quite homogeneous mantle source under steady melting conditions. The trends identified in the major element diagrams of Fig. 5 imply that fractionation of olivine, plagioclase, and augite has played a major role in the differentiation of NS1 samples. The sharp decrease of TiO_2 in the segregation vesicles and Cleft dacite shows evidence for the crystallization of Fe–Ti oxides around $\text{MgO}=2\text{--}4$ wt.%. The fact that the NS2 and Parks Plateau samples distribute in the same trends as NS1 in all major and compatible trace element diagrams (Fig. 5b–e) suggests that the corresponding contrasted primary melts have recorded roughly comparable differentiation processes. In particular, subaphyric Ni-rich samples have been collected on both sites. Their anomalously high Ni and MgO values are consistent neither with mineral

accumulation, nor with fractional crystallization, nor with source heterogeneity, as the isotopic ratios of the corresponding samples are not distinguishable from the other WBD samples (Fig. 7). Such chemical features might have been acquired during equivalent petrogenetic processes in both magmatic systems. The Ni-rich samples distribute roughly along straight lines in the TiO_2 and P_2O_5 versus MgO and Ni versus La diagrams of Fig. 5b and d–e. Linear chemical variations, together with the fact that a few Ni-rich lavas are ferrobasalts, suggest a binary mixing process between felsic and mafic end-members.

To extend the WBD Ni–Mg# correlation toward mafic terms in the Fig. 8 diagram (leaving the Ni-rich samples apart), we made the assumption that olivine is the main liquidus phase that controls the concentrations of these two elements in melts with $\text{Mg}\#>65$. Concomitant plagioclase crystallization would have no effect on MgO, FeO, and Ni. Equilibrium olivine was added to the most mafic, fresh and subaphyric sample BV2960-7 ($\text{Mg}\#=64.9$), with an increment of 1% and assuming Rayleigh fractionation, until reproducing a composition close to that of the olivine-cumulative lava BN22-14 (Fig. 8). We adjusted the MgO content in olivine at each step by considering a $^{\text{Fe-Mg}}K_D$ value of 0.3 (Roeder and

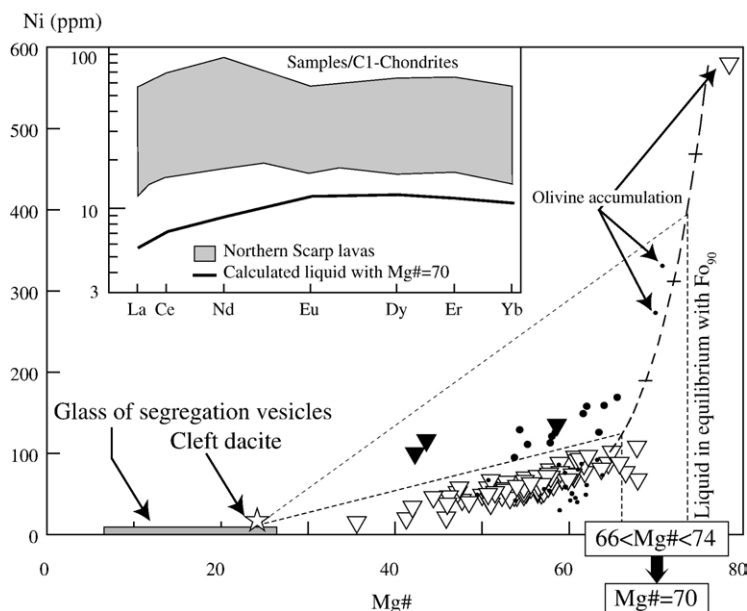


Fig. 8. Ni (ppm) versus Mg# diagram for the Northern Scarp and Parks Plateau lavas. The dashed curve is the mafic extension of the Ni–Mg# hyperbolic correlation, calculated from the most mafic, fresh, and subaphyric sample BV2960-7 (see text for the method). Dark gray field indicates the Mg# composition of the glass of segregation vesicles. The Cleft segment dacite (Stakes et al., 2006) is used to approach the felsic end-member in the mixing model. The supposed mixing field is bounded by dashed lines and is used to propose a mean Mg# and REE composition of the mafic end-member (see text for further explanation). Inset: REE pattern of the calculated refilling melt together with field of the Northern Scarp lavas, NS2 samples not included (Sun and McDonough, 1989). Symbols as in Fig. 5.

Emslie, 1970) and we considered a partition coefficient of Ni in olivine directly related to the liquid composition ($d^{\text{Ni}} = (124.13/\text{MgO}_{\text{liq}}) - 0.897$, Hart and Davis, 1978).

6. The dive BV2958: petrologic investigation of crystallization under hydrous conditions coupled with magma mixing

6.1. The dive BV2958

The dive BV2958, located 27 km east of the axis (Fig. 2), was chosen for a detailed petrologic study owing to several reasons. (i) The collected samples cover a significant range of time, since the vertical stratigraphy overlaps three magnetic periods (from Brunhes to Jaramillo, Fig. 2). (ii) The samples present remarkable petrographic features: both types of including relations between plagioclase and clinopyroxene phenocrysts are observed, and the dike BV2958-2 contains one coarse-grained xenolith (0.6*0.5 cm) made up of highly zoned plagioclases, bearing recrystallized glass inclusions (Fig. 9b and d, inset). (iii) From a chemical point of view, the samples collected during this dive are fresh (LOI < 1 wt.%) and show a large range of whole rock compositions, from quite mafic (Mg# = 58.7, BV2958-2) to ferrobaltic (Mg# > 42.3, BV2958-3 and -4, Table 2). This compositional range is extended by the glass compositions of segregation vesicles in sample BV2958-1. In addition, two olivine-poor, Ni-rich lavas (BV2958-3 and -4), interpreted as mixing products, occur just below the Brunhes/Matuyama isochrone.

6.2. Plagioclase as a marker of magmatic processes

Plagioclase, one of the commonest igneous minerals, has been extensively studied to return to magma chamber evolution and dynamics during the crystal growth because it shows more pronounced chemical zoning than any other mineral group. Changes in the major element composition of plagioclase are controlled by a large number of chemical and physical parameters (mainly melt composition, volatile content, and temperature, Smith and Brown, 1988).

Chemical traverses have been made in the plagioclase xenolith of the dike BV2958-2 and in phenocrysts of the overlying lavas BV2958-3 and -4. Representative analyses of the profiles are shown in Table 1. The chemical profiles are plotted in An versus MgO diagrams (Fig. 9) in order to set their compositions back in the two trends previously defined by using the whole plagioclase dataset (Fig. 3). These profiles are also compared to the compositions of theoretical plagioclases crystallizing in equilibrium with the host rocks (BV2958-2, -3, and -4, see calculation method in Fig. 9).

The outermost edges of plagioclase crystals are characterized by a MgO increase without any change in the An content (Fig. 3, not shown in Fig. 9), which probably records local kinetic effects. After lava eruption, the crystal growth rates are higher than the rates of element diffusion through the melt and it leads to the formation of a chemical boundary layer at the crystal-melt interface. So as not to take into account these chemical effects, analyses with MgO > 0.3 wt.% will not be considered further.

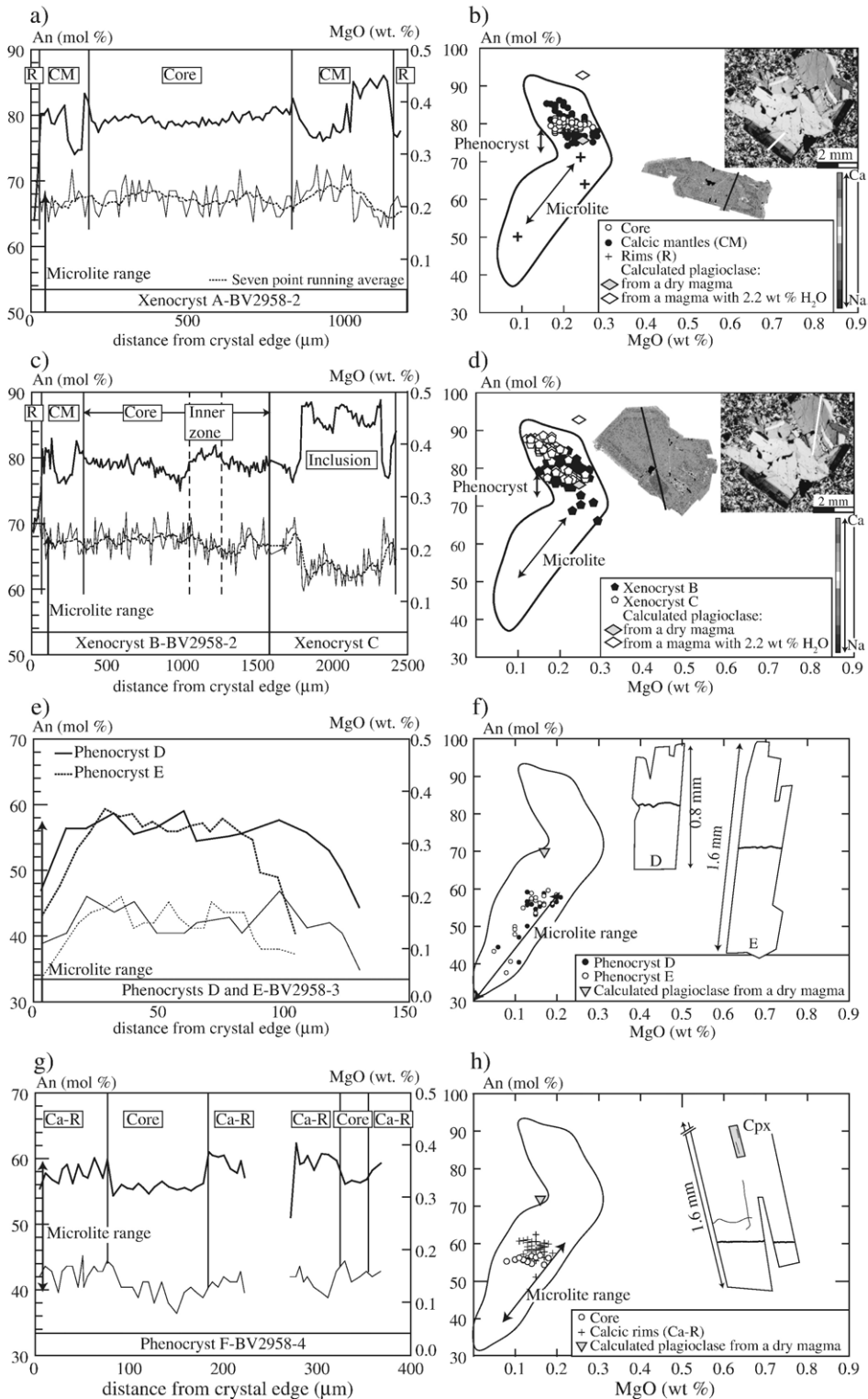
The concomitant decrease of An and MgO in phenocrysts and microlites observed in Trend 1 (Fig. 9f and h) may reflect melt differentiation both in magma chamber (phenocrysts) and during groundmass (microlites) crystallization. The composition of phenocrysts of the BV2958-3 and -4 lavas plot within this trend (Fig. 9).

By contrast, in Trend 2, as the xenocrysts of the dike BV2958-2 illustrate, An and MgO contents in plagioclase phenocrysts are negatively correlated and reach very high (An_{>70}, Fig. 9) and low values, respectively. Such a negative An–MgO correlation has already been observed in plagioclases from a MORB cumulate xenolith (EPR 9°50'N: Ridley et al., 2006, Fig. 3). The trend has been reproduced experimentally by considering a diffusion coefficient for MgO that strongly depends on An content (Costa et al., 2003). In this trend, MgO in plagioclase is no longer valuable in estimating MgO in the equilibrium melt. Furthermore, the An-rich plagioclases (An_{>85}) are not in equilibrium with any known natural anhydrous basaltic melts (Ridley et al., 2006). Following Panjasa-watong et al. (1995), Kohut and Nielsen (2003), and Ridley et al. (2006), such An-rich plagioclase xenocrysts

Fig. 9. An and MgO profiles in plagioclase crystals of the dive BV2958 samples and position of the profile analyses in the An versus MgO diagram. Selected analyses are given in Table 1. Locations of the profiles inside the crystals are shown. Theoretical plagioclase compositions plotted in the An versus MgO diagram are deduced from the host rock analyses, considering the following equilibrium constant of plagioclase-melt exchange reactions for anorthite and albite: $K_D^{\text{Ca-Na}} = 1.3$ for anhydrous melt (Baker and Egger, 1987) and $K_D^{\text{Ca-Na}} = 5.5$ for melt with 2.2 wt.% of H₂O (Sisson and Grove, 1993). MgO content in plagioclase is deduced from the partition coefficient of Mg between plagioclase and melt ($d^{\text{Mg}} = 0.035$, Ginibre et al., 2002). a–d) Plagioclase xenocrysts of the dike BV2958-2. To emphasize the large-scale tendencies, a seven-point running average is applied to the MgO data. e and f) Plagioclase phenocrysts of the pillow-lava BV2958-3. g and h) Plagioclase phenocryst of the pillow-lava BV2958-4. R = rim, CM = calcic mantle, Ca-R = calcic rim.

present in anhydrous MORBs would have crystallized in equilibrium with a melt characterized by an unusually high CaO/Na₂O ratio (>8). However, such melts have

never been sampled. Since such high An compositions have also been interpreted to be the result of high water contents in the host melt (Hattori and Sato, 1996;



Kuritani, 1998; Ginibre et al., 2002; Landi et al., 2004; Berndt et al., 2005), we prefer to envisage the occurrence of local hydrated areas within a composite magma reservoir beneath the ridge. Such a hypothesis is supported by further petrologic hydration markers found in other samples of the dive BV2958 (clinopyroxene inclusion in plagioclase phenocrysts and fO_2 values in the BV2958-3 and -4 lavas). Consequently, we calculated theoretical compositions of plagioclases crystallizing in equilibrium with BV2958-2, both under anhydrous conditions and with 2.2 wt.% of H_2O in the magma (Fig. 9b and d). Addition of H_2O in the liquid clearly shifts the plagioclase composition toward high An content (from An_{76} to An_{93} , in the studied case) and allows reproducing the An-rich compositions observed in the Trend 2 (up to An_{91}).

6.3. BV2958-2: mushy boundary layer crystallization

The An and MgO profiles are shown in Fig. 9a–d, together with the Ca distribution maps collected in two plagioclases of the BV2958-2 xenolith. MgO contents display short-wavelength fluctuations of variable amplitude. In the core of Xenocryst A, An is quite constant (An_{77-81}) but MgO shows great variations (0.17 to 0.27 wt.%, Fig. 9a and b). The core is sharply surrounded by a calcic mantle (An_{79-86}) split by large An-poor zones (An_{74-78}) where MgO correlates negatively with An. The rims of the crystal have low-An (An_{50-71}), low-MgO, and microlite-like compositions. The right side of Xenocryst B includes a small (0.4 mm wide) normally zoned plagioclase crystal (Xenocryst C), composed of an An-rich core (An_{84-89}) abruptly cut by less calcic margins (An_{76-84} , Fig. 9c). MgO and An in Xenocryst C are negatively correlated as well (Fig. 9c and d). In host Xenocryst B, rims and calcic mantles are still observed, but there the plagioclase core is characterized by a quite calcic (An_{79-82}) and MgO-poor inner zone, bounded by An drops. Then, An gradually increases to achieve the calcic mantle composition. Except in the xenocryst rims, An contents of Xenocrysts A, B, and C are higher than for a plagioclase crystallizing from the host melt BV2958-2 under anhydrous conditions (Fig. 9b and d).

Calculation of equilibrium plagioclase compositions suggests that the most An-rich compositions (An_{86} for Xenocryst-A calcic mantles and An_{89} for Xenocryst-C core) can result from the addition of less than 2 wt.% H_2O in the magma. On the other hand, the phenocryst compositions are quite in equilibrium with the host rock, under anhydrous conditions (Fig. 9b and d). H_2O -rich melt compositions may not have prevailed in the

whole magma reservoir but may reflect local conditions. The zoning patterns recorded in Xenocrysts A, B, and C could be explained by a mechanical transport through a H_2O gradient. Such a Trend 2-type evolution, extending toward An-rich compositions, has already been observed by Kuritani (1998) in phenocrysts of alkali basalts from the Rishiri stratovolcano. It has been interpreted as resulting from crystallization in a hydrated mushy boundary layer. Beneath spreading ridges, magma chambers are thought to be composite (Sinton and Detrick, 1992). In the thin melt lens, compositions are mostly mafic, as the BV2958-2 bulk rock composition suggests, and quite anhydrous, as usually presumed for MORBs (Michael and Chase, 1987). The melt lens is underlain by a large mushy crystallization zone, where H_2O -rich compositions can be locally achieved, due to an input of hydrothermal and/or magmatic water expelled from the adjacent rocks. Xenocrysts are thought to have crystallized alternately from these different zones: calcic mantles of Xenocrysts A and B and core of Xenocryst C would have crystallized in the hydrated mushy zone, whereas less calcic compositions would have recorded crystallization in or near the melt lens. The An-poor zones disturbing the calcic mantles might reveal rhythmic crystal motions between both zones. Magma tapping has preferentially sampled the easily removable basaltic liquid from the melt lens, together with a few crystals from locally hydrated areas of the mushy zone. Crystallization after magma eruption has been recorded by the An-poor, microlite-like crystal rims.

6.4. BV2958-3 and BV2958-4: hydration and magma mixing

The plagioclase phenocrysts of the lavas BV2958-3 and -4 present contrasted chemical profiles and distinct An and MgO contents (Trend 1, Fig. 9e–h) with respect to the xenocrysts of the dike BV2958-2 (Trend 2). Thus, they show evidence for different conditions of crystallization. In BV2958-3, Phenocrysts D and E are normally zoned (core with An_{53-59} and rims with An_{37-50}) and their Trend 1-type microlite-like compositional variations predominantly reflect post-emplacement crystallization of the host lava. In contrast, Phenocryst F of BV2958-4 exhibits a clear reversal zoning: in the chemical profile made through the bifid termination of the crystal, each branch contains a core (An_{54-57}) surrounded by more calcic rims (An_{57-75} , Fig. 9g and h).

In the An versus MgO diagram, the profile analyses plot toward lower An than the equilibrium plagioclases crystallizing in anhydrous conditions (Fig. 9f and h). We calculated the mean MgO content and Ca/Na ratio of the

anhydrous melts supposed to be in equilibrium with the cores of Phenocrysts D, E, and F. They are evolved liquids ($\text{Ca}/\text{Na} \sim 0.8$ and $\text{MgO} \sim 3.6$ wt.%), with compositions comparable to those of the segregation vesicles or the Cleft dacite. Such calculations, together with the observed inverse zoning, suggest that the core of Phenocryst F would have crystallized in a dacitic magma whereas its calcic rims would equilibrate with a more mafic liquid. This interpretation is consistent with the Ni-rich compositions of the subaphyric and evolved host lavas (BV2958-3 and -4), a feature that we previously interpreted as resulting from a mixing event.

In addition, BV2958-3 and -4 present petrologic evidence for H_2O -influenced crystallization. First, they are some of the few WDB samples in which the augite crystals are systematically included in plagioclase phenocrysts. Such textural relationships are usually indicative of H_2O in magma (Landi et al., 2004). Moreover, $f\text{O}_2$ values, determined from BV2958-3 groundmass Fe–Ti oxides, plot slightly above the FMQ buffer (Fig. 4) and are higher than those of common MORBs (Christie et al., 1986; Bezou and Humler, 2005; Lee et al., 2005). High $f\text{O}_2$ values are the expression of oxidized conditions of crystallization, possibly in connection with relatively high H_2O pressures. Such an interpretation is consistent with the high vesicularity (second boiling) observed in BV2958-3.

The combination of petrologic studies of the dike BV2958-2 (plagioclase xenocrysts) and the overlying pillow-lavas BV2958-3 and -4 (plagioclase phenocrysts, equilibration of Fe–Ti oxide pairs) can be used to track the mechanisms operating in the magma chamber during a limited interval of time. Dacitic residual H_2O -rich melts from the mushy zone, a relic of which is the xenolith observed in BV2958-2, either spread to the whole reservoir or are confined to localized areas. Then, they mix with mafic resident magmas. Such a mixing might explain the Ni-rich intermediate lava compositions (ferrobasalts BV2958-3 and -4) together with the inverse zoning of Phenocryst F. The hydration associated with this mixing event was sufficient to delay plagioclase crystallization and increase $f\text{O}_2$ values but not enough to cause An-rich plagioclase crystallization far away from the mushy zone.

7. An open magma chamber model

The geochemical and petrologic study of the dive BV2958 revealed the occurrence of mixing events in a composite magma reservoir. The chemical characteristics of the samples BV2958-3 and -4 (i.e. Ni-rich compositions), indicative of blending, are shared by other samples

from both the Northern Scarp and Parks Plateau, which allows generalizing mixing to all the WDB samples. BV2958-3 and -4 plagioclase compositions have shown that the felsic end-member is probably dacitic. This composition will be represented here by the dacite collected on the Cleft segment (Stakes et al., 2006). The Mg# value of the mafic end-member has to be bracketed between those of (i) the liquid in equilibrium with the analyzed forsteritic olivine Fo_{90} (Mg#=74) and (ii) the intersection of the Ni-Mg# hyperbolic correlation with the line originating from the dacite and bordering downward the Ni-rich compositions (Mg#=66, Fig. 8). Subsequently, linear regressions between Mg# and REE contents (except Sm and Gd, only analyzed in a few samples) have been calculated from 80 fresh, subaphyric, likely cogenetic (variations of La/Nb, Nd/Zr, and La/Yb lesser than 2σ), and Ni-poor lavas from the Northern Scarp. Afterward, these regressions have been used to estimate the REE composition of a mean mafic end-member (Mg#=70). The corresponding calculated pattern shows lower REE concentrations than the Northern Scarp lavas (Fig. 8). The Mg# value of the mafic end-member is close to that of primary MORBs (Kinzel and Grove, 1992; Nielsen et al., 1995), which implies that the corresponding melt has undergone little differentiation subsequently to the replenishment.

Using some Northern Scarp dives through the extrusive unit, further evidence of replenishment is shown by the distribution of Mg# with depth. The interpretation of the Mg# variations with depth might be complicated along the upper part of the scarp. Indeed, the magnetic data (Tivey, 1996) together with the minimal deformation and tilting (Karson et al., 2002) suggest that the uppermost lavas could be emplaced by late flows channeled off-axis. In this case, the contact between the uppermost and underlying lavas represents a time gap (Fig. 10). The closest dives, spaced by less than 3 km, can be considered as sampling equivalent sections of crust as such a distance is in the width range of the axial graben of the Cleft segment (Canales et al., 2005; Stakes et al., 2006). Consequently, these dives will be combined to increase the sampling density and the length of the vertical traverses (Figs. 2 and 10). For each group of selected dives, Mg# is plotted against depth (Fig. 10). The selected dives cover the central part of the Northern Scarp, from 25 to 44.5 km east of the axis. Samples of isotopic group NS2 will not be included in the coming discussion as they are issued from different parental melts.

The Mg# evolution of the previously studied dive BV2958, combined with the dive BN18, is plotted in Fig. 10b. Even if the three other dive groups cross over an oldest crust (Matuyama and Anomaly 2 magnetic

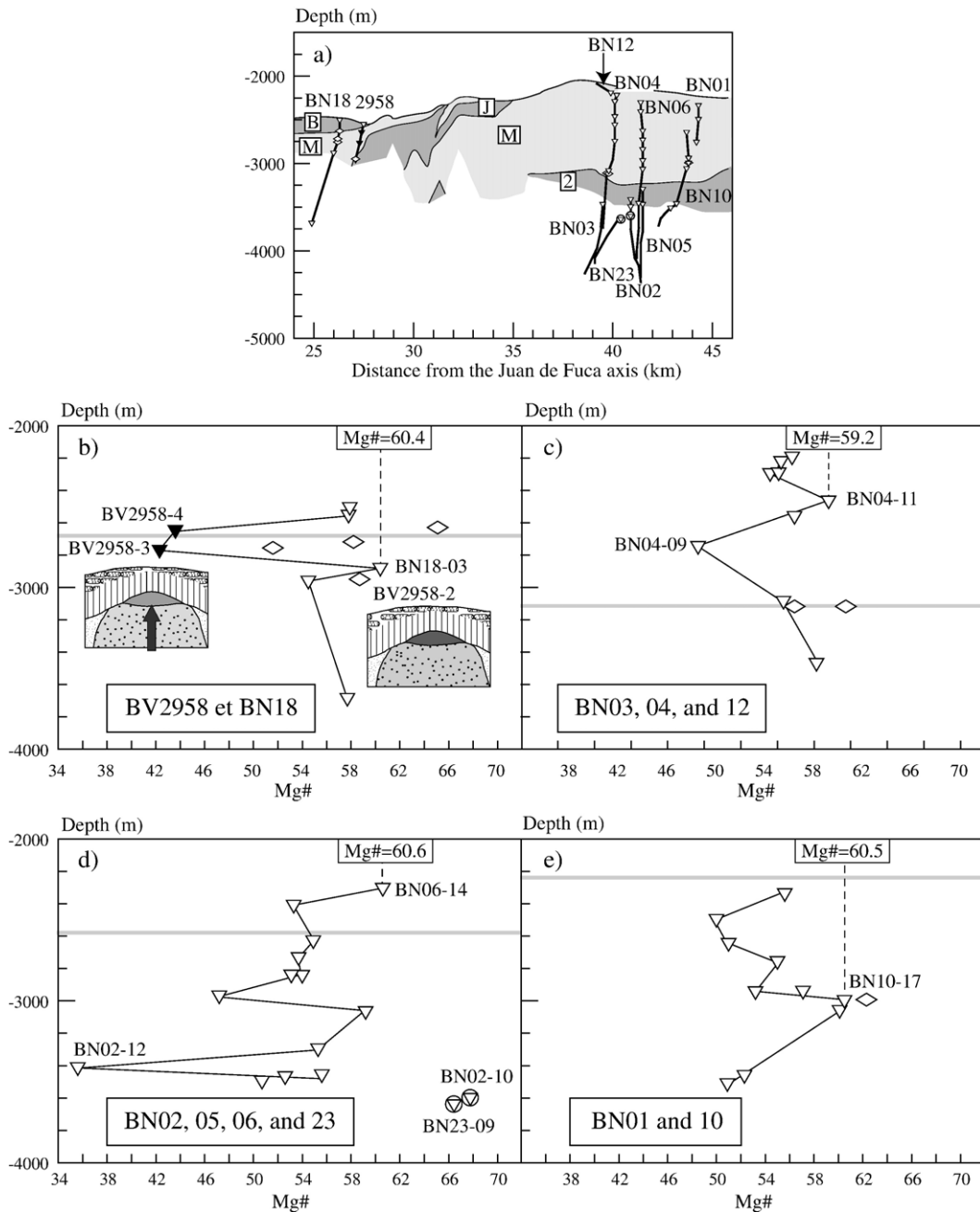


Fig. 10. Evolution of Mg# with depth in extrusive unit for four groups of dives (see text for the selection criteria). a) Position of the selected dives along the Northern Scarp superimposed on the magnetic cross section. b) Dives BV2958 and BN18. Sketches of the proposed model of refilling and mixing are shown (dark gray: mafic magma, light gray: dacitic magma). c) Dives BN03, 04, and 12. d) Dives BN02, 05, 06, and 23. e) Dive BN01 and 10. In each diagram, the unconformity at the base of the uppermost lavas is symbolized by a gray line (Karson et al., 2002) and the name of the key samples and Mg# in the most mafic composition are given. Symbols as in Fig. 5.

periods, Fig. 10a), Mg# varies with depth in a comparable way with, from bottom to top, a change from mafic to intermediate terms followed by a return to mafic compositions. Moreover, the most mafic compositions reached in extrusive samples for each dive are particularly

homogeneous ($58.2 \leq \text{Mg\#} \leq 60.6$ in 8 samples). The most evolved compositions are either ferrobasalts or evolved basalts with Mg# ranging from 47 to 51 (Fig. 10b–e). These similarities suggest that: (i) replenishment is a widespread event; (ii) this event has

governed the magmatic system over a significant period of time; (iii) the replenishment melt composition remained quite constant.

8. Conclusions

As pointed out by Pollock et al. (2005) using the Blancovin dives, the uppermost lavas that possibly flowed several kilometers away from the axis, tend to be among the most primitive observed along a vertical path. Our data have been used to characterize the time evolution of the geochemistry with more details. We have pointed out that the differentiation degree does not decrease continuously with depth but shows a more complex pattern that can be interpreted as the result of periodic replenishment of the magma reservoir beneath the Cleft axis. In our interpretation, ferrobasalts are produced by a mixing process between dacitic and mafic end-members in such an open and long-lived magma system. The evolved compositions probably result from differentiation in the cooler mushy zones, as Stakes et al. (2006) proposed. Such models cast doubt on the interpretation of Juteau et al. (1995), in which ferrobasalts are viewed as products of closed-system differentiation in short-lived magma reservoirs during the progressive transition from propagation to accretion.

Acknowledgements

Microprobe studies were performed with the help of M. Bohn. Detailed and constructive comments by three anonymous reviewers helped us to improve this manuscript. We also thank Dr. Foley for its editorial assistance. Contribution no. 1035 of the IUEM, European Institute for Marine Studies (Brest, France).

Appendix A. Supplementary data

Supplementary data associated with this article can be found, in the online version, at doi:10.1016/j.lithos.2007.06.009.

References

- Andersen, D.J., Lindsley, D.H., 1985. New (and final!) models for the Ti-magnetite/ilmenite geothermometer and oxygen barometer. Abstract AGU 1985 Spring Meeting. Eos Transactions, American Geophysical Union, vol. 66, p. 416.
- Baker, D.R., Eggler, D.H., 1987. Compositions of anhydrous and hydrous melts coexisting with plagioclase, augite, and olivine or low-Ca pyroxene from 1 atm to 8 kbar: application to the Aleutian volcanic center of Akta. *American Mineralogist* 72, 12–28.
- Barrat, J.A., Keller, F., Amosse, J., 1996. Determination of rare earth elements in sixteen silicate reference samples by ICP-MS after Tm addition and ion exchange separation. *Geostandards Newsletter* 20, 133–139.
- Berndt, J., Koepke, J., Holtz, F., 2005. An experimental investigation of the influence of water content and oxygen fugacity on differentiation of MORB at 200 MPa. *Journal of Petrology* 46, 135–167.
- Bezos, A., Humler, E., 2005. The $\text{Fe}^{3+}/\Sigma\text{Fe}$ ratio of MORB glasses and their implications for mantle melting. *Geochimica et Cosmochimica Acta* 69, 711–725.
- Byerly, G.R., 1980. The nature of differentiation trends in some volcanic rocks from the Galapagos spreading center. *Journal of Geophysical Research* 85, 3797–3810.
- Canales, J.P., Detrick, R.S., Carbotte, S.M., Kent, G.M., Diebold, J.B., Harding, A.J., Babcock, J.M., Nedimovic, M.R., Van Ark, E., 2005. Upper crustal structure and axial topography at intermediate spreading ridges: seismic constraints from the southern Juan de Fuca ridge. *Journal of Geophysical Research* 110. doi:10.1029/2005JB003630.
- Caroff, M., Lagabrielle, Y., Spadea, P., Auzende, J.-M., 1997. Geochemical modeling of nonsteady-state magma chambers: a case study from an ultrafast spreading ridge, East Pacific Rise, 17–19°S. *Geochimica et Cosmochimica Acta* 61, 4367–4374.
- Chadwick, J., Perfit, M.R., Ridley, W.I., Jonasson, I.R., Kamenov, G., Chadwick, W.W.J., Embley, R.W., Le Roux, P., Smith, M.C., 2005. Magmatic effects of the Cobb hot spot on the Juan de Fuca Ridge. *Journal of Geophysical Research* 110, B03101. doi:10.1029/2003JB002767.
- Christie, D.M., Carmichael, I.S.E., Langmuir, C.H., 1986. Oxidation states of mid-ocean ridge basalt glasses. *Earth and Planetary Science Letters* 79, 397–411.
- Cohen, R.S., Evensen, N.M., Hamilton, P.J., O’Nions, R.K., 1980. U–Pb, Sm–Nd and Rb–Sr systematics of Mid-Ocean Ridge Basalt glasses. *Nature* 283, 149–153.
- Costa, F., Chakraborty, S., Dohmen, R., 2003. Diffusion coupling between trace and major elements and a model for calculation of magma residence times using plagioclase. *Geochimica et Cosmochimica Acta* 67, 2189–2200.
- Cotsonika, L.A., Perfit, M.R., Smith, M.C., Kamenov, G.D., Stakes, D.S., Ridley, W.I., Wallace, P., 2005. The occurrence and origin of andesites and dacites from the Southern Juan de Fuca Ridge. Eos, Transactions, American Geophysical Union. Joint Assembly Supplement, vol. 86, pp. 04–V13A.
- Cotten, J., Le Dez, A., Bau, M., Maury, R.C., Dulski, P., Fourcade, S., Bohn, M., Brousse, R., 1995. Origin of anomalous rare-earth element and yttrium enrichments in subaerially exposed basalts: evidence from French Polynesia. *Chemical Geology* 119, 115–138.
- Cousens, B.L., Allan, J.F., Leybourne, M.I., Chase, R.L., Van Wagoner, N., 1995. Mixing of magmas from enriched and depleted mantle sources in the northeast Pacific: West Valley segment, Juan de Fuca Ridge. *Contributions to Mineralogy and Petrology* 120, 337–357.
- Dauteuil, O., 1995. Fault pattern from Seabeam processing: the western part of the Blanco Fracture Zone (NE Pacific). *Marine Geophysical Researches* 17, 17–35.
- Davis, A.S., Clague, D.A., 1987. Geochemistry, mineralogy, and petrogenesis of basalts from the Gorda ridge. *Journal of Geophysical Research* 92, 10476–10483.
- Davis, A.S., Clague, D.A., White, W.M., 1998. Geochemistry of basalt from Escabana Trough: evidence for sediment contamination. *Journal of Petrology* 39, 841–858.
- Delaney, J.D.E., Spiess, F.N., Colony, W.E., Karsten, J.L., Kelley, D.S., Nehlig, P., 1987. A complete deep-tow swath map of

- south-facing wall of the Blanco Trough, Juan de Fuca region. *Eos, Transactions, American Geophysical Union, Fall Meeting Supplement*, vol. 68, p. 1509.
- Dosso, L., Hanan, B.B., Bougault, H., 1991. Sr–Nd–Pb geochemical morphology between 10°N and 17°N on the Mid-Atlantic Ridge: a new MORB isotope signature. *Earth and Planetary Science Letters* 106, 29–43.
- Dunn, R.A., Toomey, D.R., 2000. Three-dimensional seismic structure and physical properties of the crust and shallow mantle beneath the East Pacific Rise at 9°30'N. *Journal of Geophysical Research* 105, 23537–23555.
- Embley, R.W., Wilson, D.S., 1992. Morphology of the Blanco Transform Fault Zone-NE Pacific: implications for its tectonic evolution. *Marine Geophysical Researches* 14, 25–45.
- Flutelot, C., 1997. Propagation de segments de dorsales océaniques et modélisation pétro-géochimique de l'évolution des réservoirs magmatiques. Ph.D. dissertation. University of Brest, France.
- Gaetani, G.A., DeLong, S.E., Wark, D.A., 1995. Petrogenesis of basalts from the Blanco Trough, northeast Pacific: inferences for off-axis melt generation. *Journal of Geophysical Research* 100, 4197–4214.
- Ginibre, C., Wörner, G., Kronz, A., 2002. Minor- and trace-element zoning in plagioclase: implications for magma chamber processes at Paríacota volcano, northern Chile. *Contributions to Mineralogy and Petrology* 143, 300–315.
- Goldstein, S.J., Murrell, M.T., Janecky, D.R., Delaney, J.R., Clague, D.A., 1991. Geochronology and petrogenesis of MORB from the Juan de Fuca and Gorda ridges by ²³⁸U–²³⁰Th disequilibrium. *Earth and Planetary Science Letters* 107, 25–41.
- Hart, S.R., Davis, K.E., 1978. Nickel partitioning between olivine and silicate melt. *Earth and Planetary Science Letters* 40, 203–219.
- Hattori, K., Sato, H., 1996. Magma evolution recorded in plagioclase zoning in 1991 Pinatubo eruption products. *American Mineralogist* 81, 982–994.
- Hegner, E., Tatsumoto, M., 1987. Pb, Sr, and Nd isotopes in basalts and sulfides from the Juan de Fuca ridge. *Journal of Geophysical Research* 92, 11380–11386.
- Ito, E., White, W.M., Goepel, C., 1987. The O, Sr–Nd, and Pb isotope geochemistry of Mid-Ocean Ridge Basalts. *Chemical Geology* 62, 157–176.
- Juteau, T., Bideau, D., Dauteuil, O., Manac'h, G., Naidoo, D.D., Nehlig, P., Ondreas, H., Tivey, M.A., Whipple, K.X., Delaney, J.R., 1995. A submersible study in the Western Blanco Fracture Zone, N.E. Pacific: structure and evolution during the last 1.6 Ma. *Marine Geophysical Researches* 17, 399–430.
- Karson, J.A., Maurice, A.T., Delaney, J.R., 2002. Internal structure of uppermost oceanic crust along the Western Blanco Transform Scarp: implications for subaxial accretion and deformation at the Juan de Fuca Ridge. *Journal of Geophysical Research* 107. doi:10.1029/2000JB000051.
- Kinzler, R.J., Grove, T.L., 1992. Primary magmas of Mid-Ocean Ridge Basalts 2. Applications. *Journal of Geophysical Research* 97, 6907–6926.
- Kohut, E.J., Nielsen, R.L., 2003. Low-pressure phase equilibria of anhydrous anorthite-bearing mafic magmas. *Geochemistry Geophysics Geosystems* 4, 1057. doi:10.1029/2002GC000451.
- Kuritani, T., 1998. Boundary layer crystallization in a basaltic magma chamber: evidence from Rishiri volcano, northern Japan. *Journal of Petrology* 39, 1619–1640.
- Lagabrielle, Y., Cormier, M.-H., 1999. Formation of large summit troughs along the East Pacific Rise as collapse calderas: an evolutionary model. *Journal of Geophysical Research* 104, 12971–12988.
- Landi, P., Métrich, N., Bertagnini, A., Rosi, M., 2004. Dynamics of magma mixing and degassing recorded in plagioclase at Stromboli (Aeolian Archipelago, Italy). *Contributions to Mineralogy and Petrology* 147, 213–227.
- Le Bas, M.J., Le Maitre, R.W., Streckeisen, A., Zanettin, B., 1986. A chemical classification of volcanic rocks based on the total alkali-silica diagram. *Journal of Petrology* 27, 745–750.
- Lee, C.T.A., Leeman, W.P., Canil, D., Li, Z.-X.A., 2005. Similar V/Sc systematics in MORB and arc basalts: implications for the oxygen fugacities of their mantle source region. *Journal of Petrology* 46, 2313–2336.
- Lepage, L.D., 2003. ILMAT: an Excel worksheet for ilmenite-magnetite geothermometry and geobarometry. *Computers & Geosciences* 29, 673–678.
- Manac'h, G., Lécuyer, C., Juteau, T., 1999. A fluid inclusion and stable isotope study of hydrothermal circulation in a transform zone: Western Blanco Depression, northeast Pacific. *Journal of Geophysical Research* 104. doi:10.1029/1998JB900069.
- Michael, P.J., Chase, R.L., 1987. The influence of primary magma composition, H₂O and pressure on Mid-Ocean Ridge Basalt differentiation. *Contributions to Mineralogy and Petrology* 96, 245–263.
- Middlemost, E.A.K., 1989. Iron oxydation ratios, norms and the classification of volcanic rocks. *Chemical Geology* 77, 19–26.
- Naidoo, D.D., 1998. Accretion of the upper oceanic crust. Ph.D. dissertation. University of Washington, Seattle.
- Nielsen, R.L., Crum, J., Bourgeois, R., Hascall, K., Forsythe, L.M., Fisk, M.R., Christie, D.M., 1995. Melt inclusions in high-An plagioclase from the Gorda Ridge: an example of the local diversity of MORB parent magmas. *Contributions to Mineralogy and Petrology* 122, 34–50.
- Niu, Y., Bideau, D., Hekinian, R., Batiza, R., 2001. Mantle compositional control on the extent of mantle melting, crust production, gravity anomaly, ridge morphology, and ridge segmentation: a case study at the Mid-Atlantic Ridge 33–35°N. *Earth and Planetary Science Letters* 186, 383–399.
- Panjasawatong, Y., Danyushevsky, L.V., Crawford, A.J., Harris, K.L., 1995. An experimental study of the effects of melt composition on plagioclase-melt equilibria at 5 and 10 kbar: implications for the origin of high An plagioclase in arc and MORB magmas. *Contributions to Mineralogy and Petrology* 118, 420–435.
- Pollock, M.A., Klein, E.M., Karson, J.A., Tivey, M.A., 2005. Temporal and spacial variability in the composition of lavas exposed along the Western Blanco Transform Fault. *Geochemistry Geophysics Geosystems* 6. doi:10.1029/2005GC001026.
- Rhodes, J.M., Morgan, C., Liias, R.A., 1990. Geochemistry of Axial Seamount lavas: magmatic relationship between the Cobb hotspot and the Juan de Fuca ridge. *Journal of Geophysical Research* 95, 12713–12733.
- Ridley, W.I., Perfit, M.R., Smith, M.C., Fornari, D.J., 2006. Magmatic processes in developing oceanic crust revealed in a cumulate xenolith collected at the East Pacific Rise, 9°50'N. *Geochemistry Geophysics Geosystems* 7, Q12004. doi:10.1029/2006GC001316.
- Roeder, P.L., Emslie, R.F., 1970. Olivine-liquid equilibria. *Contributions to Mineralogy and Petrology* 29, 275–289.
- Singh, S.C., Kent, G.M., Collier, J.S., Harding, A.J., Orcutt, J.A., 1998. Melt to mush variations in crustal magma properties along the ridge crest at the southern East Pacific Rise. *Nature* 394, 874–878.
- Sinton, J.M., Detrick, R.S., 1992. Mid-ocean ridge magma chambers. *Journal of Geophysical Research* 97, 197–216.
- Sinton, J.M., Wilson, D.S., Christie, D.M., Hey, R.N., Delaney, J.R., 1983. Petrologic consequences of ridge propagation on oceanic

- spreading ridges. *Earth and Planetary Science Letters* 62, 193–207.
- Sinton, J.M., Smaglik, S.M., Mahoney, J.J., Macdonald, K.C., 1991. Magmatic processes at superfast spreading mid-ocean ridges: glass compositional variations along the East Pacific Rise 13°–23°S. *Journal of Geophysical Research* 96, 6133–6155.
- Sisson, T.W., Grove, T.L., 1993. Experimental investigations of the role of H₂O in calc-alkaline differentiation and subduction zone magmatism. *Contributions to Mineralogy and Petrology* 113, 143–166.
- Smith, J.V., Brown, W.L., 1988. Feldspar minerals. 1. Crystal structures, physical, chemical, and microtextural properties. Springer Verlag, Berlin. 828p.
- Smith, M.C., Perfit, M.R., Jonasson, I.R., 1994. Petrology and geochemistry of basalts from the southern Juan de Fuca ridge: controls on the spatial and temporal evolution of mid-ocean ridge basalts. *Journal of Geophysical Research* 99, 4787–4812.
- Smith, S.E., Casey, J.F., Bryan, W.B., Dmitriev, L., Silantyev, S., Magakyan, R., 1998. Geochemistry of basalts from the Hayes Transform region of the Mid-Atlantic ridge. *Journal of Geophysical Research* 103, 5305–5329.
- Stakes, D.S., Perfit, M.R., Tivey, M.A., Caress, D.W., Ramirez, T.M., Maher, N., 2006. The Cleft revealed: geologic, magnetic, and morphologic evidence for construction of upper oceanic crust along the southern Juan de Fuca Ridge. *Geochemistry Geophysics Geosystems* 7. doi:10.1029/2005GC001038.
- Sun, S.S., McDonough, W.F., 1989. Chemical and isotopic systematics of oceanic basalts: implication for mantle composition and processes. In: Saunders, A.D., Norry, M.J. (Eds.), *Magmatism in the Ocean Basins*. Geological Society Special Publication, London, pp. 313–345.
- Tivey, M.A., 1994. Fine-scale magnetic anomaly field over the southern Juan de Fuca ridge: axial magnetization low and implications for crustal structure. *Journal of Geophysical Research* 99, 4833–4855.
- Tivey, M.A., 1996. Vertical magnetic structure of ocean crust determined from near-bottom magnetic field measurements. *Journal of Geophysical Research* 101, 20275–20296.
- Tivey, M.A., Johnson, H.P., Fleutelot, C., Hussenoeder, S.A., Lawrence, R., Waters, C., Wooding, B., 1998. Direct measurement of magnetic reversal polarity boundaries in a cross-section of oceanic crust. *Geophysical Research Letters* 25, 3631–3634.
- Volpe, A.M., Goldstein, S.J., 1993. ²²⁶Ra–²³⁰Th disequilibrium in axial and off-axis mid-ocean ridge basalts. *Geochimica et Cosmochimica Acta* 57, 1233–1241.
- Wendt, J.I., Regelous, M., Niu, Y., Hékinian, R., Collerson, K.D., 1999. Geochemistry of lavas from the Garrett Transform Fault: insights into mantle heterogeneity beneath the eastern Pacific. *Earth and Planetary Science Letters* 173, 271–284.
- White, W.M., Hofmann, A.W., Puchelt, H., 1987. Isotope geochemistry of Pacific Mid-Ocean Ridge Basalts. *Journal of Geophysical Research* 92, 4881–4893.
- Wilson, D.S., 1992. Focused mantle upwelling beneath mid-ocean ridges: evidence from seamount formation and isostatic compensation of topography. *Earth and Planetary Science Letters* 113, 41–55.
- Wilson, D.S., Hey, R.N., Nishimura, C., 1984. Propagation as a mechanism of reorientation of Juan de Fuca Ridge. *Journal of Geophysical Research* 89, 9215–9225.

Imprégnation magmatique de la lithosphère océanique : Étude microstructurale et géochimique de séries gabbroïques forées à la dorsale Médio-Atlantique

Résumé : Le puits IODP U1309D (Exp. IODP 304-305, 30°N) et le Site ODP 1275 (Leg ODP 209, 15°45'N) ont permis d'échantillonner deux core complexes océaniques de la dorsale Médio-Atlantique. Les roches récupérées sont principalement gabbroïques dont certaines très primitives et riches en olivine (ol >70%). Dans le puits U1309D, les compositions en éléments en trace des poëcloblastes de clinopyroxène et de plagioclase des roches riches en olivine indiquent qu'ils précipitent depuis le même magma dans toutes les lithologies. La composition en éléments en trace des olivines est en déséquilibre avec ces deux minéraux. Les fabriques cristallographiques de l'olivine sont faibles avec une concentration sur [001] inhabituelle, néanmoins compatibles avec une déformation plastique de haute température, avec l'activation du système de glissement (010) [100] communément décrit dans le manteau asthénosphérique. L'étude conjointe des caractéristiques géochimiques et microstructurales de ces roches met en lumière une histoire complexe de cristallisation dans un système ouvert où de larges volumes de magma de type MORB ont percolé et interagi avec le manteau appauvri superficiel. Ces roches riches en olivine représenteraient le résidu ultime de ces réactions liquide-manteau. Au site 1275, la formation des roches les plus évoluées de la série n'apparaît pas liée à l'événement d'imprégnation formant les roches riches en olivine. Ces roches correspondent à des injections tardives de magma qui ont entièrement cristallisé en profondeur sous forme de plutons intrusifs. Les résultats présentés dans ce mémoire sont compatibles avec une formation des core complexes océaniques associée à une activité magmatique relativement importante, et à une cristallisation complète de tout ou partie de ces magmas dans la lithosphère sans contre-partie volcanique en surface.

Mot-clés : Troctolite, gabbro, olivine, manteau, croûte, imprégnation magmatique, HR-LA-ICPMS, éléments en trace, orientations préférentielles cristallographiques, EBSD, core complexe océanique, dorsale Médio-Atlantique, Integrated Ocean Drilling Program.

Magmatic impregnation of oceanic lithosphere: Microstructural and geochemical study of gabbroic sequences drilled at Mid-Atlantic Ridge

Abstract : IODP Hole U1309D (IODP Exp. 304-305, 30°N) and ODP Site 1275 (ODP Leg 209, 15°45'N) sampled two oceanic core complexes, at the Mid-Atlantic Ridge. The recovered rocks are mostly gabbroic with some very primitive and olivine rich (Ol>70%). In Hole U1309D, trace element compositions of clinopyroxene and plagioclase poikiloblasts from olivine-rich rocks indicate that they crystallized from the same melt in all lithologies. Olivine trace element compositions are in disequilibrium with the two other minerals. Olivine crystallographic preferred orientations are weak, with a relatively strong uncommon [001] concentration but consistent with deformation by dislocation creep with activation of the high-temperature (010) [100] slip system, commonly described in asthenospheric mantle. The joint study of geochemical processes and microstructures in these rocks suggest a complex crystallization history in an open system with percolation of large volume of MORB-type melt and interaction with the depleted shallow mantle. Olivine-rich rocks are interpreted as the ultimate residue of these melt-mantle reaction processes. At Site 1275, the formation of the more evolved rocks of the gabbroic series is not related to the impregnation event creating olivine-rich rocks. These rocks represent late magmatic injections, which are completely crystallized at depth as intrusive gabbroic bodies. The results presented in this thesis are consistent with the formation of oceanic core complexes associated with relatively strong magmatic activity, and with the crystallization of most of melt in the lithosphere without basaltic counterpart erupted on the seafloor.

Keywords: troctolite; gabbro; olivine; mantle; crust; melt impregnation; trace elements; HR-LA-ICPMS; crystallographic preferred orientations; EBSD, oceanic core complex; Mid-Atlantic Ridge; Integrated Ocean Drilling Program

Discipline : Structure et évolution de la Terre et des autres planètes

Laboratoire : Géosciences Montpellier, UMR 5243, université Montpellier 2, CC 60, 34095 Montpellier Cedex 5, France